Feature Papers of Drones
Volume II

Edited by
Diego González-Aguilera and Pablo Rodríguez-Gonzálvez

Printed Edition of the Topical Collection Published in *Drones*

MDPI

Feature Papers of Drones-Volume II

Feature Papers of Drones-Volume II

Editors

Diego González-Aguilera
Pablo Rodríguez-Gonzálvez

MDPI

Editors

Diego González-Aguilera
University of Salamanca
Spain

Pablo Rodríguez-Gonzálvez
University of León
Spain

This is a reprint of articles from the Topical Collection published online in the open access journal *Drones* (ISSN 2504-446X) (available at: https://www.mdpi.com/journal/drones/topical_collections/FP_Drones).

For citation purposes, cite each article independently as indicated on the article page online and as indicated below:

LastName, A.A.; LastName, B.B.; LastName, C.C. Article Title. *Journal Name* **Year**, *Volume Number*, Page Range.

Contents

Preface to "Feature Papers of Drones-Volume II"

The present book is divided into two volumes (Volume I: articles 1–23, and Volume II: articles 24–54) which compile the articles and communications submitted to the Topical Collection "Feature Papers of Drones" during the years 2020 to 2022 describing novel or new cutting-edge designs, developments, and/or applications of unmanned vehicles (drones).

Articles 1–8 are devoted to the developments of drone design, where new concepts and modeling strategies as well as effective designs that improve drone stability and autonomy are introduced.

Articles 9–16 focus on the communication aspects of drones as effective strategies for smooth deployment and efficient functioning are required. Therefore, several developments that aim to optimize performance and security are presented. In this regard, one of the most directly related topics is drone swarms, not only in terms of communication but also human-swarm interaction and their applications for science missions, surveillance, and disaster rescue operations.

To conclude with the volume I related to drone improvements, articles 17–23 discusses the advancements associated with autonomous navigation, obstacle avoidance, and enhanced flight planning.

Articles 24–41 are focused on drone applications, but emphasize two types: firstly, those related to agriculture and forestry (articles 24–35) where the number of applications of drones dominates all other possible applications. These articles review the latest research and future directions for precision agriculture, vegetation monitoring, change monitoring, forestry management, and forest fires. Secondly, articles 36–41 addresses the water and marine application of drones for ecological and conservation-related applications with emphasis on the monitoring of water resources and habitat monitoring.

Finally, articles 42–54 looks at just a few of the huge variety of potential applications of civil drones from different points of view, including the following: the social acceptance of drone operations in urban areas or their influential factors; 3D reconstruction applications; sensor technologies to either improve the performance of existing applications or to open up new working areas; and machine and deep learning developments.

Diego González-Aguilera and Pablo Rodríguez-Gonzálvez
Editors

Article

Pasture Productivity Assessment under Mob Grazing and Fertility Management Using Satellite and UAS Imagery

Worasit Sangjan [1], Lynne A. Carpenter-Boggs [2], Tipton D. Hudson [3] and Sindhuja Sankaran [1,*

[1] Department of Biological Systems Engineering, Washington State University, Pullman, WA 99164, USA
[2] Department of Crop and Soil Sciences, Washington State University, Pullman, WA 99164, USA
[3] Department of Animal Science, Washington State University Extension, Kittitas County, Ellensburg, WA 98926, USA
*   Correspondence: sindhuja.sankaran@wsu.edu; Tel.: +1-509-335-8828

Abstract: Pasture management approaches can determine the productivity, sustainability, and ecological balance of livestock production. Sensing techniques potentially provide methods to assess the performance of different grazing practices that are more labor and time efficient than traditional methods (e.g., soil and crop sampling). This study utilized high-resolution satellite and unmanned aerial system (UAS) imagery to evaluate vegetation characteristics of a pasture field location with two grazing densities (low and high, applied in the years 2015–2019) and four fertility treatments (control, manure, mineral, and compost tea, applied annually in the years 2015–2019). The pasture productivity was assessed through satellite imagery annually from the years 2017 to 2019. The relation and variation within and between the years were evaluated using vegetation indices extracted from satellite and UAS imagery. The data from the two sensing systems (satellite and UAS) demonstrated that grazing density showed a significant effect ($p < 0.05$) on pasture crop status in 2019. Furthermore, the mean vegetation index data extracted from satellite and UAS imagery (2019) had a high correlation ($r \geq 0.78$, $p < 0.001$). These results show the potential of utilizing satellite and UAS imagery for crop productivity assessment applications in small to medium pasture research and management.

Keywords: grazing density; nutrient; pasture management; forage grass; remote sensing

1. Introduction

Pasture management is vital to ensure adequate forage quantity and quality in support of domestic animal production. In addition, several countries have utilized the integration of livestock into cropping systems to contribute to the ecological sustainability of agriculture [1–4]. Domestic livestock is grown in pastures, grasslands, and natural areas; well-managed grazing results in reducing soil erosion from tillage and heavy grazing, improving soil fertility through the application of manure, maintaining ruminants' natural digestive systems, and converting otherwise unusable plant material into more nutritious animal products, such as meat and milk [5–7].

Livestock grazing over a large area requires dynamic decision-making to appropriately allocate pasture forage for animals; this must consider pasture growth's spatial and temporal variation associated mainly with the weather, soil nutrients, and grazing management [8,9]. Systematic monitoring of plant community and soil health to inform this decision-making in larger grazed areas can be time-consuming and labor-intensive. Moreover, destructive sampling can limit the amount of vegetation available as animal feed. Thus, novel methods and techniques to gather information on the forage quality of paddocks using less labor could improve the management of large swaths of land [10,11].

Remote sensing technologies offer distinctive advantages, providing high spatial and temporal resolutions; these techniques are inexpensive, time-effective, non-destructive, and applicable in areas inaccessible to humans [12–15]. Satellite and unmanned aerial

system (UAS) are the typical platforms used for acquiring remotely-sensed imagery [16,17]. Applications include grassland vegetation mapping and phenomena detection related to crop-livestock research/management, such as yield and biomass at large spatial scales, to optimize process/output efficiency [18,19].

Satellite imagery has been commonly utilized to observe large pastures, such as advanced very high-resolution radiometer–AVHRR [20,21], moderate resolution imaging spectroradiometer–MODIS [22,23], the Landsat fleet [24,25], and Sentinel-2 [26,27]. In addition, synthetic aperture radar (SAR) sensors have also been applied from TerraSAR-X [28,29] and Sentinel-1 sources [30,31]. UAS-mounted cameras/sensors can offer high-resolution spectral data, providing more details to describe the plant/crop status in the field. Nevertheless, the issue of coverage area and the efficiency of resource utilization (personnel, travel) for continuous monitoring restrict the wide usage of UAS applications in rangeland systems [32,33]. In the same way, although the satellite platform can provide medium to high temporal resolution (~1–15 days), the spatial resolution is inadequate to delineate forage performances of small to medium pasture parcels (<1 ha) [34,35]. This research, therefore, aims to expand our understanding of the inter-relationships between these two remote sensing data for productivity evaluation in small to medium-sized pasture paddocks.

In this study, the primary objective was to utilize remotely sensed indices derived from satellite and UAS imagery to assess the biophysical connections/transitions of diverse grazing density and fertility management on a sustainably managed ranch pasture. The specific goals were to (1) examine the effects of two strategies of planned grazing management differing by the density and timing, and four soil fertility treatments on pasture productivity through replicated research, applying related remotely sensed data to investigate the sensitivity/quality of the two sensing platforms for estimating pasture biophysical changes; and (2) to evaluate relationships between digital traits extracted from satellite and UAS data to determine the applicability of different remote sensing platforms in small to medium-sized pasture paddocks for pasture characterization, research, and management.

2. Materials and Methods

2.1. Study Area

The study was established in 2015 in an existing irrigated pasture on a commercial ranch in Cheney, Washington (Figure 1a). The location of the study area (GPS: 47°29′25.2″ N, 117°43′26.6″ W) was on the edge of the semi-arid region leading up to the Selkirk Mountains foothills, and the soil type was gravelly silt loam, with a significant phosphorus deficit. The area has a Mediterranean climate with Köppen's climatic type of Csb; the summers (mid-June to mid-September) are short and warm with an average maximum temperature of 29–30 °C in July, and winters (mid-November to the end of February) are cold with an average minimum temperature of −4.50 °C in December. The wet season is from late October to early June (maximum precipitation in December at about 83.80 mm average and minimum in July at about 12.70 mm average). The weather data during the research period (2015–2020) was acquired from the National Oceanic and Atmospheric Administration (NOAA)–National Centers for Environmental Information (NECI) of the U.S. Department of Commerce (https://www.ncdc.noaa.gov/cag/; accessed on 20 July 2021) is presented in Figure 1b.
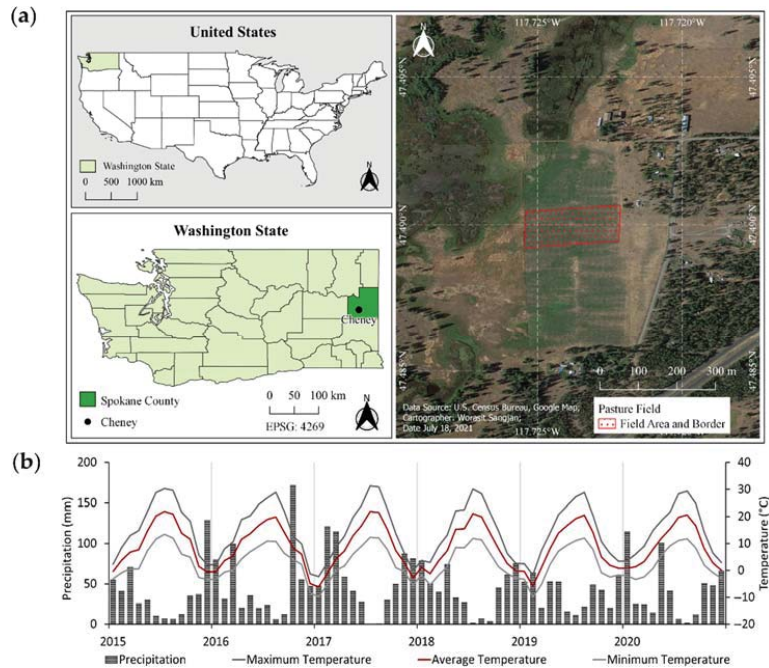
Figure 1. Location and weather data of the study area (**a**) the study location in Cheney, WA, United States, and (**b**) monthly meteorological data of Spokane County in Washington State, US, from January 2015 to December 2020 acquired from NOAA–NECI.

Plant species composition in the study area was evaluated in June 2015 before grazing, which was clearly driven by soil type and moisture. Cheatgrass and drought-tolerant annual forbs dominated with remnant perennial grasses in the drier soil on the eastern side. More mesic soil was found towards the west side (near a wetland) of the study area, where perennial grass and mesic pasture forbs dominated. Dominant species by weight were primarily western wheatgrass, tumble mustard, cheatgrass, and alfalfa.

2.2. Experimental Design and Grazing Methodology

The study area's experimental design was a strip plot consisting of four replicates (four blocks) and eight treatments over 3.24 ha (Figure 2). Cattle grazing was managed using planned rotational grazing at two different stocking densities: (1) low density (LD); and (2) high density (HD), using an approach referred to as "mob grazing" at high stocking densities of livestock for a short period of time (hours or days). At both livestock densities, cattle were moved into a grazing area with the aid of electrical fences, allowed to graze and trample aboveground forage biomass, and removed. The land was then left ungrazed until the following year [36,37]. These two strategies were overlaid with four soil fertility management to address pre-existing phosphorus and sulfur fertility limitations in this irrigated pasture: control (no fertility supplement), one year aged manure (2800 kg dry manure ha^{-1}, supplying 55 kg ha^{-1} N, 22.40 kg ha^{-1} P$_2$O$_5$, 80 kg ha^{-1} K$_2$O, 8 kg ha^{-1} S), organic registered phosphorus and sulfur fertilizers (22.40 kg ha^{-1} S as gypsum and 22.40 kg ha^{-1} P$_2$O$_5$ as bonemeal), and non-aerated compost tea (supplying 5 kg ha^{-1} N, 2 kg ha^{-1} P$_2$O$_5$, 7 kg ha^{-1} K$_2$O). Fertility treatments were applied annually.
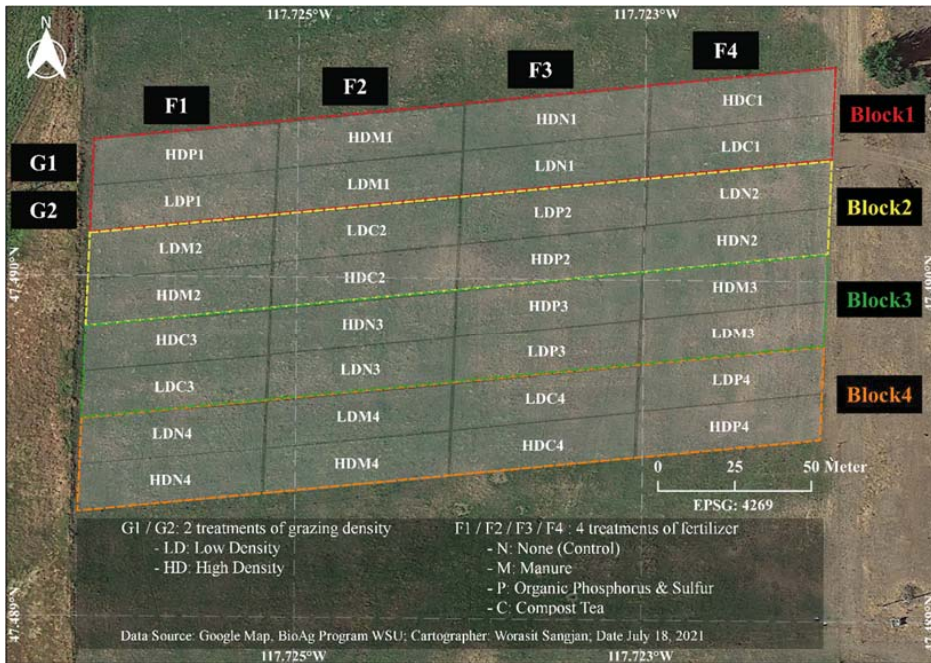
Figure 2. Experimental design of the study area consisted of two different grazing managements: LD—low density and HD—high density with four soil fertility management: N—no fertility supplement (control), M—partially-aged manure, P—organic forms of phosphorus, and sulfur fertilizers, and C—non-aerated compost tea.

The HD grazing was applied once in June or July each year from 2015 to 2019 when the fields were predominantly covered by forage. Each 0.40 ha HD paddock was separated by electric fencing. Grazing duration in HD was in accordance with mob grazing methodology, using a target utilization level as a trigger of timing to move animals to the next strip [38]. The LD grazing represented a seasonal-sustainable grazing rate from June to September each year. Thus, LD removed approximately 40% of available forage, and HD targeted 80–90% forage removal and trampling at each grazing event, monitored by an experienced rancher's visual estimation.

Throughout the study, cattle (400–500 kg mature body weight) were used as forage "harvesters" to a targeted level of forage removal for each grazing density in each paddock. The rancher used 100 to 119 animal units (454 kg equivalent live weight (LW) per animal unit) of cattle in HD. All cattle were applied on one 0.40 ha HD paddock at a time for a stock density of 113,000 to 135,000 kg LW ha^{-1} for 12 h. After all HD paddocks were grazed, two cow-calf pairs or 2.40 animal units grazed all LD paddocks together (1.60 ha), a stock density of approximately 700 kg LW ha^{-1}, for 100 days.

2.3. Image Acquisition

2.3.1. Satellite Imagery

Two remote sensing platforms, satellite, and UAS, were utilized to acquire raw data. Satellite imagery was the PlanetScope Analytic Ortho Scene (Level 3B) provided by Planet Labs Inc. (San Francisco, CA, USA). PlanetScope Dove satellite comprises over 180 CubeSats 3U form factor (10 × 10 × 30 cm) on the constellation having the capability to image all of the Earth's land surface each day. The ground sampling distance of PlanetScope imagery is 3.70 m at a reference altitude of 475 km, and pixel size is 3 m after the orthorectified

process. Ortho scenes are radiometrically-, sensor-, and geometrically-corrected, including atmospherically corrected using the 6S radiative transfer model with ancillary data from the MODIS for surface reflectance 4-band imageries that were utilized in the study (https://www.planet.com/products/planet-imagery/; accessed on 20 July 2021). Images from 2017 to 2019 of cloud-free PlanetScope scenes were acquired on dates before the grazing period and downloaded through the Planet's Education Research Program (https://api.planet.com; accessed on 20 June 2020). The information about its specific attributes and raw image acquisition date are shown in Table 1.

Table 1. Parameters and information for sensors applied in the study.

Parameter/Sensor	PlanetScope (Level 3B)	DJI Phantom 4 Pro	RedEdge
Type	Multispectral	Visible (RGB [1])	Multispectral
Platform	Satellite	UAS	UAS
Spatial resolution	3 m	0.62 cm [2]	3.44 cm [3]
Spectral band (nm)	Blue: 455–515 Green: 500–590 Red: 590–670 NIR: 780–860	Blue, Green, and Red: 390~700	Blue: 475 ± 10 Green: 560 ± 10 Red: 668 ± 5 Red Edge: 717 ± 5 NIR [4]: 840 ± 20
Acquisition date	5 June 2017 8 June 2018 28 May 2019	28 May 2019	28 May 2019

[1] RGB: Red-Green-Blue spectral bands; [2] Raw images were acquired at 25 m UAS flight altitude; [3] Raw images were acquired at 50 m UAS flight altitude; [4] NIR: Near-Infrared.

2.3.2. UAS Imagery

High-resolution UAS imageries were acquired from two quadcopters. DJI-Phantom 4 Pro with an onboard visible camera (DJI Inc., Los Angeles., CA, USA), as described in Table 1, was utilized to collect raw RGB images. Pix4Dcapture (Pix4D S.A., Lausanne, Switzerland) was used for mission planning, such that the images were captured by setting a flight pattern as a single grid with 80% front and 70% side overlap and speed at about 2.50 m s^{-1}. In order to receive good image accuracies, UAS flight altitude was set at 25 m, and images were captured with two missions. The high-resolution RGB imagery was utilized to accurately geolocate/georeference each pasture plot of the multispectral imagery from satellite and UAS sources.

ATI-AgBotTM (Aerial Technology International, Oregon City, OR, USA) mounted with a RedEdge camera (Table 1) (Micasense Inc., Seattle, WA, USA) was employed to capture multispectral images. Similar mission planning with 3 m s^{-1} UAS speed and 50 m flight altitude using Mission Planner software (http://ardupilot.org/planner; accessed on 20 July 2021) was established. Before each flight, 80 × 50 cm boards that could be seen in the resulting UAS orthomosaic images were placed at each ground control point position to assist in georeferencing process. In addition, a 30 × 30 cm white reference panel having 99% reflectance from RGB to NIR spectral range (Spectralon® Diffuse Reflectance Targets, SRS-99-120, Labsphere Inc., North Sutton, NH, USA) was also placed in the field during image acquisition of both UAS missions for radiometric correction.

2.4. Image Pre-Processing

2.4.1. Pre-Processing on Satellite Imagery

Figure 3 summarizes the satellite imagery pre-processing steps performed utilizing an open-source Python 3 (Python Core Team, 2015) program to fully spatially align and precisely evaluate the pixels or areas transforming through time, as provided in [39]. In this process, AROSICS, the open-source image co-registration software for multi-sensor satellite imagery that uses the Fourier shift theorem to perform intensity-based registration and identify sub-pixel shifts [40], was used. All images in the time series were compared

against the first image (reference image), which was the satellite image from 2019, as this image could be georeferenced with the UAS RGB image. Later, the multivariate alteration detection (MAD) algorithm [41] was employed to find invariant pixels between the target (2017 or 2018 satellite image) and the reference image (2019 satellite image) for normalizing the radiometry between the images. The MAD was selected due to its robustness against diverse atmospheric conditions and its appropriateness as a precursor to various normalization techniques.
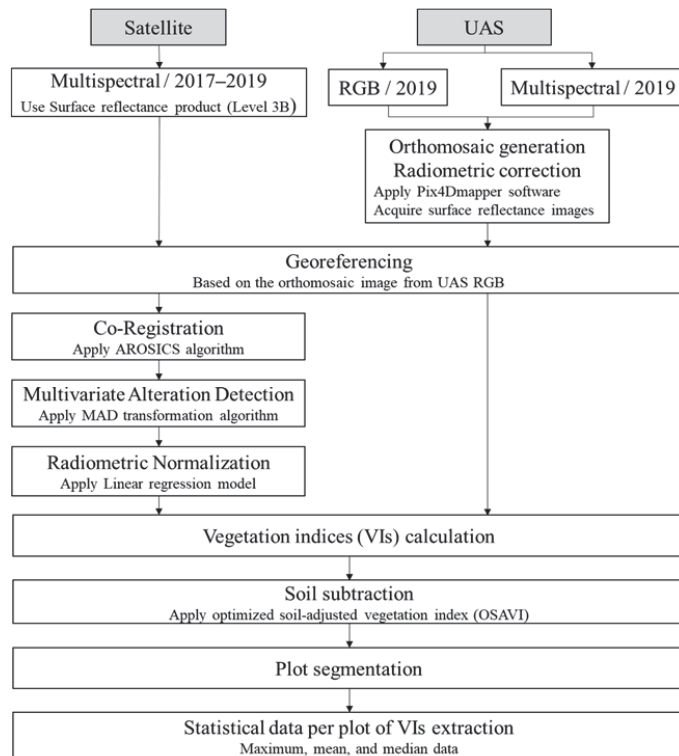
Figure 3. Image processing pipeline used to process both satellite and UAS imagery.

Based on [39,41], the MAD component images at a no-change probability threshold of 95% were set to select the representing invariant features, which were the highest likelihood pixels and their spectral values. This process, combined with a linear regression approach, was used to generate a transformation between the two radiometries of the reference and target images. Moreover, 65% of invariant pixels were used to train the model, and the remaining were for testing purposes. In order to minimize the residuals and compensate for spectral values offset between the two images, both slope and intercept were automatically adjusted through the algorithm. With the linear regression model, the image appearance was preserved and not over-corrected, which simplified the image/result interpretability. Therefore, utilizing the MAD algorithm, the spatial resolution of the images in the series was maintained, and any parameters on the reference image were transformed to the images in series, but the atmospheric or cross-sensor normalization variation was compensated.

2.4.2. Pre-Processing on Satellite Imagery

Raw RGB and multispectral images from UAS platforms were pre-processed (Figure 3), applying the structure-from-motion software Pix4Dmapper (Pix4D S.A., Lau-

sanne, Switzerland) to derive an orthomosaic image of the study area with 0.62 cm and 3.44 cm spatial resolution, respectively. In the process, the software improved the radiometric quality of the images automatically by considering the scene illumination, reference panel, and sensor specifications to create reflectance imagery. The 2019 surface reflectance images from the satellite and UAS platform were rectified to the correct location between different images using the Georeferencer tool in open-source software QGIS (QGIS.org, 2021, version 3.10.4), similar to those described in [42].

2.5. Image Processing

Vegetation indices (VIs) were constructed utilizing the algorithm created in Python 3 using the Rasterio library (https://rasterio.readthedocs.io/en/latest/#; accessed on 20 July 2021). The satellite images after normalization and multispectral surface reflectance images from UAS after georeferencing were used in this method (Figure 3). The VIs, especially those commonly used in agricultural applications with a potential to estimate pasture productivity or aboveground biomass or yield estimation, were derived (Table 2).

Table 2. Summary of vegetation indices that were extracted in the study.

Vegetation Index		Formulation	Ref.
Chlorophyll Index Green	CIgreen	$\frac{NIR}{Green} - 1$	[43]
Enhanced Vegetation Index 2	EVI2	$\frac{2.5 \times (NIR - Red)}{1 + NIR + (2.4 \times Red)}$	[44]
Green Leaf Index	GLI	$\frac{2 \times Green - Red - Blue}{2 \times Green + Red + Blue}$	[45]
Green Normalized Difference Vegetation Index	GNDVI	$\frac{NIR - Green}{NIR + Green}$	[46]
Leaf Area Index	LAI	$3.618 \times EVI\,^1 - 0.118$	[47]
Modified Chlorophyll Absorption Ratio Index 2	MCARI2	$\frac{1.5 \times [(2.5 \times (NIR - Red)) - (1.3 \times (NIR - Green))]}{\sqrt{(2 \times NIR + 1)^2 - (6 \times NIR - 5 \times \sqrt{Red}) - 0.5}}$	[48]
Modified Soil Adjusted Vegetation Index 2	MSAVI2	$\frac{2 \times NIR + 1 - \sqrt{(2 \times NIR + 1)^2 - (8 \times (NIR - Red))}}{2}$	[49]
Normalized Difference Vegetation Index	NDVI	$\frac{NIR - Red}{NIR + Red}$	[50]
Optimized Soil Adjusted Vegetation Index	OSAVI	$\frac{NIR - Red}{NIR + Red + 0.16}$	[51]
Wide Dynamic Range Vegetation Index	WDRVI	$\frac{b \times NIR - Red}{b \times NIR + Red}; b = 0.15$	[52]

[1] EVI: Enhanced Vegetation Index = $2.5 \times \frac{NIR - Red}{NIR + (6 \times Red) - (7.5 \times Blue) + 1}$, ref. [53].

The OSAVI [51] was utilized to estimate a threshold to create a soil mask that was eliminated from each VI image. Then, the polygons defining each pasture study plot were digitized in a *.shp format using QGIS software as it is complex to generate the shapefile using an algorithm because the plots were not of uniform grid pattern (Figure 2). The shapefile of plot segmentation was imported to the created algorithm, and the Python libraries: NumPy (https://numpy.org/; accessed on 20 July 2021) and Rasterstats (https://pythonhosted.org/rasterstats/#; accessed on 20 July 2021) were applied to extract statistical data (maximum, mean, and median) of each VI image from each plot and to export the data in a comma-separated values file format.

2.6. Data Analysis

The effect of grazing density and fertility management on pasture productivity were assessed from all calculated VIs in each year independently and also the comparison between the year of study (2017–2019) using analysis of variance (ANOVA) in R programing language (version 3.2.5, R core Team, 2017). Agricolae (version 1.3-3, ref. [54]) in R was utilized to test the variance in strip-plot design, divided into three parts: horizontal-factor analysis (grazing density), vertical-factor analysis (fertility management), and interaction analysis. Fisher's least significant difference (LSD) test was followed to compute the

significant differences among the mean data (α = 0.05 and adjusting probability value method = Bonferroni). The tests created multiple comparisons of treatments by means of Fisher's LSD and a grouping of treatments. The analysis method described above was applied for the two datasets—first, the original dataset, the originally extracted VI data from all treatments. Second, the normalized dataset was the original VI data normalizing based on VI data from a no fertility supplement (control) paddock in each block of the study area to minimize the influence of different meteorological conditions each year on the crop growth and development and thus the investigated VI data. Furthermore, the linear relationship of extracted VIs between satellite and UAS imagery was evaluated using Pearson's correlation analysis.

3. Results

3.1. Pasture Productivity over Time

Satellite and UAS data were acquired before grazing to study the effect of applied treatments on the plots. Figure 4 displayed some of the spatial variability (satellite and UAS) of vegetation indices such as NDVI, EVI2, and MCARI2, representing the pasture productivity from the years 2017–2019. The plot segmentation layer presented the pattern of the pasture productivity in different blocks of treatments changed over the study period. Moreover, the range of VI data from satellite and UAS images was dissimilar, which could be because of the difference in spectral bands, as described in Table 1; however, the patterns of VI spatial distributions were similar.

The digital traits generated for each image demonstrated the highest data values for areas where high pasture productivity occurred as a dark green area. The crop productivity differences in the years 2017 and 2018 were low. However, in 2019, especially as observed from EVI2 and MCARI2 from satellite images, revealed a high vegetation probability of over 40–50% in the HD area. In addition, for UAS data, the VIs map also correspondingly distinguished that 40–50% of HD area had high VI values.

A comparative analysis utilizing box-and-whisker plots of the extracted mean statistic of EVI2 and MCARI2 from the satellite dataset (Figure 5) revealed the applied treatment effects, different treatment comparisons, and pasture productivity trends through the studied time period. Figure 5 demonstrated that the treatments involving 2015 and 2016 did not affect the 2017 pasture productivity data as the mean of the EVI2 and MCARI2 from different treatments (grazing density and fertility management) were consistent and showed low variability. Similar results were observed for the year 2018. Nevertheless, the mean values of EVI2 and MCARI2 from the two datasets (original and normalized) in 2019 revealed the difference in mean values between low and high grazing density. Notably, the mean VI values were most different between LD and HD, where organic phosphorus and sulfur fertilizers had been applied.

3.2. Treatment Effects

ANOVA in both the original and normalized datasets indicated that the grazing density significantly affected the digital traits (VIs) extracted from satellite and UAS imagery in 2019 (Figure 6). In contrast, fertility management and the interaction between both treatments were not significant in 2017–2019, as observed using remote sensing data. However, the extracted median of CIgreen value calculated from satellite data showed a significant interaction of both treatments' effects ($p < 0.10$) in the original dataset. In the normalized dataset, especially in UAS data, the fertility management effect was found to be significant from the extracted maximum of GLI ($p < 0.05$) and also in the extracted median of LAI ($p < 0.10$) and MSAVI2 ($p < 0.10$).
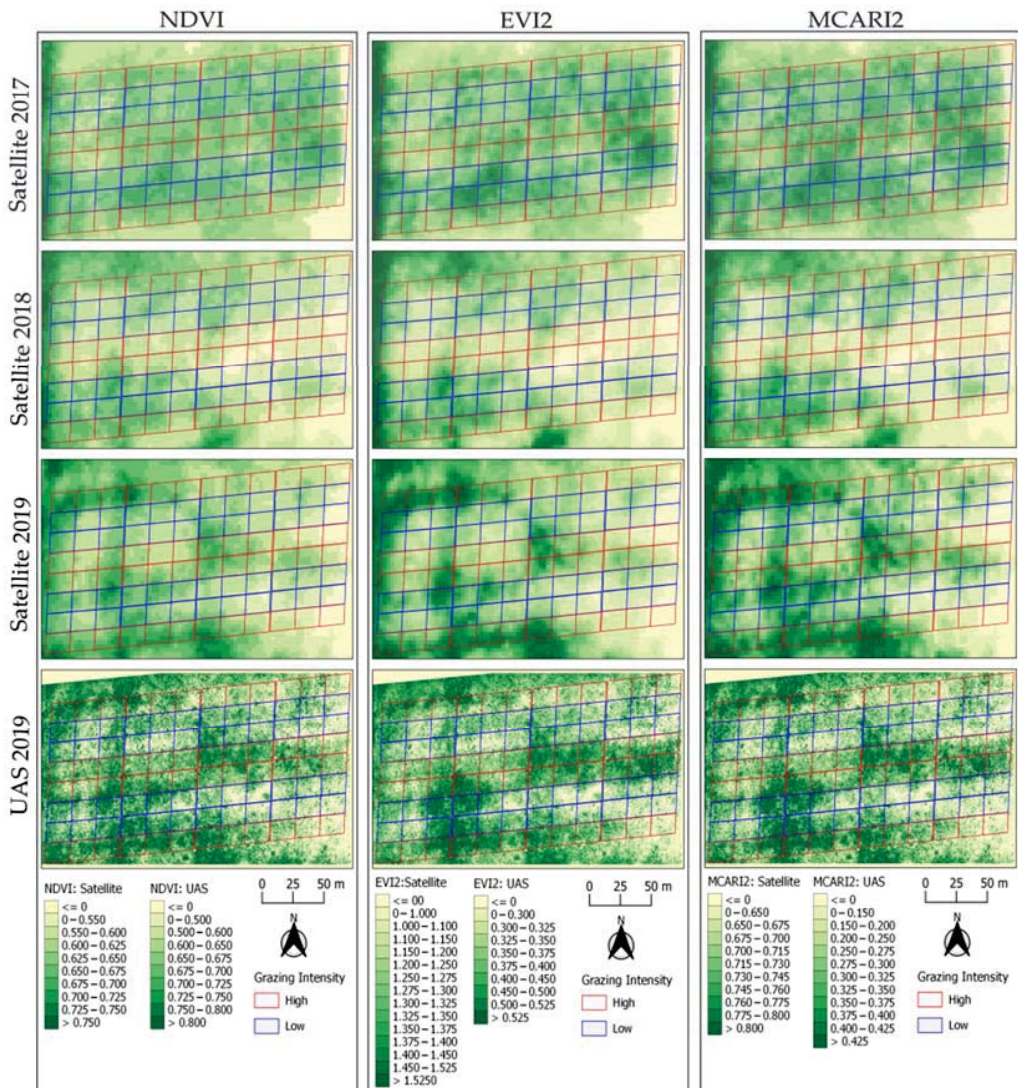
Figure 4. Vegetation index maps of the study area constructed from satellite (2017–2019) and UAS (2019) imagery.

The satellite data results revealed that the different grazing densities affected the VIs values (vegetation characteristics) after four seasons (2015–2018) of applying the treatments. Moreover, all selected VIs from both sensing platforms in 2019 from the original dataset displayed similar results, especially from the extracted mean VI data. The VIs showed the potential for observing differences/effects among treatments (at least $p < 0.10$), excluding GLI from UAS imagery. Correspondingly, the normalized dataset demonstrated the extracted mean and median VI values from the satellite sensing platform, including the extracted maximum (except NDVI and WDRVI) and mean VI values (except CIgreen and WDRVI) from UAS in 2019 could estimate variation in vegetative cover.
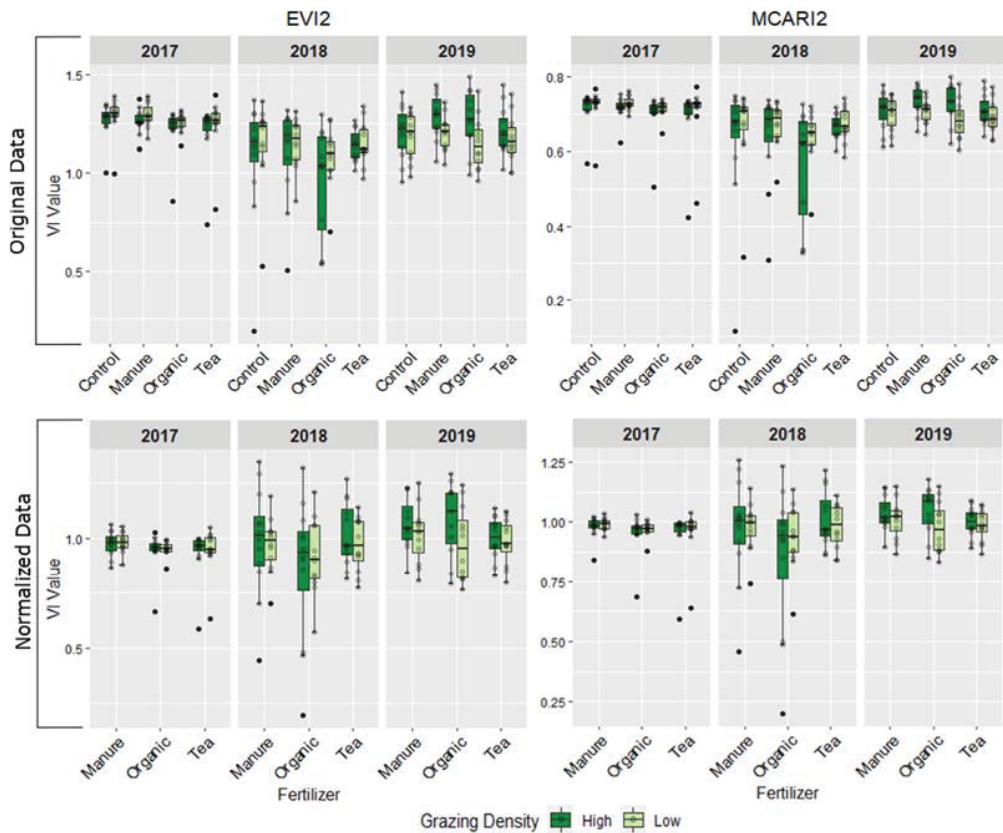
Figure 5. Box-and-whisker plots of extracted mean statistical VI data, EVI2 and MCARI2, created from satellite images from 2017 to 2019 to represent the pasture productivity changing on different grazing intensities and fertility management over the study period between original data and normalized data.

The EVI2, LAI, MCARI2, MSAVI2, and OSAVI extracted from satellite and UAS imagery (original dataset) were consistent in differentiating the grazing density effect. The normalized dataset revealed minor differences, especially using median data from UAS imagery. Nevertheless, EVI2, MSAVI2, and OSAVI showed a consistent and high impact from grazing density than other VI data ($p < 0.05$; excluding the extracted mean VI values from the UAS imagery had $p < 0.10$). EVI2 and MCARI2 data showing the effect of grazing density are shown in Figure 7. The results demonstrated that the mean of HD was significantly different from LD (both sensing platforms and datasets). This comparison indicated that implementing high grazing density could result in high canopy vigor in pasture systems, as observed from the remote sensing data.
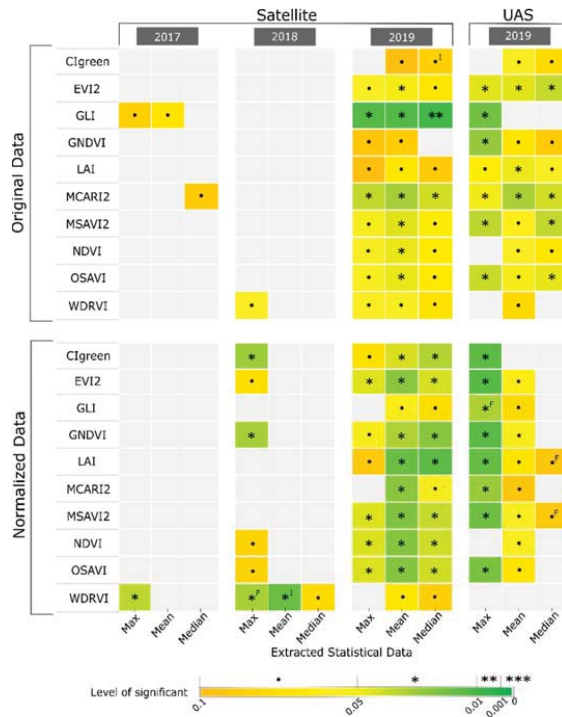
Figure 6. Grazing density effects on VI data extracted from satellite and UAS imagery. F: main effect from fertility management; I: interaction effect from grazing density and fertility management.
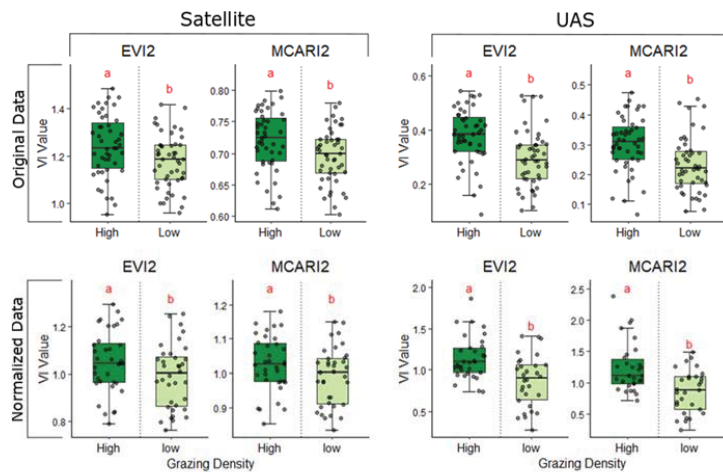
Figure 7. Effects of grazing density on the mean EVI2 and MCARI2 data extracted from satellite and UAS imagery in 2019. Different letters above each bar indicate statistically different means between grazing density treatments ($p < 0.05$, except the normalized data of UAS imagery $p < 0.10$; ANOVA; Fisher's LSD test).

3.3. Correlation between Satellite and UAS Data

The congruence between satellite and UAS imagery for evaluating pasture productivity was investigated on the normalized dataset using mean and median VI values (Figure 8). Pearson correlation coefficients were stable and high ($r \geq 0.75$, $p < 0.001$) between VIs extracted from the two sensing systems, especially CIgreen, MCARI2, and NDVI. Furthermore, the Pearson correlation coefficient of the extracted mean data, except GLI and WDRVI, revealed high correlations ($r \geq 0.78$, $p < 0.001$) between the VIs from satellite and UAS imagery. Given the difference in resolution (3.40 cm for UAS and 3 m for satellite imageries), these findings are encouraging.
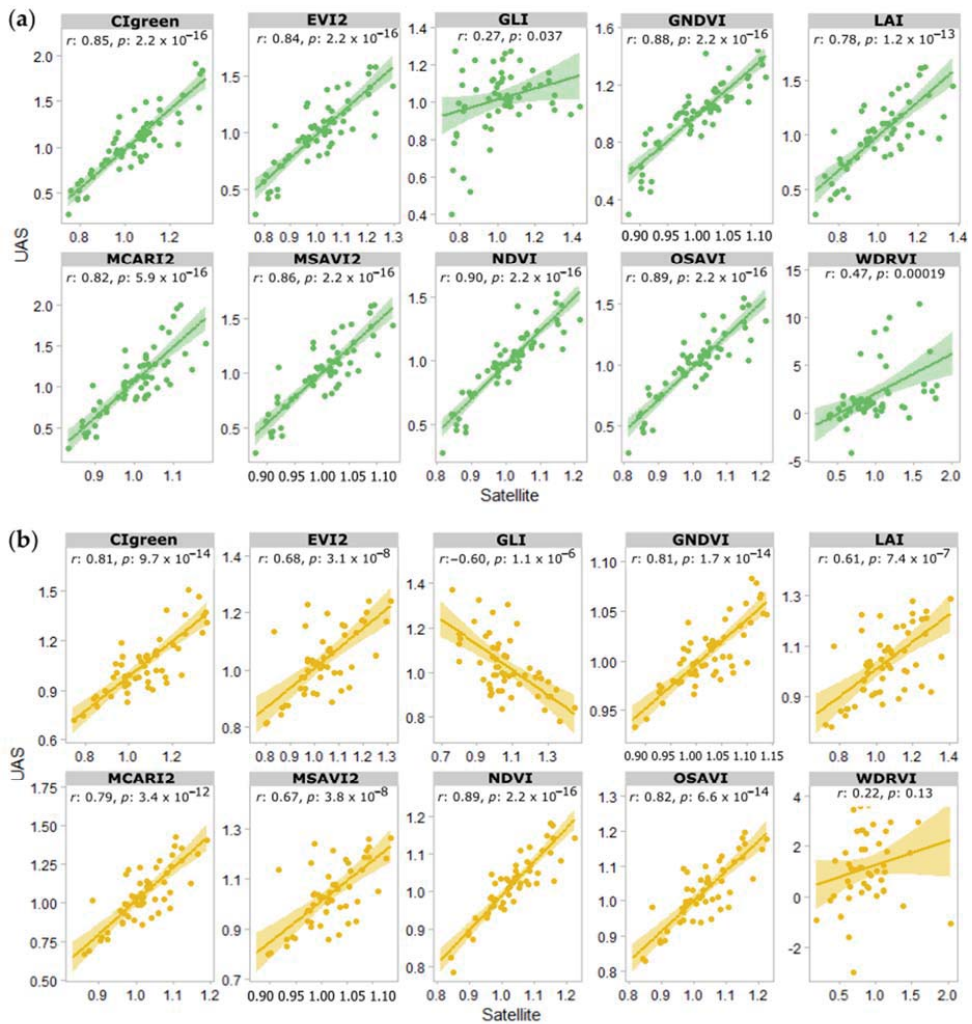
Figure 8. Scatter plots demonstrating the relationship of the extracted VI values from satellite and UAS sensing platforms in 2019 (**a**) mean data and (**b**) median data.

4. Discussion

The results from this study indicate that both the satellite and UAS imagery have the potential to assess pasture productivity (based on applied treatments and/or natural variability). The benefits of utilizing satellite imagery over UAS imagery would be the efficient utilization of resources (no equipment/training required to collect data, saved travel time) while capturing data across a larger region/area. One of the key challenges in this study was identifying the treatment areas across the imagery (especially satellite), where the higher resolution UAS imagery was useful. If satellite imagery were utilized for similar studies, ground control points or checkpoints with accurate GPS information on the boundary are recommended for the accurate positioning of the target plots and more straightforward image processing. Nevertheless, the co-registration and normalization during the pre-processing of the satellite images allowed the consolidation of data for the same location and spectral range across the different years in the study. Similar methods can also be deployed for evaluating the long-term evaluation of pasture health using historical data.

Figure 4 shows the higher spatial image resolution of UAS imagery in comparison to satellite imagery. In general, higher resolution imagery (such as UAS imagery) reduces the mixed pixels in the images (contain more pure pixels), resulting in better discrimination between vegetation and soil. Contrarily, the satellite imagery showed some spectral mixing. The mixing of vegetative and soil pixels with a high concentration of organic matter may influence and increase the vegetation index data [51,55], as observed in Figure 7.

The normalization with respect to control treatment was performed to eliminate the effect of different weather conditions across the years. Nevertheless, the results showed similar patterns as observed from the trends in the original and normalized datasets. The location of different paddocks did influence the vegetation development. The drier soil on the east side and the field entrance for the cattle on the northeast side displayed lower vegetation than the west side, which was closer to the wet area, as presented in Figure 4.

This study demonstrated that the high spatial resolution satellite imagery could be used for small to medium pasture field research/management, as the processed images are able to recognize the variation in vegetation growth or crop status. Furthermore, the product offers daily temporal coverage and a viable cost-affordable option in terms of spatial resolution (3 m pixel resolution), thereby allowing the researchers/farmers to check their crop/plant status over time. However, the satellite imagery used in this study did not have a red-edge spectrum that can be utilized to estimate leaves' chlorophyll content over a canopy [56,57], which may be useful to assess crop stress. More recent images (SuperDove satellites) have 8 spectral bands, including red edge bands.

The two sensing platforms (satellite and UAS) required different image acquisition and processing approaches to get crop information [58,59]. The data acquisition using UAS required travel to the imaging site, planning of the flight mission, and operating the UAS to collect data. The UAS platform can provide high resolution data that can be applied to monitor specific/interested crops and cropping regions, with plausible application of precision agriculture technologies. In contrast, satellite imagery acquisition and operation are more established than the UAS, where the imaging can be tasked through prior arrangement with the satellite imagery providing company. The database of satellite images is also vast, and historical data can be acquired for several agricultural applications, including the study of variability and changes in the cropping areas and overall health, as presented in this study.

Progress in remote sensing technology from both sensors and platforms (satellite and UAS) provides considerable benefits to pasture/grassland science. The production of grassland in terms of spatial and temporal patterns has been evaluated using vegetation indices extracted from the sensing imagery [60–62]. In addition, vegetation indices integrated with ground-truth data have been used to develop empirical models for estimating the productivity/biomass on pastures [63–66]. The most utilized remote sensing data for pasture management for large grassland areas were from satellite sources such as Formosat-2,

Lansat, MODIS, and Sentinel-1. The applications included classification, detection, and analysis of applied management practices such as mowing, grazing, or a combination of the two operations [67–71]. Thus, with the capability of high-resolution satellite imagery (as used in this study), pasture research/management in small to medium areas can be a suitable application.

5. Conclusions

This research paper presents the application of vegetation indices extracted from satellite and UAS imagery for assessing crop status/vigor of a small to medium pasture under different grazing density and fertility management. The major findings can be summarized below.

1. The high-resolution satellite imagery (~3 m pixel^{-1} in this study)—with radiometric calibration and atmospheric correction—can be used to assess overall crop productivity in small to medium-sized pasture paddocks (8–10 ha in this study). The remote sensing data showed an effect of the grazing density on crop productivity (2019), while the effects of the fertility treatments and the interaction between the two treatments were absent.

2. Satellite and UAS-based vegetation indices (mean) showed a similar trend as evaluated using 2019 data.

These results offer great benefits to farmers, ranchers, and researchers alike as pasture management can be investigated and evaluated using sensing data. These tools can be resource-efficient, allowing short and long-term assessment of crop health and productivity.

References

1. Garrett, R.D.; Niles, M.T.; Gil, J.D.; Gaudin, A.; Chaplin-Kramer, R.; Assmann, A.; Assmann, T.S.; Brewer, K.; de Faccio Carvalho, P.C.; Cortner, O.; et al. Social and ecological analysis of commercial integrated crop livestock systems: Current knowledge and remaining uncertainty. *Agric. Syst.* **2017**, *155*, 136–146. [CrossRef]
2. Moraine, M.; Duru, M.; Therond, O. A social-ecological framework for analyzing and designing integrated crop-livestock systems from farm to territory levels. *Renew. Agric. Food Syst.* **2017**, *32*, 43–56. [CrossRef]
3. Poffenbarger, H.; Artz, G.; Dahlke, G.; Edwards, W.; Hanna, M.; Russell, J.; Sellers, M.; Liebman, M. An economic analysis of integrated crop-livestock systems in Iowa, USA. *Agric. Syst.* **2017**, *157*, 51–69. [CrossRef]
4. Cortner, O.; Garrett, R.D.; Valentim, J.F.; Ferreira, J.; Niles, M.T.; Reis, J.; Gil, J. Perceptions of integrated crop-livestock systems for sustainable intensification in the Brazilian Amazon. *Land Use Policy* **2019**, *82*, 841–853. [CrossRef]

5. Alves, B.J.; Madari, B.E.; Boddey, R.M. Integrated crop–livestock–forestry systems: Prospects for a sustainable agricultural intensification. *Nutr. Cycl. Agroecosystems* **2017**, *108*, 1–4. [CrossRef]
6. Hanrahan, L.; McHugh, N.; Hennessy, T.; Moran, B.; Kearney, R.; Wallace, M.; Shalloo, L. Factors associated with profitability in pasture-based systems of milk production. *J. Dairy Sci.* **2018**, *101*, 5474–5485. [CrossRef]
7. de Souza Filho, W.; de Albuquerque Nunes, P.A.; Barro, R.S.; Kunrath, T.R.; de Almeida, G.M.; Genro, T.C.M.; Bayer, C.; de Faccio Carvalho, P.C. Mitigation of enteric methane emissions through pasture management in integrated crop-livestock systems: Trade-offs between animal performance and environmental impacts. *J. Clean. Prod.* **2019**, *213*, 968–975. [CrossRef]
8. Andersson, K.; Trotter, M.; Robson, A.; Schneider, D.; Frizell, L.; Saint, A.; Lamb, D.; Blore, C. Estimating pasture biomass with active optical sensors. *Adv. Anim. Biosci.* **2017**, *8*, 754–757. [CrossRef]
9. Breunig, F.M.; Galvão, L.S.; Dalagnol, R.; Dauve, C.E.; Parraga, A.; Santi, A.L.; Flora, D.P.D.; Chen, S. Delineation of management zones in agricultural fields using cover–crop biomass estimates from PlanetScope data. *Int. J. Appl. Earth Obs. Geoinf.* **2020**, *85*, 102004. [CrossRef]
10. Legg, M.; Bradley, S. Ultrasonic proximal sensing of pasture biomass. *Remote Sens.* **2019**, *11*, 2459. [CrossRef]
11. Gargiulo, J.; Clark, C.; Lyons, N.; de Veyrac, G.; Beale, P.; Garcia, S. Spatial and temporal pasture biomass estimation integrating electronic plate meter, Planet CubeSats and Sentinel-2 satellite data. *Remote Sens.* **2020**, *12*, 3222. [CrossRef]
12. Gitelson, A.A.; Vina, A.; Ciganda, V.; Rundquist, D.C.; Arkebauer, T.J. Remote estimation of canopy chlorophyll content in crops. *Geophys. Res. Lett.* **2005**, *32*, L08403. [CrossRef]
13. Sankaran, S.; Khot, L.R.; Espinoza, C.Z.; Jarolmasjed, S.; Sathuvalli, V.R.; Vandemark, G.J.; Miklas, P.N.; Carter, A.H.; Pumphrey, M.O.; Knowles, N.R.; et al. Low-altitude, high-resolution aerial imaging systems for row and field crop phenotyping: A review. *Eur. J. Agron.* **2015**, *70*, 112–123. [CrossRef]
14. Sangjan, W.; Sankaran, S. Phenotyping architecture traits of tree species using remote sensing techniques. *Trans. ASABE* **2021**, *64*, 1611–1624. [CrossRef]
15. Valencia-Ortiz, M.; Sangjan, W.; Selvaraj, M.G.; McGee, R.J.; Sankaran, S. Effect of the solar zenith angles at different latitudes on estimated crop vegetation indices. *Drones* **2021**, *5*, 80. [CrossRef]
16. Zhang, C.; Marzougui, A.; Sankaran, S. High-resolution satellite imagery applications in crop phenotyping: An overview. *Comput. Electron. Agric.* **2020**, *175*, 105584. [CrossRef]
17. Sangjan, W.; McGee, R.J.; Sankaran, S. Optimization of UAV-based imaging and image processing orthomosaic and point cloud approaches for estimating biomass in a forage crop. *Remote Sens.* **2022**, *14*, 2396. [CrossRef]
18. Schellberg, J.; Verbruggen, E. Frontiers and perspectives on research strategies in grassland technology. *Crop Pasture Sci.* **2014**, *65*, 508–523. [CrossRef]
19. Dos Reis, A.A.; Werner, J.P.S.; Silva, B.C.; Figueiredo, G.K.D.A.; Antunes, J.F.G.; Esquerdo, J.C.D.M.; Coutinho, A.C.; Lamparelli, R.A.C.; Rocha, J.V.; Magalhães, P.S.G. Monitoring pasture aboveground biomass and canopy height in an integrated crop–livestock system using textural information from PlanetScope imagery. *Remote Sens.* **2020**, *12*, 2534. [CrossRef]
20. Chen, Y.; Fei, X.; Groisman, P.; Sun, Z.; Zhang, J.; Qin, Z. Contrasting policy shifts influence the pattern of vegetation production and C sequestration over pasture systems: A regional-scale comparison in Temperate Eurasian Steppe. *Agric. Syst.* **2019**, *176*, 102679. [CrossRef]
21. Miao, L.; Sun, Z.; Ren, Y.; Schierhorn, F.; Müller, D. Grassland greening on the Mongolian Plateau despite higher grazing intensity. *Land Degrad. Dev.* **2021**, *32*, 792–802. [CrossRef]
22. Paltsyn, M.Y.; Gibbs, J.P.; Iegorova, L.V.; Mountrakis, G. Estimation and prediction of grassland cover in western Mongolia using MODIS-derived vegetation indices. *Rangel. Ecol. Manag.* **2017**, *70*, 723–729. [CrossRef]
23. Veloso, G.A.; Ferreira, M.E.; Júnior, L.G.F.; da Silva, B.B. Modelling gross primary productivity in tropical savanna pasturelands for livestock intensification in Brazil. *Remote Sens. Appl. Soc. Environ.* **2020**, *17*, 100288. [CrossRef]
24. Wang, J.; Xiao, X.; Bajgain, R.; Starks, P.; Steiner, J.; Doughty, R.B.; Chang, Q. Estimating leaf area index and aboveground biomass of grazing pastures using Sentinel-1, Sentinel-2 and Landsat images. *ISPRS J. Photogramm. Remote Sens.* **2019**, *154*, 189–201. [CrossRef]
25. Fernando, G.; Víctor, C. Pasture Monitoring Applying Normalized Difference Vegetation Index (NDVI) Time Series with Sentinel-2 and Landsat 8 Images, to Improve Milk Production at Santa Mónica Farm, Imbabura, Ecuador. In *Computational Science and Its Applications–ICCSA 2020*; Gervasi, O., Murgante, B., Misra, S., Garau, C., Blečić, I., Taniar, D., Apduhan, B.O., Rocha, A.M.A.C., Tarantino, E., Torre, C.M., et al., Eds.; Springer International Publishing: Cham, Switzerland, 2020; pp. 560–575. [CrossRef]
26. Ara, I.; Harrison, M.T.; Whitehead, J.; Waldner, F.; Bridle, K.; Gilfedder, L.; da Silva, J.M.; Marques, F.; Rawnsley, R. Modelling seasonal pasture growth and botanical composition at the paddock scale with satellite imagery. *Silico Plants* **2021**, *3*, diaa013. [CrossRef]
27. Chen, Y.; Guerschman, J.; Shendryk, Y.; Henry, D.; Harrison, M.T. Estimating pasture biomass using Sentinel-2 imagery and machine learning. *Remote Sens.* **2021**, *13*, 603. [CrossRef]
28. Schuster, C.; Schmidt, T.; Conrad, C.; Kleinschmit, B.; Förster, M. Grassland habitat mapping by intra-annual time series analysis–Comparison of RapidEye and TerraSAR-X satellite data. *Int. J. Appl. Earth Obs. Geoinf.* **2015**, *34*, 25–34. [CrossRef]
29. Roth, A.; Marschalk, U.; Winkler, K.; Schättler, B.; Huber, M.; Georg, I.; Künzer, C.; Dech, S. Ten years of experience with scientific TerraSAR-X data utilization. *Remote Sens.* **2018**, *10*, 1170. [CrossRef]

30. Fauvel, M.; Lopes, M.; Dubo, T.; Rivers-Moore, J.; Frison, P.L.; Gross, N.; Ouin, A. Prediction of plant diversity in grasslands using Sentinel-1 and-2 satellite image time series. *Remote Sens. Environ.* **2020**, *237*, 111536. [CrossRef]
31. De Vroey, M.; Radoux, J.; Defourny, P. Grassland mowing detection using sentinel-1 time series: Potential and limitations. *Remote Sens.* **2021**, *13*, 348. [CrossRef]
32. Gao, R.; Kong, Q.; Wang, H.; Su, Z. Diagnostic feed values of natural grasslands based on multispectral images acquired by small unmanned aerial vehicle. *Rangel. Ecol. Manag.* **2019**, *72*, 916–922. [CrossRef]
33. Insua, J.R.; Utsumi, S.A.; Basso, B. Estimation of spatial and temporal variability of pasture growth and digestibility in grazing rotations coupling unmanned aerial vehicle (UAV) with crop simulation models. *PLoS ONE* **2019**, *14*, e0212773. [CrossRef] [PubMed]
34. Zhou, Y.; Gowda, P.H.; Wagle, P.; Ma, S.; Neel, J.P.; Kakani, V.G.; Steiner, J.L. Climate effects on tallgrass prairie responses to continuous and rotational grazing. *Agronomy* **2019**, *9*, 219. [CrossRef]
35. Reinermann, S.; Asam, S.; Kuenzer, C. Remote sensing of grassland production and management—A review. *Remote Sens.* **2020**, *12*, 1949. [CrossRef]
36. Billman, E.D.; Williamson, J.A.; Soder, K.J.; Andreen, D.M.; Skinner, R.H. Mob and rotational grazing influence pasture biomass, nutritive value, and species composition. *Agron. J.* **2020**, *112*, 2866–2878. [CrossRef]
37. Guretzky, J.A.; Mamo, M.; Schacht, W.H.; Volesky, J.D.; Wingeyer, A.B. Mob grazing increases trampling but not litter deposition on a Nebraska Sandhills subirrigated meadow. *Crop Forage Turfgrass Manag.* **2020**, *6*, e20047. [CrossRef]
38. Green, S.; Brazee, B. *Harvest Efficiency in Prescribed Grazing*; Technical Note No. TN Range No. 73; USDA National Resources Conservation Service: Boise, ID, USA, 2012.
39. Leach, N.; Coops, N.C.; Obrknezev, N. Normalization method for multi-sensor high spatial and temporal resolution satellite imagery with radiometric inconsistencies. *Comput. Electron. Agric.* **2019**, *164*, 104893. [CrossRef]
40. Scheffler, D.; Hollstein, A.; Diedrich, H.; Segl, K.; Hostert, P. AROSICS: An automated and robust open-source image co-registration software for multi-sensor satellite data. *Remote Sens.* **2017**, *9*, 676. [CrossRef]
41. Canty, M.J.; Nielsen, A.A.; Schmidt, M. Automatic radiometric normalization of multitemporal satellite imagery. *Remote Sens. Environ.* **2004**, *91*, 441–451. [CrossRef]
42. Quirós Vargas, J.J.; Zhang, C.; Smitchger, J.A.; McGee, R.J.; Sankaran, S. Phenotyping of plant biomass and performance traits using remote sensing techniques in pea (*Pisum sativum*, L.). *Sensors* **2019**, *19*, 2031. [CrossRef]
43. Gitelson, A.A.; Gritz, Y.; Merzlyak, M.N. Relationships between leaf chlorophyll content and spectral reflectance and algorithms for non-destructive chlorophyll assessment in higher plant leaves. *J. Plant Physiol.* **2003**, *160*, 271–282. [CrossRef] [PubMed]
44. Jiang, Z.; Huete, A.R.; Didan, K.; Miura, T. Development of a two-band enhanced vegetation index without a blue band. *Remote Sens. Environ.* **2008**, *112*, 3833–3845. [CrossRef]
45. Louhaichi, M.; Borman, M.M.; Johnson, D.E. Spatially located platform and aerial photography for documentation of grazing impacts on wheat. *Geocarto Int.* **2001**, *16*, 65–70. [CrossRef]
46. Gitelson, A.A.; Kaufman, Y.J.; Merzlyak, M.N. Use of a green channel in remote sensing of global vegetation from EOS-MODIS. *Remote Sens. Environ.* **1996**, *58*, 289–298. [CrossRef]
47. Boegh, E.; Soegaard, H.; Broge, N.; Hasager, C.B.; Jensen, N.O.; Schelde, K.; Thomsen, A. Airborne multispectral data for quantifying leaf area index, nitrogen concentration, and photosynthetic efficiency in agriculture. *Remote Sens. Environ.* **2002**, *81*, 179–193. [CrossRef]
48. Haboudane, D.; Miller, J.R.; Pattey, E.; Zarco-Tejada, P.J.; Strachan, I.B. Hyperspectral vegetation indices and novel algorithms for predicting green LAI of crop canopies: Modeling and validation in the context of precision agriculture. *Remote Sens. Environ.* **2004**, *90*, 337–352. [CrossRef]
49. Qi, J.; Chehbouni, A.; Huete, A.R.; Kerr, Y.H.; Sorooshian, S. A modified soil adjusted vegetation index. *Remote Sens. Environ.* **1994**, *48*, 119–126. [CrossRef]
50. Rouse, J.W.; Haas, R.H.; Schell, J.A.; Deering, D.W. Monitoring vegetation systems in the Great Plains with ERTS. *NASA Spec. Publ.* **1974**, *351*, 309–317.
51. Rondeaux, G.; Steven, M.; Baret, F. Optimization of soil-adjusted vegetation indices. *Remote Sens. Environ.* **1996**, *55*, 95–107. [CrossRef]
52. Gitelson, A.A. Wide dynamic range vegetation index for remote quantification of biophysical characteristics of vegetation. *J. Plant Physiol.* **2004**, *161*, 165–173. [CrossRef]
53. Huete, A.; Didan, K.; Miura, T.; Rodriguez, E.P.; Gao, X.; Ferreira, L.G. Overview of the radiometric and biophysical performance of the MODIS vegetation indices. *Remote Sens. Environ.* **2002**, *83*, 195–213. [CrossRef]
54. De Mendiburu, F. Agricolae: Statistical Procedures for Agricultural Researc, R Package Version 1.3–3; Comprehensive R Arch. *Network*. 2020. Available online: https://CRAN.R-project.org/package=agricolae (accessed on 18 July 2021).
55. Schowengerdt, R.A. *Remote Sensing: Models and Methods for Image Processing*; Elsevier: Amsterdam, The Netherlands, 2006.
56. Delegido, J.; Verrelst, J.; Meza, C.M.; Rivera, J.P.; Alonso, L.; Moreno, J. A red-edge spectral index for remote sensing estimation of green LAI over agroecosystems. *Eur. J. Agron.* **2013**, *46*, 42–52. [CrossRef]
57. Dong, T.; Liu, J.; Shang, J.; Qian, B.; Ma, B.; Kovacs, J.M.; Walters, D.; Jiao, X.; Geng, X.; Shi, Y. Assessment of red-edge vegetation indices for crop leaf area index estimation. *Remote Sens. Environ.* **2019**, *222*, 133–143. [CrossRef]

58. Matese, A.; Toscano, P.; Di Gennaro, S.F.; Genesio, L.; Vaccari, F.P.; Primicerio, J.; Belli, C.; Zaldei, A.; Bianconi, R.; Gioli, B. Intercomparison of UAV, aircraft and satellite remote sensing platforms for precision viticulture. *Remote Sens.* **2015**, *7*, 2971–2990. [CrossRef]

59. Akumu, C.E.; Amadi, E.O.; Dennis, S. Application of drone and worldview-4 satellite data in mapping and monitoring grazing land cover and pasture quality: Pre-and post-flooding. *Land* **2021**, *10*, 321. [CrossRef]

60. Gao, Q.; Schwartz, M.W.; Zhu, W.; Wan, Y.; Qin, X.; Ma, X.; Liu, S.; Williamson, M.A.; Peters, C.B.; Li, Y. Changes in global grassland productivity during 1982 to 2011 attributable to climatic factors. *Remote Sens.* **2016**, *8*, 384. [CrossRef]

61. Qamer, F.M.; Xi, C.; Abbas, S.; Murthy, M.S.; Ning, W.; Anming, B. An assessment of productivity patterns of grass-dominated rangelands in the Hindu Kush Karakoram region, Pakistan. *Sustainability* **2016**, *8*, 961. [CrossRef]

62. Kath, J.; Le Brocque, A.F.; Reardon-Smith, K.; Apan, A. Remotely sensed agricultural grassland productivity responses to land use and hydro-climatic drivers under extreme drought and rainfall. *Agric. For. Meteorol.* **2019**, *268*, 11–22. [CrossRef]

63. Wylie, B.; Howard, D.; Dahal, D.; Gilmanov, T.; Ji, L.; Zhang, L.; Smith, K. Grassland and cropland net ecosystem production of the US Great Plains: Regression tree model development and comparative analysis. *Remote Sens.* **2016**, *8*, 944. [CrossRef]

64. Magiera, A.; Feilhauer, H.; Waldhardt, R.; Wiesmair, M.; Otte, A. Modelling biomass of mountainous grasslands by including a species composition map. *Ecol. Indic.* **2017**, *78*, 8–18. [CrossRef]

65. Yin, G.; Li, A.; Wu, C.; Wang, J.; Xie, Q.; Zhang, Z.; Nan, X.; Jin, H.; Bian, J.; Lei, G. Seamless upscaling of the field-measured grassland aboveground biomass based on gaussian process regression and gap-filled landsat 8 OLI reflectance. *ISPRS Int. J. Geo-Inf.* **2018**, *7*, 242. [CrossRef]

66. Zeng, N.; Ren, X.; He, H.; Zhang, L.; Zhao, D.; Ge, R.; Li, P.; Niu, Z. Estimating grassland aboveground biomass on the Tibetan Plateau using a random forest algorithm. *Ecol. Indic.* **2019**, *102*, 479–487. [CrossRef]

67. Dusseux, P.; Vertès, F.; Corpetti, T.; Corgne, S.; Hubert-Moy, L. Agricultural practices in grasslands detected by spatial remote sensing. *Environ. Monit. Assess.* **2014**, *186*, 8249–8265. [CrossRef] [PubMed]

68. Tamm, T.; Zalite, K.; Voormansik, K.; Talgre, L. Relating Sentinel-1 interferometric coherence to mowing events on grasslands. *Remote Sens.* **2016**, *8*, 802. [CrossRef]

69. Lopes, M.; Fauvel, M.; Girard, S.; Sheeren, D. Object-based classification of grasslands from high resolution satellite image time series using Gaussian mean map kernels. *Remote Sens.* **2017**, *9*, 688. [CrossRef]

70. John, R.; Chen, J.; Giannico, V.; Park, H.; Xiao, J.; Shirkey, G.; Ouyang, Z.; Shao, C.; Qi, J. Grassland canopy cover and aboveground biomass in Mongolia and Inner Mongolia: Spatiotemporal estimates and controlling factors. *Remote Sens. Environ.* **2018**, *213*, 34–48. [CrossRef]

71. Taravat, A.; Wagner, M.P.; Oppelt, N. Automatic grassland cutting status detection in the context of spatiotemporal Sentinel-1 imagery analysis and artificial neural networks. *Remote Sens.* **2019**, *11*, 711. [CrossRef]

A Review of Unmanned System Technologies with Its Application to Aquaculture Farm Monitoring and Management

Naomi A. Ubina [1,2] and Shyi-Chyi Cheng [1,*]

[1]   Department of Computer Science and Engineering, National Taiwan Ocean University,
      Keelung City 202, Taiwan; 20857002@mail.ntout.edu.tw

[2]   College of Computing Studies, Information and Communication Technology, Isabela State University,
      Cabagan 3328, Isabela, Philippines

*   Correspondence: csc@mail.ntou.edu.tw

Abstract: This paper aims to provide an overview of the capabilities of unmanned systems to monitor and manage aquaculture farms that support precision aquaculture using the Internet of Things. The locations of aquaculture farms are diverse, which is a big challenge on accessibility. For offshore fish cages, there is a difficulty and risk in the continuous monitoring considering the presence of waves, water currents, and other underwater environmental factors. Aquaculture farm management and surveillance operations require collecting data on water quality, water pollutants, water temperature, fish behavior, and current/wave velocity, which requires tremendous labor cost, and effort. Unmanned vehicle technologies provide greater efficiency and accuracy to execute these functions. They are even capable of cage detection and illegal fishing surveillance when equipped with sensors and other technologies. Additionally, to provide a more large-scale scope, this document explores the capacity of unmanned vehicles as a communication gateway to facilitate offshore cages equipped with robust, low-cost sensors capable of underwater and in-air wireless connectivity. The capabilities of existing commercial systems, the Internet of Things, and artificial intelligence combined with drones are also presented to provide a precise aquaculture framework.

Keywords: drone technology; aquaculture; precision aquaculture; aquaculture monitoring; aquaculture drones; internet of things

1. Introduction

Fisheries and aquaculture play an essential role in feeding the growing population and are critical for the livelihood of millions of people in the world. Based on the long-term assessment by the Although the Food and Agriculture Organization (FAO) has assessed the continuous declination of marine fish resources [1], many interventions were made by government institutions, private organizations, and individuals to increase awareness of the importance of the world's fishery resource. Strict implementation of fishing regulations and water environment conservation has increased fishery production and sustainability. Despite these developments and with the expected increasing population of 8.5 billion by 2030, the increase in demand for marine commodities cannot be sustained any longer by wild fish stocks. Aquaculture is involved in farming of fish, shellfish, and other aquatic plants and have been a great help in food security. In the past years, it is the fastest-growing product in the food sector [2] and is emerging as an alternative to commercial fishing [3]. With this trend, the expansion of aquaculture plays a significant role in ensuring food sufficiency, improved nutrition, food availability, affordability, and security.

In 2018, world aquaculture reached 114.5 million tons of production record [1], making this industry marketable and promising. However, with the increasing global population, aquaculture production must also continue to increase to meet the food demand of the growing population. With this significant contribution of the aquaculture industry in alleviating poverty [4–6] and increasing income [5,6], employment [3,7], economic growth [8–10],

reducing hunger for food, and increasing the nutrition of the population [9,11,12], one of the main challenges in aquaculture production is sustainability [13].

1.1. Challenges in Aquaculture Production, Supervision and Management

One of the indicators of the success of an aquaculture venture depends on the correct selection of the aquaculture site. Aquaculture farm types vary from small-scale rural farms to large-scale commercial systems. For choosing a farm location, a good quality water source is a must since surface water such as river, stream, or spring is prone to pollutions. They are also intermittently available since it is affected by weather such as drought or typhoons. Aquaculture farms are in lakes, rivers, reservoirs (extensive aquaculture), coastal lagoons, land-based coastal, in-shore, and offshore areas [14].

Coastal lagoons are shallow estuarine systems; they are productive and highly vulnerable [15]. Aquaculture in coastal lagoons is more heterogeneous in terms of cultivated species, techniques, extent [16], which can lead to reduced water quality, habitat destruction, and biodiversity loss which limits or restricts fish and shellfish farming concessions [17]. Land-based farming is also becoming famous due to less environmental impact on coastal areas and reducing the cost of transportation. Compared with open-water fish farming, monitoring is easy due to accessibility, and quick adjustments can be made to achieve optimal living conditions of aquaculture products [18]. Despite this, land-based coastal aquaculture is more constrained [14], and mass mortalities due to disease spread is fast, and sudden change in water temperature is also apparent.

In-shore farm locations are close to the open fishing grounds with minimal shore currents. However, concerns such as wind and wave protection currents brought by small boat fishers [19] are also evident. Offshore aquaculture farms' locations are in the deep-sea water. Since they are far from the shore, this reduces the negative environmental impact of fish farming. Despite the higher investment requirements for this farm location and some requiring importation of cages and equipment from other countries [14], its utilization offers a great potential to expand the industry in many parts of the world. Currents and greater depths generally increase the assimilation capacity and energy of the offshore environment and offer vast advantages for aquaculture farming. Since offshore cages are far away from the coast, there is an increased cost in terms of management and daily routine operations for farm visits and monitoring [20]. Recent technological innovations in offshore cage systems make it possible for aquaculture operations in the open ocean, and this industry is rapidly increasing in different parts of the world.

Aquaculture production is very costly considering the requirement in terms of human labor and feeds. The big aquaculture farms are located offshore in deep and open ocean waters, allowing them to produce with a large number. Many of the offshore fish cages are submerged in water and they can only be reached by boats and ships. This method limits the accessibility with additional capital costs [21]. Meanwhile, feeds have the highest share during the production period [22]. Farming systems are also diverse in terms of methods, practices, and facilities. The presence of climate change highly affects the quality of aquaculture production (e.g., change in water temperature, water becomes acidic); it has now become a threat to sustainable global fish production [2]. Global food loss and waste are also severe problems and concerns. Proper handling from production, harvest to consumption is also essential to prevent the identified problems and preserve the production quality [1].

Aside from feeding, farming in the grow-out phase involves tasks such as size grading and distribution of fish to maintain acceptable stocking densities, monitoring water quality and fish welfare, net cleaning, and structural maintenance. All these operations are significant to obtain good growth to ensure fish welfare. Attaining profitability and sustainability in production requires a high degree of regularity in all these operations [23].

Offshore aquaculture farms that have large-scale productions require high manual labor and close human interactions to perform monitoring and management. Proper farm management requires regular monitoring, observation, and recording. For example, to

monitor the growth of the fish, the farmer must evaluate the utilization of the feeds utilized and assess the fish growth to optimize stocking, transfer, and harvests. According to FAO, the extent of farm monitoring depends on the educational level and skill of the farmer, the farmer's interest in good management and profit, the size and organization of the aquaculture farm, and the external assistance available to farmers. Commercial farms need a close monitor of fish stocks. Farmers should also be aware of various parameters for growth measurement, production, and survival of aquaculture stocks. In ensuring this achievement, farms visits should be at least once a day to check if water quality is good and if fish are healthy. Close fish monitoring determines growth, the efficiency of feeding, and adjustment of daily feeding ratio to save feed costs. Checking the adequacy of the stocking rate will enable the transfer of larger fish or marketed immediately and if the stock has reached the target weights, production and harvesting schedule can be changed [24].

According to Wang et al. [25], intelligent aquaculture is now moving beyond data toward decision-making. Intelligent aquaculture farms should be capable of carrying out all-around fine control on various elements such as intelligent feeding, water quality control, behavior analysis, biomass estimation, disease diagnosis, equipment working condition, and fault warning. It is significant to collect data from the aquaculture site to monitor and use technologies, such as sensors and unmanned systems to integrate artificial intelligence (AI) for a smarter fish farm. As an example, with feeding management considerations, feed cost has the highest share in the production period [22]. So, there is a need to reduce the cost to maximize the profit by making sure that the fish is not overfed, which is an added cost, or making sure that fish is not underfed, which affects the fish growth and density, thus, affect the production quality. Bait machines help automate the feeding process, but for it to be fully optimized, information is required of the level of fish feeding satiety or hunger. Information such as disturbance on the water surface can be a basis to determine the level of fish hunger or feeding intensity. Such information can be captured by the UAV using its camera sensors and sends the information to the cloud to perform data analysis using AI services such as deep learning techniques to evaluate the fish feeding intensity level. The analysis results will be forwarded to the baiting machine to determine how much food to dispense. If fish feeding intensity is high, the feeding machine continues to give food, and otherwise, when it is none, it will stop giving food [26].

1.2. Aquaculture's Technological Innovation for Precision Farming

With the challenges mentioned for aquaculture production, there is a need to identify and adopt various strategies. To address these previously mentioned issues, technology integration in the past decades has become famous for automating or helping aquaculture farmers monitor and manage their farms for improved aquaculture sustainability. Technological innovations (such as breeding systems, feeds, vaccines) and non-technological innovations (e.g., improved regulatory frameworks, organizational structures, market standards) have enabled the growth of the aquaculture industry. Radical and systemic innovations are necessary to achieve the ecological and social sustainability of aquaculture [27]. Integrating smart fish farming as a new scientific method can optimize and efficiently use available resources. It will also promote sustainable development in aquaculture through deep integration of the Internet of Things (IoT), big data, cloud computing, artificial intelligence, and other modern technologies. A new mode of fishing production is achieved with its real-time data collection, quantitative decision making, intelligent control, precise investment, and personalized service [28]. Various technological innovations are already available to improve aquaculture production and management [29]. The availability of unmanned vehicles equipped with aerial cameras, sensors, and computational capability is very famous for site surveillance [30].

Precision fish farming described by Føre et al. [31] aims to apply control engineering principles in fish production to improve farm monitoring, control, and allow documentation of biological processes. This method makes it possible for commercial aquaculture to transition from a traditional experience-based production method to a knowledge-based

production method using emerging technologies and automated systems that address the challenges of aquaculture monitoring and management. Precision fish farming aims to improve the accuracy, precision, and repeatability of farming operations. The preciseness facilitates more autonomous and continuous biomass/animal monitoring. It also provides higher reliable decision support and reduces dependences from manual labor and subjective assessments to improve worker safety and welfare. Furthermore, O'Donncha and Grant [32] described precision aquaculture as a set of disparate and interconnected sensors deployed to monitor, analyze, interpret, and provide decision support for farm operations. Precision farming in the ocean will help farmers respond to natural fluctuations and impact operations using real-time sensor technologies and will no longer rely on direct human observations and human-centric data acquisition. Thus, artificial intelligence (AI) and IoT connectivity now support farm decision-making.

Unmanned vehicles or aircraft is one of the emerging technologies for various personal, businesses, and governments, particularly in the military field intended for different purposes. Recently, it has become well-utilized in agriculture and aquaculture in managing and monitoring fish due to its availability and affordability [33]. They are capable of reaching remote areas requiring a small amount of time and effort. Users can control the flight or navigation using only a remote control or a mobile application. When UAVs were introduced around the 20th century, their intended function was for military purposes [34–36]. However, in the last few years, drones' capability has prospered and is now capable of accomplishing multiple and simultaneous functions. Such capabilities are aerial photography [37], shipping and delivery [38–40], data collection [41,42], search and rescue operations during disasters or calamities [43], agricultural crop monitoring [44], natural calamity monitoring, and tracking [45]. UAVs were also successfully integrated into marine science and conservation. In the paper of de Lima et al. [46], the authors provided an overview of the application of unoccupied aircraft systems (UAS) to conserve marine science. As part of their study, they used electro-optical RGB cameras for multispectral, thermal infrared, and hyperspectral systems. Their applications of UAS in marine science and conservation include animal morphometrics and individual health, animal population assessment, behavioral ecology, habitat assessment and coastal geomorphology, management, maritime archaeology and infrastructure, pollutants, and physical and biological oceanography. Some of these mentioned applications could also be utilized in the aquaculture environment.

Today, drones have been successful in collecting environmental data and fish behavior at the aquaculture site for monitoring [47]. In the work of Ubina et al. [30], an autonomous drone performs visual surveillance to monitor fish feeding activities, detect nets, moorings, cages, and detect suspicious objects (e.g., people, ships). The drone is capable of flying above the aquaculture site to perform area surveillance and auto-navigate based on the instructions or commands provided. The autonomous drone can understand the position of the target objects through the information provided by the cloud, which makes it more intelligent than the usual drone navigation scheme. It becomes an intelligent flying robot to capture distant objects and valuable data. The drone can also execute a new route based on the path planning generated by the cloud, unlike the non-autonomous drone, which only follows a specific path [30]. Their autonomous capability reduces the need for human interactions; actual site monitoring and inspection activities can be controlled or reduced [23].

The paper is organized as follows: Section 2 is the methodology; Section 3 provides the unmanned vehicle system platforms. Section 4, on the other hand, presents the framework of the aquaculture monitoring management using unmanned vehicles while in Section 5 is the unmanned vehicles capability as communication gateway and IoT device data collector. Section 6 provides how unmanned vehicles are used for site surveillance, Section 7 is for aquaculture farm monitoring and management function, and Section 8 contains the regulations and requirements for unmanned vehicle system operations. Lastly, Section 9 is the challenges and future trends, and Section 10 is the conclusions.

2. Methodology

This paper's purpose is to conduct a review of literature and studies conducted for unmanned systems' applicability to perform aquaculture monitoring and surveillance. The majority of the literature search was made using the Web of Science (WOS) database. Factors considered in the preference of articles include relevance to the related keywords provided for the search and the number of paper citations. There were no restrictions on the date of publication. Figure 1 is the taxonomy used for keyword extraction in the Web of Science database to determine the trend and the number of works involving unmanned vehicle systems for aquaculture. The authors also used Google Scholar, IEEE Xplore and Science Direct to search for related works.
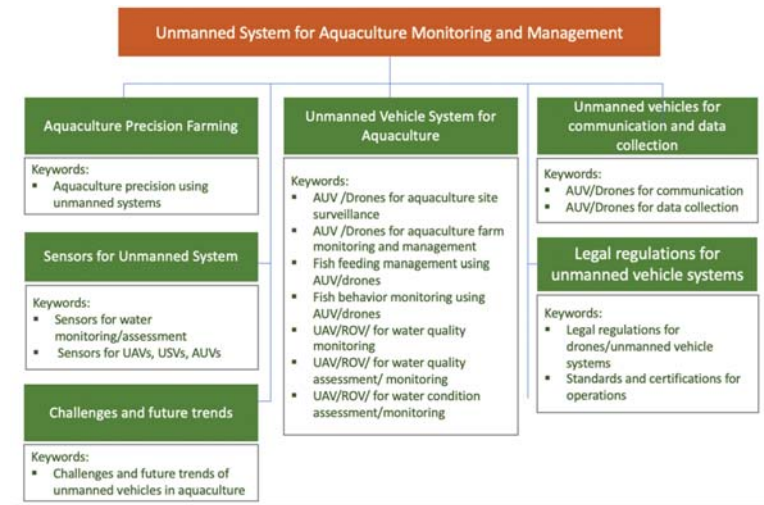
Figure 1. Taxonomy for keyword extraction in the database search.

The articles from the keyword search were the basis in identifying the capabilities, progress, gaps, and challenges of unmanned vehicle systems for aquaculture site monitoring and management. We also conducted data analysis based on the search results from the WOS database to know the trend or research interest based on the number of published journal articles for each year. Graphs were generated to present the result of the analysis. Samples of the results are in Figures 2–4.
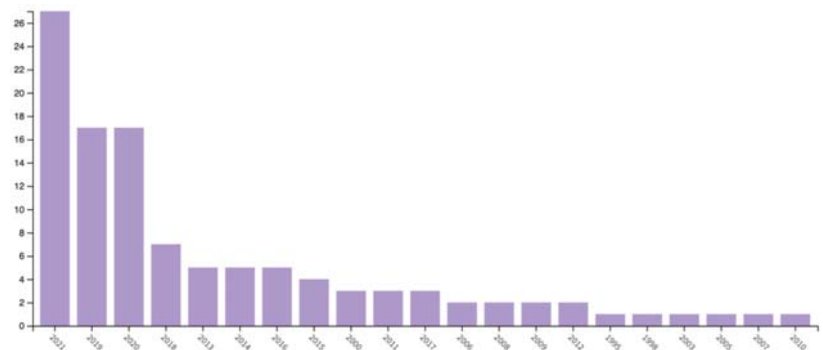
Figure 2. Publication result by year using the keyword aquaculture precision farming.
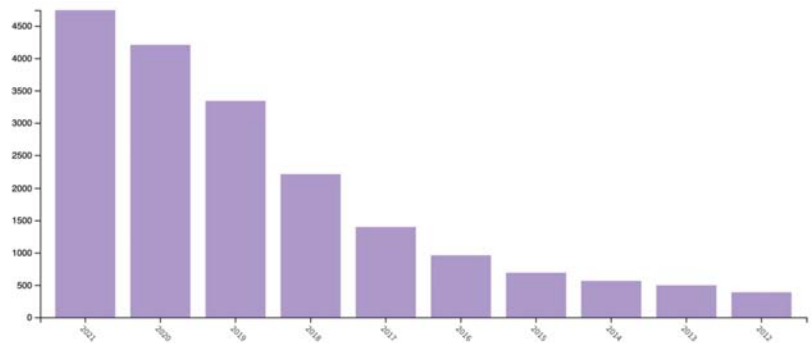
Figure 3. Publication result by year using the keywords "aquaculture precision" and "unmanned vehicle" or "unmanned system".
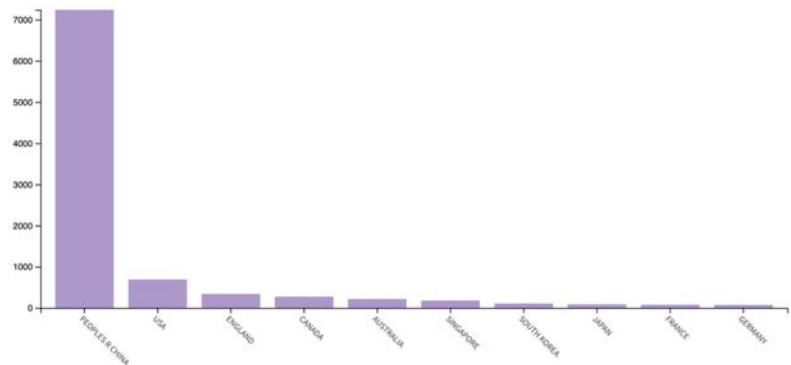
Figure 4. Publication result by country using the keywords "aquaculture" and "unmanned vehicle" or "unmanned system".

3. Unmanned Vehicle System Platforms

Unmanned vehicles can improve mission safety, repeatability and reduce operational costs [48]. The tasks performed by unmanned vehicles are typically dangerous or relatively expensive to use humans to execute. In addition, they are assigned jobs that are simple but repetitive and less expensive to implement without humans [49]. Low-cost, off-the-shelf systems are now emerging, but many still require customization [48] to meet the specific requirement for aquaculture monitoring and management. The work of Verfuss et al. [50] provides the detail of the current state-of-the-art autonomous technologies for marine species observation and detection. Although it does not focus on aquaculture, underlying principles, and requirements can be adopted in aquaculture monitoring.

In this paper, the authors describe the capabilities and limitations of unmanned vehicle systems to perform monitoring and management of aquaculture farms. The functions are to assess water quality, water pollutants, water temperature, fish feeding, water currents, drones as a communication gateway, cage detection, farm management, and surveillance of illegal fishing are content of this review paper as a mechanism to achieve precise aquaculture. There are different classifications of unmanned vehicles considered in this paper for aquaculture monitoring and management: unmanned aircraft systems, autonomous underwater vehicles, and unmanned surface vehicles. Each of the unmanned vehicle systems has its respective capabilities and limitations. However, they can be used together to collaborate and attain the goal of aquaculture monitoring and management. The strength of unmanned vehicles can address the issues or limitations of the other types to increase robustness and efficiency.

3.1. Unmanned Aircraft Systems (UAS)

Unmanned aircraft systems (UAS) or unmanned aerial vehicles (UAVs) provide an alternative platform that addresses the limitations of manned-aerial surveys. According to Jones et al. [51], UAS does not require hundreds of hundreds of dollars to perform surveillance and works best for geospatial accuracy of the acquired data and survey repeatability. A potential advantage of UASs is lower operating costs and consistency of flight path and image acquisition. UAS should be small, with an electric motor, easy to use, affordable, and record and store onboard data to prevent data loss or degradation from the transmission [50]. For real-time monitoring, UAS should send data using its wireless capability. Since they are pilotless aircraft, they can operate in dangerous environments inaccessible to humans [52]. For surveillance and monitoring, they have sensors such as cameras flying into the sky to monitor the target interests [53]. Cameras installed in UAVs can also serve as data collectors and send them into a repository system. Additionally, recent developments in UAS provide longer flight durations and improved mission safety. Although UAS has strong potential for aquaculture monitoring, its success still depends on various factors such as aircraft flight capability, type of sensor, purpose, and regulatory requirements for operations for a specific platform [54].

At the highest level, the three main UAS components are unmanned aerial vehicles, ground control, and the communication data link [55]. Low-cost or multi-rotor drones are easy to control and maneuver with the ability to take off and land vertically. Multirotor UAS has lightweight materials such as plastic, aluminum, or carbon fiber to increase efficiency, and wingspans range from 35 to 150 cm. They can be ideal for small areas and can be controlled from the deck of a small boat [56], but they are limited in terms of flight time and capacity to withstand strong wind conditions. An alternative to multi-rotor drones is single rotor or helicopter drones [57]; they are built for power and durability, with long-lasting flight time with heavy payload capability. However, single rotor drones are harder to fly, and they can be expensive and with more complex requirements.

Fixed-wing drones can travel several kilometers and fly at a high altitude and speeds and cover larger areas for surveillance. They can also carry more payloads, have more endurance which can perform long-term operations. They can be fully autonomous and do not require piloting skills [58]. Like the single rotor drones, fixed-winged drones are expensive and need the training to fly non-autonomous aircrafts. Aside from being difficult to land, they can only move forward, unlike the other two drones that can hover in the target area.

3.2. Autonomous Underwater Vehicles (AUVs)

Autonomous underwater vehicles (AUVs) or remotely operated underwater vehicles (ROV) are waterproof and submersible in the water as they are equipped with cameras to capture images and videos and other sensors to collect data such as water quality. Some of the capabilities of sensors in ROV can perform data collection such as water temperature, depth level, chemical, biological, and physical properties. They are equipped with lithium-ion batteries that enable longer or extended time [59] for navigation or data collection. AUVs are now preferred to use human divers to perform underwater inspections, which is lesser in cost and provides better safety. They can provide a 4D view of the dynamic underwater environment capable of carrying a wide range of payloads or sensors. As the ROV moves to the water, its sensors can perform spatial and time-series measurements [60].

One of the challenges of AUVs since it is submerged underwater is high navigational precision [61], communication, and localization due to the impossibility of relying on radio communications and global positioning systems [62]. There are many devised alternatives in dealing with these challenges. One of them is the integration of geophysical maps to match the sensor measurements known as Geophysical Navigation [63]. In addition, UV navigation that uses a differential-Global Navigation System (DGPs) is with high precision. When submerged in water, its position is estimated by measuring its relative speed over

the current or seabed using an Acoustic Doppler Current Profiler (ADCP). For more precise navigation, an inertial navigation unit is used with positioning from a sonar system [60].

Vehicle endurance is also one of the requirements of AUVs and should be less dependent on weather and water current or pressure. AUVs should be equipped with reliable navigation to perform surveillance functions such as fishnet inspections and fish monitoring. In the paper of Bernalte Sánche et al. [64], the authors presented the summary of navigation and mapping of UAV embedded systems for offshore underwater inspections where sensors and technologies are combined to create a functional system for improved performance. Niu et al. [60] listed in their paper the specifications of candidate sensors embedded in AUVs such as salinity, hydrocarbons, nutrients, and chlorophyll.

3.3. Unmanned Surface Vehicles (USVs)

Unmanned surface vehicles (USVs) or autonomous surface craft [65] operate on the water without human intervention. They were developed to support unmanned operations such as environmental monitoring and data gathering [62]. USVs should be easy to handle and durable in the field environment. USVs can get up close to objects or targets to quickly close to gather high-resolution images. It is also fast-moving, can cover large accurate sensors, and execute run-time missions [66]. However, the autonomy level of USVs is still limited when being deployed to conduct multiple tasks simultaneously [67]. For USV to form immense heterogeneous communication and surveillance networks, they can cooperate with other UVs such as UAVs. One unique potential of USV is to simultaneously communicate with other vehicles located either above or below the water surface areas. USVs can also act as relays between vehicles operating underwater, inland, in air, or in space [68].

Combining various unmanned vehicle systems can maximize their strengths to collaborate and perform more expansive tasks and coverage to address the limitations of each type. In its collaboration, UAVs and USVs can cruise synergically to provide richer information functioning as an electronic patrol system. A USV-UAV collaborative technique can perform tasks such as mapping and payload transportation. In this way, it can handle more complex tasks with increased robustness through redundancy, increased efficiency by task distribution, and reduced cost of operations [66]. These heterogeneous vehicles can work collaboratively to achieve large-scale and comprehensive monitoring. Although there are still many open research issues for heterogeneous vehicle collaboration [69], the possibility of its exploration should increase performance, adaptability, flexibility, and fault tolerance [66].

4. Unmanned Vehicles and Sensors

Unmanned systems' navigation and monitoring capabilities concerning several quantities in their environment strictly depend on their sensors [70], measurement systems, and data processing algorithms. Sensor fault detection is also essential to ensure safety and reliability. UVs have different numbers, types, and combinations of sensors mounted in various ways to measure information using specific, diverse, and customized algorithms. Therefore, finding an optimal sensor that can perform various tasks, applications, and types is an unsolvable problem. Individual sensor specifications and characteristics affect the performance of UV aside from other factors such as operating conditions and environment [71]. One of the primary purposes of the sensor is to collect data relevant to a mission beyond plat-form navigation. Examples of data collected by sensors include acoustic profiles, radar, and infrared signatures, electro-optical images, local ocean depth, and turbidity. Major sensor subtypes are sonar, radar, environmental, and light or optic sensors [72]. Generally, aerial systems rely on electro-optical imaging sensors, while underwater and surface vehicles mostly rely on acoustic methods [48].

UAV's flight position and orientation are determined by combining accelerometers, tilt sensors and, gyroscopes [71]. Aside from GPS, and based on Table 1, USVs can also use radars or inertial navigation systems (INS) if the satellite signal is unavailable. Since UAVs

are vulnerable to weather conditions such as rain or wind, they should be equipped with wind-resistant equipment. Visual cameras can have shockproof and waterproof casings for protection. Extreme wind, rain, or storms can cause UAVs to deviate from intended missions, or small UAVs cannot operate in such weather conditions. UAVs must adapt to atmospheric density and temperature changes to preserve their aerodynamic performance.

Table 1. Navigational payloads characteristics.

Major Subtype	Capability	Design Trade-Off	Challenges or Limitations	Source
Inertial	Data collection from accelerometers and gyroscopes to determine position, orientation, and velocity; measures line accelerations and angular velocities; provides high-frequency time.	Data-processing capability, power inefficient, sensor calibration.	Requires data processing and data fusion from multiple sensors to correct drift errors; accuracy deteriorates along time when operating in stand-alone mode.	[72,73]
GPS	Continuous 3D positioning in the coverage area.	Data rate of communication link, signal frequency	GPS is susceptible to intercept and jamming and is not available in the underwater environment; suffers from numerical errors, atmospheric effect, and multipath errors.	[72,74]
Acoustics	Uses acoustic transponders to determine the position relative to receivers or features (e.g., seafloor); enables accurate and reliable positioning even in low visibility environment; robustness to environmental disturbances.	Sensor geometry	Some sensors require fixed infrastructure and bottom-lock; water presents environmental constraints, and some systems have speed restrictions.; Limited to performing surface navigations.	[72,75,76]
Radar	Combines radar imagery with sea charts to determine the positioning.	Sensor geometry, power inefficiency, and data-processing capability; aircraft size.	Using radar as a navigational tool requires feature-rich environments and is limited to use above water.; Its accuracy decreases as the size of the aircraft decreases.	[72,77]
Depth	Measure of ambient pressure of the water column to calculate depth; insensitive to changes in lighting conditions with 3D information; provides the metric distance; provides low-level stability control and high-level navigation and motion planning.	Sensor configuration; Sensor fusion.	Limitations are minimal. measurement sensors will function at lower depths than projected platforms are intended to go.	[72,78,79]
Orientation	Calculate the heading of the platform using one or several sensors.	Power inefficient	Degraded performance when accelerated.	[72,80]
Light and optics	Uses environmental features or landmarks (e.g., stars, pipeline) to determine position; low cost, high reliability, high accuracy, and real-time performance.	Data-processing capability	Environmental constraints, such as water and fog, limit accuracy.	[72,81,82]

The most common sensor payload is cameras. Although smaller cameras are lighter and easier to deploy, larger cameras provide better image quality. RGB digital cameras provide high-spatial-resolution. The spatial resolution of the RGB sensor determines the quality of the acquired images [71]. The work of Liu et al. [83] provided a detailed discussion of the various sensors shown in Table 2.

Table 2. Characteristics of exteroceptive sensors; adapted from Balestrieri et al., Liu et al. and Qiu et al. [71,83,84].

Characteristics	Type of Sensor							
	Lidar	Radar	Ultrasonic	Monocular Camera	Stereo Camera	Omni-directional Camera	Infrared Camera	Event Camera
Illumination	-	-	-	Yes	Yes	Yes	No	Yes
Weather	Yes	No	-	Yes	Yes	Yes	Yes	Yes
Color and texture	No	No	No	Yes	Yes	Yes	No	No
Depth Information	Yes	Yes	Yes	No	Yes	No	No	No
Area of coverage (m)	<200 m	<200 m	<5 m	Range operational environment dependent	<100 m	Range operational environment dependent	Range operational environment dependent	Range operational environment dependent
Level of accuracy	High	Medium	Low	High	High	High	Low	Low
Size	Large	Small	Small	Small	Medium	Small	Small	Small
Affordability	Low	Medium	High	High	High	High	High	High

One of the challenges to facilitate image and video collection in the underwater environment is data quality, and AUV should be capable of collecting high-definition data for monitoring. Image captures of AUV are affected by the amount of light available in the underwater environment is poor due to the scattering light or turbidity for shallow coastal water [71]. AUVs are not capable of GPS signals; instead, they depend on acoustics, sonar, cameras, INSs, or combinations of such systems to navigate. For sonars, they are highly utilized for detection, tracking, and identification, but it is limited since sound propagation depends on temperature and salinity, and calibration is also required [72].

For unmanned surface vehicles, the water environment is affected by wind, waves, currents, sea fog, and water reflection [85]. There are remedies or solutions to dealing with these environmental disturbances to make the USV more robust. Monocular vision is strongly affected by weather and illumination conditions, which requires a high amount of calculating costs when obtaining high-resolution images [71]. Image stabilization, image defogging, wave information perception, and multi-camera methods are some solutions to deal with the factors affecting image quality due to weather conditions. For stereo vision, its lenses can calculate the flight time to generate a depth map that serves as an obstacle map for near-field collision avoidance. They can also extract color and motion from the environment but can be affected by weather and illumination conditions such as a narrow field of view. Likewise, infrared visons can operate during day and night since they can overcome problems caused by light conditions (night and fog). Omnidirectional cameras can have a large field view but require high computational cost; images from this type of camera are affected by illumination and weather conditions, as well. Infrared cameras also have good quality performance at night but are limited to providing color and texture information, and their accuracy is low. Event cameras are good in reducing the transmission and processing time but generate low-resolution outputs, and like others, it is affected by weather and illumination conditions [85]. Table 3 shows the advantages and limitations of various USV sensors.

Table 3. Advantages and limitations of various sensors for USVs.

Type of Sensor	Advantages	Limitations	Source
Radar	Long detection range; not affected by weather and broad-area imagery; high depth resolution and accuracy.	Skewed data from fast turning maneuvers; limited small and dynamic target detection capability; affected by high waves and water reflectivity.	[71,85]
LIDAR	Performs well for near-range obstacle detection; suitable for spatial classification (position and speed); it can present point cloud data of the surface features with high accuracy and high resolution.	Sensor noise and calibration errors; affected by the weather environment and vehicle movements.	[71,84,85]
Acoustics	No visual restrictions; High depth resolution and accuracy.	Limited detecting range in each scanning; affected by noise from near-surface area; low spatial resolution.	[85,86]
Visual sensor	High lateral and temporal resolution; simple and low weight in practical application.	Low depth resolution and accuracy; challenge to real-time implementation; dependent on light and weather conditions such as rains.	[71,84,85,87]
Infrared sensor	Applicable for dark condition; low power requirement; small size and easy deployment.	Indoor or evening use only; sunlight interference; low accuracy; impressionable to interference and distance.	[71,85]
Inertial Measurement Unit (IMU) Sensors	Small size, low cost, and efficient power consumption; better performance for dynamic orientation calculation.	Sensitive to accumulated error and magnetic environment, or signal noise; regular calibration maintenance.	[85,88]
GPS/Differential GPS	Small size, low acquisition cost, and efficient power consumption.	Susceptible to closed or covered area and magnetic environment; Delays, orbital errors and receiver clock errors.	[85,89]

To determine underwater quality sensors, factors to be considered are physical, chemical, and biological parameters [90]. In the paper of Bhardwaj et al. [91], the authors enumerated the requirements for aquaculture sensors. First, sensors should sense data over long periods without being cleaned, maintained, or replaced. Second, they should have a low energy demand to maximize the energy or power of the UV to perform longer monitoring. Third, sensors require waterproof isolation or the requirement such as avoiding corrosion and biofouling. Fourth, since organisms in the sea can alter the sensor surface and change the transparency and color, the potential flight path must be properly designed. Fifth, sensors should have no harmful effect on the fish. Avoid sensors that use ultraviolet light, acoustic beams that can be felt by the fish, and magnetic fields that can disturb fish activities. In addition, sensors should not alter fish swimming or feeding activities. Sensors must then be low maintenance, low cost, low battery-consuming, robust, waterproof, non-metallic, withstand biofouling, and have no effects on organisms. Modern real-time water quality sensors such as optical and bio-sensors have higher sensitivity, selectivity, and quick response time with the possibility of real-time analysis of data [92].

Although sensor fusion is possible, it could add cost to the operation and UV pay-loads. Its integration will complement the various strengths and capabilities to achieve higher accuracy and increased system robustness. When selecting a sensor, one must consider the cost, specifications, application requirements, power, and environmental conditions.

5. Framework of the Aquaculture Monitoring and Management Using Unmanned Vehicles

The architecture presented in Figure 5 provides a framework on how a drone works with sensors such as underwater cameras and water quality devices. These sensors are installed in the fish cage to collect data through a WIFI communication channel to transmit data to a cloud system. The cloud server serves as a repository and is equipped with data processing and analytics capabilities using AI-based techniques (e.g., computer vision, deep learning). The enormous amount of data collected from the underwater environment using sensors provides a non-invasive and non-intrusive method. This approach can achieve real-time image analysis for aquaculture operators [47]. Different data can be collected from the aquaculture site using these sensors to monitor the behavior of fish and the water quality of the aquaculture farm. The collected data informs the aquaculture farmers and enables them to provide immediate farm interventions to ensure farm produce and processes are optimized and of high quality to help increase production and income. The data collected, such as the level of food satiety of fish, as a specific example, are analyzed and transformed into meaningful information to dispense food from the smart feeding machine. A high level of satiety means continuous dispensing of food, while a low level of satiety means the amount of food dispensed is reduced or stopped. Real-time information with these mechanisms will achieve optimal aquaculture performance.
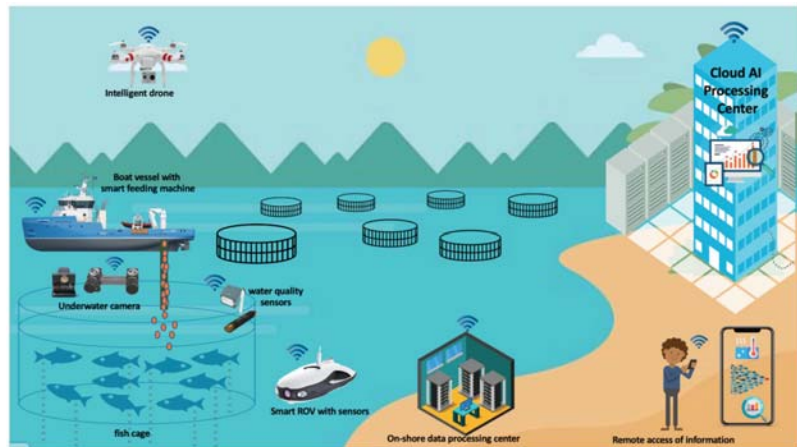
Figure 5. Architecture for aquaculture monitoring and management using drones.

In addition to the ability of the unmanned vehicles to capture or collect data from the aquaculture site, its mobility could be used as a communication channel connecting underwater cameras and sensors to the cloud as a Wi-Fi gateway that provides more services for precise aquaculture. Since the cameras installed in aerial drones have limitations and cannot capture underwater events, fish cages are equipped with stationary cameras (e.g., sonar, stereo camera systems) and other sensors to perform specific tasks. The drone now eliminates long cables for connection with improved reliable connection and communication [30]. Aerial drones work best for functions that involve mapping, site surveillance, inspection, and photogrammetric surveys. AUV and USV, on the other hand, can do other monitoring and assessment functions such as water quality and conditions that cannot be fully addressed by aerial drones. There are additional costs and technical requirements for this method. However, one can take advantage of its more extensive area and scope for monitoring functions.

With this ability, users, such as aquaculture farm owners, can remotely monitor their aquaculture farms and assess fish welfare and stock. With the vast and varied amount of data collection from the aquaculture site, data-driven management of fish production

is now possible. This scheme improves the ability of farmers to monitor, control, and document biological processes on their farms so that they can understand the environmental conditions that affect the welfare and growth of fish [93].

6. Unmanned Vehicles as Communication Gateway and IoT Device Data Collector

In developed countries where access to the Internet is not a problem, the Internet of Things (IoT) is helpful to farmers. This new connectivity help increase production, reduce operating costs, and enhance labor efficiency. The Internet of Things (IoT) has made promising and remarkable progress in collecting data and establishing real-time processing through the cloud using wireless communication channels. With the presence of 5G technology, it is a great advantage to combine UAVs and IoT to extend coverage to rural or remote areas [94], which are the locations of aquaculture farms; thus, it is just appropriate to exploit this capability. The presence of LTE 45/5G networks and mobile edge computing now broadens the coverage of UAVs [95] and is even capable of performing real-time video surveillance [96].

The drone as a flying gateway is equipped with LTE cellular networks to base stations and a lightweight antenna to collect data. UAVs acts as the intermediate node allowing data collection from sensors and transmitting them to their target destinations. The drone then flies to the location of the IoT devices to offer additional coverage or support to the aquaculture farm in case there are problems with the wired connection of the devices. The gateway can receive sensor data and send these collected data to the servers [94] to integrate additional processing strategies, such as artificial intelligence and deep learning techniques. A drone can also serve as a node of the wireless sensor network where IoT communication is not available to receive the collected data from the node. Then it moves to an area where wireless IoT communication is possible and transfers the data to the IoT server [97]. Various sensor devices can connect to aquaculture cages and farms, such as underwater cameras and water quality sensors; Arduino [94] and Raspberry Pi can be embedded as part of an IoT platform, as shown in Figure 6.
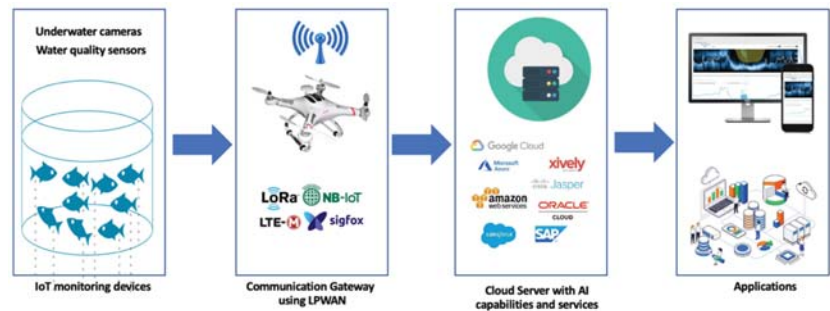
Figure 6. IoT platform using drone as a communication gateway.

In maximizing the drone's capability, it is significant to optimize its energy consumptions. The work of Min et al. [97] proposes a dynamic rendezvous node estimation scheme considering the average drone speed and data collection latency to increase the data collection success rate. Many devices can be embedded on the drone to provide a better wireless communication network. The Lower Power Wide Area Network (LPWAN) gateway onboard can be installed in the UAV. The LoRa gateway is famous for its coverage and lower power consumption in its deployment.

Short-range communication devices are convenient to enable communication between sensors and gateways, such as Bluetooth, ZigBee, and Wi-Fi. However, with drones as a communication gateway, Lower Power Wide Area Network (LPWAN) is much of an advantage to provide extended communication coverage. The different types of LPWAN in Table 4 present their advantages and disadvantages. A comparative study with LP-

WAN technologies for large-scale IoT deployment and smart applications based on IoT is utilized [98,99]. In the work of Yan et al. [100], a comprehensive survey was made on UAV communication channel modeling, taking into account the propagation losses and link fading, including the challenges and open issues for the development of UAV communication.

Table 4. Comparison of LPWAN wireless technologies.

Type of LPWAN Technology	Coverage	Data Rate	Pros	Cons	Source/s
LoRa	Urban: 5 km Rural: 20 km	50 kbps	Wider coverage; Low power consumption; Low cost	Not open standard; No direct connection between devices.	[94,95,101–103]
SigFox	Urban: 10 km Rural: 40 km	100 kbps	Lowest bandwidth; Open standard; Low power consumption; High receiver sensitivity; Widest coverage; Low cost	High latency in communication; Small quantities of data	[101–105]
NB-IoT	Urban: 1 km Rural: 10 km	200 kbps	Low bandwidth; High airtime; Strong signal; low energy consumption; Excellent security	Higher cost as compared to other LPWAN technologies	[101,103]

With this capability of drones as a communication gateway, it can now serve as a medium to help achieve the goal of precise aquaculture. The drone can now provide wireless communication for IoT devices to send data to the cloud for processing, thus acting as a data collection medium. Data acquisition using UAVs is less expensive and more convenient than hiring manned aircraft, especially in remote and inaccessible places such as offshore aquaculture farms. UAVs, when combined with deep learning, can provide tremendous innovation for aquaculture farm management.

With all the identified potentials of drones as a communication channel [106], cameras, and sensors (e.g., stereo camera system, sonar devices) to capture the underwater environment is promising. The drone collects and then sends the data to the cloud to employ AI services using computer vision and deep learning techniques. The processed information provides information to users about the current conditions of the aquaculture farms. Fish survey activities [107] that can be performed includes fish behavior detection such as schooling [108–110], swimming [111–113], stress response [110,114,115], tracking [116,117], and feeding [112,118,119]. To determine the satiety or feeding level of fish used for demand feeder includes fish feeding intensity evaluation [26,120] and detection of uneaten food pellets [120,121]. The video collected from the aquaculture site through the drones can help estimate fish growth [122,123], fish count [124–126], and fish length and density estimation [127–131] as a device to transmit this information to the cloud for processing and data analytics to make predictions or estimates [132,133].

7. Aquaculture Site Surveillance Using Unmanned Vehicles

Illegal fishing is a global problem that threatens the viability of fishing industries and causes profit loss to farmers. On-the-ground surveillance is the typical way to monitor or minimize this practice [134], but with a very high operational cost. Submersible drones and UAVs are now capable of detecting illegal fishing activities [135] and are lower in terms of cost [136,137].

An unmanned system surveillance composed of fish farmers, vessels, and fish stocks was used to detect unauthorized fishing vessels [138] with an advantage in speed and size, making them capable of being unnoticed when performing surveillance. Automatic

ship classification is relevant for maritime surveillance in detecting illegal fishing activities, which immensely affects the income of aquaculture farmers. Gallego [139] uses drones to capture aerial images for the detection and classification of ships. In the work of Marques et al. [140], aerial image sequences acquired by sensors mounted on a UAV detect vessels using sea vessel detection algorithms. A surveillance system framework was proposed using drone aerial images, drone technology, and deep learning [141] to eliminate illegal fishing activities. The ship is detected to identify its position and then classify the hull plate vessels to determine among them are authorized or not. The drone provides visual information using its installed camera. Additionally, crabs are highly valued commercial commodities, and also used drones with infrared cameras to detect crab traps and floats [134,135] to prevent illegal activities.

Remote sensing platforms or technologies with global positioning system capabilities, such as drones, have the ability for marine spatial planning to provide a wide spatial-temporal range for marine and aquaculture surveillance [142]. The drone is also applied to 3D mapping [143], aerial mapping [144], and low-altitude photogrammetric survey [145]. A semantic scene modeling was integrated to manage aquaculture farms using autonomous drones and a cloud-based aquaculture surveillance system as an AIoT platform. The scene modeling algorithm transfers information to the drone using the aquaculture cloud to monitor fish, persons, nets, and feeding levels daily. The drone acts as an intelligent flying robot to manage aquaculture sites [146].

The UAV with an onboard camera was also used for cage detection. The UAV's GPS is a guide to approximate the location of the cages, and applying image recognition methods follows to obtain the fish cage and the relative position of the UAV. This collected information will be the basis of the drone to adjust its position and proceed to the target object [147]. Additionally, UAVs could also be used for cage farming environment inspection [29] without requiring the installation of a hardware system in each cage which entails a higher cost in farming. Even a single UAV system can fly around all fish cages to capture data of the aquaculture cage environment, thus, a drastic reduction of the aquaculture operation cost. An inventory of salmon spawning nests is executed using UAVs to capture high-resolution images and videos to identify spawning locations and habitat characteristics; its abundance and distribution are metrics to monitor and evaluate adult salmon populations [148].

In Japan, they developed an agile ROV to perform underwater surveillance that provides real-time monitoring. The designed ROV is for easy transport, short startup time, effortless control, capable of high-resolution images at a low cost [149]. Drones are also applied to fishery damage assessment of natural hazards. It can survey fish groups, assist in salvage operations, and conduct aquaculture surveys and management after disasters [150]. In India, an autonomous AUV replaced the expensive sonar equipment to perform surveillance and relays the data and the global positioning system location. The drone provides a mechanism to serve as a bird's eye view to monitor the surrounding ocean surface like a person with normal vision can see [151]. Autonomous vehicles are also applied to increase spatial and temporal coverage. They can transit remote target areas with real-time observations with more potential than traditional ship-based surveys. Unmanned surface vehicles with two sail drones (USVs) were equipped with echo sounders to perform acoustic observations [152].

In the work of Livanos et al. [153], an AUV prototype was proposed as an IoT-enabled device. Machine vision techniques were incorporated to enable correct positioning and intelligent navigation in the underwater environment where GPS locations are limited due to its physical limitation to transmit communication signals through wireless networks. The AUV was programmed to record video and scan the fish cage net area and save this information in its onboard memory storage. Its navigation scheme is based on a combined optical recognition/validation system with photogrammetry as applied to a reference target of known characteristics attached to the fishnet. The AUV captures video data of the fish cage area under a relatively close distance successively to address the fishnet consistency

problem. The AUV architecture is cost-effective to automate the inspection of aquaculture cages equipped and accomplished a real-time behavior capability.

In the work of Kellaris e al. [154], drones were evaluated as monitoring tools for seaweeds using a low-cost aircraft. Compared to satellites and typical airborne systems as sources of images, drones achieve a very high spatial resolution that addresses the problems on habitats with high heterogeneity and species differentiation, which apply to seaweed habitat. A sample of the captured image for aquaculture site surveillance using a drone is in Figure 7. With the application of drones in surveying, it is now more accessible with a more large-scale range and scope of integration to aquaculture, fisheries, and marine-related applications. Table 5 shows the different types of drones and the embedded sensors for site surveillance and their corresponding applications.

Figure 7. Aerial view of in-land aquaculture site with scene modelling with detected objects such as fish pen, cages and house for site surveillance.

Table 5. Unmanned vehicles and its application to aquaculture site surveillance.

Type of Unmanned Vehicle Used	Applications	Attached Sensors	Reference/s
Customized and augmented UAV with delta wing design	Surveillance	Thermal camera, location transmitter, RF signal generator	[151]
Customized ROV	Underwater surveillance	GoPro HD Hero2	[149]
Hexacopter AUV	Cage detection	On-board camera	[147]
Customized rotorcraft AUV	Cage inspection	Lidar	[29]
Customized AUV using BlueROV2	Inspection of aquaculture net pens to identify holes or fouling of nets	AUV camera	[153]
Phantom 3 Professional senseFly eBee	Mapping	Sony EXMOR 4K RGBCanon PowerShot S110 RGB	[144]
Customized UAV	Photogrammetric survey	Super-wide-angle camera	[145]
Phantom 4 Pro V2.0	Scene modeling	Built-in camera	[146]
UAV type not specified	Ship classification and detection	Color camera and wide-angle lens	[140,141]
DJI Phantom 3 Professional quadcopter drone	Sea-weed habitat mapping	Sony EXMOR camera	[154]

As much as possible, the position of offshore aquaculture cages is relatively close to onshore facilities to minimize distance-related costs of transport and maintenance services [155]. Table 6 provides the characteristics of the three aquaculture farm locations: coast, off-coast, and offshore based on physical and hydrodynamical settings. In the table, the work of Chu et al. [156], they provided a review on the cage and containment tanks designs for offshore fish farming and Holmer [157] provided the characteristics. The limitations in terms of accessibility to aquaculture farms is affected by weather conditions.

Table 6. Characteristics of coast, off-coast, and offshore aquaculture farms; adapted from Chu et al., Holmer and Marine Fish Farms [156–158].

| Location of the Aquaculture Farm | Characteristics | | | |
| | Physical | | Exposure | |
	Distance from the Shore	Visibility from the Shore	Waves	Accessibility
Coastal	<500 m	Visible	Small to moderate exposure	100%
Off-Coast	500 m to 3 km	Usually visible	High to huge exposure	>90%
Off-Shore	>3 km	Not visible	Huge exposure	>80%

The data provided in the table, especially the distance of the cages from the shore, are significant since they help determine the capability of the unmanned vehicle to perform navigation and monitoring. In Taiwan, the distance from the shore to the offshore cages range from 2 to 11 km, while the inshore cages are one kilometer away. The distance of the fish cages from the shore is significant in terms of the amount of time the unmanned vehicle needs to travel. Commercial UAVs are widely used for inspection since they are low-cost, but they are limited in terms of flight hours and payload capacity. Table 7 shows the characteristics of the UAV's performance measures.

Table 7. Characteristics of UAV types; adapted from Gupta et al., Fotouhi et l., Shi et al. and Delavarpour et al. [58,159–161].

Characteristics	Rotary-Wing	Fixed-Wing	Hybrid
Weight (kg)	0.01 to 100	0.1 to 400,000	1.5 to 65
Payload (kg)	0 to 50	0 to 1000	0 to 10
Ceiling altitude (km)	4	0.1 to 300	-
Endurance (m)	6 to 180	60 to 3000	180 to 480
Range	0.05 to 200 km	2 to 20 mil	-
Power source	Battery	Fuel or battery	Fuel or battery
Hover	Yes	No	Yes
Autonomy	Yes	No	Yes
Take-off/Landing	Vertical	Conventional	Vertical
Control Complexity	Simple	Complex	Most Complex
Flight System	Simple	Complex	Complex
Energy Efficiency	Less	More	More

Since the battery life of UAVs to perform extended navigation is limited most especially those with small size [162] (16 to 30 min for commercial drones), this restricts its operational range. For example, DJI Mavic Air 2, a quadcopter drone UAV that costs approximately $800, has only 34 min flight time. Meanwhile, military drones have longer flying times, but cost millions of dollars. Fixed-wing drones with longer flight hours (120 min), such as Autel's Dragonfish [163], cost around $99,000. Hybrid drones such as the SkyFront Perimeter 8 multirotor can fly up to 5 h [164]. UAV's flying time is also affected by the payload it carries; the fewer payloads, UAV will have a longer navigation time.

UAVs are also limited in their capacity to fly during bad weather. There are commercially available drones that can fly in windy conditions. But this scenario can be extremely difficult and challenging. One has to undergo a drone training course to make sure that setups are optimized to fly in difficult conditions, or one has to purchase high-end AUVs that cost hundreds of thousands of dollars, but many could not afford or might find it not practical. There are consumer-grade drone models that are available for windy conditions. The DJI Mavic Pro 2 can handle up to 15 mph though there are claims that it can reach a wind resistance up to 24 mph. Some commercially available drones can still fly in windy conditions but cannot withstand a tropical depression or a typhoon with at least sustained gusts of 30 mph. Although there are many efforts and studies for commercial-grade unmanned vehicle systems to advance their robustness and adapt to harsh weather conditions, this vision remains a challenge.

The capability of commercial-grade UVs to perform long-term mission is a challenge as well. The locations of coastal farms are close to the shore, so the flight time is shorter, and more time to perform navigation and its assigned mission compared to offshore farms, which are kilometers from the shore. In the case of offshore farms, if a UV takes off from the shore, it can no longer maximize its power once it reaches its destination since the battery is consumed for traveling. Thus, only limited time is available to perform its supposed function. However, there are many ways to extend and maximize their performance, such as lower altitude and smaller payloads. Instead of taking off from the shore or land area, they can take off from the barge. To assist the smart feeding machine for the fish feeding process, as an example, UV can take off from the barge or ship and does not need to travel a long distance from the shore. The operator can fly or control the UAV from the barge; it can return when finished monitoring. With this, there will be more time for the desired or target mission.

Aquaculture farms need to be visited at least once a day, and this is done during feeding time. The duration of a UV's mission depends on the function it must perform. Performing a water quality will not require some hours since the UV can get a water sample and perform analysis right away if it is equipped with sensors to measure water quality. On the other hand, monitoring the feeding activity requires longer hours; large offshore aquaculture farms have 24 cages where each cage is 100 m (standard size) in terms of the circumference. For each cage, there is an approximate distance of 5 m away from each other. To perform feeding in such conditions, it takes around 15 to 20 min to feed one cage, and 24 cages require almost a day of feeding activity. With the amount of time to monitor the feeding of the fish, one commercial-grade UV is not sufficient since it has limited power. Thus, multiple vehicles are needed to carry out a complete monitoring mission and data collection. During harsh weather conditions, fish cages are submerged in the water, and no fish feeding activity is carried out.

8. Aquaculture Farm Monitoring and Management

Drones are capable of monitoring fish farms in aquaculture, especially on offshore sites. Its affordability and mobility have allowed for a more open scope and access to difficult areas to reach and with high risks. The continued mechanization and automation of farm monitoring using drones, sensors, and artificial intelligence will enable farmers to inspect their farms, acquire more information needed for decision making, manage and interact with their farms efficiently. Furthermore, with the rapid growth of the aquaculture industry, drones will enable the monitoring of the growing farm site. Drones can replace the supply and demand for laborers and high-cost work in the aquaculture industry, thus ensuring that the management of the fish farm becomes stable by reducing farm deaths. To enable monitoring of the growing environment at the aquaculture farm site, using a drone as an image collection device, an integrated controller for posture stabilization and a remote device to control drones can capture underwater images in real-time [165].

An aquatic platform [166] composed of USVs and buoys has a self-organizing capability performing a mission and path planning in the water environment. This platform can

communicate with other devices, sense the environment (water or air), and serve as a communication channel using data gateways stations (DTS). The data taken by the USVs and Buoys using the attached sensors are forwarded to the server to be accessible to aquaculture workers to improve or maintain the aquaculture performance. Sousa et al. [167] designed and developed an innovative electric marine ASV (autonomous surface vehicle) with a simplified sail system controlled by electric actuators. This vehicle is capable of exploration and patrolling. Aside from reducing cost, since no fuel is required, it will be capable of endless autonomy, maximizes the limited energy to manage sails using propulsion power using solar cells and wind generators.

Aerial and underwater drones also have enormous potential to monitor offshore kelp aquaculture farms. Giant kelps with their same growth rate and versatility make them an attractive aquaculture crop that requires high-frequency monitoring to ensure success, maximize production, and optimize its nutritional content and biomass. Regular monitoring of these offshore farms can use sensors mounted to aerial and underwater drones. A small unoccupied aircraft system (sUAS) can carry a lightweight optical sensor. It can then estimate the canopy area, density, and tissue nitrogen content based on time and space scales, which are significant to observe changes in kelp. To provide a natural image of the kelp forest canopy, sUAS have sensors such as color, multispectral and hyperspectral tcameras [168].

An integrated system to count wild scallops based on vision was developed by Rasmussen et al. [169] to measure population health. Sequential images were collected using AUV and used convolutional neural networks (CNNs) to process those collected images for object detection. The images used as a dataset were captured by a downward-pointing digital camera installed in the nose of the AUV. In the work of Ferraro [170], UAV was also used to collect color photos and side-scan sonar images of the seafloor to perform a quantitative estimate of incidental mortality using a precise and non-invasive method for sea scallops. AUV was also used to capture a reliable image of the seafloor to determine the density and size of the scallops, thus providing an accurate set of data for site surveys. It also offers an efficient and productive platform to collect sea scallop images for stock assessment since it can be quickly deployed and retrieved [171].

Oysters were also detected and counted using ROVs for small-size aquaculture/oyster farms with robotics and artificial intelligence for monitoring. The ROV's front is mounted with a camera and two led lights. The camera feed streams to the remote machine, then used by the operator to perform underwater navigation. Additionally, the ROV was equipped with an additional GoPro camera and LED lights to view the seafloor. A graphic user interface called Qground Control (QGC) was installed to acquire underwater images of oysters by the ROV. The QGC sends commands to the device and receives the camera and other sensory information on the ground station machine or remote machine; the ROV can be controlled manually or automatically controlled. For manual control of the ROV, control commands are sent to the QGC through a wireless controller [172]. The Argus Mini, an observation class ROV built for inspection and intervention operations in shallow waters and can be used in offshore, inshore, and fish farming industries. It is equipped with six thrusters in which four are placed in the horizontal plane, and two are in the vertical plane to guarantee actuation in 4 degrees of freedom to resist water surges, sways, heaves, and yaw. The ROV is equipped with sensors to perform net cage inspection [173].

An underwater drone was developed integrating 360 degrees panoramic camera, deep learning, and open-source hardware to investigate and observe the environment such as the sea, aquarium, and lakes for fish recognition in real-time. The drone was also equipped with Raspberry Pi to compute module with GPU for processing and achieving real-time panoramic image generation [174]. Other application of UV includes periodic fish cage inspection [175], fish behavior observation [176], salmon protection [177], and fish tracking [178]. Table 8 presents the different application of unmanned vehicles for aquaculture farm monitoring and management.

Table 8. UVs and its application to aquaculture farm monitoring and management.

Application	Type of UV Used	Attached Devices/Sensors	Reference/s
Oyster detection and counting	BlueRobotics BlueROV2	GoPro camera and led lights	[172]
Assessment of the population/ stocks of wild scallops	Gavia AUV	Downward-pointing digital camera	[169]
	Telegavia UAV	a Point Grey Grasshopper 14S5C/M-C model with Sony ICZ285AL CCD	[170]
	Teledyne Gavia AUV	Nose cone camera, GeoSwath phase measuring bathymetric sonar, Marine Sonic side-scan sonar)	[171]
Monitoring of the growth environment at the farm site	Customized ROV	USB camera based on LIFI	[165]
Offshore kelp monitoring	DJI Phantom 4 Pro	20 MP (1″ CMOS sensor, 84° FOV) color camera	[168]
Recognition of fish species	Underwater drone (type not specified)	360-degree panoramic camera with two 235-degree fisheye lenses	[174]
Salmon protection	Underwater laser drone	Stereo camera system	[177]
Fish cage inspection	BlueROV2 of BlueRobotics	Camera	[175]
Observation of fish behavior	Customized UAV	Cameras with power LEDs and water quality sensors	[56]
Fish tracking	AggieAir	Visual camera, near-infrared (NIR) camera, thermal infrared camera, and air quality sensors	[178]

8.1. Fish Feed Management

The welfare of fish in aquaculture comes from improving standards and quality for fish production technologies and aquaculture products. The well-being of fish has direct implications for production and sustainability. Fish under good welfare conditions are less susceptible to disease, hence, manifest better growth and higher food conversion rate providing better quality [179]. There are many indicators to assess fish welfare, such as fish behavior and characteristics.

Many developed technologies can automate processes, such as underwater cameras to observe fish behavior and characteristics and provide visual observations in fish cages. However, installation and configuration of underwater cameras are laborious, particularly in an offshore area. They should be equipped with cables for communication and transmission and power source for continuous data collection. There are underwater cameras that are equipped with batteries but can only work for a limited time. For such cameras, it is necessary for physical installation, and it will be difficult to keep changing and charging the battery now and then. For underwater cameras with a power source (e.g., solar power), when the source malfunctions, these devices cannot perform data collection and surveillance. With these limitations, drones become helpful as an alternative or added support for underwater cameras to provide visual functionalities for fish behaviors and characteristics.

Feeding management in aquaculture is a challenging task since the visibility of the feeding process is limited, and it is laborious to have a precise measurement. Machine feeders became available to assist fish farmers in dispensing food. However, such a mechanism, when not accurately monitored, would lead to food waste and profit loss. Feeding using pellets that floats above the water should be observed when to discontinue or continue feeding. In the work of Ubina et al. [26], a drone equipped with an RGB camera captures the surveillance video of the water surface using optical flows to measure fish feeding level as shown in Figure 8. The authors conducted various experiments such as the different altitudes and viewing angles to determine the best visuals and features of the fish feeding. The images were processed using a deep convolutional neural network to classify

the different feeding levels. The drone provides a non-invasive way for fish observation, which is more reliable than human investigations and observations.
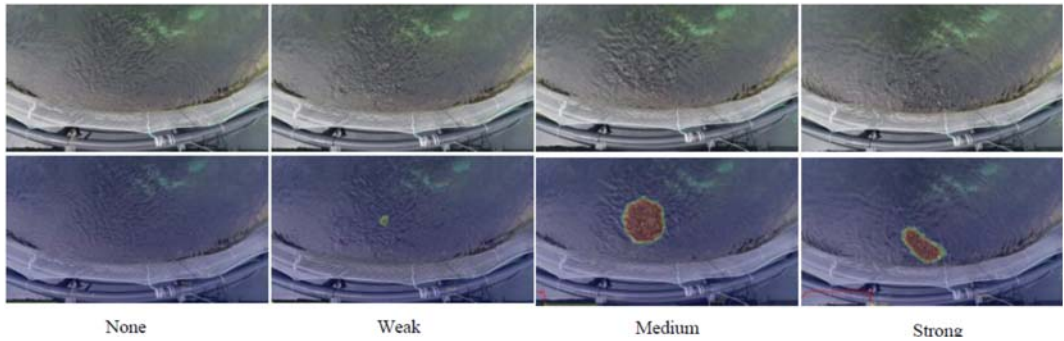
Figure 8. Image capture of the drone to evaluate fish feeding intensity using four different feeding intensity levels and the detected optical flow [26].

For a typical fish feeding to offshore locations, the feeds are transported in a boat or ship (see Figure 9). Then the pellets are dispensed using machine feeders, creating an annular feed distribution pattern across the water surface, and covering a limited percentage of the surface area. As an alternative method to determine the distribution of the pellets in the water surface, a UAV of Skøien et al. [121] was used to observe and characterize the motion and measure the spatial distribution of the pellets of the feed spreaders in sea cage aquaculture where the camera is always perpendicular to the water surface. The UAV also recorded the pellet surface impacts from the air together with the position and direction of the spreader. For this work, the UAV is fast with minimal equipment installation and a viable alternative in collecting pellets which can help farmers achieve feeding optimization.
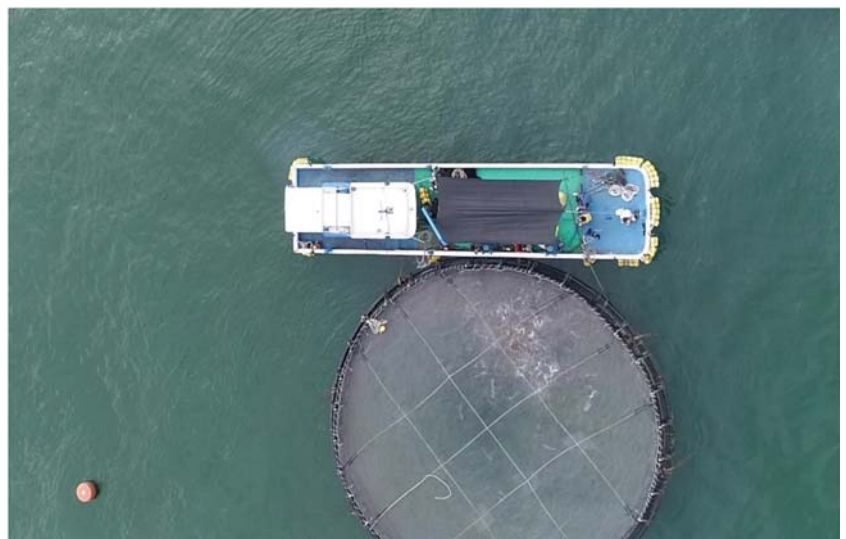
Figure 9. The aerial footage using UAV to facilitate optimized feeding using feeders transported in boats.

To estimate the spatial distribution of feed pellets in salmon fish cages, a UAV provides a simple and faster setup, as it covers a large area of the surface of the sea cage. The UAV captures the aerial videos using a 4K camera from a top-view position of the hamster wheel in the fish cage during the feeding experiment. The UAV used for this work was DJI Inspire 1 and was positioned above the rotor spreader. But images taken outdoors are challenging, and it needs immediate adjustment to lighting conditions changes. These difficulties are induced by the reflection of the clouds on the water surface area and sometimes caused by slight variations in the camera position. For accurate estimations, the splashes of the dropping pellets must be identified and extracted to count or measure the splashes relative to the spreader in the image. A technique was integrated using top-head imaging as a processing step to extract brighter pixels from the image corresponding to splashes [180].

8.2. Fish Behavior Observation

A bio-interactive (BA-1) AUV monitors fish interactively and can stay in the environment where the fish resides. It can be swimming together with the fish to monitor their movements in a pen-free offshore aquaculture system. The vehicle can provide a stimulus to the fish and observe their behavior caused by stimulation. The UAV was designed to have hovering and cruising capability with bio-interactive functionality with an LED lighting system. It can also operate simultaneously with other BA-1 AUVs as its multiple AUVs capability feature. The BA-1 is equipped with sensors to perform navigation, collision avoidance, localization, self-status monitoring, and payload. The device was tested in tanks and aquaculture pens with sea bream species. Once the fish becomes familiar with the vehicle, it can come close to the demand feeding system to receive the bait [181] and assist in the smart feeding process.

A UAV device with GoPro cameras for its video recording tracks monitors the behavior in space and time of GPS-tagged sunfish. For communication, the vehicle uses Wi-Fi or GSM/HSDPA. Remotely sensed environmental characteristics were extracted for each position of sunfish and used as parameters to determine their behavioral patterns [182]. Spatial movements of fish are vital in maintaining fish populations and monitoring their progress. A multi-AUV state-estimator system helps determine the 3D position of tagged fish, also its distance and depth measurements. The system is composed of two AUVs with a torpedo-shaped vehicle. The attached rear propeller in the UAV determines the location, and the four fins control the pitch, raw, and yaw of the device. It is also equipped with two processors that communicate with the sensors and actuators [183]. A stereovision AUV was utilized to assess the size and abundance of ocean perch in temperate water. The AUV hovers above the target area with a constant altitude of 2 m and with a slow flying speed above the seafloor as it captures images using a pair of downward-looking Pixelfly HiRes (1360 × 1024 pixel) digital cameras [184].

8.3. Water Quality and Pollutants Detection and Assessment

Fish are in close contact with water, which is one of the most critical factors for fish welfare, which requires continuous and close monitoring. Poor water quality can lead to acute and chronic health and welfare problems, so water quality should be at optimal levels. Aquaculture is also significantly affected by climate change which results in changes in abiotic (sea temperature, oxygen level, salinity, and acidity) and biotic conditions (primary production and food webs) that will significantly cause disturbance in growth and size [1]. Parameters that reflect water quality [179] include temperature, conductivity, pH, oxygen concentration, and nitrogenous compounds such as ammonia, nitrate, and nitrite concentration. Traditional water assessments and predictions collect water samples and submit them for laboratory inspections, or some have physical-chemical test devices carried [185]. This method is a burdensome one and requires a physical presence to conduct water quality assessments. Many aquaculture farms rely on mechanical equipment to ensure water quality, which includes oxygenation pumps, independent rescue power systems, and aeration/oxygenation equipment. Although they are helpful, they have

limitations when installed in open-sea cages or offshore aquaculture sites and require additional configurations and setup. Drones have become very helpful to perform on-site water monitoring, sampling, and testing due to their high mobility, reliability, and flexibility to carry water quality sensors. A combination of UAV and wireless sensor network (WSN) in the work of Wang et al. [186] was designed for a groundwater quality parameter and the acquisition of drone spectrum information. Their proposed approach provides a new mechanism on how remote sensing with UAVs can rapidly monitor water quality in aquaculture.

An electrochemical sensor array to predict and assess water quality data using the pH of the water, dissolved oxygen, and ammonia nitrogen is carried by a floating structure UAV in T shape that can take off and land on the water surface. The sensor bears the capability of real-time detection and transmits its result to the sever backstage using the cloud server through a wireless network [185]. Furthermore, catastrophic events such as spills of hazardous agents (e.g., oil) in the ocean can cause massive damage to aquaculture products. To detect similar leaks like the fluorescent dye in the water, Powers et al. [187] used USV by mounting a fluorescence sensor underneath for detection. An unmanned aircraft system (UAS) visualized the fluorescent dye, and the USV takes samples from different areas of the dye plume.

Water sample collection based on in situ measurable water quality indicators can increase the efficiency and precision of collected data. To achieve the goal of preciseness, an adaptive water sampling device was developed using a UAV with multiple sensors capable of measuring dissolved oxygen, pH level, electrical conductivity, temperature, and turbidity. The device was tested using seven locations and was successful in providing water quality assessment [188]. In addition, in the works of Ore et al. [189], Dunbabin et al. [190] and Doi et al. [191], UAVs were used to obtain water samples that require less effort and faster data collection.

An extensive study on how drone technology assists in water sampling to achieve the goal of biological and physiological chemical data from the water environment can be found in the work of Lally et al. [192] and was characterized mainly using remote sensing. Spectral images captured by UAV were also used to assess water quality, such as algae blooms, to determine the chlorophyll content of the water [193], turbidity, and colored dissolved organic matter [194]. Other studies also show the use of drones with attached thermal cameras, such as miniaturized thermal infrared [195], to capture images for measuring surface water temperature, and environmental contamination [196].

The work of Sibanda et al. [197] shows a systematic review to assess the quality and quantity of water using UAVs. In Table 9, dissolved oxygen, turbidity, pH level, ammonia nitrogen, nitrate, water temperature, chlorophyll-a, redox potential, phytoplankton counts, salinity, colored dissolved organic matter (CDOM), fluorescent dye, and electrical conductivity were among the collected parameters for water monitoring. Additionally, the DJI brand of drones is the commonly used commercial type. Some UAVs have sensors specific to their functions (e.g., dissolve oxygen sensors test dissolve oxygen). Many customized UAVs were also used to perform a water quality assessment to meet the specific needs of each work and as an improvement to existing commercial capabilities such as navigation, strength, and mobility capabilities.

Table 9. Type of UVs and parameters used for water quality assessment and monitoring.

Measurement Indicators	Type/Brand of; UV Used	Sensors/Devices Installed	Sampling Location	Reference/s
Dissolved oxygen	DJI M600 pro	k4 multispectrometer camera	Inland	[186]
	Customized Six-rotor UAV	Dissolved oxygen sensor	Open sea	[185]
	AUV Tantan	Conductivity, temperature, and depth (CD) sensors	Open sea	[198]
	Customized multi-rotor UAV	Sensor nodes, water sampling cartridge	Ponds, lakes	[188]
	Customized multirotor UAV with hovercraft	Dissolved oxygen sensor	Lake	[199]
Turbidity	DJI M600 pro	k4 multispectrometer camera	Inland	[186]
	AUV Tantan	Conductivity, temperature, and depth (CD) sensors	Open sea	[198]
	Customized multirotor UAV	Sensor nodes, water sampling cartridge	Ponds, lakes	[188]
	Quad-copter (DJI Phantom 2 Vision Plus) and hexa-copter (DJI Spreading Wings S800	RGB Camera	Open sea	[170]
	Customized multirotor UAV with hovercraft	Turbidity sensor	Lake	[199]
pH Level	Six-rotor UAV	pH nitrogen sensor	Open sea	[185]
	AUV Tantan	Conductivity, temperature, and depth (CD) sensors	Open sea	[198]
	Customized multirotor UAV	Sensor nodes, water sampling cartridge	Ponds, lakes	[188]
	Customized multirotor UAV with hovercraft	pH level sensor	Lake	[199]
Ammonia nitrogen	Six-rotor UAV	Ammonia nitrogen sensor	Open sea	[185]
	Customized UAV	Ammonia nitrogen sensor	Lake	[200]
Nitrate	Customized AUV "Dorado"	Gulper water samples	Bay and offshore water	[201]
Temperature	UAV Tantan	Conductivity, temperature, and depth (CD) sensors	Open sea	[198]
	DJI Octocopter UAV	FLIR T450sc Thermal camera; Infrared camera	Coastal water	[202]
	Customized multirotor UAV	Sensor nodes, water sampling cartridge	Ponds, lakes	[188]
Chlorophyll-a	UAV Tantan	Conductivity, temperature, and depth (CD) sensors	Open sea	[198]
	Customized AUV "Dorado"	Gulper water samples	Bay and offshore water	[201]
	Remo-M UAV	Sequoia multispectral sensor with 4 cameras to capture spectral images (algae blooms)	Streams	[193]
	Customized UAV	Portable fluorometers	Streams	[193]
	Quad-copter (DJI Phantom 2 Vision Plus) and hexa-copter (DJI Spreading Wings S800).	RGB Camera	Open sea	[194]
Redox Potentia	UAV Tantan	Conductivity, temperature, and depth (CD) sensors	Open sea	[198]

Table 9. *Cont.*

Measurement Indicators	Type/Brand of ; UV Used	Sensors/Devices Installed	Sampling Location	Reference/s
Phytoplankton counts	Customized AUV "Dorado"	Gulper water sampler	Bay and offshore water	[201]
Salinity	DJI Octocopter UAV	FLIR T450sc Thermal camera and infrared camera	Coastal water	[202]
	DJI Phantom 3 Professional UAV	MicaSense RedEdge-M multispectral camera	Lagoon ; (Shallow water)	[203]
Colored dissolved organic matter (CDOM)	Quad-copter (DJI Phantom 2 Vision Plus) and hexa-copter (DJI Spreading Wings S800	RGB Camera	Open sea	[194]
Fluorescent dye	Clearpath Robotics Kingfisher M200 USV (dye detection and tracking) and DJI Phantom UAV (image capture)	Fluorometer (fluorescence sensor)	Freshwater lake	[187]
Electrical conductivity	Customized multirotor UAV	Sensor nodes, water sampling cartridge	Ponds, lake	[188]
	Customized multi-rotor UAV with hovercraft	Electrical conductivity sensor	Lake	[199]

8.4. Water Quality Condition

Aquaculture farms have raised environmental concerns, and an increase in aquaculture production will pose a huge environmental challenge. Climate change is considered a threat to aquaculture production [21]. Sea-level rise, frequent and extreme weather (e.g., winds and storms) events are also projected to increase in the future [1]. For sustainable growth in aquaculture production, it is necessary to adapt to climate to produce more fish, and environmental impacts could not affect its operations.

UVs are commonly applied for image acquisition in the field of geophysical science to generate high-resolution maps. There is an increasing demand for high-performance geophysical observational methodologies, and UV technology combined with optical sensing to quantify the character of water surface flows is a possibility. Water surface flow affects the growth and health of aquaculture products with its environmental impacts from sea lice, escaped fish, and release of toxic chemicals and organic emissions to the water area [204]. It is also essential for farming fish in cages for replenishment of oxygen and removal of organic waste [156]. Water velocity also has a profound impact on fish metabolism, growth, behavior, and welfare. A higher velocity can boost the growth of farmed fish. In the work of Li et al. [205], it determines the protein content of the fish muscle using moderate swimming exercise. Using moderate water velocity exhibited a higher level of the protein content of the fish muscle. The growth performance of Atlantic salmon was also monitored using lower salinity and higher water velocity with positive effects on the growth of the salmon [98]. Another positive influence of higher velocity on fish welfare is in the work of Tauro et al. [204], where improvements of flesh texture, general robustness, and lower aggression lead to a reduced stress response. On the other hand, very high velocities increase oxygen need and anaerobic metabolism and cause exhaustion, reduced growth, and affect fish welfare. Moreover, excessive current flow causes the fish to excessively use its energy in swimming. Outrageous waves in an offshore environment, on the other hand, damages cage structures and moorings and can cause fish injury. A severe wave condition can be a hazardous situation and can cause an interruption in the routines or operations of farmers [156].

With the mentioned importance of measuring water surface flow and velocity for fish growth, drones can be integrated to perform such functions. Flying drones [204] were used to observe the water environment to produce accurate surface flow maps of submeter

water bodies. This aerial platform enables complete remote measurements for on-site surveys. To measure the water velocities that integrate UVs, the work of Detertm and Weitbrecht [99] shows its effectivity to perform such function. A technique on how a drone can retrieve a two-dimensional wavenumber spectrum of sea waves from sun glitter images was proposed by [206], which shows the potential of the drone to investigate the surface wave field. Airborne drones were compared with satellite images to determine the state of the sea in the ocean and the dynamics of the coastal areas. Optical technologies that use spatial resolution optical images derive anomalies in the elevation of the water surface induced by wind-generated ocean waves [207].

In Table 10, UVs are equipped with cameras to collect data from the water environment. The majority of UV used are the commercial DJI Phantom, which is famous for its affordability and is sought-after but is reported to have a small amount of image distortion that can affect the images. According to Streßer et al. [208] and Fairleyet al. [209], some fixes were made with the gimbal pitch to make it independent of the aircraft's motion.

Table 10. Application of UVs to perform water condition monitoring.

Application	Type of UV Used	Attached Sensors/; Devices	Environment	Reference/s
Surface flow/current measurement	DJI Phantom 2 quadrotor	Zenmuse H3-2D gimbal and a GoPro Hero 3 camera	Open sea	[204]
	DJI Phantom III Professional	Self-stabilizing camera gimbal	River	[208]
	DJI Phantom 3 Professional	Brushless gimbal and 4K video camera	River	[210]
	Custom-built unmanned aerial platform	Lightweight camera gimbal; GoPro Hero 3	Water tunnel and water stream	[211]
	AscTec Falcon 8	Sony NEX-5N	River	[212]
	Custom built torpedo-shaped AUV	Pressure sensors	Sea	[213]
Measurement of large-scale surface velocity fields	DJI Phantom FC40	4K GoPro Hero 3+ Black Edition camera	River	[99]
Speed of wave crest	DJI Phantom 2 Vision+	Camera	Coast	[214]
Derive spatial and dynamic characteristics of waves.	DJI Mavic Pro	Acoustic Doppler Current Profiler	Coast	[207]
Surface flow observation	DJI Phantom 2	H3-2D gimbal, a GoPro Hero 3 camera, and a system of four green lasers	Stream	[215]
Field measurements of tidal elevation (water depth), wave spectrum, wave height, and wave period	DJI, S1000	Scanning lidar (Hokuyo, UTM-30LX)	Coast	[216]
Monitoring the topography of a dynamic tidal inlet	eBee flying wing	Canon Powershot ELPH110 HS RGB camera	Coast	[217]
Velocities of tidal streams	DJI M210v2 RTK	Zenmuse X7 lens	Tidal stream	[209]
Water surface detection and cleaning	Customized multi-function USV	OmniVision Image Sensor; Pixy CMUcam5	Shallow lake	[213]
Flow velocity and direction	ATOMIC 792–4 p	USB Camera	River	[218]
Surface gravity waves	Wave Glider Float	MicroStrain GPS + AHRS	Bay	[219]
Surface meteorology and wind power density	Wave Glider—American Liquid Robotics	Oceanographic sensors	Offshore-Ocean	[220]

9. Legal Regulations and Requirements for Unmanned Vehicle Systems

Potential users of unmanned vehicle systems, especially unmanned aerial systems (UAS), should be aware of the current and proposed regulations to understand their

potential impacts and restrictions. The permitted sites for UAS should be first determined; flight restrictions for UAS in the offshore locations of aquaculture sites should be within the allowable time of the day. One of the challenges to consider when using UAS is that regulations are not fully established and are currently changing. The user must always check the updated rules in advance [54] of the scheduled flight or mission.

9.1. Standards and Certifications

New policies and regulations for UAS must be planned and implemented to ensure there is a safe, reliable, and efficient use of the vehicles. Developing standards is one of the most crucial issues for UAS since UAVs should be interoperable with the existing systems. In managing the electromagnetic spectrum and bandwidth, it is critical of UAVs not to be operating in crowded frequency and bandwidth spectrum. It is also essential to be aware of the published standardization agreements by NATO for UAVs. This standard defines the standard message formats and data protocols. It provides a standard interface between UAVs and ground coalitions. It also represents the coalition-shared database that allows information sharing between intelligent sources. In the US, the Federal Aviation Administration (FAA) has provided certification for remote pilots, including commercial operators [221]. UAVs used for public operations should have a certificate from the FAA; operators must comply with all federal and laws, rules, and regulations of each area, state or country [222].

9.2. Regulations and Legal Issues

In Canada, drones weighing from 250 g to 25 kg must be registered with Transport Canada, and pilots must have a drone pilot certificate. Pilots must mark their drones with their registration number before flying and drones should be seen at all times. While flying, they should be below 122 m in the air. The places where drones are prohibited to fly include 5.6 km from airports or 1.9 km from heliports. In the US, each state has its respective laws and regulatory requirements. In Taiwan, drones are prohibited to fly in sensitive areas such as government or military installations. Drone flights are permitted only within a visual line of sight and are limited to daylight hours between sunrise and sunset without prior authorization. A drone operator permit is required if the drone weighs more than 2 kg. In Germany, drones weighing more than 5 kg should obtain authorization from the aviation authority. When applying for permission, a map indicating the launch area and operating space, consent declaration from the property owner, timing, technical details about the UAS, data privacy statement, and a letter of no objection from the competent regulatory or law enforcement agency [223].

UAV regulations and policies of different countries have some common ground. However, they still differ in many aspects in terms of requirements and implementation. When used for a specific purpose, according to Demir et al. [222], aviation regulations determine the rules for the AUV minimum flight requirements. In most countries, UAVs are used in separate airspace zones. National regulations are also laid out to ensure safe operations of different UAVs in their respective national airspaces.

The operation requirements for unmanned maritime vehicles are also not yet clearly defined and regulated in terms of current domestic law or international conventions. There is no definite legal framework exists to regulate its use since permits and licenses are required based on a few narrow circumstances. The growing population and popularity of unmanned vehicles do not indicate causing danger to the oceans, in the future, but with is a possibility of potential implications of their widespread. Although there are regulatory gaps, there are options available to obtain permission for AUV operations to make the ocean a safer place for humans and animals [224]. Additionally, due to the varied types of AUV and their wide range of applications, it is also challenging to know their respective legal status for different operations, as their regulations vary significantly [225]. Operators should be aware of the prohibitions of such vehicles to avoid future problems or legal implications of their actions. The moral and ethical use of unmanned systems should also

be considered by potential users to ensure that UAVs do not participate in illegal activities or morally doubtful operations.

10. Challenges and Future Trends

Unmanned systems have shown significant contributions to aquaculture management and monitoring to attain precision aquaculture. Table 11 shows the different functionalities identified in this paper with their strengths and limitations. However, despite all the functionalities, unmanned systems still have drawbacks and shortcomings and how improvements and modifications can be made to improve their performance.

Table 11. Application of drones to aquaculture management and monitoring to achieve precise aquaculture with its corresponding advantages and disadvantages.

	Application to Aquaculture	Advantages	Disadvantages
1.	Communication gateway and data collector	■ Provide wireless communication to IoT devices installed in the aquaculture cage in remote and high-risk areas. ■ Less expensive than manned aircrafts in collecting data. ■ Can now provide wide coverage area using LPWAN devices. ■ High volume of data can be collected	■ Limited power and energy source. ■ Limited navigation time.
	Aquaculture site surveillance and monitoring		
a.	Remote sensing	■ Less atmospheric interference for remote sensing applications than satellite images ■ High spatial resolution for airborne image captures	■ Limited payload and capacity and difficulty in processing large data sets such as high-definition videos. ■ Limited capacity in terms of memory, processor, and energy.
b.	Site surveillance	■ Provides safe and effective alternative to humans to conduct surveillance ■ Bigger coverage area	■ Trade-off between additional payload and navigation time. ■ Limited under undesirable weather conditions
2.	Aquaculture farm management and monitoring		
a.	Fish feeding management	■ Can be integrated with cloud computing for live monitoring.	■ Small-sized images are captured, which makes it difficult to detect objects as compared to underwater cameras when a drone is used to capture images.
b.	Fish behavior observation	■ Noninvasive and noncontact method of observation. ■ Can replace humans and is accessible by remote monitoring. ■ Eliminates the cable requirement used by underwater cameras installed in fish cages for communication.	■ Requires more stable and predictable weather for efficient monitoring results. ■ Determine the sufficient altitude to capture small images.
c.	Water quality and pollutants detection and assessment	■ Remote sample collection, assessment and monitoring of water quality. ■ Does not require samples to be tested in laboratories. ■ Provide a real-time result. ■ Spectral images can be evaluated water quality. ■ UAVs with hovercraft can glide on water surface to gather water samples.	■ Images captured by drones is affected by weather conditions such as sun glint, wind speed, and clouds. ■ Glint, foam and shadows could be evident in the images; need to consider suitable weather condition in capturing images. ■ Does not cover varied sampling capabilities.
d.	Water condition	■ Provides complete remote surveys. ■ Can yield accurate surface flow maps of the water. ■ Low-cost data collection method.	■ Camera shakes affects the distortion of images. ■ Drones are limited by their physical instability which indices motion. ■ The captured images can be affected by weather conditions.

UAVs utilized for wireless perspective can act as a base station in the cellular network providing communication links to terrestrial users or functioning as a relay in a wireless communication network. However, drones for wireless sensor networks have low transmission power, and many may not wirelessly communicate for a longer range or duration. There are technical challenges of providing a communication link between sensor nodes

and drones, such as network planning, sensor positioning, drone battery limitations, and trajectory optimization. With those challenges, there is a need to optimize the drone flight path planning based on the locations of the sensors to minimize flight time and overcome battery limitations [101]. To optimize path planning capability, algorithms such as the traveling salesman problem, A Star (A*) algorithm [226], Dijkstra algorithm [226], and modified and improved Dijkstra algorithm [227,228] could be utilized. Optimizing the drone's flight capability would reduce cost, faster execution of missions, and increase navigation time, so there is a need to improve existing path planning algorithms to optimize the drone's navigation time.

To increase the battery life, the installation of more batteries may be a solution. However, such a remedy will increase the weight of the aircraft [58]; UAVs are designed to be lightweight for efficiency, so they operate longer and can cover a wider area. Adding a load to the drone can affect its weight shifting or create a disproportion of its structure. To increase UAV navigation time and for prolonged flight endurance, solar-powered aircraft can also be considered. With solar-powered batteries, there is no need to charge and refuel. This scheme reduces drone operational costs, but heavy and bulky solar panels to collect solar energies are not feasible for drones. In addressing such limitations, there are already available next-generation solar panels that are flexible, thin, and lightweight called gallium arsenide (GaAs) solar cells, which are highly efficient solar cells [229]. In the future, we can see more developments of power-solar drones using next-generation solar panels. In maximizing UAV's potential, using low-cost components can be considered; programmable microprocessors can connect the solar power source and a battery power source. In addition, there should be more investigation on auto-pilot settings such as airspeed, altitude, and turning radius to optimize flight endurance [230].

A docking station for drones as future development enables these vehicles of automated inductive charging of batteries at sea level. This station has a very narrow depth within the fish cage that will act as a power supply and data up-loading/transfer from the AUVG to the external servers for data processing. Once completed a mission or when the battery level becomes critical, the AUV will be directed to the docking station. Without any physical malfunctions, drones can permanently reside in fish cages and provide near real-time information on the condition of aquaculture farms [153].

Satellite images have the widest coverage compared to drone-captured but with the lowest quality and resolution. Although satellite images are best for mapping, they are strongly affected by clouds and fogs. AUVs provide image captures with better resolution and image quality for aquaculture site surveillance and monitoring. Many drones perform in situ surveillance, but they are lightweight and small with limited computational resources. Integrating AI and deep learning techniques could be computationally demanding and increase the drone's power consumption. It escalates its capacity for processing, the required analysis shifts to the cloud for processing, and the drone now becomes a 24-h surveillance system [231] with an increase in navigation time [232] and functionality [233]. Now that the high-volume data processing is eliminated, the drone can promptly collect a high volume of data in just a few hours.

For UAVs with attached camera sensors used as image capture devices, there are problems with the quality of the detected images. Raw captured images have low contrast [169], and small image size, which requires a post-processing procedure to improve image quality. One of the challenges of drone captures is weather conditions, where image capture is under suboptimal conditions, are highly variable, and is hard to predict. The sunglint effect also affects the water surface. Image enhancement and corrections are needed to improve the image quality and reduce noise [154]. Each image captured based on its specific function can employ explicit techniques to address a particular issue. For example, to solve the limitations of detecting objects, such as scallops, post-processing techniques specifically for small-sized images could be integrated. Despite the availability of image enhancement algorithms, underwater captured images continue to be a big challenge since they suffer from low contrast, low visibility, and blurriness due to light attenuation [234].

Water surface environments are active, and they continue to move, shrink, expand, or change their appearance with time [235]. Addressing these difficulties could employ and combine various techniques to process both underwater and above-water images. Each sensor type (e.g., sonar, stereo camera) also requires different processing techniques, which adds challenges to image enhancement integration. The use of sonar cameras depends on the wavelength of sounds, and the images generated are low contrast, and objects are blurred. For stereo camera systems, adjustments such as camera calibration are necessary. The use of deep learning is a well-proven technique to improve the image quality of surface water and underwater images to achieve a high precision rate. In practice, underwater video cameras are the most affordable data collector and highest quality and resolution for underwater surveillance, but they are difficult to install and configure.

There are many challenges in using unmanned systems to capture water movements to measure water velocity, such as camera shakes that affect the distortions of images or videos taken [99]. Physical instability of UAV induces motion in acquired videos that can significantly affect the accuracy of camera-based measurements, such as velocimetry. There are data-processing techniques or methods to deal with drone instability. The digital image stabilization (DIS) method uses the visual information of the videos in the form of physically static features to estimate and then compensate for such motions. In the work of Ljubičić et al. [236], seven tools were carefully investigated in terms of stabilization accuracy under various conditions, robustness, computational complexity, and user experience. Future work should aim to provide stability to aerial devices. Sensors carried by drones to perform meteorological surveillance combined with IoT, artificial intelligence, and cloud technology connected through a mobile communication channel provide optimal impact to the aquaculture industry, making it more sustainable and profitable.

One of the challenges of unmanned systems is to withstand typhoons with strong winds, heavy rains, and other calamities to increase their autonomous capabilities. Unmanned underwater vehicles (UUVs) should operate in harsh environments under high ocean currents and heavy hydraulic pressure; their navigation and maneuverability can still be strongly affected by oceans and water density [71]. Commercial graded are low-cost UAVs but are limited since their design is for operation in a stable or controlled environment. Commercially graded UAVs are low-cost in terms of acquisition, but only a few are with the capability to operate in such conditions. One of the few claims that their product is capable of such bad weather conditions is bbcom secure Deutschland GmbH [237], a company based in Germany. The company designed the unmanned aerial system (UAS) to be easy to use with low operating cost and capable of real-time video up to 17 sea miles away from the shore with 4 h of safe flying operation time even in harsh weather conditions. It is also capable of a maximum speed of 90 mph and can perform vertical take-off and landing and remote control with easy handling.

In the work of Elkolali et al. [238], a low-cost and solar-powered USV was designed for water quality monitoring that can operate in conditions that are dangerous and risky for human safety. However, adverse weather and water conditions such as rain and extreme wind or rough and choppy water can strongly affect USV's mission results and operations. Many business solutions are offering specialized packages combining high-quality unmanned vehicles and customized software applications for aquaculture farm and water monitoring. Blueye [239] has a complete package including underwater drones and software to perform aquaculture monitoring to reduce the risk and minimize the use of divers to inspect aquaculture cages. The mini ROV has four powerful thrusters combined with a unique hull design to perform high-quality underwater inspections in tough weather conditions where very few ROVs are capable of doing it safely. Saildrone [220] developed a USV that is a capable, proven, and trusted platform for collecting high-quality ocean data for a wide variety of applications with uncrewed wind-powered vehicles using renewable energy, wind, and solar. Their vehicles are equipped with state-of-the-art sensors for data collection, and they can cover more than 500,000 nautical miles in the most extreme weather conditions. Deep Trekker's ROV is battery operated and ensures no contamination to the

environment or fish health. It was tested in several locations where ROVs faced extreme weather and sea conditions daily. Water samples can still be collected under the ice at various depths [240]. FIFISH PRO W6, an industrialized class ROV platform, is equipped with an all-new powerful and patented Q-Motor system, a depth of 350 m of dive, with an intelligent stabilization system against strong currents [241].

11. Conclusions

This paper assesses progress and identifies opportunities and challenges of utilizing unmanned systems to manage and monitor aquaculture farms. The different capabilities of drones were identified as a communication gateway and data collector, aquaculture site surveillance, and aquaculture farm management and monitoring. Some of the challenges for offshore aquaculture site management and monitoring were also part of this paper. The utilization of technological innovation using unmanned vehicle systems addressed these difficulties to achieve the goal of precision aquaculture.

We also presented three platforms for unmanned vehicles with corresponding functions and limitations. UAS or UAVs are best suited for aerial surveys, site surveillance, monitoring and inspection, and photogrammetric surveys. However, there were also some UAVs for water observation, such as the surface flow map. Unmanned vehicles equipped with LTE cellular networks and LPWAN technologies can act as a communication gateway and IoT data collector. Fairweather condition is a requirement for surveys and inspections. Most AUVs have difficulties operating in a strong wind environment, and many cannot fly during harsh weather conditions. AUVs capable to operate in such condition is very expensive and highly complicated as it also requires government certifications and formal training for operation.

AUVs, ROVs, and USVs equipped with sensors can collect data for analysis using water temperature, depth level, chemical, biological, and physical properties. Some relevant parameters to monitor water quality are temperature, oxygen level, salinity, acidity, conductivity, pH level, oxygen concentration, and nitrogenous compounds such as ammonia, nitrate, and nitrite concentration. USVs are widely utilized to monitor water conditions such as surface flow and velocity measurement. DJI Phantom commercial unmanned system is the most preferred type based on the collected works of literature. There were also some customized unmanned systems. The common sensors used for UAVs are acoustic cameras but there are also some vehicles equipped with thermal cameras. To provide motion stability for data capturing using cameras, gimbal pitch can be added although this concern should be further investigated to provide better stability, most especially for AUVs. For water velocity captures, camera shakes are evident that causes distortions to images. The capacity to operate despite a strong water current or pressure should be fully considered in selecting an underwater vehicle. There are AUVs and ROVs that were designed for this condition, but it comes with a higher price. Others might consider choosing low-cost vehicles with fewer capabilities and strengths for economic considerations. Furthermore, UAVs are more sensitive to unpredictable weather conditions such as strong winds and rains since they operate in the air.

Many unmanned system performances have limitations in terms of power or battery, which affects the mission or operation due to longer navigation time and slower mission execution. Many countermeasures were devised to optimize the navigation time of UVs. Some integrate flight path planning to reduce flight time, sensor positioning, and trajectory optimizations. There are also solar-powered UVs with efficient solar cells for an increased power source for longer navigation coverage. Multiple drones could also be used during surveillance to address the drone's limitations in terms of navigation time. To correct image blurriness, low contrast, low visibility, and small-sized captures, image enhancement, and corrections to improve quality and reduce noise; deep learning and computer vision techniques and algorithms are capable of such functions.

There is no unmanned system capable of performing all aquaculture operations and functions. These systems can collaborate to perform complex tasks to increase robust-

ness and efficiency. Collaboration of heterogeneous vehicles can achieve larger scale and comprehensive monitoring. Despite many open issues for such kind of collaboration, the possibility of exploring its capability can help achieve high performance, adaptability, flexibility, and fault tolerance.

Different sensors were also presented, including their corresponding characteristics and limitations. Sensors are also susceptible to harsh weather conditions. For AUVs, sensors are affected by winds, waves, sea fog, and water reflection. There are various restoration methods in dealing with these concerns, such as incorporating image stabilization or image defogging. For water quality sensors, factors to consider in its integration can be low maintenance, low cost, low battery consumption, robust, waterproof, non-metallic, resistant to biofouling, and have no effects on organisms. The possibility of sensor fusion can be exploited to take advantage of UVs potentials and achieve higher precision.

Practicing awareness and continuous updates on the regulations must be practiced to avoid the legal implications of not following the law. The standardized policies for UVs operations are still not mature since regulations are different in each country although there are some common grounds. The wide range and varied types of UVs and their applications is an added challenge that requires operators and owners to be aware of the legal status and regulations of each operation. With a various and wide range of commercially available UVs in the market, compromise and trade-offs between the type of vehicle, installed sensors, power, manpower requirement, and cost are for the user's decision to weigh how to achieve maximum performance and potential based on their corresponding functions. To maximize the potential of a UV, each type should be maximized based on its strength and capabilities. There is no single unmanned system that can perform all the desired functions at once for aquaculture management and monitoring. Thus, each type can collaborate to achieve a bigger coverage for aquaculture monitoring and management. The integration of unmanned systems can be exploited to serve as a cutting-edge technology to provide robust, timely, efficient, reliable, and sustainable aquaculture. As these systems integrate more and more technologies, they can extend their functionalities to perform more capability for aquaculture production. UVs can be combined with sensors and robotics with artificial intelligence and deep learning techniques to process big data.

Unmanned systems are already widely used in fisheries science and marine conservation, such as megafauna, but the literature and research work on the application of such system in aquaculture can still be further explored to achieve maturity; more undertakings should be made for successful integration of such systems in the field of aquaculture. Although there were successful implementations that were stated in this work, state-of-the-art technologies and devices should continue for unmanned systems to provide better and more powerful aquaculture precision farming functionalities.

References

1.   FAO. *The State of World Fisheries and Aquaculture 2020. Sustainability in Action*; FAO: Rome, Italy, 2020. [CrossRef]
2.   Ahmed, N.; Thompson, S.; Glaser, M. Global Aquaculture Productivity, Environmental Sustainability, and Climate Change Adaptability. *Environ. Manag.* **2019**, *63*, 159–172. [CrossRef] [PubMed]
3.   Grealis, E.; Hynes, S.; ODonoghue, C.; Vega, A.; van Osch, S.; Twomey, C. The economic impact of aquaculture expansion: An input-output approach. *Mar. Policy* **2017**, *81*, 29–36. [CrossRef]
4.   Béné, C.; Arthur, R.; Norbury, H.; Allison, E.; Beveridge, M.; Bush, S.; Campling, L.; Leschen, W.; Little, D.; Squires, D.; et al. Contribution of Fisheries and Aquaculture to Food Security and Poverty Reduction: Assessing the Current Evidence. *World Dev.* **2016**, *79*, 179–196. [CrossRef]
5.   Kassam, L. Assessing the Contribution of Aquaculture to Poverty Reduction in Ghana. Ph.D. in Development Economics, University of London, London, UK, 2013. [CrossRef]
6.   Genschick, S.; Kaminski, A.; As, K.; Cole, S. *Aquaculture in Zambia: An Overview and Evaluation of the Sector's Responsiveness to the Needs of the Poor*; Working Paper: FISH-2017-08; CGIAR Research Program on Fish Agri-Food Systems: Penang, Malysia; Department of Fisheries: Lusaka, Zambia, 2017.
7.   Stevenson, J.; Irz, X. Is Aquaculture Development an Effective Tool for Poverty Alleviation? *A Review of Theory and Evidence. Cah. Agric.* **2009**, *18*, 292–299. [CrossRef]
8.   Sribhibhadh, A. Role of Aquaculture in Economic Development Within Southeast Asia. *J. Fish. Res. Board Can.* **2011**, *33*, 114. [CrossRef]
9.   FAO. *Commercial Aquaculture and Economic Growth, Poverty Alleviation and Food Securi: Assessment Framework. FAO Fisheries and Aquaculture Technical Paper*; FAO: Rome, Italy, 2009; ISBN 9251063370.
10.   Shamsuzzaman, M.M.; Mozumder, M.; Mitu, S.; Ahamad, A.; Bhyuian, S. The economic contribution of fish and fish trade in Bangladesh. *Aquac. Fish.* **2020**, *5*, 174–181. [CrossRef]
11.   Jennings, S.; Stentiford, G.; Leocadio, A.; Jeffery, K.; Metcalfe, J.; Katsiadaki, I.; Auchterlonie, N.; Mangi, S.; Pinnegar, J.; Ellis, T.; et al. Aquatic food security: Insights into challenges and solutions from an analysis of interactions between fisheries, aquaculture, food safety, human health, fish and human welfare, economy and environment. *Fish Fish.* **2016**, *17*, 893–938. [CrossRef]
12.   Pradeepkiran, J.A. Aquaculture role in global food security with nutritional value: A review. *Transl. Anim. Sci.* **2019**, *3*, 903–910. [CrossRef]
13.   Frankic, A.; Hershner, C. Sustainable aquaculture: Developing the promise of aquaculture. *Aquac. Int.* **2003**, *11*, 517–530. [CrossRef]
14.   FAO. *Report of the Consultation on the Application of Article 9 of the FAO Code of Conduct for Responsible Fisheries in the Mediterranean Region*; FAO: Rome, Italy, 1999.
15.   Gaertner-Mazouni, N.; De Wit, R. Exploring new issues for coastal lagoons monitoring and management. *Estuar. Coast. Shelf Sci.* **2012**, *114*, 1–6. [CrossRef]
16.   Perez-Ruzafa, A.; Marcos, C. Fisheries in coastal lagoons: An assumed but poorly researched aspect of the ecology and functioning of coastal lagoons. *Estuar. Coast. Shelf Sci.* **2012**, *110*, 15–31. [CrossRef]
17.   Aliaume, C.; Chi, D.; Viaroli, T.; Zaldívar, P. Coastal lagoons of Southern Europe: Recent changes and future scenarios. *Transit. Waters Monogr.* **2007**, *1*, 1–12. [CrossRef]
18.   Yin, G.; Ong, M.; Lee, J.; Kim, T. Numerical simulation of oxygen transport in land-based aquaculture tank. *Aquaculture* **2021**, *543*, 736973. [CrossRef]
19.   Fiander, L.; Graham, M.; Murray, H.; Boileau, R. Land based multi-trophic aquaculture research at the wave energy research centre. Available online: https://nrc-publications.canada.ca/fra/voir/objet/?id=543d494b-95b1-4c30-ab48-7463b14e29ab (accessed on 2 November 2021).
20.   Benetti, D.; Benetti, G.; Rivera, J.; Sardenberg, B.; O'Hanlon, B. Site Selection Criteria for Open Ocean Aquaculture. *Mar. Technol. Soc. J.* **2010**, *44*, 22–35. [CrossRef]
21.   Naylor, R.L.; Hardy, R.W.; Buschmann, A.H.; Bush, S.R.; Cao, L.; Klinger, D.H.; Little, D.C.; Lubchenco, J.; Shumway, S.E.; Troell, M. A 20-year retrospective review of global aquaculture. *Nature* **2021**, *591*, 551–563. [CrossRef]
22.   Baki, B.; Yucel, Ş. Feed cost/production income analysis of seabass (Dicentrarchus labrax) aquaculture. *Int. J. Ecosyst. Ecol. Sci.* **2017**, *7*, 859–864.
23.   Bjelland, H.A.; Føre, M.; Lader, P.; Kristiansen, D.; Holmen, I.; Fredheim, A.; Grøtli, E.; Fathi, D.; Oppedal, F.; Utne, I.; et al. Exposed Aquaculture in Norway. In Proceedings of the Oceans 2015 MTS/IEEE Washington, Washington, DC, USA, 19–22 October 2015; pp. 1–10. [CrossRef]
24.   FAO. FAO Training Series: Simple Methods for Aquaculture. Available online: https://www.fao.org/fishery/docs/CDrom/FAO_Training/FAOTraining/General/f1e.htm (accessed on 2 November 2021).
25.   Wang, C.; Li, Z.; Wang, T.; Xu, X.; Zhang, X.; Li, D. Intelligent fish farm—The future of aquaculture. *Aquacult. Int.* **2021**, *29*, 2681–2711. [CrossRef] [PubMed]
26.   Ubina, N.; Cheng, S.C.; Chang, C.C.; Chen, H.Y. Evaluating fish feeding intensity in aquaculture with convolutional neural networks. *Aquac. Eng.* **2021**, *94*, 102178. [CrossRef]
27.   Joffre, O.; Klerkx, L.; Dickson, M.; Verdegem, M. How is innovation in aquaculture conceptualized and managed? A systematic literature review and reflection framework to inform analysis and action. *Aquaculture* **2017**, *470*, 128–148. [CrossRef]

28. Yang, X.; Song, Z.; Liu, J.; Gao, Q.; Dong, S.; Zhou, C. Deep learning for smart fish farming: Applications, opportunities and challenges. *Rev. Aquac.* **2020**, *13*, 12464. [CrossRef]
29. Cai, Y.-E.; Juang, J.-G. Path planning and obstacle avoidance of UAV for cage culture inspection. *J. Mar. Sci. Technol.* **2020**, *28*, 14. [CrossRef]
30. Ubina, N.A.; Cheng, S.-C.; Chen, H.-Y.; Chang, C.-C.; Lan, H.-Y. A Visual Aquaculture System Using a Cloud-Based Autonomous Drones. *Drones* **2021**, *5*, 109. [CrossRef]
31. Føre, M.; Frank, K.; Norton, T.; Svendsen, E.; Alfredsen, J.A.; Dempsterd, T.; Eguiraun, H.; Watsong, W.; Stahlb, A.; Sundea, L.M.; et al. Precision fish farming: A new framework to improve production in aquaculture. *Biosyst. Eng.* **2018**, *173*, 176–193. [CrossRef]
32. O'Donncha, F.; Grant, J. Precision Aquaculture. *IEEE Internet Things Mag.* **2019**, *2*, 26–30. [CrossRef]
33. Murugan, D.; Garg, A.; Singh, D. Development of an Adaptive Approach for Precision Agriculture Monitoring with Drone and Satellite Data. *IEEE J. Sel. Top. Appl. Earth Obs. Remote Sens.* **2017**, *10*, 5322–5328. [CrossRef]
34. Krishna, K.R. *Agricultural Drones, A Peaceful Pursuit*, 1st ed.; Apple Academic Press, Inc.: Palm Bay, FL, USA, 2021; ISBN 97801077188-595-0.
35. Ko, Y.; Kim, J.; Duguma, D.G.; Astillo, P.V.; You, I.; Pau, G. Drone Secure Communication Protocol for Future Sensitive Applications in Military Zone. *Sensors* **2021**, *21*, 2057. [CrossRef] [PubMed]
36. Choudhary, G.; Sharma, V.; You, I. Sustainable and secure trajectories for the military Internet of Drones (IoD) through an efficient Medium Access Control (MAC) protocol. *Comput. Electr. Eng.* **2019**, *74*, 59–73. [CrossRef]
37. Liu, C.-C.; Chen, J.-J. Analysis of the Weights of Service Quality Indicators for Drone Filming and Photography by the Fuzzy Analytic Network Process. *Appl. Sci.* **2019**, *9*, 1236. [CrossRef]
38. Cokyasar, T. Optimization of battery swapping infrastructure for e-commerce drone delivery. *Comput. Commun.* **2021**, *168*, 146–154. [CrossRef]
39. Wang, D.; Hu, P.; Du, J.; Zhou, P.; Deng, T.; Hu, M. Routing and Scheduling for Hybrid Truck-Drone Collaborative Parcel Delivery With Independent and Truck-Carried Drones. *IEEE Internet Things J.* **2019**, *6*, 10483–10495. [CrossRef]
40. Rahman, M.S.; Khalil, I.; Atiquzzaman, M. Blockchain-Powered Policy Enforcement for Ensuring Flight Compliance in Drone-Based Service Systems. *IEEE Netw.* **2021**, *35*, 116–123. [CrossRef]
41. Pan, Q.; Wen, X.; Lu, Z.; Li, L.; Jing, W. Dynamic Speed Control of Unmanned Aerial Vehicles for Data Collection under Internet of Things. *Sensors* **2018**, *18*, 3951. [CrossRef]
42. Yao, J.; Ansari, N. QoS-Aware Power Control in Internet of Drones for Data Collection Service. *IEEE Trans. Veh. Technol.* **2019**, *68*, 6649–6656. [CrossRef]
43. Kurt, A.; Saputro, N.; Akkaya, K.; Uluagac, A.S. Distributed Connectivity Maintenance in Swarm of Drones During Post-Disaster Transportation Applications. *IEEE Trans. Intell. Transp. Syst.* **2021**, *22*, 6061–6073. [CrossRef]
44. Maddikunta, P.K.R.; Hakak, S.; Alazab, M.; Bhattacharya, S.; Gadekallu, T.R.; Khan, W.Z.; Pham, Q. Unmanned Aerial Vehicles in Smart Agriculture: Applications, Requirements, and Challenges. *IEEE Sens. J.* **2021**, *21*, 17608–17619. [CrossRef]
45. Avanzato, R.; Beritelli, F. An Innovative Technique for Identification of Missing Persons in Natural Disaster Based on Drone-Femtocell Systems. *Sensors* **2019**, *19*, 4547. [CrossRef]
46. de Lima, R.L.P.; Paxinou, K.; Boogaard, C.F.; Akkerman, O.; Lin, F.-Y. In-Situ Water Quality Observations under a Large-Scale Floating Solar Farm Using Sensors and Underwater Drones. *Sustainability* **2021**, *13*, 6421. [CrossRef]
47. Chang, C.C.; Wang, J.H.; Wu, J.L.; Hsieh, Y.Z.; Wu, T.D.; Cheng, S.C.; Chang, C.C.; Juang, J.G.; Liou, C.H.; Hsu, T.H.; et al. Applying Artificial Intelligence (AI) Techniques to Implement a Practical Smart Cage Aquaculture Management System. *J. Med. Biol. Eng.* **2021**, *41*, 652–658. [CrossRef]
48. Verfuß, U.K.; Aniceto, A.S.; Harris, D.V.; Gillespie, D.; Fielding, S.; Jiménez, G.; Johnston, P.F.; Sinclair, R.R.; Sivertsen, A.; Solbo, S.; et al. A review of unmanned vehicles for the detection and monitoring of marine fauna. *Mar. Pollut. Bull.* **2019**, *140*, 17–29. [CrossRef]
49. Nicholls, R.; Ryan, J.; Mumm, H.; Lonstein, W.; Carter, C.; Shay, J.; Mai, R.; Hood, J.-P.; Jackson, M. *Unmanned Vehicle Systems and Operations on Air, Sea and Land*; New Prairie Press (Kansas State University): Manhattan, KS, USA, 2020; ISBN 978-1-944548-30-8.
50. Verfuss, U.K.; Aniceto, A.S.; Biuw, M.; Fielding, S.; Gillespie, D.; Harris, D.; Jimenez, G.; Johnston, P.; Plunkett, R.; Sivertsen, A.; et al. Wyatt Literature Review: Understanding the Current State of Autonomous Technologies to Improve/Expand Observation and Detection of Marine Species. Available online: https://fdocuments.in/document/literature-review-understanding-the-current-state-literature-review-understanding.html (accessed on 2 December 2021).
51. Jones, G.P.; Pearlstine, L.G.; Percival, H.F. An assessment of small unmanned aerial vehicles for wildlife research. *Wildl. Soc. Bull.* **2006**, *34*, 750–758. [CrossRef]
52. Otto, A.; Agatz, N.; Campbell, J.; Goden, B.; Pesch, E. Optimization approaches for civil applicates of unmanned aerial vehicles (UAVs) or aerial drones: A survey. *Networks* **2018**, *72*, 411–458. [CrossRef]
53. Savkin, A.V.; Huang, H. Proactive Deployment of Aerial Drones for Coverage over Very Uneven Terrains: A Version of the 3D Art Gallery Problem. *Sensors* **2019**, *19*, 1438. [CrossRef] [PubMed]
54. Watts, A.; Perry, J.; Smith, S.; Burgess, M.; Wilkinson, B.; Szantoi, Z.; Ifju, P.; Percival, H. Small Unmanned Aircraft Systems for Low-Altitude Aerial Surveys. *J. Wildl. Manag.* **2010**, *74*, 1614–1619. [CrossRef]
55. Colomina, I.; Molina, P. Unmanned aerial systems for photogrammetry and remote sensing: A review. *ISPRS J. Photogramm. Remote Sens.* **2014**, *92*, 79–97. [CrossRef]

56. Johnston, D. Unoccupied Aircraft Systems in Marine Science and Conservation. *Annu. Rev. Mar. Sci.* **2019**, *11*, 439–463. [CrossRef]
57. Klaer, P.; Huang, A.; Sévigny, P.; Rajan, S.; Pant, S.; Patnaik, P.; Balaji, B. An Investigation of Rotary Drone HERM Line Spectrum under Manoeuvering Conditions. *Sensors* **2020**, *20*, 5940. [CrossRef] [PubMed]
58. Delavarpour, N.; Koparan, C.; Nowatzki, J.; Bajwa, S.; Sun, X. A Technical Study on UAV Characteristics for Precision Agriculture Applications and Associated Practical Challenges. *Remote Sens.* **2021**, *13*, 1204. [CrossRef]
59. Panda, J.P.; Mitra, A.; Warrior, H.V. A review on the hydrodynamic characteristics of autonomous underwater vehicles. *Proc. Inst. Mech. Eng. Part M J. Eng. Marit. Environ.* **2020**, *235*, 15–29. [CrossRef]
60. Niu, H.; Adams, S.; Lee, K.; Husain, T.; Bose, N. Applications of Autonomous Underwater Vehicles in Offshore Petroleum Industry Environmental Effects Monitoring. *J. Can. Pet. Technol.* **2007**, *48*, 12–16. [CrossRef]
61. Bahr, A.; Leonard, J.J.; Fallon, M.F. Cooperative Localization for Autonomous Underwater Vehicles. *Int. J. Robot. Res.* **2009**, *28*, 714–728. [CrossRef]
62. Jung, J.; Park, J.; Choi, J.; Choi, H. Autonomous Mapping of Underwater Magnetic Fields Using a Surface Vehicle. *IEEE Access* **2018**, *6*, 62552–62563. [CrossRef]
63. González-García, J.; Gómez-Espinosa, A.; Cuan-Urquizo, E.; García-Valdovinos, L.G.; Salgado-Jiménez, T.; Cabello, J.A.E. Autonomous Underwater Vehicles: Localization, Navigation, and Communication for Collaborative Missions. *Appl. Sci.* **2020**, *10*, 1256. [CrossRef]
64. Bernalte Sánche, P.; Papaelias, M.; García Márquez, F.P. Autonomous underwater vehicles: Instrumentation and measurements. *IEEE Instrum. Meas. Mag.* **2020**, *23*, 105–114. [CrossRef]
65. Manley, J.E. Unmanned surface vehicles, 15 years of development. In Proceedings of the OCEANS 2008, Quebec, QC, Canada, 15–18 September 2008; pp. 1–4. [CrossRef]
66. Zhu, M.; Wen, Y.-Q. Design and Analysis of Collaborative Unmanned Surface-Aerial Vehicle Cruise Systems. *J. Adv. Transp.* **2019**, *2019*, 1323105. [CrossRef]
67. Ma, S.; Guo, W.; Song, R.; Liu, Y. Unsupervised learning based coordinated multi-task allocation for unmanned surface vehicles. *Neurocomputing* **2021**, *420*, 227–245. [CrossRef]
68. Breivik, M.; Hovstein, V.; Fossen, T. Straight-Line Target Tracking for Unmanned Surface Vehicles. *Model. Identif. Control.* **2008**, *29*, 131–149. [CrossRef]
69. Li, P.; Wu, X.; Shen, W.; Tong, W.; Guo, S. Collaboration of Heterogeneous Unmanned Vehicles for Smart Cities. *IEEE Netw.* **2019**, *33*, 133–137. [CrossRef]
70. Yeong, D.J.; Velasco-Hernandez, G.; Barry, J.; Walsh, J. Sensor and Sensor Fusion Technology in Autonomous Vehicles: A Review. *Sensors* **2021**, *21*, 2140. [CrossRef]
71. Balestrieri, E.; Daponte, P.; De Vito, L.; Lamonaca, F. Sensors and Measurements for Unmanned Systems: An Overview. *Sensors* **2021**, *21*, 1518. [CrossRef]
72. Martin, B.; Tarraf, D.; Whitmore, T.; Deweese, J.; Kenney, C.; Schmid, J.; DeLuca, P. *Advancing Autonomous Systems: An Analysis of Current and Future Technology for Unmanned Maritime Vehicles*; RAND Corporation: Santa Monica, CA, USA, 2019.
73. Molina, P.; Fortuny, P.; Colomina, I.; Remy, M.; Camara de Macedo, K.; Zúnigo, Y.; Vaz, E.; Luebeck, D.; Moreira, J.; Blázquez, M. Navigation and remote sensing payloads and methods of the SARVANT unmanned aerial system. *ISPRS-Int. Arch. Photogramm. Remote Sens. Spat. Inf. Sci.* **2013**, *11*, 275–280. [CrossRef]
74. Chen, L.; Wang, S.; McDonald-Maier, K.; Hu, H. Towards autonomous localization and mapping of AUVs: A survey. *Int. J. Intell. Unmanned Syst.* **2013**, *1*, 97–120. [CrossRef]
75. Kapoor, R.; Ramasamy, S.; Gardi, A.; Schyndel, R.V.; Sabatini, R. Acoustic Sensors for Air and Surface Navigation Applications. *Sensors* **2018**, *18*, 499. [CrossRef] [PubMed]
76. Kapoor, R.; Gardi, A.; Sabatini, R. Network Optimisation and Performance Analysis of a Multistatic Acoustic Navigation Sensor. *Sensors* **2020**, *20*, 5718. [CrossRef]
77. Hosseini, N.; Jamal, H.; Haque, J.; Magesacher, T.; Matolak, D.W. UAV Command and Control, Navigation and Surveillance: A Review of Potential 5G and Satellite Systems. In Proceedings of the 2019 IEEE Aerospace Conference, Big Sky, MT, USA, 2–9 March 2019; pp. 1–10. [CrossRef]
78. Chen, C.; Jafari, R.; Kehtarnavaz, N. Improving Human Action Recognition Using Fusion of Depth Camera and Inertial Sensors. *IEEE Trans. Hum. Mach. Syst.* **2015**, *45*, 51–61. [CrossRef]
79. Jung, J.; Lee, J.Y.; Jeong, Y.; Kweon, I.S. Time-of-Flight Sensor Calibration for a Color and Depth Camera Pai. *IEEE Trans. Pattern Anal. Mach. Intell.* **2015**, *37*, 1501–1513. [CrossRef]
80. Araguás, G.; Paz, C.; Gaydou, D.; Paina, G.P. Quaternion-based Orientation Estimation Fusing a Camera and Inertial Sensors for a Hovering UAV. *J. Intell. Robot. Syst.* **2015**, *77*, 37–53. [CrossRef]
81. Liu, Z.; Zhang, R.; Wang, Z.; Guan, L.; Li, B.; Chu, J. Integrated polarization-dependent sensor for autonomous navigation. *J. Micro/Nanolithogr. MEMS MOEMS* **2015**, *14*, 015001. [CrossRef]
82. Li, S.; Liu, Z. Autonomous navigation and guidance scheme for precise and safe planetary landing. *Aircr. Eng. Aerosp. Technol.* **2019**, *81*, 516–521. [CrossRef]
83. Liu, O.; Yuan, S.; Li, Z. A Survey on Sensor Technologies for Unmanned Ground Vehicles. In Proceedings of the 2020 3rd International Conference on Unmanned Systems (ICUS), Harbin, China, 27–28 November 2020; pp. 638–645. [CrossRef]

84. Qiu, R.; Wei, S.; Zhang, M.; Li, H.; Sun, H.; Liu, G.; Li, M. Sensors for measuring plant phenotyping: A review. *Int. J. Agric. Biol. Eng.* **2018**, *11*, 1–17. [CrossRef]
85. Liu, Z.; Zhang, Y.; Yu, X.; Yuan, C. Unmanned surface vehicles: An overview of developments and challenges. *Annu. Rev. Control* **2016**, *41*, 71–93. [CrossRef]
86. Saberioon, M.; Gholizadeh, A.; Cisar, P.; Pautsina, A.; Urban, J. Application of Machine Vision Systems in Aquaculture with Emphasis on Fish: State-of-the-Art and Key Issues. *Rev. Aquac.* **2017**, *9*, 369–387. [CrossRef]
87. Furukawa, F.; Laneng, L.A.; Ando, H.; Yoshimura, N.; Kaneko, M.; Morimoto, J. Comparison of RGB and Multispectral Unmanned Aerial Vehicle for Monitoring Vegetation Coverage Changes on a Landslide Area. *Drones* **2021**, *5*, 97. [CrossRef]
88. Ferrete Ribeiro, N.; Santos, C. Inertial measurement units: A brief state of the art on gait analysis. In Proceedings of the 2017 IEEE 5th Portuguese Meeting on Bioengineering, University of Coimbra, Coimbra, Portugal, 16–18 February 2017; pp. 1–4. [CrossRef]
89. Kumar, D.; Singh, R.; Kaur, R. Global Positioning System. In *Spatial Information Technology for Sustainable Development Goals*; Sustainable Goals Series; Springer International Publishing AG: Berlin/Heidelberg, Germany, 2019. [CrossRef]
90. Kruse, P. Review on water quality sensors. *J. Phys. D Appl. Phys.* **2018**, *51*, 203002. [CrossRef]
91. Bhardwaj, J.; Gupta, K.K.; Gupta, R. A review of emerging trends on water quality measurement sensors. In Proceedings of the 2015 International Conference on Technologies for Sustainable Development (ICTSD), Mumbai, India, 4–6 February 2015; pp. 1–6. [CrossRef]
92. Parra, L.; Lloret, G.; Lloret, J.; Rodilla, M. Physical Sensors for Precision Aquaculture: A Review. *IEEE Sens. J.* **2018**, *18*, 3915–3923. [CrossRef]
93. O'Donncha, F.; Stockwell, C.L.; Planellas, S.R.; Micallef, G.; Palmes, P.; Webb, C.; Filgueira, R.; Grant, J. Data Driven Insight Into Fish Behaviour and Their Use for Precision Aquaculture. *Front. Anim. Sci.* **2021**, *2*, 695054. [CrossRef]
94. Moheddine, A.; Patrone, F.; Marchese, M. UAV and IoT Integration: A Flying Gateway. In Proceedings of the 26th IEEE International Conference on Electronics, Circuits and Systems (ICECS), Genova, Italy, 27–29 November 2019; pp. 121–122. [CrossRef]
95. Motlagh, N.H.; Bagaa, M.; Taleb, T. UAV based IoT platform: A crowd surveillance use case. *IEEE Commun. Mag.* **2017**, *55*, 128–134. [CrossRef]
96. Qazi, S.; Siddiqui, A.S.; Wagan, A.I. UAV based real time video surveillance over 4G LTE. In Proceedings of the 2015 International Conference on OpenSource Systems & Technologies (ICOSST), Lahore, Pakistan, 17–19 December 2015; pp. 141–145. [CrossRef]
97. Min, H.; Jung, J.; Kim, B.; Hong, J.; Heo, J. Dynamic Rendezvous Node Estimation for Reliable Data Collection of a Drone as a Mobile IoT Gateway. *IEEE Access* **2019**, *7*, 184285–184293. [CrossRef]
98. Ytrestøyl, T.; Takle, H.; Kolarevic, J.; Calabrese, S.; Timmerhaus, G.; Rosseland, B.O.; Teien, H.C.; Nilsen, T.O.; Handeland, S.O.; Stefansson, S.O.; et al. Performance and welfare of Atlantic salmon (Salmo salar) post-smolts in RAS; importance of salinity and water velocity. *J. World Aquac. Soc.* **2020**, *51*, 12682. [CrossRef]
99. Detertm, M.; Weitbrecht, V. A low-cost airborne velocimetry system: Proof of concept. *J. Hydraul. Res.* **2015**, *53*, 532–539. [CrossRef]
100. Yan, C.; Fu, L.; Zhang, J.; Wang, J. A Comprehensive Survey on UAV Communication Channel Modeling. *IEEE Access* **2019**, *7*, 107769–107792. [CrossRef]
101. Behjati, M.; Mohd Noh, A.B.; Alobaidy, H.A.H.; Zulkifley, M.A.; Nordin, R.; Abdullah, N.F. LoRa Communications as an Enabler for Internet of Drones towards Large-Scale Livestock Monitoring in Rural Farms. *Sensors* **2021**, *21*, 5044. [CrossRef] [PubMed]
102. Sanchez-Iborra, R.; Sanchez-Gomez, J.; Ballesta-Viñas, J.; Cano, M.-D.; Skarmeta, A.F. Performance Evaluation of LoRa Considering Scenario Conditions. *Sensors* **2018**, *18*, 772. [CrossRef] [PubMed]
103. Rompagroup. Internet of Things Part 3: LPWAN Technogies. Available online: https://www.rompagroup.com/news/internet-of-things-part-3-lpwan-technologies.aspx (accessed on 28 November 2021).
104. Mekki, K.; Bajic, E.; Chaxel, F.; Meyer, F. A comparative study of LPWAN technologies for large-scale IoT deployment. *ICT Express* **2019**, *5*, 1–7. [CrossRef]
105. Digi. A Comparison of LPWAN Technologies. Available online: https://www.digi.com/blog/post/lpwan-technology-comparison (accessed on 28 November 2021).
106. Sharma, A.; Vanjani, P.; Paliwal, N.; Wijerathn Basnayaka, C.M.; Jayakody, D.N.; Wang, H.-C.; Muthuchidambaranathan, P. Communication and Networking Technologies for UAVs: A Survey. *J. Netw. Comput. Appl.* **2020**, *168*, 102739. [CrossRef]
107. Niu, B.; Li, G.; Peng, F.; Wu, J.; Zhang, L.; Li, Z. Survey of Fish Behavior Analysis by Computer Vision. *J. Aquac. Res. Dev.* **2018**, *9*, 1000534. [CrossRef]
108. Manna, D.; Maiti, A.; Samanta, G.P. Analysis of a predator-prey model for exploited fish populations with schooling behavior. *J. Appl. Math. Comput.* **2018**, *317*, 35–48. [CrossRef]
109. Banerjee, S.; Alvey, L.; Brown, P.; Yue, S. An assistive computer vision tool to automatically detect changes in fish behavior in response to ambient odor. *Sci. Rep.* **2021**, *11*, 1002. [CrossRef] [PubMed]
110. Xu, J.; Liu, Y.; Cui, S.; Miao, X. Behavioral responses of tilapia (Oreochromis niloticus) to acute fluctuations in dissolved oxygen levels as monitored by computer vision. *Aquac. Eng.* **2006**, *35*, 207–217. [CrossRef]
111. Pinkiewicz, T.; Purser, J.; Williams, R.N. A computer vision system to analyse the swimming behaviour of farmed fish in commercial aquaculture facilities: A case study using cage-held Atlantic salmon. *Aquac. Eng.* **2011**, *45*, 20–27. [CrossRef]

112. Zhao, J.; Bao, W.; Zhang, F.; Ye, Z.; Liu, Y.; Shen, M.; Zhu, S. Assessing appetite of the swimming fish based on spontaneous collective behaviors in a recirculating aquaculture system. *Aquac. Eng.* **2017**, *78*, 118–124. [CrossRef]
113. Jakka, N.; Rao, T.; Rao, J. Locomotor Behavioral Response of Mosquitofish (Gambusia affinis) to Subacute Mercury Stress Monitored by Video Tracking System. *Drug Chem. Toxicol.* **2007**, *30*, 383–397. [CrossRef] [PubMed]
114. Israeli, D.; Kimmel, E. Monitoring the behavior of hypoxia-stressed Carassius auratus using computer vision. *Aquac. Eng.* **1996**, *16*, 423–440. [CrossRef]
115. Kane, A.S.; Salierno, J.D.; Gipson, G.T.; Molteno, T.C.A.; Hunter, C. A video-based movement analysis system to quantify behavioral stress responses of fish. *Water Res.* **2004**, *38*, 3993–4001. [CrossRef]
116. Ben-Simon, A.; Ben-Shahar, O.; Segev, R. Measuring and tracking eye movements of a behaving archer fish by real-time stereo vision. *J. Neurosci. Meth.* **2009**, *184*, 235–243. [CrossRef] [PubMed]
117. AlZubi, H.; Al-Nuaimy, W.; Buckley, J.; Sneddon, L.; Young, I. Real-time 3D fish tracking and behaviour analysis. In Proceedings of the 2015 IEEE Jordan Conference on Applied Electrical Engineering and Computing Technologies (AEECT), Amman, Jordan, 3–5 November 2015; pp. 1–5. [CrossRef]
118. Ziyi, L.; Xian, L.; Liangzhong, F.; Huanda, L.; Li, L.; Ying, L. Measuring feeding activity of fish in RAS using computer vision. *Aquac. Eng.* **2014**, *60*, 20–27. [CrossRef]
119. Wang, G.; Muhammad, A.; Liu, C.; Du, L.; Li, D. Automatic Recognition of Fish Behavior with a Fusion of RGB and Optical Flow Data Based on Deep Learning. *Animals* **2021**, *11*, 2774. [CrossRef]
120. Parsonage, K.D.; Petrell, R.J. Accuracy of a machine-vision pellet detection system. *Aquac. Eng.* **2003**, *29*, 109–123. [CrossRef]
121. Skøien, K.; Alver, M.; Zolich, A.; Alfredsen, J.A. Feed spreaders in sea cage aquaculture—Motion characterization and measurement of spatial pellet distribution using an unmanned aerial vehicle. *Comput. Electron. Agric.* **2016**, *129*, 27–36. [CrossRef]
122. Difford, G.F.; Boison, S.A.; Khaw, H.L.; Gjerde, B. Validating non-invasive growth measurements on individual Atlantic salmon in sea cages using diode frames. *Comput. Electron. Agric.* **2020**, *173*, 105411. [CrossRef]
123. Azzaydi, M.; Madrid, J.A.; Zamora, S.; Sánchez-Vázquez, F.J.; Mart Nez, F.J. Effect of three feeding strategies (automatic, ad libitum demand-feeding and time-restricted demand-feeding) on feeding rhythms and growth in European sea bass (Dicentrarchus labrax L). *Aquaculture* **1998**, *163*, 285–296. [CrossRef]
124. Ditria, E.M.; Lopez-Marcano, S.; Sievers, M.; Jinks, E.L.; Brown, C.J.; Connolly, R.M. Automating the Analysis of Fish Abundance Using Object Detection: Optimizing Animal Ecology with Deep Learning. *Front. Mar. Sci.* **2020**. [CrossRef]
125. Connolly, R.; Fairclough, D.; Jinks, E.; Ditria, E.; Jackson, G.; Lopez-Marcano, S.; Olds, A.; Jinks, K. Improved accuracy for automated counting of a fish in baited underwater videos for stock assessment. *Front. Mar. Sci.* **2021**, *8*, 1511. [CrossRef]
126. Fan, L.; Liu, Y. Automate fry counting using computer vision and multi-class least squares support vector machine. *Aquaculture* **2013**, *380–383*, 91–98. [CrossRef]
127. Almansa, C.; Reig, L.; Oca, J. The laser scanner is a reliable method to estimate the biomass of a Senegalese sole (Solea senegalensis) population in a tank. *Aquac. Eng.* **2015**, *69*, 78–83. [CrossRef]
128. Gümüş, E.; Yılayaz, A.; Kanyılmaz, M.; Gümüş, B.; Balaban, M.O. Evaluation of body weight and color of cultured European catfish (Silurus glanis) and African catfish (Clarias gariepinus) using image analysis. *Aquac. Eng.* **2021**, 93. [CrossRef]
129. Zhang, L.; Wang, J.; Duan, Q. Estimation for fish mass using image analysis and neural network. *Comput. Electron. Agric.* **2020**, *173*, 105439. [CrossRef]
130. Costa, C.; Antonucci, F.; Boglione, C.; Menesatti, P.; Vandeputte, M.; Chatain, B. Automated sorting for size, sex and skeletal anomalies of cultured seabass using external shape analysis. *Aquac. Eng.* **2013**, *52*, 58–64. [CrossRef]
131. Shieh, A.; Petrell, R.J. Measurement of fish size in atlantic salmon (Salmo salar l.) cages using stereographic video techniques. *Aquac. Eng.* **1998**, *17*, 29–43. [CrossRef]
132. Måløy, H.; Aamodt, A.; Misimi, E. A spatio-temporal recurrent network for salmon feeding action recognition from underwater videos in aquaculture. *Comput. Electron. Agric.* **2019**, *167*, 105087. [CrossRef]
133. Lopez-Marcano, S.; Jinks, E.L.; Buelow, C.A.; Brown, C.J.; Wang, D.; Kusy, B.; Ditria, E.M.; Connolly, R.M. Automatic detection of fish and tracking of movement for ecology. *Ecol. Evol.* **2021**, *11*, 8254–8263. [CrossRef]
134. Provost, E.J.; Butcher, P.A.; Coleman, M.A.; Bloom, D.; Kelaher, B.P. Aerial drone technology can assist compliance of trap fisheries. *Fish. Manag. Ecol.* **2020**, *27*, 12420. [CrossRef]
135. Bloom, D.; Butcher, P.A.; Colefax, A.P.; Provost, E.J.; Cullis, B.R.; Kelaher, B.P. Drones detect illegal and derelict crab traps in a shallow water estuary. *Fish. Manag. Ecol.* **2019**, *26*, 311–318. [CrossRef]
136. Wong, P.; Nguyen, D.; Abukmail, A.; Brown, R.; Ryan, R.; Pagnutti, M. Low Cost Unmanned Aerial Vehicle Monitoring Using Smart Phone Technology. In Proceedings of the 2015 12th International Conference on Information Technology—New Generations, Las Vegas, NV, USA, 13–15 April 2015; pp. 286–291. [CrossRef]
137. Saska, M.; Krajník, T.; Faigl, J.; Vonásek, V.; Přeučil, L. Low-cost MAV platform AR-drone in experimental verifications of methods for vision based autonomous navigation. In Proceedings of the 2012 IEEE/RSJ International Conference on Intelligent Robots and Systems, Vilamoura-Algarve, Portugal, 7–12 October 2012; pp. 4808–4809. [CrossRef]
138. Toonen, H.M.; Bush, S.R. The digital frontiers of fisheries governance: Fish attraction devices, drones and satellites. *J. Environ. Policy Plan.* **2018**, *22*, 1–13. [CrossRef]
139. Gallego, A.-J.; Pertusa, A.; Gil, P. Automatic Ship Classification from Optical Aerial Images with Convolutional Neural Networks. *Remote Sens.* **2018**, *10*, 511. [CrossRef]

140. Marques, J.S.; Bernardino, A.; Cruz, G.; Bento, M. An algorithm for the detection of vessels in aerial images. In 2014 Proceedings of the 11th IEEE International Conference on Advanced Video and Signal Based Surveillance (AVSS), Seoul, Korea, 26–29 October 2014; pp. 295–300. [CrossRef]

141. Prayudi, A.; Sulistijono, I.A.; Risnumawan, A.; Darojah, Z. Surveillance System for Illegal Fishing Prevention on UAV Imagery Using Computer Vision. In Proceedings of the 2020 International Electronics Symposium (IES), Surabaya, Indonesia, 29–30 September 2020; pp. 385–391. [CrossRef]

142. Jossart, J.; Theuerkauf, S.J.; Wickliffe, L.C.; Morris, J.A., Jr. Applications of Spatial Autocorrelation Analyses for Marine Aquaculture Siting. *Front. Mar. Sci.* **2020**, *6*, 806. [CrossRef]

143. Nex, F.; Remondino, F. UAV for 3D mapping applications: A review. *Appl. Geomat.* **2014**, *6*, 1–15. [CrossRef]

144. Madawalagama, S.; Munasinghe, N.; Dampegama, S.; Samarakoon, L. Low-cost aerial mapping with consumer-grade drones. In Proceedings of the 37th Asian Conference on Remote Sensing, Colombo, Sri Lanka, 17–21 October 2016.

145. Zongijan, L. UAV for mapping—Low altitude photogrammetric survey. *Int. Arch. Photogramm. Remote Sens. Spat. Inf. Sci.* **2008**, *37*, 1183–1186.

146. Chen, H.-Y.; Cheng, S.-C.; Chang, C.-C. Semantic scene modeling for aquaculture management using an autonomous drone. In Proceedings of the International Workshop on Advanced Imaging Technologies 2020 (IWAIT 2020), Yogyakarta, Indonesia, 5–7 January 2020; Volume 11515, p. 18. [CrossRef]

147. Chen, C.-X.; Juang, J.-G. Vision Based Target Recognition for Cage Aquaculture Detection. *J. Mar. Sci. Technol.* **2020**, *28*, 2. [CrossRef]

148. Shelby, K.; Staci, L. WDFW to Use Drone to Count Spawning of Salmon Nests. 2020. Available online: https://wdfw.wa.gov/news/wdfw-use-drone-count-spawning-salmon-nests-0 (accessed on 15 November 2021).

149. Yamamoto, I.; Morinaga, A.; Lawn, M. Agile ROV for underwater surveillance. *J. Mar. Sci. Technol.* **2020**, *28*, 3. [CrossRef]

150. Gou, H.-Y. Drone Applications in Farming Management in Taiwan. Food and Fertilizer Technology Center for the Asian and Pacific Region. Available online: https://ap.fftc.org.tw/article/1640 (accessed on 22 November 2021).

151. Ahilan, T.; Adityan, V.A.; Kailash, S. Efficient Utilization of Unmanned Aerial Vehicle (UAV) for Fishing through Surveillance for Fishermen. *Int. J. Aerosp. Mec. Eng.* **2015**, *9*, 1468–1471.

152. Robertis, A.; Lawrence-Slavas, N.; Jenkins, R.; Wangen, I.; Calvin, W.; Mordy, C.M.; Meinig, C.; Levine, M.; Peacock, D.; Tabisola, H. Long-term measurements of fish backscatter from Saildrone unmanned surface vehicles and comparison with observations from a noise-reduced research vessel. *ICES J. Mar. Sci.* **2019**, *76*, 2459–2470. [CrossRef]

153. Livanos, G.; Zervakis, M.; Chalkiadakis, V.; Moirogiorgou, K.; Giakos, G.; Papandroulakis, N. Intelligent Navigation and Control of a Prototype Autonomous Underwater Vehicle for Automated Inspection of Aquaculture net pen cages. In Proceedings of the 2018 IEEE International Conference on Imaging Systems and Techniques (IST), Krakow, Poland, 16–18 October 2018; pp. 1–6. [CrossRef]

154. Kellaris, A.; Gil, A.; Faria, L.; Amaral, R.; Moreu, I.; Neto, A.I.; Yesson, C. Using low-cost drones to monitor heterogeneous submerged seaweed habitats: A case study in the Azores. *Aquat. Conserv. Mar. Freshw. Ecosyst.* **2019**, *29*, 1909–1922. [CrossRef]

155. Percy, D.R.; Hishamunda, N.; Kuemlangan, B. Governance in marine aquaculture: The legal dimension. In *Expanding Mariculture Farther Offshore: Technical, Environmental, Spatial and Governance Challenges, Proceedings of the FAO Technical Workshop, Orbetello, Italy, 22–25 March 2010*; Lovatelli, A., Aguilar-Manjarrez, J., Soto, D., Eds.; FAO Fisheries and Aquaculture Proceedings No. 24; FAO: Rome, Italy, 2013; pp. 245–262.

156. Chu, Y.; Wang, C.M.; Park, J.C.; Lader, P. Review of cage and containment tank designs for offshore fish farming. *Aquaculture* **2020**, *519*, 734928. [CrossRef]

157. Holmer, M. Environmental issues of fish farming in offshore waters: Perspectives, concerns and research needs. *Aquac. Environ. Interact.* **2010**, *1*, 57–70. [CrossRef]

158. Marine Fish Farms—Requirements for Site Survey Analyses, Design, Dimensioning, Production, Installation and Operation. *Reference Number NS 9415:2009*; Standards Norway: Lillesand, Norway, 2009.

159. Gupta, A.; Afrin, T.; Scully, E.; Yodo, N. Advances of UAVs toward Future Transportation: The State-of-the-Art, Challenges, and Opportunities. *Future Transp.* **2021**, *1*, 326–350. [CrossRef]

160. Fotouhi, A.; Qiang, H.; Ding, M.; Hassan, M.; Giordano, L.G.; Garcia-Rodriguez, A.; Yuan, J. Survey on UAV Cellular Communications: Practical Aspects, Standardization Advancements, Regulation, and Security Challenges. *IEEE Commun. Surv. Tutor.* **2019**, *21*, 3417–3442. [CrossRef]

161. Shi, Y.; Thomasson, J.; Murray, S.; Pugh, N.; Rooney, W.; Rajan, N.; Gregory, R.; Morgan, C.; Neely, H.; Rana, A.; et al. Unmanned Aerial Vehicles for High-Throughput Phenotyping and Agronomic Research. *PLoS ONE* **2016**, *11*, e0159781. [CrossRef]

162. Zhang, C.; Kovacs, J.M. The application of small unmanned aerial systems for precision agriculture: A review. *Precis. Agric.* **2012**, *13*, 693–712. [CrossRef]

163. Advexure Unmanned Systems and Solutions. Available online: https://advexure.com/pages/autel-dragonfish (accessed on 22 December 2021).

164. Skyfront. Available online: https://skyfront.com/perimeter-8/ (accessed on 22 December 2021).

165. Yoo, S.; Ju, Y.; Kim, J.; Kim, E.K. Design and Development of Underwater Drone for Fish Farm Growth Environment Management. *J. Korea Inst. Electron. Commun. Sci.* **2020**, *15*, 959–966.

166. Sousa, D.; Hernandez, D.; Oliveira, F.; Luís, M.; Sargento, S. A Platform of Unmanned Surface Vehicle Swarms for Real Time Monitoring in Aquaculture Environments. *Sensors* **2019**, *19*, 4695. [CrossRef]
167. Sousa, D.; Sargento, S.; Pereira, A.; Luis, M. Self-adaptive Team of Aquatic Drones with a Communication Network for Aquaculture. *Prog. Artif. Intell.* **2019**, 569–580. [CrossRef]
168. Bell, T.W.; Nidzieko, N.J.; Siegel, D.A.; Miller, R.J.; Cavanaugh, K.C.; Nelson, N.B.; Reed, D.C.; Fedorov, D.; Moran, C.; Snyder, J.N.; et al. The Utility of Satellites and Autonomous Remote Sensing Platforms for Monitoring Offshore Aquaculture Farms: A Case Study for Canopy Forming Kelps. *Front. Mar. Sci.* **2020**, *7*, 1083. [CrossRef]
169. Rasmussen, C.; Zhao, J.; Ferraro, D.; Trembanis, A. Deep Census: AUV-Based Scallop Population Monitoring. In Proceedings of the 2017 IEEE International Conference on Computer Vision Workshops (ICCVW), Venice, Italy, 22–29 October 2017; pp. 2865–2873. [CrossRef]
170. Ferraro, D. Estimating Sea Scallop Incidental Mortality from Photogrammetric before-after-Control-Impact Surveys. Master's Thesis, University of Delaware, Newark, DE, USA, 2016.
171. Walker, J.; Trembanis, A.; Miller, D. Assessing the use of a camera system within an autonomous underwater vehicle for monitoring the distribution and density of sea scallops (Placopecten magellanicus) in the Mid-Atlantic Bight. *Fish. Bull.* **2016**, *114*, 261–273. [CrossRef]
172. Sadrfaridpour, B.; Aloimonos, Y.; Yu, M.; Tao, Y.; Webster, D. Detecting and Counting Oysters. In Proceedings of the 2021 IEEE International Conference on Robotics and Automation (ICRA), Xi'an, China, 30 May–5 June 2021; pp. 2156–2162. [CrossRef]
173. Bjerkeng, M.; Kirkhus, T.; Caharija, W.; Thielemann, J.T.; Amundsen, H.B.; Johan Ohrem, S.; Ingar Grøtli, E. ROV Navigation in a Fish Cage with Laser-Camera Triangulation. *J. Mar. Sci. Eng.* **2021**, *9*, 79. [CrossRef]
174. Meng, L.; Hirayama, T.; Oyanagi, S. Underwater-Drone with Panoramic Camera for Automatic Fish Recognition Based on Deep Learning. *IEEE Access* **2018**, *6*, 17880–17886. [CrossRef]
175. Chalkiadakis, V.; Papandroulakis, N.; Livanos, G.; Moirogiorgou, K.; Giakos, G.; Zervakis, M. Designing a small-sized autonomous underwater vehicle architecture for regular periodic fish-cage net inspection. In Proceedings of the IEEE International Conference on Imaging systems and Techniques, Beijing, China, 18–20 October 2017; pp. 1–6.
176. Karimanzira, D.; Jacobi, M.; Pfützenreuter, T.; Rauschenbach, T.; Eichhorn, M.; Taubert, R.; Ament, C. First testing of an AUV mission planning and guidance system for water quality monitoring and fish behavior observation in net cage fish farming. *Inf. Process. Agric.* **2014**, *1*, 131–140. [CrossRef]
177. Dumiak, M. Lice-hunting underwater drone protects salmon. *IEEE Spectr.* **2017**, *54*, 9–10. [CrossRef]
178. Jensen, A.; Chen, Y. Tracking tagged fish with swarming Unmanned Aerial Vehicles using fractional order potential fields and Kalman filtering. In Proceedings of the 2013 International Conference on Unmanned Aircraft Systems (ICUAS), Atlanta, GA, USA, 28–31 May 2013; pp. 1144–1149. [CrossRef]
179. Segner, H.; Reiser, S.; Ruane, N.; Rösch, R.; Steinhagen, D.; Vehanen, T. Welfare of Fishes in Aquaculture. In *FAO Fisheries and Aquaculture Circular No. 1189*; FAO: Budapest, Hungary, 2019.
180. Lien, A.; Schellewald, C.; Stahl, A.; Frank, K.; Skøien, K.; Tjølsen, J. Determining spatial feed distribution in sea cage aquaculture using an aerial camera platform. *Aquac. Eng.* **2019**, *87*, 102018. [CrossRef]
181. Kondo, H.; Shimizu, E.; Choi, J.-K.; Nakane, K.; Matsushima, M.; Nagahashi, K.; Nishida, Y.; Matsui, R. Biointeractive Autonomous Underwater Vehicle "BA-1". In Proceedings of the 2010 IEEE/OES Autonomous Underwater Vehicles, Monterey, CA, USA, 1–3 September 2010; pp. 1–7. [CrossRef]
182. Sousa, L.L.; López-Castejón, F.; Gilabert, J.; Relvas, P.; Couto, A.; Queiroz, N.; Caldas, R.; Dias, P.S.; Dias, H.; Faria, M.; et al. Integrated Monitoring of Mola mola Behaviour in Space and Time. *PLoS ONE* **2016**, *11*, e0160404. [CrossRef]
183. Lin, Y.; Kastein, H.; Peterson, T.; White, C.; Lowe, C.G.; Clark, C.M. A multi-AUV state estimator for determining the 3D position of tagged fish. In Proceedings of the 2014 IEEE/RSJ International Conference on Intelligent Robots and Systems, Chicago, IL, USA, 14–18 September 2014; pp. 3469–3475. [CrossRef]
184. Seiler, J.; Williams, A.; Barrett, N. Assessing size, abundance and habitat preferences of the Ocean Perch Helicolenus percoides using a AUV-borne stereo camera system. *Fish. Res.* **2012**, *129–130*, 64–72. [CrossRef]
185. Yao, D.; Cheng, L.; Wu, Q.; Zhang, G.; Wu, B.; He, Y. Assessment and prediction of fishery water quality using electrochemical sensor array carried by UAV. In Proceedings of the 2019 IEEE International Symposium on Olfaction and Electronic Nose (ISOEN), Fukuoka, Japan, 26–29 May 2019; pp. 1–4. [CrossRef]
186. Wang, L.; Yue, X.; Wang, H.; Ling, K.; Liu, Y.; Wang, J.; Hong, J.; Pen, W.; Song, H. Dynamic Inversion of Inland Aquaculture Water Quality Based on UAVs-WSN Spectral Analysis. *Remote Sens.* **2020**, *12*, 402. [CrossRef]
187. Powers, C.; Hanlon, R.; Schmale, D.G., III. Tracking of a Fluorescent Dye in a Freshwater Lake with an Unmanned Surface Vehicle and an Unmanned Aircraft System. *Remote Sens.* **2018**, *10*, 81. [CrossRef]
188. Koparan, C.; Koc, A.B.; Privette, C.V.; Sawyer, C.B. Adaptive Water Sampling Device for Aerial Robots. *Drones* **2020**, *4*, 5. [CrossRef]
189. Ore, J.P.; Elbaum, S.; Burgin, A.; Detweiler, C. Autonomous aerial water sampling. *J. Field Robot.* **2015**, *32*, 1095–1113. [CrossRef]
190. Dunbabin, M.D.; Grinham, A.; Udy, J.W. An autonomous surface vehicle for water quality monitoring. In Proceedings of the 2009 Australasian Conference on Robotics and Automation (ACRA), Sydney, Australia, 2–4 December 2019; p. 13.

191. Doi, H.; Akamatsu, Y.; Watanabe, Y.; Goto, M.; Inui, R.; Katano, I.; Nagano, M.; Takahara, T.; Minamoto, T. Water sampling for environmental DNA surveys by using an unmanned aerial vehicle: Drone water sampling for eDNA. *Limnol. Oceanogr. Methods* **2017**, *15*, 10214. [CrossRef]
192. Lally, H.; O'Connor, I.; Jensen, O.; Graham, C.T. Can drones be used to conduct water sampling in aquatic environments? *A review. Sci. Total Environ.* **2019**, *670*, 569–575. [CrossRef] [PubMed]
193. Kim, E.-J.; Nam, S.-H.; Koo, J.-W.; Hwang, T.-M. Hybrid Approach of Unmanned Aerial Vehicle and Unmanned Surface Vehicle for Assessment of Chlorophyll-a Imagery Using Spectral Indices in Stream, South Korea. *Water* **2021**, *13*, 1930. [CrossRef]
194. Zeng, C.; Richardson, M.; King, D. The impacts of environmental variables on water reflectance measured using a lightweight unmanned aerial vehicle (UAV)-based spectrometer system. *ISPRS J. Photogramm. Remote Sens.* **2017**, *130*, 217–230. [CrossRef]
195. Kelly, J.; Kljun, N.; Olsson, P.-O.; Mihai, L.; Liljeblad, B.; Weslien, P.; Klemedtsson, L.; Eklundh, L. Challenges and Best Practices for Deriving Temperature Data from an Uncalibrated UAV Thermal Infrared Camera. *Remote Sens.* **2019**, *11*, 567. [CrossRef]
196. Lega, M. Using Advanced Aerial Platforms and Infrared Thermography to Track Environmental Contamination. *Environ. Forensics* **2012**, *13*, 332–338. [CrossRef]
197. Sibanda, M.; Mutanga, O.; Chimonyo, V.G.P.; Clulow, A.D.; Shoko, C.; Mazvimavi, D.; Dube, T.; Mabhaudhi, T. Application of Drone Technologies in Surface Water Resources Monitoring and Assessment: A Systematic Review of Progress, Challenges, and Opportunities in the Global South. *Drones* **2021**, *5*, 84. [CrossRef]
198. Kumagai, M.; Ura, T.; Kuroda, Y.; Walker, R. A new autonomous underwater vehicle designed for lake environment monitoring. *Adv. Robot.* **2002**, *16*, 17–26. [CrossRef]
199. Esakki, B.; Ganesan, S.; Mathiyazhagan, S.; Ramasubramanian, K.; Gnanasekaran, B.; Son, B.; Park, S.W.; Choi, J.S. Design of Amphibious Vehicle for Unmanned Mission in Water Quality Monitoring Using Internet of Things. *Sensors* **2018**, *18*, 3318. [CrossRef]
200. Cheng, L.; Tan, X.; Yao, D.; Xu, W.; Wu, H.; Chen, Y. A Fishery Water Quality Monitoring and Prediction Evaluation System for Floating UAV Based on Time Series. *Sensors* **2021**, *21*, 4451. [CrossRef] [PubMed]
201. Pennington, J.; Blum, M.; Chavez, F. Seawater sampling by an autonomous underwater vehicle: "Gulper" sample validation for nitrate, chlorophyll, phytoplankton, and primary production. *Limnol. Oceanogr. Methods* **2016**, *14*, 14–23. [CrossRef]
202. Lee, E.; Yoon, H.; Hyun, S.P.; Burnett, W.C.; Koh, D.-C. Unmanned aerial vehicles (UAVs)-based thermal infrared (TIR) mapping, a novel approach to assess groundwater discharge into the coastal zone. *Limnol. Oceanogr. Methods* **2016**, *14*, 725–735. [CrossRef]
203. Taddia, Y.; Russo, P.; Lovo, S. Multispectral UAV monitoring of submerged seaweed in shallow water. *Appl. Geomat.* **2020**, *12*, 19–34. [CrossRef]
204. Tauro, F.; Porfiri, M.; Grimaldi, S. Surface flow measurements from drones. *J. Hydrol.* **2016**, *540*, 240–245. [CrossRef]
205. Li, X.M.; Yuan, J.M.; Fu, S.F.; Zhang, Y.G. The effect of sustained swimming on the growth performance, muscle cellularity and flesh quality of juvenile qingbo (Spinibarus sinensis). *Aquaculture* **2016**, *456*, 287–295. [CrossRef]
206. Yurovskaya, M.; Kudryavtsev, V.; Shirokov, A.; Nadolya, I. Field measurements of the sea surface wave spectrum from photos of sunglitter taken from drone. *Geology* **2018**, *15*, 245–257. [CrossRef]
207. Almar, R.; Bergsma, E.W.J.; Catalan, P.A.; Cienfuegos, R.; Suarez, L.; Lucero, F.; Nicolae Lerma, A.; Desmazes, F.; Perugini, E.; Palmsten, M.L.; et al. Sea State from Single Optical Images: A Methodology to Derive Wind-Generated Ocean Waves from Cameras, Drones and Satellites. *Remote Sens.* **2021**, *13*, 679. [CrossRef]
208. Streßer, M.; Carrasco-Álvarez, R.; Horstmann, J. Video-Based Estimation of Surface Currents Using a Low-Cost Quadcopter. *IEEE Geosci. Remote Sens. Lett.* **2017**, *14*, 1–5. [CrossRef]
209. Fairley, I.; Williamson, B.; McIlvenny, J.; Lewis, M.; Neill, S.; Masters, I.; Williams, A.; Reeve, D. A preliminary assessment of the use of drones to quantify current velocities at tidal stream sites. In Proceedings of the European Wave and tidal Energy Conference, Plymouth, UK, 5–9 September 2021.
210. Horstmann, J.; Stresser, M.; Carrasco, R. Surface currents retrieved from airborne video. In Proceedings of the OCEANS 2017, Aberdeen, UK, 19–22 June 2017; pp. 1–4. [CrossRef]
211. Tauro, F.; Pagano, C.; Phamduy, P.; Grimaldi, S.; Porfiri, M. Large-Scale Particle Image Velocimetry from an Unmanned Aerial Vehicle. *IEEE/ASME Trans. Mechatron.* **2015**, *20*, 3269–3275. [CrossRef]
212. Eltner, A.; Sardemann, H.; Grundmann, J. Technical Note: Flow velocity and discharge measurement in rivers using terrestrial and unmanned-aerial-vehicle imagery. *Hydrol. Earth Syst. Sci.* **2020**, *24*, 1429–1445. [CrossRef]
213. Hoth, J.; Kowalczyk, W. Determination of Flow Parameters of a Water Flow Around an AUV Body. *Robotics* **2019**, *8*, 5. [CrossRef]
214. Matsuba, Y.; Sato, S. Nearshore bathymetry estimation using UAV. *Coast. Eng. J.* **2018**, *60*, 1–9. [CrossRef]
215. Tauro, F.; Petroselli, A.; Arcangeletti, E. Assessment of drone-based surface flow observations. *Hydrol. Processes* **2015**, *30*, 10698. [CrossRef]
216. Huang, Z.C.; Yeh, C.-Y.; Tseng, K.-H.; Hsu, W.-Y. A UAV-RTK-lidar system for wave and tide measurements in coastal zones. *J. Atmos. Ocean. Technol.* **2018**, *35*, 1557–1570. [CrossRef]
217. Long, N.; Millescamps, B.; Guillot, B.; Pouget, F.; Bertin, X. Monitoring the Topography of a Dynamic Tidal Inlet Using UAV Imagery. *Remote Sens.* **2016**, *8*, 387. [CrossRef]
218. Sanjou, M.; Shigeta, A.; Kato, K.; Aizawa, W. Portable unmanned surface vehicle that automatically measures flow velocity and direction in rivers. *Flow Meas. Instrum.* **2021**, *80*, 101964. [CrossRef]

219. Jha, R. Wave Measurement Methodology and Validation from Wave Glider Unmanned Surface Vehicle. In Proceedings of the 2018 OCEANS—MTS/IEEE Kobe Techno-Oceans (OTO), Port Island, Kobe, 28–31 May 2018; pp. 1–7. [CrossRef]
220. Offshore Wind Solutions. Available online: https://www.saildrone.com/ (accessed on 25 December 2021).
221. Federal Aviation Administration. Available online: https://www.faa.gov/uas/commercial_operators/ (accessed on 24 December 2021).
222. Demir, K.; Cicibaş, H.; Arica, N. Unmanned Aerial Vehicle Domain: Areas of Research. *Def. Sci. J.* **2015**, *65*, 319–329. [CrossRef]
223. Drone Laws for a Safer Airspace. Available online: https://drone-laws.com/ (accessed on 24 December 2021).
224. Showalter, S. The legal status of autonomous underwater vehicles. *Mar. Technol. Soc. J.* **2004**, *38*, 80–83. [CrossRef]
225. Norris, A. Legal Issues Relating to Unmanned Maritime Systems Monograph. Available online: https://www.iqpc.com/media/1002182/50661.pdf (accessed on 24 December 2021).
226. Dhulkefl, E.; Durdu, A. Path Planning Algorithms for Unmanned Aerial Vehicles. *Int. J. Trend Sci. Res. Dev.* **2019**, *3*, 359–362. [CrossRef]
227. Danancier, K.; Ruvio, D.; Sung, I.; Nielsen, P. Comparison of Path Planning Algorithms for an Unmanned Aerial Vehicle Deployment Under Threats. *IFAC-Pap. OnLine* **2019**, *52*, 1978–1983. [CrossRef]
228. Medeiros, F.; Silva, J. A Dijkstra Algorithm for Fixed-Wing UAV Motion Planning Based on Terrain Elevation. In Proceedings of the 20th Brazilian Conference on Advances in Artificial Intelligence, São Bernardo do Campo, Brazil, 23–28 October 2010; p. 6404. [CrossRef]
229. PVtech. Alta Devices Sets GaAs Solar Efficiency Record at 29.1% Joins NASA Space Station Testing. Available online: https://www.pv-tech.org/alta-devices-sets-gaas-solar-cell-efficiency-record-at-29-1-joins-nasa-spac/ (accessed on 28 November 2021).
230. Chu, Y.; Ho, C.; Lee, Y.; Li, B. Development of a Solar-Powered Unmanned Aerial Vehicle for Extended Flight Endurance. *Drones* **2021**, *5*, 44. [CrossRef]
231. Chae, H.; Park, J.; Song, H.; Kim, Y.; Jeong, H. The IoT based automate landing system of a drone for the round-the-clock surveillance solution. In Proceedings of the 2015 IEEE International Conference on Advanced Intelligent Mechatronics (AIM), Busan, Korea, 7–11 July 2015; pp. 1575–1580. [CrossRef]
232. Yu, Y.; Lee, S.; Lee, J.; Cho, K.; Park, S. Design and implementation of wired drone docking system for cost-effective security system in IoT environment. In Proceedings of the 2016 IEEE International Conference on Consumer Electronics (ICCE), Las Vegas, NV, USA, 7–11 January 2016; pp. 369–370. [CrossRef]
233. Mahmoud, S.; Mohamed, N.; Al-Jaroodi, J. Integrating UAVs into the Cloud Using the Concept of the Web of Things. *J. Robot.* **2015**, *2015*, 631420. [CrossRef]
234. Almutiry, O.; Iqbal, K.; Hussain, S.; Mahmood, A.; Dhahri, H. Underwater images contrast enhancement and its challenges: A survey. *Multimed. Tools Appl.* **2021**. [CrossRef]
235. Karpatne, A.; Khandelwal, A.; Chen, X.; Mithal, V.; Faghmous, J.; Kumar, V. Global Monitoring of Inland Water Dynamics: State-of-the-Art, Challenges, and Opportunities. In *Computational Sustainability*; Studies in Computational Intelligence; Lässig, J., Kersting, K., Morik, K., Eds.; Springer: Cham, Switzerland, 2016; p. 645. [CrossRef]
236. Ljubičić, R.; Strelnikova, D.; Perks, M.; Eltner, A.; Peña-Haro, S.; Pizarro, A.; Dal, S.; Silvano, F.; Scherling, U.; Vuono, P.; et al. A comparison of tools and techniques for stabilising UAS imagery for surface flow observations. *Adv. River Basin Monit.* **2021**. [CrossRef]
237. Bbm Secure Maritime Division. Fight Illegal Fishing Economical Coastal Surveillance. Available online: https://bbcomsecure.com/resources/bbsec_IUU_Fishing_economical_costal_surveilance_system.pdf (accessed on 15 December 2021).
238. Elkolali, M.; Al-Tawil, A.; Much, L.; Schrader, R.; Masset, O.; Sayols, M.; Jenkins, A.; Alonso, S.; Carella, A.; Alcocer, A. A low-cost wave/solar powered unmanned surface vehicle. In Proceedings of the Global Oceans Singapore, Singapore, 5–14 October 2020; pp. 1–10. [CrossRef]
239. Blueye. Aquaculture. Available online: https://www.blueyerobotics.com/page/aqua-culture (accessed on 25 December 2021).
240. Aquaculture ROVs for Net Inspections, Patching, Mort Pushing, and Site Selection. Available online: https://www.deeptrekker.com/industries/aquaculture (accessed on 25 December 2021).
241. Enterprise Grade ROV Platform Powerful & Precise, Advanced Add-Ons, Exceptional Stability, Superior Battery. Available online: https://www.qysea.com/products/fifish-w6/ (accessed on 25 December 2021).

The Relationship between Drone Speed and the Number of Flights in RFID Tag Reading for Plant Inventory

Jannette Quino [1], Joe Mari Maja [2,*], James Robbins [3], James Owen, Jr. [4], Matthew Chappell [5], Joao Neto Camargo [6] and R. Thomas Fernandez [7]

[1] Edisto Research and Education Center, 64 Research Road, Blackville, SC 29817, USA; jquino@clemson.edu
[2] Department of Agricultural Science, Clemson University, 240 McAdams Hall, Clemson, SC 29634, USA
[3] Division of Agriculture, University of Arkansas, CES, 2301 S. University Ave., Little Rock, AR 72204, USA; jrobbins@uada.edu
[4] USDA-ARS Application Technology Research Unit, 1680 Madison Ave., Wooster, OH 44691, USA; jim.owen@usda.gov
[5] Tidewater Agricultural Research & Extension Center, Virginia Tech, 6321 Holland Road, Suffolk, VA 23437, USA; chappell@vt.edu
[6] Embrapa Digital Agriculture, Avenida Andre Tosello 209, Campus da Unicamp, Barao Geraldo, Campinas 130083-886, SP, Brazil; joao.camargo@embrapa.br
[7] Department of Horticulture, Michigan State University, 1066 Bogue St., East Lansing, MI 48824, USA; fernan15@msu.edu
* Correspondence: jmaja@clemson.edu

Abstract: Accurate inventory allows for more precise forecasting, including profit projections, easier monitoring, shorter outages, and fewer delivery interruptions. Moreover, the long hours of physical labor involved over such a broad area and the effect of inefficiencies could lead to less accurate inventory. Unreliable data and predictions, unannounced stoppages in operations, production delays and delivery, and a considerable loss of profit can all arise from inaccurate inventory. This paper extends our previous work with drones and RFID by evaluating: the number of flights needed to read all tags deployed in the field, the number of scans per pass, and the optimum drone speed for reading tags. The drone flight plan was divided into eight passes from southwest to northwest and back at a horizontal speed of 2.2, 1.7, and 1.1 m per second (m/s) at a vertically fixed altitude. The results showed that speed did not affect the number of new tags scanned (p-value > 0.05). Results showed that 90% of the tags were scanned in less than four trips (eight passes) at 1.7 m/s. Based on these results, the system can be used for large-scale nursery inventory and other industries that use RFID tags in outdoor environments. We presented two novel measurements on evaluating RFID reader efficiency by measuring how fast the reader can read and the shortest distance traveled by the RFID reader over tag.

Keywords: speed; RFID; inventory; drones; labor; forecast

1. Introduction

According to the United States Department of Agriculture's National Agricultural Statistics Service [1], 91.1 million acres of land are projected to be used for plant production for 2021. Specialty crops, including floriculture and nursery products, accounted for $13.8 billion in sales in 2019; the nursery industry is a multibillion-dollar enterprise that relies on inventory and monitoring to forecast sales, production requirements, and quality improvements [2]. The information collected in an inventory is used for planning that includes labor requirements, space requirements, production timing, and sales and demand trends, including product pricing [3]. However, obtaining individual plant information about the location or number of plants in the field is labor intensive and time-consuming. Since this process is done manually, there may be inefficiencies, including missing data, due to human error. Furthermore, it is difficult to avoid mistakes due to a lack of reliable equipment to gather data [4].

Increased personnel or labor alone cannot alleviate the current inventory inefficiencies. The number of hours required in the field is considerable, and workers will be scarce as the horticultural industry's labor supply declines. The decline of workers is because most entry-level employees would prefer to work in a position that requires less physical exertion [5]. Similarly, just 20% of the workers in the nursery are permanent, with the remaining 80% being temporary [6]. Thus, accessibility to laborers will be a persistent issue.

Small unmanned aircraft systems (sUAS) can fly at low altitudes and carry various sensors to gather real-time data; thus, being a viable alternative for ground-based data collection in nursery systems [7]. Aside from inventory data, sUAS is used for crop scouting and loss assessment, yield estimation and monitoring, irrigation and drainage planning, sampling of plant pathogens in the air, diagnosis of herbicide injury in crops, and efficient use of chemicals and pesticides [8]. Additionally, researchers have worked on RFID used for identification, harvesting, and crop histology [9–11]. An RFID system was used to track, capture remotely, and handle data in a vineyard [12]. RFID systems and Global Positioning System (GPS) used to monitor and track plant information can be updated in real-time. Geographic Information System (GIS) software can be used to visualize information location to edit and manage data changes in the area. RFID technology combined with GPS was used in plant pathology and genomics [13] and citrus fruit harvesting in Florida [14].

Passive RFID tags and sUAS can be combined to gather information about nursery plants in the field. The passive tag at the Ultra-high frequency (UHF) band ranges from 0 distance to 12 m and has a faster data rate [15]. However, UHF is more susceptible to interference. It usually works between 860–960 MHz band [16]. Preliminary results showed that the drone flying at a speed of 6 km per hour (kph) at an altitude of between 4.5 and 6.0 m can scan tags on a static position with the front of the tags orientated to face upward toward the antenna [17]. Knox Nursery in Winter Garden, Florida, operates a greenhouse using a ground-based Ultra-High Frequency (UHF) RFID tag platform [18]. As a result, there was an increase in productivity and the number of hours required to update the inventory report has decreased from three days to two hours, demonstrating a drop in labor costs. In addition, individual plants can be tagged or labeled using RFID; allowing them to be compared to geo-referenced data from transplant machines.

The deployment of mobile platforms such as sUAS to integrate RFID technology will ensure the ability to collect information over large areas, encompassing numerous products, taxa, or stock-keeping units (SKU), while further reducing the amount of labor and time spent in the field. In the long run, it can improve efficiency by lowering the operational cost of obtaining nursery data, resulting in higher productivity, better inventory management, and subsequent product forecasting. The following are the objectives of this experiment:

- To evaluate the number of flights needed to read all tags deployed in the field
- To determine the number of scans per pass, and
- To determine the optimal drone speed for reading.

2. Materials and Methods

2.1. Study Site, Drone and RFID Tags

Clemson University Edisto Research and Education Center (EREC) in Blackville, SC, was the study site location. The Matrice 600 Pro (Matrice 600 Pro, Shenzhen DJI Sciences and Technologies Ltd., Shenzhen, China) (Figure 1a) sUAS carried the 2.6 kg RFID–Reader Module (RFID-RM) (Figure 1b) used to scan the RFID tags [17]. The sUAS can handle a maximum payload of 6 kg, including six TB47S batteries. Figure 2 shows the RFID tag used in this experiment based on prior work. Figure 3 shows the placement of the tags at the study site.

(**a**)   (**b**)

Figure 1. (**a**) DJI Matrice 600 Pro, and (**b**) RFID Reader Module (RFID-RM).

Figure 2. The RFID tag design (Avery Dennison Corp., Glendale, CA, USA) used in the experiment.

Figure 3. RFID tags at the study site facing upward.

2.2. RFID-Reader Module (RFID-RM) and Dashboard

A Lithium battery of 12-volt, 2200-mAh, 3-cell supplied power to the RFID-RM. The RFID-RM, once powered, sent all information to a remote computer via 450 Mhz transceivers. The RFID-RM reader chip was set to use the maximum power and operates at a frequency of 900 Mhz [17]. The current firmware was written in C and can be easily updated to change the polling frequency and duration of the reading.

A dashboard was developed to display RFID tag ID, GPS, Received Signal Strength Indicator (RSSI), Phase Angle, and battery information of the RFID-RM. The original dashboard in Figure 4a was developed to display all tag information without a map. The new dashboard in Figure 4b has a view map option button to show the map and the approximate location of the tags. It also has an indicator that the GPS signal is fixed. This information is an indicator that the system is now ready to collect data. Another new

feature is the ability to display the approximate location of the tags on a map and the plotting of the reader coordinates in reference to the tag locations (Figure 4c). A logging area is also added to view the count summary of the new tags per pass, and the RFID tag or Electronics Product Code (EPC) Tagbytes are displayed in the order they were scanned. Furthermore, when a user clicks the disconnect button, the data collected are automatically saved in a folder with a timestamped filename.

(**a**)

(**b**)

(**c**)
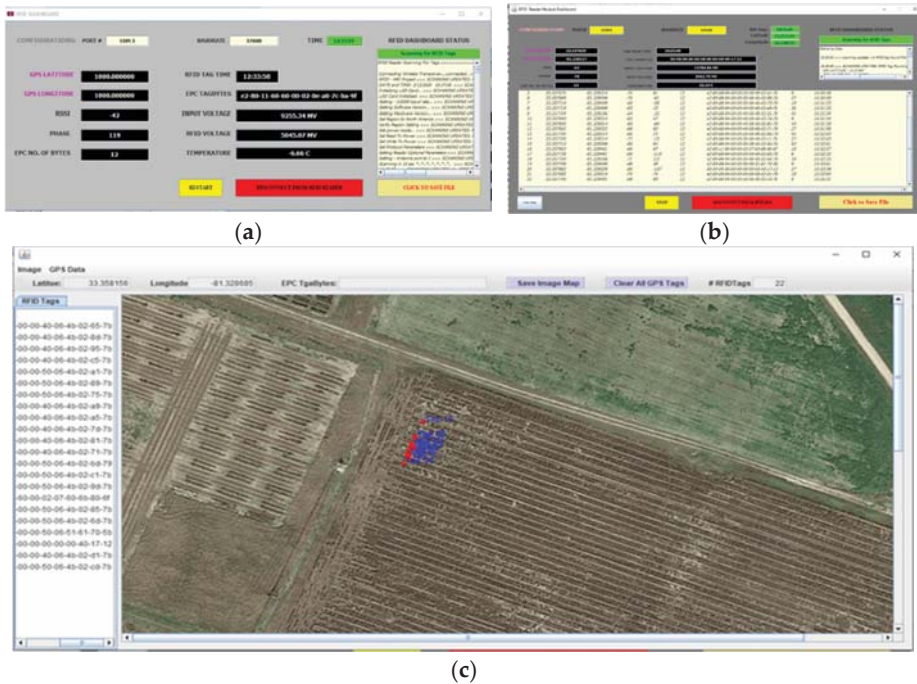
Figure 4. The (**a**) old Dashboard version, (**b**) new version of the Dashboard, and (**c**) Map showing the approximate location of the different RFID tags in the field.

2.3. Weather Condition

The weather conditions were obtained from the Clemson University- EREC Station Summary of Weather Conditions (www.edistorecweather.net, accessed on 19 August 2021). Table 1 shows the weather report during the data collection.

Table 1. Clemson University-EREC Station Summary of Weather Conditions.

Wind Speed	4.8 kph~9.7 kph
Average Wind Speed	1.4 kph~4.5 kph
Predominant Wind Speed	NE, E, ENE
Humidity Level	78.8~85.2%
Temperatures	28.3~30.7° Centigrade
Atmospheric Pressure	101,998.0~102,028.5 Pa

2.4. The Tag Layout

Twenty identical tags were attached to a 1.8-m-long round wood dowel. There were four dowels in total, with six tags attached to the first three dowels and the final two tags on the fourth dowel. The dowel was marked with black stripes to arrange the tags from tag 1 to tag 20. The dowels were placed on top of a tripod stand 1.2 m above the ground. Prior to

the drone flights, the dowel was rotated so that the tags face upward due to our previous finding on the best position of the tag. To keep the dowel from rolling, it was placed on top of the foam and taped down. Figure 5 depicts the tags spread sideways by 0.3 m from the center of one tag to the center of the adjacent tag. The total distance measured between tags 1 and 20 was 5.8 m. The spacing of the tags (0.3 m) was based on the normal distance of the pots in nursery production [19].

Figure 5. The tags spaced at 0.30 m, facing upward.

2.5. The Number of Tags Scanned

The distance between the drone and the tag was held at 4.5 m. The flight altitude was set to 5.7 m with the tags positioned 1.2 m from the ground. Two flag sticks were used as a guide for the drone flight path. The RFID-RM was attached to the drone with the antenna pointing downward to the tags. Due to the limitations of the drone's battery, the trips were reduced to three flights per speed to accommodate four trips for a total of eight passes per speed. A single trip consists of two passes, one forward and one backward (Figure 6). Three drone speeds were evaluated; 2.2 m/s (8 kph), 1.7 m/s (6 kph), and 1.1 m/s (4 kph) to compare the scan rate. During the data collection process, some tags were scanned or read multiple times in a single pass, while others were not scanned at all. Tags that are scanned for the first time after being listed in the log area are considered new or unique tags.

Figure 6. Drone flying at 5.7 m AGL toward the tags.

2.6. Inverse Rate

Drone travel time and the number of tags scanned were used to determine the inverse rate (seconds per tag [spt]) of each pass. The spt is a value that describes how long it takes to scan a tag in each pass. The drone travel time is the time it will take the drone to travel from tag 1 to tag 20 at a set speed (Equation (1)). As shown in Table 2, the drone travel time is 3.5 s to complete one pass covering 5.8 m at a speed of 1.7 m/s. Consequently, spt was calculated by dividing the number of tags scanned per pass by the drone travel time (Equation (2)).

$$v = {}^d/_t \tag{1}$$

where:

v = drone speed (m/s);
d = total distance (meters) flown by the drone in one pass;
t = drone travel time (seconds).

Table 2. Drone travel time per pass.

Speed (v) Meters per Sec	Total Distance (d) Meters	Drone Travel Time (t) Seconds
2.2 m/s (8 kph)	5.8	2.6
1.7 m/s (6 kph)	5.8	3.5
1.1 m/s (4 kph)	5.8	5.2

$$spt = \frac{t}{T} \tag{2}$$

where:

spt = seconds per tag;
t = drone travel time (seconds);
T = new tags scanned per pass.

2.7. RFID-RM Efficiency

To determine the efficiency of the RFID-RM in reading tags at a fixed speed, it is important to determine the distance traveled by the drone to scan the next available tag (meters per tag [mpt]). The mpt is calculated by multiplying the spt with the drone speed (Equation (3)).

$$mpt = spt \times v \tag{3}$$

where:

mpt = meters per tag

spt = seconds per tag
v = speed (m/s)

2.8. Statistical Analysis

A single factor Analysis of Variance (ANOVA) without replication is used to analyze the data. The hypothesis is that the speed of the drone and the number of passes will influence the number of new or unique tag readings.

3. Results

3.1. The Number of New Tags Scanned

Figure 7 shows the total number of tag readings, which includes tags that have been scanned multiple time as well as newly scanned tags. A forward speed of 1.7 m/s resulted in the greatest number of tags read (451) and 2.2 m/s yielded the fewest (281). Figure 8 shows the percentage of new tags read for each pass based on the three drone speeds. The first pass resulted in the highest percentage of tag read across all three speeds. Values ranged from 25% to 30%. Starting with the fifth pass, the percentage of news tags read never exceeded 5% for any drone speed. In general, across all drone speeds, the percentage of new tags read decreased after the fourth pass. Figure 9 summarizes the cumulative total of tag readings at each pass and at three drone speeds.
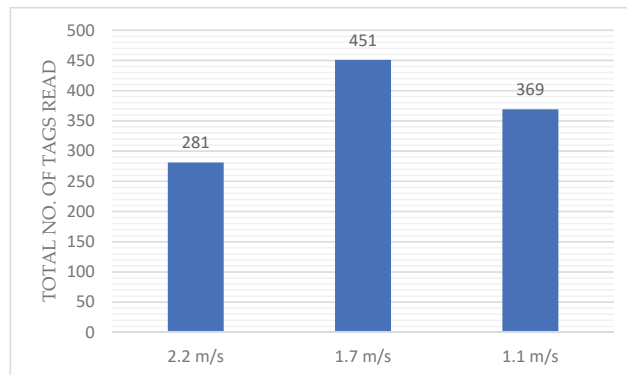
Figure 7. The effect of drone speed on the number of total tags reading (includes multiple reads per tag).
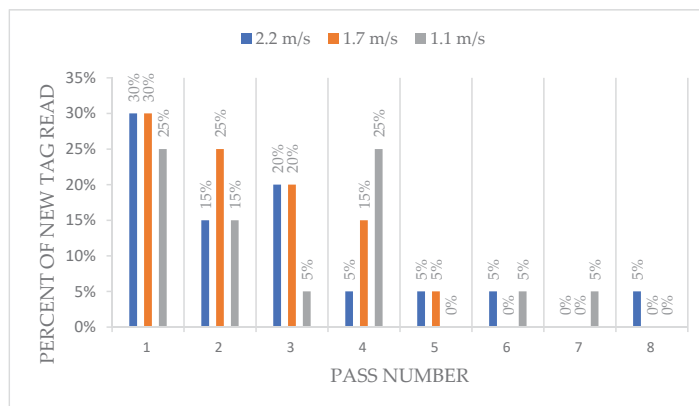
Figure 8. Percent of new tags read at three speeds of the drone for eight passes.
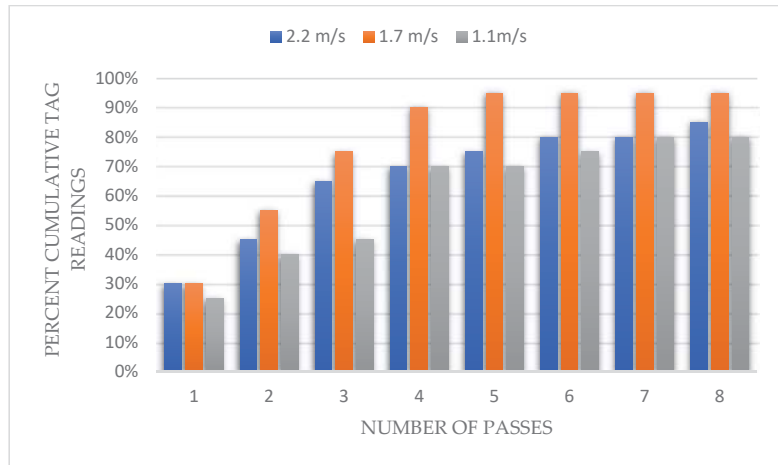
Figure 9. The cumulative tag readings in each pass at three drone speeds.

3.2. Inverse Rate

At a speed of 2.2 m/s, the inverse rate ranged from 0 at pass number seven to 0.146 at pass number six as shown in Figure 10. An inverse rate of zero indicates that no tags were read. At a speed of 1.7 m/s, the inverse rate ranged from 0.039 at pass number four to 0.128 at pass number seven. The inverse rate at a speed of 1.1 m/s ranged from 0.048 at pass number four to 0.580 at pass number five.
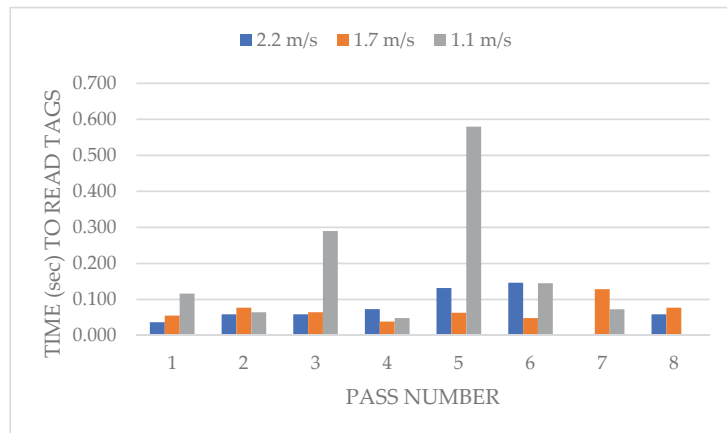
Figure 10. The number of seconds per tag (inverse rate) for each pass and each drone speed as calculated using Equation (2).

Figure 11 summarizes the effect of drone speed on the number of seconds it takes to read one new tag on each of the eight passes. Results indicate the inverse rate for new tags is between 0.439 at pass number one and 2.632 at pass number four, five, six and seven. At a speed of 1.7 m/s, the inverse rate is between 0.578 at pass number one and 3.467 at pass number five. The inverse rate of 1.1 m/s is between 1.043 at pass number one and 5.216 at pass numbers three, six and seven. Contrary to Figure 10, Figure 11 only shows the unique tag read on multiple passes. Tags which were already read on the first few passes were not counted.
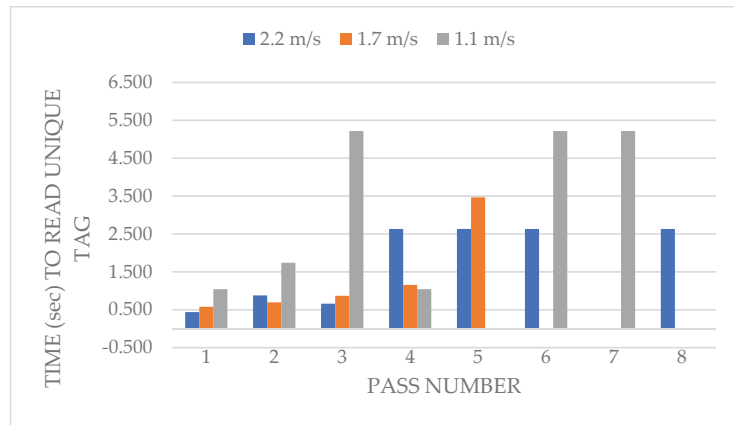
Figure 11. The time required to read each new tag for each pass at three drone speeds.

3.3. RFID-RM Efficiency

Figure 12 shows that at a speed of 2.2 m/s, the RFID-RM efficiency in terms of readings all tags is between 0.080 at pass number one and 0.322 at pass number six. Furthermore, at a speed of 1.7 m/s, the RFID-RM efficiency is between 0.064 at pass number four and 0.214 at pass number seven. The RFID-RM efficiency of 1.1 m/s is between 0.054 at pass number four and 0.643 at pass number five.
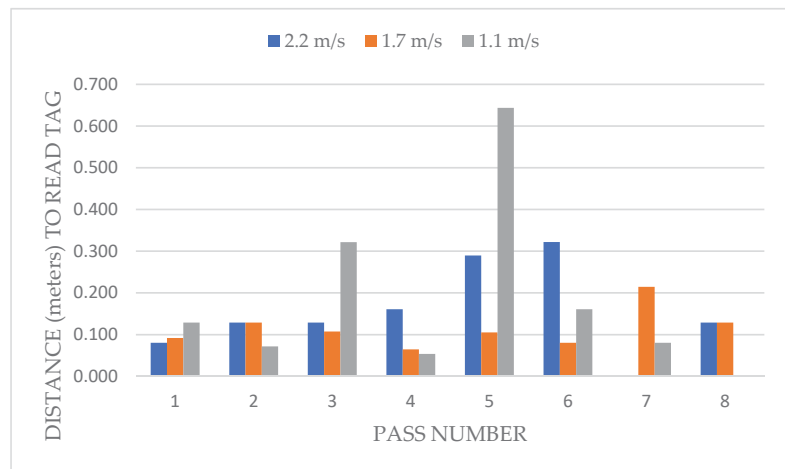
Figure 12. The distance covered to read tag for each pass as calculated using Equation (3).

Figure 13 shows that at a speed of 2.2 m/s, the RFID-RM efficiency for unique tags was between 0.96 at pass number one and 5.79 at pass number four, four, six and seven. At a speed of 1.7 m/s, the RFID-RM efficiency is between 0.96 at pass number one and 5.8 at pass number five. While the RFID-RM efficiency of 1.1 m/s is between 1.158 at pass number one and 5.79 at pass number three, six and seven.
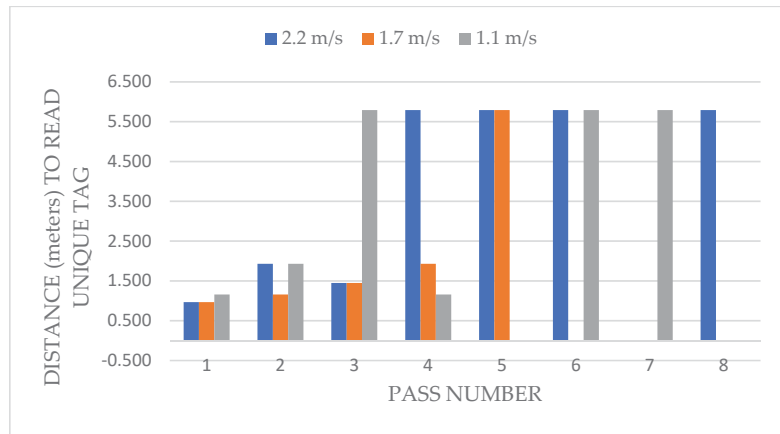
Figure 13. The distance covered to read unique tag for each pass at three different speeds.

3.4. Statistical Analysis

The ANOVA evaluates whether there is a statistically significant difference between each pass reading and how the RFID reader detects tags at variable speeds. The ANOVA parameters are the source of variation, Sum of Squares (SS), degree of freedom (df), Mean Squares (MS), F statistical (F), (*p*-value) a measure of the probability of the test results gathered on how likely that the same tag readings would occur by random chance, and F critical (F crit). Furthermore, F, *p*-value, and the F crit values are the values that would determine the significance level of the source of variation. The value F > F crit is the same as *p*-value < alpha, which rejects the null hypothesis. In this experiment, the source of variation is the number of passes and the drone speeds. The SS, df, MS are values used to compute the F, F crit, and the *p*-value. The SS is derived by getting the count for each speed reading multiplied by the difference between the speed and grand mean. The grand mean is the average of all the readings, adding the total new tag readings divided by the total count. In addition, the df is the difference between groups minus 1 (8 passes − 1 = 7). The MS is the square of the difference between the mean, and the data collected, while the F results from the mean square of the number of passes divided by the mean square in each pass. The *p*-value of 0.000126 measures the probability that an observed difference could occur is computed using F, df between groups as the numerator and df within groups as the denominator. F crit is computed using three arguments, the alpha value, numerator df between groups (between each pass), and the denominator df within each pass.

The number of passes made by drone scanning new/unique tags has an influence on the number of tags read (*p*-value = 0.000126); however, the three speeds used for this experiment are not significant (*p*-value = 0.941182) (see Table 3).

Table 3. Anova results for scanning a new/unique tag.

Source of Variation	SS	df	MS	F	*p*-Value	F Crit
No. of Passes	81.3	7	11.6	9.3	0.000126	2.7
Drone Speeds	0.6	2	0.3	0.1	0.941182	3.5

4. Discussion

Prior to these experiments, the hypothesis was that the speed of the drone and the number of passes has an influence on the reading of unique or new tags. Results from our experiments suggest that only the number of passes will affect the number of new tags read. At 2.2 m/s, the label scanning is between 0.037 and 0.146 spt. At 1.1 m/s the label scanning is between 0.048 and 0.580 spt. The result also shows that the total time required

to collect tag information is determined by the drone's speed and the length of the flight path [20,21]. In addition, at speeds of 1.1 to 2.2 m/s, the scan time ranged from 0.01 to 0.15 has a common overlap. Based on our results, the effect of the number of readings when the drone changes speed is not significant.

Furthermore, the first pass results in the highest percentage of new tags scanned across all speeds. On the fifth pass, the scan rate begins to drop. However, 1.7 m/s scanned a total of 95 percent of new tags on the fifth pass, the highest percentage among the three speeds. The scan rate trend increases from the first to the fourth pass and then a decreasing trend from the fifth to the eighth pass. In addition, after the scan rate reaches 70% of the tags scanned, the scan rate also shows a decreasing trend. The decreasing trend was since only 30% of new tags are still available for reading.

There were instances where readings were not reported, starting at the pass 5 onwards. In Figure 9, no readings were recorded at a drone speed of 2.2 m/s for pass 7 and 1.1 m/s for pass 8. Figure 10 also shows that at pass 5, at the speed 1.1 m/s did not register any readings, but readings were registered on passes 6 and 7. The same instances can be found in Figures 11 and 12, where no readings were registered at various speeds. This could be attributed to how the RFID-RM is responding to tag readings. Every tag read goes into an interrupt service routine where it collects all available information before the reader will be available for reading another tag. Although the tags are of the same manufacturer, some tags may respond quicker and thus create multiple instances of the interrupt, thus, delaying the reader. Moreover, the physical constraints feature of radio frequency poses a barrier to advanced anti-collision techniques for RFID chips, due to the interference from the transition signal's scattering and reflection [22].

We presented two novel measurements on evaluating RFID reader efficiency by measuring how fast the reader can read and the shortest distance traveled of the RFID reader reading a tag. These two measurements can be used to compare other RFID readers developed by different manufacturers.

5. Conclusions

Based on results from this experiment, the first three flights have the highest number of unique tags scanned. The time required to scan tags repeatedly is 0.04 s per tag (spt), and the minimum distance is 0.064 m per tag (mpt) at a speed of 1.7 m/s. New tags can be scanned in the first five passes at a percentage between 70 to 95 percent. The first pass results in the most readings (30%), and gradually decreases as the number of passes increases. The decline is attributable to a reduction in the quantity of new scannable tags.

Finally, when scanning new tags, the pass number is essential. At least two flights equivalent to four passes will get a scan rate of 70% to 90%. It takes 0.578 to 3.467 spt to scan at a speed of 1.7 m/s with a minimum distance of 0.96 mpt. It is important to note that due to the placement of plants in the field at close proximity, this experiment showed that the drone must perform multiple passes on the same location to gather an accurate inventory. This limitation has been shown in the results of this work. The distance of the tags was based on the distance between the pots in a real nursery production.

This technology is a potential tool in obtaining automated, aireal based nursery inventory data that would reduce labor hours in the field for data retrieval. Once the pandemic has subsided, we will conduct the field testing in large nurseries.

References

1. USDA NASS. US Farmers Expect to Plant More Corn and Soybean Acreage. 2021. Available online: https://www.nass.usda.gov/Newsroom/2021/03-31-2021.php (accessed on 9 July 2021).
2. USDA NASS. U.S. Horticulture Operations Report $13.8 Billion in Sales. 2019. Available online: https://www.nass.usda.gov/Newsroom/archive/2020/12-08-2020.php (accessed on 23 September 2021).
3. Hall, C.R. Managing Plant Material Inventory. Ornamental Production. 2021. Available online: https://aggie-horticulture.tamu.edu/ornamental/economic-fact-sheets/managing-plant-material-inventory/ (accessed on 29 June 2021).
4. West, B. Nursery Inventory Management. Lawn and Landscape (Market Leadership). 2020. Available online: https://www.lawnandlandscape.com/article/nursery-inventory-management (accessed on 18 May 2021).
5. Owen, J.S.; Lebude, A.; Calabro, J.; Boldt, J.; Gray, J.; Altland, J. Research Priorities of the Environmental Horticultural Industry Founded through Consensus. *J. Environ. Hortic.* **2019**, *37*, 120–126. [CrossRef]
6. Abayomi, E.J.; Ridolfo, H. The Effects of Currently Reported Data on Data Quality: An Analysis of the Agricultural Labor Survey. 2017. Available online: https://www.nass.usda.gov/Education_and_Outreach/Reports,_Presentations_and_Conferences/reports/conferences/JSM/JSM_2017_Abayomi-Ridolfo.pdf (accessed on 18 May 2021).
7. de Castro, A.; Maja, J.M.; Owen, J.; Robbins, J.; Pena, J. Experimental approach to detect water stress in ornamental plants using suas-imagery. *Proc. SPIE* **2018**, *10664*, 106640N. [CrossRef]
8. Ehsani, R.; Maja, J. The Rise of Small UAVs in Precision Agriculture. 2013. Available online: https://elibrary.asabe.org/pdfviewer.asp?param1=s:/8y9u8/q8qu/tq9q/5tv/HH/72IGHJ/IG/K/hBIG_K_HO.5tv&param2=L/IK/IGIH&param3=HJG.HIN.ILL.IGJ&param4=44296 (accessed on 28 May 2021).
9. Bowman, K.D. Identification of Woody Plants with Implanted Microchips. *Am. Soc. Hortic. Sci.* **2005**, *15*, 352–354. [CrossRef]
10. Ampatzidis, Y.; Vougioukas, S. Field Experiments for evaluating the incorporation of RFID and barcode registration and digital weighing technologies in manual fruit harvesting. *Comput. Electron. Agric.* **2009**, *66*, 166–172. [CrossRef]
11. Luvisi, A.; Panattoni, A.; Bandinelli, R.; Rinaldelli, E.; Pagano, M.; Gini, B.; Triolo, E. RFID microchip internal implants: Effects on grapevine histology. *Sci. Hortic.* **2010**, *124*, 349–353. [CrossRef]
12. Luvisi, A.; Pagano, M.; Bandinellie, R.; Rinaldelli, E.; Gini, B.; Scarton, M.; Triolo, E. Virtual vineyard for grapevine management purposes: A RFID/GPS application. *Comput. Electron. Agric.* **2011**, *75*, 368–371. [CrossRef]
13. Kumagai, M.H.; Miller, P. Development of electronic barcodes for use in plant pathology and functional genomics. *Plant Mol. Biol.* **2006**, *61*, 515–523. [CrossRef] [PubMed]
14. Ampatzidis, Y.; Vougioukas, S.; Bochtis, D.; Tsatsarelis, C. A yield mapping system for hand-harvested fruits based on RFID and GPS location technologies: Field testing. *Precis. Agric.* **2008**, *10*, 63–72. [CrossRef]
15. About-RFID. Available online: https://www.impinj.com/about-rfid/types-of-rfid-systems#:~{}:text=Passive%20RFID%20systems%20can%20operate,typically%20less%20than%2010%20m (accessed on 10 November 2020).
16. Fernandez, R. RFID: How It Works and What It Can Do for the Green Industry. *Am. Hort Newsl.* **2014**, *9*, 6–11. Available online: https://www.researchgate.net/publication/271194305_RFID_How_It_Works_And_What_It_Can_Do_For_The_Green_Industry (accessed on 8 September 2020).
17. Quino, J.; Maja, J.; Robbins, J.; Fernandez, R.; Owen, J.S.; Chappell, M. RFID and drones: The next generation of plant inventory. *AgriEngineering* **2021**, *3*, 168–181. [CrossRef]
18. Saraswat, D.; Robbins, J. High-Tech Tags. Nursery Management. 2011. Available online: https://www.nurserymag.com/article/nm1111-rfid-technology-tags/ (accessed on 28 May 2021).
19. R.A. Dudley Nurseries, Inc. Available online: https://www.radudley.com/plants-archive (accessed on 23 September 2021).
20. Buffi, A.; Motroni, A.; Nepa, P.; Tellini, B.; Cioni, R. A SAR-based measurement method for Passive-Tag positioning with a Flying UHF-RFID Reader. *IEEE Trans. Instrum. Meas.* **2019**, *68*, 845–853. [CrossRef]
21. Siachalou, S.; Megalou, S.; Tzitzis, A.; Tsardoulias, E.; Bletsas, A.; Sahalos, J.; Yioultsis, T.; Dimitriou, A.G. Robotic Inventorying and Localization of RFID Tags Exploiting Phase-Fingerprinting. In Proceedings of the 2019 IEEE International Conference on RFID Technology and Applications (RFID-TA), Pisa, Italy, 25–27 September 2019; pp. 362–367. [CrossRef]
22. Yang, P.; Wu, W.; Moniri, M.; Chibelushi, C.C. Efficient Object Localization Using Sparsely Distributed Passive RFID Tags. *IEEE Trans. Ind. Electron.* **2013**, *60*, 5914–5924. [CrossRef]

MDPI

Article

Comparison of RGB and Multispectral Unmanned Aerial Vehicle for Monitoring Vegetation Coverage Changes on a Landslide Area

Flavio Furukawa [1],*, Lauretta Andrew Laneng [1], Hiroaki Ando [1], Nobuhiko Yoshimura [2], Masami Kaneko [2] and Junko Morimoto [1]

[1] Laboratory of Ecosystem Management, Graduate School of Agriculture, Hokkaido University, Sapporo 060-8587, Japan; lla@for.agr.hokudai.ac.jp (L.A.L.); hiro-pufferfish-1997@eis.hokudai.ac.jp (H.A.); jmo1219@for.agr.hokudai.ac.jp (J.M.)

[2] Department of Environmental and Symbiotic Science, Rakuno Gakuen University, Ebetsu 069-8501, Japan; n-yoshim@rakuno.ac.jp (N.Y.); kaneko@rakuno.ac.jp (M.K.)

* Correspondence: furuka@for.agr.hokudai.ac.jp

Abstract: The development of UAV technologies offers practical methods to create landcover maps for monitoring and management of areas affected by natural disasters such as landslides. The present study aims at comparing the capability of two different types of UAV to deliver precise information, in order to characterize vegetation at landslide areas over a period of months. For the comparison, an RGB UAV and a Multispectral UAV were used to identify three different classes: vegetation, bare soil, and dead matter, from April to July 2021. The results showed high overall accuracy values (>95%) for the Multispectral UAV, as compared to the RGB UAV, which had lower overall accuracies. Although having lower overall accuracies, the vegetation class of the RGB UAV presented high producer's and user's accuracy over time, comparable to the Multispectral UAV results. Image quality played an important role in this study, where higher accuracy values were found on cloudy days. Both RGB and Multispectral UAVs presented similar patterns of vegetation, bare soil, and dead matter classes, where the increase in vegetation class was consistent with the decrease in bare soil and dead matter class. The present study suggests that the Multispectral UAV is more suitable in characterizing vegetation, bare soil, and dead matter classes on landslide areas while the RGB UAV can deliver reliable information for vegetation monitoring.

Keywords: landslides; unmanned aerial vehicle (UAV); multispectral; RGB; vegetation monitoring

1. Introduction

The evolution of remote sensing technology allows a feasible method for gathering detailed information for mapping land-cover changes [1], drought monitoring [2], and analyzing complex attributes [3,4] over space and time. This technology uses different types of sensor onboard satellites, airborne or unmanned aerial vehicles (UAVs), and provides different methods of vegetation classification at large and small scales. Remote sensing offers a practical approach to designing strategies for the management of forest disaster such as evaluating landslide-prone areas through airborne, UAV, and ground-based remote sensing [5], as well as for evaluating changes in vegetation cover after a wildfire for post-fire management by using satellite-based remote sensing and UAV [6].

To deal with the need to assess forest disasters for quick management decisions, the advancement of satellite-based remote sensing applications was initiated for detecting areas affected by natural disasters such as windthrow and landslide for forest restoration or forest disaster management purposes [7], assessing vegetation recovery [8], detecting and mapping [9,10] of landslide areas, and creating historical landslide inventories [11]. Although playing an important role in forest disaster management, satellite-based remote sensing has some limitations in terms of spatial and temporal resolution of the data.

Local cloudiness, low temporal and spatial resolution, and gaps on the image create a complex task for vegetation classification [2,12,13]. Recently, very high spatial resolution satellites are available, delivering data of around 30 cm per pixel [14]; despite a high spatial resolution, this could be a limitation in understanding changes happening on smaller scales [15]. A one-day temporal resolution satellite dataset is also available [16], but cloud cover can still be a hindrance to acquiring the desired dataset.

Nevertheless, the evolution of UAV technologies has brought RGB sensors and multispectral sensors to UAVs for more detailed information as compared to satellite-based remote sensing, making it possible to acquire centimeter-level imagery at any time. In terms of cost and availability, multispectral UAVs cost much more and have lower availability while UAVs coupled with RGB sensors are more affordable and accessible. However, RGB UAVs are limited for remote sensing analysis, especially on complex and heterogeneous forest-covered areas, due to the sensor having an RGB array filter [17]. Despite these limitations, Ruwaimana et al., [18] proved that the application of UAVs for vegetation classification on mangrove ecosystems provided higher accuracy concerning object-based and pixel-based classification compared to satellite imagery. The implementation of UAV systems gained attention not only due to their efficiency to map land cover [19,20] vegetation on a coastal dune [21] but also as an effective tool in mapping and characterizing burned areas affected by wildfires [22], as well as landslide displacement mapping [23].

Comparing the performance between satellite image and aerial photo for vegetation mapping [18], testing the applicability of UAVs for mapping and monitoring geohazard areas [24], as well as characterizing and monitoring landslides, [25] have been well documented. Yet there is still a gap in understanding how RGB and multispectral sensors on UAVs perform in assessing the regrowth of vegetation in an area affected by a natural disaster such as a landslide. In order to understand the condition of the affected area to make management decisions, it is important to determine the vegetation coverage to understand its regrowth on a landslide area on a small scale [26,27], and to evaluate the area's ability to undergo a natural regeneration process on a regional scale. Besides, the presence of debris including fallen logs and litter provides a potential for vegetation regrowth by sprouting and seedbanks [28] and by the colonization of early successional plant species [29–31]. Moreover, due to unstable bare soil conditions, vegetation regrowth is slow or non-existent on hillslopes [32].

Therefore, we mapped a landslide area considering three different classes (i.e., vegetation, bare soil, and dead matter) to assess the changes in coverage pattern focusing on vegetation growth throughout four months using two different types of UAV. This study aimed to compare the performance of an RGB UAV and a multispectral UAV using a pixel-based classification approach, to understand how the spectral resolution and the type of sensor can deliver precise information for vegetation mapping on a landslide area. The findings from this study can provide baseline information for forest managers and ecologists in selecting the applicable system and to assist in deciding on further management practice in the affected area, especially in understanding post-landslide regeneration. Thus, this study was designed for the following objectives: (1) to understand the differences between the UAV systems for vegetation mapping in a landslide area assessing the parameters that affect the datasets; (2) to monitor the monthly changes of vegetation, bare soil, and dead matter areas in landslides for the management of vegetation recovery.

2. Materials and Methods

2.1. Study Area

In 2018, the northernmost island of Japan, Hokkaido, was affected by the Hokkaido Eastern Iburi Earthquake, with a magnitude of 6.7 [33] and several aftershocks. The seism triggered over 4000 ha of landslides around different municipalities in western Atsuma town [34].

This study was conducted in an area of surface failure of approximately 8 ha in the Uryu District at Atsuma town (42°43′20.3″ N, 141°55′22.5″ E) (Figure 1). The area was

characterized by moderate terrain with a predominant slope and an angle of less than 40 degrees, and the elevation ranged from 57m to 121m. Soil structure consists of Neogene sedimentary rock, i.e., sandstone, siltstone, mudstone, and a conglomerate that was covered by a thick pyroclastic fall deposit from the Tarumae Volcano [34,35]. The area was covered mostly by deciduous trees, fallen trees, and bare soil, an effect of the landslide, with grasses and shrubs such as Japanese sweet-coltsfoot (*Petasites japonicus* (Siebold et Zucc.) Maxim.), dwarf bamboo (*Sasa* spp.), and wild berries (*Rubus* spp.), etc.
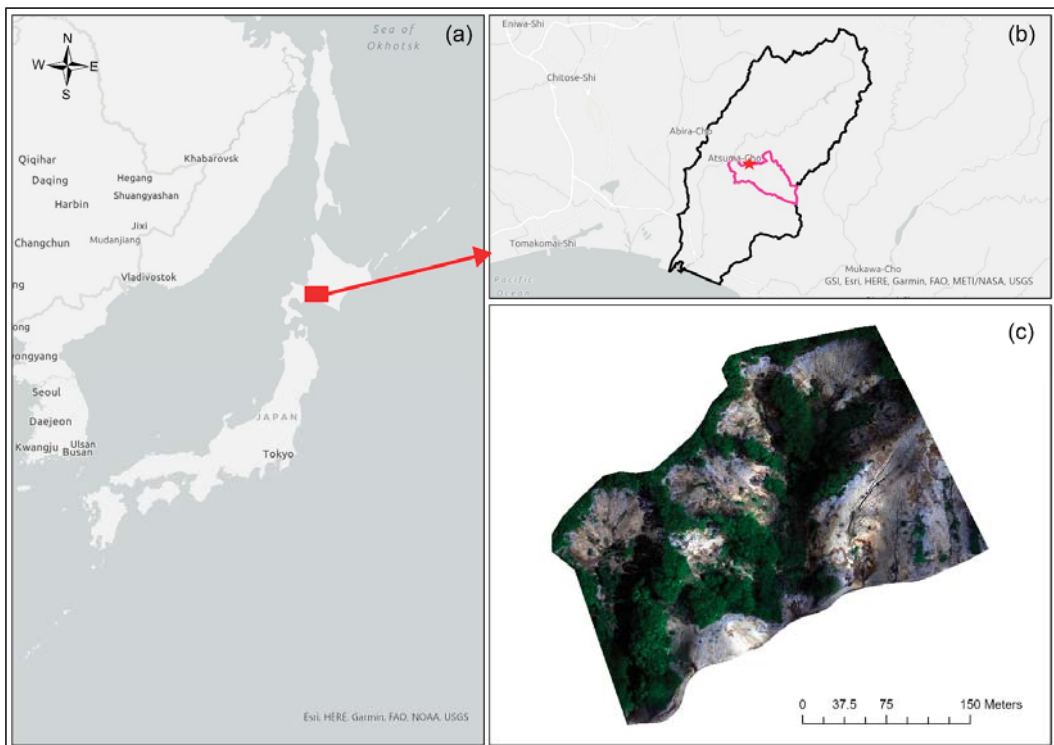
Figure 1. (**a**) The study area located in Hokkaido, Japan, (**b**) at Atsuma town (black boundary), and in Uryu district (pink boundary) located at 42°43′20.3″ N, 141°55′22.5″ E (red star); (**c**) with the true color ortho-mosaic taken with the Multispectral UAV on 9 June.

2.2. Datasets

For acquisition of the aerial images to create the ortho-mosaics for analysis, two different UAVs were used: the DJI Phantom 4 Pro, and the DJI Phantom 4 Multispectral. The DJI Phantom 4 Pro has a 1-inch CMOS RGB sensor, which acquires the red, green, and blue wavelengths in the same sensor, delivering one 5472 × 3648 pixels RGB image per shot. On the other hand, the DJI Phantom 4 Multispectral, has six 1/2.9-inch CMOS sensors, one RGB sensor for visible imaging and five monochrome sensors for multispectral imaging in different spectral bands: blue, green, red, red-edge, and near-infrared. Each band generates one image of 1600 × 1300 pixels, totalizing six images per shot. The DJI Phantom 4 Multispectral also had a Real-Time Kinect (RTK) GNSS system built in for centimeter position accuracy, but for this study, we compared only the sensors of each UAV: the RGB sensor of DJI Phantom 4 Pro (RGB UAV) and the multispectral sensor from DJI Phantom 4 Multispectral (Multispectral UAV).

The data was taken in four different flight campaigns in 2021: 14 April, 12 May, 9 June, and 9 July, with all images taken in the morning. The weather condition on 14 April and 9 July was cloudy, while being sunny on 12 May and 9 June, with no clouds (Figure 2).
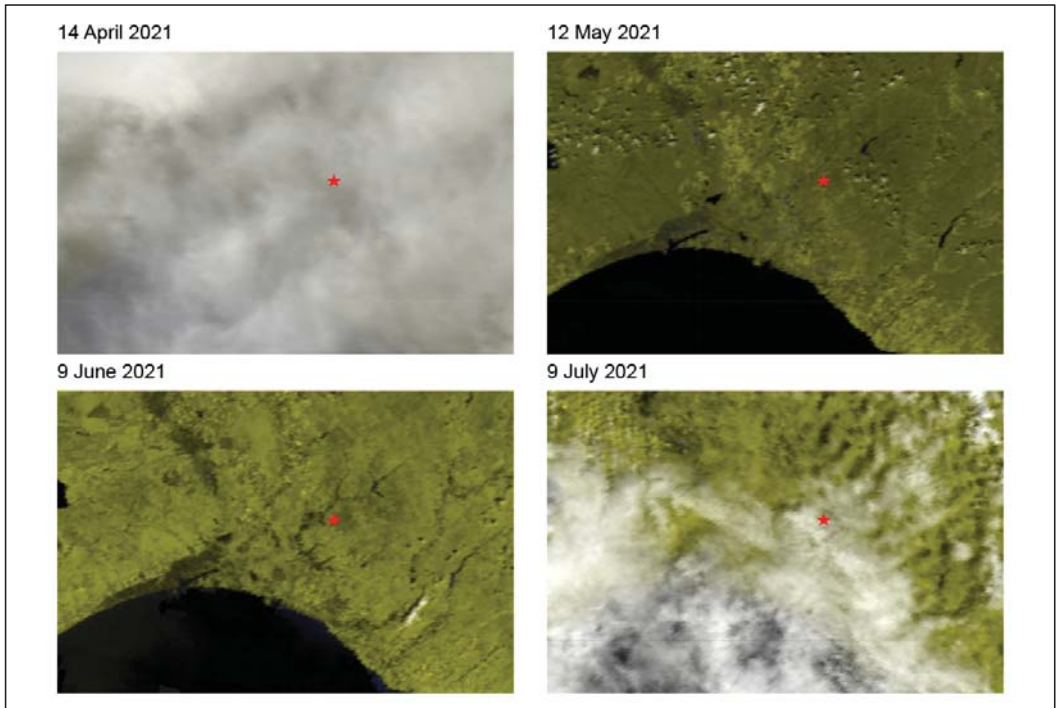
Figure 2. Cloud cover over the study site (red star) in each date, assessed using Modis M0D09GQ.006 Terra Surface Reflectance Daily Global 250 m, acquired in the morning [36].

For each flight campaign, we first flew the Multispectral UAV followed by the RGB UAV (around 14 min each flight), with 5 min in between flights to reduce the displacement of shadow areas. The UAVs were flown at 120 m of altitude, capturing images with 80% overlap and 80% side-lap to create the ortho-mosaics via photogrammetry processing. For the Multispectral UAV, images of a calibration reflectance panel were taken to be used on the calibration of the multispectral images inside the photogrammetry software [37].

To register the RGB and Multispectral ortho-mosaics, 15 ground control points (GCPs) made from plywood were placed along the study site and the position of each point was collected using the Drogger RTK GNSS system [38] connected to the ICHIMILL virtual reference station (VRS) [39] service provided by Softbank Japan [40]. The accuracy of each point position was around 2 cm.

For each flight campaign, a field survey was also conducted. Using the Drogger RTK system connected to an android tablet with the open-source application Open Data Kit (ODK) [41], we collected ground truth points to classify the ortho-mosaics and validate the classification results. Inside the ODK application, a questionnaire form was previously created containing the classes to be chosen on the field, and photos were taken with the tablet (Figure 3).

Figure 3. (**a**) The red dot is the vegetation class obtained by ODK with the RTK system accuracy (2 cm) on the Multispectral UAV ortho-mosaic in true color, and (**b**) the respective photo of a Japanese sweet-coltsfoot for verification on 12 May.

2.3. Data Processing

To create the ortho-mosaics, we used the photogrammetry technique for UAVs [42], where each image dataset was processed on Agisoft Metashape [43] with the GCPs taken on the field to improve the position accuracy of the ortho-mosaic. For the Multispectral UAV, the 5 monochrome images were automatically merged creating a multispectral ortho-mosaic, and the images were also calibrated in the software using the calibration reflectance panel images to convert the digital numbers into reflectance values. All ortho-mosaics were later uploaded into Google Earth Engine [44] and resampled to the same spatial resolution of 5.5 cm using the bilinear interpolation mode.

2.4. Classification and Accuracy Assessment

The processing workflow is shown in Figure 4. To identify vegetation cover in the study area, three different classes were established: vegetation, bare soil, and dead matter (dead leaves, fallen trees, and tree branches). To create the reference dataset, an empirical test was made and 30 samples for each class were selected to conduct the study. The reference dataset was composed of samples taken on the field and samples selected from a visual interpretation of the ortho-mosaic, totalizing 90 samples. For each date, the same reference dataset was used for the RGB and the multispectral dataset.

The classification and the assessment for this study were made by applying the cross-validation method [45], using 5 k-folds inside Google Earth Engine. The built-in support vector machine classifier with the linear kernel type [46] was selected to classify the ortho-mosaics. This method was chosen due to its robustness in assessing the predictor model, which in this study was mainly influenced by the ortho-mosaic.

First, the reference data was divided into five different folds randomly, where four folds (80% of the reference dataset) were used to train the classifier and one fold (20% of the reference dataset) to test the classifier. A total of five iterations were made to test all folds.

For each iteration, we created a classification model based on the training dataset and the support vector machine classifier. Then, the classification model generated a prediction map which was put against the independent testing dataset to achieve a confusion matrix. The confusion matrix delivered three different results: overall accuracy, producer's accuracy (PA), and user's accuracy (UA).
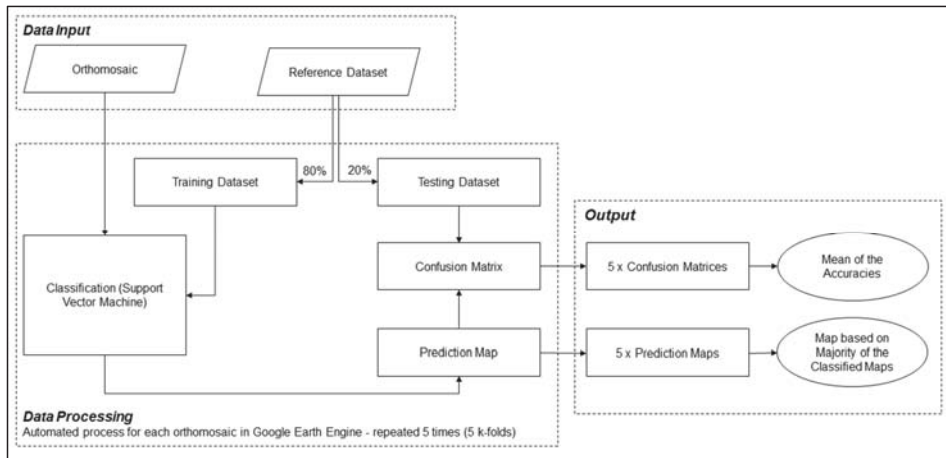
Figure 4. The processing workflow for each dataset.

The final assessment values for each ortho-mosaic were created considering the mean of the accuracies of all five confusion matrices. To create the final classification map of each ortho-mosaic, an aggregation was made considering the majority of classes among the five iterations for each pixel; the final classification map presented a straightforward portrayal of confidence for the study site, which identified the model's fit and stability. Whilst not directly measuring mapping accuracy, the relative confidence of the methodology can provide valuable information to support the interpretation of the maps [47].

3. Results

3.1. UAV Orthomosaics

Figure 5 shows that the higher spatial resolution of the RGB UAV created ortho-mosaics with more details compared to the Multispectral UAV ortho-mosaic, even though the data were resampled to 5.5 cm.
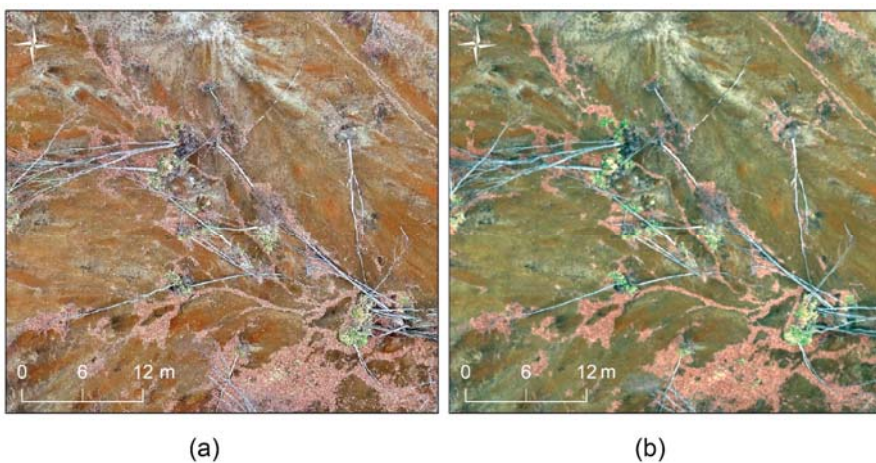
Figure 5. (**a**) The RGB UAV in true color ortho-mosaic resampled to 5.5 cm, (**b**) the Multispectral UAV in true color ortho-mosaic resampled to 5.5 cm. The RGB UAV ortho-mosaic has a sharper image compared to the Multispectral UAV ortho-mosaic.

The RGB and Multispectral UAV ortho-mosaic colors and amount of shadow were also influenced by the weather condition (Figure 2). Due to the cloudy condition and rain on the previous days of 14 April and 9 July [48,49], the ortho-mosaics were generated with brownish soil and without any shadow effect. During the sunny condition on 12 May and 9 June, the ortho-mosaics were generated with whitish soil and shadow effects (Figure 6).
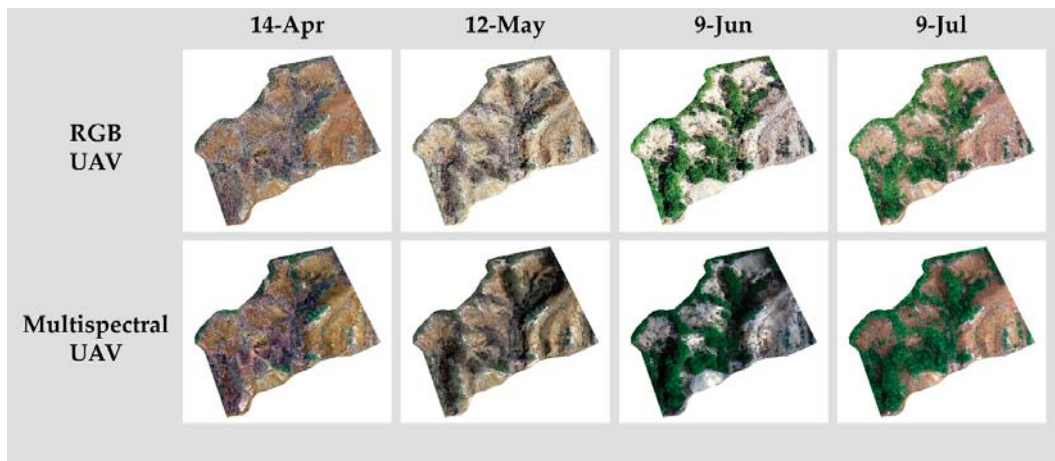
Figure 6. The RGB UAV and Multispectral UAV ortho-mosaics generated by Agisoft Metashape on 14 April, 12 May, 9 June and 9 July. The soil color on 14 April and 9 July was brownish with no shadow, while on 12 May and 9 June, the soil was whitish with shadow areas.

3.2. Performance of the UAV's Imagery

The performance of the UAV's imagery was accessed considering the overall accuracies calculated from the mean of all five K-folds of each dataset (Table 1). The Multispectral UAV delivered higher percentages (more than 95%) throughout the months. On the other hand, the RGB UAV presented slightly lower overall values, with the highest values on 14 April (94.44%) and on 9 July (90%), while for pm 12 May and 9 June, the values were 72.22% and 64.44% respectively.

Table 1. Overall accuracies for the Multispectral UAV and RGB UAV on each date with the respective weather condition.

		14-Apr	**12-May**	**9-Jun**	**9-Jul**
	Weather	Cloudy	Sunny	Sunny	Cloudy
Overall	RGB	94.44%	72.22%	64.44%	90.00%
Accuracy	Multispectral	97.78%	95.56%	96.67%	98.89%

Looking into the PA and UA of all classes (i.e., vegetation, bare soil, and dead matter) (Table 2), the RGB UAV had the highest values for the three classes on April 14th and July 9th, while lower values were found on 12 May and 9 June, mainly on bare soil and dead matter classes. The Multispectral UAV was more consistent compared to the overall accuracies in Table 1, and both PA and UA showed high values throughout the months for all three classes, above 90%.

Table 2. Producer's and user's accuracy of the vegetation, bare soil, and dead matter classes.

		14-Apr		12-May		9-Jun		9-Jul	
		PA	UA	PA	UA	PA	UA	PA	UA
Vegetation	RGB	100.00%	100.00%	93.78%	88.50%	93.33%	86.00%	100.00%	92.00%
	Multispectral	97.78%	97.14%	96.00%	96.67%	100.00%	100.00%	97.14%	100.00%
Bare Soil	RGB	87.14%	94.17%	43.05%	63.00%	68.00%	46.63%	81.43%	92.67%
	Multispectral	100.00%	100.00%	100.00%	94.64%	96.00%	97.14%	100.00%	100.00%
Dead Matter	RGB	91.00%	94.07%	82.26%	64.12%	49.79%	59.33%	90.64%	84.33%
	Multispectral	96.00%	96.00%	91.31%	97.14%	97.50%	95.00%	100.00%	97.50%

PA: Producer's Accuracy, UA: User's Accuracy.

3.3. Classification Results

The classification results created through the aggregation considering the majority classes for the five prediction maps are shown in Figure 7.
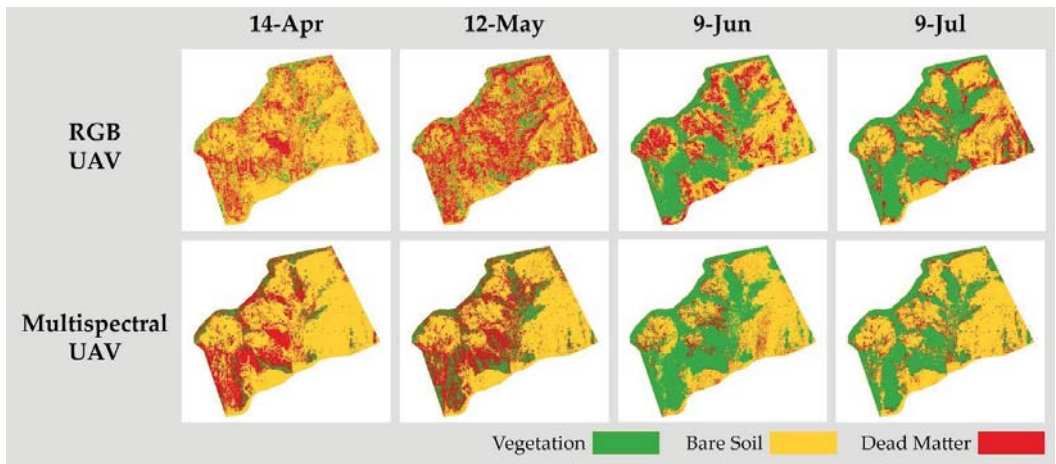
Figure 7. Classification results from the Multispectral UAV and the RGB UAV on each date.

Despite the high accuracy values on the Multispectral UAV, the visual interpretation showed some disparities when compared to the respective ortho-mosaics (Figure 8). Misclassification mainly occurred on the shadowed area (Figure 8a), where both bare soil and dead matter areas were misclassified as vegetation class (Figure 8b).
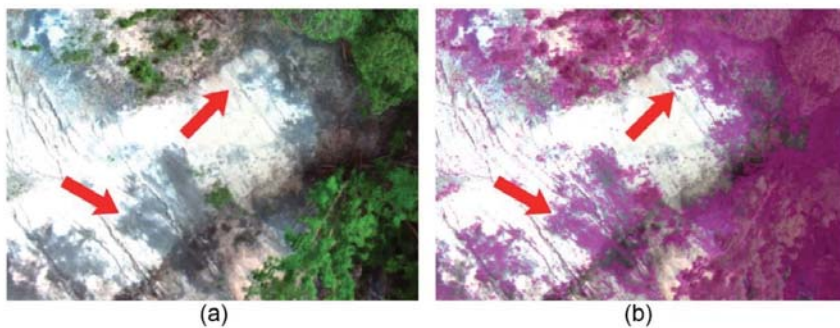
Figure 8. (**a**) The Multispectral UAV ortho-mosaic in true color on 9 June, (**b**) vegetation class (pink), misclassifying bare soil and dead matter areas (red arrows).

The RGB UAV generated more misclassification throughout the study area. On 12 May and 9 June, it was clear to see the misclassification of the dead matter class on bare areas (Figures 6 and 7). A closer look on 12 May (Figure 9) showed misclassification occurring even in no shadow areas.
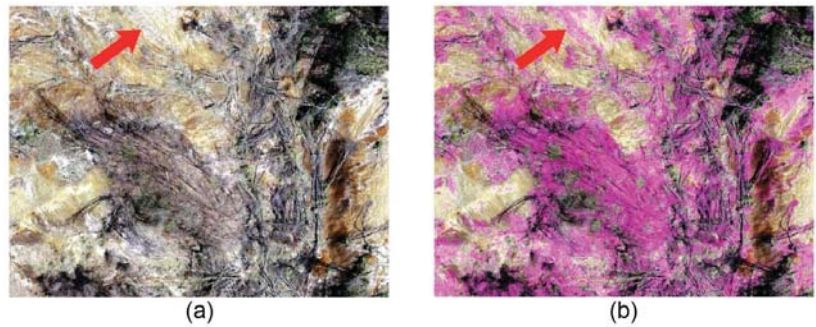
Figure 9. (**a**) The RGB UAV ortho-mosaic in true color on 12 May, (**b**) the dead matter class (pink), misclassifying bare areas (red arrows).

The comparison among the classified maps in terms of class coverage (i.e., vegetation, bare soil, and dead matter) over the months, showed a similar pattern in the RGB UAV and the Multispectral UAV from April to June (Figure 10), where we found an increase in the vegetation class and a decrease in both bare soil and dead matter classes.
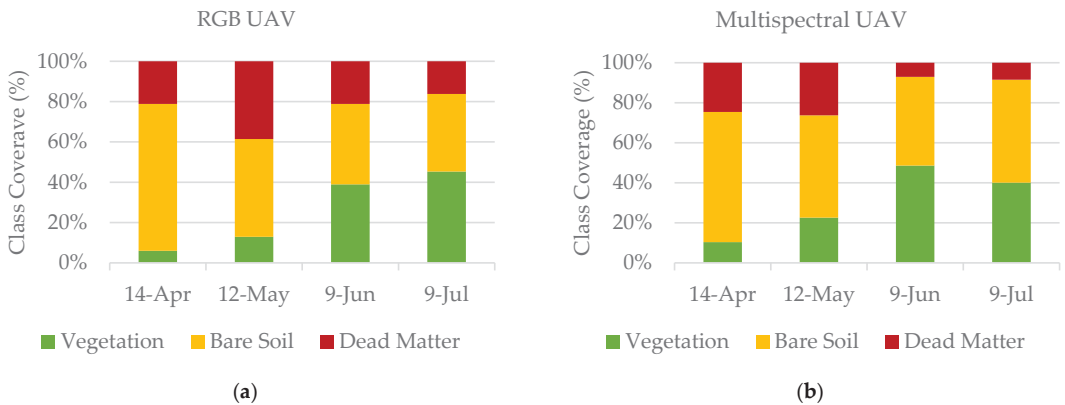
Figure 10. The graph shows the class coverage (%) generated from the (**a**) RGB UAV and (**b**) Multispectral UAV over time.

In the Multispectral UAV, the proportion for the vegetation class on 9 June was higher when compared to 9 July, while values for bare soil increased during the same period. This was due to the misclassification that happened in the shadowed area of 9 June (Figure 8). Another problem also occurred on the RGB UAV, where there was an increase in the dead matter class from 14 April to 12 May, misclassified by the inclusion of the dead matter class on bare areas (Figure 9).

Comparing the vegetation class of RGB UAV and Multispectral UAV, besides presenting high values of PA and UA, it was possible to see a similar pattern of vegetation growth around the already vegetated areas (Figure 11). On the other hand, for the bare soil and dead matter classes, the similarities were much smaller when comparing the RGB UAV and the Multispectral UAV (Figures 12 and 13), as expected by the low values of the PA and UA accuracies from these classes on the RGB UAV.
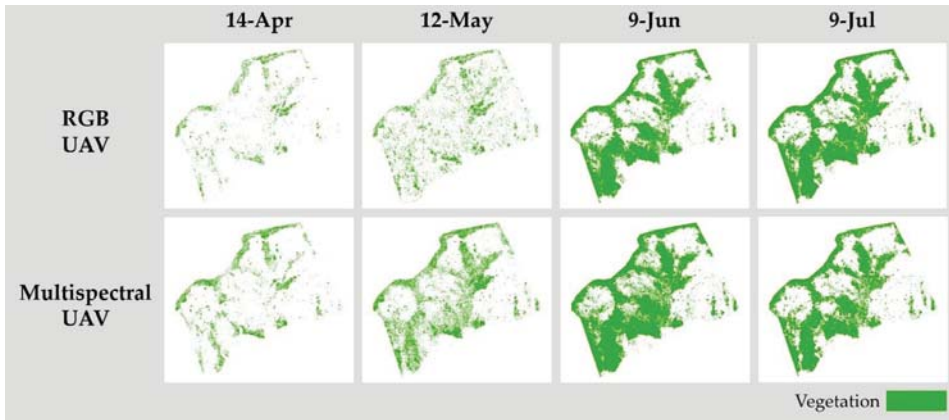
Figure 11. Change of vegetation class over the months from the RGB and multispectral UAV.
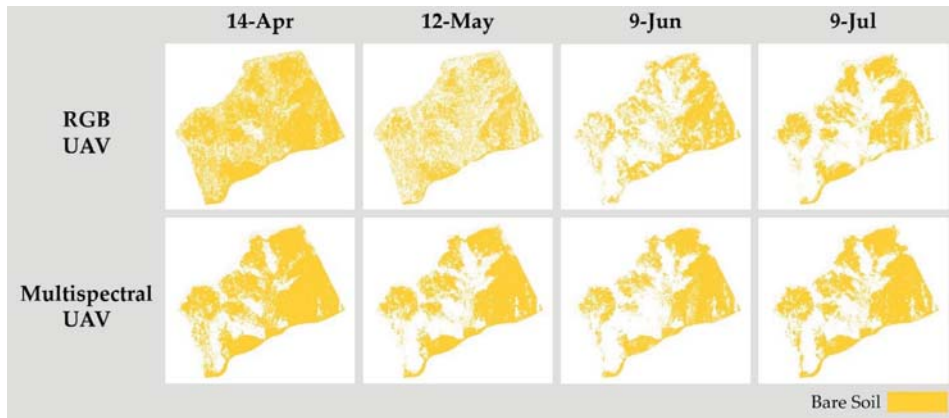
Figure 12. Change of bare soil class over the months from the RGB and multispectral UAV.
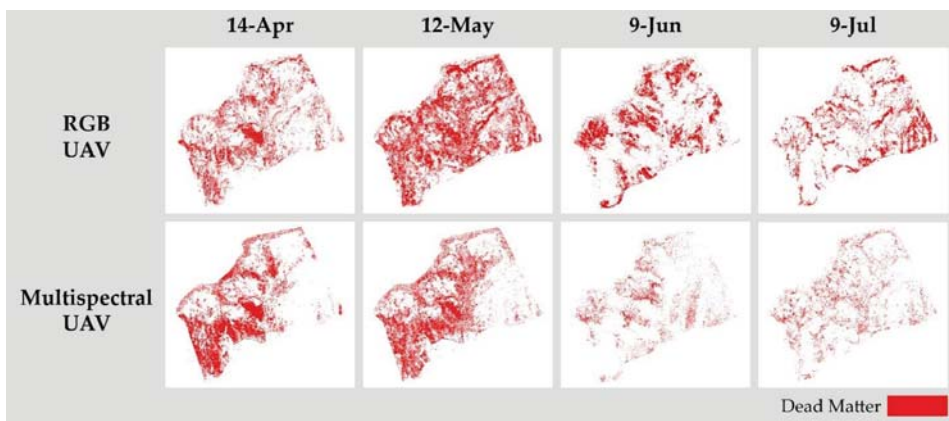
Figure 13. Change of dead matter class over the months from the RGB and multispectral UAV.

4. Discussion

4.1. Comparison between the RGB UAV and the Multispectral UAV

The evaluation of the performance of each UAV showed that the Multispectral UAV delivered more consistent results for every class, while the RGB UAV, even though more detailed (higher spatial resolution), suffered from the smaller number of bands and the type of sensor [50], generating a more speckled classification map. On the other hand, even though having five distinct spectral bands and higher accuracy values, the Multispectral UAV generated some misclassification, mainly on shadowed areas [51,52].

Apart from the misclassification of shadowed areas, the weather conditions played an important role in this study, mainly for the RGB UAV. Cloudy days with brownish soil had better results compared to sunny weather with whitish soil, delivering higher accuracy values for both RGB UAV and Multispectral UAV. This was also confirmed by Duffy et al. [51], which suggests that cloudy days had consistent lighting conditions, improving the homogeneity of the spectral signatures.

Even though the RGB UAV and the Multispectral UAV generated misclassifications, they could still provide valuable information regarding the monitoring of classes' coverage changes on a landslide area. The RGB UAV delivered impressive results, being able to monitor vegetation growth in detail despite the low cost of the system. Although the visual analysis showed a discrepancy between the RGB UAV classification map and the respective ortho-mosaics on the bare soil and dead matter classes, when comparing the area of coverage by the classes both UAV systems had similar patterns, with the vegetation class reflecting a gradual increase from April to June along with the decrease in bare soil and dead matter classes over these months.

Considering the pixel-based classification approach, the Multispectral UAV is recommended, due to its ability to acquire data on the red edge and near-infrared wavelengths, optimal for vegetation analysis. On the other hand, the higher spatial resolution of the RGB UAV could enable a more accurate visual inspection of the geohazard areas as reported by Rossi et al. [24]. Future studies using an object-based classification approach are suggested to understand the difference between the two UAV systems considering spatial resolution [18]. Therefore, both the RGB UAV and the Multispectral UAV proved suitable for evaluating the capability of the area to undergo a natural regeneration process, at a centimeter-level.

4.2. Vegetation, Bare Soil, and Dead Matter Monitoring

The results showed not only the possibility of monitoring changes throughout the months, but also locating where the changes happened. This is key since monitoring pattern changes from dead matter to vegetation class could provide an initial understanding of the potential of vegetation regeneration on the landslides area. The applied methodology also proved suitable for areas with a dominance of deciduous forest, where the identification of the dead matter was possible after the winter season when the trees had no foliage.

The vegetation growth around the already vegetated areas confirms that the condition of unstable soil after landslides, preventing seeds from nearby intact forests to germinate due to the erosion of soil, infertile soil, and other abiotic factors, slows down or impedes the regeneration process. The availability of decomposing material, i.e., fallen trees and leaf litter, favor the initial stage of plant succession on the landslide area [53,54] by protecting the seeds or saplings from rolling down due to soil erosion. as well improving soil fertility through the decomposition process.

The expansion in vegetation coverage observed during the four consecutive months could indicate that a post-landslide regeneration occurred in the affected area. This suggests that the increase in vegetation recovery on the landslides area might improve stability, especially on the bare soil area, in order to support seed germination and the growth of saplings, though this process would take a long time [53,55]. Thus, monitoring the pattern changes through time comparing the three classes, i.e., vegetation, bare soil, dead matter, contributes to a more detailed ecological research planning. Due to the role of

landslide areas in regenerating high vegetation species richness after disturbance [55,56], the annual vegetation growth dataset is suggested to infer the potential of the study area for dynamic regeneration.

5. Conclusions

Overall, the present study reveals that Multispectral UAVs are more applicable for characterizing vegetation, bare soil, and dead matter in areas affected by landslides, highlighting that cloudy weather and brownish soil are recommended to create a more reliable dataset. However, the RGB UAV can play an important role if the purpose is to monitor vegetation development, which is a positive achievement, especially in terms of accessibility and availability of the tool. In addition, the monitoring of vegetation, bare soil, and dead matter classes over four months suggests the initial recovery of vegetation on the landslide area. This indicates that the monthly annual dataset and multi-year dataset will serve a better understanding of the dynamic process of initial vegetation recovery. Future work is suggested using an object-based classification approach, in order to take advantage of the higher spatial resolution of the RGB UAV dataset.

Author Contributions: Conceptualization, F.F., L.A.L. and J.M.; data curation, H.A.; formal analysis, F.F.; investigation, F.F. and H.A.; methodology, F.F.; project administration, F.F.; resources, M.K.; software, F.F.; supervision, M.K. and J.M.; validation, N.Y.; visualization, L.A.L.; writing—original draft, F.F. and L.A.L.; writing—review & editing, F.F., L.A.L., N.Y. and J.M. All authors have read and agreed to the published version of the manuscript.

Institutional Review Board Statement: Not applicable.

Informed Consent Statement: Not applicable.

Data Availability Statement: Not applicable.

Conflicts of Interest: The authors declare no conflict of interest.

References

1. Hansen, M.C.; Loveland, T.R. A review of large area monitoring of land cover change using Landsat data. *Remote Sens. Environ.* **2012**, *122*, 66–74. [CrossRef]
2. West, H.; Quinn, N.; Horswell, M. Remote sensing for drought monitoring & impact assessment: Progress, past challenges and future opportunities. *Remote Sens. Environ.* **2019**, *232*, 111291. [CrossRef]
3. Blaschke, T. Object based image analysis for remote sensing. *ISPRS J. Photogramm. Remote Sens.* **2010**, *65*, 2–16. [CrossRef]
4. Langner, A.; Titin, J.; Kitayama, K. The Application of Satellite Remote Sensing for Classifying Forest Degradation and Deriving Above-Ground Biomass Estimates. *Angew. Chem. Int. Ed.* **2012**, *6*, 23–40.
5. Casagli, N.; Frodella, W.; Morelli, S.; Tofani, V.; Ciampalini, A.; Intrieri, E.; Raspini, F.; Rossi, G.; Tanteri, L.; Lu, P. Spaceborne, UAV and ground-based remote sensing techniques for landslide mapping, monitoring and early warning. *Geoenviron. Dis.* **2017**, *4*, 1–23. [CrossRef]
6. Martinez, J.L.; Lucas-Borja, M.E.; Plaza-Alvarez, P.A.; Denisi, P.; Moreno, M.A.; Hernández, D.; González-Romero, J.; Zema, D.A. Comparison of Satellite and Drone-Based Images at Two Spatial Scales to Evaluate Vegetation Regeneration after Post-Fire Treatments in a Mediterranean Forest. *Appl. Sci.* **2021**, *11*, 5423. [CrossRef]
7. Furukawa, F.; Morimoto, J.; Yoshimura, N.; Kaneko, M. Comparison of Conventional Change Detection Methodologies Using High-Resolution Imagery to Find Forest Damage Caused by Typhoons. *Remote Sens.* **2020**, *12*, 3242. [CrossRef]
8. Lin, C.-Y.; Lo, H.-M.; Chou, W.-C.; Lin, W.-T. Vegetation recovery assessment at the Jou-Jou Mountain landslide area caused by the 921 Earthquake in Central Taiwan. *Ecol. Modell.* **2004**, *176*, 75–81. [CrossRef]
9. Hervás, J.; Barredo, J.I.; Rosin, P.L.; Pasuto, A.; Mantovani, F.; Silvano, S. Monitoring landslides from optical remotely sensed imagery: The case history of Tessina landslide, Italy. *Geomorphology* **2003**, *54*, 63–75. [CrossRef]
10. Chen, W.; Li, X.; Wang, Y.; Chen, G.; Liu, S. Forested landslide detection using LiDAR data and the random forest algorithm: A case study of the Three Gorges, China. *Remote Sens. Environ.* **2014**, *152*, 291–301. [CrossRef]
11. Martha, T.R.; Kerle, N.; van Westen, C.J.; Jetten, V.; Vinod Kumar, K. Object-oriented analysis of multi-temporal panchromatic images for creation of historical landslide inventories. *ISPRS J. Photogramm. Remote Sens.* **2012**, *67*, 105–119. [CrossRef]

12. Fuentes-Peailillo, F.; Ortega-Farias, S.; Rivera, M.; Bardeen, M.; Moreno, M. Comparison of vegetation indices acquired from RGB and Multispectral sensors placed on UAV. In Proceedings of the 2018 IEEE International Conference on Automation/XXIII Congress of the Chilean Association of Automatic Control (ICA-ACCA), Concepcion, Chile, 17–19 October 2018; pp. 1–6.
13. Al-Wassai, F.A.; Kalyankar, N.V. Major Limitations of Satellite images. *J. Glob. Res. Comput. Sci.* **2013**, *4*, 51–59.
14. MAXAR–CONSTELLATION. Available online: https://www.maxar.com/constellation (accessed on 30 July 2021).
15. Woodcock, C.E.; Strahler, A.H. The factor of scale in remote sensing. *Remote Sens. Environ.* **1987**, *21*, 311–332. [CrossRef]
16. Planet Labs Inc Satellite Imagery and Archive. Available online: https://www.planet.com/products/planet-imagery/ (accessed on 2 July 2021).
17. Vanamburg, L.K.; Trlica, M.J.; Hoffer, R.M.; Weltz, M.A. Ground based digital imagery for grassland biomass estimation. *Int. J. Remote Sens.* **2006**, *27*, 939–950. [CrossRef]
18. Ruwaimana, M.; Satyanarayana, B.; Otero, V.; Muslim, A.M.; Syafiq, A.M.; Ibrahim, S.; Raymaekers, D.; Koedam, N.; Dahdouh-Guebas, F. The advantages of using drones over space-borne imagery in the mapping of mangrove forests. *PLoS ONE* **2018**, *13*, e0200288. [CrossRef] [PubMed]
19. Kalantar, B.; Mansor, S.B.; Sameen, M.I.; Pradhan, B.; Shafri, H.Z.M. Drone-based land-cover mapping using a fuzzy unordered rule induction algorithm integrated into object-based image analysis. *Int. J. Remote Sens.* **2017**, *38*, 2535–2556. [CrossRef]
20. Bellia, A.F.; Lanfranco, S. A Preliminary Assessment of the Efficiency of Using Drones in Land Cover Mapping. *Xjenza* **2019**, *7*, 18–27. [CrossRef]
21. Suo, C.; McGovern, E.; Gilmer, A. Coastal Dune Vegetation Mapping Using a Multispectral Sensor Mounted on an UAS. *Remote Sens.* **2019**, *11*, 1814. [CrossRef]
22. Lazzeri, G.; Frodella, W.; Rossi, G.; Moretti, S. Multitemporal Mapping of Post-Fire Land Cover Using Multiplatform PRISMA Hyperspectral and Sentinel-UAV Multispectral Data: Insights from Case Studies in Portugal and Italy. *Sensors* **2021**, *21*, 3982. [CrossRef]
23. Lucieer, A.; Jong, S.M.d.; Turner, D. Mapping landslide displacements using Structure from Motion (SfM) and image correlation of multi-temporal UAV photography. *Prog. Phys. Geogr.* **2014**, *38*, 97–116. [CrossRef]
24. Rossi, G.; Tanteri, L.; Tofani, V.; Vannocci, P.; Moretti, S.; Casagli, N. Multitemporal UAV surveys for landslide mapping and characterization. *Landslides* **2018**, *15*, 1045–1052. [CrossRef]
25. Rossi, G.; Nocentini, M.; Lombardi, L.; Vannocci, P.; Tanteri, L.; Dotta, G.; Bicocchi, G.; Scaduto, G.; Salvatici, T.; Tofani, V.; et al. Integration of multicopter drone measurements and ground-based data for landslide monitoring. In *Landslides and Engineered Slopes. Experience, Theory and Practice*; CRC Press: Boca Raton, FL, USA, 2016; Volume 3, pp. 1745–1750. ISBN 9781138029880.
26. Hirata, Y.; Tabuchi, R.; Patanaponpaiboon, P.; Poungparn, S.; Yoneda, R.; Fujioka, Y. Estimation of aboveground biomass in mangrove forests using high-resolution satellite data. *J. For. Res.* **2014**, *19*, 34–41. [CrossRef]
27. Dixon, D.J.; Callow, J.N.; Duncan, J.M.A.; Setterfield, S.A.; Pauli, N. Satellite prediction of forest flowering phenology. *Remote Sens. Environ.* **2021**, *255*, 112197. [CrossRef]
28. Walker, L.R.; Velázquez, E.; Shiels, A.B. Applying lessons from ecological succession to the restoration of landslides. *Plant Soil* **2009**, *324*, 157–168. [CrossRef]
29. Chećko, E.; Jaroszewicz, B.; Olejniczak, K.; Kwiatkowska-Falińska, A.J. The importance of coarse woody debris for vascular plants in temperate mixed deciduous forests. *Can. J. For. Res.* **2015**, *45*, 1154–1163. [CrossRef]
30. Narukawa, Y.; Iida, S.; Tanouchi, H.; Abe, S.; Yamamoto, S.I. State of fallen logs and the occurrence of conifer seedlings and saplings in boreal and subalpine old-growth forests in Japan. *Ecol. Res.* **2003**, *18*, 267–277. [CrossRef]
31. Xiong, S.; Nilsson, C. The effects of plant litter on vegetation: A meta-analysis. *J. Ecol.* **1999**, *87*, 984–994. [CrossRef]
32. Buma, B.; Pawlik, Ł. Post-landslide soil and vegetation recovery in a dry, montane system is slow and patchy. *Ecosphere* **2021**, *12*, e03346. [CrossRef]
33. Japan Meteorological Agency Information on the 2018 Hokkaido Eastern Iburi Earthquake. Available online: http://www.jma.go.jp/jma/menu/20180906_iburi_jishin_menu.html (accessed on 14 July 2021).
34. Zhang, S.; Wang, F. Three-dimensional seismic slope stability assessment with the application of Scoops3D and GIS: A case study in Atsuma, Hokkaido. *Geoenviron. Dis.* **2019**, *6*, 9. [CrossRef]
35. Osanai, N.; Yamada, T.; Hayashi, S.; Kastura, S.; Furuichi, T.; Yanai, S.; Murakami, Y.; Miyazaki, T.; Tanioka, Y.; Takiguchi, S.; et al. Characteristics of landslides caused by the 2018 Hokkaido Eastern Iburi Earthquake. *Landslides* **2019**, *16*, 1517–1528. [CrossRef]
36. MOD09GQ v006. Available online: https://doi.org/10.5067/MODIS/MOD09GQ.006 (accessed on 13 July 2021).
37. Agisoft Metashape Version 1.5 Agisoft Downloads User Manuals. Available online: https://www.agisoft.com/downloads/user-manuals/ (accessed on 4 July 2021).
38. DG-PRO1RWS RTK W-Band Gnss Receiver. Available online: https://www.bizstation.jp/ja/drogger/dg-pro1rws_index.html (accessed on 14 July 2021).
39. Retscher, G. Accuracy Performance of Virtual Reference Station (VRS) Networks. *J. Glob. Position. Syst.* **2002**, *1*, 40–47. [CrossRef]
40. Softbank ichimill IoT Service. Available online: https://www.softbank.jp/biz/iot/service/ichimill/ (accessed on 16 July 2021).
41. Hartung, C.; Lerer, A.; Anokwa, Y.; Tseng, C.; Brunette, W.; Borriello, G. Open data kit. In Proceedings of the 4th ACM/IEEE International Conference on Information and Communication Technologies and Development—ICTD '10, London, UK, 13–16 December 2010; ACM Press: New York, NY, USA, 2010; pp. 1–12.

42. Remondino, F.; Barazzetti, L.; Nex, F.; Scaioni, M.; Sarazzi, D. UAV photogrammetry for mapping and 3D modeling—Current status and future perspectives. *Int. Arch. Photogramm. Remote Sens. Spat. Inf. Sci.* **2012**, *38*, 25–31. [CrossRef]
43. Agisoft. Available online: https://www.agisoft.com/ (accessed on 26 July 2021).
44. Gorelick, N.; Hancher, M.; Dixon, M.; Ilyushchenko, S.; Thau, D.; Moore, R. Google Earth Engine: Planetary-scale geospatial analysis for everyone. *Remote Sens. Environ.* **2017**, *202*, 18–27. [CrossRef]
45. Mosier, C.I.I. Problems and Designs of Cross-Validation 1. *Educ. Psychol. Meas.* **1951**, *11*, 5–11. [CrossRef]
46. Cortes, C.; Vapnik, V. Support-vector networks. *Mach. Learn.* **1995**, *20*, 273–297. [CrossRef]
47. Mitchell, P.J.; Downie, A.-L.; Diesing, M. How good is my map? A tool for semi-automated thematic mapping and spatially explicit confidence assessment. *Environ. Model. Softw.* **2018**, *108*, 111–122. [CrossRef]
48. Japan Meteorological Agency. Available online: https://www.data.jma.go.jp/obd/stats/etrn/view/hourly_a1.php?prec_no=21&block_no=0124&year=2021&month=4&day=13&view= (accessed on 20 July 2021).
49. Japan Meteorological Agency. Available online: https://www.data.jma.go.jp/obd/stats/etrn/view/hourly_a1.php?prec_no=21&block_no=0124&year=2021&month=7&day=8&view= (accessed on 20 July 2021).
50. Coburn, C.A.; Smith, A.M.; Logie, G.S.; Kennedy, P. Radiometric and spectral comparison of inexpensive camera systems used for remote sensing. *Int. J. Remote Sens.* **2018**, *39*, 4869–4890. [CrossRef]
51. Duffy, J.P.; Cunliffe, A.M.; DeBell, L.; Sandbrook, C.; Wich, S.A.; Shutler, J.D.; Myers-Smith, I.H.; Varela, M.R.; Anderson, K. Location, location, location: Considerations when using lightweight drones in challenging environments. *Remote Sens. Ecol. Conserv.* **2018**, *4*, 7–19. [CrossRef]
52. Adler-Golden, S.M.; Matthew, M.W.; Anderson, G.P.; Felde, G.W.; Gardner, J.A. Algorithm for de-shadowing spectral imagery. In *Imaging Spectrometry VIII*; Shen, S.S., Ed.; SPIE Digital Library: Bellingham, WA, USA, 2002; Volume 4816, p. 203.
53. Walker, L.R.; Zarin, D.J.; Fetcher, N.; Myster, R.W.; Johnson, A.H. Ecosystem Development and Plant Succession on Landslides in the Caribbean. *Biotropica* **1996**, *28*, 566. [CrossRef]
54. Shiels, A.B.; Walker, L.R.; Thompson, D.B. Organic matter inputs create variable resource patches on Puerto Rican landslides. *Plant Ecol.* **2006**, *184*, 223–236. [CrossRef]
55. Guariguata, M.R. Landslide Disturbance and Forest Regeneration in the Upper Luquillo Mountains of Puerto Rico. *J. Ecol.* **1990**, *78*, 814. [CrossRef]
56. Pang, C.; Ma, X.K.; Lo, J.P.; Hung, T.T.; Hau, B.C. Vegetation succession on landslides in Hong Kong: Plant regeneration, survivorship and constraints to restoration. *Glob. Ecol. Conserv.* **2018**, *15*, e00428. [CrossRef]

Article

Quantifying the Spatial Variability of Annual and Seasonal Changes in Riverscape Vegetation Using Drone Laser Scanning

Jonathan P. Resop [1,*], Laura Lehmann [2] and W. Cully Hession [2]

[1] Department of Geographical Sciences, University of Maryland, College Park, MD 20740, USA
[2] Department of Biological Systems Engineering, Virginia Tech, Blacksburg, VA 24060, USA;
  lauteany@vt.edu (L.L.); chession@vt.edu (W.C.H.)
[*] Correspondence: resop@umd.edu

Abstract: Riverscapes are complex ecosystems consisting of dynamic processes influenced by spatially heterogeneous physical features. A critical component of riverscapes is vegetation in the stream channel and floodplain, which influences flooding and provides habitat. Riverscape vegetation can be highly variable in size and structure, including wetland plants, grasses, shrubs, and trees. This vegetation variability is difficult to precisely measure over large extents with traditional surveying tools. Drone laser scanning (DLS), or UAV-based lidar, has shown potential for measuring topography and vegetation over large extents at a high resolution but has yet to be used to quantify both the temporal and spatial variability of riverscape vegetation. Scans were performed on a reach of Stroubles Creek in Blacksburg, VA, USA six times between 2017 and 2019. Change was calculated both annually and seasonally over the two-year period. Metrics were derived from the lidar scans to represent different aspects of riverscape vegetation: height, roughness, and density. Vegetation was classified as scrub or tree based on the height above ground and 604 trees were manually identified in the riverscape, which grew on average by 0.74 m annually. Trees had greater annual growth and scrub had greater seasonal variability. Height and roughness were better measures of annual growth and density was a better measure of seasonal variability. The results demonstrate the advantage of repeat surveys with high-resolution DLS for detecting seasonal variability in the riverscape environment, including the growth and decay of floodplain vegetation, which is critical information for various hydraulic and ecological applications.

Keywords: UAVs; lidar; streams; canopy height; roughness; vegetation density; change detection

1. Introduction

A riverscape is a spatially heterogeneous landscape representing a complex ecosystem that comprises the stream beds, banks, channels, riparian zones, floodplains, and basins spanning the many interconnected reaches of a river system [1–3]. Fausch et al. [1] proposed a "continuous view" of this riverscape environment is necessary at multiple spatial and temporal scales to properly study ecological processes. This "continuous view" is possible through state-of-the-art remote-sensing technologies, such as digital imagery and laser scanning, which can measure the physical properties of the riverscape at both fine and coarse scales [2]. Carbonneau et al. [2] combined a 0.03 m aerial image and a 5 m digital elevation model (DEM) over a 16 km stream reach to extract physical riverscape measures over multiple scales, such as channel width and depth, particle size, and slope, which were used to estimate the spatial distribution of salmon habitat patches. Dietrich et al. [3] used helicopter-based imagery and structure-from-motion (SfM) to derive a 0.1 m DEM for a 32 km stream reach, calculated metrics such as channel width, slope, and sinuosity along 3 m cross-sections, and explored their relationships with various land class and geomorphic variables. These studies demonstrated the need for multi-scale analyses for ecological studies involving riverscape environments and the benefit of applying remotely-sensed data over not just a large extent but also at a high resolution.

Remote sensing technologies, such as imagery and lidar, rely on a range of platforms including satellite, aerial, terrestrial, mobile, and, more recently, drone systems for measuring physical riverscape properties. Farid et al. [4] classified riparian zone vegetation using 0.5 m resolution canopy elevation models and intensity rasters derived from aerial laser scanning (ALS) data. Heritage and Hetherington [5] scanned a 150 m reach with terrestrial laser scanning (TLS) to create a high-resolution (0.01 m) DEM. Resop et al. [6] applied TLS to a 100 m reach to classify cobble and boulders and calculate percent in-stream rock cover at 0.02 m resolution. Woodget et al. [7] used drone-based imagery and SfM to survey a 120 m reach and classify riverscape features, such as cobble, boulders, gravel, grass, and trees. Yang et al. [8] compared 0.25 m drone-based and 10 m satellite-based multispectral imagery to classify vegetation in a coastal area and found the higher-resolution drone data resulted in improved delineation of features, such as mangroves. Drone laser scanning (DLS), or unmanned aerial vehicle (UAV)-based lidar, is well suited in particular for measuring fine details in riverscapes due to its resolution and survey extent. Resop et al. [9] found that DLS (at 0.1 m resolution) was more accurate than ALS for measuring physical features in the riverscape and detecting micro-changes in the environment, such as streambank profiles and small herbaceous vegetation. While these studies demonstrated the ability of remote sensing for surveying and classifying riverscapes at multiple scales, they all take place over a single survey representing a single moment in time. More studies are needed that take advantage of repeat surveys for better measuring the temporal variability of riverscape features.

A number of studies have used lidar to detect physical changes in riverscapes. Huang et al. [10] combined 1 m ALS-derived inundation maps from 2007 and 2009 with 30-m Landsat images to monitor inundated area change. Anders et al. [11] estimated geomorphological changes based on 2 m ALS-derived digital terrain models (DTMs) from 2003 and 2011. While these studies demonstrate the benefits of lidar for annual change detection, many riverscape processes occur seasonally (in particular, those involving vegetation), which requires multiple surveys per year to properly monitor. The lack of widespread and continuous ALS data is a significant limitation for lidar-based change detection studies [12]. More often than not, locations only have a single ALS dataset at best, which means other remotely-sensed data, such as SfM or coarser-resolution satellite imagery, are required for change detection. In addition, ALS from high-altitude aircraft has limited resolution, typically around 0.5 or 1 m, which is not fine enough to detect small changes in vegetation [9].

A more flexible lidar platform than ALS, such as terrestrial, mobile, or drone, is required for more frequent surveys at higher resolution. Lidar platforms such as TLS and mobile laser scanning (MLS) have shown to be successful for measuring change over repeat surveys and have been used to measure streambank retreat, bluff erosion, and riparian vegetation change [13–18]; however, these studies typically scan a limited extent, such as a single streambank. For example, Resop and Hession [13] scanned an 11 m streambank six times over two years with TLS (at 0.02 m resolution) and observed seasonal variations in streambank retreat rates, demonstrating the advantage of repeat surveys. More research is needed to study the potential of DLS for detecting vegetation change along entire riverscapes at high resolution.

There are many metrics available to quantify riverscape vegetation, such as height, roughness, and density. These metrics have a history of being derived using lidar data, most commonly with ALS, for a range of ecological applications. Vegetation height, represented by a canopy height model (CHM), has been used to estimate tree height, above-ground biomass, bulk density, and canopy fuel weight over large extents [19,20]. Vegetation roughness, a measure of the level of smoothness or roughness [21], is related to a commonly used parameter in flood modeling, the hydraulic roughness, which is estimated over the channel and floodplain based on a combination of topographic and vegetative complexity [22]. Vegetation density, represented by metrics such as the laser penetration index (LPI), has been used to estimate percent canopy cover or leaf area index (LAI) [20,23].

These vegetation metrics could be quantified at high resolution using DLS and vegetation change could be measured seasonally with repeat surveys.

Many approaches have been used to estimate canopy height: (1) vector-based normalization of point clouds, (2) raster-based differences between digital surface models (DSMs) representing surface features and DTMs representing ground, and (3) full waveform lidar approaches. Vector-based methods normalize point cloud elevations to derive height above ground and are commonly used for tree detection [24–26]. Raster-based methods classify lidar points as vegetation or ground returns and rasterize them into DSMs representing maximum vegetation elevation and DTMs representing ground elevation with the difference resulting in a normalized digital surface model (nDSM) or CHM [9,20,27]. If full waveform lidar data is available, which is less common and generally has larger footprints, then canopy height can be estimated through decomposition of the waveform peaks [28,29]. Raster-based methods are most often used due to the flexibility of fixed-grid data formats for a variety of applications and because they are most practical for DLS due to the high resolution and discrete format of the point clouds.

Two approaches have been used to estimate vegetative roughness: (1) calculating roughness based on the variability of lidar point elevation within a moving window and (2) classifying lidar-derived rasters based on observed or calibrated roughness values. Mundt et al. [21] estimated roughness as a way to classify sagebrush distribution using the standard deviation of normalized ALS point heights within 4.6 m raster pixels. Dorn et al. [27] applied a supervised classification to ALS-derived CHMs to classify vegetation (i.e., grass, shrub, forest) corresponding to Manning's roughness (n) values from Chow [30]. Both methods have been effective at estimating roughness, but have only recently been explored with DLS. Prior et al. [31] estimated Manning's n from both DLS- and SfM-derived CHMs through empirical methods as well as by classifying vegetation (i.e., grass, scrub, small trees, and large trees) and calibrating roughness with observed stream velocity data and 2D HEC-RAS.

Multiple metrics have been used to measure vegetation density, ranging from canopy cover, crown closure, gap fraction, or LAI. Lidar metrics estimating density take advantage of the physics of laser pulses passing through gaps in the canopy and include both vector-based and raster-based approaches. Vector-based methods classify lidar points as vegetation or ground and then calculate the LPI, defined as the ratio of ground points to total points in a given area [23,32]. Alternatively, raster-based methods derive a CHM at high resolution to define locations of canopy cover and then calculate the percent of canopy pixels within a coarser resolution grid or sample area [20,26]. Both approaches have a similar conceptual background and result in a raster representing the percent vegetation density or cover but have not yet been applied to DLS data.

The objectives of this study were: (1) to scan a reach of Stroubles Creek six times over two years (between April 2017 and March 2019) at high resolution with DLS; (2) to produce three lidar-based metrics of riverscape vegetation (i.e., height, roughness, and density); (3) to classify distinct vegetation classes in the riverscape (i.e., scrub and tree) and locate them with respect to the stream channel; and (4) to calculate and compare annual and seasonal changes in vegetation metrics spatially over the riverscape.

2. Materials and Methods

2.1. Study Area

The study area was a 0.65 km reach of Stroubles Creek located in Blacksburg, VA, USA (Figure 1). This reach has a history of agricultural use and underwent a stream restoration that was completed in May 2010 [33]. The restoration consisted of best management practices such as livestock exclusion, bank reshaping, and riparian vegetation planting [33]. The Stream Research, Education, and Management (StREAM) Lab at Virginia Tech continuously monitor water quality, stream flow, and weather at sampling bridges located along the reach as part of ongoing research efforts [34]. Resop and Hession [13] monitored streambank retreat on an 11 m bank of this reach using TLS between 2007 and 2009 and found

that TLS was more accurate than traditional surveying methods for measuring topographic change; however, the stationary nature of TLS limited the study to a single streambank and was not ideal for larger extents. Resop et al. [9] scanned multiple streambanks and the floodplain using DLS in 2017, demonstrating the potential of DLS to perform change detection over the entire riverscape. Prior et al. [31] used DLS and SfM data for this reach from 2018 to estimate hydraulic roughness based on vegetation height and velocity data.

Figure 1. The study area, a 0.65 km reach of Stroubles Creek, showing the approximate extent of the drone laser scanning (DLS) surveys. The actual extent varied slightly between scans.

2.2. Lidar Data Collection

The drone used for this study was an AeroVironment Vapor35 (Arlington, VA, USA). The lidar system on board was a YellowScan Surveyor Core (Saint-Clément-de-Rivière France). The drone weighed approximately 13.6 kg with a payload (i.e., the lidar system) of about 2.3 kg. The battery provides a practical maximum flight time of 40 min at an altitude

of 20 m above ground level (AGL). The lidar operated with a pulse rate of 300 kHz, used a near-infrared (NIR) wavelength of 905 nm and recorded up to two returns per pulse. Additional technical details for the drone and lidar systems can be found in Resop et al. [9], which used the same system to compare DLS and ALS for the same study area.

The reach was scanned six times over two years: 5 April 2017, 2 August 2017, 9 November 2017, 3 April 2018, 9 October 2018, and 20 March 2019. Three scans occurred during the leaf-off dormant vegetation season (April 2017, April 2018, and March 2019) and three scans occurred during the leaf-on season at varying stages of foliage (August 2017, November 2017, and October 2018; Figure 2). The extent was mostly similar for all six scans (Figure 1). Each flight consisted of six flightlines and accounted for overlap between swaths. All scans flew at a consistent altitude (about 20 m AGL), launch location, and speed to produce similar point densities, with the exception of the March 2019 scan, which tested a higher pulse density.
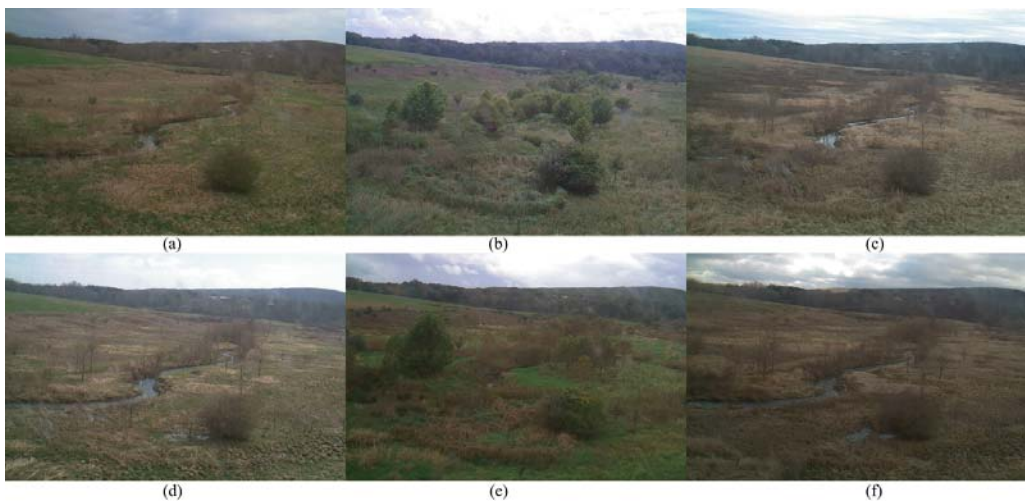
Figure 2. Photos of the study area, Stroubles Creek, taken downstream of the concrete bridge from an on-site tower camera around the same dates as the drone scans: (**a**) April 2017, (**b**) August 2017, (**c**) January 2018 (Note: Due to a malfunction in the tower camera, this is the closest photo to the November 2017 scan), (**d**) April 2018, (**e**) October 2018, (**f**) March 2019.

2.3. Lidar Data Preprocessing

The lidar data were georeferenced with the on-board GPS and local National Geodetic Survey CORS base station data [9]. For each scan, the DLS data was processed into six LAS files, one for each swath. The LAS files for each scan were added to a LAS dataset, projected to WGS 1984 UTM Zone 17N, and further classified and rasterized with ArcGIS 10.6 (Redlands, CA, USA) and LAStools (Gilching, Germany). Data analysis and visualization were performed with Python 3.7.7 and various open-source modules (e.g., numpy, pandas, matplotlib, sklearn).

The study area contained three prominent structures that served as control points to compare the DLS point clouds between scans: one concrete bridge used for vehicles at the north end of the reach and two wooden sampling bridges in the middle and south end of the reach (Figure 1). For each scan, lidar points representing bridges were manually classified as building with ArcGIS. Points representing other anthropogenic features (e.g., cars and people conducting the flights) were also classified as building so they would be ignored in further analysis.

During point cloud post-processing and georeferencing, an issue of concern occurred—some LAS files were not properly aligned with respect to the others. Two misalignment

phenomena were observed: (1) within each scan, one of the six LAS files might be misaligned with respect to the other five, and (2) between each of the six scans, there might be an elevation bias. This issue was easily observed at bridges, which made it appear as if there were multiple bridges at the same location (Figure 3).
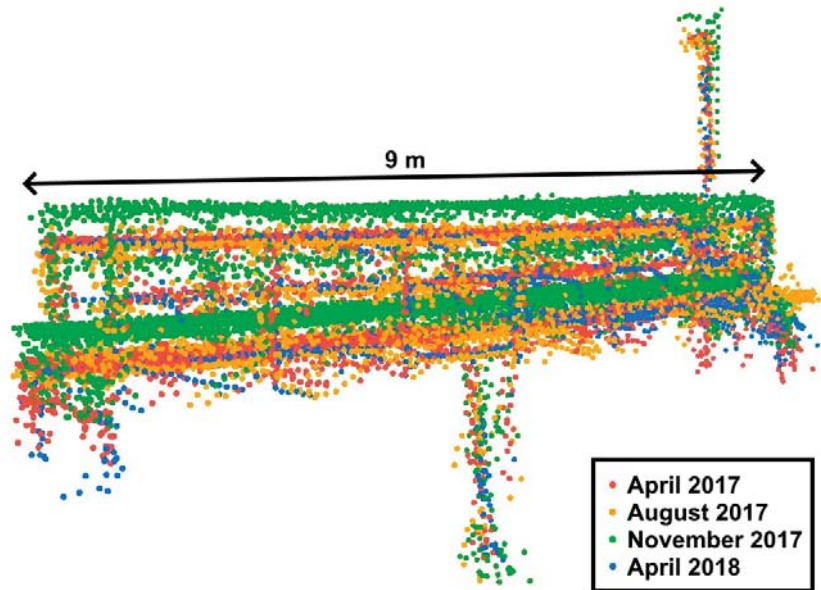
Figure 3. An example misaligned point cloud representing one of the wooden sampling bridges that cross the stream showing an elevation bias in the November 2017 scan (i.e., the green points) relative to the other scans before correction with CloudCompare.

Misaligned LAS files were corrected with the open-source software CloudCompare 2.10 (https://www.cloudcompare.org/ accessed on 2 July 2021). A two-stage process was used: (1) within each scan to correct misaligned LAS files and (2) between each scan and the April 2017 baseline scan to correct bias. The three bridges were used as control points during alignment. Points were finely registered with the "Iterative Closest Point (ICP)" tool to a root mean squared difference (RMSD) of 0.00001 m and a transformation matrix was calculated. The transformation matrix was then applied to the entire point cloud. After correcting all six scans, the elevation bias was calculated between all scans and the April 2017 baseline scan as a measure of relative accuracy.

The extent of each lidar scan was delineated with ArcGIS [9]. The "LAS Point Statistics as Raster" tool created a 0.1-m raster representing all pixels with at least one point. The "Expand" and "Shrink" tools performed a morphological closing and removed small data gaps. The final raster was converted to a polygon representing the scan extent. Key differences in extents include the November 2017 scan, which had a smaller extent south of the concrete bridge, and the March 2019 scan, which had a larger extent expanding out into the floodplain (Figure 4). The extent intersection was calculated with the "Intersect" tool to normalize comparisons between scans. The "annual extent intersection" (between April 2017, April 2018, and March 2019) was 11.02 ha and the "seasonal extent intersection (between all scans) was 8.29 ha (Figure 4).
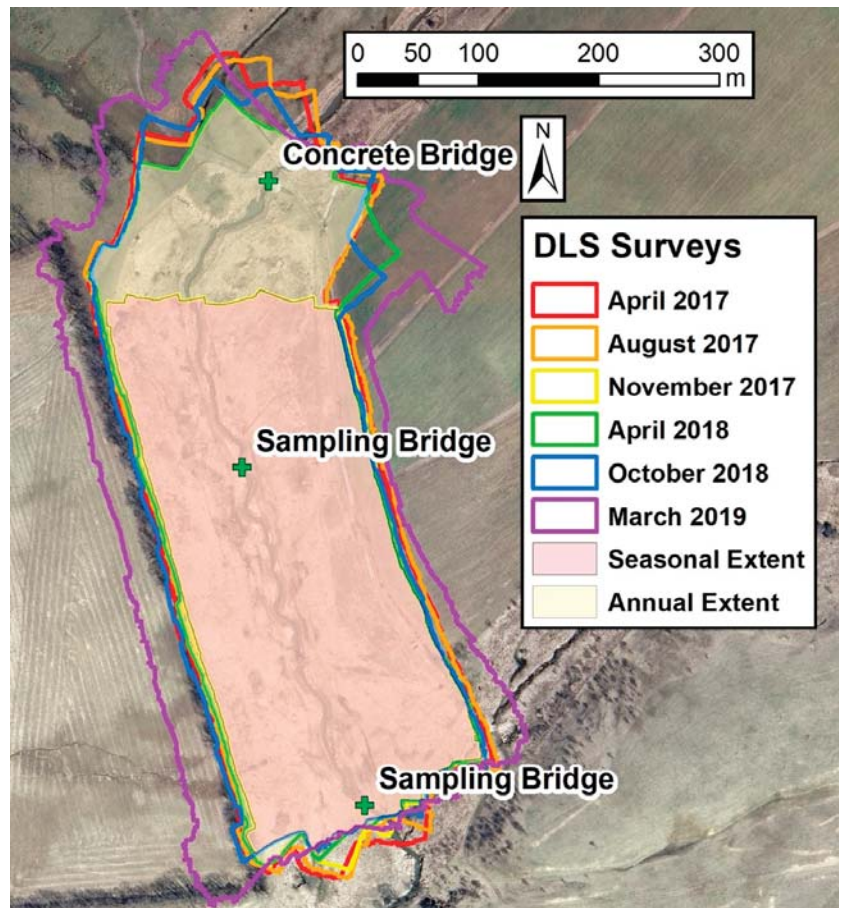
Figure 4. The extent of each drone laser scanning (DLS) survey as well as the extent intersection of all six scans ("Seasonal Extent") and of only the annual leaf-off season scans (April 2017, April 2018, and March 2019; "Annual Extent").

2.4. Lidar Data Classification

With respect to the lidar data collected for this study, noise was rare and most likely represented data artifacts, such as "bird hits." The "Classify LAS Noise" tool in ArcGIS identified outlier points based on absolute minimum and maximum elevation thresholds. Afterwards, the point clouds from each scan were inspected with the "Profile View" tool and any remaining outliers were manually classified as noise.

After manually classifying building and noise, automated classification tools in ArcGIS were used to classify ground and vegetation points [9]. The "Classify LAS Ground" tool identified ground and "Classify LAS by Height" classified the remaining points as unassigned or vegetation based on a height threshold of 0.1 m (Table 1). Points with a height greater than 0.1 m were classified as vegetation and points less than 0.1 m were classified as unassigned. The unassigned class served as a measure of uncertainty, as these points were within the precision of DLS [35] and could represent ground or vegetation.

Table 1. Lidar point data classes used in this study.

Class	Definition
Ground	Points most likely representing bare earth topography
Unassigned	Points between 0 m < height above ground < 0.1 m
Vegetation	Points between 0.1 m < height above ground < 15 m
Building	Points identified as human-made or built structures (e.g., bridges or cars)
Noise	Points identified as noise (e.g., bird-hits or lidar artifacts)

Researchers have observed that point clouds from a YellowScan lidar, which is based on the Velodyne Puck (San Jose, CA), can result in a "thickness" of points of a few centimeters when scanning flat ground, producing surfaces that are not as "crisp" as they should [36]. This phenomenon was observed in the point clouds produced for this study. Upon investigation, a cross-section of points along the concrete bridge at the northern end of the study area showed an approximate 0.05 m thickness of what should have been a solid surface. To account for this thickness, the unassigned class, representing points with a height above ground less than 0.1 m, was used in addition to the ground class to define terrain for bare earth models (i.e., DTMs).

The automated classification algorithms produced two common misclassifications: (1) ground points misclassified as vegetation on high-gradient stream banks and (2) vegetation points misclassified as ground under dense canopy [9]. These misclassifications need to be corrected manually due to limitations in current lidar point classification algorithms. Unfortunately, the manual correction of large point clouds, especially from DLS, is very time-consuming and labor-intensive [9]. The April 2017 scan was corrected previously [9], but the other five scans were not fully verified. An investigation into a more efficient classification correction process was outside the scope of this study.

2.5. Lidar Vegetation Metrics

Three lidar metrics were selected to represent riverscape vegetation: (1) height (canopy height model; CHM), (2) roughness (vegetative roughness index; VRI), and (3) density (lidar vegetation index; LVI; Table 2). All three metrics were calculated in raster format for each DLS survey using data processing pipelines created with Model Builder in ArcGIS. All outputs had a pixel size of 0.1 m. Based on an average point spacing of 0.047 m over the six scans, this is about five lidar points per pixel.

Table 2. Metrics produced from drone laser scanning (DLS) data to represent different components of riverscape vegetation.

Lidar Vegetation Metrics	Definition	Value Range	Units
Canopy height model (CHM)	Measure of vegetation height (veg. elev.) − (ground elev.)	0 to ~13	Meters
Vegetative roughness index (VRI)	Measure of vegetative roughness St. dev. of vegetation height	0 to ~9	Meters
Lidar vegetation index (LVI)	Measure of vegetation density (count veg.)/(count all points)	0 to 1	Decimal Percent

The CHM was derived from two rasters: the DTM (i.e., the minimum ground and unassigned point elevation per pixel) and the DSM (i.e., the maximum vegetation point elevation per pixel) [9]. The DTM and DSM were calculated with the "LAS Dataset to Raster" tool (Figure 5). The difference between DSM and DTM resulted in a normalized digital surface model (nDSM) [9]. Data gaps (e.g., water surfaces and lidar shadows) and pixels with a height less than 0.1 m (i.e., the smallest height of vegetation points), were assigned zero values to produce the final CHM. The CHM ranged from 0 m (i.e., bare earth) to about 13 m (i.e., the height of the tallest tree).
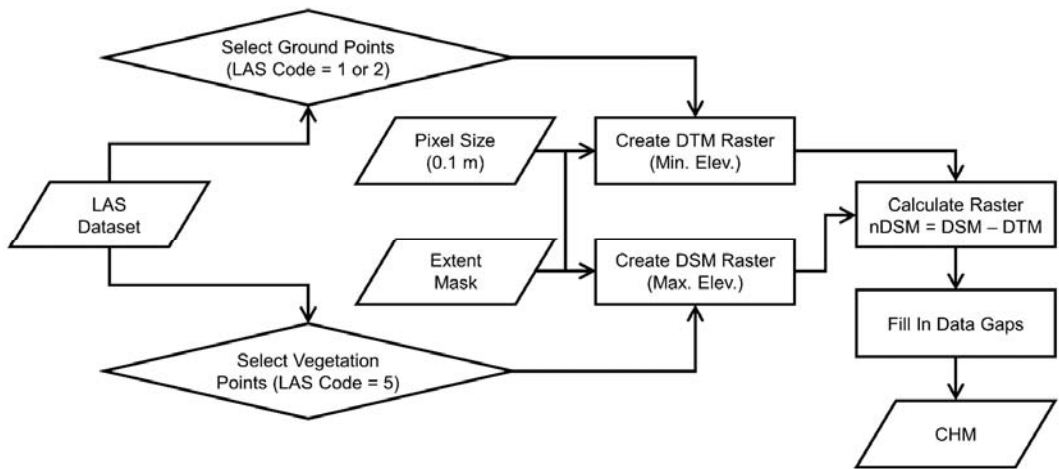
Figure 5. The workflow deriving the canopy height model (CHM) based on the maximum height above ground of lidar vegetation points in each raster pixel.

The vegetative roughness index (VRI) estimated the local variability of vegetation height. The VRI was calculated with the "LAS Height Metrics" tool as the standard deviation of vegetation point height per pixel (Figure 6). Points with a height less than 0.1 m were ignored. Low standard deviations corresponded to smooth surfaces while high standard deviations corresponded to rough surfaces. Data gaps were assigned a VRI of zero. The VRI ranged from about 0 m, representing relatively uniform vegetation, to 9 m, representing more complex vegetation.
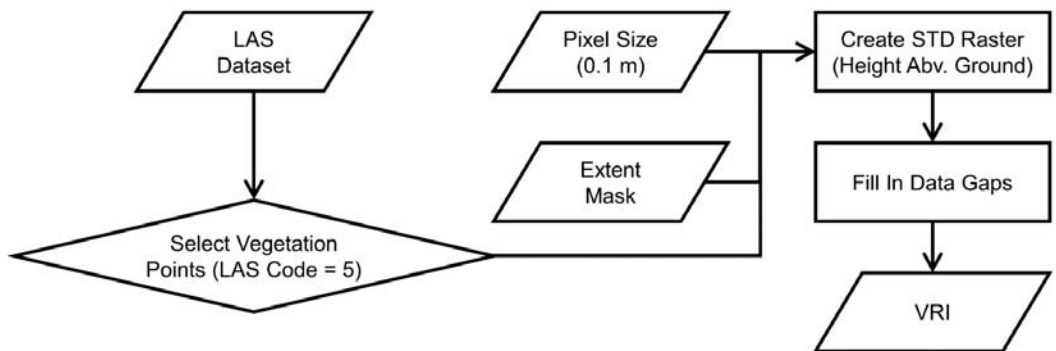
Figure 6. The workflow estimating the vegetative roughness index (VRI) based on the standard deviation of vegetation height within each raster pixel.

The lidar vegetation index (LVI) represented the percentage of vegetation points per pixel. While CHM and VRI were both absolute measures, the LVI was the only relative measure. The number of vegetation points per pixel was calculated with the "LAS Point Statistics as Raster" tool and then the number of total points per pixel was calculated (Figure 7). The vegetation point count was divided by the total point count on a pixel-by-pixel basis, resulting in a decimal percentage. Data gaps were assigned an LVI of zero. The LVI ranged from zero, representing no vegetation or open canopy, to one, representing heavy vegetation or dense canopy.
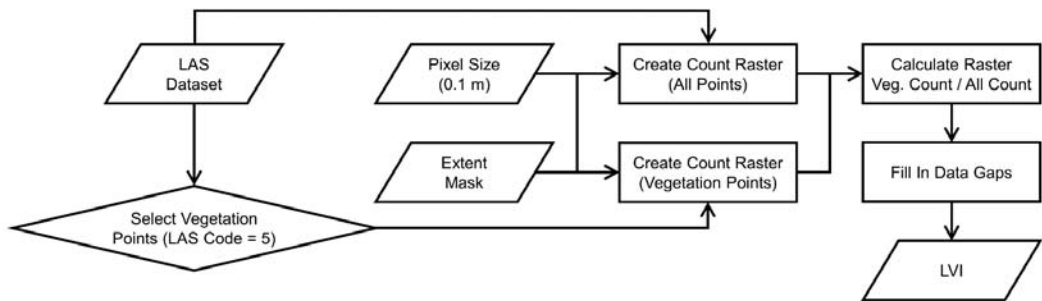
Figure 7. The workflow calculating the lidar vegetation index (LVI) based on the percentage of vegetation points within each raster pixel as a measure of density.

2.6. Vegetation Classification, Distance to Water, and Tree Identification

The CHM for each scan was classified into the following land classes: ground, scrub, and tree. These classes were defined with a simple threshold method based on a manual investigation of vegetation in the riverscape. Pixels with a CHM value (i.e., height above ground) less than 0.1 m were classified as ground, pixels between 0.1 and 2 m were classified as scrub, and pixels greater than 2 m were classified as tree.

The CHM for the April 2017 baseline was used to establish the stream location. A land class for water was defined by taking advantage of the physics of NIR lidar pulses, which are absorbed by water surfaces and result in "No Data" pixels. The "LAS Point Statistics as Raster" tool counted the lidar points in each 0.1 m pixel and those with more than three points represented ground. The "Expand" and "Shrink" tools were used to close small data gaps. At this point, "No Data" gaps represented the water surface. Once the water class was defined, the "Euclidean Distance" tool was used to determine the distance between each pixel in the riverscape and the stream.

To quantify the annual growth of vegetation, trees were manually identified from the April 2017 CHM based on pixels classified with a height greater than 2 m. The riverscape was inspected, crowns were identified, and stems were marked. The environment for this study had a fairly open canopy, so it was easy to manually identify trees. Each identified tree was verified by inspecting the point cloud. The "Buffer" tool created 0.5 m buffers around each tree stem and the maximum tree height was calculated from the CHMs for April 2017, April 2018, and March 2019.

2.7. Annual and Seasonal Change Detection

Annual and seasonal changes were calculated for each vegetation metric (Table 2). The overall two-year period was represented by the April 2017 to March 2019 scans. Annual change was measured between leaf-off scans (April 2017 to April 2018 and April 2018 to March 2019) within the annual extent intersection (Figure 4). Seasonal change was measured between all six DLS scans within the seasonal extent intersection (Figure 4).

An effective method of identifying pixel-level change is to calculate DEMs of difference (DoDs) by subtracting rasters representing two moments in time: the newer raster minus the older raster [12,37,38]. For CHMs, change represented vegetation growth or decay [15]. For VRIs, change represented increased roughness or smoothness. For LVIs, change represented increased or decreased vegetation density. Change was determined to be significant, as opposed to noise, by applying a minimum level of detection (LoD), representing the uncertainty of the lidar sensor [37,38]. An LoD of 0.05 m was used for the CHM and VRI DoDs [35], which is consistent with LoDs used by change detection studies involving lidar at a similar range [17]. For the LVI DoD, the unassigned class (Table 1) represented the point classification uncertainty.

3. Results

3.1. Point Density Comparison and Elevation Bias between the Six Lidar Scans

The point count varied significantly between the scans due to extent differences (Figure 4), ranging from 42.6 to 70.1 million points. When considering only the seasonal extent intersection the point counts were more consistent (Table 3). Most scans contained between 41.7 and 43.0 million points with the exception of the March 2019 scan, which contained 51.2 million points due to a higher pulse density. While most scans were consistent (491 to 502 pulses/m^2), the March 2019 scan had a pulse density of 590 pulses/m^2.

Table 3. Drone laser scanning (DLS) statistics for each scan within the extent intersection.

Scan Date	Point Count	Point Density (All Returns/m^2)	Pulse Density (First Returns/m^2)
April 2017	41,661,008	502.43	492.39
August 2017	42,148,141	508.30	501.89
November 2017	42,389,739	511.21	490.65
April 2018	42,994,259	518.51	501.61
October 2018	42,584,883	513.57	500.07
March 2019	51,135,652	616.69	590.30

Agreement between the six DLS scans was determined based on the average elevation (Z) bias between DEMs produced from each scan and the April 2017 baseline. Bridge DEMs were created using points representing the concrete bridge and two sampling bridges. Before aligning the data in CloudCompare, the average Z bias was as large as 1.15 m (March 2019) with smaller biases of 0.23 m (November 2017) and −0.11 m (October 2018; Figure 3). After alignment, the average Z biases ranged from −0.03 m to 0.01 m over all six scans (Table 4), which is well within the precision of YellowScan lidar systems [35].

Table 4. The average elevation (Z) bias between each drone laser scanning (DLS) survey and the April 2017 scan after all point clouds were aligned with CloudCompare.

Scan Date	Mean Z Bias (m) Bridge DEMs	Mean Z Bias (m) Ground DTMs
April 2017	Baseline	Baseline
August 2017	−0.02	0.25
November 2017	−0.01	0.06
April 2018	0.01	−0.01
October 2018	−0.02	0.17
March 2019	−0.03	−0.03

Between DTMs, the average Z biases had a wider range, −0.03 m to 0.25 m (Table 4). The scans with a higher bias included August 2017 (0.25 m), October 2018 (0.17 m), and November 2017 (0.06 m), which occurred during leaf-on seasons. The Z bias was negatively correlated to the time of year. Going forward in time from August to October to November, as the amount of vegetation decreased there was a lower likelihood of vegetation understory misclassified as ground, which decreased the bias. For the other leaf-off scans (April 2018 and March 2019), the bias was within the precision of the lidar system (−0.01 m and −0.03 m, respectively) [35].

3.2. Annual and Seasonal Change of Lidar Point Classifications

The three primary data classes were ground, unassigned, and vegetation (Table 1). Vegetation represented objects with a height above ground greater than 0.1 m that were not identified as a built structure, which allowed DLS to detect not just trees and bushes but also small herbaceous vegetation [9]. The scans were clipped to the seasonal extent intersection and the point statistics (percent terrain vs. percent vegetation) were compared. As expected,

the percent vegetation varied periodically throughout the seasons as associated with the growth and decay of vegetation in the riverscape, with a maximum of 56% in August 2017 (leaf-on) and a minimum of 12% in April 2017 (leaf-off; Figure 8). During the leaf-on scans, there was a clear negative trend in the percent vegetation going forward in time from August (56%) to October (45%) to November (38%), likely due to the decay of leaves over the autumn season.
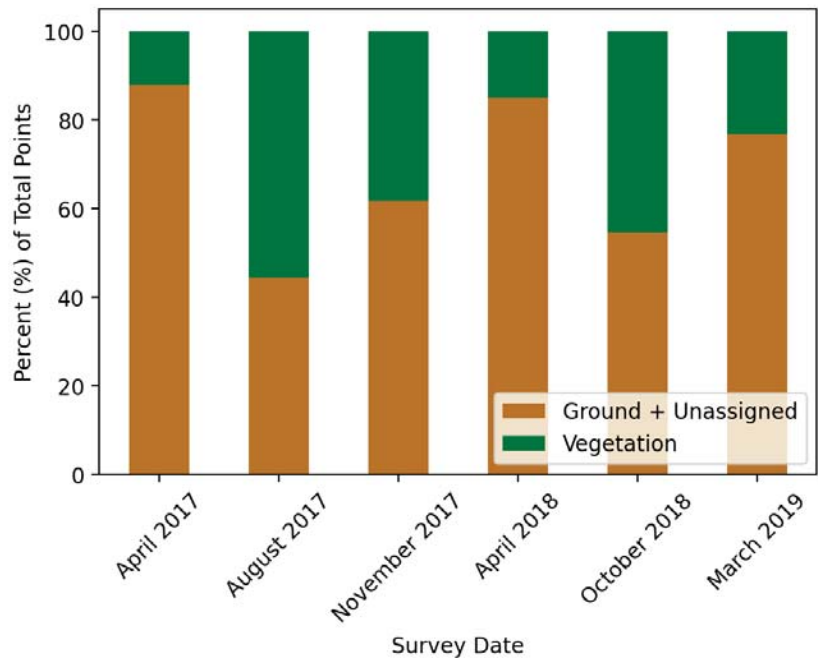
Figure 8. Drone laser scanning (DLS) point classifications within the extent intersection over all six scans showing the seasonal variation between terrain points and vegetation points.

There was a gradual increase in percent vegetation over time between the leaf-off scans going forward in time from April 2017 (12%) to April 2018 (15%) to March 2019 (23%; Figure 8). This positive trend was likely reflecting the annual growth of vegetation in the riverscape. The higher pulse density during the March 2019 scan (Table 3) may have contributed to the higher percent vegetation observed for this scan, but the level of influence is not clear.

3.3. Annual Change of Maximum Tree Height

A total of 604 trees were identified in the April 2017 CHM based on a manual inspection of areas classified as tree (CHM > 2 m; Figure 9). The average tree growth over the two-year period was 1.48 m. A majority of trees had positive growth ($n = 570$; mean = 1.62 m) while a few had negative growth ($n = 34$; mean = -0.96 m). Most trees with negative growth fell due to natural causes over the two-year period. Tree growth was greatest from 2018 to 2019 (mean = 0.83 m) compared to the period 2017 to 2018 (mean = 0.65 m). Based on the tree's distance to stream (i.e., pixels classified as water), trees within 20 m grew faster ($n = 544$; mean = 1.56 m) over the two-year period compared to trees farther than 20 m ($n = 60$; mean = 0.70 m).
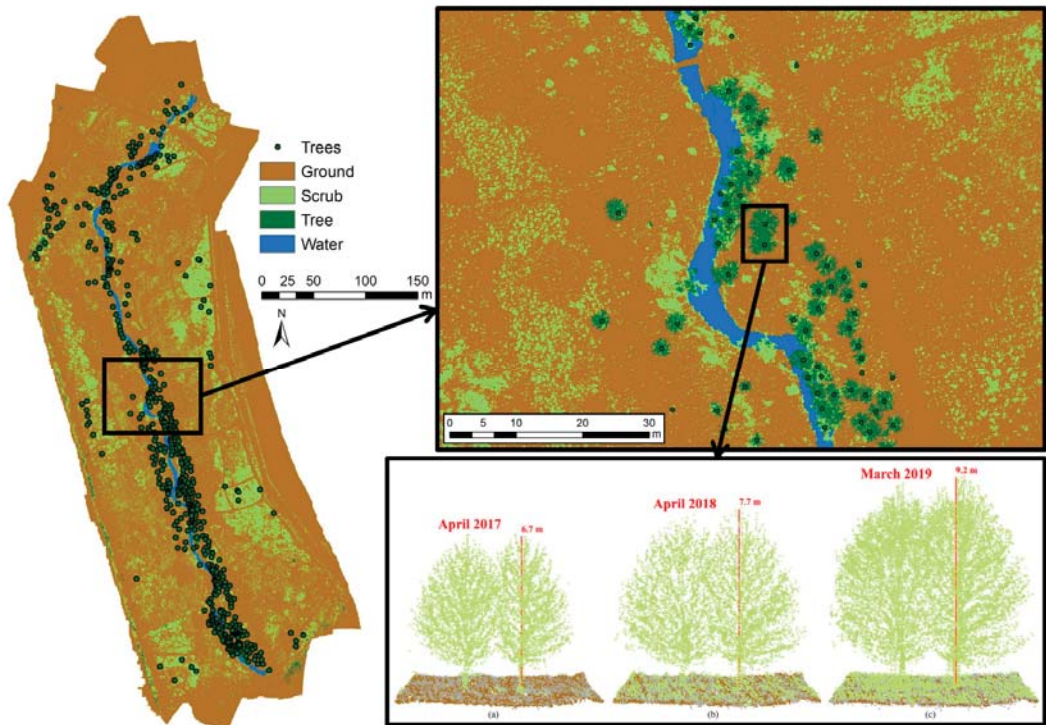
Figure 9. Trees taller than 2 m were identified from the April 2017 canopy height model (CHM) and maximum tree height was measured for: (**a**) April 2017; (**b**) April 2018; (**c**) March 2019.

Not only did the trees show steady average growth (April 2017 = 4.37 m, April 2018 = 5.02 m, March 2019 = 5.84 m), but the variability or standard deviation of height increased over time as well (April 2017 = 1.28 m, April 2018 = 1.58 m, March 2019 = 1.90 m). This positive trend in standard deviation demonstrates not just an increase in tree height over time but also tree height diversity and variability (Figure 10). Overall, the annual scans showed a consistent, steady growth of woody vegetation over the riverscape.
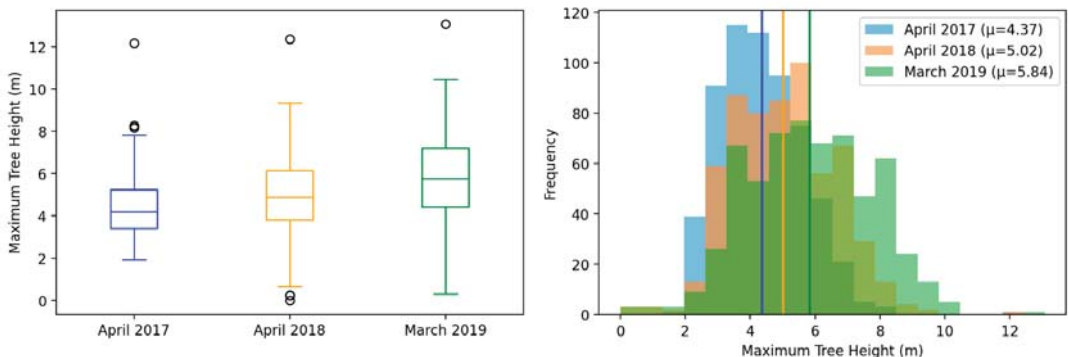
Figure 10. Maximum tree height statistics of the 604 trees identified in the riverscape for each of the three leaf-off scans. The average and standard deviation of maximum tree height increased over the two-year period.

3.4. Baseline Lidar Vegetation Metrics

The vegetation metrics (CHM, VRI, and LVI) were derived for the April 2017 scan as a baseline (Figure 11). The CHM ranged from 0 m (bare ground) to 12.97 m (the height of the tallest tree). The VRI ranged from 0 m (smooth surfaces) to 8.41 m (rough surfaces). The LVI ranged from 0 (open terrain) to 1 (dense vegetation). The April 2017 scan was classified as: ground (CHM < 0.1 m), scrub (0.1 m < CHM < 2 m) and tree (CHM > 2 m; Figure 9). As expected, pixels classified as ground had a value close to zero for all three metrics. For pixels classified as vegetation, tree areas consistently had higher vegetation metrics than scrub areas. The biggest difference was between average height (CHM; scrub = 0.48 m and tree = 3.52 m), which is to be expected since the classes were determined based on height. The differences between roughness (VRI; scrub = 0.08 m and tree = 0.67 m) and density (LVI; scrub = 0.45 and tree = 0.61) were much smaller.
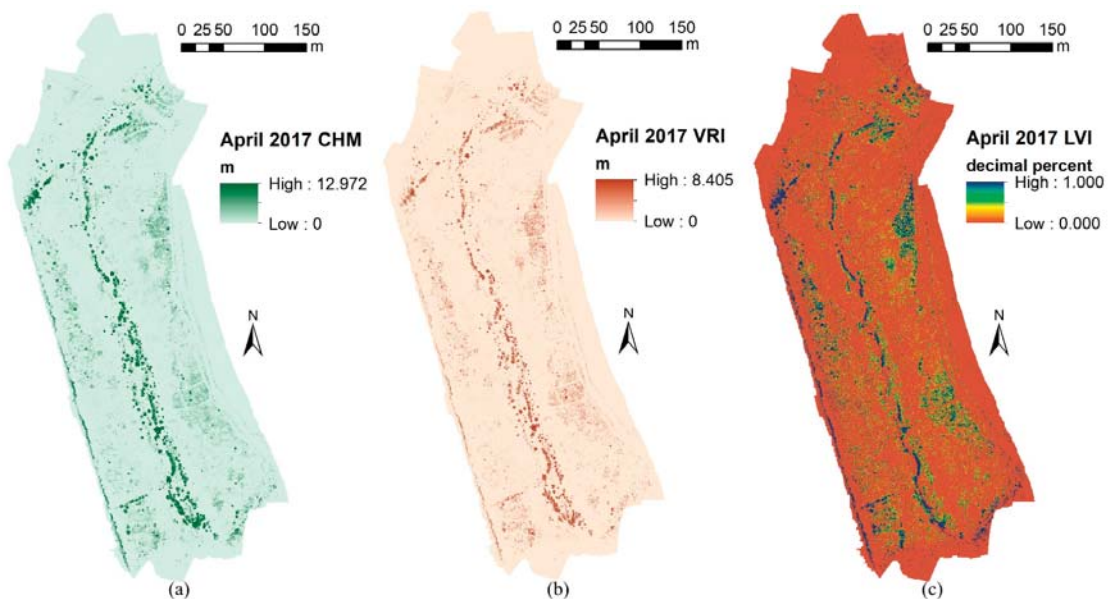
Figure 11. Lidar vegetation metrics for April 2017 showing: (**a**) height (CHM); (**b**) roughness (VRI); (**c**) density (LVI).

Very weak negative correlations were observed between CHM (R^2 = 0.12) and VRI (R^2 = 0.07) with respect to the distance to the stream channel, but overall the taller and rougher vegetation tended to be located closer to the stream (Figure 12). There was no correlation between LVI (R^2 = 0.01) and distance to stream; however, it is important to note that within the stream channel itself the LVI ~ 1 due to the fact that the water surface absorbed the lidar pulses resulting in a lack of ground points measured by the lidar system (Figure 11).

3.5. Annual Change of Lidar Vegetation Metrics

The vegetation metrics for the annual leaf-off scans (April 2017, April 2018, and March 2019) were overlaid with each vegetation class (scrub and tree) and clipped to the annual extent intersection (total area = 11.02 ha). Both scrub and tree areas increased steadily over the two-year period (Figure 13). Scrub, as a percent of the total area, increased from 15.28% for April 2017 to 22.02% for April 2018 to 36.04% for March 2019 while tree area increased from 2.83% to 4.02% to 5.31%. In tree areas, all three metrics increased over the two-year period (Figure 13). An increase in height (CHM) was driven by annual tree growth (Figure 10). However, increases in roughness (VRI) and density (LVI) were

likely also influenced by the growth of understory. On the other hand, scrub areas did not show any significant annual trends with respect to any metric (Figure 13). Annual variations in scrub vegetation were likely impacted by the growth of new scrub and decay of old scrub, while trees had more consistent growth without much change in the overall tree population.
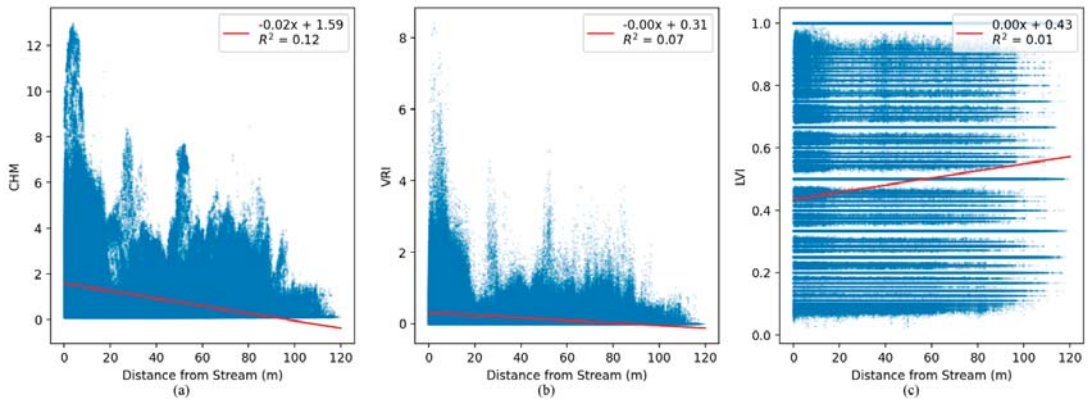
Figure 12. The relationship between vegetation metrics and distance to stream for April 2017: (**a**) height (CHM); (**b**) roughness (VRI); (**c**) density (LVI).
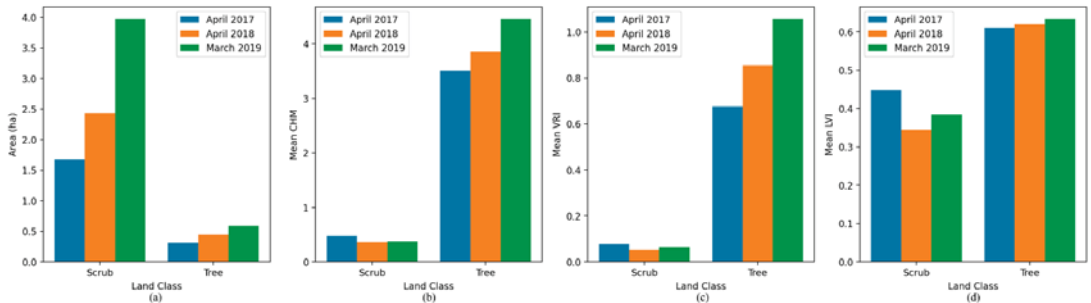
Figure 13. Trends in annual vegetation change over the riverscape: (**a**) total land class area; (**b**) average height (CHM); (**c**) average roughness (VRI); (**d**) average density (LVI).

There was a clear increase in total scrub and tree area over each year (Figure 13). By looking at the 0.1 m pixel-level change, one can investigate how land class changed from one year to the next. From April 2017 to April 2018, scrub area increased from 1.68 ha to 2.43 ha; however, a majority (75%) of the April 2018 scrub area was previously ground (Figure 14) and a majority (62%) of the April 2017 scrub area became ground in April 2018. This same trend was observed between April 2018 and March 2019 when the scrub area increased from 2.43 ha to 3.97 ha and again a majority (69%) was previously ground (Figure 14) and a near majority (48%) of the previous scrub became ground. This demonstrates the volatility of scrub areas and could have dramatic effects on physical riverscape properties such as hydraulic roughness from year to year. In contrast, tree areas showed more consistency. From April 2017 to April 2018 to March 2019 the tree area increased from 0.31 ha to 0.44 ha to 0.59 m. Unlike scrub area, a majority of the tree area in both 2018 and 2019 was previously classified as tree, 54% and 65%, respectively (Figure 14).
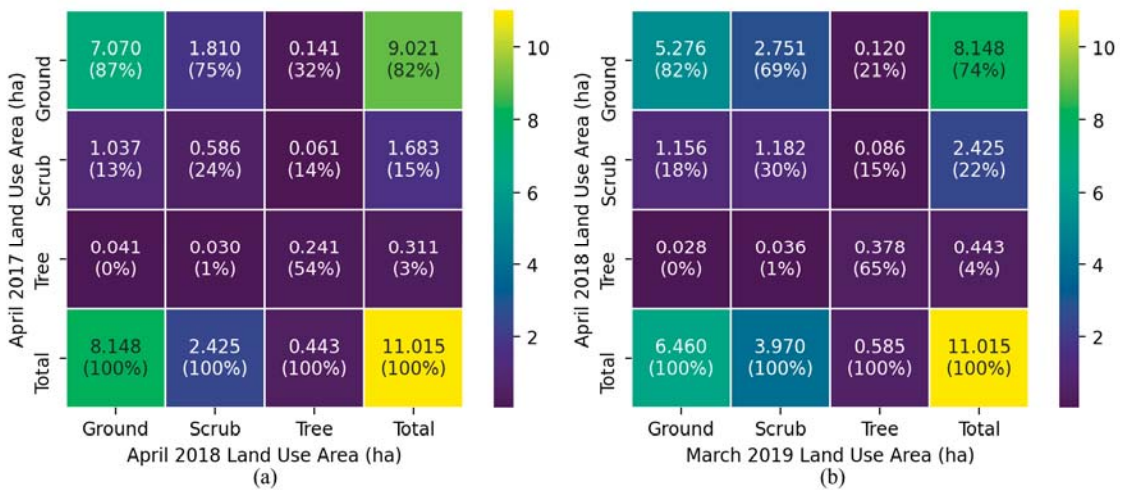
Figure 14. Change matrices representing the pixel-level change in land class between: (**a**) April 2017 and April 2018; (**b**) April 2018 and March 2019.

Looking at the DoDs, one can observe the pixel-level growth and decay of vegetation spatially over the riverscape and temporally over the two-year study (Figure 15). The DoDs for height (CHM) and roughness (VRI) showed similar trends; although, the CHM had a greater overall magnitude of change compared to the VRI. Most of the positive change in vegetation occurred near the stream channel and was primarily due to the growth of trees. Farther into the floodplain, there was more spatial variability in the growth and decay of scrub. From year to year, some sections of scrub showed positive change and some showed negative change. Overall, tree areas showed greater growth in CHM and VRI over the two-year period compared to scrub areas (Figure 16). On the other hand, vegetation density (LVI) consistently had positive change over the entire riverscape (Figure 15) and the change was similar between scrub and trees (Figure 16). This consistent growth in vegetation density suggests that while scrub and trees are growing at different rates, the canopy density and vegetation understory is increasing more uniformly.

The vegetation metrics did not show much correlation with distance to stream. However, when selecting only tree areas, some annual trends were observed. There was a negative correlation for tree height and roughness with distance to stream (Figure 17). The negative correlation increased in magnitude over time from April 2017 to April 2018 to March 2019 (Figure 17). Generally, trees grew faster within 20 m of the stream compared to trees farther than 20 m. The average CHM growth from 2017 to 2019 was 1.03 m within 20 m and 0.07 m farther than 20 m. The average increase in VRI over the same period was 0.40 m within 20 m and 0.12 m farther than 20 m. While tree height and roughness showed a negative correlation with distance to stream, vegetation density showed a positive correlation over the two-year period (Figure 17). This positive correlation in tree areas decreased over time from 2017 to 2019 as the average LVI increased by +0.05 within 20 m but decreased by −0.09 farther than 20 m. Overall, the annual trend for all three metrics showed a greater increase in vegetation closer to the stream. While these annual trends were observed in tree areas, there were no significant correlations or trends observed in scrub areas. This is likely a result of the volatility of the scrub area over the riverscape that was previously described.

3.6. Seasonal Change of Lidar Vegetation Metrics

All six scans were clipped to the seasonal extent intersection (total area = 8.29 ha). Based on the change in vegetation area, two periods were associated with growth (April 2017

to August 2017 and April 2018 to October 2018) and three periods were associated with decay (August 2017 to November 2017, November 2017 to April 2018, and October 2018 to March 2019; Figure 18). These trends were similar to what was previously observed when looking at the classified lidar point clouds (Figure 8). Much like the observations of annual change for individual trees and the pixel-level change of the vegetation metrics, tree areas gradually increased in height (CHM) and roughness (VRI) over time (Figure 18). On the other hand, scrub areas were more constant for both metrics (Figure 18). Density (LVI) was highly variable for both scrub and trees (Figure 18).
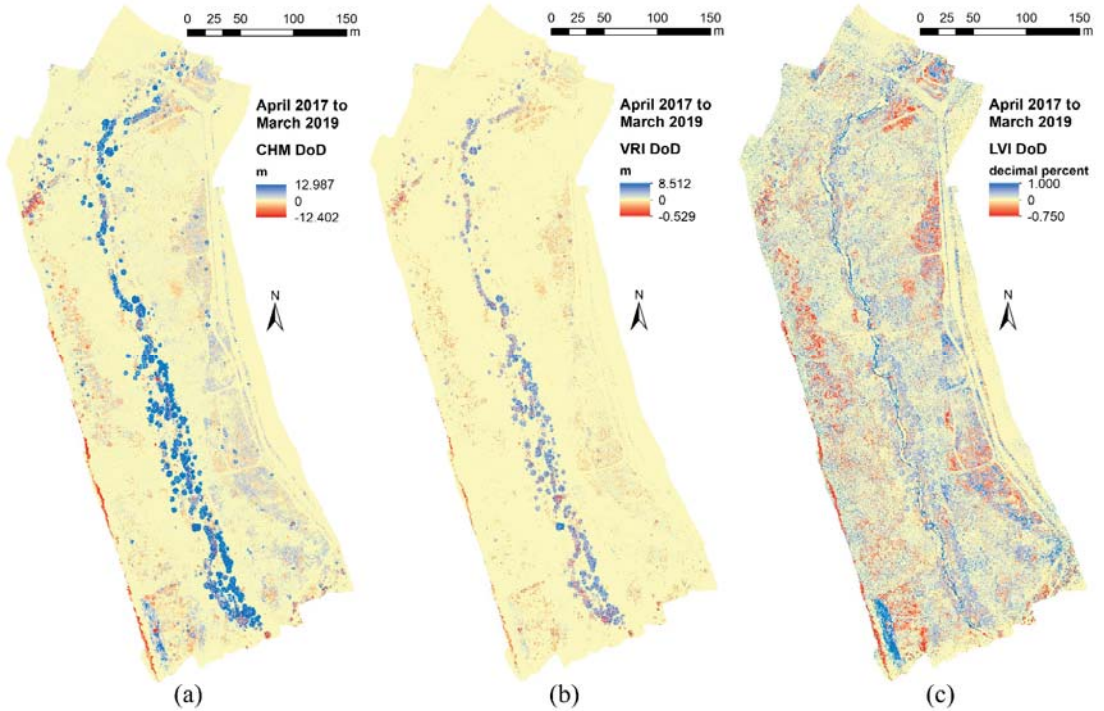
Figure 15. DEMs of Difference (DoDs) over the two-year study from April 2017 to March 2019 representing pixel-level change in: (**a**) height (CHM); (**b**) roughness (VRI); (**c**) density (LVI).
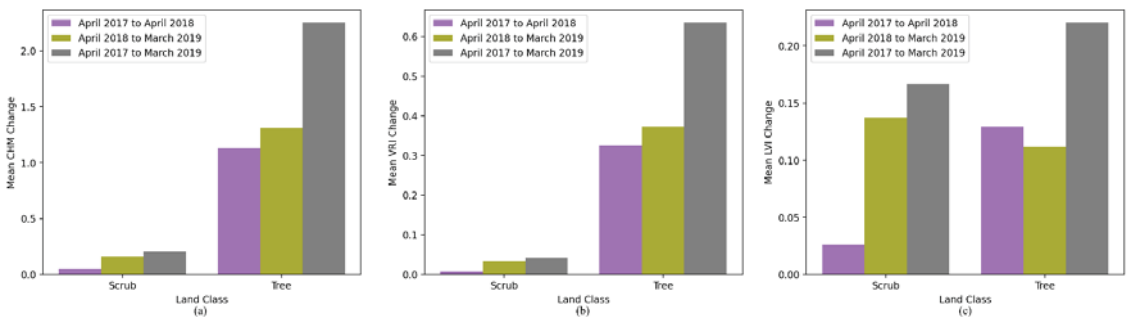
Figure 16. The average pixel-level annual change in each metric, (**a**) height (CHM), (**b**) roughness (VRI), and (**c**) density (LVI), over each land class and over each year in the two-year study.
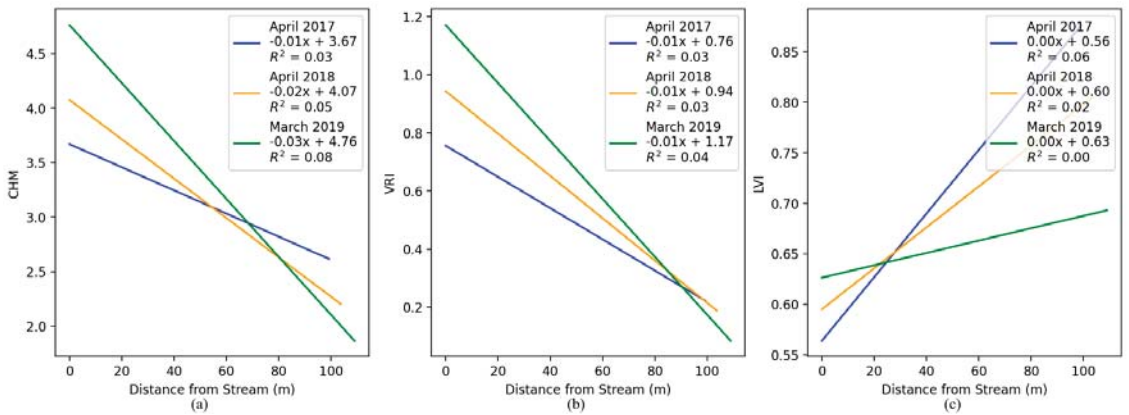
Figure 17. Linear regression models relating vegetation metrics and distance to stream annually over time for tree areas: (**a**) height (CHM); (**b**) roughness (VRI); (**c**) density (LVI).
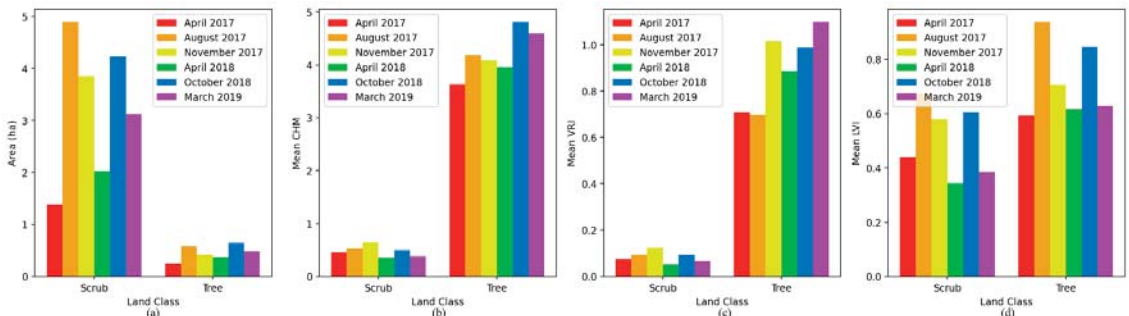
Figure 18. Trends in seasonal vegetation change over the riverscape: (**a**) total land class area; (**b**) average height (CHM); (**c**) average roughness (VRI); (**d**) average density (LVI).

Temporal linear regression was used to remove the annual trend of each metric for scrub and tree areas and isolate the seasonal variability, which was represented by the normalized root mean squared error (NRMSE) of the regression residuals (Table 5). Out of all the combinations of lidar metric and land class, only height and roughness in tree areas had significant annual trends (both had $R^2 = 0.70$). Both scrub and tree areas demonstrated seasonal variability for height and roughness; however, the variability was greater for scrub (CHM NRMSE = 17.8%; VRI NMRSE = 25.6%) compared to trees (CHM NRMSE = 5.1%; VRI NMRSE = 9.2%). Vegetation density did not have any significant annual trends. However, it was highly seasonally variable for both scrub areas (LVI NRMSE = 23.1%) and tree areas (LVI NRMSE = 17.8%).

No temporal trends could be observed for the average vegetation density (LVI) when viewing the data sequentially (Figure 18). However, by reordering the scans as they would fall in a single growing season, a trend emerges representing vegetation decay (Figure 19). The scans were reordered August (2017) to October (2018) to November (2017) to April (2018). This time shift does not work well for height and roughness since these are absolute measures and are affected by annual vegetation growth. On the other hand, density is a relative measure based on the local percentage of vegetation points. By reordering the scans seasonally, one can observe a negative trend in LVI over both scrub and tree areas (Figure 19). This trend likely represents the seasonal decay of vegetation in

the riverscape as foliage falls and DLS is able to penetrate further through the canopy to record ground points.

Table 5. Regression results showing the annual trend (based on R^2) and seasonal variability (based on normalized root mean squared error [NRMSE]) for each metric and land class.

Vegetation Metric	Scrub Land Class Areas		Tree Land Class Areas	
	Annual Trend (R^2)	Seasonal Variability (NRMSE)	Annual Trend (R^2)	Seasonal Variability (NRMSE)
Height (CHM)	0.16	17.8%	0.70	5.1%
Roughness (VRI)	0.08	25.6%	0.70	9.2%
Density (LVI)	0.08	23.1%	0.00	17.8%
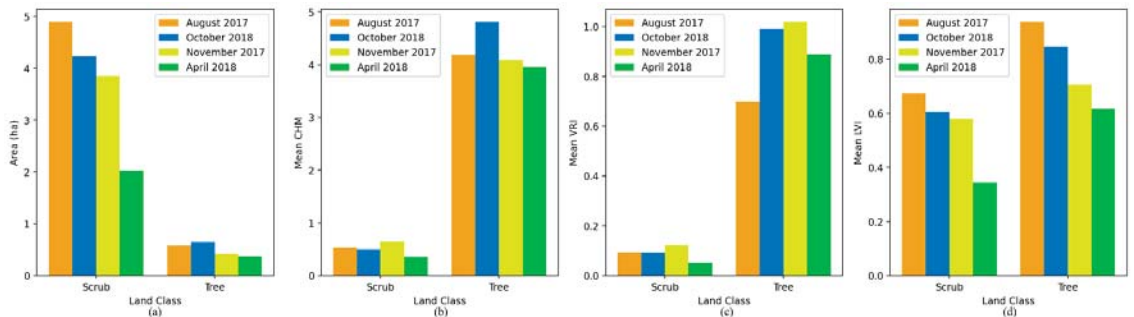
Figure 19. Trends in seasonal vegetation decay over the riverscape going from August (2017) to October (2018) to November (2017) to April (2018): (**a**) total land class area; (**b**) average height (CHM); (**c**) average roughness (VRI); (**d**) average density (LVI).

4. Discussion

Limitations with the Current Study and Future Research

One of the limitations of raster-based analysis is that only a single Z value is allowed per pixel. When quantifying height or classifying different types of vegetation this limitation does not allow for an accurate representation of complex environments; in particular, when multiple vegetation types exist at the same location. For example, when grass or scrub grows under a tree canopy. With traditional image-based remote sensing, these distinctions are often impossible to make. However, since lidar can penetrate through the tree canopy, it is possible to derive lidar measures that represent this vegetation diversity. Many applications take advantage of this aspect of lidar data by generating metrics such as average height, standard deviation, point density, and height percentiles to represent forest structure [20]. The lidar metrics generated in this study, representing height, roughness, and density, allowed for different perspectives of vegetation structure. These metrics could allow for more complex vegetation classes, such as combinations of grass, scrub, and trees. This could be accomplished using machine learning algorithms [20], but would require additional field data for model training.

Another area of uncertainty is the impact of pixel size or resolution on the calculation of the vegetation metrics. It is expected that two of the metrics, VRI (which deals with roughness, defined by the standard deviation of height) and LVI (which deals with density, defined by the percentage of vegetation points) are both heavily influenced by the pixel size, as these metrics are dependent on the number of lidar points in each pixel. As the size of the pixel increases, more lidar points are included, which results in a more generalized rather than localized value for each pixel. A sensitivity analysis is needed to determine the effect of pixel size on each of these metrics, but this is an area of future study.

In this study, we quantified and classified riverscape vegetation at 0.1-m resolution using an active system (i.e., DLS). Other studies have classified vegetation using passive systems, such as drone-based imagery [7,8,31]. Woodget et al. [7] used drone-based imagery and SfM to create 0.02-m DEMs and classified images with a mean elevation error of 0.05 m, similar to the elevation errors observed in our study. Yang et al. [8] used multispectral drone-based imagery to create 0.25 m classified images. Prior et al. [31] created 0.1 m classified images from DLS and SfM, but the datasets were collected in different years. Both remote sensing technologies have advantages and disadvantages. Lidar is better suited for producing 3D point clouds and penetrating vegetation canopy. Imagery is better suited for collecting a range of spectral information. There is a long history of data fusion applications that have combined active and passive remote sensing datasets to take advantage of their respective strengths [21]. The results of this study could theoretically be improved by combining the DLS data with SfM data. However, such data fusion would require collecting both lidar and imagery data at each survey, presenting additional field management challenges, and was outside the scope of this study.

5. Conclusions

Comparing the annual and seasonal change of all three lidar vegetation metrics (height [CHM], roughness [VRI], and density [LVI]) over both vegetation classes (scrub and tree), the following trends and patterns emerge over the two-year period:

1. Trees were defined by annual change, while seasonal variability dominated scrub.
2. Trees closer to the stream (within 20 m) grew faster than trees farther from the stream (greater than 20 m), although this trend was not observed with scrub.
3. The trends observed in height (CHM) and roughness (VRI) were very similar and the differences were mainly in terms of the scale of each metric between scrub and trees.
4. Height (CHM) and roughness (VRI) were more influenced by annual change.
5. Density (LVI) was more influenced by seasonal variability.

Based on these results, it is clear that all three metrics are representing different aspects of the riverscape vegetation as it changes both annually and seasonally. It is recommended that for any fluvial application able to utilize high-resolution survey data such as from DLS, whether it is for ecological modeling or hydraulic modeling, to consider integrating all three metrics as possible explanatory variables to describe the dynamic physical changes occurring to vegetation over the riverscape.

Author Contributions: Conceptualization, J.P.R.; data curation, L.L.; formal analysis, J.P.R.; funding acquisition, W.C.H.; methodology, J.P.R. and L.L.; supervision, W.C.H.; writing—original draft, J.P.R.; writing—review and editing, W.C.H. and L.L. All authors have read and agreed to the published version of the manuscript.

Conflicts of Interest: The authors declare no conflict of interest.

References

1. Fausch, K.D.; Torgersen, C.E.; Baxter, C.V.; Li, H.W. Landscapes to Riverscapes: Bridging the Gap between Research and Conservation of Stream Fishes. *BioScience* **2002**, *52*, 483–498. [CrossRef]
2. Carbonneau, P.; Fonstad, M.A.; Marcus, W.A.; Dugdale, S.J. Making Riverscapes Real. *Geomorphology* **2012**, *137*, 74–86. [CrossRef]
3. Dietrich, J.T. Riverscape Mapping with Helicopter-Based Structure-from-Motion Photogrammetry. *Geomorphology* **2016**, *252*, 144–157. [CrossRef]

4. Farid, A.; Rautenkranz, D.; Goodrich, D.C.; Marsh, S.E.; Sorooshian, S. Riparian Vegetation Classification from Airborne Laser Scanning Data with an Emphasis on Cottonwood Trees. *Can. J. Remote Sens.* **2006**, *32*, 15–18. [CrossRef]
5. Heritage, G.; Hetherington, D. Towards a Protocol for Laser Scanning in Fluvial Geomorphology. *Earth Surf. Process. Landf.* **2007**, *32*, 66–74. [CrossRef]
6. Resop, J.P.; Kozarek, J.L.; Hession, W.C. Terrestrial Laser Scanning for Delineating In-Stream Boulders and Quantifying Habitat Complexity Measures. *Photogramm. Eng. Remote Sens.* **2012**, *78*, 363–371. [CrossRef]
7. Woodget, A.S.; Austrums, R.; Maddock, I.P.; Habit, E. Drones and Digital Photogrammetry: From Classifications to Continuums for Monitoring River Habitat and Hydromorphology. *Wiley Interdiscip. Rev. Water* **2017**, *4*, 1–20. [CrossRef]
8. Yang, B.; Hawthorne, T.L.; Torres, H.; Feinman, M. Using Object-Oriented Classification for Coastal Management in the East Central Coast of Florida: A Quantitative Comparison between UAV, Satellite, and Aerial Data. *Drones* **2019**, *3*, 60. [CrossRef]
9. Resop, J.P.; Lehmann, L.; Hession, W.C. Drone Laser Scanning for Modeling Riverscape Topography and Vegetation: Comparison with Traditional Aerial Lidar. *Drones* **2019**, *3*, 35. [CrossRef]
10. Huang, C.; Peng, Y.; Lang, M.; Yeo, I.-Y.; McCarty, G. Wetland Inundation Mapping and Change Monitoring Using Landsat and Airborne LiDAR Data. *Remote Sens. Environ.* **2014**, *141*, 231–242. [CrossRef]
11. Anders, N.S.; Seijmonsbergen, A.C.; Bouten, W. Geomorphological Change Detection Using Object-Based Feature Extraction from Multi-Temporal LiDAR Data. *IEEE Geosci. Remote Sens. Lett.* **2013**, *10*, 1587–1591. [CrossRef]
12. Okyay, U.; Telling, J.; Glennie, C.L.; Dietrich, W.E. Airborne Lidar Change Detection: An Overview of Earth Sciences Applications. *Earth-Sci. Rev.* **2019**, *198*, 102929. [CrossRef]
13. Resop, J.P.; Hession, W.C. Terrestrial Laser Scanning for Monitoring Streambank Retreat: Comparison with Traditional Surveying Techniques. *J. Hydraul. Eng.* **2010**, *136*, 794–798. [CrossRef]
14. O'Neal, M.A.; Pizzuto, J.E. The Rates and Spatial Patterns of Annual Riverbank Erosion Revealed through Terrestrial Laser-Scanner Surveys of the South River, Virginia. *Earth Surf. Process. Landf.* **2011**, *36*, 695–701. [CrossRef]
15. Saarinen, N.; Vastaranta, M.; Vaaja, M.; Lotsari, E.; Jaakkola, A.; Kukko, A.; Kaartinen, H.; Holopainen, M.; Hyyppä, H.; Alho, P. Area-Based Approach for Mapping and Monitoring Riverine Vegetation Using Mobile Laser Scanning. *Remote Sens.* **2013**, *5*, 5285–5303. [CrossRef]
16. Day, S.S.; Gran, K.B.; Belmont, P.; Wawrzyniec, T. Measuring Bluff Erosion Part 1: Terrestrial Laser Scanning Methods for Change Detection. *Earth Surf. Process. Landf.* **2013**, *38*, 1055–1067. [CrossRef]
17. Flener, C.; Vaaja, M.; Jaakkola, A.; Krooks, A.; Kaartinen, H.; Kukko, A.; Kasvi, E.; Hyyppä, H.; Hyyppä, J.; Alho, P. Seamless Mapping of River Channels at High Resolution Using Mobile LiDAR and UAV-Photography. *Remote Sens.* **2013**, *5*, 6382–6407. [CrossRef]
18. Leyland, J.; Hackney, C.R.; Darby, S.E.; Parsons, D.R.; Best, J.L.; Nicholas, A.P.; Aalto, R.; Lague, D. Extreme Flood-Driven Fluvial Bank Erosion and Sediment Loads: Direct Process Measurements Using Integrated Mobile Laser Scanning (MLS) and Hydro-Acoustic Techniques. *Earth Surf. Process. Landf.* **2017**, *42*, 334–346. [CrossRef]
19. Andersen, H.-E.; McGaughey, R.J.; Reutebuch, S.E. Estimating Forest Canopy Fuel Parameters Using LIDAR Data. *Remote Sens. Environ.* **2005**, *94*, 441–449. [CrossRef]
20. Huang, W.; Dolan, K.; Swatantran, A.; Johnson, K.; Tang, H.; O'Neil-Dunne, J.; Dubayah, R.; Hurtt, G. High-Resolution Mapping of Aboveground Biomass for Forest Carbon Monitoring System in the Tri-State Region of Maryland, Pennsylvania and Delaware, USA. *Environ. Res. Lett.* **2019**, *14*, 095002. [CrossRef]
21. Mundt, J.T.; Streutker, D.R.; Glenn, N.F. Mapping Sagebrush Distribution Using Fusion of Hyperspectral and Lidar Classifications. *Photogramm. Eng. Remote Sens.* **2006**, *72*, 47–54. [CrossRef]
22. Arcement, G.J.; Schneider, V.R. *Guide for Selecting Manning's Roughness Coefficients for Natural Channels and Flood Plains*; United States Geological Survey: Denver, CO, USA, 1989.
23. You, H.; Wang, T.; Skidmore, A.K.; Xing, Y. Quantifying the Effects of Normalisation of Airborne LiDAR Intensity on Coniferous Forest Leaf Area Index Estimations. *Remote Sens.* **2017**, *9*, 163. [CrossRef]
24. Kato, A.; Moskal, L.M.; Schiess, P.; Swanson, M.E.; Calhoun, D.; Stuetzle, W. Capturing Tree Crown Formation through Implicit Surface Reconstruction Using Airborne Lidar Data. *Remote Sens. Environ.* **2009**, *113*, 1148–1162. [CrossRef]
25. Jakubowski, M.K.; Li, W.; Guo, Q.; Kelly, M. Delineating Individual Trees from Lidar Data: A Comparison of Vector- and Raster-Based Segmentation Approaches. *Remote Sens.* **2013**, *5*, 4163–4186. [CrossRef]
26. Wu, X.; Shen, X.; Cao, L.; Wang, G.; Cao, F. Assessment of Individual Tree Detection and Canopy Cover Estimation Using Unmanned Aerial Vehicle Based Light Detection and Ranging (UAV-LiDAR) Data in Planted Forests. *Remote Sens.* **2019**, *11*, 908. [CrossRef]
27. Dorn, H.; Vetter, M.; Höfle, B. GIS-Based Roughness Derivation for Flood Simulations: A Comparison of Orthophotos, LiDAR and Crowdsourced Geodata. *Remote Sens.* **2014**, *6*, 1739–1759. [CrossRef]
28. Lefsky, M.A.; Harding, D.J.; Keller, M.; Cohen, W.B.; Carabajal, C.C.; Espirito-Santo, F.D.B.; Hunter, M.O.; de Oliveira, R. Estimates of Forest Canopy Height and Aboveground Biomass Using ICESat. *Geophys. Res. Lett.* **2005**, *32*. [CrossRef]
29. Zhou, T.; Popescu, S. Waveformlidar: An R Package for Waveform LiDAR Processing and Analysis. *Remote Sens.* **2019**, *11*, 2552. [CrossRef]
30. Chow, V.T. *Open-Channel Hydraulics*; McGraw-Hill: New York, NY, USA, 1959; ISBN 978-0-07-085906-7.

31. Prior, E.M.; Aquilina, C.A.; Czuba, J.A.; Pingel, T.J.; Hession, W.C. Estimating Floodplain Vegetative Roughness Using Drone-Based Laser Scanning and Structure from Motion Photogrammetry. *Remote Sens.* **2021**, *13*, 2616. [CrossRef]
32. Barilotti, A.; Sepic, F.; Abramo, E.; Crosilla, F. Improving the Morphological Analysis for Tree Extraction: A Dynamic Approach to Lidar Data. In Proceedings of the ISPRS Workshop on Laser Scanning 2007 and SilviLaser 2007, Espoo, Finland, 12–14 September 2007.
33. Wynn, T.; Hession, W.C.; Yagow, G. *Stroubles Creek Stream Restoration*; Virginia Department of Conservation and Recreation: Richmond, VA, USA, 2010.
34. Wynn-Thompson, T.; Hession, W.C.; Scott, D. StREAM Lab at Virginia Tech. *Resour. Mag.* **2012**, *19*, 8–9. [CrossRef]
35. YellowScan YellowScan Surveyor: The Lightest and Most Versatile UAV LiDAR Solution. Available online: https://www.yellowscan-lidar.com/products/surveyor/ (accessed on 21 March 2020).
36. Isenburg, M. Processing Drone LiDAR from YellowScan's Surveyor, a Velodyne Puck Based System. Available online: https://rapidlasso.com/2017/10/29/processing-drone-lidar-from-yellowscans-surveyor-a-velodyne-puck-based-system/ (accessed on 4 September 2021).
37. Wheaton, J.M.; Brasington, J.; Darby, S.E.; Sear, D.A. Accounting for uncertainty in DEMs from repeat topographic surveys: Improved sediment budgets. *Earth Surf. Process. Landf.* **2010**, *35*, 136–156. [CrossRef]
38. Williams, R. DEMs of Difference. *Geomorphol. Tech.* **2012**, *2*, 1–17.

drones

Article

UAV-Based Classification of Cercospora Leaf Spot Using RGB Images

Florian Görlich [1], Elias Marks [1,*,†], Anne-Katrin Mahlein [2], Kathrin König [3], Philipp Lottes [1,4] and Cyrill Stachniss [1,4]

[1] Institute of Geodesy and Geoinformation, University of Bonn, 53115 Bonn, Germany; s7flgoer@uni-bonn.de (F.G.); philipp.lottes@uni-bonn.de (P.L.); cyrill.stachniss@igg.uni-bonn.de (C.S.)

[2] Institute of Sugar Beet Research, 37079 Göttingen, Germany; mahlein@ifz-goettingen.de

[3] Strube Research GmbH & Co. KG, 38387 Söllingen, Germany; k.koenig@strube.net

[4] Pheno-Inspect GmbH, 46047 Oberhausen, Germany; philipp.lottes@phenoinspect.de

* Correspondence: elias.marks@uni-bonn.de

† Current address: Photogrammetry & Robotics Lab, University of Bonn, Nussallee 15, 53115 Bonn, Germany.

Abstract: Plant diseases can impact crop yield. Thus, the detection of plant diseases using sensors that can be mounted on aerial vehicles is in the interest of farmers to support decision-making in integrated pest management and to breeders for selecting tolerant or resistant genotypes. This paper investigated the detection of Cercospora leaf spot (CLS), caused by *Cercospora beticola* in sugar beet using RGB imagery. We proposed an approach to tackle the CLS detection problem using fully convolutional neural networks, which operate directly on RGB images captured by a UAV. This efficient approach does not require complex multi- or hyper-spectral sensors, but provides reliable results and high sensitivity. We provided a detection pipeline for pixel-wise semantic segmentation of CLS symptoms, healthy vegetation, and background so that our approach can automatically quantify the grade of infestation. We thoroughly evaluated our system using multiple UAV datasets recorded from different sugar beet trial fields. The dataset consisted of a training and a test dataset and originated from different fields. We used it to evaluate our approach under realistic conditions and analyzed its generalization capabilities to unseen environments. The obtained results correlated to visual estimation by human experts significantly. The presented study underlined the potential of high-resolution RGB imaging and convolutional neural networks for plant disease detection under field conditions. The demonstrated procedure is particularly interesting for applications under practical conditions, as no complex and cost-intensive measuring system is required.

Keywords: UAV-based monitoring; agricultural robotics; plant disease detection; RGB images; Cercospora leaf spot; CNNs; semantic segmentation; phenotyping

1. Introduction

Our society relies on sustainable crop production for obtaining food, feed, and other resources [1]. Plant diseases can have strong negative effects on the achievable yield, heavily influencing the efficiency of farmlands. To address this problem in the short term, farmers need to detect the occurrence and spread of diseases in time to take adequate countermeasures. This is known as the concept of integrated pest management. To tackle the problem in the long run, plant breeders aim at developing new, more tolerant, or resistant varieties concerning yield-affecting plant diseases. Besides preventing the adverse effects on crop yield, cultivating these innovative crop varieties allows reducing the application of chemical plant protection products, resulting in benefits for the environment. Plant breeding considers the performance of varieties in diverse environments [2]. Therefore, the selection of preferable genotypes is time and cost intensive, often referred to as the so-called phenotyping bottleneck [3].

UAVs have been applied to many fields in recent years, and examples of these are cinematography [4], wind field estimation [5], and remote cameras [6]. Furthermore, UAVs are attractive platforms for monitoring agricultural fields and breeding plots as they allow for flexible image-based monitoring and enable the in-depth analysis of such image data retrospectively [7,8]. Therefore, UAVs represent a valuable tool for farmers and breeders to minimize the effort needed to detect and quantify diseases in crop fields.

An exemplary disease impacting yield in sugar beet is Cercospora leaf spot, caused by the fungal pathogen *Cercospora beticola (Sacc.)*. Causing yield losses approaching 40%, CLS is the most important foliar disease in sugar beet production. The first symptoms caused by the perthotrophic pathogen *C. beticola* are leaf spots with a reddish-brown margin of typically 2 to 5 mm in diameter [9]; see the bottom left of Figure 1. Later, the disease spreads, and the spots merge into a more extensive symptom distributed across entire leaves, as visible in Figure 1, bottom-right.
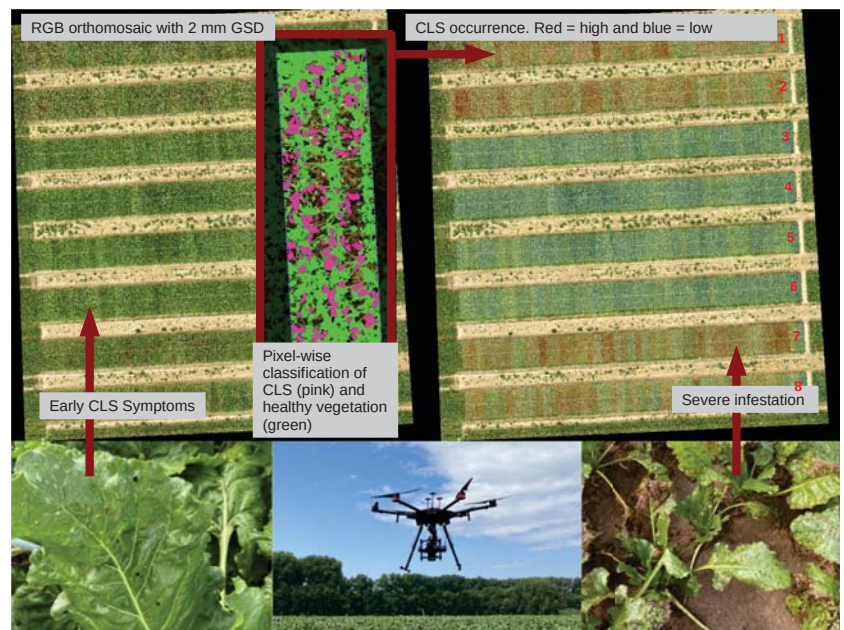
Figure 1. We aimed at predicting the occurrence of Cercospora leaf spot (CLS) for the entire field trial. We first separated the RGB orthomosaic into small plots that corresponded to the breeder's plot structure for variety testing. These plots were divided into eight strips, which are numbered in red. For each plot, we performed a pixel-wise classification into the classes CLS (pink), healthy vegetation (green), and background (no color). Finally, we illustrate the plot-based infection level for the entire field in semantic maps, where a red plot refers to high infection and blue refers to no infection. We flew a DJI M600 equipped with a Phase One IMX 100 megapixel RGB camera.

Finding new sugar beet varieties with CLS tolerance or resistance poses multiple challenges to the breeder. It requires a time-intensive observation of the breeding plots—a task that offers a great potential for UAV-based monitoring support. For the breeder, it is essential to know when and where outbreaks of the disease occur in the trial sites consisting of hundreds or thousands of trial plots and how each individual genotype is affected by the plant disease regarding several epidemiological parameters. In many cases, the disease starts from a primary inoculum in the soil and afterward spreads radially, generating so-called CLS nests [10]. Therefore, it is important to automize the detection and quantification of CLS among a vast amount of tested genotypes to capture the gradual

change of CLS resistance, as well as the detection of nests in breeding trials. Furthermore, early detection and identification in an automated and easy-to-execute way are key for the successful adoption of disease control in agricultural practice.

We addressed the problem of CLS occurrence detection and quantification in a breeding trial by analyzing UAV imagery. UAVs equipped with RGB cameras serve as an excellent platform to obtain fast and spatially detailed information of field environments such as the breeding trials we analyzed. An example is illustrated in Figure 1. We focused on detection at the pixel level to estimate the amount of CLS and provided this information in concise semantic maps to breeders. We aimed at dealing with different environmental conditions and agronomic diversity regarding plant appearances, soil conditions, and light conditions during capturing. Furthermore, our goal was to provide high performance also in unseen conditions, which can occur in unknown field sites and trials. To correlate our method with the approaches currently used for plant disease monitoring, we compared the predictions of our approach to the infection scores estimated by plant experts as the ground truth.

The main scientific contribution of this work was a novel, vision-based classification approach that uses fully convolutional neural networks (FCNs) that operate on RGB images to determine the occurrence of CLS in real fields. We proposed a detection pipeline that performs the pixel-wise classification of the RGB images into the classes CLS, healthy vegetation, and background. The FCN, on which our method was based, uses an encoder-decoder structure for the semantic segmentation of the images. We trained it end-to-end: the input to the network were raw images of the plots, and the loss was computed directly on the semantic maps. It neither relies on a certain pre-segmentation of the vegetation, nor any pre-extraction of handcrafted features. In contrast to Jay et al. [11], who targeted a leaf spot-level evaluation, we aimed at detecting CLS symptoms at the pixel scale to help breeders detect the infection earlier, allowing an improved evaluation of the temporal and spatial dynamics of the spread in breeding trials. Our approach was also intended for growers to quantify CLS at different levels to identify management thresholds in the context of integrated pest management. An exemplary output of our approach is illustrated in the center of Figure 1.

In sum, we make the following three key claims about our work. First, our approach can detect CLS with high-performance results when testing on data captured under similar field conditions, i.e., when trained and tested on images coming from the same agricultural field under similar conditions during a single flight. Second, our approach generalizes to unseen data when trained on datasets captured in different fields and under changing light and environmental field conditions. Third, we show that our proposed classification system's results correlate well to field experts' scoring results assessing CLS disease severity visually. This paper used several UAV datasets from diverse experimental field trials to explicitly evaluate our approach under these claims.

2. Related Work

In general, semantic segmentation can be applied in different fields of applications. These are, for instance, autonomous driving [12], medical analysis [13,14], video analysis [15], segmentation of 3D environments [16], joint semantic-instance segmentation [17], and many other domains.

Regarding classification approaches, Lottes et al. [18] proposed an FCN that can determine the localization of plant stems and a pixel-wise semantic map of crops and weeds at the same time. The difference from our approach is that we used UAV imagery instead of ground vehicle-captured images. In addition to this, another proposed network by Lottes et al. [19] sought to improve the previously presented crop and weed segmentation by performing a generalization.

Milioto et al. [20] proposed a CNN, which can classify sugar beet plants, weeds, and background in real time. They used images taken from a ground robot and did not tackle diseases. Another proposed approach by Mortensen et al. [21] aimed to classify several crop

species within overloaded data. This task was also performed by semantic segmentation based on FCNs.

Various classification systems have been proposed to detect plant diseases such as CLS on sugar beet in the past. Most of these systems perform the classification task using classical machine learning methods such as clustering [22], spectral indices [23], or support vector machines (SVMs) [24–28]. More recently, the wide adoption of neural networks has led to classification approaches based on convolutional neural networks (CNNs) [11,29–34].

Jay et al. [11] proposed an approach focusing on comparing the capability of UGVs and UAVs to determine a CLS scoring, which refers to the infection of a plot by *C. beticola*. Therefore, spatially high-resolution RGB images for UGV and spatially coarser resolved multi-spectral images for UAV find use. In contrast to our approach, they used multi-spectral images captured by a UAV instead of the RGB imagery. For the assessment, the parameters disease incidence (occurrence of single symptoms on a specific unit) and disease severity are relevant. In Jay et al., both of these were addressed and were represented by the canopy cover (green fraction), as well as the spot density [11]. They found that using high-resolution RGB imagery by UGV capturing led to a good extraction of low and high CLS scoring values. In contrast, the spatially coarser multi-spectral imagery used in UAV capturing is only applicable for high scoring values [11].

Facing the problem of powdery mildew on cucumber leaves, Lin et al. [35] proposed a CNN for semantic segmentation, which enables the pixel-wise segmentation and determination of powdery mildew on leaf images. This related approach differs from ours because we used RGB images, which are not previously segmented as the network's input. Moreover, we used imagery captured by a UAV instead of images captured from a close point of view. Besides disease detection, also nutrient deficiencies can be identified using RGB data and deep learning as shown by Yi et al. [36]. This information can then be used to provide targeted fertilization and optimize field management.

In contrast to the aforementioned prior work, our network can detect CLS and differentiate symptomatic pixels from healthy sugar beet plants and background with high-performance results. Second, our method generalizes well to unseen data, using RGB images of various field conditions. To the best of our knowledge, we are therefore the first to propose an end-to-end learned semantic segmentation approach determining the occurrence of CLS within breeders' real fields.

3. Classification System for Plant Disease Detection

The primary objective of our work was to detect and quantify CLS in sugar beet trials robustly. With our approach, we can provide breeders with information about the disease severity within their fields on a plot basis. We developed a semantic segmentation pipeline that explicitly distinguishes between the classes CLS, healthy sugar beet, and background, i.e., mostly soil.

Our approach was designed to process three-channel RGB images as the input. The output is a pixel-wise pseudo probability distribution over the class labels mentioned above. We picked per pixel the class label with the highest probability and obtained the final class map with the same resolution as the original image.

Our fully convolutional network was based on the architecture that we proposed in our previous work [18] for semantic segmentation and stem detection. Fully convolutional DenseNets, proposed by Jégou et al. [37], inspired the architectural design for our semantic segmentation approach. Their FC-DenseNet architecture was based on DenseNet, which was introduced by Huang et al. [38].

In general, the architecture of our approach is structured into three different parts: pre-processing, image encoding, and feature decoding. Figure 2 illustrates our FCN approach's general processing pipeline.
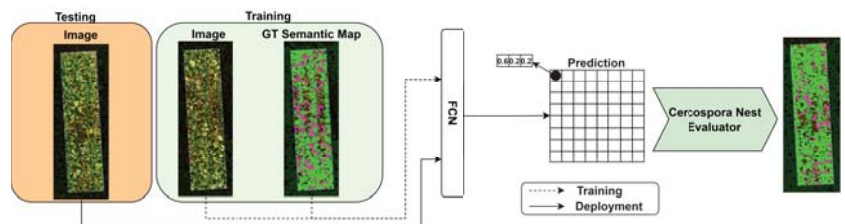
Figure 2. Overview of the approach, developed with precision farming applications in mind. It briefly illustrates the FCN approach for the classification of CLS based on RGB images only.

3.1. Preprocessing

Our pipeline begins with an automatic preprocessing step of the network's input. By aligning the distributions of the training and test data, preprocessing the network's inputs can improve the classification system's generalization capabilities. It includes transforming the pixel values, typically ranging between $[0, 255]$, into the range of $[0, 1]$. This transformation is carried out by subtracting each channel's mean value and dividing this result by each channel's standard deviation, i.e., a standardization. Afterward, we zero centered the data to $[-0.5, 0.5]$.

3.2. Encoder Structure

The preprocessing step is followed by the encoder, which serves as a feature extractor. Our encoder incorporates five fully convolutional dense building blocks for the densely compressed feature extraction of the network's input. The basic building block in our FCN's encoder structure follows the idea of the so-called fully convolutional DenseNet (FC-DenseNet) [37]. It combines the recently proposed densely connected CNNs, which are organized as dense blocks [38], with fully convolutional networks (FCN) [39]. The dense connectivity pattern iteratively concatenates all computed feature maps of subsequent convolutional layers in a feed-forward fashion. These dense connections encourage deeper layers to reuse features that were produced by earlier layers. Additionally, it supports the gradient flow in the backward pass and thus a stable training. After passing the RGB input images through the encoder, they are transformed into a more compressed and high-level representation.

3.3. Decoder Structure

Our decoder structure closely follows the previously described encoder. It is used to bring the compressed feature representation of the input volume back to the original resolution. The decoder achieves this by applying learned transposed convolutions to the dense feature representations until the resolution of the original input image is matched. Additionally, we included skip connections between the encoder and decoder, supporting the restoration of the spatial information, which might get lost within the encoder structure. Each pixel contains, within the original-sized output, assignment probabilities of belonging to each possible class after passing through a final softmax layer.

The resulting output is a semantic map in which the pixel-wise final class labels are stated. The final class label assignment is based on choosing the class having the highest assignment probability.

4. Experimental Evaluation

Our experiments were designed to show our method's capabilities and support our key claims, which were: (i) our approach can detect CLS with high performance when testing under similar field conditions; (ii) our approach generalizes well to changing conditions; (iii) the classification system's results of our proposed approach correlate well to field experts' scoring results. Hence, our classification system can robustly classify CLS

and is a valuable tool for the evaluation of genotypes in the breeding process or plant varieties in registration or recommendation trials.

4.1. Experimental Setup

Data assessment was performed in official breeding trials all over Germany. At each experimental site, several sugar beet genotypes are cultivated in a randomized plot design, and each plot consists of 3 rows. The data set was from different time points during the vegetation period, and all characteristic phases of CLS infection from healthy to severe were observed. Reference ground truth data for calibration in Experiment 3 were assessed at one trial side in North-Rhine-Westphalia in September. We show an illustration for one of these plots in Figure 1.

In the trials that we analyzed, the infection by *Cercospora beticola* was not inoculated, but appeared naturally as the plants grew on fields that are prone to this disease.

The manually labeled portion of the datasets consisted of around 80 sugar beet plots. Various visual appearances of infested and healthy sugar beets, changing light conditions, and environmental conditions were present in the datasets. In total, we recorded and manually labeled the datasets among 16 different locations across Germany.

The images were captured by a Phase One IMX 100 megapixel RGB camera attached to a M600 drone manufactured by DJI. This drone has a payload of 6 kg, so it can easily carry the employed camera.

4.2. Parameters

In our experiments, we trained all networks from scratch using previously generated random image patches with a resolution of 320×320 pixels. During training, we considered $K = 2$ pairs $(m\hat{y}, my)$ within each batch. Hereby, $m\hat{y}$ denotes the predicted semantic map, and my represents the ground truth labels of the image patches, each represented as a vector. Moreover, we applied randomized augmentations to the training image patches to reduce overfitting of the model.

We used a positive weighted cross-entropy loss function to evaluate the difference between the predicted semantic map and the ground truth semantic map. It is calculated as follows:

$$
\begin{aligned}
\mathcal{L}_{\text{CE}}(y, \hat{y}) = \frac{1}{K} \sum_{k=1}^{K} \sum_{c=1}^{C=3} &\left(1 - y_c^k\right) \cdot \hat{y}_c^k + \\
&\left(1 + (\omega_c - 1) \cdot y_c^k\right) \cdot \\
&\left(\log\left(1 + \exp^{-|\hat{y}_c^k|}\right) + \max\left(-\hat{y}_c^k, 0\right)\right),
\end{aligned}
$$

where k represents the current image. Additionally, ω_c denotes the weight of class c; $\hat{y}_c^k$ is the predicted semantic map of image k; and y_c^k represents the provided ground truth semantic map of image k. The weights ω_c depend on the occurrence of each class within the training dataset. We assigned 10, 1, and 1 for the respective classes of CLS, healthy vegetation, and background.

We trained our network through 150 epochs and chose 0.005 as the initial learning rate. We also introduced a learning rate schedule that improved convergence by decreasing the learning rate after a predefined number of epochs. To improve generalization, we used a dropout rate of 0.33. As our parameter initialization values, we sampled a random set from a uniform distribution with a lower boundary of 0.05 and an upper boundary of 0.15. For gradient-based parameter optimization, we used the Adam algorithm by Kingma et al. [40].

4.3. Performance under Similar Field Conditions

In this first experiment, we evaluated our network's performance results in detecting CLS within every single plot when testing on data captured in the same agricultural field

(but in a different area) where the training data were acquired. In addition, we ensured that the used images were captured under similar light and environmental field conditions. Therefore, we used a dataset that contained 38 plot images recorded in the same sugar beet field within one flight. Exemplary images used within this experimental setup are visualized in Figure 3.
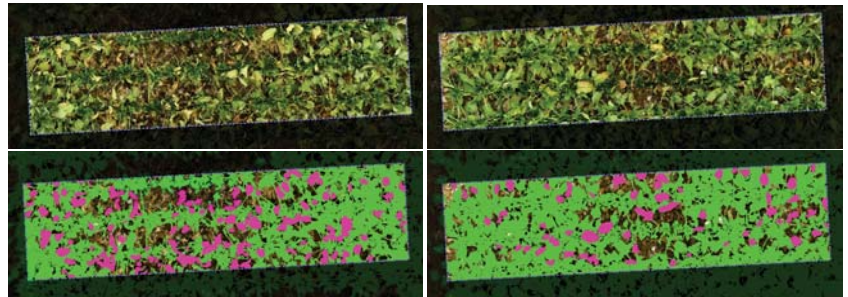
Figure 3. A single plots' RGB and corresponding ground truth information. The pixels labeled as Cercospora leaf spot (CLS) are in pink, whereas healthy vegetation is represented by green pixels. Note that this is a single plot from the field illustrated in Figure 1, but rotated 90°.

We captured these plot images in the field shown in Figure 1. We split the total amount of 38 RGB images into a training and test dataset with a ratio of 50/50. Thus, we used 19 plot images for training and 19 pictures solely for testing. As previously mentioned, these performance results can be seen as the upper boundary of the experimental setup explained in Section 4.4, as the training and test data came from a rather similar distribution.

In Table 1, we show exemplary output results of our first experimental setup.

Visually, the performance results under similar conditions led to rather good classification results for the class CLS. We came to this view because, as depicted in Table 1, almost all pixels labeled as CLS within the ground truth were correctly predicted by our network as CLS. Hence, the class CLS's recall value should be high, which was confirmed by a corresponding value of around 85%. The performance results of this experimental setup are summarized in Table 2. As can be seen in Table 2, the high recall of 85% contrasts with a rather low precision value of around 33%. The reason for the low precision value is also visible in Table 1. Our network predicted the class CLS at more pixel locations within the prediction map than were actually labeled as infected in the ground truth. This is especially recognizable in the upper left corner of the test image in the last row of Table 1, where there are much more CLS-labeled pixels in the predicted semantic map in comparison to the ground truth. In the table, it can be seen that the network correctly predicted leaves that were totally damaged, while it tended to overestimate the spread of the infection in leaves that were only partially affected.

In general, the classification of the class background worked highly satisfactorily, recognizable by very the high-performance results in terms of the intersection over union (IoU), precision, and recall. This observation was confirmed both visually and with numbers, such as an IoU of 90%, a precision of around 98%, and a recall of around 91%. In contrast, the class vegetation only showed high-performance results when facing a precision value of 96%. That means almost all pixels predicted as vegetation were labeled within the ground truth as vegetation as well. The IoU value of 73%, as well as the recall of around 76% were not as good as the corresponding values for the class background, but this was because most pixels wrongly classified as CLS actually belonged to the vegetation class. The wrongly assigned pixels resulted in a low IoU and recall for the vegetation class.

Table 1. Visualization of the resulting output of the CLS classification. In the first image from the left, we show the original RGB image. In the rightmost image, we visualize the agreement between the pixel-wise labels of the predicted semantic map (third image from the left) and the pixel-wise labels of the ground truth semantic map (second image from the left) using green pixels (agreement) and red pixels (disagreement). Within the semantic maps, we represent the class CLS as red pixels and the class healthy vegetation as green pixels, and all remaining pixels belong to the class background.

Image Patch	Ground Truth	Prediction	Agreement
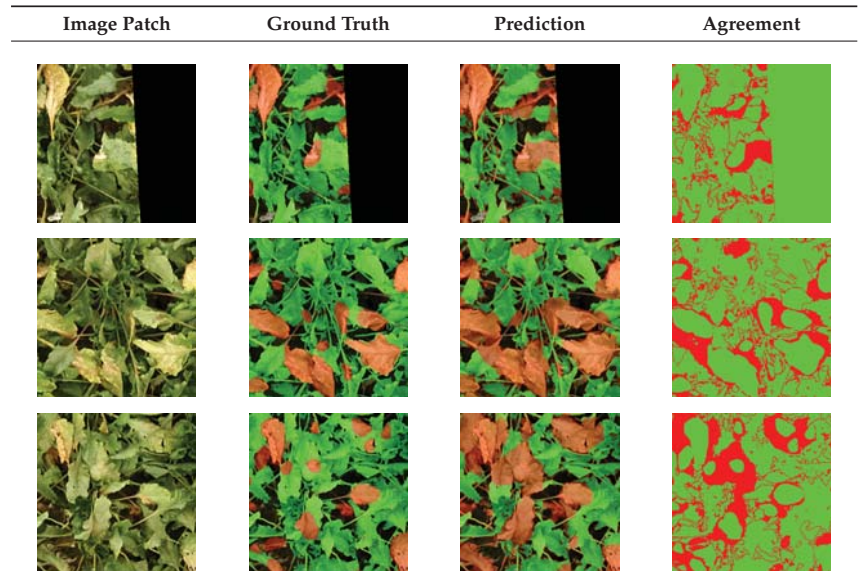
Table 2. Class-wise evaluation of the pixel-wise classification performance of the classes CLS, healthy vegetation, and background. Classification performance for the first experiment under similar field conditions. We evaluated using the IoU, precision, recall, and F1 scores. All presented results are given in %.

Class-Wise Evaluation under Similar Field Conditions				
Classes	**IoU**	**Precision**	**Recall**	**F1 Score**
CLS	31.39	33.27	84.75	47.78
healthy vegetation	73.44	96.32	75.57	84.69
background	90.00	98.43	91.31	94.74
∅	64.94	76.00	83.87	75.74

4.4. Performance under Changing Conditions

Within the second experiment, we examined whether our trained classification model achieved a good performance in detecting the CLS disease, which developed on a subset of the plants, even under changing light and environmental conditions during the capturing process. Hence, we aimed to reach a certain generalization capability of our network to different environment variables. The symptom development of CLS is dynamic. Early symptoms differ in size, color, and shape from a late symptoms [41]. Furthermore, different leaf stages (young or old leaves) can be diseased preferably. This poses a big challenge to the classifier by itself. Moreover, different lightning and points of view in the analyzed images made the classification problem even harder. Therefore, we used image data captured at 16 different locations at different times of the day to ensure a broad spectrum of environmental conditions during the capturing process. Figure 4 in comparison to Figure 3 shows one exemplary plot image, which illustrates that in differently located sugar

beet fields, the light and environmental conditions, as well as plant appearances and soil conditions could vary dramatically.
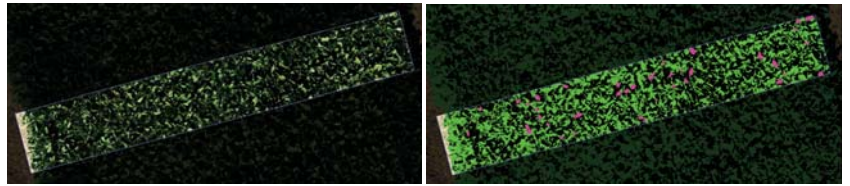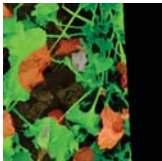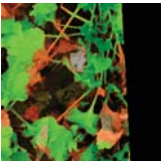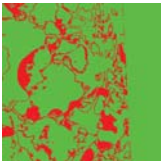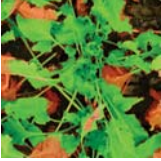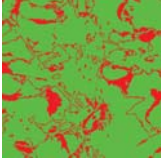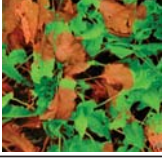
Figure 4. The images show an exemplary plot at another location in comparison to the breeder's field visualized in Figure 1 and Table 1. In different sugar beet field locations, the conditions can strongly differ from one another.

Within this experiment, we used 38 plot images, captured at 15 different locations, for training. We then used 38 plots from another location as the testing dataset. By this data partitioning, we aimed at providing enough training information from different perspectives to the network. We, therefore, expected our approach to generalize well enough to correctly classify the test set acquired under unseen conditions.

In Table 3, we show exemplary output results of our second experimental setup.

Table 3. Visualization of the resulting output of the CLS classification. In the first image from the left, we show the original RGB image. In the rightmost image, we visualize the agreement between the pixel-wise labels of the predicted semantic map (third image from the left) and the pixel-wise labels of the ground truth semantic map (second image from the left) using green pixels (agreement) and red pixels (disagreement). Within the semantic maps, we represent the class CLS as red pixels and the class healthy vegetation as green pixels, and all remaining pixels belong to the class background.

Image Patch	Ground Truth	Prediction	Agreement

The visual evaluation of these results showed that, generally, the classification of CLS-labeled pixels was characterized by a good performance regarding the recall. This was in line with the previous experiment, and we saw a certain generalization. As is visible in the top and bottom row of Table 3, almost all occurring CLS-labeled pixels were classified correctly by our network. Only a few false-negative pixels classified as CLS

were recognizable. This generally happened only when the network predicted a small part of the damaged leaf instead of the entire infected surface. In the bottom row of Table 3, the network extended its CLS prediction to the background in some parts, especially in the upper left corner of the image. We imputed this to very similar colors of the soil and rotten leaves.

We can confirm this observation by considering the performance results regarding the IoU, precision, recall, and F1 score [42]. We show these results in Table 4. Concerning the class CLS, the pixels labeled with this specific class were recognized with a recall of about 67%. However, the precision was 33%, as in the first experiment. This was in line with our observations in Table 3, in which the predicted semantic map included most CLS-labeled pixels of the ground truth semantic map, but extended this prediction to certain soil and vegetation areas.

The classes healthy vegetation and background showed high-performance results with respect to the IoU, precision, and recall. Especially the class background with an IoU of around 89%, a precision of around 98%, and a recall value of around 90% was classified well. Furthermore, the class vegetation showed satisfying results with an IoU of 79%, a precision of around 93%, and a recall of 84%.

Table 4. Class-wise evaluation of the pixel-wise classification performance of the classes CLS, healthy vegetation, and background. Classification performance for the second experiment under changing field conditions. We evaluated using the IoU, precision, recall and F1 scores. All presented results are given in %.

Class-Wise Evaluation under Changing Field Conditions				
Classes	**IoU**	**Precision**	**Recall**	**F1 Score**
CLS	28.60	33.37	66.69	44.48
healthy vegetation	78.99	92.58	84.33	88.26
background	88.50	98.47	89.73	93.90
∅	65.36	74.81	80.25	75.55

In general, the achieved recall for the class CLS of around 67% was acceptable, but compared to the remaining two classes, the performance results were less precise. Considering the fact that the test images were captured under light conditions, as well as plant and soil appearances never seen by the network, the resulting recall value of the class CLS was quite good. This was especially true when considering the upper boundary, which we determined in our first experimental setup in Section 4.3. Regarding the precision, the performance results of the generalized network were identical to the upper bound value.

Regarding the classes healthy vegetation and background, both networks' resulting performances did not strongly differ from one another. That means the generalization of soil and vegetation did not seem to be challenging for our approach.

In conclusion, the performance results of the first two experimental setups, the classification of CLS, led to quite satisfying performance results regarding the recall. When considering the precision instead, the classification did not perform as well. In this regard, it should be noted that the detection of CLS is a difficult problem also for an expert human operator. Especially in early disease stages, symptoms are hard to detect accurately as they result in an appearance that is only slightly different from a healthy leaf. We, therefore, performed a third experiment, presented in the next section, to show that the performance of our approach led to a quantification of the spread of CLS, which was comparable to the one obtained by experts examining the plants visually on site.

4.5. Comparison of the Estimated Level of Infection and the Experts' Scoring Results

To correlate our network output with the experts' scoring results in the third experiment, we needed to derive a value that was comparable to the scoring values used by them. We further refer to these derived values as infection levels. They describe the severity of

infection by CLS on sugar beet plants within the individual plots via an ordinal rating scale. For this evaluation, an expert went into the field to determine the infection level of the plots. Therefore, the determination of the infection level is a time-consuming and expensive task for farmers and breeders. Since the fields were organized into plots, each of these single plots was assigned a score. This single number represented the infection level of CLS on the sugar beet plants within this certain plot. The infection level was a number in the range between 1 and 9. No infection or a very small infection was set as 1; 5 meant a mediocre infection; and 9 represented very heavily infested plants [43].

The ground truth data were provided by the breeding company Strube Research and were based on the experts' scoring of the infection level of CLS for 336 plots. The trial was comprised of 84 entries, which were laid out over 2 strips. The entries of the trial were replicated 4 times. Two of those replicates were treated with fungicide (Strips 3-4 and 5-6), and the other two were not treated with fungicide (Strips 1-2 and 7-8). We expected high infection levels in the strips where no fungicide was applied and lower scores for the other strips. The eight strips with 42 entries each are numbered in Figure 1. The data used in this experiment were collected by two experts with 12 and 25 years of experience, respectively. They used an evaluation scheme developed by Strube and used for 20 years to ensure a consistent interpretation of the symptoms.

In order to compare the classification system's results, we first needed to derive comparable values. Therefore, we analyzed the classified image pixels' distribution within the predicted semantic map, which we obtained after applying the previously trained classifier. We focused on the resulting semantic map we obtained using the classifier trained under similar conditions (Section 4.3) and the one obtained under changing conditions (Section 4.4).

In the infection level estimation process, we only considered the pixels that were predicted as CLS, since healthy vegetation and background were not relevant for this task. To convert the number of pixels predicted as CLS into the infection level score, we first defined the lower and upper boundaries. For the first boundary, we calculated the average occurrence of CLS pixels within all plots that were rated as Infection Level 1 in the ground truth defined by the experts. We then defined as 1 the infection level off all plots with a number of pixels classified as infected that was lower than or equal to the calculated average. We used this averaging instead of simply assigning the lowest value to the first score, which was more in line with the expert evaluation. The same procedure was applied by us to find the amount of CLS pixels relative to Infection Level 8, taking into consideration the most infected plots instead. We here used the score of 8 instead of the maximum possible infection level of 9 since the ground truth data contained only infection levels in the range between 1 and 8. This allowed us to actually define the plots with the lowest-rated infection level as 1 instead of interpolating them to a higher score. Based on our predicted infection levels' lower and upper boundary, we performed linear interpolation to find the occurrence frequencies of CLS corresponding to the different scores. By finding the score corresponding to an occurrence frequency that was closest to the one of a given plot, we could assign this score to the plot. This resulted in an estimated infection level for every single plot. Now, we could compare these predictions with the corresponding expert's ground truth scoring values.

Figure 5 contains the results obtained from the images of both the classifier trained under similar, as well as the one trained under changing conditions. In the leftmost image in the upper row, we see a histogram showing the difference between the ground truth value and the corresponding predicted infection level. Here, the estimated infection levels were based on the semantic maps predicted using the classifier, which was trained under similar field conditions (Section 4.3). Underneath, in the bottom row's leftmost figure, we show the histogram of the differences between the ground truth and the prediction based on the semantic maps obtained using the classifier trained under changing field conditions (Section 4.4). In the upper row's central figure, we present the difference between the ground truth and the predicted infection level for each plot, based on the output of the

classifier trained under similar conditions. Below this plot, we show the counterpart based on the classifier trained under changing field conditions. We visualize the predicted infection level of the plots based on the two classifiers on the right-hand side.
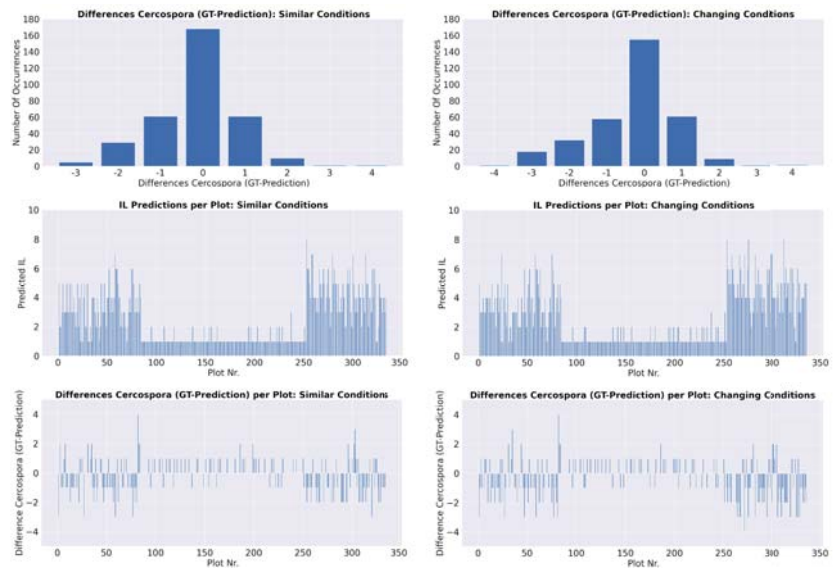
Figure 5. Results of the infection level (IL) determination of CLS based on the predicted semantic maps. The upper line contains the results based on the semantic maps we obtained using the classifier trained under similar conditions, whereas the lower line consists of the results based on using the classifier trained under changing conditions.

As clearly visible within both histograms, the most occurring difference between the ground truth and the prediction was 0, equaling 29.8%. In addition, regarding the differences ± 1 often occurring within the histograms, they could be observed in 51.5% of the plots. This led to the insight that the estimation of the infection levels based on our networks' semantic maps correlated well to the experts' scoring values. We came to this conclusion because in practice, the infection level determination is highly subjective and depends on each expert [44,45]. This led to the fact that, sometimes, an expert evaluates an area with a different scoring value than another expert would have done. Therefore, a deviation of ± 1 of the experts' scores seemed reasonable. The resulting accuracy with a ± 1 tolerance was 81.2%.

The plots on the right-hand side correlate to the ground truth data distribution we explained at the beginning of this section. Both classifiers predicted rather high infection levels for the first two rows of the breeder's field, small scores for Rows 3 to 6, and high CLS infection in Rows 7 and 8.

5. Conclusions

In this paper, we showed that we could determine Cercospora leaf spot (CLS) with a high recall, but a rather low precision, in the presence of mostly healthy sugar beet plants when using data that were captured under similar field conditions as the testing data. Additionally, we could classify healthy vegetation and background with F1 scores higher than 80%. Moreover, we demonstrated that we achieved a certain generalization regarding various light and environmental conditions during the data acquisition while classifying CLS's occurrence, underlined by a recall of around 66% for the class CLS. This generalization was also observable when considering the F1 score values of the classes healthy vegetation and background, which were higher than 88%. Considering the fact

that this work was a proof-of-concept, the resulting performance of CLS detection was acceptable and showed that this approach is worth being studied further. Most of the false negatives were classified as healthy vegetation, which in our opinion were derived mostly from the difficulty of visually determining the CLS symptoms, which made it almost impossible to label the data with very high accuracy. Here also the resolution of the images played a big role. We showed that this approach is already valuable by verifying that estimated infection levels derived from the semantic map predicted by our network correlated well with the experts' scoring values. Still, there is room for improvement by using a bigger dataset, and experts could be involved in the labeling process to obtain a better ground truth. Furthermore, an increased resolution of the RGB images would most likely improve the result, especially regarding the detection of early symptoms.

Author Contributions: Conceptualization, E.M. and P.L.; methodology, F.G., E.M., P.L. and C.S.; software, F.G. and P.L.; validation, P.L.; formal analysis, F.G., A.-K.M. and P.L.; investigation, F.G., E.M. and P.L.; resources, P.L. and C.S.; data curation, F.G., K.K. and P.L.; writing—original draft preparation, F.G. and P.L.; writing—review and editing, E.M., A.-K.M., K.K., P.L. and C.S.; supervision, P.L. and C.S.; project administration, P.L.; funding acquisition, P.L. and C.S. All authors have read and agreed to the published version of the manuscript.

Institutional Review Board Statement: Not applicable.

Informed Consent Statement: Not applicable.

Data Availability Statement: The data presented in this study are available on request from the corresponding author. The data are not publicly available due to ownership reasons.

Conflicts of Interest: The authors declare no conflict of interest.

References

1. Savary, S.; Willocquet, L. Modeling the Impact of Crop Diseases on Global Food Security. *Annu. Rev. Phytopathol.* **2020**, *58*, 313–341. [CrossRef]
2. Mahlein, A.K.; Kuska, M.T.; Thomas, S.; Wahabzada, M.; Behmann, J.; Rascher, U.; Kersting, K. Quantitative and qualitative phenotyping of disease resistance of crops by hyperspectral sensors: Seamless interlocking of phytopathology, sensors, and machine learning is needed! *Curr. Opin. Plant Biol.* **2019**, *50*, 156–162. [CrossRef] [PubMed]
3. Furbank, R.T.; Tester, M. Phenomics—Technologies to relieve the phenotyping bottleneck. *Trends Plant Sci.* **2011**, *16*, 635–644. [CrossRef] [PubMed]
4. Bonatti, R.; Wang, W.; Ho, C.; Ahuja, A.; Gschwindt, M.; Camci, E.; Kayacan, E.; Choudhury, S.; Scherer, S. Autonomous aerial cinematography in unstructured environments with learned artistic decision-making. *J. Field Robot.* **2020**, *37*, 606–641. [CrossRef]
5. Patrikar, J.; Moon, B.; Scherer, S. Wind and the City: Utilizing UAV-Based In-Situ Measurements for Estimating Urban Wind Fields. In Proceedings of the (IROS) IEEE/RSJ International Conference on Intelligent Robots and Systems, Las Vegas, NV, USA, 25–29 October 2020.
6. Pavan Kumar, B.N.; Balasubramanyam, A.; Patil, A.K.; Chethana, B.; Chai, Y.H. GazeGuide: An Eye-Gaze-Guided Active Immersive UAV Camera. *Appl. Sci.* **2020**, *10*, 1668. [CrossRef]
7. Radoglou-Grammatikis, P.; Sarigiannidis, P.; Lagkas, T.; Moscholios, I. A compilation of UAV applications for precision agriculture. *Comput. Netw.* **2020**, *172*, 107148. [CrossRef]
8. Christiansen, M.P.; Laursen, M.S.; Jørgensen, R.N.; Skovsen, S.; Gislum, R. Designing and Testing a UAV Mapping System for Agricultural Field Surveying. *Sensors* **2017**, *17*, 2703. [CrossRef]

9. Weiland, J.; Koch, G. Sugarbeet leaf spot disease (*Cercospora beticola* Sacc.) dagger. *Mol. Plant Pathol.* **2004**, *5*, 157–166. [CrossRef]
10. Imbusch, F.; Liebe, S.; Erven, T.; Varrelmann, M. Dynamics of cercospora leaf spot disease determined by aerial spore dispersal in artificially inoculated sugar beet fields. *Plant Pathol.* **2021**, *70*, 853–861. [CrossRef]
11. Jay, S.; Comar, A.; Benicio, R.; Beauvois, J.; Dutartre, D.; Daubige, G.; Li, W.; Labrosse, J.; Thomas, S.; Henry, N.; et al. Scoring Cercospora Leaf Spot on Sugar Beet: Comparison of UGV and UAV Phenotyping Systems. *Plant Phenomics* **2020**, 1–18. [CrossRef]
12. Treml, M.; Arjona-Medina, J.; Unterthiner, T.; Durgesh, R.; Friedmann, F.; Schuberth, P.; Mayr, A.; Heusel, M.; Hofmarcher, M.; Widrich, M.; et al. Speeding up semantic segmentation for autonomous driving. In Proceedings of the MLITS, NIPS Workshop, Barcelona, Spain, 9 December 2016; Volume 2, p. 7.
13. Quan, T.M.; Hildebrand, D.G.; Jeong, W.K. Fusionnet: A deep fully residual convolutional neural network for image segmentation in connectomics. *arXiv* **2016**, arXiv:1612.05360.
14. Ronneberger, O.; Fischer, P.; Brox, T. U-net: Convolutional networks for biomedical image segmentation. In Proceedings of the International Conference on Medical Image Computing and Computer-Assisted Intervention, Munich, Germany, 5–9 October 2015; pp. 234–241.
15. Athar, A.; Mahadevan, S.; O*s*ep, A.; Leal-Taixé, L.; Leibe, B. STEm-Seg: Spatio-temporal Embeddings for Instance Segmentation in Videos. In Proceedings of the European Conference on Computer Vision (ECCV), Glasgow, UK, 23–28 August 2020.
16. Engelmann, F.; Bokeloh, M.; Fathi, A.; Leibe, B.; Nießner, M. 3D-MPA: Multi Proposal Aggregation for 3D Semantic Instance Segmentation. In Proceedings of the IEEE Conference on Computer Vision and Pattern Recognition (CVPR), Seattle, WA, USA, 13–19 June 2020.
17. Weber, M.; Luiten, J.; Leibe, B. Single-Shot Panoptic Segmentation. *arXiv* **2019**, arXiv:1911.00764.
18. Lottes, P.; Behley, J.; Chebrolu, N.; Milioto, A.; Stachniss, C. Joint Stem Detection and Crop-Weed Classification for Plant-specific Treatment in Precision Farming. In Proceedings of the IEEE/RSJ International Conference on Intelligent Robots and Systems (IROS), Madrid, Spain, 1–5 October 2018.
19. Lottes, P.; Behley, J.; Milioto, A.; Stachniss, C. Fully Convolutional Networks with Sequential Information for Robust Crop and Weed Detection in Precision Farming. *IEEE Robot. Autom. Lett. RA-L* **2018**, *3*, 3097–3104. [CrossRef]
20. Milioto, A.; Lottes, P.; Stachniss, C. Real-time Semantic Segmentation of Crop and Weed for Precision Agriculture Robots Leveraging Background Knowledge in CNNs. In Proceedings of the IEEE International Conference on Robotics & Automation (ICRA), Brisbane, Australia, 21–25 May 2018.
21. Mortensen, A.; Dyrmann, M.; Karstoft, H.; Jörgensen, R.N.; Gislum, R. Semantic Segmentation of Mixed Crops using Deep Convolutional Neural Network. In Proceedings of the International Conference of Agricultural Engineering (CIGR), Aarhus, Denmark, 26–29 June 2016.
22. Zhang, S.; Wang, H.; Huang, W.; You, Z. Plant diseased leaf segmentation and recognition by fusion of superpixel, K-means and PHOG. *Optik* **2018**, *157*, 866–872. [CrossRef]
23. Mahlein, A.K.; Rumpf, T.; Welke, P.; Dehne, H.W.; Plümer, L.; Steiner, U.; Oerke, E.C. Development of spectral indices for detecting and identifying plant diseases. *Remote Sens. Environ.* **2013**, *128*, 21–30. [CrossRef]
24. Bhange, M.; Hingoliwala, H. Smart farming: Pomegranate disease detection using image processing. *Procedia Comput. Sci.* **2015**, *58*, 280–288. [CrossRef]
25. Padol, P.B.; Yadav, A.A. SVM classifier based grape leaf disease detection. In Proceedings of the 2016 Conference on Advances in Signal Processing (CASP), Pune, India, 9–11 June 2016.
26. Kaur, P.; Pannu, H.; Malhi, A. Plant disease recognition using fractional-order Zernike moments and SVM classifier. *Neural Comput. Appl.* **2019**, *31*, 8749–8768. [CrossRef]
27. Singh, V.; Misra, A.K. Detection of plant leaf diseases using image segmentation and soft computing techniques. *Inf. Process. Agric.* **2017**, *4*, 41–49. [CrossRef]
28. Zhou, R.; Kaneko, S.; Tanaka, F.; Kayamori, M.; Shimizu, M. Image-based field monitoring of Cercospora leaf spot in sugar beet by robust template matching and pattern recognition. *Comput. Electron. Agric.* **2015**, *116*, 65–79. [CrossRef]
29. Amara, J.; Bouaziz, B.; Algergawy, A. A Deep Learning-Based Approach for Banana Leaf Diseases Classification. Datenbanksysteme für Business, Technologie und Web (BTW 2017) Workshopband 2017; pp. 79–88. Available online: https://www.semanticscholar.org/paper/A-Deep-Learning-based-Approach-for-Banana-Leaf-Amara-Bouaziz/9fcecc67da35c6af6defd6825875a49954f195e9 (accessed on 21 March 2021).
30. Ferentinos, K.P. Deep learning models for plant disease detection and diagnosis. *Comput. Electron. Agric.* **2018**, *145*, 311–318. [CrossRef]
31. Mohanty, S.P.; Hughes, D.P.; Salathé, M. Using deep learning for image-based plant disease detection. *Front. Plant Sci.* **2016**, *7*, 1419. [CrossRef] [PubMed]
32. Ozguven, M.M.; Adem, K. Automatic detection and classification of leaf spot disease in sugar beet using deep learning algorithms. *Phys. A Stat. Mech. Its Appl.* **2019**, *535*, 122537. [CrossRef]
33. Sladojevic, S.; Arsenovic, M.; Anderla, A.; Culibrk, D.; Stefanovic, D. Deep Neural Networks Based Recognition of Plant Diseases by Leaf Image Classification. *Comput. Intell. Neurosci.* **2016**, 1–11. Available online: https://www.hindawi.com/journals/cin/2016/3289801/ (accessed on 21 March 2021). [CrossRef] [PubMed]

34. Wang, G.; Sun, Y.; Wang, J. Automatic image-based plant disease severity estimation using deep learning. *Comput. Intell. Neurosci.* **2017**, 1–8. Available online: https://www.hindawi.com/journals/cin/2017/2917536/ (accessed on 21 March 2021). [CrossRef] [PubMed]
35. Lin, K.; Gong, L.; Huang, Y.; Liu, C.; Pan, J. Deep learning-based segmentation and quantification of cucumber Powdery Mildew using convolutional neural network. *Front. Plant Sci.* **2019**, *10*, 155. [CrossRef]
36. Yi, J.; Krusenbaum, L.; Unger, P.; Hüging, H.; Seidel, S.; Schaaf, G.; Gall, J. Deep Learning for Non-Invasive Diagnosis of Nutrient Deficiencies in Sugar Beet Using RGB Images. *Sensors* **2020**, *20*, 5893. [CrossRef]
37. Jégou, S.; Drozdzal, M.; Vazquez, D.; Romero, A.; Bengio, Y. The one hundred layers tiramisu: Fully convolutional densenets for semantic segmentation. In Proceedings of the IEEE Conference on Computer Vision and Pattern Recognition Workshops, Honolulu, HI, USA, 21–26 July 2017; pp. 11–19.
38. Huang, G.; Liu, Z.; Maaten, L.; Weinberger, K.Q. Densely Connected Convolutional Networks. In Proceedings of the IEEE Conference on Computer Vision and Pattern Recognition (CVPR), Honolulu, HI, USA, 21–26 July 2017.
39. Long, J.; Shelhamer, E.; Darrell, T. Fully Convolutional Networks for Semantic Segmentation. In Proceedings of the IEEE Conference on Computer Vision and Pattern Recognition (CVPR), Boston, MA, USA, 7–12 June 2015.
40. Kingma, D.P.; Ba, J. Adam: A method for stochastic optimization. *arXiv* **2014**, arXiv:1412.6980.
41. Mahlein, A.K.; Steiner, U.; Hillnhütter, C.; Dehne, H.W.; Oerke, E.C. Hyperspectral imaging for small-scale analysis of symptoms caused by different sugar beet disease. *Plant Methods* **2012**, *8*, 1–13. [CrossRef]
42. Sasaki, Y. The Truth of the F-Measure. Teach Tutor Mater 2007. Available online: https://www.cs.odu.edu/~mukka/cs795sum09dm/Lecturenotes/Day3/F-measure-YS-26Oct07.pdf (accessed on 21 March 2021).
43. Wilbois, K.P.; Schwab, A.; Fischer, H.; Bachinger, J.; Palme, S.; Peters, H.; Dongus, S. Leitfaden für Praxisversuche. Available online: https://orgprints.org/2830/3/2830-02OE606-fibl-wilbois-2004-leitfaden_praxisversuche.pdf (accessed on 25 May 2020).
44. Nutter, F., Jr.; Esker, P.; Netto, R.; Savary, S.; Cooke, B. Disease Assessment Concepts and the Advancements Made in Improving the Accuracy and Precision of Plant Disease Data. *Eur. J. Plant Pathol.* **2007**, *115*, 95–103. [CrossRef]
45. Bock, C.; Barbedo, J.; Del Ponte, E.; Bohnenkamp, D.; Mahlein, A.K. From visual estimates to fully automated sensor-based measurements of plant disease severity: Status and challenges for improving accuracy. *Phytopathol. Res.* **2020**, *2*, 1–30. [CrossRef]

Unmanned Aerial Vehicles for Wildland Fires: Sensing, Perception, Cooperation and Assistance

Moulay A. Akhloufi [1,*], Andy Couturier [1] and Nicolás A. Castro [2]

[1] Perception, Robotics, and Intelligent Machines Research Group (PRIME), Department of Computer Science, Université de Moncton, 18 Antonine-Maillet Ave, Moncton, NB E1A 3E9, Canada; eac6996@umoncton.ca

[2] Electronics Engineering Department, Universidad Técnica Federico Santa María, Valparaíso 2340000, Chile; nicolas.castro.12@sansano.usm.cl

[*] Correspondence: moulay.akhloufi@umoncton.ca

Abstract: Wildfires represent a significant natural risk causing economic losses, human death and environmental damage. In recent years, the world has seen an increase in fire intensity and frequency. Research has been conducted towards the development of dedicated solutions for wildland fire assistance and fighting. Systems were proposed for the remote detection and tracking of fires. These systems have shown improvements in the area of efficient data collection and fire characterization within small-scale environments. However, wildland fires cover large areas making some of the proposed ground-based systems unsuitable for optimal coverage. To tackle this limitation, unmanned aerial vehicles (UAV) and unmanned aerial systems (UAS) were proposed. UAVs have proven to be useful due to their maneuverability, allowing for the implementation of remote sensing, allocation strategies and task planning. They can provide a low-cost alternative for the prevention, detection and real-time support of firefighting. In this paper, previous works related to the use of UAV in wildland fires are reviewed. Onboard sensor instruments, fire perception algorithms and coordination strategies are considered. In addition, some of the recent frameworks proposing the use of both aerial vehicles and unmanned ground vehicles (UGV) for a more efficient wildland firefighting strategy at a larger scale are presented.

Keywords: unmanned aerial systems; UAV; autonomous systems; wildland fire; forest fires; fire detection

1. Introduction

Wildland fires are an important threat in rural and protected areas. Their control and mitigation are difficult as they can quickly spread to their surroundings, potentially burning large land areas and getting close to urban areas and cities. The occurrence of wildland fires results into substantial costs to the economy, ecosystems and climate [1]. Nevertheless, their frequency is on the rise. In fact, there has been an increase in the intensity and frequency of wildland fires in comparison to the past 10,000 years [2]. In the western U.S. alone, wildland fires increased by 400% in the last decades [3,4]. In 2018, 8.8 million acres ($35,612.34$ km^2) were burned by more than 58,083 wildland fires in the U.S. [5]. In Northern California, a single fire, known as "Camp Fire", ended up killing 85 people. This fire was the most destructive in California history burning 153,336 acres (620.53 km^2) and destroying 18,733 structures. Losses were estimated to $16.5 billion [3]. Experts estimate that wildland fires will increase in the coming years mainly as a result of climate change [6].

With wildland fires being a multifaceted issue, many different elements are relevant to the efforts to reduce their impact. Aspects such as meteorology, drought monitoring, vegetation status monitoring can help the prevention and the preparation to wildland fires. Other aspects such as fire suppression actions and post-fire recovery strategies must also be taken into account after the appearance of fire. Many of these aspects have been studied with unmanned aerial vehicles (UAVs). However, in the literature, two elements

seem more prominent in relation to UAVs. First, the time span between the start of a fire and the arrival of firefighters. This response time needs to be reduced to a minimum in order to decrease the chances of the fire spreading to unmanageable levels. The second key element is the evaluation of the extent of the event and the monitoring of the emergency response. As manual wildland fire assessment is rendered difficult by several factors (e.g., limited visibility), the consideration of this aspect is necessary in order to elaborate better fighting strategies. These two key elements can only be properly addressed through the development of reliable and efficient systems for early stage fire detection and monitoring. As a result of this need, interest has grown in the research community and led to a large number of publications on the subject.

Remote sensing has been widely researched in the field as it allows the observation of wildland fire events without unnecessarily exposing humans to dangerous activities. For instance, satellite images have been used to report the fire risks [7] and the detection of active fires [8,9]. Wireless sensor networks (WSNs) have also been proposed for wildland fire detection [10], monitoring [11] and risk assessment [12]. However, both types of systems have practical limitations. Satellite imagery has limited resolution. Therefore, the data relevant to an area are often averaged and constrained to a single-pixel making it difficult to detect small fires [13]. Furthermore, satellites have limited ground coverage and necessitate a significant amount of time before being able to resurvey the same region. Limited precision and the lack of real-time data reporting are therefore rendering satellite imagery unsuitable for continuous monitoring. As for WSNs, they operate as an infrastructure that needs to be deployed beforehand. As the sensors are installed in the forest, their coverage and resolution are proportional to the investment that is made in their acquisition and deployment. Moreover, in the event of a fire, the sensors are destroyed, leading to additional replacement costs. Maintenance difficulties, the lack of power independence and the fact that they are not scalable due to their static nature are all factors known to limit their coverage and effectiveness [14]. As a result of the previous systems' shortcomings, unmanned aerial vehicles (UAVs) have been proposed as a more convenient technology for this task. Their maneuverability, autonomy, easy deployment and relatively low cost are all attributes that made UAV the technology of choice for future wildland fire management efforts.

UAV technologies have seen an important progression in the last decade and they are now used in a wide range of applications. UAV has become smaller, more affordable and now have better computation capabilities than in the past making them reliable tools for remote sensing missions in hostile environments [15]. Furthermore, UAVs can fly or hover over specific zones to retrieve relevant data in real time with cameras or other airborne sensors. As a result, research has shown their benefits for surveillance and monitoring of wildland fire as well as tasks related to post-fire damage evaluation [16–20]. Additionally, UAVs have exhibited a positive economic balance in favor of their use in wildland fire emergencies [21,22]. This makes UAVs both a practical and an economical solution. Therefore, research efforts have been oriented towards the development of frameworks and techniques using UAVs with the goal of delivering optimal fire detection, coverage and firefighting.

The subject of this paper is a summarization of the literature pertaining to use of UAVs in the context of wildland fires. Research in this area revolve more predominantly around fire detection and monitoring, therefore the core of this review will be concentrated on technologies and approaches aimed at tackling these challenges. However, this paper also touches on other subjects when relevant such as fire prognosis and firefighting but less extensively as fewer works are available on the subject in the literature. The only other related works believed to exist are the work of Yuan et al. [19] and Bailon-Ruiz and Lacroix [23]. Yuan et al. [19] touch on subjects such as UAV wildland fire monitoring, detection, fighting, diagnosis and prognosis, image vibration elimination and cooperative control of UAVs. While the subject of this work overlaps with ours, it was performed 5 years ago and since then a lot of research has been produced on the subject. In fact, most of the papers reviewed have been published in 2015 or after and are not present in Yuan et al. [19]. Therefore,

this work is much more current than Yuan et al. [19]. Bailon-Ruiz and Lacroix [23] have been published in 2020, and are therefore much more current. The authors discuss two components of the field of UAV wildfire remote sensing: system architecture (single UAV or multiple UAV) and autonomy level. The reviewed works are characterized by similar attributes (mission types, decision level, collaboration level, fielded) and include unique attributes such as information processing and airframe, while this paper also analyzes unique attributes such as sensing mode and coordination. Attributes such as information processing and airframe indicate that Bailon-Ruiz and Lacroix [23] put more focus on the type of UAV and the software that runs on it while this paper is focusing on sensing and communication. The most notable difference between both works is the depth of analysis of the reviewed works and the extent of the reviewed literature. While Bailon-Ruiz and Lacroix [23] discusses system architecture and autonomy level only, this paper discusses these topics as well as sensing instruments, fire detection and segmentation, available fire datasets, fire geolocation and modeling and UAV-unmanned ground vehicles (UGV) systems for wildfires. This paper also reviews more recent works (16 vs. 10 published in 2015 or after), more works in total (27 vs. 19), and this paper's reference count is more than three times higher (121 vs. 35) indicating a more in-depth discussion of concepts related to the reviewed works which in turn requires more referencing. Following these observations, it is believed that this paper is a significant contribution and is very relevant to the field.

The final goal of this review is to provide insight into the field towards the development of cooperative autonomous systems for wildland fires. Observations made after evolving for many years in the field indicate that the research community has provided many pieces of the solution to the problems that are wildland fires. However, these pieces, especially recent ones, often fail to come together in a unified framework to form a multi-faceted solution to the underlying issue. A lot more could be accomplished by combining fire detection, monitoring, prognosis and firefighting under the same system. Therefore, this paper reviews fire assistance components, sensing modalities, fire perception approaches, relevant datasets and UAV/UGV coordination and cooperation strategies. In fact, this paper's review approach is to break apart the reviewed works in these categories instead of discussing all the aspects of a reviewed work in the same paragraph. The idea is to bring existing approaches into light in such a way that it would be easier in the future to combine them into more complete systems instead of seeing them as individual systems. These subjects lead to the last section of this paper where cooperative autonomous systems are discussed and where all previously discussed technologies come together under the umbrella of a single framework.

2. Fire Assistance

Remote sensing with aerial systems presents multiple advantages in the context of emergency assistance. Their high maneuverability allows them to dynamically survey a region, follow a defined path or navigate autonomously. The wide range of sensors that can be loaded onboard allows the capture of important data which can be used to monitor the situation of interest and plan an emergency response. The ability to remotely control UAVs helps reduce the risk for humans and remove them from life-threatening tasks. The automation of maneuvers, planning and other mission-related tasks through a computer interface improves distant surveillance and monitoring. Advances in these aspects have a direct impact on the firefighting resource management.

UAV fire assistance systems in the literature can be characterized using four attributes: sensing modalities and instruments, type of task performed, coordination strategies with multiple UAVs or with the ground control station (GCS) and the approach to experimental validation. Figure 1 is a visual representation of these characteristics and their implementation in the reviewed works. These components are designed to perform one or more tasks related to fire emergencies. Within the reviewed works, the most prevalent tasks are the fire detection and monitoring. Fire prognosis and firefighting are also present in some works, but have received less interest from researchers. Fire detection and monitoring

is based on recognition techniques, a field of research that has seen significant advances in the last decades. Meanwhile, fire prognosis and fighting has practical limitations that hinder research on the subject hence the imbalance in the research interest. Prognosis requires complex mathematical models that must be fed with data that can be difficult to acquire in real time and in unknown environments. Fire fighting, on the other hand, requires expensive combat equipment that is even more expensive for large wildland fires. Moreover, close proximity with fires can pose a significant risk for the vehicle integrity and lead to its loss. However, some initial research has been done to design a UAV capable of fighting fires [24–26] and more recently some drone manufacturers have steeped in to tackle this problem as well [27]. It is clear that more work remains to be done for these vehicles to be affordable and technically viable.

Figure 1. Characteristics of the reviewed works.

One key component of an airborne fire assistance system is the type of UAV used. UAVs have different sizes, maneuverability and endurance capacities. These characteristics in themselves have a strong influence on the overall architecture of the system. There

is a wide selection of aerial systems ranging from large UAVs with long endurance and high-processing capabilities to small UAVs with short flight times and limited processing capabilities [28,29]. Large vehicles are expensive but have higher payload and can carry more sensors and other instruments. On the other hand, smaller vehicles are more affordable but with limited payload. The instruments onboard the vehicles vary between the reviewed systems, but some are essential to navigation and localization and therefore found in almost all UAVs. Global Navigation Satellite System (GNSS) and Inertial Navigation System (INS) fall into this last category. Furthermore, almost all of the vehicles in the reviewed works have at least one kind of imagery sensor used for different purposes including fire perception. Temperature sensors are also present in some of the proposed fire assistance systems, but as shown in Section 3, they are less common.

Sensor measurements are the inputs of fire perception algorithms that process the data to detect the presence of the fire. The processing can be performed either onboard the UAV or by a computer located at a GCS. Fire perception can also, in some cases, be performed by a human operator inspecting the data from a GCS. It seems that a lot of efforts in research are devoted to the automation of fire perception and the optimization of the processing while at the same time preserving the accuracy of the overall system. Computer vision and machine learning techniques are commonly used for this purpose.

The last component fire assistance systems is the coordination strategy, it provides the framework for the deployment of the flight missions. Surveillance missions are usually planned beforehand and aim to search wide areas, prioritizing areas with higher fire risks. These missions can be accomplished by humans manually operating UAVs or autonomously. The coordination strategy in itself becomes more critical during the monitoring of a fire propagation as it is necessary to adapt the flight plan to the fire spread. This is even more relevant if there are multiple UAVs collaborating to the mission during a fire emergency. For this purpose, multiple coordination strategies were proposed in the literature.

For example, a UAV could hover near a fire spot and alert the rest of the fleet to proceed with fire confirmation [30]. More complex planning is also possible, by requiring a consensus on the task to be performed by each unit [31] or by flying in a specific formation around the fire perimeter [32]. In both cases, a concrete description of the task and the autonomous decision scheme must be defined for the system to be effective. Section 7 gives more details about the coordination strategies using a single or multiple UAVs.

Tables 1–3 present an overview of the reviewed fire assistance systems. Table 1 contains the year of publication and the validation process used by the authors. Table 2 presents the sensing modalities used to perform fire perception and the tasks performed. Note that some of the works do not specify sensing instruments and the authors assume that the necessary instruments are available onboard the UAV. Table 3 contains the level of autonomy, the organization of the system and the coordination strategy. Not that in some works the system is only theorized and many assumptions are made and some information might not be specified as it is not relevant to the central subject of the work. This is especially the case with works validated in simulations that do not always define a specific hardware platform.

Table 1. Reviewed works' characteristics.

Authors	Year	Validation
Casbeer et al. [32]	2006	Simulation
Martins et al. [33]	2007	Simulation
Merino et al. [30,34,35]	2007	Practical
Sujit et al. [36]	2007	Simulation
Alexis et al. [37]	2009	Simulation
Ambrosia et al. [17]	2011	Practical
Bradley and Taylor [38]	2011	Near practical
Hinkley and Zajkowski [18]	2011	Practical
Kumar et al. [39]	2011	Simulation
Martínez-de Dios et al. [40]	2011	Practical
Pastor et al. [41]	2011	None
Belbachir et al. [42]	2015	Simulation
Karma et al. [43]	2015	Practical
Merino et al. [44,45]	2015	Practical
Ghamry and Zhang [46,47]	2016	Simulation
Ghamry et al. [31]	2017	Simulation
Sun et al. [48]	2017	Near practical
Yuan et al. [49]	2017	Simulation
Yuan et al. [50–53]	2017	Near practical
Lin et al. [54]	2018	Simulation
Wardihani et al. [55]	2018	Practical
Zhao et al. [56]	2018	Simulation
Pham et al. [57,58]	2018	Simulation
Julian and Kochenderfer [59]	2019	Simulation
Aydin et al. [26]	2019	Near practical
Jiao et al. [60,61]	2020	Near practical
Seraj and Gombolay [62]	2020	Simulation

Table 2. Reviewed works' sensors and performed tasks.

Authors	Sensing Mode	Tasks
Casbeer et al. [32]	IR	Monitoring
Martins et al. [33]	NIR, Visual	Detection
Merino et al. [30,34,35]	IR, Visual	Detection, Monitoring
Sujit et al. [36]	Not specified	Monitoring
Alexis et al. [37]	Not specified	Monitoring
Ambrosia et al. [17]	Multispectral	Detection, Diagnosis
Bradley and Taylor [38]	IR	Detection
Hinkley and Zajkowski [18]	IR	Monitoring
Kumar et al. [39]	IR	Monitoring, Fighting
Martínez-de Dios et al. [40]	IR, Visual	Monitoring, Diagnosis
Pastor et al. [41]	IR, Visual	Detection, Monitoring
Belbachir et al. [42]	Temperature	Detection
Karma et al. [43]	Not specified	Monitoring
Merino et al. [44,45]	IR, Visual	Detection, Monitoring
Ghamry and Zhang [46,47]	Not specified	Detection, Monitoring
Ghamry et al. [31]	Not specified	Fighting
Sun et al. [48]	Visual	Detection, Monitoring
Yuan et al. [49]	IR	Detection

Table 2. *Cont.*

Authors	Sensing Mode	Tasks
Yuan et al. [50–53]	Visual	Detection
Lin et al. [54]	Temperature	Monitoring
Wardihani et al. [55]	Temperature	Detection
Zhao et al. [56]	Visual	Detection
Pham et al. [57,58]	IR, Visual	Monitoring
Julian and Kochenderfer [59]	Not specified	Monitoring
Aydin et al. [26]	IR, Visual	Fighting
Jiao et al. [60,61]	Visual	Detection
Seraj and Gombolay [62]	Visual	Monitoring

Table 3. Reviewed works' system architecture.

Authors	Autonomy	Organization	Coordination
Casbeer et al. [32]	Autonomous	Multiple UAV	Decentralized
Martins et al. [33]	Autonomous	Single UAV	None
Merino et al. [30,34,35]	Autonomous	Multiple UAV	Centralized
Sujit et al. [36]	Autonomous	Multiple UAV	Decentralized
Alexis et al. [37]	Autonomous	Multiple UAV	Decentralized
Ambrosia et al. [17]	Piloted	Single UAV	None
Bradley and Taylor [38]	Piloted	Single UAV	None
Hinkley and Zajkowski [18]	Piloted	Single UAV	None
Kumar et al. [39]	Autonomous	Multiple UAV	Decentralized
Martínez-de Dios et al. [40]	Piloted	Single UAV	None
Pastor et al. [41]	Piloted	Single UAV	None
Belbachir et al. [42]	Autonomous	Multiple UAV	Centralized
Karma et al. [43]	Piloted	Multiple UAV and UGV	Centralized
Merino et al. [44,45]	Autonomous	Multiple UAV	Centralized
Ghamry and Zhang [46,47]	Autonomous	Multiple UAV	Centralized
Ghamry et al. [31]	Autonomous	Multiple UAV	Decentralized
Sun et al. [48]	Piloted	Single UAV	None
Yuan et al. [49]	Not specified	Single UAV	None
Yuan et al. [50–53]	Not specified	Single UAV	None
Lin et al. [54,63]	Autonomous	Multiple UAV	Centralized
Wardihani et al. [55]	Near autonomous	Single UAV	None
Zhao et al. [56]	Piloted	Single UAV	None
Pham et al. [57,58]	Autonomous	Multiple UAV	Decentralized
Julian and Kochenderfer [59]	Autonomous	Multiple UAV	Decentralized
Aydin et al. [26]	Autonomous	Multiple UAV	Centralized
Jiao et al. [60,61]	Not specified	Single UAV	None
Seraj and Gombolay [62]	Autonomous	Multiple UAV	Decentralized

3. Sensing Instruments

Sensors provide the necessary data for navigation and for firefighting monitoring and assistance. In outdoor scenarios, GNSS and INS provide real-time UAV localization. They are also used to georeference the captured images thus allowing geographical mapping of fires. While these sensors are of interest to localize fires, the following section will instead focus on sensors that are able to detect fires. Fires have specific signatures that can be composed of different elements such as heat, flickering, motion, brightness, smoke and bio-product [64]. These elements can be measured using suitable sensing instruments. Cameras are the sensing instruments that offer the most versatility in their measurement. Visual and infrared (IR) sensors onboard UAVs can be used to capture a rich amount of information. In relation to cameras, Table 4 provides a list of the spectral bands used in the literature reviewed in this section. The table is provided in hopes that it will help researchers identify pertaining spectral bands for their application or identify areas of the spectrum that needs more attention for future works.

Table 4. Visual and IR electromagnetic spectrum.

Spectral Band	Wavelength (μm)
Visible	0.4–0.75
Near Infrared (NIR)	0.75–1.4
Short Wave IR (SWIR)	1.4–3
Mid Wave IR (MWIR)	3–8
Long Wave IR (LWIR)	8–15

3.1. Infrared Spectrum

At room temperature, the radiation peak of matter is located within the thermal infrared band which ranges from 0.7 μm to 1000 μm. Specialized sensors are available and can capture images in different sub-bands of the IR spectrum. Wildfire temperatures can be as high as 1000 °C (1800 °F), leading to a peak radiation in the mid-wave infrared (MWIR) sub-band [64,65]. Therefore, a sensor operating in the MWIR spectral band is best suited for fire perception. However, until recently, the form factor of MWIR sensors and their cost limited their use for low-cost small and medium UAVs [66]. To overcome these restrictions in smaller aerial vehicles, recent fire detection systems are still using NIR, SWIR or LWIR sensors. The use of these sub-bands is possible due to the fact that the higher temperature of fires also shifts the distribution of the object radiation in shorter wavelengths. Therefore, it is not necessary to use MWIR sensors directly as the effect of the peak can be observed in these other bands as well. However, a disadvantage of using NIR and SWIR is that objects under sunlight are often reflecting radiation in these sub-bands creating false positives. In such conditions, fire hot spots still remain detectable but their contrast is reduced during day time flights [64].

Characteristics put aside, IR sensors remain the most commonly used sensors in fire assistance systems due to their ability to detect heat. Bradley and Taylor [38], Casbeer et al. [32], Hinkley and Zajkowski [18], Kumar et al. [39] and Yuan et al. [49] are among the authors who have proposed methods based solely on the IR spectrum (see Table 2).

3.2. Visible Spectrum

Visible spectrum cameras are widely available and commonly used in various applications. They come in a wide variety of resolutions, form factors and cost. Their versatility offers a valuable alternative in wildland fire research from both technical and commercial perspectives. Moreover, the ever continuing reduction in visible cameras size and weight makes them perfect candidates for UAVs.

Data provided by these sensors are images in grayscale or RGB format. This allows the development of computer vision techniques using color, shape, temporal changes and motion in images or a sequence of images. Some of the vision-based techniques are presented in Section 4. Although, they are versatile and widely available, visible light sensors must be carefully selected for night-time operations as some sensors perform poorly in low light conditions. Despite some of their limitations, they equip almost all UAVs and make them good candidates for wildland fires study.

Yuan et al. [50–53], Sun et al. [48] and Zhao et al. [56] are among the authors that propose systems that rely only on the use of visible spectrum cameras (see Table 2).

3.3. Multispectral Cameras

Using each spectral band alone comes with its limitations. To tackle these limitations some authors propose the use of multiple cameras and combine multiple spectra. This allows the use of data fusion techniques to increase the accuracy of fire detection in complex situations and under different lighting conditions. Esposito et al. [67] developed a multispectral camera operating in the LWIR, NIR and visible spectrum mounted on a UAV. In a NASA Dryden's project, Ikhana UAS [17,68], a Predator B unmanned aircraft system adapted for civilian missions, was built to carry a multispectral sensor that operates in

16 different bands from visible to LWIR spectrum. Despite their interesting characteristics, in both cases, the weight of these combined sensors limited their implementation to large airborne platforms only. To address this problem, other alternatives combine smaller sensors such as visible spectrum sensors and IR sensors. Martínez-de Dios et al. [30] used this approach to capture and project the IR data onto visible images. This generated a superposition of the data leading to pixels being represented with four intensity values red, green, blue and IR. The authors report improvements in fire detection with mixed segmentation techniques that make use of the four-channel values.

3.4. Other Sensors

Various sensors other than cameras have also been proposed to detect and confirm the presence of fires. Some authors proposed the use of chemical sensors which can detect concentrations of hazardous compounds [43]. Spectrometry measures is another approach that can be used to detect the characteristics of burned vegetation and confirm a fire [64]. Again, in both cases, the size of the sensors seems to limit their use.

Temperature sensors have also been used by Belbachir et al. [42,55] to generate heat maps and detect/locate fires. Lin et al. [54,63] also theorized the use of temperature sensors to estimate a fire contour and rate of spread in the context of fire modeling. Most of the authors are using temperature sensors in the context of a simulation and therefore assume their availability without referring to real hardware. However, Wardihani et al. [55] performed a real-world validation of their proposed solution and successfully demonstrated the use of a 2×2 pixel resolution non-contact infrared sensor with a field of view of five degrees to measure temperatures. While interesting, these sensors are limited in comparison to IR cameras that can provide richer data. This reflects on the reviewed works and the reported results are more limited than with IR cameras.

4. Fire Detection and Segmentation

Research has shown the effectiveness of UAVs as a remote sensing tool in firefighting scenarios [17,18,43]. They are very useful even in simple tasks such as observing the fire from a static position and streaming the video sequence to human operators. This simple use case already allows firefighters to have an aerial view of the spreading fire and plan containment measures. However, single man-controlled UAVs, even if they are useful for small emergencies, do not scale up in large scenarios. Therefore, the automation of the detection and the monitoring of fires can help deliver an optimal coverage of the fire area with the help of multiple UAVs and with less human intervention. Furthermore, the gathered data can later be processed to analyze the fire, estimate its Rate of Spread (ROS) [69], volume [40] or perform post fire damage evaluation [17].

To perform fire-related tasks autonomously, systems must address different subtasks such as fire geolocation, fire modeling and even path planning and coordination between UAVs. For that purpose, sensor data are often initially processed to detect fire and extract fire-related measures. The derived information is then passed on to the different subsystems. For fire detection, authors are usually able to directly extract fire-like pixels based on color cues or IR intensities and do not require further analysis. However, monitoring tasks usually require further analysis to estimate the fire perimeter or burned areas. In that context, computed measures (e.g., segmentation) are provided as input to fire models to estimate the fire propagation over time.

This section reviews some fire detection and segmentation techniques found in the literature.

4.1. Fire Segmentation

Fire segmentation is the process of extracting pixels corresponding to fire in an image. The criteria by which a pixel is selected vary from one method to another. The selection criteria are also the main factor affecting the accuracy of the detection. In general, fire segmentation uses the pixel values of a visual spectrum image (e.g., color space segmentation)

or the intensities of an IR image. Motion segmentation can also be used to extract the fire using its movement over a sequence of images.

4.1.1. Color Segmentation

Images are built of pixel units that can have different encoding (e.g., grayscale, color). In color images, pixels are composed of three values in the red, green and blue channels (RGB). Other color spaces are also possible such as YCbCr, HSI, CIELAB, YUV, etc. [70]. In IR images the pixels have one channel value representing temperature (MWIR and LWIR) or reflectance (NIR, SWIR).

In the COMETS project [30,34,35], the authors employed a lookup table with fire-like colors (RGB values) that were extracted from a learned fire color histogram. The image pixels were compared to the table and the values that were not found were considered as non-fire. A non-calibrated LWIR camera is used to capture qualitative images with radiation values relative to the overall temperature of the objects in the scene. The heat peak observed in the resulting image depends on the current scenario. A training process was carried out to learn the thresholds to be applied to the IR images for binarization. Images with and without fires were considered as well as different lighting conditions and backgrounds. This permitted the selection of the appropriate threshold to apply during deployment in known conditions. Ambrosia et al. [17] selected fixed thresholds for each IR spectral band. They also varied the bands used for day-and-night missions. During night-time, the MWIR and LWIR bands were used and during the day, the NIR band was added. The results show that fixed threshold adapts poorly to unexpected conditions but can be tuned to perform better in known environments.

Yuan et al. [49–53] used color space segmentation. The images are converted from RGB to the CIELAB color space before further processing. Sun et al. [48] proposed the use of YCbCr color space. In both cases, a set of rules were developed based on empirical calculations performed on captured fire images. For example, Sun et al. [48] considered pixels as fires if their values followed the following rules: $Y > Cb$, $Cr > Cb$, $Y > Y_{mean}$, $Cb < Cb_{mean}$ and $Cr > Cr_{mean}$. The mean sub-index indicates the channel mean value of the corresponding image. Otsu thresholding technique [71] was used in [49] to segment IR images.

Color value rule-based segmentation approaches are computationally efficient, but lack robustness during detection. Results show that objects with a color similar to fire are often mislabeled as fire and trigger false alarms. A combination of rules in different color spaces and the addition of IR can increase the detection accuracy. More complex algorithms that are time and space aware have also been shown to increase the accuracy of the fire detection [72–82]. The majority of them have not been integrated with UAVs.

In recent years, deep learning algorithms have shown impressive results in different areas. Relating to UAVs, past work using deep convolutional neural networks (CNN) dealt mainly with fire detection [56,83,84]. Deep fire segmentation techniques proposed recently have shown the potential of developing an efficient wildland fire segmentation system [85]. The used dataset in this last work included some aerial wildland fire images [86]. Deep segmentation of wildland fires is still lacking in UAV applications.

4.1.2. Motion Segmentation

Fire segmentation using static images help reduce the search space, but often objects with a similar color to fire can be detected and lead to false positives. Yuan et al. [49–53] and Sun et al. [48] proposed the use of Lukas-Kanade optical flow algorithm [87] to consider fire movements. With the detection of corresponding feature points in consecutive image frames, a relative motion vector can be computed. The mean motion vector matches the UAV's motion except for moving objects in the ground. Fire flames are among those objects because of their random motion. By detecting feature points within regions with both random movements and fire-like colors, the fire can be confirmed and the false alarm rate reduced.

4.2. Fire Detection and Features Extraction

The data fed to a detection system are analyzed in order to find patterns that confirm the occurrence of an event. Patterns are recognized by computing different features which can be strong or weak signatures for a specific application. In the case of fire detection with UAVs, the most popular features are color, brightness and motion. Research focusing on fire detection considers the fusion of more features to obtain better results in the classification stage. These features can be categorized by the level of abstraction at which they are extracted: pixel, spatial and temporal.

Color cues are widely used in the first step to extract fire-like pixels. This reduces the search space for further processing with more computationally expensive detection algorithms. For example, the RGB mean values of a Region of Interest (RoI) and the absolute color differences ($|R - B|$, $|R - G|$, $|B - G|$) can be thresholded [88] or used to train a classification algorithm [89]. In the work of Duong and Tinh [90], the authors further added the intensity mean, the variance and the entropy values of the ROI to the feature vector. Other features used in the literature include color histograms of ROI [75] and color spatial dispersion measures [73].

After the detection of the ROI, other features can be extracted. Some authors consider spatial characteristics to determine the fire perimeter complexity by relating the convex hull to the perimeter ratio and the bounding rectangle to perimeter ratio [91]. The distance between the blob centroid position within the bounding box has also been considered in this work.

Texture is another spatial characteristic often used for fire detection. The main texture descriptors proposed for this task are Local Binary Patterns (LBP) [92–95] and Speeded Up Robust Features (SURF) [75,78]. These operators characterize local spatial changes in intensity or color in an image and return a feature vector that can be used as input for classification. SURF [96] is computationally expensive but allows for scale and rotation invariant matching. LBP [97] needs less processing power and extracts the mean relation between pixels in a small area using the 8 neighbors of a pixel. Some authors [98,99] also used the Harris corner detector [100], which is a computationally efficient feature point extractor.

Deep learning is another approach that has been used for fire detecting. It allows the automatic learning of low- and high-level features instead of hand crafting them as it was the case with the previous approaches described. Zhao et al. [56] developed such an approach in the form of a 15-layer CNN called Fire_Net. The proposed architecture is inspired by AlexNet [101] and is made of a succession of convolutions, ReLUs and max poolings that end with a fully connected layer followed by a softmax layer. The approach is able to classify image patches as fire or not fire with a 98% accuracy outperforming many other similar deep learning or learning-based approaches tested by the authors on the same data. Jiao et al. [60,61] also proposed a deep learning approach but based on the YOLOv3 architecture [102]. The solution is an object detection approach able to provide bounding boxes around objects of interest. In this case, the network is trained on 3 classes: smoke, fire and combination of smoke and fire. Initially, the authors used a YOLOv3-tiny architecture and on-board computations. The system was able to reach a precision of 83% and a frame rate of 3 to 6 fps [60]. In a more recent contribution [61], the same authors were able to reach a detection precision of 91% and a frame rate of over 80 fps by performing the computation on a GPU located in the GSC instead.

The features reviewed above are extracted from single images. When a video sequence is available, the temporal variation in color, shape and position of some blobs can be extracted. In the work of Ko et al. [103], the fire blob shape variation is computed by a skewness measure of the distance from the perimeter points to the blob's centroid. Foggia et al. [104] measured shape changes by computing the perimeter to area ratio variation over multiple frames. The authors also detected the blob movements by matching them in contiguous frames and to compute the centroid displacement. Fire tends to move slowly upwards, thus blobs that do not comply with this rule can be discarded [72,103,105].

The centroid displacement can also be an input for further classification [72,91,106]. A similarity evaluation is employed by Zhou et al. [91]. They measure the rate of change of overlapping areas of blobs in contiguous frames. This gives a practical representation of the speed at which the region of interest is moving and if it is growing or decreasing in size. Fire flickering can also be identified by considering specific measures such as intensity variation [107], the number of high-pass zero crossing in the wavelet transform [108] or the number of changes from fire to non-fire pixels inside a region [109]. Wang et al. [110] implemented a long-term movement gradient histogram, which accumulates the motion changes. The histogram is fitted to a curve which is used to evaluate if the area corresponds to a fire or not. Kim and Kim [111] proposed a Brownian motion estimator that measures the correlation of two random vectors [112]. The vectors are composed of channel values, the first intensity derivative and the second intensity derivative. Therefore, the Brownian motion estimator describes the dynamic dependence between a series of regions across multiple frames. Temporal features consider a time window for the fire evaluation. Then, some empirical criteria are established to determine the optimal thresholds and duration of the events in order to trigger a fire alarm.

Among the features described so far, there are some features that are more oriented towards fire detection. Features such as color, blob centroid displacement and flickering are some of the most popular. Some novel approaches such as the Brownian correlation or the histogram of gradients have been less explored but are nevertheless interesting. A comparison of these different features and an evaluation of which one has a greater impact on the fire detection accuracy and false positive rate would be very useful. Unfortunately, such a comprehensive comparison does not seem to have been published yet. However, as most of these features are not computationally expensive, ensembling the features can improve the performance and reduce the false detection rate. Table 5 gives an overview of the features used depending on the input.

Table 5. Image input and extracted features.

Input	Statistical Measures	Spatial Features	Temporal Features
Color, IR and radiance images	Mean value, mean difference, color histogram, variance and entropy.	LBP, SURF, shape, convex hull to the perimeter rate, bounding box to the perimeter rate.	Shape and intensity variations, centroid displacement, ROI overlapping, fire to non-fire transitions, movement gradient histograms and Brownian correlation.
Wavelet transform	Mean energy content.	Mean blob energy content.	Diagonal filter difference. High-pass filter zero crossing of wavelet transform on area variation.

4.3. Considerations in UAV Applications

Additional features can improve the fire detection. Features that are obtained by temporal analysis evaluate the difference between contiguous frames. In simple scenarios, where the camera is static and the background is not complex, frame subtractions can help detect moving pixels. In the presence of complex and dynamic backgrounds, Gaussian mixture models and other sophisticated background modeling techniques can be considered.

However, the video streams from UAVs have fast motions and no classical background subtraction method would give satisfying results because of the assumption of a static camera. Even in a situation where the UAV is hovering over a fixed position, the images are still affected by wind turbulence and vibrations. Therefore, in order to be able to apply these motion analysis techniques, it is necessary to consider image alignment and video stabilization. The usual approach is to find strong feature points that can be tracked over a sequence of frames. Merino et al. [44], in their fire assistance system, used a motion

estimation approach based on feature points matching known as sparse motion field. From the matched points, they estimate a homography matrix that maps the pixels in an image with the pixels in the previous frame. This allows mapping every image to a common coordinated frame for alignment. SURF [96] and ORB [113] are two feature point methods that were used for extracting salient features prior to the image alignment. It seems that the impacts and the benefits of the image alignment have not yet been addressed in the literature relating to fire and smoke detection but some researchers such as [44] consider it important for their fire assistance system to work properly.

5. Wildland Fire Datasets

A large number of fire detection approaches use a classification method that relies on learning algorithms. The main challenges of machine learning is to build or to find a large enough dataset with low bias. Such a dataset should contain positive examples with high feature variance and negative examples consisting of standard and challenging samples.

Deep learning techniques need even larger datasets for training. Data augmentation techniques can help in this regard but it requires a sufficiently large dataset to start. Well-developed research fields such as face or object recognition have already large datasets that have been built and vetted by the community. These datasets are considered suitable for the development and benchmarking of the new algorithms in their respective fields. In the case of fire detection, no such widely employed dataset is available yet. Some effort has been made toward this direction. Steffens et al. [114] captured a set of 24 videos from hand-held cameras and robot mounted cameras. The ground-truth was defined by bounding boxes around the fire. Foggia et al. [104] compiled a collection of 29 videos of fire and smoke but did not provide ground-truth data. Chino et al. [93] gathered around 180 fire images to test their BowFire algorithm and made the dataset available with manually segmented binary images representing the ground-truth for the fire area. However, the main problem with these datasets is the lack of wildland fire samples. This could be problematic for the development of a fire detection module for wildland fire assistance systems. Aerial fire samples in the form of videos are also necessary for the development of UA-based systems.

In [86], the authors collected images and videos to build the Corsican fire database. This dataset is specifically built for wildland fires. It also contains multimodal images (visual and NIR images) of fires. The images have their corresponding binary masks representing the ground-truth (segmented fire area). Other information is also available such as smoke presence, location of capture, type of vegetation, dominant color, fire texture level, etc. The dataset contains some aerial wildland fire views, but their number is limited.

The wildland fire UAV research is still lacking a dataset that can help improve the development of the algorithms needed in a wildland fire assistance system. Table 6 contains a brief description of the main fire research datasets.

Table 6. Fire datasets.

Dataset	Description	Wildland Fires	Aerial Footage	Annotations
FURG [114]	14,397 fire frames in 24 videos from static and moving cameras.	No	No	Fire bounding boxes
BowFire [93]	186 fire and non-fire images.	No	No	Fire masks
Corsican Fire DB [86]	500 RGB and 100 multimodal images.	All	Few	Fire masks
VisiFire [104]	14 fire videos, 15 smoke videos, 2 videos containing fire-like objects.	17 videos	7 videos	No

6. Fire Geolocation and Fire Modeling

In a wildland fire scenario, when a fire is detected, the vehicle must alert the GCS and send the fire's geolocation to deploy the firefighting resources. In the reviewed literature, two different levels of approach are studied for detection alert. Some authors are using a local approach where the position of the fire is reported at first contact. Other authors go

further by taking a global approach to the problem by identifying and locating the entire perimeter of the fire.

The simplest alerting approach is to directly provide the geographical coordinates of the UAV using the onboard GPS when a fire is first detected. This can be performed with good accuracy when the UAV is flying at low altitudes and has its data acquisition sensor pointing to the ground with a 90-degree angle. This approach is employed by Wardihani et al. [55] using a downward pointing temperature sensor to locate fire hotspots. A similar approach is possible with a camera located on the bottom of a UAV and oriented downward. However, for a camera located on the front side of the UAV, it is required to compute a projection of the camera plane onto a global coordinate system using an homography. This transformation allows mapping pixel coordinates to the ground plane. This approach performs well when the UAV pose estimation is reliable and when the ground is mostly planar. Some difficulties arise in the presence of uneven surfaces. Some authors [17,30,41,44,45] have circumvented this limitation by exploiting a previously known Digital Elevation Map (DEM) of the surveyed area. DEM allows for the estimation of the location from where a ray corresponding to a fire pixel originated and thus improves the fire location estimation. DEMs can induce some errors. To reduce these errors, a UAV fleet looking at the same hotspot can first detect the fire and then use different views of the UAV to refine the estimations [30].

In order to better characterize ongoing wildfires, some authors have studied fire modeling in order to provide global information such as the fire boundaries and its behavior. The simplest models are using an elliptic shape which is fitted to the fire and where each ellipse axis increases at some given rate. For example, Ghamry and Zhang [46,47], Ghamry et al. [69] applied an elliptical model to estimate the fire perimeter. Here, the rate at which the ellipse axis grows depends on the direction towards which the wind blows and its speed. This allowed the authors to estimate the perimeter of the fire and then define a UAV team formation for further monitoring.

More complex fire models with more variables and data inputs have also been studied. These more advanced models often try to estimate the rate of spread (ROS) of the fire based on wind speed and direction, terrain slopes, vegetation density, weather and other variables. These models are often tested in a simulation. For example, Kumar et al. [39], Pham et al. [57,58], Lin et al. [54,63] and Seraj and Gombolay [62] used the FARSITE model to test their coordination strategies under various scenarios. Some of these models were not suitable for real-time fire estimation because their complexity significantly increased the computation time. However, Lin et al. [54,63] proposed a convergent Kalman filter-based methodology to provide data to a scalar field wildfire model that is executable on-board a UAV and requires low computation resources. The proposed approach was able to provide estimations of the wildfire ROS and the fire front contour.

Some authors used a different approach to model and characterize the fire. For example, Martínez-de Dios et al. [40] used multiple images to extract geometric features from the fire such as the base perimeter, the height and the inclination. The extraction is performed using computer vision techniques (e.g., image segmentation). The authors propose the use of multiple visible-NIR multimodal stereo vision systems to extract the fire area. Each stereo system provides an approximate 3D model of the fire. The models captured using multiple views are registered to get the fire 3D model. This 3D model is tracked over time to compute different fire characteristics such as height, width, inclination, perimeter, area, volume, ROS and their evolution over time.

Bradley and Taylor [38] divided the environment into cells and assigned a fire probability to each cell using IR images. This method takes into account the uncertainty in the position of the UAV and therefore applies a Gaussian weighting scheme to the probabilities. The authors then apply a Sequential Monte Carlo (SMC) method to compose a Georeferenced Uncertainty Mosaic (GUM) which is then used to locate the fire. Belbachir et al. [42] model the fire as a static cone of heat sourcing from the fire center and dissipating with an altitude and a horizontal distance. Based on this assumption, they

construct a grid of fire probabilities with the temperature measures. The fire is detected when the probabilities are above a defined threshold. Lin and Liu [63] also generate an occupancy grid by using temperature sensors and by associating temperatures to cells. They also compute the gradient of the grid and estimate the fire center, ROS and perimeter.

7. Coordination Strategy

Coordination strategy is an important component when deploying autonomous UAVs. The coordination strategy establishes the procedure for communication, task allocation and planning procedures. Based on the communication links established during the mission, three main schemes can be distinguished. First, for a single vehicle, there is no coordination strategy as the UAV does not need to communicate with other UAVs. For multiple UAVs, the path planning and task allocation are often resolved by an optimization process or assumed to be so. One approach is to centralize the path planning and decision process in the GCS and only allows the UAV to communicate with it but not between each other. Another approach is to tackle the problem of coordinating multiple entities in a distributed and decentralized manner. Each vehicle can connect to other UAVs, allowing for distributed decision-making and communication with the GCS is only for reporting observations but not for planning.

7.1. Single UAV

The viability of single UAVs, either large airships or small aerial systems, has been evaluated for wildland fire surveillance and monitoring. The Ikhana UAS [17] was deployed in western US between 2006 and 2010. It was a single large and high endurance vehicle with powerful sensory systems for autonomous fire detection. The decision strategy and the path planning were performed by human operators. Similarly, Wardihani et al. [55] used small quadcopter UAV and manually defined flight paths using a mission planner software in order to survey a region and detect hotspots. Pastor et al. [41] proposed a semi-autonomous system in which a single UAV would sweep a rectangular area, locate hotspots and then return to a nearby ground station. A human could control the UAV and order it to stay over the hotspot location to confirm visually if it corresponds to a real fire or not. Martins et al. [33] used an entirely autonomous navigation system where the UAV only received waypoints from where to start surveillance. When a hotspot is detected, the UAV approaches the source, hovers over the target and confirms the fire. The experimental tests showed very interesting results for fire detection and monitoring tasks.

While single UAV strategies are interesting for their simplicity, they remain very limited in relation to large-scale wildland fires. For this reason, the more advanced and mature solutions use team-based systems that help increase the coverage area.

7.2. Centralized

The addition of more UAVs to the mission increases the area covered by the systems. In a centralized team strategy, all UAVs are coordinated by a single GCS. This scheme can lead to a more accurate fire georeferencing and less false alarms by allowing for a global situation awareness at all times. Another advantage of centralized communications is that it makes centralized processing easy and therefore makes it possible to use smaller and more affordable UAVs as they do not require high-processing power. The main drawback of this approach is the need for a functional communication network that can connect to all UAVs at all times which is not always possible when the fire areas are remote.

Martínez-de Dios et al. [30] proposed a simple centralized approach where data from multiple UAVs is combined to correct and reduce the uncertainty of fire georeferencing. After a fire is detected by a unit, nearby vehicles are sent to the same region to perform a fire confirmation.

Belbachir et al. [42] proposed a greedy algorithm for fire detection using a probability grid. For this purpose, each UAV selects, in a greedy way, the path that provides more

information. The UAVs visit cells that have not yet been visited and which are within the direction where the temperature increases.

Ghamry and Zhang [46] distributed the UAVs uniformly around the fire perimeter using an elliptical formation. This allows the UAVs to keep their paths at even angles around the estimated fire center. Ghamry and Zhang [47] added the ability to restructure the formation if a UAV is damaged or has to leave for refueling. To achieve this fault-tolerant behavior, when a UAV needs to leave the formation, all communications with it are stopped. Other vehicles automatically notice the missing UAV and start performing a reformation process. In this system, prior to the monitoring task, the fleet flies in a leader–follower formation where the leader gets a predetermined flight path and the rest follow it at specific distances and angles. In the work of Lin et al. [54], Lin and Liu [63], UAVs are directed to fly uniformly in formation around an estimated fire center. In this approach, a Kalman filter is used to estimate the fire contour and the fire center movements, allowing the UAVs to fly and adapt their formation accordingly.

While incomplete, initial results by Aydin et al. [26] are worthy of mention as it is one of the only works to tackle fire fighting directly. The authors theorized a collaboration model where scout UAVs would spot wildfires and monitor the risk of spread to structures. Relay UAVs would then be used to extend the communication range and allow the scouts to contact firefighting UAVs carrying fire-extinguishing balls. It is believed that 10 UAVs each carrying 10 1.3 kg fire-extinguishing balls would be able to extinguish an area of approximately 676 m^2 per sortie. While the extinguishing capacity of the fire-extinguishing balls was validated, the UAV coordination strategy has not been tested yet. However, this approach remains promising for wildfire fighting.

7.3. Decentralized

In a decentralized communication scheme, the UAVs are communicating between each other in order to collaborate for path planning and optimal area coverage. The interaction with the GCS is reduced to a minimum and usually only happens at the beginning of a flight to receive initial flight coordinates or at the end of a flight for observation reporting and data transfers. The system is able to perform more tasks in an autonomous manner and even to cover larger areas by using some UAVs as communication relays. The main advantages of such an approach are reliability as a link with the GCS is not required to be active at all times and the possibility for operations in remote areas where global communication links are impractical. However, the added complexity imposes new challenges as distributed coordination algorithms need to be developed and implemented. In the literature, these systems were mainly used for optimal fire perimeter surveillance and task allocation.

Alexis et al. [37] describe a UAV rendezvous-based consensus algorithm which aims to equally distribute the path length of the UAV around the fire perimeter. UAVs depart in pairs and in opposite directions around the fire perimeter. They set rendezvous locations where they share knowledge about the traveled paths, the current state of the fire perimeter and other units encountered. If the update shows that the fire perimeter has evolved, then each UAV will select new rendezvous locations in such a way that the distance traveled by each of the UAVs is almost the same. The authors have shown through simulations that the algorithm converges and the recomputing of rendezvous points allows efficient adaptation of the UAV formation to an evolving fire perimeter. The optimal distribution of UAVs around a fire perimeter has also been studied by Casbeer et al. [32]. They demonstrated that in order to reduce the length of time between data uploads to the GCS, the UAVs must depart in pairs, travel in opposite directions and be evenly spaced around the perimeter. To achieve optimal perimeter tracking, they designed a control loop to keep half of the bottom-facing IR camera over hotspot pixels and the other half over non-fire area.

For monitoring, Pham et al. [57,58] proposes a collaborative system in which UAVs are sent to monitor a fire and optimally cover the fire area. This formation is achieved by detecting neighboring UAVs and reducing camera view overlaps while considering the location of the fire front. The UAVs are also allowed to increase or decrease their altitude in

order to control the resolution of the captured imagery to provide optimal observational capabilities. This behavior is accomplished with the application of a force field-based algorithm that simulates the attraction of a UAV by the fire front and its repeal from the other UAVs. The attraction and repulsion forces are adapted by considering the fire front confidence and the estimated field of view of each UAV. One problem with this approach is that the visibility reduction induced by smoke is not taken into account which can put the vehicle in a dangerous situation.

Another coordination strategy was proposed to perform optimal task allocation within a team of UAVs. The tasks can be surveillance, monitoring or firefighting. Ghamry et al. [31] proposed an auction-based firefighting coordination algorithm. In this algorithm, a fire is first detected and then the UAV must coordinate themselves to act upon each known fire spot. To achieve this task, each vehicle generates a bid valued by a cost function of its distance from the fire spot. In this manner, the UAV with the best offer for the task will be assigned to it. Sujit et al. [36] also proposed a similar auction-based collaboration algorithm but with the ability to consider a minimal number of UAVs to watch each hotspot. Both contributions distributed the UAVs equally around the fire perimeter.

Decentralized approaches have also been used for direct fire fighting using fire suppressants. Kumar et al. [39] proposed such a coordination protocol where the planned path of each UAV is optimized to minimize the distance to a detected fire perimeter. As a second phase, the path of UAVs carrying fire suppressants is optimized by minimizing the distance to the fire center. This allows the solution to monitor a fire situation and provide optimal fire suppressant delivery.

Recently, new control approaches based on deep reinforcement learning (DRL) started to appear in the literature. One of the very first with such an approach for wildfire monitoring has been proposed by Julian and Kochenderfer [59]. The authors first formulated the problem as a partially observable Markov decision process (POMDP) solvable with DRL. A simulation environment being required for DRL, they also defined a simplified stochastic wildfire model using a 100×100 fire presence grid. This environment was used to train a simulated fixed-wing agent with a decision process based on a CNN. Multiple agent using the same CNN can be spawned in the same environment to simulate a multi-UAV system. While the authors defined different DRL approaches, the best performing approach used a collaborative belief map shared and updated by all agents indicating the state of the wildfire. A reward function rewarding newly discovered burning cells by any aircraft is used to encourage good fire monitoring and collaboration between agents. An aircraft proximity penalty is also added to encourage aircraft separation. Simulation results show that the approach is able to outperform a baseline receding-horizon controller, scale with different numbers of aircraft and adapt to different fire area shapes. However, the approach remains limited as the environment modeling is oversimplified, the UAVs are assumed to maintain a steady altitude, a constant speed and fly at different altitudes as collision avoidance is not implemented.

While new approaches are interesting, research on objective function optimization-based distributed control frameworks is still very active and continues to generate state-of-the-art results. This is the case with the approach proposed by Seraj and Gombolay [62]. The authors used a dual-criterion objective function based on a Kalman uncertainty residual propagation and a weighted multi-agent consensus protocol. An adaptive extended Kalman filter (AEKF) is used to leverage the fire propagation model (FARSITE) and the observation model. The approach includes an uncertainty-based controller built through the combination of a fire front location uncertainty map and a human uncertainty map. This allows the system to take into account GPS-equipped human firefighters on the ground in order to ensure their safety while considering the fire front location like other similar methods. A second controller (formation controller) is encouraging the UAV team to maintain a formation consensus for maximizing the coverage. The approach is using the theory of artificial potential field to generate artificial forces to pull or push on the UAV in order to attain an optimal state. Following a simulation,

the solution was able to outperform both a state-of-the-art model-based distributed control algorithm and a DRL baseline strongly confirming the relevance of the approach.

This paper only reviews decentralized communication frameworks used in wildland fire contexts. However, many solutions in the literature are presented as general communication solutions without corresponding applications. This is the case with the work of Pignaton de Freitas et al. [115] that proposed a multipurpose localization service to inform all UAVs in the formation of the other UAVs position. One interesting and rarely seen feature of the system is its ability to estimate the position of UAVs that are not received due to communication errors. This illustrates that researchers in the field should not only refer to wildfire-related works when the time comes to design new systems and that some works outside of the field may be important to consider.

8. Cooperative Autonomous Systems for Wildland Fires

UAVs can play an important role in the detection and monitoring of large wildland fires. Multiple UAVs can collaborate in the extraction of important data and improve firefighting strategies. Moreover, aerial vehicles can cooperate with unmanned ground vehicles (UGV) in operational firefighting scenarios.

One type of cooperation can consist of the use of UGV to carry small short endurance UAVs to detected fire areas and be used as refueling stations. Ghamry et al. [69] proposed such a system, where a coordinated leader–follower strategy is used. UAVs are carried by UGV to a desired location and deployed to explore preassigned areas. If a UAV detects a fire, an alert is sent to the leading UGV and to the rest of the fleet. The leader computes new optimal trajectories for the UAVs in order to monitor the fire perimeter. Phan and Liu [116] present another firefighting collaborative UAV-UGV strategy. A hierarchical UAV-UGV system composed of a large leading airship and cooperative UAV and UGV is proposed. When a fire is detected, the vehicles are deployed for fire monitoring. In this scenario, UAVs and UGVs are supposed to have the capacity to carry water and combat fire. The UAVs are deployed in an optimal flying formation over the fire front area. UGV are sent to prevent the fire propagation and limit its spread using water and fire retardants. Auction-based algorithms are implemented to allocate the tasks to each vehicle. Viguria et al. [117] also proposed the use of task allocation by an auction-based algorithm. In their framework, the vehicles can perform various tasks such as surveillance, monitoring, fire extinguishing, transportation and acts as a communication relay. A human or the GCS can generate a list of tasks that need to be fulfilled. Each robot sends a bid for each task and the one with the best offer wins and can proceed to execute the task. The offers are based on specific cost functions for each task that consider the vehicle distance, fuel level and capabilities.

Akhloufi et al. [118] proposed a multimodal UAV-UGV cooperative framework for large-scale wildland fire detection and segmentation, 3D modeling and strategical firefighting. The framework is composed of multiple UAVs and UGVs operating in a team-based cooperative mode. Figure 2 illustrates the proposed framework [118]. The vehicles are equipped with a multimodal stereo-vision system such as the ones developed for ground-based fire detection and 3D modeling [119–122]. The stereo system includes multispectral cameras operating in the visible and NIR spectrum for efficient fire detection and segmentation. Each stereo system provides an approximate 3D model of the fire. The models captured using multiple views are registered using inertial measurements, geospatial data and the extracted features using computer vision to build the propagating fire front 3D model [119–121]. Based on the 3D model of the fire, the UAVs and UGVs can be positioned strategically to capture complementary views of the fire front. This 3D model is tracked over time to compute different three-dimensional fire characteristics such as height, width, inclination, perimeter, area, volume, ROS and their evolution over time. The extracted three-dimensional fire characteristics can be fed to a mathematical fire propagation model to predict the fire behavior and spread over time. The obtained data make it possible to alert and inform about the risk levels in the surrounding areas. The predicted fire propagation can be mapped and used in an operational firefighting strategy. Furthermore, this information can be used for the

optimal deployment of UAVs and UGVs in the field. This type of framework can be combined with other firefighting resources such as firefighters, aerial firefighting aircraft and future fire extinguisher drones.

(**a**) The acquisition of 3D fire front data. UAVs and UGVs equipped with multimodal stereo cameras, IMU and GPS.
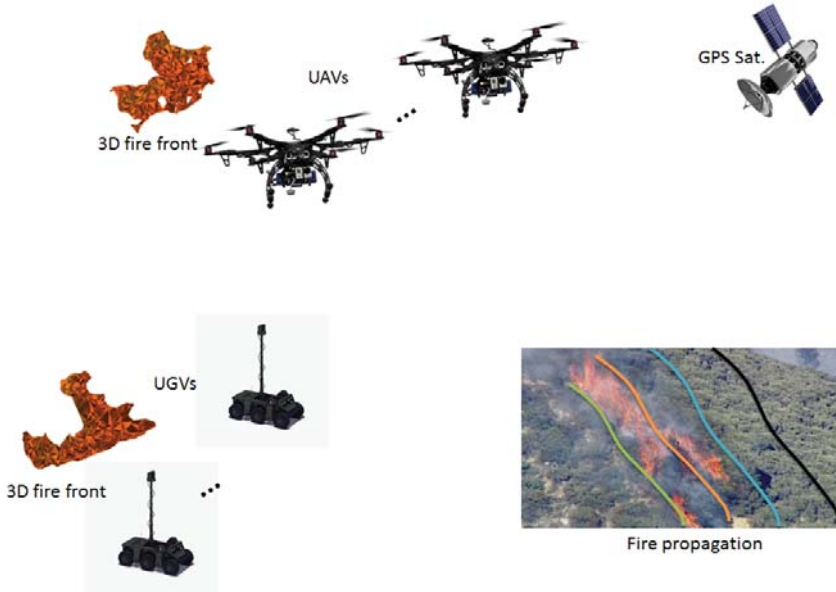
(**b**) The modeling and prediction. Registered 3D fire front, weather, topographic and vegetation data are used to predict the fire propagation and map it.
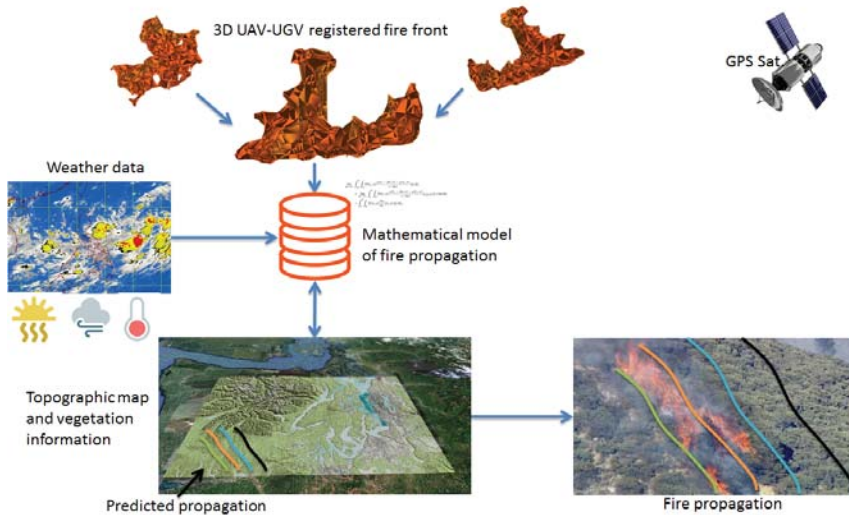
Figure 2. Unmanned aerial vehicle-unmanned ground vehicle (UAV-UGV) multimodal framework for wildland fires assistance.

9. Conclusions

This paper presents a survey of different approaches for the development of UAV fire assistance systems. Sensing instruments, fire perception algorithms and different coordination strategies have been described. UAVs can play an important role in the fight against wildland fires in large areas. With the decrease in their prices and their wider commercial availability, new applications in this field will emerge. However, some limitations remain such as autonomy, reliability and fault tolerance. Further research is needed to overcome these limitations. Security is also a concern, as there are risks associated with having UAVs flying over firefighters or close to aircraft carrying water and fire retardants. Nevertheless, the benefits of using UAVs are significant and this could lead to innovations aiming to solve these problems.

On the perception side, most of the developed techniques rely on classical computer vision algorithms. However, the emergence of some work in the field of deep learning has been witnessed in recent years, especially for fire detection, but it remains in the early stages of development. Furthermore, some datasets containing wildland fire images that can be used for the development of computer vision algorithms were presented. Unfortunately, only a small number of them contains aerial views of wildland fires. In addition, the lack of a large dataset limits the development of advanced deep learning algorithms. Such datasets would be important for the future of the field as they can serve to benchmark approaches and compare them quantitatively. Therefore, deep learning and the construction of new large-scale aerial wildfire datasets represents interesting research opportunities for future contributions by researchers in the field.

In this work, frameworks proposing cooperative autonomous systems where both aerial and ground vehicles contribute to wildland firefighting were also discussed. While these frameworks are mostly theoretical and limited to simulations, they provide interesting ideas about a more complete wildland firefighting system. Future research in these areas can provide new approaches for the further development of autonomous operational systems without or with little human intervention.

References

1. Jolly, W.; Cochrane, M.; Freeborn, P.; Holden, Z.; Brown, T.; Williamson, G.; Bowman, D. Climate-induced variations in global wildfire danger from 1979 to 2013. *Nat. Commun.* **2015**, *6*, 7537. [CrossRef]
2. Kelly, R.; Chipman, M.; Higuera, P.; Stefanova, I.; Brubaker, L.; Hu, F. Recent burning of boreal forests exceeds fire regime limits of the past 10,000 years. *Proc. Natl. Acad. Sci. USA* **2013**, *110*. [CrossRef] [PubMed]
3. Amadeo, K. Wildfire Facts, Their Damage, and Effect on the Economy. 2019. Available online: https://www.thebalance.com/wildfires-economic-impact-4160764 (accessed on 30 December 2019).
4. Westerling, A.L.; Hidalgo, H.G.; Cayan, D.R.; Swetnam, T.W. Warming and Earlier Spring Increase Western U.S. Forest Wildfire Activity. *Science* **2006**, *313*, 940–943. [CrossRef]
5. Insurance Information Institute. Facts + Statistics: Wildfires. Available online: https://www.iii.org/fact-statistic/facts-statistics-wildfires (accessed on 30 December 2019).
6. U.S. Global Change Research Program. Climate Science Special Report: Fourth National Climate Assessment. 2017. Available online: https://science2017.globalchange.gov/chapter/8/ (accessed on 30 December 2019).

7. Chien, S.; Doubleday, J.; Mclaren, D.; Davies, A.; Tran, D.; Tanpipat, V.; Akaakara, S.; Ratanasuwan, A.; Mandl, D. Space-based sensorweb monitoring of wildfires in Thailand. In Proceedings of the 2011 IEEE International Geoscience and Remote Sensing Symposium, Vancouver, BC, Canada, 24–29 July 2011; pp. 1906–1909. [CrossRef]
8. Chiaraviglio, N.; Artés, T.; Bocca, R.; López, J.; Gentile, A.; Ayanz, J.S.M.; Cortés, A.; Margalef, T. Automatic fire perimeter determination using MODIS hotspots information. In Proceedings of the 2016 IEEE 12th International Conference on e-Science, Baltimore, MD, USA, 24–27 October 2016; pp. 414–423. [CrossRef]
9. Fukuhara, T.; Kouyama, T.; Kato, S.; Nakamura, R.; Takahashi, Y.; Akiyama, H. Detection of small wildfire by thermal infrared camera with the uncooled microbolometer array for 50-kg class satellite. *IEEE Trans. Geosci. Remote Sens.* **2017**, *55*, 4314–4324. [CrossRef]
10. Yoon, I.; Noh, D.K.; Lee, D.; Teguh, R.; Honma, T.; Shin, H. Reliable wildfire monitoring with sparsely deployed wireless sensor networks. In Proceedings of the 2012 IEEE 26th International Conference on Advanced Information Networking and Applications, Fukuoka, Japan, 26–29 March 2012; pp. 460–466. [CrossRef]
11. Tan, Y.K.; Panda, S.K. Self-autonomous wireless sensor nodes with wind energy harvesting for remote sensing of wind-driven wildfire spread. *IEEE Trans. Instrum. Meas.* **2011**, *60*, 1367–1377. [CrossRef]
12. Lin, H.; Liu, X.; Wang, X.; Liu, Y. A fuzzy inference and big data analysis algorithm for the prediction of forest fire based on rechargeable wireless sensor networks. *Sustain. Comput. Informatics Syst.* **2018**, *18*, 101–111. [CrossRef]
13. Marder, J. NASA Tracks Wildfires From Above to Aid Firefighters Below. 2019. Available online: https://www.nasa.gov/feature/goddard/2019/nasa-tracks-wildfires-from-above-to-aid-firefighters-below (accessed on 30 December 2019).
14. Bumberger, J.; Remmler, P.; Hutschenreuther, T.; Toepfer, H.; Dietrich, P. Potentials and Limitations of Wireless Sensor Networks for Environmental. In Proceedings of the AGU Fall Meeting, San Francisco, CA, USA, 9–13 December 2013; Volume 2013.
15. Nex, F.; Remondino, F. Preface: Latest Developments, Methodologies, and Applications Based on UAV Platforms. *Drones* **2019**, *3*, 26. [CrossRef]
16. Ollero, A.; de Dios, J.M.; Merino, L. Unmanned aerial vehicles as tools for forest-fire fighting. *For. Ecol. Manag.* **2006**, *234*, S263. [CrossRef]
17. Ambrosia, V.; Wegener, S.; Zajkowski, T.; Sullivan, D.; Buechel, S.; Enomoto, F.; Lobitz, B.; Johan, S.; Brass, J.; Hinkley, E. The Ikhana unmanned airborne system (UAS) western states fire imaging missions: from concept to reality (2006–2010). *Geocarto Int.* **2011**, *26*, 85–101. [CrossRef]
18. Hinkley, E.A.; Zajkowski, T. USDA forest service—NASA: unmanned aerial systems demonstrations—Pushing the leading edge in fire mapping. *Geocarto Int.* **2011**, *26*, 103–111. [CrossRef]
19. Yuan, C.; Youmin, Z.; Zhixiang, L. A survey on technologies for automatic forest fire monitoring, detection, and fighting using unmanned aerial vehicles and remote sensing techniques. *Can. J. For. Res.* **2015**, *45*, 783–792. [CrossRef]
20. Skorput, P.; Mandzuka, S.; Vojvodic, H. The use of Unmanned Aerial Vehicles for forest fire monitoring. In Proceedings of the 2016 International Symposium ELMAR, Zadar, Croatia, 12–14 September 2016; pp. 93–96. [CrossRef]
21. Restas, A. Forest Fire Management Supporting by UAV Based Air Reconnaissance Results of Szendro Fire Department, Hungary. In Proceedings of the 2006 First International Symposium on Environment Identities and Mediterranean Area, Corte-Ajaccio, France, 10–13 July 2006; pp. 73–77. [CrossRef]
22. Laszlo, B.; Agoston, R.; Xu, Q. Conceptual approach of measuring the professional and economic effectiveness of drone applications supporting forest fire management. *Procedia Eng.* **2018**, *211*, 8–17. [CrossRef]
23. Bailon-Ruiz, R.; Lacroix, S. Wildfire remote sensing with UAVs: A review from the autonomy point of view. In Proceedings of the 2020 International Conference on Unmanned Aircraft Systems (ICUAS), Athens, Greece, 1–4 September 2020; pp. 412–420. [CrossRef]
24. Twidwell, D.; Allen, C.R.; Detweiler, C.; Higgins, J.; Laney, C.; Elbaum, S. Smokey comes of age: unmanned aerial systems for fire management. *Front. Ecol. Environ.* **2016**, *14*, 333–339. [CrossRef]
25. Qin, H.; Cui, J.Q.; Li, J.; Bi, Y.; Lan, M.; Shan, M.; Liu, W.; Wang, K.; Lin, F.; Zhang, Y.F.; et al. Design and implementation of an unmanned aerial vehicle for autonomous firefighting missions. In Proceedings of the 2016 12th IEEE International Conference on Control and Automation (ICCA), Kathmandu, Nepal, 1–3 June 2016; pp. 62–67. [CrossRef]
26. Aydin, B.; Selvi, E.; Tao, J.; Starek, M.J. Use of fire-extinguishing balls for a conceptual system of drone-assisted wildfire fighting. *Drones* **2019**, *3*, 17. [CrossRef]
27. Johnson, K. DJI R&D Head Dreams of Drones Fighting Fires by the Thousands in 'Aerial Aqueduct'. 2019. Available online: https://venturebeat.com/2019/04/20/dji-rd-head-dreams-of-drones-fighting-fires-by-the-thousands-in-aerial-aqueduct/ (accessed on 30 December 2019).
28. Watts, A.; Ambrosia, V.; Hinkley, E. Unmanned Aircraft Systems in Remote Sensing and Scientific Research: Classification and Considerations of Use. *Remote Sens.* **2012**, *4*, 1671–1692. [CrossRef]
29. Abdullah, Q.A. iGEOG 892 Geospatial Applications of Unmanned Aerial Systems (UAS): Classification of the Unmanned Aerial Systems. Available online: https://www.e-education.psu.edu/geog892/node/5 (accessed on 5 August 2020).
30. Martínez-de Dios, J.; Merino, L.; Ollero, A.; Ribeiro, L.M.; Viegas, X. Multi-UAV experiments: application to forest fires. In *Multiple Heterogeneous Unmanned Aerial Vehicles*; Springer: Berlin/Heidelberg, Germany, 2007; pp. 207–228. [CrossRef]

31. Ghamry, K.; Kamel, M.; Zhang, Y. Multiple UAVs in forest fire fighting mission using particle swarm optimization. In Proceedings of the 2017 International Conference on Unmanned Aircraft Systems (ICUAS), Miami, FL, USA, 13–16 June 2017; pp. 1404–1409. [CrossRef]
32. Casbeer, D.; Kingston, D.; Beard, R.; McLain, T. Cooperative forest fire surveillance using a team of small unmanned air vehicles. *Int. J. Syst. Sci.* **2006**, *37*, 351–360. [CrossRef]
33. Martins, A.; Almeida, J.; Almeida, C.; Figueiredo, A.; Santos, F.; Bento, D.; Silva, H.; Silva, E. Forest fire detection with a small fixed wing autonomous aerial vehicle. *IFAC* **2007**, *40*, 168–173. [CrossRef]
34. Merino, L.; Caballero, F.; Martínez-de Dios, J.; Ollero, A. Cooperative fire detection using Unmanned Aerial Vehicles. In Proceedings of the 2005 IEEE International Conference on Robotics and Automation, Barcelona, Spain, 18–22 April 2005; pp. 1884–1889. [CrossRef]
35. Merino, L.; Caballero, F.; Martínez-de Dios, J.; Ferruz, J.; Ollero, A. A cooperative perception system for multiple UAVs: Application to automatic detection of forest fires. *J. Field Robot.* **2006**, *23*, 165–184. [CrossRef]
36. Sujit, P.; Kingston, D.; Beard, R. Cooperative forest fire monitoring using multiple UAVs. In Proceedings of the 2007 46th IEEE Conference on Decision and Control, New Orleans, LA, USA, 12–14 December 2007; pp. 4875–4880. [CrossRef]
37. Alexis, K.; Nikolakopoulos, G.; Tzes, A.; Dritsas, L. Coordination of helicopter UAVs for aerial forest-fire surveillance. In *Applications of Intelligent Control to Engineering Systems*; Springer: Dordrecht, The Netherlands, 2009; Volume 39, Chapter 7, pp. 169–193.
38. Bradley, J.; Taylor, C. Georeferenced mosaics for tracking fires using unmanned miniature air vehicles. *J. Aerosp. Comput. Inf. Commun.* **2011**, *8*, 295–309. [CrossRef]
39. Kumar, M.; Cohen, K.; Homchaudhuri, B. Cooperative control of multiple uninhabited aerial vehicles for monitoring and fighting wildfires. *J. Aerosp. Comput. Inf. Commun.* **2011**, *8*, 1–16. [CrossRef]
40. Martínez-de Dios, J.; Merino, L.; Caballero, F.; Ollero, A. Automatic forest-fire measuring using ground stations and Unmanned Aerial Systems. *Sensors* **2011**, *11*, 6328–6353. [CrossRef] [PubMed]
41. Pastor, E.; Barrado, C.; Royo, P.; Santamaria, E.; Lopez, J.; Salami, E. Architecture for a helicopter-based unmanned aerial systems wildfire surveillance system. *Geocarto Int.* **2011**, *26*, 113–131. [CrossRef]
42. Belbachir, A.; Escareno, J.; Rubio, E.; Sossa, H. Preliminary results on UAV-based forest fire localization based on decisional navigation. In Proceedings of the 2015 Workshop on Research, Education and Development of Unmanned Aerial Systems (RED-UAS), Cancún, Mexico, 23–25 November 2015; pp. 377–382. [CrossRef]
43. Karma, S.; Zorba, E.; Pallis, G.C.; Statheropoulos, G.; Balta, I.; Mikedi, K.; Vamvakari, J.; Pappa, A.; Chalaris, M.; Xanthopoulos, G.; et al. Use of unmanned vehicles in search and rescue operations in forest fires: Advantages and limitations observed in a field trial. *Int. J. Disaster Risk Reduct.* **2015**, *13*, 307–312. [CrossRef]
44. Merino, L.; Caballero, F.; Martínez-de Dios, J.R.; Maza, I.; Ollero, A. An unmanned aircraft system for automatic forest fire monitoring and measurement. *J. Intell. Robot. Syst.* **2012**, *65*, 533–548. [CrossRef]
45. Merino, L.; Martínez-de Dios, J.; Ollero, A. Cooperative unmanned aerial systems for fire detection, Monitoring, and Extinguishing. In *Handbook of Unmanned Aerial Vehicles*; Springer: Dordrecht, The Netherlands, 2015; Chapter 112, pp. 2693–2722.
46. Ghamry, K.; Zhang, Y. Cooperative control of multiple UAVs for forest fire monitoring and detection. In Proceedings of the 2016 12th IEEE/ASME International Conference on Mechatronic and Embedded Systems and Applications (MESA), Auckland, New Zealand, 29–31 August 2016; pp. 1–6. [CrossRef]
47. Ghamry, K.; Zhang, Y. Fault-tolerant cooperative control of multiple UAVs for forest fire detection and tracking mission. In Proceedings of the 2016 3rd Conference on Control and Fault-Tolerant Systems (SysTol), Barcelona, Spain, 7–9 September 2016; pp. 133–138. [CrossRef]
48. Sun, H.; Song, G.; Wei, Z.; Zhang, Y.; Liu, S. Bilateral teleoperation of an unmanned aerial vehicle for forest fire detection. In Proceedings of the 2017 IEEE International Conference on Information and Automation (ICIA), Macau, China, 18–20 July 2017; pp. 586–591. [CrossRef]
49. Yuan, C.; Liu, Z.; Zhang, Y. Fire detection using infrared images for UAV-based forest fire surveillance. In Proceedings of the 2017 International Conference on Unmanned Aircraft Systems (ICUAS), Miami, FL, USA, 13–16 June 2017; pp. 567–572. [CrossRef]
50. Yuan, C.; Liu, Z.; Zhang, Y. UAV-based forest fire detection and tracking using image processing techniques. In Proceedings of the 2015 International Conference on Unmanned Aircraft Systems (ICUAS), Denver, CO, USA, 9–12 June 2015; pp. 639–643. [CrossRef]
51. Yuan, C.; Liu, Z.; Zhang, Y. Vision-based forest fire detection in aerial images for firefighting using UAVs. In Proceedings of the 2016 International Conference on Unmanned Aircraft Systems, Arlington, VA, USA, 7–10 June 2016; pp. 1200–1205. [CrossRef]
52. Yuan, C.; Ghamry, K.; Liu, Z.; Zhang, Y. Unmanned aerial vehicle based forest fire monitoring and detection using image processing technique. In Proceedings of the 2016 IEEE Chinese Guidance, Navigation and Control Conference (CGNCC), Nanjing, China, 12–14 August 2016; pp. 1870–1875. [CrossRef]
53. Yuan, C.; Liu, Z.; Zhang, Y. Aerial images-based forest fire detection for firefighting using optical remote sensing techniques and unmanned aerial vehicles. *J. Intell. Robot. Syst.* **2017**, *88*, 635–654. [CrossRef]
54. Lin, Z.; Liu, H.H.; Wotton, M. Kalman filter-based large-scale wildfire monitoring with a system of UAVs. *IEEE Trans. Ind. Electron.* **2018**, *66*, 606–615. [CrossRef]
55. Wardihani, E.; Ramdhani, M.; Suharjono, A.; Setyawan, T.A.; Hidayat, S.S.; Helmy, S.W.; Triyono, E.; Saifullah, F. Real-time forest fire monitoring system using unmanned aerial vehicle. *J. Eng. Sci. Technol.* **2018**, *13*, 1587–1594.

56. Zhao, Y.; Ma, J.; Li, X.; Zhang, J. Saliency Detection and Deep Learning-Based Wildfire Identification in UAV Imagery. *Sensors* **2018**, *18*, 712. [CrossRef]
57. Pham, H.; La, H.; Feil-Seifer, D.; Deans, M. A distributed control framework for a team of unmanned aerial vehicles for dynamic wildfire tracking. In Proceedings of the 2017 IEEE/RSJ International Conference on Intelligent Robots and Systems (IROS), Vancouver, BC, Canada, 24–28 September 2017; pp. 6648–6653. [CrossRef]
58. Pham, H.X.; La, H.M.; Feil-Seifer, D.; Deans, M.C. A distributed control framework of multiple unmanned aerial vehicles for dynamic wildfire tracking. *IEEE Trans. Syst. Man Cybern. Syst.* **2018**, *50*, 1537–1548. [CrossRef]
59. Julian, K.D.; Kochenderfer, M.J. Distributed wildfire surveillance with autonomous aircraft using deep reinforcement learning. *J. Guid. Control. Dyn.* **2019**, *42*, 1768–1778. [CrossRef]
60. Jiao, Z.; Zhang, Y.; Xin, J.; Mu, L.; Yi, Y.; Liu, H.; Liu, D. A deep learning based forest fire detection approach using UAV and YOLOv3. In Proceedings of the 2019 1st International Conference on Industrial Artificial Intelligence (IAI), Shenyang, China, 23–25 July 2019; pp. 1–5. [CrossRef]
61. Jiao, Z.; Zhang, Y.; Mu, L.; Xin, J.; Jiao, S.; Liu, H.; Liu, D. A YOLOv3-based Learning Strategy for Real-time UAV-based Forest Fire Detection. In Proceedings of the 2020 Chinese Control And Decision Conference (CCDC), Hefei, China, 22–24 August 2020; pp. 4963–4967. [CrossRef]
62. Seraj, E.; Gombolay, M. Coordinated control of uavs for human-centered active sensing of wildfires. In Proceedings of the 2020 American Control Conference (ACC), Denver, CO, USA, 1–3 July 2020; pp. 1845–1852. [CrossRef]
63. Lin, Z.; Liu, H. Enhanced cooperative filter for wildfire monitoring. In Proceedings of the 2015 54th IEEE Conference on Decision and Control (CDC), Osaka, Japan, 15–18 December 2015; pp. 3075–3080. [CrossRef]
64. Allison, R.; Johnston, J.; Craig, G.; Jennings, S. Airborne optical and thermal remote sensing for wildfire detection and monitoring. *Sensors* **2016**, *16*, 1310. [CrossRef] [PubMed]
65. Johnston, J.; Wooster, M.; Lynham, T. Experimental confirmation of the MWIR and LWIR grey body assumption for vegetation fire flame emissivity. *Int. J. Wildland Fire* **2014**, *23*, 463–479. [CrossRef]
66. Ball, M. FLIR Unveils MWIR Thermal Camera Cores for Drone Applications. 2018. Available online: https://www.unmannedsystemstechnology.com/2018/12/new-mwir-thermal-camera-cores-launched-for-drone-applications/ (accessed on 30 December 2019).
67. Esposito, F.; Rufino, G.; Moccia, A.; Donnarumma, P.; Esposito, M.; Magliulo, V. An integrated electro-optical payload system for forest fires monitoring from airborne platform. In Proceedings of the 2007 IEEE Aerospace Conference, Big Sky, MT, USA, 3–10 March 2007; pp. 1–13. [CrossRef]
68. National Aeronautics and Space Administration. Ikhana UAV Gives NASA New Science and Technology Capabilities. 2007. Available online: https://www.nasa.gov/centers/dryden/news/NewsReleases/2007/07-12.html (accessed on 30 December 2019).
69. Ghamry, K.; Kamel, M.; Zhang, Y. Cooperative forest monitoring and fire detection using a team of UAVs-UGVs. In Proceedings of the 2016 International Conference on Unmanned Aircraft Systems, Arlington, VA, USA, 7–10 June 2016; pp. 1206–1211. [CrossRef]
70. Fairchild, M.D. *Color Appearance Models*, 3rd ed.; John Wiley & Sons Ltd.: Chichester, West Sussex, UK, 2013.
71. Otsu, N. A Threshold Selection Method from Gray-Level Histograms. *IEEE Trans. Syst. Man Cybern.* **1979**, *9*, 62–66. [CrossRef]
72. Lei, S.; Fangfei, S.; Teng, W.; Leping, B.; Xinguo, H. A new fire detection method based on the centroid variety of consecutive frames. In Proceedings of the 2017 2nd International Conference on Image, Vision and Computing (ICIVC), Chengdu, China, 2–4 June 2017; pp. 437–442. [CrossRef]
73. Wang, T.; Shi, L.; Yuan, P.; Bu, L.; Hou, X. A new fire detection method based on flame color dispersion and similarity in consecutive frames. In Proceedings of the 2017 Chinese Automation Congress (CAC), Jinan, China, 20–22 October 2017; pp. 151–156. [CrossRef]
74. Chou, K.; Prasad, M.; Gupta, D.; Sankar, S.; Xu, T.; Sundaram, S.; Lin, C.; Lin, W. Block-based feature extraction model for early fire detection. In Proceedings of the 2017 IEEE Symposium Series on Computational Intelligence (SSCI), Hawaii, HI, USA, 27 November–1 December 2017; pp. 1–8. [CrossRef]
75. Shi, L.; Long, F.; Zhan, Y.; Lin, C. Video-based fire detection with spatio-temporal SURF and color features. In Proceedings of the 2016 12th World Congress on Intelligent Control and Automation (WCICA), Guilin, China, 12–15 June 2016; pp. 258–262. [CrossRef]
76. Abdullah, M.; Wijayanto, I.; Rusdinar, A. Position estimation and fire detection based on digital video color space for autonomous quadcopter using odroid XU4. In Proceedings of the 2016 International Conference on Control, Electronics, Renewable Energy and Communications (ICCEREC), Bandung, Indonesia, 13–15 September 2016; pp. 169–173. [CrossRef]
77. Steffens, C.; Botelho, S.; Rodrigues, R. A texture driven approach for visible spectrum fire detection on mobile robots. In Proceedings of the 2016 XIII Latin American Robotics Symposium and IV Brazilian Robotics Symposium (LARS/SBR), Recife, Brazil, 8–12 October 2016; pp. 257–262. [CrossRef]
78. Choi, J.; Choi, J.Y. Patch-based fire detection with online outlier learning. In Proceedings of the 2015 12th IEEE International Conference on Advanced Video and Signal Based Surveillance (AVSS), Karlsruhe, Germany, 25–28 August 2015; pp. 1–6. [CrossRef]

79. Poobalan, K.; Liew, S. Fire detection based on color filters and Bag-of-Features classification. In Proceedings of the 2015 IEEE Student Conference on Research and Development (SCOReD), Kuala Lumpur, Malaysia, 13–14 December 2015; pp. 389–392. [CrossRef]
80. Zhang, H.; Zhang, N.; Xiao, N. Fire detection and identification method based on visual attention mechanism. *Opt. Int. J. Light Electron Opt.* **2015**, *126*, 5011–5018. [CrossRef]
81. Toulouse, T.; Rossi, L.; Akhloufi, M.; Celik, T.; Maldague, X. Benchmarking of wildland fire colour segmentation algorithms. *IET Image Process.* **2015**, *9*, 1064–1072. [CrossRef]
82. Verstockt, S.; Kypraios, I.; Potter, P.; Poppe, C.; Walle, R. Wavelet-based multi-modal fire detection. In Proceedings of the 19th European Signal Processing Conference, Barcelona, Spain, 29 August–2 September 2011; pp. 903–907.
83. Kyrkou, C.; Theocharides, T. Deep-Learning-Based Aerial Image Classification for Emergency Response Applications Using Unmanned Aerial Vehicles. *arXiv* **2019**, arXiv:1906.08716.
84. Lee, W.; Kim, S.; Lee, Y.; Lee, H.; Choi, M. Deep neural networks for wild fire detection with unmanned aerial vehicle. In Proceedings of the 2017 IEEE International Conference on Consumer Electronics (ICCE), Las Vegas, NV, USA, 8–10 January 2017; pp. 252–253. [CrossRef]
85. Akhloufi, M.A.; Tokime, R.B.; Elassady, H. Wildland fires detection and segmentation using deep learning. In Proceedings of the SPIE 10649, Pattern Recognition and Tracking XXIX, International Society for Optics and Photonics, Orlando, FL, USA, 15–19 April 2018; Volume 10649. [CrossRef]
86. Toulouse, T.; Rossi, L.; Campana, A.; Celik, T.; Akhloufi, M. Computer vision for wildfire research: An evolving image dataset for processing and analysis. *Fire Saf. J.* **2017**, *92*, 188–194. [CrossRef]
87. Bruhn, A.; Weickert, J.; Schnörr, C. Lucas/Kanade meets Horn/Schunck: Combining local and global optic flow methods. *Int. J. Comput. Vis.* **2005**, *61*, 211–231. [CrossRef]
88. Asatryan, D.; Hovsepyan, S. Method for fire and smoke detection in monitored forest areas. In Proceedings of the 2015 Computer Science and Information Technologies (CSIT), Yerevan, Armenia, 28 September–2 October 2015; pp. 77–81. [CrossRef]
89. Yuan, C.; Liu, Z.; Zhang, Y. Learning-based smoke detection for unmanned aerial vehicles applied to forest fire surveillance. *J. Intell. Robot. Syst.* **2018**, *93*, 337–349. [CrossRef]
90. Duong, H.; Tinh, D.T. An efficient method for vision-based fire detection using SVM classification. In Proceedings of the 2013 International Conference on Soft Computing and Pattern Recognition (SoCPaR), Hanoi, Vietnam, 15–18 December 2013; pp. 190–195. [CrossRef]
91. Zhou, Q.; Yang, X.; Bu, L. Analysis of shape features of flame and interference image in video fire detection. In Proceedings of the 2015 Chinese Automation Congress (CAC), Wuhan, China, 27–29 November 2015; pp. 633–637. [CrossRef]
92. Chen, X.; Zhang, X.; Zhang, Q. Fire alarm using multi-rules detection and texture features classification in video surveillance. In Proceedings of the 2014 7th International Conference on Intelligent Computation Technology and Automation, Changsha, China, 25–26 October 2014; pp. 264–267. [CrossRef]
93. Chino, D.; Avalhais, L.; Rodrigues, J.; Traina, A. BoWFire: Detection of fire in still images by integrating pixel color and texture analysis. In Proceedings of the 2015 28th SIBGRAPI Conference on Graphics, Patterns and Images, Salvador, Brazil, 26–29 August 2015; pp. 95–102. [CrossRef]
94. Chi, R.; Lu, Z.M.; Ji, Q.G. Real-time multi-feature based fire flame detection in video. *IET Image Process.* **2017**, *11*, 31–37. [CrossRef]
95. Favorskaya, M.; Pyataeva, A.; Popov, A. Verification of smoke detection in video sequences based on spatio-temporal local binary patterns. *Procedia Comput. Sci.* **2015**, *60*, 671–680. [CrossRef]
96. Bay, H.; Ess, A.; Tuytelaars, T.; Gool, L.V. Speeded-Up Robust Features (SURF). *Comput. Vis. Image Underst.* **2008**, *110*, 346–359. [CrossRef]
97. Ojala, T.; Pietikäinen, M.; Harwood, D. A comparative study of texture measures with classification based on featured distributions. *Pattern Recognit.* **1996**, *29*, 51–59. [CrossRef]
98. Avalhais, L.; Rodrigues, J.; Traina, A. Fire detection on unconstrained videos using color-aware spatial modeling and motion flow. In Proceedings of the 2016 IEEE 28th International Conference on Tools with Artificial Intelligence (ICTAI), San Jose, CA, USA, 6–8 November 2016; pp. 913–920. [CrossRef]
99. Li, K.; Yang, Y. Fire detection algorithm based on CLG-TV optical flow model. In Proceedings of the 2016 2nd IEEE International Conference on Computer and Communications (ICCC), Chengdu, China, 14–17 October 2016; pp. 1381–1385. [CrossRef]
100. Harris, C.; Stephens, M. A combined corner and edge detector. In Proceedings of the Fourth Alvey Vision Conference, Manchester, UK, 31 August–2 September 1988; pp. 147–152.
101. Krizhevsky, A.; Sutskever, I.; Hinton, G.E. Imagenet classification with deep convolutional neural networks. *Adv. Neural Inf. Process. Syst.* **2012**, *25*, 1097–1105. [CrossRef]
102. Redmon, J.; Farhadi, A. Yolov3: An incremental improvement. *arXiv* **2018**, arXiv:1804.02767.
103. Ko, B.; Jung, J.; Nam, J. Fire detection and 3D surface reconstruction based on stereoscopic pictures and probabilistic fuzzy logic. *Fire Saf. J.* **2014**, *68*, 61–70. [CrossRef]
104. Foggia, P.; Saggese, A.; Vento, M. Real-time fire detection for video-surveillance applications using a combination of experts based on color, shape, and motion. *IEEE Trans. Circuits Syst. Video Technol.* **2015**, *25*, 1545–1556. [CrossRef]

105. Buemi, A.; Giacalone, D.; Naccari, F.; Spampinato, G. Efficient fire detection using fuzzy logic. In Proceedings of the 2016 IEEE 6th International Conference on Consumer Electronics—Berlin (ICCE-Berlin), Berlin, Germany, 5–7 September 2016; pp. 237–240. [CrossRef]

106. Cai, M.; Lu, X.; Wu, X.; Feng, Y. Intelligent video analysis-based forest fires smoke detection algorithms. In Proceedings of the 2016 12th International Conference on Natural Computation, Fuzzy Systems and Knowledge Discovery (ICNC-FSKD), Changsha, China, 13–15 August 2016; pp. 1504–1508. [CrossRef]

107. Zhao, Y.; Tang, G.; Xu, M. Hierarchical detection of wildfire flame video from pixel level to semantic level. *Expert Syst. Appl.* **2015**, *42*, 4097–4104. [CrossRef]

108. Stadler, A.; Windisch, T.; Diepold, K. Comparison of intensity flickering features for video based flame detection algorithms. *Fire Saf. J.* **2014**, *66*, 1–7. [CrossRef]

109. Barmpoutis, P.; Dimitropoulos, K.; Grammalidis, N. Real time video fire detection using spatio-temporal consistency energy. In Proceedings of the 2013 10th IEEE International Conference on Advanced Video and Signal Based Surveillance, Krakow, Poland, 27–30 August 2013; pp. 365–370. [CrossRef]

110. Wang, H.; Finn, A.; Erdinc, O.; Vincitore, A. Spatial-temporal structural and dynamics features for Video Fire Detection. In Proceedings of the 2013 IEEE Workshop on Applications of Computer Vision (WACV), Clearwater, FL, USA, 15–17 January 2013; pp. 513–519. [CrossRef]

111. Kim, S.; Kim, T. Fire detection using the brownian correlation descriptor. In Proceedings of the 2016 IEEE International Conference on Consumer Electronics-Asia (ICCE-Asia), Seoul, Korea, 26–28 October 2016; pp. 1–4. [CrossRef]

112. Székely, G.; Rizzo, M. Brownian distance covariance. *Ann. Appl. Stat.* **2009**, *3*, 1236–1265. [CrossRef]

113. Rublee, E.; Rabaud, V.; Konolige, K.; Bradski, G. ORB: An efficient alternative to SIFT or SURF. In Proceedings of the 2011 International Conference on Computer Vision, Barcelona, Spain, 6–13 November 2011; pp. 2564–2571. [CrossRef]

114. Steffens, C.; Rodrigues, R.; Botelho, S. An unconstrained dataset for non-stationary video based fire detection. In Proceedings of the 2015 12th Latin American Robotics Symposium and 2015 3rd Brazilian Symposium on Robotics (LARS-SBR), Uberlandia, Brazil, 29–31 October 2015; pp. 25–30. [CrossRef]

115. Pignaton de Freitas, E.; da Costa, L.A.L.F.; Felipe Emygdio de Melo, C.; Basso, M.; Rodrigues Vizzotto, M.; Schein Cavalheiro Corrêa, M.; Dapper e Silva, T. Design, Implementation and Validation of a Multipurpose Localization Service for Cooperative Multi-UAV Systems. In Proceedings of the 2020 International Conference on Unmanned Aircraft Systems (ICUAS), Athens, Greece, 1–4 September 2020; pp. 295–302. [CrossRef]

116. Phan, C.; Liu, H. A cooperative UAV/UGV platform for wildfire detection and fighting. In Proceedings of the 2008 Asia Simulation Conference—7th International Conference on System Simulation and Scientific Computing, Beijing, China, 10–12 October 2008; pp. 494–498. [CrossRef]

117. Viguria, A.; Maza, I.; Ollero, A. Distributed Service-Based Cooperation in Aerial/Ground Robot Teams Applied to Fire Detection and Extinguishing Missions. *Adv. Robot.* **2010**, *24*, 1–23. [CrossRef]

118. Akhloufi, M.A.; Castro, N.A.; Couturier, A. UAVs for wildland fires. In Proceedings of the SPIE 10643, Autonomous Systems: Sensors, Vehicles, Security, and the Internet of Everything. International Society for Optics and Photonics, Orlando, FL, USA, 15–19 April 2018; Volume 10643. [CrossRef]

119. Akhloufi, M.A.; Toulouse, T.; Rossi, L. Multiple spectrum vision for wildland fires. In Proceedings of the SPIE 10661, Thermosense: Thermal Infrared Applications XL. International Society for Optics and Photonics, Orlando, FL, USA, 15–19 April 2018; Volume 10661, p. 1066105. [CrossRef]

120. Toulouse, T.; Rossi, L.; Akhloufi, M.A.; Pieri, A.; Maldague, X. A multimodal 3D framework for fire characteristics estimation. *Meas. Sci. Technol.* **2018**, *29*, 025404. [CrossRef]

121. Akhloufi, M.; Toulouse, T.; Rossi, L.; Maldague, X. Multimodal three-dimensional vision for wildland fires detection and analysis. In Proceedings of the 2017 Seventh International Conference on Image Processing Theory, Tools and Applications (IPTA), Montreal, QC, Canada, 28 November–1 December 2017; pp. 1–6. [CrossRef]

122. Akhloufi, M.; Toulouse, T.; Rossi, L.; Maldague, X. Three-dimensional infrared-visible framework for wildland fires. In Proceedings of the 14th International Workshop on Advanced Infrared Technology and Applications (AITA), Quebec City, QC, Canada, 27–29 September 2017; pp. 65–69.

Article

Spray Deposition on Weeds (Palmer Amaranth and Morningglory) from a Remotely Piloted Aerial Application System and Backpack Sprayer

Daniel Martin [1,*], Vijay Singh [2,†], Mohamed A. Latheef [1] and Muthukumar Bagavathiannan [2]

[1] Agricultural Research Service, United States Department of Agriculture, Aerial Application Technology Research Unit, 3103 F & B Road, College Station, TX 77845, USA; mohamed.latheef@usda.gov

[2] Department of Soil and Crop Sciences, Texas A&M University, College Station, TX 77845, USA; v.singh@vt.edu (V.S.); Muthu@tamu.edu (M.B.)

* Correspondence: dan.martin@usda.gov

† Present address: Eastern Shore Agricultural Research and Extension Center, Virginia Polytechnic Institute and State University, Painter, VA 23420, USA.

Abstract: This study was designed to determine whether a remotely piloted aerial application system (RPAAS) could be used in lieu of a backpack sprayer for post-emergence herbicide application. Consequent to this objective, a spray mixture of tap water and fluorescent dye was applied on Palmer amaranth and ivyleaf morningglory using an RPAAS at 18.7 and 37.4 L·ha^{-1} and a CO_2-pressurized backpack sprayer at a 140 L·ha^{-1} spray application rate. Spray efficiency (the proportion of applied spray collected on an artificial sampler) for the RPAAS treatments was comparable to that for the backpack sprayer. Fluorescent spray droplet density was significantly higher on the adaxial surface for the backpack sprayer treatment than that for the RPAAS platforms. The percent of spray droplets on the abaxial surface for the RPAAS aircraft at 37.4 L·ha^{-1} was 4-fold greater than that for the backpack sprayer at 140 L·ha^{-1}. The increased spray deposition on the abaxial leaf surfaces was likely caused by rotor downwash and wind turbulence generated by the RPAAS which caused leaf fluttering. This improved spray deposition may help increase the efficacy of contact herbicides. Test results indicated that RPAASs may be used for herbicide application in lieu of conventional backpack sprayers.

Keywords: UAV; UAS; RPAAS; aerial application; backpack sprayer; spray deposition; droplet spectra; palmer amaranth; morningglory

1. Introduction

Weeds are one of the major limiting factors to the production of agricultural crops and cause significant yield loss in crop farming systems throughout the world [1–3]. It is estimated that weeds in corn and soybean alone would reduce yield by 50%, costing growers $43 billion in economic loss annually in the United States and Canada according to a recent study conducted by the Weed Science Society of America in conjunction with Kansas State University spanning over a seven-year period [4–6]. In general, broadleaf weeds are more competitive than grasses and early germinating weeds reduce yield more than weeds which emerge later in the growing season [7]. In many parts of the world, weed control with herbicides has gained traction in lieu of tillage and it is purported to improve environmental conditions including a reduction in soil erosion, fuel use and greenhouse gas emissions [8].

Recently, the use of unmanned aerial application systems (UASs) or remotely piloted aerial application systems (RPAASs) for field mapping, weed classification by species, plant stress detection,

biomass and field nutrition estimation and application of pest control products in small-farm operations and site-specific management of crop pests in difficult terrains not easily accessible to manned aircraft has received increased attention around the globe [9–12]. RPAASs have the potential to occupy this niche because of their ability to fly at low altitudes and to hover close to plant canopies at different application heights and ground speeds with precision and safety. RPAASs are remotely piloted telemetrically and can fly autonomously using preprogrammed georeferenced flight paths. In precision agriculture, data on soil variability and crop characteristics to optimize field applications of seed, fertilizer and irrigation can be collected by remote sensing [13–15]. Huang et al. [16] developed UAS systems for digital imaging to identify glyphosate-resistant weeds and to determine crop injury from dicamba herbicide. Göktoğan et al. [17] used a rotary wing UAS to locate, classify and map alligator weed and *Salvinia* in an inaccessible aquatic habitat. Using multispectral cameras, Castaldi et al. [18] acquired aerial images of weed patches in maize fields and developed prescription maps for herbicide application. Peña et al. [19] found strong correlation between on-ground weed coverage and that estimated by aerial remote imagery captured by an UAV ($r^2 = 0.89$). Moreover, Peña et al. [19] reported that the determination of weed-free and low to moderate weed density areas would likely facilitate the growers to reduce herbicide application in maize fields. Although several researchers have reported that spray drones offer good potential for site-specific herbicide application in commercial farms or for monitoring weed populations over much larger areas [20], hardly any data exist on the use of RPAAS in controlling weeds. Exceptions to these reports was that of Ahmad et al. [21], who recently reported that the operational parameters, 2 m application height and 2 m s^{-1} flight speed provided the highest average herbicide spray deposition on weed canopy.

Backpack sprayers are the preferred method for applying herbicides in small-farm operations, in small plot weed science research trials and in rangelands where selective application to patches of invasive species is required [22,23]. Research data comparing applications of pest control products made by backpack sprayers with spray drones are limited. Spray application rates for backpack sprayers are usually between 94 and 318 L·ha^{-1} at 207 to 345 kPa pressure, with nozzle flow rates varying between 0.4 and 0.8 L·min^{-1}. The walking speed of the operator is usually held at 1.4 m·s^{-1} [22,24]. However, RPAAS vehicles are typically programmed to apply pesticides between 2 and 4 m application height and 1 and 7 m·s^{-1} ground speed. The spray application rates usually vary between 19 and 38 L·ha^{-1} [25]. These key differences can affect spray pattern uniformity, droplet spectra and application rates and efficacy of pest control products [22,26–28]. It is, therefore, essential to characterize and compare spray deposition and droplet spectra characteristics produced by these two delivery systems under field conditions. Such fundamental studies are required to assess whether RPAASs could be used in lieu of backpack sprayers for herbicide applications.

This research was designed to evaluate conventional ground and novel aerial spray technologies for herbicide applications against weed populations. This study was conducted in a soybean field pre-seeded with Palmer amaranth (*Amaranthus palmeri* S. Watson) and ivyleaf morningglory (*Ipomoea hederacea* (L.) Jacq.), summer annual and most problematic weeds [29–31].

2. Materials and Methods

The field experiments were conducted at Texas A&M research farm near College Station, TX, USA (30°32′17″ N; 96°25′19″ W). Four blocks, each 15 m wide × 12 m long, with 3 m between each block, were established with a 5 m strip of land earmarked at random for each treatment (Figure 1). The experimental units were assembled in a randomized complete block design with four replications to overcome heterogeneity in field conditions, relative to weed density and edaphic conditions between replicated blocks. Soybean was drill seeded at 320,000 seeds·ha^{-1} with 76 cm row spacing on 15 May 2018. Weed seeds were broadcasted after soybean planting and were lightly incorporated into the soil. Weed density and size were recorded before spray application. Palmer amaranth and ivyleaf morningglory densities were 19 and 28 plants·m^{-2}, respectively at the time of spray application.

The widest areas of the leaf blades of Palmer amaranth were ca. 7 cm long and 4 cm wide, while those of ivyleaf morning glory were ca. 9 cm long and 7 cm wide when the test was conducted.
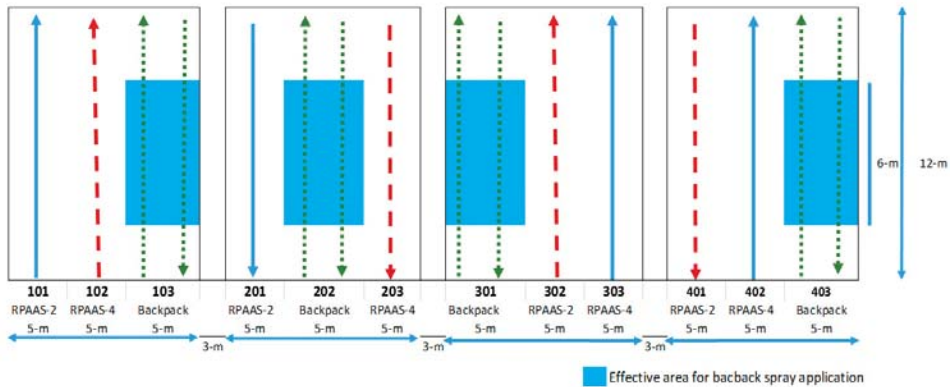
Figure 1. Field plot layout of the study on Palmer amaranth and ivyleaf morningglory. Backpack spray application was evaluated only for the 6 m × 5 m sections of the plots indicated in blue.

Two spray treatments (18.7 and 37.4 L·ha^{-1}) were applied with a RPAAS (model V6A, Homeland Surveillance and Electronics, Seattle, WA), and one treatment (140 L·ha^{-1}) was applied with a custom-made CO_2 backpack sprayer (Figure 2A,B), respectively, show V6A aircraft and backpack sprayer). These treatments are described in the text for brevity as acronyms, RPAAS-2, RPAAS-4, and BP-15, each representing spray application rates of 2, 4 and 15 gallons per acre or 18.7, 37.4 and 140 L·ha^{-1}, respectively. This study was conducted on 27 June 2018 (Study 1) and was repeated in time and space two weeks later on 11 July 2018 (Study 2). The details about the spray treatment setups, operating parameters for the backpack sprayer and the RPAAS aircraft, including spray pressure, spray rates, nozzle type and orifice, aircraft ground speed, walking speed for the backpack sprayer and application height are provided in Table 1. Initially, four TTI110-015 nozzles were installed on the RPAAS. However, due to the low pump capacity, a pressure of only 345 kPa was achievable. For the RPAAS, the outboard nozzles were positioned 0.41 m away from the inboard nozzles, which were 0.82 m apart (Figure 3). Spray pattern testing was conducted with this setup according to the conventional pattern-testing technique described earlier [25]. Briefly, four spray passes were conducted with water and fluorescent dye and patterns from each of the passes were averaged to yield a representative spray pattern for the aircraft. The results showed a symmetrical pattern with an effective swath of 4.6 m (15 ft) (Figure 4). During the field study, only three of the four nozzles were operational (the left outboard nozzle was non-functional), likely due to the daylight visible dye used in the study for image analysis, which reduced system pressure. This pressure was not enough to open the check valves on all the nozzles. As a result, only three of the four nozzles were operational for Study 1, and a full spray pattern for each nozzle was not achieved. With an effective swath of 4.6 m and a ground speed of 4 m·s^{-1} for three operational nozzles, the resulting spray application rate was 17.8 L·ha^{-1}. Two of these passes would yield an application rate of 35.6 L·ha^{-1}. For Study 2, only the two inboard nozzles were used to achieve a pressure of 414 kPa, which activated both nozzles and provided a full spray pattern for each nozzle. Spray pattern testing for this two-nozzle configuration was not conducted.

Table 1. Spray application setups for the backpack sprayer and the RPAAS aircraft in Study 1 and Study 2.

Treatment	Application Rate (L·ha⁻¹)	Nozzle Orifice	# of Nozzles	Nozzle Spacing (cm)	Flow Rate/Nozzle (L·m⁻¹)	Pressure (kPa)	Speed (m·s⁻¹)	Height (m)
RPAAS-2	18.7	TTI 110-015 [a]	4 [b]	*	0.65	345	4	3
RPAAS-4	37.4	TTI 110-015 [a]	4 [b]	*	0.65	345	4 [c]	3
BP-15	140	TTI 110-015 [a]	4	51	0.56	276	1.25	0.51

[a] TeeJet Technologies, Wheaton, Ill. [b] In Study 1, only three nozzles were operational for the RPAAS aircraft because of lack of adequate pressure due to large nozzle orifice size. In Study 2, the number of nozzles was reduced to two, which provided a full nozzle spray pattern at 414 kPa. The two nozzles used were the inboard nozzles which remained in their original positions. [c] This treatment was flown twice at this speed to achieve double the application rate. * Please see Figure 2.

(**A**)

(**B**)

Figure 2. (**A**) V6A aircraft in flight. (**B**) The backpack sprayer with spray boom, nozzles, spray tank, and pressure gage.
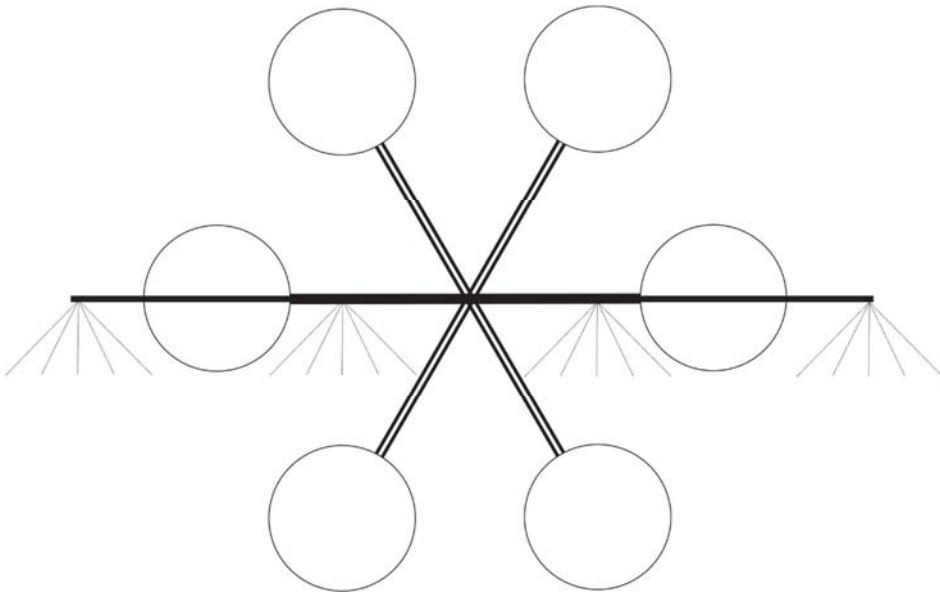
Figure 3. Schematic of HSE V6A, showing rotor configurations and corresponding nozzle locations on spray boom. Circles represent rotor positions.
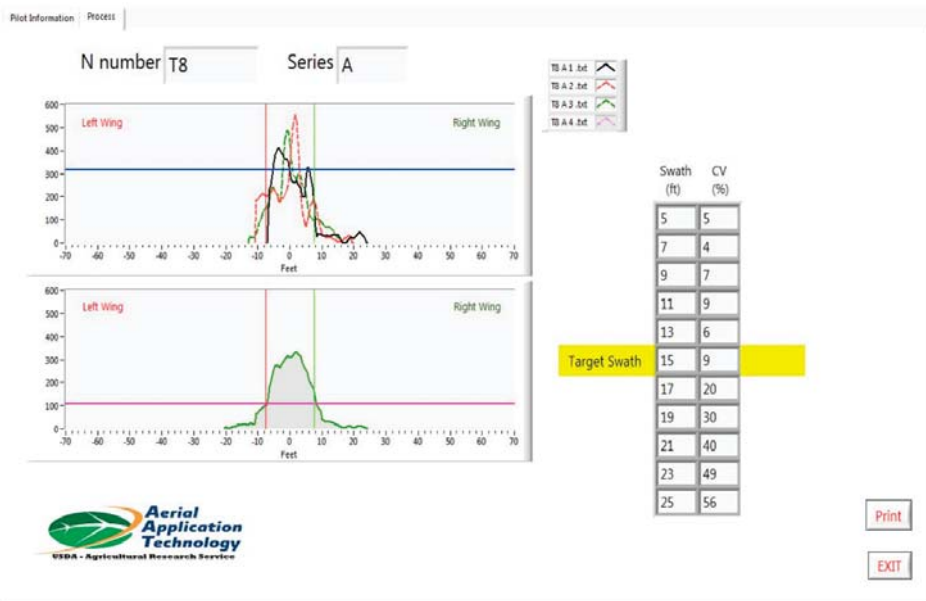
Figure 4. Pattern test results for RPAAS with the four-nozzle configuration. The top graph shows the pattern of individual passes. The bottom graph shows the average of the four passes. The table on the right shows the coefficient of variation (CV) at different swath widths. An effective swath of 4.6 m (15 ft) was chosen because it was the largest swath width with a CV < 15%.

The spray solution was comprised of a daylight visible fluorescent dye (Tintex Rocket Red, TX-13, DayGlo Color Corporation, Cleveland, OH, USA) at 10% *v/v* mixed with tap water. The fluorescent dye was used to quantify spray droplets on Palmer amaranth and morningglory leaves using the digital imaging technique documented previously [32,33].

2.1. Sampling of Spray Deposition

Water-sensitive paper (WSP) samplers (26 mm × 76 mm) (Spraying Systems, Wheaton, Ill.) were paper clipped to a metal plate (100 mm × 100 mm) and placed on a 0.3 m × 0.3 m wooden board. WSPs were oriented towards the upwind side of the metal plate to keep them flat and secured. There were four artificial samplers placed in each backpack treatment plot and five samplers in each RPAAS treatment plot. WSP samplers were diagonally placed in the test plots with the first sampling location 2 m in from the edge of each plot and subsequent locations 2 m farther down and 1 row over from the previous location.

After five minutes of drying time, WSPs were placed inside film negative sleeves. The spray droplets (Figure 5) captured on them were analyzed in the laboratory by the DropletScan™ scanner-based software system [34]. The droplet spectra parameters examined were $D_{v0.1}$, $D_{v0.5}$, $D_{v0.9}$, droplet density (droplets/cm^2), percent area coverage and spray efficiency (proportion of spray relative to the target application rate). $D_{v0.1}$ is the droplet diameter (µm), where 10% of the spray volume is contained in droplets smaller than this value. Similarly, $D_{v0.5}$ and $D_{v0.9}$ are droplet diameters, where 50% and 90% of the spray volumes, respectively, are contained in droplets smaller than these values.

Typical WSP Droplet Data

RPAAS-18.7 L·ha^{-1}

RPAAS-37.4 L·ha^{-1}
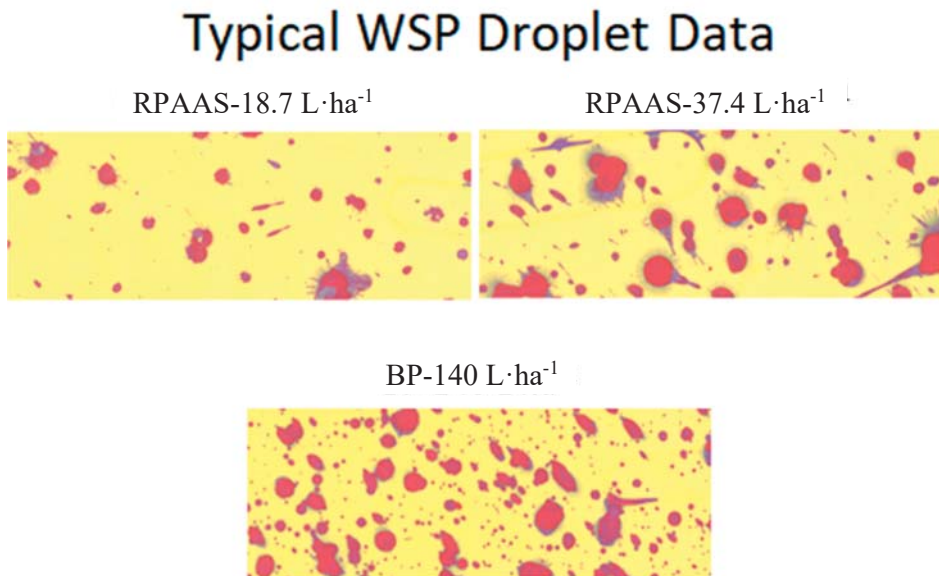
BP-140 L·ha^{-1}

Figure 5. Spray droplet images captured on WSP samplers in each of the three treatments. The RPAAS at 18.7 L·ha^{-1}, RPAAS-4 at 37.4 L·ha^{-1} and Backpack Sprayer at 140 L·ha^{-1}.

2.2. Fluorescent Imaging

Five leaves of Palmer amaranth and morningglory were collected from each replicated block close to where the wooden boards containing the WSP samplers were placed. A total of 20 leaf samples of each weed species were collected from each treatment for the RPAAS platform. However, four leaves of each species were collected for the BP-15 treatment, with a total of 16 leaf samples per species per treatment.

Leaves were imaged in the laboratory using a digital single-lens reflex camera (Model Alpha 7R, Sony Corp., Tokyo, Japan), secured to an adjustable camera stand. The camera was equipped with a macro lens (Close-up + 4 Polaroid) and UV filter (49 mm) to help zoom in and obtain a closer view of the droplets, while maintaining high spatial resolution (*ca.* 30 µm). Each leaf was placed on an integrated platform at the base of the camera stand where the abaxial and adaxial surfaces of the leaves were imaged. A blue LED light at a wavelength of 470 nm (StellarNet Inc., Tampa, FL, USA) illuminated the droplets during the imaging process. After imaging, the photographs of both the top and bottom leaf surfaces were processed using ImageJ, a public domain, Java-based image processing software. The image processing procedure used in the study was similar to that described earlier by Martin [32]. However, some modifications were made to accommodate the larger droplet spectrum produced by the TT110-015 nozzles used in the study. Lab color space was used to detect the droplets, with the red threshold color chosen to align with the Rocket Red color of the fluorescent dye. In Lab color space, the 'L', 'a' and 'b' minimum and maximum values were set to 55 and 255, 179 and 205, and 52 and 115, respectively. Spray droplet particles were determined by setting the minimum and maximum pixel area size of the droplets between 10 and 4000 pixels. Circularity values were set between 0.00 and 1.0 to include all of the droplets, regardless of shape. The Show: Outlines option displayed the outlines of the individual droplets and the images were saved for the top and the bottom leaf surfaces. Figure 6 illustrates the enhanced (Figure 6A), selected (Figure 6B) and computer drawings (Figure 6C) of the image of spray droplets on the top surface of a Palmer amaranth leaf as an example.

(**A**)
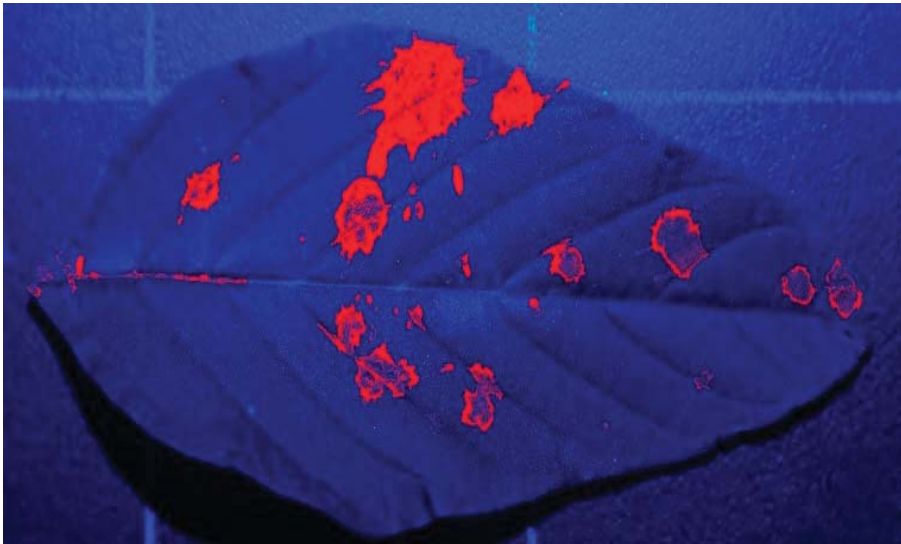
Figure 6. *Cont.*
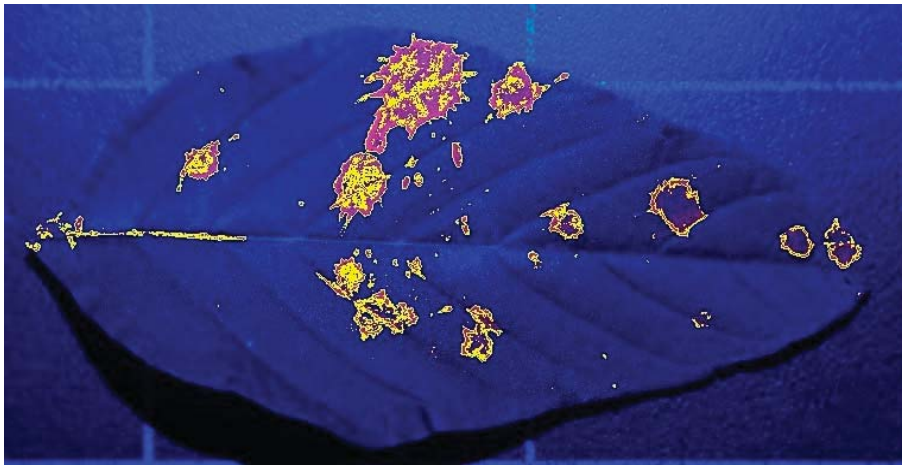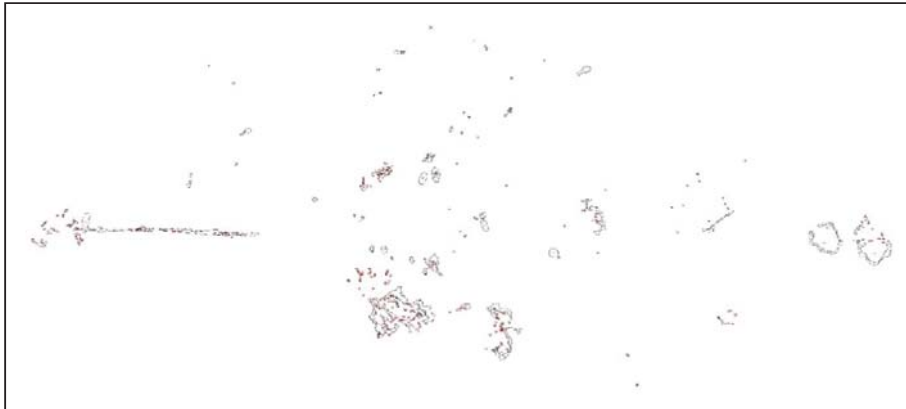
Figure 6. Fluorescent images of a Palmer amaranth leaf processed by ImageJ software: enhanced image of spray droplets (**A**), selected image of spray droplets (**B**) and the computer drawing of spray droplets (**C**).

Thus, the fluorescent imaging provided data on the number of droplets found in each sample of leaves collected. Spray droplet density (droplets/cm^2) on the adaxial and abaxial surfaces of the weed foliage was calculated using the area of each leaf determined by a leaf area meter (Model 3100, Li-Cor, Lincoln, NE, USA). Because the droplet density data were highly variable, the percentage of spray droplets on the adaxial and abaxial surfaces of the leaves was calculated for each sample collected from the designated locations in each treated block to compare the treatments using a common format.

2.3. Data Analysis

Spray deposits, as a percentage of the target application rate, were highly variable and comprised of values ranging from 0 to 100%. Because of the high variability of the data, they were transformed to arcsine $\sqrt{p}$, where p = original variates in proportions [35]. The spray droplet density of the fluorescent imaging data was transformed to log $(x + 1)$, where x = the original variate. When the mean is positively correlated with the variance, the logarithmic transformation is likely to remedy the situation, and make the variance independent of the mean [36]. Figure 7 shows the functional

relationship between the variance and the mean, with an R^2 of 0.9033 ($p < 0.0001$; df = 14) and a highly significant slope coefficient ($b = 70.7$; $t = 11.4$; $p < 0.0001$), which indicates that the data do not meet the assumptions of the analysis of variance. The adequacy of the transformation in stabilizing the variance was achieved following transformation by calculating the correlation coefficient between the two parameters (Figure 8) as suggested by several researchers [36–39]. The coefficient of determination between the two parameters was 0.11, with a non-significant slope coefficient ($b = 0.37$; $t = 1.32$; $p > 0.21$). The transformed fluorescent droplet density data were used for statistical analysis. All other data were analyzed without transformation. The analysis of variance of the data was conducted using the Proc GLIMMIX procedure (SAS) and least square means were separated using the lines option at $p < 0.05$ when sample size was equal [40]. The replicated block effects were not significant for any of the data discussed in this study.
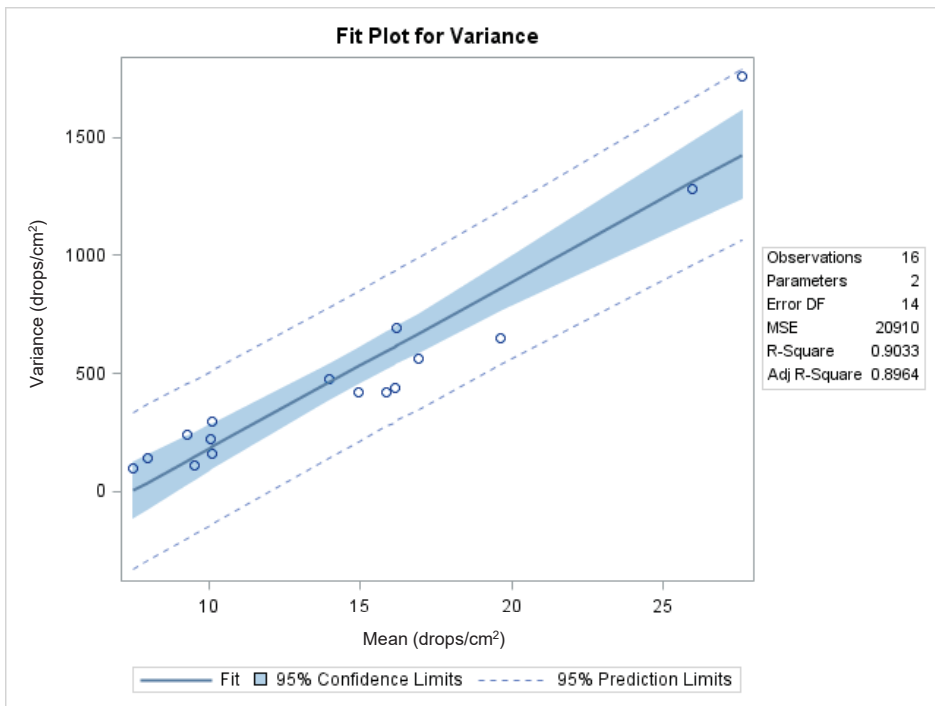
Figure 7. Relationship between the original variance and original mean of spray droplet density of the fluorescent imaging data.
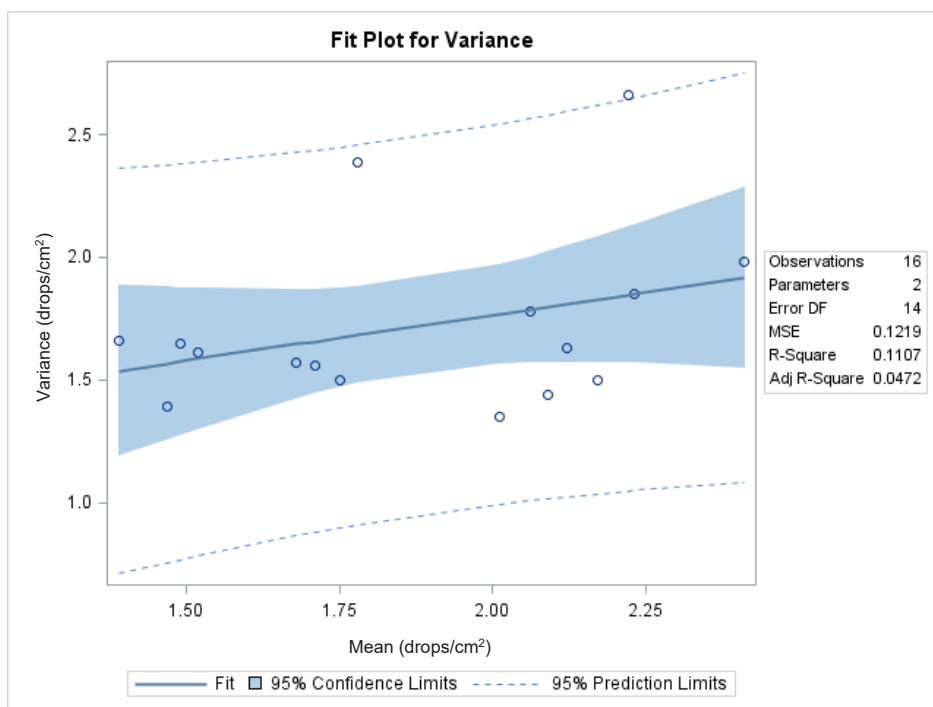
Figure 8. Relationship between the transformed variance and transformed mean of spray droplet density of the fluorescent imaging data in log (*x* + 1) transformed scale, where *x* is the original variate.

3. Results

Meteorological data for each test/replication combination are presented in Table 2. Mean temperature and relative humidity remained relatively constant. Wind speed was variable; however, the angular deviation of the wind from row orientation was well within 40° used for studies designed to mitigate spray drift [41]. Moreover, each test plot was separated by 5 m from each other as shown in Figure 1 to mitigate the effect of cross winds that can move spray deposits between plots.

Table 2. Meteorological data during the test periods.

Temperature (C)	Relative Humidity (%)	Wind Speed (km/h)	Wind Direction (°)	Crosswind [a]
		Test 1		
31.7–33.2	59–67	(8.8–13.9)	175–200	15–40°
		Test 2		
33.7–34.5	55.1–57.8	(7.2–10.2)	174–200	15–41°

[a] Angular deviation of the wind from row orientation (215°).

3.1. Spray Droplet Spectra on WSPs

The spray droplet characteristics revealed from the WSP samplers ($D_{v0.1}$ and $D_{v0.5}$) were not significantly different between treatments in Study 1 (Table 3). However, the $D_{v0.9}$ of the deposits was higher for the backpack sprayer than those for the RPAAS aircraft, as would be expected since the backpack sprayer was operated at a lower pressure. The spray droplet spectra ($D_{v0.1}$, $D_{v0.5}$ and $D_{v0.9}$) were not significantly different between treatments in Study 2, likely due to the small

sample size collected. Numerically, the backpack sprayer again yielded a larger droplet spectrum. The spray droplet density (drops/cm^2) and % area coverage were higher for the high-volume treatment (140 L·ha^{-1}) applied with the backpack sprayer than those for the low-volume treatments (18.7 and 37.4 L·ha^{-1}) applied with the RPAAS platform in both Study 1 and Study 2 (Tables 3 and 4).

Table 3. Spray droplet spectra parameters sampled by WSP collectors in Study 1 [a].

Treatment	$D_{v0.1}$ (μm)	$D_{v0.5}$ (μm)	$D_{v0.9}$ (μm)	Droplet Density (Drops/cm^2)	Coverage (%)
RPAAS-2	253.6 a	517.4 a	617.5 b	24.4 b	3.5 b
RPAAS-4	286.6 a	482.1 a	625.2 b	26.5 b	6.0 b
BP-15	342.8 a	651.8 a	839.4 a	49.2 a	18.6 a
$F_{2,53}$	1.55 [ns]	2.57 [ns]	3.48 *	6.24 **	24.1 **
p	0.22	0.09	0.04	0.0037	0.0001

[a] Least square means were separated using the lines option at $p = 5\%$. Means followed by the same lower-case letter are not significantly different. [ns] = Not significant. *, ** significant and highly significant, respectively. "a" and "b" represent means separation.

Table 4. Spray droplet parameters sampled by WSP collectors in Study 2 [a].

Treatment	$D_{v0.1}$ (μm)	$D_{v0.5}$ (μm)	$D_{v0.9}$ (μm)	Droplet Density (Drops/cm^2)	Coverage (%)
RPAAS-2	246.5 a	490.9 a	644.0 a	16.9 b	4.9 b
RPAAS-4	263.3 a	540.4 a	706.6 a	38.7 b	10.3 b
BP-15	276.7 a	574.3 a	768.8 a	51.1 a	19.8 a
$F_{2,53}$	0.29 [ns]	0.75 [ns]	0.98 [ns]	5.72 **	7.84 **
p	0.75	0.48	0.38	0.0056	0.001

[a] Least square means were separated using the lines option at $p = 5\%$. Means followed by the same lower-case letter are not significantly different. [ns] = Not significant. ** significant and highly significant, respectively.

The spray application efficiency, which is the percent of spray deposits collected on artificial samplers relative to the theoretical application rate, in Study 1 and Study 2 is shown in Figures 9 and 10, respectively. The spray application efficiency for each treatment was the same for Study 1 ($F = 1.94$; $p > 0.15$; df = 2,49) as it was for Study 2 ($F = 0.73$; $p > 0.48$; df = 2,53).
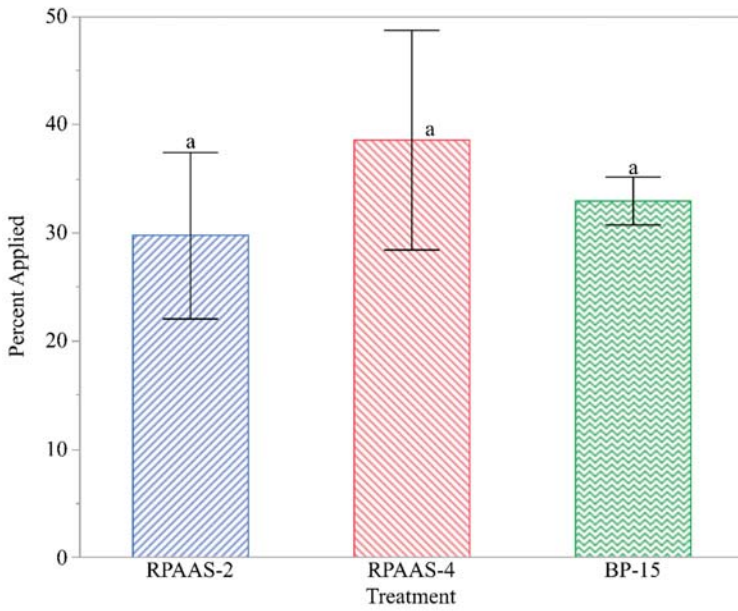
Figure 9. Percent of spray deposits collected on WSP samplers relative to target application rate in Study 1. Data analysis was based upon arcsine transformation. Bars with original means ± SEM with the same lower-case letter are not significantly different ($p > 0.05$).
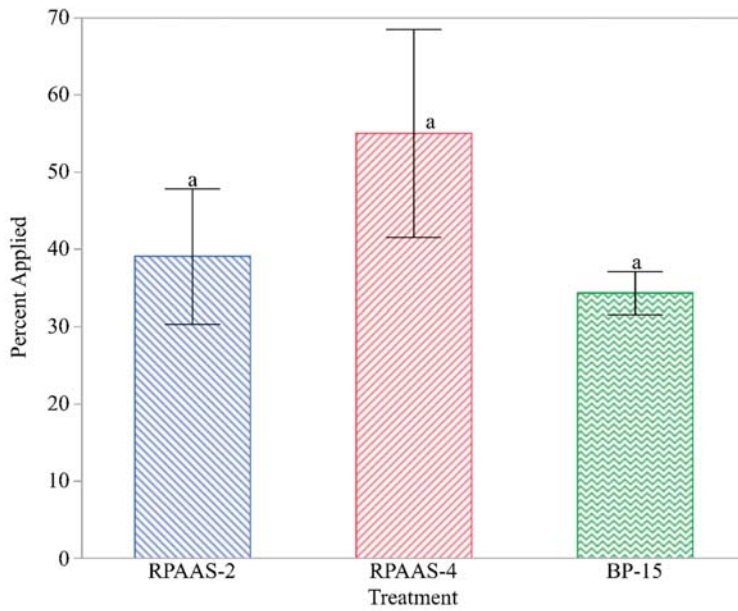
Figure 10. Percent of spray deposits collected on WSP samplers relative to target application rate in Study 2. Data analysis was based upon arcsine transformation. Bars with original means ± SEM with the same lower-case letter are not significantly different ($p > 0.05$).

3.2. Fluorescent Droplets on Weed Leaves

Droplet density, determined by fluorescent imaging on adaxial and abaxial surfaces of Palmer amaranth and ivyleaf morningglory leaves for the RPAAS platforms and the backpack sprayer in Studies 1 and 2, are shown in Tables 5 and 6, respectively. Transformed means are presented in original scale to maintain clarity. Droplet density varied between treatments and leaf surfaces for both Palmer amaranth and morningglory in Studies 1 and 2. Interactions between the treatments and the leaf surfaces were observed for both studies and for both weed species. Droplet density on the adaxial leaf surfaces of Palmer amaranth and morningglory leaves was higher for the BP-15 treatment than those for the RPAAS platforms in Studies 1 and 2. The abaxial leaf surfaces of both weed species had greater droplet density with RPAAS-4 compared to RPAAS-2 treatment and that the RPAAS-4 treatment resulted in greater droplet density on the abaxial leaf surfaces of morningglory than the BP-15 treatment. Droplet density test results for Study 2 were similar to Study 1 (Table 6).

Table 5. Fluorescent imaging of spray droplet density (drops/cm^2) on the top and the bottom surface of weed leaves in Study 1.

Treatment	Palmer Amaranth		Morningglory	
	Top	Bottom	Top	Bottom
RPAAS-2	13.09 b	0.83 d	9.98 b	0.94 d
RPAAS-4	15.55 b	3.86 c	8.99 b	3.42 c
BP-15	36.45 a	3.12 c	29.77 a	0.90 d
Treatment (T)	$F = 14.4$; $p < 0.0001$; df = 2,102		$F = 7.4$; $p > 0.0009$; df = 2,106	
Surface (S)	$F = 85.6$; $p < 0.0001$; df = 1,102		$F = 123.5$; $p < 0.0001$; df = 1,106	
T × S	$F = 4.3$; $p > 0.016$; df = 2,102		$F = 4.3$; $p > 0.016$; df = 2,106	

Droplet density data were transformed to log $(x + 1)$. Original means within each column followed by the same lower-case letters are not significantly different ($p = 5\%$).

Table 6. Fluorescent imaging of spray droplet density (drops/cm^2) on the top and the bottom surface of weed leaves in Study 2.

Treatment	Palmer Amaranth		Morningglory	
	Top	Bottom	Top	Bottom
RPAAS-2	22.30 b	1.75 d	14.08 b	2.43 d
RPAAS-4	42.14 b	5.80 c	21.48 b	5.44 c
BP-15	63.83 a	3.28 cd	51.76 a	1.86 d
Treatment (T)	$F = 4.1$; $p > 0.02$; df = 2,94		$F = 4.9$; $p > 0.0094$; df = 2,106	
Surface (S)	$F = 268.9$; $p < 0.0001$; df = 1,94		$F = 189.7$; $p < 0.0001$; df = 1,106	
T × S	$F = 3.9$; $p > 0.02$; df = 2,94		$F = 16.3$; $p > 0.0001$; df = 2,106	

Data were transformed to log $(x + 1)$. Original means within each column followed by the same lower-case letters are not significantly different ($p = 5\%$).

Tables 7 and 8 describe the percent of spray droplets deposited in the adaxial and abaxial leaf surfaces of weed foliage in Study 1 and Study 2, respectively. In Study 1, the proportion of spray droplets on Palmer amaranth was significantly higher on the abaxial leaf surface when the spray rate was 37.4 L·ha^{-1} (20.76%) than when the spray rate was 18.7 L·ha^{-1} (9.30%) for the RPAAS platform. Likewise, the proportion of spray droplets on morningglory was significantly higher on the abaxial leaf surface when the spray rate was 37.4 L·ha^{-1} (30.25%) than when the spray rate was 18.7 L·ha^{-1} (9.50%). In Study 2, similar results were evident. The proportion of spray droplets on the abaxial leaf surface for the Palmer amaranth was 20.93% vs. 6.28%, while that for the morningglory was 27.54% vs. 12.47% for the 37.4 and 18.7 L·ha^{-1} spray rates, respectively. The BP-15 treatment resulted in deposition of only 6% of the total droplets on abaxial surface (average of both weeds) in both studies. The RPAAS-4 treatment in both studies deposited approximately 25% of the total droplets on abaxial surface (average of both weeds), which was four times than that of BP-15 treatment (Tables 7 and 8).

Table 7. Fluorescent imaging of percent of spray droplets in the top and the bottom surface of weed leaves in Study 1.

Treatment	Palmer Amaranth		Morningglory	
	Top	Bottom	Top	Bottom
RPAAS-2	90.70 a	9.30 d	90.50 a	9.50 d
RPAAS-4	79.24 b	20.76 c	69.75 b	30.25 c
BP-15	91.34 a	8.66 d	96.52 a	3.48 d
Treatment (T)	$F = 0.0; p > 1.0;$ df = 2,102		$F = 0.1; p > 1.0;$ df = 2,98	
Surface (S)	$F = 493.2; p < 0.00001;$ df = 1,102		$F = 416.0; p < 0.00001;$ df = 1,98	
T × S	$F = 5.7; p < 0.0045;$ df = 2,102		$F = 21.7; p < 0.0001;$ df = 2,98	

Means within each column followed by the same lower-case letters are not significantly different ($p = 5\%$).

Table 8. Fluorescent imaging of percent of spray droplets in the top and the bottom surface of weed leaves in Study 2.

Treatment	Palmer Amaranth		Morningglory	
	Top	Bottom	Top	Bottom
RPAAS-2	93.72 a	6.28 d	87.53 a	12.47 d
RPAAS-4	79.07 b	20.93 c	72.46 b	27.54 c
BP-15	92.91 a	7.09 d	94.89 a	5.11 d
Treatment (T)	$F = 0.0; p > 1.0;$ df = 2,106		$F = 0.0; p > 1.0;$ df = 2,106	
Surface (S)	$F = 635.2; p < 0.00001;$ df = 1,106		$F = 632.5; p < 0.0001;$ df = 1,106	
T × S	$F = 10.1; p < 0.0045;$ df = 2,106		$F = 22.5; p < 0.0001;$ df = 2,106	

Means within each column followed by the same lower-case letters are not significantly different ($p = 5\%$).

4. Discussion

4.1. Spray Droplet Spectra

The percent of applied spray on WSPs did not significantly differ among treatments in either of the two studies. The total percent spray deposits on WSP samplers (mean ± SEM) were 31.7 ± 5.3, 40.3 ± 8.1 and 33.0 ± 2.3 for RPAAS-2, RPAAS-4, and the backpack treatments, respectively, in Study 1. The total spray deposits (mean ± SEM) were 42.4 ± 8.9, 59.8 ± 12.2 and 36.7 ± 9.1 for RPAAS-2, RPAAS-4, and the backpack treatments, respectively, in Study 2. Although these values were numerically different, statistical differences between treatments were not realized likely due to small sample size. However, test results indicate that although all of the spray application systems were equally effective in the delivery of spray deposits as sampled on artificial collectors, none of the systems were able to produce 100% of the targeted spray rates.

Our data agree with Wang et al. [42], who reported that the amount of imidacloprid ($\mu g/cm^2$) deposited on wheat did not vary between an RPAAS and a conventional backpack sprayer. In another study on wheat, Wang et al. found that with higher spray volume (>18.8 $L \cdot ha^{-1}$) and with coarser nozzles, deposition of tebuconazole fungicide with a spray drone was similar to that of a conventional backpack sprayer, but the deposition was depressed at the lower spray application rate (<9.0 $L \cdot h^{-1}$) with fine nozzles. Hill and Inaba [43] studied the deposition of deltamethrin and permethrin formulations on WSP samplers and found a significant linear relationship between μg of the chemicals/WSP and spray droplets per cm^2 with similar size droplet spectra. This indicates that droplet density from non-active spray applications should be a good indicator of active formulation spray deposits. Test results reported by Hill and Inaba and Wen et al. [44] indicate that the spray quality assessments with WSPs are reliable when using conventional hydraulic spray nozzles.

Despite the difference in operational parameters between the RPAAS platforms and the backpack sprayer, no significant difference in $Dv_{0.5}$ between the RPAAS and the backpack treatments were observed. The operational parameters used in this study were closer to those used by Qin et al. [45],

who reported testing a UAV flown at 3.5 m height and 4 m/s ground speed with a fungicide over a wheat canopy and compared that to a backpack sprayer operated at 0.5 m height and 0.8 to 1.0 m s^{-1} ground speed. Although the spray volume (140 L·ha^{-1}) applied with the backpack sprayer was 3.7 to 7.5 times greater than those of the RPAAS treatments, droplet size was not affected by the carrier volume. In a laboratory study, Creech et al. [26] evaluated the effects of nozzle type, orifice size, herbicide active ingredients, pressure, and carrier volume on the droplet spectra of the spray, and found that when averaged across all the experimental variables, the herbicide carrier volume had the least effect on $D_{v0.5}$ spray droplets. When the carrier volume increased from 47 to 187 L·ha^{-1}, $D_{v0.5}$ increased only by 5%, indicating that the droplet size of the herbicides tested was not highly dependent on spray volume. Even though the 37.6 L·ha^{-1} application rate was achieved by making two passes over the research plots, there is no expectation that this should change the resulting droplet spectrum.

4.2. Fluorescent Droplets on Weed Leaves

Data reported herein indicate that the backpack sprayer with a 140 L·ha^{-1} spray volume produced only 6% of the total number of applied spray droplets on the abaxial surface, while the RPAAS aircraft with a 37.4 L·ha^{-1} spray volume produced a 4-fold increase in the number of spray droplets on the abaxial surface. Thus, it is likely that this would help improve the efficacy of contact herbicides against weed foliage, because it increases the probability of a spray droplet occupying an active site on the under surface of the leaf. These data suggest that leaf fluttering caused by rotor downwash likely caused this increased spray deposition on the abaxial surfaces of Palmer amaranth and morningglory leaves.

The results reported here corroborate research data which indicate that downwash and wind turbulence created by rotor blades of RPAAS aircraft assist in droplet deposition and canopy penetration [46–52]. For instance, Qing et al. [48] studied the movement of spray plumes in the laboratory at different rotor speeds, using an 8-rotor RPAAS and found that the spray angle of the nozzles was reduced with an increase in the speed of the downwash flow and spray droplets tended to move towards the direction of the rotors. The reduction in nozzle spray angle is known to be highly correlated with an increase in air velocity past a nozzle. Songchao et al. [53] used a single rotor unmanned helicopter to study downwash distribution using a computational fluid dynamics model and found that the downwash covered an area equivalent to the rotor radius of 3.0 m in size with a boundary velocity of 0.5 m·s^{-1}. This appears to indicate that the downwash effect extends beyond the immediate vicinity of the aircraft. Yang et al. [54] reported that the downwash airflow of the RPAAS rotor caused a pressure differential between the upper and lower surfaces of the leaf producing a torque and thus enabling the spray droplets to penetrate as much as 4-fold to the bottom surface of the leaf.

5. Conclusions

The spray application efficiency described as the percent of spray deposits collected on an artificial sampler for the RPAAS systems at the 18.7 and 37.4 L·ha^{-1} spray rates was comparable to that for the backpack sprayer at a 140.0 L·ha^{-1} spray rate. The spray droplets, $D_{v0.5}$, deposited on an artificial collector were statistically similar for both backpack and RPAAS treatments, although these spray platforms were operated at different heights and ground speeds. Test results suggest that if the nozzles were kept similar for the remotely piloted aerial and the conventional ground spray application systems, operational protocols (application height and ground speed) may not significantly influence the spray droplet spectra characteristics. Higher-volume treatment (140 L·ha^{-1}) applied with the backpack sprayer resulted in greater fluorescent droplet density on the adaxial leaf surface compared to the lower-volume RPAAS treatments. However, the highest spray rate RPAAS platform (37.4 L·ha^{-1}) resulted in the deposition of the largest proportion of droplets on the abaxial surface of weed foliage, relative to the total number of depositing droplets. This suggests that the rotor downwash and wind turbulence created by the RPAAS aircraft when operated at a ground speed of 4.0 m·s^{-1} to achieve 37.4 L·ha^{-1} spray application rate likely helped flip leaves over and enabled spray deposition onto the lower surface of weed canopy. It is important to note that the spray application rate (37.4 L·ha^{-1}) was

achieved by flying the aircraft twice over the test plots at 4 m·s^{-1} and this could have likely helped to increase spray deposition on the abaxial surfaces of weed leaves. However, if the 37.4 L·ha^{-1} spray application rate was achieved with a single pass of the aircraft, it would have required a 2 m s^{-1} ground speed, and the slower ground speed would have increased the residence time of the aircraft over the weed canopy, thus increasing the downwash effect of the rotors. Whether or not a single pass of the aircraft with a delivery volume at 37.4 L·ha^{-1} would similarly increase under-leaf surface deposition remains conjectural and should be investigated. Test results suggest that RPAAS systems may be used for herbicide applications against post-emergence weeds in lieu of conventional backpack sprayers. Data reported here indicate that further research should be conducted to evaluate herbicidal efficacy of spray applications from the RPAAS platforms compared to backpack sprayers.

Author Contributions: Conceptualization, D.M., V.S. and M.B., methodology, D.M., V.S., post M.B.; formal analysis, M.A.L.; writing—original draft preparation, D.M. post M.A.L., writing—review and editing, M.A.L., D.M., post V.S. All authors have read and agreed to the published version of the manuscript.

Conflicts of Interest: The authors declare no conflict of interest. Disclaimer: The use of trade, firm, or corporation names in this publication is for the information and convenience of the reader. Such use does not constitute an official endorsement or approval by the United States Department of Agriculture or the Agricultural Research Service of any product or service to the exclusion of others that may be suitable.

References

1. Buchanan, G.A.; Burns, E.R. Influence of weed competition on cotton. *Weed Sci.* **1970**, *18*, 149–154. [CrossRef]
2. Staniforth, D.W.; Weber, C.R. Effects of annual weeds on the growth and yield of soybeans 1. *Agron. J.* **1956**, *48*, 467–471. [CrossRef]
3. Cousens, R. A simple model relating yield loss to weed density. *Ann. Appl. Biol.* **1985**, *107*, 239–252. [CrossRef]
4. University, K.S. Left Uncontrolled, Weeds Would Cost Billions in Economic Losses Every Year. *ScienceDaily*. 2016. Available online: https://www.sciencedaily.com/releases/2016/05/160516130720.htm (accessed on 18 September 2020).
5. Soltani, N.; Dille, J.; Burke, I.; Everman, W.; VanGessel, M.; Davis, V.; Sikkema, P. Potential corn yield losses due to weeds in North America. *Weed Technol.* **2016**, *30*. [CrossRef]
6. Gianessi, L.P.; Nathan, P.R. The Value of Herbicides in U.S. Crop Production. *Weed Technol.* **2007**, *21*, 559–566. [CrossRef]
7. Sikkema, P.H.; Hamill, A.S. Weed costs per day (2). In *New Perspectives into Research on Early Weed Control*; Syngenta: Basel, Switzerland, 2005; p. 4.
8. Gianessi, L.P. The increasing importance of herbicides in worldwide crop production. *Pest. Manag. Sci.* **2013**, *69*, 1099–1105. [CrossRef]
9. Hassler, S.C.; Baysal-Gurel, F. Unmanned Aircraft System (UAS) Technology and Applications in Agriculture. *Agronomy* **2019**, *9*, 618. [CrossRef]
10. Pflanz, M.; Nordmeyer, H.; Schirrmann, M. Weed mapping with UAS imagery and a Bag of Visual Words based image classifier. *Remote Sens.* **2018**, *10*, 1530. [CrossRef]
11. Rasmussen, J.; Nielsen, J.; Streibig, J.; Jensen, J.; Pedersen, K.; Olsen, S. Pre-harvest weed mapping of Cirsium arvense in wheat and barley with off-the-shelf UAVs. *Precis. Agric.* **2019**, *20*, 983–999. [CrossRef]
12. Bah, M.D.; Hafiane, A.; Canals, R. Weeds Detection in UAV Imagery Using SLIC and the Hough Transform. In Proceedings of the 2017 Seventh International Conference on Image Processing Theory, Tools and Applications (IPTA), Montreal, QC, Canada, 28 November–1 December 2017; pp. 1–6.
13. Baluja, J.; Diago, M.P.; Balda, P.; Zorer, R.; Meggio, F.; Morales, F.; Tardaguila, J. Assessment of vineyard water status variability by thermal and multispectral imagery using an unmanned aerial vehicle (UAV). *Irrig. Sci.* **2012**, *30*, 511–522. [CrossRef]

14. Ge, Y.; Thomasson, J.A.; Sui, R. Remote sensing of soil properties in precision agriculture: A review. *Front. Earth Sci.* **2011**, *5*, 229–238. [CrossRef]

15. Saari, H.; Pellikka, I.; Pesonen, L.; Tuominen, S.; Heikkilä, J.; Holmlund, C.; Mäkynen, J.; Ojala, K.; Antila, T. Unmanned Aerial Vehicle (UAV) Operated Spectral Camera System for Forest and Agriculture Applications. In *Remote Sensing for Agriculture, Ecosystems, and Hydrology XIII*; Neale, C.M.U., Maltese, A., Eds.; SPIE—International Society for Optics and Photonics: Bellingham, WA, USA, 2011; p. 81740H.

16. Huang, Y.; Reddy, K.N.; Fletcher, R.S.; Pennington, D. UAV Low-altitude remote sensing for precision weed management. *Weed Technol.* **2018**, *32*, 2–6. [CrossRef]

17. Göktoğan, A.H.; Sukkarieh, S.; Bryson, M.; Randle, J.; Lupton, T.; Hung, C. A rotary-wing unmanned air vehicle for aquatic weed surveillance and management. *J. Intell. Robot. Syst.* **2010**, *57*, 467. [CrossRef]

18. Castaldi, F.; Pelosi, F.; Pascucci, S.; Casa, R. Assessing the potential of images from unmanned aerial vehicles (UAV) to support herbicide patch spraying in maize. *Precis. Agric.* **2017**, *18*, 76–94. [CrossRef]

19. Peña, J.M.; Torres-Sánchez, J.; de Castro, A.I.; Kelly, M.; López-Granados, F. Weed mapping in early-season maize fields using object-based analysis of unmanned aerial vehicle (UAV) images. *PLoS ONE* **2013**, *8*, e77151. [CrossRef]

20. Rasmussen, J.; Nielsen, J.; Garcia-Ruiz, F.; Christensen, S.; Streibig, J.C. Potential uses of small unmanned aircraft systems (UAS) in weed research. *Weed Res.* **2013**, *53*, 242–248. [CrossRef]

21. Ahmad, F.; Qiu, B.; Dong, X.; Ma, J.; Huang, X.; Ahmed, S.; Chandio, F.A. Effect of operational parameters of UAV sprayer on spray deposition pattern in target and off-target zones during outer field weed control application. *Comput. Electron. Agric.* **2020**, *172*, 105350. [CrossRef]

22. Meyer, C.J.; Norsworthy, J.K.; Kruger, G.R.; Barber, T. Effects of Nozzle Selection and Ground Speed on Efficacy of Liberty and Engenia Applications and Their Implication on Commercial Field Applications. *Weed Technol.* **2016**, *30*, 401–414. [CrossRef]

23. DiTomaso, J.M.; Smith, B.S. Linking ecological principles to tools and strategies in an EBIPM program. *Rangelands* **2012**, *34*, 30–34. [CrossRef]

24. Bellinder, R.R.; Kirkwyland, J.J.; Wallace, R.W.; Colouhoun, J.B. Weed Control and Potato (Solanum tuberosum) yield with banded herbicides and cultivation. *Weed Technol.* **2000**, *14*, 30–36. [CrossRef]

25. Martin, D.E.; Woldt, W.E.; Latheef, M.A. Effect of Application Height and Ground Speed on Spray Pattern and Droplet Spectra from Remotely Piloted Aerial Application Systems. *Drones* **2019**, *3*, 83. [CrossRef]

26. Creech, C.F.; Henry, R.S.; Fritz, B.K.; Kruger, G.R. Influence of herbicide active ingredient, nozzle type, orifice size, spray pressure, and carrier volume rate on spray droplet size characteristics. *Weed Technol.* **2015**, *29*, 298–310. [CrossRef]

27. McKinlay, K.; Ashford, R.; Ford, R. Effects of drop size, spray volume, and dosage on paraquat toxicity. *Weed Sci.* **1974**, *22*, 31–34. [CrossRef]

28. Wolf, T.M.; Liu, S.H.; Caldwell, B.C.; Hsiao, A.I. Calibration of greenhouse spray chambers: The importance of dynamic nozzle patternation. *Weed Technol.* **1997**, *11*, 428–435. [CrossRef]

29. Culpepper, A.S.; Webster, T.M.; Sosnoskie, L.M.; York, A.C.; Nandula, V. Glyphosate-resistant Palmer amaranth in the United States. In *Glyphosate Resistance in Crops and Weeds: History, Development, and Management*; John Wiley & Sons: Hoboken, NJ, USA, 2010; pp. 195–212.

30. Norsworthy, J.K. Use of soybean production surveys to determine weed management needs of South Carolina farmers. *Weed Technol.* **2003**, *17*, 195–201. [CrossRef]

31. Ward, S.M.; Webster, T.M.; Steckel, L.E. Palmer amaranth (Amaranthus palmeri): A review. *Weed Technol.* **2013**, *27*, 12–27. [CrossRef]

32. Martin, D. A fluorescent imaging technique for quantifying spray deposits on plant leaves. *At. Sprays* **2014**, *24*, 367–373. [CrossRef]

33. Martin, D.E.; Latheef, M.A. Aerial electrostatic spray deposition and canopy penetration in cotton. *J. Electrost.* **2017**, *90*, 38–44. [CrossRef]

34. Whittney, R.W.; Gardisser, D.R. *DropletScan Operators Manual*; WRK of Oklahoma and WRK of Arkansas: Stillwater, OK, USA, 2003.

35. Sokal, R.R.; Rohlf, R.R. *Biometry—The principles and Practice of Statistics in Biological Research*; W. H. Freeman and Company: San Francisco, CA, USA, 1969.

36. Guppy, J.; Harcourt, D. Spatial pattern of the immature stages and teneral adults of *Phyllophaga spp.*(Coleoptera: Scarabaeidae) in a permanent meadow. *Can. Entomol.* **1970**, *102*, 1354–1359. [CrossRef]

37. Harcourt, D. Population dynamics of *Leptinotarsa decemlineata* (Say) in eastern Ontario: I. Spatial pattern and transformation of field counts. *Can. Entomol.* **1963**, *95*, 813–820. [CrossRef]

38. Mukerji, M.; Harcourt, D. Spatial pattern of the immature stages of *Hylemya brassicae* on cabbage. *Can. Entomol.* **1970**, *102*, 1216–1222. [CrossRef]

39. Miller, C.; Mukerji, M.; Guppy, J. Notes on the spatial pattern of *Hypera postica* (Coleoptera: Curculionidae) on alfalfa. *Can. Entomol.* **1972**, *104*, 1995–1999. [CrossRef]

40. Westfall, P.H.; Tobias, R.D.; Wolfinger, R.D. *Multiple Comparisons and Multiple Tests Using SAS*; SAS Institute: Cary, NC, USA, 2011.

41. Nuyttens, D.; De Schampheleire, M.; Baetens, K.; Sonck, B. The Influence of Operator-Controlled Variables on Spray Drift from Field Crop Sprayers. *Trans. Asabe* **2007**, *50*, 1129–1140. [CrossRef]

42. Wang, G.; Lan, Y.; Yuan, H.; Qi, H.; Chen, P.; Ouyang, F.; Han, Y. Comparison of spray deposition, control efficacy on wheat aphids and working efficiency in the wheat field of the unmanned aerial vehicle with boom sprayer and two conventional knapsack sprayers. *Appl. Sci.* **2019**, *9*, 218. [CrossRef]

43. Hill, B.; Inaba, D. Use of water-sensitive paper to monitor the deposition of aerially applied insecticides. *J. Econ. Entomol.* **1989**, *82*, 974–980. [CrossRef]

44. Wen, Y.; Zhang, R.; Chen, L.; Huang, Y.; Yi, T.; Xu, G.; Li, L.; Hewitt, A.J. A new spray deposition pattern measurement system based on spectral analysis of a fluorescent tracer. *Comput. Electron. Agric.* **2019**, *160*, 14–22. [CrossRef]

45. Qin, W.; Xue, X.; Zhang, S.; Gu, W.; Wang, B. Droplet deposition and efficiency of fungicides sprayed with small UAV against wheat powdery mildew. *Int. J. Agric. Biol. Eng.* **2018**, *11*, 27–32. [CrossRef]

46. Xinyu, X.; Kang, T.; Weicai, Q.; Yubin, L.; Huihui, Z. Drift and deposition of ultra-low altitude and low volume application in paddy field. *Int. J. Agric. Biol. Eng.* **2014**, *7*, 23–28.

47. Fengbo, Y.; Xinyu, X.; Ling, Z.; Zhu, S. Numerical simulation and experimental verification on downwash air flow of six-rotor agricultural unmanned aerial vehicle in hover. *Int. J. Agric. Biol. Eng.* **2017**, *10*, 41–53. [CrossRef]

48. Qing, T.; Ruirui, Z.; Liping, C.; Min, X.; Tongchuan, Y.; Bin, Z. Droplets movement and deposition of an eight-rotor agricultural UAV in downwash flow field. *Int. J. Agric. Biol. Eng.* **2017**, *10*, 47–56.

49. Wen, S.; Han, J.; Ning, Z.; Lan, Y.; Yin, X.; Zhang, J.; Ge, Y. Numerical analysis and validation of spray distributions disturbed by quad-rotor drone wake at different flight speeds. *Comput. Electron. Agric.* **2019**, *166*, 105036. [CrossRef]

50. Tan, Y.; Chen, J.; Norton, T.; Wang, J.; Liu, X.; Yang, S.; Zheng, Y. The computational fluid dynamic modeling of downwash flow field for a six-rotor UAV. *Front. Agric. Sci. Eng.* **2018**, *5*, 159–167.

51. Yang, S.; Liu, X.; Chen, B.; Li, S.; Zheng, Y. CFD Models and Verification of the Downwash Airflow of an Eight-Rotor UAV. In Proceedings of the 2019 ASABE Annual International Meeting, St. Joseph, MI, USA, 7–10 July 2019; p. 1.

52. Yang, S.; Zheng, Y.; Liu, X. Research Status and Trends of Downwash Airflow of spray UAVs in Agriculture. *Int. J. Precis. Agric. Aviat.* **2019**, *2*, 1–8. [CrossRef]

53. Songchao, Z.; Xinyu, X.; Zhu, S.; Lixin, Z.; Yongkui, J. Downwash distribution of single-rotor unmanned agricultural helicopter on hovering state. *Int. J. Agric. Biol. Eng.* **2017**, *10*, 14–24. [CrossRef]

54. Yang, Z.; Qi, L.; Wu, Y. Influence of UAV Rotor Down-Wash Airflow for Droplet Penetration. In Proceedings of the 2018 ASABE Annual International Meeting, Detroit, MI, USA, 29 July–1 August 2018; p. 1.

An Approach for Route Optimization in Applications of Precision Agriculture Using UAVs

Kshitij Srivastava [1], Prem Chandra Pandey [2,*] and Jyoti K. Sharma [2]

[1] Department of Electrical Engineering, Shiv Nadar University, Greater Noida 201314, India; ks435@snu.edu.in
[2] Center for Environmental Sciences & Engineering, Shiv Nadar University, Greater Noida 201314, India; jyoti.sharma@snu.edu.in
* Correspondence: Prem26bit@gmail.com or prem.pandey@snu.edu.in

Abstract: This research paper focuses on providing an algorithm by which (Unmanned Aerial Vehicles) UAVs can be used to provide optimal routes for agricultural applications such as, fertilizers and pesticide spray, in crop fields. To utilize a minimum amount of inputs and complete the task without a revisit, one needs to employ optimized routes and optimal points of delivering the inputs required in precision agriculture (PA). First, stressed regions are identified using VegNet (Vegetative Network) software. Then, methods are applied for obtaining optimal routes and points for the spraying of inputs with an autonomous UAV for PA. This paper reports a unique and innovative technique to calculate the optimum location of spray points required for a particular stressed region. In this technique, the stressed regions are divided into many circular divisions with its center being a spray point of the stressed region. These circular divisions would ensure a more effective dispersion of the spray. Then an optimal path is found out which connects all the stressed regions and their spray points. The paper also describes the use of methods and algorithms including travelling salesman problem (TSP)-based route planning and a Voronoi diagram which allows applying precision agriculture techniques.

---

1. Introduction

One of the main objectives of the United Nations is to have sustainable agriculture which can enhance agricultural productivity to meet the food supply-demand of the increasing population without overexploiting and wasting natural resources [1]. The estimated population is likely to reach nine billion from seven billion by 2050 [2,3]. Significant pressure is expected on agricultural systems to meet the continuously increasing needs of the population, thus escalating human pressures on the environment [3–6]. Farming is predominantly done on limited space or regions, which are decreasing day by day due to several factors, such as conversion to other land use categories, e.g., farmland to residential, commercial and industrial buildings [7,8]. With the limited land area available, agriculture will have more pressure for increased crop yield to enhance productivity as well as maintain the food quality to cope up with the increasing population's demands. Several parameters, such as soil moisture, nutrients, such as nitrogen, phosphorus, and potassium [9], water holding capacity, pH and other variables affect crop productivity and thus require continuous monitoring to prevent crop stress. At present, the identification process of stressed regions and preventive measures are performed manually, while the identification of stressed regions is assessed using visual image interpretation using remote sensing and GIS. Moreover, at most of the places, other agricultural applications, such as spraying of pesticides or fertilizers, are performed manually too. This leads to an increased cost and

inefficient use of resources, along with wastage of input resources. To maintain quality and enhance the productivity of crops, precision agriculture (PA) has to be adopted by farmers worldwide [10,11].

In recent decades, there has been an increase in the number of techniques and methods employed in agriculture to enhance crop yield and productivity. Pesticides have been used against insects and pests, while fertilizers are used to improve the fertility of the soil by adding major nutrients to enhance crop productivity [12,13]. Moreover, wastage of these agricultural inputs is more common during steps and processes which, overall, impact the expenses in agriculture. In recent years, there has been a gradual shift towards mechanization in agriculture for harvesting, spraying and drip irrigation which has helped to optimize the amount of water used and reduce the wastage.

In the present era, PA is a new concept that has been introduced in agricultural practices to improve agricultural crop yields and help in decision making using advanced geospatial tools and techniques for analysis [14,15]. This is used worldwide nowadays to reduce labor costs, minimize the time duration and assist in the proper management of fertilizers, pesticides and irrigation activities throughout the field in less time [16]. PA also helps in understanding the soil condition and its parameters over time and aims at addressing this soil spatial variability, but for these tasks, spectral images of the land are required [17]. Therefore, a new concept of PA has been introduced to tackle these problems, such as minimizing wastage of agricultural resources inputs and reducing labor time to increase the productivity of the crops [18]. PA is the science of improving crop yields with assisted management using high technology sensors and analysis tools. Advanced multispectral imaging equipment offers innovations in the practical application of PA techniques. This is useful for the valuation of crop stresses, quality of soils and the vegetative cover, as well as for yield estimation [19,20]. The technique also adopts a concept to minimize the wastages and effective management of fertilizers and pesticides for increased crop yields [18]. The everyday practices of agriculture can be observed by UAVs for soil monitoring, early weed detection, disease and pest control, nutrient assessment and fertilizer applications at different spatial scales [21–23]. These innovative technologies have been implemented and are in demand for new opportunities in PA by farmers to provide stressed maps, pest infestation maps, soil condition, disease control and yield maps [22–25].

The above concepts, when implemented in agricultural practices, undoubtedly result in increased agricultural productivity by protecting crops against pests, insects, disease and any stress. Concepts and methods to provide fertilizers at a particular stressed region effectively at appropriate times are also promoted. To realize this, spectral images and thermal images are obtained from the UAVs, which have a high spatial resolution compared to satellite images and are less susceptible to weather conditions [26–28]. These are useful for regional mapping and analysis where limited areas are being considered and are in focus.

Spectral and reflectance images from UAVs are incorporated for analysis and assessment in agricultural research and agricultural tasks, as well as decision making [29,30]. In 2008, Nebikera conceptualized the use of the spectral camera on drones for aerial imaging and analysis [31]. Research has demonstrated the usage of these spectral images to assess stressed regions as well as stressed crops based on different soil parameters, water content and plant chlorophyll contents [32]. This was recently demonstrated in our previous study [33] by the development of VegNet (Vegetative Network) software to assess crop stress in a large field by extracting different vegetative indices, such as NDVI (normalized difference vegetation index) [34], NDRE (normalized red difference index) [35], EVI (enhanced vegetation index) [36]. We also incorporated other reflectance indices, such as NDVI, TCARI/OSAVI (transformed chlorophyll absorption in reflectance index/optimized soil adjusted vegetation index), etc. These indices were derived from spectral images and demonstrated that they have a positive correlation to stress indicators (water or nutrients). Both TCARI/OSAVI are very sensitive to chlorophyll content variations which are useful to assess the stress condition of vegetation [37]. The spectral images were employed for the detection of stressed regions in the agricultural fields using the VegNet software application (please refer to [33]). VegNet is an application that was developed with the aim of providing the necessary tools to detect stressed crop locations using spectral images obtained from UAVs, and providing the

stressed crops' condition and location and the area covered by those stressed crops. It has been shown that VegNet has the flexibility to use any combination of reflectance indices, or even thermal indices, for detection of stressed regions.

In the past, UAVs have been used for monitoring agricultural fields with spectral images and then calculating the above-mentioned indices which indicate deficiencies in the field. Even the usage of UAVs in non-agricultural activities, such as monitoring natural resources, such as land, water and rivers [38–40], as well as in disaster management [41], has rapidly increased in the past few years. In 2015, Gao [26] demonstrated the use of UAVs for water stress assessment using thermal indices and canopy conductance measurements. Hence, both thermal imagery and spectral imagery obtained from UAVs providing reflectance indices and thermal indices have shown great potential to determine field stress heterogeneity. In 2019, authors developed an application based on a combination of reflectance indices to detect stressed regions in agricultural fields [33].

The soil parameters and use of spectral indicators for water content extraction, plant chlorophyll content and so on have been demonstrated in past research. This was done by extracting different vegetative indices, such as NDVI, NDRE and EVI. While these findings are very helpful in gaining new insights about a farm, these sophisticated vegetative indicators make little sense for a nonprofessional. Even if farmers get to know about the deficiency of nutrients in their crops and the locations of stressed regions, they will still be taking corrective steps manually, which is inefficient and time-consuming, hence optimized use of machinery is suggested. UAVs are also increasingly being used in PA activities, such as administering inputs, apart from monitoring. Thus, UAVs have been employed in supporting PA mapping to effectively manage and provide optimized inputs to agricultural fields, such as water, fertilizers and pesticides, to increase the quality and yield of crops [42,43]. There is still a lot of progress to be made in the way in which corrective measures are applied, such as spraying water, pesticides or fertilizers. Therefore, a system has to be brought to the forefront that addresses the technological gaps and applies the benefits of PA for increasing farm productivity.

Software and information technology (IT) solutions have been developed by researchers on a variety of aspects of precision farming [44–47]. Most of them have focused on PA by using it primarily for monitoring and analysis purposes and not focused on IT-based mechanization and automation [48]. One of the research papers has tried focusing on providing integrated UAV-based PA using an aerial farm robot that takes care of all agriculture-related activities, such as cropping, planting and fertilizing [49]. It used UAVs that were attached with detachable instruments for this purpose. In this system, they applied fertilizer to all parts of the field equally without any regard for spatial nutrient differences in the land. However, what was needed was for the fertilizer to be applied only on stressed regions and not to all the parts of the field, so there must be a feedback mechanism for nutrient deficient regions and application of fertilizer [48]. Analysis using spectral indices will help in identifying stressed regions and will help in site-specific input applications.

Recent studies have focused on studying the effects of several UAV design parameters on spraying outcomes. Qin et al. illustrated and discussed the influence of spraying parameters, such as the operation height and operation velocity of the UAV, on droplet deposition [50]. Studies also revealed spray factors, such as the speed and distance of UAVs for droplet size, distribution and distribution uniformity [51]. It studied factors, such as the speed and distance of UAVs for droplet size, distribution and distribution uniformity. Most of these papers have focused on the spraying while in motion. In contrast, the present paper suggests spraying fertilizers while the UAV is flying over the spray position. This method of spraying would reduce some of the factors associated with UAVs.

All the past research works have been done on spraying fertilizers and pesticides from UAVs on farms and stressed regions of particular shapes and sizes. This paper will open up the possibilities of working in farms and stressed regions of irregular shapes and sizes which were not addressed earlier. There are a few algorithms that can work on farms of all shapes and sizes, and our algorithm is one among them. One of the early research papers used multiple drones on a full field where the drones were spraying parallel to one another in various rows of the farm [52]. However, the method

proposed was not site-specific and no algorithm was proposed for traversing the field. It required the crops to be planted in rows which are to be fed into the system for spraying. In 2013, a unique approach was given where centroidal Voronoi tessellation was used to spread swarm UAVs to cover an infected region. It claimed that the most effective solution, then, is to attack around the infection and contain the situation before fully eradicating the infection. Voronoi divided the region into many parts and drones started spraying from each Voronoi centroid [53]. It could attend to any stressed region, ensure to limit the amount of spraying over healthy plants and avoid overlapping of pesticide spraying. Nevertheless, this method required many UAVs for attending to a single stressed region, making it very resource-intensive. In 2017, another article looked at using UAVs to find stressed regions and then spraying on the stressed patches using a tractor with many spraying nozzles that could be turned on and off depending upon the patches [54]. However, the authors failed to provide an algorithm for spraying on the stressed regions. In 2019, another study looked into site-specific management during the vineyard spraying process. Here, the authors also used UAVs to find stressed regions. They divided the stressed regions into three different zones indicating different levels of canopy vigor. The application map was divided into small and irregular rectangles. The width of the rectangle was decided such that it corresponded to the working width of the sprayer [55]. However, the problem with this approach is that this division of stressed regions is done in the form of a rectangular shape, which is not the most appropriate approach since the spraying happens over a circular area. Hence, rectangular divisions should be replaced with circular divisions to ensure more effective dispersion. This paper combines all the deficiencies present in earlier research to come out with an algorithm for proper spraying of inputs by drones. It provides continuous feedback to the system to allow for spraying of fertilizers on all shapes of stressed regions. Finally, it brings out an optimized route covering all the stressed regions and spray points.

Nevertheless, so far, these UAVs may not have been following optimum paths and routes to deliver inputs in large agricultural fields, wasting time by visiting the same place repeatedly [42,43]. In the past, researchers have addressed this problem by initiating research on route planning for vehicles delivering resources [56] and also for energy saving schemes in machinery utilized in agricultural systems [57]. Cabreira et al. (2019) and Galceran et al. (2013) reviewed the important path planning algorithms used in UAVs [58,59]. Most of the algorithms, such as back-and-forth coverage path planning algorithms, were suitable for continuous spraying in a region. These algorithms used turning maneuvers which increased the time and energy spent at corners, thus giving irregular spraying at the corners of the regions [59]. Other algorithms used were grid-based algorithms, such as the Wavefront algorithm, which utilized regions made of grids for making paths [59]. But grid-based or rectangular divisions-based algorithms are not efficient for spraying as explained in the previous paragraphs. Therefore, to avoid wastage of resources, such as fertilizers or pesticides, by spraying the same places, the paths of UAV movement need to be controlled. Therefore, an optimal path and route should be devised which will allow UAVs to visit the identified region and spray points only once in their trip, thus reducing time and resources [60,61].

This paper removes all the problems associated with the previous research to come out with an algorithm for proper spraying of inputs by drones. The present study attempts to implement an optimal path and route to ensure the effective spraying of fertilizers and pesticides at the identified stressed regions using the optimal path and route quickly, for effective PA. The UAVs will be carrying the fertilizer spray or pesticide spray as per user needs or requirements with shortest optimum trip length covering all points with only a single visit by the UAVs. This article also demonstrates some practical experiences of a travelling salesman problem (TSP), Euclidean distance metrics and a Voronoi diagram, which have been applied to provide optimal paths, routes and points for spraying, using UAVs to deliver effective inputs to agricultural activities to increase crop yields and save time as well as resources from being wasted.

In the present work, Section 2 describes the study area briefly, while Section 3 deals with the materials and methodology adopted in the present study. The various shortcomings of previous

research as well as many novel methods have been suggested which are significant improvements over past research. In Section 3, the paper discusses, in detail, the proposed algorithm used in this paper. In Section 4, the results are discussed, which were obtained with the proposed algorithm. In Section 5, we brief about the challenges faced with the proposed method, and in Section 6, we discuss future improvements that could be possible. At the end, the paper is concluded by recommending some ideas for achieving higher crop productivity.

2. Study Area

The study area chosen for the present study was an agrarian region located around Devagiri village in Haveri Tehsil, Haveri district, located in the state of Karnataka, India. The district has an area of 4851.56 square km and it lies between the latitudinal coordinates of 14.19–15.09° N and longitudinal coordinates of 75.01–75.50° E [33]. Agricultural activities dominate in part of the study area. Maize, paddy, sorghum, and chili are the major crops cultivated in this region. The total land under irrigation in the selected region in Haveri Tehsil is 86.2 km^2, including all varieties of horticulture, vegetable, spice and plantation crops. Spectral images were acquired using UAVs covering the test site (with 490 sq. m), spanning across a length of 3 km in multiple drone flights. These images were acquired in the month of October in the year 2018.

3. Materials and Methods

This section provides the specifications of the UAVs and methodology adopted in the present study. Figure 1 illustrates the schematic diagram with the overall methodology adopted in the present study.
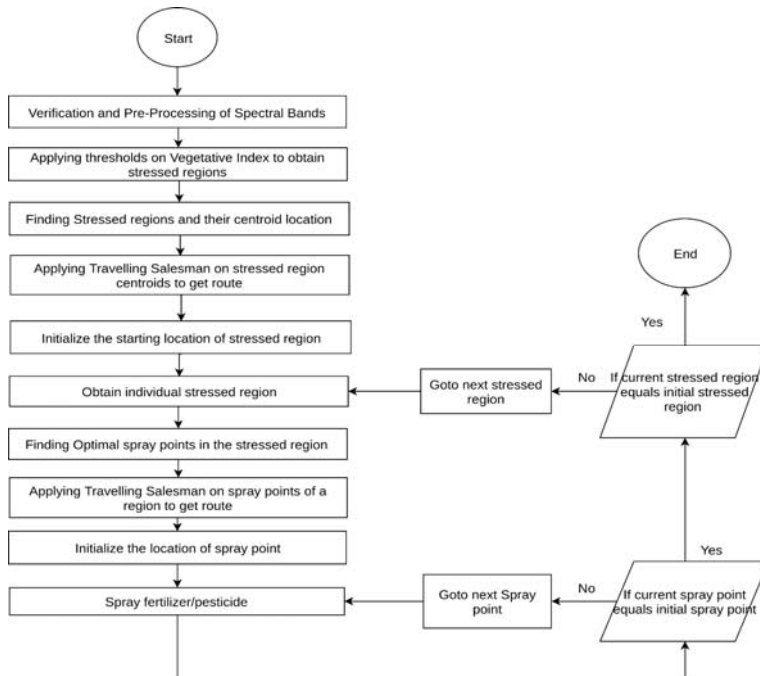
Figure 1. Schematic diagram illustrating the overall methodology adopted in the present study.

3.1. Specifications of UAV

The specifications of the UAV employed for capturing spectral images are discussed in this section and a detailed specification is illustrated in Table 1. A quadcopter UAV (as shown in Figure 2) was

used for this study. It has four brushless direct current (BLDC) motors [62] with carbon fiber propellers and is powered by 10,000 mAh lithium-ion batteries. BLDC motors have the ability to deliver precise control, therefore making them suitable for flying drones. The autonomous flight path of the UAV was designed using mission planner software, and the flight parameters, points and paths were configured in such a way to ensure proper capturing of spectral images for the whole field [63]. Therefore, the necessary instructions were fed into the system to configure the autopilot system. The UAV consists of a Pixhawk PX4 flight controller (FC) having components attached, such as a power system, a global positioning system (GPS), an external compass, a radio control system, etc. The flight controller's function is to generate a control signal for each motor in response to a user's control input [64,65]. It uses sensors to determine vehicle state, which is needed for stabilization, and to enable autonomous control. The vehicle state includes its position, altitude, direction, speed, airspeed, rates of rotation in different directions and battery level of the UAV. The UAV was controlled using a radio communication (RC) controller [66]. This RC controller transmitted control signals to the receiver on the UAV. A GPS sensor was integrated into this flight controller so that the UAV could know the exact locations [67]. A light detection and ranging (LIDAR) sensor was integrated into the UAV so that it could estimate the height of flight [68].

Table 1. Specifications of the UAV employed in the present study.

Details/Parts of Drone	Items	Specifications
Drone frame	Frame	Carbon fiber
	Type	Quadcopter
Drone motor	Type	Brushless direct current motor (BLDC)
	Typical endurance	40 to 60 min
	Weight	85 g
	Speed	330 KV
Digital spectral camera	Camera make	MicaSense Red Edge™ 3 Multispectral Camera
	Spectral bands	Blue, green, red, red edge, near-IR
	Megapixel	3.6 MP
	Capture rate	1 capture per second
	Storage	SD card
Battery	Technology	Lithium-ion batteries
	Max battery capacity	10,000 mAh
RC controller	Make	FS-i6S transmitter
	No. of channels	10
	Frequency range	2.4055–2.475 GHz
	Modulation system	GFSK
	2.4G mode	AFHDS 2A
Light detection and ranging (LIDAR)	Make	TF02-Pro 40m IP65 LiDAR
	Operating range	0.1–40 m
	Weight	50 g
	Frequency	1–1000 Hz
GPS	Oscillator	Crystal
	Technology	GPS, GLONASS
	Memory	ROM
	Navigation update rate	up to 10 Hz
PX4 controller	Main chip	STM32F427
	CPU	180 MHz ARM® Cortex® M4
	RAM	256 KB SRAM
	Connectivity	1× I2C, 1× CAN, 1× ADC, 4× UART
	Sensors	Gyroscope, accelerometer, 3-axis gyroscope, barometer

Figure 2. Illustration of the UAV employed in the study.

A multispectral camera was mounted on the UAV for extraction of multi-spectral band imagery of the agricultural fields. The images were captured in sunny and cloud-free conditions at a height of 121 m from the ground level for a flight duration ranging from 27 to 30 min. An overlap triggering mode was used for capturing the images and the overlap percentage was set at 70% between images taken at a speed of 15 m/s and giving a resolution of 8 cm per pixel [69]. The camera had a downwelling light sensor (DLS) which measured the ambient light during flight and exposure settings were automatically optimized for each capture to prevent blurring or over-exposure [70].

3.2. Algorithm

This paper presents an algorithm which has been designed for automated spraying on stressed regions with fertilizers, and pesticides. The steps followed in the methodology are presented briefly here and discussed in the later section.

❏   Spectral images were acquired from UAVs used to assess the stressed region in the agricultural field.
❏   VegNet Software was developed to locate stressed areas in the agricultural field using spectral indices (refer to [33]). These stressed regions may have been affected by water stress, nutrient deficiency, disease or pest damage, and could be assessed using a combination of spectral indices discussed in our previous article [33].
❏   Individual stress regions were separated from each other using the flood filling method, and their centroid was calculated.
❏   Each stressed region's boundary was delineated using mathematical morphological operations and was then transformed into a convex region using the Graham scan convex hull algorithm.
❏   Using the Voronoi diagram and Voronoi iteration process, the optimal spray points were calculated for each stressed region.
❏   Thereafter, the shortest path from the starting point traversing through each stressed region and its spray points was found using a TSP-based route planning solution.

The next step of the process involved the identification of stressed and unhealthy regions from the spectral images. As discussed in the previous sections, we used the VegNet software to identify the stressed regions [33]. These stressed regions indicated some sort of deficiencies which could be reduced with the help of appropriate fertilizers. The proposed method of spraying with UAVs took into consideration that an equal quantity of spray would be administered irrespective of the degree of

deficiency. To decide the equipment to be used for spraying, parameters such as the radius and area to be covered in single spray and the type and quantity of fertilizer to be sprayed were considered.

When the thresholds were identified and applied to the spectral image, the stressed areas were obtained using VegNet software application. These stressed regions were small regions in the farm separated from each other by some distance. These were then extracted to get the individual stressed regions. The flood filling method is one of two popular methods for extraction of individual regions in a binary image. In this method, a region is filled in all directions starting from a single point within the region. This method searches for an unlabeled foreground pixel, labels it and marks it "visited" to all the neighboring pixels in the region [71,72].

In this method, the 8-connected component was used as a metric for the identification of connected image regions. Hence, by employing the flood filling algorithm, each stressed region could be obtained. Therefore, later on, the centroid of each stressed region could be obtained from these stressed regions.

The next procedure involved finding the shortest path from the starting point and traversing through each stressed region's centroid. Therefore, this method found the shortest path through each stressed region and then, for each stressed region, the shortest path for traversing each spray region was determined. The problem of finding the shortest path through each of these points is called the TSP. The travelling salesman is a classical problem in computer science and operations research. It can be described as a graph with N nodes. All the nodes are connected to each other with an edge that has a corresponding weight and cost attached to it. The cost describes how "difficult" it is to traverse this edge on the graph. The objective of the salesman is to visit all the N cities (nodes) by visiting each node only once, finishing where he started and keeping the traversal costs as low as possible. Since there are N factorial combinations for N nodes, it is impossible to go through all the possible combinations if N is large; therefore, some scientific methods have been formed for solving the problem. Some of the popular ones are the Branch and Bound algorithm [73] and local search algorithms, such as the 2-opt algorithm [74]. In 1975, Chisman used a variation of the travelling salesman problem called the clustered travelling salesman problem [75]. Here, a group of nodes (clusters) must be visited contiguously in an optimal order. There exist several sets of clusters within the problem. This method was developed for optimizing, simultaneously, the ordering of nodes within each cluster and the ordering of clusters. Therefore, in our problem, the stressed regions act as clusters while the spray points inside them are the nodes of each cluster.

In order to find the spray points for each stressed region, their boundary was calculated. This was performed with the help of mathematical morphological operations. The boundaries of the stressed regions inside spectral image A can be calculated as A—(A ⊖ B) where B is a 3 × 3 square structuring element. Here (A ⊖ B) denotes erosion of A by B where erosion is another mathematical morphological operation [76,77]. Figure 4 shows the boundary of the stressed region identified in the study site.

The boundary points obtained from each stressed region were used to find a convex hull for the points. A convex hull is the smallest convex set that contains a set of points enclosed within it. Figure 7 shows the boundary as well as the corresponding convex hull of the stressed region. A convex hull is a primary requirement for implementing the algorithm proposed in this paper. The aim of the convex hull is to make the structure of the stressed region into the shape of a polygon that resembles the original shape while containing all the stressed regions inside of it. The convex polygon shape would help in the storage, manipulation and analysis of these stressed regions as opposed to earlier work with images. There are many algorithms called convex hull algorithms that are used to achieve the convex hull. Some of the popular ones are the Graham scan algorithm proposed by [78] and the gift-wrapping algorithm developed by Jarvis [79]. The algorithm given below is the Graham scan algorithm.

3.3. Graham Scan Algorithm

In Algorithm 1, ccw (counterclockwise) is a function which denotes the counterclockwise rotation. ccw > 0 if three points make a counterclockwise turn clockwise if ccw < 0, and collinear if ccw = 0.

The method utilizes the unique approach of covering each region with circles, with the idea borrowed from the covering of convex regions by base stations towers used in telecommunications [80]. This idea was introduced in the context of mobile communication for efficient base station placement problems in a convex region such that each point in the convex region is covered by at least one base station of equal radius. The present research is based on the above idea, with the convex region being the stressed region and the base station being the location where the fertilizer has to be applied, optimizing the base station location for the k points [80].

Algorithm 1. Function GrahamScanAlgorithm(points)

---

points = list of points
stack = EmptyStack()

P0 = lowest y-coordinate and leftmost point
sort points by polar angle with P0, if several points have the same polar angle then only keep the farthest
for point in points:
while count stack > 1 and ccw(next_to_top(stack), top(stack), point) < 0:
stack.pop()
stack.push(point)
return stack
End

Since finding the number of points for spreading is also a task, this method was applied iteratively and the points were increased one by one till almost all of the convex region was covered and the maximum circumscribing radius was obtained, approximately equal to the radius chosen for the spray. The algorithm initially started with a rough estimate of the number of points needed to cover the convex region, i.e., equal to the total area of the convex region divided by the area of the spray. Then, the number of points was increased iteratively and optimized until most of the stressed area was covered by spray, i.e., 97% of stressed region in our case, and the maximum radius of the enclosed circle was less than or equal to the radius of the spray. We chose 97% in our case because we wanted to find a balance between the minimum number of circles required to cover a region and to cover the maximum amount of area. The number of points, as well as their location, was the answer which was finally obtained. Table 2 shows the number of spray points and area of the stressed region not covered by spray in the selected region after completion of optimization processes. This table shows that eight points were selected, covering more than 97% of the stressed region and had a maximum circumscribing radius equal to the spray radius. Thus, eight points and their optimized locations became the answer for that particular stressed region. These points were further used for route planning, See Algorithm 2.

Algorithm 2. Function find_optimum_points(convex_region, spray_radius)

Number of points (N) = floor(area of convex region/pi spray_radius * spray_radius)*
while True:
Points (P) = Find N random points inside the convex region
Points (P), max_radius = optimum_location_algorithm(convex_region, points, spray_radius)
If ((area_covered_by_points(convex_region, spray_radius) > 97%) and (max_radius =< spray_radius))
return Points (P)
Else:
Number of points (N) = (N) + 1
End

Table 2. Number of spray points in the selected region and area of stressed region not covered by spray after completing the optimization process.

Number of Spray Points	Percentage of Area of Stressed Region Not Covered by Spray Region	Radius of Maximum Circumcircle of a Voronoi Region at the Last Iteration
5	24.24%	0.48712 m
6	9.14%	0.51512 m
7	5.92%	0.45808 m
8	0.28%	0.40368 m

3.4. Voronoi Diagram

The fundamental data structure used in this method is the Voronoi diagram [81] of the point set P, (P is the list of points in the convex region), denoted by VOR(p) for formulating the update mechanism of the members in P to achieve optimum placement. VOR(p) divides the convex region Π into n disjoint convex polygon region such that:

(i)   each region contains a member of P;
(ii) the region containing point Pi P is denoted by vor(pi);
(iii) for any arbitrary point q inside a Voronoi region, i.e., q vor(qi), (pi, q) δ(pj, q) <= for all pj ϵ P. Here, δ(p,q) denotes the Euclidean distance of the pair of points.

In this paper, we consider vor(qi) as a closed convex region for each point. So, if a part of the region is outside the convex region then vor(qi)$\cap\Pi$ is used as vor(qi).

The way to optimize the points in the region is to find the positions of all the points P inside the region such that the maximum range required is as quickly as possible. The algorithm is iterative, so it perturbed the points P until it finally attained a local minimum. This algorithm is also called the Voronoi iteration algorithm or Lloyd's algorithm [82]. At each iteration, a circumscribing circle (Ci) for each vor(pi) was calculated using the algorithm [83]. Ri became the radius of the circumscribing circle (Ci). In order to cover a convex polygon by a spray with a minimal range, the spray should be placed at the center of the circumscribed polygon of the convex region and assigned a range of spray equal to the radius of the circle. As such, the maximum radius was calculated for all the circumscribing circles, which was equal to ρ. This maximum radius was minimized until the circle radius matched the spray radius and the number of iterations did not exceed the limit, i.e., cross the particular value of 40 in our case. We choose 40 in this case because most of the optimizations take place in the first few iterations; after that it converges to another value. The last iterations would lead to a very small decrease in the maximum radius, which is the value that we were optimizing (see Table 3). Therefore, 40 iterations ensured that only major iterations took place in the algorithm and reduced the time for running further optimization processes.

Table 3. Radius of the maximum circumscribing circle for all the iterative optimization steps when N = 8 points were selected for covering a stressed region.

Optimization Steps	Radius (in Meters)	Optimization Steps	Radius (in Meters)	Optimization Steps	Radius (in Meters)	Optimization Steps	Radius (in Meters)
1	0.5572	11	0.4521	21	0.4212	31	0.4080
2	0.49	12	0.4470	22	0.4191	32	5.092 0.4073
3	0.4636	13	0.4429	23	0.4172	33	0.4066
4	0.4607	14	0.4394	24	0.4156	34	0.4060
5	0.4628	15	0.4364	25	0.4140	35	0.4056
6	0.4591	16	0.4336	26	0.4128	36	0.4052
7	0.4584	17	0.4309	27	0.4116	37	0.4048
8	0.4576	18	0.4286	28	0.4105	38	0.4044
9	0.4564	19	0.4260	29	0.4096	39	0.4041
10	0.4547	20	0.4234	30	0.4088	40	0.4036

The number of points was increased iteratively until most of the stressed area was covered with a spray, i.e., 97% of stressed region in our case, and the maximum radius of the enclosed circle was less than or approximately equal to the radius of the spray. If these spray point positions covered more than 97% of the area and had a maximum radius which was less than or equal to the spray radius, then these points became the spray points of the stressed region.

3.5. Voronoi Iteration Algorithm or Lloyd's Algorithm

Lloyd's algorithm starts with an initial placement of some number k of points. It then repeatedly executes the following relaxation steps:

- The Voronoi diagram of the k sites is computed.
- Each cell of the Voronoi diagram is integrated and the centroid is computed.
- Each site is then moved to the centroid of its Voronoi cell.

This relaxation step terminated when the new set of points met some convergence criteria. Algorithm 3 was very crucial in obtaining the optimum location of these points so that the spray radius would become equal to the maximum circumscribing radius of the region.

Algorithm 3. Function optimum_location_algorithm(convex_region, points, spray_radius)

---

set of points P = {p1, p2, ... pk } inside the convex polygon.
iter_count = 0
ρ (maximum radius) = 0
while iter_count < 40 and ρ > spray_radius
Find the voronoi diagram for the points P
Compute the circumscribing circle Ci for each vor(pi)
r_i be the radius of C_i
Move p_i to the center of C_i and assign range r_i o to it
ρ == max{ri , i = 1, 2...}
iter_count += 1
return Points (P), (maximum radius) ρ
End

After finding the locations for the application of fertilizer for a particular stressed region, the TSP-based algorithm was, again, applied to obtain the shortest path traversing all the points. When the drone had traversed all the points in the stressed region, it then moved on to the next stressed region. Figure 9 shows the stressed region along with spray points and spray regions in the stressed region. Figure 11 shows the optimized path through all the stress points in the region.

Most drones today are configured with mission planner software which can be used to create automated missions. This is done by programming the micro-controller manually or programmatically to automated paths using the input of latitude, longitude, altitude and time delays. This automated mission ensures that these drones would not have to be controlled manually thus removing any risk of a crash or manual error. Ardu Pilot's Mission Planner software has the ability to create automated paths using Python scripts [84].

4. Results and Discussion

This section discusses the outcomes derived from the paper, i.e., finding the optimal points for spraying stressed regions and the optimal path to follow while covering all possible points in the field without re-visiting single points. For assessing the stress regions, a combination of spectral indices or thermal indices were obtained as per user needs and requirements, or the user could employ any techniques or methods to assess the stressed regions. Results will demonstrate the advantages of using TSP-based algorithms using UAVs within agricultural plots to reduce associated costs with labor and

fertilizer spraying, thereby realizing the goal of this study for optimal route to visit each stressed point only once, and cover the entire agricultural area in a minimum time interval.

As discussed in previous sections, VegNet software helped in providing the stressed location and regions of stress in the farm holdings (please refer to [33]). Figure 3 illustrates the stressed regions identified in the agricultural regions, highlighted with yellow color, and the blue color represents the non-stressed regions. Figure 3a represents whole agricultural fields while Figure 3b illustrates a very small part of the agricultural holdings. We thus had this small piece of agriculture field to which we applied the algorithm present in this paper. Figure 4 shows the optimum route to be taken to reach each stressed region, which was obtained after applying an algorithm for solving this problem of clustered TSP. Figure 4 demonstrates the application of the (Travelling salesman) TS algorithm on the stressed regions in the agricultural field in order to find the optimum path to each stressed region. Each stressed region is illustrated with a different color and the blue line shows the optimal path to the centroid of each stressed region.

(**a**) (**b**)
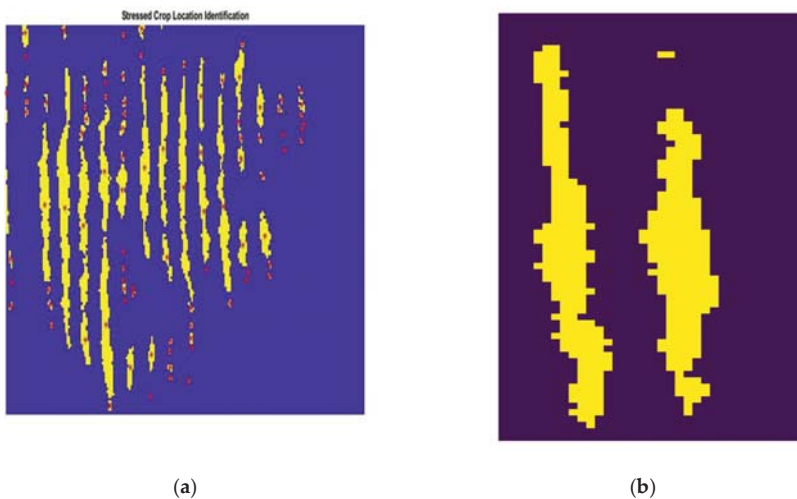
Figure 3. (**a**) Stressed regions in the whole agricultural field and (**b**) a selection of stressed regions for a small region highlighted in yellow.

Using flood filling algorithms, we selected stressed regions from the cluster of stressed regions, as shown in Figure 5. Thereafter, the boundary of each stressed region was delineated from the selected region. The delineated boundaries of the stressed regions can be seen in Figure 6. Thereafter comes the role and importance of the convex hull, which uses the delineated boundaries of the stressed regions in order to get a polygon that resembles their original shapes. The convex shape helps in the storage, manipulation and analysis of stressed regions which is a primary requirement for implementing the proposed algorithm. A typical convex hull applied on the delineated boundary of the stressed region can be seen in Figure 7.

The algorithm then estimated the minimum number of circles required for covering the stressed region using the stressed region's area and the area of spray region. Let this number be N. Then, N random points were found in the stressed region. For these random points, a Voronoi diagram was made and the corresponding circumscribing circles (for each region of the Voronoi diagram) were obtained. Then began the iterative optimization process where the locations of the points kept on updating so that a minimum number of sprays was required to cover a stressed region. The number of points was increased iteratively until most of the stressed area was covered with spray, i.e., 97% of the stressed region, and the maximum radius of the enclosed circle was less than or approximately equal to the radius of the spray. If these spray points positions covered more than 97% of the area and had a

maximum radius which was less than or equal to the spray radius, then these points became the spray points of the stressed region.
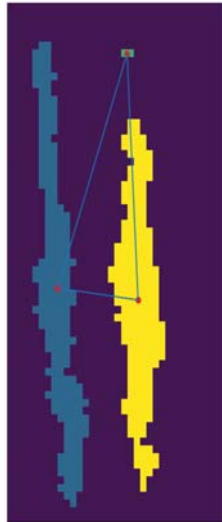
Figure 4. Applying travelling salesman (TS) on the stressed region, with different stressed regions highlighted by different colors.

Figure 5. A stressed region selected from the cluster of stressed regions (as shown in Figure 3a,b).

Table 2 shows the number of spray points and area of the stressed region not covered by spray in the selected region after the optimization process. This table shows that as the number of points was increased, the percentage of stressed region area not covered by the spray region decreased. When eight points were selected, more than 97% of the stressed area was covered and had a maximum radius less than or equal to the spray radius. If the number of points was increased after this, then there was a very marginal decrease in the percentage of stressed region area not covered by the spray region. On the other hand, there would be a large requirement of spray liquid which would lead to overuse of fertilizer and pesticides. Table 3 shows the optimization steps when eight spray points were

selected. The maximum circumcircle radius kept on decreasing in each step until there was very little change in the last few steps where the algorithm ended. Figure 8 shows the Voronoi diagram and the corresponding circumscribing circles after optimization, where different regions of Voronoi are shown with different colors. Here, the maximum radius of the circumscribing circle was 5.046 units, i.e., 40.4 cm, which is shown in the last step of optimization in Table 3. The maximum radius of the circumscribing circle, i.e., 40.4 cm, was almost equal to the spray radius from the UAVs, i.e., 40 cm (1 unit = 1 pixel = 8 cm).
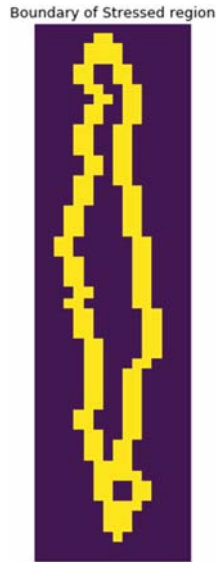
Figure 6. Boundary of the stressed region.
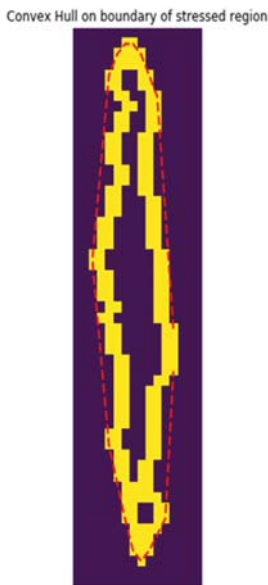
Figure 7. Convex hull on the boundary of stressed region.
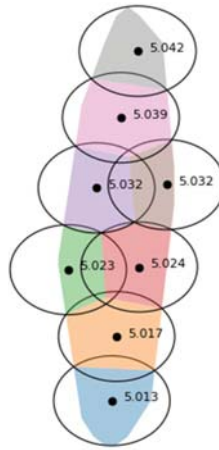
Figure 8. Voronoi diagram and the corresponding circumscribing circles for Voronoi regions at an iterative optimization step.

This optimization provides optimal points in the stressed regions which uses these points to provide the optimal path and route to deliver services in the fields at appropriate points with accuracy. Thus, optimal points are required to ensure the route of the UAVs to reach at each point without re-visiting the same place in its complete trip. In our study, optimum route was identified using TSP based algorithm and Voronoi Diagram which has been illustrated in Figure 9. Thus, Figure 9 shows the coverage of the stressed crops with a fixed amount of radius i.e., radius of the spray from UAVs. In our case study, the optimal route has been shown in the application of UAVs for spraying the fertilizer at each point and spray radius of fertilizer by UAVs equal to 0.4 m (as shown in Figure 9). Here, all the circles will be of the same radius. We have also provided the different stressed regions in Figure 10a and illustrated how Drone is covering all the three types of stressed regions along with overlap areas. Table 4 provides the information about the overlap regions for these three stressed regions (based on the area covered by stressed regions). Therefore, this optimal points and optimal path route will use the shortest possible route to cover the agricultural fields completely in possibly less time frame. The advantages of this study is that it will provide the coverage of entire field in a minimum period with full coverage without re-visiting. Figure 11 indicates the optimal route through all spray points in the stressed region with a fixed spray radius of 40 cm. Hence, the optimised path is derived through all the spray points generated using TSP based algorithms.

A few important studies can be highlighted here that briefly demonstrated the spraying of fertilizers and pesticides on farms of a particular shape and size, which were easy to maneuver, and design algorithms. In 2013, one article demonstrated the optimization of maneuvering near boundaries and the loading and unloading of inputs of an agricultural machine [85]. The method suggested works only for specific field geometries with all parts of the field being sprayed irrespective of whether an area is stressed or not. Furthermore, previous papers divided the stressed regions into various small rectangles for spraying, but this shape is not the most appropriate one for spraying since the spraying happens over a circular area. Therefore, a circular shape was chosen for dividing the stressed region in this study. In comparison, some authors demonstrated easier methods of maneuvering with the help of UAVs. Similarly, Cabreira et al. [58] discussed coverage path planning to cover every region of interest considering the different area shapes [58]. Some others discussed algorithms, such as back-and-forth coverage path planning algorithms, which are suitable for continuous spraying in a region. These algorithms used turning maneuvers which increased the time and energy spent at corners, thus giving irregular spraying at the corners of the regions. One article discussed the development of a coverage trajectory with a minimal required time for UAVs for better navigation for

any specific task [60]. Here, the authors used rectangular grids to divide a stressed region and then used path planning algorithms to find an optimized path. However, it is not the best idea to divide a stressed region which has a very irregular shape into rectangular grids. This is because the grids might contain areas which do not require these inputs which leads to unnecessary spraying. These grid-based spray systems would not be optimal as applying a circular spray motion on a rectangular cell is not preferred. This may lead to missed spraying or over-spraying in some areas.
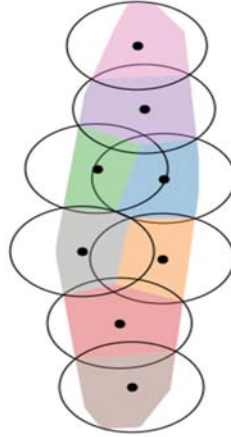
Figure 9. Fertilizer spray with radius of 0.40 m on the spray points in the stressed region (here, all the circles are of the same radius).
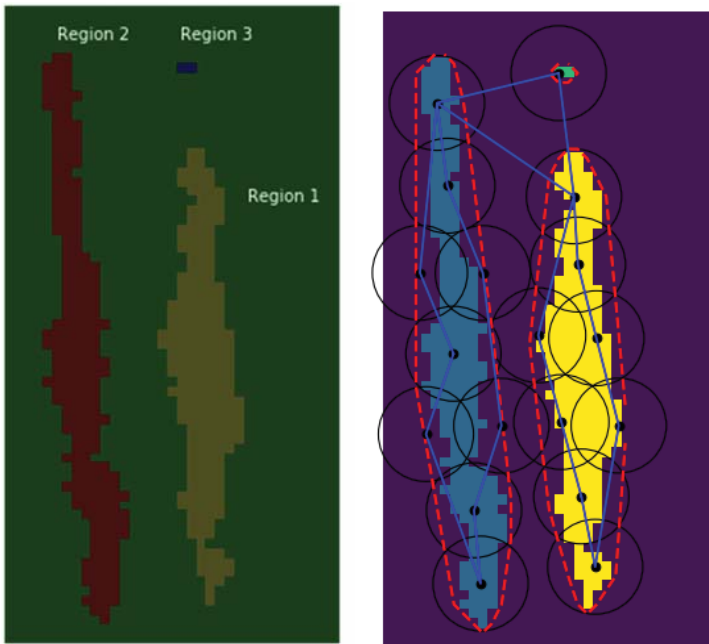
Figure 10. (**a**) Stressed regions in test site with different area marked as region I, II and III (based on the area covered) and (**b**) Path covered for all the stressed regions and their respective spray points (Total Distance covered = 227.73 × 0.08 m = 18.2984 m).

Table 4. Statistics for the overlap and area covered for the test site during the optimal route and field coverage (area for overlap for stressed wise percentage).

Region	Percentage of Area Not Covered	Percentage of Area with Overlap
Region I	0.04%	25.69%
Region II	2.12%	12.96%
Region III	0%	0%
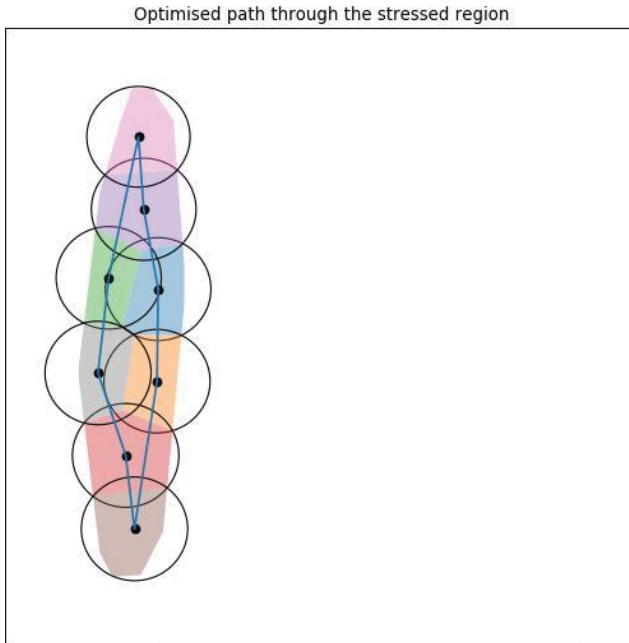
Figure 11. Optimized path through all the spray points in the stressed region.

This paper will help to spray inputs only on the stressed area where it is required and where there is nutrient deficiency. We also suggest spraying inputs while the UAV is flying still over the spray position. This method of spraying would reduce some of the spraying factors associated with UAVs. We have tried to combine all the shortcomings from earlier research to come out with an algorithm for proper spraying of pesticides by drones which provides continuous feedback to the system for allowing spraying of fertilizers on all shapes of stressed regions. Finally, the algorithm outputs an optimized route covering all the stressed regions and spray points. The tasks of administering pesticides and fertilizer, when done by traditional means, take a lot of time and are not efficient processes. However, by using the proposed method, the task of administering fertilizer and pesticide can be completed in a shorter time frame, with optimum resources and with a high level of accuracy.

5. Challenges

This section deals with the challenges and hurdles associated with the UAVs and discusses the future work scope, conclusion and recommendations. There are numerous challenges associated with UAVs which will be the main focus before delivering the application part for the optimal path and route. The first challenge is the usage of drones as they are more difficult to control as they move rapidly in all possible directions, and they can be difficult to control in adverse weather conditions, such as rain or high wind turbulence. However, most drones now come with automated navigation software that enables autonomous flight, requiring no input from the user apart from route instructions.

The UAV's size and weight are also challenges to the user, along with their operational flight time, which depend upon the battery being used. Drones have a limited battery capacity; therefore, they have a short time flight. To compensate for this, larger batteries can be used which makes them more expensive. UAVs also cannot carry a heavy load; therefore, they would need to be refilled with inputs and their batteries recharged before flying again. Therefore, the resupply trips should be incorporated into the route planning, depending on the type of input being administered and size of the field. Drones also require a large memory for storing and processing high resolution spectral images. Drone operations are heavily regulated by most governments and require a license to be operated in certain regions and places due to security and safety issues. Along with challenges in the hardware, there exist some challenges with the software too, despite the presence of a large number of open-source libraries for the implementation of software and availability of affordable graphical processing units (GPUs). Irrespective of the above-mentioned challenges, UAVs are widely used by overcoming these challenges, somehow, either by using a short flight duration, low spectral resolution data (not acquiring hyperspectral data) or by spending money on expensive batteries to operate over large land holdings.

6. Future Work

This section deals with future research directions. In this paper, a simple method of fertilizer and pesticide application by drone has been discussed which automates the process of identification and application of fertilizer automatically, without any need for human decision-making and manual labor. This paper used only one of the many vegetative indexes available in the research literature for finding stressed regions with a deficiency of a particular nutrient. The future work of this paper could be the integration of various kinds of vegetative indices which indicate various kinds of nutrient deficiencies. These deficiencies could be used to predict the overall health of the crop. This paper proposes a method for spraying only one fertilizer at a time, but the method could be developed so that multiple fertilizers and pesticides could be sprayed onto the stressed region, thus improving the process efficiency and reducing the cost. This would result in a reduction in the number of steps which need to be taken to find and rectify each deficient nutrient, while a centralized system could be developed to address all the deficiencies with a single spray of fertilizers/pesticides. As agricultural machines spend a significant part of their time on non-productive operations, with more time spent on turns and repetitions, the technique described will help to reduce these non-productive operations.

This paper focused on administering an equal amount of fertilizer to the stressed region irrespective of the degree of nutrient deficiency. However, ideally, there should be a focus on applying the fertilizer based on the degree of fertilizer and nutrient deficiency. Therefore, a novel method will be much needed in the future which can administer fertilizer based on the degree of deficiency of fertilizers in respect to volume requirement. This method could lead to the development of more sophisticated software, with which farmers can estimate their total revenue and losses due to the stressed regions. This could be done by integrating various kinds of real-time global prices and real-time sensor data with the yield prediction data obtained through the drone. Another future scope is the usage of artificial intelligence which is being used in a wide range of complex tasks, ranging from speech processing to self-driving cars and, more recently, in geospatial applications (remote sensing and geographical information systems). Many artificial intelligence applications are currently being researched and developed to use hyperspectral data for prediction of the yield and health of crops. These data could be used for PA activities and would help in increasing the agricultural crop yields and income. Autonomous UAVs have great potential to exploit agricultural applications to improve and enhance crop yields and productivity, with improved accuracy in spraying route and higher time efficiency, as well proper coverage. This applicability can be applied to other research domains as well, such as forestry, ocean and defense. Another suitable application could be the use of this method for extinguishing forest fires that could be detected by UAVs. This method can help to timely extinguish fires and prevent them from spreading using optimal route calculation and maintaining the route of interest by not deviating from

optimum path. With the more advanced development of UAVs which are capable of lifting higher loads, this method can be used for precision irrigation so that the optimum amount of water can be used.

7. Conclusions and Recommendations

The paper discussed the results, challenges and future scopes of the methodology for using UAVs in precision agriculture. The results demonstrated the advantages of using TSP algorithms for UAVs within agricultural plots to reduce associated costs with labor and fertilizer spraying. This paper described a method by which automated UAVs can be used efficiently in providing inputs, such as pesticides and fertilizers, for precision agriculture. The method uses optimal points and route to provide these inputs to the stressed regions of the farm, thus covering the entire agricultural area using optimal amounts of inputs over a minimal distance and in minimum time. These optimal outcomes are generated from TSP-based algorithms and Voronoi diagrams implemented on spectral images acquired through UAVs. The spectral images are employed to locate and assess the stressed regions in large landholdings, using a spectral indices-based application (for details, refer to [33]). A few recommendations for future work using UAVs for PA applications that can be used by farmers to enhance crop yields (prevent crop damage) have also been given. Some of the recommendation points are listed below:

- Employ a combination of spectral indices or thermal indices to assess the stress regions in terms of soil moisture, nutrient deficiency and disease condition.
- Employ any techniques or methods to assess the stressed regions which employ accurate methods and applications for the above.
- Utilize route planning and an optimal path that can be used in any field shape and size.
- Implement an optimal path and route for other agricultural applications, such as pesticides and insecticides.
- Implement these techniques while sowing the seeds, effectively and in proper rows.
- Use advanced techniques of calculating an optimal path and route during harvesting to manage large landholdings to make it cost effective and time-saving.

Implementation of the points outlined above would greatly improve the productivity of large landholdings and farms while decreasing the need for manual labor and repetitive concerns for stressed point location through remote sensing application instead of knowledge-based field visiting information. In this paper, we concluded with a key recommendation to employ UAVs to find an optimized route to completely cover stressed areas efficiently and without wastage of input resources during the spraying process which is tackled with the TSP solving technique. However, there is a need for evolving much more efficient algorithms for a true sense of PA in a sustainable way to meet the future requirements of PA.

References

1. United Nations. Sustainable Development Website—United Nations. Food Security and Nutrition and Sustainable Agriculture. 2019. Available online: https://sustainabledevelopment.un.org/topics/foodagriculture (accessed on 13 March 2019).

2. United Nations Population. Global Issues—Population Website—United Nations. 2019. Available online: https://www.un.org/en/sections/issues-depth/population/ (accessed on 13 March 2019).
3. Bruinsma, J. The resource outlook to 2050: By how much do land, water and crop yields need to increase by 2050. *Expert Meet. How Feed World* **2009**, *2050*, 24–26. Available online: http://www.fao.org/3/a-ak971e.pdf (accessed on 20 February 2020).
4. Millennium Ecosystem Assessment. *Ecosystems and Human Well-Being*; Island Press: Washington, DC, USA, 2005; Volume 5.
5. Goodland, R. The concept of environmental sustainability. *Ann. Rev. Ecol. Syst.* **1995**, *26*, 1–24. [CrossRef]
6. WHO. Ecosystems and Human Well-Being, Health Synthesis. 2005. Available online: http://www.bioquest.org/wp-content/blogs.dir/files/2009/06/ecosystems-and-health.pdf (accessed on 20 August 2019).
7. Lamine, S.; Petropoulos, G.P.; Brewer, P.A.; Srivastava, P.K.; Bachari, N.E.; Manevski, K.; Kalaitzidis, C.; Macklin, M.G. Heavy Metal Soil Contamination Detection Using Combined Geochemistry and Field Spectroradiometry in the United Kingdom. *Sensors* **2019**, *19*, 762. [CrossRef] [PubMed]
8. Sharma, L.; Pandey, P.C.; Nathawat, M. Assessment of land consumption rate with urban dynamics change using geospatial techniques. *J. Land Use Sci.* **2012**, *7*, 135–148. [CrossRef]
9. Pandey, P.C.; Mandal, V.; Katiyar, S.; Kumar, P.; Tomar, V.; Patairiya, S.; Ravisankar, N.; Gangwar, B. Geospatial Approach to Assess the Impact of Nutrients on Rice Equivalent Yield Using MODIS Sensors'-Based MOD13Q1-NDVI Data. *IEEE Sens. J.* **2015**, *15*, 6108–6115. [CrossRef]
10. Mondal, P.; Basu, M. Adoption of precision agriculture technologies in India and in some developing countries: Scope, present status and strategies. *Prog. Nat. Sci.* **2009**, *19*, 659–666. [CrossRef]
11. Tey, Y.S.; Brindal, M. Factors influencing the adoption of precision agricultural technologies: A review for policy implications. *Precis. Agric.* **2012**, *13*, 713–730. [CrossRef]
12. Thomas, D.E.; Weyerhaeuser, H.; Saipathong, P.; Onpraphai, T. Negotiated land use patterns to meet local and societal needs. In Proceedings of the Cultures and Biodiversity Congress 2000, Yunnan, China, 20–30 July 2000; Yunnan Science and Technology Press: Yunnan, China, 2000; pp. 414–433. Available online: http://old.worldagroforestry.org/downloads/Publications/PDFS/PP00160.pdf (accessed on 15 March 2020).
13. Mogili, U.R.; Deepak, B.B.V.L. Review on Application of Drone Systems in Precision Agriculture. *Procedia Comput. Sci.* **2018**, *133*, 502–509. [CrossRef]
14. Somayeh Tohidyan, F.; Rezaei-Moghaddam, K. Impacts of the precision agricultural technologies in Iran: An analysis experts' perception & their determinants. *Inf. Process. Agric.* **2018**, *5*, 173–184. [CrossRef]
15. Whelan, B.M.; McBratney, A.B.; Boydell, B.C. The Impact of Precision Agriculture. In Proceedings of the ABARE Outlook Conference, the Future of Cropping in NW NSW, Moree, UK, 15 July 1997; p. 5.
16. Mulla, D.J. Twenty five years of remote sensing in precision agriculture: Key advances and remaining knowledge gaps. *Biosyst. Eng.* **2013**, *114*, 358–371. [CrossRef]
17. Schnug, E.; Panten, K.; Haneklaus, S. Sampling and nutrient recommendations—The future. *Commun. Soil Sci. Plant Anal.* **1998**, *29*, 1455–1462. [CrossRef]
18. Singh, P.; Pandey, P.C.; Petropoulos, G.P.; Pavlides, A.; Srivastava, P.K.; Koutsias, N.; Kwal Deng, K.A.; Yangson, B. Hyperspectral remote sensing in precision agriculture: Present status, challenges, and future trends. In *Hyperspectral Remote Sensing: Theory and Applications*; Pandey, P.C., Srivastava, P.K., Baltzer, H., Eds.; Elsevier: Amsterdam, The Netherlands, 2020; Chapter 8; pp. 121–146. [CrossRef]
19. Bagheri, N.; Ahmadi, H.; Alavipanah, S.K.; Omid, M. Multispectral remote sensing for site-specific nitrogen fertilizer management. *Pesqui. Agropecu. Bras.* **2013**, *48*, 1394–1401. [CrossRef]
20. Wójtowicz, M.; Wójtowicz, A.; Piekarczyk, J. Application of remote sensing methods in agriculture. *Commun. Biometry Crop Sci.* **2016**, *11*, 31–50.
21. Hruska, R.C.; Mitchell, J.J.; Anderson, M.; Glenn, N.F. Radiometric and Geometric Analysis of Hyperspectral Imagery Acquired from an Unmanned Aerial Vehicle. *Remote Sens.* **2012**, *4*, 2736–2752. [CrossRef]
22. Uto, K.; Seki, H.; Saito, G.; Kosugi, Y. Characterization of Rice Paddies by a UAV-Mounted Miniature Hyperspectral Sensor System. *IEEE J. Sel. Top. Appl. Earth Obs. Remote Sens.* **2013**, *6*, 851–860. [CrossRef]
23. Zarco-Tejada, P.J.; Gonzalez-Dugo, V.; Berni, J.; Jimenez-Berni, J.A. Fluorescence, temperature and narrow-band indices acquired from a UAV platform for water stress detection using a micro-hyperspectral imager and a thermal camera. *Remote Sens. Environ.* **2012**, *117*, 322–337. [CrossRef]
24. Stehr, N.J. Drones: The Newest Technology for Precision Agriculture. *Nat. Sci. Educ.* **2015**, *44*, 89–91. [CrossRef]

25. Von Bueren, S.K.; Burkart, A.; Hueni, A.; Rascher, U.; Tuohy, M.P.; Yule, I.J. Deploying four optical UAV-based sensors over grassland: Challenges and limitations. *Biogeosciences* **2015**, *12*, 163–175. [CrossRef]

26. Gago, J.; Douthe, C.; Coopman, R.; Gallego, P.P.; Ribas-Carbo, M.; Flexas, J.; Escalona, J.; Medrano, H. UAVs challenge to assess water stress for sustainable agriculture. *Agric. Water Manag.* **2015**, *153*, 9–19. [CrossRef]

27. Honkavaara, E.; Saari, H.; Kaivosoja, J.; Pölönen, I.; Hakala, T.; Litkey, P.; Mäkynen, J.; Pesonen, L. Processing and Assessment of Spectrometric, Stereoscopic Imagery Collected Using a Lightweight UAV Spectral Camera for Precision Agriculture. *Remote Sens.* **2013**, *5*, 5006–5039. [CrossRef]

28. Schmale David, G., III; Dingus, B.R.; Reinholtz, C.; Schmale, D.G. Development and application of an autonomous unmanned aerial vehicle for precise aerobiological sampling above agricultural fields. *J. Field Robot.* **2008**, *25*, 133–147. [CrossRef]

29. Cheein, F.A.A.; Carelli, R. Agricultural Robotics: Unmanned Robotic Service Units in Agricultural Tasks. *IEEE Ind. Electron. Mag.* **2013**, *7*, 48–58. [CrossRef]

30. Freeman, P.K.; Freeland, R.S. Agricultural UAVs in the U.S.: Potential, policy, and hype. *Remote Sens. Appl. Soc. Environ.* **2015**, *2*, 35–43. [CrossRef]

31. Nebiker, S.; Annen, A.; Scherrer, M.; Oesch, D. A light-weight multispectral sensor for micro UAV—Opportunities for very high resolution airborne remote sensing. *Int. Arch. Photogramm. Remote Sens. Spat. Inf. Sci.* **2008**, *37*, 1193–1199.

32. Fischer, A. A model for the seasonal variations of vegetation indices in coarse resolution data and its inversion to extract crop parameters. *Remote Sens. Environ.* **1994**, *48*, 220–230. [CrossRef]

33. Srivastava, K.; Bhutoria, A.J.; Sharma, J.K.; Sinha, A.; Pandey, P.C. UAVs technology for the development of GUI based application for precision agriculture and environmental research. *Remote Sens. Appl. Soc. Environ.* **2019**, *16*, 100258. [CrossRef]

34. Huete, A. A soil-adjusted vegetation index (SAVI). *Remote Sens. Environ.* **1988**, *25*, 295–309. [CrossRef]

35. Horler, D.N.H.; Dockray, M.; Barber, J. The red edge of plant leaf reflectance. *Int. J. Remote Sens.* **1983**, *4*, 273–288. [CrossRef]

36. Huete, A.R.; Liu, H.Q.; Batchily, K.V.; Van Leeuwen, W. A comparison of vegetation indices over a global set of TM images for EOS-MODIS. *Remote Sens. Environ.* **1997**, *59*, 440–451. [CrossRef]

37. Haboudane, D.; Miller, J.R.; Tremblay, N.; Zarco-Tejada, P.J.; Dextraze, L. Integrated narrow-band vegetation indices for prediction of crop chlorophyll content for application to precision agriculture. *Remote Sens. Environ.* **2002**, *81*, 416–426. [CrossRef]

38. Gonçalves, J.A.; Henriques, R. UAV photogrammetry for topographic monitoring of coastal areas. *ISPRS J. Photogramm. Remote Sens.* **2015**, *104*, 101–111. [CrossRef]

39. Pinto, E.; Santana, P.; Barata, J. On collaborative aerial and surface robots for environmental monitoring of water bodies. In *Doctoral Conference on Computing, Electrical and Industrial Systems*; Springer: Berlin/Heidelberg, Germany, 2013; pp. 183–191.

40. Watanabe, Y.; Kawahara, Y. UAV Photogrammetry for Monitoring Changes in River Topography and Vegetation. *Procedia Eng.* **2016**, *154*, 317–325. [CrossRef]

41. Li, C.-C.; Zhang, G.-S.; Lei, T.-J.; Gong, A.-D. Quick image-processing method of UAV without control points data in earthquake disaster area. *Trans. Nonferrous Met. Soc. China* **2011**, *21*, s523–s528. [CrossRef]

42. Matese, A.; Toscano, P.; Di Gennaro, S.F.; Genesio, L.; Vaccari, F.P.; Primicerio, J.; Belli, C.; Zaldei, A.; Bianconi, R.; Gioli, B.; et al. Intercomparison of UAV, Aircraft and Satellite Remote Sensing Platforms for Precision Viticulture. *Remote Sens.* **2015**, *7*, 2971–2990. [CrossRef]

43. Muzari, W.; Gatsi, W.; Muvhunzi, S. The Impacts of Technology Adoption on Smallholder Agricultural Productivity in Sub-Saharan Africa: A Review. *J. Sustain. Dev.* **2012**, *5*, 69. [CrossRef]

44. Anderson, K.R. A reevaluation of an efficient algorithm for determining the convex hull of a finite planar set. *Inf. Process. Lett.* **1978**, *7*, 53–55. [CrossRef]

45. Xuemei, L.; Yuyan, D.; Lixing, D. Study on precision agriculture monitoring framework based on WSN. In Proceedings of the 2008 2nd International Conference on Anti-Counterfeiting, Security and Identification, Guiyang, China, 20–23 August 2008.

46. López-Riquelme, J.; Pavón-Pulido, N.; Navarro-Hellín, H.; Soto-Valles, F.; Torres-Sánchez, R. A software architecture based on FIWARE cloud for Precision Agriculture. *Agric. Water Manag.* **2017**, *183*, 123–135. [CrossRef]

47. Nash, E.; Korduan, P.; Bill, R. Applications of open geospatial web services in precision agriculture: A review. *Precis. Agric.* **2009**, *10*, 546–560. [CrossRef]
48. Hunt, E.R.; Hively, W.D.; Daughtry, C.S.; McCarty, G.W.; Fujikawa, S.J.; Ng, T.L.; Tranchitella, M.; Linden, D.S.; Yoel, D.W. Remote sensing of crop leaf area index using unmanned airborne vehicles. In Proceedings of the Pecora 17—The Future of Land Imaging, Going Operational, Denver, CO, USA, 18–20 November 2008.
49. Burema, H.; Filin, A. Aerial Farm Robot System for Crop Dusting, Planting, Fertilizing and Other Field Jobs. U.S. Patent No. 9,382,003, 5 July 2016.
50. Qin, W.-C.; Qiu, B.-J.; Xue, X.; Chen, C.; Xu, Z.-F.; Zhou, Q. Droplet deposition and control effect of insecticides sprayed with an unmanned aerial vehicle against plant hoppers. *Crop. Prot.* **2016**, *85*, 79–88. [CrossRef]
51. Zhou, L.P.; He, Y. Simulation and optimization of multi spray factors in UAV. In Proceedings of the 2016 ASABE Annual International Meeting, Lake Buena Vista, FL, USA, 17–20 July 2016; American Society of Agricultural and Biological Engineers: Saint Joseph, MI, USA, 2016. [CrossRef]
52. Yao, L.; Jiang, Y.; Zhiyao, Z.; Shuaishuai, Y.; Quan, Q. A pesticide spraying mission assignment performed by multi-quadcopters and its simulation platform establishment. In Proceedings of the 2016 IEEE Chinese Guidance, Navigation and Control Conference (CGNCC), Nanjing, China, 12–14 August 2016.
53. Stark, B.; Rider, S.; Chen, Y. Optimal pest management by networked unmanned cropdusters in precision agriculture: A cyber-physical system approach. *IFAC Proc. Vol.* **2013**, *46*, 296–302. [CrossRef]
54. Castaldi, F.; Pelosi, F.; Pascucci, S.; Casa, R. Assessing the potential of images from unmanned aerial vehicles (UAV) to support herbicide patch spraying in maize. *Precis. Agric.* **2016**, *18*, 76–94. [CrossRef]
55. Campos, J.; Llop, J.; Gallart, M.; García-Ruiz, F.; Gras, A.; Salcedo, R.; Gil, E. Development of canopy vigour maps using UAV for site-specific management during vineyard spraying process. *Precis. Agric.* **2019**, *20*, 1136–1156. [CrossRef]
56. Norbert, D. Route Planning System for Agricultural Work Vehicles. U.S. Patent 6,128,574, 3 October 2000. Available online: https://patentimages.storage.googleapis.com/86/bd/48/076423c308fe7b/US6128574.pdf (accessed on 25 June 2020).
57. Rodias, E.; Berruto, R.; Busato, P.; Bochtis, D.; Sørensen, C.G.; Zhou, K. Energy Savings from Optimised In-Field Route Planning for Agricultural Machinery. *Sustainability* **2017**, *9*, 1956. [CrossRef]
58. Cabreira, T.M.; Brisolara, L.B.; Ferreira, P.R., Jr. Survey on Coverage Path Planning with Unmanned Aerial Vehicles. *Drones* **2019**, *3*, 4. [CrossRef]
59. Galceran, E.; Carreras, M. A survey on coverage path planning for robotics. *Robot. Auton. Syst.* **2013**, *61*, 1258–1276. [CrossRef]
60. Nam, L.H.; Huang, L.; Li, X.J.; Xu, J.F. An approach for coverage path planning for UAVs. In Proceedings of the 2016 IEEE 14th International Workshop on Advanced Motion Control (AMC), Auckland, New Zealand, 22–24 April 2016; pp. 411–416. [CrossRef]
61. Tokekar, P.; Hook, J.V.; Mulla, D.; Isler, V. Sensor Planning for a Symbiotic UAV and UGV System for Precision Agriculture. *IEEE Trans. Robot.* **2016**, *32*, 1498–1511. [CrossRef]
62. Tarot. Tarot 4008 Martin Long Flight Time BLDC Motor Specifications. 2019. Available online: http://www.tarotrc.com/Product/Detail.aspx?Lang¼en&Id¼9fc38c24-b74d-469d-b568-3d5ea644874a (accessed on 17 December 2019).
63. Planner, Mission. Ardupilot—Mission Planner Documentation. 2019. Available online: http://ardupilot.org/planner/index.html (accessed on 5 December 2018).
64. Alsalam, B.H.Y.; Morton, K.; Campbell, D.; Gonzalez, F. Autonomous UAV with vision based on-board decision making for remote sensing and precision agriculture. In Proceedings of the 2017 IEEE Aerospace Conference, Big Sky, MT, USA, 4–11 March 2017; pp. 1–12.
65. Pixhawk. Pixhawk-4 User Guide and Documentation-PixHawk. 2019. Available online: https://docs.px4.io/v1.9.0/en/flight_controller/pixhawk4.html (accessed on 23 March 2019).
66. FlySky. FlySky FS-i6S RC Transmitter with Receiver. 2019. Available online: https://www.flysky-cn.com/fsi6s (accessed on 10 November 2019).
67. U-Blox. U-Blox Neo-7M GPS Module Specifications and Documentation. 2019. Available online: https://www.u-blox.com/en/product/neo-7-series (accessed on 27 January 2019).
68. Benewafke. Benewake TF02 LiDAR (Mid-Range Distance Sensor) User Guide and Documentation—Benewake. 2019. Available online: http://en.benewake.com/product/detail/5c345c9de5b3a844c4723299 (accessed on 15 February 2019).

69. MicaSense. MicaSense RedEdge—MX Spectral Camera Specifications. 2019. Available online: https://www.micasense.com/rededge-mx (accessed on 15 November 2019).
70. Walsh, O.S.; Shafian, S.; Marshall, J.M.; Jackson, C.; McClintick-Chess, J.R.; Blanscet, S.M.; Swoboda, K.; Thompson, C.; Belmont, K.M.; Walsh, W.L. Assessment of UAV Based Vegetation Indices for Nitrogen Concentration Estimation in Spring Wheat. *Adv. Remote Sens.* **2018**, *7*, 71–90. [CrossRef]
71. Pavlidis, T. Filling algorithms for raster graphics. *Comput. Graph. Image Process.* **1979**, *10*, 126–141. [CrossRef]
72. James, D.F.; Van Dam, A. *Fundamentals of Interactive Computer Graphics*; Addison-Wesley Longman Publishing Co., Inc.: Boston, MA, USA, 1982; Volume 2, ISBN 0-201-14468-9.
73. Little, J.D.C.; Murty, K.G.; Sweeney, D.W.; Karel, C. An Algorithm for the Traveling Salesman Problem. *Oper. Res.* **1963**, *11*, 972–989. [CrossRef]
74. Croes, G.A. A Method for Solving Traveling-Salesman Problems. *Oper. Res.* **1958**, *6*, 791–812. [CrossRef]
75. Chisman, J.A. The clustered traveling salesman problem. *Comput. Oper. Res.* **1975**, *2*, 115–119. [CrossRef]
76. Serra, J. *Image Analysis and Mathematical Morphology*; Academic Press: New York, NY, USA, 1982.
77. Soille, P. *Morphological Image Analysis, Principles and Applications*; Academic Press, Inc.: Orlando, FL, USA, 1999; ISBN 0126372403.
78. Graham, R.L. An efficient algorith for determining the convex hull of a finite planar set. *Inf. Process. Lett.* **1972**, *1*, 132–133. [CrossRef]
79. Jarvis, R. On the identification of the convex hull of a finite set of points in the plane. *Inf. Process. Lett.* **1973**, *2*, 18–21. [CrossRef]
80. Das, G.K.; Das, S.; Nandy, S.C.; Sinha, B.P. Efficient algorithm for placing a given number of base stations to cover a convex region. *J. Parallel Distrib. Comput.* **2006**, *66*, 1353–1358. [CrossRef]
81. De Berg, M.; Van Kreveld, M.; Overmars, M.; Cheong, O. *Computational Geometry*; Springer: Berlin/Heidelberg, Germany, 1997; pp. 1–17. [CrossRef]
82. Lloyd, S. Least squares quantization in PCM. *IEEE Trans. Inf. Theory* **1982**, *28*, 129–137. [CrossRef]
83. Megiddo, N. Linear-time algorithms for linear programming in R^3 and related problems. *SIAM J. Comput.* **1983**, *12*, 759–776. Available online: http://theory.stanford.edu/~{}megiddo/pdf/lp3.pdf (accessed on 5 August 2020). [CrossRef]
84. Mission Planning. Mission Planning—Copter Documentation. 2019. Available online: www.ardupilot.org/copter/docs/common-mission-planning.html (accessed on 25 June 2019).
85. Spekken, M.; De Bruin, S. Optimized routing on agricultural fields by minimizing maneuvering and servicing time. *Precis. Agric.* **2012**, *14*, 224–244. [CrossRef]

High Resolution Geospatial Evapotranspiration Mapping of Irrigated Field Crops Using Multispectral and Thermal Infrared Imagery with METRIC Energy Balance Model

Abhilash K. Chandel [1,2]**, Behnaz Molaei** [1,2]**, Lav R. Khot** [1,2,*]**, R. Troy Peters** [1,2] **and Claudio O. Stöckle** [2,*]

1   Center for Precision and Automated Agricultural Systems, Irrigated Agriculture Research and Extension Center, Washington State University, Prosser, WA 99350, USA; abhilash.chandel@wsu.edu (A.K.C.); behnaz.molaei@wsu.edu (B.M.); troy_peters@wsu.edu (R.T.P.)
2   Department of Biological Systems Engineering, Washington State University, Pullman, WA 99164, USA
*   Correspondence: lav.khot@wsu.edu (L.R.K.); stockle@wsu.edu (C.O.S.)

Abstract: Geospatial crop water use mapping is critical for field-scale site-specific irrigation management. Landsat 7/8 satellite imagery with a widely adopted METRIC (Mapping Evapotranspiration at high Resolution with Internalized Calibration) energy balance model (LM approach) estimates accurate evapotranspiration (ET) but limits field-scale spatiotemporal (30 m pixel^{-1}, ~16 days) mapping. A study was therefore conducted to map actual ET of commercially grown irrigated-field crops (spearmint, potato, and alfalfa) at very high-resolution (7 cm pixel^{-1}). Six small unmanned aerial system (UAS)-based multispectral and thermal infrared imagery campaigns were conducted (two for each crop) at the same time as the Landsat 7/8 overpass. Three variants of METRIC model were used to process the UAS imagery; UAS-METRIC-1, -2, and -3 (UASM-1, -2, and -3) and outputs were compared with the standard LM approach. ET root mean square differences (RMSD) between LM-UASM-1, LM-UASM-2, and LM-UASM-3 were in the ranges of 0.2–2.9, 0.5–0.9, and 0.5–2.7 mm day^{-1}, respectively. Internal calibrations and sensible heat fluxes majorly resulted in such differences. UASM-2 had the highest similarity with the LM approach (RMSD: 0.5–0.9, ET$_{dep,abs}$ (daily ET departures): 2–14%, r (Pearson correlation coefficient) = 0.91). Strong ET correlations between UASM and LM approaches (0.7–0.8, 0.7–0.8, and 0.8–0.9 for spearmint, potato, and alfalfa crops) suggest equal suitability of UASM approaches as LM to map ET for a range of similar crops. UASM approaches (Coefficient of variation, CV: 6.7–24.3%) however outperformed the LM approach (CV: 2.1–11.2%) in mapping spatial ET variations due to large number of pixels. On-demand UAS imagery may thus help in deriving high resolution site-specific ET maps, for growers to aid in timely crop water management.

Keywords: actual evapotranspiration; high spatiotemporal resolution; multispectral imagery; thermal infrared imagery; METRIC energy balance model; irrigated field crops

1. Introduction

Satellite-based remote sensing (RS) has been extensively used with energy balance models for regional scale evapotranspiration (ET) mapping [1–8]. One such widely adopted model is Mapping ET at high-resolution with Internalized Calibration (METRIC) [9,10]. The METRIC model uses Landsat 5/7/8, or Terra and Aqua satellite based multispectral and thermal infrared imagery data to compute ET as an energy balance residue. METRIC is advantageous for its independence from surface conditions, stabilized sensible heat flux (H) estimations, and internal calibration using hot and cold

anchor pixels. This internal calibration compensates for any computational biases that arise from atmospheric dynamics, surface albedo, net radiation (R_n), surface temperature (T_s), air temperature (T_a), soil heat flux (G), and wind speed (u). The METRIC model has been evaluated for a wide range of irrigated field and orchard/tree crops under different agroclimatic zones, with studies reporting ET estimation errors in the ranges of 1 to 11% [11–22].

Conventional METRIC uses high orbiting satellite imagery and as a result has low spatial (~30 m pixel^{-1} for Landsat and 1 km pixel^{-1} for Terra and Aqua satellites) and temporal resolution (~16 days for Landsat) ET maps. Cloud cover is an additional challenge. Alternatively, the ET mapping can be improved spatiotemporally using unmanned aerial system (UAS)-based imagery data [23–25] that can be collected on-demand [7,26–29]. Recent UAS technology advancements have enabled rapid assessment of crop vigor and soil characteristics, crop water requirements, disease infestation, and yield prediction [23,26–30]. Pertinent to ET estimation, Chavez et al. [27] have used airborne imagery data with METRIC and reported daily ET errors of 9% for corn and sorghum grown on experimental plots. Similarly, Ortega-Farias et al. [31] have estimated ET using UAS imagery for a drip irrigated olive orchard and reported maximum errors below 7%. Brenner et al. [32] have estimated latent heat fluxes (LE) from energy balance model for irrigated grassland and observed errors below 10%. They also reported strong correlations of up to 0.9 between estimated LE and that measured with eddy covariance system. Furthermore, Paul et al. [33] have reported suitability of UAS based imagery in conjunction with METRIC model to estimate ET with maximum errors below 11% for irrigated forage, corn, and sorghum crops. All these studies have experimentally illustrated potential of UAS based RS data for accurate ET estimation. However, ET mapping of commercial crop fields from the grower's perspective has been limited for site-specific irrigation management. Additionally, the differences in spatial ET mapping due to in-field elevation variability and near-site available meteorological inputs have not been evaluated with respect to the conventional satellite-based METRIC approach.

Agricultural growers typically use standard crop coefficients or point soil moisture measurements for irrigation scheduling and supply water at a constant rate to the entire field. This results in either under or over irrigation. Satellite imagery also restricts site-specific irrigation management due to low spatiotemporal resolutions. Alternatively, ET mapping with UAS imagery could be directly applicable to growers. This study therefore assesses the suitability of UAS-based imagery to geospatially map actual ET at very high-resolution relative to the satellite-based imagery. The spatial ET differences resulting due to local field conditions and near-site meteorological inputs are also assessed. The specific objectives are: (1) ET mapping of irrigated spearmint, potato, and alfalfa crops under commercial operations using UAS-based multispectral and thermal infrared imagery with variants of METRIC energy balance model, and (2) parametric comparison of the model outputs and spatial ET variation assessment potentials from UAS imagery with that from satellite (Landsat 7/8) imagery.

2. Materials and Methods

2.1. Field Sites

Selected were commercial sites (Table 1) planted with spearmint (Cultivar (cv.) Native) in Toppenish, potato (cv. Russet Burbank) in Paterson, and alfalfa (cv. FD-4) in Prosser in Washington state (Figure 1). All sites received limited rainfall (<60 mm), and seasonal mean air temperatures up to 20 °C and cumulative reference ET between 1000 to 1200 mm were observed.

Table 1. Details of the field site and weather parameters for 2018 growth season.

Parameter	Site 1	Site 2	Site 3
Crop	Spearmint	Potato	Alfalfa
Location, WA	Toppenish (46°22′19.16′′ N, 120°27′21.91′′ W)	Paterson (45°59′43.52′′ N, 119°33′57.58′′ W)	Prosser (46°17′35.16′′ N, 119°44′38.82′′ W)
Irrigation system	Center pivot	Center pivot	Wheel-line
Study plot size (m × m)	175 × 135	275 × 170	300 × 140
Mean wind speed (m s^{-1})	1.8	2.1	2.6
Mean relative humidity (%)	46.9	55.5	52.9
Total precipitation (mm)	25	53	57.2
Mean air temperature (°C)	20.1	18.2	18
Cumulative seasonal reference ET (alfalfa-based, mm)	1042	1153	1216
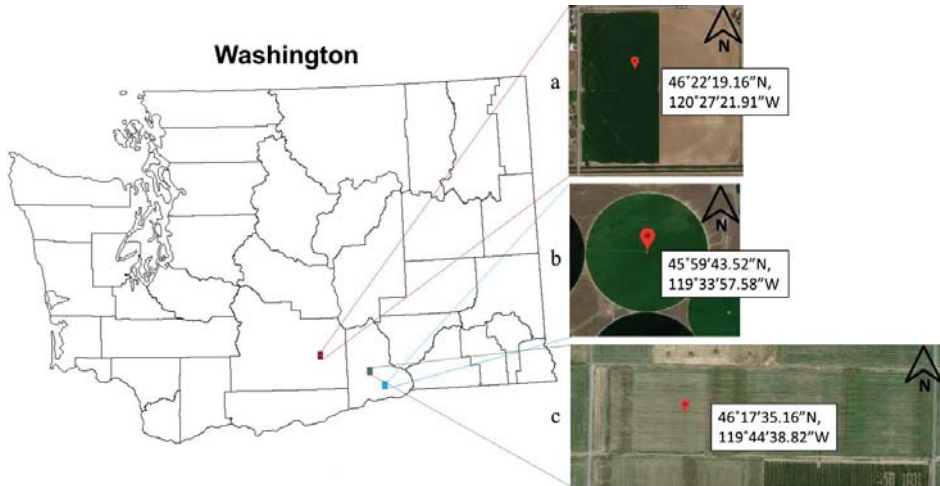
Figure 1. Geolocations of (**a**) spearmint, (**b**) potato, and (**c**) alfalfa crop study sites (Source: Google Maps).

2.2. Data Acquisition Campaigns

2.2.1. UAS-Based Imagery

A UAS (ATI AgBOT™, Aerial Technology International, Wilsonville, OR, USA) was deployed for imagery data acquisition (Figure 2). On-board was a multispectral imaging sensor (RedEdge 3, MicaSense, Inc., Seattle, WA, USA) with Blue (B, 475 ± 10 nm), Green (G, 560 ± 10 nm), Red (R, 668 ± 5 nm), Red Edge (RE, 717 ± 5 nm), and Near Infrared (NIR, 840 ± 20 nm) wavebands and a radiometric calibrated thermal infrared imaging sensor (11,000 ± 3000 nm, Tau 2 640, FLIR Systems, Wilsonville, OR, USA). Image-specific geotags for the multispectral sensor were received from the global positioning system (GPS) receiver on-board UAS and that for thermal sensor were received from an independent GPS receiver (ThermalCapture GPS, TeAx Technology GmbH, Wilnsdorf, Germany). On-board the UAS was also a downwelling light sensor (DLS, MicaSense, Inc., Wilnsdorf, WA, USA) facing skyward to embed the solar irradiance data in the imagery spectrum during flights.

UAS flights were configured using a ground control software (MissionPlanner, version 1.3.49, Ardupilot, USA) for altitude of 100 m above ground level (AGL) to acquire multispectral and thermal images at ground sampling resolutions of 7 and 13 cm pixel^{-1}, respectively. The software aided in configuring the multispectral sensor to acquire images at 85% front and 75% side overlaps. The thermal imaging sensor was configured independently to acquire frames at 3 Hz to ensure image overlaps of 90–95%. Imagery data was stored on-board in respective memory cards for the two sensors. A calibrated reflectance panel (CRP, Micasense Inc., Seattle, WA, USA) was imaged before and after

each flight and these reference images were used for radiometric calibration of the multispectral imagery (Figure 2).

Total six UAS flights were conducted in summers of 2018 (two missions/site × 3 sites) during the dates and approximate times of the Landsat 7/8 overpass. UAS imagery for spearmint crop was collected 10 days before the first harvest (dataset-1) and 37 days before the second harvest (dataset-2). Imagery for the potato crop was acquired 72 days (dataset-3) and 48 days before harvest (DBH, dataset-4). Data for the alfalfa crop was collected 2 days before the first harvest (dataset-5) and 7 days before the second harvest (dataset-6).
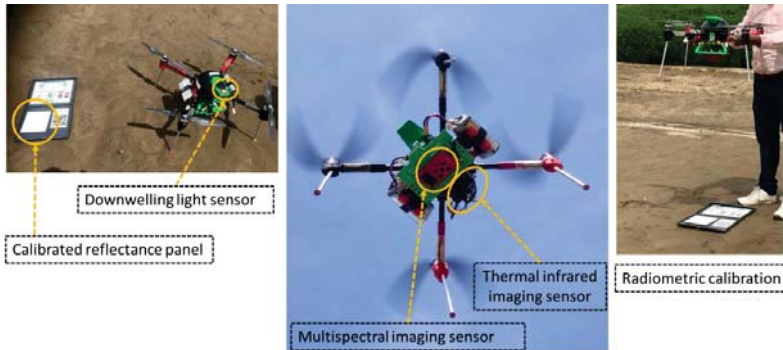
Figure 2. High-resolution imagery campaigns with optical sensors integrated with the small unmanned aerial system.

2.2.2. Satellite-Based Imagery and Weather Data

Landsat 7/8 imagery datasets and 1-arc SRTM (Shuttle Radar Topography Mission) digital elevation models (DEM) were downloaded for the data collection days (Table 2). Weather data logged at every 15 min was downloaded from the nearest (1–5 km) stations (AgWeatherNet, Washington State University, Washington, WA, USA). All the data collected on a day were grouped to have a total of six datasets (see Table 2) ready for analysis.

Table 2. Summary of datasets used as inputs to METRIC energy balance.

Dataset	DOY	DBH	Crop	UAS Imagery	Landsat 7/8 Imagery	Weather & Scene Metadata
1	175	10	Spearmint	√	√	√
2	224	37	Spearmint	√	√	√
3	184	72	Potato	√	√	√
4	208	48	Potato	√	√	√
5	191	2	Alfalfa	√	√	√
6	223	7	Alfalfa	√	√	√

DOY: day of year, DBH: days before harvest, √: subset data, scene metadata: date, time, sun azimuth and solar elevation angles during flights.

2.3. Imagery Analysis and METRIC Models Implementation

2.3.1. Preprocessing

UAS imagery was initially processed to obtain orthomosaics of the study site(s) through a series of image stitching operations (Figure 3a) in a photogrammetry and mapping software (Pix4D Mapper, Pix4D, Inc., Lausanne, Switzerland). Independent surface temperature orthomosaic was then georeferenced and resampled to the multispectral orthomosaic (7 cm pixel^{-1}) in Quantum Geographic Information System (QGIS) platform (ver.2.18.16, Open Source). The "Georeferencer" tool with "Thin Plate Spline" as the transformation type was used for georeferencing and the "Nearest Neighborhood" method was used for resampling. Five surfaces reflectance (B, G, R, RE, and NIR

(Figure 3b)), one surface temperature (Figure 3c) and a DEM orthomosaic were obtained for each UAS mission.
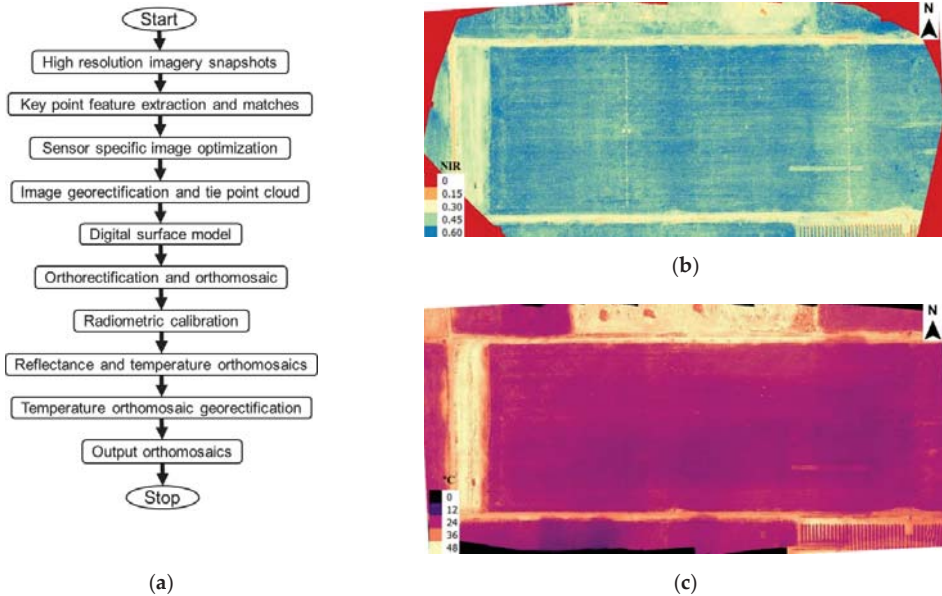
Figure 3. Images showing (**a**) preprocessing flow chart and unmanned aerial system imagery derived (**b**) near-infrared, and (**c**) temperature orthomosaics of the alfalfa field site (DBH: 2, DOY: 191).

2.3.2. METRIC Model Implementation

The METRIC model is detailed in Allen et al. [9]. Briefly, model computes R_n, G, H and residual LE within the blending height (100–200 m AGL) which can be converted to actual water loss to the atmosphere (ET). METRIC eliminates the need for accurate surface temperature (T_s) measurements. It uses ground weather station-based reference ET (ET_r, alfalfa crop based) for internal calibration and reduction of biases related to satellite imagery. The internal calibration indexes near-surface temperature gradients to the radiometric T_s using extreme hot and cold anchor pixels. The model was primarily developed for agricultural fields and does not need crop specific inputs. This enhances METRIC's applicability to high-resolution RS data. Small UAS based RS data captures distinct features of soil, vegetation, or mixed regions that can improve internal calibration of METRIC model with respect to the study environment [26–29,33].

Conventional METRIC maps regional ET for 185×185 km scene size and all its assumptions might not necessarily apply at the field-scale. Therefore, METRIC model was implemented with three variant approaches. The resulting approaches are named as UAS-METRIC-1, -2, and -3 (UASM-1, -2, and -3) with pertinent modification highlights summarized in Table 3. UASM-1 (Figure 4) was implemented to observe relative differences only due to UAS imagery specific inputs that include (i) scene metadata from flight missions, (ii) surface albedo from on-board multispectral imager, and (iii) high-resolution DEM. All other equations were identical as the conventional METRIC. Similar to LM, leaf area index (LAI) in UASM-1 was calculated using soil adjusted vegetation index (SAVI) with background adjustment factor (L) of 0.1 for high crop cover [34,35]. UASM-2 was employed for two reasons: (i) possibility to reduce model input data needs from the grower perspective and (ii) to assess pertinent differences caused by the DEM typical to flat agricultural fields located in non-terrain regions. Implementation of UASM-2

was identical to UASM-1 except that UASM-2 used a flat DEM for local field conditions. This scenario forced surface slopes and aspects to zero and elevation as the mean of all pixels in the DEM.
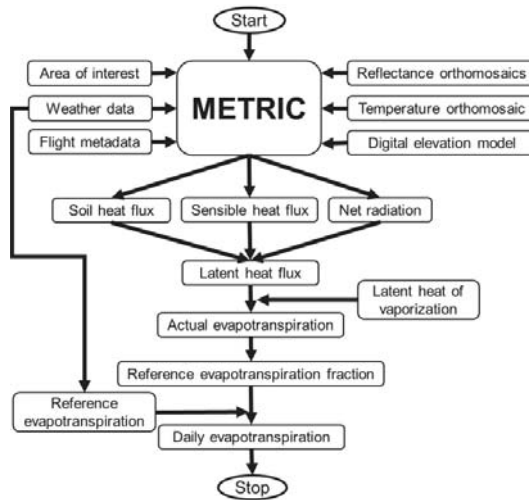
Figure 4. Flow chart for processing UAS-based imagery data with Mapping Evapotranspiration at High Resolution with Internalized Calibration (METRIC) energy balance model.

UASM-3 considered site-specific energy balance inputs typical to agricultural field plots imaged in this study. Pertinent modifications include (i) DEM as per field conditions (as in UASM-2), (ii) LAI calculation from spatial fraction canopy cover (FCC), (iii) incoming shortwave radiation (ISWR) from the nearest open field weather station, (iv) incoming longwave radiation (ILWR) calculation using air temperature (T_a), and (v) momentum roughness length (MRL) calculated without surface slope (S) adjustments. The LAI calculation in UASM-3 were based on the fact that surface features (i.e., soil, vegetation, and mixed) could be distinctively captured in every pixel [28–30] of high-resolution imagery. FCC was first derived from the normalized difference vegetation index (NDVI) [28,36,37] and soil was segmented using NDVI vegetation threshold mask (>0.3) to ensure LAI for the vegetation only. ISWR measurements from the nearest weather station may be assumed as actual shortwave radiation on the surface for the fact that these are open-field stations installed at 2 m AGL and located within 5 km radius from the study sites. Moreover, conventional ISWR calculation might get affected by cloud cover and other atmospheric dynamics [38,39]. T_a from nearest weather station was used to calculate ILWR and can be assumed constant for a field (Stefan Boltzmann's law, [40]).

For comparisons, Landsat imagery was processed through the conventional METRIC model as described in a "R package" (water, [41,42]), hereafter abbreviated as LM (Landsat-METRIC) approach. Level-2 surface reflectance products were downloaded for Landsat 8 while such products were calculated within the package for Landsat 7 datasets. Similar to the LM approach, all UASM approaches performed an energy balance within the blending height and used the conventional automated approach of selecting anchor pixels.

2.4. Output Comparisons

This study aimed at evaluating spatial ET maps from UAS based remote sensing (RS) data relative to satellite-based RS data for crops grown in commercial farming operations. As the conventional METRIC model is well-established for spatial ET mapping for its corroboration in over 25 countries and in almost all types of agroclimatic zones [22], the additional field validation was deemed not necessary, i.e., outside the scope of the study. Thus, we did not conduct ground-reference ET measurements.

Table 3. METRIC model modifications for UAS imagery compared to the conventional Landsat-METRIC (LM) approach.

Parameter	LM	UASM-1	UASM-2	UASM-3
Metadata	Landsat 7/8 based	UAS flight based		
Surface albedo	Landsat 7/8 imager based	UAS imager based		
Digital elevation model (DEM)	SRTM grids	Derived corresponding to small UAS-based imagery		
		Considers variable elevation, slope and aspect per pixel	Considers constant elevation by forcing slope and aspects to zero	
Leaf area index (LAI)		$LAI = -(ln[(0.69-SAVI)/0.59])/0.91$ $SAVI = ((1+L)\times(R_{NIR}-R_R))/(L+(R_{NIR}+R_R)),\ L=0.1$		$LAI = (-ln(1-FCC))/K$ $FCC = (NDVI-NDVI_{min})/(NDVI_{max}-NDVI_{min})$ $FCC = 0$ for $NDVI < 0.3$
Incoming shortwave radiation (ISWR)	$R_{s\downarrow} = G_{sc} \times cos\theta_{rel} \times \tau_{sw}/d^2$			
	$cos\theta_{rel}$ calculated for non-horizontal surface using surface slopes and aspect.		$cos\theta_{rel}$ calculated for horizontal surface by forcing surface slope and aspect to zero.	Measured directly from the nearest open field weather station.
Incoming longwave radiation (ILWR)	$R_{L\downarrow} = \varepsilon_a \sigma Ts^4$			$R_{L\downarrow} = \varepsilon_a \sigma T_a^4$
Momentum roughness length (MRL)	$Z_{om,mtn} = Z_{om} \times (1 + (((180\times S)/\pi)-5)/20)$		$Z_{om} = 0.018 \times LAI$	No adjustment

NDVI: Normalized difference vegetation index, **SAVI**: Soil adjusted vegetation index, **K**: Solar extinction coefficient, **R$_{NIR}$**: Reflectance in near-infrared band, **R$_R$**: Reflectance in red band, **L**: Soil background adjustment factor, **θ$_{rel}$**: Angle of incidence, **τ$_{sw}$**: Atmospheric transmissivity, **d**: Relative earth-sun distance, **G$_{sc}$**: Solar constant, **ε$_a$**: Atmospheric emissivity, **σ**: Stefan Boltzmann's constant, **T$_s$**: Surface temperature, **T$_a$**: Air temperature, and **S**: Surface slope derived from DEM and **Z$_{om,mtn}$**: Momentum roughness length adjusted for varying elevation surface.

Since the energy balance computations with LM approach were performed for images of 180 km × 180 km dimension, intermediate and final output maps were clipped to the study site areas covered by the UAS flights. The mean, standard deviation (SD), and coefficients of variation (CV, %) to assess spatial variability capturing potentials of ET pixels from LM (ET_{LM}) and UASM-1, -2, and -3 approaches (ET_{UASM}) were calculated. Percentage absolute departures of mean ET ($ET_{dep,abs}$, Equation (1)) from all UAS-based approaches with respect to that from the LM approach were also calculated. Next, ET maps from all UAS-based approaches were resampled to the resolution equal to ET maps from LM approach (30 m pixel^{-1}) using the "Nearest Neighborhood" method and region of interest (ROI) samples were randomly extracted. Sample ET from these ROIs were compared using root mean square difference (RMSD) and Pearson's linear correlation (*r*) at 5% significance (RStudio, Inc., Boston, MA, USA).

$$ET_{dep,abs} \ (\%) = (|ET_{UASM} - ET_{LM}| \times 100)/ET_{LM} \tag{1}$$

3. Results

Major energy balance computations from the UASM and LM approaches are presented in the following subsections. Results pertinent to spearmint (Table 4, Figures 5a–d and 6), potato (Table 5, Figures 5e–h and 7), and alfalfa crops (Table 6, Figures 5i–l and 8) are also presented.

3.1. Crop Vigor

The UAS imagery mapped crop vigor indicators of SAVI (Mean: 0.7–0.9, SD: 0.1–0.2) and NDVI (Mean: 0.8–0.9, SD: 0.1–0.2) similar to the Landsat imagery mapped SAVI (Mean: 0.7–0.85, SD: ~0.02) and NDVI (Mean: 0.8–0.9, SD: 0.02–0.1). The mean LAI from LM approach ranged between 4–6 m^2 m^{-2} and that from UASM-1/-2 and -3 ranged from 5.1–5.8 m^2 m^{-2} and 3.5–5.9 m^2 m^{-2}, respectively. Mean FCC ranges were 0.91–0.93 (SD: ~0.14) for spearmint, 0.92–0.93 (SD: ~0.1) for potato, and 0.8–0.9 (SD: 0.1–0.24) for the alfalfa fields. All these estimates show high density vegetation also observed at the sites.

3.2. Net Radiation, Soil Heat and Sensible Heat Fluxes

The mean ISWR ranges from the LM, UASM-1, -2, and -3 approaches were 819–903, 817–927, 818–921, and 737–949 W m^{-2}, respectively. Mean ILWR ranges from those approaches were 337–396, 296–347, 296–347, and 321–375 W m^{-2}, respectively. Mean outgoing longwave radiation (OLWR) from the LM, UASM-1, -2, and -3 approaches ranged between 440–514, 381–451, 381–451, and 381–451 W m^{-2}, respectively and R_n ranges were 508–594, 596–685, 596–685, and 564–716 W m^{-2}. Mapped G from the LM, UASM-1, -2, and -3 approaches were in the ranges of 23.8–63.6, 19.4–35.9, 19.4–35.9, and 18.2–36.1 W m^{-2}, respectively and mean H ranges were 60–181, 114–237, 126–250, and 127–233 W m^{-2}, respectively.

3.3. Daily Evapotranspiration

The mean ranges of mapped instantaneous ET (ET_{inst}) from the LM, UASM-1, -2, and -3 approaches were 0.5–0.7, 0.5–0.7, 0.5–0.7, and 0.5–0.7 mm h^{-1}, respectively and pertinent ET_rF ranges were 0.7–0.9, 0.74–0.95, 0.7–1, and 0.7–0.93, respectively. ET_{r24} for the six datasets were 9.4, 5.2, 6.3, 6.5, 8.8, and 8.5 mm day^{-1}. The mean of mapped daily ET from LM, UASM-1, -2, and -3 approaches were in the ranges of 4–7, 4.3–8.4, 4.1–6.7, and 3.9–8.2 mm day^{-1}, respectively. Ranges of absolute departures of daily ET ($ET_{dep,abs}$) from UASM-1, -2, and -3 were 0.4–20.8, 2.0–14.4, and 2.2–21% of ET_{LM}, respectively for the selected crops. Highest correlations and minimum RMSDs (Figures 6–9) were observed for UASM-2 (*r*: 0.66–0.9, RMSD: 0.5–0.9) followed by UASM-1 (*r*: 0.65–0.9, RMSD: 0.2–2.9) and UASM-3 (*r*: 0.65–0.9, RMSD: 0.5–2.7) approaches compared to the LM approach.

Table 4. Summary of intermediate and final energy balance outputs for spearmint crop.

Approach	LM				UASM-1				UASM-2				UASM-3			
	Mean		SD		Mean		SD		Mean		SD		Mean		SD	
Parameter (Unit) / DBH	10	37	10	37	10	37	10	37	10	37	10	37	10	37	10	37
$SAVI$	0.8	0.9	0.03	0.01	0.8 *	0.8 *	0.1 *	0.1 *	0.8 *	0.8 *	0.1 *	0.1 *	0.8 *	0.8 *	0.1 *	0.1 *
$NDVI$	0.9	0.9	0.02	0.02	0.9 *	0.9 *	0.1 *	0.1 *	0.9 *	0.9 *	0.1 *	0.1 *	0.9 *	0.9 *	0.1 *	0.1 *
FCC	-	-	-	-	-	-	-	-	-	-	-	-	0.9	0.9	0.2	0.1
LAI (m² m⁻²)	5.8	6.0	0.3	0.1	5.5 *	5.7 *	1.2 *	1.0 *	5.5 *	5.7 *	1.2 *	1.0 *	5.5	5.9	1.6	0.9
MRL (m)	0.1	0.1	0.004	0.001	0.1	0.1	0.02	0.02	0.1	0.1	0.02	0.02	0.1	0.1	0.03	0.02
$ISWR$ (W m⁻²)	903	820	0.02	0.01	899	817	6.1	8.3	901	820	0.01	0.01	934	737	-	-
$ILWR$ (W m⁻²)	396	352	4.4	3.8	347 *	296 *	24.2 *	11.0 *	347 *	296 *	24 *	11.0 *	349	334	-	-
$OLWR$ (W m⁻²)	515	455	5.7	4.9	451 *	382 *	29.7 *	13.2 *	451 *	382 *	29.7 *	13.2 *	451	381	29.7	13.5
Net radiation (R_n, W m⁻²)	594	508	17.3	11.3	677 *	596 *	16.3 *	17.7 *	677 *	596 *	16.3 *	17.7 *	707	564	29.2	22.3
Soil heat flux (G, W m⁻²)	48.3	23.8	8	3.6	35 *	19.4 *	22 *	8.4 *	35.2 *	19.4 *	22 *	8.4 *	36	18.2	20.2	7.2
Sensible heat flux (H, W m⁻²)	106	168	13.5	12	188	237	87	41	165	250	87	39	194	234	80	29.5
ET_{inst} (mm h⁻¹)	0.66	0.47	0.04	0.02	0.67	0.50	0.15	0.08	0.65	0.48	0.15	0.08	0.65	0.46	0.15	0.08
ET_rF	0.73	0.78	0.05	0.04	0.74	0.83	0.16	0.13	0.71	0.79	0.16	0.13	0.72	0.76	0.16	0.13
ET_{r24} (mm day⁻¹)	9.43 *	5.2 *	0	0	9.43 *	5.16 *	0	0	9.43 *	5.16 *	0	0	9.43 *	5.16 *	0	0
Daily ET (mm day⁻¹)	6.99	4.01	0.22	0.20	6.96	4.26	1.53	0.67	6.72	4.09	1.5	0.65	6.79	3.92	1.53	0.65
$ET_{dep,abs}$ (%)	0.43	-	-	-	0.43	6.23	-	-	3.86	2.00	-	-	2.86	2.24	-	-

$ET_{dep,abs}$ (%): Percentage absolute ET departure with respect to LM approach, **SD**: Standard deviation, and * indicates same values for different approaches on same data collection day.

Table 5. Summary of intermediate and final energy balance outputs for potato crop.

Approach	LM				UASM-1				UASM-2				UASM-3			
	Mean		SD		Mean		SD		Mean		SD		Mean		SD	
Parameter (Unit) / DBH	72	48	72	48	72	48	72	48	72	48	72	48	72	48	72	48
$SAVI$	0.86	0.82	0.02	0.03	0.85 *	0.85 *	0.09 *	0.07 *	0.85 *	0.85 *	0.09 *	0.07 *	0.85 *	0.85 *	0.09 *	0.07 *
$NDVI$	0.90	0.85	0.02	0.02	0.90 *	0.88 *	0.09 *	0.06 *	0.90 *	0.88 *	0.09 *	0.06 *	0.90 *	0.88 *	0.09 *	0.06 *
FCC	-	-	-	-	-	-	-	-	-	-	-	-	0.93	0.92	0.12	0.08
LAI (m² m⁻²)	6	4.02	0	0.46	5.83 *	5.82 *	0.85 *	0.70 *	5.83 *	5.82 *	0.85 *	0.70 *	5.52	5.11	0.71	0.62
MRL (m)	0.08	0.04	0	0.006	0.09	0.09	0.01	0.01	0.11	0.1	0.02	0.01	0.1	0.09	0.01	0.01
$ISWR$ (W m⁻²)	903.5	854.9	0.01	0.01	927.1	873.4	7.35	9.95	921.3	865.6	0.003	0.003	949	889	-	-
$ILWR$ (W m⁻²)	337.2	370.3	4.38	3.68	314.3 *	335.8 *	4.14 *	9.99 *	314.3 *	335.8 *	4.14 *	9.99 *	321.3	375.4	-	-
$OLWR$ (W m⁻²)	439.6	478.5	5.71	4.02	409.9 *	434.7 *	4.11 *	12.04 *	409.9 *	434.7 *	4.11 *	12 *	409.8	434.6	4.05	12
Net radiation (R_n, W m⁻²)	565.5	546.6	9.22	6.68	685.2 *	617 *	15.0 *	18.42 *	685.2 *	617 *	15.0 *	18.4 *	715.8	675.3	17.4	20.5

Table 5. *Cont.*

Approach	LM				UASM-1				UASM-2				UASM-3			
	Mean		SD		Mean		SD		Mean		SD		Mean		SD	
Parameter (Unit)																
DBH	72	48	72	48	72	48	72	48	72	48	72	48	72	48	72	48
Soil heat flux (G, W m^{-2})	29	46.9	3.94	5.50	22.5 *	29.9 *	9.53 *	10.97 *	22.5 *	29.9 *	9.53 *	11 *	23.5	32.6	9.50	10.8
Sensible heat flux (H, W m^{-2})	133	91.8	13.4	6.35	175.3	180.5	71.7	17.78	201.1	134.8	67.6	20.5	202.5	218.7	67.5	12.4
ET_{Inst} (mm h^{-1})	0.59	0.61	0.02	0.01	0.71	0.60	0.13	0.04	0.68	0.67	0.12	0.05	0.72	0.62	0.13	0.05
ET,F	0.75	0.89	0.03	0.02	0.91	0.88	0.10	0.06	0.86	0.98	0.10	0.07	0.91	0.92	0.10	0.07
ET_{r24} (mm day^{-1})	6.27 *	6.47 *	0	0	6.27 *	6.47 *	0	0	6.27 *	6.47 *	0	0	6.27 *	6.47 *	0	0
Daily ET (mm day^{-1})	4.71	5.76	0.17	0.12	5.69	5.71	0.63	0.42	5.39	6.35	0.60	0.45	5.71	5.95	0.63	0.44
$ET_{dep,abs}$ (%)	-	-	-	-	20.8	0.87	-	-	14.4	10.2	-	-	21.2	3.30	-	-

* indicates same values for different approaches on same data collection day.

Table 6. Summary of intermediate and final energy balance outputs for alfalfa crop.

Approach	LM				UASM-1				UASM-2				UASM-3			
	Mean		SD		Mean		SD		Mean		SD		Mean		SD	
Parameter (Unit)																
DBH	2	7	2	7	2	7	2	7	2	7	2	7	2	7	2	7
SAVI	0.83	0.68	0.01	0.19	0.85 *	0.73 *	0.07 *	0.20 *	0.85 *	0.73 *	0.07 *	0.20 *	0.85 *	0.73 *	0.07 *	0.20 *
NDVI	0.83	0.83	0.11	0.08	0.82 *	0.81 *	0.17 *	0.22 *	0.82 *	0.81 *	0.17 *	0.22 *	0.82 *	0.81 *	0.17 *	0.22 *
FCC	-	-	-	-	-	-	-	-	-	-	-	-	0.92	0.80	0.08	0.24
LAI (m^2 m^{-2})	5.31	4.74	0.68	1.24	5.25 *	5.05 *	1.53 *	0.98 *	5.25 *	5.05 *	1.53 *	0.98 *	5.05	3.54	0.96	1.18
MRL (m)	0.07	0.06	0.02	0.02	0.08	0.08	0.01	0.02	0.09	0.09	0.003	0.02	0.09	0.04	0.02	0.01
ISWR (W m^{-2})	886.1	822.9	0.02	0.02	902.3	840.4	9.19	9.90	889.2	821.3	0.003	0.003	872	804.5	-	-
ILWR (W m^{-2})	367.2	367	7.00	6.89	324.1 *	312.2 *	27.8 *	20.7 *	324.1 *	312.2 *	27.8 *	20.7 *	331.9	346.7	-	-
OLWR (W m^{-2})	475.1	477.6	8.58	8.34	419.2 *	401.9 *	32.5 *	23.2 *	419.2 *	401.9 *	32.5 *	23.2 *	419.5	401.8	32.5	23.1
Net radiation (R_n, W m^{-2})	592.5	534.7	9.03	5.73	661.4 *	620.7 *	28.7 *	29.1 *	661.4 *	620.7 *	28.7 *	29.1 *	654.6	639.8	53.5	46.7
Soil heat flux (G, W m^{-2})	63.6	44.6	15.3	15.7	35.9 *	27.6 *	25.6 *	21.1 *	35.9 *	27.6 *	25.6 *	21.1 *	33.7	27.7	20.2	19
Sensible heat flux (H, W m^{-2})	181	59.9	33.7	30.3	119.5	114.3	70	51.8	238.4	126.3	47	49.8	126.9	137.5	46.2	34
ET_{Inst} (mm h^{-1})	0.53	0.64	0.07	0.06	0.74	0.70	0.18	0.14	0.57	0.68	0.14	0.14	0.72	0.69	0.17	0.14
ET,F	0.67	0.74	0.08	0.07	0.95	0.81	0.22	0.16	0.73	0.79	0.18	0.16	0.93	0.80	0.22	0.16
ET_{r24} (mm day^{-1})	8.84 *	8.48 *	0	0	8.84 *	8.48 *	0	0	8.84 *	8.48 *	0	0	8.84 *	8.84 *	0	0
Daily ET (mm day^{-1})	5.90	6.26	0.73	0.59	8.40	6.88	1.95	1.39	6.43	6.71	1.56	1.36	8.18	6.82	1.91	1.38
$ET_{dep,abs}$ (%)	-	-	-	-	42.4	9.90	-	-	8.98	7.19	-	-	38.6	8.95	-	-

* indicates same values for different approaches on same data collection day.
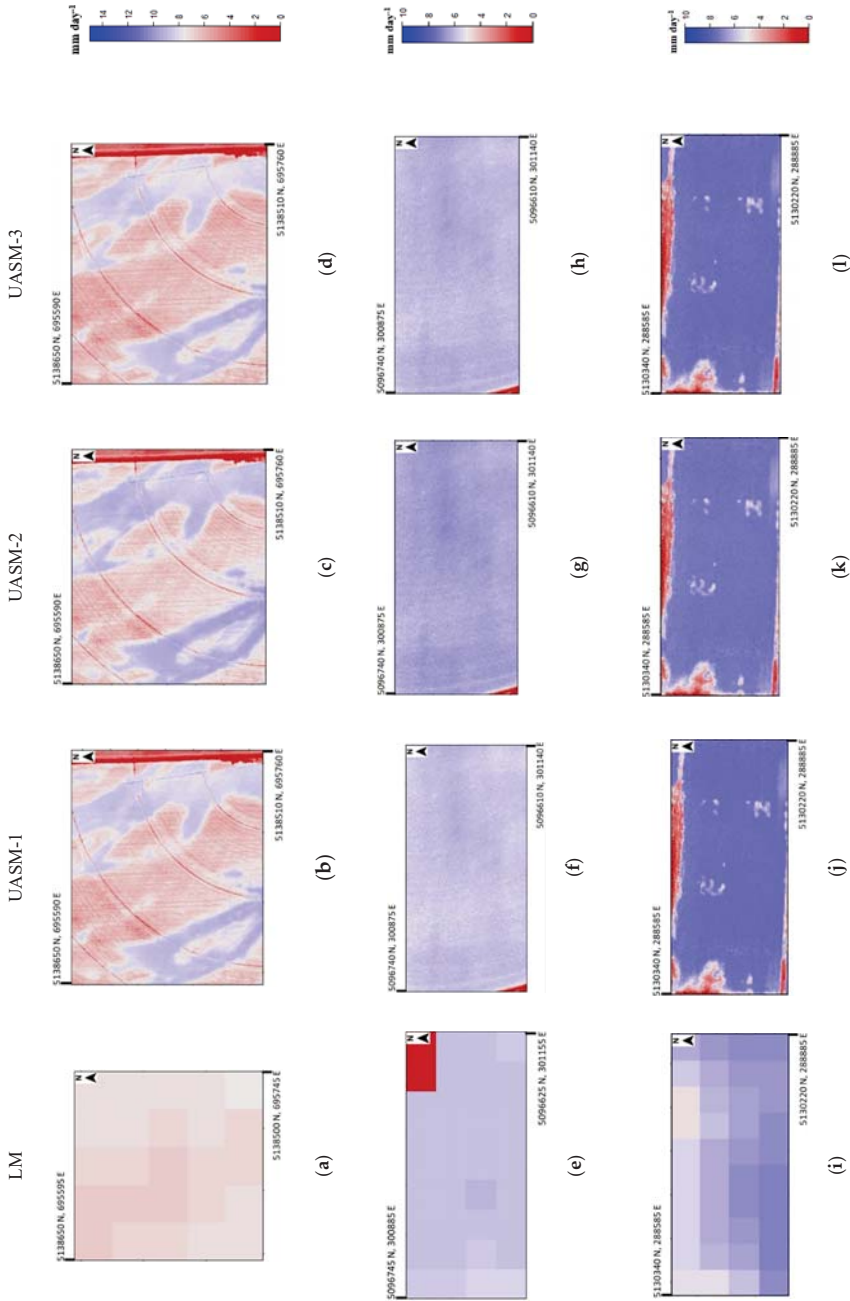
Figure 5. Sample daily ET maps from LM and very high resolution UASM-1, UASM-2, and UASM-3 approaches for spearmint (**a**–**d**), potato (**e**–**h**), and alfalfa (**i**–**l**) field crops.
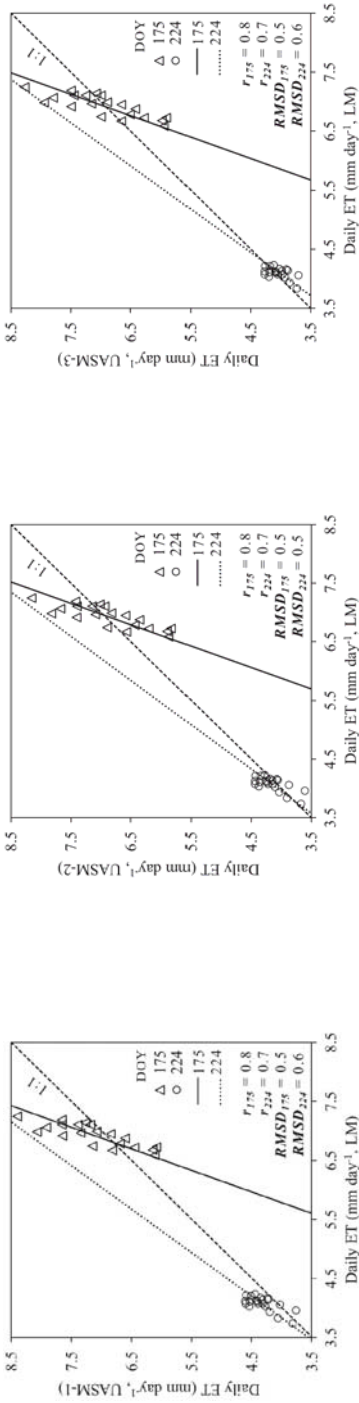
Figure 6. ET comparison plots between (**a**) LM and UASM-1, (**b**) LM and UASM-2, and (**c**) LM and UASM-3 approaches for spearmint crop.
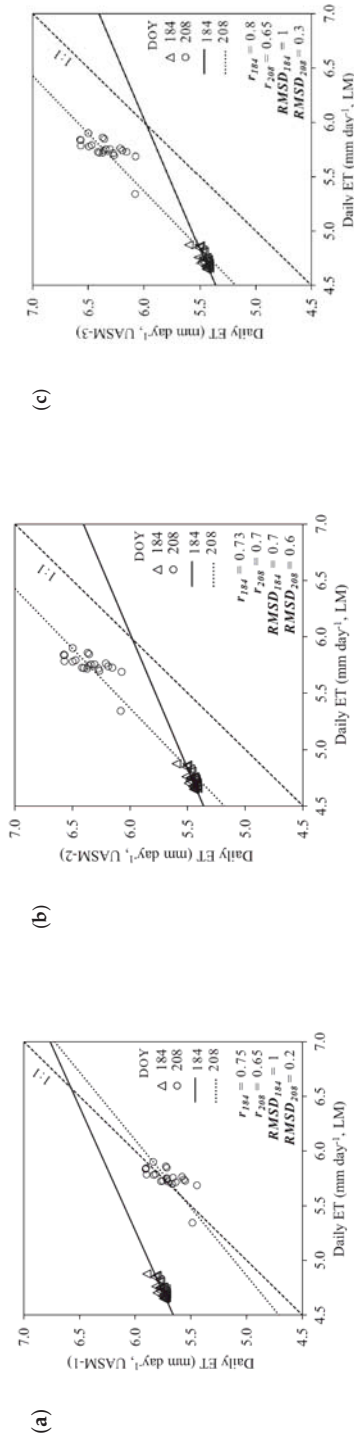
Figure 7. ET comparison plots between (**a**) LM and UASM-1, (**b**) LM and UASM-2, and (**c**) LM and UASM-3 approaches for potato crop.
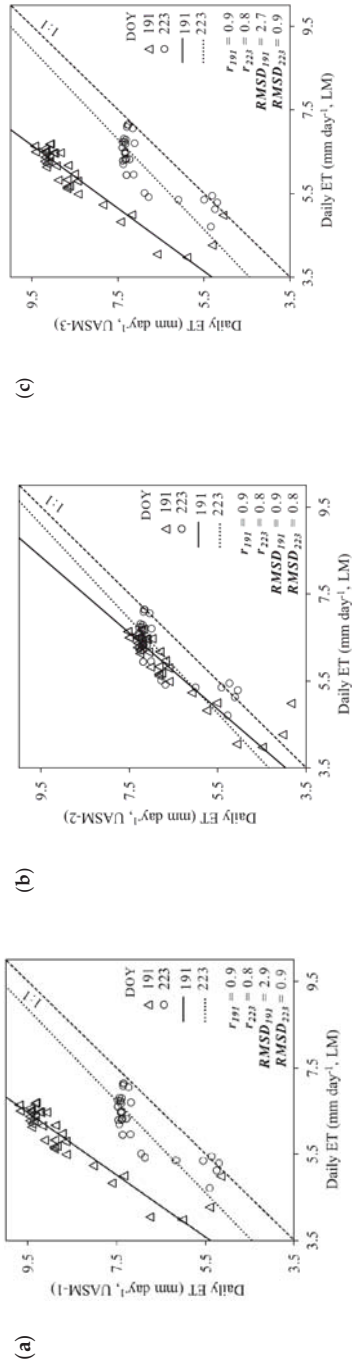
Figure 8. ET comparison plots between (**a**) LM and UASM-1, (**b**) LM and UASM-2, and (**c**) LM and UASM-3 approaches for alfalfa crop.
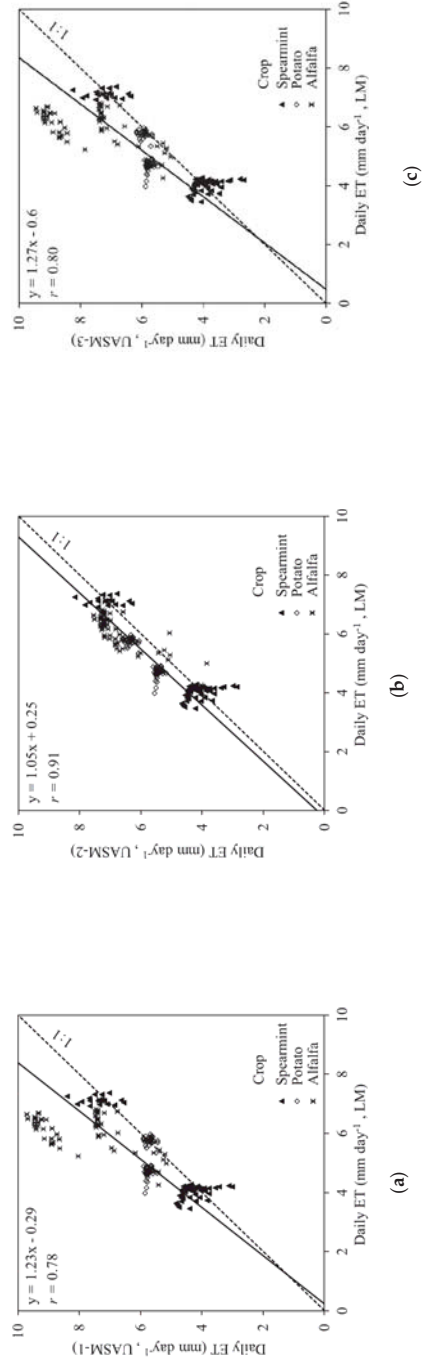
Figure 9. Combined ET comparison plots between (**a**) LM and UASM-1, (**b**) LM and UASM-2, and (**c**) LM and UASM-3 approaches.

4. Discussion

4.1. Crop Vigor

High spatial variability in crop vigor was captured by the UAS imagery. Soil background adjustment factor (L) of 0.1 as in the LM calculated similar SAVI with the UAS imagery for selected crops [34,35]. Higher NDVI compared to SAVI for some datasets may be due to the saturation effects ignored in SAVI [43]. Soil-segmented FCC mapped similar LAI from UASM-3 as from the LM approach. MRL estimates from UAS and Landsat imagery were also similar. Slight differences in MRL from UASM-1 and -2 approaches were mainly due to surface slope factor in the case of UASM-1 approach and that between UASM-1 and -3 approaches were due to LAI and DEM inputs.

4.2. Net Radiation and Soil Heat Flux

The ISWR from LM, UASM-1, and -2 approaches were similar and slight differences were due to the DEM inputs. ISWR from UASM-3 approach was different due to its direct measurement source (nearest weather station). Such ISWR measurements may be assumed actual compared to the standard computations for the weather stations installed near study sites (within 5 km) approximately at 2 m height [38,39]. Higher ILWR estimates from the LM approach compared to UASM-1 and -2, were primarily due to higher T_s. Minor ILWR differences between LM and UASM-1 or -2 approaches would be due to slightly different DEMs used to calculate atmospheric transmissivities. ILWR computation in UASM-3 approach used T_a as the input (Stefan Boltzmann's law) instead of the T_s [40] and no variation for use of a single value may be assumed realistic at field level. OLWR differences between LM and UASM approaches were primarily due to differences in T_s from pertinent imaging systems. Similar OLWR from UASM-1, -2, and -3 approaches showed no effect of LAI differences that contribute only 1% to the surface emissivity calculations. R_n and G estimate differences between UASM and LM approaches can be attributed to differences between ISWR, ILWR, OLWR and surface albedo computations. While no R_n and G differences between UASM-1 and UASM-2 approaches were due to negligible differences between ISWR, ILWR, and OLWR. Such differences between UASM-1 and UASM-3 approaches were due to the ISWR and ILWR differences. Since high LAI was observed in all imaging campaigns, slightly high variations in OLWR and R_n may be expected during initial days of plantation (Low LAI).

4.3. Sensible Heat Flux

Differences between H estimates from LM and UASM approaches were primarily due to T_s differences, and secondarily due to different internal calibrations. As the Landsat 7/8 imagery has coarse resolution (~30 m pixel^{-1}), it might not be readily possible to find uniform hot and cold anchor pixels. This demands for additional flexibility in anchor pixel identification also suggested by Jaafar et al. [42]. Contrarily, it was easier with the UAS-based approaches (~7 m pixel^{-1}) to identify anchor pixels within the imaged field area (Table 7). Irrigated crops would have also facilitated identification of highly transpiring cold anchor pixels alike the reference alfalfa. H differences between UASM-1, -2, and -3 could be due to LAIs, MRLs, R_n, and G differences in the different cold pixels that resulted in different internal calibrations.

4.4. Daily Evapotranspiration

Similar ET was mapped from all UASM approaches compared to the LM approach (Figures 5–9). However, UASM approaches showed larger potential for assessing spatial variations in field ET maps (Figure 10) due to large number of pixels [21]. The ET differences between LM, UASM-1, and -3 approaches were large for dataset-5 (alfalfa field) and dataset-3 (potato field) primarily due to the internal calibration differences, H and R_n differences. The ET_rF for alfalfa crop in dataset-6 was high compared to dataset-5 showing more matured crop at 2 DBH than 7 DBH. Notable ET_rF differences between LM and UASM approaches could also be due to accumulated differences between

the intermediate outputs. ET_rFs for selected crops did not exceed 1.1, complying to the cold anchor pixel assumption ($1.05 \times ET_r$, [9]). UASM-3 approach (METRIC model modified to local conditions) can also provide reliable geospatial ET maps as LM. As also reported by Paul et al. [33], G and H differences between LM and UAS approaches did not influence daily ET maps for irrigated field crops due to small magnitudes. UASM approaches indicate their versatility for geospatial ET mapping for a range of similar crops as spearmint, potato and alfalfa (*r*: 0.8–0.9). However, additional parametrization may be needed for different crop physiologies [21,27]. An average 10% uncertainty of UASM approaches for point scale ET might be acceptable as discussed in prior research studies that used similar UAS imagery with METRIC model [29,33]. Flight missions within solar noon ± 2 h could have produced comparable and reasonable ET_rF used for 24-h [44].

Table 7. Details of hot and cold anchor pixels identified in the LM and UASM approaches.

DBH	Approach	Pixel	Spearmint		Potato		Alfalfa	
			NDVI	Ts	NDVI	Ts	NDVI	Ts
10 (Spearmint) 72 (Potato) 2 (Alfalfa)	LM	Hot	0.21	336.15	0.28	321.07	0.19	330.26
		Cold	0.87	300.86	0.82	299.34	0.86	298.66
	UASM-1	Hot	0.27	320.43	0.26	319.18	0.25	323.54
		Cold	0.93	294.65	0.89	296.92	0.9	296.54
	UASM-2	Hot	0.27	320.43	0.26	319.18	0.25	323.54
		Cold	0.81	295.82	0.85	295.03	0.88	294.42
	UASM-3	Hot	0.27	320.43	0.26	319.18	0.25	323.54
		Cold	0.87	293.2	0.87	294.55	0.85	293.43
37 (Spearmint) 48 (Potato) 7 (Alfalfa)	LM	Hot	0.19	333.47	0.15	326.78	0.17	331.3
		Cold	0.91	301.37	0.96	306	0.86	300.52
	UASM-1	Hot	0.24	317.94	0.27	326.85	0.21	319.11
		Cold	0.85	297.8	0.91	294.84	0.87	297.51
	UASM-2	Hot	0.24	317.94	0.27	326.85	0.21	319.11
		Cold	0.86	298.58	0.92	294.61	0.85	296.88
	UASM-3	Hot	0.24	317.94	0.27	326.85	0.21	319.11
		Cold	0.88	295.57	0.89	295.96	0.89	294.98
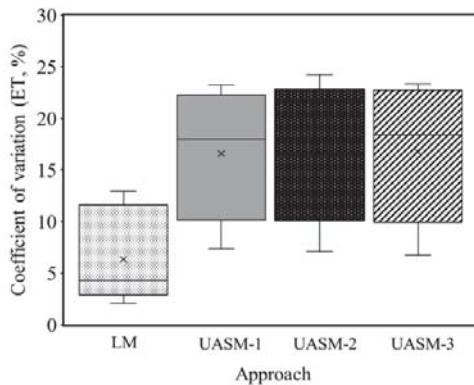
Figure 10. Spatial daily ET variation potential assessments from LM, UASM-1, -2, and -3 approaches.

5. Conclusions

Agricultural growers are highly dependent on generalized crop coefficients or point measurements (soil moisture, sap flow, etc.) for irrigation scheduling and are restrictive towards satellite-based remote sensing approaches due to low spatiotemporal resolution and cloud cover issues. Considering the critical need for geospatial ET mapping towards precision irrigation management, ET of irrigated field crops was mapped using very high resolution multispectral and thermal infrared imagery.

Three variants of standard METRIC energy balance model modified as per UAS and local conditions were used to process UAS imagery and their performance was evaluated relative to standard LM approach.

Increased spatial resolution did not influence the mean field-scale ET (low RMSD: 0.2–1.0 mm day^{-1}, ET$_{dep,abs}$: 0.4–21.2%, and r: 0.7–0.9). However, high spatial ET variation potential was assessed in UAS derived maps (6.7–24.3%) compared to the Landsat satellite derived maps (2.1–11.2%). Variants of UASM models performed very similar to the LM approach for irrigated field crops; spearmint (ET$_{dep,abs}$: 0.4–6.2% and r: 0.7–0.8), potato (ET$_{dep,abs}$: 0.9–21.2% and r: 0.7–0.8), and alfalfa (ET$_{dep,abs}$: 7.2–9.9% and r: 0.8–0.9). UASM-2 showed highest similarity with the LM approach (RMSD: 0.5–0.9 mm day^{-1} and r: 0.7–0.9) for very similar energy balance outputs. ET differences between LM and UAS based approaches were majorly due to the internal calibrations differences that could have been affected slightly by the spatial resolution. UASM-1 could be advantageous for agricultural fields with elevation variability and resulting temperature differences due to lapse rates. UASM-1 uses high-resolution UAS imagery derived DEM inputs that can be accurately compared to the satellite based DEMs. UASM-2 could be advantageous for the crop fields where spatial variability in ground elevation is negligible, as it also reduces additional DEM data requirement for ET mapping. UASM-3 uses actual meteorological parameters of ISWR and T$_a$ (for ILWR) measured by the automated weather station near the field site. UASM-3 could also be advantageous for ensuring LAI calculation for the areas with vegetation only, as supported by high spatial resolution to distinctly capture soil, vegetation and mixed pixels. UASM-1 and UASM-3 could also be merged for field-relevant energy balance inputs such as meteorological parameters and ground elevation variabilities to obtain more realistic crop water use maps.

ET mapping at high spatiotemporal resolution provides more control over timely monitoring of spatial crop water requirements where restrictions of cloud cover interference and imagery acquisition at 16-day interval could be avoided unlike LM approach. LM based approaches may assist in review of seasonal water distribution rights while UASM approaches may assist in irrigation water savings through grower friendly and on-demand site-specific irrigation prescription maps/tools.

Author Contributions: Conceptualization, A.K.C., B.M., and L.R.K.; data curation, A.K.C. and B.M.; funding acquisition, L.R.K., R.T.P., and C.O.S.; drone flights, A.K.C. and B.M.; investigation, A.K.C. and B.M.; methodology, A.K.C., L.R.K., and C.O.S.; project administration, L.R.K., R.T.P., and C.O.S.; resources, L.R.K., R.T.P., and C.O.S.; software, A.K.C.; supervision, L.R.K., R.T.P., and C.O.S.; validation, A.K.C. and B.M.; visualization, A.K.C., B.M., L.R.K., R.T.P., and C.O.S.; writing—original draft, A.K.C.; and writing—review and editing, A.K.C., B.M., L.R.K., R.T.P., and C.O.S. All authors have read and agreed to the published version of the manuscript.

References

1. Kustas, W.P.; Norman, J.M. Use of remote sensing for evapotranspiration monitoring over land surfaces. *Hydrol. Sci. J.* **1996**, *41*, 495–516. [CrossRef]
2. Quattrochi, D.A.; Luvall, F.J.C. Thermal infrared remote sensing for analysis of landscape ecological processes: Methods and applications. *Landsc. Ecol.* **1999**, *14*, 577–598. [CrossRef]
3. Overgaard, J.; Rosbjerg, D.; Butts, M.B. Land-surface modelling in hydrological perspective? a review. *Biogeosciences* **2006**, *3*, 229–241. [CrossRef]
4. Schmidt, M.; King, E.A.; McVicar, T.R. A user-customized Web-based delivery system of hypertemporal remote sensing datasets for Australasia. *Photogramm. Eng. Rem. Sens.* **2006**, *72*, 1073–1080. [CrossRef]
5. Farahani, H.; Howell, T.; Shuttleworth, W.; Bausch, W.C. Evapotranspiration: Progress in measurement and modeling in agriculture. *Trans. Am. Soc. Agric. Biol. Eng.* **2007**, *50*, 1627–1638. [CrossRef]

6. Glenn, E.P.; Huete, A.R.; Nagler, P.L.; Hirschboeck, K.K.; Brown, P. Integrating remote sensing and ground methods to estimate evapotranspiration. *Crit. Rev. Plant Sci.* **2007**, *26*, 139–168. [CrossRef]

7. Gowda, P.H.; Chavez, J.L.; Colaizzi, P.D.; Evett, S.R.; Howell, T.A.; Tolk, J.A. Remote sensing based energy balance algorithms for mapping ET: Current status and future challenges. *Trans. Am. Soc. Agric. Biol. Eng.* **2007**, *50*, 1639–1644.

8. Verstraeten, W.W.; Veroustraete, F.; Feyen, J. Assessment of evapotranspiration and soil moisture content across different scales of observation. *Sensors* **2008**, *8*, 70–117. [CrossRef]

9. Allen, R.G.; Tasumi, M.; Trezza, R. Satellite-based energy balance for mapping evapotranspiration with internalized calibration (METRIC)-Model. *J. Irrig. Drain. Eng.* **2007**, *133*, 380–394. [CrossRef]

10. Allen, R.G.; Tasumi, M.; Morse, A.; Trezza, R.; Wright, J.L.; Bastiaanssen, W.; Kramber, W.; Lorite, I.J.; Robison, C.W. Satellite-based energy balance for mapping evapotranspiration with internalized calibration (METRIC)—Applications. *J. Irrig. Drain. Eng.* **2007**, *133*, 395–406. [CrossRef]

11. Trezza, R. Evapotranspiration Using a Satellite-Based Surface Energy Balance with Standardized Ground Control. Ph.D. Thesis, Utah State University, Logan, UT, USA, 2002.

12. Tasumi, M.; Allen, R.G.; Trezza, R.; Wright, J.L. Satellite-based energy balance to assess within-population variance crop coefficient curves. *J. Irrig. Drain. Eng.* **2005**, *131*, 94–139. [CrossRef]

13. Gonzalez-Dugo, M.P.; Neale, C.M.U.; Mateos, L.; Kustas, W.P.; Prueger, J.H.; Anderson, M.C.; Li, F. A comparison of operational remote sensing-based models for estimating crop evapotranspiration. *Agric. For. Meteorol.* **2009**, *149*, 1843–1853. [CrossRef]

14. Chávez, J.L.; Howell, T.A.; Gowda, P.H.; Copeland, K.S.; Prueger, J.H. Surface aerodynamic temperature modeling over rainfed cotton. *Trans. Am. Soc. Agric. Biol. Eng.* **2010**, *53*, 759–767.

15. Allen, R.; Irmak, A.; Trezza, R.; Hendrickx, J.M.; Bastiaanssen, W.; Kjaersgaard, J. Satellite-based ET estimation in agriculture using SEBAL and METRIC. *Hydrol. Process.* **2011**, *25*, 4011–4027. [CrossRef]

16. Anderson, M.C.; Allen, R.G.; Morse, A.; Kustas, W.P. Use of Landsat thermal imagery in monitoring evapotranspiration and managing water resources. *Remote Sens. Environ.* **2012**, *122*, 50–65. [CrossRef]

17. Santos, C.; Lorite, I.J.; Allen, R.G.; Tasumi, M. Aerodynamic Parameterization of the Satellite-Based Energy Balance (METRIC) Model for ET Estimation in Rainfed Olive Orchards of Andalusia, Spain. *Water Resour. Manag.* **2012**, *26*, 3267–3283. [CrossRef]

18. Paço, T.A.; Pôças, I.; Cunha, M.; Silvestre, J.C.; Santos, F.L.; Paredes, P.; Pereira, L.S. Evapotranspiration and crop coefficients for a super intensive olive orchard. An application of SIMDualKc and METRIC models using ground and satellite observations. *J. Hydrol.* **2014**, *519*, 2067–2080. [CrossRef]

19. Pôças, I.; Paço, T.A.; Cunha, M.; Andrade, J.A.; Silvestre, J.; Sousa, A.; Santos, F.L.; Pereira, L.S.; Allen, R.G. Satellite-based evapotranspiration of a super-intensive olive orchard: Application of METRIC algorithms. *Biosyst. Eng.* **2014**, *128*, 69–81. [CrossRef]

20. Carrasco-Benavides, M.; Ortega-Farías, S.; Lagos, L.; Kleissl, J.; Morales-Salinas, L.; Kilic, A. Parameterization of the satellite-based model (METRIC) for the estimation of instantaneous surface energy balance components over a drip-irrigated vineyard. *Remote Sens.* **2014**, *6*, 11342–11371. [CrossRef]

21. la Fuente-Sáiz, D.; Ortega-Farías, S.; Fonseca, D.; Ortega-Salazar, S.; Kilic, A.; Allen, R. Calibration of metric model to estimate energy balance over a drip-irrigated apple orchard. *Remote Sens.* **2017**, *9*, 670. [CrossRef]

22. McShane, R.R.; Driscoll, K.P.; Sando, R. *A Review of Surface Energy Balance Models for Estimating Actual Evapotranspiration with Remote Sensing at High Spatiotemporal Resolution over Large Extents*; Scientific Investigations Report; Department of the Interior and U.S. Geological Survey: Reston, VA, USA, 2017.

23. Zhang, C.; Kovacs, J.M. The application of small unmanned aerial systems for precision agriculture: A review. *Precis. Agric.* **2012**, *13*, 693–712. [CrossRef]

24. Vargas, J.J.Q.; Khot, L.R.; Peters, R.T.; Chandel, A.K.; Molaei, B. Low Orbiting Satellite and Small UAS-Based High-Resolution Imagery Data to Quantify Crop Lodging: A Case Study in Irrigated Spearmint. *IEEE Geosci. Remote Sens.* **2019**, *17*, 755–759. [CrossRef]

25. Ranjan, R.; Chandel, A.K.; Khot, L.R.; Bahlol, H.Y.; Zhou, J.; Boydston, R.A.; Miklas, P.N. Irrigated pinto bean crop stress and yield assessment using ground based low altitude remote sensing technology. *Inf. Process. Agric.* **2019**, *6*, 502–514. [CrossRef]

26. Berni, J.A.; Zarco-Tejada, P.J.; Suárez, L.; Fereres, E. Thermal and narrowband multispectral remote sensing for vegetation monitoring from an unmanned aerial vehicle. *IEEE Trans. Geosci. Remote Sens.* **2009**, *47*, 722–738. [CrossRef]

27. Chávez, J.L.; Gowda, P.H.; Howell, T.A.; Garcia, L.A.; Copeland, K.S.; Neale, C.M.U. ET mapping with high-resolution airborne remote sensing data in an advective semiarid environment. *J. Irrig. Drain. Eng.* **2012**, *138*, 416–423. [CrossRef]

28. Elarab, M. The Application of Unmanned Aerial Vehicle to Precision Agriculture: Chlorophyll, Nitrogen, and Evapotranspiration Estimation. Ph.D. Thesis, Utah State University, Logan, UT, USA, 2016.

29. Chávez, J.L.; Torres-Rua, A.; Boldt, W.E.; Zhang, H.; Robertson, C.; Marek, G.; Wang, D.; Heeren, D.; Taghvaeian, S.; Neale, C.M. A Decade of Unmanned Aerial Systems in Irrigated Agriculture in the Western US. *Appl. Eng. Agric.* **2020**, *36*, 423–436. [CrossRef]

30. Sankaran, S.; Khot, L.R.; Espinoza, C.Z.; Jarolmasjed, S.; Sathuvalli, V.R.; Vandemark, G.J.; Miklas, P.N.; Carter, A.H.; Pumphrey, M.O.; Knowles, N.R.; et al. Low-altitude, high-resolution aerial imaging systems for row and field crop phenotyping: A review. *Eur. J. Agron.* **2015**, *70*, 112–123. [CrossRef]

31. Ortega-Farías, S.; Ortega-Salazar, S.; Poblete, T.; Kilic, A.; Allen, R.; Poblete-Echeverría, C.; Ahumada-Orellana, L.; Zuñiga, M.; Sepúlveda, D. Estimation of energy balance components over a drip-irrigated olive orchard using thermal and multispectral cameras placed on a helicopter-based unmanned aerial vehicle (UAV). *Remote Sens.* **2016**, *8*, 638. [CrossRef]

32. Brenner, C.; Thiem, C.E.; Wizemann, H.D.; Bernhardt, M.; Schulz, K. Estimating spatially distributed turbulent heat fluxes from high-resolution thermal imagery acquired with a UAV system. *Int. J. Remote Sens.* **2017**, *38*, 3003–3026. [CrossRef]

33. Paul, G. Evaluation of Surface Energy Balance Models for Mapping Evapotranspiration Using very High Resolution Airborne Remote Sensing Data. Ph.D. Thesis, Kansas State University, Manhattan, KS, USA, 2013.

34. Candiago, S.; Remondino, F.; De Giglio, M.; Dubbini, M.; Gattelli, M. Evaluating Multispectral Images and Vegetation Indices for Precision Farming Applications from UAV Images. *Remote Sens.* **2015**, *7*, 4026–4047. [CrossRef]

35. Jorge, J.; Vallbe, M.; Soler, J.A. Detection of irrigation in homogeneities in an olive grove using the NDRE vegetation index obtained from UAV images. *Eur. J. Remote Sens.* **2019**, *52*, 169–177. [CrossRef]

36. Duchemin, B.; Hadria, R.; Erraki, S.; Boulet, G.; Maisongrande, P.; Chehbouni, A.; Escadafal, R.; Ezzahar, J.; Hoedjes, J.C.B.; Kharrou, M.H.; et al. Monitoring wheat phenology and irrigation in Central Morocco: On the use of relationships between evapotranspiration, crops coefficients, leaf area index and remotely-sensed vegetation indices. *Agric. Water Manag.* **2006**, *79*, 1–27. [CrossRef]

37. Smith, A.M.; Bourgeois, G.; Teillet, P.M.; Freemantle, J.; Nadeau, C. A comparison of NDVI and MTVI2 for estimating LAI using CHRIS imagery: A case study in wheat. *Can. J. Remote Sens.* **2008**, *34*, 539–548. [CrossRef]

38. Sun, Z.; Gebremichael, M.; Wang, Q.; Wang, J.; Sammis, T.; Nickless, A. Evaluation of clear-sky incoming radiation estimating equations typically used in remote sensing evapotranspiration algorithms. *Remote Sens.* **2013**, *5*, 4735–4752. [CrossRef]

39. Stettz, S.; Zaitchik, B.F.; Ademe, D.; Musie, S.; Simane, B. Estimating variability in downwelling surface shortwave radiation in a tropical highland environment. *PLoS ONE* **2019**, *14*, e0211220. [CrossRef]

40. Prata, A.J. A new long-wave formula for estimating downward clear-sky radiation at the surface. *Q. J. R. Meteorol. Soc.* **1996**, *122*, 1127–1151. [CrossRef]

41. Olmedo, G.F.; Ortega-Farías, S.; de la Fuente-Sáiz, D.; Fonseca-Luengo, D.; Fuentes-Peñailillo, F. Water: Tools and Functions to Estimate Actual Evapotranspiration Using Land Surface Energy Balance Models in R. *R. J.* **2016**, *8*, 352–369. [CrossRef]

42. Jaafar, H.H.; Ahmad, F.A. Time series trends of Landsat-based ET using automated calibration in METRIC and SEBAL: The Bekaa Valley, Lebanon. *Remote Sens. Environ.* **2020**, *238*, 111034. [CrossRef]

43. Huete, A. A soil-adjusted vegetation index (SAVI). *Remote Sens. Environ.* **1988**, *25*, 295–309. [CrossRef]

44. Jackson, R.; Hatfield, J.; Reginato, R.; Idso, S.; Pinter, P. Estimation of daily evapotranspiration from one time-of-day measurements. *Agric. Water Manag.* **1983**, *7*, 351–362. [CrossRef]

Vegetation Extraction Using Visible-Bands from Openly Licensed Unmanned Aerial Vehicle Imagery

Athos Agapiou [1,2]

[1]   Remote Sensing and Geo-Environment Lab, Department of Civil Engineering and Geomatics,
     Faculty of Engineering and Technology, Cyprus University of Technology, Saripolou 2-8, Limassol 3036,
     Cyprus; athos.agapiou@cut.ac.cy; Tel.: +357-25-002471
[2]   Eratosthenes Centre of Excellence, Saripolou 2-8, Limassol 3036, Cyprus

Abstract: Red–green–blue (RGB) cameras which are attached in commercial unmanned aerial vehicles (UAVs) can support remote-observation small-scale campaigns, by mapping, within a few centimeter's accuracy, an area of interest. Vegetated areas need to be identified either for masking purposes (e.g., to exclude vegetated areas for the production of a digital elevation model (DEM) or for monitoring vegetation anomalies, especially for precision agriculture applications. However, while detection of vegetated areas is of great importance for several UAV remote sensing applications, this type of processing can be quite challenging. Usually, healthy vegetation can be extracted at the near-infrared part of the spectrum (approximately between 760–900 nm), which is not captured by the visible (RGB) cameras. In this study, we explore several visible (RGB) vegetation indices in different environments using various UAV sensors and cameras to validate their performance. For this purposes, openly licensed unmanned aerial vehicle (UAV) imagery has been downloaded "as is" and analyzed. The overall results are presented in the study. As it was found, the green leaf index (GLI) was able to provide the optimum results for all case studies.

Keywords: vegetation indices; RGB cameras; unmanned aerial vehicle (UAV); empirical line method; Green leaf index; open aerial map

1. Introduction

Unmanned aerial vehicles (UAVs) are widely applied for monitoring and mapping purposes all around the world [1–4]. The use of relatively low-cost commercial UAV platforms can produce high-resolution visible orthophotos, thus providing an increased resolution product in comparison to the traditional aerial or satellite observations. Throughout the years, the technological development in sensors and the decrease in the cost of the UAV sensors has popularized them both to experts as well as amateurs [5,6]. While several countries have lately adopted restrictions due to safety reasons, UAVs are still being used for mapping relatively small areas (in comparison to aerial and satellite observations) [7].

Today a variety of UAVs and cameras exist in the market, providing a plethora of options to end-users. As [8] mentioned in their work, UAVs can be classified according to the characteristics of the drones, such as their size, ranging from nano (<30 mm) to large size (>2 m) drones, their maximum take-off weight (from less than 1 kg to more than 25 kg), their range of operation, etc. In addition, existing UAVs' cameras can also be classified into visible red–green–blue (RGB), near-infrared (NIR), multispectral, hyperspectral, and thermal cameras.

Once the stereo pairs of the images are taken from the UAV camera sensors, these are processed using known control points and orthorectified based on the digital surface model (DSM) produced by the triangulation of the stereo pairs [9]. In many applications, the detection of vegetated areas is essential, as in the case of monitoring agricultural areas or forests [10–13]. Even if vegetation is not a

goal of a study, vegetation needs to be masked out to produce a digital elevation model (DEM) and provide realistic contours of the area.

Vegetated areas can usually be detected using the near-infrared part of the spectrum (approximately between 760–900 nm). At this spectral range, healthy vegetation tends to give high reflectance values in comparison to the visible bands (red–green–blue, RGB) [14]. The sudden increase in reflectance at the near-infrared part of the spectrum is a unique characteristic of healthy vegetation. For this reason, the specific spectral window has been widely exploited in remote sensing applications. Indeed, numerous vegetation indices based on different mathematical equations have been developed in the last decades, aiming to detect healthy vegetation, taking into consideration atmospheric effects and the soil background reflectance noise [15]. One of the most common vegetation indexes applied in remote sensing applications is the so-called normalized difference vegetation index (NDVI), which is estimated using the reflectance values of the near-infrared and the red bands of multispectral images [16].

However, in most UAV cameras, the near-infrared part of the spectrum which is sensitive to vegetation is absent. UAVs cameras are normally sensitive to recording the visible part of the spectrum (red–green–blue), thus making the detection of vegetated areas quite challenging. In addition, radiometric calibration of the images is needed to convert the raw digital numbers (DNs) into reflectance values. To do this, calibration targets and field campaigns are essential to have a good approximation of the backscattered radiance of the various targets observed in the orthophotos [17,18].

This study aims to investigate the detection of vegetated areas based on limited metadata information, and with no information regarding the reflectance properties of targets visible in the orthophoto. For this reason, five orthophotos from openly licensed an unmanned aerial vehicle (UAV) imagery repository was used, while simplifying linear regression models were established to convert the DNs of the images to reflectance values. Once this was accomplished, then more than ten (10) different visible vegetation indices were applied, and their results are discussed. The methodology presented here can, therefore, be used in products where knowledge is limited, and the extraction of vegetation is needed to be carried out in a semi-automatic way.

2. Materials and Methods

For the needs of the current study, five different datasets were selected through the OpenAerialMap platform [19]. The OpenAerialMap relies on a set of open-source tools, where users can upload their products, such as orthophotos, filling basic metadata information, to support their re-use. OpenAerialMap provides a set of tools for searching, sharing, and using openly licensed satellite and unmanned aerial vehicle (UAV) imagery. The platform is operated by the Open Imagery Network (OIN). All images uploaded in the platform are publicly licensed under the Creative Commons (CC) license (CC-BY 4.0), thus allowing both sharing and adaptation of the content from third parties and other users.

The case studies were selected based on the following criteria: (1) have a different context, (2) have a different geographical distribution, (3) captured by different UAV/camera sensors, and (4) quality of the final orthophoto. In the end, the following case studies were identified and downloaded for further processing (Table 1). A preview of these areas can be found in Figure 1. Case study 1 was a 6 cm-resolution orthophoto, from a highly urbanized area (Figure 1a), located in the Philippines, where vegetation was randomly scattered. A mixed environment was selected as the second case study from St. Petersburg in Russia (Figure 1b), where both high trees, grassland, and buildings were visible. A UAV corridor mapping along a river near the Arta city, Greece, was the third case study (Figure 1c). At the same time, it should be mentioned that watergrass was also visible in this orthophoto.

Table 1. Case studies selected through the OpenAerialMap [19].

No.	Case Study	Location	UAV Camera Sensor	Named Resolution	Preview
1	Highly urbanized area	Taytay, Philippines	DJI Mavic 2 Pro	6 cm	Figure 1a
2	Campus	St. Petersburg, Russia	DJI Mavic 2 Pro	5 cm	Figure 1b
3	River-corridor	Arta, Greece	DJI FC6310	5 cm	Figure 1c
4	Picnic area	Ohio, USA	SONY DSC-WX220	6 cm	Figure 1d
5	Agricultural area	Nîmes, France	Parrot Anafi	5 cm	Figure 1e
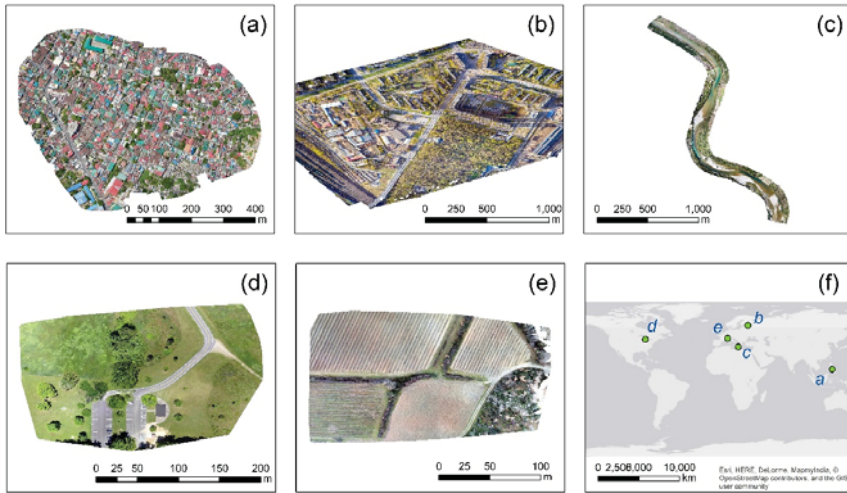
Figure 1. Case studies selected through the OpenAerialMap [19]. (**a**) a highly urbanized area, at Taytay, Philippines, (**b**) a campus at St. Petersburg, Russia, (**c**) a river near Arta, Greece, (**d**) a picnic area at Ohio, USA, (**e**) an agricultural area at Nîmes, France, and (**f**) the geographical distribution of the selected case studies.

The next case study referred to a picnic area at Ohio, USA, with low vegetation (grass) and some sporadic high trees (Figure 1d), while the last case study was an agricultural field near Nîmes, France. All orthophotos have a named resolution of few centimeters (5–6 cm), without the ability to evaluate further geometric distortions of the images (e.g., radial distortion, root mean square error, maximum horizontal and vertical error, and distribution of the control points). Therefore, these orthophotos were further processed "as is". The first two orthophotos were obtained using the DJI Mavic 2 Pro, while the DJI FC6310 model was used for the case study of Greece. The SONY DSC-WX220 and Parrot Anafi UAV models were used for the last two case studies.

Once the orthophotos were downloaded, the digital numbers (DN) of each band were calibrated using the empirical line method (ELM) [18]. The ELM is a simple and direct approach to calibrate DN of images to approximated units of surface reflectance in the case where no further information is available as in our example. The ELM method aims to build a relationship between at-sensor radiance and at-surface reflectance by computing non-variant spectral targets and comparing these measurements with the respective DNs in the image. The calibration of raw DNs to surface reflectance factor is based on a linear relationship for each image band using reflectance targets of the image. The derived prediction equations can consider changes in illumination and atmospheric effects [20]. In our case study, since no additional information was available, the impact of the atmospheric effects was ignored. The ELM for the RGB UAV sensed data could be estimated using the following equation:

$$\rho_{(\lambda)} = A * DN + B, \tag{1}$$

where $\rho_{(\lambda)}$ is the reflectance value for a specific band (range 0%–100%), DNs are the raw digital numbers of the orthophotos, and A and B are terms which can be determined using a least-square fitting approach. Figure 2 illustrates the basic concept of the ELM calibration.
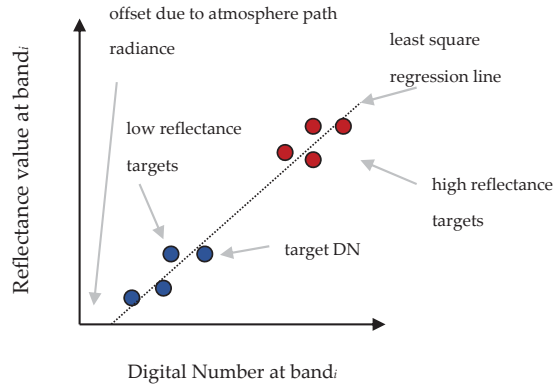
Figure 2. Empirical line method (ELM) schematic diagram.

In the case where no appropriate targets were used, a simple normalization of the orthophotos was followed using image statistics per each band. Once the orthophotos were radiometrically calibrated, with pixel values between 0 and 1, various visible vegetation indices were applied. In specific, we implemented ten (10) different equations, as shown in more detail in Table 2. The following vegetation indices were applied to all case studies: (1) Normalized green–red difference index, (2) green leaf index, (3) visible atmospherically resistant index, (4) triangular greenness index, (5) red–green ratio index, (6) red–green–blue vegetation index, (7) red–green ratio index, (8) modified green–red vegetation index, (9) excess green index, and (10) color index of vegetation. These indices explore in different ways the visible bands (red–green–blue). The outcomes were then evaluated and compared with random points defined in the orthophotos. The overall results are provided in the next section.

Table 2. Vegetation indices used in this study.

No.		Vegetation Index	Equation	Ref.
1	**NGRDI**	Normalized green red difference index	$(\rho_g - \rho_R)/(\rho_g + \rho_r)$	[21]
2	**GLI**	Green leaf index	$(2 * \rho_g - \rho_r - \rho_b)/(2 * \rho_g + \rho_r + \rho_b)$	[22]
3	**VARI**	Visible atmospherically resistant index	$(\rho_g - \rho_r)/(\rho_g + \rho_r - \rho_b)$	[23]
4	**TGI**	Triangular greenness index	$0.5 * [(\lambda_r - \lambda_b)(\rho_r - \rho_g) - (\lambda_r - \lambda_g)(\rho_r - \rho_b)]$	[24]
5	**IRG**	Red–green Ratio index	$\rho_r - \rho_g$	[25]
6	**RGBVI**	Red–green–blue vegetation index	$(\rho_g * \rho_g) - (\rho_r * \rho_b)/(\rho_g * \rho_g) + (\rho_r * \rho_b)$	[26]
7	**RGRI**	Red–green ratio index	ρ_r / ρ_g	[27]
8	**MGRVI**	Modified green–red vegetation index	$(\rho_g{}^2 - \rho_r{}^2)/(\rho_g{}^2 + \rho_r{}^2)$	[26]
9	**ExG**	Excess green index	$2 * \rho_g - \rho_r - \rho_b$	[28]
10	**CIVE**	Color index of vegetation	$0.441* \rho_r - 0.881 * \rho_g + 0.385 * \rho_b + 18.787$	[29]

where ρ_b is the reflectance at the blue band, ρ_g is the reflectance at the green band, ρ_r is the reflectance at the red band, λ_b is the wavelength of the blue band, and λ_r is the wavelength of the red band.

3. Results

3.1. Radiometric Calibration of the Raw Orthophotos

After the detailed examination of the selected orthophotos, high target reflectance pixels were identified and mapped in three out of the five case studies. These targets were selected, namely in case study 1 (Figure 3a) and case study 2 (Figure 3b). For both these orthophoto, smooth white roofs were found, and the average DN value per band was extracted. A similar procedure was also implemented

for the fourth case study (Figure 3c), where a white high reflectance asphalt area was evident in the southern part of the image. In contrast, no dark objects, such as deep water reservoirs, newly-placed asphalt, or other black targets, were visible in these images. Therefore the ELM was applied using as-known input parameters of the DNs from these high reflectance targets. For the rest orthophotos (case study 3 and case study 5), no visible variant targets could be detected in the images due to their environment. In these cases, an image normalization between 0 and 1, using the image statistics, was implemented.

Case study 1 (Figure 1a)   Case study 2 (Figure 1b)   Case study 4 (Figure 1d)
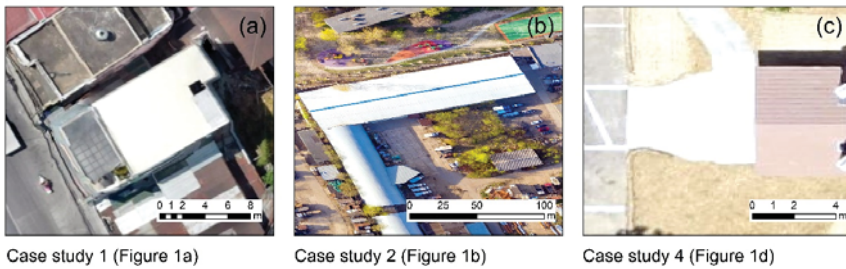
Figure 3. High reflectance targets selected for case study 1 (**a**), case study 2 (**b**), and case study 4 (**c**). For case studies 3 and 5, no appropriate targets were found, and an image-based normalization was applied.

Upon the radiometric calibration, several spectral signatures from different targets in the range of the visible part of the spectrum (i.e., approximately between 450 and 760 nm) were plotted. This is an easy way to understand if the simplified EML and image normalization procedures that we followed here did not distort the reflectance of the targets. Figure 4 presents the results from the reflectance analysis regarding the first case study (similar findings were also reported for the other case studies). Three types of targets are presented here: vegetation (first row of Figure 4), asphalt (second row of Figure 4), and soil (third row of Figure 4). Figure 4a,d,g shows the general location of these targets, while a closer look at these targets is shown in Figure 4b,e,h, respectively. The spectral signature diagram of the three targets can be seen in the last column of Figure 4 (Figure 4c,f,i). The vegetation spectral profile (Figure 4c) followed the typical spectral behavior of healthy vegetation within this part of the spectrum with low reflectance values in the blue and red part of the spectrum and higher reflectance in the green band. Asphalt targets (Figure 4f) had a similar reflectance value for all three bands, while its relatively high reflectance (i.e., between 60%–75%) can be explained due to the type of the asphalt and its age. The soil spectral profile (Figure 4i) showed a similar pattern with the asphalt with a slight increase in the reflectance as we moved from the blue to the red part of the spectrum. Other types of targets (not shown here) had a reflectance pattern as those expected from the literature, which is an indicator that the ELM did not distort any spectral band, and provided, as best as possible, reasonable outcomes.
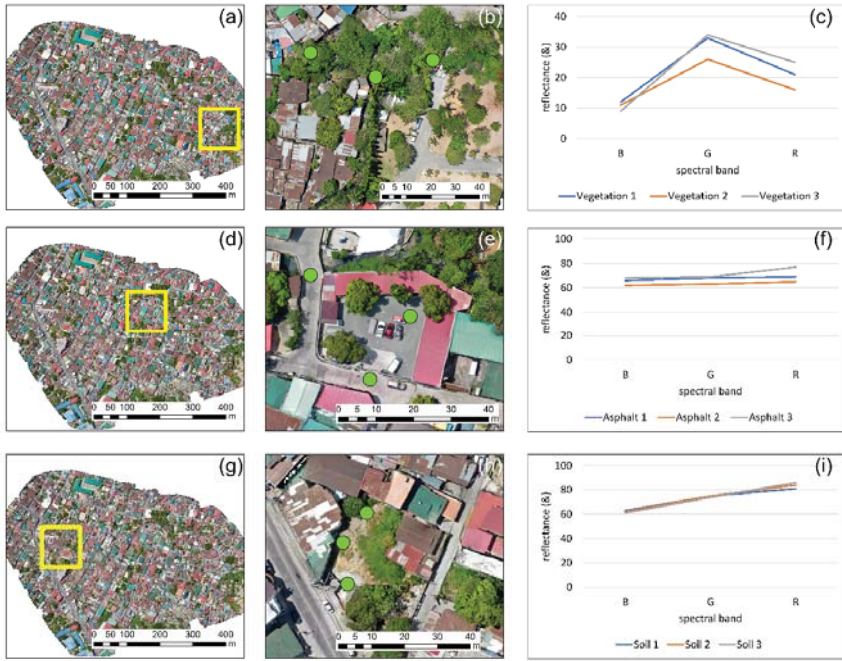
Figure 4. High reflectance targets selected for case study 1 (**a**), case study 2 (**b**), and case study 4 (**c**). For case studies 3 and 5, no appropriate targets were found, and an image-based normalization was applied.

3.2. Vegetation Indices

Once the orthophotos were radiometrically corrected, all vegetation indices mentioned in Table 2 were applied. The final results of this implementation for case studies 1 and 4 are shown in Figures 5 and 6, respectively. The calibrated RGB orthophoto of each case study is shown in Figures 5a and 6a, while the normalized green–red difference index is shown in Figures 5b and 6b. Similarly, Figures 5c–k and 6c–k show the results from the green leaf index, visible atmospherically resistant index, triangular greenness index, red–green ratio index, red–green–blue vegetation index, red–green ratio index, modified green–red vegetation index (i), excess green index, and color index of vegetation (k), respectively. Vegetated areas are highlighted with the light grayscale tone, while non-vegetated areas with the darkest tone of grey.

As shown in Figures 5 and 6, all vegetation indices were able to enhance vegetation in both areas; however, the best performance was observed for Figure 5b,f,i. For Figure 6, a clearer view of the vegetated areas can be detected in Figure 6e. Similar findings were also observed in the rest of the case studies not shown here, indicating that visible vegetation indices using the RGB color can enhance healthy vegetation; however, their performance rate is based on the context of the image. Indeed, for instance, the triangular greenness index in Figure 5e tended to give poor results since vegetation was not well enhanced in the urban environment. However, the same index was the best for the picnic area in Figure 6e.
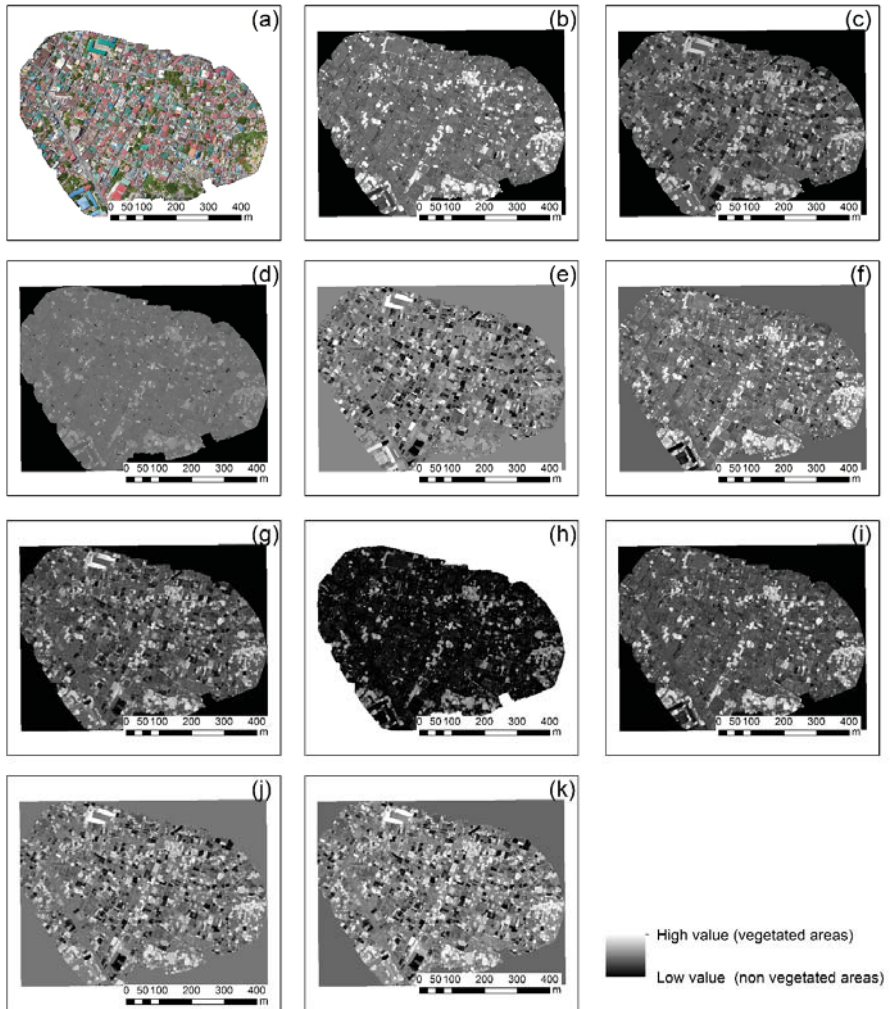
Figure 5. Vegetation indices results applied in the red–green–blue (RGB) orthophoto of the case study No. 1 (**a**), normalized green–red difference index (**b**), green leaf index (**c**), visible atmospherically resistant index (**d**), triangular greenness index (**e**), red–green ratio index (**f**), red–green–blue vegetation index (**g**), red–green ratio index (**h**), modified green–red vegetation index (**i**), excess green index (**j**), and color index of vegetation (**k**). Vegetated areas are highlighted with the light grayscale tone, during non-vegetated areas with darkest tone of gray.
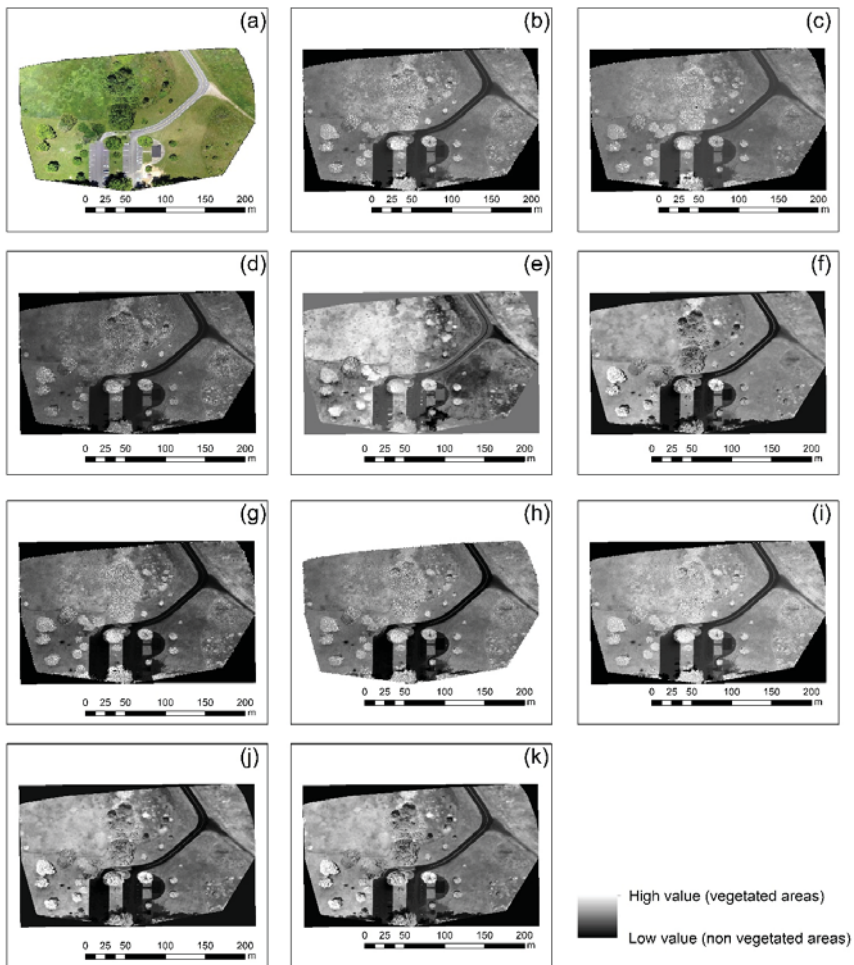
Figure 6. Vegetation indices results applied in the RGB orthophoto of the case study No. 4 (**a**), normalized green–red difference index (**b**), green leaf index (**c**), visible atmospherically resistant index (**d**), triangular greenness index (**e**), red–green ratio index (**f**), red–green–blue vegetation index (**g**), red–green ratio index (**h**), modified green–red vegetation index (**i**), excess green index (**j**), and color index of vegetation (**k**). Vegetated areas are highlighted with the light grayscale tone while non-vegetated areas with the darkest tone of grey.

Extraction of the vegetated regions using RGB cameras can be quite problematic, regardless of the vegetation index applied, in an environment similar to the one of case study 3 (along a river). Figure 7 below shows a closer look at the northern part of the river for all ten vegetation indices mentioned in Table 2. While some indices can enhance the vegetation along the river, as the case of the normalized green–red difference index (Figure 7b), the river itself can also be characterized as "vegetated areas". This is due to the low level of water in the river and the apparent watergrass within the river.

Therefore, as it was found from the visual interpretation of the results, the RGB vegetation indices can enhance vegetated areas. However, they can also give false results. For this reason, a statistical comparison for all vegetation indices and all case studies was applied.
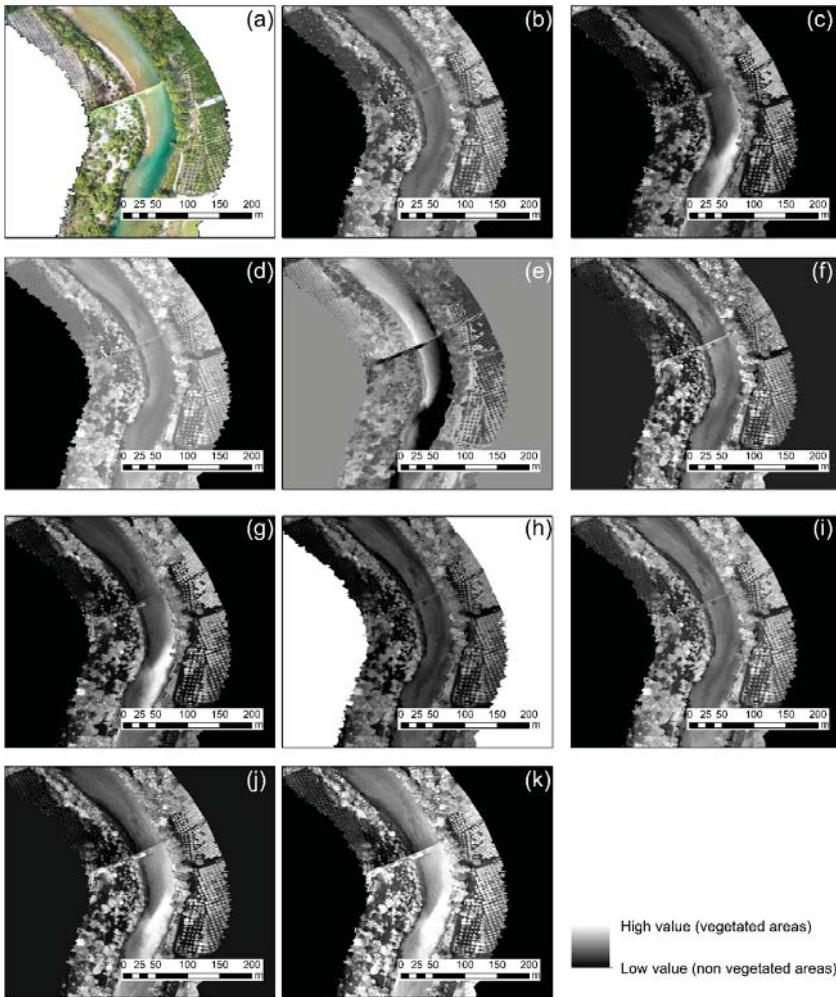
Figure 7. Vegetation indices results applied in the RGB orthophoto of the case study No. 3 (close look) (**a**), normalized green–red difference index (**b**), green leaf index (**c**), visible atmospherically resistant index (**d**), triangular greenness index (**e**), red–green ratio index (**f**), red–green–blue vegetation index (**g**), red–green ratio index (**h**), modified green–red vegetation index (**i**), excess green index (**j**), and color index of vegetation (**k**). Vegetated areas are highlighted with the light grayscale tone while non-vegetated areas with the darkest tone of grey.

3.3. Statistics

To evaluate the overall performance of the ten vegetation indices (see Table 2) per case study, several points were distributed in each orthophoto (100 in total per case study). These points were randomly positioned either over vegetated areas (trees, grass, etc.) or scattered in other types of targets (e.g., asphalt, roofs, water, etc.). The geographical distributions of the points per case study are visualized in Figure 8, while Figure 9 presents the allocation of the random points for "vegetated" and "non-vegetated areas". As expected in orthophotos with limited vegetation, such as the case study of No. 1, the number of points characterized as "vegetation" was less than the "non-vegetation" points (14 and 86 points, respectively).
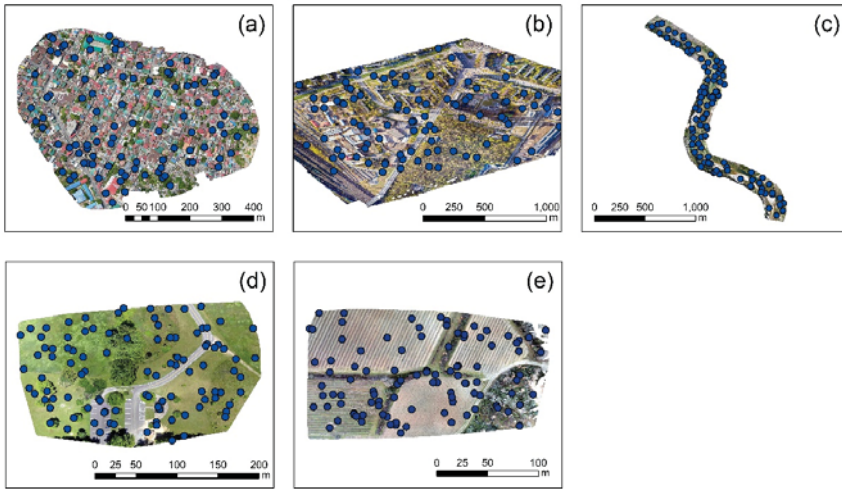
Figure 8. Case studies selected through the OpenAerialMap. (**a**) a highly urbanized area, at Taytay, Philippines, (**b**) a campus at St. Petersburg, Russia, (**c**) a river near Arta, Greece, (**d**) a picnic area at Ohio, USA, (**e**) an agricultural area at Nîmes, France.
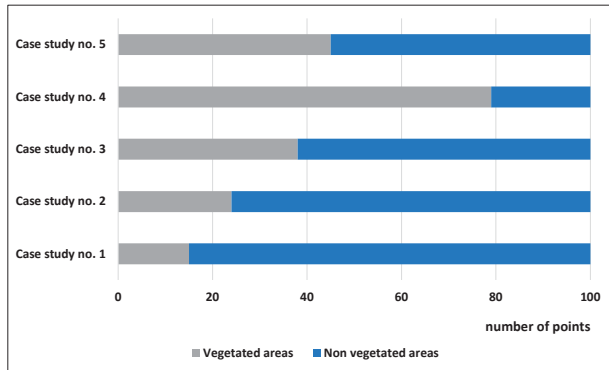
Figure 9. Overall distribution of the 100 random points over "vegetated" and "non-vegetated" areas for the five different case studies.

The normalized difference between the mean value for each index over "vegetated areas" and "non-vegetated" areas is presented in Table 3. Blue color indicates the lowest normalized difference value, while red color, the highest value per vegetation index (V_1 to V_{10}). Overall the normalized difference spanned from 1.2% to 269% for all indices and case studies. For the NGRDI (Normalized green red difference index, V_1 of Table 3), the lowest value was observed for case study No. 3, which visualized an area along a river near Arta, Greece. The highest values were reported for the small agricultural area of case study No. 5. The normalized difference of the NGRDI index for all case studies was between 50% to 107%. Similar observations were reported for the green leaf index (GLI) and Visible atmospherically resistant index (VARI) indies (V_2 and V_3 of Table 3, respectively). An analogous pattern was also reported for the red–green ratio index (IRG), red–green–blue vegetation index (RGBVI), modified green–red vegetation index (MGRVI), and excess green index (ExG) indices (V_5, V_6, V_8, and V_9 of Table 3, respectively). For the triangular greenness index (TGI) (V_4 of Table 3), the lowest normalized difference was once again reported for case study No. 3, but the highest one for the urban

areas of case study No. 1. The same area also gave the highest relatives values for the red–green ratio index (RGRI) (V_7 of Table 3). Finally, for the color index of vegetation (CIVE) (V_{10} of Table 3), the lowest score was reported for case study No. 5, and the highest at the picnic area in case study No. 4.

Table 3. The normalized difference for "vegetated" and "non-vegetated" areas for all vegetation indices (V_1 to V_{10}) mentioned in Table 2 for each case study.

	V_1	V_2	V_3	V_4	V_5	V_6	V_7	V_8	V_9	V_{10}
Case study No. 1	82.2	99.7	56.5	269.1	72.7	94.7	32.5	81.0	94.6	64.8
Case study No. 2	78.7	86.6	83.8	83.4	2.2	54.5	1.9	115.3	89.0	21.2
Case study No. 3	49.8	57.8	42.5	52.0	23.2	50.0	14.4	42.3	28.7	20.1
Case study No. 4	80.7	88.5	81.6	100.0	72.5	87.5	29.3	78.1	90.9	80.4
Case study No. 5	107.2	144.8	98.9	67.4	97.6	163.7	1.2	107.2	132.5	2.9

In general, we can state that case study No. 3 (river area) tended to give low differences between the vegetated and non-vegetated areas despite the vegetation index applied, indicating that this is by far the most challenging environment to work with and to try to discriminate vegetation from the rest areas. In contrast, high separability for all indices could be seen for case study No. 5 (agricultural area) and case study No. 1 (urban areas).

Based on the results of Table 3, we have then relatively compared the normalized difference for all case studies per vegetation index, setting the vegetation No. 1 (NGRDI) as a reference index. The results of this analysis are shown in Figure 10. The normalized difference indicates the percentage difference between (index $_{No.\ i}$ − index $_{No.\ 1}$)/index $_{No.\ 1}$. Therefore, the negative values in Figure 10 suggest that the specific index provided the poorest results in comparison with the NGRDI index (vegetation No. 1). In contrast, high values imply that the particular index gives better results compared to the NGRDI index. Vegetation indices that are closed to zero signify that they have similar performance with the reference index (NGRDI).
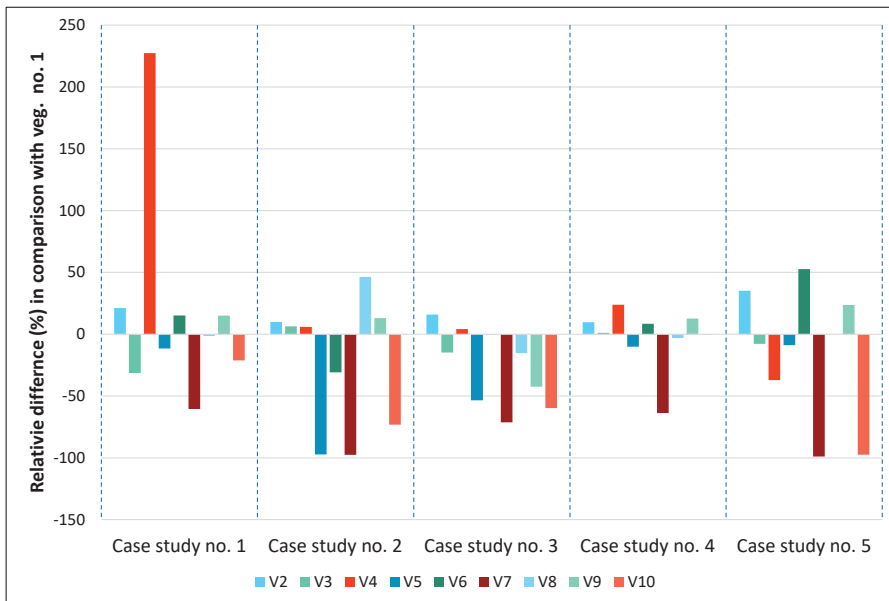
Figure 10. The relative difference of vegetation indices No. 2 to No. 10 in comparison to vegetation index No. 1.

From the results of Figure 10, we can observe that the most promising index was vegetation No. 2, namely the green leaf index (GLI), which provided better results in comparison with the NGRDI index for all case studies. Its performance ranged from 10% to 35%. This is the only index that provided better results for all case studies. Good performance for all case studies, with the exception of case study No. 3 (a river near Arta, Greece), was the vegetation index No. 9 (excess green index, ExG), as it provides a relative difference in comparison with the NGRDI index between 12% and 23% for case studies 1 and 2, and 4 and 5. In contrast, for case study No. 3, the specific index tended to give the worst performance (42%) in comparison with the reference index. Vegetation indices 5, 7, and 10 (IRG, red–green ratio index; RGRI, red–green ratio index, and CIVE, color index of vegetation, respectively) seemed not to perform better than the reference index for all case studies.

However, it is important to notice that for each case study, the optimum index varied, which is also aligned with the previous findings of Table 3. For case study 1 (a highly urbanized area, at Taytay, Philippines), the best index was No. 4 (TGI, triangular greenness index), for case study 2 (a campus at St. Petersburg, Russia), the best index was vegetation No. 8 (MGRVI, modified green–red vegetation index). For case study 3 (a river near Arta, Greece), the best index was vegetation No. 2 (GLI, green leaf index). Finally, for the last two case studies, No. 4 and No. 5, indicating a picnic area at Ohio, USA, and an agricultural area at Nîmes, France, respectively, the best indices were again vegetation No. 4 (TGI, triangular greenness index) and vegetation No. 6 (RGBVI, red–green–blue vegetation index).

4. Discussion

The results presented in the previous section, provide some very helpful information regarding the extraction of vegetation in visible orthophotos, in various environments. It was shown that the application of vegetation indices based on visible bands could highlight vegetated areas and, therefore, enhance healthy vegetation. Indeed, the results presented in Figures 5 and 6 indicate that several indices could perform a high separability between vegetated and non-vegetated areas, while from the findings of Table 3, itis demonstrated that for each case study there was a unique index that could highlight these two different areas, with a relative difference ranging from 57% up to 269%. The differences between the vegetated and non-vegetated areas were also found to be statistically significant for all case studies, after the application of a *t*-test with a 95% confidence level.

While this is true, the context of some orthophotos can also be characterized as quite challenging as the case study No. 3. The results from the application of all indices are shown in Figure 7, which shows that the detection of vegetated areas could also have several false positives within the river basin.

Beyond the spectral complexity and heterogeneity of the orthophoto, some other factors, not discussed in the paper, can also influence the overall performance of the indices. Initially, the spectral response filters of each camera used for these orthophotos were different. Differences in the sensitivity of the cameras to capture in specific wavelengths the backscattered reflectance values can be significant, as was demonstrated in the past from other studies [30]. In addition, the resolution of the orthophoto was not always optimum for each case study. Recent studies [31,32] have shown that the optimum resolution for remote sensing applications is connected not only to the spatial characteristics of the targets under investigation but also with their spectral properties. Finally, assumptions made during the radiometric calibration of the orthophotos need to be taken into consideration. At the same time, a pre-flight plan with special targets and spectroradiometric campaigns can minimize these errors.

5. Conclusions

Vegetation extraction has attracted the interest of researchers all around the world due to its importance of monitoring agricultural areas, forests, etc. While their detection is based on the exploitation of the near-infrared part of the spectrum, the tremendous increase in low altitude platforms, such as the UAVs, equipped with only visible cameras, has made this task quite challenging.

In this paper, we explored openly licensed unmanned aerial vehicle (UAV) imagery from the OpenAerialMap platform, selecting five different case studies, with different contexts and UAV sensors. Since these products were downloaded "as is", it was necessary to apply a radiometric correction before any further processing. For this reason, the EML image-based technique was applied for some case studies (namely case studies Nos. 1, 2, and 4), while for the rest of the case studies (Nos. 3 and 5), normalization of the orthophotos based on image statistics was applied. This procedure does not require any knowledge of either ground targets or field campaigns with spectroradiometers and spectral reflectance targets, which could not be performed in this study (i.e., after the UAV flight). Once the radiometric calibration was applied and verified using spectral signatures profiles of targets on the UAVs, then various visible vegetation indices were applied to all case studies. The results were further elaborated to examine the performance of each index. From the findings of this study, two aspects can be highlighted:

- *Finding 1:* The best vegetation index for all case studies was the green leaf index (GLI), which explores all visible bands of the RGB cameras. The specific index was able to provide better results robustly in all different environments. However:
- *Finding 2:* The performance of each index varied per case study as expected. Therefore, for each different orthophoto, there was a visible index that highlights better the vegetated areas.

The findings of this study can be applied in any RGB orthophoto, taken either from a low altitude system or even aerial images. Given the wide application of ready-to-fly (RTF) drones with a cost of approximatively less than 2000 euros, RGB cameras will continue to play an important role in the near future for small survey campaigns. While field campaigns and particular targets are necessary to calibrate the reflectance of the images, if these are, for any reason, absent, then a similar approach presented here can be followed. In the future, specialized vegetation indices can be developed for addressing specific needs, thus making the extraction of vegetation an easier and more straightforward procedure. Given the various phenological growth stages of vegetation, a dynamic threshold method can be investigated in the future for specific types of vegetation (e.g., crops) towards the automatic extraction of vegetation from RGB orthophotos. These vegetation-specific optimum thresholds could eventually be use to mask or extract the vegetated areas. Finally, a different approach for the extraction of vegetation based on supervised classification analysis can be performed in the future.

Conflicts of Interest: The authors declare no conflict of interest

References

1. García-Berná, J.A.; Ouhbi, S.; Benmouna, B.; García-Mateos, G.; Fernández-Alemán, J.L.; Molina-Martínez, J.M. Systematic Mapping Study on Remote Sensing in Agriculture. *Appl. Sci.* **2020**, *10*, 3456. [CrossRef]
2. Pensieri, M.G.; Garau, M.; Barone, P.M. Drones as an Integral Part of Remote Sensing Technologies to Help Missing People. *Drones* **2020**, *4*, 15. [CrossRef]
3. Feng, Q.; Yang, J.; Liu, Y.; Ou, C.; Zhu, D.; Niu, B.; Liu, J.; Li, B. Multi-Temporal Unmanned Aerial Vehicle Remote Sensing for Vegetable Mapping Using an Attention-Based Recurrent Convolutional Neural Network. *Remote Sens.* **2020**, *12*, 1668. [CrossRef]

4. Pinton, D.; Canestrelli, A.; Fantuzzi, L. A UAV-Based Dye-Tracking Technique to Measure Surface Velocities over Tidal Channels and Salt Marshes. *J. Mar. Sci. Eng.* **2020**, *8*, 364. [CrossRef]

5. Pajares, G. Overview and current status of remote sensing applications based on unmanned aerial vehicles (UAVs). *Photogramm. Eng. Remote Sens.* **2015**, *81*, 281–330. [CrossRef]

6. Cummings, A.R.; McKee, A.; Kulkarni, K.; Markandey, N. The Rise of UAVs. *Photogramm. Eng. Remote Sens.* **2017**, *83*, 317–325. [CrossRef]

7. Stöcker, C.; Bennett, R.; Nex, F.; Gerke, M.; Zevenbergen, J. Review of the Current State of UAV Regulations. *Remote Sens.* **2017**, *9*, 459. [CrossRef]

8. Jiménez López, J.; Mulero-Pázmány, M. Drones for Conservation in Protected Areas: Present and Future. *Drones* **2019**, *3*, 10. [CrossRef]

9. Hashemi-Beni, L.; Jones, J.; Thompson, G.; Johnson, C.; Gebrehiwot, A. Challenges and Opportunities for UAV-Based Digital Elevation Model Generation for Flood-Risk Management: A Case of Princeville, North Carolina. *Sensors* **2018**, *18*, 3843. [CrossRef] [PubMed]

10. Yang, M.-D.; Tseng, H.-H.; Hsu, Y.-C.; Tsai, H.P. Semantic Segmentation Using Deep Learning with Vegetation Indices for Rice Lodging Identification in Multi-date UAV Visible Images. *Remote Sens.* **2020**, *12*, 633. [CrossRef]

11. Marino, S.; Alvino, A. Agronomic Traits Analysis of Ten Winter Wheat Cultivars Clustered by UAV-Derived Vegetation Indices. *Remote Sens.* **2020**, *12*, 249. [CrossRef]

12. Lima-Cueto, F.J.; Blanco-Sepúlveda, R.; Gómez-Moreno, M.L.; Galacho-Jiménez, F.B. Using Vegetation Indices and a UAV Imaging Platform to Quantify the Density of Vegetation Ground Cover in Olive Groves (*Olea Europaea* L.) in Southern Spain. *Remote Sens.* **2019**, *11*, 2564. [CrossRef]

13. Yeom, J.; Jung, J.; Chang, A.; Ashapure, A.; Maeda, M.; Maeda, A.; Landivar, J. Comparison of Vegetation Indices Derived from UAV Data for Differentiation of Tillage Effects in Agriculture. *Remote Sens.* **2019**, *11*, 1548. [CrossRef]

14. Hennessy, A.; Clarke, K.; Lewis, M. Hyperspectral Classification of Plants: A Review of Waveband Selection Generalisability. *Remote Sens.* **2020**, *12*, 113. [CrossRef]

15. Agapiou, A.; Hadjimitsis, D.G.; Alexakis, D.D. Evaluation of Broadband and Narrowband Vegetation Indices for the Identification of Archaeological Crop Marks. *Remote Sens.* **2012**, *4*, 3892–3919. [CrossRef]

16. Rouse, J.W.; Haas, R.H.; Schell, J.A.; Deering, D.W.; Harlan, J.C. *Monitoring the Vernal Advancements and Retrogradation (Greenwave Effect) of Nature Vegetation*; NASA/GSFC Final Report; NASA: Greenbelt, MD, USA, 1974.

17. Xu, K.; Gong, Y.; Fang, S.; Wang, K.; Lin, Z.; Wang, F. Radiometric Calibration of UAV Remote Sensing Image with Spectral Angle Constraint. *Remote Sens.* **2019**, *11*, 1291. [CrossRef]

18. Iqbal, F.; Lucieer, A.; Barry, K. Simplified radiometric calibration for UAS-mounted multispectral sensor. *Eur. J. Remote Sens.* **2018**, *51*, 301–313. [CrossRef]

19. OpenAerialMap (OAM). Available online: https://openaerialmap.org (accessed on 19 May 2020).

20. Pompilio, L.; Marinangeli, L.; Amitrano, L.; Pacci, G.; D'andrea, S.; Iacullo, S.; Monaco, E. Application of the empirical line method (ELM) to calibrate the airborne Daedalus-CZCS scanner. *Eur. J. Remote Sens.* **2018**, *51*, 33–46. [CrossRef]

21. Tucker, C.J. Red and photographic infrared linear combinations for monitoring vegetation. *Remote Sens. Environ.* **1979**, *8*, 127–150. [CrossRef]

22. Louhaichi, M.; Borman, M.M.; Johnson, D.E. Spatially located platform and aerial photography for documentation of grazing impacts on wheat. *Geocarto Int.* **2001**, *16*, 65. [CrossRef]

23. Gitelson, A.A.; Kaufman, Y.J.; Stark, R.; Rundquist, D. 2002. Novel algorithms for remote estimation of vegetation fraction. *Remote Sens. Environ.* **2002**, *80*, 76–87. [CrossRef]

24. Hunt, E.R.; Daughtry, C.S.T.; Eitel, J.U.H.; Long, D.S. Remote sensing leaf chlorophyll content using a visible band index. *Agron. J.* **2011**, *103*, 1090–1099. [CrossRef]

25. Gamon, J.A.; Surfus, J.S. Assessing leaf pigment content and activity with a reflectometer. *New Phytol.* **1999**, *143*, 105–117. [CrossRef]

26. Bendig, J.; Yu, K.; Aasen, H.; Bolten, A.; Bennertz, S.; Broscheit, J.; Gnyp, M.L.; Bareth, G. Combining UAV-based plant height from crop surface models, visible, and near infrared vegetation indices for biomass monitoring in barley. *Int. J. Appl. Earth Obs. Geoinf.* **2015**, *39*, 79–87. [CrossRef]

27. Verrelst, J.; Schaepman, M.E.; Koetz, B.; Kneubuehler, M. Angular sensitivity analysis of vegetation indices derived from chris/proba data. *Remote Sens. Environ.* **2008**, *112*, 2341–2353. [CrossRef]

28. Woebbecke, D.M.; Meyer, G.E.; Vonbargen, K.; Mortensen, D.A. Color indexes for weed identification under various soil, residue, and lighting conditions. *Trans. ASAE* **1995**, *38*, 259–269. [CrossRef]

29. Kataoka, T.; Kaneko, T.; Okamoto, H.; Hata, S. Crop growth estimation system using machine vision. In Proceedings of the 2003 IEEE/ASME International Conference on Advanced Intelligent Mechatronics, Kobe, Japan, 20–24 July 2003; pp. 1079–1083.

30. Agapiou, A.; Alexakis, D.D.; Hadjimitsis, D.G. Spectral sensitivity of ALOS, ASTER, IKONOS, LANDSAT and SPOT satellite imagery intended for the detection of archaeological crop marks. *Int. J. Dig. Earth* **2012**, *7*(5), 351–372. [CrossRef]

31. Tran, T.-B.; Puissant, A.; Badariotti, D.; Weber, C. Optimizing Spatial Resolution of Imagery for Urban Form Detection—The Cases of France and Vietnam. *Remote Sens.* **2011**, *3*, 2128–2147. [CrossRef]

32. Agapiou, A. Optimal Spatial Resolution for the Detection and Discrimination of Archaeological Proxies in Areas with Spectral Heterogeneity. *Remote Sens.* **2020**, *12*, 136. [CrossRef]

Comparing UAS LiDAR and Structure-from-Motion Photogrammetry for Peatland Mapping and Virtual Reality (VR) Visualization

Margaret Kalacska [1,*], J. Pablo Arroyo-Mora [2] and Oliver Lucanus [1]

[1] Applied Remote Sensing Lab, Department of Geography, McGill University, Montreal, QC H3A 0G4, Canada; oliver.lucanus2@mcgill.ca

[2] Flight Research Laboratory, National Research Council of Canada, 1920 Research Private, Ottawa, ON K1A 0R6, Canada; juanpablo.arroyo-mora@nrc-cnrc.gc.ca

[*] Correspondence: margaret.kalacska@mcgill.ca

Abstract: The mapping of peatland microtopography (e.g., hummocks and hollows) is key for understanding and modeling complex hydrological and biochemical processes. Here we compare unmanned aerial system (UAS) derived structure-from-motion (SfM) photogrammetry and LiDAR point clouds and digital surface models of an ombrotrophic bog, and we assess the utility of these technologies in terms of payload, efficiency, and end product quality (e.g., point density, microform representation, etc.). In addition, given their generally poor accessibility and fragility, peatlands provide an ideal model to test the usability of virtual reality (VR) and augmented reality (AR) visualizations. As an integrated system, the LiDAR implementation was found to be more straightforward, with fewer points of potential failure (e.g., hardware interactions). It was also more efficient for data collection (10 vs. 18 min for 1.17 ha) and produced considerably smaller file sizes (e.g., 51 MB vs. 1 GB). However, SfM provided higher spatial detail of the microforms due to its greater point density (570.4 vs. 19.4 pts/m^2). Our VR/AR assessment revealed that the most immersive user experience was achieved from the Oculus Quest 2 compared to Google Cardboard VR viewers or mobile AR, showcasing the potential of VR for natural sciences in different environments. We expect VR implementations in environmental sciences to become more popular, as evaluations such as the one shown in our study are carried out for different ecosystems.

Keywords: bog; drone; Oculus Quest 2; Mer Bleue; SfM; UAV; augmented reality; AR

1. Introduction

Peatlands cover a significant area globally (≈3%), and in particular of northern regions (e.g., ≈12% of Canada), and they have an increasingly important role in carbon sequestration and climate change mitigation [1–4]. Ongoing monitoring of peatlands over large spatial extents through the use of satellite-based Earth observation products is needed to understand their response to climate change (e.g., [5–7]). However, given their generally poor accessibility and the fine-scale topographic variation of vegetation microforms (often <1 m in height), satellite-based mapping requires validation from ground data (e.g., water table depth, species composition, biochemistry) [8,9]. Unmanned aerial systems (UAS) have shown potential for characterizing these ecosystems at fine scales [9–11]. In general terms, microtopographic features such as hollows and hummocks are key elements that are closely related to complex and associated hydrological, ecophysiological, and biogeochemical processes in peatlands [12]. Hummocks are elevated features composed of vascular plants overlaying mosses that consistently remain above the water table, while hollows are lower lying areas with primarily exposed mosses [13]. The multitemporal characterization of hollows and hummocks at submeter scales is key to validating satellite-derived products such as phenology tracking, net ecosystem exchange estimation, etc. [9].

To date, mapping microtopography with UAS has relied on two main technologies: light detection and ranging (LiDAR) and structure-from-motion (SfM) multiview stereo (MVS) photogrammetry (hereinafter referred to as SfM) with variable results for each technology (e.g., [14–16]). LiDAR is an active remote sensing technology that uses a pulsed laser generally between 800 and 1500 nm for terrestrial applications, to measure ranges, i.e., the variable distances from the instrument to objects on the surface of the Earth. It does so by measuring the exact time it takes for the pulses to return after they are reflected off objects or the ground [17]. In contrast, SfM is a passive remote sensing technique that uses overlapping offset photographs from which to reconstruct the landscape [18,19]. In forested areas, LiDAR pulses can penetrate the canopy and allow for the development of both canopy and surface terrain models [17], while SfM only provides a surface model of the highest layer, often the canopy, as seen from the photographs [20]. Comparatively, across ecosystems, SfM is shown to produce higher density point clouds than those from LiDAR. Previously in peatlands, mapping microtopography has been compared between UAS SfM and airborne LiDAR (e.g., [16]). Many studies have also employed airborne LiDAR for large-scale peatland assessments (e.g., [21–26]). Terrestrial laser scanning (TLS) has also been shown to successfully map microforms at very high spatial detail (e.g., [27]). However, no formal study has rigorously compared UAS LiDAR and SfM for mapping peatland microtopography.

Because peatlands are both fragile ecosystems and in general have poor accessibility, tools to remotely study, access, and visualize peatland structure in 3D are needed for advancing our understanding of their response to climate change. Although not a new technology [28], the recent advances in virtual reality (VR) [29], with its applications in medicine [30], conservation [31], geosciences [32,33], e-tourism [34,35], and education [36], among others, provide novel opportunities to study peatlands and other ecosystems remotely without disturbance [37]. VR is technology (hardware and software) that generates a simulated environment which stimulates a "sense of being present" in the virtual representation [38]. In contrast, augmented reality (AR) superimposes the virtual representation on the real world through glasses or other mobile digital displays, in turn supplementing reality rather than replacing it [39]. Thus, through VR, users experience an immersive experience of the field conditions in a cost-effective and repeatable manner. For instance, [29] showcases the advantages of VR, such as the quantification and analysis of field observations, which can be performed at multiple scales. While early implementations required extensive and expensive hardware, such as CAVE (CAVE Automatic Virtual Environments) [38], recent commercial grade VR systems that utilize improved head mounted displays (HMD), such as Oculus Rift, Sony PlayStation VR, HTC Vive Cosmos, etc., allow for outstanding visualization capabilities and sharing of scientific output through web-based platforms.

Our study aims to bridge the implementation of 3D models derived from UAS (LiDAR and SfM) and VR/AR visualization. Thus, our objectives are to (1) compare SfM and LiDAR point cloud characteristics from a peatland; (2) compare the representation of peatland microtopography from the SfM and LiDAR data; and (3) provide a qualitative evaluation of VR and AR usability and quality of visualization of the two point clouds. We further discuss the potential of VR in peatland research and provide web-based examples of the study area. While we primarily focus on VR due to the maturity of the technology and its suitability for scientific data visualization, we also briefly compare the point clouds in AR. To our knowledge, ours is the first study to compare microtopography between LiDAR and SfM for a peatland, in addition to investigating peatland VR/AR models derived from UAS data.

2. Materials and Methods

2.1. Study Area

This study was carried out at Mer Bleue, an ≈8500 year-old ombrotrophic bog near Ottawa in Ontario, Canada (Figure 1). A bog is a type of peatland commonly found in

northern regions. Bogs are acidic, nutrient-poor ecosystems, receiving incoming water and nutrients only from precipitation and deposition. Mer Bleue is slightly domed, with peat depth decreasing from >5 m across most its area to ≈30 cm along the edges. It has a hummock–hollow–lawn microtopography with a mean relief between hummocks and hollows of <30 cm [40,41]. While the water table depth is variable throughout the growing season, it generally remains below the surface of the hollows [42]. Malhotra et al. (2016) [43] found a strong association between spatial variations in vegetation composition, water table depth, and microtopography. However, the strength of the association varied spatially within the bog. Mosses, predominantly *Sphagnum capillifolium, S. divinum,* and *S. medium* (the latter two species were formerly referred to as *S. magellanicum*) [44] form the ground layer of the bog and can be seen exposed in low lying hollows. Vascular plants comprise the visible upper plant canopy of the hummocks (Figure 1). The most common vascular plant species are dwarf evergreen and deciduous shrubs (*Chamaedaphne calyculata, Rhododendron groenlandicum, Kalmia angustifolia, Vaccinium myrtilloides*), sedges (*Eriophorum vaginatum*), and trees (*Picea mariana, Betula populifolia,* and *Larix laricina*) [45]. Hummocks have been estimated to account for 51.2% and hollows for 12.7% of the total area [46]. Trees and water bodies (open and vegetated) around the margins of the peatland, which are heavily impacted by beavers, comprise the remaining classes.

Figure 1. *Cont.*

Figure 1. (**A**) Map of Mer Bleue, near Ottawa in Ontario, Canada. Locations where photographs B–E were taken are indicated on the map. (**B**) UAV photograph facing north, taken in October; (**C**) photograph facing SE across the study area, taken in June; (**D**) UAV photograph of the southern margin of the study area where dense stands of *Typha latifolia* (cattail) grow in areas of permanent slow-moving water impacted by beavers. Photograph facing west, taken in May. (**E**) Photograph facing the treed bog, taken in June. A 360° aerial panorama acquired in late June can be viewed at https://bit.ly/mbpano2017 (accessed on 14 April 2021).

2.2. Airframe

We used a Matrice 600 Pro (M600P) (DJI, Shenzhen, China) for both the RGB photograph and LiDAR acquisitions (Figure 2, Table A1). The M600P is a six-rotor unmanned aerial vehicle (UAV) with a maximum takeoff weight of 21 kg (10.2 kg payload) (DJI Technical Support, 2017) that uses an A3 Pro flight controller with triple redundant GPS, compass, and IMU units. We integrated a differential real-time kinetic (D-RTK) GPS (dual-band, four-frequency receiver) module with the A3 Pro [47] for improved precision of navigation [10]. For both datasets, DJI Ground Station Pro was used for flight planning and for the automated flight control of the M600P.

Figure 2. M600P RTK enabled UAV with the (**A**) Canon DSLR and (**B**) LiAIR S220.

2.3. Structure from Motion Photogrammetry

A Canon 5D Mark III digital single-lens reflex (DSLR) camera with a Canon EF 24–70 mm f/2.8L II USM Lens set to 24 mm was used for the RGB photograph acquisition in June (Table A1). This is a full frame (36 × 24 mm CMOS) 22.1 MP camera with an image size of 5760 × 3840 pixels (6.25 μm pixel pitch). At 24 mm, the field of view of the lens is 84°. With the camera body and lens combined, the total weight was 1.9 kg. The camera was mounted on a DJI Ronin MX gimbal (2.3 kg) for stabilization and orientation control (Figure 2a). The camera's ISO was set to 800 to achieve fast shutter speeds of 1/640 to 1/1000 s at f/14 to f/16. The photographs were acquired from nadir in Canon RAW, (.cr2) format and were subsequently converted to large JPG (.jpg) files in Adobe Lightroom® with minimal compression. Because the M600P does not automatically geotag the photographs acquired by third party cameras, geotags were acquired separately.

Geotagging was achieved through a postprocessing kinematic (PPK) workflow with an M+ GNSS module and Tallysman TW4721 antenna (Emlid, St. Petersburg, Russia) to record the position and altitude each time the camera was triggered (5 Hz update rate for GPS and GLONASS constellations) (Table A1). A 12 × 12 cm aluminum ground plane was used for the antenna to reduce multipath and electromagnetic interference and to improve signal reception. The camera was triggered at two second intervals with a PocketWizard MultiMax II intervalometer (LPA Design, South Burlington, VT, USA). A hot shoe adaptor between the camera and the M+ recorded the time each photograph was taken with a resolution of <1 μs (i.e., flash sync pulse generated by the camera). The setup and configuration steps are described in [48]. The weight of the M+ GNSS module, the Tallysman antenna, the intervalometer and cables were 300 g combined. Photographs were acquired from an altitude of 50 m AGL with 90% front overlap and 85% side overlap. With the aforementioned camera characteristics, i.e., altitude and overlap, the flight speed was set to 2.5 m/s by the flight controller. The total flight time required was ≈18 min.

Base station data from Natural Resources Canada's Canadian Active Control System station 943020 [49] (9.8 km baseline) was downloaded with precise clock and ephemeris data for PPK processing of the M+ geotags. The open-source RTKLib software v2.4.3B33 [50] was used to generate a PPK corrected geotag for each photograph. A lever arm correction was also applied to account for the separation of the camera sensor from the position of the TW4721 antenna.

We used Pix4D Enterprise v4.6.4 (Pix4D S.A, Prilly, Switzerland) to carry out an SfM-MVS workflow to generate the dense 3D point cloud (Table A1). Unlike UAV integrated cameras with camera orientation written to the EXIF data, the DSLR photographs lack this information. However, these initial estimates are not necessary because during processing, Pix4D calculates and optimizes both the internal (e.g., focal length) and external camera parameters (e.g., orientation). In addition to the camera calibration and optimization in the initial processing step, an automatic aerial triangulation and a bundle block adjustment

are also carried out [51]. Pix4D generates a sparse 3D point cloud through a modified scale-invariant feature transform (SIFT) algorithm [52,53]. Next, the point cloud is densified with an MVS photogrammetry algorithm [54]. For this comparison, we did not generate the raster digital surface model (DSM) through Pix4D (see Section 2.5).

SfM Point Cloud Accuracy

Two separate flights (≈12 min total flight time) with the same equipment described above were carried out ≈30 min earlier in a vegetated field, 300 m south of the primary bog study area. This field was located on mineral soil and therefore is less impacted by foot traffic than the fragile bog ecosystem. In an area of 0.2 ha, twenty targets to be used as check points were placed flat on the ground. Their positions were recorded with an Emlid Reach RS+ single-band GNSS receiver (Emlid, St Petersburg, Russia) (Table A1). The RS+ received incoming NTRIP corrections from the Smartnet North America (Hexagon Geosystems, Atlanta, GA, USA) NTRIP casting service on an RTCM3-iMAX (individualized master–auxiliary) mount point utilizing both GPS and GLONASS constellations. The accuracy of the RS+ with the incoming NTRIP correction was previously determined in comparison to a Natural Resources Canada High Precision 3D Geodetic Passive Control Network station, and it was found to be <3 cm X, Y, and 5.1 cm Z [55]. The photographs from the camera and geotags were processed the same way as described above with RTKlib and Pix4D up to the generation of the sparse point cloud (i.e., prior to the implementation of the MVS algorithm). Horizontal and vertical positional accuracies of the sparse 3D point cloud were determined from the coordinates of the checkpoints within Pix4D. The results of this accuracy assessment are used as an estimate of the positional accuracy of the SfM model of the study area within the bog where no checkpoints were available.

2.4. LiDAR

We used a LiAIR S220 integrated UAS LiDAR system (4.8 kg) (GreenValley International, Berkeley, CA, USA) hard mounted to the M600P in August (Figure 2b) (Table A1). The system uses a Hesai Pandar40P 905 nm laser with a ±2 cm range accuracy, a range of 200 m at 10% reflectivity, and a vertical FOV of –25° to +15° [56,57]. The Pandar40P is a 40-channel mechanical LiDAR that creates the 3D scene through a 360° rotation of 40 laser diodes. The majority of the lasers (channels 6–30) are within a +2° to –6° range of the FOV [58]. The integrated S220 system utilizes an RTK enabled INS (0.1° attitude and azimuth resolution) with an external base station and a manufacturer stated relative final product accuracy of ±5 cm. The system includes an integrated Sony a6000 mirrorless camera that is triggered automatically during flight. These JPG photographs are used to apply realistic RGB colors to the point cloud in postprocessing.

Two flights at 50 m AGL and 5 m/s consisting of 6 parallel flight lines (40 m apart) were carried out. Importantly, prior to the flight lines, two figure 8s were flown to calibrate the IMU. The same figure 8s were repeated after the flight lines prior to landing. Total flight time was ≈10 min. The LiAcquire software (GreenValley International, Berkeley, CA, USA) provided a real-time view of the point cloud generation.

LiAcquire and LiNAV were used for the postprocessing of trajectory data and the geotagging of the RGB photographs. The LiDAR360 software (GreenValley International, Berkeley, CA, USA) was then used to correct the boresight error, carry out a strip alignment, merge individual strips, and calculate quality metrics consisting of analyses of the overlap, elevation difference between flight lines, and trajectory quality.

2.5. Analysis

The open source CloudCompare Stereo v2.11.3 (https://www.danielgm.net/cc/) (accessed on 14 April 2021) software was used to analyze the point clouds (Table A1). After the initial positional difference between the point clouds was computed, the LiDAR point cloud was coarsely aligned to the SfM point cloud followed by a refinement with an iterative closest point (ICP) alignment. Each point cloud was detrended to remove

the slope of the bog surface. The point clouds were then clipped to the same area and compared. Characteristics including the number of neighbor points, point density, height distribution, surface roughness (distance between a point and the best fitting plane of its nearest neighbors), and the absolute difference between point clouds were calculated. DSMs at 10 and 50 cm pixel sizes were also created from each dataset. CloudCompare was used to generate the DSMs rather than Pix4D and LiDAR360 respectively to ensure differences in the surfaces are not due to varying interpolation methodology between the different software. The average method with the nearest neighbor interpolation (in case of empty cells) was chosen for the rasterization of the point clouds.

To classify the hummocks and hollows, the DSMs were first normalized in MATLAB v2020b (MathWorks, Natick, MA, USA) by subtracting the median elevation in a sliding window of 10 × 10 m [59]. Hummocks were defined as having a height range 5–31 cm above the median and hollows as >5 cm below the median. These thresholds were defined on the basis of expert knowledge of the site. In the SfM data, this corresponded to the 55th–90th percentile of the height for hummocks and the bottom 38th percentile for hollows. In the LiDAR data, it corresponded to the 48th–71st percentile of the height for hummocks, and the bottom 40th percentile for hollows. A decision tree was used to assign the DSM pixels to hummock, hollow, and other classes based on their normalized height value.

To quantify the shape and compare the apparent complexity of the microforms from the SfM and LiDAR, we calculated the 3D Minkowski–Bouligand fractal dimension (D) of the surface of the bog [60]. The 3D fractal dimension combines information about an object/surface across different spatial scales to provide a holistic quantification of the shape [61]. The point clouds were converted to triangular meshes at rasterization scales of 10 and 50 cm in CloudCompare. The fractal dimension, D, was then calculated following the methodology described in [61]. The fractal dimension is a scale-independent measure of complexity. As defined by [62], fractals are "used to describe objects that possess self-similarity and scale-independent properties; small parts of the object resemble the whole object". Here, D is a measure of the complexity of the bog surface as modeled by the triangular mesh objects from the SfM and LiDAR data sources. The value of D ranges from 0 to 3, with higher values indicating more complexity in the shapes. In this case, the complexity quantified by D is related to the irregularity pattern [61], with more regular shapes having lower values.

Lastly, empirical semivariograms were used to compare the scale dependence of the hummock–hollow microtopography to determine whether the scale of the vegetation pattern captured by the SfM and LiDAR datasets is similar. The spatial dependence of the height of the vegetation can be inferred from the semivariogram which plots a dissimilarity measure (γ) against distance (h). The range, sill, and nugget describe the properties of the semivariogram. The range indicates the spatial distance below which the height values are autocorrelated. The sill indicates the amount of variability and the nugget is a measure of sampling error and fine-scale variability. Previous application of empirical semivariograms to terrestrial LiDAR data from a peatland indicated the hummock–hollow microtopography had an isotropic pattern with a range of up to 1 m, and in sites with increased shrub cover, the range increased to 3–4 m [27]. The empirical semivariograms were calculated in MATLAB v2020b for a subset of the open bog that did not include boardwalks.

In order to generate the PLY files (i.e., Polygon file format, .ply) needed for VR and AR visualization, the horizontal coordinates (UTM) were reduced in size (i.e., number of digits before the decimal) using a global shift. In this case, 459,400 was subtracted from the easting and 5,028,400 from the northing. Binary PLY files were then generated with CloudCompare.

Both VR (Section 2.6) and AR (Section 2.7) visualizations were compared to a standard web-based 3D point cloud viewer as a baseline. We used a Windows server implementation of Potree v1.8 [63], a free open-source WebGL based point cloud renderer to host the point clouds (https://potree.github.io/) (accessed on 14 April 2021).The Potree Converter

application was used to convert the LAS files (.las) into the Potree file and folder structure used by the web-based viewer for efficient tile-based rendering. In addition to navigation within the point cloud, user interactions include measurements of distance and volume and the generation of cross sections.

2.6. Virtual Reality Visualization

We tested the VR visualization of the point clouds with an Oculus Quest 2 headset (Facebook Technologies LLC, Menlo Park, CA. USA) (Table A1). The Oculus Quest 2 released in 2020, is a relatively low cost, consumer-grade standalone VR HMD. It has 6 GB RAM and uses the Qualcomm Snapdragon XR2 chip running an Android-based operating system. The model we tested had 64 GB of internal storage. The fast-switching LCD display has 1832 × 1920 pixels per eye at a refresh rate of 72–90 Hz (depending on the application, with 120 Hz potentially available in a future update).

In order to access point cloud visualization software, the Oculus Quest 2 was connected to a Windows 10 PC through high-speed USB 3. In this tethered mode, the Oculus Link software uses the PC's processing to simulate an Oculus Rift VR headset and to access software and data directly from the PC. The PC used had an Intel Core i7 4 GHz CPU, 64 GB RAM, and an NVIDIA GeForce GTX 1080 GPU. The PLY files were loaded in VRifier (Teatime Research Ltd., Helsinki, Finland), a 3D data viewer package that runs on Steam VR, a set of PC software and tools that allow for content to be viewed and interacted with on VR HMDs. The two touch controllers were used to navigate through the point clouds as well as to capture 2D and 360-degree "photographs" from within the VR environment.

As a simple and low-cost alternative VR visualization option, we also tested two Google Cardboard compatible viewers, a DSCVR viewer from I Am Cardboard (Sun Scale Technologies, Monrovia, CA, USA), and a second generation Google Official 87002823-01 Cardboard viewer (Google, Mountain View, CA, USA) (Table A1). These low-tech viewers can be used with both iOS and Android smartphones by placing the phone in the headset and viewing VR content through the built-in lenses. The LiDAR and SfM point clouds were uploaded to Sketchfab (https://sketchfab.com) (accessed on 14 April 2021) (in PLY format), an online platform for hosting and viewing interactive and immersive 3D content. The models were accessed through the smartphone's web browser. The entire LiDAR point cloud was viewable with the smartphone's web browser, but the SfM model was subset to an area of 0.3 ha of the open bog and an 0.4 ha area of the treed bog due to the maximum 200 MB file size upload limitations of our Sketchfab subscription. The PLY models were scaled in Sketchfab relative to a 1.8 m tall observer.

2.7. Augmented Reality Visualization

In comparison to consumer VR systems, AR head-up-displays and smart glasses capable of visualizing scientific data are predominantly expensive enterprise grade (e.g., Magic Leap 1, Epson Moverio series, Microsoft Hololens, Vuzix Blade, etc.) systems. Therefore, we tested mobile AR using webhosted data viewed through an iOS/Android smartphone application. The point clouds in PLY format were uploaded to Sketchfab, and the models were accessed in AR mode via the Sketchfab iOS/Android smartphone application. The entire LiDAR point cloud was viewable with the smartphone application, but the SfM model was subset to an area of 788 m^2 due to RAM limitations of the phones tested (i.e., iPhone XR, 11 Pro, 12 Pro and Samsung Galaxy 20 FE).

3. Results

3.1. SfM-MVS Point Cloud

Each of the 333 bog photographs was geotagged with a fixed PPK solution (AR ratio μ = 877.3 ± 302, range of 3–999.99). The precision of the calculated positions was μ = 1.2 ± 0.6 cm (easting), μ = 1.6 ± 0.7 cm (northing), and μ = 3.2 ± 1.3 cm (vertical). The final ground sampling distance (GSD) of the bog point cloud was 1.2 cm. Pix4D found a median of 58,982 keypoints per photograph and a median of 26,459.9 matches

between photographs. Total processing time in Pix4D was ≈ 2.5 h (Intel® Xeon® Platinum 8124M CPU @ 3.00GHz, 69 GB RAM). The average density of the final point cloud was 2677.96 point per m^3 (40,605,564 total points).

In the field south of the bog, the point cloud was generated with a GSD of 1.8 cm, and similar to the bog dataset, all photographs were geotagged with a fixed PPK solution. Pix4D found a median of 75,786 keypoints per photograph and a median of 23,202.9 matches between photographs. The positional accuracy of this point cloud in relation to the checkpoints was RMSE$_x$ = 5 cm, RMSE$_y$ = 6 cm, and RMSE$_z$ = 5 cm. These values serve as an estimate of the positional accuracy of the bog point cloud.

3.2. LiDAR Point Cloud

The individual LiDAR strip quality metrics calculated by LiDAR360 are shown in Table 1. These metrics are calculated for each entire strip, including edges and turns that were not used in the final dataset. At an acquisition height of 50 m AGL, the width of the individual LiDAR strips was ≈80 m with neighboring strips overlapping by 50–52%. As expected, the treed portion of the bog had the greatest elevation difference between neighboring strips (13.1–17.3 cm) compared to the open bog predominantly comprised of hummocks and hollows (5.8–7.1 cm).

Table 1. Quality metrics of the full individual LiDAR strips calculated from LiDAR360.

Quality Metric	Value
Overlap between strips (%)	50.8–52.2
RMSE before boresight correction (cm)	8.6
RMSE after correction (cm)	8.4
Elevation difference between strips, RMSE$_z$ (HU–HO) (cm)	5.8–7.1
Elevation difference between strips, RMSE$_z$ (trees) (cm)	13.1–17.3
[1] Average density (pts/m^2)	25.3–31.2
[1] Density range (pts/m^2)	1–270
Trajectory deformation (%)	0.22–0.55

[1] These values represent the full strips, including edges without overlap, turns, and infrastructure (sheds) that were cut from the final dataset.

3.3. Point Cloud Comparisons

The final SfM and LiDAR point clouds covering 1.71 ha are shown in Figure 3. The SfM dataset has 30,413,182 points while the LiDAR dataset has 1,010,278 points (Table 2). As a result, the SfM point cloud is 19.6 times larger (LAS format) than the LiDAR dataset. The data acquisition time was nearly double for the SfM (18 vs. 10 min), and the computation time to generate the 3D point cloud was at least 10 times greater than for the LiDAR dataset. Considering the time needed to process the geotags and prepare the photographs (i.e., convert from CR2 to JPEG and color correct if necessary), the SfM point cloud takes even longer to generate.

The increased detail obtained from the ≈30x more points in the SfM dataset is apparent in Figure 3, resulting in a more realistic reconstruction of the bog. The several "no data" areas in the LiDAR dataset (shown in black) and the linear pattern of point distribution are artefacts from the mechanical laser diodes spinning during acquisition in a system hard mounted on a moving platform (Figure 2b).

Figure 4 illustrates the point density of the two datasets. The SfM dataset has an average density of 570.4 ± 172.8 pts/m^2 while the LiDAR dataset has an average density of 19.4 ± 7.5 pts/m^2. In both data sets, the lowest density is in the treed bog.
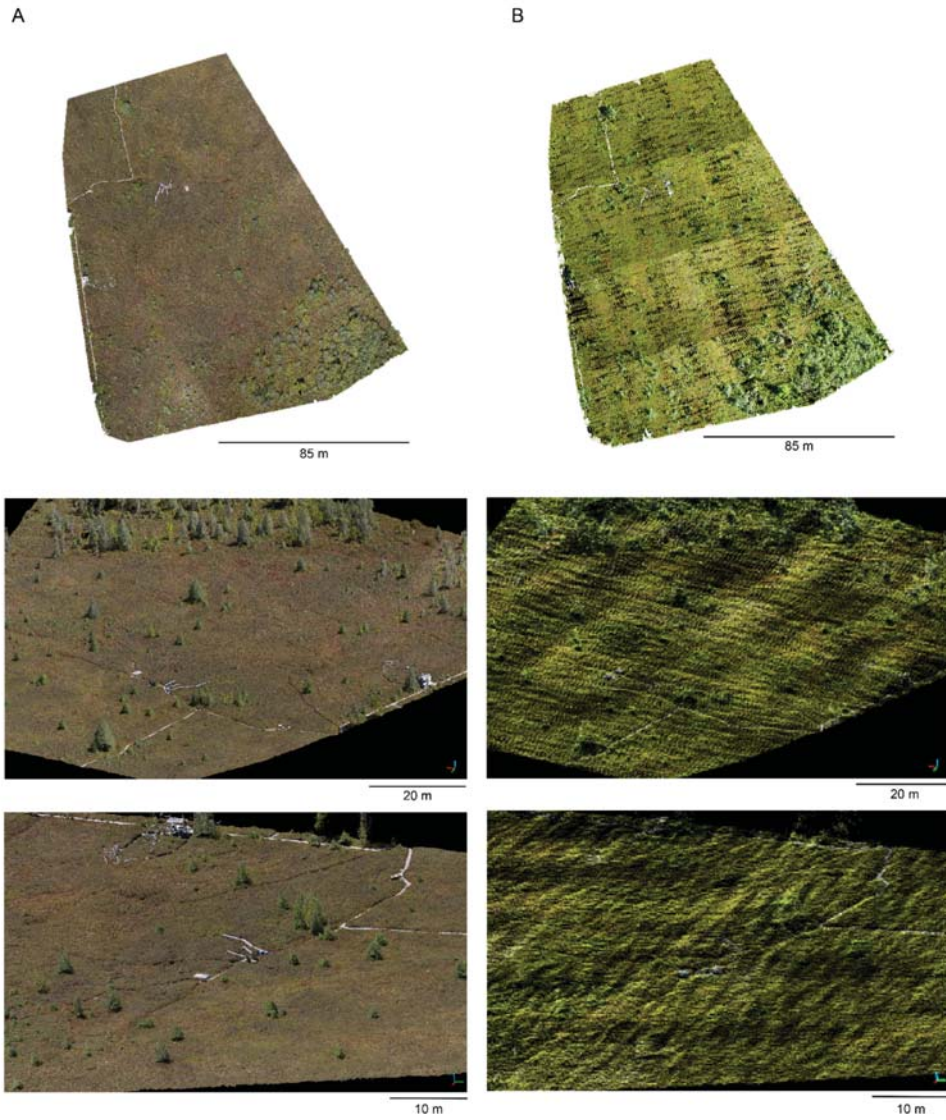
Figure 3. The final 1.71 ha point clouds for the bog study area from (**A**) SfM and (**B**) LiDAR at three increasing levels of scale.

Table 2. Comparison between the final bog SfM and LiDAR datasets.

Characteristic	SfM	LiDAR
Area (ha)	1.71	1.71
Acquisition altitude (m)	50	50
Acquisition speed (m/s)	2.5	5
[1] Total flight time (min)	≈18	≈10
Average Density (pts/ha)	≈17.7M	≈0.6M
Total number of points	30,413,182	1,010,278
Density as pts/m^2 ($\mu \pm \sigma$)	570.4 ± 172.8	19.4 ± 7.5
[2] File size, LAS format (total area in MB)	1000	51
[2] File size, LAS format (MB/ha)	585	30
[2] File size, PLY format (total area in MB)	445	15
[2] File size, PLY format (MB/ha)	260.2	8.8
[3] Computation time (min)	≈150	≈15

[1] Includes transit from takeoff area and the two sets of figure 8s required for the LiDAR INS calibration after takeoff and before landing, and does not include time on the ground between flights. [2] These files contain only six columns: x, y, z coordinates and R, G, B color intensity. [3] Does not include time needed to covert or geotag the photographs for the SfM.
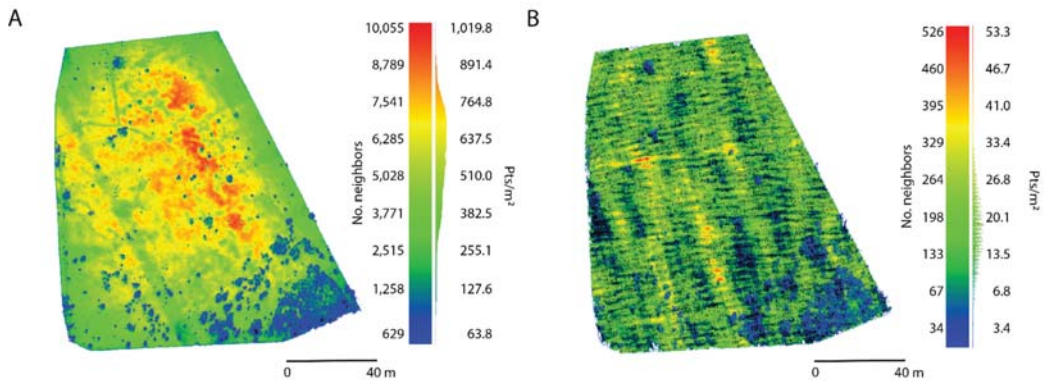
Figure 4. Point density of the (**A**) SfM and (**B**) LiDAR datasets. The number of neighbors is the count of points within a sphere with a 1 m radius. The pts/m^2 represents the number of points within a surface area of 1 m^2. The distribution next to the color bars represents the histogram of the height values. No data shown in black.

Despite the differences in point density, the gross microtopography and presence of both large and small trees can be seen in both datasets (Figure 5). A *t* location-scale distribution was found to best fit the vegetation height from both datasets based on the AIC criterion (Table 3, Figure 6). This distribution better represents data with a heavier tail (i.e., more outliers) than a Gaussian one. In this case, relatively fewer points representing the trees are the outliers. The distribution is described by three parameters, location (μ), scale (σ) and shape (ν). Larger values of ν indicate a lesser tail and, therefore, a distribution more similar to a Gaussian. A two-sample Kolmogorov–Smirnov test indicates the height values are from different continuous distributions (k = 0.11, *p* = 0, α = 0.05). Figure 6 shows that the SfM's distribution is slightly wider (σ = 1.591) than that of the LiDAR (σ = 0.1151).
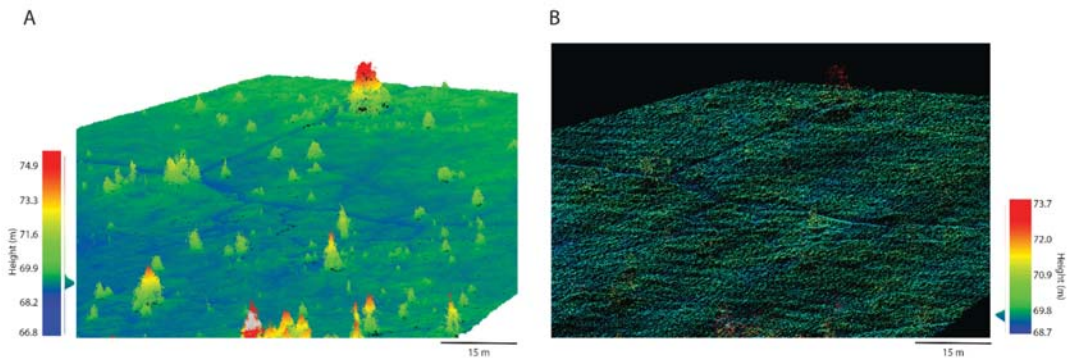
Figure 5. Subset of the point clouds illustrating the height of the vegetation (m ASL) for a subset of the point cloud from (**A**) SfM and (**B**) LiDAR. The distribution next to the color bars represents the histogram of the height values.

Table 3. Parameters of the best-fit t location-scale distributions of height (m ASL) from the two datasets; μ = location, σ = scale, ν = shape, CI = confidence interval.

Dataset	AIC	μ	σ	ν	CI μ	CI σ	CI ν
SfM-MVS	1.0879×10^7	69.436	0.1591	1.87	69.4359–69.4361	0.1590–0.1592	1.816–1.819
LiDAR	8.2967×10^4	69.470	0.1151	1.40	69.4697–69.4703	0.1148–0.1154	1.397–1.407
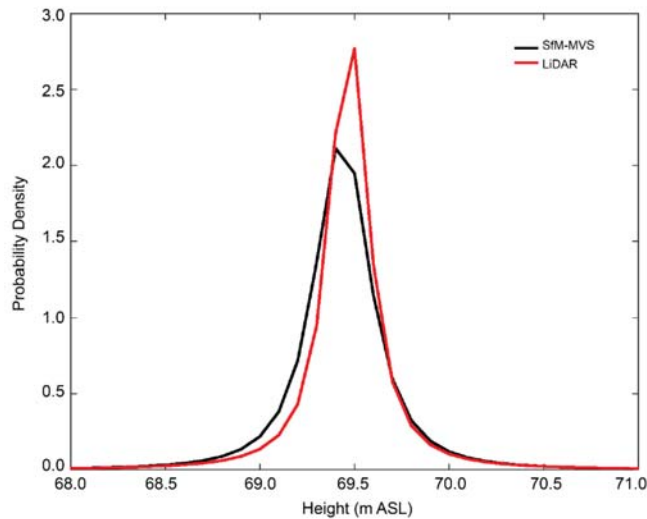
Figure 6. Best-fit t location-scale distribution probability density functions of height for the SfM and LiDAR datasets.

Prior to alignment in CloudCompare, there was a 15 $\pm$ 22 cm vertical and 50 $\pm$ 7 cm horizontal offset between the point clouds. After ICP, the horizontal offset decreased to 10.5 $\pm$ 11.5 cm. The sparseness of the LiDAR point cloud precluded a closer horizontal alignment. Vertically, the difference in height varies by spatial location (average of 4 $\pm$ 13 cm) (Figure 7) due to a more pronounced depression in center of the SfM-MVS dataset where the bog has a higher density of hollows. However, when the uncertainties of the height values of both the SfM and LiDAR surfaces are taken into account, the height differences are minimal for the majority of the study area.
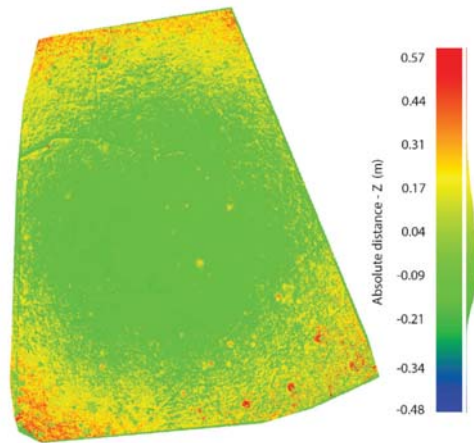
Figure 7. Difference in height between the SfM and LiDAR point clouds. The distribution next to the color bar represents the histogram of the difference in height.

The values of surface roughness (Figure 8) reveal similarities across both datasets, with the trees and boardwalks differentiated from the hummocks and hollows with higher values of roughness. In the SfM dataset, hummocks (roughness ≈ 0.1–0.35) can be better differentiated from hollows (roughness ≈ 0.06). From the LiDAR dataset, the sparseness of the point cloud results in incomplete definition of the hummocks (roughness ≈ 0.05–0.29).
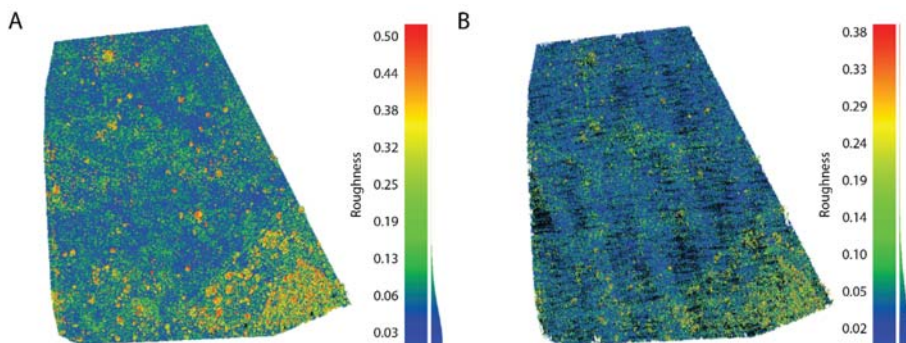
Figure 8. Surface roughness for (**A**) SfM and (**B**) LiDAR datasets calculated with a kernel size of 1 m (the radius a sphere centered on each point). The distributions next to the color bars represent the histogram of the roughness values.

After rasterization, the density of the points averaged per pixel of the 10 cm DSM was 17.6 ± 7.3 pts/px from the SfM and 0.6 ± 1.1 pts/px from the LiDAR. At a 50 cm pixel size, the density increased to 437.5 ± 144.4 pts/px for the SfM and 14.5 ± 8.3 pts/px for the LiDAR. The low point density for the LiDAR at the 10 cm pixel size resulted in interpolation artefacts. From the DSMs, the percentages of classified hummocks and hollows are similar between the SfM and LiDAR classifications (Table 4). In both cases, the proportions of the two microforms decreased with increasing pixel size, most notably for the SfM hummock class (loss of 5%). For both pixel sizes, the estimated total area of hummocks and hollows is lower from the LiDAR DSM than those generated from the SfM.

Table 4. Percentage of hummocks (HU) and hollows (HO) in the study area classified from the SfM and LiDAR DSMs.

Pixel Size	SfM HO	SfM HU	LiDAR HO	LiDAR HU
10 cm	28.8	28.6	29.9	25.6
50 cm	27.8	23.6	22.1	24.0

Comparisons of transects (Figure 9) across the profile of a tree and hummocks and hollows, from the 10 cm DSM of each dataset, reveal similarities in the heights along the transects. The remaining horizontal offset between the two datasets is most apparent in the profile of the tree (Figure 9a), but it can also be seen in the hummocks and hollows (Figure 9b) to a lesser degree. The incomplete resolution of the tree crown can be seen in the transect across the tree with sections dropping to ground level due to the low density of the LiDAR. At the finer resolution of the height in the hummocks and hollows transect, a vertical offset of 10–20 cm can be seen between the SfM and LiDAR data. This transect is located near the center of the study area and as can be seen in Figure 7, the difference in height between the datasets in that section is 9–21 cm.
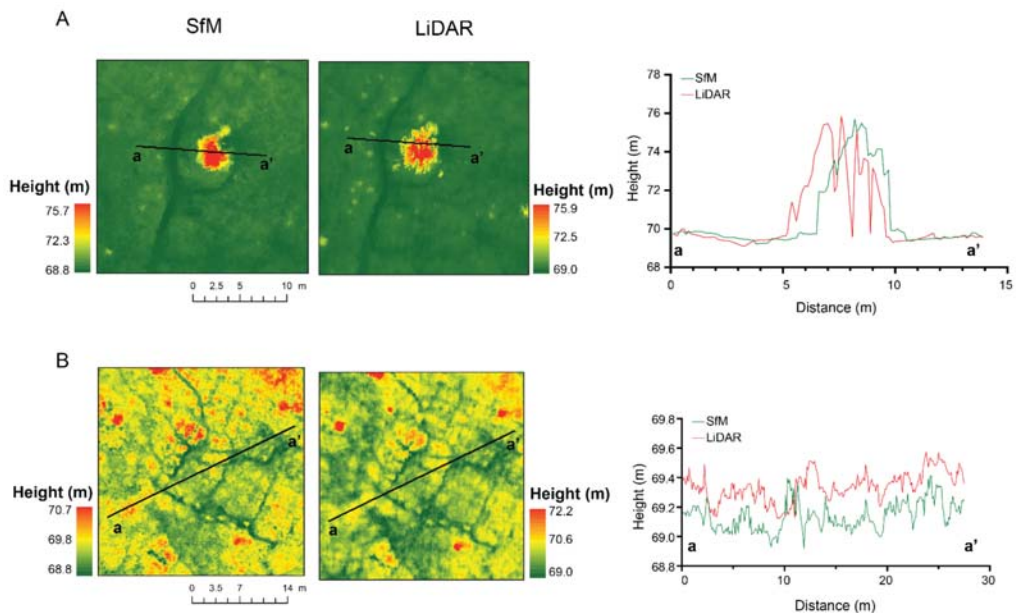
Figure 9. Comparison of transects across a profile of a tree (**A**) and hummocks and hollows (**B**) for the SfM and LiDAR datasets. The panels on the left illustrate the DSMs from which the transects were extracted.

The 3D fractal dimension reveals opposite patterns of complexity between the 10 and 50 cm scales for the SfM and LiDAR derived triangular meshes (Table 5). At both scales, the LiDAR data have higher values of D, indicating greater complexity of the 3D shape of the bog surface. However, this is likely influenced by the sparseness of the point cloud resulting in artefacts following interpolation producing artificial complexity. The lowest value of D (1.36), obtained for the 10 cm SfM data, indicates that at that scale, the microtopography of the bog is more regular. At 50 cm, some of the lawns (height values spanning ±5 cm around the median) that are intermediate between the hummocks and the hollows are grouped together with either the neighboring hummock or hollow, resulting in a more distinct boundary between microforms and a more irregular pattern and greater value of D (1.81).

Table 5. Value of the 3D Minkowski–Bouligand fractal dimension (D) for the SfM and LiDAR.

Pixel Size	SfM	LiDAR
10 cm	1.36	1.86
50 cm	1.81	1.83

Similar to the findings of [27], we also found that the bog has an isotropic (nondirectional) semivariogram (from both SfM and LiDAR). From the SfM, the range was approximately 2.5 m with a sill of 0.06 and a nugget of 0.01. The LiDAR had similar results with a range of approximately 2.7 m, a sill of 0.05, and a nugget of 0.01. The semivariograms from both datasets support a hummock–hollow pattern. The longer range value of the LiDAR indicates it was able to resolve a less well-defined pattern between the hummocks and hollows than the SfM.

Lastly, based on the system implementations and acquisition of the data, Table 6 summarizes the main strengths and weaknesses of SfM and LiDAR data acquisition for 3D surface reconstruction of the bog.

Table 6. Comparison of general SfM and LiDAR acquisition strengths and weaknesses.

Characteristic	SfM	LiDAR
Acquisition	Slow	Fast
System initialization	Starts acquisition after takeoff	Requires INS calibration after takeoff and before landing
Line spacing	Narrow (e.g., 15 m @ 50 m AGL with 80% sidelap)	Wide (e.g., 40 m @ 50 m AGL with 50% overlap)
Processing time	Slow	Fast
Resolution of spatial detail	Ultra-high	Moderate
User friendliness	Low–high [1]	High
Consistency of results	Moderate–high	High
Potential for component failure	Low–high [2]	Low
Payload implementation	Easy–difficult [3]	Easy
File size	Large	Small
Payload weight (kg)	4.5	4.8

[1] System described here has a low user-friendliness (i.e., complex to operate) but integrated systems (e.g., Phantom 4 RTK [55]) are more user friendly. [2] System described here has a high potential for component failure unlike integrated systems. [3] The DSLR setup described here requires precise balancing of the camera on the gimbal, which can be difficult and time consuming to achieve in the field. This is not a concern for integrated systems.

3.4. Web-Based Visualization

Both point clouds could be visualized in full spatial extent through a web browser from both a desktop computer (Figure 10) and smartphone. Navigation was simple and intuitive using either the mouse (desktop) or by swiping across the screen (smartphone). For both datasets, virtually no lag was experienced when interacting with the point clouds. The basic tools, which included measuring distances and areas and drawing cross sections (Figure 10b), further allowed the user to explore the characteristics of the bog. While interactivity and usability were high, this baseline implementation lacked the "sense being present" within the data. The overall definition of the detail in the point clouds depended on the speed of the internet connection. The server used Cat6 Ethernet to a gigabit broadband connection. From the user side, slow connections, especially on a mobile browser (e.g., HSPA-3G 3.5–14 Mbps), resulted in the point clouds requiring more time to load at full resolution especially for the SfM model (i.e., tens of seconds). On an LTE mobile internet connection (197 Mbps), there was no difference in the speed the models would load (i.e., <5 s) in comparison to a high-speed Wi-Fi or Ethernet connection (i.e., 150–800 Mbps). This web-based implementation is the simplest to access, requiring the user only to click a URL.
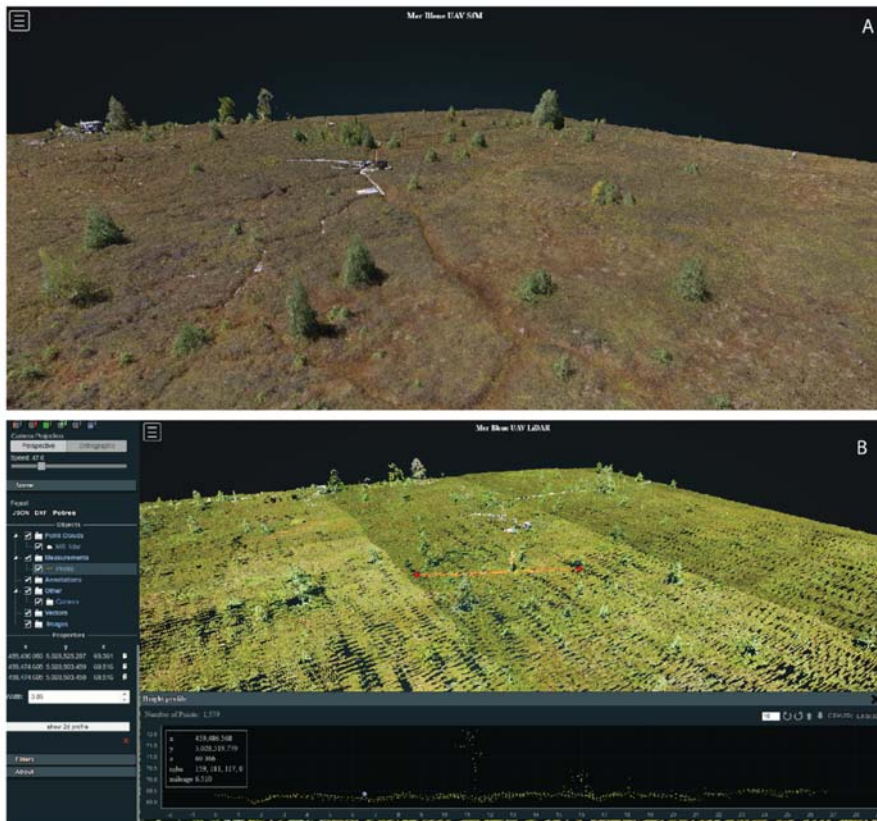
Figure 10. Screen captures illustrating the (**A**) SfM and (**B**) LiDAR point clouds in the web-based Potree viewer. The LiDAR data are shown with the cross-section tool enabled, illustrating that while the microtopography is difficult to see in the point cloud due to the low density of points, when viewed as a cross section, the difference in elevation between the hummocks and hollows is visible. The point clouds can be viewed at https://bit.ly/MB_SfM (accessed on 14 April 2021) and https://bit.ly/MB_lidar (accessed on 14 April 2021), respectively.

3.5. Virtual Reality Visualization

3.5.1. Oculus Quest 2

Similar to the web-based visualization, the full point clouds could be loaded and displayed in the HMD through VRifier (Figure 11). The LiDAR point cloud loaded near instantaneously while ≈15–20 s were needed for the SfM model to load. The Oculus Quest 2 provided a full immersive experience with a higher "sense of being present" in the data than what was achieved by the web-based visualization. In this VR implementation, the importance of point density was apparent. With the SfM model, the user has the "next best" experience to being in the bog in person due to the high level of detail while the low point density of the LiDAR resulted in a less realistic experience because of the gaps in the data. Similar to the web-based viewer, the ability to scale the model easily with the touch controllers enhanced the immersive experience.
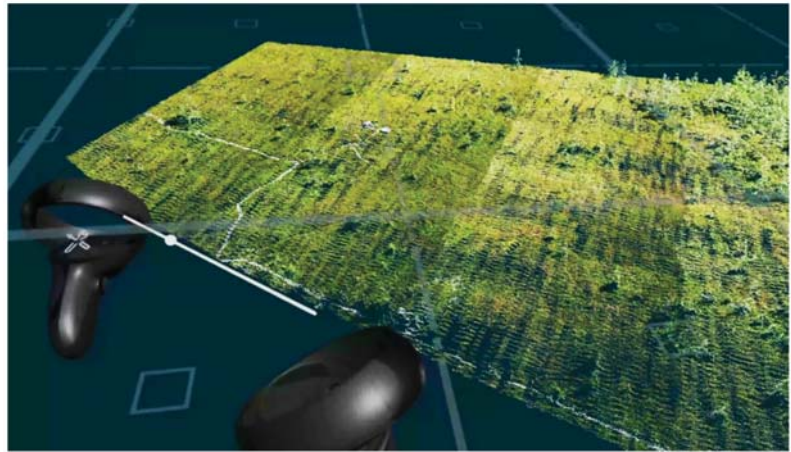
Figure 11. Video from VRifier illustrating the experience navigating the SfM and LiDAR point clouds on the Oculus Quest 2 headset. The input PLY files and video are available for download from https://doi.org/10.5281/zenodo.4692367 (accessed on 14 April 2021).

While generation of the PLY files was straightforward, the setup and integration of the Oculus Quest 2 and the desktop PC were more complicated, requiring the installation and configuration of several software packages and drivers. As of April 2021, VRifier was still in development, and not all features had been implemented. While it was possible to navigate through the point cloud and capture 2D and 3D panoramas (Figure 12) from within VRifier, tools to measure distances or areas were not available. When combined, the software packages (i.e., VRifier, Steam, various Oculus services) committed between 1.5–3 GB of the PC's RAM and 2.5–3% of the CPU during the visualization of the models.
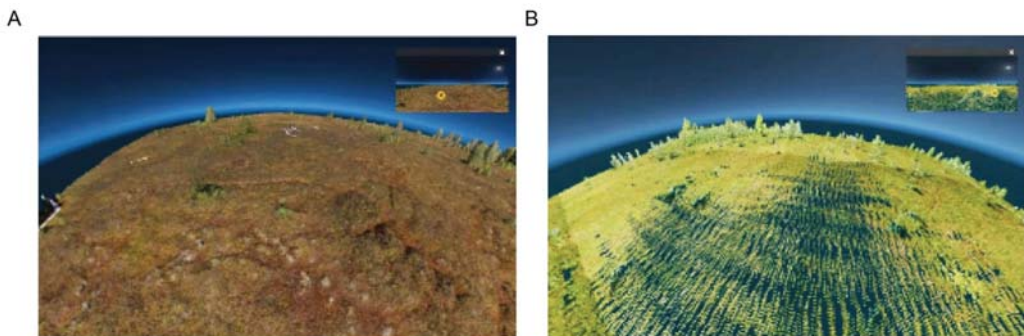
Figure 12. Videos illustrating 360° panoramas of the (**A**) SfM and (**B**) LiDAR point clouds within VRifier. These panoramas are being viewed on the Insta360 Player but can be opened by most 360° photograph viewers. The 360° panoramas are available for download from https://doi.org/10.5281/zenodo.4692367 (accessed on 14 April 2021).

One of the most useful options from within VRifier was the generation of the 360° panoramas (Figure 12). These files (PNG format, .png) can be readily shared, and many free programs are available to view them in 360° format. While they do not provide the navigation element of the immersive experience, these files are a suitable alternative for sharing geospatial data visualization.

3.5.2. Google Cardboard

Other than the web-browser, the Google Cardboard headsets wwere the easiest for visualizing the 3D models. However, the quality of the stereoscopic 3D effect depended on smartphone model used due to the differences in screen size. For example, it was not possible to avoid duplication artefacts with the iPhone XR (screen size 6.06") with either viewer, but on the iPhone 11 Pro (screen size 5.85"), both viewers worked well in showing clear 3D content. Both viewers are intended to work with screens 4–6" in size. With the Google 87002823-01 Cardboard viewer, navigation through teleportation within the model was straightforward, but it did not work with the DSCVR headset, in which the experience was more similar to viewing a static 360° 3D photograph. Despite the 3D effect, it was less immersive than with the Oculus Quest 2 implementation.

3.6. Augmented Reality Visualization

We found the density of the 3D point clouds and the resultant file sizes to be a limiting factor in the usability of the mobile AR viewer. While the entire LiDAR point cloud (14 MB in .ply) could be opened in the Sketchfab application (Figure 13a), the SfM model had to be reduced in overall extent to 788 m^2 (20 MB in .ply) (Figure 13b). In addition, the relatively small screen size of the smartphones did not allow for fine scale investigation of the models. Nevertheless, the ability to "walk through" and in-spect the models from different viewpoints by simply rotating the phone allowed for a partially immersive experience. With the LiDAR data, the sparseness of the point cloud resulted in the user being able to see through the model to the real-world ground below (Figure 13b), and the hummock–hollow microtopography was very difficult to discern. From the SfM model, gross microtopographic features could be seen on the screen, but because of the small spatial extent of the subset dataset, very little of the bog's spatial structure could be examined. Table 7 summarizes a comparison between the main consid-erations of the different point cloud visualizations in VR and AR tested here for the SfM and LiDAR point clouds.

Table 7. Qualitative comparison between main considerations for visualization of the LiDAR and SfM point clouds.

Characteristic	Web-Based	Oculus Quest 2 VR	Google Cardboard (VR)	Mobile AR
Sense of being present	Low	High	Moderate	Low
Ease of use	High	Moderate	Moderate–high	High
Ease of setup	Moderate	Low	High	High
File size supported	Ultra-large	Ultra-large	Moderate	Limited
Equipment cost (setup)	High	Moderate	Low	Low
Equipment cost (user)	Low/high	Moderate	Low	Low
Long-term cost effectiveness	High	High	Low–high	Low
Requires internet	Yes/No [1]	No [2]	Yes/No [3]	Yes

[1] A local PC installation of the Potree viewer that does not require access to the internet to view the models is available. [2] After initial setup, internet access is not required. [3] Models could be saved locally to the smartphone and accessed without internet.

Figure 13. Videos illustrating a screen recording of the AR visualization of the (**A**) SfM and (**B**) LiDAR point clouds through the iOS Sketchfab application. The models can be viewed in AR at https://skfb.ly/onuU9 (LiDAR) (accessed on 14 April 2021) and https://skfb.ly/onuUs (SfM) (accessed on 14 April 2021).

4. Discussion

Microtopography and vegetation patterns at various scales can provide important information about the composition and environmental gradients (e.g., moisture and aeration) in peatlands. Ecological functions, greenhouse gas sequestration, and emission and hydrology can further be inferred from detailed analyses of the vegetation patterns [27,43]. As expected, our study revealed differences between SfM and LiDAR bog microtopography characterizations. The greatest difference is the spatial detail defining the microforms in the point clouds or DSMs. This is a result of the varying point densities, i.e., 570.4 ± 172.8 pts/m^2 from the SfM versus 19.4 ± 7.5 pts/m^2 from the LiDAR. Despite being sparser than the SfM, the UAS LiDAR data are considerably higher in density than conventional airborne LiDAR data from manned aircraft due to the low altitude of the UAS data collection. For example, airborne LiDAR data over the same study area produced a point cloud with a density of 2–4 pts/m^2 [59]. Similarly, the authors in [64] reported a point density of 1–2 pts/m^2 from airborne LiDAR for wetlands in Eastern Canada. Nevertheless, the point density achieved here for the LiDAR is lower than that reported by other UAS systems used to study forested ecosystems (e.g., up to 35 pts/m^2 [65]).

Contrary to most forest ecosystems with a solid mineral soil ground layer, the ground layer of the bog is composed of living *Sphagnum* sp. moss over a thick peat column (several meters) with high water content, which prevents the pulses from encountering a solid non-vegetated surface below. Furthermore, the shrubs that comprise the hummocks have a complex branch architecture. A laser pulse encountering vegetation is likely to undergo foliage structural interference, resulting in reduced amplitude of return in comparison to solid open ground [66]. Luscombe et al. (2015) [67] showed that dense bog vegetation disrupts the return of the laser pulses and can result in an uncertain representation of the microform topography. Similar to the authors in [22,25] who found that penetration of the laser pulses into hummock shrub canopy was low from airborne LiDAR, because the vegetation blocked the pulse interaction with the ground beneath hummocks, our results

also did not show multiple returns over the hummocks. As can be seen in the cross section of the LiDAR point cloud (Figure 9b), the points follow the elevation of the top of the canopy. A similar phenomenon was noted in other ecosystems with short dense vegetation such as crops and grasslands [27]. The SfM also cannot distinguish between the tops of the hummocks and the moss ground layer beneath. Our results were also similar to those by the authors [23,24] who found that exposed *Sphagnum* sp. mosses are good planar reflectors for LiDAR, which allows for mapping the surface details in open bogs.

As input to models that require a DSM as part of the workflow or as a covariate, e.g., peat burn intensity mapping [68], biomass estimation [59], and peat depth estimation [21], either the SfM or LiDAR would be sufficient. Both retain the gross microtopography of the bog, with similar semivariogram ranges and complexity (at the 50 cm scale). LiDAR should be used with caution at fine scales of interpolation due to the artefacts introduced from the low point density. Where fine scale detail is required (<10 cm), the SfM provides better results.

While both technologies provide valuable datasets of the bog, they are optimized for different scenarios (Table 6). The SfM dataset is better suited for studies that require fine spatial detail over a smaller area (<10 ha). The longer time for data acquisition and processing make this technology more feasible for localized studies. In contrast, the more efficient LiDAR is better suited to acquiring data over larger areas at lower spatial detail. At the expense of total area covered, from a lower altitude and with a slower flight speed the point density of the LiDAR could be increased, but further testing is required to determine by how much in this ecosystem. Both payloads are of moderate weight, 4.5 kg for the SfM and 4.8 kg for the LiDAR (Table 6) and as such require a UAS with enough payload capacity (e.g., M600P used in our study).

When manipulating the point clouds on a desktop PC or viewing them through the web-based Potree viewer, the difference in file size (1 GB for the SfM vs. 51 MB for the LiDAR LAS files) is not apparent when navigating within or interacting with the dataset. Even with a slow mobile internet connection, the Potree viewer remained useable. The file size also was not an important consideration when viewing the point clouds in VR with the Oculus Quest 2. Because the HMD is tethered to the PC during this operation and the desktop computer is rendering the data, the full datasets can be readily interacted with. When mobile VR (e.g., Google Cardboard) or mobile AR was used, the file size of the SfM dataset hindered the user experience. The main limitation for mobile VR was the file size of the cloud-based hosting platform (i.e., Sketchfab) and RAM capacity of the smartphones for AR. Potentially, the commercial AR implementations developed for medical imaging would not have the same file size restrictions, although these were not tested here.

All VR and AR visualizations provided a sense of agency through the user's ability to turn their head or smartphone and explore the bog through a full 360° panorama and change their perspective or scale of observation. While this ability is also true for the 360° panoramas captured within VRifer, dynamic agency was only fully achieved by motion tracking in the VR and AR implementations. As described by [69], this is an important distinction between a desktop digital experience and immersive technology. Such transformative developments in visualization lead to the user becoming "part of" the digital representation as opposed to the digital content remaining distinct from the user's experience [69]. Of the VR and AR tested here, only the Oculus Quest 2 rendered a visually immersive experience. In comparison to other VR implementations such as CAVEs and video walls with smart glasses, the full 360° panoramic view of the VR HMD cannot be matched [70].

Visualization technology is important because it allows users to study areas of interest in virtual environments in 3D, and it facilitates the interaction of groups in different locations, the collection of data in time and space, and the ability to view the object studied in environments with varying scales. In addition to its use in scientific queries, the immersive digital content is a further benefit for educational material and for the individual exploration of questions related to the datasets. Adding virtual models of the

region of interest accessible with immersive VR or AR technology greatly benefits the overall understanding and interest in the subject matter [71,72]. Because VR/AR content is interactive, the datasets can now be manipulated by each person with different questions or interests.

With the popularization of this technology for gaming and entertainment, there has been both a surge in development and improvement in the quality of the hardware but also a decrease in price in consumer grade VR headsets. Therefore, it is becoming more feasible to equip teams to use this technology both for meetings and also for virtual collaboration to work with datasets and colleagues from anywhere in the world. Popular for virtual tech support, AR lags behind VR in technological maturity for geospatial visualization. Nevertheless, with more compact datasets, such as the LiDAR point cloud, these 3D scenes can be displayed from most modern smartphones, making it both easily accessible and readily available to share interactive files. With the majority of VR and AR development in fields other than geospatial sciences (e.g., gaming, marketing, telepresence), there is a need for improved functionality and the ability of the specialized software to effectively handle the large files produced from technologies such as SfM and LiDAR [73].

Despite their promise, neither VR nor AR can replicate virtual environments with sufficient detail or fidelity to be indistinguishable from the real world. They are not a substitute for fieldwork, nor firsthand in situ field experiences. Rather, they are tools to augment and enhance geospatial visualization, data exploration, and collaboration.

5. Conclusions

It is only a matter of time before peatland ecosystem models (e.g., [74–76]) become adapted for 3D spatially explicit input. Fine-scale microtopographic ecohydrological structures that can be represented from either UAS SfM or LiDAR would provide the resolution needed for models to quantify how peatland structure and function changes over time [67], which can lead to insights into the ecohydrological feedbacks [43]. We show that vegetation structure can be reliably mapped from UAS platforms using either SfM or LiDAR. This is important in sites such as Mer Bleue where the spatial structure of the peatland accounts for 20–40% of the vegetation community distribution [43] and associated ecohydrology. Given the scarcity of UAS LiDAR studies in peatlands (compared to the SfM literature), additional research in peatlands (and other wetlands) is essential. New relatively low-cost LiDAR technologies, such as the DJI's Zenmuse L1 (point rate of 240,000 pts/s, up to 3 returns and manufacturer stated high vertical and horizontal accuracy), could provide new opportunities to expand the use of LiDAR in peatlands and other ecosystems.

Appendix A

Table A1. Summary of equipment and software used in this study.

Category	Model	Purpose
UAS airframe	DJI Matrice 600 Pro	Data acquisition platform
RGB camera	Canon 5D Mark III	SfM photograph acquisition
Camera gimbal	DJI Ronin MX	SfM photograph acquisition
GNSS receiver	Emlid M+	Geotagging SfM photographs
GNSS receiver	Emlid RS+	Check point acquisition
LiDAR	LiAIR S220	LiDAR data acquisition
VR HMD	Oculus Quest 2	VR visualization
AR/VR viewer	iPhone XR, 11 Pro, 12 Pro, Samsung Galaxy 20 FE	Mobile AR visualization
VR viewer	Google Official 87002823-01 Cardboard	VR visualization
VR viewer	I am Cardboard DSCVR	VR visualization
Software	Pix4D	SfM-MVS photogrammetry
Software	RTKLib *	SfM geotag PPK
Software	LiAcquire	LiDAR acquisition
Software	LiNAV	LiDAR postprocessing
Software	LiDAR360	LiDAR postprocessing
Software	CloudCompare Stereo *	Point cloud processing/analysis
Software	MATLAB	Analysis
Software	ProcessOBJ *	Analysis
Software	Potree Converter *	Preprocessing point clouds for web-based visualization
Software	Potree Server *	Mobile and PC 3D visualization
Software	VRifier *	VR visualization
Web-based AR/VR viewer	Sketchfab [1,2]	Mobile AR visualization

[1] There is a free plan for individuals with limitations to file size uploaded. [2] Free for users to view models. Open source and free software are designated with an asterisk (*).

References

1. Leifeld, J.; Menichetti, L. The underappreciated potential of peatlands in global climate change mitigation strategies. *Nat. Commun.* **2018**, *9*, 1071. [CrossRef] [PubMed]
2. Tarnocai, C.; Kettles, I.M.; Lacelle, B. *Peatlands of Canada Database*; Research Branch, Agriculture and Agri-Food: Ottawa, ON, Canada, 2005.
3. Tanneberger, F.; Tegetmeyer, C.; Busse, S.; Barthelmes, A.; Shumka, S.; Moles Mariné, A.; Jenderedjian, K.; Steiner, G.M.; Essl, F.; Etzold, J.; et al. The peatland map of Europe. *Mires Peat* **2017**, *19*, 1–17.
4. Minasny, B.; Berglund, Ö.; Connolly, J.; Hedley, C.; de Vries, F.; Gimona, A.; Kempen, B.; Kidd, D.; Lilja, H.; Malone, B.; et al. Digital mapping of peatlands—A critical review. *Earth Sci. Rev.* **2019**, *196*, 102870. [CrossRef]
5. Poulin, M.F.; Careau, D.; Rochefort, L.; Desrochers, A. From Satellite Imagery to Peatland Vegetation Diversity: How Reliable Are Habitat Maps? *Ecol. Soc.* **2002**, *6*, 16. [CrossRef]
6. Sonnentag, O.; Chen, J.M.; Roberts, D.A.; Talbot, J.; Halligan, K.Q.; Govind, A. Mapping tree and shrub leaf area indices in an ombrotrophic peatland through multiple endmember spectral unmixing. *Remote Sens. Environ.* **2007**, *109*, 342–360. [CrossRef]
7. Kalacska, M.; Arroyo-Mora, J.P.; Soffer, R.J.; Roulet, N.T.; Moore, T.R.; Humphreys, E.; Leblanc, G.; Lucanus, O.; Inamdar, D. Estimating Peatland Water Table Depth and Net Ecosystem Exchange: A Comparison between Satellite and Airborne Imagery. *Remote Sens.* **2018**, *10*, 687. [CrossRef]
8. Kalacska, M.; Lalonde, M.; Moore, T.R. Estimation of foliar chlorophyll and nitrogen content in an ombrotrophic bog from hyperspectral data: Scaling from leaf to image. *Remote Sens. Environ.* **2015**, *169*, 270–279. [CrossRef]
9. Arroyo-Mora, J.P.; Kalacska, M.; Soffer, R.; Ifimov, G.; Leblanc, G.; Schaaf, E.S.; Lucanus, O. Evaluation of phenospectral dynamics with Sentinel-2A using a bottom-up approach in a northern ombrotrophic peatland. *Remote Sens. Environ.* **2018**, *216*, 544–560. [CrossRef]
10. Arroyo-Mora, J.P.; Kalacska, M.; Inamdar, D.; Soffer, R.; Lucanus, O.; Gorman, J.; Naprstek, T.; Schaaf, E.S.; Ifimov, G.; Elmer, K.; et al. Implementation of a UAV–Hyperspectral Pushbroom Imager for Ecological Monitoring. *Drones* **2019**, *3*, 12. [CrossRef]
11. Girard, A.; Schweiger, A.K.; Carteron, A.; Kalacska, M.; Laliberté, E. Foliar Spectra and Traits of Bog Plants across Nitrogen Deposition Gradients. *Remote Sens.* **2020**, *12*, 2448. [CrossRef]
12. Belyea, L.R.; Clymo, R.S. Feedback control of the rate of peat formation. *Proc. R. Soc. Lond. Ser. B: Biol. Sci.* **2001**, *268*, 1315–1321. [CrossRef]

13. Eppinga, M.B.; Rietkerk, M.; Borren, W.; Lapshina, E.D.; Bleuten, W.; Wassen, M.J. Regular Surface Patterning of Peatlands: Confronting Theory with Field Data. *Ecosystems* **2008**, *11*, 520–536. [CrossRef]

14. Nouwakpo, S.K.; Weltz, M.A.; McGwire, K. Assessing the performance of structure-from-motion photogrammetry and terrestrial LiDAR for reconstructing soil surface microtopography of naturally vegetated plots. *Earth Surf. Process. Landf.* **2016**, *41*, 308–322. [CrossRef]

15. Kalacska, M.; Chmura, G.L.; Lucanus, O.; Bérubé, D.; Arroyo-Mora, J.P. Structure from motion will revolutionize analyses of tidal wetland landscapes. *Remote Sens. Environ.* **2017**, *199*, 14–24. [CrossRef]

16. Lovitt, J.; Rahman, M.M.; McDermid, G.J. Assessing the Value of UAV Photogrammetry for Characterizing Terrain in Complex Peatlands. *Remote Sens.* **2017**, *9*, 715. [CrossRef]

17. Dubayah, R.O.; Drake, J.B. Lidar Remote Sensing for Forestry. *J. For.* **2000**, *98*, 44–46. [CrossRef]

18. Ullman, S. The Interpretation of Structure from Motion. *Proc. R. Soc. Lond. Ser. B Biol. Sci.* **1979**, *203*, 405–426. [CrossRef]

19. Westoby, M.J.; Brasington, J.; Glasser, N.F.; Hambrey, M.J.; Reynolds, J.M. 'Structure-from-Motion' photogrammetry: A low-cost, effective tool for geoscience applications. *Geomorphology* **2012**, *179*, 300–314. [CrossRef]

20. Iglhaut, J.; Cabo, C.; Puliti, S.; Piermattei, L.; O'Connor, J.; Rosette, J. Structure from Motion Photogrammetry in Forestry: A Review. *Curr. For. Rep.* **2019**, *5*, 155–168. [CrossRef]

21. Gatis, N.; Luscombe, D.J.; Carless, D.; Parry, L.E.; Fyfe, R.M.; Harrod, T.R.; Brazier, R.E.; Anderson, K. Mapping upland peat depth using airborne radiometric and lidar survey data. *Geoderma* **2019**, *335*, 78–87. [CrossRef]

22. Hopkinson, C.; Chasmer, L.E.; Sass, G.; Creed, I.F.; Sitar, M.; Kalbfleisch, W.; Treitz, P. Vegetation class dependent errors in lidar ground elevation and canopy height estimates in a boreal wetland environment. *Can. J. Remote Sens.* **2014**, *31*, 191–206. [CrossRef]

23. Korpela, I.; Haapanen, R.; Korrensalo, A.; Tuittila, E.-S.; Vesala, T. Fine-resolution mapping of microforms of a boreal bog using aerial images and waveform-recording LiDAR. *Mires Peat* **2020**, *26*, 1–24. [CrossRef]

24. Korpela, I.; Koskinen, M.; Vasander, H.; Holopainen, M.; Minkkinen, K. Airborne small-footprint discrete-return LiDAR data in the assessment of boreal mire surface patterns, vegetation, and habitats. *For. Ecol. Manag.* **2009**, *258*, 1549–1566. [CrossRef]

25. Richardson, M.C.; Mitchell, C.P.J.; Branfireun, B.A.; Kolka, R.K. Analysis of airborne LiDAR surveys to quantify the characteristic morphologies of northern forested wetlands. *J. Geophys. Res.* **2010**, *115*, 115. [CrossRef]

26. Langlois, M.N.; Richardson, M.C.; Price, J.S. Delineation of peatland lagg boundaries from airborne LiDAR. *J. Geophys. Res. Biogeosci.* **2017**, *122*, 2191–2205. [CrossRef]

27. Anderson, K.; Bennie, J.; Wetherelt, A. Laser scanning of fine scale pattern along a hydrological gradient in a peatland ecosystem. *Landsc. Ecol.* **2009**, *25*, 477–492. [CrossRef]

28. Gigante, M.A. 1—Virtual Reality: Definitions, History and Applications. In *Virtual Reality Systems*; Earnshaw, R.A., Gigante, M.A., Jones, H., Eds.; Academic Press: Cambridge, MA, USA, 1993; pp. 3–14.

29. Le Mouélic, S.; Enguehard, P.; Schmitt, H.H.; Caravaca, G.; Seignovert, B.; Mangold, N.; Combe, J.-P.; Civet, F. Investigating Lunar Boulders at the Apollo 17 Landing Site Using Photogrammetry and Virtual Reality. *Remote Sens.* **2020**, *12*, 1900. [CrossRef]

30. Li, L.; Yu, F.; Shi, D.; Shi, J.; Tian, Z.; Yang, J.; Wang, X.; Jiang, Q. Application of virtual reality technology in clinical medicine. *Am. J. Transl. Res.* **2017**, *9*, 3867–3880.

31. Leigh, C.; Heron, G.; Wilson, E.; Gregory, T.; Clifford, S.; Holloway, J.; McBain, M.; Gonzalez, F.; McGree, J.; Brown, R.; et al. Using virtual reality and thermal imagery to improve statistical modelling of vulnerable and protected species. *PLoS ONE* **2019**, *14*, e0217809. [CrossRef]

32. Ching-Rong, L.; Loffin, R.B.; Stark, T. Virtual reality for geosciences visualization. In Proceedings of the 3rd Asia Pacific Computer Human Interaction (Cat. No.98EX110), Shoan Village Center, Kangawa, Japan, 15–17 July 1998; pp. 196–201.

33. Billen, M.I.; Kreylos, O.; Hamann, B.; Jadamec, M.A.; Kellogg, L.H.; Staadt, O.; Sumner, D.Y. A geoscience perspective on immersive 3D gridded data visualization. *Comput. Geosci.* **2008**, *34*, 1056–1072. [CrossRef]

34. Berger, H.; Dittenbach, M.; Merkl, D.; Bogdanovych, A.; Simoff, S.; Sierra, C. Opening new dimensions for e-Tourism. *Virtual Real.* **2006**, *11*, 75–87. [CrossRef]

35. Bruno, F.; Barbieri, L.; Lagudi, A.; Cozza, M.; Cozza, A.; Peluso, R.; Muzzupappa, M. Virtual dives into the underwater archaeological treasures of South Italy. *Virtual Real.* **2017**, *22*, 91–102. [CrossRef]

36. Chang, Y.-L.; Tien, C.-L. Development of mobile augmented-reality and virtual-reality simulated training systems for marine ecology education. In Proceedings of the 24th International Conference on 3D Web Technology, Los Angeles, CA, USA, 26–28 July 2019; pp. 1–3.

37. Huang, J.; Lucash, M.S.; Scheller, R.M.; Klippel, A. Walking through the forests of the future: Using data-driven virtual reality to visualize forests under climate change. *Int. J. Geogr. Inf. Sci.* **2020**, *10*, 1–24. [CrossRef]

38. Liberatore, M.J.; Wagner, W.P. Virtual, mixed, and augmented reality: A systematic review for immersive systems research. *Virtual Real.* **2021**. [CrossRef]

39. Scavarelli, A.; Arya, A.; Teather, R.J. Virtual reality and augmented reality in social learning spaces: A literature review. *Virtual Real.* **2020**, *25*, 257–277. [CrossRef]

40. Lafleur, P.M.; Hember, R.A.; Admiral, S.W.; Roulet, N.T. Annual and seasonal variability in evapotranspiration and water table at a shrub-covered bog in southern Ontario, Canada. *Hydrol. Process.* **2005**, *19*, 3533–3550. [CrossRef]

41. Bubier, J.L.; Moore, T.R.; Crosby, G. Fine-scale vegetation distribution in a cool temperate peatland. *Can. J. Bot.* **2006**, *84*, 910–923. [CrossRef]

42. Lafleur, P.M.; Roulet, N.T.; Bubier, J.L.; Frolking, S.; Moore, T.R. Interannual variability in the peatland-atmosphere carbon dioxide exchange at an ombrotrophic bog. *Glob. Biogeochem. Cycles* **2003**, *17*, 13. [CrossRef]
43. Malhotra, A.; Roulet, N.T.; Wilson, P.; Giroux-Bougard, X.; Harris, L.I. Ecohydrological feedbacks in peatlands: An empirical test of the relationship among vegetation, microtopography and water table. *Ecohydrology* **2016**, *9*, 1346–1357. [CrossRef]
44. Hassel, K.; Kyrkjeeide, M.O.; Yousefi, N.; Prestø, T.; Stenøien, H.K.; Shaw, J.A.; Flatberg, K.I. Sphagnum divinum (sp. nov.) and S. medium Limpr. and their relationship to S. magellanicum Brid. *J. Bryol.* **2018**, *40*, 197–222. [CrossRef]
45. Moore, T.R.; Bubier, J.L.; Frolking, S.E.; Lafleur, P.M.; Roulet, N.T. Plant biomass and production and CO$_2$ exchange in an ombrotrophic bog. *J. Ecol.* **2002**, *90*, 25–36. [CrossRef]
46. Arroyo-Mora, J.; Kalacska, M.; Soffer, R.; Moore, T.; Roulet, N.; Juutinen, S.; Ifimov, G.; Leblanc, G.; Inamdar, D. Airborne Hyperspectral Evaluation of Maximum Gross Photosynthesis, Gravimetric Water Content, and CO$_2$ Uptake Efficiency of the Mer Bleue Ombrotrophic Peatland. *Remote Sens.* **2018**, *10*, 565. [CrossRef]
47. DJI. *D-RTK User Manual*; DJI: Schenzen, China, 2017.
48. Lucanus, O.; Kalacska, M. UAV DSLR Photogrammetry with PPK Processing. Available online: https://www.protocols.io/view/uav-dslr-photogrammetry-with-ppk-processing-bjm2kk8e (accessed on 30 March 2020).
49. Natural Resources Canada. Station Report. Available online: https://webapp.geod.nrcan.gc.ca/geod/data-donnees/station/report-rapport.php?id=943020 (accessed on 1 March 2021).
50. Takasu, T.; Yasuda, A. Development of the low-cost RTK-GPS receiver with an open source program package RTKLIB. In Proceedings of the International Symposium on GPS/GNSS, Jeju, Korea, 11 April 2009; pp. 4–6.
51. Pix4D. Initial Processing > Calibration. Available online: https://support.pix4d.com/hc/en-us/articles/205327965-Menu-Process-Processing-Options-1-Initial-Processing-Calibration (accessed on 1 March 2021).
52. Strecha, C.; Kung, O.; Fua, P. Automatic mapping from ultra-light UAV imagery. In Proceedings of the 2012 European Calibration and Orientation Workshop, Barcelona, Spain, 8–10 February 2012; pp. 1–4.
53. Strecha, C.; Bronstein, A.; Bronstein, M.M.; Fua, P. LDAHash: Improved Matching with Smaller Descriptors. *IEEE Trans. Pattern Anal. Mach. Intell.* **2012**, *34*, 66–78. [CrossRef]
54. Strecha, C.; von Hansen, W.; Van Gool, L.; Fua, P.; Thoennessen, U. On Benchmarking camera calibration and multi-view stereo for high resolution imagery. In Proceedings of the IEEE Conference on Computer Vision and Pattern Recognition, Anchorage, AK, USA, 23–28 June 2008.
55. Kalacska, M.; Lucanus, O.; Arroyo-Mora, J.P.; Laliberté, É.; Elmer, K.; Leblanc, G.; Groves, A. Accuracy of 3D Landscape Reconstruction without Ground Control Points Using Different UAS Platforms. *Drones* **2020**, *4*, 13. [CrossRef]
56. GreenValley Interantional. LiAir 220 UAV 3D Mapping System. Available online: https://www.greenvalleyintl.com/wp-content/uploads/2019/09/LiAir220.pdf (accessed on 1 March 2021).
57. Hesai. Pandar40P 40-Channel Mechanical LiDAR. Available online: https://www.hesaitech.com/en/Pandar40P (accessed on 10 March 2021).
58. Hesai. *Pandar40P 40-Channel Mechanical LiDAR User Manual*; Hesai: Shanghai, China; p. 74.
59. Inamdar, D.; Kalacska, M.; Arroyo-Mora, J.; Leblanc, G. The Directly-Georeferenced Hyperspectral Point Cloud (DHPC): Preserving the Integrity of Hyperspectral Imaging Data. *Front. Remote Sens. Data Fusion Assim.* **2021**, *2*, 675323. [CrossRef]
60. Backes, A.R.; Eler, D.M.; Minghim, R.; Bruno, O.M. Characterizing 3D shapes using fractal dimension. In *Progress in Pattern Recognition, Image Analysis, Computer Vision, and Applications SE-7*; Bloch, I., Cesar, R., Jr., Eds.; Springer: Berlin/Heidelberg, Germany, 2012; pp. 14–21.
61. Reichert, J.; Backes, A.R.; Schubert, P.; Wilke, T.; Mahon, A. The power of 3D fractal dimensions for comparative shape and structural complexity analyses of irregularly shaped organisms. *Methods Ecol. Evol.* **2017**, *8*, 1650–1658. [CrossRef]
62. Halley, J.M.; Hartley, S.; Kallimanis, A.S.; Kunin, W.E.; Lennon, J.J.; Sgardelis, S.P. Uses and abuses of fractal methodology in ecology. *Ecol. Lett.* **2004**, *7*, 254–271. [CrossRef]
63. Schuetz, M. *Potree: Rendering Large Point Clouds in Web Browsers*; Vienna University of Technology: Vienna, Austria, 2016.
64. LaRocque, A.; Phiri, C.; Leblon, B.; Pirotti, F.; Connor, K.; Hanson, A. Wetland Mapping with Landsat 8 OLI, Sentinel-1, ALOS-1 PALSAR, and LiDAR Data in Southern New Brunswick, Canada. *Remote Sens.* **2020**, *12*, 2095. [CrossRef]
65. Davenport, I.J.; McNicol, I.; Mitchard, E.T.A.; Dargie, G.; Suspense, I.; Milongo, B.; Bocko, Y.E.; Hawthorne, D.; Lawson, I.; Baird, A.J.; et al. First Evidence of Peat Domes in the Congo Basin using LiDAR from a Fixed-Wing Drone. *Remote Sens.* **2020**, *12*, 2196. [CrossRef]
66. Garroway, K.; Hopkinson, C.; Jamieson, R. Surface moisture and vegetation influences on lidar intensity data in an agricultural watershed. *Can. J. Remote Sens.* **2014**, *37*, 275–284. [CrossRef]
67. Luscombe, D.J.; Anderson, K.; Gatis, N.; Wetherelt, A.; Grand-Clement, E.; Brazier, R.E. What does airborne LiDAR really measure in upland ecosystems? *Ecohydrology* **2015**, *8*, 584–594. [CrossRef]
68. Chasmer, L.E.; Hopkinson, C.D.; Petrone, R.M.; Sitar, M. Using Multitemporal and Multispectral Airborne Lidar to Assess Depth of Peat Loss and Correspondence With a New Active Normalized Burn Ratio for Wildfires. *Geophys. Res. Lett.* **2017**, *44*, 11851–11859. [CrossRef]
69. Klippel, A.; Zhao, J.; Oprean, D.; Wallgrün, J.O.; Stubbs, C.; La Femina, P.; Jackson, K.L. The value of being there: Toward a science of immersive virtual field trips. *Virtual Real.* **2019**, *24*, 753–770. [CrossRef]

70. Cerfontaine, P.A.; Mreyen, A.-S.; Havenith, H.-B. Immersive visualization of geophysical data. In Proceedings of the 2016 International Conference on 3D Imaging, Liege, Belgium, 13–14 December 2008.
71. Karanth, S.; Murthy S., R. Augmented Reality in Visual Learning. In *ICT Analysis and Applications*; Springer: Singapore, 2021; pp. 223–233.
72. Raiyn, J. The Role of Visual Learning in Improving Students' High-Order Thinking Skills. *J. Educ. Pract.* **2016**, *7*, 115–121.
73. Nesbit, P.R.; Boulding, A.; Hugenholtz, C.; Durkin, P.; Hubbard, S. Visualization and Sharing of 3D Digital Outcrop Models to Promote Open Science. *GSA Today* **2020**, *30*, 4–10. [CrossRef]
74. Frolking, S.; Talbot, J.; Jones, M.C.; Treat, C.C.; Kauffman, J.B.; Tuittila, E.-S.; Roulet, N. Peatlands in the Earth's 21st century climate system. *Environ. Rev.* **2011**, *19*, 371–396. [CrossRef]
75. Wu, J.; Roulet, N.T.; Moore, T.R.; Lafleur, P.; Humphreys, E. Dealing with microtopography of an ombrotrophic bog for simulating ecosystem-level CO2 exchanges. *Ecol. Model.* **2011**, *222*, 1038–1047. [CrossRef]
76. Gong, J.; Roulet, N.; Frolking, S.; Peltola, H.; Laine, A.M.; Kokkonen, N.; Tuittila, E.-S. Modelling the habitat preference of two key *Sphagnum* species in a poor fen as controlled by capitulum water content. *Biogeosciences* **2020**, *17*, 5693–5719. [CrossRef]

Application of Drone Technologies in Surface Water Resources Monitoring and Assessment: A Systematic Review of Progress, Challenges, and Opportunities in the Global South

Mbulisi Sibanda [1,*], Onisimo Mutanga [2], Vimbayi G. P. Chimonyo [3,4], Alistair D. Clulow [5], Cletah Shoko [6], Dominic Mazvimavi [7], Timothy Dube [7] and Tafadzwanashe Mabhaudhi [3]

1   Department of Geography, Environmental Studies and Tourism, University of the Western Cape, Private Bag X17, Bellville 7535, South Africa

2   Discipline of Geography and Environmental Science, School of Agricultural Earth and Environmental Sciences, University of KwaZulu-Natal, Private Bag X01, Scottsville, Pietermaritzburg 3209, South Africa; mutangao@ukzn.ac.za

3   Centre for Transformative Agricultural and Food Systems, School of Agricultural, Earth & Environmental Sciences, University of KwaZulu-Natal, P/Bag X01, Pietermaritzburg 3209, South Africa; v.chimonyo@cgiar.org (V.G.P.C.); mabhaudhi@ukzn.ac.za (T.M.)

4   International Maize and Wheat Improvement Center (CIMMYT)-Zimbabwe, Mt Pleasant, Harare P.O. Box MP 163, Zimbabwe

5   Discipline of Agrometeorology, School of Agricultural, Earth and Environmental Sciences, University of KwaZulu-Natal, Private Bag X01, Scottsville, Pietermaritzburg 3209, South Africa; clulowa@ukzn.ac.za

6   Division of Geography, School of Geography, Archaeology and Environmental Studies, University of the Witwatersrand, 1 Jan Smuts Avenue, Braamfontein, Johannesburg 2000, South Africa; cletah.shoko@wits.ac.za

7   Institute of Water Studies, Department of Earth Sciences, University of the Western Cape, Private Bag X17, Bellville 7535, South Africa; dmazvimavi@uwc.ac.za (D.M.); tidube@uwc.ac.za (T.D.)

*   Correspondence: msibanda@uwc.ac.za; Tel.: +27-(21)-959-2668

Abstract: Accurate and timely information on surface water quality and quantity is critical for various applications, including irrigation agriculture. In-field water quality and quantity data from unmanned aerial vehicle systems (UAVs) could be useful in closing spatial data gaps through the generation of near-real-time, fine resolution, spatially explicit information required for water resources accounting. This study assessed the progress, opportunities, and challenges in mapping and modelling water quality and quantity using data from UAVs. To achieve this research objective, a systematic review was adopted. The results show modest progress in the utility of UAVs, especially in the global south. This could be attributed, in part, to high costs, a lack of relevant skills, and the regulations associated with drone procurement and operational costs. The progress is further compounded by a general lack of research focusing on UAV application in water resources monitoring and assessment. More importantly, the lack of robust and reliable water quantity and quality data needed to parameterise models remains challenging. However, there are opportunities to advance scientific inquiry for water quality and quantity accounting by integrating UAV data and machine learning.

Keywords: drones; green water; integrated water management strategies; remote sensing; small-holder farms; water productivity

1. Introduction

Freshwater accounts for only 2.5% of the total amount of water on the earth's surface, and about 1.5% of that amount is accessible for biophysical processes [1]. Meanwhile, freshwater is a fundamental input in agricultural production, numerous manufacturing industries, and a basic need for domestic uses. Specifically, agriculture accounts globally for

about 70% of the total freshwater usage, mostly through irrigation [2,3]. Intense competition for water between different sectors will increase with an increase in the world population increase from the current 7.8 billion to about 9.7 billion by 2050. Consequently, global agricultural production is expected to increase by 60 to 70% [4], which will substantially increase water demand.

In the global south, particularly Southern Africa, water resources are unevenly distributed, and this is compounded by climate variability (i.e., an unpredictable seasonality of precipitation). The quality and quantity of available water affect all water users, including crop irrigation. Based on the recent findings presented by Bronkhorst et al [5], irrigation agriculture contributes to 25–30% of South Africa's agricultural production, and is responsible for up to 90% of high-value crops production and 25 to 49% of industrial crop production; however, it uses 60% of freshwater resources [5,6]. Meanwhile, urban and rural water use (including domestic use) consume 30% of available water resources. In this regard, there is an urgent need to identify accurate and efficient methods for assessing the quality and quantity of available surface water resources. The quantity and quality of available water resources are conventionally determined from in situ measurements, which in some cases can be time-consuming and costly [7]. In situ measurements do not always provide adequate spatial representativeness, and information may not be readily available to users such as farmers. In situ measurements may not always provide information about the temporal variability of available water, which is necessary for managing crop irrigation [7].

Earth observation and geospatial technologies have been widely proven to provide synoptic, timely, and spatially explicit data of various aspects of the earth's surface, including the spatio–temporal variability of both the quality and quantity of available water [7]. The literature shows that clean water generally absorbs electromagnetic energy mostly from the visible section (green) to the longer wavelengths in the infrared sections [8,9]. Subsequently, water has been detected and discriminated from other landcover types in this regard. Furthermore, this attribute of clean water has facilitated the determination of water quantity (surface volumes, spatial extent) and quality of surface water resources based on earth observation data and geospatial approaches. Earth observation facilities have been proven useful in accurately and efficiently characterising various attributes of surface water resources. These include the moderate-resolution imaging spectroradiometer (MODIS) [10], Landsat [11], SPOT [12], and Worldview [13], Medium Resolution Imaging Spectrometer (MERIS) [14], to mention a few. Work by Gholizadeh et al. [7] comprehensively details parameters that have been widely used to estimate water quality using remote sensing techniques. However, Gholizadeh et al. [7] extensively illustrate the application of remote sensing techniques at regional and landscape scales. Additionally, freely available satellite-borne earth observation facilities such as the Landsat and Sentinel 2 multispectral instrument remain inapplicable for local to farm-scale water resources monitoring and management.

Unmanned aerial vehicle systems (UAVs), also known as drones, have emerged as a potential alternative for mapping and monitoring the quality and quantity of water resources at local scales. This is because drones are flexible, relatively cheaper in comparison to in situ measurements and spaceborne remote sensing, and can be flown at low altitudes, offering very high spatial resolution data, with high prospects of timely and accurately characterising water quality and quantity for smallholder irrigation farms (Xiang et al., 2019). Dissimilar to satellite and other air-borne sensors, UAVs could be used in monitoring hazards (i.e., after landslides, floods, fires) [15] because they generate near-real-time, fine resolution, spatially explicit information. Despite the usefulness of UAVs, their application in agriculture, rural development, and, more importantly, water resources management, remains limited. Although some studies have sought to assess the literature on the utility of drones for a water resources assessment [7,16,17], the studies do not provide a systematic review that focuses on characterising water quality and quantity in the context of smallholder farming in the global south. To the best of our knowledge, the aforementioned studies did

not conduct any bibliometric analysis to evaluate progress, gaps, and challenges faced by the global south in utilising drone technologies for mapping and monitoring the quality and quantity of surface water bodies. In this regard, this paper seeks to review and offer an in-depth systematic assessment of literature on progress, challenges, and opportunities in the utilisation of UAVs in mapping and monitoring surface water resources for improving crop water production in smallholder farms in the global south.

2. Materials and Methods

This study sought to conduct a systematic literature review on assessing the quality and quantity of water using UAVs. The review was structured into two sections. The first section sought to establish the progress attained using drone technologies to map and monitor open water bodies and identify existing gaps. The second section then outlined the challenges and opportunities for applying drone technologies in mapping and monitoring open water bodies for improving crop water production. To address these sections, the literature search and analysis were conducted in three phases

2.1. Phase 1: Literature Search

The initial step of the literature search was to identify keywords, terms, and phrases used in the actual search strings. The review's objective was copied and pasted into Google Scholar, and the top three articles—Gholizadeh et al. [7], Lally et al. [16], and Cancela et al. [18]—were downloaded and reviewed for keywords, terms, and phrases. We identified the following keywords and their variants: "unmanned aerial vehicle(s)", "drone(s)", "Remote sensing", "GIS", "crop water use" "irrigation", "water productivity", "water use efficiency", "water bodies", "dam(s)", "reservoir(s)" OR "river(s)", water quality", "water quantity", and "water volume". The query strings used across the databases are presented in Table 1. The searches were restricted to titles, abstracts, and keywords.

Table 1. Key search words used in this study.

Search Platform	Search Criterion	Total Number of Articles	Number of Articles Retained
SCOPUS	(TITLE-ABS-KEY (("unmanned aerial vehicle" OR "drone*" OR "Remote sensing*" OR "GIS") AND ("crop water use" OR "irrigate*" OR "water productivity" OR "water use efficiency") AND ("water bodies*" OR "dam*" OR "reservoir*" OR "River*") AND ("water quality" or "water quantity" or volume or "water volume" or "water reflectance"))) and not (TITLE-ABS-KEY("groundwater" or "groundwater")) AND (LIMIT-TO (DOCTYPE,"ar"))	136	70
Web of Science	TS= (("unmanned aerial vehicle" OR "drone*" OR "Remote sensing*" OR "GIS") AND ("crop water use" OR "irrigate*" OR "water productivity" OR "water use efficiency") AND ("water bodies*" OR "dam*" OR "reservoir*" OR "River*") AND ("water quality" or "water quantity" or volume or "water volume" or "water reflectance")) NOT ("groundwater" or "ground water"))	108	52
Science Direct	(("unmanned aerial vehicle" OR "drone" OR "Remote sensing" OR "GIS") AND ("irrigation canal" OR "Dams) AND ("water quality" OR volume or "water reflectance") NOT ("groundwater"))	73	32
Google Scholar	(("unmanned aerial vehicle" OR "drone" OR "Remote sensing" OR "GIS") AND ("irrigation canal" OR "Dams) AND ("water quality" OR volume or "water reflectance")	63	60
Articles considered before screening after removing duplicates			214
Articles on UAV applications in water			56

SCOPUS, Web of Science, and Science Direct were utilised to establish literature based on specified keywords. The literature search was framed based on the PRISMA statement (Table 1). Since the current work was adding to what has already been established, the literature search was not restricted to the above databases. We used Google Scholar to identify and include articles that SCOPUS, Web of Science, and Science Direct had not indexed. The search covered the period from 1980 to January 2021.

Initially, the literature searches from SCOPUS, Web of Science, and Science Direct retrieved 136, 108, and 73 articles, respectively (Table 1, Figure 1). All retrieved literature were compiled in EndNote in preparation for screening. Specifically, the bibliographic information of the articles was used at this stage. The first screening procedure was the removal of duplicates considering that the key search terms were similar. In the second step, literature that were not written in English were excluded from the analysis. The following step involved examining whether each article was based on detecting and/or predicting surface water quantity or quality. Full-length articles of the selected abstracts were then sought and downloaded. Subsequently, 214 articles were retained after the screening procedure (Figure 1). A Microsoft Excel spreadsheet was then created to capture the details of each study. The spreadsheet was then reduced to consider only the studies that had specifically utilised drones in mapping and modelling the quality and quantity of surface water bodies. Fifty-six articles were considered on the drones' database (Table 1). The developed database was later used for quantitative assessment of the captured information.
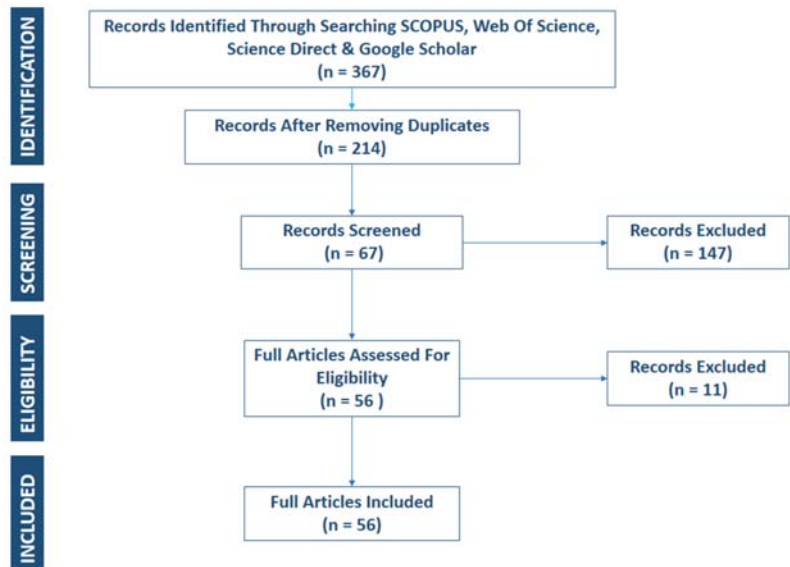
Figure 1. Selection of the studies considered in this review.

2.2. Phase 2: Data Extraction

The database created from the previous phase was used to identify and comprehensively outline the existing progress, gaps, challenges, and opportunities in using drone technologies to map and model the quality and quantity of surface water bodies. To address these objectives of the study, the second phase extracted data from the identified articles. Specifically, information on the year the study was conducted, the study site, type of the surface water body, water quality parameter, sensor, vegetation indices, prediction or classification algorithms, and optimal spectral variables derived were captured. The categorical variables were then converted into numerical variables in preparation for data analysis. Meanwhile, key bibliometric information was also extracted during this phase.

The bibliometric data extracted included author names, country, year of publication, the title of the article, name of the journal, and abstract. A few studies and grey literature that were not captured by the review were included at this phase. Subsequently, this phase was also regarded as evaluating the systematic review's relevance and quality assessment stage.

2.3. Phase 3: Data Analysis

Identified literature and extracted data were subjected to quantitative and qualitative analysis. For the quantitative analysis, basic statistical frequencies were conducted. Furthermore, exploratory trend analysis was conducted in assessing progress on the utility and applicability of satellite and drone-based sensors in mapping and modelling the quality and quantity of surface water bodies. Bibliometric analysis was also conducted to reveal trends of key terms in monitoring surface water bodies. Bibliometric analysis is a quantitative method used to assess published articles and has become helpful in evaluating peer-reviewed studies in a specific field of research [19,20]. The evolutionary trends were inferred by statistically assessing the occurrence and co-occurrence of key terms used to map and monitor surface water bodies using VOSviewer software [21]. The titles and abstracts of articles in the final database (with 214 articles in Table 1), as well as the database of articles that specifically used drones, derived datasets (with 56 articles in Table 1) were used in the VOSviewer to investigate how concepts and topics have evolved in mapping and monitoring the quality and quantity of surface water bodies. Considering that only the occurrence, co-occurrence of key terms, and frequency distributions were computed, bias assessment was not conducted. Meanwhile, the Preferred Reporting Items for Systematic Reviews and Meta-Analyses checklist (http://www.prisma-statement.org/, accessed on 19 July 2021) was used as a guideline to avoid biased reporting [22,23]. The peer review system of the *Drones* MPDI Journal was also used in evaluating findings presented in this study.

The review was then presented in two sections to address the research objectives. The first section explored the progress attained, hitherto, in mapping and modelling the quality and quantity of surface water bodies using remotely sensed data. This section presented and detailed literature trends quantitatively evaluating the quality and quantity of surface water bodies. Specifically, water quality and quantity parameters, earth observation sensors (cameras), sensor platforms, algorithms, and optimal spectral variables that were used to date were showcased throughout this phase. The final phase then outlined and discussed the challenges, gaps, and opportunities existing in the context of knowledge creation in mapping and modelling the quality and quantity of surface water bodies using drone-derived remotely sensed data.

3. Results

3.1. Searched Literature Characteristics

In evaluating the evolution and topical concepts of mapping and monitoring the quality and quantity of open water bodies, results showed that the utilisation of drone-based "remote sensing" "application" "case studies" trending mostly in "small reservoirs" of "China" around 2017 (Figure 2). The period from 2018 to 2020 represents an intensification in terms of the imagery analysis in the evaluation of water quality. This period was marked by the application of hyperspectral drone cameras in mapping water quality (Figure 2). Meanwhile, Figure 3 illustrates three topical clusters, green, blue, and red, in monitoring water. The key terms from the blue cluster were "UAV', 'remote sensing', ('image'), 'application,' 'mapping', 'chlorophyll', 'concentration', 'low cost', and 'measurement', which directly imply the utility of UAVs as a low-cost remote sensing system associated with mapping chlorophyll concentrations (Figure 3). The second-largest cluster linked to UAVs was in red and had 'reservoir', 'lake', 'dam', 'basin', 'area', 'volume', 'area', 'data', and Landsat. This articulates the major water quantity parameters, i.e., volume area, that were widely characterised using Landsat data and 'GIS 'techniques. The third cluster in green had 'water quality', 'water', 'model', 'river', 'turbidity', and 'irrigation' as the key terms in

order of importance (Figure 3). This cluster presented the linkages between chlorophyll
and turbidity concentrations which were previously modelled using satellite-borne data
mainly in the context of evaluating the quality of crop irrigation water.
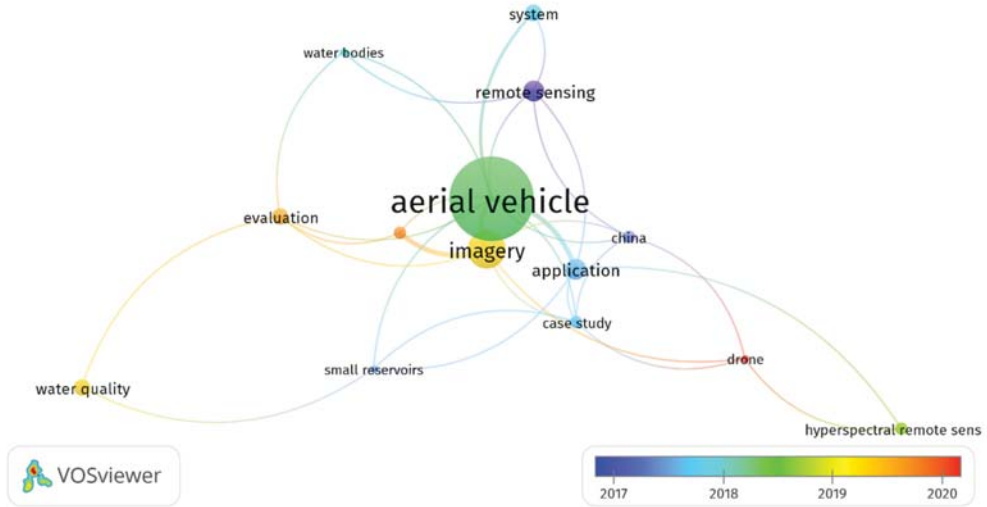
Figure 2. Direction and revolution of topical concepts in mapping and monitoring the quality and quantity of open water
bodies' derived using data from abstracts and titles.
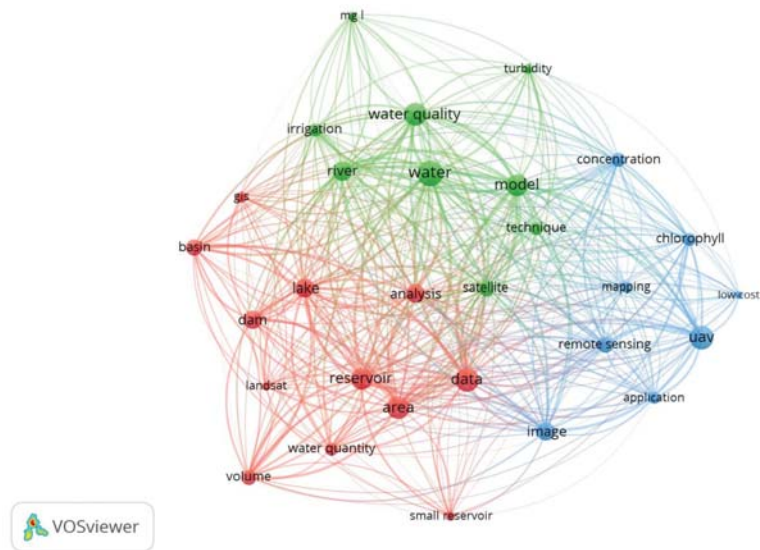
Figure 3. Topical concepts in mapping and monitoring the quality and quantity of open water bodies'
derived using data from abstracts and titles.

3.2. Progress in Modelling Water Quality and Quantity

Generally, progress is noted in detecting, mapping, and monitoring surface water
resources, using remotely sensed data (Figure 3). As in Gholizadeh, Melesse and Reddi [7],
the results of this study illustrated that most of the studies that utilised earth observation
data sought to characterise water quality more than water quantity (Figure 3). The widely

researched water quality parameters included conductivity [24,25], pH [25,26], Cl⁻ [24], dissolved oxygen [27], total suspended solids (TSS) [28,29], chlorophyll [30–33], turbidity [34–36], K^+, ammonium nitrogen (NH₄-N), sodium (Na⁺), BOD, magnesium (Mg), total phosphorous, orthophosphate (PO₄–P), temperature and total nitrogen, iron (Fe), COD, zinc (Zn), calcium (Ca), manganese (Mn), salinity, copper (Cu), bicarbonate HCO^{3-}, sodium-absorbed ratio (SAR), coliform, cadmium (Cd), chromium (Cr), Ca^{2+}, HCO^{3-}, and total hardness in order of frequency, as illustrated in Figure 4b. These parameters were mostly characterised using satellite remotely sensed data.
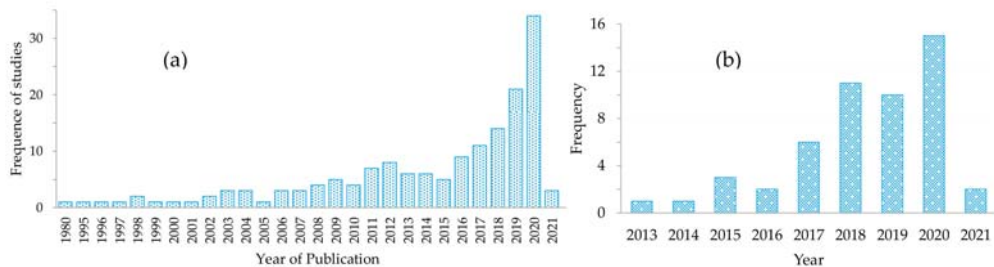
Figure 4. Frequency of studies that mapped surface water resources per year based on (**a**) both satellite and drone-borne sensors. (**b**) Drone-borne sensors.

The use of satellite remotely sensed data in mapping and modelling water quality and quantity has of late received extensive attention. This is illustrated by the steady increase in the number of studies that applied remote sensing techniques in mapping and monitoring water quality and quantity (Figure 4a). Meanwhile, a significant number of studies ventured into the utility of drones (Figure 4b). This study showed that works that utilised UAVs in mapping and monitoring water quality and quantity appeared around 2013 (Figure 4b). The studies that evaluated the utility of drone-derived data for mapping the quantity of water were significantly less than those that sought to assess the quality of water. Specifically, only fourteen studies assessed the level of water, whereas thirty-seven studies assessed water quality parameters based on drone remotely sensed data. However, the majority of the aforementioned studies were conducted based on drone remotely sensed data, principally mapped and monitored chlorophyll content [30,32,33,37,38] and turbidity in lakes, ponds, and dams (Figure 5b) [34–36].

The quality of irrigation water that is generally considered acceptable should be colourless, odourless, foamless with minimum turbidity, TDS below 1000 mg L^{-1} at circumneutral pH, and a specific conductance below 1.5 mmhos/m [39–41]. COD, ZSD, TP, conductivity, pH, TSS, DO, and turbidity are critical attributes of water that need to be frequently monitored if high-quality crops and full potential harvests are to be attained.

For irrigation water, COD is a critical attribute that needs to be frequently monitored. COD and biochemical oxygen demand (BOD) are appropriate indicators for organic matter concentrations in irrigation water. When COD and BOD are high in irrigation water, much of the oxygen in the water will be consumed during the decomposition of organic matters resulting in an anaerobic condition [42]. In this process, soil oxides such as Fe^{3+}, Mn^{5+} and SO_4^{2-} will exhaust oxygen to reduce the oxidation–reduction potential. Subsequently, the generated iron, manganese, sulphides, and organic acids may limit crop uptake and the absorption of nutrients. This frequently results in stunted growth, poor quality, and reduced harvests.
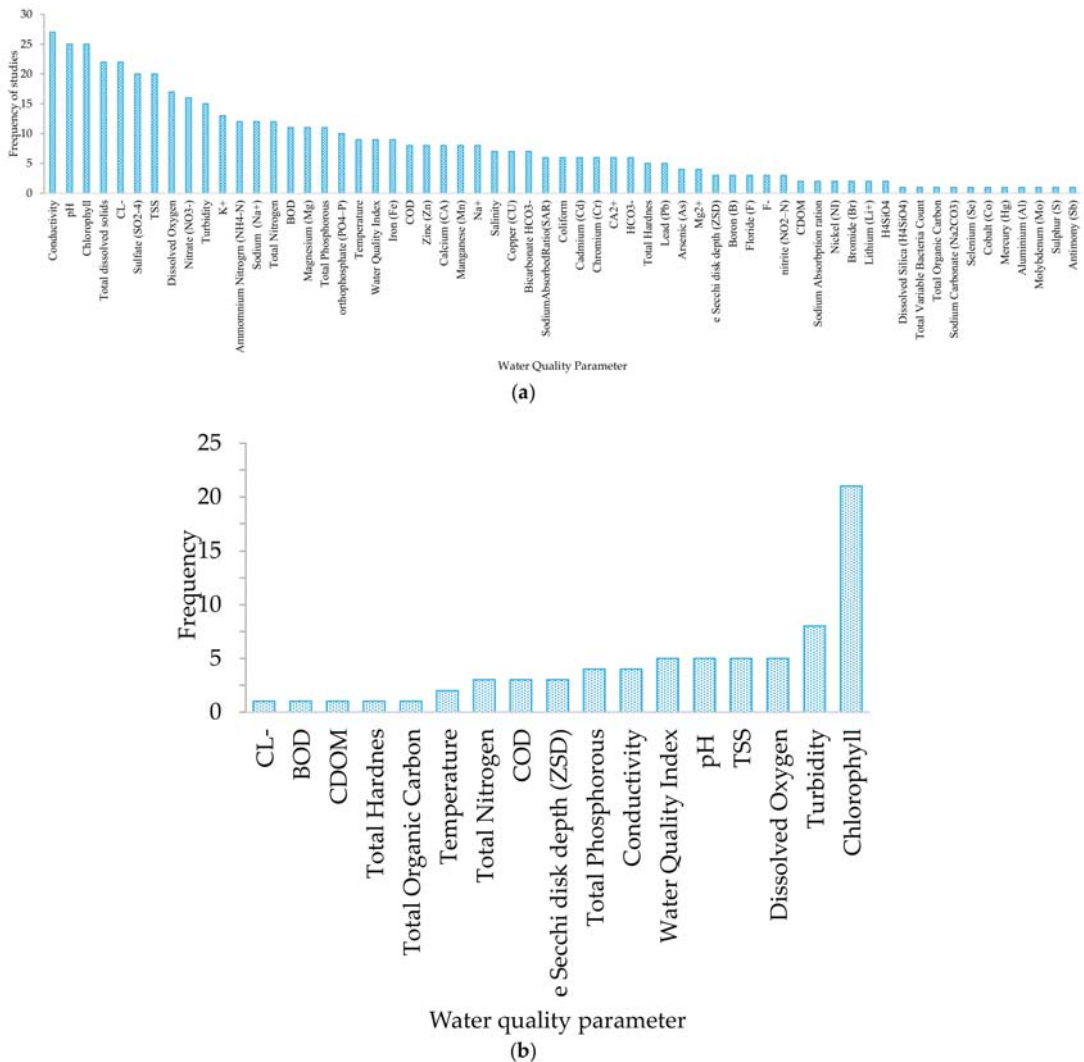
Figure 5. Frequency of studies that considered a specific water quality parameter based on (**a**) all satellite and drone-borne sensors. (**b**) Drone-borne sensors only.

ZDS is an indicator of turbidity and the total number of suspended particles in irrigation water [39]. A high concentration of suspended particles tends to result in an altered colour of the water and lower ZDS measurements. Higher concentrations of suspended sediments result in the clogging of irrigation equipment such as sprinklers. Therefore, high turbidity or TSS impedes irrigation by drippers and sprinklers [43].

In terms of the spatial distribution, the majority of studies that have hitherto ventured into the utility of drones in mapping water quality parameters such as chlorophyll, turbidity, DO, TSS, and pH were mostly conducted in China, the USA, Latin America, Europe, and Australia (Figure 6). This could be attributed to the fact that the earliest drone technologies began in Europe, the USA, and China between 1849 and 1916. Since then, the technology has been spreading. However, very few studies have been conducted in the global south,

especially in Africa. Subsequently, there is a need to consider and prioritise water quality parameters such as chlorophyll, turbidity, DO, TSS, and pH when devising irrigation water quality assessment techniques, especially in the global south.
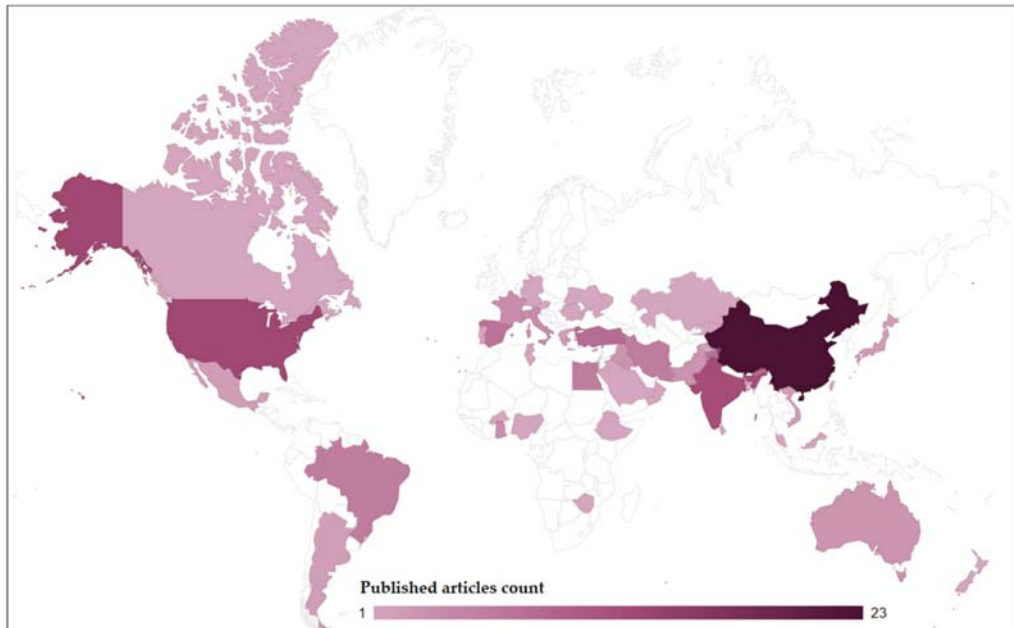
Figure 6. Spatial distribution of UAV-based remote sensing studies in the context of open water bodies.

3.3. Types of Sensor Platforms

Some of the most widely used satellite platforms are the Landsat, Shuttle Radar topographic mission, MODIS, SPOT, and Sentinel 2 MSI (Figure 4b). Studies involving mapping and monitoring the quality and quantity of surface water bodies based on satellite-borne remotely sensed data have drastically increased. This could be attributed to the significant increase in earth observation technologies. However, no studies were conducted using both satellite and drone data simultaneously (Figure 3). As illustrated in the characterisation of literature, t-studies based on UAVs remotely sensed data only picked up in 2013 (Figures 2 and 6). The increase in the research effort and attention towards the utility of UAVs in relation to satellite-borne data could be explained by that they offer near-real-time, fine resolution, and remotely sensed data suitable for high-throughput quantification of water quantity and quality at user-defined revisit frequencies.

Satellite platforms of freely available datasets such as Sentinel 2 and Landsat tend to be limited by cloud cover and relatively coarser spatial and temporal resolutions, which are difficult to implement at farm scales. The findings of this study also illustrated that 77% of the studies in mapping surface water resources using drones were conducted based on the multi-copter platform systems, and 23% were based on fixed-wing platforms (Table 1). Interestingly, innovative octocopters and hovercrafts have also been harnessed for this particular purpose [25,44]. The dominance of the multi-copter platforms in water resources mapping could be because they are relatively cheaper than fixed-wing platforms [45,46]. Specifically, in their comparative study, Brito et al. (2019) noted that the superiority of the multirotor platforms was established better in the context of two-dimensional mapping surfaces, as is the case with mapping agricultural fields and surface water resources. Above all, the multi-copter platforms were associated with a capability for vertical take-off and

landing (VTOL). Most of the DJI multi-copters can VTOL [46]. This makes it easy to utilise multi-copter drones in any environment. However, batteries are their major setback [46]. The weight of multi-copter drone batteries and their capacity limits their flight duration significantly. Specifically, 35% of the studies noted in this study utilised the DJI multi-copter series from the Chinese company, Shenzhen DJI Sciences and Technologies Ltd (Figure 7). This was the most widely used platform based on the findings of this study. Generally, the DJI Matrice and the Phantom series were the dominant DJI platforms noted in our study. This could be attributed to the fact that the DJI Matrice platforms seem to be compatible platforms that can be integrated with many types of sensors, as illustrated in Table 2, when compared to other platforms.
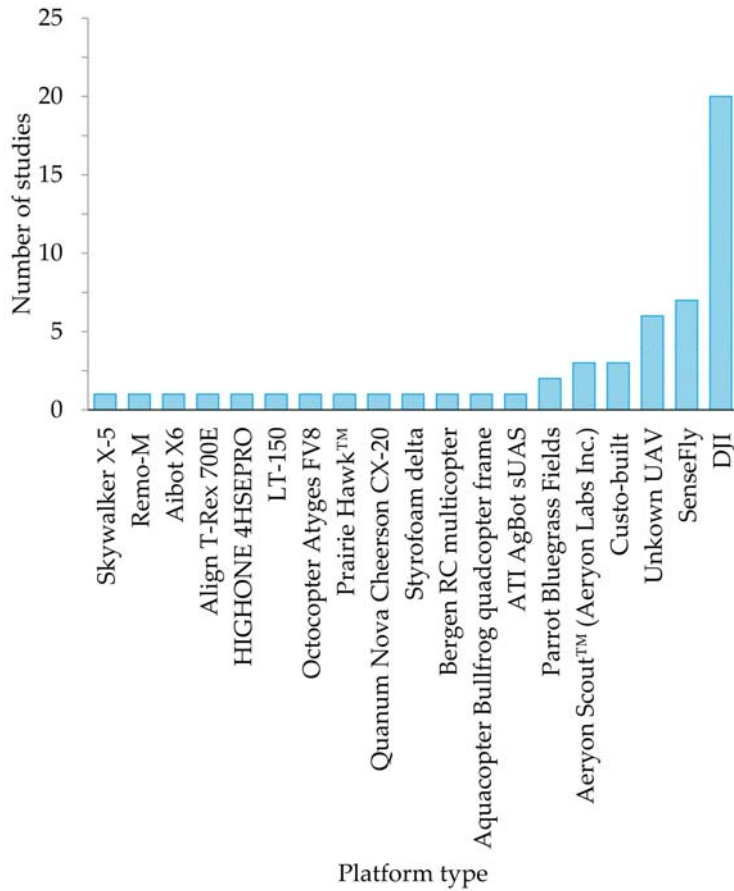
Figure 7. Frequency and types of UAV platforms that were used in mapping water quality and quantity.

Table 2. Platforms and sensors that were used in mapping water quality.

UAV_Platform	Platform Type	UAV_Sensor	No Bands	No RGB Bands	No RE Bands	No NIR Bands
custom-built multirotor quadcopter-UAV	Quadcopter Quadcopter					
Aeryon Scout™ (Aeryon Labs Inc.)	Quadcopter	3S™	1			
Aibot X6	Quadcopter	NIKKOR AF-S 24–85 mm f/3.5–4.5G ED VR	1			
Aibot X6	Quadcopter	Velodyne HDL-32E	1			
Styrofoam delta	Fixed-wing	Sony NEX-5N_APS-C CMOS	1			
Aeryon SkyRanger	Quadcopter	Aeryon HDZoom31	3	3		
Aeryon SkyRanger	Quadcopter	HDZoom30	3	3		
Aibot X6	Quadcopter	Nikon D800	3	3		
Align T-Rex 700E	Helicopter	Nikon D5100	3	3		
DJI hexacopter Spreading Wings S900	Quadcopter	SONY RX-100, ARS 30X radar	3	3		
DJI M 600 Pro	Quadcopter	K4 multi-spectrometer	3	3	1	
DJI MAVIC 2	Quadcopter	HD integrated, L1D-20c model	3	3		
DJI Phantom	Quadcopter	GoPro Hero 3	3	3		
DJI Phantom 3	Quadcopter	Digital Camera	3	3		
DJI Phantom 4	Quadcopter	inBuilt	3	3		
DJI Phantom 4	Quadcopter	Sony IMX117 Exmor-R™, CMOS	3	3		
DJI Phantom-4-pro	Quadcopter	1″CMOS	3	3		
DJI S 800 EVO Hexacopter	Quadcopter	Canon EOS 5DS R	3	3		
Prairie Hawk™	Fixed-wing	GoPro™ HERO3,	3	3		
Prairie Hawk™	Fixed-wing	Sony IMX117 Exmor-R™, CMOS	3	3		
Quanum Nova Cheerson CX-20	Quadcopter	GoPro Hero 4 Black Edition, Feiyu Mini 3D Pro	3	3		
Quanum Nova Cheerson CX-21	Quadcopter	GoPro Hero 4 Black Edition, Feiyu Mini 3D Pro	3	3		
senseFly	Fixed-wing	Canon ELPH 110HS	3	3		
SenseFly Swinglet CAM	Fixed wing	Canon ELPH 110HS	3	3		
Skywalker X-5	Quadcopter	Sony RX100 20 MP	3	3		
ITALDRON HIGHONE 4HSEPRO	Quadcopter	SONY Alpha 7R,	3			
senseFly eBee	Fixed-wing	MicaSense Parrot Sequoia	4	2	1	
senseFly eBee	Fixed wing	Canon Powershot S110	4	2		1
senseFly eBee	Fixed wing	Canon Powershot S110	4	2		1
DJI Phantom 3 Professional	Quadcopter	Sentera	4	3		
DJI Phantom 3 Professional	Quadcopter	Sentera	4	3		
DJI Phantom 4	Quadcopter	Sequoia	4	3	1	1
Parrot Bluegrass Fields	Quadcopter	Sequoia	4	3	1	1
Remo-M	Fixed-wing	Sequoia	4	3	1	1
senseFly eBee	Fixed-wing	Sequoia	4	3	1	1
senseFly eBee	Fixed-wing	Sequoia	4	3	1	1
ATI AgBOT sUAS	Quadcopter	MicaSense RedEdge	5	3	1	
DJI Inspire 1 v2	Quadcopter	MicaSense	5	3	1	
DJI Inspire-2	Quadcopter	MicaSense RedEdge-M	5	3	1	1
DJI M600 multirotor	Quadcopter	MicaSense RedEdge multispectral	5	3	1	1
Octocopter ATyges FV8	Octocopter	MicaSense RedEdge-M	6	3	1	1
DJI	Quadcopter	MAIA WV	9	4	1	
Aquacopter Bullfrog quadcopter frame	Quadcopter	Ocean Optics	>200	3	1	
Bergen RC multi-copter	Quadcopter	Ocean Optics	>200	3	1	
DJI M600	Quadcopter	Gaia Sky-mini	>200	3	1	
DJI Phantom 2 Vision Plus	Quadcopter	Ocean Optics STS-VIS	>200	3	1	
LT-150	Fixed wing	AvaSpec-dual	>200	3		
DJI Matrice 600 Pro	Quadcopter	Headwall Nano-Hyperspec	270	3	1	
DJI MATRICE M600 Pro	Quadcopter	Headwall Nano-Hyperspec	270	3	1	
DJI MATRICE M600 Pro	Quadcopter	Headwall Nano-Hyperspec	270	3	1	
DJI S 800 EVO Hexacopter	Quadcopter	Headwall Nano-Hyperspec	270	3	1	

Meanwhile, fixed-wing drone platforms' superiority was reported in mapping linear features (i.e., rivers and roads) [45]. They were also associated with longer flight durations [46]. However, the disadvantage of the fixed-wing drones is that they require a runway, making it challenging to operate them in any environment [46]. Despite these differences, the current drive in the drone technology industry is to harness the VTOL of multi-copters with a long flight time associated with fixed-wing platforms through creating a hybrid VTOL fixed-wing UAV [46].

3.4. Sensors and Spectral Wavebands

In terms of the sensors, the results of this review showed that from the satellite-borne sensors, Landsat, had been the widest-used sensors for characterising irrigation water quality across the world (Figure 7). Specifically, Landsat 5 was the most widely used sensor with 39 studies, followed by Landsat 8 Operational land Instrument (OLI) with

18 studies and then Landsat 1 with only three studies. These findings were similar to those of Gholizadeh, Melesse, and Reddi [7], who also echoed the dominance of Landsat data in mapping and monitoring water quality. This could be attributed to the fact that Landsat is the longest mission that has been consistently supplying remotely sensed data suitable for a wide variety of applications, including water quality and quantity parameters, without any charges. However, the moderate spatial resolution of Landsat datasets of a 30 m ground sampling distance has limited its applications to regional and landscape scales. Subsequently, there has been a gap at local scales since the available VHSR sensors such as Worldview and QuickBird are associated with high costs.

The advent of drone technologies has seen the utility of sensors, such as Nikon (NIKKOR AF-S 24–85 mm f/3.5–4.5G ED VR) and the Nikon D800 [47], GoPro Hero 4 Black Edition [48], Feiyu Mini 3D Pro [48], Sony [44], and CMOS [49] to the multispectral sensors such as the MicaSense, Parrot Sequoia [28,50–55] Sentera [38], MicaSense RedEdge multi-spectral [29,56], and the hyperspectral sensors such as Headwall Photonics Inc (207 bands), Ocean Optics STS-VIS (640 bands) [27], AvaSpec-dual Gaia (640 bands) [35,57], Sky-mini Nano-Hyperspec [30], Canon EOS 5DS R, and Headwall Nano-Hyperspec (640 bands) for local-scale water remote sensing applications (Table 2). However, as the spectral resolution of drone sensors increases, the associated costs also increase linearly. From our results, it can be observed that the most widely used sensors were the Cannon, Sony, MicaSense, and the Nikon.

Nevertheless, most of the Cannon, Sony, and Nikon sensors acquire images only in the visible section of the electromagnetic spectrum. They cover the red, green, and blue (RGB) regions of the electromagnetic spectrum (Figure 8). The RGB sections of the electromagnetic spectral alone do not offer sufficient data for extensive applications in areas such as characterising water quality despite their relatively limited costs and very high spatial resolutions in relation to other robust sensors. Meanwhile, the MicaSense series are multispectral cameras that acquire data not only in the visible section, but also cover the red edge and the near-infrared sections of the electromagnetic spectrum at a very high spatial resolution. This makes these the most sought after in the context of characterising a wide variety of applications ranging from the characterisation of vegetation traits to water levels and quality [26,28,29,56]. For example, the MicaSense RedEdge multispectral sensor covers the RGB and the RedEdge, NIR and the thermal infrared portions of the electromagnetic spectrum at an optimal ground sampling distance beyond 4 cm depending on the flight height. These spectral settings make this sensor comparable to the renowned Sentinel 2 multispectral instrument that also covers almost the same spectral regions, save for the thermal infrared section. Based on the findings of this study, there is a growing interest in the utility of hyperspectral sensors in mapping water quality and quantity. Specifically, these hyperspectral sensors cover the spectrum range between 300 and 1000 nm of the electromagnetic spectrum (Table 3). The major advantage of hyperspectral remotely sensed data in water quality remote sensing is the sensitivity to small changes in water quality parameters such as chlorophyll and TSS concentrations. Hyperspectral wavebands have a narrow spectral resolution of about 1–3.5 nm, making them more sensitive in relation to the multispectral drone cameras that are generally broader.

Table 3. Details of drone based hyperspectral sensors.

Spectrometer	Wavelength Range	Optical Resolution (nm)	Signal to Noise	Weight
Ocean Insight STS-VIS	350–800	1.5, 12.0, 3.0, 6.0	>1500 (at max signal)	60 g
AvaSpec-dual	360–1000	1	~100–400 (VIS)	58 g
Gaia Sky-mini Hyperspectral	400–1000	3.5nm		1.5 kg
NANO-HYPERSPEC	400–1000	2.5		1.2/0.5 (lb/kg)
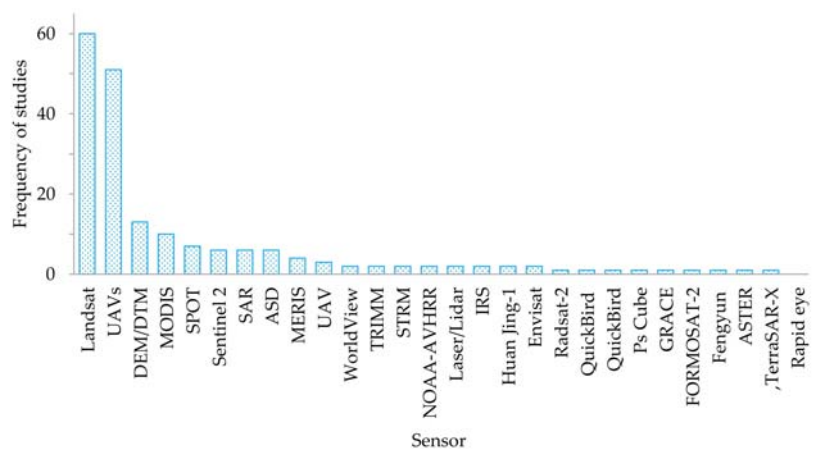
Figure 8. Satellite-borne sensors that were used in mapping surface water resources.

Table 3 illustrates a summary of the technical details of the hyperspectral sensors that were used in mapping water quality and quantity using drones. These sensors typically covered the visible to the NIR sections of the electromagnetic spectrum at very high spatial resolutions. The visible and NIR infrared (VIS-NIR) sections of the electromagnetic spectrum have been widely proven to be instrumental in assessing water quality. The premise that could explain the high frequency in the utility of the RGB spectrum (illustrated in Figure 8) was the relatively lesser costs associated with such three-band sensors. Furthermore, as aforementioned, the ease associated with interpreting the spectral signature of water in the visible and the near-infrared. However, there seems to be limited efforts to evaluate other sections of the electromagnetic spectrum in relation to the VIS–NIR in characterising water quality parameters. Based on the performance of hyperspectral data in other areas of research [58,59], there is a need to test the robustness and capability of the narrow spectral channels in detecting various water quality parameters.

3.5. The Role of Drone Data Derived Vegetation Indices and Machine Algorithms in Remote Sensing Water Quality and Quantity

Numerous vegetation indices were derived from drone remotely sensed data for characterising surface water quality and quantity. The most widely used sections of the electromagnetic spectrum in detecting water quality parameters were the visible section (blue and green) and the NIR wavebands. In this regard, vegetation indices such as the red and near-infrared (NIR), Surface Algal Bloom Index (SABI) [60], two-band algorithm (2BDA) [26], NDVI, and Green NDV [33], as well as band combinations and differencing such as (R+NIR/G) were used mostly in characterising chlorophyll content as well as TSS. As was suggested in many studies, the combination of sensitive spectral variables with robust and efficient algorithms produce accurate models. This study noted that algorithms such as linear regression (LR), image differencing, matching pixel-by-pixel (mpp), artificial neural networks (ANN), and the Manning–Strickler and adaptive cosine estimator were utilised in characterising mostly water quality parameters (Figure 9). The mpp based algorithms were also detected during the bibliometric analysis illustrated in Figure 3 (red cluster). Despite being a parametric estimator, LR was the most widely used algorithm because it is simple to implement [61] across various statistical platforms ranging from Microsoft Excel to R statistics. Since LR is a parametric statistic, it requires the data to suit specific assumptions such as normality that are often a challenge to attain. In this regard, there is a need for more efforts in assessing the utility of robust machine learning algorithms such as stochastic gradient boosting, random forest, and the ANN in mapping water quality based on drone remotely sensed data (Figure 10).
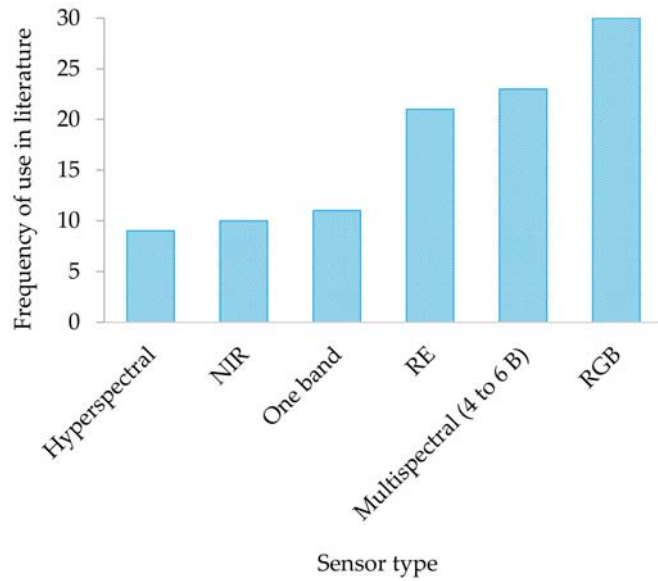
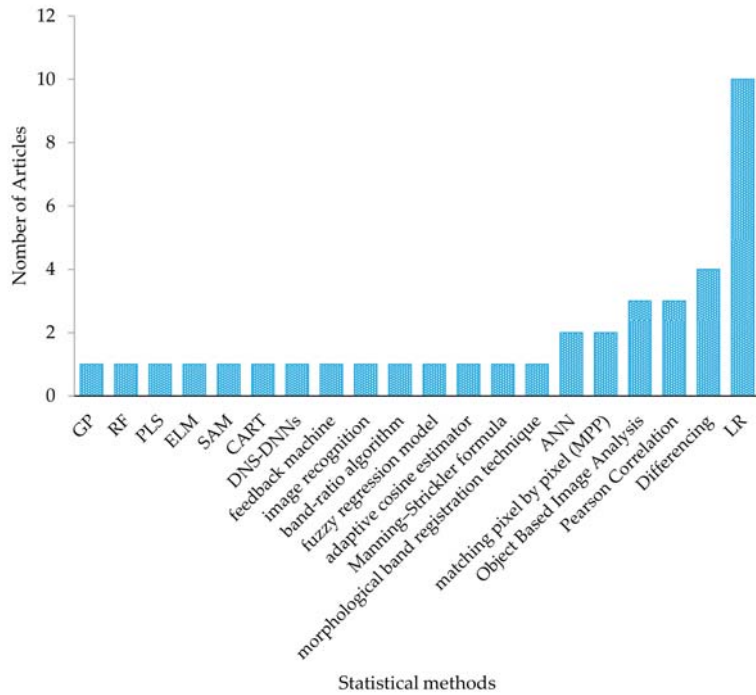**Figure 9.** Spectral resolutions of drone sensors illustrated in Table 1.

Figure 10. Algorithms used to detect and map water quality and quantity using drone remotely sensed data.

4. Discussion

4.1. Evolution of Drone Technology Applications in Remote Sensing Water Quality and Quantity

Results in this study showed that the application of drones dates back to the late 1940s. Initially, drones were developed on the offensive as cheap and less risky military airborne fighting machines. With modernisation and the ease of prohibitive regulations, drones became a significant source of spatial data. Specifically, between 2012 and 2014, the United States of America eased the regulations that restricted UAVs for other purposes. Subsequently, the entire global village began to venture into utilising drones in earth observation. It was also observed that studies on the utility of UAVs in mapping and monitoring water quality and quantity are significantly increasing (Figure 4b) [16]. This could be explained by the advancement in drone and sensor technologies as well as the easing of restrictive regulations associated with drone technologies.

Meanwhile, results showed that more efforts from the community of practice were widely exerted towards mapping water quality in relation to water quantity. Specifically, only fourteen studies assessed the level of water, whereas thirty-seven studies assessed water quality parameters based on drone remotely sensed data [44,47–49,62–72]. A few examples of studies that mapped water levels included Ridolfi and Manciola [63] who used a method that was based on the Ground Control Points (GCPs) to detect water levels, where water level values were measured using drone-derived data. Meanwhile, Adongo et al. [64] assessed the utility of undertaking bathymetric surveys combined with geographic information systems (GIS) functionalities in remotely determining the reservoir volume of nine irrigation dams in three northern regions of Ghana. On the other hand, the majority of water quality-related studies that were conducted based on drone remotely sensed data, principally mapped and monitored the chlorophyll content [30,32,33,37,38] and turbidity in lakes, ponds and dams (Figure 5b) [34–36]. This trend was also revealed through the bibliometric analysis illustrated in Figure 3. Other water quality parameters that were of interest include the chemical oxygen demand (COD) [26,35,73], Secchi disk depth (ZSD) [26,34,74], total nitrogen [35], total phosphorous [35,73], conductivity [24–26,73], water quality index [73], pH [27,75], total suspended solids (TSS) [28,29,76], dissolved Oxygen (DO) [75,77], and turbidity [35,48], in order of importance illustrated by their frequency in the literature.

4.2. Challenges in the Application of Drone Technologies with Special Reference to the Global South

The major challenge associated with many regions is the statutory regulations that govern the operation of UAVs [77–79]. In many countries, there are still stringent restrictions regarding where and how UAVs are supposed to be operated [16]. In some countries of the global south, the take-off mass, the maximum altitude of flight, and the operational areas of drones tend to be regulated [16]. For instance, the South African Civil Aviation Authority (SACAA) stipulates that remotely piloted aircraft or toy aircraft should not be operated at 50 m or closer to any person or group of persons. It states that remotely piloted aircraft or toy aircraft must not be operated at an altitude higher than 45.72 m (150 ft) from the ground unless approved by the Director of Civil Aviation of the SACAA. Remotely piloted aircraft or toy aircraft weighing more than 7 kg should be operated only if approved by the SACAA (http://www.caa.co.za/pages/rpas/remotely%20piloted%20aircraft%20systems.aspx, accessed on 19 July 2021). The size of the UAV which is often associated with its batteries, engine efficiency, load, and type of UAV (fixed-wing or multi-rotor) tends to determine the length of time it can spend on a single flight plan and the size of the area it can cover [46,79]. In this regard, the regulation on the mass of UAV at taking off tends to indirectly restrict the areal extent that can be covered as well as the size of the camera to be mounted for research purposes, amongst other uses [16,68]. Specifically, due to the weight restrictions, many of the sensor types that are frequently used tend to be lightweight, small-size, and general consumer grades with limited spectral resolutions [15]. Moreover, SACAA states that Remotely Piloted Aircraft Systems (RPAs) shall not be operated beyond the visual-line-of-sight (BVLOS). Insufficient flight autonomy to cover large areas [50] limits the areal extent that can be covered by drones to a farm or field scale. Meanwhile, a supporting regulation

and operationalisation of BVLOS drone technology applications will facilitate coverage of greater areas on a single mission. Covering a greater area on a single mission improves the cost-effectiveness in the acquisition of VHR imagery. This will increase the prospects of drone applications in covering large dams and lakes in mapping and monitoring water quality and quantity. Further advancements and improvements towards the automation of drone operations will sanction routine monitoring and mapping applications. This study shows that single and three-band cameras are the most widely used sensors in characterising water quality parameters (Table 1 and Figure 6).

The SACAA stipulates a need for a pilot license to operate UAVs for commercial purposes in South Africa. However, the Eighth Amendment of the Civil Aviation Regulations, 2011, which came into operation on 1 July 2015, contains Part 101 on Remotely Piloted Aircraft Systems, states that

> *"2.3 . . . the SACAA acknowledges that many entrepreneurs interested in obtaining a Remotely Piloted Aircraft Systems Operator Certificate (ROC) to provide aerial services, for example, real estate photography, academia etc. are not aviation professionals. As such, they have limited aviation backgrounds, and a lack knowledge about existing flight and airspace regulations. To protect the safety of the public and for these individuals to become viable UAS operators, they need to be aware of the requirements and the process. UAS operators, in turn, must be informed on the current regulations, policies and procedures to develop safe business practices in a similar fashion to professional "manned" aviation companies" (source: http://www.caa.co.za/RPAS%20AICs/AIC%20 007-2015.pdf , accessed on 19 July 2021).*

Meanwhile, the process of acquiring a licence costs about USD1500–2000. On the other hand, the prices of drone platforms and cameras remain high and beyond the reach of many researchers. Drone platforms with the capability of mounting various cameras generally vary between USD1000 and 10,000, inclusive of the sensor; hence, they are not accessible for research purposes in most Southern African countries. Only the affordable small platforms restricted in terms of sensors type (spectral and spatial resolution), flight height, and flight time are easily accessible and widely used for recreational purposes. This current review highlights the current state of affairs (opportunities and challenges) associated with research using cutting-edge drone technologies, especially to some of the countries in the global south. Although highlighting limitations such as the lack of funding, laboratories, and human capacity, this study sought to expose the plausible opportunities associated with these technologies. In this regard, this work will invoke ways in which researchers in countries of the global south can be aware of the prospects of UAV technologies and seek collaborations with countries of the global north. For instance, UNICEF, Virginia Polytechnic Institute, and State University, commonly known as Virginia Tech, joined the Government of Malawi in establishing The African Drone and Data Academy (ADDA) (https://www.unicef.org/malawi/african-drone-and-data-academy-malawi, accessed on 19 July 2021). The ADDA aimed to be a centre of excellence for dually equipping young people in Malawi and the African region with necessary 21st-century skills, while strengthening the drone ecosystem for a more effective humanitarian and development response in Southern Africa.

Mapping water volume using drone remotely sensed data is also one of the major challenges in the global south and across all continents. In mapping such complex channel bathymetric characteristics, there is a need for robust sensor systems that could penetrate water in detecting the water body's volume. Active sensors could be suitable for this procedure in conjunction with robust machine learning algorithms.

4.3. Research Gaps and Opportunities

The following gaps were identified from the results of this study in the context of irrigation water quantity and quality monitoring based on drone remotely sensed data:

- There are a limited number of studies that have sought to evaluate the utility of drone remotely sensed data in the global south;

- The assessment of water quality using multispectral and hyperspectral drone sensors has not attracted much attention from the research community;
- There are very few studies that have assessed the utility of robust nonparametric machine learning algorithms for water;
- Few studies have sought to evaluate and exploit the possible synergies between drone and satellite bone datasets, especially since the launch of Sentinel 2 MSI, which is freely available;
- Limited research attention has been given towards mapping water quality and quantity in open water reservoirs supplying smallholder farms;
- Furthermore, as noted in the literature (Lally et al., 2019; Koparan et al., 2018a), there is still a gap in the real-time use of drone-mounted monitoring probes in testing and monitoring water quality parameters.

4.4. Way Forward: Closing the Gaps in the Utilisation of Drone Technology in Mapping Water Quality and Quantity

Research efforts need to be promoted to evaluate UAVs' utility in monitoring irrigation water quality and quantity, especially in the global south's smallholder farms that are susceptible to climate variability shocks and unpredictable rains. As the fourth industrial revolution is progressing, UAVs are emerging as an innovative source of near-real-time spatial data for mapping and monitoring surface water resources to improve the agricultural sector productivity. Drone data have high prospects of providing well-calibrated, time-efficient, and spatially explicit data models on water quantity and quality. In this regard, the application of multispectral sensors in characterising surface water levels and water quality needs to be conducted if a sustainable utilisation of water resources and water security is to be achieved in the light of the rapidly growing population and its associated water demands. Since the current focus in the agricultural sector is towards reducing the amount of irrigation water while increasing agricultural productivity, timely and accurate fine spatial resolution data derived using drones such as the DJI series in concert with multispectral sensors such as the Mica sense and hyperspectral sensors such as the Headwall Nano-Hyperspec could be useful in detecting and mapping the spatio–temporal variability of available irrigation water quality and volume at field levels. Field-level near real-time fine resolution, spatially explicit information on water quality, and quantity models are useful in informing smallholder farmers in the field and policymakers away from the fields about water leakages occurring at the grassroots level. Near-real-time fine resolution and information on water quality and quantity will help farmers plan their irrigation schedules, resulting in limited water leakages and losses while improving productivity. This is very critical in reducing further strains on the already stressed-out water resources. This evidence-based, timely information on the available water resources is critical for farmers to suit their irrigation water management strategies based on in-field spatial variability and seasonal changes in water quantity and quality. Subsequently, formulating robust and effective local-to-regional frameworks and policies to facilitate sustainable utilisation and water management are more likely to be achieved.

5. Conclusions

The objective of this study was to conduct a systematic review, assess progress, opportunities, and challenges for using drone-derived remotely sensed data to map and model water quality and quantity. The utility of UAVs globally in mapping and monitoring the amount of surface water and its quality at a farm scale is still in its infancy. This is partly due to high costs, a lack of personnel with the requisite skills, and the stringent regulations of securing and operating drones. Nevertheless, drones are cutting-edge technology with high prospects of providing spatially explicit, timely, robust, and reliable surface water resources accounting. There is a need to swiftly embrace this technology to minimize water leakages for improving on-farm irrigation strategies, and draw local, regional, and national strategies and policies focusing on the sustainable utilisation of water to reduce the strain on the already stressed water resources. There is room for research on a wide range of

aspects on the quality and quantity of irrigation water in situ, which require research efforts and integration with other upcoming innovative technologies such as artificial intelligence and deep learning computer advances.

References

1. Stephens, G.L.; Slingo, J.M.; Rignot, E.; Reager, J.T.; Hakuba, M.Z.; Durack, P.J.; Worden, J.; Rocca, R. Earth's water reservoirs in a changing climate. *Proc. R. Soc. A* **2020**, *476*, 20190458. [CrossRef] [PubMed]
2. FAO. *World Food and Agriculture—Statistical Pocketbook*; FAO: Rome, Italy, 2018.
3. Finley, J.W.; Seiber, J.N. The nexus of food, energy, and water. *J. Agric. Food Chem.* **2014**, *62*, 6255–6262. [CrossRef]
4. Fischer, G. World food and agriculture to 2030/50. In *Technical Paper for the Expert Meeting on "How to Feed the World"*; FAO: Rome, Italy, 2009; pp. 24–26.
5. Bronkhorst, S.; Pengelly, C.; Seyler, H. *Water 2017 Market Intelligence Report*; Greencape: Cape Town, South Africa, 2017.
6. Von Bormann, T.; Gulati, M. *The Food Energy Water Nexus: Understanding South Africa's Most Urgent Sustainability Challenge*; WWF-SA: Western Cape, South Africa, 2014; pp. 1–35.
7. Gholizadeh, M.H.; Melesse, A.M.; Reddi, L. A comprehensive review on water quality parameters estimation using remote sensing techniques. *Sensors* **2016**, *16*, 1298. [CrossRef]
8. Palmer, K.F.; Williams, D. Optical properties of water in the near infrared. *JOSA* **1974**, *64*, 1107–1110. [CrossRef]
9. Lee, Z.; Carder, K.L.; Arnone, R.A. Deriving inherent optical properties from water color: A multiband quasi-analytical algorithm for optically deep waters. *Appl. Opt.* **2002**, *41*, 5755–5772. [CrossRef] [PubMed]
10. Ovakoglou, G.; Alexandridis, T.K.; Crisman, T.L.; Skoulikaris, C.; Vergos, G.S. Use of MODIS satellite images for detailed lake morphometry: Application to basins with large water level fluctuations. *Int. J. Appl. Earth Obs. Geoinf.* **2016**, *51*, 37–46. [CrossRef]
11. Dube, T.; Sibanda, M.; Shoko, C. Examining the variability of small-reservoir water levels in semi-arid environments for integrated water management purposes, using remote sensing. *Trans. R. Soc. S. Afr.* **2016**, *71*, 115–119. [CrossRef]
12. Sallam, A.; Alharbi, A.B.; Usman, A.R.; Hussain, Q.; Ok, Y.S.; Alshayaa, M.; Al-Wabel, M. Environmental consequences of dam construction: A case study from Saudi Arabia. *Arab. J. Geosci.* **2018**, *11*, 1–12. [CrossRef]
13. Ismail, M. Remote Sensing as a Tool in Assessing Water Quality. *Life Sci. J.* **2012**, *9*, 246–252.
14. Campbell, G.; Phinn, S.R.; Dekker, A.G.; Brando, V.E. Remote sensing of water quality in an Australian tropical freshwater impoundment using matrix inversion and MERIS images. *Remote Sens. Environ.* **2011**, *115*, 2402–2414. [CrossRef]
15. Xiang, T.-Z.; Xia, G.-S.; Zhang, L. Mini-Unmanned Aerial Vehicle-Based Remote Sensing: Techniques, applications, and prospects. *IEEE Geosci. Remote Sens. Mag.* **2019**, *7*, 29–63. [CrossRef]
16. Lally, H.; O'Connor, I.; Jensen, O.; Graham, C. Can drones be used to conduct water sampling in aquatic environments? A review. *Sci. Total Environ.* **2019**, *670*, 569–575. [CrossRef] [PubMed]
17. Yao, H.; Qin, R.; Chen, X. Unmanned Aerial Vehicle for Remote Sensing Applications—A Review. *Remote Sens.* **2019**, *11*, 1443. [CrossRef]
18. Cancela, J.J.; González, X.P.; Vilanova, M.; Mirás-Avalos, J.M. Water management using drones and satellites in agriculture. *Water* **2019**, *11*, 874. [CrossRef]
19. Small, H. Co-citation in the scientific literature: A new measure of the relationship between two documents. *J. Am. Soc. Inf. Sci.* **1973**, *24*, 265–269. [CrossRef]

20. Lozano, S.; Calzada-Infante, L.; Adenso-Díaz, B.; García, S. Complex network analysis of keywords co-occurrence in the recent efficiency analysis literature. *Scientometrics* **2019**, *120*, 609–629. [CrossRef]
21. Van Eck, N.J.; Waltman, L. Software survey: VOSviewer, a computer program for bibliometric mapping. *Scientometrics* **2010**, *84*, 523–538. [CrossRef]
22. Moher, D.; Shamseer, L.; Clarke, M.; Ghersi, D.; Liberati, A.; Petticrew, M.; Shekelle, P.; Stewart, L.A. Preferred reporting items for systematic review and meta-analysis protocols (PRISMA-P) 2015 statement. *Syst. Rev.* **2015**, *4*, 1–9. [CrossRef]
23. Shamseer, L.; Moher, D.; Clarke, M.; Ghersi, D.; Liberati, A.; Petticrew, M.; Shekelle, P.; Stewart, L.A. Preferred reporting items for systematic review and meta-analysis protocols (PRISMA-P) 2015: Elaboration and explanation. *BMJ* **2015**, *349*, g7647. [CrossRef] [PubMed]
24. Koparan, C.; Koc, A.; Privette, C.; Sawyer, C.; Sharp, J. Evaluation of a UAV-Assisted Autonomous Water Sampling. *Water* **2018**, *10*, 655. [CrossRef]
25. Koparan, C.; Koc, A.B.; Privette, C.V.; Sawyer, C.B. In Situ Water Quality Measurements Using an Unmanned Aerial Vehicle (UAV) System. *Water* **2018**, *10*, 264. [CrossRef]
26. Cillero Castro, C.; Dominguez Gomez, J.A.; Delgado Martin, J.; Hinojo Sanchez, B.A.; Cereijo Arango, J.L.; Cheda Tuya, F.A.; Diaz-Varela, R. An UAV and Satellite Multispectral Data Approach to Monitor Water Quality in Small Reservoirs. *Remote Sens.* **2020**, *12*, 1514. [CrossRef]
27. Zeng, C.; Richardson, M.; King, D.J. The impacts of environmental variables on water reflectance measured using a lightweight unmanned aerial vehicle (UAV)-based spectrometer system. *ISPRS J. Photogramm. Remote Sens.* **2017**, *130*, 217–230. [CrossRef]
28. Larson, M.D.; Simic Milas, A.; Vincent, R.K.; Evans, J.E. Multi-depth suspended sediment estimation using high-resolution remote-sensing UAV in Maumee River, Ohio. *Int. J. Remote Sens.* **2018**, *39*, 5472–5489. [CrossRef]
29. Ying, H.; Xia, K.; Huang, X.; Feng, H.; Yang, Y.; Du, X.; Huang, L. Evaluation of water quality based on UAV images and the IMP-MPP algorithm. *Ecol. Inform.* **2021**, *61*, 101239. [CrossRef]
30. Kwon, Y.S.; Pyo, J.; Kwon, Y.-H.; Duan, H.; Cho, K.H.; Park, Y. Drone-based hyperspectral remote sensing of cyanobacteria using vertical cumulative pigment concentration in a deep reservoir. *Remote Sens. Environ.* **2020**, *236*, 416. [CrossRef]
31. Kim, G.; Baek, I.; Stocker, M.D.; Smith, J.E.; Van Tassell, A.L.; Qin, J.; Chan, D.E.; Pachepsky, Y.; Kim, M.S. Hyperspectral Imaging from a Multipurpose Floating Platform to Estimate Chlorophyll-a Concentrations in Irrigation Pond Water. *Remote Sens.* **2020**, *12*, 2070. [CrossRef]
32. Cheng, K.H.; Chan, S.N.; Lee, J.H.W. Remote sensing of coastal algal blooms using unmanned aerial vehicles (UAVs). *Mar. Pollut. Bull.* **2020**, *152*, 110889. [CrossRef]
33. Guimarães, T.; Veronez, M.; Koste, E.; Gonzaga, L.; Bordin, F.; Inocencio, L.; Larocca, A.; de Oliveira, M.; Vitti, D.; Mauad, F. An Alternative Method of Spatial Autocorrelation for Chlorophyll Detection in Water Bodies Using Remote Sensing. *Sustainability* **2017**, *9*, 416. [CrossRef]
34. Su, T.-C.; Chou, H.-T. Application of Multispectral Sensors Carried on Unmanned Aerial Vehicle (UAV) to Trophic State Mapping of Small Reservoirs: A Case Study of Tain-Pu Reservoir in Kinmen, Taiwan. *Remote Sens.* **2015**, *7*, 10078–10097. [CrossRef]
35. Zhang, Y.; Wu, L.; Ren, H.; Liu, Y.; Zheng, Y.; Liu, Y.; Dong, J. Mapping Water Quality Parameters in Urban Rivers from Hyperspectral Images Using a New Self-Adapting Selection of Multiple Artificial Neural Networks. *Remote Sens.* **2020**, *12*, 336. [CrossRef]
36. Vogt, M.C.; Vogt, M.E. Research Article: Near-Remote Sensing of Water Turbidity Using Small Unmanned Aircraft Systems. *Environ. Pract.* **2017**, *18*, 18–31. [CrossRef]
37. Flynn, K.; Chapra, S. Remote Sensing of Submerged Aquatic Vegetation in a Shallow Non-Turbid River Using an Unmanned Aerial Vehicle. *Remote Sens.* **2014**, *6*, 12815–12836. [CrossRef]
38. McEliece, R.; Hinz, S.; Guarini, J.-M.; Coston-Guarini, J. Evaluation of Nearshore and Offshore Water Quality Assessment Using UAV Multispectral Imagery. *Remote Sens.* **2020**, *12*, 2258. [CrossRef]
39. Malakar, A.; Snow, D.D.; Ray, C. Irrigation Water Quality—A Contemporary Perspective. *Water* **2019**, *11*, 1482. [CrossRef]
40. Frenkel, H. Reassessment of water quality criteria for irrigation. In *Ecological Studies: Analysis and Synthesis*; Springer-Verlag: New York, NY, USA, 1984.
41. Bauder, T.A.; Waskom, R.; Sutherland, P.; Davis, J. *Irrigation Water Quality Criteria*; Colorado State University: Fort Collins, CO, USA, 2011.
42. Jeong, H.; Kim, H.; Jang, T. Irrigation water quality standards for indirect wastewater reuse in agriculture: A contribution toward sustainable wastewater reuse in South Korea. *Water* **2016**, *8*, 169. [CrossRef]
43. Sengupta, M.E.; Keraita, B.; Olsen, A.; Boateng, O.K.; Thamsborg, S.M.; Pálsdóttir, G.R.; Dalsgaard, A. Use of Moringa oleifera seed extracts to reduce helminth egg numbers and turbidity in irrigation water. *Water Res.* **2012**, *46*, 3646–3656. [CrossRef]
44. Schumann, G.J.-P.; Muhlhausen, J.; Andreadis, K.M. Rapid Mapping of Small-Scale River-Floodplain Environments Using UAV SfM Supports Classical Theory. *Remote Sens.* **2019**, *11*, 982. [CrossRef]
45. Brito, R.C.; Lorencena, M.C.; Loureiro, J.F.; Favarim, F.; Todt, E. A comparative approach on the use of unmanned aerial vehicles kind of fixed-wing and rotative wing applied to the precision agriculture scenario. In Proceedings of the 2019 IEEE 43rd Annual Computer Software and Applications Conference (COMPSAC), Milwaukee, WI, USA, 15–19 July 2019; pp. 522–526.

46. Zaludin, Z.; Harituddin, A.S.M. Challenges and Trends of Changing from Hover to Forward Flight for a Converted Hybrid Fixed Wing VTOL UAS from Automatic Flight Control System Perspective. In Proceedings of the 2019 IEEE 9th International Conference on System Engineering and Technology (ICSET), Shah Alam, Malaysia, 7 October 2019; pp. 247–252.

47. Tymków, P.; Jóźków, G.; Walicka, A.; Karpina, M.; Borkowski, A. Identification of Water Body Extent Based on Remote Sensing Data Collected with Unmanned Aerial Vehicle. *Water* **2019**, *11*, 338. [CrossRef]

48. Ventura, D.; Bonifazi, A.; Gravina, M.F.; Belluscio, A.; Ardizzone, G. Mapping and Classification of Ecologically Sensitive Marine Habitats Using Unmanned Aerial Vehicle (UAV) Imagery and Object-Based Image Analysis (OBIA). *Remote Sens.* **2018**, *10*, 1331. [CrossRef]

49. Lou, H.; Wang, P.; Yang, S.; Hao, F.; Ren, X.; Wang, Y.; Shi, L.; Wang, J.; Gong, T. Combining and Comparing an Unmanned Aerial Vehicle and Multiple Remote Sensing Satellites to Calculate Long-Term River Discharge in an Ungauged Water Source Region on the Tibetan Plateau. *Remote Sens.* **2020**, *12*, 2155. [CrossRef]

50. Olivetti, D.; Roig, H.; Martinez, J.-M.; Borges, H.; Ferreira, A.; Casari, R.; Salles, L.; Malta, E. Low-Cost Unmanned Aerial Multispectral Imagery for Siltation Monitoring in Reservoirs. *Remote Sens.* **2020**, *12*, 1855. [CrossRef]

51. Kim, E.-J.; Nam, S.-H.; Koo, J.-W.; Hwang, T.-M. Hybrid Approach of Unmanned Aerial Vehicle and Unmanned Surface Vehicle for Assessment of Chlorophyll-a Imagery Using Spectral Indices in Stream, South Korea. *Water* **2021**, *13*, 1930. [CrossRef]

52. Brinkhoff, J.; Hornbuckle, J.; Barton, J.L. Assessment of Aquatic Weed in Irrigation Channels Using UAV and Satellite Imagery. *Water* **2018**, *10*, 1497. [CrossRef]

53. Yang, B.; Hawthorne, T.L.; Torres, H.; Feinman, M. Using object-oriented classification for coastal management in the east central coast of Florida: A quantitative comparison between UAV, satellite, and aerial data. *Drones* **2019**, *3*, 60. [CrossRef]

54. Freitas, P.; Vieira, G.; Canário, J.; Folhas, D.; Vincent, W.F. Identification of a threshold minimum area for reflectance retrieval from thermokarst lakes and ponds using full-pixel data from Sentinel-2. *Remote Sens.* **2019**, *11*, 657. [CrossRef]

55. Wojcik, K.A.; Bialik, R.J.; Osinska, M.; Figielski, M. Investigation of Sediment-Rich Glacial Meltwater Plumes Using a High-Resolution Multispectral Sensor Mounted on an Unmanned Aerial Vehicle. *Water* **2019**, *11*, 2405. [CrossRef]

56. Kim, W.; Jung, S.; Moon, Y.; Mangum, S.C. Morphological Band Registration of Multispectral Cameras for Water Quality Analysis with Unmanned Aerial Vehicle. *Remote Sens.* **2020**, *12*, 2024. [CrossRef]

57. Shang, S.; Lee, Z.; Lin, G.; Hu, C.; Shi, L.; Zhang, Y.; Li, X.; Wu, J.; Yan, J. Sensing an intense phytoplankton bloom in the western Taiwan Strait from radiometric measurements on a UAV. *Remote Sens. Environ.* **2017**, *198*, 85–94. [CrossRef]

58. Mutanga, O.; Van Aardt, J.; Kumar, L. Imaging spectroscopy (hyperspectral remote sensing) in southern Africa: An overview. *S. Afr. J. Sci.* **2009**, *105*, 193–198. [CrossRef]

59. Khan, M.J.; Khan, H.S.; Yousaf, A.; Khurshid, K.; Abbas, A. Modern trends in hyperspectral image analysis: A review. *IEEE Access* **2018**, *6*, 14118–14129. [CrossRef]

60. Alawadi, F. Detection of surface algal blooms using the newly developed algorithm surface algal bloom index (SABI). In *Remote Sensing of the Ocean, Sea Ice, and Large Water Regions 2010*; International Society for Optics and Photonics: Bellingham, WA, USA, 2010; p. 782506.

61. Harrington, J.A., Jr.; Schiebe, F.R.; Nix, J.F. Remote sensing of Lake Chicot, Arkansas: Monitoring suspended sediments, turbidity, and Secchi depth with Landsat MSS data. *Remote Sens. Environ.* **1992**, *39*, 15–27. [CrossRef]

62. Templin, T.; Popielarczyk, D.; Kosecki, R. Application of low-cost fixed-wing UAV for inland lakes shoreline investigation. *Pure Appl. Geophys.* **2018**, *175*, 3263–3283. [CrossRef]

63. Ridolfi, E.; Manciola, P. Water Level Measurements from Drones: A Pilot Case Study at a Dam Site. *Water* **2018**, *10*, 297. [CrossRef]

64. Adongo, T.A.; Kyei-Baffour, N.; Abagale, F.K.; Agyare, W.A. Assessment of reservoir sedimentation of irrigation dams in northern Ghana. *Lake Reserv. Manag.* **2020**, *36*, 87–105. [CrossRef]

65. Tamminga, A.; Hugenholtz, C.; Eaton, B.; Lapointe, M. Hyperspatial remote sensing of channel reach morphology and hydraulic fish habitat using an unmanned aerial vehicle (uav): a first assessment in the context of river research and management. *River Res. Appl.* **2015**, *31*, 379–391. [CrossRef]

66. Rahman, M.M.; McDermid, G.J.; Strack, M.; Lovitt, J. A New Method to Map Groundwater Table in Peatlands Using Unmanned Aerial Vehicles. *Remote Sens.* **2017**, *9*, 1057. [CrossRef]

67. Lovitt, J.; Rahman, M.M.; Saraswati, S.; McDermid, G.J.; Strack, M.; Xu, B. UAV Remote Sensing Can Reveal the Effects of Low-Impact Seismic Lines on Surface Morphology, Hydrology, and Methane (CH4) Release in a Boreal Treed Bog. *J. Geophys. Res. Biogeosciences* **2018**, *123*, 1117–1129. [CrossRef]

68. Flener, C.; Vaaja, M.; Jaakkola, A.; Krooks, A.; Kaartinen, H.; Kukko, A.; Kasvi, E.; Hyyppa, H.; Hyyppa, J.; Alho, P. Seamless Mapping of River Channels at High Resolution Using Mobile LiDAR and UAV-Photography. *Remote Sens.* **2013**, *5*, 6382–6407. [CrossRef]

69. Bandini, F.; Olesen, D.; Jakobsen, J.; Kittel, C.M.M.; Wang, S.; Garcia, M.; Bauer-Gottwein, P. Technical note: Bathymetry observations of inland water bodies using a tethered single-beam sonar controlled by an unmanned aerial vehicle. *Hydrol. Earth Syst. Sci.* **2018**, *22*, 4165–4181. [CrossRef]

70. Gao, A.; Wu, S.; Wang, F.; Wu, X.; Xu, P.; Yu, L.; Zhu, S. A Newly Developed Unmanned Aerial Vehicle (UAV) Imagery Based Technology for Field Measurement of Water Level. *Water* **2019**, *11*, 124. [CrossRef]

71. Feng, Q.; Liu, J.; Gong, J. Urban Flood Mapping Based on Unmanned Aerial Vehicle Remote Sensing and Random Forest Classifier—A Case of Yuyao, China. *Water* **2015**, *7*, 1437–1455. [CrossRef]

72. Rossi, L.; Mammi, I.; Pelliccia, F. UAV-derived multispectral bathymetry. *Remote Sens.* **2020**, *12*, 3897. [CrossRef]
73. Kageyama, Y.; Takahashi, J.; Nishida, M.; Kobori, B.; Nagamoto, D. Analysis of Water Quality in Miharu Dam Reservoir, Japan, using UAV Data. *IEEJ Trans. Electr. Electron. Eng.* **2016**, *11*, S183–S185. [CrossRef]
74. Su, T.-C. A study of a matching pixel by pixel (MPP) algorithm to establish an empirical model of water quality mapping, as based on unmanned aerial vehicle (UAV) images. *Int. J. Appl. Earth Obs. Geoinf.* **2017**, *58*, 213–224. [CrossRef]
75. Banerjee, B.P.; Raval, S.; Maslin, T.J.; Timms, W. Development of a UAV-mounted system for remotely collecting mine water samples. *Int. J. Min. Reclam. Environ.* **2018**, *34*, 385–396. [CrossRef]
76. Guimarães, T.T.; Veronez, M.R.; Koste, E.C.; Souza, E.M.; Brum, D.; Gonzaga, L.; Mauad, F.F. Evaluation of Regression Analysis and Neural Networks to Predict Total Suspended Solids in Water Bodies from Unmanned Aerial Vehicle Images. *Sustainability* **2019**, *11*, 2580. [CrossRef]
77. Wang, L.; Yue, X.; Wang, H.; Ling, K.; Liu, Y.; Wang, J.; Hong, J.; Pen, W.; Song, H. Dynamic Inversion of Inland Aquaculture Water Quality Based on UAVs-WSN Spectral Analysis. *Remote Sens.* **2020**, *12*, 402. [CrossRef]
78. Rhee, D.S.; Kim, Y.D.; Kang, B.; Kim, D. Applications of unmanned aerial vehicles in fluvial remote sensing: An overview of recent achievements. *KSCE J. Civ. Eng.* **2017**, *22*, 588–602. [CrossRef]
79. Cracknell, A.P. UAVs: Regulations and law enforcement. *Int. J. Remote Sens.* **2017**, *38*, 3054–3067. [CrossRef]

Monitoring Dynamic Braided River Habitats: Applicability and Efficacy of Aerial Photogrammetry from Manned Aircraft versus Unmanned Aerial Systems

M Saif I. Khan [1,*], Ralf Ohlemüller [2], Richard F. Maloney [3] and Philip J. Seddon [1]

1   Zoology Department, Otago University, Dunedin 9016, New Zealand; philip.seddon@otago.ac.nz
2   School of Geography, Otago University, Dunedin 9016, New Zealand; ralf.ohlemuller@otago.ac.nz
3   Department of Conservation, Dunedin 9016, New Zealand; rmaloney@doc.govt.nz
*   Correspondence: mdsaiful.khan@otago.ac.nz

Abstract: Despite growing interest in using lightweight unmanned aerial systems (UASs) for ecological research and conservation, review of the operational aspects of these evolving technologies is limited in the scientific literature. To derive an objective framework for choosing among technologies we calculated efficiency measures and conducted a data envelopment productivity frontier analysis (DEA) to compare the efficacy of using manned aircraft (Cessna with Aviatrix triggered image capture using a 50 mm lens) and UAS (Mavic Pro 2) for photogrammetric monitoring of restoration efforts in dynamic braided rivers in Southern New Zealand. Efficacy assessment was based on the technological, logistical, administrative, and economic requirements of pre (planning), peri (image acquiring) and post (image processing) phases. The results reveal that the technological and logistic aspects of UASs were more efficient than manned aircraft flights. Administratively, the first deployment of UASs is less efficient but was very flexible for subsequent deployment. Manned aircraft flights were more productive in terms of the number of acquired images, but the ground resolution of those images was lower compared with those from UASs. Frontier analysis confirmed that UASs would be economical for regular monitoring of habitats—and even more so if research personnel are trained to fly the UASs.

Keywords: unmanned aerial systems (UAS); aerial photogrammetry; habitat monitoring; braided river habitats; efficiency; data envelopment analysis (DEA)

1. Introduction

The use of digital aerial imagery for habitat monitoring is an evolving technology [1]. Increasing computational power, the availability of low-cost unmanned aerial systems (UASs), and the development of software for image analysis have made aerial imagery using UASs a tool of growing interest among conservation researchers and practitioners [2]. Since these technologies are relatively new, there is only a handful of scientific papers discussing their operational complexities [3]. It will be useful to have a comparative summary of available technology with information about their applicability and efficiency for a given purpose such as habitat monitoring [4–6], wildlife monitoring [7–9], vegetation change analysis [10,11], forest inventory [12], monitoring agricultural productivity [13,14] etc.

Braided rivers are one of the most dynamic ecosystems of the world [15]. The unique geomorphology and hydrological regime give rise to a range of habitats along the braided riverbeds [16]. These diverse microhabitats are often endangered due to the growing threat of habitat modifications induced by the upstream hydrological change and invasion by introduced flora and fauna [15]. Monitoring the consequences of these impacts is important for conserving the unique and often endemic flora and fauna of these habitats [17]. Braided river systems are prone to changes, as the complex spatial and fluvial arrangements are easily altered by fluctuations in the upstream flow regime [15]. The dynamic nature of the

braided river ecosystem makes habitat monitoring challenging as changes often happen within a short period following local weather events, such as high precipitation in the catchments. Lack of accessibility, logistics, and resources can be additional challenges. Remote sensing methods are being increasingly used in such situations [6].

There are many candidate remote sensing technologies to choose from, ranging from satellite imagery to lightweight unmanned aerial vehicles (UASs) [18], as well as aerial photographs using flights with manned aircraft [19]. Unmanned aerial systems are also referred to as unmanned aerial vehicles (UAVs). The term "unmanned" is sometimes argued as not being gender-neutral and "unoccupied" is suggested as an alternative [20]. However, we have persisted with the terms "manned" and "unmanned" as these are widely used. Each of these remote sensing methods have a wide range of features to choose from. For example, UASs vary in flying technology from fixed-wing or multi-rotor [21] and can be equipped with various sensors including RGB [11], infra-red [22], thermal bands [9], or even laser scanners [23]. Reviews of different UAS technologies are available in the literature [21], but the technology is ever-evolving and new choices are added to the mix relatively frequently. There are also varying options for flight planning, operating, image acquisition, and image processing software [24]. However, there is a lack in the scientific literature of objective comparison of technological alternatives for a given application [1]. Cost-based decision making often underestimates logistical, administrative, and other technological challenges [3]. There is need for a comprehensive framework that can incorporate these different aspects and can still objectively compare different technologies and assess their efficiencies for a given purpose. In this study, we assess the applicability of aerial photogrammetry for monitoring changes in the habitat features of the Aparima River, a braided river in Southern New Zealand, and compare the efficacy of using manned aircraft versus unmanned aerial vehicles (UASs).

2. Materials and Methods

2.1. Study Site

A 10 km stretch of the Aparima River (46.0003° S, 168.1095° E) is being monitored for changes in habitat features due to ongoing commercial gravel extraction from the riverbed. The goal of the monitoring is to assess the changes and inform habitat management solutions to maintain habitat suitability for a range of native species. In this research, manned aircraft and unmanned aerial photogrammetry tools are compared in order to select an economically viable and technologically suitable remote sensing monitoring system.

2.2. Manned Aircraft and Unmanned Flight Missions

The manned aircraft flights were performed with a Cessna 180 customized to carry aerial photogrammetry equipment [19]. Onboard was an Aviatrix aerial photography system capable of triggering photographs at pre-fixed points along the planned flight lines. Altitude above ground level, and image resolution and the number of flight lines was also pre-set. The camera used was a Canon EOS 5DS r with a Sigma 50 mm lens. The flight planning was carried out in Flight Planner Pro software from Aeroscientific (Adelaide, Australia), licensed through the Department of Conservation. The image sizes were 8688 × 5792 pixels with 50% sidewise and 68% forward overlaps. Three manned aircraft flight missions were carried out in February 2018, December 2019, and October 2020 at 608 m, 518 m, and 304 m altitude above ground level (AGL), respectively. All manned aircraft flights were performed at a speed of 166.70 km/h.

The unmanned flights were carried out with a commercially available Mavic2 pro quadcopter (DJI, China) carrying a 20 MP Hasselblad camera with a 28 mm equivalent focal length. The image sizes for unmanned flights were 5472 × 3648 pixels with 70% overlaps. Flight planning for UASs was carried out with Pix4D software (Prilly, Switzerland) and the same software was used to fly the UAS with DJI control on a Samsung A10 mobile phone. The unmanned flights took place in October 2020 and November 2020. One site at the

Northern end of the study area was performed on both the October and November missions, before and after a flood event of the riverbed habitat induced by high precipitation in late October. The flooding event possibly triggered the abandonment of colony exploration by white fronted terns (*Sterna striata*) in that site. The abandonment was a potential indicator of changes in habitat features. The re-deployment of the UAS within this short period was carried out to search for the changes in the habitat due to the flooding event. The average speed of UAS flights was 16.80 km/h and all were performed at 50 m altitude AGL. No ground control points (GCPs) were used for manned aircraft or UAS flights.

The manned aircraft flights covered the whole 10 km stretch of the Aparima River study area covering on average 863 ha. The unmanned flights covered three subsections of this larger area, comprising Northern and Southern ends, and a central area, a total of more than 83 ha (Figure 1). When necessary, the manned aircraft flight image geotags were updated using ExifTool software (Kingston, ON, Canada) [25] by syncing with the aviatrix trigger time log. All image processing analyses, including image mosaicking, were carried out in ESRI ArcGIS Pro 2.5, Redlands, CA, USA.
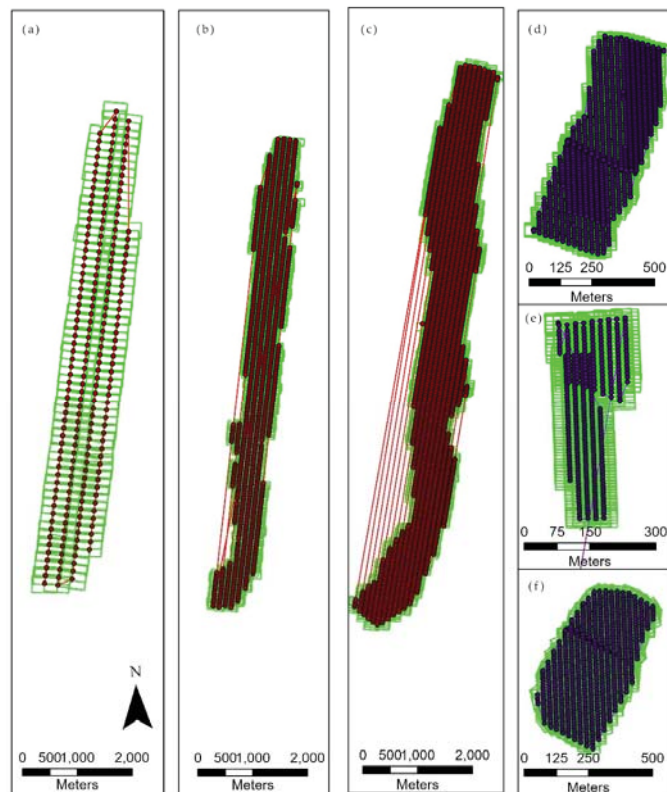
Figure 1. Flight plans and image footprints of flight missions over the Aparima River (**a**) Manned aircraft flight 2018, (**b**) Manned aircraft flight 2019, (**c**) Manned aircraft flight 2020, (**d**) unmanned flight 2020 over the Northern end, (**e**) unmanned flight 2020 over the central area, (**f**) unmanned flight 2020 over the Southern end of the manned aircraft flights. The image mosaics of these areas are included in Figure 2.
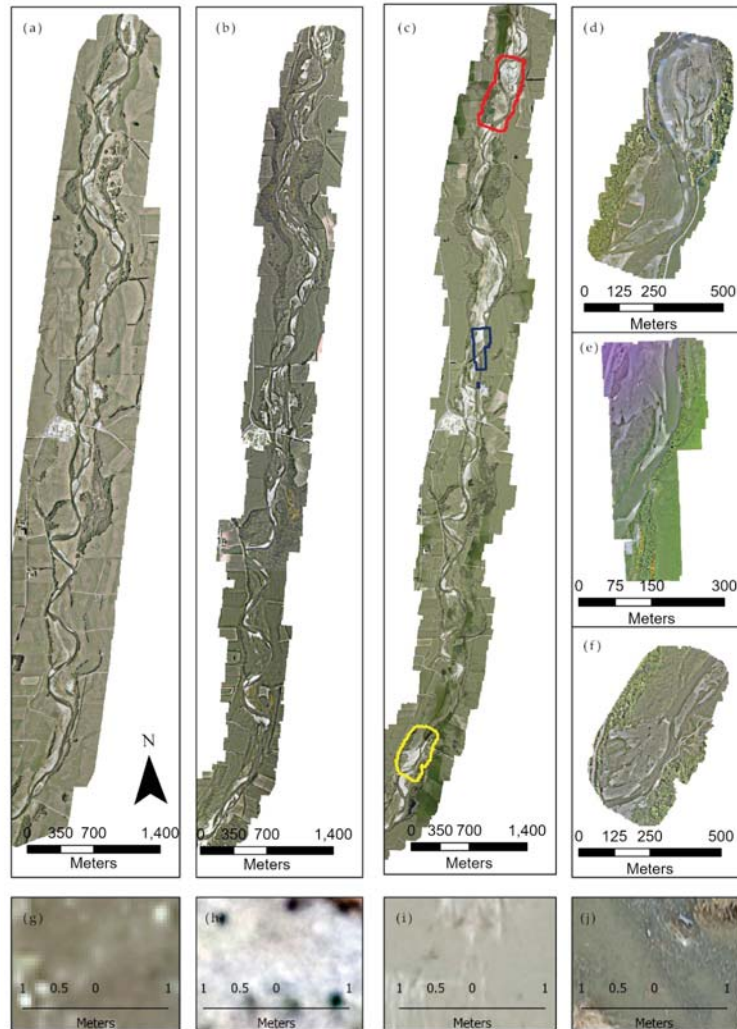
Figure 2. Output image mosaics from different manned aircraft and unmanned flight missions over the Aparima River: (**a**) Manned aircraft flight 2018, (**b**) Manned aircraft flight 2019, (**c**) Manned aircraft flight 2020, (**d**) unmanned flight 2020 over the Northern end, (**e**) unmanned flight 2020 over the central area, (**f**) unmanned flight 2020 over the Southern end, (**g**) zoomed in subsection of manned aircraft flight 2018, (**h**) zoomed in subsection of manned aircraft flight 2019, (**i**) zoomed in subsection of manned aircraft flight 2020, (**j**) zoomed in subsection of unmanned flight 2020 over the Northern end. Red, blue, and yellow polygons on 1e delineates the Northern, central and Southern sections performed with UASs. The zoomed in subsections (**1g,1h,1i,1j**) showcases the ground resolution difference among the flight missions.

2.3. Input Resource Assessment

For a better insight into the aerial imaging technology, we have separated aerial photography operations into pre-, peri-, and post-flying phases. The pre-flying phase includes flight planning and mobilizing resources for the flying operation. The peri-flying phase includes the actual flight operation and image acquisition. The post-flying phase includes image sorting, storage, and various image analysis techniques. For ease

of comparison, we have considered orthophoto mosaicking of the acquired images as the minimum step to be completed in the image processing phase.

Each of these three phases has technological, logistical, administrative, and economic aspects to assess. Technological resource assessment includes software and hardware availability, the required operating system or platform, and the trained personnel to operate these tools. Logistics refers to organizing the required resources for the operation. The administrative aspect is considered separately from logistics as it deals with compliance with various rules and guidelines for undertaking flight missions for aerial photography.

2.3.1. Technological Aspects

Technological complexity is subjective depending on the previous experience of the user. For a more objective assessment, the days of training required for someone who is generally enthusiastic about the technology is used as a proxy for the training needs. The data are generated from available formal training manuals, and the least number of days needed for basic functional engagement with the technology is considered. For example, for drone flying, diploma courses of a few months are available. However, for basic engagement, a two-day course and some hands-on flying experience is a basic necessity. Consequently, 30 days is considered as a proxy for drone flying training needs. For manned aircraft flight, however, flying the plane and managing the aerial imagery tools (Aviatrix system) are two distinct sets of skills. In our case, it was the same person who was the pilot who simultaneously managed the Aviatrix system on board. However, for resource assessment, we have considered the requirement as two trained skillsets. Any time requirement is rounded up to the next full day.

2.3.2. Administrative Aspects

For the administrative assessment, we considered the number of days required to secure the consent of all relevant stakeholders as an indicator of operational requirement. Stakeholders were selected based on the rules and guidelines in place for flying airplanes and drones. The stakeholders included air traffic control authorities, local councils, government organizations, and private owners. The time required for consent was considered as a whole, as the consent process could move simultaneously once initial communication had been established.

2.3.3. Economic Assessment

For the economic assessment, the cost of procuring all the services and equipment was considered. This includes the overall time required in technological, administrative, and logistical fronts for the different flying phases. For recurring monitoring missions, we included the establishment cost in the first mission and only included the resources that were required for any subsequent mission. For a manned aircraft flight, the cost of customization required to equip the airplane for aerial imaging is available from the reporting by the New Zealand Department of Conservation [19]. The lead time required for the customization of the manned aircraft flight is included as the logistics organization time for the first flight as a required investment. The cost of a drone flight is taken from the advertised price of the drone available for sales in New Zealand [26]. For our case, we borrowed the drone from the Department of Conservation's Maukahuka project [27]. The communication required to organize the drone is taken as a substitute for the time required for procuring a drone from the market. No customization was required for the drone itself.

Apart from the quantitative assessments, we used information synthesis on different operational complexities as a qualitative assessment. For example, this would include an assessment of the particular software, which has restricted access or limitations on being used in the field because of the unavailability of a portable platform. Where possible, we have directly compared the resource requirement for the two technologies. The analytical frame used for these analyses is presented in Table 1.

Table 1. Analytical framework for comparing manned aircraft and unmanned flying technologies for aerial photography.

Aspects	Criteria	Data Definition	Analysis	Notes
Technological	Software Hardware Human resources	Availability, accessibility, and complexity No. of personnel;days required to become trained	Qualitative analysis: information synthesis Descriptive statistics and Efficiency measures	Data envelopment analysis (DEA) production frontier analysis is carried out for all aspects Includes trained and untrained personnel required for operation
Logistics	Acquiring and organizing resources Time	Cost (USD) Days	Descriptive statistics and efficiency measures	Includes the cost of ground operations Time required for organizing ground operation
Administrative	Approval/consents	Days	Descriptive statistics and Efficiency measures	Consent stakeholders include organizations and private owners
Economical	Time Money	Total number of days Total money (USD)	Descriptive statistics and Efficiency measures	Includes both preparedness and operational time and money

2.4. Efficiency Measurements and Data Envelopment Analysis (DEA)

For quantitative efficiency assessment, we used Farrell efficiency within the data envelopment assessment (DEA) framework [28,29]. Farrell measures of efficiency are based on proportional changes to input or output, i.e., how much input can proportionally be reduced while maintaining the same output (input efficiency), and with the same amount of input how much can we proportionally increase the productivity (output efficiency) [11]. The input–based Farrell efficiency or just input efficiency, for a technology where input is x and output is y, is defined as

$$Efficiency\ (Input),\ E_i = min\ \{\ E_i > 0\ |\ (E_i x;\ y)\}$$

In other words, it is the maximum proportional reduction of all inputs x that still can produce y amount. An input efficiency measure of 0:7 would indicate that the technology can save 30% off all inputs while producing the same outputs. Similarly, output–based Farrell efficiency or output efficiency is defined as

$$Efficiency\ (Output),\ E_o = max\ \{\ E_o > 0\ |\ (x;\ E_o y)\}$$

In other words, the maximal proportional increment of all outputs y that is possible for a given inputs x. An output efficiency measure of 1:2 suggests that the output can be increased by 20% without any additional input [28]. Simply put, the input efficiency is the actual input divided by the minimum input required, while the output efficiency is the actual output divided by expected output [28]. Again, in general terms, efficiency is measured by output divided by inputs. However, for a set of observed productivity scenario, the efficiency is scaled to the different input sets. The efficiency measure reported here is adjusted through the parameters used in the benchmarking procedure such as free disposability hull, variable returns to scale, decreasing returns to scale, etc. The reported efficiencies here are on a scale of 0 to 1, with 1 being the optimum effi-ciency [28–30].

The non-parametric DEA analysis is a widely used method for comparing production efficiency among different firms using varying technologies [29,31–33]. The chosen frontier type for DEA analysis was FDH+, which is a combination of free disposability hull (FDH) and constant return to scale [28,30]. FDH is a stair-way shaped frontier and the least restrictive on input data [28]. The free disposability implies that increased input results in the same or in higher productivity. The choice of these efficiency measures and frontier analysis is inspired by it being able to be used with low data availability, while being non-parametric requires the least amount of data transformation. The key productivity indicator (KPI) used for efficiency analysis is the number of the image acquired or processed. Area coverage and the desired ground resolution of those images were also included for discussing different aspects of efficiency. Since coarser (numerically higher) ground resolution means lower productivity, multiplicative inverse, or reciprocal of ground resolution, i.e., 1/ground resolution in cm was used in a quantitative analysis of efficiency. To make the fractions an integer, the reciprocal was normalized by multiplying by 100. We used the R package benchmarking [30] for all efficiency measurements and DEA production frontier analysis.

3. Results

3.1. Resource Assessment and Efficiency Measures

3.1.1. Technological

For manned aircraft flight, flight planner pro software was used. The software is licensed to the Department of Conservation. A demonstration version is available only by contacting the company and they also provide orientation and training sessions for the software as needed for any potential customer. Even though this is useful, there are certain challenges to accessing the service, as one must prove genuine intent as a potential buyer. The flight planner is available on PC and can be taken on board the flight with the Aviatrix

system. An Aviatrix trigger box is available on order through aero scientific, which is a more restrictive accessibility than for other platforms available off the shelf.

For UAS, Pix4D software suite was used for flight planning and control of the drone during flight. The suite has software for flight planning and has extensions for operating flights on various platforms. Most of the drone flight planning and flying control interface comes as an application (app) to be used on Android mobiles and Apple iOS. This is convenient during field operation as adjustments and modifications can be easily accommodated. Similar software can be used for image analysis of both manned aircraft and unmanned flights. However, the images that were taken through manned aircraft flights needed to go through GPS geotagging correction as camera GPS tags are not always able to keep up with the image capture rate, and often record the same GPS location for multiple images.

Technologically, manned aircraft and unmanned flights have similar personnel requirements. For the peri-flying phase, the manned aircraft flight would need people trained with two distinct skill sets, whereas unmanned flights can be undertaken by one trained person and one supporting person (Supplementary Materials Table S1) to keep the UAS under constant manual viewing. However, the training needs for the peri-flying phase is much higher for manned aircraft flights than for unmanned flights (Table 2).

Whereas the manned aircraft flights generally have more outputs in terms of images captured or processed (Table 3), the image quality as indicated by ground resolution is higher for UASs (Table 3; Figure 2).

These findings are reflected in the efficiency measures (Table 4) where under technological efficiency, on average, manned aircraft flights are estimated to be about 90% efficient compared to the efficiency of unmanned flights through different flying phases (Table 4). The overall efficiency of the technological aspect for manned aircraft flights was about 76% that of the unmanned flights. The detailed efficiency measures for all the flight missions are included in Supplementary Materials Table S2.

Table 2. Average input across manned aircraft and unmanned aerial missions through their different phases of flying.

| Flying Phase | Flight Type | Technological | | Logistical | | Administrative | Operational | | | Economical | |
		Skillsets (No)	Training (Days)	Days	Cost (US$)	(Days)	Cost (US$)	Execution (Days)	Total Days	Total Cost (US$)	
Pre	Manned	1.00	5.67	3.00	490.00	3.00	700	2.00	13.67	1190.00	
	Unmanned	1.00	3.00	1.67	140.00	4.67	25.67	1.00	10.33	165.67	
Peri	Manned	2.00	117.33	166.67	11,946.67	2.00	3710	1.00	287.00	15,656.67	
	Unmanned	2.00	10.67	5.00	956.67	2.33	700	1.00	19.00	1656.67	
Post	Manned	1.00	10.67	3.67	490.00	1.00	70.00	20.00	35.33	560.00	
	Unmanned	1.00	10.67	1.33	490.00	1.00	32.67	2.33	15.33	522.67	
Overall	Manned	4.00	133.67	172.67	12,926.67	6.00	4480	23.00	335.33	17,406.67	
	Unmanned	4.00	24.33	6.00	1586.67	8.00	758.33	4.33	42.67	2345.00	

Table 3. Outputs and key performance indicators (KPI) for different manned aircraft and unmanned flight missions over the Aparima River.

Flight Missions	Flight Type	Flying Time	Area Coverage (ha)	Ground Resolution: Reciprocal Normalized (Planned cm)	Image Processed (No)
First	Manned	February 2018	974.48	17 (5.8 cm)	223
	Unmanned (South)	October 2020	20.60	125 (0.8 cm)	682
Second	Manned	December 2019	615.63	23 (4.3 cm)	1087
	Unmanned (Central, North)	November 2020	32.18	125 (0.8 cm)	1509
Third	Manned	October 2020	999.24	36 (2.8 cm)	2287
	Unmanned (North)	November 2020	30.81	125 (0.8 cm)	1559
Overall (Average)	Manned	2018–2020	863.12	25.33	1199.00
	Unmanned	2020	27.86	125.00	1250.00

Table 4. Average efficiency of manned and unmanned flights through different flying phases over the Aparima River.

Flying Phase	Flight Type	Average Efficiency			
		Technological	Logistical	Administrative	Economic
Pre	Manned	0.90	0.66	0.71	0.59
	Unmanned	1.00	0.78	0.73	0.75
Peri	Manned	0.90	0.48	0.90	0.39
	Unmanned	1.00	1.00	0.89	0.74
Post	Manned	0.90	0.67	0.90	0.49
	Unmanned	1.00	0.83	1.00	0.71
Overall	Manned	0.76	0.55	0.81	0.39
	Unmanned	1.00	0.88	0.79	0.73

3.1.2. Logistical

The logistics requirement is the highest for the peri-flying phase for both manned aircraft and unmanned flights. However, the logistical requirement, both in terms of time and cost, for manned aircraft flights is noticeably higher than for unmanned flights (Table 4). In terms of efficiency, overall, the manned aircraft flights are on an average 33% less efficient than unmanned flights (Table 4). For the pre- and post-flying phase, the logistics requirements for manned aircraft flights are still higher than for unmanned flights. The lower logistics requirement for UAS makes this more flexible, especially for re-deployments.

3.1.3. Administrative

The administrative input requirement for unmanned flights is higher than for manned aircraft flights, especially for the pre-flying phase (Table 2; Supplementary Materials Table S1). The unmanned flights require consent from any private landowners that have private land within the flight range. This adds to the time required for both planning and flying phases for unmanned flights (Supplementary Materials Table S1). Since flight planning could bypass the subsequent consent requirement, unmanned flights still perform more efficiently than manned aircraft flights on average for the pre-flying phase (Table 4). However, since consent is required each time an unmanned mission is performed it becomes less efficient than a manned aircraft flight. Overall, the administrative efficiency of manned aircraft flights was higher (Table 4).

3.1.4. Economic

From the economic aspect, unmanned flights required considerably lower inputs in terms of time and money throughout all flying phases (Table 2). The same trend is reflected in efficiency measures, and overall, the manned aircraft flights, on average, were about 39% efficient, whereas unmanned flights were 73% efficient (Table 4).

3.2. Re-Deployment of Unmanned Aerial Vehicles (UASs) Following a Flooding Event of the Riverbed

The Aparima River experienced a flooding event in late October 2020. It was immediately after the second UAS mission for acquiring photographs of the Northern end of the project site (Figure 2). Before the weather event, white fronted terns (*S. striata*) were exploring the site for potential colony establishment with an estimated 70 individuals observed in that site for few weeks spanning from September to October, 2020. However, after the weather event, the terns abandoned the site and did not return that summer. This was a good opportunity to assess the changes in the habitat due to the weather event within two weeks of the flooding event in early November. Although detailed image analysis (Figure 3) remains outside the scope of this article, a quick visual inspection reveals erosion of the sandy site as floodwater forced through the riverbed (Figure 3e,f). The ability to rapidly deploy a UAS enabled documentation of the sudden changes in habitat features. This would not have been possible with a manned aircraft flight, given the long period required for logistic requirements.
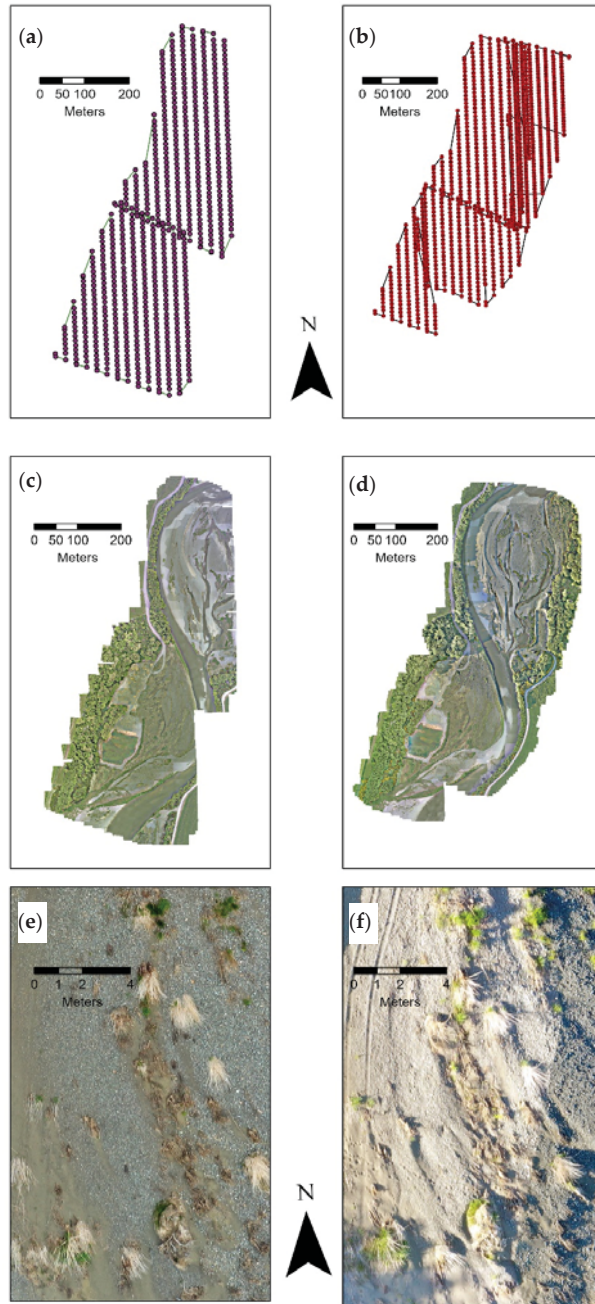
Figure 3. Image mosaics of same site at the Aprima River, New Zealand, before and after a flooding event. Images were acquired with unmanned aerial system (UAS): (**a,b**) show flight path and photo centres of flight missions, respectively, in October 2020 and November 2020; (**c,d**) show the image mosaics; and (**e,f**) are zoomed in subsections of the same area before and after the flooding event occurred in late October 2020 at the site.

3.3. Comparison of Manned Aircraft and Unmanned Flights Through Data Envelopment Productivity Frontier Analysis (DEA)

The DEA frontier analysis shows that across all four aspects of aerial imaging, manned aircraft flights (Figure 4, solid lines) missions had higher productivity potential, i.e., higher output efficiency over unmanned flights (Figure 4, dashed lines). The unmanned flights have lower input requirements indicating the input efficiency of the unmanned flights (Figure 4).
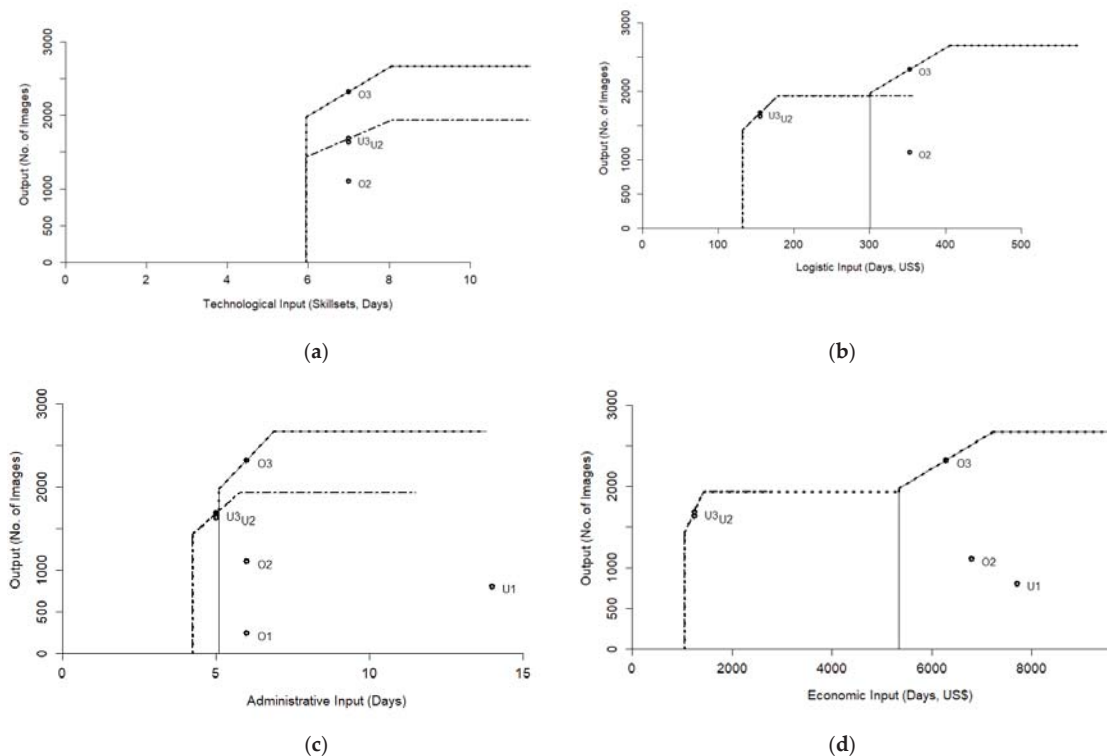
Figure 4. Frontier analysis for different aspects efficiency to compare manned aircraft and unmanned aerial imaging techniques for different flying phases: (**a**) Technological, (**b**) administrative, (**c**) logistical and (**d**) economic; the solid line represents manned aircraft flight production frontier, the dashed line represents unmanned flight production frontier and the dotted line represents the combination of manned aircraft and unmanned flight production frontier. Where the frontier lines cross the *x*-axis indicates the minimum input required for any productivity to occur and the highest y-values the lines reach represents the highest production possible. O1, O2, and O3 are the first, second, and third manned aircraft flights where U1, U2, and U3 are unmanned flights in the same sequence.

Technologically, the manned aircraft and unmanned flights have similar minimum input requirements and manned aircraft flights will have higher productivity given the same inputs (Figure 4a). Unmanned flights need lower inputs for administrative, logistical, and economic components (Figures 2c,d and 4b). However, it is the minimum input requirement (where the frontier crosses the *x*-axis representing inputs) that clearly shows that unmanned flights had much less initial investment and less time required for flight deployments.

4. Discussion

The results indicate that UASs have higher input efficiency, as minimum resource requirement for deploying UASs are lower than that for manned aircraft flights. Results also re-affirm that manned aircraft flights have higher output efficiency in acquiring more images and area coverage than UASs. However, UASs, are performed at a lower height, and usually have improved ground resolution of acquired images. More importantly, UAS missions are much more flexible than manned aircraft flights for subsequent deployment for monitoring dynamic habitats.

4.1. UASs Have Higher Input Efficiency Than Manned Aircraft Flights

The cost of arranging for UAS flights was much lower than for the manned aircraft flights. Moreover, the manned aircraft flights needed further customization to fit cameras and other accessories and therefore required approval from the Civil Aviation Authority [8]. Commercial aerial survey flights usually have these arrangements in place and are not included in the cost-only analysis. However, these requirements added to the pre-flying phase input, especially for the first fight mission of the manned aircraft flights, both in terms of time and money. These inputs are indicative of the technological complexities of the manned aircraft flights.

The manned aircraft flight operation is also much more training intensive than UASs. Flying a manned aircraft flight for aerial photography, where one needs to fly along a pre-planned flight line at a fixed speed, requires a long-term commitment for training and accumulation of flying experience. On the contrary, UAS operations are much easier to learn and implement. With only relatively brief training, project personnel can readily operate a UAS to obtain aerial photographs of the area of interest.

The lower cost of UAS-based aerial photography for a small area is considered one of the reasons for the growing use of UASs in various remote sensing operations [34], including aerial photography for monitoring conservation projects [2]. Apart from investment, UASs are considered safer as there is a lower risk to life and property in an event of an accident [35]. The critical public concern for drone usage is privacy [18] and this is reflected in UAS flying and usage guidelines mandating that consent must be secured from all private landowners and people present within the UAS flying zone. Even though manned aircraft flights could capture high-resolution images of the same area and people, there is no legal requirement for specific consent for image acquisition [36]. Securing flight consent is one notable feature, falling within the administrative category of flight operations, where the input requirements for UASs are higher than for manned aircraft flights. The other aspect where higher input is required for UAS operation is the need for arranging logistics on the ground including finding a secure launching and landing site near the flight path [3]. In all other aspects, UASs have higher input efficiency than manned aircraft flight missions for aerial photography.

4.2. Output Efficiency of Manned Aircraft Flights Are Higher Than UASs for Aerial Photography

Manned aircraft flights have the potential to acquire more images and over a larger area than the UASs during flying missions, because the UASs are restricted by speed and battery power. The ability to acquire and process more images can be translated into larger area coverage or improved ground resolution or to cover the same area in fewer images.

The need for UASs to be always visible to the pilot and co-observer also limits the extent of the flying area from each launching site [3]. The area coverage of manned aircraft flights was significantly higher than the UASs for all three flight missions (Table 3). Accordingly, the average overall cost of manned aircraft flights (US$18.75/ha) was much lower than for UASs (US$104.28). However, for image quantity, the average cost is reversed as the manned aircraft flights cost (US$ 66.81/image) is much higher than for UASs (US$2.97/image). On the other hand, the ground resolution of aerial images taken from UASs is finer (0.8 cm) than that of manned aircraft flights (average 4.3 cm, Table 3). These

contrasting figures highlight the importance of a holistic analysis for comparing new technologies.

The area coverage and ground resolution can be adjusted by flying at different heights according to the intended end use of the aerial images. It is the number of acquired and processed images that is independent of the user's choice or requirement. Therefore, the number of images was considered a key performance indicator (KPI) for frontier analysis. As noted earlier, ground resolution of images acquired from manned aircraft flights can be improved by flying at a lower height. However, there are administrative restrictions on flight heights. For manned aircraft flights in New Zealand, the lowest flight height is set at 304 m above ground level for settlements and 152 m for other areas. A flight plan with lower altitude AGL will need special approval from the Civil Aviation Authority (CAA), New Zealand [37]. Ground resolution of the resultant image can also be lowered or by using a lens of higher focal length. In either case, the field of view for such images will be reduced [8], necessitating more images to be taken to cover the area of interest. Maintaining the image triggering sequence with a shorter time interval between photocentres is challenging, and the potential for missing images also increases. Correcting the GPS tags of these photos can also become challenging as the image timing sequence will likely be shorter than a second and thereby difficult to align with triggering time. On the other hand, the flight restriction for UASs is at the higher height. The highest UASs are permitted to fly in New Zealand is 122 m [38], and there are similar regulations for flying UASs in many countries of the world [39]. Additionally, the safety concern and reaction of wildlife such as birds can limit how low a UAS can be performed [40], putting a cap on the image ground resolution for a given camera setting. In any case, despite the lower ground resolution, the output efficiency of manned aircraft flights remains higher than for UASs in terms of the number of images acquired and by having higher ground coverage.

4.3. High UAS Flexibility for Monitoring Dynamic Ecosystems

The productivity frontier analysis indicates that deploying UASs requires much less time and money than commissioning a manned aircraft flight for an aerial image mission (Figure 4). This input efficiency provides UAS missions with very high flexibility in arranging aerial image missions at short notice. The low cost of procuring a UAS would make the hardware accessible at all times, even at a project level. In contrast, along with the maintenance and other associated costs, procuring a manned aircraft flight on short notice would likely be unrealistic at a project level. As the manned aircraft flights are specialized, even outsourcing the services needs a considerable lead time to secure a slot for the mission. This is a key constraint for monitoring dynamic ecosystems such as braided rivers, where weather events might rapidly change flow regimes and necessitate that monitoring takes place within only a few days, as demonstrated in the case of the Aprima river weather event in October 2020 (Figure 3). UASs have been used for detecting temporal changes in both biotic and abiotic habitat features such as detecting spring phenomenon [18], erosion monitoring [41], etc. The high temporal resolution of image sequences using UASs can also be a key to detecting vegetation changes [42]. Overall, flexibility in re-deployment is key to the temporal flexibility of UASs is a positive attribute of UASs for monitoring dynamic habitats.

Even technologically, drone operations are more flexible than manned aircraft flights, especially for pre- and peri-flying phases. The flexibility comes from the availability of flight planning and operating software suites such as Pix4D, which can be used through everyday platforms such as mobile smartphones. It is also useful to be able to adjust flight plans according to changing field conditions. For our second unmanned mission, due to high winds, we adjusted our mission by slightly reducing the area to conserve the battery power used to stabilize the drone against the wind. Such flexibility for adjusting flight missions in response to local conditions is limited for manned aircraft flight missions.

4.4. Use of Frontier Analysis in Future Research

It would be interesting to assess the efficiency of varying aerial flight mission settings (flight height, camera, and focal length of manned aircraft flights and UASs) through a scenario analysis. In this article, we demonstrated efficiency measure using the number of images as a performance indicator. However, it is possible to use other performance indicators such as ground resolution or area, which are used as outputs. The DEA productivity analytical framework can be used for any such analysis. The productivity frontier draws a general threshold for productivity (minimum input requirement and maximum possible output) and the free disposability allows the input-output observations to move proportionately along that frontier [28,30]. If a mission setting falls under the curve, it is operating at a lower efficiency. Additionally, the frontier analysis is considered better able to handle the difference in scale issue than some other analyses and is used for technological comparison in other fields [29]. With this, researchers and project managers can make use of the DEA productivity frontier analysis for selecting technology and setting for aerial photography missions, including flexibility of re-deployment for frequent monitoring.

5. Conclusions

Management of dynamic ecosystems such as braided riverbeds typically requires monitoring at high frequencies over large spatial extents. We applied an established and easy-to-use method for comparing two aerial imaging technologies to be used for monitoring dynamic braided river habitats. This provides some insight into the field operations of both manned aircraft and unmanned aerial image flight missions and demonstrates a way to make technological choices in research and conservation practice.

We assessed the applicability of aerial photogrammetry for monitoring habitat restoration efforts in the Aparima River, a braided river in Southern New Zealand, and compared the efficacy of using manned aircraft and unmanned aerial vehicles. We found that technologically manned aircraft and unmanned flights have similar efficiency. Even though manned aircraft flights have the potential to cover a larger area, manned aircraft flights are constrained by the need for high initial investment both in terms of money and personnel training. Outsourcing from specialized aerial photography aviation companies can also be costly and will have limited availability due to demands elsewhere. UASs require much less initial investment and it is relatively easy to train project personnel to fly UASs for aerial photography missions. The low lead time required for UAS flying makes them flexible for deployment, which is very critical for monitoring the dynamic braided river habitats.

Ella Sussex for helping as a ground observer for the UAS flights. Clement Lagrue coordinated the UAS flights including ensuring the consents of the different stakeholders involved. We would also like to thank Grant McGregor and Wreys Bush Concrete for support and facilitating groundwork including communication with local landowners. Special thanks to Hugh Robertson and Canterbury Aviation for their services in conducting the manned aircraft flight missions. We are also thankful for the contributions of the three anonymous reviewers and academic editor whose comments have significantly improved the content of this manuscript.

Conflicts of Interest: The authors declare no conflict of interest.

References

1. Coops, N.C.; Goodbody, T.R.H.; Cao, L. Four Steps to Extend Drone Use in Research. *Nature* **2019**, *572*, 433–435. [CrossRef] [PubMed]
2. Koh, L.P.; Wich, S.A. Dawn of Drone Ecology: Low-Cost Autonomous Aerial Vehicles for Conservation. *Trop. Conserv. Sci.* **2012**, *5*, 121–132. [CrossRef]
3. Duffy, J.P.; Cunliffe, A.M.; DeBell, L.; Sandbrook, C.; Wich, S.A.; Shutler, J.D.; Myers-Smith, I.H.; Varela, M.R.; Anderson, K. Location, Location, Location: Considerations When Using Lightweight Drones in Challenging Environments. *Remote Sens. Ecol. Conserv.* **2018**, *4*, 7–19. [CrossRef]
4. Ventura, D.; Bonifazi, A.; Gravina, M.F.; Ardizzone, G.D. Unmanned Aerial Systems (Uass) for Environmental Monitoring: A Review with Applications in Coastal Habitats. *Aer. Robots Aerodyn. Control Appl.* 2017. [CrossRef]
5. Carlson, B.Z.; Hébert, M.; Van Reeth, C.; Bison, M.; Laigle, I.; Delestrade, A. Monitoring the Seasonal Hydrology of Alpine Wetlands in Response to Snow Cover Dynamics and Summer Climate: A Novel Approach with Sentinel-2. *Remote Sens.* **2020**, *12*, 1959. [CrossRef]
6. Long, N.; Millescamps, B.; Guillot, B.; Pouget, F.; Bertin, X. Monitoring the Topography of a Dynamic Tidal Inlet Using UAV Imagery. *Remote Sens.* **2016**, *8*, 387. [CrossRef]
7. Francis, R.J.; Lyons, M.B.; Kingsford, R.T.; Brandis, K.J. Counting Mixed Breeding Aggregations of Animal Species Using Drones: Lessons from Waterbirds on Semi-Automation. *Remote Sens.* **2020**, *12*, 1185. [CrossRef]
8. Burke, C.; Rashman, M.; Wich, S.; Symons, A.; Theron, C.; Longmore, S. Optimizing Observing Strategies for Monitoring Animals Using Drone-Mounted Thermal Infrared Cameras. *Int. J. Remote Sens.* **2019**, *40*, 439–467. [CrossRef]
9. Scholten, C.N.; Kamphuis, A.J.; Vredevoogd, K.J.; Lee-Strydhorst, K.G.; Atma, J.L.; Shea, C.B.; Lamberg, O.N.; Proppe, D.S. Real-Time Thermal Imagery from an Unmanned Aerial Vehicle Can Locate Ground Nests of a Grassland Songbird at Rates Similar to Traditional Methods. *Biol. Conserv.* **2019**, *233*, 241–246. [CrossRef]
10. Havrilla, C.A.; Villarreal, M.L.; DiBiase, J.L.; Duniway, M.C.; Barger, N.N. Ultra-High-Resolution Mapping of Biocrusts with Unmanned Aerial Systems. *Remote Sens. Ecol. Conserv.* **2020**, *6*, 441–456. [CrossRef]
11. Agapiou, A. Vegetation Extraction Using Visible-Bands from Openly Licensed Unmanned Aerial Vehicle Imagery. *Drones* **2020**, *4*, 27. [CrossRef]
12. Rahlf, J.; Breidenbach, J.; Solberg, S.; Næsset, E.; Astrup, R. Digital Aerial Photogrammetry Can Efficiently Support Large-Area Forest Inventories in Norway. *For. Int. J. For. Res.* **2017**, *90*, 710–718. [CrossRef]
13. Wynn, C.R. Drone Technology: Is It Worth the Investment in Agriculture. Ph.D. Thesis, The University of Nebraska, Lincoln, NE, USA, 2019.
14. López-Granados, F.; Torres-Sánchez, J.; Serrano-Pérez, A.; de Castro, A.I.; Mesas-Carrascosa, F.-J.; Peña, J.-M. Early Season Weed Mapping in Sunflower Using UAV Technology: Variability of Herbicide Treatment Maps against Weed Thresholds. *Precis. Agric.* **2016**, *17*, 183–199. [CrossRef]
15. Gray, D.P. Ecological Connectivity in Braided Riverscapes. Ph.D. Thesis, University of Canterbury, Christchurch, New Zealand, 2010.
16. O'Donnell, C.F.J.; Sanders, M.D.; Woolmore, C.B.; Maloney, R. *Management and Research Priorities for Conserving Biodiversity on New Zealand's Braided Rivers*; Department of Conservation: Wellington, New Zealand, 2016; ISBN 978-0-478-15097-1.
17. Piégay, H.; Grant, G.; Nakamura, F.; Trustrum, N. Braided River Management: From Assessment of River Behaviour to Improved Sustainable Development. In *Braided Rivers*; Smith, G.H.S., Best, J.L., Bristow, C.S., Petts, G.E., Eds.; Blackwell Publishing Ltd.: Oxford, UK, 2006; pp. 257–275, ISBN 978-1-4443-0437-4.
18. Berra, E.F.; Gaulton, R.; Barr, S. Assessing Spring Phenology of a Temperate Woodland: A Multiscale Comparison of Ground, Unmanned Aerial Vehicle and Landsat Satellite Observations. *Remote Sens. Environ.* **2019**, *223*, 229–242. [CrossRef]
19. Greene, T.C.; Sprague, R.; Schutter, A.D.; Schurink, C.; Briden, K.; Earl, R. *Use of Aerial Remote Sensing to Detect Pre-Coning Wilding Conifers in a Dry Grassland Environment*; Department of Conservation: Wellington, New Zealand, 2020; ISBN 978-0-9951392-5-1.
20. Joyce, K.E.; Anderson, K.; Bartolo, R.E. Of Course We Fly Unmanned—We're Women! *Drones* **2021**, *5*, 21. [CrossRef]
21. Vergouw, B.; Nagel, H.; Bondt, G.; Custers, B. Drone Technology: Types, Payloads, Applications, Frequency Spectrum Issues and Future Developments. In *The Future of Drone Use: Opportunities and Threats from Ethical and Legal Perspectives*; Custers, B., Ed.; Information Technology and Law Series; T.M.C. Asser Press: The Hague, The Netherlands, 2016; pp. 21–45, ISBN 978-94-6265-132-6.

22. Lopez-Vicente, M.; Lana-Renault, N.; Maria Garcia-Ruiz, J.; Navas, A. Assessing the Potential Effect of Different Land Cover Management Practices on Sediment Yield from an Abandoned Farmland Catchment in the Spanish Pyrenees. *J. Soils Sediments* **2011**, *11*, 1440–1455. [CrossRef]
23. Dash, J.P.; Watt, M.S.; Paul, T.S.H.; Morgenroth, J.; Pearse, G.D. Early Detection of Invasive Exotic Trees Using UAV and Manned Aircraft Multispectral and LiDAR Data. *Remote Sens.* **2019**, *11*, 1812. [CrossRef]
24. Lewis, D.; Phinn, S.; Arroyo, L. Cost-Effectiveness of Seven Approaches to Map Vegetation Communities—A Case Study from Northern Australia's Tropical Savannas. *Remote Sens.* **2013**, *5*, 377–414. [CrossRef]
25. Harvey, P. Exiftool Application Documentation. Available online: https://exiftool.org/exiftool_pod.html (accessed on 25 April 2021).
26. DJI New Zealand—DJI Ferntech Authorised Retail Store in New Zealand. Available online: https://www.ferntech.co.nz/ (accessed on 30 March 2021).
27. Department of Conservation, N.Z. Maukahuka Project Updates. Available online: https://www.doc.govt.nz/our-work/maukahuka-pest-free-auckland-island/maukahuka-updates/ (accessed on 30 March 2021).
28. Bogetoft, P.; Otto, L. *Benchmarking with DEA, SFA, and R*; International Series in Operations Research & Management Science; Springer: New York, NY, USA, 2011; ISBN 978-1-4419-7960-5.
29. Battese, G.E.; Rao, D.S.P.; O'Donnell, C.J. A Metafrontier Production Function for Estimation of Technical Efficiencies and Technology Gaps for Firms Operating under Different Technologies. *J. Product. Anal.* **2004**, *21*, 91–103. [CrossRef]
30. Otto, P.B.; Otto, L. Benchmarking: Benchmark and Frontier Analysis Using DEA and SFA; 2020. R package version 0.29. Available online: https://cran.r-project.org/web/packages/Benchmarking/Benchmarking.pdf (accessed on 30 March 2021).
31. Daraio, C.; Kerstens, K.H.J.; Nepomuceno, T.C.C.; Sickles, R. Productivity and Efficiency Analysis Software: An Exploratory Bibliographical Survey of the Options. *J. Econ. Surv.* **2019**, *33*, 85–100. [CrossRef]
32. Bogetoft, P. *Performance Benchmarking: Measuring and Managing Performance*; Management for Professionals; Springer: New York, NY, USA, 2012; ISBN 978-1-4614-6042-8.
33. Stroobants, J.; Bouckaert, G. Benchmarking Local Public Libraries Using Non-Parametric Frontier Methods: A Case Study of Flanders. *Libr. Inf. Sci. Res.* **2014**, *36*, 211–224. [CrossRef]
34. Boucher, P. Domesticating the Drone: The Demilitarisation of Unmanned Aircraft for Civil Markets. *Sci. Eng. Ethics* **2015**, *21*, 1393–1412. [CrossRef] [PubMed]
35. Sandbrook, C. The Social Implications of Using Drones for Biodiversity Conservation. *Ambio* **2015**, *44*, 636–647. [CrossRef]
36. AskUs | Article | Are Aerial Photographs of My Property a Privacy Issue? | Office of the Privacy Commissioner. Available online: https://privacy.org.nz/tools/knowledge-base/view/489 (accessed on 25 March 2021).
37. Aviation Concerns | Aviation.Govt.Nz. Available online: https://www.aviation.govt.nz/safety/aviation-concerns/ (accessed on 30 March 2021).
38. Intro to Part 101 Rules for Unmanned Aircraft | Aviation.Govt.Nz. Available online: https://www.aviation.govt.nz/drones/rules-and-regulations-for-drones-in-new-zealand/part-101-rules-for-drones/ (accessed on 30 March 2021).
39. Stöcker, C.; Bennett, R.; Nex, F.; Gerke, M.; Zevenbergen, J. Review of the Current State of UAV Regulations. *Remote Sens.* **2017**, *9*, 459. [CrossRef]
40. Mulero-Pázmány, M.; Jenni-Eiermann, S.; Strebel, N.; Sattler, T.; Negro, J.J.; Tablado, Z. Unmanned Aircraft Systems as A New Source of Disturbance for Wildlife: A Systematic Review. *PLoS ONE* **2017**, *12*, e0178448. [CrossRef]
41. Meinen, B.U.; Robinson, D.T. Agricultural Erosion Modelling: Evaluating Usle and Wepp Field-Scale Erosion Estimates Using Uav Time-Series Data. *Environ. Model. Softw.* **2021**, *137*, 104962. [CrossRef]
42. Van Iersel, W.; Straatsma, M.; Addink, E.; Middelkoop, H. Monitoring Height and Greenness of Non-Woody Floodplain Vegetation with UAV Time Series. *ISPRS J. Photogramm. Remote Sens.* **2018**, *141*, 112–123. [CrossRef]

Assessing the Potential of Remotely-Sensed Drone Spectroscopy to Determine Live Coral Cover on Heron Reef

Valerie J. Cornet [1,*] **and Karen E. Joyce** [2]

1   College of Science and Engineering, James Cook University Bebegu Yumba Campus, Townsville, QLD 4811, Australia
2   College of Science and Engineering/TropWATER, James Cook University Nguma-bada Campus, Cairns, QLD 4878, Australia; karen.joyce@jcu.edu.au
*   Correspondence: valerie.cornet@my.jcu.edu.au

Abstract: Coral reefs, as biologically diverse ecosystems, hold significant ecological and economic value. With increased threats imposed on them, it is increasingly important to monitor reef health by developing accessible methods to quantify coral cover. Discriminating between substrate types has previously been achieved with in situ spectroscopy but has not been tested using drones. In this study, we test the ability of using point-based drone spectroscopy to determine substrate cover through spectral unmixing on a portion of Heron Reef, Australia. A spectral mixture analysis was conducted to separate the components contributing to spectral signatures obtained across the reef. The pure spectra used to unmix measured data include live coral, algae, sand, and rock, obtained from a public spectral library. These were able to account for over 82% of the spectral mixing captured in each spectroscopy measurement, highlighting the benefits of using a public database. The unmixing results were then compared to a categorical classification on an overlapping mosaicked drone image but yielded inconclusive results due to challenges in co-registration. This study uniquely showcases the potential of using commercial-grade drones and point spectroscopy in mapping complex environments. This can pave the way for future research, by increasing access to repeatable, effective, and affordable technology.

Keywords: remote sensing; coral reefs; drones; linear unmixing; R; Google Earth Engine

1. Introduction

Coral reefs are some of the most biologically diverse ecosystems on the planet, providing key ecosystem services to coastal communities through tourism, food security, and coastal protection [1]. However, reefs around the world are currently experiencing decline, through mass coral bleaching, ocean acidification, and water quality reduction [2]. Due to both their ecological and economic importance, more accessible and cost-effective methods to map and monitor the decline of coral reefs are needed.

Many monitoring programs have focused on studying reefs locally using in situ field methods [3]. Due to the various difficulties of working in aquatic environments, there is increasing pressure to develop better, wide-scale methods to map and monitor coral reef benthos [4,5]. Collecting data through using remote sensing therefore complements research conducted in the field. By developing more affordable and repeatable methods in remote sensing, research can be made more accessible and efficient. This is particularly useful in locations that are hard to access as the improved capacity to survey remote areas can facilitate repeated monitoring [6]. This can be achieved at broad spatial and temporal scales, using platforms such as drones, aircrafts, or satellites.

Drone-based remote sensing presents a wide array of advantages with regard to local, detailed assessments of study sites. With advances in the technological field over the years, the cost of using drone-mounted sensors has decreased, making consumer-grade drones accessible to many whilst reducing the need for expertise in operating commercial grade

drone technology [7]. Increased battery life has led to increased flight time, and decreased payload weight has made drones lighter and more user friendly [8]. Additionally, on-demand deployment has the advantage of choosing favourable weather conditions for collecting data [9]. Drones provide the benefit of flying under the cloud cover, resulting in greater flexibility in terms of data collection time frames compared to satellites and aircrafts. Furthermore, since external limitations presented by the environment influences the accuracy of benthic mapping studies, reducing the distance between the sensor and the subject reduces atmospheric effects on readings [10]. These combined benefits give drones competitive advantage over other remote sensing platforms.

However, there are disadvantages in using drones that need to be considered as well. Data processing errors often occur within the quantitative analysis and classification steps. As for errors in data collection, these are presented by the sensors and platforms, the classification steps, and the environment. When collecting data with drones, it is important to note that the platform moves. When doing so, attached spectrometers do not always point directly downwards. This means that spectral readings may not always be taken from the area of interest [11]. Errors in data collection from drones may also occur through geopositioning, as the accuracy of the GPS location determined by the drone is not always exact. This is particularly the case in commercial-grade drones, as the inertial navigation systems that measure position information are often of low to medium accuracy to save costs and payload weight [12]. Similar to the inaccuracies present by drones' GPS, in-water validation imagery collected in situ are also subject to spatial inaccuracy. This, along with scale differences in field data justify the difficulties to use field data for direct comparisons to aerial mapping [13].

Mapping and monitoring using remote sensing often relies on being able to accurately record colour or light interactions in the environment [14]. This includes using spectrometers to make measurements of reflection, absorption, and transmission, and finding patterns or 'spectral signatures' that may be unique to features of interest—in this case, live coral, algae, rock, and sand. This information can be collected using imaging spectrometers (e.g., hyperspectral scanners) or with individual point based spectroscopy [14]. Spectroscopy has been used to distinguish between live coral and other coral reef benthos in the past, but these studies have largely been limited to in situ underwater or close-range measurements [15–20]. Capturing data in that way is time intensive and provides limited coverage.

However, drone-based spectroscopy provides the opportunity to extend the coverage, providing a tool for rapid data collection. While other research has documented the potential for using small and lightweight imaging spectrometers on drone platforms (e.g., [21], little work has been done to test the extent to which the more affordable point-based spectrometers can also capture categorical and continuous variable information about the benthos and water column.

In using drones, a major consideration is the influence of the water column and the nature of its influence under different light and environmental conditions, such as waves. With varying depths and water quality, there is likely increased confusion between more spectrally similar classes such as algae and coral due to uneven attenuation throughout spectral signatures [18]. For example, it has been found that with higher chlorophyll or sediment content in the water, more algae will likely be classified as coral [22]. Lee et al. [23] proposed a widely used inversion model that uses diffuse attenuation coefficients as functions of light absorption and scattering. This model was built upon to derive water column properties and water depth, which has been widely used in water column correction [24,25]. Classification of benthic groups was successfully achieved by Goodman and Ustin [24] through combining Lee et al. [25]'s semi-analytical inversion model with linear spectral unmixing, which allowed for the correction of the water column and achieved an overall accuracy of 80% for all substrate groups. BRUCE, a model built upon Lee et al. [25]'s algorithm achieved an overall accuracy of 79% in mapping benthic substrates [26]. However, in

clear, unturbid, and shallow waters under 5 metres, water column correction is not always necessary to capture accurate measurements of the benthos.

This study tests the extent to which consumer-grade drones are capable of providing fine resolution information on coral reefs. This type of data offers a low-cost resource that has the potential to overcome separability issues between classes such as coral and algae, as well as a level of detail and information that cannot be provided by multispectral and RGB data. By using drones, there is the potential to bridge the scale gaps presented between field and satellite-based assessments. Achieving this would help pave the way for future research in the field of remote sensing, as it would demonstrate how accessible technology such as consumer-grade drones and public spectral endmember libraries can be used by anyone. As such, the aim of this study is to quantify the amount of various benthic substrates using drone-based spectroscopy on Heron Reef.

2. Materials and Methods

2.1. Study Site

Data were collected at Heron Reef (23.44° S, 151.91° E), a shallow, lagoonal coral reef located on the Southern end of the Great Barrier Reef, Australia (Figure 1). The shallow depth of the reef and the clear water afforded by its offshore location allow for effective spectral data collection. As it is a lagoonal reef, the depth remains relatively constant across the reef.
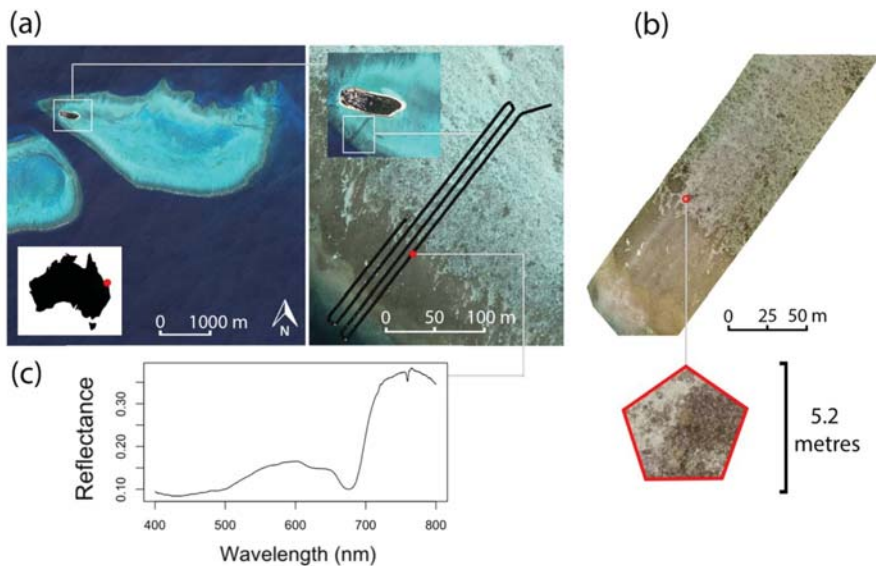
Figure 1. (**a**) Heron Reef study site. Image obtained from Google Earth and shows Heron Island, Heron Reef and the lagoon, along with the primary drone flight used to establish workflow. Drone flight is indicated as a series of black points. Satellite images were obtained from Google Earth. (**b**) Mosaicked RGB image of reef and study area on Google Earth Engine. Note that in Google Earth Engine the creation of completely circular areas is not possible and therefore the use of a pentagon was used to get the closest equivalence for linear unmixing results. (**c**) Example spectrum from drone flight sampled from the high coral cover region of the reef.

2.2. Data Collection

2.2.1. Public Spectral Library

We used a spectral library of known features to calibrate and validate our drone spectroscopy mapping model. For the purpose of this study, we defined the benthic

substrate features of interest (spectral endmembers) as live coral, algae, sand, and rock as these are the most common generalised substrate groups found at the study site [27]. Representative spectra were chosen from the public spectral library of substrata collected in situ on Heron Island in 2006 by Dr. Christian Roelfsema and Dr. Stuart Phinn [28]. The public library consisted of endmember spectra that were recorded at shallow depths using a dive torch as a light source 5 cm away from the subject and a white panel was used as a baseline to calibrate the respective spectrometers. The dark current of the spectrometer (concurrent to the thermal variation) was also accounted for, removing the effects of dark current noise. Recordings of the digital number obtained were converted to reflectance values through the equation below, where dark current is written as Dark, Target refers to the reflectance of the target, and White refers to the reflectance of the white panel:

$$R = \frac{(\text{Target} - \text{Dark})}{(\text{White} - \text{Dark})} \tag{1}$$

2.2.2. Drone Spectroscopy

Spectroscopy data were collected using an Ocean Optics STS-Vis 15° field of view spectrometer, which measured reflectance at bands within the effective spectral range of 350 to 800 nm mounted on a 3DR Solo drone [29]. At a flying altitude of 20 m, this achieved an approximate spectral and spatial resolution of 0.13 nm and 5.2 m, respectively (Figure 2). Point spectroscopy data were collected approximately four times per second and each data point was attributed with the time and coordinates of the drone at the time of capture. The drone was flown up and down adjacent flight paths using a trajectory perpendicular to the shore in order to obtain a cross-reef-flat study area (Figure 1a). Data were calibrated to reflectance using a 99% Spectralon® reference panel (Labsphere) [22]. A Phantom 4 Pro, with an RGB camera also captured photos over the same region for accuracy assessment.
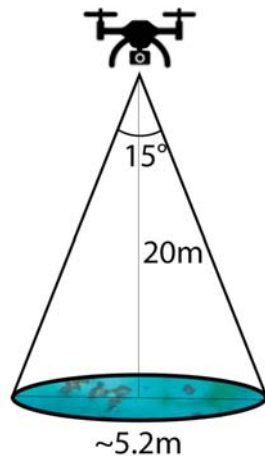
Figure 2. Drone footprint of flight path for spectrometer data collection. Since drone was flown at a constant height of 20 m, a point resolution of approximately 5.2 m diameter was achieved.

2.3. Data Processing

As seen in Figure 3, there are three subsequent steps in the methods tested which are described below. As it relies entirely on running the code written on R and Google Earth Engine, there is no need for expertise regarding commercial software, nor is there the need to obtain licenses for paid software (see Supplementary Materials).
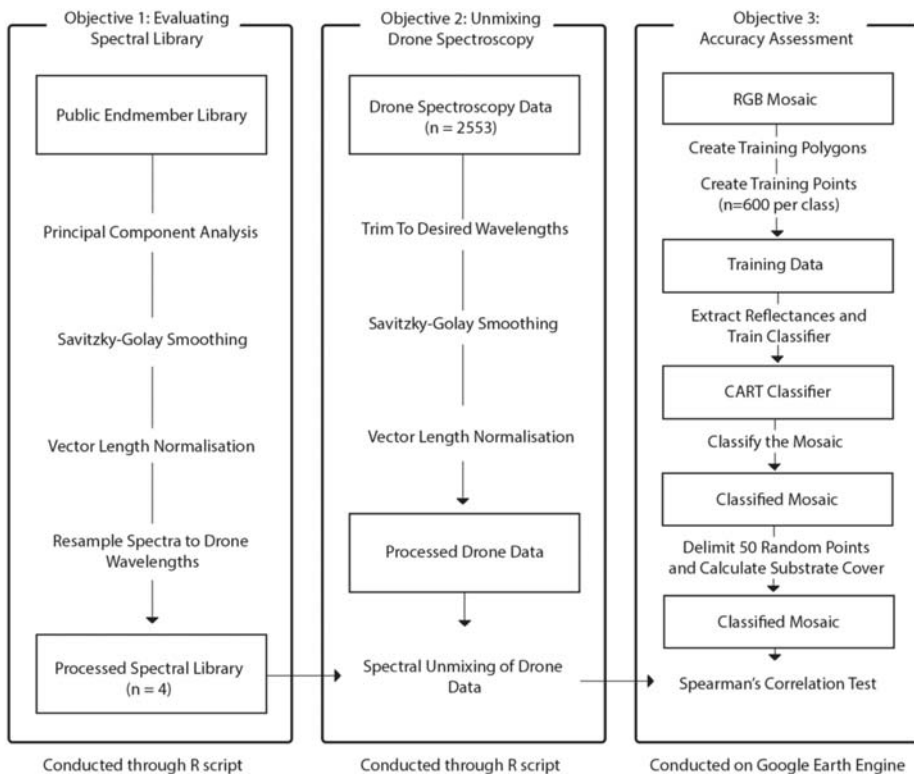
Figure 3. Workflow of the study. Each column represents the workflow to achieve the three objectives. The first column demonstrates the steps to obtain and modify the spectral library from a public database to obtain the four spectra for live coral, sand, algae, and rock. The second column shows the steps to obtain the processed drone data. These two datasets will be used in combination to derive the fractional contributions of each endmember class. The third column shows the steps of the accuracy assessment. The output datasets are shown in boxes and unboxed comments represent the steps for each objective.

2.3.1. Evaluating the Spectral Library

To choose endmember spectra, a principal component analysis (PCA) was conducted on all the endmembers present in the public library [30]. This method to visualise the maximum variation seen between data points has been used in studies proving its use in endmember determination [31]. Spectra that were projected far apart from other substrate classes and within their own substrate class were chosen. Preliminary review comparing spectral signatures to known "pure" endmember signatures was conducted to confirm suitability of the endmember.

Spectra were processed to create the final endmember library of the four substrate classes (Figure 3). Spectra were smoothed through Savitzy–Golay smoothing and normalised for vector length. Vector length normalisation involves calculating the length of reflectance vectors and dividing reflectance values by the vector length [32]. This ensures that a focus is given on the shape of the spectral signatures in the spectral unmixing step rather than the absolute values. Finally, the spectra were tested for collinearity using the detect.lindep()function in R from the plm package [33,34]. There should be no collinearity or linear dependence detected between endmember spectra as this is likely to lead to misclassification.

2.3.2. Evaluating Drone Spectroscopy

A separate endmember library consisting of endmembers sampled from the hyperspectral drone data were created through conducting a principal component analysis of the data and choosing the "purest" endmembers found clustered furthest apart. This was used as a comparison to the public endmember library in order to evaluate the pros and cons of each. Sampling within the studied dataset gives the advantage of providing spectra that will inherently be sourced from the same sensor and in the same environmental conditions. However, the likelihood of providing "pure" spectra is low due to the resolution of the spectroscopy data and the fine scale of spatial heterogeneity of the reef benthos.

Spectral reflectance values of the final endmembers were corrected for through smoothing and normalising in the same manner as the drone data, as explained above. Spectra were then resampled in order to coordinate with the wavelengths sampled in the drone spectroscopy dataset. Resampling was conducted through the resample() function in the spectrolab package using R [33,35]. The algorithm will then be used to separate these endmembers and determine the fractional contribution of each endmember. Through this, live coral cover may be estimated. This section of the workflow was processed in R (Figure 3) [33].

2.3.3. Unmixing Drone Spectroscopy

Spectra were imported into and processed in R in the appropriate format to run the code (columns as wavelengths and rows as individual points) and work through the steps of objective 2 in the workflow (Figure 3) [33]. Prior to the unmixing step, spectra from the drone data were also smoothed using Savitzy–Golay smoothing and normalised, through vector length normalisation [32,36]. Spectra collected by the drone were subset to record reflectance between 400 and 750 nm due to the opaque nature of the water column at wavelengths above and atmospheric scattering below that in the visible spectrum. Data reduction serves in reducing dimensionality of the dataset, which further facilitates algorithm performance, complexity, and data storage [37]. Due to the time limitations presented by the study and the aim of shaping a more accessible, repeatable, and relatively simple workflow, water column was not corrected for using radiative transfer equations. Previous studies have confirmed that classification of reef substrata using the aforementioned spectral range remains possible at depths shallower than six meters, which was the case for this study [38].

A single endmember spectral mixture analysis (SMA) was conducted to unmix endmembers for the hyperspectral data obtained. This was chosen because previous studies, have established its ability to unmix benthic classes, its accessibility of unmixing algorithms, and the lower computational power needed compared to MESMA or non-linear SMAs. Single endmember unmixing functions as a linear unmixing method. This assumes a linear contribution of endmembers to the spectra. This implies that the fractional spatial contribution of an endmember will equal the fractional spectral contribution an endmember will have on a spectrum. Although it is unlikely that the nature of spectral mixing among reef substrata is completely linear, most coral reef benthic studies that have used this method have yielded positive results [20,39]. The lack of perfect linearity in coral reef systems could be explained by the morphologic nature of coral colonies, where spectral reflectance may differ depending on the viewing angle of the colony [40]. This is also important when considering different substrate types overlaying one another. For example, a coral colony may have a dead top that might present as turf algae, whilst the rest of the coral colony below classifies as live coral. Despite this, using a linear unmixing model provides the additional advantage of being less sensitive to collinearity between endmembers [41]. This is useful for this study as live coral spectra and algae spectra are known to be highly similar, resulting in an increased likelihood of estimation errors if a non-linear model is used.

Non-negative and least squares (NNLS) constraints were applied to carry out simultaneous inversion of the data and endmember determination. The inversion step allows the fractional abundances retrieved to be constrained to be non-negative, meaning that all

fractions within a pixel will be positive, rendering the results more realistic over unconstrained methods. The model was not forced to sum to one, to give a better indication of the unexplained spectral contributions by endmembers. If the summed fractional contributions obtained from the linear unmixing step are significantly less than one, this will indicate the inability of the set of endmembers to fully explain the spectral signature of the hyperspectral data point. The linear unmixing algorithm chosen was performed through R using the unmix() function in the package RStoolbox [33,42]. It was chosen as the model implies sparsity within the pixel of certain endmembers, meaning that some endmembers within a hyperspectral pixel can be set to zero. This is important as not all endmembers will necessarily be present in all pixels. NNLS unmixing is also widely used in the field of marine studies due to its simplicity and proven ability to yield more accurate results than unconstrained unmixing [43,44]. In addition, NNLS unmixing also decreases fractional retrieval error over unconstrained methods, especially in waters under 5 m of depth, which was the case for this study's dataset. Previous studies have demonstrated that the highest accuracy of classification occurs when the fractional percentage of the endmembers cover over 25% of the pixel recorded [45]. As coral colonies on Heron Reef can span over an area larger than one pixel (>5 m wide), accurately determining live coral cover using this method is likely.

2.4. Accuracy Assessment

Using RGB/multispectral drone data collected along the same flight paths, an accuracy assessment was conducted. An RGB image was created by mosaicking images collected along the flight path. Live coral cover was estimated for each RGB image through supervised classification using Google Earth Engine, based on the methods of Bennett et al. [13] yielding high classification accuracy of over 85% for live coral. The workflow in this study was modified to suit the format of the dataset and to calculate substrate cover for point sizes comparable to those obtained by drone spectroscopy (Figure 3).

Within the multispectral images, polygons delimiting each substrate class were created to train the classification. The same number of random points across substrate classes were then selected within these polygons to ensure equal sampling and validation of the training data. The Classification and Regression Tree (CART) algorithm was chosen, as the most suitable when compared to Random Forest [46]. To calculate live coral cover, 50 randomly generated corresponding points of overlapping coordinates with the hyperspectral drone data were marked. A pentagonal area of 2.6 m radius was then demarcated for each point and the live coral cover within each area was calculated. This radius was chosen to equate the circular area of the spectral point's 5.2 m diameter. Note that in Google Earth Engine the creation of completely circular areas is not possible and therefore the use of a pentagon was used to get the closest equivalent of linear unmixing results. The accuracy of live coral cover assessment through spectral unmixing was then assessed using a Spearman's correlation test between the measured live coral cover (recorded from the RGB classification) and the percentage values obtained from spectral unmixing. This was also conducted for the substrate classes of algae, rock, and sand. Through conducting the linear spectral unmixing, the root mean square error was also obtained for each endmember for an additional measure of error for each individual endmember.

3. Results

By combining drone spectroscopy data and a public spectral library, linear unmixing of the spectroscopy points collected on the drone flight was achieved. Over 82% of the spectral variance seen in the drone spectroscopy dataset was explained by the chosen endmembers. With statistically significant correlations between live coral, rock, and sand cover derived from the linear unmixing and the RGB classifications, we highlight the potential for using drone spectroscopy in mapping coral reef habitats.

3.1. Evaluating Spectral Libraries

The PCA was conducted on a total of 101 spectra from a public spectral library that were divided into eight substrate classes. There was a lack of distinct clusters for all substrate classes, but with most coral spectra forming a cluster with low scores in the first principal component (Figure 4a). Spectra '56' was chosen as it was projected furthest away from the highest density of algae spectra, with high scores in the first component. The coral spectra chosen was of an Acropora colony, which was deemed appropriate due to the common nature of Acropora in shallow, lagoonal waters, but also specifically at Heron Reef in the area of the data capture [47]. The projections of algae spectra also led to the choice of spectrum '67', which was that of turf algae. This was also deemed appropriate due to turf algae generally being the most abundant algal assemblage found on coral reefs [48,49]. For both sand and bare rock, due to the low number of spectra present in the public spectral library, spectra '80' and '48', respectively were chosen, being positioned away from the other chosen spectra.

The four spectra were normalised, smoothed, and tested for linear dependence, for which results indicated a lack thereof. Spectral signature shapes were compared to known endmember spectra in the literature to validate the likeliness to "pure" spectra. Comparison to the spectra published by Joyce and Phinn [43] confirmed that spectra chosen for the endmember library were suitable (Figure 4b).

3.2. Evaluating Drone Spectroscopy

To challenge the use of public libraries, a PCA was conducted on the drone spectroscopy data to evaluate the potential for endmember extraction within the dataset. As seen in Figure 5i, no clear clusters can be seen, but points were projected across the plot in three directions (a, b, and c). Points projected around "b" and "c" were, respectively situated with low and high scores in the first principal component, whereas points around "a" were projected with high scores in the first and second principal components (Figure 5i). Situating these spectra on a map indicated these represent deep water, coral, and sand (Figure 5ii). This was validated upon further inspection of the spectral signatures, with the deep-water signature showing a characteristic continuous dip in reflectance past 750 nm (Figure 5iii). However, due to the spatial resolution of the drone data (circular area of 5.2 m diameter) and the heterogeneous nature of coral reefs, it was unlikely that the extracted spectra were as "pure" as those obtained from the public spectral library. The difference in spectral signature between the extracted spectra and the public spectral library spectra could also be attributed to endmember heterogeneity, where the extracted endmembers for coral could have represented different species or even bleached corals. Despite some clustering in the plot, it was difficult to confidently extract "pure" algae and rock endmembers, thus reinforcing the advantages of using the public spectral library.

3.3. Unmixing Drone Spectroscopy

A total of 2553 reflectance measurements were unmixed during the spectral unmixing step using the selected endmember library. Spectral unmixing of the drone data using the endmember library created revealed a live coral coverage ranging from 0 to 24% across the drone flight path studied. An increasing coral cover gradient can be observed progressing away from the island (Figure 6a). Similarly, rock cover decreased along the same gradient, but was found in lower density compared to live coral, ranging from 0 to 17% (Figure 6b). Conversely, sand cover is higher on the sandy reef areas with sand cover ranging from 0 to 64%, as expected. Data points where no sand influenced the spectral signatures all coincide with the highly structured section of the reef preceding the reef slope (Figure 6c). Algae showed the greatest range of percentage cover, of 0 to 69%. As seen on Figure 7d, most points displayed a percentage algal cover between 25 and 60%, which is high compared to the other substrate classes.
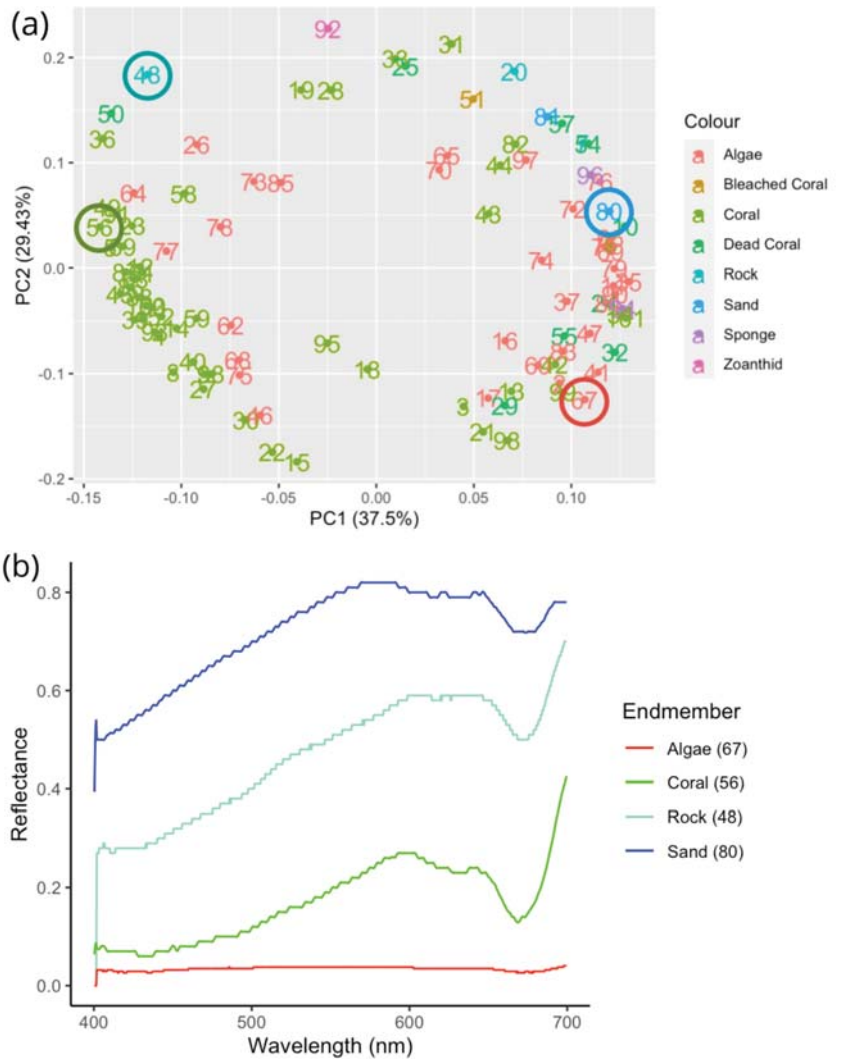
Figure 4. (**a**) Principal component analysis of endmember spectral signatures. Chosen endmembers are circled in green (coral), red (algae), green-blue (rock), and blue (sand). Various other substrate classes are also included from the spectral library but were not included in the formation of the final endmember library. The first principal component accounts for 37.5% of the variation, whilst the second component accounts for 29.43%, indicating a lack of full explanation of variance by the first two principal components. (**b**) Spectral signatures of chosen endmembers. Spectra were all smoothed using Savitzy–Golay smoothing and normalised for vector length.
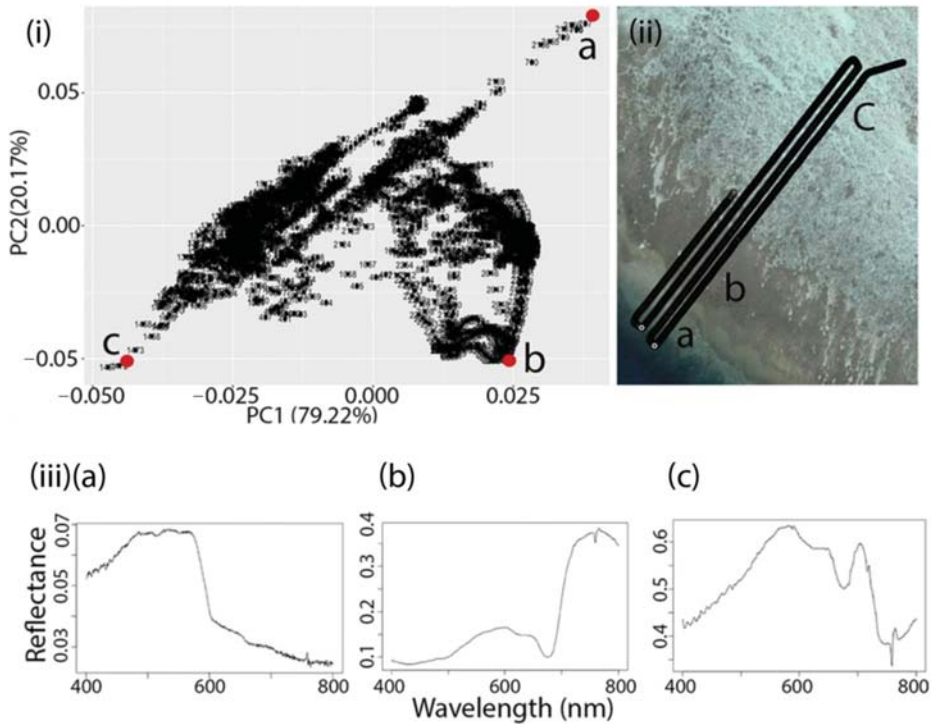
Figure 5. (**i**) Principal component analysis of hyperspectral drone data, (**ii**) Map of drone flight, (**iii**) Spectral signatures of self-sampled spectra. Spectra were chosen from the points that clustered the furthest apart, where "a" is likely to represent deep water, "b" coral, and "c" sand. Note that spectra are unlikely to be pure but serve as the purest spectra within the drone dataset. Axes are not shown to the same scale for better visualisation of spectral trends.
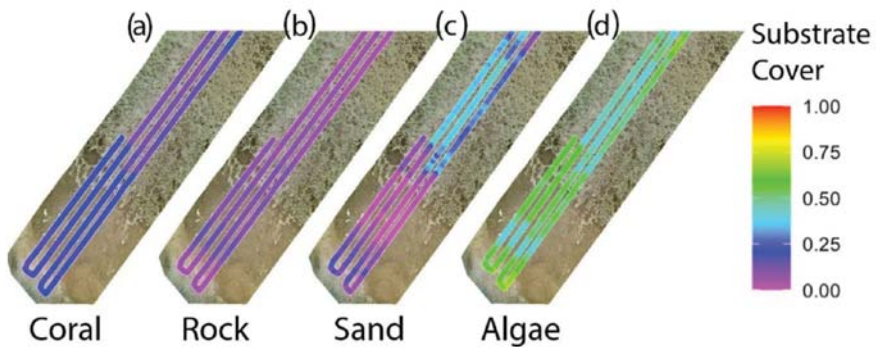
Figure 6. (**a**) Percentage benthic habitat type estimated from linear unmixing using drone spectroscopy: (**a**) Coral, (**b**) rock, (**c**) sand, and (**d**) algae. Results were overlaid on a map of the study area in question. Substrate cover is shown from a scale of 0 to 1. The model yielded an RMSE of 0.00204.
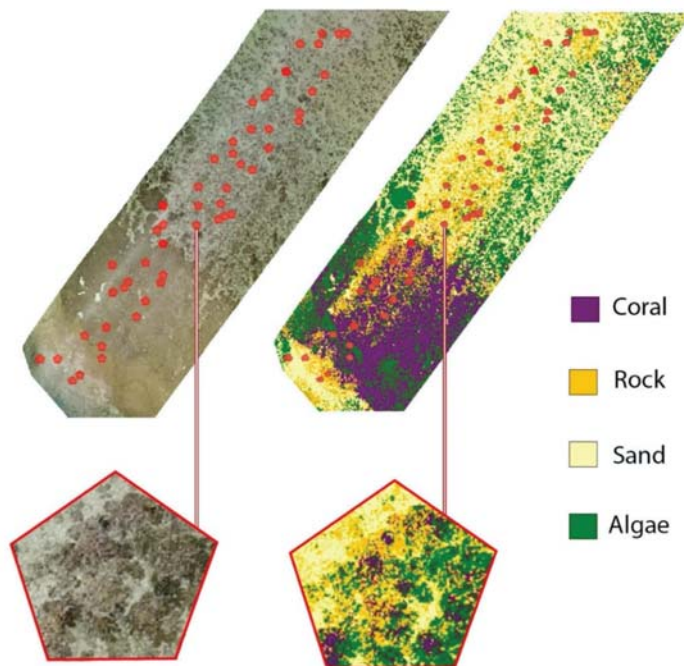
Figure 7. Mosaicked RGB image of the corresponding study region showing the fifty randomly generated pentagons to calculate substrate cover with a classified map of the four substrate classes: coral (purple), rock (orange), sand (yellow), and algae (green).

As fractional contributions of endmembers were not forced to sum to one (100%), the unexplained fractional contributions may be explained by endmembers that were not included in the endmember library, such as species within the same class with variable spectra or completely separate substrate classes such as marine biota or mud. Overall, the summed percentage cover of the four endmembers for all points ranged from 82 to 100%, showing that the endmembers chosen were able to account for at least 82% of the spectral mixing seen within each drone point. Over 78% of data points studied showed total percentages of over 90%. This demonstrates that the use of only four endmembers can produce a relatively representative map.

3.4. Accuracy Assessment

To check the validity of the results, an accuracy assessment was conducted to compare the unmixing results to a classification of fifty polygonal areas (Figure 7). As seen on the classified mosaicked image, the inner reef flat showed the greatest number of pixels being classified as sand. Further towards the crest, algae is the dominant substrate class, with coral and rock substrate types increasing in this area as well (Figure 7).

Retrieving fractional contributions by linear unmixing revealed an unsurprising spatial distribution of the endmembers unmixed. Spearman's correlation tests revealed a significant moderate correlation between live coral cover derived from spectral unmixing and from RGB classification ($r_s = 0.408$, $S = 13085$, $p = 0.00297$) (Table 1). Results estimated a mean live coral cover of 17% and 14%, respectively for the unmixing and RGB classifications. As seen on Figure 8a, this was predominantly the case at low to moderate coral cover (Figure 8a). Although a correlation is seen, in order to better test the correlation between the unmixing results and the RGB classification, a greater range in coral cover would need to be tested.

Table 1. Results of Spearman's correlation test. Significant correlations are highlighted in bold.

Substrate Type	r_s	S	p
Live Coral	0.408	13,085	**0.00297**
Algae	0.115	19,570	0.424
Sand	0.620	8392.8	**1.208×10^{-6}**
Rock	0.505	10,943	**0.000158**
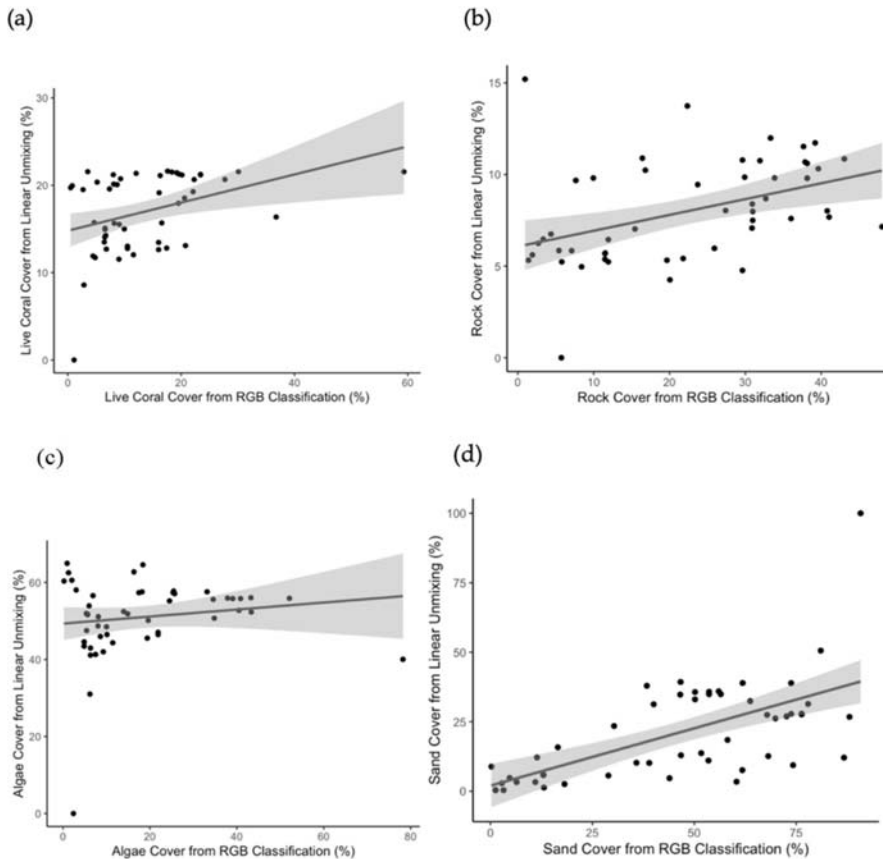
Figure 8. Relationship between substrate cover determined from linear unmixing and from the RGB classification. The black line represents the best fit line and the grey area indicates the 95% confidence interval. (**a**) Regression results for live coral cover, (**b**) Rock cover, (**c**) Algae cover, and (**d**) Sand cover. Axes are not shown to the same scale for better visualisation of individual trends.

Similar to live coral, rock cover yielded a moderate correlation between classification results (r_s = 0.505, S = 10943, p = 0.000158). However, rock cover was underestimated in the linear unmixing process when compared to the RGB classification (Figure 8b). This underestimation may have been the result of misclassification within the accuracy assessment, by falsely classifying other benthic types as rock. Confusion between rock and algae is especially likely due to the difficulties in distinguishing turf algae that may be overgrown on rock or dead coral specimens. This would have resulted in an overestimation of rock in the RGB classification.

On the other hand, algae cover was shown to have a low and insignificant correlation between unmixing and RGB classification results (rs = 0.115, S = 19570, p = 0.424) (Figure 8c). Again, this may be due the inability of distinguishing between turf algae and other benthic groups in the RGB classification, but could also be linked to human error in the training step, being limited by less spectral information and inefficient spatial resolution to confidently classify groups.

Sand classified by linear unmixing had the highest correlation with that obtained from the accuracy assessment, likely meaning that the sand measured is in truth, sand (rs = 0.620, S = 8392.8, p = 1.208 $\times$ 10^{-6}). Sand was underestimated in the linear unmixing process, which could potentially be explained by error in the unmixing step, but also could be attributed to misclassification in the RGB classification (Figure 8d). Sand could have been underrepresented due to the unmixing algorithm detecting spectral influences from other substrate classes such as algae and small biota that may be too small to be visualised with the resolution available from the RGB image. Sand may also be variable in origin, grain size, and mineralogy, and therefore one endmember may not explain the spectral mixing caused by both silicate sand and carbonate sand from bioeroders such as parrotfish and physical erosion.

4. Discussion

4.1. Using Public Spectral Libraries

Successfully using public spectral libraries for these types of analyses encourages mapping efforts by making unmixing studies more accessible (by decreasing the need for field collection of endmembers), as well as opening doors for the facilitation of endmember determination [28]. It is important to note that determining endmembers arguably remains the most crucial step in the spectral unmixing process [50]. Acting as the first step along with the pre-processing of data, minimising error is vital, as error caused from insufficient or unrepresentative endmember selection can propagate errors in all subsequent steps of the analysis.

Despite yielding positive unmixing results, direct improvements to the methods can be achieved in the future through additional selective steps. Choosing endmembers from the PCA plot is the only step that is not automated in the linear unmixing workflow and relies on user choice. Although the endmembers chosen were successful in unmixing the drone spectroscopy points in this study, the methods used in choosing endmembers should be automated to remove bias and ensure repeatability. The method is also flawed in that choosing endmembers that cluster far apart on a PCA plot could lead to the extraction of anomalies, leading to the use of endmembers that are not representative of their substrate class. This stresses the need for standardised endmember determination methods. Examples of methods include endmember determination include iterative endmember selection (IES) or endmember average RMSE (EAR) [50]. Using automated steps such as these will help in standardising the proposed workflow of this study and ensure that the choice of suitable endmembers is statistically backed.

With marine public spectral libraries becoming more accessible and complete, it may be soon possible to find pure spectra with matching sensors and environmental conditions as those collected for individual studies, facilitating the pre-processing step by decreasing the need for extensive normalisation of datasets. In order to achieve this, future data collection methods should aim to standardise methods for collecting spectra for libraries and provide additional information on the factors affecting intra-specific variability, such as developmental stage, tidal position, and bathymetric position [51]. Public databases are commonly used in the fields of mineral exploration and canopy analysis, where organisation and individual researchers have combined efforts to develop shared libraries for a range of different materials, both natural and anthropogenic. To minimise the variation in spectra caused by differences in data collection techniques, various standardisation methods have been proposed, such as continuous wavelet analysis, a form of scaling spectra [52]. By doing this, spectral libraries become increasingly transferrable between

studies and the use of spectra from different libraries can be made possible. Shared public databases such as USGS, SPECMIN, and SPECCHIO also help in identifying the requirements of a spectral library, by using a Database Management System (DBMS) that stores spectral information in relational tables [53]. However, this does not necessarily enforce data integrity, reinforcing the need for standardisation methods during data collection.

4.2. Benthic Distribution on Heron Reef

According to the current Reef Check Australia Health Report of Heron Island, the reef comprises of approximately 37% live coral, similar to the 36% in 2017, the year the drone spectroscopy data were collected [54]. In that year, across 17 sites studied, hard coral cover ranged between 3% and 65%, which is the range within which the unmixed fractional contributions fell within. The highest coral cover was highest at the reef slopes and the lowest on sandy reef flats, which agreed with findings by the Reef Check Report [54]. Although the unmixing results fall within the live coral cover range found by Reef Check, comparing results to monitoring studies must always be done with caution, as these in situ studies often overestimate live coral. This is often the case due to bias in choosing monitoring sites, where the sandy regions tend to be monitored less frequently. Additionally, the findings of this study were based on one single drone flight and therefore may not serve as an accurate representation for the benthic distribution on the rest of Heron Reef. This could explain the slightly lower overall coral coverage yielded by the unmixing at 17% compared to the estimated 37% found by Reef Check.

For algae, a previous study by Roelfsema et al. [55] found that chlorophyll a concentrations found in Heron Reef sediments were among the highest reported for any marine sediments. This was especially the case on the windward side of the reef, which is where the drone data from this study was captured. The sediments sampled were used to quantify benthic microalgal communities [46]. The high levels of benthic microalgae could be a factor explaining the dominance of algae seen in the findings of the spectral unmixing, as the endmember of algae could have extracted the fractional contributions of turf, macro- and microalgae combined. Similarly, this could also explain the low rock cover found through the unmixing process, as rock covered by turf algae is likely to have a spectral signature similar to that of the turf algae endmember used.

4.3. Sources of Error and Potential Improvements

Weak correlations in the accuracy assessment may be attributed to error in the data collection and error in misclassification during data processing. Whilst errors in the data processing generally occur in the quantitative analysis and classification steps, errors in data collection are accumulated through the sensors and platforms, the classification steps, and the water column, as previously mentioned [56]. As this study involved combining three separate datasets, errors produced within collecting or processing of all three need to be considered.

4.3.1. Sources of Error from Sensors and Platforms

As discussed, sources of error from sensors and platforms may arise due to the instability of the moving drone platform and inaccuracies in geopositioning. To avoid this, spectrometers may be attached on a gimbal. However, not all commercial-grade drones have a built-in gimbal and attaching one will add additional weight and cost. Errors in geopositioning present implications for the accuracy assessment step, as matching up the coordinates between the drone spectroscopy data and the mosaicked RGB image will not be exact. This could explain the lack of correlation seen in the accuracy assessment, as spatial inaccuracy, even minimal, can lead to significant changes in substrate cover in a heterogeneous environment. As the spectroscopy data are not in the form of imagery and do not provide spatial context, matching up of data through landmark structures is not possible. This highlights one of the drawbacks of this study's chosen accuracy assessment.

4.3.2. Sources of Error from the Classification Steps

It must be noted that the accuracy assessment used in this study serves as one option to testing accuracy without the need for underwater data collection. The RGB classification in itself presents inaccuracies, as it relies on visual classification by the user and is therefore prone to human error and bias. It is also limited by the amount of spectral information it holds and is more likely to confuse benthic groups such as coral and algae [27]. Therefore, the classification obtained from the linear unmixing has the potential to show higher accuracy compared to that obtained from the RGB image. To improve the RGB classification accuracy, more polygons and points could have been used to train the classifier and sun glint could be added as a substrate group to minimise misclassification. In making sure that we collect data in the most appropriate way in the first place, we minimize artefacts due to sampling and environmental conditions [57]. As this study establishes a protocol where in situ underwater validation was not conducted as part of it, further testing is recommended for future studies to validate this.

As previously discussed, GPS location errors also arise during underwater validation and images collected underwater in situ cannot be compared at the same scale. Efforts to minimise GPS location errors include the use of georeferenced quadrat sampling in estimating benthic cover, combined to underwater photography [13]. However, this would greatly increase data collection effort and does not address the issue of scale. An alternative would be to conduct an accuracy assessment using imagery collected from the same drone and at the same time of drone spectroscopy collection. This would reduce spatial discrepancies between the spectroscopy dataset and the validation data, as both would be collected from the same source. Although this may serve as a credible accuracy assessment, the need to develop more effective methods for validation is highlighted.

Aside from the accuracy assessment, misclassification errors could have occurred in the linear unmixing step. These errors could be linked to inefficient data reduction, the absence of representative endmembers, or the confounding presence of the water column. Studies have found that many of the differences between coral and algae lie between 520 and 580nm and therefore linear unmixing could have been conducted on a dataset where these wavelengths were given a greater weighting [13]. Hochberg et al. [27] used a multivariate stepwise selection procedure to isolate the wavelengths that best differentiate between substrate classes. Spectral feature selection is another method that relies on extracting endmembers that minimise intra-class variability and maximise inter-class variability [58]. These methods remove less meaningful information in the dataset for more efficient classification. Inefficient data reduction could therefore be improved by focusing on wavelengths where diagnostic features of substrate classes can be found, but the disadvantages of losing data must be considered.

Inaccurate estimation of benthic cover could have also occurred in the linear unmixing step by not including certain endmember classes (biota such as holothurians) or not accounting for endmember variability within the analysis [59]. Due to the inherent spectral variation that occurs within and between species of the same class, using one endmember spectra per substrate class leads to an oversimplification of the model that does not incorporate the heterogeneous nature of coral reef habitats [50]. Algae comes in the form of more than turf, with various species of red, brown, green, fleshy and calcareous algae, whereas corals can be classified as bleached, blue, brown or soft/gorgonians, that each differ in spectral signatures [60]. In order to account for spectral variability within endmember classes, previous studies have used averages of various species and yielded a lower overall RMSE.

Alternatively, implementing MESMA instead of single endmember SMA accounts for endmember variability [45,61]. Using MESMA, where different endmember spectra can be chosen depending on the pixel, has shown to yield lower RMSE values in coral reef unmixing studies in the past [62,63]. However, MESMA can also be flawed as it cannot fully incorporate the heterogeneous nature of coral reefs, only choosing one endmember spectra per class in each pixel or point [62]. To evaluate its potential with point spectroscopy data

such as that used in this study, further research should be conducted. Results can then be compared to those from studies in which endmember variability is not accounted for, or where an average signature is used to represent one endmember class.

There are significant biological implications associated with grouping species together within endmember classes or omitting substrate classes. Although some mapping studies may not require the differentiation within algal and coral groups, the use of such proxies for coral reef health could be misleading. Generally, an increase in turf or macroalgae over time can represent a phase shift from coral-dominated to algae-dominated reefs, indicating a decline in reef health as the presence of some algae affects coral recruitment and survival [48]. However, observed increases in crustose coralline algae (a red alga) can instead be an indicator of increasing coral reef health [48,64]. Although this study is a development and test of a workflow that does not include testing biology, it is important to consider for future applications of the technique what biological implications the dataset being used can have.

4.3.3. Sources of Error from the Environment

This study was conducted on a shallow study site, when environmental conditions were good and water quality was high, and therefore it was an optimal study site to test the effectiveness of the workflow in ideal conditions. If this method were to be applied in deeper water, water column correction would be needed. Lee et al. [25]'s algorithm consistently showed improvements in classification accuracy when applied. This should be used to build upon the workflow in this paper, for future studies requiring water column correction. Combining a semi-analytical model with linear unmixing on hyperspectral imagery has been achieved with positive results by Goodman and Ustin [24] and Klonowski et al. [65], demonstrating the potential for using such models on spectroscopy data. It is important to note that water column correction remains a difficult task, explaining the choice to exclude it from this study, for the sake of simplicity in using it for shallow reefs. Nonetheless, through the use of linear unmixing techniques, this workflow serves as a first step towards scaling mapping of hyperspectral point data and can be added to in order to incorporate water column correction.

4.4. Examples of Future Applications

Although accurate measurements have been done using the relatively more affordable RGB data, there are benefits of using data with a greater amount of information. Mapping studies, such as that by Bennett et al. [13] focused on using RGB images to extract substrate cover, instead of spectroscopy, and showed the pros and cons of doing so. Although yielding positive results, the paper highlighted the difficulties in differentiating between certain substrate types such as live coral and rock, where live coral cover estimates are often overestimated due to rock being classified as coral. The reason for the use of spectroscopy in this project was to assess whether the use of a greater number of wavebands within the data would help to differentiate between similar looking substrate classes. In the case of estimating live coral cover, or the cover of other types of substrata, a 1D coverage could be an effective way to obtain estimates whilst ensuring a higher accuracy of classification than provided through the use of RGB images. Using such data can be useful for more sophisticated information extraction purposes in the future.

Although spectroscopy has been shown to successfully help in monitoring live coral cover, it is not limited by this application. Since it provides a way to access complex datasets without the need for extensive expertise in remote sensing, the proposed workflow could be used in various fields such as quantitative mapping, through monitoring bleaching and reef health, without being restricted by the environmental and time limitations offered by a satellite. Joyce and Phinn [66] used hyperspectral imagery to derive chlorophyll content of coral reef substrates. Quantifying pigment concentrations using drones may serve as early warnings for bleaching or health monitoring on the reef for conservation managers. Drone spectroscopy could be further applied to quantitative mapping by quantifying in

situ fluorescence spectra of benthic substrates, which if further tested, could open doors to quantifying photosynthetic potential of the substrata [67]. This gives an indication of applications of drone spectroscopy that need to be tested, which could facilitate monitoring through directly quantifying key variables. Developing this workflow for mapping substrate cover demonstrated a relatively simple application, but helps to present a method that enables a range of other more sophisticated applications. The applications are endless and the simplicity of running the code makes these applications achievable.

5. Conclusions

Overall, using drone spectroscopy data shows promise for mapping benthic cover on Heron Reef. This type of data offers a low-cost resource that has the potential to provide a level of detail and information that cannot be provided by multispectral and RGB data.

The process of determining endmembers in this study was able to account for over 82% of the spectral mixing throughout all spectral measurements collected from a consumer-grade drone and was able to moderately determine the exact fractional contributions of live coral, sand, and rock. Although there still remains the need to further refine current workflows, this method provides an accessible process that can be applied to data collected by affordable technology. Due to this, future research should focus on testing the effectiveness of using drone spectroscopy for specific applications, such as quantitative mapping or detecting coral bleaching. Further recommended steps to improve the study include an automated endmember selection step, bathymetric retrieval, and water column correction.

This highlights the importance of this study, as it can hopefully help further wide-scale research and monitoring programs, not only in highly studied sites, but in remote areas. With the increase in accessibility to both drone hyperspectral data and public spectral libraries, high spectral resolution information will be made available for mapping studies for a range of various research, as the applications for remote sensing are endless.

Conflicts of Interest: The authors declare no conflict of interest.

References

1. Laurans, Y.; Pascal, N.; Binet, T.; Brander, L.; Clua, E.; David, G.; Rojat, D.; Seidl, A. Economic valuation of ecosystem services from coral reefs in the South Pacific: Taking stock of recent experience. *J. Environ. Manag.* **2013**, *116*, 135–144. [CrossRef]
2. Hedley, J.D.; Roelfsema, C.M.; Chollett, I.; Harborne, A.R.; Heron, S.F.; Weeks, S.; Skirving, W.J.; Strong, A.E.; Eakin, C.M.; Christensen, T.R.L.; et al. Remote Sensing of Coral Reefs for Monitoring and Management: A Review. *Remote Sens.* **2016**, *8*, 118. [CrossRef]
3. Page, C.A.; Field, S.N.; Pollock, F.J.; Lamb, J.; Shedrawi, G.; Wilson, S.K. Assessing coral health and disease from digital photographs and in situ surveys. *Environ. Monit. Assess.* **2016**, *189*, 18. [CrossRef] [PubMed]
4. Hochberg, E.J.; Atkinson, M.J.; Andréfouët, S. Spectral reflectance of coral reef bottom-types worldwide and implications for coral reef remote sensing. *Remote Sens. Environ.* **2003**, *85*, 159–173. [CrossRef]
5. Casella, E.; Collin, A.; Harris, D.; Ferse, S.; Bejarano, S.; Parravicini, V.; Hench, J.L.; Rovere, A. Mapping coral reefs using consumer-grade drones and structure from motion photogrammetry techniques. *Coral Reefs* **2017**, *36*, 269–275. [CrossRef]
6. Mumby, P.J.; Skirving, W.; Strong, A.E.; Hardy, J.T.; LeDrew, E.F.; Hochberg, E.J.; Stumpf, R.P.; David, L.T. Remote sensing of coral reefs and their physical environment. *Mar. Pollut. Bull.* **2004**, *48*, 219–228. [CrossRef]
7. Levy, J.; Hunter, C.; Lukacazyk, T.; Franklin, E.C. Assessing the spatial distribution of coral bleaching using small unmanned aerial systems. *Coral Reefs* **2018**, *37*, 373–387. [CrossRef]
8. Tang, L.; Shao, G. Drone remote sensing for forestry research and practices. *J. For. Res.* **2015**, *26*, 791–797. [CrossRef]
9. Hamylton, S.M. Mapping coral reef environments: A review of historical methods, recent advances and future opportunities. *Prog. Phys. Geogr.* **2017**, *41*, 803–833. [CrossRef]
10. Joyce, K.E.; Phinn, S.R.; Roelfsema, C.M. The costs and benefits of image acquisition and pre-processing for coral reef remote sensing. *Backscatter J. Alliance Mar. Rem. Sens.* **2005**, *16*, 23–26.
11. Gurtner, A.; Greer, D.G.; Glassock, R.; Mejias, L.; Walker, R.A.; Boles, W.W. Investigation of Fish-Eye Lenses for Small-UAV Aerial Photography. *IEEE Trans. Geosci. Remote. Sens.* **2009**, *47*, 709–721. [CrossRef]
12. Wang, G.; Zhang, M.; Huang, Y.; Zhang, L.; Wang, F. Robust Two-Dimensional Spatial-Variant Map-Drift Algorithm for UAV SAR Autofocusing. *Remote Sens.* **2019**, *11*, 340. [CrossRef]
13. Bennett, M.K.; Younes, N.; Joyce, K. Automating Drone Image Processing to Map Coral Reef Substrates Using Google Earth Engine. *Drones* **2020**, *4*, 50. [CrossRef]
14. Parsons, M.; Bratanov, D.; Gaston, K.J.; Gonzalez, F. UAVs, Hyperspectral Remote Sensing, and Machine Learning Revolutionizing Reef Monitoring. *Sensors* **2018**, *18*, 2026. [CrossRef]
15. Minghelli-Roman, A.; Chisholm, J.R.; Marchioretti, M.; Jaubert, J.M. Discrimination of coral reflectance spectra in the Red Sea. *Coral Reefs* **2002**, *21*, 307–314. [CrossRef]
16. Caras, T.; Karnieli, A. Ground-level spectroscopy analyses and classification of coral reefs using a hyperspectral camera. *Coral Reefs* **2013**, *32*, 825–834. [CrossRef]
17. Hochberg, E.J.; Atkinson, M.J. Spectral discrimination of coral reef benthic communities. *Coral Reefs* **2000**, *19*, 164–171. [CrossRef]
18. Holden, H.; LeDrew, E. Accuracy assessment of hyperspectral classification of coral reef features. *Geocarto Int.* **2000**, *15*, 7–14. [CrossRef]
19. Joyce, K.E. A method for mapping live coral cover using remote sensing. Ph.D. Thesis, The University of Queensland, Queensland, Austrilia, 2005.
20. Hedley, J.D.; Mumby, P.J.; Joyce, K.E.; Phinn, S.R. Spectral unmixing of coral reef benthos under ideal conditions. *Coral Reefs* **2003**, *23*, 60–73. [CrossRef]
21. Salazar-Vazquez, J.; Mendez-Vazquez, A. A plug-and-play Hyperspectral Imaging Sensor using low-cost equipment. *HardwareX* **2020**, *7*, e00087. [CrossRef]
22. Biggar, S.F.; Labed, J.; Santer, R.P.; Slater, P.N.; Jackson, R.D.; Moran, M.S. Laboratory Calibration Of Field Reflectance Panels. *Recent Adv. Sens. Radiom. Data Process. Remote Sens.* **1988**, *924*, 232–240.
23. Lee, Z.; Carder, K.L.; Mobley, C.D.; Steward, R.G.; Patch, J.S. Hyperspectral remote sensing for shallow waters I A semianalytical model. *Appl. Opt.* **1998**, *37*, 6329–6338. [CrossRef] [PubMed]
24. Goodman, J.A.; Ustin, S.L. Classification of benthic composition in a coral reef environment using spectral unmixing. *J. Appl. Remote Sens.* **2007**, *1*, 011501.
25. Lee, Z.; Carder, K.L.; Chen, R.F.; Peacock, T.G. Properties of the water column and bottom derived from Airborne Visible Infrared Imaging Spectrometer (AVIRIS) data. *J. Geophys. Res. Space Phys.* **2001**, *106*, 11639–11651. [CrossRef]

26. Dekker, A.G.; Phinn, S.R.; Anstee, J.M.; Bissett, P.; Brando, V.E.; Casey, B.; Fearns, P.; Hedley, J.; Klonowski, W.; Lee, Z.P.; et al. Intercomparison of shallow water bathymetry, hydro-optics, and benthos mapping techniques in Australian and Caribbean coastal environments. *Limnol. Oceanogr. Methods* **2011**, *9*, 396–425. [CrossRef]

27. Hochberg, E.J.; Atkinson, M.J. Capabilities of remote sensors to classify coral, algae, and sand as pure and mixed spectra. *Remote Sens. Environ.* **2003**, *85*, 174–189. [CrossRef]

28. Roelfsema, C.; Phinn, S. Spectral reflectance library of selected biotic and abiotic coral reef features in Heron Reef. Pangaea. Data Collection. 2006. Available online: https://doi.pangaea.de/10.1594/PANGAEA.804589 (accessed on 25 October 2020).

29. Burkart, A.; Cogliati, S.; Schickling, A.; Rascher, U. A Novel UAV-Based Ultra-Light Weight Spectrometer for Field Spectroscopy. *IEEE Sens. J.* **2013**, *14*, 62–67. [CrossRef]

30. Bateson, A.; Curtiss, B. A method for manual endmember selection and spectral unmixing. *Remote Sens. Environ.* **1996**, *55*, 229–243. [CrossRef]

31. Andreou, C.; Karathanassi, V. Using principal component analysis for endmember extraction. In Proceedings of the 2011 3rd Workshop on Hyperspectral Image and Signal Processing: Evolution in Remote Sensing, Lisbon, Portugal, 6–9 June 2011; pp. 1–4.

32. Afseth, N.K.; Segtnan, V.H.; Wold, J.P. Raman Spectra of Biological Samples: A Study of Preprocessing Methods. *Appl. Spectrosc.* **2006**, *60*, 1358–1367. [CrossRef]

33. R Core Team. R: A Language and Environment for Statistical Computing. R Foundation for Statistical Computing: Vienna, Austria. 2013. Available online: http://www.R-project.org/ (accessed on 25 October 2020).

34. Croissant, Y.; Millo, G. Panel Data Econometrics inR: TheplmPackage. *J. Stat. Softw.* **2008**, *27*, 1–43. [CrossRef]

35. Meireles, J.; Schweiger, A.; Cavender-Bares, J. Spectrolab: Class and Methods for Hyperspectral Data in R. R package version 0.0.2. 2017. Available online: https://cran.r-project.org/web/packages/spectrolab (accessed on 26 October 2020). [CrossRef]

36. Stevens, A.; Ramirez-Lopez, L. An Introduction to the Prospectr Package. *R Package Vignette*, R Package Version 0.1. 2014. Available online: https://www.researchgate.net/publication/255941339_An_introduction_to_the_prospectr_package (accessed on 26 October 2020).

37. Bioucas-Dias, J.M.; Plaza, A.; Dobigeon, N.; Parente, M.; Du, Q.; Gader, P.; Chanussot, J. Hyperspectral Unmixing Overview: Geometrical, Statistical, and Sparse Regression-Based Approaches. *IEEE J. Sel. Top. Appl. Earth Obs. Remote Sens.* **2012**, *5*, 354–379. [CrossRef]

38. Kutser, T.; Dekker, A.G.; Skirving, W. Modeling spectral discrimination of Great Barrier Reef benthic communities by remote sensing instruments. *Limnol. Oceanogr.* **2003**, *48*, 497–510. [CrossRef]

39. Bajjouk, T.; Mouquet, P.; Ropert, M.; Quod, J.-P.; Hoarau, L.; Bigot, L.; Le Dantec, N.; Delacourt, C.; Populus, J. Detection of changes in shallow coral reefs status: Towards a spatial approach using hyperspectral and multispectral data. *Ecol. Indic.* **2019**, *96*, 174–191. [CrossRef]

40. Joyce, K.E.; Phinn, S.R. Bi-directional reflectance of corals. *Int. J. Remote Sens.* **2002**, *23*, 389–394. [CrossRef]

41. Chen, X.; Chen, J.; Jia, X.; Wu, J. Impact of collinearity on linear and nonlinear spectral mixture analysis. In Proceedings of the 2010 2nd Workshop on Hyperspectral Image and Signal Processing: Evolution in Remote Sensing, Reykjavik, Iceland, 14–16 June 2010; pp. 1–4.

42. Leutner, B.; Horning, N.; Schwalb-Willmann, J. RStoolbox: Tools for Remote Sensing Data Analysis. R package version 0.2.6. 2019. Available online: https://CRAN.R-project.org/package=RStoolbox (accessed on 20 October 2020).

43. Joyce, K.E.; Phinn, S.R. Spectral index development for mapping live coral cover. *J. Appl. Remote Sens.* **2013**, *7*, 073590. [CrossRef]

44. Williams, M.D.; Parody, R.J.; Fafard, A.J.; Kerekes, J.P.; Van Aardt, J. Validation of Abundance Map Reference Data for Spectral Unmixing. *Remote Sens.* **2017**, *9*, 473. [CrossRef]

45. Bell, T.W.; Okin, G.S.; Cavanaugh, K.C.; Hochberg, E.J. Impact of water characteristics on the discrimination of benthic cover in and around coral reefs from imaging spectrometer data. *Remote Sens. Environ.* **2020**, *239*, 111631. [CrossRef]

46. Wicaksono, P.; Aryaguna, P.A.; Lazuardi, W. Benthic Habitat Mapping Model and Cross Validation Using Machine-Learning Classification Algorithms. *Remote Sens.* **2019**, *11*, 1279. [CrossRef]

47. Scopelitis, J.; Andrefouet, S.; Phinn, S.R.; Done, T.J.; Chabanet, P. Coral colonisation of a shallow reef flat in response to rising sea level: Quantification from 35 years of remote sensing data at Heron Island, Australia. *Coral Reefs* **2011**, *30*, 951–965. [CrossRef]

48. Vermeij, M.J.A.; Van Moorselaar, I.; Engelhard, S.; Hörnlein, C.; Vonk, S.M.; Visser, P.M. The Effects of Nutrient Enrichment and Herbivore Abundance on the Ability of Turf Algae to Overgrow Coral in the Caribbean. *PLoS ONE* **2010**, *5*, e14312. [CrossRef] [PubMed]

49. Swierts, T.; Vermeij, M.J. Competitive interactions between corals and turf algae depend on coral colony form. *PeerJ* **2016**, *4*, e1984. [CrossRef]

50. Dennison, P.E.; Roberts, D.A. Endmember selection for multiple endmember spectral mixture analysis using endmember average RMSE. *Remote Sens. Environ.* **2003**, *87*, 123–135. [CrossRef]

51. Olmedo-Masat, O.; Raffo, M.; Rodríguez-Pérez, D.; Arijón, M.; Sánchez-Carnero, N. How Far Can We Classify Macroalgae Remotely? An Example Using a New Spectral Library of Species from the South West Atlantic (Argentine Patagonia). *Remote Sens.* **2020**, *12*, 3870. [CrossRef]

52. Rivard, B.; Feng, J.; Gallie, A.; Sanchez-Azofeifa, A. Continuous wavelets for the improved use of spectral libraries and hyperspectral data. *Remote Sens. Environ.* **2008**, *112*, 2850–2862. [CrossRef]

53. Hueni, A.; Nieke, J.; Schopfer, J.; Kneubühler, M.; Itten, K.I. The spectral database SPECCHIO for improved long-term usability and data sharing. *Comput. Geosci.* **2009**, *35*, 557–565. [CrossRef]

54. Salmond, J.; Loder, J.; Roelfsema, C.; Passenger, J. *Reef Check Australia 2017 Heron Reef Health Report 2017*; Reef Check Foundation Ltd.: Brisbane, Australia, 2017.

55. Roelfsema, C.; Phinn, S.; Dennison, W. Spatial distribution of benthic microalgae on coral reefs determined by remote sensing. *Coral Reefs* **2002**, *21*, 264–274. [CrossRef]

56. Congalton, R.G. Remote sensing and geographic information system data integration: Error sources and research issues. *Photogramm. Eng. Remote Sens.* **1991**, *57*, 677–687.

57. Joyce, K.E.; Duce, S.; Leahy, S.M.; Leon, J.; Maier, S.W. Principles and practice of acquiring drone-based image data in marine environments. *Mar. Freshw. Res.* **2019**, *70*, 952. [CrossRef]

58. Guo, B.; Gunn, S.R.; Damper, R.I.; Nelson, J.D.B. Band Selection for Hyperspectral Image Classification Using Mutual Information. *IEEE Geosci. Remote Sens. Lett.* **2006**, *3*, 522–526. [CrossRef]

59. Williamson, J.E.; Duce, S.; Joyce, K.E.; Raoult, V. Putting sea cucumbers on the map: Projected holothurian bioturbation rates on a coral reef scale. *Coral Reefs* **2021**, 1–11. [CrossRef]

60. Leiper, I.; Phinn, S.; Dekker, A.G. Spectral reflectance of coral reef benthos and substrate assemblages on Heron Reef, Australia. *Int. J. Remote Sens.* **2011**, *33*, 3946–3965. [CrossRef]

61. Hamylton, S. Estimating the coverage of coral reef benthic communities from airborne hyperspectral remote sensing data: Multiple discriminant function analysis and linear spectral unmixing. *Int. J. Remote Sens.* **2011**, *32*, 9673–9690. [CrossRef]

62. Okin, G.S.; Clarke, K.D.; Lewis, M.M. Comparison of methods for estimation of absolute vegetation and soil fractional cover using MODIS normalized BRDF-adjusted reflectance data. *Remote Sens. Environ.* **2013**, *130*, 266–279. [CrossRef]

63. Meyer, T.; Okin, G. Evaluation of spectral unmixing techniques using MODIS in a structurally complex savanna environment for retrieval of green vegetation, nonphotosynthetic vegetation, and soil fractional cover. *Remote Sens. Environ.* **2015**, *161*, 122–130. [CrossRef]

64. Vermeij, M.; Dailer, M.; Smith, C. Crustose coralline algae can suppress macroalgal growth and recruitment on Hawaiian coral reefs. *Mar. Ecol. Prog. Ser.* **2011**, *422*, 1–7. [CrossRef]

65. Klonowski, W.M.; Fearns, P.R.; Lynch, M.J. Retrieving key benthic cover types and bathymetry from hyperspectral imagery. *J. Appl. Remote Sens.* **2007**, *1*, 011505. [CrossRef]

66. Joyce, K.E.; Phinn, S.R. Hyperspectral analysis of chlorophyll content and photosynthetic capacity of coral reef substrates. *Limnol. Oceanogr.* **2003**, *48*, 489–496. [CrossRef]

67. Fux, E.; Mazel, C. Unmixing coral fluorescence emission spectra and predicting new spectra under different excitation conditions. *Appl. Opt.* **1999**, *38*, 486–494. [CrossRef]

The Use of UAVs for the Characterization and Analysis of Rocky Coasts

Alejandro Gómez-Pazo [1,2,*] and Augusto Pérez-Alberti [1,3]

1   CRETUS Institute, University of Santiago de Compostela, 15782 Santiago de Compostela, Spain; augusto.perez@usc.es
2   Departament of Geography, Faculty of Geography and History, University of Santiago de Compostela, 15782 Santiago de Compostela, Spain
3   Departament of Soil Science and Agricultural Chemistry, Faculty of Biology, Campus Vida, University of Santiago de Compostela, 15782 Santiago de Compostela, Spain
*   Correspondence: a.gomez@usc.es

Abstract: Rocky coasts represent three quarters of all coastlines worldwide. These areas are part of ecosystems of great ecological value, but their steep configuration and their elevation make field surveys difficult. This fact, together with their lower variation rates, explains the lower numbers of publications about cliffs and rocky coasts in general compared with those about beach-dune systems. The introduction of UAVs in research, has enormously expanded the possibilities for the study of rocky coasts. Their relative low costs allow for the generation of information with a high level of detail. This information, combined with GIS tools, enables coastal analysis based on Digital Models and high spatial resolution images. This investigation summarizes the main results obtained with the help of UAVs between 2012 and the present day in rocky coastline sections in the northwest of the Iberian Peninsula. These investigations have particularly focused on monitoring the dynamics of boulder beaches, cliffs, and shore platforms, as well as the structure and function of ecosystems. This work demonstrates the importance of unmanned aerial vehicles (UAVs) for coastal studies and their usefulness for improving coastal management. The Galician case was used to explain their importance and the advances in the UAVs' techniques.

Keywords: UAV; rocky coast; Galicia; ecosystems; geomorphic change detection; GIS

1. Introduction

Rocky coasts are of great importance within the global context. This typology occupies three quarters of all coastlines worldwide, and cliff sections are found in 52% of coastal areas at the global level [1,2]. While these environments could be expected to show lower variation rates than other areas, such as sedimentary systems, they have been found to be characterized by a great dynamism [3]. Although many studies have been performed on rocky coasts, the overall research on these areas has been restricted by several limitations, such as spatial and temporal resolution or the relative importance of different erosion factors, which can generate very different shapes with similar values [2].

In Spain, coastal cliffs with slopes greater than 32° represent 21.88% of the total coastal area, and 80% of them have elevations below 100 m. These values are relatively similar in Galicia, where 15.29% of cliffs have slopes greater than 32°, and 6% of them have elevations above 200 m at their highest point [4,5]. In this regard, it is worth highlighting that, since rocky coasts show a wide variability, multiple factors affect and modify their characteristics and determine their evolution. In the case of Galicia, those factors are summarized in Figure 1 [4]. Lithological differences, such as different degrees of fracturing, play a key role in cliff behavior, with different lithological types having higher or lower degrees of vulnerability and different degrees of predisposition to the occurrence of mass movements [6,7] or other erosive processes related to bioerosion [8,9].
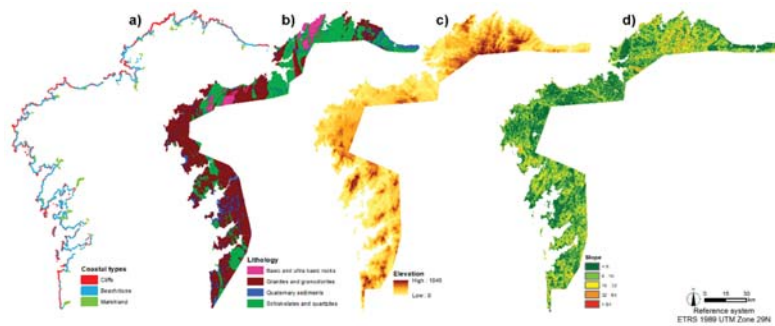
Figure 1. Main characteristics of the Galician coastline. (**a**) Coastal types in Galicia; (**b**) lithology of coastal areas in Galicia; (**c**) elevation of the Galician coast, in meters; and (**d**) slope in the same sector.

Another key element in the behavior of coastal systems is the type of structures associated with cliff toes. In this respect, there is a great diversity, ranging from shore platforms to heterometric boulder accumulations and sedimentary beaches [4]. All these elements determine coastal evolution and must be taken into account for any study related to coastal characterization or dynamic analysis. Moreover, the forms present at a given moment are part of the natural heritage, and this can play a relevant role in coastal evolution [10]. Indeed, in the Galician case, it is necessary to understand the past cold processes in order to explain the current coastal landscape [10].

Other factors add to the slower rates of change; among them, it is worth highlighting the difficulties of access, which have historically led to a lower degree of attention from researchers. Moreover, sedimentary areas have generally been considered more important due to their social and economic relevance, which has promoted their study [11]. This lack of attention to rocky coasts has been clearly evidenced by Naylor et al. [12], who reported an increase in this type of work in recent years, covering a wide variety of environments such as shore platforms [11,13], boulder beaches [14,15], and cliffs [16,17].

In general terms, the first studies on rocky coasts, performed only a few decades ago, focused on describing study areas by analyzing topographic maps and field surveys [18,19]. These works provided a first approach to the landscape of these areas and an interpretation of their possible evolution. Since then, new techniques and devices have been applied to understand the evolution of rocky coasts, among which the following are worth highlighting: TMEM (transverse micro-erosion meters) [11,20–24], TLS (terrestrial laser scanning) [25,26], LiDAR (light detection and ranging) [27–29], hardness testers [30–32], aerial and satellite images [33–36], or sensors as RFID (radio frequency identification) [14,37–39] among others (Figure 2).
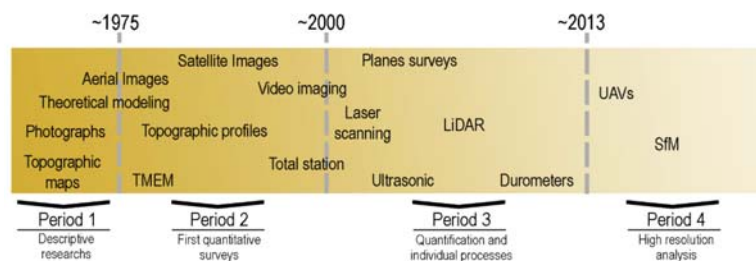
Figure 2. Timeline showing the evolution of research about rocky coasts. The position of the different techniques and methods along the timeline represents the date they were first used to study rocky coasts. Abbreviations: TMEM (transverse micro-erosion meters); LiDAR (light detection and ranging); UAV (unmanned aerial vehicles), and SfM (structure from motion).

This improvement in research on rocky coasts has been related to technical and technological advances (Figure 2), which have partly solved the problems associated with measurements in these areas [40]. This fact can be clearly observed in the above-mentioned references, as well as in the diagram represented in Figure 2. The last decade has seen a great improvement both in research in general and in studies on rocky coasts in particular. This improvement has been related to the increasing number of researchers employing UAVs (unmanned aerial vehicles). These have been applied to different fields, such as vegetation analysis [41] or wildfire research [42]. In the context of coastal research, these devices have gained importance in the last decade, allowing for new works about coastal areas in general [43,44] and rocky areas in particular [13,44–46], without the need for complicated and expensive field surveys. In this sense, it is worth mentioning the study by Pérez-Alberti et al. [47,48], as the first application of UAVs on rocky coasts, in this case boulder beaches, published in [46]. The use of UAVs allowed quantifying topographic variations and current dynamics with a great level of detail and spatial continuity. This fact was often not possible with classic field surveys, such as topographic profiles, or with aerial images, due to their low spatial and temporal resolution. Even in a novel field such as the use of UAVs on rocky coasts, great technical and methodological advances have taken place, from an early period related to photointerpretation of high resolution images [45,46] to more recent works using photogrammetric techniques such as DSM (digital surface models) generated through SfM (structure from motion) techniques, which enhance the possibilities for quantification [3,49–51].

The aim of this research was to emphasize the importance of rocky coasts in general and to analyze how UAVs can improve research about the different environments present in these areas. These allowed for a detailed analysis of the dynamics of boulder beaches, shore platforms, and cliff ecosystems. For this purpose, the results of several studies performed in the last decade using UAVs as a key tool are shown, paying special attention to their methods and results. These investigations summarize the main results obtained in the Galician coast, a sector with a great variability of coastal typologies. These studies allowed understand their usefulness in other sectors with similar characteristics. Moreover, this project provides a review on the evolution of techniques and methodologies applied to the study of rocky coasts and outlines the future of these devices both for general research and for the study of rocky coasts, as a potentially helpful tool for new researchers in rocky coastal environments.

2. Materials and Methods

2.1. Study Areas

This study is included in a project about rocky coast dynamics and evolution in Galicia (NW Iberian Peninsula) started in 2012 and currently ongoing. The first results have been published in communications by Pérez-Alberti. [47,48]. In this case, four sites were selected for measurement and analysis. Their locations are shown in Figure 3, while Figure 4 shows photographs of the four sites.

2.1.1. Oia (Pontevedra)

Oia is located in the SW coast of Galicia. This area has been monitored since 2012 [47,48], and previous works have analyzed variations in a natural boulder beach based on information from UAVs using different techniques. It constitutes one of the first areas analyzed with these vehicles. As described in previous works [3,37,47,48], the boulder beach is approximately 20 m wide and 100 m long. This boulder beach is located at the edge of a shore platform and is limited by two rocky promontories to the north and south. The majority of boulders come from the erosion of the back cliff formed by fluvio-nival deposits in a cold environment more than 40,000 years ago [48]. The beach is composed of heterometric boulders, with the largest ones exceeding 60 cm along their major axis, and it sits at the northern section, while decametric clasts are accumulated in the southern section. The substrate is dominated by intensely fractured two-mica granites. This area shows low

elevations, reaching 8.56 m at the cliff toe, while a major portion of the shore platform and part of the boulder beach belong to the intertidal level (Figure 5a). Figure 5b shows the slopes of this site, which show a great variability that is clearly related to the boulder accumulations that define their landscape.
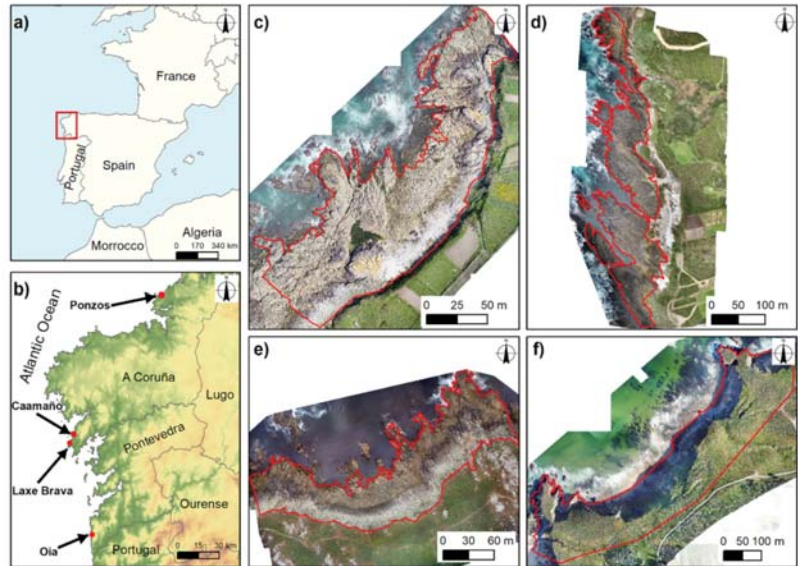
Figure 3. Location of study sites. (**a**) Location of Galicia in Europe; (**b**) location of the study sites (red points) in the western coast of Galicia; (**c**) Oia study site (41.998; −8.879); (**d**) Caamaño shore platform (42.655; −9.041); (**e**) Laxe Brava site (42.598; −9.075); and (**f**) Ponzos cliff site (43.561; −8.254).
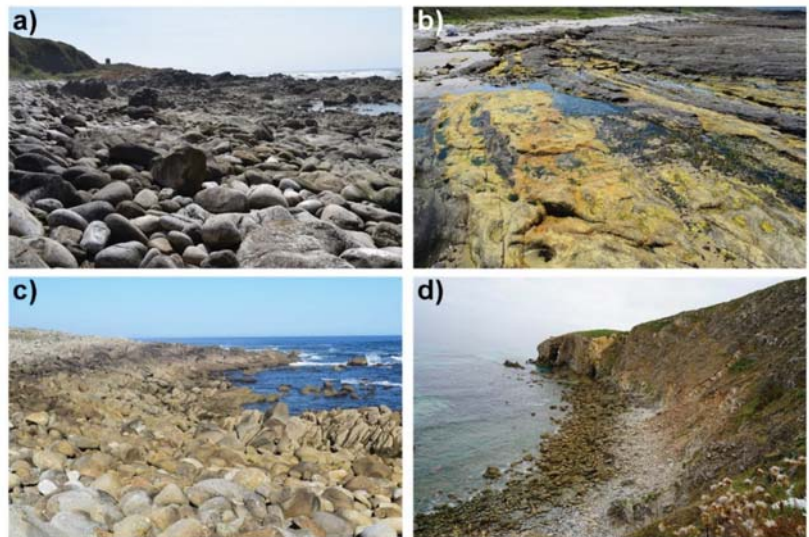
Figure 4. Photographs of study sites. (**a**) Oia boulder beach; (**b**) part of the Caamaño shore platform with its lithological variations; (**c**) Laxe Brava boulder beach; and (**d**) north section of Ponzos cliff site.
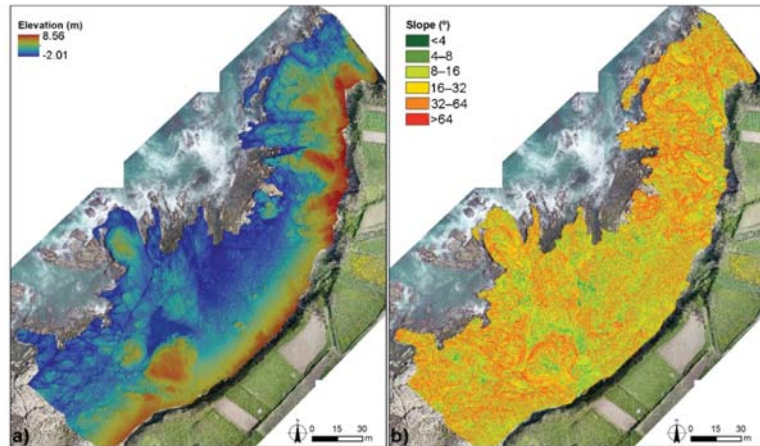
Figure 5. Main characteristics of the Oia site. (**a**) Elevation in meters; (**b**) slope in degrees. Figure adapted from [3].

Oia is located in a mesotidal region, and the beach is exposed to waves from the northwest, the main direction of waves during winter storms, which are of great importance for the dynamics of this site.

2.1.2. Laxe Brava (A Coruña)

The Laxe Brava site includes a boulder beach associated with a 45–65 m wide shore platform. As in the previous case, this area has been studied in detail using UAVs since 2012, and the first results have been published in communications by Pérez-Alberti [47,48]. This area is fully composed of two-mica granites that, as in the case of Oia, are intensely fractured. The origin of boulders in Laxe Brava is the shore platform and its edge, since no cliffs or any other similar forms that could provide boulders to this beach, are present in the continental area. This origin is related to wave action in the foreshore, combined with frost weathering during glacial periods.

Mean boulder size is 66 cm along the major axis. However, some larger boulders, even exceeding 200 cm in some cases, are found especially in the landward zone, where the current marine influence does not activate these boulders, although some larger boulders located in the most dynamic area have been observed to change positions in recent years. Among these large landward-located boulders are other smaller-sized boulders that have been moved during extreme events in the winter.

Figure 6a shows elevation in this area, which is homogeneous in the active boulder area and reaches 20 m in the distal sections of the platform and along the edge of the study site, which protects part of this area from marine influence. As in the previous case, Figure 6b clearly shows boulder distribution based on their contour in the slope map, which becomes smoother in the landward beach zone.

Laxe Brava is located in one of the most energetic coastal sections of the Iberian Peninsula, where waves above 9 m are frequent during winter storms [46]. As in the case of Oia, their orientation is N-NW; thus, the boulder beach is exposed to the main component of storm waves while being partially protected from SW waves by a rocky promontory located west of the accumulation zone.

2.1.3. Caamaño (A Coruña)

Like Laxe Brava, the Caamaño site is located in the Barbanza Peninsula. This site is a large, 600 m-long shore platform facing west. Its width varies between 50 and 120 m. This area does not have a main sedimentary deposit, showing only small areas with clasts

and sediments cemented by iron and accumulated in small hollows, which stand out amid the mostly horizontal shore platform. This platform is dominated by two-mica granites and schists. This lithological variety adds interest to the analysis of this site, since it allows comparing the behavior of these different rock types when subjected to similar erosive factors.
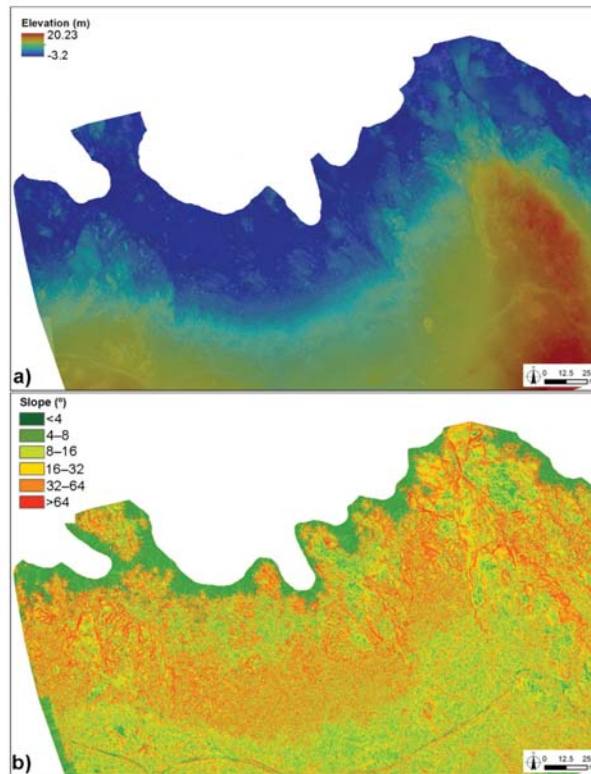
Figure 6. Main characteristics of the Laxe Brava site. (**a**) Elevation in meters; (**b**) Slope in degrees.

Figure 7a shows elevation distribution throughout the entire site. In this case, the shore platform area reaches an elevation of 4 m. The highest values occur in the southern area, while elevation is below 3 m in the rest of the shore platform. As for the slope, major differences were observed between the central section, with lower values, and the edges, with the highest slopes (Figure 7b).

The marine influence in this case is similar to that observed in Laxe Brava, with a great impact of winter storms and waves from the NW. The most relevant differences relative to the previous site is orientation: Caamaño does not directly receive the influence of high waves from the NW.

2.1.4. Ponzos (A Coruña)

Ponzos is a cliff site located in the northwestern coast of Galicia, near the city of Ferrol. This area is characterized by cliffs above 50 m with beaches at their base, related to rocky promontories and with a wide lithological heterogeneity. This variety is composed of schists and biotite–muscovite orthogneisses related to paragneisses with a medium and high degree of metamorphism in the southwest edge, as well as small granite seams near schist areas.
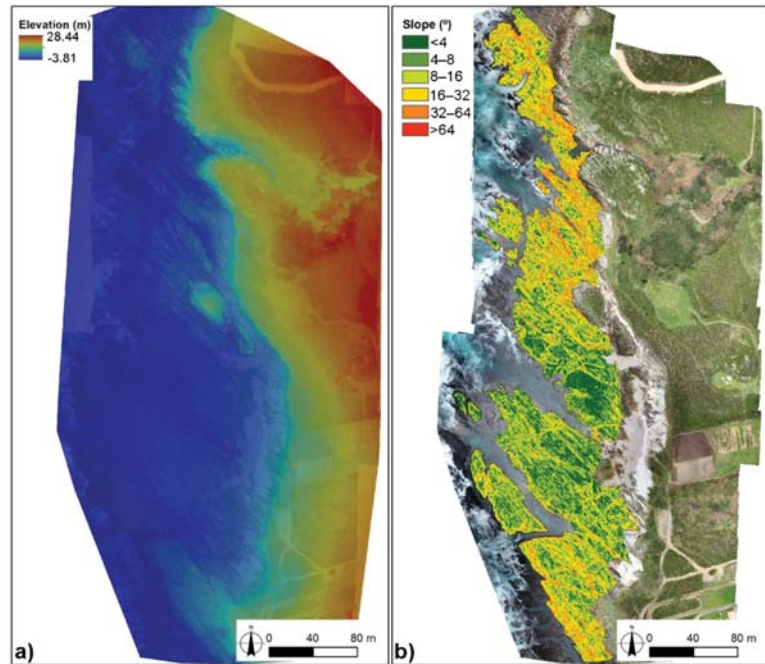
Figure 7. Main characteristics of the Caamaño shore platform. (**a**) Elevation in meters; (**b**) slope in degrees.

In this case, the analysis focused on an 800-m-long section selected as a pilot area to validate different tools for monitoring cliff areas. Figure 8a clearly shows the elevation distribution in this area, with cliffs exceeding 100 m in the central section. Moreover, an analysis of the slopes (Figure 8b) confirmed the wide variety of this zone. These variations are related to the materials accumulated at the cliff toe and to the presence of almost vertical areas, especially in the central section, many of them exceeding 75°.

Ponzos is also located in a high-energy coastline, with a mesotidal level where significant wave height exceeds 5 m for 3.79% of the time during winters. This fact is relevant for the redistribution of materials at the cliff toe and in sedimentary areas in general. Moreover, in order to understand the dynamic of cliffs, it is necessary to take into account that the analyzed section is located in an area where rainfall exceeds 1000 mm/year, with minimum values during the summer.

2.2. Material

All the processes and studies included in this research have as their key element the use of UAVs to characterize and analyze variations in different rocky coasts. It is worth noting that significant changes in UAV devices and associated cameras and in their quality have taken place during the study period. Table 1 summarizes the main characteristics of each flight.
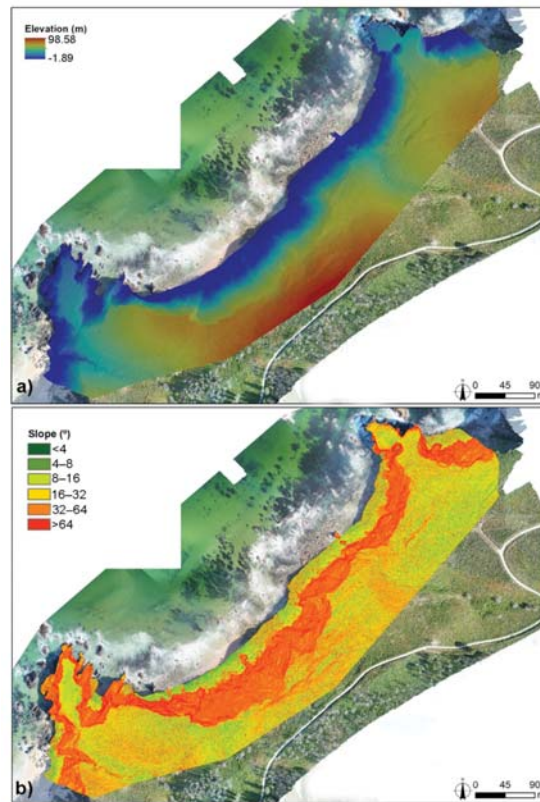
Figure 8. Main characteristics of the Ponzos site. (**a**) Elevation in meters; (**b**) slope in degrees.

Table 1. Dates and main characteristics of the UAV flights analyzed in this study.

Year	Zone	UAV Model	Camera Resolution	Spatial Resolution (cm)
1 July 2012	Oia	Microdrones md4-200	10 MP	1.80
22 July 2012	Laxe Brava	Microdrones md4-200	10 MP	1.50
20 May 2013	Oia	Microdrones md4-200	10 MP	1.50
8 May 2013	Laxe Brava	Microdrones md4-200	10 MP	1.50
28 March 2014	Oia	Microdrones md4-200	17 MP	1.80
9 June 2014	Laxe Brava	Microdrones md4-200	17 MP	1.50
2 March 2015	Caamaño	Microdrones md4-200	17 MP	1.40
23 May 2016	Oia	Microdrones md4-200	20 MP	1.80
5 August 2016	Laxe Brava	Microdrones md4-200	20 MP	1.30
26 May 2016	Ponzos	Microdrones md4-200	20 MP	5.00
11 September 2018	Ponzos	DJI Phantom 4 Pro	20 MP	2.98

2.3. Methods

The process for image acquisition in the study sites is explained in detail in previous publications [3,45,46] and consisted of the placement of GCPs (ground control points) and their positioning through a GPS device, in this case a Stonex S8 GNSS device. These were used to determine the exact position of the acquired images. The flight area was then defined, and routes were created, along with other parameters such as flight elevation, overlap, and the outline of the analyzed section. After completing the flights, the collected information was processed to yield a comprehensive image of the areas of interest through

the generation of a mosaic with UAV photographs and the design of a point cloud to obtain elevation values at each point [45,46].

Once UAV data were processed, various approaches were taken to analyze the areas. First, high-resolution aerial images were used to map the elements present in Oia and Laxe Brava. This approach was based on photointerpretation techniques using ArcGIS (licensed to the USC) to identify variations in the position of thousands of boulders in both sectors [45,46]. This methodology have some problems as the time necessary to mapping all boulders and the uncertainty associated to the person that drawing the boulder contour.

More recent projects have also employed high-resolution images using SfM techniques. This technique was used to generate digital surface models (DSM) to analyze spatial and volumetric variations. based on this information, techniques such as geomorphic change detection (GCD) [52] were applied to identify and quantify differences among several dates, through a raster file with the DEMs of difference (DoD), and to identify the areas with the greater losses or gains during the analyzed period [3,53]. In these analyses a Limit of Detection (LoD) was applied based on the uncertainty of raw data and the processes. This value varied in both sectors, 3.71 cm in Oia and 1.5 cm in Laxe Brava. The uncertainty estimation and its reduction is one of the most important elements to improve these studies.

To characterize shore platforms, high-resolution images and DSMs generated from UAV flights were employed. Photographs were used to distinguish lithologies in the shore platform, while the DSM was used to analyze the elevation, slope, and roughness of these areas. Using both data sources, joints were then traced to analyze platform evolution. In the specific case of Caamaño, this remote information has been complemented with field surveys to identify surface hardness using a durometer (Proceq Equotip 3) [54], thus obtaining a more comprehensive view of the behavior of this site.

In the monitoring of rocky ecosystems, the necessary processes for their correct management are much more costly than in the previous cases in terms of time and resources. As a first approach, variations in the cliff sector were analyzed for two years (2016–2018), detecting mass movements and variations in cliff profiles [52,55]. Moreover, in this case, variations in the cliff top were analyzed to estimate the evolution of the cliff during the aforementioned period using DSAS (Digital Shoreline Analysis System) [55], widely used in coastal studies [56–58]. In this sense, this type of study must be complemented with future field surveys by installing sensors to monitor soil humidity or by analyzing the flora and fauna of each site in order to understand their behavior and importance.

3. Evolution of UAVs Studies in Galician Coast and Their Future

3.1. Boulder Beach Dynamics

Similar methodologies were applied in the two studied boulder beaches in Galicia, ranging from visual analysis between the winters of 2012–2013 and 2013–2014 [45,46], to more quantitative methods such as the analysis of volumetric variations during the 2014–2016 period [3,53]. The analysis of boulder contour in both sectors revealed differences between Oia and Laxe Brava sites (Figure 9c,d).

The first area showed the highest percentage of relocated boulders. This fact is related to the lower size of boulders. However, size by itself is not sufficient to explain the differences, because in some cases, larger boulders moved while smaller ones remained in place. For this reason, it is essential to understand that the beach environment is key to explaining their dynamics, with a great emphasis on the degree of confinement [37]. Boulder groups could have a more reduced movement capacity, while isolated boulders have a greater degree of freedom to move around.

In the case of Laxe Brava, the number of relocated boulders notably increased from 17.5% to 47.8% between the first and second winter. Movements covering the greatest distances were observed in the seaward zone, between 0 and 4 m, and in the eastern section, where mobility increased between 4 and 6 m. In Oia, the movement rate was greater during the winter of 2013–14 (87.6%) than in the previous winter (53.0%). These variations mainly involved boulders between 0.5 and 6 m in diameter and occurred mainly in the central and

northern sections of the study site, far away from the protection of the rocky promontory to the southwest. In both areas, variations were related to the higher frequency of storms during the winter of 2013–14 [59], which promoted boulder mobilization.
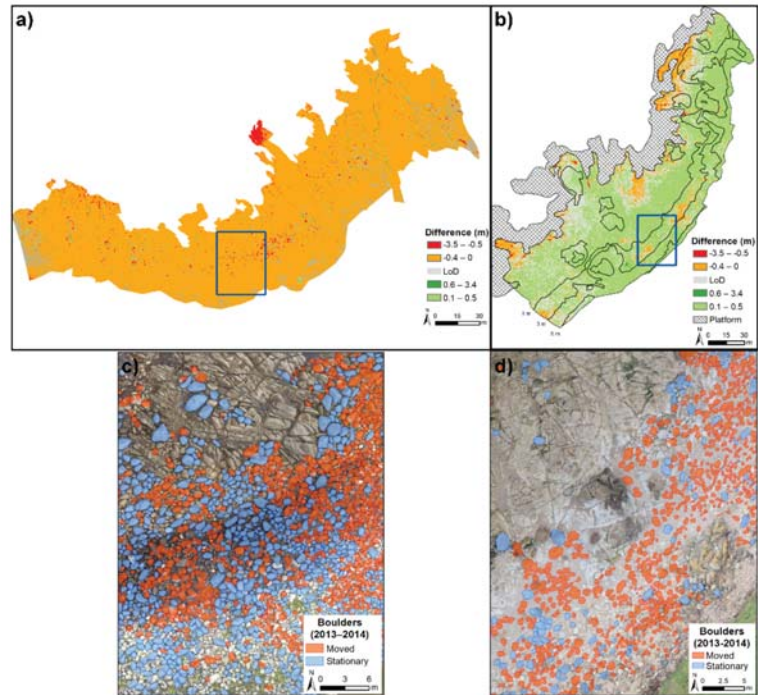
Figure 9. Analysis of spatial variations and variations in boulder position in Laxe Brava and Oia. (**a**) Elevation difference in the Laxe Brava site between 2014 and 2016; the blue polygon represents the area detailed in (**c**); (**b**) variations in elevation in the Oia area during the 2014–2016 period; the blue polygon represents the area detailed in (**d**); (**c**) boulders movement in Laxe Brava during the 2013–2014 period; and (**d**) variations in boulder position in Oia between 2013 and 2014. Figures adapted from [3,45,46,53].

In both areas, boulder movement did not occur individually, but rather occurred in groups; this fact led to important variations in beach profile, which is usually 8°. Greater boulder sizes led to steeper beach profiles and, therefore, more energy would be necessary to initiate movement. In this sense, it is worth noting that waves are not the only factor for boulder mobilization; the hydrostatic overload derived from the water mass arriving to the coast is also important. For this reason, major mobility events must be related to storms and wave height, as well as to tides.

Based on the results obtained with the previous method, DSMs were used, focusing on data from the 2014–2016 period. In Laxe Brava, a decrease in elevation was observed throughout almost the whole analyzed site (97.81%), corresponding to a net volume variation of -5141.32 m^3. Similarly, to Oia, erosion concentrated in the lower section of the beach, while accretion was limited to small areas, especially in the center of the study area.

In the case of Oia, 80% of the area was found to undergo an accretion process, with erosion concentrated in the seaward sector and with lower variations in the southern part, the most protected from winter storms (Figure 9b). For this period, net difference was 1461.07 m^3. The greatest variations occurred in the central section, consistently with findings by previous works [45,46]. The differences in dynamics between both sectors

were very similar to those revealed by previous analyses using aerial images and boulder contours (Figure 9a).

One of the main advantages of the latter technique is the collection of continuous data about spatial variations in both areas. This allowed having a more accurate idea about the dynamics affecting these boulder beaches and improved the quantitative results (Table 2). In this sense, it is necessary to highlight the uncertainty associated with this type of analysis due to the presence of spaces between boulders in rocky environments, which affect accretion/erosion values, and which could not be quantified [3,60].

Table 2. Variations in Laxe Brava and Oia in all the analyzed periods, based on [3,45,46,53].

Period	Laxe Brava	Oia	Technique
2012–2013	17.5%	53.0%	Moved boulders
2013–2014	47.8%	87.6%	Moved boulders
2014–2016	$117.97 \pm 3.26 \text{ m}^3$	$1891.63 \pm 170.13 \text{ m}^3$	Accretion (DoD)
2014–2016	$5259.29 \pm 121.96 \text{ m}^3$	$430.55 \pm 30.75 \text{ m}^3$	Erosion (DoD)

For this type of study, it is necessary to combine these methods with other techniques to improve our understanding of the existing dynamics. In this context, the Oia site has been selected to introduce RFID sensors in recent years. These devices have allowed monitoring the positions of boulders since 2016 and verifying the behavior of this beach as described in the aforementioned studies, therefore leading to a better understanding of their evolutionary dynamics [37].

3.2. Shore Platform Analysis Using UAV Data

The use of UAVs allowed for the detailed characterization of the Caamaño shore platform. This area shows relevant lithological differences between sections dominated by schists and by granites. In this sense, this study revealed that granitic areas form islands with a higher elevation than their surroundings at the lower part of the shore platform. This is related to the greater resistance to erosion displayed by this type of rock. Moreover, this lithology shows higher degrees of roughness and steeper slopes, a fact that can be qualitatively observed in aerial images, as shown in Figure 4.

Figure 10 summarizes the main characteristics of a specific section of the Caamaño shore platform. First, joints were traced due to their key role in understanding platform evolution and analyzing the more erodible areas. These values are closely related to roughness and slope (Figure 10b,d), which explains the importance of taking these variables into account for shore platform characterization. As for elevation, Figure 10c clearly shows hollow areas in the platform and also allows identifying the most resistant materials by the higher elevations with which they appear.

Taking a closer look at lithological differences, this research demonstrated that granites had high roughness values, especially in the upper platform areas (0.44), while values for schists were similar in all areas (0.32–0.37). Using Proceq Equotip 3, resistance was found to be higher for granite (424.89) than for schist (332.22). These values could be related to remote sensing variables. This type of research not only allows for shore platform characterization [15,61], but, thanks to the detailed examination of their future dynamics [13], it can identify differences in behavior among various lithological types and reveal how physical and biological factors can influence their evolution [8].
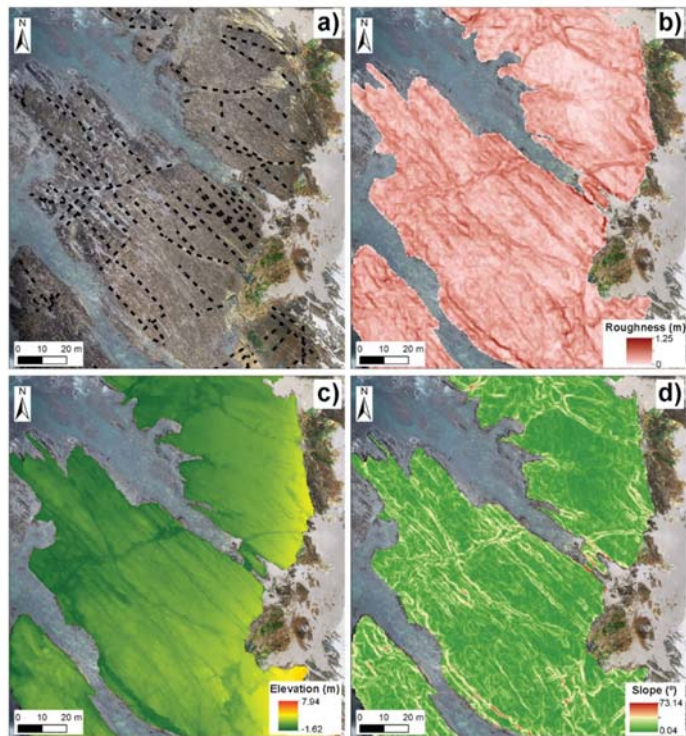
Figure 10. Analyzed parameters in the Caamaño shore platform. (**a**) The main joints are shown black dashed lines; (**b**) roughness in the shore platform section; (**c**) elevation in meters; (**d**) slope of shore platform in degrees.

3.3. Management of Rocky Ecosystems Using UAV Data

Ecosystem characterization and monitoring are key aspects in the field of coastal management. This study provides a first approach to the evolution of a Galician rocky coastal cliff applying photointerpretation and spatial statistic techniques. Nevertheless, this is only one of the necessary elements for this type of research. To describe ecosystems in detail, it is necessary to generate reports about the species, the floristic and faunal composition, and to analyze trace species that indicate a high environmental quality, as well as to characterize soils and of the degree of anthropization [5]. All these parameters require great efforts in terms of field surveys, which must be performed in different seasons and with a specific frequency to understand the evolution of these sectors.

Despite the great usefulness of UAVs, some analyses could be performed through field surveys to thoroughly understand the areas and the species inhabiting them. However, remote sensing information enabled a close analysis of the evolution of mass movements in this area, as well as of the retreat of cliff tops. Both elements are key parameters to understand ecosystem evolution and functionality. The improvement of technologies in the last decades had a great importance in this field, with an important increase in accuracy level [62,63].

In this project, an important dynamism could be observed in the Ponzos site, with major landslides affecting the cliff section and mobilizing more than 4000 m^3 of material in two years (Figure 11). A similar dynamic was observed regarding cliff-top behavior, with a mean retreat of 0.9 m. Other areas found along the coastline are vulnerable to factors such as rock fracturing, sediment accumulation at cliff toes, or rainfall [5]. It is worth emphasizing

the importance of continental factors in the alteration of cliff areas, among which rainfall accumulation is a fundamental element to understanding mass movements [64].
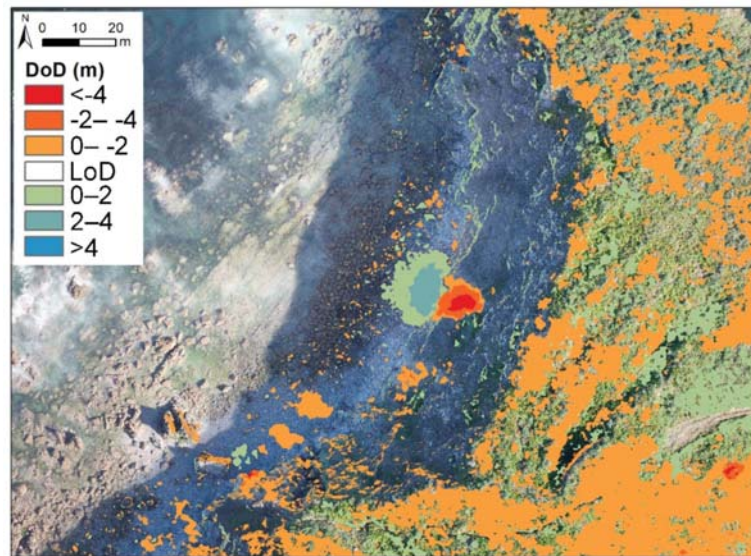
Figure 11. DEMs of difference (DoD) in the Ponzos south section between 2016–2018.

The mass movements occurred in the south sector zone during the analyzed period have been outlined. Other mass movements have previously appeared in this area, and further analyses are required in order to understand their evolution [65]. In this sense, UAVs are a fundamental tool to identify cliff dynamics and, therefore, to improve coastal management thanks to the creation of inventories of the most vulnerable areas [64,66], while avoiding activities that could potentially be dangerous for the area's inhabitants and infrastructures.

UAVs can be extremely useful to estimate vegetation status and soil humidity in this type of research. For these purposes, multiband cameras enable a quantitative approach [67].

3.4. Improvements in Research with the Use of UAVs

The arrival of UAVs to coastal geomorphology research has two main elements. The first, as already mentioned, is related to an improvement in spatial resolution. In addition, the relatively low cost of these devices allows for faster image acquisition and for a more comprehensive temporal coverage in comparison with other technologies such as satellite or aerial images [68–70]. This improvement currently enables detailed analyses of the influence of marine and continental factors on the evolution of rocky areas, thanks to the possibility of surveying study areas between storms or after extreme rainfall events [71,72]. Moreover, in coastal cliffs or steep slopes, other data sources (e.g., satellite or aerial images) do not allow a detailed analysis about their dynamics. In steep zones, the pixel size of these images avoids the variations identification.

The application of UAVs to geomorphological studies and, more generally, to studies about ecosystem behavior did not initially target rocky coasts, nor are these the most relevant areas in this field. Nowadays, multiple studies have used UAVs to monitor sedimentary systems [73,74], vulnerable areas as coastal lagoons [75], saltmarshes [76], mangroves [77], estuaries [78], and other coastal areas that require detailed analysis [79–81], as well as in the general coastal context [68,73].

All the aforementioned sectors had been previously studied, but the technical advances associated with UAVs have improved the time series and have allowed acquiring better and more accurate qualitative data at mesoscale. These facts have allowed expanding the knowledge about the natural environment in general and about rocky coasts in particular.

3.5. The Future of UAVs in Coastal Research

Based on the number of projects generated in the last decade and on their relevance, it is clear that the increase in coastal research using UAVs will continue to follow a positive trend in the near future. The wide possibilities of their associated methodologies, together with fast data acquisition and low costs, have promoted their use, especially in sectors where field surveys are not easy to perform either due to costs or to other factors.

It is worth emphasizing the importance of combining the information obtained through UAVs with other data to improve results and generate better and more accurate explanations about coastal evolution. In line with this, it is worth emphasizing the combined use of instruments such as durometers in shore platforms, which, together with DSM analysis, can expand our knowledge about these areas and their evolution. In the case of Oia, the information acquired by the flight was merged with data obtained by other techniques, such as RFID sensors, to determine the directions and measure the distances of boulder movements. This combination of information from different sources helps to understand the variations observed in DSMs [37].

Moreover, as has been observed in other fields such as in wildfire research [82], UAVs are likely to constitute a key tool to monitor coastal environments in the future. They could play an important role in improving coastal management projects by updating the actions applied in protected spaces and other sensitive areas according to variations related to global change. It is precisely in relation to global change and its consequences where UAVs could be of great importance to analyze how alterations in physical factors could impact the territory.

In relation to the aforementioned, research carried out on cliffs, shore platforms, and boulder beaches has revealed the importance of understanding soil temperature and humidity for rock alteration processes, particularly at the start of mass movements in cliff areas. For this reason, multiband sensors in UAVs could be immensely useful to monitor sectors such as Ponzos during heavy rainfall periods. The use of multispectral sensors is a logical evolution that will allow analyzing seasonal variations in vegetation, as well as soil characteristics, such as humidity or other physicochemical parameters, to understand landscape evolution in detail [67,83,84].

4. Conclusions

This study shows the importance of UAVs for rocky coastal research. These instruments have allowed for a detailed analysis of the dynamics affecting rocky coasts.

The associated methodologies allowed confirming the high dynamism of rocky areas, such as boulder beaches, by measuring variations in the position of elements or volumetric differences. These studies allow comparing near sectors to understand the factors controlling their dynamics and explain the possible differences (e.g., the behavior in Oia and Laxe Brava during the same period).

The use of UAVs combined with other techniques is of enormous value to expand the knowledge about rocky coasts. As previously observed, their combination with field surveys in accessible areas is of crucial importance for a correct environmental characterization. Clear examples of this are shore platforms, where the relation with durometer values allows a more realistic approach to the platform characteristics, and boulder beaches, where currently the use of UAVs are related to RFID sensors. This combination improves the knowledge about the boulders displacements.

The techniques employed, as well as the uncertainty associated with these analyses, could be improved in the future by increasing processing capabilities and by performing

more studies using similar techniques. In this sense, the application of multispectral cameras could greatly impact our understanding of coastal areas.

The use of UAVs for ecosystem monitoring and coastal management is expected to increase in the future within the context of global change. These devices allow an accurate characterization of land uses and ecosystems distribution.

References

1. Bird, E.C.F. *Coastal Geomorphology: An Introduction*, 2nd ed.; John Wiley & Sons: Chichester, UK, 2008; ISBN 9780470723968.
2. Young, A.P.; Carilli, J.E. Global distribution of coastal cliffs. *Earth Surf. Process. Landf.* **2019**, *44*, 1309–1316. [CrossRef]
3. Gómez-Pazo, A.; Pérez-Alberti, A.; Trenhaile, A. Recording inter-annual changes on a boulder beach in Galicia, NW Spain using an unmanned aerial vehicle. *Earth Surf. Process. Landf.* **2019**, *44*, 1004–1014. [CrossRef]
4. Perez-Alberti, A.; Gomez-Pazo, A. The Rocky Coasts of Northwest Spain. In *The Spanish Coastal Systems*; Springer: Berlin/Heidelberg, Germany, 2019; pp. 27–47. ISBN 9783319931692.
5. Aranda, M.; Gracia, F.J.; Pérez-Alberti, A. *Selección y Descripción de Variables que Permitan Diagnosticar el Estado de Conservación del Parámetro 'Estructura y Función' de los Diferentes Tipos de Hábitat Costeros*; Ministerio para la Transición Ecológica: Madrid, Spain, 2019.
6. Marques, F. Regional Scale Sea Cliff Hazard Assessment at Sintra and Cascais Counties, Western Coast of Portugal. *Geosciences* **2018**, *8*, 80. [CrossRef]
7. Del Río, L.; Gracia, F.J.; Benavente, J. Mass Movements and Cliff Retreat along the SW Spanish Coast. *J. Coast. Res.* **2009**, *SI*, 717–721.
8. Naylor, L.A.; Coombes, M.A.; Viles, H.A. Geomorphology Reconceptualising the role of organisms in the erosion of rock coasts: A new model. *Geomorphology* **2012**, *157–158*, 17–30. [CrossRef]
9. Naylor, L.A.; Viles, H.A.; Carter, N.E.A. Biogeomorphology revisited: Looking towards the future. *Geomorphology* **2002**, *47*, 3–14. [CrossRef]
10. Pérez-Alberti, A.; Blanco-Chao, R.; Vázquez, M.; Valcárcel, M. Dinámica y evolución de las costas rocosas. El ejemplo de Galicia. In *Geomorfología Litoral. Procesos Activos*; de Andrés, J.R., Gracia, F.J., Eds.; ITGME. Ministerio de Ciencia y Tecnología: Madrid, Spain, 1999; pp. 175–185.
11. Trenhaile, A.S. The effect of Holocene changes in relative sea level on the morphology of rocky coasts. *Geomorphology* **2010**, *114*, 30–41. [CrossRef]
12. Naylor, L.A.; Stephenson, W.J.; Trenhaile, A.S. Rock coast geomorphology: Recent advances and future research directions. *Geomorphology* **2010**, *114*, 3–11. [CrossRef]
13. Swirad, Z.M.; Rosser, N.J.; Brain, M.J. Identifying mechanisms of shore platform erosion using Structure-from-Motion (SfM) photogrammetry. *Earth Surf. Process. Landf.* **2019**, *44*, 1542–1558. [CrossRef]
14. Hastewell, L.; Inkpen, R.; Bray, M.; Schaefer, M. Quantification of contemporary storm-induced boulder transport on an intertidal shore platform using radio frequency identification technology. *Earth Surf. Process. Landf.* **2020**, *45*, 1601–1621. [CrossRef]
15. Perez-Alberti, A.; Trenhaile, A.S.; Pires, A.; Lopez-Bedoya, J.; Chamine, H.I.; Gomes, A. The effect of boulders on shore platform development and morphology in Galicia, north west Spain. *Cont. Shelf Res.* **2012**, *48*, 122–137. [CrossRef]
16. Mancini, F.; Castagnetti, C.; Rossi, P.; Dubbini, M.; Fazio, N.L.; Perrotti, M.; Lollino, P. An integrated procedure to assess the stability of coastal rocky cliffs: From UAV close-range photogrammetry to geomechanical finite element modeling. *Remote Sens.* **2017**, *9*, 1235. [CrossRef]
17. Vann Jones née Norman, E.C.; Rosser, N.J.; Brain, M.J.; Petley, D.N. Quantifying the environmental controls on erosion of a hard rock cliff. *Mar. Geol.* **2015**, *363*, 230–242. [CrossRef]
18. Blanco Chao, R.; Pérez Alberti, A. Formas litorales en la costa noroccidental gallega: Los sectores acantilados entre Cabo Prioriño (Ferrol) y Punta Frouxeira (Valdoviño). *Geographicalia* **1996**, *33*, 3–28. [CrossRef]

19. Sunamura, T. *Geomorphology of Rocky Coasts*; Wiley: Chichester, UK, 1992; ISBN 0471917753.
20. Naylor, L.A.; Stephenson, W.J. On the role of discontinuities in mediating shore platform erosion. *Geomorphology* **2010**, *114*, 89–100. [CrossRef]
21. Inkpen, R.J.; Stephenson, W. Statistical analysis of the significance of site topography and erosion history on erosion rates on intertidal shore platforms, Kaikoura Peninsula, South Island, New Zealand. *Geomorphology* **2006**, *81*, 18–28. [CrossRef]
22. Stephenson, W.J.; Finlayson, B.L. Measuring erosion with the micro-erosion meter-Contributions to understanding landform evolution. *Earth Sci. Rev.* **2009**, *95*, 53–62. [CrossRef]
23. Stephenson, W.J.; Kirk, R.M.; Hemmingsen, S.A.; Hemmingsen, M.A. Decadal scale micro erosion rates on shore platforms. *Geomorphology* **2010**, *114*, 22–29. [CrossRef]
24. Trudgill, S.T. The subaerial and subsoil erosion of limestones on Aldabra Atoll, Indian Ocean. *Z. Geomophologie* **1976**, *26*, 201–210.
25. Letortu, P.; Costa, S.; Maquaire, O.; Delacourt, C.; Augereau, E.; Davidson, R.; Suanez, S.; Nabucet, J. Retreat rates, modalities and agents responsible for erosion along the coastal chalk cliffs of Upper Normandy: The contribution of terrestrial laser scanning. *Geomorphology* **2015**, *245*, 3–14. [CrossRef]
26. Jaud, M.; Letortu, P.; Théry, C.; Grandjean, P.; Costa, S.; Maquaire, O.; Davidson, R.; Le Dantec, N. UAV survey of a coastal cliff face—Selection of the best imaging angle. *Meas. J. Int. Meas. Confed.* **2019**, *139*, 10–20. [CrossRef]
27. Matsumoto, H.; Dickson, M.E.; Masselink, G. Systematic analysis of rocky shore platform morphology at large spatial scale using LiDAR-derived digital elevation models. *Geomorphology* **2017**, *286*, 45–57. [CrossRef]
28. Le Mauff, B.; Juigner, M.; Ba, A.; Robin, M.; Launeau, P.; Fattal, P. Coastal monitoring solutions of the geomorphological response of beach-dune systems using multi-temporal LiDAR datasets (Vendée coast, France). *Geomorphology* **2018**, *304*, 121–140. [CrossRef]
29. Thébeaudeau, B.; Trenhaile, A.S.; Edwards, R.J. Modelling the development of rocky shoreline profiles along the northern coast of Ireland. *Geomorphology* **2013**, *203*, 66–78. [CrossRef]
30. Aoki, H.; Matsukura, Y. A new technique for non-destructive field measurement of rock-surface strength: An application of the Equotip hardness tester to weathering studies. *Earth Surf. Process. Landf.* **2007**, *32*, 1759–1769. [CrossRef]
31. Viles, H.; Goudie, A.; Grab, S.; Lalley, J. The use of the Schmidt Hammer and Equotip for rock hardness assessment in geomorphology and heritage science: A comparative analysis. *Earth Surf. Process. Landf.* **2011**, *36*, 320–333. [CrossRef]
32. Feal-Pérez, A.; Blanco-Chao, R. Characterization of abrasion surfaces in rock shore environments of NW Spain. *Geo Mar. Lett.* **2013**, *33*, 173–181. [CrossRef]
33. Lim, M.; Rosser, N.J.; Allison, R.J.; Petley, D.N. Erosional processes in the hard rock coastal cliffs at Staithes, North Yorkshire. *Geomorphology* **2010**, *114*, 12–21. [CrossRef]
34. Cenci, L.; Disperati, L.; Persichillo, M.G.; Oliveira, E.R.; Alves, F.L.; Phillips, M. Integrating remote sensing and GIS techniques for monitoring and modeling shoreline evolution to support coastal risk management. *GISci. Remote Sens.* **2018**, *55*, 355–375. [CrossRef]
35. Federici, B.; Corradi, N.; Ferrando, I.; Sguerso, D.; Lucarelli, A.; Guida, S.; Brandolini, P. Remote sensing techniques applied to geomorphological mapping of rocky coast: The case study of Gallinara Island (Western Liguria, Italy). *Eur. J. Remote Sens.* **2019**, *52*, 123–136. [CrossRef]
36. Horikawa, K.; Sunamura, T. A study on erosion of coastal cliffs by using aerial photographs. *Coast. Eng. Jpn.* **1967**, *10*, 67–83. [CrossRef]
37. Gómez-Pazo, A.; Pérez-Alberti, A.; Trenhaile, A. Tracking clast mobility using RFID sensors on a boulder beach in Galicia, NW Spain. *Geomorphology* **2021**, *373*, 107514. [CrossRef]
38. Hastewell, L.J.; Schaefer, M.; Bray, M.; Inkpen, R. Intertidal boulder transport: A proposed methodology adopting Radio Frequency Identification (RFID) technology to quantify storm induced boulder mobility. *Earth Surf. Process. Landf.* **2019**, *44*, 681–698. [CrossRef]
39. Casamayor, M.; Alonso, I.; Cabrera, J.; Rodríguez, S.; Sánchez-García, M. Long term recovery rates obtained using RFID technology at a mixed beach. *Geol. Acta* **2015**, *13*, 85–96. [CrossRef]
40. Viles, H. Technology and geomorphology: Are improvements in data collection techniques transforming geomorphic science? *Geomorphology* **2016**, *270*, 121–133. [CrossRef]
41. Masek, J.G.; Hayes, D.J.; Joseph Hughes, M.; Healey, S.P.; Turner, D.P. The role of remote sensing in process-scaling studies of managed forest ecosystems. *For. Ecol. Manag.* **2015**, *355*, 109–123. [CrossRef]
42. Cruz, H.; Eckert, M.; Meneses, J.; Martínez, J.F. Efficient forest fire detection index for application in Unmanned Aerial Systems (UASs). *Sensors* **2016**, *16*, 893. [CrossRef] [PubMed]
43. Gonçalves, J.A.; Henriques, R. UAV photogrammetry for topographic monitoring of coastal areas. *ISPRS J. Photogramm. Remote Sens.* **2015**, *104*, 101–111. [CrossRef]
44. Boesl, F.; Engel, M.; Eco, R.C.; Galang, J.N.B.; Gonzalo, L.A.; Llanes, F.; Quix, E.; Brückner, H. Digital mapping of coastal boulders—high-resolution data acquisition to infer past and recent transport dynamics. *Sedimentology* **2019**, *67*, 1393–1410. [CrossRef]
45. Pérez-Alberti, A.; Trenhaile, A.S. Clast mobility within boulder beaches over two winters in Galicia, northwestern Spain. *Geomorphology* **2015**, *248*, 411–426. [CrossRef]
46. Pérez-Alberti, A.; Trenhaile, A.S. An initial evaluation of drone-based monitoring of boulder beaches in Galicia, north-western Spain. *Earth Surf. Process. Landf.* **2015**, *40*, 105–111. [CrossRef]

47. Pérez-Alberti, A.; Pires, A.; López, M. Photogrammetric evaluation of rocky coasts using UAV mapping system. In Proceedings of the 8th IAG International Conference, Paris, France, 27–31 August 2013.

48. Pérez-Alberti, A. Boulder mobility and shore platform erosion in southern Galicia, Northwestern Spain. In Proceedings of the 8th International conference (AIG) on Geomorphology "Geomorphology and sustainability" (Abstracts), Paris, France, 27–31 August 2013; p. 857.

49. Cook, K.L. An evaluation of the effectiveness of low-cost UAVs and structure from motion for geomorphic change detection. *Geomorphology* **2017**, *278*, 195–208. [CrossRef]

50. Gómez-Gutiérrez, Á.; Gonçalves, G.R. Surveying coastal cliffs using two UAV platforms (multirotor and fixed-wing) and three different approaches for the estimation of volumetric changes. *Int. J. Remote Sens.* **2020**, *41*, 8143–8175. [CrossRef]

51. Clapuyt, F.; Vanacker, V.; Van Oost, K. Reproducibility of UAV-based earth topography reconstructions based on Structure-from-Motion algorithms. *Geomorphology* **2016**, *260*, 4–15. [CrossRef]

52. Wheaton, J.M.; Brasington, J.; Darby, S.E.; Sear, D.A. Accounting for uncertainty in DEMs from repeat topographic surveys: Improved sediment budgets. *Earth Surf. Process. Landf.* **2010**, *35*, 136–156. [CrossRef]

53. Gómez-Pazo, A.; Perez-Alberti, A. El uso de imágenes de alta resolución en el estudio de los cambios volumétricos en playas de bloques. El ejemplo de Laxe Brava (Ribeira, NO Península Ibérica). In Proceedings of the X Jornadas de Geomorfología Litoral, Castelldefells, Spain, 4–6 September 2019; pp. 201–204.

54. Coombes, M.A.; Feal-Pérez, A.; Naylor, L.A.; Wilhelm, K. A non-destructive tool for detecting changes in the hardness of engineering materials: Application of the Equotip durometer in the coastal zone. *Eng. Geol.* **2013**, *167*, 14–19. [CrossRef]

55. Himmelstoss, E.A.; Henderson, R.E.; Kratzmann, M.G.; Farris, A.S. *Digital Shoreline Analysis System (DSAS) Version 5.0 User Guide*; USGS: Reston, VA, USA, 2018.

56. Castedo, R.; de la Vega-Panizo, R.; Fernández-Hernández, M.; Paredes, C. Measurement of historical cliff-top changes and estimation of future trends using GIS data between Bridlington and Hornsea—Holderness Coast (UK). *Geomorphology* **2015**, *230*, 146–160. [CrossRef]

57. Puig, M.; Del Río, L.; Plomaritis, T.A.; Benavente, J. Contribution of storms to shoreline changes in mesotidal dissipative beaches. Case study in the Gulf of Cadiz (SW Spain). *Nat. Hazards Earth Syst. Sci.* **2016**, *16*, 2543–2557. [CrossRef]

58. Puig, M.; Del Río, L.; Plomaritis, T.A.; Benavente, J. Influence of storms on coastal retreat in SW Spain. *J. Coastal Res.* **2014**, *70*, 193–198. [CrossRef]

59. Masselink, G.; Castelle, B.; Scott, T.; Dodet, G.; Suanez, S.; Jackson, D.; Floc'h, F. Extreme wave activity during 2013/2014 winter and morphological impacts along the Atlantic coast of Europe. *Geophys. Res. Lett.* **2016**, *43*, 2135–2143. [CrossRef]

60. James, M.R.; Chandler, J.H.; Eltner, A.; Fraser, C.; Miller, P.E.; Mills, J.P.; Noble, T.; Robson, S.; Lane, S.N. Guidelines on the use of Structure from Motion Photogrammetry in Geomorphic Research. *Earth Surf. Process. Landf.* **2019**, *44*, 2081–2084. [CrossRef]

61. Trenhaile, A.S. Rock coasts, with particular emphasis on shore platforms. *Geomorphology* **2002**, *48*, 7–22. [CrossRef]

62. Lim, M.; Petley, D.N.; Rosser, N.J.; Allison, R.J.; Long, A.J.; Pybus, D. Combined digital photogrammetry and time-of-flight laser scanning for monitoring cliff evolution. *Photogramm. Rec.* **2005**, *20*, 109–129. [CrossRef]

63. Quinn, J.D.; Rosser, N.J.; Murphy, W.; Lawrence, J.A. Identifying the behavioural characteristics of clay cliffs using intensive monitoring and geotechnical numerical modelling. *Geomorphology* **2010**, *120*, 107–122. [CrossRef]

64. Valenzuela, P.; Zêzere, J.L.; Domínguez-Cuesta, M.J.; Mora García, M.A. Empirical rainfall thresholds for the triggering of landslides in Asturias (NW Spain). *Landslides* **2019**, *16*, 1285–1300. [CrossRef]

65. Bea Abelairas Derrumbe en la zona nudista de Ponzos. *La Voz Galicia*, 7 March 2017.

66. Valenzuela, P.; Domínguez-Cuesta, M.J.; Mora García, M.A.; Jiménez-Sánchez, M. Rainfall thresholds for the triggering of landslides considering previous soil moisture conditions (Asturias, NW Spain). *Landslides* **2018**, *15*, 273–282. [CrossRef]

67. Wigmore, O.; Mark, B.; McKenzie, J.; Baraer, M.; Lautz, L. Sub-metre mapping of surface soil moisture in proglacial valleys of the tropical Andes using a multispectral unmanned aerial vehicle. *Remote Sens. Environ.* **2019**, *222*, 104–118. [CrossRef]

68. Turner, I.L.; Harley, M.D.; Drummond, C.D. UAVs for coastal surveying. *Coast. Eng.* **2016**, *114*, 19–24. [CrossRef]

69. Gomez-Pazo, A.; Perez-Alberti, A.; Otero Pérez, X.L. Recent Evolution (1956–2017) of Rodas Beach on the Cíes Islands, Galicia, NW Spain. *J. Mar. Sci. Eng.* **2019**, *7*, 125. [CrossRef]

70. Splinter, K.D.; Harley, M.D.; Turner, I.L. Remote sensing is changing our view of the coast: Insights from 40 years of monitoring at Narrabeen-Collaroy, Australia. *Remote Sens.* **2018**, *10*, 1744. [CrossRef]

71. Biolchi, S.; Denamiel, C.; Devoto, S.; Korbar, T.; Macovaz, V.; Scicchitano, G.; Vilibić, I.; Furlani, S. Impact of the October 2018 storm Vaia on coastal boulders in the northern Adriatic Sea. *Water* **2019**, *11*, 2229. [CrossRef]

72. Nagle-McNaughton, T.; Cox, R. Measuring change using quantitative differencing of repeat structure-from-motion photogrammetry: The effect of storms on coastal boulder deposits. *Remote Sens.* **2020**, *12*, 42. [CrossRef]

73. Mancini, F.; Dubbini, M.; Gattelli, M.; Stecchi, F.; Fabbri, S.; Gabbianelli, G. Using unmanned aerial vehicles (UAV) for high-resolution reconstruction of topography: The structure from motion approach on coastal environments. *Remote Sens.* **2013**, *5*, 6880–6898. [CrossRef]

74. Guisado-Pintado, E.; Jackson, D.W.T.; Rogers, D. 3D mapping efficacy of a drone and terrestrial laser scanner over a temperate beach-dune zone. *Geomorphology* **2019**, *328*, 157–172. [CrossRef]

75. Long, N.; Millescamps, B.; Guillot, B.; Pouget, F.; Bertin, X. Monitoring the topography of a dynamic tidal inlet using UAV imagery. *Remote Sens.* **2016**, *8*, 387. [CrossRef]

76. Pinton, D.; Canestrelli, A.; Fantuzzi, L. A UAV-based dye-tracking technique to measure surface velocities over tidal channels and salt marshes. *J. Mar. Sci. Eng.* **2020**, *8*, 364. [CrossRef]
77. Yin, D.; Wang, L. Individual mangrove tree measurement using UAV-based LiDAR data: Possibilities and challenges. *Remote Sens. Environ.* **2019**, *223*, 34–49. [CrossRef]
78. Jaud, M.; Grasso, F.; Le Dantec, N.; Verney, R.; Delacourt, C.; Ammann, J.; Deloffre, J.; Grandjean, P. Potential of UAVs for monitoring mudflat morphodynamics (Application to the Sein e Estuary, France). *ISPRS Int. J. Geo Inf.* **2016**, *5*, 50. [CrossRef]
79. Letortu, P.; Jaud, M.; Grandjean, P.; Ammann, J.; Costa, S.; Maquaire, O.; Davidson, R.; Le Dantec, N.; Delacourt, C. Examining high-resolution survey methods for monitoring cliff erosion at an operational scale. *GIScience Remote Sens.* **2017**, *55*, 457–476. [CrossRef]
80. Muñoz Narciso, E.; García, H.; Sierra Pernas, C.; Pérez-Alberti, A. Study of geomorphological changes by high quality DEMs, obtained from UAVs-Structure from Motion in highest continental cliffs of Europe: A Capelada (Galicia, Spain). *Geophys. Res. Abstr. EGU Gen. Assem.* **2017**, *19*, 2017–2692. [CrossRef]
81. Horacio, J.; Muñoz-Narciso, E.; Trenhaile, A.S.; Pérez-Alberti, A. Remote sensing monitoring of a coastal-valley earthflow in northwestern Galicia, Spain. *Catena* **2019**, *178*, 276–287. [CrossRef]
82. Allison, R.S.; Johnston, J.M.; Craig, G.; Jennings, S. Airborne optical and thermal remote sensing for wildfire detection and monitoring. *Sensors* **2016**, *16*, 1310. [CrossRef] [PubMed]
83. Jay, S.; Maupas, F.; Bendoula, R.; Gorretta, N. Retrieving LAI, chlorophyll and nitrogen contents in sugar beet crops from multi-angular optical remote sensing: Comparison of vegetation indices and PROSAIL inversion for field phenotyping. *F. Crop. Res.* **2017**, *210*, 33–46. [CrossRef]
84. Klosterman, S.; Melaas, E.; Wang, J.; Martinez, A.; Frederick, S.; O'Keefe, J.; Orwig, D.A.; Wang, Z.; Sun, Q.; Schaaf, C.; et al. Fine-scale perspectives on landscape phenology from unmanned aerial vehicle (UAV) photography. *Agric. For. Meteorol.* **2018**, *248*, 397–407. [CrossRef]

Article

Modeling Streamflow and Sediment Loads with a Photogrammetrically Derived UAS Digital Terrain Model: Empirical Evaluation from a Fluvial Aggregate Excavation Operation

Joseph P. Hupy [1,*] and Cyril O. Wilson [2]

[1] School of Aviation and Transportation Technology, Purdue University, West Lafayette, IN 47907, USA
[2] Department of Geography, University of Wisconsin–Eau Claire, Eau Claire, WI 54701, USA; wilsonc@uwec.edu
[*] Correspondence: jhupy@purdue.edu; Tel.: +1-765-496-6201

Abstract: Soil erosion monitoring is a pivotal exercise at macro through micro landscape levels, which directly informs environmental management at diverse spatial and temporal scales. The monitoring of soil erosion can be an arduous task when completed through ground-based surveys and there are uncertainties associated with the use of large-scale medium resolution image-based digital elevation models for estimating erosion rates. LiDAR derived elevation models have proven effective in modeling erosion, but such data proves costly to obtain, process, and analyze. The proliferation of images and other geospatial datasets generated by unmanned aerial systems (UAS) is increasingly able to reveal additional nuances that traditional geospatial datasets were not able to obtain due to the former's higher spatial resolution. This study evaluated the efficacy of a UAS derived digital terrain model (DTM) to estimate surface flow and sediment loading in a fluvial aggregate excavation operation in Waukesha County, Wisconsin. A nested scale distributed hydrologic flow and sediment loading model was constructed for the UAS point cloud derived DTM. To evaluate the effectiveness of flow and sediment loading generated by the UAS point cloud derived DTM, a LiDAR derived DTM was used for comparison in consonance with several statistical measures of model efficiency. Results demonstrate that the UAS derived DTM can be used in modeling flow and sediment erosion estimation across space in the absence of a LiDAR-based derived DTM.

Keywords: streamflow; sediment loading; unmanned aerial systems; drones; digital terrain model

1. Introduction

Unmanned aerial systems, hereafter referred to as UAS, are now widely recognized in the remote sensing community as a valid geospatial data collection tool. Their utility extends into a wide variety of applications, including but not limited to general mapping, precision agriculture, forestry, wetlands, mining, excavation, and hydrology [1–4]. While UAS platforms can be equipped with a wide array of sensor types, i.e., meteorological, gas, and particle sensors, the majority of current UAS platforms are equipped with imaging sensors [5,6]. UAS are a useful platform to gather imagery over small to moderately sized areas due to their relatively low cost and for their overall versatility when compared to traditional satellite and manned aircraft remote sensing platforms. Manfreda [7], detailed how traditional manned aircraft and satellites were limited in their ability to gather remotely sensed data based on their altitude constraints and their inability to gather information over certain areas within a given set of time constraints and temporal frequency needs. Furthermore, both satellite and fixed-wing aircraft cannot achieve the centimeter to sub-centimeter spatial resolution that UAS delivers.

The versatility of a UAS platform is best described as being able to fly 'low and slow', which means that a UAS platform equipped with a small format camera sensor can fly

at a low altitude over a pre-defined area to gather remotely sensed images at resolutions unattainable with traditional platforms, and at a temporal frequency deemed necessary. When UAS imagery is gathered by the platform sensor at a constant altitude, and with enough overlap, the imagery can be processed using structure-from-motion with multi-view stereo (hereafter referred to as SfM) methods to generate a three-dimensional point cloud model [8–10]. This point cloud can then be used to generate a digital surface or terrain model (DSM/DTM). A DSM contains all above ground surface features, such as vegetation and buildings, while a DTM only contains the bare ground.

Software companies, such as Pix4D, Agisoft, and Socet Set, have revolutionized the field of photogrammetry by transforming the laborious and time-consuming conventional photogrammetric method into more efficient and optimized workflows such as the scale invariant feature transform [11] and its associated SfM algorithm [12–14] including the BAE Systems Socet Set [15]. This new development is timely and welcome in the processing of UAS imagery and extraction of derivatives and is slowly being adopted into the mainstream of many different fields that rely on geospatial data. While the increased use of UAS data is indeed a boon to the geospatial community, the ease of creating SfM derived data products such as a point cloud, DSM, DTM, and orthomosaic means that both the limitations and potential of such data need to be realized.

Despite airborne and terrestrial LiDAR's accuracy in generating surface and terrain models for use in diverse applications, it is expensive to collect and process, and therefore has limits to its widespread use [7,16,17]. Furthermore, because of the altitude of the platform used, airborne Lidar data is often not available at the 1−2 cm spatial resolution that one can obtain using UAS derived SfM methods [9,18]. While progress has been made toward equipping UAS platforms with LiDAR sensors, the technology remains both cost prohibitive and unreachable for most researchers and UAS users [7,17]. Scientific investigations in the emerging frontier of UAS SfM approaches are needed to better understand the potentially concealed functionalities of photogrammetrically derived UAS data, which might be beneficial in certain research and market niches.

Extraction and excavation-based activities associated with vegetation removal, such as open pit mines, construction sites, barren farm-fields, and post-hazard events (e.g., slope failure) are well-suited for UAS derived DSM and/or DTM analysis [19–21]. The lack of vegetation cover associated with surface disturbance on excavated surfaces makes them ideal for modeling both drainage and erosion potential. In an applied sense, the erosion associated with surface drainage at sites devoid of vegetation cover can impact day to day operations at the site. Excessive erosion at construction and mining sites also can mean being subjected to fines and citations from regulatory bodies. Most mining and construction operations are aware of erosion modeling techniques available with LiDAR data, but understand the financial and temporal limitations in place to be able to use such datasets and are seeking means to model surface drainage with technology that is more attainable, such as UAS derived DTM from SfM models.

While LiDAR derived terrain models in hydrologic applications have their place as an essential data source [18], traditional photogrammetrically derived products like digital elevation models (DEMs) are still an important source of topographic information that informs hydrologic applications [22,23]. Historically, such DEM products have been retrieved from medium resolution optical and microwave images [7,24,25]. Quite recently, photogrammetrically derived DSM and DTM from high resolution UAS imagery has been emerging in the hydrologic literature [18,26–28]. Photogrammetrically derived UAS data has been used to model surface flow within and outside urban areas [17,29,30], spatial and temporal variability of riverbed hydraulic conductivity [31], channel morphology [32], streambank topography [33], streambank erosion [27], and gully erosion in agricultural and urban watersheds [34,35]. Stocker [34] demonstrated that the photogrammetrically derived data from UAS can measure gully erosion in farmland in a way that LiDAR technology could not due to the increased spatial and temporal resolution that UAS models provide. Gudino-Elizondo et al. [35] reported that UAS derived DSM was effective in estimating

gully erosion rates in an urban catchment. While the use of UAS derived dataset to estimate specific types of erosion rates in different catchment characteristics is welcome, we currently know very little on the use and effectiveness of this relatively new dataset to estimate runoff and erosion rates on diverse land cover types [35]. Moreover, an investigation of this phenomenon within the lens of a nested scale distributed hydrologic modeling framework has great potential to unlock the efficacy of UAS derived DTM for the monitoring of runoff and erosion rates across space.

Nested-scale hydrologic modeling framework has proven effective in predicting stream flow and water pollutants when model input data are not available at the same scale [36–38]. Didszun and Uhlenbrook [38] applied a nested-scale approach to investigate hydrologic responses at scales < 1 km^2 and $\geq$ 40 km^2; they reported slight variation in hydrologic responses at the smallest scale attributed to varying topography. Van der Velde [36] concluded that hydrologic models configured within a nested-scale framework improves prediction of stream discharge and nitrate loads. In a related vein, Zeiger and Hubbart [37] echoed the efficacy of a nested-scale experimental hydrologic modeling design to predict suspended sediment loads. The overarching objective of this study is to assess the potential of a UAS photogrammetrically derived DTM for modeling surface runoff and sediment loading in an open pit fluvial aggregate mining operation experiencing high amounts of erosion. Specifically, this study addresses the following objectives: (1) to develop a downscaling calibration and validation framework for a large-scale hydrologic water quality model and extend to a smaller UAS dataset areal extent; (2) to evaluate the suitability of UAS derived DTM for surface runoff and erosion modeling within an open pit fluvial aggregate mining operation.

2. Materials and Methods

2.1. Study Area

This study was conducted in an open pit fluvial aggregate excavation operation in Waukesha county, near the village of Delafield, Wisconsin, USA. (Figure 1). The operation uses extracted aggregate materials from the open pit for its activities in paving and construction. The data acquisition area covers 10 ha with elevation values ranging between 314 m and 287 m above mean sea level. Due to the erosion issues that the site was experiencing, a request was made to have the area flown with a UAS to potentially identify areas where significant erosion was occurring. The steep slopes and loosely consolidated material made a ground-based survey both impractical and dangerous (Figure 2). The study area is sparsely vegetated (<15%) due to excavation and extraction activities at the site. Average annual precipitation at the site is 87.9 mm. The nearest climatic records from Waukesha, WI show average temperatures in January range from –11.8 to –2.3 °C. Average July temperatures fall within the 27.7 to 15.4 °C range. Soils in the study area are designated as an open gravel pit soil unit and classified as Psammic Fluvent [39].

2.2. UAS Data Collection and Processing

All data was gathered in June 2015 by MenetAero LLC, a UAS service provider who specializes in UAS data acquisition. The Platform used to collect imagery was a DJI Matrice 600 Pro with D-RTK, allowing for reliable flight paths and altitude consistency during flight. Image collection was facilitated by a gimbal based Zenmuse X5 RGB camera equipped with a 15 mm lens (Table 1).
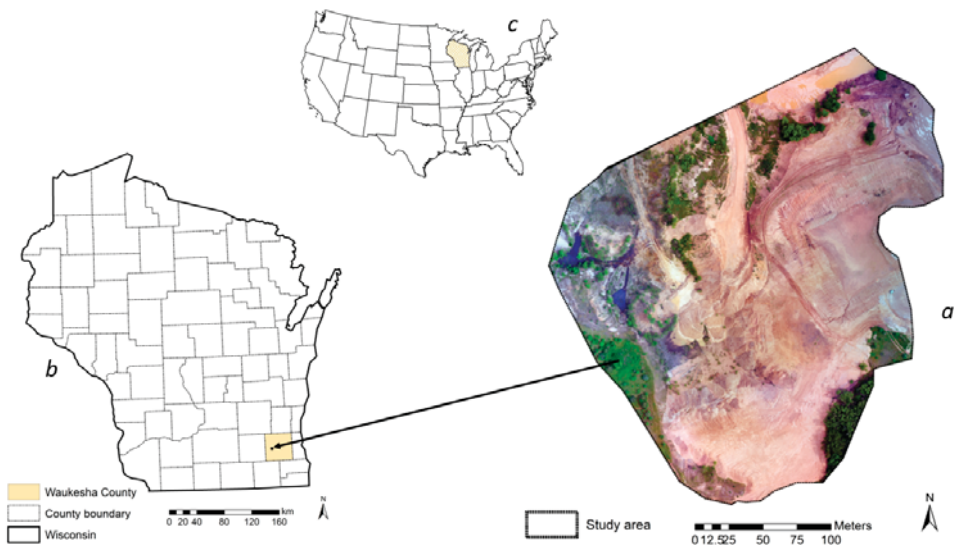
Figure 1. Map of the study area: Excavation operation site (*a*), Wisconsin (*b*), USA (*c*).
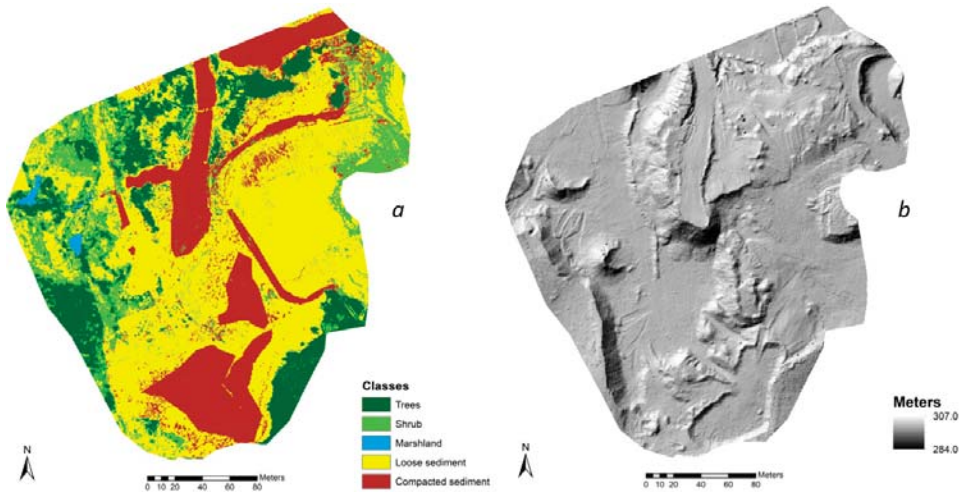
Figure 2. Optical UAS imagery derived land cover (*a*) and hillshade DTM based on UAS point cloud (*b*).

Flight altitude at image capture was 80 m with 80% frontal and lateral overlap. The images were saved onto a 32 GB Generation V SanDisk SD card in Jpeg format. Image geolocation was stored to the image exif file using the WGS 84 geographic coordinate system. This coordinate system is what most UAS platforms utilize to record data related to their GPS log and is the default setting for the DJI platform. It should be noted here that the Matrice 600 Platform, although equipped with D-RTK GPS, did not communicate with the Pix4D Capture application to geolocate the imagery with RTK precision. Spatial accuracy was achieved by the placement and survey of ground control markers prior to the flight. A Trimble R2 GNSS integrated system was used to acquire coordinate locations at six ground control points (GCPs) distributed accordingly across the flight area. To ensure survey quality, redundant check shots were also recorded at each GCP with a variance

tolerance of 0.01 m horizontally and 0.02 m vertically. GCPs were recorded using the projected Universal Transverse Mercator coordinate system with a WGS 84 datum. This was chosen to match the desired processed data output projection and coordinate system for further use in a Geographic Information System with other forms of geospatial data.

Table 1. Survey data collection parameters and equipment specifications.

Data Collection Date	6 June 2015
UAS platform	DJI Matrice 600 Pro w/RTK
UAS mission planning application	Pix4D Capture
Flight path overlap	80% lateral and frontal
Area covered	12.23 hectares
Number of images acquired	125
Sensor/platform altitude	80 m
Ground sampling distance	2.07 cm
Camera model	Zenmuse X5
Camera focal length	15 mm
Camera resolution	16 megapixels
Image coordinate system	WGS84 (egm96)
GNSS integrated survey system	Trimble R2
Ground control point (GCP) coordinate system	WGS84/UTMzone 16N (egm96)
Number of GCPs	6
Number of check shots per GCP	6
Check points/shot tolerance	0.01 m horizontal/0.02 m vertical

Pix4D Structure from Motion Multi-View Stereo (SfM MVS) software (version 3.1.23) was used to generate a point cloud, digital surface model, orthomosaic image, and subsequent derivative data products that allowed for further analysis within LP360, ESRI ArcMap Desktop (version 10.7) software, and image processing utilities. Calibration, validation, subsequent processing, and error reporting details associated with SfM model creation utilized in this study are summarized in Table 2 and adhere as best as possible to guidelines put for by James [40]. Following the initial processing phase, where the geolocated images are used to generate a low-density point cloud, the dataset was adjusted for both horizontal and vertical accuracy using the GCP markers. The dataset was then reoptimized and used to generate a high-density point cloud (las format) with 0.058 m RMS error.

Utilizing a hybrid approach, the UAS photogrammetrically derived point cloud was classified into ground and above ground points with the aid of LP360 software (GeoCue Group, Madison, AL, USA). The small fraction of above ground points was a result of shrubs and trees in dispersed throughout study area (Figures 1a and 2a). In the first stage of point cloud classification, we employed the adaptive triangulated irregular network (TIN) ground filter to separate ground points from non-ground points [41,42]. The adaptive TIN-based ground filter generates tiles over the point cloud dataset and identifies the lowest point in each tile as a potential candidate ground point [41]. Next a triangulated irregular network (TIN) is generated from the earmarked lowest points. The algorithm then utilizes thresholds that encapsulates elevation difference and angle closest to a TIN face to iteratively remove non-ground points. Detailed description of the adaptive TIN-based ground filter can be found in Axelsson [41]. In stage two, a two-dimensional profile window that is equipped with vertical manual classification tools was utilized to improve on stage one automated classification. Following the successful classification of ground points, a 3.6 cm DTM was derived by interpolating ground points using a triangulation

algorithm. The output spatial resolution of the DTM was set at 3.6 cm to be consistent with the nominal point spacing (NPS) of the classified ground points. A 14.3 cm LiDAR DTM was derived from an already classified LiDAR ground points for Waukesha County collected late spring 2015 [43]. The LiDAR derived DTM spatial resolution was determined by the NPS of LiDAR ground points (~7 points per m^2). We used triangulation interpolation method to generate a LiDAR derived DTM to be consistent with that of the UAS derived DTM mentioned above. The final processing of the UAS and LiDAR derived DTMs was the generation of a hillshade for visualization purposes.

Table 2. Calibration, processing, and error reporting detail summary table.

SfM Processing Software	Pix4D (Version 3.1.23)
Number of calibrated images	125/125 (100%)
Median keypoints per image	35,170
Matches per calibrated image	13,384
GCP mean RMS error	X(m) 0.002254 Y(m) − 0.013442 Z(m) 0.064130
Overall GCP mean RMS error	0.058
Absolute camera position uncertainties	Mean X(m) 0.028 Mean Y(m) 0.024
Number of 2D keypoint observations for bundle block adjustment	1,600,420
Number of 3D keypoint observations for bundle block adjustment	575,499
Mean reprojection error (pixels)	0.162
Point cloud density	Optimal

In hydrologic modeling, land use/land cover (LULC) are needed to establish parameters related to erosion potential. LULC data was derived from the orthomosaic image of the study area collected during the UAS flight mission. We employed a two-stage hybrid classification framework to generate land cover information for the study area. Object-based image analysis (OBIA) followed by the implementation of a random forest classifier was utilized in stage one image processing [44,45]. The determination of spectral and spatial segmentation parameters was informed by local variance of heterogeneity; following this, image objects were generated by a multiresolution segmentation algorithm [46,47]. Equation (1) illustrates a simplified example of the major segmentation parameters employed in OBIA.

$$F_s = C_w * r_c + (1 - C_w) * r_s$$
$$\text{and } 0 \leq C_w \leq 1 \tag{1}$$

where F_s is segmentation function; C_w is weight given to color; r_c illustrates color criterion; and r_s denotes spatial criterion. The random forest classifier was trained to classify image objects in conjunction with textural and contextual information [47]. In stage two, output of random forest classification was integrated in an expert system ruleset classifier [48] with the use of ancillary data to improve on the result of stage 1 classification. Ancillary data was obtained by creating patches to fix misclassification encountered during stage 1. Image classification accuracy was conducted by collecting 300 ground reference points via stratified random sampling from a high-resolution National Agriculture Imagery Program (NAIP) imagery collected at the same temporal scale as the orthomosaic imagery [39,49]. Overall image classification accuracy is 89%. At the end of image processing, five classes were produced: Trees, shrub, marshland, loose sediment, and compacted sediment (Figure 2a).

2.3. Flow and Sediment Model Construction

The Soil and Water Assessment Tool (SWAT) was employed to model flow and sediment loading in the study area. SWAT is a fully distributed model that aids in the evaluation of land management practices on flow and water quality in river basins over time [50,51]. For a SWAT model to be successfully implemented, it requires LULC, soil, elevation, and climate variables. Soil data was obtained from the soil survey geographic (SSURGO) data [52] while climate data was acquired from SWAT database. For a SWAT model to produce results that are close to reality, it must be calibrated and validated. We constructed two SWAT models for the UAS derived DTM and the LiDAR derived DTM, respectively. Due to the unavailability of observed streamflow data within the UAS image acquisition area, a nested downscaling approach was developed and applied in operationalizing model calibration and validation. We reconstructed the hydrologically active area covered by the closest USGS streamflow gauging station (4 km upstream) to the UAS study extent. The larger watershed (199 km^2) encapsulated the UAS study area and accounted for the hydrologically active area of the observed streamflow data (Figure 3). An ungauged SWAT model with a warmup period of 15 years (2000−2014) was initially operationalized for this larger calibration study area. Following this, the model was calibrated and validated to obtain the appropriate coefficients for 17 key SWAT parameters (Table 3) that were found to be highly sensitive at this large spatial scale and extendible to the smaller UAS spatial scale.
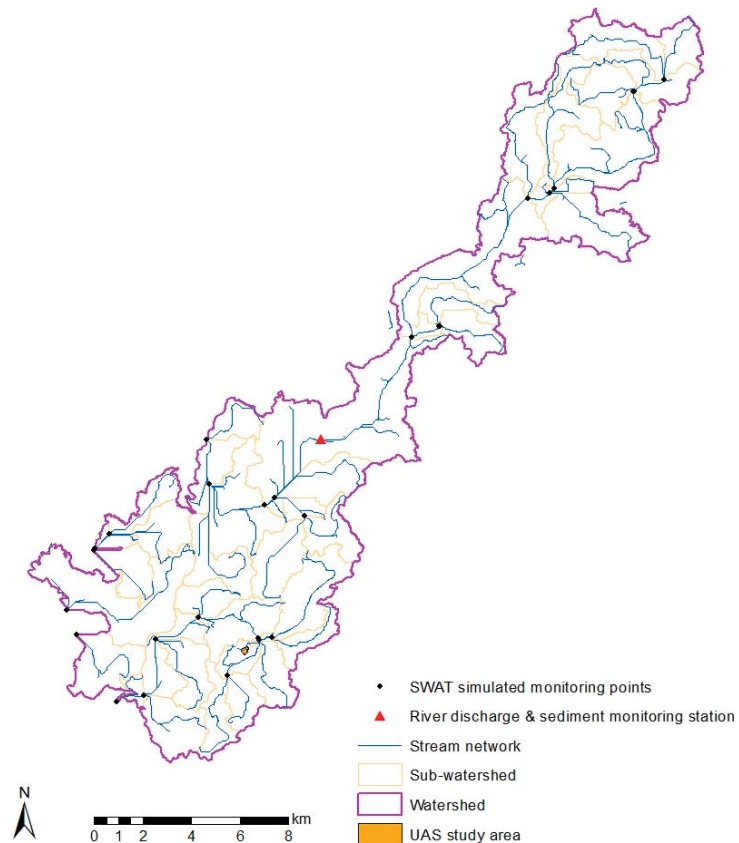
Figure 3. Simplified SWAT large extent calibration and validation model for study area.

Table 3. Fitted SWAT model calibration parameters and their coefficients.

Parameter	Description	Minimum Value	Maximum Value	Fitted Value
CN2	Curve number for soil moisture 2	34.0	98.0	69.30
ALPHA_BF	Baseflow alpha factor (1/days)	0	0.1	0.62
GW_DELAY	Ground water delay time (days)	20.0	450	153.70
GWQMN	Threshold dept of water in shallow aquifer (mm H_2O)	0.0	300.0	153.90
ESCO	Soil evaporation compensation factor	0.0	1.0	0.91
SURLAG	Surface runoff lag coefficient	1.0	24.0	11.60
CH_K2	Effective hydraulic conductivity in main channel	6.0	25.0	18.56
CH_N2	Manning's "n" value for the main channel	−0.01	0.3	0.02
SHALLST	Initial depth of water in the shallow aquifer (mm H_2O)	0.0	1000	239
GWHT	Initial groundwater height (m)	0.0	25.0	21.7
RCHRG_DP	Deep aquifer percolation fraction	0.0	1.0	0.29
TIMP	Snowpack temperature lag factor	0.0	1.0	0.09
SMFMX	Maximum melt rate for snow during year (mm H_2O/°C-day)	0.0	10.0	0.53
SMFMN	Minimum melt rate for snow during year (mm H_2O/°C-day)	0.0	10.0	7.7
SMTMP	Snowmelt base temperature (°C)	−5.5	5.0	−3.75
SOL_AWC	Available water capacity for the soil layer (mm H_2O/mm soil)	0.0	1.0	0.27
PRF	Sediment routing factor in main channel	0.0	2.0	1.80

We employed Sequential Uncertainty Fitting version 2(SUFI-2) program embedded in SWAT-CUP 2012 to calibrate and validate the models [53,54]. SUFI2 fits SWAT output simulated data to observed data and in the process adjust the coefficients of SWAT model parameters during model calibration [55]. In evaluating how well a model is calibrated, SUFI-2 utilizes two major criteria. The *P*-factor which provides a measure of SUFI-2's ability to capture uncertainty while the *R*-factor gauges the quality of model calibration [56]. Equation (2) depicts the *R*-factor.

$$R = \frac{\frac{1}{p} \sum_{i=1}^{p} (B_{s,97.5\%} - B_{s,2.5\%})i}{\sigma_{obs}} \tag{2}$$

where p is the number of parameters fitted, $B_{s,97.5\%}$ and $B_{s,2.5\%}$ represents the upper and lower bounds of the 95PPU (95% prediction uncertainty) for a simulated variable B_s, σ_{obs} is the standard deviation of the observed data. Values for *R*-factor range between 0 and infinity. An *R*-factor of zero demonstrates a perfect fit between simulated and measured data. Figure 3 illustrates a simplified SWAT model used in calibration at the larger spatial extent.

Due to the paucity of monitoring stations in the watershed, a temporal split sampling was used in the calibration and validation for flow [57]. The model was calibrated for

flow between August−2015 and August−2016 while validation was implemented between August−2017 and August−2018. To obtain the appropriate calibrated coefficients for the parameters outlined in Table 3, we executed 10,000 iterations. The best simulation that produced the appropriate coefficients for the parameters was achieved at iteration 9457. Following the successful model calibration and validation for flow at the larger spatial extent, the simulated flow value at the subbasin that mostly coincides with the UAS study area location was used as an observed data to calibrate and validate the UAS DTM and LiDAR derived DTM models for flow, respectively. To evaluate the efficacies of model calibration and validation for (i) the large extent SWAT model, and (ii) the UAS DTM and LiDAR derived DTM models for flow, three additional statistical measures besides that outlined in Equation (2) were employed.

The first additional statistical measure used to evaluate model effectiveness for calibration and validation is the Nash–Sutcliffe (NS) coefficient [58]. Equation (3) illustrates the Nash–Sutcliffe coefficient:

$$E = 1 - \frac{\sum_{i=1}^{n} (O_i - S_i)^2}{\sum_{i=1}^{n} (O_i - \overline{O})^2} \tag{3}$$

where E is the Nash–Sutcliffe coefficient of model efficiency, O_i is observed data; $\overline{O}$ is the mean of observed data; S_i is simulated value, while n is the total number of observations. Possible values of NS range between $-\infty$ and 1.0. A Nash–Sutcliffe statistic of 1.0 suggest a perfect fit between simulated and observed data, NS values between zero and 1 are generally regarded as tolerable levels of model performance, while NS values less than zero illustrates that the mean of observed data is a preferred predictor compared to the simulated values. Another model efficiency criterion that we employed is the index of agreement (d) which is calculated according to the following equation [59]:

$$d = 1 - \frac{\sum_{i=1}^{n} (O_i - S_i)^2}{\sum_{i=1}^{n} (|S_i - \overline{O}| + |O_i - \overline{O}|)^2} \quad 0 \leq d \geq 1 \tag{4}$$

where d is the index of agreement, O_i is observed signal, $\overline{O}$ is the mean of observed signal, S_i is simulated value, while n is the number of observations. An index of agreement value of 1 suggest perfect fit between simulated and observed while zero depicts no association. We further employed the root mean square error (RMSE) in evaluating model predictive power [60]. The RMSE statistics quantifies the predicted error (residuals) vis à vis the units of the simulated value into a single measure of model efficiency. The RMSE is calculated according to the following equation:

$$RMSE = \sqrt{\frac{\sum_{i=1}^{n} (O_i - S_i)^2}{n}} \tag{5}$$

where O_i and S_i represent observed and simulated values of a sample size n. Values for RSME range between 0 and ∞, where RMSE of zero suggest perfect fit between observed and simulated information.

Calibration of suspended sediments was not performed due to the unavailability of suspended sediment observed data covering the accepted period of model calibration and validation, outside SWAT warm up period (2000–2014). Notwithstanding, one pivotal sediment related SWAT parameter (PRF) that is tied to flow parameters was calibrated thus providing an indirect calibration for suspended sediment (Table 3).

Figure 4 shows a simplified SWAT model constructed for the UAS spatial extent using a LiDAR derived DTM (Figure 4a) and a photogrammetrically derived point cloud DTM (Figure 4b). In each of the models, the watershed was automatically delineated into 60 sub-basins with very similar characteristics of monitoring points, stream network, and sub-basin sizes and morphology.
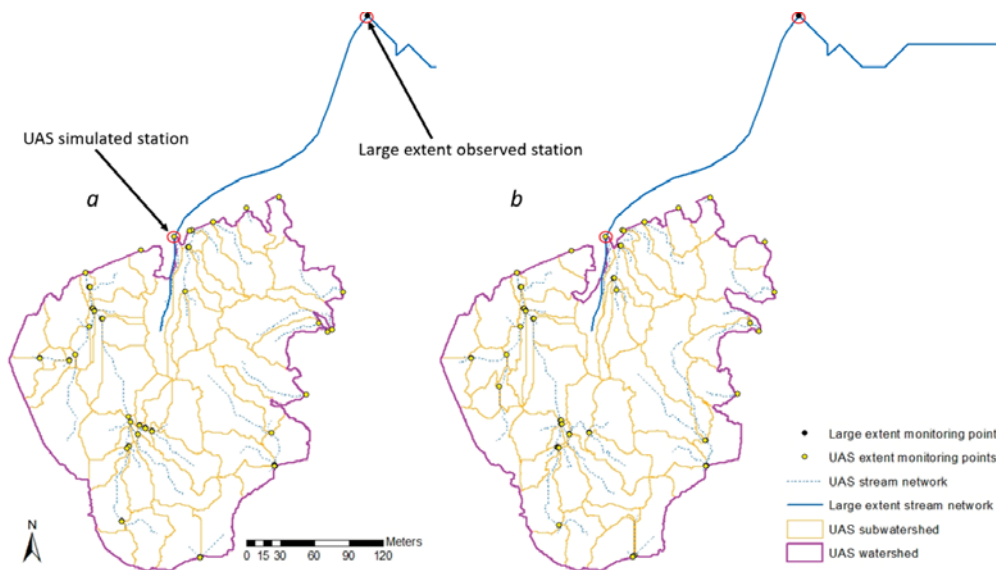
Figure 4. Simplified SWAT UAS extent calibration and validation model for study area: LiDAR derived DTM (*a*) Photogrammetrically derived DTM (*b*).

Both models were calibrated and validated for flow at the monitoring points marked with red circle in Figure 4a,b. The warmup period including calibration and validation period for the SWAT models was consistent with that assigned to the large spatial extent illustrated in Figure 3.

3. Results and Discussion

3.1. Model Calibration and Validation at the Larger Spatial Extent

The SWAT model was calibrated for flow between August 2015 through August 2016 at a monthly timestep. In Figure 5, the statistical measures of model efficiency clearly demonstrate that the simulated flow is within acceptable threshold of the USGS measured data. Moreover, all the measures of model efficiency demonstrated that the 17 SWAT parameters outlined in Table 3 did a decent job in fitting the simulated data to the USGS observed streamflow data. The extent of model uncertainty captured by the 95PPU (>76%) further attest to the effectiveness of the model calibration. The R-factor (R), Nash–Sutcliffe (E), and index of agreement (d) shows strong association between simulated and observed data. Despite the relatively low RMSE, the overwhelmingly excellent efficiency of the other criteria suggests that the model calibration is robust.

Note: R is *R*-factor, E is Nash–Sutcliffe coefficient of simulation efficiency, d is index of agreement, and RMSE is root mean square error.

The SWAT model was validated for flow between August 2017 and August 2018 at a monthly time interval. The model evaluation criteria of R, E, and d (Figure 6) are not that different from those demonstrated for model calibration and suggest a strong validation of the model, though one can conclude the model was slightly better calibrated compared to its validation. Notwithstanding, all the statistical criteria strongly suggest that the model was constructed in a manner that closely matches surface fluvial hydrologic characteristics. Figure 6 also shows that a large fraction (>80%) of model uncertainty was captured by the 95PPU. The widely used model efficiency values generated by Nash–Sutcliffe, index of agreement, and the RMSE are within acceptable levels reported in other studies [61–63].
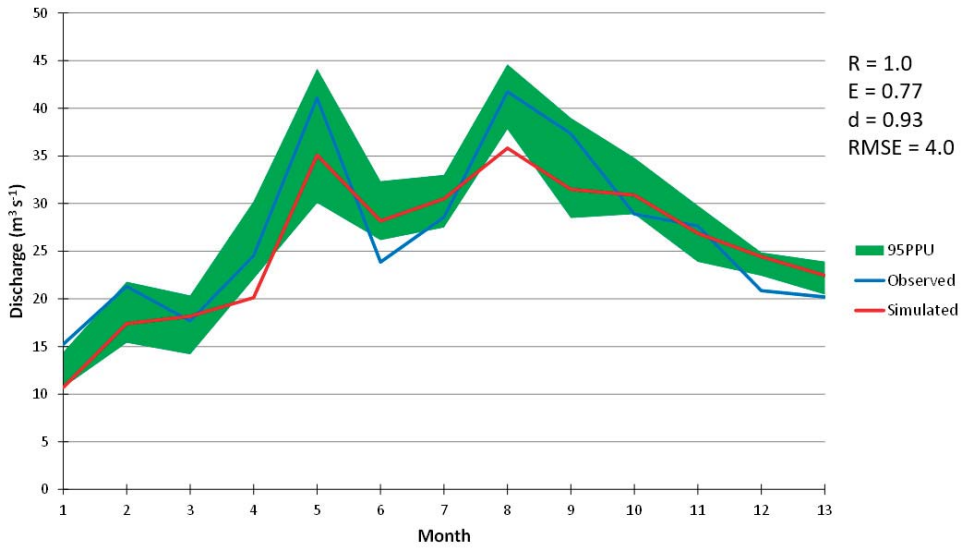
Figure 5. SWAT large extent model calibration subbasin 18 (8/2015–8/2016).
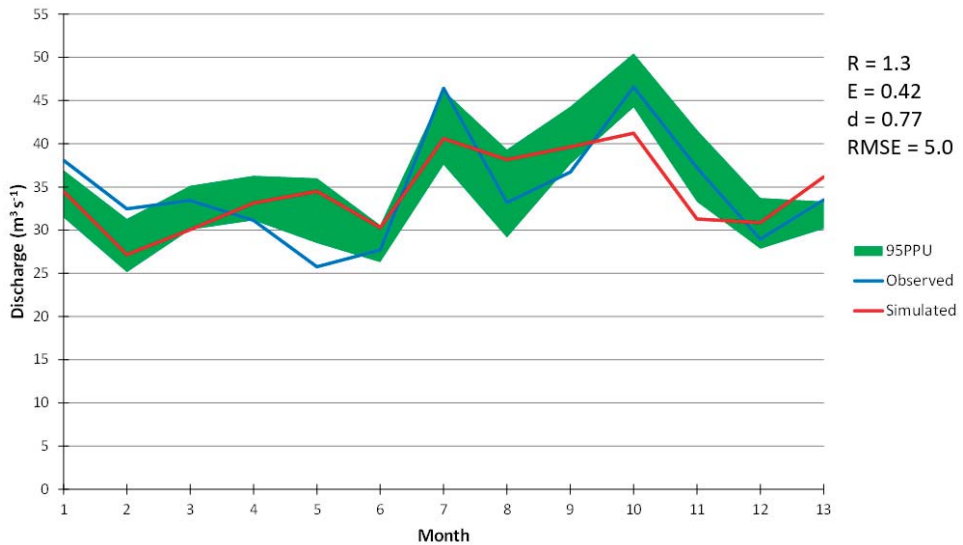
Figure 6. SWAT large extent model validation subbasin 18 (8/2017–8/2018).

Note: R is *R*-factor, E is Nash–Sutcliffe coefficient of simulation efficiency, d is index of agreement, and RMSE is root mean square error.

3.2. Model Calibration and Validation at the UAS Spatial Scale

Following the successful calibration of the large spatial extent SWAT model, the fitted parameter coefficients were transferred to the nested UAS spatial scale models. Moreover, the predicted streamflow at the sub-basin closest to the UAS spatial extent watershed was used for calibrating and validating the models. It has been shown that model parameters and their coefficients are regionally transferrable within a watershed if the efficiency

value statistics are reproducible at a different sub-basin [64]. Calibration results for the UAS derived DTM and Lidar derived DTM demonstrated that both models fall within an acceptable threshold of model calibration efficiency despite the LiDAR derived DTM having a relatively higher R-factor, Nash–Sutcliffe, and index of agreement (Figure 7). Notwithstanding, both models had identical RMSE which turned out to be higher than that obtained at the larger spatial extent scale of calibration. The models generated by the LiDAR DTM and the UAS DTM, respectively also illustrated that a high fraction (>70%) of model uncertainty was captured during calibration as can be seen by the 95PPU. As a result of the model calibration, it can be subsequently concluded that a photogrammetrically derived DTM from a UAS point cloud is effective in modeling flow. Jeziorska et al., [30] reported that a UAS derived terrain model is more effective in accounting for flow morphology and patterns over a lidar derived DTM in areas not covered by vegetation because of its increased spatial resolution. We attribute the slightly lower values of R, E, and d in the UAS derived terrain model to the uncertainty in interpolated terrain beneath the few areas within the watershed that are covered by trees and shrub and also to the single flow (D-8) algorithm used by SWAT. Studies have shown that a multiple flow algorithm better estimates flow compared to single flow algorithm [65,66]. Figure 8 shows the validation results for the LiDAR derived DTM and UAS derived DTM. Both models are within the acceptable threshold of validation based on their simulation efficiency despite the Lidar based DTM scoring slightly higher values compared to the UAS derived DTM in three of the four model efficiency criteria used (Figure 8).
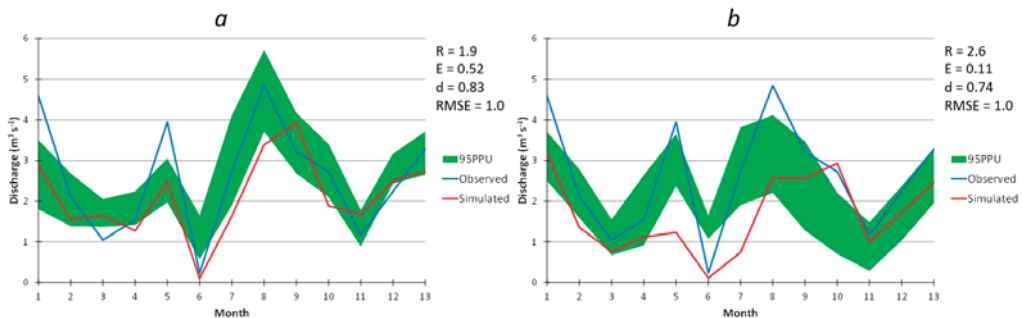
Figure 7. SWAT UAS extent model calibration 8/2015–8/2016: (*a*) Lidar point cloud DTM and (*b*) Photogrammetrically derived point cloud DTM. Note: R is *R*-factor, E is Nash–Sutcliffe coefficient of simulation efficiency, d is index of agreement, and RMSE is root mean square error.
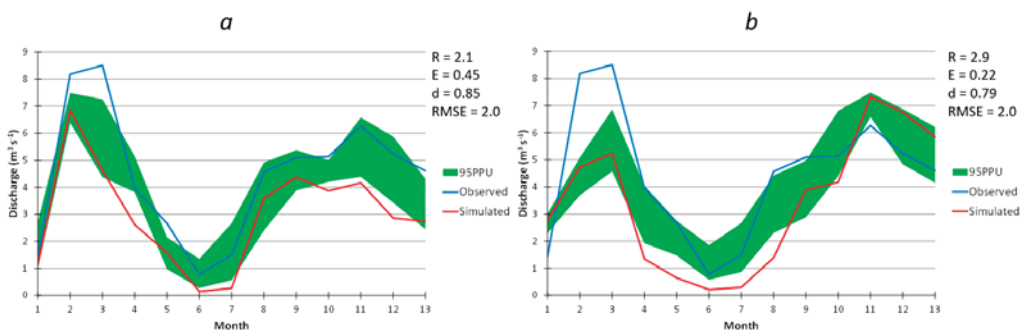
Figure 8. SWAT UAS extent model validation 8/2017–8/2018: (*a*) Lidar point cloud DTM and (*b*) Photogrammetrically derived point cloud DTM. Note: R is *R*-factor, E is Nash–Sutcliffe coefficient of simulation efficiency, d is index of agreement, and RMSE is root mean square error.

Validation results for the two models display close similarities when compared to the results generated by calibration. This suggest that a UAS-derived DTM can serve as an alternative dataset to model streamflow in the absence of lidar DTM provided that the study area has minimal to no vegetation cover. When vegetation cover dominates a study area, ground/terrain models generated by UAS-derived point cloud contains higher errors [67,68] and may not be suitable for modeling streamflow. Since surface runoff is mostly controlled by terrain, we recommend that a UAS derived DTM used for estimating flow and eventual sediment erosion be collected over areas with minimum high vegetation cover, such as trees (<10%). Moreover, as demonstrated by Jensen and Mathews [69], the point cloud should be classified into ground points using a robust algorithm such as the adaptive TIN ground filter employed in this study followed by a manual classification of the automated classified ground points to further eliminate above ground features. The resulting DTM generated from the hybrid classified ground points can be used in modeling flow across space in the absence of a LiDAR derived DTM. This refined UAS derived DTM has great potential to extend the applications of UAS data.

3.3. Assessment of Sediment Erosion at the UAS Spatial Scale

The calibrated and validated SWAT models for the LiDAR point cloud DTM and photogrammetrically derived point cloud DTM were used to model the amount of sediment being eroded and washed from the watershed at the sub-basin level. Figure 9 compares the sediment loads generated by the two models. The photogrammetrically derived point cloud DTM accounted for a slightly higher sediment loading from the watershed compared to that obtained from the LiDAR derived DTM (Figure 9). In sub-basins covered with loose sediment and gentle slopes, the amount of sediment eroded is identical between the LiDAR derived DTM and the UAS-derived point cloud DTM. However, this is not the case in sub-basins that have rugged terrain where the UAS derived DTM generated greater sediment loads compared to the LiDAR derived DTM. We speculate that this difference might be ascribed to the higher spatial resolution of the UAS derived DTM (3.6 cm) compared to the relatively lower spatial resolution of the LiDAR derived DTM (14.3 cm). Digital terrain models derived from UAS point cloud have been shown to be more effective in accounting for streambank erosion [27,33] and measuring gully erosion rates [34] compared to LiDAR -derived DTMs. This effectiveness demonstrates how photogrammetrically derived SfM terrain when used in scenarios with little to no vegetative ground cover, can serve as a low-cost viable alternative to more costly methods that rely on LiDAR data.
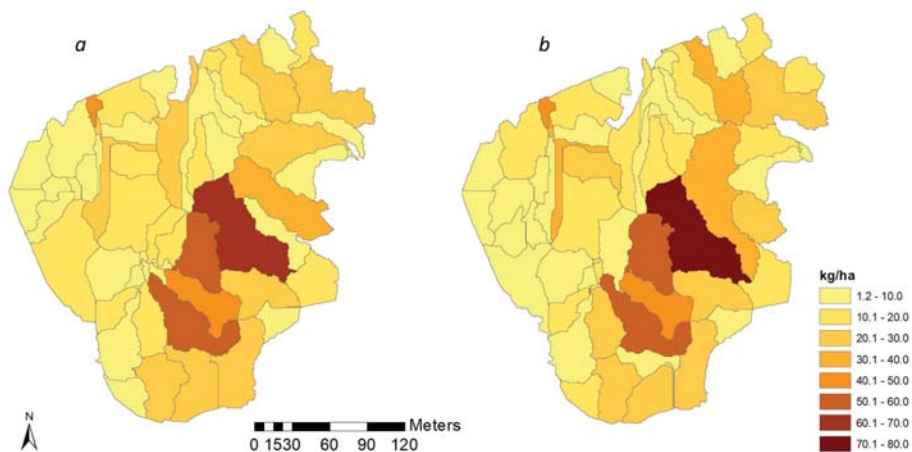
Figure 9. Comparison of sediment erosion generated by (*a*) LiDAR point cloud DTM and (*b*) Photogrammetrically derived point cloud DTM.

Additional research is needed to better compare UAS and LiDAR derived DTMs collected at identical spatial and temporal resolution over non-vegetated terrain to comprehensively evaluate the efficacy of the UAS derived DTM in estimating flow and erosion of sediment. Moreover, the key difference unearthed in this study where both DTMs performed identically in gentle slopes and loose sediments but differently in rugged terrain needs further testing in similar site setting. As the cost of lighter payload LiDAR sensors developed for drone platforms becomes cheaper [70], hydrologic modeling of flow and nonpoint source pollutants which have been historically conducted at moderate to large scales will become more practical at the smaller UAS spatial scale thus providing a more effective tool for monitoring of erosion at mining sites.

4. Conclusions

Unmanned Aerial Systems have been long recognized for their ability to acquire imagery over areas of interest with spatial resolutions that can provide incredible amounts of detail, both temporally and spatially. Coupled with their ability to be quickly deployed over small areas on a frequent basis, UAS have rapidly demonstrated themselves as a valid data collection tool in many geomorphic and geologic applications. While UAS derived data products, such as DSM and DTM have been used in many forms of fluvial research, the integration of UAS derived DTM in a nested scale distributed hydrologic modeling that this study investigated is a unique domain in UAS application. In this research we assessed the feasibility and efficacy of a photogrammetrically derived DTM in modeling sediment erosion across space. The nested scale hydrologic modeling framework successfully downscaled streamflow data from a larger spatial extent and applied to a smaller UAS spatial scale. In this study, we have demonstrated that it is possible to extend the use of UAS derived DTM from river and other narrow transects to the entire image area in modeling erosion potentials. We built on the literature which mostly agrees that the higher spatial resolution obtained from UAS derived products facilitates the modeling of erosion at the transect level. The study also demonstrates that with the tools of model calibration and validation, it is possible to utilize UAS derived DTM to model flow and sediment load estimation in the absence of measured data at the UAS spatial scale. Notwithstanding, we caution that if LiDAR data is available at a higher temporal and spatial frequency, such as the recent lighter payload lidar sensors that can be mounted on UAS platforms, it should be used to monitor flow and sediment loading rather than a photogrammetrically derived DTM especially if the study area is covered with significant vegetation. The nested scale methodology developed and utilized in this study can be extended to similar fluvial aggregate excavation operations. The hydrologic modeling framework serves as an excellent example of how UAS data can serve as a low-cost alternative to LiDAR in terms of decision making and lowering overhead costs in a variety of extraction-based industries. Future research should evaluate the quality and accuracy of models over areas with diverse amounts of vegetation cover and provide a direct comparison of DTM models gathered via LiDAR and UAS imagery, respectively.

References

1. Huang, S.; Tang, L.; Hupy, J.P.; Wang, Y.; Shao, G. A Commentary Review on the Use of Normalized Difference Vegetation Index (NDVI) in the Era of Popular Remote Sensing. *J. For. Res.* **2021**, *32*, 1–6. [CrossRef]
2. Demario, A.; Lopez, P.; Plewka, E.; Wix, R.; Xia, H.; Zamora, E.; Gessler, D.; Yalin, A.P. Water Plume Temperature Measurements by an Unmanned Aerial System (UAS). *Sensors* **2017**, *17*, 306. [CrossRef] [PubMed]
3. Bellvert, J.; Zarco-Tejada, P.J.; Girona, J.; Fereres, E. Mapping Crop Water Stress Index in a 'Pinot-Noir' Vineyard: Comparing Ground Measurements with Thermal Remote Sensing Imagery from an Unmanned Aerial Vehicle. *Precis. Agric.* **2014**, *15*, 361–376. [CrossRef]
4. Lelong, C.C.D.; Burger, P.; Jubelin, G.; Roux, B.; Labbe, S.; Baret, F. Assessment of Unmanned Aerial Vehicles Imagery for Quantitative Monitoring of Wheat Crop in Small Pots. *Sensors* **2008**, *8*, 3557–3585. [CrossRef] [PubMed]
5. Singh, K.K.; Frazier, A.E. A Meta-Analysis and Review of Unmanned Aircraft System (UAS) Imagery for Terrestrial Applications. *Int. J. Remote. Sens.* **2018**, *39*, 5078–5098. [CrossRef]
6. Tang, L.; Shao, G. Drone Remote Sensing for Forestry Research and Practices. *J. For. Res.* **2015**, *26*, 791–797. [CrossRef]
7. Manfreda, S.; McCabe, M.F.; Miller, P.E.; Lucas, R.; Pajuelo Madrigal, V.; Mallinis, G.; Ben-Dor, E.; Helman, D.; Estes, L.; Ciraolo, G.; et al. On the Use of Unmanned Aerial Systems for Environmental Monitoring. *Remote. Sens.* **2018**, *10*, 641. [CrossRef]
8. Zhang, H.; Aldana-Jague, E.; Clapuyt, F.; Wilken, F.; Vanacker, V.; Van Oost, K. Evaluating the Potential of Post-processing Kinematic (PPK) Georeferencing for UAV-Based Structure-from-Motion (SfM) Photogrammetry and Surface Change Detection. *Earth Surf. Dyn.* **2019**, *7*, 807–827. [CrossRef]
9. Westoby, M.J.; Lim, M.; Hogg, M.; Pound, M.J.; Dunlop, L.; Woodward, J. Cost-Effective Erosion Monitoring of Coastal Cliffs. *Coast. Eng.* **2018**, *138*, 152–164. [CrossRef]
10. Clapuyt, F.; Vanacker, V.; Van Oost, K. Reproducibility of UAV-Based Earth Topography Based on Structure-from-Motion Algorithms. *Geomorphology* **2016**, *260*, 4–15. [CrossRef]
11. Lowe, D. Object Recognition from Local Scale-Invariant Features. In Proceedings of the IEEE Transactions on Pattern Analysis and Machine Intelligence, Kerkyra, Greece, 20–27 September 1999.
12. Snavely, N. Scene Reconstruction and Visualization from Internet Photo Collections: A Survey. *IPSJ Trans. Comput. Vis. Appl.* **2011**, *3*, 44–66. [CrossRef]
13. Snavely, N.; Seitz, S.M.; Szeliski, R. Modeling the World from Internet Photo Collections. *Int. J. Comput. Vis.* **2008**, *80*, 189–210. [CrossRef]
14. Fonstad, M.A.; Dietrich, J.T.; Courville, B.C.; Jensen, J.L.; Carbonneau, P.E. Topographic Structure from Motion: A New Development in Photogrammetric Measurement. *Earth Surf. Process. Landforms* **2013**, *38*, 421–430. [CrossRef]
15. Miller, P.; Kunz, M.; Mills, J.; King, M.; Murray, T.; James, T.; Marsh, S. Assessment of Glacier Volume Change Using ASTER-Based Surface Matching of Historical Photography. *IEEE Trans. Geosci. Remote. Sens.* **2009**, *47*, 1971–1979. [CrossRef]
16. Resop, J.P.; Lehmann, L.; Hession, W.C. Drone Laser Scanning for Modeling Riverscape Topography and Vegetation: Comparison with Traditional Aerial Lidar. *Drones* **2019**, *3*, 35. [CrossRef]
17. Leitão, J.P.; De Vitry, M.M.; Scheidegger, A.; Rieckermann, J. Assessing the Quality of Digital Elevation Models Obtained from Mini Unmanned Aerial Vehicles for Overland Flow Modelling in Urban Areas. *Hydrol. Earth Syst. Sci.* **2016**, *20*, 1637–1653. [CrossRef]
18. Tauro, F.; Porfiri, M.; Grimaldi, S. Surface Flow Measurements from Drones. *J. Hydrol.* **2016**, *540*, 240–245. [CrossRef]
19. Padró, J.-C.; Carabassa, V.; Balagué, J.; Brotons, L.; Alcañiz, J.M.; Pons, X. Monitoring Opencast Mine Restorations Using Unmanned Aerial System (UAS) Imagery. *Sci. Total. Environ.* **2019**, *657*, 1602–1614. [CrossRef] [PubMed]
20. Park, S.; Choi, Y. Applications of Unmanned Aerial Vehicles in Mining from Exploration to Reclamation: A Review. *Minerals* **2020**, *10*, 663. [CrossRef]
21. Ren, H.; Zhao, Y.; Xiao, W.; Hu, Z. A Review of UAV Monitoring in Mining Areas: Current Status and Future Perspectives. *Int. J. Coal Sci. Technol.* **2019**, *6*, 1–14. [CrossRef]
22. Baltsavias, E.P. A Comparison between Photogrammetry and Laser Scanning. *ISPRS J. Photogramm. Remote Sens.* **1999**, *54*, 83–94. [CrossRef]
23. Rocha, J.; Duarte, A.; Silva, M.; Fabres, S.; Vasques, J.; Revilla-Romero, B.; Quintela, A. The Importance of High Resolution Digital Elevation Models for Improved Hydrological Simulations of a Mediterranean Forested Catchment. *Remote. Sens.* **2020**, *12*, 3287. [CrossRef]
24. Ballatore, P. Extracting Digital Elevation Models from SAR Data through Independent Component Analysis. *Int. J. Remote. Sens.* **2011**, *32*, 3807–3817. [CrossRef]

25. Ghuffar, S. DEM Generation from Multi Satellite PlanetScope Imagery. *Remote. Sens.* **2018**, *10*, 1462. [CrossRef]
26. Husson, E.; Ecke, F.; Reese, H. Comparison of Manual Mapping and Automated Object-Based Image Analysis of Non-Submerged Aquatic Vegetation from Very-High-Resolution UAS Images. *Remote. Sens.* **2016**, *8*, 724. [CrossRef]
27. Hamshaw, S.D.; Engel, T.; Rizzo, D.M.; O'Neil-Dunne, J.; Dewoolkar, M.M. Application of Unmanned Aircraft System (UAS) for Monitoring Bank Erosion along River Corridors. *Geomatics, Nat. Hazards Risk* **2019**, *10*, 1285–1305. [CrossRef]
28. Kang, B.; Kim, J.G.; Kim, D.; Kang, D.H. Flow Estimation using Drone Optical Imagery with Non-uniform Flow Modeling in a Controlled Experimental Channel. *KSCE J. Civ. Eng.* **2019**, *23*, 1891–1898. [CrossRef]
29. Petrasova, A.; Mitasova, H.; Petras, V.; Jeziorska, J. Fusion of High-Resolution DEMs for Water Flow Modeling. *Open Geospat. Data Softw. Stand.* **2017**, *2*, 205. [CrossRef]
30. Jeziorska, J.; Mitasova, H.; Petrasova, A.; Petras, V.; Divakaran, D.; Zajkowski, T. Overland Flow Analysis Using Time Series of sUAS Derived Data. *ISPRS Ann. Photogramm. Remote Sens. Spat. Inf. Sci.* **2016**, *III*, 159–166. [CrossRef]
31. Tang, Q.; Schilling, O.S.; Kurtz, W.; Brunner, P.; Vereecken, H.; Franssen, H.-J.H. Simulating Flood-Induced Riverbed Transience Using Unmanned Aerial Vehicles, Physically Based Hydrological Modeling, and the Ensemble Kalman Filter. *Water Resour. Res.* **2018**, *54*, 9342–9363. [CrossRef]
32. Tamminga, A.D.; Hugenholtz, C.H.; Eaton, B.C.; Lapointe, M. Hyperspatial Remote Sensing of Channel Reach Morphology and Hydraulic Fish Habitat Using an Unmanned Aerial Vehicle (UAV): A First Assessment in the Context of River Research and Management. *River Res. Appl.* **2015**, *31*, 379–391. [CrossRef]
33. Meinen, B.U.; Robinson, D.T. Streambank Topography: An Accuracy Assessment of UAV-Based and Traditional 3D Reconstructions. *Int. J. Remote. Sens.* **2019**, *41*, 1–18. [CrossRef]
34. Stocker, C.; Eltner, A.; Karrasch, P. Measuring Gullies by Synergetic Application of UAV and Close Range Photogram-Metry–A Case Study from Andalusia, Spain. *Catena* **2015**, *132*, 1–11. [CrossRef]
35. Gudino-Elizondo, N.; Biggs, T.W.; Castillo, C.; Bingner, R.L.; Langendoen, E.J.; Taniguchi, K.T.; Kretzschmar, T.; Yuan, Y.; Liden, D. Measuring Ephemeral Gully Erosion Rates and Topographical Thresholds in an Urban Watershed Using Unmanned Aerial Systems and Structure from Motion Photogrammetric Techniques. *Land Degrad. Dev.* **2018**, *29*, 1896–1905. [CrossRef]
36. Van der Velde, Y.; Rozemeijer, J.C.; De Rooij, G.H.; Van Geer, F.C.; Torfs, P.J.J.F. Improving Catchment Discharge Predic-Tions by Inferring Flow Route Contributions from a Nested-Scale Monitoring and Model Setup. *Hydrol. Earth Syst. Sci.* **2011**, *15*, 913–930. [CrossRef]
37. Zeiger, S.; Hubbart, J.A. Quantifying Suspended Sediment Flux in a Mixed-Land-Use Urbanizing Watershed Using a Nest-Ed-Scale Study Design. *Sci. Total Environ.* **2016**, *542*, 315–323. [CrossRef] [PubMed]
38. Didszun, J.; Uhlenbrook, S. Scaling of Dominant Runoff Generation Processes: Nested Catchments Approach Using Multiple Tracers. *Water Resour. Res.* **2008**, *44*. [CrossRef]
39. USDA (United States Department of Agriculture). 2019 National Agriculture Imagery Program. Available online: http://nrcs.usda.gov (accessed on 14 June 2019).
40. James, M.R.; Chandler, J.H.; Eltner, A.; Fraser, C.; Miller, P.E.; Mills, J.P.; Noble, T.; Robson, S.; Lane, S.N. Guidelines on the Use of Structure-from-Motion Photogrammetry in Geomorphic Research. *Earth Surf. Process. Landforms* **2019**, *44*, 2081–2084. [CrossRef]
41. Axelsson, P. DEM Generation from Laser Scanner Data Using Adaptive Tin Models. In *The International Archives of the Photogrammetry and Remote Sensing*; 2000; Volume 33, pp. 110–117. Available online: https://www.isprs.org/proceedings/XXXIII/congress/part4/111_XXXIII-part4.pdf (accessed on 1 February 2021).
42. Serifoglu, C.; Gungor, O.; Yilmaz, V. Performance Evaluation of Different Filtering Algorithms for UAV-Based Point Clouds. The International Archives of the Photogrammetry. *Remote Sens. Spat. Inf. Sci.* **2016**, *41*. [CrossRef]
43. Waukesha County. Elevation/Imagery Data Download Application, Waukesha County. 2020. Available online: http://data-waukeshacounty.opendata.arcgis.com/datasets/12b0cdf25d5a458ca74b97cd23ad8135 (accessed on 6 July 2019).
44. Blaschke, T. Object Based Image Analysis for Remote Sensing. *ISPRS J. Photogramm. Remote. Sens.* **2010**, *65*, 2–16. [CrossRef]
45. Rodriguez-Galiano, V.; Ghimire, B.; Rogan, J.; Chica-Olmo, M.; Rigol-Sanchez, J. An Assessment of the Effectiveness of a Random Forest Classifier for Land-Cover Classification. *ISPRS J. Photogramm. Remote. Sens.* **2012**, *67*, 93–104. [CrossRef]
46. Drăguţ, L.; Tiede, D.; Levick, S.R. ESP: A Tool to Estimate Scale Parameter for Multiresolution Image Segmentation of Remotely Sensed Data. *Int. J. Geogr. Inf. Sci.* **2010**, *24*, 859–871. [CrossRef]
47. Wilson, C.O.; Liang, B.; Rose, S.J. Projecting Future Land Use/Land Cover by Integrating Drivers and Plan Prescriptions: The Case for Watershed Applications. *GIScience Remote. Sens.* **2018**, *56*, 511–535. [CrossRef]
48. Kahya, O.; Bayram, B.; Reis, S. Land Cover Classification with an Expert System Approach Using Landsat ETM Imagery: A Case Study of Trabzon. *Environ. Monit. Assess.* **2008**, *160*, 431–438. [CrossRef] [PubMed]
49. Congalton, R.G. A Review of Assessing the Accuracy of Classifications of Remotely Sensed Data. *Remote. Sens. Environ.* **1991**, *37*, 35–46. [CrossRef]
50. Arnold, J.G.; Allen, P.M.; Bernhardt, G. A Comprehensive Surface-Ground Flow Model. *J. Hydrol.* **1993**, *142*, 47–69. [CrossRef]
51. Arnold, J.G.; Srinivasan, R.; Muttiah, R.S.; Williams, J.R. Large Area Hydrologic Modeling and Assessment Part I: Model Development. *JAWRA J. Am. Water Resour. Assoc.* **1998**, *34*, 73–89. [CrossRef]
52. Soil Survey Staff, Natural Resources Conservation Service, United States Department of Agriculture. Soil Survey Geographic (SSURGO) Database for Waukesha and Washington Counties, Wisconsin. Available online: https://data.nal.usda.gov/dataset/soil-survey-geographic-database-ssurgo (accessed on 6 June 2020).

53. Abbaspour, K.C. User Manual for SWAT-CUP 2012. SWAT Calibration and Uncertainty Programs. (105 pp.) Dubendorf, Switzerland: Ewag: Swiss Fed. Inst. Of Aquat. Sci. and Technol. 2018. Available online: http://www.eawag.ch/forschung/siam/software/swat/index (accessed on 5 June 2018).
54. Wilson, C.O. Land Use/Land Cover Water Quality Nexus: Quantifying Anthropogenic Influences on Surface Water Quality. *Environ. Monit. Assess.* **2015**, *187*, 1–23. [CrossRef]
55. Abbaspour, K.C.; Vaghefi, S.A.; Srinivasan, R. A Guideline for Successful Calibration and Uncertainty Analysis for Soil and Water Assessment: A Review of Papers from the 2016 International SWAT Conference. *Water* **2017**, *10*, 6. [CrossRef]
56. Rouholahnejad, E.; Abbaspour, K.; Vejdani, M.; Srinivasan, R.; Schulin, R.; Lehmann, A. A Parallelization Framework for Calibration of Hydrological Models. *Environ. Model. Softw.* **2012**, *31*, 28–36. [CrossRef]
57. Wilson, C.; Weng, Q. Assessing Surface Water Quality and Its Relation with Urban Land Cover Changes in the Lake Calumet Area, Greater Chicago. *Environ. Manag.* **2010**, *45*, 1096–1111. [CrossRef] [PubMed]
58. Nash, J.E.; Sutcliffe, J.V. River Flow Forecasting through Conceptual Models: Part 1—A Discussion of Principles. *J. Hydrol.* **1970**, *10*, 282–290. [CrossRef]
59. Willmott, C.J. On the Validation of Models. *Phys. Geogr.* **1981**, *2*, 184–194. [CrossRef]
60. Ritter, A.; Munoz, C. Performance Evaluation of Hydrological Models: Statistical Significance for Reducing Subjectivity in Goodness-of-Fit Assessments. *J. Hydrol.* **2013**, *480*, 33–45. [CrossRef]
61. Krysanova, V.; Müller-Wohlfeil, D.-I.; Becker, A. Development and Test of a Spatially Distributed Hydrological/Water Quality Model for Mesoscale Watersheds. *Ecol. Model.* **1998**, *106*, 261–289. [CrossRef]
62. Eckhardt, K.; Arnold, J. Automatic Calibration of a Distributed Catchment Model. *J. Hydrol.* **2001**, *251*, 103–109. [CrossRef]
63. Krause, P.; Boyle, D.P.; Bäse, F. Comparison of Different Efficiency Criteria for Hydrological Model Assessment. *Adv. Geosci.* **2005**, *5*, 89–97. [CrossRef]
64. Bárdossy, A. Calibration of Hydrological Model Parameters for Ungauged Catchments. *Hydrol. Earth Syst. Sci.* **2007**, *11*, 703–710. [CrossRef]
65. Pei, T.; Qin, C.-Z.; Zhu, A.-X.; Yang, L.; Luo, M.; Li, B.; Zhou, C. Mapping Soil Organic Matter Using the Topographic Wetness Index: A Comparative Study Based on Different Flow-Direction Algorithms and Kriging Methods. *Ecol. Indic.* **2010**, *10*, 610–619. [CrossRef]
66. Wilson, J.P.; Lam, C.S.; Deng, Y. Comparison of the Performance of Flow-Routing Algorithms Used in GIS-Based Hydrologic Analysis. *Hydrol. Process.* **2007**, *21*, 1026–1044. [CrossRef]
67. Graham, A.; Coops, N.C.; Wilcox, M.; Plowright, A. Evaluation of Ground Surface Models Derived from Unmanned Aerial Systems with Digital Aerial Photogrammetry in a Disturbed Conifer Forest. *Remote. Sens.* **2019**, *11*, 84. [CrossRef]
68. Lizuka, K.; Itoh, M.; Shiodera, S.; Matsubara, T.; Dohar, M.; Watanabe, K. Advantages of Unmanned Aerial Vehicle (UAV) Photogrammetry for Landscape Analysis Compared with Satellite Data: A Case Study of Postmining Sites in Indonesia. *Cogent Geosci.* **2018**, *4*, 1–15.
69. Jensen, J.L.R.; Mathews, A.J. Assessment of Image-Based Point Cloud Products to Generate a Bare Earth Surface and Estimate Canopy Heights in a Woodland Ecosystem. *Remote. Sens.* **2016**, *8*, 50. [CrossRef]
70. Almeida, D.; Broadbent, E.; Zambrano, A.; Wilkinson, B.; Ferreira, M.; Chazdon, R.; Meli, P.; Gorgens, E.; Silva, C.; Stark, S.; et al. Monitoring the Structure of Forest Restoration Plantations with a Drone-Lidar System. *Int. J. Appl. Earth Obs. Geoinf.* **2019**, *79*, 192–198. [CrossRef]

Temperature Profiling of Waterbodies with a UAV-Integrated Sensor Subsystem

Cengiz Koparan, Ali Bulent Koc *, Calvin Sawyer and Charles Privette

Department of Agricultural Sciences, Clemson University, Clemson, SC 29634, USA;
ckopara@g.clemson.edu (C.K.); CALVINS@clemson.edu (C.S.); privett@clemson.edu (C.P.)
* Correspondence: bulent@clemson.edu; Tel.: +1-864-656-0496

Abstract: Evaluation of thermal stratification and systematic monitoring of water temperature are required for lake management. Water temperature profiling requires temperature measurements through a water column to assess the level of thermal stratification which impacts oxygen content, microbial growth, and distribution of fish. The objective of this research was to develop and assess the functions of a water temperature profiling system mounted on a multirotor unmanned aerial vehicle (UAV). The buoyancy apparatus mounted on the UAV allowed vertical takeoff and landing on the water surface for in situ measurements. The sensor node that was integrated with the UAV consisted of a microcontroller unit, a temperature sensor, and a pressure sensor. The system measured water temperature and depth from seven pre-selected locations in a lake using autonomous navigation with autopilot control. Measurements at 100 ms intervals were made while the UAV was descending at 2 m/s until it landed on water surface. Water temperature maps of three consecutive depths at each location were created from the measurements. The average surface water temperature at 0.3 m was 22.5 °C, while the average water temperature at 4 m depth was 21.5 °C. The UAV-based profiling system developed successfully performed autonomous water temperature measurements within a lake.

Keywords: autonomous; hexacopter; water quality; water stratification; water temperature

1. Introduction

Evaluation of the physiochemical parameters of lake water is crucial for lake management and water quality monitoring. Water temperature is one of the physiochemical parameters that has a significant impact on water chemistry. Change in water temperature can trigger several phenomena in a waterbody. Some of these phenomena can occur naturally, causing no harm to the aquatic system, while others can cause negative impacts on water quality. Thermal stratification occurs at a depth of 3.6 m in many lakes where layers are formed with different temperatures [1]. These layers are categorized from top to bottom where the warmest layer is on the top and the coolest layer is at the bottom as the epilimnion, the thermocline, and the hypolimnion [2]. A lake can be considered as stratified when the temperature difference between the epilimnion and the hypolimnion is greater than 1 °C [3]. An inverse stratification, where coolest layer forms on the top while the warmer layer rests at the bottom, occurs during winter [4]. This phenomenon can impact many aspects of the lake, such as spatial distribution of fish, microbial growth, and oxygen content [5]. Other than the thermal stratification, water temperature can be the direct indicator of dissolved oxygen (DO), toxic absorption, and salinity [6]. The growth rate of algae and aquatic plants are influenced by change in temperature, where reduced DO due to increased temperature can cause harmful effects to the aquatic life [7]. Other factors such as discharge of industrial wastes, forest harvesting, and agricultural runoff can affect water temperature [8]. Therefore, periodic evaluation of the thermal stratification, as well as systematic monitoring of water temperature, are important for water quality monitoring and lake management.

Water temperature monitoring systems vary depending on the size of the targeted waterbody. The most common water temperature monitoring systems are manual sampling with multi-parameter sensors and buoy-based submersible sensor systems that can provide real time water temperature measurements from water columns [5,9]. The multi-parameter sensors and the buoy-based temperature sensors come with different configurations depending on the desired monitoring depth and sampling conditions [10]. Buoy-based temperature sensors are formed by thermistors that are embedded along a single cable, forming a thermistor chain [11]. The total number of thermistors and the distance between each thermistor vary depending on the depth, width, and other hydrological properties of the lake [12,13]. A buoy-based thermistor chain can make synchronous water temperature measurements at various depths, thus providing information for water column profiling. Multi-parameter sensors are useful for rapid water temperature monitoring from shore; however, they require transport vehicles and extensive labor. Buoy-based thermistors are at a fixed location and the spatial resolution of the measurements depends on the number of thermistors. Buoy-based systems must be installed for a longer period with limited numbers due to cost and maintenance constraints. Because shallow lakes stratify for short periods of time, the installation of buoy-based systems can be impractical and expensive [14]. An easily deployable system that can collect water temperature measurements with high spatial resolution within a short period of time could be applicable in shallow waters.

Unmanned aerial vehicles (UAVs) offer advantages over current multi-parameter sensors and buoy-based systems for water temperature profiling when it comes to lake management and water quality monitoring. UAVs are mobile and easily deployable from nearby location to a waterbody. Recent studies have utilized remote sensing and UAVs for monitoring the surface temperature of waterbodies. Thermal infrared remote sensing has been used for measuring surface water temperature in rivers and lakes for practical applications [15]. UAV-based thermal infrared mapping to assess groundwater discharge into coastal zones has been studied [16]. In addition to remote sensing, temperature sensor-integrated UAVs have been tested for water temperature measurements in lakes [17,18]. These UAV-based systems acquire temperature measurements from an applicable depth while hovering above water surface. Aerial measurements with a UAV while hovering above a water surface increases the battery use, thereby limiting the number of samples that can be taken [19]. UAV systems rely on sensitive navigational sensor technology to fix their position in the air. When it comes to water sampling at a lower altitude, many things can go wrong, resulting in crash landing into the water. The hover altitude of UAV depends on wind speed, sensor calibration, and payload swing motion. These factors prevent the precise depth of the water temperature measurements [20]. Therefore, more reliable UAV-based water temperature measurement approach is required to provide water column temperature data.

Our previous studies introduced the development, application, and evaluation of UAVs for water quality monitoring. First, a water sampling UAV for aerial water sample collection was designed and evaluated [21]. Second, an in situ water quality measurement UAV was designed and utilized for autonomous water quality measurements within an agricultural pond [19]. Third, the water collection apparatus and the sensor node were combined in the same UAV with a relatively larger payload capacity [22]. Fourth, the combined UAV was re-designed for adaptive water sampling where the decision for water collection was made based on in situ water quality measurements with the onboard sensor node.

The objective of this research was to develop and test a water temperature measurement system UAV for lake temperature profiling and monitoring. The in situ water quality measurement UAV reported in Koparan et al. [19] was re-modeled by replacing the sensor node with a depth and temperature sensors and the buoyancy apparatus on the UAV was modified for safer water-landing. The novelty of the system presented here is that the UAV starts measuring the temperature and depth when the temperature and pressure probes are in the water while descending. Another key feature of the system is that the UAV can land on the water surface and take off from the water surface rather than hovering during measurements.

2. Materials and Methods

2.1. UAV and Sensor Node Components

The system developed for water temperature profiling consisted of a hexacopter UAV and a sensor node. The UAV was custom designed and the technical specifications were provided in a previous publication [19]. The gross weight of the aircraft was 3100 g (UAV and payload). The weight of the UAV was 2,300g and the payload (sensor node) was 800g including a second battery, microcontroller unit with protective case, temperature and pressure probes, extension cord (10 m), and protective steel case for the probes. The second battery was a Li-Po battery (7.4 V, 2.200 mAh, Venom, Rathdrum, ID, USA). The voltage to the microcontroller was regulated using a second battery with a battery eliminator circuit (BEC). A separate battery for the sensor node allowed dismounting the unit for standalone measurements without using the UAV.

The pressure and temperature sensors were embedded as a single unit by the manufacturer (Bar02, Blue Robotics, Torrance, CA, USA). An integration of this single unit with a microcontroller unit (Arduino Mega 2560, Ivrea, Italy) was made for calibration, control, and data recording. The pressure measurements were used to determine the depth at which temperature measurements were made. The measurements were recorded in a secure digital card (SD card) (SunFounder, Shenzhen City, Guangdong Province, China) that was inserted with the microcontroller unit. A voltage converter circuit (I2C Level Converter, Blue Robotics, Torrance, CA, USA) was used with the pressure sensor to regulate voltage and to enable communication with the microcontroller unit. The pressure sensor and voltage converter circuit were waterproofed in a custom designed 3D printed case and sealed with epoxy. (Figure 1). The 3D printed case was placed in a steel tube to ensure that the pressure sensor would submerge rapidly in the water. The steel tube was coated with Flex Seal (Flex Seal, Weston, FL, USA) to prevent corrosion. The microcontroller platform was sealed in a box and mounted on the UAV. The pressure sensor was suspended with a 10 m long tether.

| (a) | (b) | (c) | (d) |
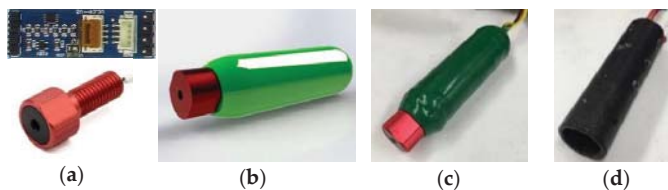
Figure 1. The sensor node assembly: (**a**) pressure sensor and voltage converter circuit, (**b**) computer aided design (CAD) of the case in SolidWorks, (**c**) pressure sensor in 3D printed and sealed case, and (**d**) steel tube to enable rapid submerge and sensor protection.

2.2. Experiment Site and Sampling Locations

The UAV-based water temperature profiling system was evaluated and tested in Lake Issaqueena (Pickens County, South Carolina). The length of the lake is 13 km, with an approximate surface area of 36 ha. The width of the lake at the largest section is 400 m. The top of the dam at Lake Issaqueena is about 15.7 m above bedrock. The water temperature averages 21.9 °C in summer, and 4 °C in winter [23]. In 2005, The South Carolina Department of Health and Environmental Control (SCDHEC) reported that water quality parameters meet the standards at this lake [24]. This lake was chosen for the experiments because the results could be used to generate new data sets for water quality monitoring. Lake Issaqueena has no boat access from neighboring Keowee River, thereby providing safe UAV flight conditions for the experiments. Figure 2 shows the UAV integrated sensor node and launch locations at the lake.
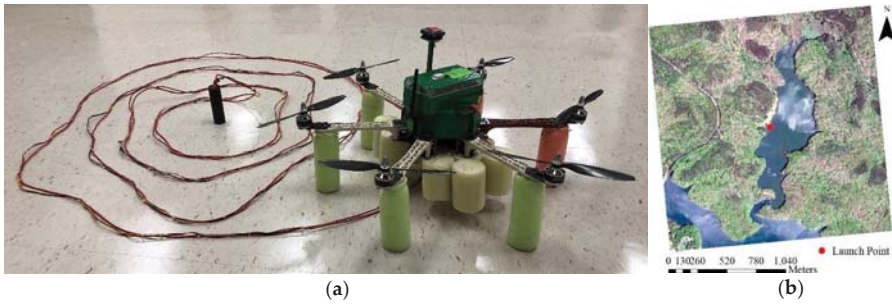
Figure 2. (**a**) Sensor node integrated with the aircraft and (**b**) the launch location in Lake Issaqueena.

Due to the flight restrictions imposed by Federal Aviation Administration (FAA) and limited battery power, the water temperature profiling experiments were conducted in a smaller portion of the lake. The FAA mandates UAV flights to be within the line of sight at a maximum altitude of 120 m above ground level [25]. Because of these limitations, the sampling locations were selected in areas where the UAV can access with the limited battery power while staying within line of sight. The UAV launch location was marked as zero and the water sampling locations were marked with numbers one to seven in the map in Figure 3. The UAV launch location was free of trees and provided flat ground for safe takeoff and landing. Water sampling locations were assigned in grid sampling fashion while scattered to provide water temperature measurements to represent the entire area within the mission plan boundary. The distance between the sampling locations were 80 m to 90 m apart from each other. The shortest flight distance was 73 m, from launch location to sampling location one, and the longest flight distance was 290 m, from launch location to sampling location seven.
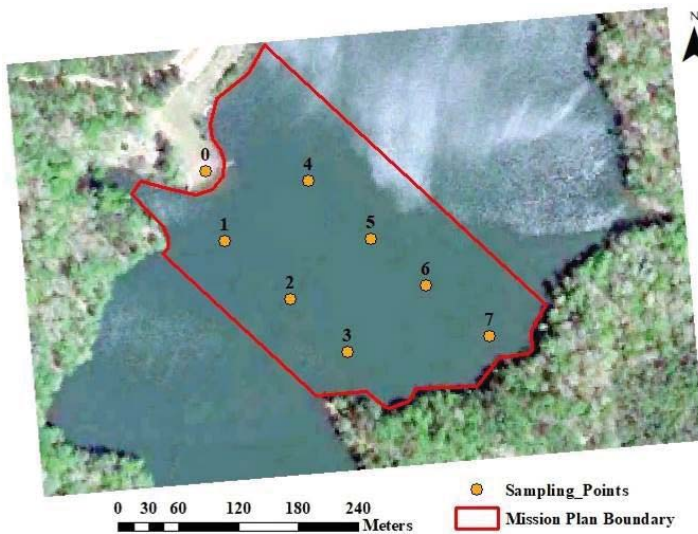
Figure 3. A section of the lake was used as the experiment site for measurements.

2.3. Water Temperature Profiling Data Collection

The experiments for water temperature profiling were conducted on 25 April 2019 at 3:00 p.m. The average air temperature from 20 m altitude to water surface was 24 °C within the mission plan boundary. The air temperature measurements were obtained from the UAV's internal temperature sensor. The UAV with integrated sensor node was deployed to each of the sampling points with

autopilot-controlled autonomous flights. The navigation altitude was set as 20 m to provide safe flight during travel as the probe was mounted on a 10 m long tether. After the navigation destination was been reached, the autopilot let the UAV slowly descend and land on the water surface for 5 s. The temperature and water depth measurements were made during the descent until landing. After completing measurements, the UAV took off and continued with the mission plan to measure water temperature and depth at the next sampling location (Figure 4). The autonomous flights were programmed with a ground control station using the open source Mission Planner (MP) software and each individual flight was assigned as a mission plan [26]. The limited battery power and long flight distances made it necessary to divide the selected area into individual mission plans. Locations one and two were included in the first mission plan, location three was included in the second, locations four and five were included in the third, location six was included in the fourth, and location seven was included in the fifth mission plan.
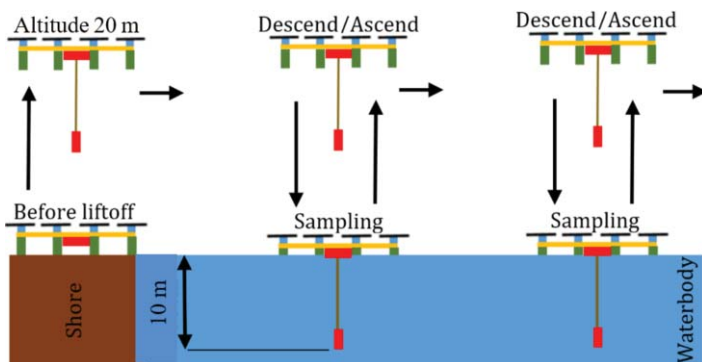
Figure 4. Applied method of water temperature measurements with the UAV.

The water depth and temperature measurements were initiated by the autopilot when the UAV arrived at the predefined sampling location at 20 m altitude. Water depth and temperature measurements were recorded at 100 ms intervals while the UAV was descending at a rate of 2 m/s for landing. A flare altitude of 10 m was assigned in the autopilot's configurations for safe, smooth, and steady landing. Flare altitude is the final stage of the auto-landing procedure where autopilot decreases the throttle and slows down the UAV to readjust the descent speed prior to landing [26].

The number of measurements at each location varied depending on the water depth. The depth measurements indicated the depth of the probe during descent; therefore, repeated measurements were expected once the probe had reached the bottom of the water column. Measurements that repeated themselves after a certain depth were assigned as the maximum water depth at that sampling location. The collected water depth and temperature data were used to create a bathymetric map and water temperature maps for visualization of water temperature distribution at the surface (0.3 m) and at the depths of 2 m and 4 m. The Inverse Distance Weighted Interpolation (IDW) method was used for processing and interpolating in ArcMap (ESRI, Redlands, CA, USA). Raster maps were developed by interpolating vector data in the Geographic Information System (GIS) to illustrate data values for intermediate locations [27]. The relationship between water depth, water temperature, and location was evaluated. The water temperature distribution was illustrated in R software (R-GUI, Vienna, Austria) driven 3D scatter plot [28].

3. Results and Discussion

The indoor depth measurements with the sensor node were 100% accurate when compared to the reference depth values within a water column. The 3D printed watertight case protected the probe and the circuits from water damage. The indoor experiments showed that the probe was submersible

in water and provided reliable water depth and temperature measurements. Table 1 shows the summary statistics of indoor tests to evaluate whether the 3D printed case affected the sensor depth measurements. The difference between the actual sensor depth values and measured sensor depth values was not significant using 0.05 level of significance (t (18) = 2.03, p = 0.57). The difference between the two depth measurements show less than a 1 percent error. The accuracy of water temperature measurements from the sensor was not investigated, because temperature measurements are reported to be within 2 °C in the manufacturer's specifications. Visual observations were made for confirming the sensor temperature measurements.

Table 1. Summary statistics for evaluation of sensor depth measurement.

	Reference		Sensor		Difference (%)	*t* Value (DF)	*p* Value
	Mean	**SD**	**Mean**	**SD**			
Probe Depth (m)	0.973	0.551	1.07	0.551	0.009	2.03 (18)	0.57

The steel tube-enclosed sensor probe descended rapidly into the bottom of the lake as was expected. The rapid descent of the pressure sensor reduced the time that the UAV had to stay at the water surface and increased the speed of data collection. Reduction of floating time on the water surface minimized battery use because the UAV's idle mode duration was reduced. The idle mode of the flight controller kept the propellers spinning at the slowest rate to ensure that UAV could take off immediately when requested to either by the mission plan or the ground control station. The water depth evaluations estimated the maximum water depth as 8.4 m within the experiment boundary near the center (Figure 5). The water depth was 7.3 m at sampling location three, as it was the deepest sampling point, while the water depth was 4 m at sampling location four.
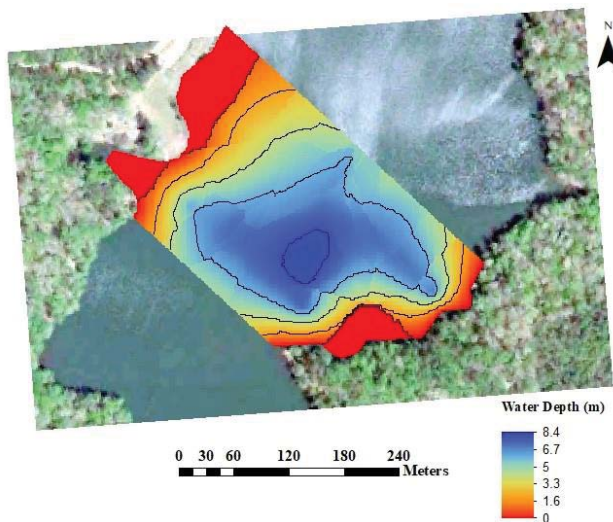
Figure 5. Water depth map of Lake Issaqueena within the mission plan boundary.

Water temperature varied at each location across the mission plan boundary and water depth. The temperature profiling experiments showed that water temperature was highest at location one, both at the water surface and at the bottom (Figure 6). The water temperature was 28 °C at the surface and 23 °C at the bottom in location one, with the highest temperature variation. The water temperature was 18.3 °C at the surface and 17.6 °C at the bottom in location six. Water temperature

at locations two and five followed the same trend, with the water temperature at the surface being 20 °C and the water temperature at the bottom being 19 °C. The trend in water temperature was the same in these two locations, because they were both located at the center in the downstream direction from northeast to southwest. A similar trend was observed at locations three and seven with a 1 °C difference in water temperature. The water temperature measurements from water columns indicate a sudden temperature change at locations two, five, and six at the depths of 3.67 m, 3.93 m, and 3.67 m, respectively. A rapid and steady water cooling was observed at these depths and the cooling continued until the bottom of the lake was reached at each location. The water temperature was steady until the depth of 1.4 m at location three. A sudden temperature drop was observed after this depth, indicating the cooling depth at the location three was less than at locations two, five, and six. Thermal stratification occurs at a depth of 3.6 m in many lakes and the temperature difference between the epilimnion and the hypolimnion must be at least greater than 1 °C [1,3]. While there was a temperature drop of more than 1 °C at an average depth of 3.8 m, it was not clear that if a thermal stratification occurred according to these measurements.
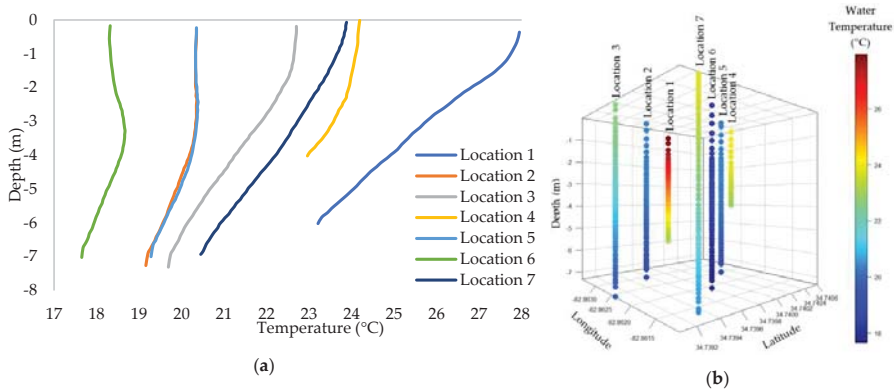
Figure 6. Water temperature distribution by location and water depth: (**a**) 2D scatter plot illustration and (**b**) 3D scatter plot illustration.

Sampling location one was closest to a stream that was located at the west corner of the experiment boundary. Increase in the water temperature might have been due to runoff after a rain event that occurred before field experiments. Change in water temperature by intermediate locations and sampling depths is illustrated in the water temperature maps in Figure 7. The maps represent the water temperature at the surface (0.3 m) and at depths of 2 m and 4 m, respectively. The average surface water temperature was recorded as 22.5 °C, while the average water temperature at the 4 m depth was 21.5 °C. The water temperature remained at around 18 °C at all depths at sampling location six. The largest water temperature drop was recorded as 3 °C at sampling location one. The difference in water temperature between sampling locations one and six was the highest at the surface, at 10 °C, and the lowest at the sampling depth of 4 m, at 6 °C.

(a)

(b)

(c)
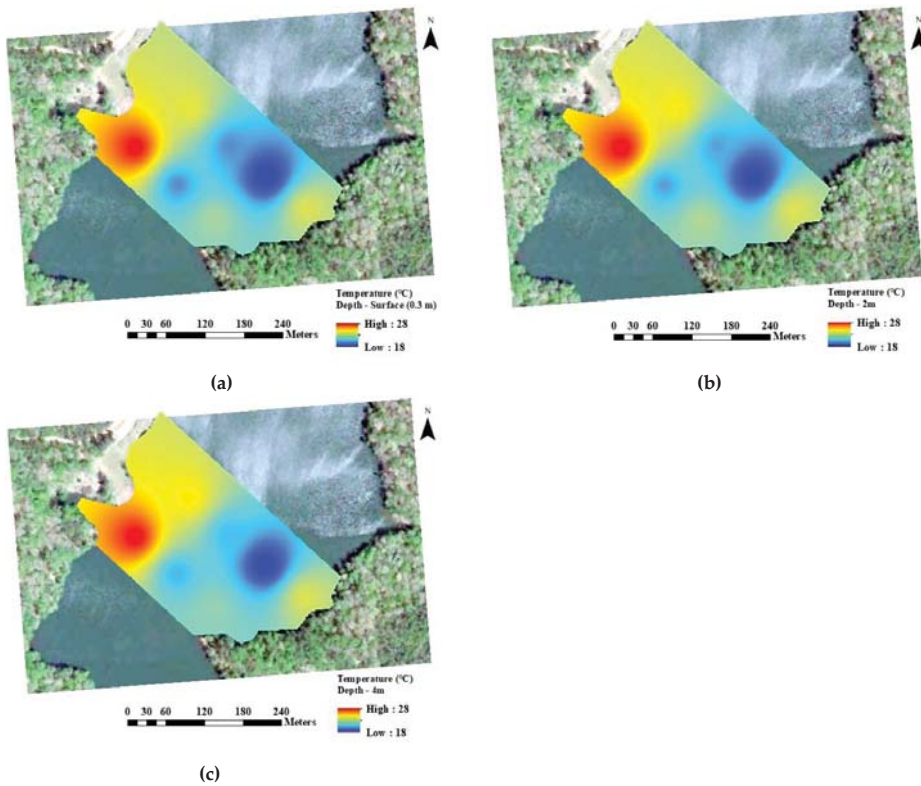
Figure 7. Water temperature maps representing change in water temperature by intermediate locations and sampling depth.

4. Conclusions

The UAV-based water temperature profiling system described here provides a different perspective to water quality monitoring practices. Its ability to remotely access waterbodies and the ease of deployment provided better and faster data collection when compared to other water quality monitoring methods. The UAV-based water temperature profiling system successfully navigated to pre-defined water sampling locations and executed mission plans for water temperature and depth measurements. The 3D printed pressure sensor case successfully prevented water leak and kept the sensors' components safe while allowing it to descend quickly throughout the water column. The maximum depth of water was 8.4 m within the selected boundary in Lake Issaqueena. A rapid water temperature drop at sampling location one was due to the stream entry into the waterbody. A rapid water temperature drop of greater than 1 °C at an average depth of 3.8 m at locations two, five, and six was observed. However, a wider data collection experiment that covers the entire lake is necessary to justify whether thermal stratification might have occurred. The length of the extension cable of the probe can be readjusted, depending on the depth of the waterbody under study, while taking the endurance and the thrust performance of the UAV and the maximum operational depth of the sensor node into consideration. Water temperature profiling with this system could be achieved within a relatively short time span, providing great advantages over other methods such as traditional sampling by boat. The UAV-assisted temperature profiling option could also reduce the costs by minimizing the required time on a site while providing coverage of a larger area with ease. Considering the maintenance time, cost, and lack of spatial resolution of fixed sensor

stations, the UAV-assisted temperature profiling system here described provides unique advantages, including advanced mobility, high spatial resolution, low cost, and fast response to disasters and other natural events.

Author Contributions: Conceptualization, C.K. and A.B.K.; Methodology, C.K., A.B.K., C.P. and C.S.; Software, C.K.; Validation, C.K., A.B.K., and C.S.; Formal Analysis, C.K.; Resources, A.B.K. and C.P.; Data Curation, C.K.; Writing—Original Draft Preparation, C.K.; Writing—Review and Editing, A.B.K., C.S. and C.P.; Visualization, C.K.; Supervision, A.B.K.; Project Administration, A.B.K.; Funding Acquisition, A.B.K. All authors have read and agreed to the published version of the manuscript.

References

1. Li, D.; Liu, S. (Eds.) Chapter 8—Water Quality Detection for Lakes. In *Water Quality Monitoring and Management*; Academic Press: Cambridge, MA, USA, 2019; pp. 221–231. [CrossRef]
2. Boehrer, B.; Schultze, M. Stratification of lakes. *Rev. Geophys.* **2008**, *46*. [CrossRef]
3. Foley, B.; Jones, I.A.N.; Maberly, S.; Rippey, B. Long-term changes in oxygen depletion in a small temperate lake: Effects of climate change and eutrophication. *Freshw. Biol.* **2011**, *57*, 278–289. [CrossRef]
4. Wang, J.; Huang, L.; Ju, J.; Daut, G.; Ma, Q.; Zhu, L.; Haberzettl, T.; Baade, J.; Mäusbacher, R.; Hamilton, A.; et al. Seasonal stratification of a deep, high-altitude, dimictic lake: Nam Co, Tibetan Plateau. *J. Hydrol.* **2020**, *584*, 124668. [CrossRef]
5. Liu, M.; Zhang, Y.; Shi, K.; Zhu, G.; Wu, Z.; Liu, M.; Zhang, Y. Thermal stratification dynamics in a large and deep subtropical reservoir revealed by high-frequency buoy data. *Sci. Total Environ.* **2019**, *651*, 614–624. [CrossRef]
6. Kurtuluş, T.; Kurtuluş, B.; Avşar, Ö.; Avşar, U. Evaluating the thermal stratification of Köyceğiz Lake (SW Turkey) using in-situ and remote sensing observations. *J. Afr. Earth Sci.* **2019**, *158*, 103559. [CrossRef]
7. Rucinski, D.K.; Beletsky, D.; DePinto, J.V.; Schwab, D.J.; Scavia, D. A simple 1-dimensional, climate based dissolved oxygen model for the central basin of Lake Erie. *J. Great Lakes Res.* **2010**, *36*, 465–476. [CrossRef]
8. Yang, K.; Yu, Z.; Luo, Y.; Yang, Y.; Zhao, L.; Zhou, X. Spatial and temporal variations in the relationship between lake water surface temperatures and water quality—A case study of Dianchi Lake. *Sci. Total Environ.* **2018**, *624*, 859–871. [CrossRef]
9. Mziray, P.; Kimirei, I.A.; Staehr, P.A.; Lugomela, C.V.; Perry, W.L.; Trolle, D.; O'Reilly, C.M.; Mgana, H.F. Seasonal patterns of thermal stratification and primary production in the northern parts of Lake Tanganyika. *J. Great Lakes Res.* **2018**, *44*, 1209–1220. [CrossRef]
10. Kirillin, G.; Shatwell, T. Generalized scaling of seasonal thermal stratification in lakes. *Earth-Sci. Rev.* **2016**, *161*, 179–190. [CrossRef]
11. Consi, T.; Anderson, G.; Barske, G.; Bootsma, H.; Hansen, T.; Janssen, J.; Klump, J.; Paddock, R.; Szmania, D.; Waples, J. *Measurement of Spring Thermal Stratification in Lake Michigan with the GLUCOS Observing System*; IEEE: New York City, NY, USA, 2009; pp. 1–5.
12. Biddanda, B.A.; Weinke, A.D.; Kendall, S.T.; Gereaux, L.C.; Holcomb, T.M.; Snider, M.J.; Dila, D.K.; Long, S.A.; VandenBerg, C.; Knapp, K.; et al. Chronicles of hypoxia: Time-series buoy observations reveal annually recurring seasonal basin-wide hypoxia in Muskegon Lake—A Great Lakes estuary. *J. Great Lakes Res.* **2018**, *44*, 219–229. [CrossRef]
13. Woolway, R.I.; Maberly, S.C.; Jones, I.D.; Feuchtmayr, H. A novel method for estimating the onset of thermal stratification in lakes from surface water measurements. *Water Resour. Res.* **2014**, *50*, 5131–5140. [CrossRef]
14. Gorham, E.; Boyce, F.M. Influence of Lake Surface Area and Depth Upon Thermal Stratification and the Depth of the Summer Thermocline. *J. Great Lakes Res.* **1989**, *15*, 233–245. [CrossRef]
15. Handcock, R.N.; Torgersen, C.E.; Cherkauer, K.A.; Gillespie, A.R.; Tockner, K.; Faux, R.N.; Tan, J. Thermal infrared remote sensing of water temperature in riverine landscapes. *Fluv. Remote Sens. Sci. Manag.* **2012**, *1*, 85–113.
16. Lee, E.; Yoon, H.; Hyun, S.P.; Burnett, W.C.; Koh, D.-C.; Ha, K.; Kim, D.-J.; Kim, Y.; Kang, K.-M. Unmanned aerial vehicles (UAVs)-based thermal infrared (TIR) mapping, a novel approach to assess groundwater discharge into the coastal zone. *Limnol. Oceanogr. Methods* **2016**, *14*, 725–735. [CrossRef]

17. Chung, M.; Detweiler, C.; Hamilton, M.; Higgins, J.; Ore, J.-P.; Thompson, S. Obtaining the Thermal Structure of Lakes from the Air. *Water* **2015**, *7*, 6467. [CrossRef]
18. DeMario, A.; Lopez, P.; Plewka, E.; Wix, R.; Xia, H.; Zamora, E.; Gessler, D.; Yalin, A.P. Water Plume Temperature Measurements by an Unmanned Aerial System (UAS). *Sensors* **2017**, *17*, 306. [CrossRef] [PubMed]
19. Koparan, C.; Koc, A.; Privette, C.; Sawyer, C. In Situ Water Quality Measurements Using an Unmanned Aerial Vehicle (UAV) System. *Water* **2018**, *10*, 264. [CrossRef]
20. Ore, J.-P.; Detweiler, C. Sensing water properties at precise depths from the air. *J. Field Robot.* **2018**, *35*, 1205–1221. [CrossRef]
21. Koparan, C.; Koc, A.; Privette, C.; Sawyer, C.; Sharp, J. Evaluation of a UAV-Assisted Autonomous Water Sampling. *Water* **2018**, *10*, 655. [CrossRef]
22. Koparan, C.; Koc, A.B.; Privette, C.V.; Sawyer, C.B. Autonomous In Situ Measurements of Noncontaminant Water Quality Indicators and Sample Collection with a UAV. *Water* **2019**, *11*, 604. [CrossRef]
23. Pilgrim, C.M.; Mikhailova, E.A.; Post, C.J.; Hains, J.J. Spatial and temporal analysis of land cover changes and water quality in the Lake Issaqueena watershed, South Carolina. *Environ. Monit. Assess.* **2014**, *186*, 7617–7630. [CrossRef] [PubMed]
24. South Carolina Department of Health and Environmental Control (SCDHEC). *State of South Carolina Monitoring Strategy for Calender Year 2018*; SCDHEC: Columbia, SC, USA, 2018.
25. Freeman, P.K.; Freeland, R.S. Agricultural UAVs in the U.S.: Potential, policy, and hype. *Remote Sens. Appl. Soc. Environ.* **2015**, *2*, 35–43. [CrossRef]
26. Ardupilot. Automatic Landing; Setting the Flare Point. Available online: http://ardupilot.org/plane/docs/automatic-landing.html (accessed on 28 May 2020).
27. Ahmad, H.R.; Aziz, T.; Rehman, Z.R.; Saifullah. Chapter 15—Spatial Mapping of Metal-Contaminated Soils A2 - Hakeem, Khalid Rehman. In *Soil Remediation and Plants*; Sabir, M., Öztürk, M., Mermut, A.R., Eds.; Academic Press: San Diego, CA, USA, 2015; pp. 415–431. [CrossRef]
28. Ligges, U.; Mächler, M. Scatterplot3d-an r Package for Visualizing Multivariate Data. Available online: https://www.econstor.eu/handle/10419/77160 (accessed on 28 May 2020).

Implementing Mitigations for Improving Societal Acceptance of Urban Air Mobility

Ender Çetin [1,*], Alicia Cano [2], Robin Deransy [3], Sergi Tres [2] and Cristina Barrado [1]

1   Computer Architecture Department, Technical University of Catalonia (UPC) BarcelonaTECH, 08860 Castelldefels, Spain; cristina.barrado@upc.edu
2   HEMAV Foundation, Esteve Terradas 1, 08860 Castelldefels, Spain; acano@hemavfoundation.com (A.C.); stres@hemavfoundation.com (S.T.)
3   European Organisation for the Safety of Air Navigation—EUROCONTROL, 91220 Brétigny-sur-Orge, France; robin.deransy@eurocontrol.int
*   Correspondence: ender.cetin@upc.edu

Abstract: The continuous development of technical innovations provides the opportunity to create new economic markets and a wealth of new services. However, these innovations sometimes raise concerns, notably in terms of societal, safety, and environmental impacts. This is the case for services related to the operation of unmanned aerial vehicles (UAV), which are emerging rapidly. Unmanned aerial vehicles, also called drones, date back to the first third of the twentieth century in aviation industry, when they were mostly used for military purposes. Nowadays, drones of various types and sizes are used for many purposes, such as precision agriculture, search and rescue missions, aerial photography, shipping and delivery, etc. Starting to operate in areas with low population density, drones are now looking for business in urban and suburban areas, in what is called urban air mobility (UAM). However, this rapid growth of the drone industry creates psychological fear of the unknown in some parts of society. Reducing this fear will play an important role in public acceptance of drone operations in urban areas. This paper presents the main concerns of society with regard to drone operations, as already captured in some public surveys, and proposes a list of mitigation measures to reduce these concerns. The proposed list is then analyzed, and its applicability to individual, urban, very large demonstration flights is explained, using the feedback from the CORUS-XUAM project. CORUS-XUAM will organize a set of very large drone flight demonstrations across seven European countries to investigate how to safely integrate drone operations into airspace with the support of the U-space.

Keywords: drones; unmanned aerial vehicles (UAV); social acceptance; urban air mobility (UAM); CORUS-XUAM

1. Introduction

Drones are flying machines ranging from insect-sized flapping crafts to large airplanes the size of a commercial airline jet [1]. Their capabilities are also wide-ranging: some drones are capable of flying for only a few minutes, while others can fly for days at a time. The applications of drones are also diverse. While the initial applications of drones were mainly for military purposes, and later for recreational purposes, drones are used today in many civil applications and in public spaces. Some of the most common commercial applications and uses for drones include agriculture (crop spraying, crop monitoring, etc.), live streaming events, emergency response, search and rescue, firefighting, disaster zone mapping, mapping and surveying, and artificial intelligence applications [2–5]. More recently, the societal utility of drones has been further enhanced in the management of the global COVID-19 pandemic, with use cases such as aerial spraying of public areas to disinfect streets, the surveillance of public spaces, and monitoring local authorities during lockdowns and quarantine [6].

The 2016 European Drones Outlook Study [7] forecasts a promising economical growth fostered by the emerging drone market. Unmanned aircraft will be part of everyday life in most of the economic sectors, as shown by the size of the bullets in Figure 1, but will have a greater impact on air travel, utilities, entertainment and media, logistics, and agriculture. Indeed, the number of drones flying in the European airspace is expected to increase from a few thousand to several hundred thousand by 2050, most notably in government and commercial activities. The annual economic benefit could exceed EUR 10 billion by 2035 in Europe and create 100,000 new direct jobs to support drone-related operations. An example of this growth is illustrated by the agricultural sector, where authors estimate that 150,000 drones will be operated by 2035. The same is true in the fields of utilities and security, where around 60,000 unmanned aircraft will be used to assist in natural disaster management or traffic control, among other tasks.
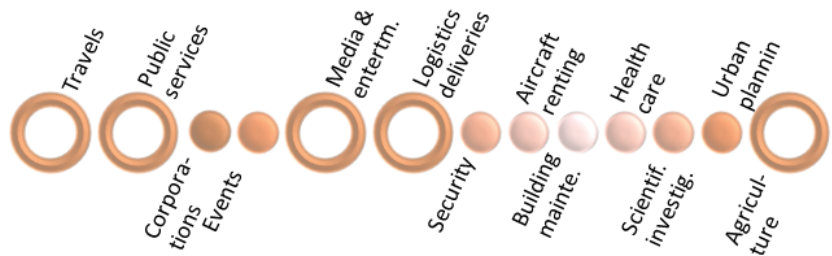
Figure 1. Drone market areas (size represents the market expectations).

However, despite the multiple operational services and the huge potential economic benefits of the drone industry, this relatively new technology will not really take off until the societal concerns associated with its widespread deployment are properly addressed.

As in the early days of aviation, safety will remain the main factor that will influence public acceptance of drones, especially as, unlike conventional commercial and general aviation, drones will often operate over moderately to densely populated areas and at lower altitudes. Visible to the naked eye, civil drone operations will raise questions about their nature and the risk they may represent for the populations and installations overflown. Noise pollution generated by drones will have to be contained to acceptable levels depending on the time of day and the frequency of operations. In addition, other societal and environmental impacts on the population, fauna, and flora will also have to be anticipated and mitigated.

Aware of these societal and environmental challenges, the CORUS-XUAM project has undertaken a review of surveys that covers the public acceptance of drones, and has initiated the identification of possible mitigation measures. The aim of this work is to address public concerns before the UAM business spread over cities, and have mitigation measures in place to facilitate a seamless acceptation of drones in our urban skies.

2. Public Surveys about Drones

The surveys reviewed are from various organizations (air traffic service providers, industry, research, universities, airspace security agencies) and countries (Australia, Germany, Brazil, USA, China, Korea, etc.), and were conducted between 2015 and 2021, 2018 being the inflection point in which drones were considered for the first time as new-entrant vehicles to share urban transport.

In 2015, Clothier et al. [8] studied the risk perception and the public acceptance of drones in Australia. The objectives of this study were to investigate whether the public perceives the risks of drones differently to that of conventionally piloted aircraft, to provide guidance for setting safety requirements for drones, and to understand how the terminology used to describe the technology influences how the public perceives the risk. In this research, it was found that that terminology had a minimal effect on public perceptions.

However, this may change as more information about the drone technology and risks and benefits of their usage becomes available to the public.

In 2016, the Office of Inspector General of the United States Postal Service published a report [9] on the public perception of drone delivery in the United States. This report refers to an online survey that was administered, in June 2016, to a sample of 18–75-year-old residents in all 50 states and the District of Columbia to understand the current state of public opinion on drone delivery for potential customers. The survey showed, among other things, that most Americans like the concept of drone delivery rather than dislike it, but that many have yet to make up their minds. Different groups have different levels of interest in drone delivery. Drone malfunctions was the main concern of the public, but other concerns included misuse, privacy, potential damage, and nuisance.

In 2017, Lidynia et al. [10] conducted a survey of 200 people, laypersons, and active users living in Germany about their acceptance and perceived barriers for drones. The survey questions were about the general evaluation of civil drone technology, barriers, demography, and further user factors. The survey results show that user diversity strongly influences the acceptance of drones and perceived barriers. Active drone pilots were more concerned by a risk of possible accidents, while laypeople were more concerned about the violation of their privacy (the routes that drones should and should not be allowed to use).

In 2018, an online survey from NATS [11], the UK airspace service provider, showed that drone acceptance can range from 45% when seen as a generic technology tool, but raises to 80% when they are used in emergency situations. A deep market study conducted by NASA [12] forecasts that, in the coming years, there will be numerous markets in which the drones will have a stake.

As a novelty, additional operations, such as passenger transport by unmanned aircraft, or "air taxis", are expected to grow exponentially. Air taxis operations will reduce the travel times of part of the commuting traffic to city centers and contribute to decongesting ground transport by up to 25% . Urban air mobility (UAM) is emerging as the new concept for drones future business. In the US, the concept will later be extended to also include manned electrical vehicles with vertical take-off and landing capabilities, known as eVTOL, under the new term advanced air mobility (AAM). The paper shows that the acceptance level raises to 55% with the development of new safety technologies, the improvement in air flow network, and automation of the flights.

In 2019, Airbus conducted also a survey [13] about the public perception of UAM. The Airbus survey covered four cities/countries around the world, Los Angeles, Mexico City, New Zealand, and Switzerland, and collected 1540 responses. Results revealed that 44.5% of respondents supported or strongly supported UAM and that 41.4% of respondents thought UAM was safe to very safe. This suggests that the initial perception of UAM is quite positive.

The same year, a meta-analysis from Legere of former US public surveys [14] and the DLR survey to 832 German citizens [15] showed acceptance levels of 60% and 49%, respectively. The meta-analysis focused on the different acceptance levels per mission, with public missions having higher acceptance than private/commercial uses. The German survey provides results about major public concerns. The most important one was the misuse of drones for crime (91%) and the violation of privacy (86%). Both surveys refer to generic (small) drones involved in missions such as police surveillance or search and rescue.

In 2020, Tan et al. [16] surveyed the opinion of more than 1000 citizens from Singapore. Delivery drones and passenger vehicles were considered to have an average acceptance of 62%.

In 2021, an EASA survey [17] obtained the highest acceptance (83%) for the UAM composed of passenger electrical vehicles, not necessarily unmanned, cargo drones, and also surveillance drones. Special emphasis was given to the different types of passenger vehicles, and also to concerns related to the environment.

In addition, surveys [18–20] had a main focus on the analysis of the demand of the future UAM services. Questions were addressed to the public as potential customers. Kloss

and Riedel surveyed almost 5000 people from Brazil, China, Germany, India, Poland, and the US. Acceptance was measured for different missions (six using eVTOL and four using cargo-drones) and they found out that only 27.3% of the people declared themselves willing to try passenger drones, mostly for commuting, business trips, or travels to/from airport). On the contrary, the willingness to use cargo drones, paying twice or more of today's cost, was 57.8%.

More positive were the responses from the Lundqvist survey. This survey was conducted on almost 500 people from five EU regions (in Holland, England, Spain, Croatia, and Poland). Respondents were mainly connected to drone operators or their business. The general positive attitude towards drones was up to approximately 70%. Specific questions about concerns included safety, environment, and privacy issues. Finally, the Park and Joo survey was conducted in South Korea on more than 1000 citizens plus 44 experts. The willingness to use UAM (both passenger and cargo) was 47%, and decreased as the automation of the vehicles increased.

In Figure 2, the surveys are visualized according to their main focus, such as public acceptance (blue) or market analysis (green). The number of surveys for each year from 2015 to 2021 can be seen on the vertical axis. The different types of drones (surveillance, cargo, and passenger) covered by each questionnaire are also indicated by a picture.
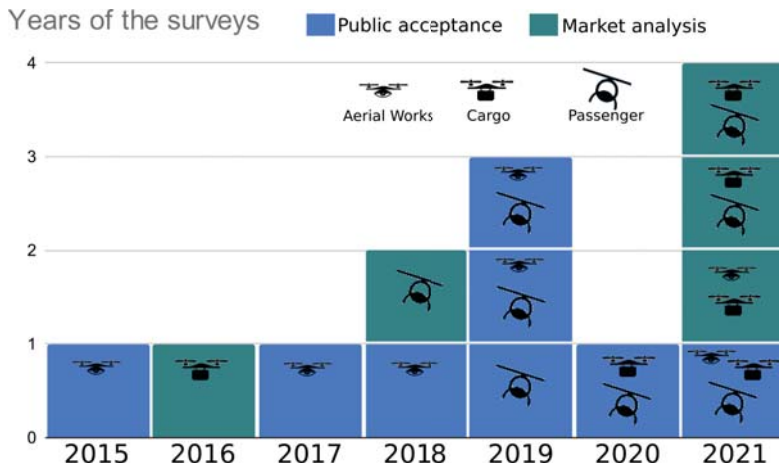
Figure 2. Summary of the surveys per year, aim, and proposed vehicles.

A growing interest in passenger drones can be observed starting from 2018 to 2021. Conversely, the interest in surveillance drones has been decreasing. This may be a reason why privacy concerns have been decreasing over the years in these surveys, while noise and environmental concerns have increased.

As an overall metric, the level of acceptances of drones and of urban air mobility are shown in Figure 3. Each bar represents one survey, and they are sorted by year to try to show any trend across time. Again, the color indicates the final focus of the survey: blue for public acceptance and green for market analysis.

As can be seen, the public acceptance has no clear trend over the years but reached the maximum in six years of 83% in 2021 (EASA survey). However, the other surveys of the same year had very different results. The way questions are proposed in these surveys partly explains these differences. In the EASA survey[17], with the highest acceptance value, the question was the "general attitude towards urban air mobility". In the Park and Joo survey [18], also conducted in 2021, but from a market analysis perspective, the question that obtained 47% of positive responses was about the "public's willingness to use UAM in its initial phase". This shows how difficult it is to compare survey results.
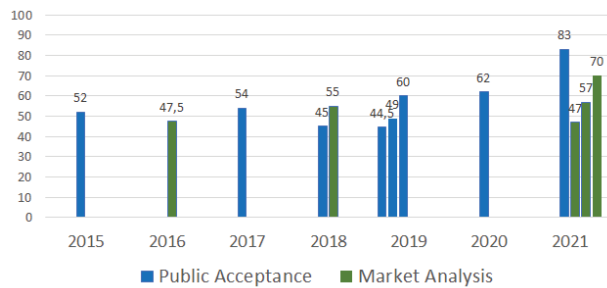
Figure 3. Acceptance levels of drones and/or UAM per survey (in %).

Surveys, in general, have a first set of questions to classify the public according to their age, gender, and economic status, but also their knowledge about drones, so that the answers can be further studied by groups. Typically, females, elders, and less-educated people have a slightly lower acceptance of drones than the other groups. On the contrary, experts in the field are generally more concerned about safety than laypersons.

Most surveys are also usually accompanied by a scenario of drone usage, and in the market study surveys, the scenarios include a forecast about the cost of the services. Many unknowns are yet to be unveiled: Will safety increase or decrease? Will the projected drone service costs/times be achievable? Will drones generate the expected economical growth? For the moment, only predictions can be provided when conducting surveys, whereas the survey results show clearly that the costs of drone services, as well as the time saved, have a high impact on responses. Drone operations related to health and welfare always have a high level of acceptance, while leisure or business related to leisure are always the least accepted drone operations.

In most recent surveys, we found that quantitative data are obtained from the questionnaire responses, while qualitative information is obtained from a set of persons who are interviewed separately, and whose responses are analyzed with more detail. Typically, this set of responses, referred to as experts, is used to validate and interpret the responses of the questionnaire. However, expert answers usually point towards a positive attitude to drones, as confirmed during the first CORUS-XUAM stakeholder workshop. This workshop analyzed the most critical elements related to UAS/UAM operations along with possible solutions that could enable a sustainable and accepted expansion of drone operations in and around the European cities. In particular, the fifth day of the workshop was dedicated to the analysis of societal impact of drone operations and possible mitigation measures. The responses to the questions in Table 1 showed a high acceptance rate among the 66 workshop participants, as in the surveys analyzed.

Table 1. Please check the option(s) that apply/applies to you.

Options (Multiple Choice)	
I am a potential passenger of a taxi-drone	63%
I am a potential client of a delivery-drone	89%

Although public opinions vary with time/country, trends seem to show that between half and three-fourths of the public accepts the deployment of business-related drone operations.

In addition to acceptance, most surveys include questions about public concerns, but they do not use an equivalent set of concerns or the same terminology. To highlight this fact, we used word clouds to process the surveys addressing "public concerns" (see Figure 4). In word clouds, the most frequently used terms within a document are displayed in larger font size.

As can be seen in these word clouds, public concerns related to drone operations are mostly focused on safety, environment, privacy, and noise. Terms such as animals, visual, and waste are classified as an environmental concern, while others, such as risk and danger, are considered as safety concerns. In addition, we see terms related to the economy, (i.e., cost and liability), or to other topics, such as regulation or ethics.

Figure 4. Word clouds highlighting the public concerns in the different surveys.

In the CORUS-XUAM, the workshop participants were asked to select the top three concerns for them, and the results are shown in Table 2. As most of them came from the aviation sector, it is not surprising to see that the safety concern was selected as the major concern.

Table 2. Please select which of the three main concerns is most important for you.

Options (Single Choice)	
Safety/(Cyber)Security	59%
Environmental impact (noise, emissions, visual,...)	33%
Privacy	9%

It is worth mentioning some specific issues that yield "not in my backyard" responses. The location of vertiports is a good example. People are open to the concept, but would not be happy to have one near their home or office.

The full list of societal concerns that can be identified by the CORUS-XUAM project is as follows:

- Environment: noise impact; emissions impact, impacts on animals and flora; recycling; impact of climate change; visual pollution; loss of privacy/intrusion; nuisance.
- Safety: safety concerns; security concerns, cybersecurity.
- Fairness: lack of transparency; cost of services; competency; liability.
- Economy: jobs; economic viability; demand.

As the environmental area has many items, and noise and privacy are highly mentioned as concerns, we treat them separately in the following sections. While analyzing each societal concern, we also hint at possible mitigation measures.

3. Materials and Methods

The procedure followed for defining the mitigation measures and analyzing them is summarized in Figure 5. First, the main societal concerns were extracted from the surveys. Aspects related to safety, the economy, the environment and noise were the result of this first step, as depicted in the figure. Next, the societal concerns were analyzed during several brainstorming sessions. For each concern, we determined possible actions that could help to minimize its negative perception. The result was a list of mitigation measures, in which each item is an individual action that can mitigate one or several concerns.
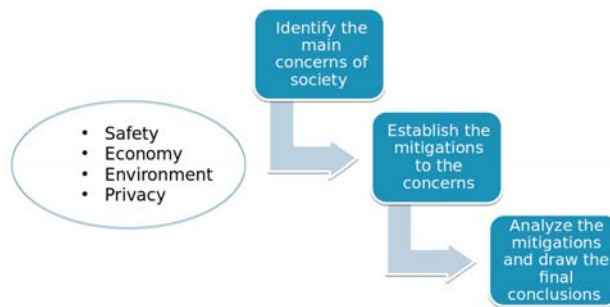
Figure 5. Mitigation analysis process.

Finally, the list of mitigation measures was analyzed to draw conclusions. As part of this process, this list was presented and discussed in the CORUS-XUAM workshop. The majority of the participants felt that it was a good start (details can be seen in Table 3) but it was still incomplete. During the debate, new potential actions were proposed and added to the existing ones.

Table 3. Opinions collected during CORUS-XUAM workshop to the question "Please select the best option to end this sentence: *The presented list of mitigations . . .*".

Options (Single Choice)	Split
Is a good starting point	85%
Has important omissions	11%
Is exhaustive and complete	4%

Once the list of mitigation actions is completed, the analysis was performed using the double classification process illustrated in Figure 6. With the workflow moving from the inside to the outside, we started collecting public concerns and then proposed actions to mitigate such concerns, and finally applied two overlapping classifications: first providing a category to each action and then a level that measures the required effort to implement that action.
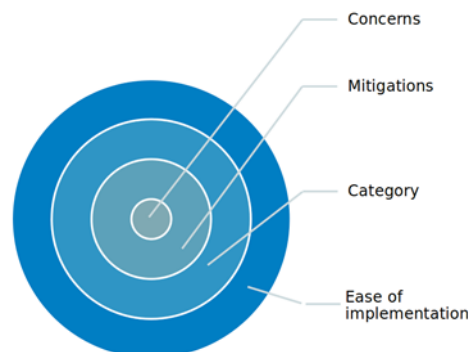
Figure 6. Mitigation measures classification procedure.

In more detail, the analysis starts by categorizing each mitigation measure according to the scope in which it can be applied. We established four different scopes, or categories, as follows:

- Regulation and policy. This category contains the mitigations that should be part of a regulation made by the authorities.

- Operational and ConOps. This category includes the mitigation measures related to rules and regulations that enable the safe integration of drones with other airspace users.
- Human response and metrics. This category relates to mitigation measures that engage the public.
- Tool and technologies. This category includes mitigation measures that can be built into or used by drones.

Figure 7 shows some examples of mitigation for each category. Note that simply rewording a mitigation slightly can move it from one category to another. For instance, "setting up countermeasures to criminal/illegal use of drones" was categorized under "tools and technologies", but rephrasing it to "make mandatory the use of countermeasures ..." would have categorized it under "regulation and policy".
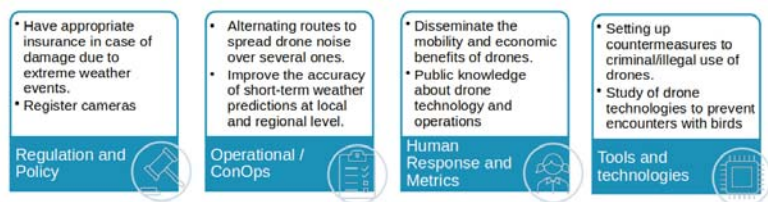
Figure 7. Examples of mitigations by category.

In addition to the category, we assigned each mitigation a second classification in three levels, "easy", "medium", and "difficult", according to its ease of implementation in terms of resources and time. Figure 8 shows some mitigation examples for each of the three levels of ease of implementation. For example, the mitigation "creating an independent authority to investigate accidents/incidents/complaints related to drone operations" is considered to be difficult to implement at the moment because it requires a high level of agreement between stakeholders. In particular, this mitigation measure shall involve regulation bodies which have to follow a lengthy period of legal procedures. In contrast, the mitigation "limit minimum altitude" is an operational action that is easy to implement.
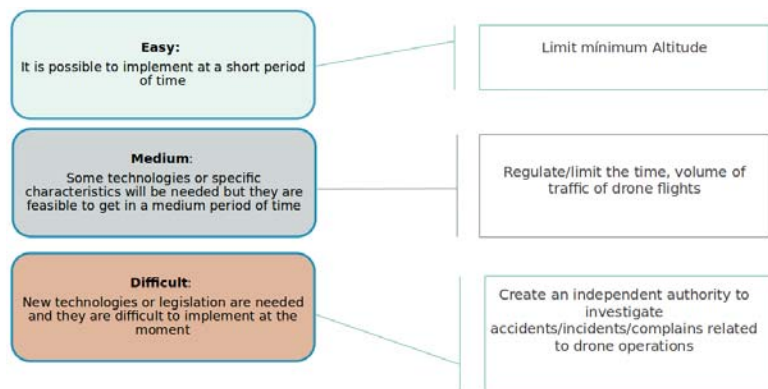
Figure 8. Examples of mitigations by ease of implementation.

3.1. Scoring of the Mitigations

Given the long list of mitigation measures, we needed a method to rank them from highest to lowest priority. The prioritization process uses a scoring value generated from a dynamic table. The dynamic table is created by reversing the rows and columns of the table used to generate the mitigation measures.

The process for scoring each individual mitigation is the result of adding up the applicability values of that mitigation measure in each and every concern.

Indeed, one mitigation that reduces visual impact may have a negative effect on the safety of the surrounding traffic, but at the same time may be neutral for natural life and for privacy. For this reason, we crossed each mitigation with each concern on the long list of concerns presented in Section 2 and set +1 for a positive impact, −1 for a negative impact, and 0 for a neutral.

This is similar to the process used in the safety operational risk assessment (SORA) methodology [21]. The final sum of the values of a mitigation provides a numerical proxy of the impact of its applicability. The higher the number, the more positive the impact.

3.2. CORUS-XUAM Mitigations Subset

As a final step for this work, we selected a subset of mitigation measures, mainly from the operational/ConOps category (but not all) that are applicable to very large (drone flight) demonstrations (VLDs) being prepared within the CORUS-XUAM project.

Very-large-scale demonstration (VLD) activities will be at the heart of CORUS-XUAM and will support the integrated operations of UAS/UAM and manned aircraft and the advanced forms of interaction through digital data exchange supported by integrated and advanced U-space services in urban, suburban, and intercity scenarios, as well as in and near ATM-controlled airspace and airports. The VLDs will focus on different types of missions such as passenger transport, delivery, emergency response, and surveillance. The VLDs will use different U-space deployment architectures and state-of-the-art technologies. They will take into account the coordination between ATC and U-space, including interaction with ATCOs and pilots. The VLDs will combine eVTOLs flights with other traffic, and operations in the CTRs of major airports. Vertiport procedures, separation, and data services will also be demonstrated [22].

The mitigation measures proposed to be tested during VLDs are mainly those that can be implemented by the U-space service providers or any other partner involved. As the VLDs are in the planning phase, at the time of writing this paper, each VLD responds differently to the proposed list of mitigation measures, depending on its mission and capacity.

4. Results

4.1. Mitigations

4.1.1. Full Mitigation List: Categories, Ease of Implementation, and Top 10 Scored

The full list of social acceptance mitigation measures identified after the CORUS-XUAM brainstorming sessions [23] is presented in Appendix A.

Figure 9 shows the percentage of categorization of the mitigation measures according to the scope in which they can be applied. The categories are explained in detail in Section 3.
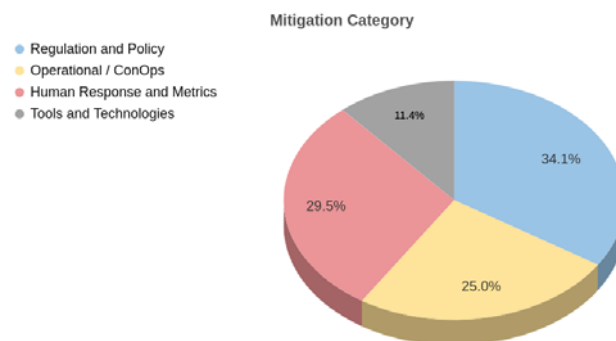
Figure 9. Mitigation categories for full list.

A categorization of the ease of implementation of each mitigation measure was established to analyze those that could be implemented and achieved with the current technologies and regulations. Figure 10 shows the percentages of the ease of implementation of the full list of mitigation measures. The aim was to identify and analyze the possible mitigation measures that could be implemented quickly.
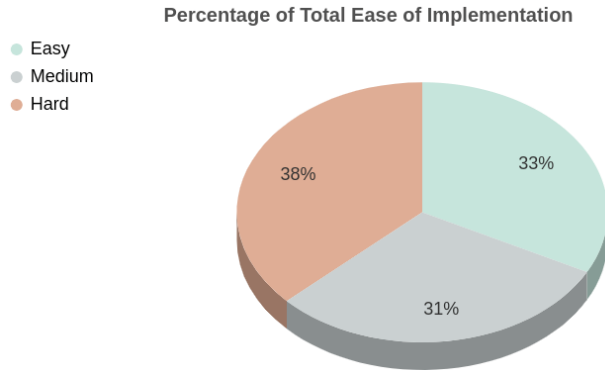
Figure 10. Percentages of total ease of implementation for full list.

The list of prioritized Top 10 mitigation measures and the concerns that can be improved upon are presented in Table 4. Figure 11 shows the ease of implementation of the ones that mitigate a bigger number of concerns; for example, mitigation "M1—limit minimum altitude" is thought to support six different concerns and be easy to implement.
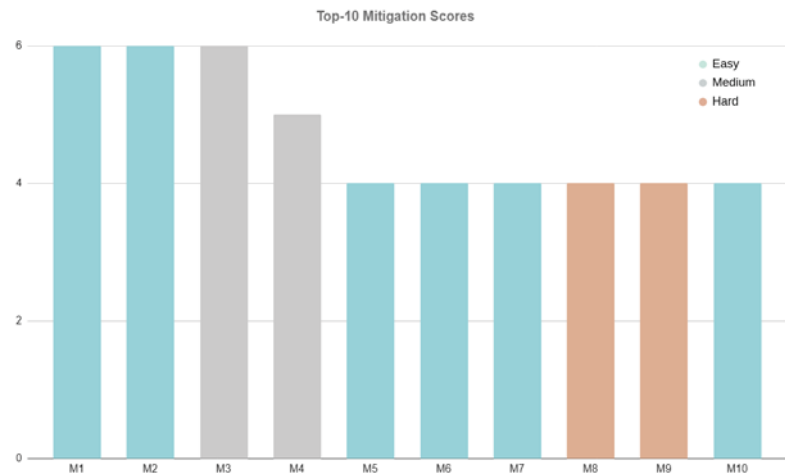
Figure 11. Mitigation scores for full list of mitigation measures.

It can be observed that more than 70% of the mitigation measures are found to be achievable in a short or medium timeframe, either because the necessary applied science exists today or because the required technologies are under development. However, 31% of the mitigation measures are still considered complex to implement, which means that there is still a long way to go in the research and development of new technologies and the regulations that make these mitigations possible.

Table 4. Prioritized top 10 mitigation measures.

M1	**Limit minimum altitude**
	The concerns addressed:
	Noise impact, impacts on animals and flora, visual pollution,
	safety concerns, security concerns, loss of privacy/intrusion

M2	**Establish no-fly zones for drones**
	The concerns addressed:
	Noise impact, impacts on animals and flora, visual pollution,
	safety concerns, security concerns, loss of privacy/intrusion

M3	**Identify a strategic location for vertiports**
	The concerns addressed:
	Noise impact, emissions impact, impacts on animals and flora,
	visual pollution, safety concerns, security concerns

M4	**Public knowledge about drone technology and operations**
	The concerns addressed:
	Loss of privacy/intrusion, lack of transparency,
	competency, economic viability, demand

M5	**Avoid/limit hovering drone flights**
	The concerns addressed:
	Noise impact, impacts on animals and flora,
	visual pollution, loss of privacy/intrusion

M6	**Promote the use of renewable energy sources to recharge batteries.** **Use of SAF for hybrid drones**
	The concerns addressed:
	Emissions impact, recycling, impact of climate change,
	economic viability, demand

M7	**Ensure proper maintenance processes and controls** **for batteries to extend their life cycle**
	The concerns addressed:
	Emissions impact, recycling, impact of climate change, safety concerns

M8	**Work with eco-friendly drones(re-cycling parts)**
	The concerns addressed:
	Emissions impact, recycling, impact of climate change, economic viability

M9	**Ensure that the cost of drone services commensurate** **with the value of the activity**
	The concerns addressed:
	Cost of services, competency, jobs, economic viability

M10	**Developing a risk and safety culture in the drone industry**
	The concerns addressed:
	Competency, jobs, economic viability, demand

4.1.2. Partial Mitigation List Applicable to VLDs: Categories, Ease of Implementation, and Top 10 Scored

The mitigation measures were selected by considering their applicability to VLDs. This partial mitigation list applicable to VLDs is in Appendix B.

In Figure 12, the percentages of categorization of the mitigation measure are shown. As can be seen in this figure, the first category, "regulation and policy", accounts for almost 43% of the mitigation categories that are applicable to VLDs. However, the fourth category, "tools and technologies", accounts for only 9.5%.
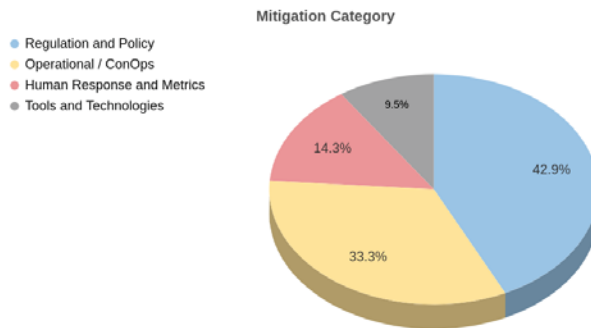
Figure 12. Mitigation categories for VLDs.

In Figure 13, the percentages of the ease of implementation considering the partial mitigation list applicable to VLDs are shown. In this figure, it can be seen that 57% of these mitigation measures can be implemented quickly. Only 10% of the partial mitigation measures are considered difficult to implement.
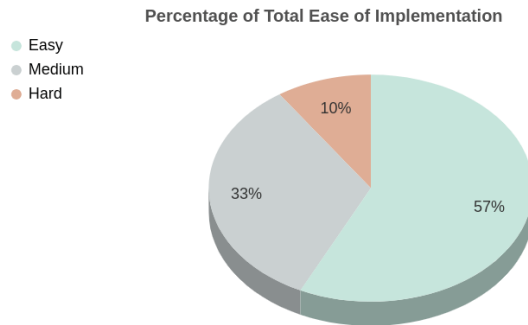
Figure 13. Percentages of total ease of implementation for VLDs.

Figure 14 and Table 5 show that most of the top 10 scored mitigation measures that are applicable to VLDs are considered to be easy to implement. Only the mitigation measure "ensure that electronic devices on drones (cameras, sensors, etc.) cannot be used to infringe on privacy" is considered to be hard to implement in a short time.
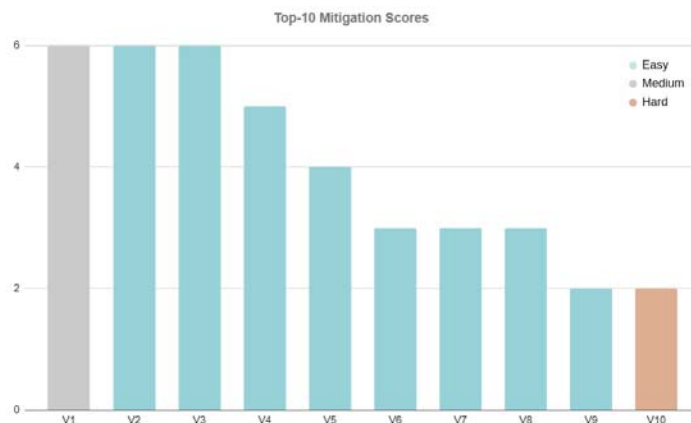
Figure 14. Mitigation scores for mitigation measures applicable to VLDs.

Table 5. TOP 10 VLDs mitigation measures.

	Mitigations
V1	Identify strategic location for vertiports.
V2	Limit minimum altitude.
V3	Establish no-fly zones for drones.
V4	Fly direct routes to avoid unnecessary path extension and minimize the time in the air.
V5	Limit hovering drone flights.
V6	Use different methods (such as advanced encryption standards or regular cyberattack tests) to improve the security of communications in the U-space system.
V7	Public engagement activities about drone technology and operations.
V8	Disseminate the environmental benefits of drones (quantification of emission savings.)
V9	General aviation pilots' engagement in activities about UAM.
V10	Ensure that electronic devices on drones (cameras, sensors, etc.) cannot be used to infringe on privacy.

5. Discussion

The application of actions to mitigate risks is the basis of the SORA methodology [21]. For instance, to reduce the energy of a falling drone, a common mitigation is the addition of a parachute. While the parachute will, in general, improve safety, it may also introduce new risks and failures, such as an undesired deployment of the parachute. We have to understand that any well-intentioned action may indirectly introduce malicious effects as well.

In the case of the proposed social concern mitigation list, we found a number of contradictory effects.

For instance, we proposed a number of mitigations in relation to the flight trajectory and noise-limiting hover time, flying direct routes, and so on—but also using alternate paths, avoiding certain areas, and limiting speeds. Although they are helpful for reducing the noise on the ground, it is not possible to apply all of them at the same time. Trade-offs need to be elaborated to avoid long route deviations due to protected zones. Other route characteristics, such as altitude, time of day, and maximum capacity, play important roles in the abatement of noise. They should all be taken into account together when selecting the best mitigation strategy for drone operations.

Another example is the location of vertiports. For safety reasons, vertiports should be located in isolated areas, with few air and ground risks, but for economical reasons they should be close to transportation hubs (persons and/or freight). Moreover, the high traffic density of a vertiport can generate a nuisance for neighbors. Using a building ceiling could mitigate this nuisance, but at the cost of increasing the flight risk. A split of opinions is very clearly shown in Table 6, obtained based on the workshop attendees' opinions. It seems clear that more research is needed to further develop this and some of the proposed mitigations.

Table 6. Which factors should be considered as constraints for the location of vertiports?

Options (Multiple Choice)	
Low population density	33%
High population density	43%
Low altitude/ground	15%
Building roofs	28%
Isolated	15%
Connected to transport hubs	65%
Others	15%

A number of mitigations have been classified as "tools and technologies". Based on research on clean energy sources, artificial intelligence or new materials are key to reducing societal concerns. A drone with low-noise propellers may be inaudible at 10–15 m of height, thus increasing the minimum altitude noise mitigation. It is especially relevant to note the object avoidance technologies, currently based on near-infrared or ultrasound sensors, that only work at low speeds. Future developments can help to avoid unexpected encounters (i.e., killing birds) at any speed.

Most societal concerns cannot be purely measured objectively. Human perception is highly subjective. A clear example is the experiment reported in the EASA survey [17] about noise. In a lab, a number of people were requested to order a list of sounds according to what they considered a nuisance. While all sounds were played all at the same volume (80 decibels, which is higher than a vacuum cleaner), responses penalized unknown noise sources more than other, known ones. As the public becomes informed and used to drone characteristic noise, this human factor will change. Moreover, according to [24], the noise of a VA-X4 taxi drone flying at 300 m produces a noise of 43 decibels, a loudness between the noise of a quiet urban night (40 dBA) and that of light urban traffic (50 dBA). A very interesting review of drone noise emissions and noise effects on humans can be found in [25]. Furthermore, the effects of drone noise with natural life, especially in birds, seems to be a growing societal concern [EASAsurvey], but scientific studies show that certain frequencies, such as drone high-frequency noise, are not audible to most birds [26].

A number of proposed mitigations can be adopted in future regulations. However, the role of governments must go beyond the regulatory aspects. Actions are needed to disseminate the benefits of drones as environmentally friendly vehicles, with a capacity for the fast transport of people and goods to be used in emergency situations and a motor of a new economic growth cycle. Simultaneously, the initial support in terms of infrastructure to be deployed (i.e., U-space) are actions needed to foster the new era of transport using drones. The development of this infrastructure still requires decisions about U-space airspace organization to be made. This is also a hot topic for research, as there does not appear to be any consensus based on the expert responses of Table 7.

Table 7. How should UAM flights be organized to mitigate ground risks and noise?

Options (Multiple Choice)	
Free flight	13%
Corridors	87%
Over the roads	35%
Over the green areas	30%
Over buildings	20%
Other	20%

Another aspect that governments and authorities should face is the fairness in regard to the access to airspace. Transparency is a tool of fairness as well as a strategy for mitigating citizen concerns about privacy, according to the responses to the workshop poll shown in Table 8.

Table 8. To which point do you agree with the following sentence: *The ability of citizens to obtain information about drone flights in their vicinity would resolve privacy concerns.*

Options (Multiple Choice)	
Strongly agree	13%
Agree	30%
Slightly agree	35%
Slightly disagree	7%
Disagree	13%
Strongly disagree	2%

On exchange, drone operators shall carefully monitor safety levels to be fully compliant with the regulations. With this paper, we hope to provide them with ideas to help them to improve the social acceptance of drone operations (and thus increase business), especially in urban environments. The authors' aim is to convince drone operators to be eager to apply the most convenient mitigations to their operations, including dissemination actions and collaboration with researchers of new environmentally friendly technologies for drones.

6. Conclusions

Many governments believe that drone-related business can provide a competitive advantage for developing their country and are taking political and economic measures to foster drone business and urban air mobility. Expectations about drones are to be widely adopted by citizens in urban areas, once some issues are addressed and resolved. The most important ones are safety and societal issues.

Safety issues are largely anticipated in traditional aviation, to reduce risks to airspace users and people, assets, and facilities on the ground. Safety is achieved through thoughtful airspace design, robust and certified industrial processes, and the use of operational mitigation measures, all of them supported by an international regulation. Societal issues are sometimes overlooked before deployment.

This paper proposes to address societal issues similar to safety risks by anticipating and reducing risks (public concerns) prior to deployment. Social acceptance can be facilitated by ensuring mitigation measures that prevent the negative impact of drones on citizens and on the environment. Public concerns are identified, and actions that mitigate them shall be implemented well in advance of urban air mobility widespread deployment. The paper presents the main concerns of society with regard to drone operations, as already captured in some public surveys, and proposes a list of mitigation measures to reduce these concerns. The proposed list was then analyzed and its applicability to individual, very large demonstration urban flights is explained, using the framework of the CORUS-XUAM project. The proposed mitigation measures do not only concern drone operators but also regulators, educational bodies, other airspace stakeholders, infrastructure providers, technology and software developers, and research centers.

Future work includes the analysis of the application of mitigations in the six very large demonstrations of CORUS-XUAM to understand their impact and to fully consolidate the mitigation list proposed in this paper. It also includes new measures and scientific work to provide more detailed data to some mitigation measures, such as the perception of noise in the ground, which will help to suggest limits on altitude and speed. Future observations are needed to understand the interaction with birds. The analysis of images captured during flights will be useful to estimate threats to privacy. Additionally, further work is needed to develop a comprehensive list of mitigation measures, identify regulatory gaps, propose suitable infrastructure deployment, or influence pilot training in the future. Social concerns need to be anticipated and mitigated in advance if urban air mobility is to become an accepted part of a modern, efficient, environmentally friendly, and competitive future mobility.

Abbreviations

The following abbreviations are used in this manuscript:

UAM	Urban air mobility
VLD	Very large demonstrations
eVTOL	Electric vertical take-off and landing vehicles
ATM	Air traffic management
UAS	Unmanned aircraft systems
ATCO	Air traffic controller
CTR	Controlled traffic region

Appendix A. Full List of Mitigations

The full set of mitigations proposed in this paper are as follows:

- Limit minimum altitude.
- Establish no-fly zones for drones.
- Identify a strategic location for vertiports.
- Design optimized arrival and departure operations.
- Public engagement activities about drone technology and operations.
- General aviation pilots' engagement in activities about UAM.
- Limit hovering drone flights.
- Use of renewable energy sources to recharge batteries. Use of sustainable aviation fuel for hybrid drones.
- Ensure proper maintenance processes and controls for batteries to extend their lifecycle.
- Work with eco-friendly drones (recycled parts).
- Ensure that the cost of drone services remains commensurate with the value of the activity.
- Developing a no-blame safety culture (see EVAIR [27]) in the drone industry.
- Regulate the authorized time of the day/week and the maximum volume of traffic of UAM services.
- Further research is needed to fully understand the unique acoustics effects of drones.
- Fly direct routes to avoid unnecessary path extension and minimize the time in the air.
- Identify the classes of drone operations that can be performed under certain extreme meteorological conditions.
- Developing an environmental protection culture in the drone industry.
- Disseminate the environmental benefits of drones (quantification of emission savings).
- Establish a minimum ingress protection code (IP) for drone manufacturers.
- Ensure that electronic devices on drones (cameras, sensors, etc.) cannot be used to infringe on privacy.
- Give law enforcement the ability to monitor drone traffic directly in U-space.
- Provide a U-space information service to citizens for the purpose of verifying the mission of a drone.
- Set up countermeasures to criminal/illegal use of drones.
- Use different methods (e.g., advance encryption standards or regular cyberattack tests) to improve the security of communications at the U-space system.

- Implement an artificial intelligence system capable of detecting any deviant behavior of a drone.
- Allow all types of business to use and provide U-space services.
- Use U-space service to identify noise hot-spots.
- Improve the accuracy of short-term weather predictions at local and regional level.
- Have appropriate insurance in case of damage due to extreme weather events.
- Authorize the use of any drone in search and rescue operations (by diverting it from its original mission), unless its mission is already of an emergency or security nature.
- Ensuring that the transport of sensitive goods and strategic people is able to be subject to reinforced anonymization/protection measures in the U-space system .
- Register cameras.
- Limit type/positions of cameras.
- Create an independent authority to investigate accidents/incidents/complains related to drone operations.
- Create a public website for the identification and monitoring of public concerns.
- Ensure that the right level of technical and operational skills/competencies/knowledge are available throughout the drone industry.
- Need for clear rules and insurance to cover potential damage from UAM to third parties, infrastructure and wildlife.
- Quantify and advertise the economic contribution of drones in terms of jobs created and number of people transported, volume and cost of goods transported .
- Advertise the mobility and economic benefits of drones.
- Alternating routes to spread drone noise over several ones.
- Equip drones with systems to prevent them from being attacked by birds of prey.
- Regulate the use of lights at night.
- Strictly limit access to video recordings during and after a drone mission.
- Regulate the speed limits of UAM flights according to the area being crossed.
- Promote comfort and ergonomic designs in the new UAM services.
- Research new technologies and operations for noise reduction and abatement.
- Create standards for noise certification.
- Develop/review the planning of urban land use to regulate UAM overflights.

Appendix B. Partial List of Mitigations Adapted to Very Large Demonstrations

The following tables show the mitigations that we believe are applicable to flight demonstrations. These mitigations have been grouped according to the areas they influence.

Table A1. List of mitigation actions on the flight plan design to reduce the social concerns of demonstration flights.

Mitigation Action	Areas
Limit hovering drone flights	noise
Fly direct routes to avoid unnecessary path extension and minimize the time in the air	noise, economy, environment
Alternating routes to spread drone noise over several ones	noise
Limit minimum altitude	privacy, noise
Set the speed limits of UAM flights according to the area being crossed	environment, noise
Respect no-fly zones for drones	environment, noise
Review the urban land use below the flight plan	environment, safety, privacy, security, noise

Table A2. List of dissemination actions to reduce the social concerns of demonstration flights.

Mitigation Action	Areas
General aviation pilots' engagement in activities about UAM	fairness, safety, economy
Public engagement activities about drone technology and operations	transparency
Disseminate the environmental benefits of drones and disseminate results (emission savings)	transparency, economy
Disseminate the mobility and economic benefits of drones	transparency, economy

Table A3. List of mitigation actions applicable to drones that reduce the social concerns of demonstration flights.

Mitigation Action	Areas
Work with eco-friendly drones (recycled parts)	environment
Study of drone technologies to prevent encounters with birds	environment, economy
Measure noise at different altitudes/spots	noise
Ensure that electronic devices on drones (cameras, sensors, etc.) cannot be used to infringe on privacy	privacy
Limit type/positions of cameras	privacy

Table A4. List of other mitigation actions applicable to drones that reduce the social concerns of demonstration flights.

Topic	Mitigation Action	Areas
Vertiport	Identify a strategic location for vertiports	safety, noise, economy
Vertiport	Design optimized arrival and departure operations	environment, economy, noise
Security	Use different methods (e.g., advance encryption standards or regular cyberattack tests) to improve the security of communications at the U-space system	(cyber)security
Security	Have a U-space service capable of detecting any deviant behavior of a drone	safety, security
Security	Strictly limit the access of third parties to video recordings during and after a drone mission	privacy

References

1. Palmer, J.; Clothier, R. Analysis of the applicability of existing airworthiness classification schemes to the unmanned aircraft fleet. In Proceedings of the 15th Australian International Aerospace Congress (AIAC15-AERO), Melbourne, Australia, 25–28 February 2013; pp. 228–244.
2. Kugler, L. Real-world applications for drones. *Commun. ACM* **2019**, *62*, 19–21. [CrossRef]
3. Chew, R.; Rineer, J.; Beach, R.; O'Neil, M.; Ujeneza, N.; Lapidus, D.; Miano, T.; Hegarty-Craver, M.; Polly, J.; Temple, D.S. Deep Neural Networks and Transfer Learning for Food Crop Identification in UAV Images. *Drones* **2020**, *4*, 7. [CrossRef]
4. Muñoz, G.; Barrado, C.; Çetin, E.; Salami, E. Deep reinforcement learning for drone delivery. *Drones* **2019**, *3*, 72. [CrossRef]

5. Skorobogatov, G.; Barrado, C.; Salamí, E. Multiple UAV systems: A survey. *Unmanned Syst.* **2020**, *8*, 149–169. [CrossRef]
6. Restás, Á.; Szalkai, I.; Óvári, G. Drone Application for Spraying Disinfection Liquid Fighting against the COVID-19 Pandemic—Examining Drone-Related Parameters Influencing Effectiveness. *Drones* **2021**, *5*, 58. [CrossRef]
7. SESAR. European Drones Outlook Study. Unlocking the Value for Europe. Available online: http://www.sesarju.eu/sites/default/files/documents/reports/European_Drones_Outlook_Study_2016.pdf (accessed on 29 November 2021).
8. Clothier, R.A.; Greer, D.A.; Greer, D.G.; Mehta, A.M. Risk perception and the public acceptance of drones. *Risk Anal.* **2015**, *35*, 1167–1183. [CrossRef] [PubMed]
9. Soffronoff, J.; Piscioneri, P.; Weaver, A. Public Perception of Drone Delivery in the United States. Available online: https://www.uspsoig.gov/sites/default/files/document-library-files/2016/RARC_WP-17-001.pdf (accessed on 17 January 2022).
10. Lidynia, C.; Philipsen, R.; Ziefle, M. Droning on about drones—Acceptance of and perceived barriers to drones in civil usage contexts. In *Advances in Human Factors in Robots and Unmanned Systems*; Springer: Cham, Switzerland, 2017; pp. 317–329.
11. NATS. New and Emerging Technologies: Drones and Digital Towers. Available online: https://www.nats.aero/static/aviation-index (accessed on 17 January 2022).
12. Hamilton, B.A. *Final Report Urban Air Mobility (UAM) Market Study*; National Aeronautics and Space Administration: McLean, WA, USA, 2018.
13. Yedavalli, P.; Mooberry, J. Airbus UTM: Defining Future Skies—An Assessment of Public Perception of Urban Air Mobility (UAM). Available online: https://storage.googleapis.com/blueprint/AirbusUTM_Full_Community_PerceptionStudy.pdf (accessed on 17 January 2022).
14. Legere, M.M. *Meta-Analysis of Public Acceptance of Unmanned Aircraft Systems in the United States*; Embry-Riddle Aeronautical University: Daytona Beach, FL, USA, 2019.
15. Eißfeldt, H.; Vogelpohl, V.; Stolz, M.; Papenfuß, A.; Biella, M.; Belz, J.; Kügler, D. The acceptance of civil drones in Germany. *CEAS Aeronaut. J.* **2020**, *11*, 665–676. [CrossRef]
16. Tan, L.K.L.; Lim, B.C.; Park, G.; Low, K.H.; Yeo, V.C.S. Public acceptance of drone applications in a highly urbanized environment. *Technol. Soc.* **2021**, *64*, 101462. [CrossRef]
17. EASA. Study on the Societal Acceptance of Urban Air Mobility in Europe. Available online: https://www.easa.europa.eu/downloads/127760/en (accessed on 29 November 2021).
18. Park, S.W.; Joo, Y. Social Acceptability of Urban Air Mobility by Aircraft Category and Autonomous Phases. Ph.D. Thesis, KDI School, Sejong, Korea, 2021.
19. Kloss, B.; Riedel, R. Up in the Air: How Do Consumers View Advanced Air Mobility? Available online: https://www.mckinsey.com/industries/aerospace-and-defense/our-insights/up-in-the-air-how-do-consumers-view-advanced-air-mobility (accessed on 30 November 2021).
20. Lundqvist, R. *Aerial Uptake Intereg Europe—Regional Analysis. Comparative Summary of Regional Questionnaire Responses*; RISE Research Institutes of Sweden: Gothenburg, Sweden, 2021; pp. 1–109.
21. AESA. *JARUS Guidelines on Specific Operations Risk Assessment (SORA)*; Final Public Release v.1.0; JARUS: Paris, France, 2017.
22. Concept of Operations for European UTM Systems–Extension for Urban Air Mobility. Available online: https://www.eurocontrol.int/project/corus-xuam/ (accessed on 30 November 2021).
23. CORUS-XUAM Website. Available online: https://corus-xuam.eu/ (accessed on 30 November 2021).
24. Vertical. The Future of Advanced Aerial Mobility. Available online: https://vertical-aerospace.com/the-future-of-advanced-aerial-mobility/ (accessed on 30 November 2021).
25. Schäffer, B.; Pieren, R.; Heutschi, K.; Wunderli, J.M.; Becker, S. Drone Noise Emission Characteristics and Noise Effects on Humans—A Systematic Review. *Int. J. Environ. Res. Public Health* **2021**, *18*, 5940.
26. Beason, R.C. What can birds hear? In Proceedings of the Vertebrate Pest Conference 2004, San Diego, CA, USA, 29 March 2004; Volume 21.
27. EUROCONTROL Voluntary ATM Incident Reporting (EVAIR) Safety Bulletin 21. Available online: https://www.eurocontrol.int/publication/eurocontrol-voluntary-atm-incident-reporting-evair-safety-bulletin-21 (accessed on 28 December 2021). [CrossRef] [PubMed]

Concept Paper
The Use of Drones in the Spatial Social Sciences

Ola Hall * and Ibrahim Wahab

Department of Human Geography, Lund University, SE-223 62 Lund, Sweden; ibrahim.wahab@keg.lu.se
* Correspondence: ola.hall@keg.lu.se; Tel.: +46-73-374-7849

Abstract: Drones are increasingly becoming a ubiquitous feature of society. They are being used for a multiplicity of applications for military, leisure, economic, and academic purposes. Their application in academia, especially as social science research tools, has seen a sharp uptake in the last decade. This has been possible due, largely, to significant developments in computerization and miniaturization, which have culminated in safer, cheaper, lighter, and thus more accessible drones for social scientists. Despite their increasingly widespread use, there has not been an adequate reflection on their use in the spatial social sciences. There is need for a deeper reflection on their application in these fields of study. Should the drone even be considered a tool in the toolbox of the social scientist? In which fields is it most relevant? Should it be taught as a course in the social sciences much in the same way that spatially-oriented software packages have become mainstream in institutions of higher learning? What are the ethical implications of its application in spatial social science? This paper is a brief reflection on these questions. We contend that drones are a neutral tool which can be good and evil. They have actual and potentially wide applicability in academia but can be a tool through which breaches in ethics can be occasioned given their unique abilities to capture data from vantage perspectives. Researchers therefore need to be circumspect in how they deploy this powerful tool which is increasingly becoming mainstream in the social sciences.

Keywords: drones; legislation; ethics; spatial social sciences

1. Introduction

The term drone (For the purposes of this paper, whenever we use the term drones, we are referring to unmanned aerial systems in their use to capture photographic data, and as this is used in the social sciences. Our focus therefore is the photographic product that can be collected from drones and not the devices themselves), originally referring to the male bee, is the everyday name for autonomous aircraft. Drones tend to evoke memories of warfare as they were first flown during the First World War, during which they were often launched using a catapult. Since then, they have been used as tools for reconnaissance, for deploying propaganda leaflets, as decoys for missile launches, or even as actual combat platforms in multiple theaters of war. In more recent times, drones have become household names for their non-military uses. There have been several attempts to delink them from their militaristic past. These efforts include popularizing more civilian-leaning names for these systems. To this end, common monikers in academic literature include unmanned aerial vehicles (UAV), remotely-piloted aircraft (RPA) or vehicle (RPV), unmanned aerial system (UAS), or the recent, gender-neutral form, uncrewed aerial vehicle (also UAV). Notwithstanding these efforts, the traditional terminology has, however, stuck, and so even now, major industry players offer 'drones' and 'mini-drones' as flagship products.

Within the last decade, drones have become a much more common feature of life. This is largely attributable to the fact that they have become relatively cheaper to manufacture compared to just two decades ago. This is mainly due to significant technological advances in computerization and miniaturization. The former has exponentially increased the processing power of computers and researchers' ability to process data from drones, even on low-cost laptops, while the latter has dramatically reduced the cost of production with

less expensive components such as carbon fiber. Increasing civilian use of drones has also accompanied improvements in features aimed at augmenting safety. These features include obstacle-avoidance and vertical take-off and land (VTOL) systems. The latter allows take-off and landing of the drone system even in challenging terrains, while the former helps prevent mid-flight collision with other aircraft, trees, or buildings.

The application of drones is expanding just as their use in multiple facets of life is growing. In addition to being used as leisure tools, drones have several applications in weather forecasting, search and rescue operations, disaster management, crowd control, and delivery of vaccines and blood for transfusion, among others. One area that has also begun seeing the increased application of drones in the last decade is academia. In this regard, both the physical as well as the social sciences have found it to be a useful tool. Some disciplines, by virtue of their subject matter and focus, find the incorporation of drones into their research agenda easier than others. For instance, in the physical sciences, the subject matter is often physical, and the unit of analysis could be rocks, stars, plants, or animals. Studying such using drones is easier and more straightforward than the social sciences, in which the subject matter is society itself and the unit of analysis is often humans. The latter are more complex units of study because they are sentient, conscious, and can modify their activities under study. Related to this are ethical dilemmas as well as questions about objectivity when we study our, as well as other, societies. Given our biases, both declared and undeclared, as well as recognized and unrecognized, there is often the need for greater reflexivity in social science studies, especially in collecting data.

Generally, social scientists employ a range of tools and methods to collect data for their studies. These methods range from experiments, surveys, interviews, focus group discussions (FGDs), participant observations, life histories, and documentation analysis, among others. While each of these methods have their strengths and weaknesses, their appropriateness depends on the context of studies. Some social science disciplines are more inclined to relying on visual methodologies than others. The social science disciplines of anthropology, archaeology, economics, geography, history, and sociology have found drones to be useful research tools. Of these, anthropology and geography are unique in their reliance on the visual and visual images to construct their knowledge [1]. Given drones' advantage of providing access to a bird's eye view of the geographical space [2], and geography's preoccupation as a spatial science, drones have found a much more accepting audience among geographers compared to other social scientists. Even within geography, not only are drones helping to bridge the gap, but they are also offering new opportunities for collaborative research between human and physical geographers given that these two subdisciplines often approach the application of drones differently [3].

In this conceptual paper, we aim to discuss the use of drones as social science research tools. In this vein, we focus the discussion on three main themes: teaching their use as a course in the social science faculties of universities, legislations governing their use across countries, and the ethical and political hurdles that need reflection in their application, particularly in the social sciences. While the civilian use of drones for surveillance and policing to fight crime is generally socially acceptable [4], there is often a certain level of uneasiness and strong pushback against a continuous, universal, and an all-seeing flying big brother in the sky [5], given the potential for abuse and concerns for privacy. These reflections are critical as drones continue to become mainstream tools in the toolbox of the social scientist.

2. Drones as Social Science Research Tools

The application of drones in the social sciences as data collection tools comes on the back of the use of satellite imagery in the same endeavours. The latter can be traced to the mid-1990s when the National Aeronautics and Space Administration (NASA) approached the research community to realize the potential of satellite imagery to specifically address questions which social scientists are preoccupied with. Notwithstanding the high expectations from this collaboration expressed in People and Pixels: Linking Remote Sensing and

Social Science [6], the results have been meagre, and their added value questioned. Much of the difficulties that limited the success of using remotely sensed satellite imagery-coarse resolution of most readily available datasets, the challenge with cloud cover, particularly in the tropics, and limitations relating to temporal resolutions have persisted. This is despite the significant strides that have been made in this area in the last two decades. It is on the back of these challenges that other platforms have been proposed as alternatives to satellites as remote sensing platforms for collecting critical data about the earth's surface. As the third generation remote sensing platform-with piloted aircraft as the first generation and earth-orbiting satellites as the second generation [7], drones are proving much more ubiquitous in terms of their application in scientific research.

There are, of course, substantial differences between drone data and satellite imagery and, as such, the two are not comparable. An important differentiating factor is the scale of application. While satellites are ideal when the macro view of the terrain is needed, due to the larger spatial coverage, drone imagery is better suited for a micro view of the landscape, given its higher-centimetre-level-resolution. Some studies have catalogued the pros and cons of each platform and shown where each performs optimally [8,9], others have been preoccupied with integrating them in a synergistic manner [10,11]. The general trend, with regard to spatial resolution, is a continuous increase, with some satellite platforms now offering sub-meter resolutions. This opens the door for greater applications that were hitherto virtually impossible. The recent use of the 1 m resolution Terra Bella satellite imagery for measuring smallholder productivity in Western Kenya is a case in point [12]. Thus, each platform and the resultant data they generate meet specific needs. In some cases, however, drone data can be up-scaled to cover larger areas. This of course, raises questions of cost-effectiveness [13].

Drones and drone imagery position the researcher and the objects of interest closer together, both physically as well as conceptually. Compared to satellite imagery, the low flying altitude, small area coverage, and the detailed visuals that drones offer create a familiar perspective, closely related to traditional field work. Unlike satellite imagery, drone imagery is usually ready to be used as a map base or in photo elicitation interviews [14–16]. They can also be processed, classified, and analyzed in a more conventional remote sensing way [17,18]. Thus, drone imagery can either be used on its merit or to improve the quality of data that other more conventional methods of data collection in the social sciences have produced. For instance, van Auken, Frisvoll [19] enumerate the advantages that photo-elicitation interviews have over more traditional social science research tools, such as the provision of tangible stimuli for more effectively tapping into informants' tacit, and often unconscious knowledge, consumption of representations, images and metaphors, and thus leading to the production of different and richer information than other techniques, while also helping to reduce differences in power, class, and knowledge between researcher and researched. In the developing world, which is invariably the 'data-poor' world, drone imagery has proven to be an indispensable tool for research.

The geographical applications of drones are perhaps more widespread than in other fields. In the sub-field of physical geography, drones have gained wide acceptance for studying rock weathering [20,21], for river bed monitoring [22,23], and for restoration [24]. In this area, studies have progressed beyond proof-of-concepts to real-world applications for geomorphological change detection and mapping, vegetation mapping, habitat classification and sediment transport path delineation [25]. Further downstream, Callow, May [26] used a drone to generate high-accuracy, centimeter-resolution digital topographic models which offer insights into the likely consequences of inundation and the dynamics that control low-gradient sedimentary landforms. It is not surprising that geography in general, and the subdiscipline of physical geography in particular, were always going to be more accepting of drones due mainly to the their 'vertical' and 'visual' character. The proliferation of drones as research tools, however, avails further opportunities for intra-discipline collaboration between physical and human geographers [3].

In agricultural geography, drone applications include mapping crop condition and yield estimation [18,27,28], crop classification [17], seedling emergence assessment, crop damage assessment, weed detection, and mapping [29]. In general terms, drones have been heralded as the right tools for making agriculture smarter, especially in Sub-Saharan Africa where the application of the first- and second-generation remote sensing platforms have met with largely limited success. This limited success is due to such factors as costs of acquisitions, cloud cover, and low spatial and temporal resolutions vis-à-vis the predominance of small farms in SSA. Multiple reviews such as those by Daponte, De Vito [30], Puri, Nayyar [31] have chronicled the use of drones in the field of smart agriculture. Iost Filho, Heldens [32] more specifically reviewed the application of drones as noninvasive crop monitoring systems in precision pest management. Three main niches exist in this subfield for drone application: (1) scouting for problems; (2) monitoring crops to prevent/reduce losses; and (3) planning crop management operations [33]. Similarly, Barbedo [34] offers a more comprehensive and critical review of the use of drones in this area, chronicling the major milestones, the main research gaps and possibilities for future research with the application of even newer techniques of machine learning on drone image analysis.

This is, however, not to assert that drones are not already useful research tools in the other subdisciplines of human geography. In tourism studies, for example, the usefulness of drones continues to grow. Here, drones are being used for monitoring and patrolling tourism activities for safety and security as well as for virtual tourism systems [35]. For virtual tourism, drones serve as destination marketing tools to produce large amounts of visually appealing footages of various destinations [36]. On the part of tourism service providers, major considerations regarding economic viability and operational feasibility need to be addressed in order to efficiently deploy drones in the tourism sector [37]. While tourists tend to have a better appreciation of the potential uses of drones compared to managers of tourist centers, there is need to set boundaries of what is acceptable [38]. Beyond tourism studies, drones are finding applications as research tools in cultural geography, health geography, rural geography, transportation geography, and urban geography, among others.

In the area of environmental geography, for instance, community drones for natural resource management and conservation is a strongly growing niche [39–42]. Much of the work in this area emanates from Latin America and, to a lesser extent, South-East Asia. Drone applications are most useful in cases where the study locations are usually difficult to physically access. A number of reviews by those such as Paneque-Gálvez, Vargas-Ramírez [43], Canal and Negro [44], Beaver, Baldwin [45], have emerged in this area that point to current and potential significant contributions that drones can be put to in natural resource management. Cummings, Cummings [46] go a step further to demonstrate how drones can be adapted in indigenous peoples' dominated settings in a collective and concerted manner. Following such a collaborative approach can help build mutually beneficial relationships, as it respects indigenous culture and customary norms, which in turn augurs well for a sustainable monitoring and protection of natural ecosystems. Vargas-Ramírez and Paneque-Gálvez [39] provide a broad overview of this growing field of community drones, finding that local knowledge is often neglected or undervalued, and emphasizing the need to recognize indigenous peoples' territorial rights. Done well, participatory action mapping (PAM) using drones can be useful for bolstering the political and legal claims of indigenous communities to counteract land grabs by foreign entities [47,48]. Conversely, unintended negative consequences of PAM include fragmentation and conflicts among indigenous communities and the facilitation of land acquisitions, either by the state or corporations, following legal recognitions [49]. There is also the need for researchers engaged in PAM to pay attention to the digital divide that often exists between them and indigenous communities, a situation which is symptomatic of broader socioeconomic and political inequalities which are largely legacies of colonialism [50].

In archaeology, drones are becoming increasingly useful in studying previously unrecognizable features. For example, Cucchiaro, Fallu [51] demonstrate that orthomosaics from drones provide an accurate and high level of detail of the terrace landscape, the archaeological features and sediment stratigraphy along an excavation trench previously unobserved. Similarly, Brown, Walsh [52] show the beneficial use of drones to map multi-faceted terraces under intensification and diversification. In landscape archaeology, Stek [53] demonstrates the utility of drones for detecting previously undocumented subsurface archaeological artifacts in mountainous, Mediterranean landscapes. Campana [54] provides an excellent review of the application of drones in archaeology and delineates five main areas of application: exploratory aerial surveys, survey of archaeological sites and landscapes, three-dimensional (3D) documentation of excavations, 3D surveys of monuments and historic buildings, and archaeological surveys of woodland areas. Just like in tourism studies, the application of drones, which makes hitherto unobservable sites accessible, also requires some safeguards to ensure that aerial photos do not contribute to looting and destruction of heritage sites [55].

Different fields incorporate drones into the fieldwork and studies to varying extents. The broad field of geography is, however, relatively more predisposed to employing drones compared to other fields because it uses the full sweep of quantitative and qualitative methods and places greater emphasis on fieldwork and mapping. This is underpinned by its special focus on spatial analysis and areal differentiation. Perhaps, through more widespread teaching of drones as a stand-alone course in the social sciences in universities, other fields might come to realize their value and how they can be adopted and utilized to suit each discipline's peculiar needs.

3. Teaching Drones in Higher Education

The teaching of drones in institutions of higher learning is fast catching on, notwithstanding the substantial capital outlay that this involves due to the infrastructure demands that it entails. The teaching can, broadly, be categorised into two main areas: (1) teaching it as hardware, including the development of technical improvements to the drone's navigation systems; and (2) teaching drone-based data capture and processing. The first is the kind of stuff that more technical departments of universities such as engineering already do, and this is not the focus of the present paper. Here we limit ourselves to the social sciences, and thus the second, which is the teaching of the capture and processing of drone-based data.

In this era of rapid data collection, drones have emerged as a well-established geospatial technology for collecting and analysing primary remote sensing data. In terms of importance, they are poised to be as revolutionary for geography in the same order of magnitude as other spatially-oriented software packages. They offer a method for collecting and accumulating data from strategic viewpoints [56] and at such fine spatial resolutions that there are many social science disciplines that can benefit from this vantage perspective. Given their ubiquity in society and increasing applications, even in the social sciences, there is increasingly obvious need for having a dedicated course on drones in research-oriented universities. To be fair, much of what we propose here, in terms of teaching drones, is already being done by many engineering departments across many universities. Our focus here relates to flying the drones, capturing spatial data in photographic format, processing these into orthomosaics, and the application of these in the social sciences and the ethical implications that this entails. It is our position that the reflexivity and reflections that arise when social scientists undertake these processes themselves are markedly different from those that arise when the orthomosaics are presented to them for analysis. Hence the need to teach these in universities to social science students even if photogrammetry has been taught for years to engineers. Herein lies the gravamen of the argument for the teaching of drones as an important tool in the toolbox of the social scientist.

Effective teaching of the principles and applications in a field such as dynamic geographic information systems and technology in higher education is usually challenging [57]

and drones are no exception in this. This is partly down to the constant change that this niche of study is subject to. Effective teaching of drones in institutions of higher learning needs to overcome two fundamental issues: teachers need to adopt and adapt new paradigms and tools while keeping up to date with newer trends in the field, and yet also develop effective methods for transferring the new competencies to students. The teaching of drones, especially when it encompasses image acquisition, data processing and interpretation, has been shown to significantly enhance students' data processing skills while enhancing their competence in handling data quality issues [58]. Consequently, this field is usually at the cutting edge of teaching and learning approaches, with traditional approaches giving way to more modern methods.

In recent times, more traditional approaches, such as pen-and-paper in lectures and laboratory exercises, are giving way to more active learning strategies such as 'flipped classrooms' [57]. Such participatory and collaborative approaches lay good foundations among students for participatory action research and popular education approaches which ensure community participation and cultural appropriateness of the methods that are employed in data collection using drones [39]. These, however, often require further training not only on the part of students, but instructors as well. On the part of instructors, there is often the need to allocate extended periods of preparation for classes to keep abreast with software updates as well as new trends and developments in the general field of geographic information science and technology [57] and the specific field of image analysis, especially using the artificial intelligence techniques of machine learning and deep learning using big data. Holloway, Kenna [59] further posit that, with regards to new technologies, such new approaches foster teamwork, peer-to-peer learning, and positively reinforce the uptake of such technologies in fieldwork.

Already, some institutions are setting the pace in teaching drones both at undergraduate and advanced levels. In the United States, the Drone Journalism programmes at the Universities of Missouri and Nebraska-Lincoln are pacesetters in drone studies. In such programmes, students are taught not only the technical skill of flying a drone mounted with cameras to collect aerial data, but also the ethics of collecting data on people in public places and the legal, safety and regulatory frameworks across various jurisdictions and areas as well as the analysis of aerial data [56]. For instance, flying regulations are different within a 2-km radius of an airport than they are for a rural area [3]. For safety reasons, special rules also apply to flying altitudes, with about 100 metres often considered a safe height. Elsewhere in continental Europe, the Oslo School of Architecture and Design is also considered an early pioneer in the teaching of drones as a course [60]. Similarly, Lund University has an aviation school which specializes in training and certification of drone pilots and is in the process of acquiring the necessary credentials from the country's transport administration. Other research-oriented universities should be following these early innovators in this endeavour. The main challenge for instructors is to cover the three fundamentals of remote sensing, these being planning, data collections, and image analysis, while minimising logistical and practical issues associated with the actual flights [61]. A further hurdle in this is securing the necessary certifications to be able to train pilots within the existing legislation framework.

Those institutions that do not have the infrastructure or which are in jurisdictions where private drone use, even for academic purposes, is significantly restricted, could liaise with already established pilot schools to train students on the technical aspects of flying while they focus on the theoretical, philosophical, ethical, and methodological aspects of drone use in the social sciences. The onus falls on geographers, both physical and human ones, to actively engage with this technology and lead cross-disciplinary discussions on not only the processing of drone data but also the ethical implications of its use. Collaborating with specialized flight training schools thus helps to overcome barriers relating to certification and licensing.

4. Legislations on Drone Use across Countries

At the core of the legislations regulating the use of drones is the need to ensure safety and minimize harm in the use of drones in civilian airspace. Professional use of drones necessarily needs to be guided by a multiplicity of legislations, from the national, regional, and even local levels. Regulations often relate to the flying of the drone itself, the safe and secure management of the communication to and from the drone system, and those relating to the ethical issues arising from the acquisition, processing, and dissemination of drone imagery. Underpinning the first two is the need to prevent airspace conflict and interference with commercial airport systems. The third is concerned with preventing breaches of confidentiality, privacy and safety of people and locations of national security importance.

Much like other technological innovations, regulations for drones have been playing catch-up with the proliferation and use of the devices [62]. Different countries have reached different regulation development stages for drones, with most countries, especially in Africa, having developed their national guidelines within the last half decade. Even among OECD countries, there is substantial heterogeneity in national legal frameworks on drone regulation [63]. Regulations on the use of drones are necessary due to the potential for breaching privacy, data protection, and public peace [64]. Regulations relating to licensing and operations therefore vary significantly across countries, even though a substantial proportion (40 to 85%) of the provisions of legislations governing drone usage is often sourced from the manual of the International Civil Aviation Organization [64]. Even where regulations have been harmonized, as is the case with the European Union (new regulations came into force in January 2021), stakeholders often find them cumbersome due to administrative and bureaucratic complexities in their interpretations [65]. The regulatory field will most likely continue to be characterized by fluidity in the foreseeable future. There are a few data repositories for information on drone regulations worldwide. A useful portal for the most up-to-date information on drone regulations for various jurisdictions can be found at: https://www.droneregulations.info/index.html (accessed on 16 June 2021). Here, one can access the specific website of respective national authorities responsible for licensing and issuing guidelines and regulations for drone pilots. The portal thus serves as a one-stop-shop for the most updated laws on the use of drones on each country.

A major challenge relating to the regulations is the restrictions they tend to come with. This is particularly true when regulatory agencies fear that lives could be at risk. In such circumstances, there is a tendency for broad restrictions which limit adoption and use of drones even for academic research [64,65]. These barriers are sometimes purely financial. For example, Kenya Airways has an entry-cost of about USD 1600 for a month-long course to obtain a license to fly a drone in Kenya [66]. This excludes other charges such as the cost of medical examination. The initial license issuance costs some USD 720 and this is renewable at a fee of about USD 460 [67]. This area is, however, in constant flux. Countries are regularly reviewing regulations to improve the ease of use of drones in their jurisdictions. In the United States, which is a pioneer in this area, drone operators are no longer required to pass a medical examination nor have liability insurance, for example. Drone pilots are only required to pass an aeronautical knowledge test rather than acquire any form of pilots' license.

Other portals exist to check drone operations and report incidents involving drones. The most popular of these is the drone incidents and intelligence system https://www.drone-detectives.com/ (accessed on 7 July 2021). The primary purpose of this portal is to safeguard public safety by allowing private individuals to report dangerous drone activities and to file accident incidents involving drones. Some of the details one can report include date and time of incident, the type/model of drone involved, and the altitude at which the drone was flying, as well as the specifics of the incident such as the proximity to airport airspace or military installations. Such reports are useful for regulatory institutions in their monitoring activities. Apart from showing incidents involving drones, Drone Detectives

is also useful in noting the various no fly zones in all countries. These are usually over military installations, airport airspace and public spaces such as parks and stadia.

Thus, while the fundamental role of these national regulations relating to drone use is to ensure public safety and security, some of the rules will have to be relaxed as drone features such as obstacle sensing and avoidance systems improve. Legislations on drones often have three main aims: (1) to regulate the use of airspaces; (2) to impose operational limitations; and (3) to outline administrative processes for permissions, licenses and authorizations [64]. The overall aim is therefore safety and security. The enactment of such rules is fundamental for further tapping into the potential benefits that drones come with in the various fields.

Several studies and reviews have been carried out in this area of regulations governing drone use and the implications of these on the industry. In the last year alone, Alamouri, Lampert [65] provided an overview of recent updates on drone regulations in the European Union and showed how regulations can help and hinder the use of the technology. Similarly, Hodgson and Sella-Villa [68] provide a review of the regulatory regimes in the United States, with particular reference to its application for academic research. They further highlight the complexities relating to restrictions on flying over critical infrastructure such as security installations when the locations of such facilities are classified for security reasons, as well as recommendations on how researchers can obtain exemptions from often sweeping restrictions. In the African context, Ayamga, Tekinerdogan [64] provide a review of the challenges that regulations pose for drone adoption and application, with specific focus on the field of agriculture. They argue that while the political commitment may be present in most Sub-Saharan African countries, regulations are often hampered by inadequate capacity to develop and enforce drone regulations.

5. Ethical and Safety Considerations

In terms of safety, drones are generally considered relatively safer than piloted aircraft for two main reasons; first, they are not piloted and so there is minimal risk of harm to the human controller in cases of a crash, and second, they do less damage on crashing because they are relatively smaller in size [69]. Modern drones also come with more safety features such as obstacle avoidance systems and return to launch buttons on controllers than their predecessors. This notwithstanding, drones come with some heightened concerns of safety due mainly also to their pilotlessness nature [70]. How safe a particular drone system would be is influenced, to some extent, by the drone configuration. For instance, rotary winged drones tend to fall stone-like in cases of rotor failure, while their fixed-wing counterparts tend to fall more gracefully. It is for this reason that drone licenses and flight permission are influenced by the type of drone.

Beyond safety is the ethical implications of research done using drones. The main issues of concern when discussing ethics in drone research are not markedly different from those that come up when using conventional research techniques like interviews, surveys, and FGDs, among others. Indeed, the key issues of privacy, confidentiality, and consent are still fundamental. The distinction of what constitutes the private sphere and public domain is critical. While drone data collection does not involve human test subjects *per se*, they often involve the observation of public places that humans are an intrinsic part of. In such contexts, it would be required that the data is recorded in a manner such that individuals are not personally identifiable, and if they were identifiable, disclosure of their identity outside of the research environment would not place them at the risk of any harm [71]. Studies that do not meet these thresholds may be subject to institutional ethics restrictions. On private property, however, studies will necessarily require consent from individuals to pass the ethics requirement. It is, for instance, not inconceivable that a drone captures an individual engaging in an illegal activity which would make them liable to criminal prosecution. The possibility of such accidental breaches of people's privacy means that drone operations over the private domain often requires researchers to obtain informed consent. Conversely, Sella-Villa [72] argues that drones are primarily data collection devices

whose impact on privacy is rather limited, as they are not substantially different from other camera-equipped technology. From this perspective, if a photograph is taken, the platform used is largely irrelevant. This notwithstanding, certain unique characteristics and qualities of drones means that their use as data collection tools in the social sciences brings to the fore key ethical concerns.

Issues regarding ethics in drone research, like in many other fields, is not a straightforward one and is often riddled with inconsistencies and contradictions; what is private can quickly become public and vice-versa. For example, can people have private moments in a public park and how does one draw the distinction? There remain many grey areas and a lack of universality in principles regarding these requirements. For instance, what constitutes private information? While the airspace may reasonably be considered public space, would flying a drone over a farmer's field in open view require consent from them? What happens if they were growing marijuana on this field? Would institutional ethics review committees require researchers to gain informed consent for such drone operations? Moreover, obtaining informed consent from individuals in a study using drones can be a daunting task. This becomes impractical where, for instance this involves an indefinite number of people in a village.. In such a scenario, a community-wide forum prior to data collection becomes prudent. Through this, researchers could inform community members of what kind of information is to be collected and assure them of the protection of their anonymity, privacy and confidentiality [71]. This could engender public trust and buy-in on drone projects. This is especially critical in resource conservation in the interest of long-term sustainability of projects long after researchers leave research communities [69].

Despite their ubiquitous nature in the last few years, the capabilities of drones means that they are an excellent tool for surveillance, since they capture data from a vantage perspective inaccessible to other technologies [72]. There is, therefore, the need to be circumspect when applying them to data collection in the social sciences [70]. There is general agreement that researchers who employ drones to collect data should ideally submit their proposals to institutional review committees or some other oversight body for vetting to ensure compliance with ethical and regulatory standards [71]. While most drone studies, based on current ethical requirements, would qualify as exempt from such stringent reviews due to the minimal risk of harm to human subjects, researchers should nonetheless be aware of the possibility of ethical breaches that the collection of data in the public domain can occasion.

6. Conclusions

The last decade has seen a significant uptake in studies that use drones either as supporting tools or even as the primary methods of data collection. Drones can have important roles to play in mixed methods, especially in the areas of natural resource conservation, agriculture, tourism, among others. In this paper, we have discussed the increasingly widespread application of drones as tools for research in the social sciences. Given the unique capabilities of drones, there is the need for adequate ethical considerations when using them in research. While they hold enormous potential in multiple fields of study, certain fields such as geography and archaeology are already more inclined to their application than others. In archaeology, drones have enabled hitherto unobserved artifacts to become accessible to researchers. This has both positive and negative implications for heritage sites and indigenous populations. The application of drones in the fields of tourism studies and archaeology thus requires additional reflexivity to ensure that their use does not contribute to exploitation and looting of sites that were hitherto inaccessible. These considerations should fit into broader national guidelines and regulatory frameworks which should, in turn, be streamlined and be made less cumbersome to engender compliance. Certain barriers, which in most countries are financial, do not augur well for the adoption of the technology to reap the full benefits of their application.

Drones are already an inexorable part of society, and so spatial social scientists should be actively engaged with the use of this tool and be engaged in debates on the application

of the technology as a tool in their increasingly dynamic toolbox. This will ensure that the benefits inherent in the use of drones are maximised without exacerbating possibilities of breaches in ethics. A key plank of this engagement is the teaching of specialised courses in drones in institutions of higher learning. Such a drone course will not only help students acquire the technical skills to operate drones but also help them explore ways in which the tool can be applied in their own research specialisations, as well as enable them to engage critically with the ethical dilemmas inherent in its application in the social sciences. This latter discussion is critical as drones are becoming an integral tool in the toolbox of the social scientist as they become cheaper, safer, and more accessible.

References

1. Rose, G. On the Need to Ask How, Exactly, Is Geography "Visual"? *Antipode* **2003**, *35*, 212–221. [CrossRef]
2. Birtchnell, T. Drones in human geography. In *Handbook on Geographies of Technology*; Warf, B., Ed.; Edward Elgar Publishing: Cheltenham, UK, 2017; pp. 231–241.
3. Garrett, B.; Anderson, K. Drone methodologies: Taking flight in human and physical geography. *Trans. Inst. Br. Geogr.* **2018**, *43*, 341–359. [CrossRef]
4. West, J.P.; Bowman, J.S. The Domestic Use of Drones: An Ethical Analysis of Surveillance Issues. *Public Adm. Rev.* **2016**, *76*, 649–659. [CrossRef]
5. Neocleous, M. Air Power as Police Power. *Environ. Plan. D Soc. Space* **2013**, *31*, 578–593. [CrossRef]
6. Livermore, D.E. *People and pixels: Linking remote sensing and social science*; National Academies Press: Washington, DC, USA, 1998.
7. Simic Milas, A.; Cracknell, A.P.; Warner, T.A. Warner, Drones–the third generation source of remote sensing data. *Int. J. Remote Sens.* **2018**, *39*, 7125–7137. [CrossRef]
8. Martinez, J.; Lucas-Borja, M.; Plaza-Alvarez, P.; Denisi, P.; Moreno, M.; Hernández, D.; González-Romero, J.; Zema, D. Comparison of Satellite and Drone-Based Images at Two Spatial Scales to Evaluate Vegetation Regeneration after Post-Fire Treatments in a Mediterranean Forest. *Appl. Sci.* **2021**, *11*, 5423. [CrossRef]
9. Matese, A.; Toscano, P.; Di Gennaro, S.F.; Genesio, L.; Vaccari, F.P.; Primicerio, J.; Belli, C.; Zaldei, A.; Bianconi, R.; Gioli, B. Intercomparison of UAV, Aircraft and Satellite Remote Sensing Platforms for Precision Viticulture. *Remote Sens.* **2015**, *7*, 2971–2990. [CrossRef]
10. Gray, P.C.; Ridge, J.T.; Poulin, S.K.; Seymour, A.C.; Schwantes, A.M.; Swenson, J.J.; Johnston, D.W. Integrating Drone Imagery into High Resolution Satellite Remote Sensing Assessments of Estuarine Environments. *Remote Sens.* **2018**, *10*, 1257. [CrossRef]
11. Padró, J.-C.; Muñoz, F.-J.; Ávila, L.Á.; Pesquer, L.; Pons, X. Radiometric Correction of Landsat-8 and Sentinel-2A Scenes Using Drone Imagery in Synergy with Field Spectroradiometry. *Remote Sens.* **2018**, *10*, 1687. [CrossRef]
12. Burke, M.; Lobell, D.B. Satellite-Based Assessment of Yield Variation and Its Determinants in Smallholder African Systems. *Proc. Natl. Acad. Sci. USA* **2017**, *114*, 2189–2194. [CrossRef]
13. Jang, G.; Kim, J.; Yu, J.-K.; Kim, H.-J.; Kim, Y.; Kim, D.-W.; Kim, K.-H.; Lee, C.W.; Chung, Y.S. Review: Cost-Effective Unmanned Aerial Vehicle (UAV) Platform for Field Plant Breeding Application. *Remote. Sens.* **2020**, *12*, 998. [CrossRef]
14. Wahab, I.; Jirström, M.; Hall, O. An Integrated Approach to Unravelling Smallholder Yield Levels: The Case of Small Family Farms, Eastern Region, Ghana. *Agriculture* **2020**, *10*, 206. [CrossRef]
15. Harper, D. Talking about pictures: A case for photo elicitation AU—Harper, Douglas. *Vis. Stud.* **2002**, *17*, 13–26. [CrossRef]
16. Glaw, X. Visual methodologies in qualitative research: Autophotography and photo elicitation applied to mental health research. *Int. J. Qual. Methods* **2017**, *16*, 1–8. [CrossRef]
17. Hall, O.; Dahlin, S.; Marstorp, H.; Bustos, M.F.A.; Öborn, I.; Jirström, M. Classification of Maize in Complex Smallholder Farming Systems Using UAV Imagery. *Drones* **2018**, *2*, 22. [CrossRef]
18. Wahab, I.; Hall, O.; Jirström, M. Remote Sensing of Yields: Application of UAV Imagery-Derived NDVI for Estimating Maize Vigor and Yields in Complex Farming Systems in Sub-Saharan Africa. *Drones* **2018**, *2*, 28. [CrossRef]
19. Van Auken, P.M.; Frisvoll, S.; Stewart, S.I. Visualising community: Using participant-driven photo-elicitation for research and application. *Local Environ.* **2010**, *15*, 373–388. [CrossRef]

20. Mol, L.; Clarke, L. Integrating structure-from-motion photogrammetry into rock weathering field methodologies. *Earth Surf. Process. Landf.* **2019**, *44*, 2671–2684. [CrossRef]
21. Verma, A.K.; Bourke, M.C. A method based on structure-from-motion photogrammetry to generate sub-millimetre-resolution digital elevation models for investigating rock breakdown features. *Earth Surf. Dyn.* **2019**, *7*, 45–66. [CrossRef]
22. Vázquez-Tarrío, D.; Borgniet, L.; Liébault, F.; Recking, A. Using UAS optical imagery and SfM photogrammetry to characterize the surface grain size of gravel bars in a braided river (Vénéon River, French Alps). *Geomorphology* **2017**, *285*, 94–105. [CrossRef]
23. Piégay, H.; Arnaud, F.; Belletti, B.; Bertrand, M.; Bizzi, S.; Carbonneau, P.; Dufour, S.; Liébault, F.; Ruiz-Villanueva, V.; Slater, L. Remotely sensed rivers in the Anthropocene: State of the art and prospects. *Earth Surf. Process. Landforms* **2020**, *45*, 157–188. [CrossRef]
24. Marteau, B.; Vericat, D.; Gibbins, C.; Batalla, R.J.; Green, D.R. Application of Structure-from-Motion photogrammetry to river restoration. *Earth Surf. Process. Landforms* **2017**, *42*, 503–515. [CrossRef]
25. Carrivick, J.L.; Smith, M.W. Fluvial and aquatic applications of Structure from Motion photogrammetry and unmanned aerial vehicle/drone technology. *Wiley Interdiscip. Rev. Water* **2019**, *6*, 1328. [CrossRef]
26. Callow, J.; May, S.; Leopold, M. Drone photogrammetry and KMeans point cloud filtering to create high resolution topographic and inundation models of coastal sediment archives. *Earth Surf. Process. Landforms* **2018**, *43*, 2603–2615. [CrossRef]
27. Yonah, I.B.; Mourice, S.K.; Tumbo, S.D.; Mbilinyi, B.P.; Dempewolf, J. Unmanned aerial vehicle-based remote sensing in monitoring smallholder, heterogeneous crop fields in Tanzania. *Int. J. Remote Sens.* **2018**, *39*, 5453–5471. [CrossRef]
28. Adewopo, J.; Peter, H.; Mohammed, I.; Kamara, A.; Craufurd, P.; Vanlauwe, B. Can a Combination of UAV-Derived Vegetation Indices with Biophysical Variables Improve Yield Variability Assessment in Smallholder Farms? *Agronomy* **2020**, *10*, 1934. [CrossRef]
29. van der Merwe, D. Drones in agriculture. In *Advances in Agronomy*; Academic Press: Cambridge, MA, USA, 2020.
30. Daponte, P.; De Vito, L.; Glielmo, L.; Iannelli, L.; Liuzza, D.; Picariello, F.; Silano, G. A review on the use of drones for precision agriculture. In Proceedings of the IOP Conference Series: Earth and Environmental Science, 1st Workshop on Metrology for Agriculture and Forestry (METROAGRIFOR), Ancona, Italy, 1–2 October 2018; 2019; Volume 275, p. 012022.
31. Puri, V.; Nayyar, A.; Raja, L. Agriculture drones: A modern breakthrough in precision agriculture. *J. Stat. Manag. Syst.* **2017**, *20*, 507–518. [CrossRef]
32. Filho, F.H.I.; Heldens, W.B.; Kong, Z.; De Lange, E.S. Drones: Innovative Technology for Use in Precision Pest Management. *J. Econ. Entomol.* **2019**, *113*, 1–25. [CrossRef]
33. Hunt, E.R.; Daughtry, C.S.T. and C.S.T. Daughtry, What good are unmanned aircraft systems for agricultural remote sensing and precision agriculture? *Int. J. Remote Sen.* **2018**, *39*, 5345–5376. [CrossRef]
34. Barbedo, J. A Review on the Use of Unmanned Aerial Vehicles and Imaging Sensors for Monitoring and Assessing Plant Stresses. *Drones* **2019**, *3*, 40. [CrossRef]
35. Song, B.D.; Ko, Y.D. Quantitative approaches for economic use of emerging technology in the tourism industry: Unmanned aerial vehicle systems. *Asia Pac. J. Tour. Res.* **2017**, *22*, 1–14. [CrossRef]
36. Stankov, U.; Kennell, J.; Morrison, A.M.; Vujičić, M. The view from above: The relevance of shared aerial drone videos for destination marketing. *J. Travel Tour. Mark.* **2019**, *36*, 808–822. [CrossRef]
37. Ko, Y.D.; Song, B.D. Application of UAVs for tourism security and safety. *Asia Pac. J. Mark. Logist.* **2021**, *33*, 1829–1843. [CrossRef]
38. Hay, B. Drone tourism: A study of the current and potential use of drones in hospitality and tourism. In *The Changing Landscape of Tourism and Hospitality: The Impact of Emerging Markets and Emerging Destinations*; Scerri, M., Hue, L.K., Eds.; Blue Mountains International Hotel Management School: Sydney, Australia, 2016; pp. 49–68.
39. Vargas-Ramírez, N.; Paneque-Gálvez, J. The Global Emergence of Community Drones (2012–2017). *Drones* **2019**, *3*, 76. [CrossRef]
40. Rush, G.P.; Clarke, L.E.; Stone, M.; Wood, M. Can drones count gulls? Minimal disturbance and semiautomated image processing with an unmanned aerial vehicle for colony-nesting seabirds. *Ecol. Evol.* **2018**, *8*, 12322–12334. [CrossRef] [PubMed]
41. Valle, R.G.; Scarton, F. Drones Improve Effectiveness and Reduce Disturbance of Censusing Common Redshanks Tringa totanus Breeding on Salt Marshes. *Ardea* **2019**, *107*, 275. [CrossRef]
42. Burke, C.; Rashman, M.; Wich, S.; Symons, A.; Theron, C.; Longmore, S. Optimizing observing strategies for monitoring animals using drone-mounted thermal infrared cameras. *Int. J. Remote Sens.* **2019**, *40*, 439–467. [CrossRef]
43. Paneque-Gálvez, J.; Vargas-Ramírez, N.; Napoletano, B.M.; Cummings, A. Grassroots Innovation Using Drones for Indigenous Mapping and Monitoring. *Land* **2017**, *6*, 86. [CrossRef]
44. Canal, D.; Negro, J.J. Use of Drones for Research and Conservation of Birds of Prey. In *Birds of Prey*; Springer: Berlin/Heidelberg, Germany, 2018; pp. 325–337.
45. Beaver, J.T.; Baldwin, R.W.; Messinger, M.; Newbolt, C.H.; Ditchkoff, S.S.; Silman, M.R. Evaluating the Use of Drones Equipped with Thermal Sensors as an Effective Method for Estimating Wildlife. *Wildl. Soc. Bull.* **2020**, *44*, 434–443. [CrossRef]
46. Cummings, A.R.; Cummings, G.R.; Hamer, E.; Moses, P.; Norman, Z.; Captain, V.; Bento, R.; Butler, K. Developing a UAV-Based Monitoring Program with Indigenous Peoples. *J. Unmanned Veh. Syst.* **2017**, *5*, 115–125. [CrossRef]
47. Radjawali, I.; Pye, O.; Flitner, M. Recognition through reconnaissance? Using drones for counter-mapping in Indonesia. *J. Peasant. Stud.* **2017**, *44*, 817–833. [CrossRef]
48. Radjawali, I.; Pye, O. Drones for justice: Inclusive technology and river-related action research along the Kapuas. *Geogr. Helvetica* **2017**, *72*, 17–27. [CrossRef]

49. Dewi, R. Gaining Recognition Through Participatory Mapping? The Role of Adat Land in the Implementation of the Merauke Integrated Food and Energy Estate in Papua, Indonesiatudy: Implementation of Merauke Integrated Food and Energy Estate, Papua, Indonesia. *Austrian J. South-East Asian Stud.* **2016**, *9*, 87–106. [CrossRef]
50. Smith, D.A.; Ibáñez, A.; Herrera, F. The importance of context: Assessing the benefits and limitations of participatory mapping for empowering indigenous communities in the Comarca Ngäbe-Buglé, Panama. *Cartogr. Int. J. R Geogr. Inf. Geovisualization* **2017**, *52*, 49–62. [CrossRef]
51. Cucchiaro, S.; Fallu, D.J.; Zhao, P.; Waddington, C.; Cockcroft, D.; Tarolli, P.; Brown, A.G. SfM photogrammetry for GeoArchaeology. In *Weathering, Soils & Paleosols*; Elsevier BV: Amsterdam, The Netherlands, 2020; Vol. 23, pp. 183–205.
52. Brown, A.; Walsh, K.; Fallu, D.; Cucchiaro, S.; Tarolli, P. European agricultural terraces and lynchets: From archaeological theory to heritage management. *World Archaeol.* **2020**, *52*, 566–588. [CrossRef]
53. Stek, T.D. Drones over Mediterranean landscapes. The potential of small UAV's (drones) for site detection and heritage management in archaeological survey projects: A case study from Le Pianelle in the Tappino Valley, Molise (Italy). *J. Cult. Herit.* **2016**, *22*, 1066–1071. [CrossRef]
54. Campana, S. Drones in Archaeology. State-of-the-art and Future Perspectives. *Archaeol. Prospect.* **2017**, *24*, 275–296. [CrossRef]
55. Jorz, V. Open Aerial Map, Drones and Archaeology: The Implications of Using Drones to Contribute and Share Aerial Data on an Open Data Repository. University of Waterloo, 2019. Available online: http://hdl.handle.net/10012/15247 (accessed on 16 June 2021).
56. Birtchnell, T.; Gibson, C. Less talk more drone: Social research with UAVs. *J. Geogr. High. Educ.* **2015**, *39*, 182–189. [CrossRef]
57. Mathews, A.J.; Wikle, T.A. GIS&T pedagogies and instructional challenges in higher education: A survey of educators. *Trans. GIS* **2019**, *23*, 892–907. [CrossRef]
58. Williams, R.D.; Tooth, S.; Gibson, M. The sky is the limit: Reconstructing physical geography from an aerial perspective. *J. Geogr. High. Educ.* **2017**, *41*, 134–146. [CrossRef]
59. Holloway, P.; Kenna, T.; Linehan, D.; O'Connor, R.; Bradley, H.; O'Mahony, B.; Pinkham, R. Active learning using a smartphone app: Analysing land use patterns in Cork City, Ireland. *J. Geogr. High. Educ.* **2019**, *45*, 47–62. [CrossRef]
60. Morrison, A.; Tronstad, R.; Martinussen, E.S. Design notes on a lonely drone. *Digit. Creativity* **2013**, *24*, 46–59. [CrossRef]
61. Hodgson, M.E.; Piovan, S.E. An indoor landscape for instruction of 3-D aerial drone imagery. *J. Geogr. High. Educ.* **2021**, 1–15. [CrossRef]
62. West, J.P.; Klofstad, C.A.; Uscinski, J.E.; Connolly, J.M. Citizen Support for Domestic Drone Use and Regulation. *Am. Politi- Res.* **2019**, *47*, 119–151. [CrossRef]
63. Tsiamis, N.; Efthymiou, L.; Tsagarakis, K.P. A Comparative Analysis of the Legislation Evolution for Drone Use in OECD Countries. *Drones* **2019**, *3*, 75. [CrossRef]
64. Ayamga, M.; Tekinerdogan, B.; Kassahun, A. Exploring the Challenges Posed by Regulations for the Use of Drones in Agriculture in the African Context. *Land* **2021**, *10*, 164. [CrossRef]
65. Alamouri, A.; Lampert, A.; Gerke, M. An Exploratory Investigation of UAS Regulations in Europe and the Impact on Effective Use and Economic Potential. *Drones* **2021**, *5*, 63. [CrossRef]
66. Otieno, B. *KQ drone licence to cost pilots Sh 180,000, in Business Daily Africa*; Nation Media: Nairobi, Kenya, 2021; Available online: https://www.businessdailyafrica.com/bd/corporate/companies/kq-drone-licence-to-cost-pilots-sh180-000-3482972 (accessed on 20 June 2021).
67. KCAA. *Unmanned Aircraft Systems—Regulatory Fees and Charges*; Kenya Civil Aviation Authority: Nairobi, Kenya, 2020; Available online: https://www.kcaa.or.ke/safety-%26-security-oversight/unmanned-aircraft-systems (accessed on 16 June 2021).
68. Hodgson, M.E.; Sella-Villa, D. State-level statutes governing unmanned aerial vehicle use in academic research in the United States. *Int. J. Remote Sens.* **2021**, *42*, 5370–5399. [CrossRef]
69. Sandbrook, C. The social implications of using drones for biodiversity conservation. *Ambio* **2015**, *44*, 636–647. [CrossRef]
70. Finn, R.L.; Wright, D. Unmanned aircraft systems: Surveillance, ethics and privacy in civil applications. *Comput. Law Secur. Rev.* **2012**, *28*, 184–194. [CrossRef]
71. Resnik, D.B.; Elliott, K.C. Using Drones to Study Human Beings: Ethical and Regulatory Issues. *Sci. Eng. Ethic-* **2019**, *25*, 707–718. [CrossRef] [PubMed]
72. Sella-Villa, D. Drones and Data: A Limited Impact on Privacy. *Univ. Richmond Law Rev.* **2021**, *55*, 991–1075.

![drones logo] *drones*

Article

On the Dominant Factors of Civilian-Use Drones: A Thorough Study and Analysis of Cross-Group Opinions Using a Triple Helix Model (THM) with the Analytic Hierarchy Process (AHP)

Chen-Hua Fu [1], Ming-Wen Tsao [2], Li-Pin Chi [3] and Zheng-Yun Zhuang [4,*]

1 Department of Information Management, College of Management, National Defense University, Taipei 11258, Taiwan; fchemail@gmail.com
2 Department of Industrial Engineering and Systems Management, College of Engineering, Feng Chia University, Taichung 40724, Taiwan; roslrtmw@gmail.com
3 Aeronautical System Research Division, National Chung-Shan Institute of Science and Technology, Taichung 40772, Taiwan; clp25669100@gmail.com
4 Department of Civil Engineering, College of Engineering, National Kaohsiung University of Science and Technology, Kaohsiung 807, Taiwan
* Correspondence: waynemcgwire@yahoo.com or wayne@nkust.edu.tw; Tel.: +886-7-3814526

Abstract: This study explores the experts' opinions during the consultation stage before law-making for civilian drones. A thorough literature study is first undertaken to have the set of influencing factors that should be suitable for the investigation from the perspective of designing and selecting civilian drones. Several rounds of surveys using the Delphi method, followed by an analytic hierarchy process (AHP), are performed to conform to the organized tree structure of constructs and factors and to obtain the knowledge about the opinions of the expert groups, with the expert sample being intentionally partitioned into three opinion groups at the beginning: academia (A), industry (I), and research institutes (R). Doing so facilitates a "mind-mining" process using the triple helix model (THM), while the opinions across the groups can also be visualized and compared. This exploits a new set of knowledge for the design and selection of civilian drones on a scientific yet empirical basis, and the observed differences and similarities among the groups may benefit their future negotiations to propose the drafts for regulating the design, manufacturing, and uses of civilian drones. As several significant implications and insights are also drawn and gained from the abovementioned results eventually, some possible research directions are worthwhile. The proposed hybrid methodological flow is another novelty.

1. Introduction

With the mature development of the Internet of Things (IoT) and mobile communication technology, especially 5G, civilian drones are widely used in many applications. The drone industry is rapidly developing, causing drones with higher technical capabilities at a lower cost to enter the market. Combined with their ease of use, drones could become the primary players in the field of surveying for commercial, government, and scientific entities [1].

A forecast of global commercial and private drone market sizes indicates that in 2020, the global drone market generated almost 22.5 billion USD in terms of global revenue. By 2025, the global drone market is expected to generate over 42.8 billion USD, with annual growth projected to beat 13.8% [2]. The market forecast also shows the market will keep growing, and the major key factor comes from civilian consumers. This means that many drone-based applications will be available for enterprises and other organizations in the future. Therefore, for the government, how to control the use of civilian drones

becomes a critical issue. On the other hand, for the aeronautics industry, the design issues of advanced civilian-use drones have also become a hot topic valued by many researchers and manufacturers. Therefore, a nexus of these possible conflicts is law-making. For example, Sah et al. [3] have pointed out that regulations are the most critical barriers to implementing drones in the logistics sector, an important application domain of civilian drones. Therefore, the significance of drone regulations is highlighted.

In Taiwan, for example, as in many developed countries or regions, many drone applications have gradually emerged recently. Many enterprises and organizations could use drones to perform different kinds of jobs for their business. Given the gradual rise of demand for drone applications and regulations, the Civil Aeronautics Administration (CAA), Taiwan R.O.C., is planning relevant regulations and certification mechanisms to manage drone applications.

However, in the recent studies related to drones, most of those studies explored the issues of applications, technologies, markets, safety, privacy, and others. Some of these studies also explored the cooperative relationships among industry (I), government (G), and academia (A) regarding military and civil drones with the triple helix model (THM) [4].

The THM is the key theory for this study. A THM model usually refers to a triangle that involves the corporations of I, G, and A parties (i.e., the vertices) to achieve some certain objective (O), e.g., for the public interest to design a large (mega) construction project, as shown in the left model in Figure 1. It is a "conceptual model" because a party's name remains non-uniformed, e.g., party I is sometimes called "Business" (B) and party A is sometimes called "University" (U), varying case by case. Despite the name varying, the interchangeable names usually connote the same party without any ambiguity. Given this model, relations and actions that happen between each pair of parties can be analyzed along with the edge in the model. Moreover, the intersections between the three parties may form yet another interesting matter to be observed. However, in this study, the THM model is slightly modified for the research purpose, and those relations and intersections (and gaps) between the group opinions that affect the law-making actions are analyzed.
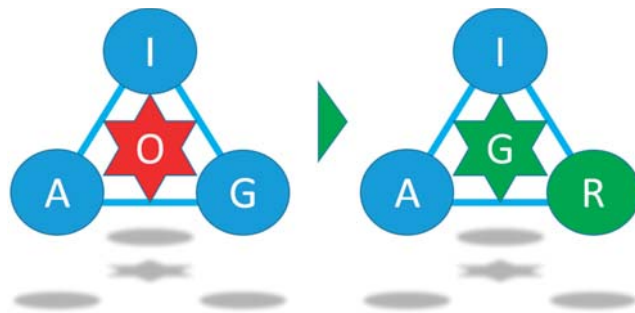
Figure 1. From conventional THM model to the proposed "modified THM".

Before drafting the relevant regulations for law-making, the CAA, the institution in charge (of the G party), consulted and collected the opinions from the other three parties, namely, academia (A) (e.g., the university-level academics), industry (I) (e.g., the largest aeronautic manufacturer), and research institutes (R) (e.g., the largest government-funded aeronautic R&D institution), in Taiwan, R.O.C. These three parties, namely, A, I, and R, may constitute another meaningful triangle in THM rather than industry, government, and academia (I, G, and A). Problems related to designing civilian drones and making reasonable legislation can be dissected and studied using the proposed and renewed THM model. In other words, among the players in the THM model, G is replaced by R, and such a replacement should be reasonable because of the following two main reasons.

First, the original THM was used to explore the military-, civil-, and dual-use drone development issues [4], so THM is based on the cooperative relationship between I, G, and

A. However, for this study, it is the case that G usually would like to entrust A, I, and R to draft the relevant regulations, and G is then responsible for legislating and implementing the law later. This is because the R party always performs some cutting-edge research on drones, so it can also give G more suggestions about newly developing directions, limits, and applications of drones. Hence, there is a change in the players in THM, i.e., for "which are triple", as required by the nature of the main aim.

Second, according to the surrogate model [5] in the engineering domain, replacing G with R to explore the design factors of civilian drones is also reasonable, because the R, if properly selected, is also G. Consider the largest domestic R&D institution chosen to be R for opinion collection in this study: could such an institution not represent G, as it is government funded? In other words, in the A-I-R THM model, R can be carefully chosen to concur with the original structure of the I-G-A THM model without breaking its rule for G. These are the reasons why we replace G with R in the "modified THM" in this study. For clarity, in this text, we refer to THM as this *modified THM model* in most of the cases.

Additionally, in this study, following the abovementioned, we argue that a systematic study of the *design factors* of civilian drones for the makers (or the *selection factors* for users, equivalently) may help to *understand the opinions of these three parties in the THM* and to *clarify the differences in their opinions*. Such knowledge may *address the emphasis of the subsequent advice* given to the government *for law-making*.

To begin with, a set of design factors are clearly established through a thorough literature study, and the Delphi method can be used to confirm whether this set of factors is effective or not. When we stand on the user's side, the temporarily civilian drone selection is a typical multiple-criteria decision-making (MCDM) problem. The analytic hierarchy process (AHP) is a very suitable approach that can be applied to understand how each group of experts (i.e., the three parties) may perceive the importance of these factors (i.e., for mind-mining [6,7]). That is, in terms of MCDM, civilian drone selection can be treated as a multi-attribute decision-making (MADM) problem that usually involves many consideration factors and the priority among these consideration factors (i.e., the significances of them), and usually, these consideration factors are the "decision criteria" in terms of MCDM, so the information about the "criteria weight vector" (CWV) can be obtained using AHP.

Prior to this, we perform a comprehensive literature study to seek and summarize a set of these factors, mounting them under some meaningful "constructs" in a tree-formed hierarchy, and confirm whether this set of factors we have included is effective or not by reference to the opinions of the domain experts using the Delphi method. Note specifically that the use of the abovementioned Delphi–AHP approach in studying the design factors has been shown to be effective in practice for other aircraft types with military purposes, e.g., next-generation fighters and MALE UAS [8,9], and/or for other UAV subjects, e.g., in Ulloa et al.'s work [10] to design a lightweight, portable, and flexible air-based PV-T module for UAV shelter hangars and in Song et al.'s work [11] to evaluate the comprehensive performance of UAV-based granular fertilizer spreaders (GFSs).

In short, this study explores the main design factors for the civilian applications of drones. It adopts several research methods, such as a literature study to collect and establish the initial set of factors, the Delphi method to confirm and solidify the set of factors, and AHP to understand the priority over these factors and how the opinions may differ (or not) among the three interest groups (A, I, and R). Inasmuch as the results would be helpful to understand the thoughts in the minds of the different groups of experts pertaining to the set of civilian drone design factors and the priority over these factors before the three groups of experts give some advice regarding the relevant regulations in the law, this study may perfectly meet the requirement and the core spirit of data-driven decision-making (DDDM) [12].

Therefore, the research question of this study is worth exploring, and *the possible contributions of this study should be two-fold*. First, as there are relatively few studies on the market and applications of civilian drones that are driven by a law-making requirement,

the results of this study may offer valuable knowledge in an empirical sense. Second, to the authors' knowledge, there seems to be no research that applies the THMs with the decision analysis (MCDM) methods, such as AHP, to explore some know-how further for drones. This study fills the gap by offering a new hybrid way to conduct the research in the methodological sense.

This introductory section placed the study in a broad context and highlighted the reason why it was conducted. Section 2 reviews the relevant literature, including a thorough literature study for the influencing factors. Section 3 explains the processes performed by using the methods and the results obtained from using these methods. Section 4 provides the discussions and implications drawn. Section 5 gives the concluding remarks and the recommendations for future works.

2. Literature Study and Methods

This section starts with the history of drones and the related works about drones (Section 2.1). This is followed by an in-depth review of the possible consideration factors (Section 2.2). In addition, except for the THM theory, which should be clear so far, a review about Delphi and AHP is also given to link these used methods with the study (Section 2.3).

2.1. Drones and Their Civilian Uses

Drones originated in 1917 when the U.S. military began conducting research and tested them during World War I. Therefore, relevant developing drivers and phases are reviewed by using this country as the example here for space reasons. In addition, the comprehension of public datasets that are available is another reason (i.e., data availability) to adopt this country as an example, at least for the researchers of this study.

After the early stage of the drone's invention, it was not taken into combat until after the Vietnam War. However, since then, advanced communication technology has increased the bandwidth of military communications satellites and the development of navigation technology, improved the remote-control capability of unmanned aerial vehicles (UAV), and made the remote operations of UAV more practical. Additionally, the geographical nature of the wars affecting Iraq and Afghanistan has increased the need for the Organization of American States to identify, locate, and attack hidden targets through continuous surveillance and rapid strikes, while minimizing collateral damage. In these applications, unmanned aircraft systems (UAS) provide asymmetrical technical advantages in these conflicts [13]. In general, over the past decades, UAS have played a critical role in non-military operations, such as supporting humanitarian relief operations in Haiti or for mine detection and chemical, biological, radiological, and nuclear reconnaissance.

The U.S. Federal Aviation Administration (FAA, USA) clearly defines the term UAV as "equipment used or intended for use in air, without an on-board pilot". In other words, UAV include all categories of aircraft, helicopters, airships, and refractive lifts without on-board pilots, and this implies that a "drone" flies autonomously or remotely without a pilot operating the aircraft. In the development history of drones, they have different designs and functions for military missions and civilian and commercial applications [14]. Because many missions are boring, dirty, or dangerous (3D) for pilots, drones are better suited for some tasks. For example, many types of drones, either large or small, are widely used by government departments or research institutes to carry out different tasks and research work [15].

Additionally, UAV can integrate with ground control stations and data links to form UAV systems (UAS). Therefore, drones involve command, control, and communications (C3) systems and must support those who control them [16]. UAS can be considered a system that includes multiple subsystems, including aircraft (often referred to as drones), payloads, control stations (often with other remote stations), aircraft launch and recovery, support, communications, transmission, etc. With advanced navigation and communication technologies, UAS have become a "new capability" available to the government (public) and commercial (civil) aviation sectors [17]. As the developing technology of

drones is becoming more and more mature, the civilian applications are growing day by day. Table 1 lists the related applications of drones in the civilian domain [18].

Table 1. The uses of drone technology in the civilian domain.

For Civilian Use	
Aerial photography	Film, video, and stills
Agriculture crops	Monitoring and spraying, herd monitoring, and cattle driving
Coastguard	Search and rescue; coastline and sea-lane monitoring
Conservation	Pollution and land monitoring
Customs and excise	Surveillance for illegal imports
Electricity companies	Power line inspection
Fire services and forestry	Fire detection and incident control
Fisheries	Fisheries protection
Gas and oil supply companies	Land survey and pipeline security
Information services	News, pictures, and featured pictures, e.g., wildlife
Lifeboat institutions	Incident investigation, guidance, and control
Local authorities	Survey and disaster control
Meteorological services	Sampling and analysis of atmosphere for forecasting
Traffic agencies	Monitoring and control of road traffic
Oil companies	Pipeline security
Ordinance survey	Aerial photography for mapping
Police authorities	Search for missing persons, security, and incident surveillance
River authorities	Water course level monitoring and flood and pollution control
Survey organizations	Geographical, geological, and archaeological surveys
Water boards	Reservoir and pipeline monitoring

Drone manufacturers and UAS suppliers worldwide are developing industry-specific solutions to meet customers' business needs effectively. Advancements in drone technology have enabled manufacturers to produce different models in sizes, weights, and shapes that can carry various devices and payloads to play roles in a wide range of applications. However, some safety issues and drone traffic management issues are the factors that could challenge the growth of the commercial drone market to some extent. The demand for drones in the commercial sector is increasing, because they increase productivity through improvements in graphical visualization and an overall reduction in project costs. Due to a significant improvement in drone control accuracy, many drone application requirements are emerging quickly in the commercial sector. Various applications related to cost reduction and time have led to the increasing use of drones. This trend could be expected to create the overall value of commercial drones. Figure 2 presents another forecast of the drone growth trend, in addition to the forecast made for 2020–2025 [2] (see Section 1), in the commercial sector in the U.S. from 2014 to 2025 [19].
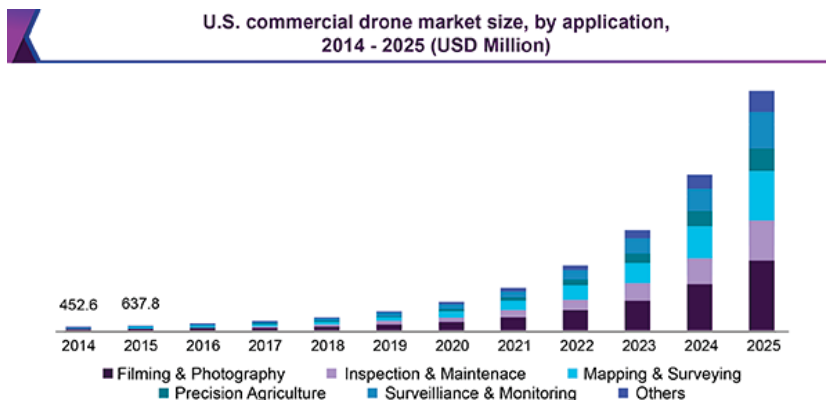
Figure 2. The forecast of the drone growth trend in the commercial sector from 2014 to 2025.

Except for the U.S., many countries around the world also used drones in the civilian sector. Currently, at least 90 countries or non-state organizations are known to operate drones [20]. However, different types of drones have different usages. For example, micro and small drones are commonly used in low-altitude and unregulated airspace. Typically, light drones smaller than 150 kg are suitable for monitoring tasks in many real-world applications.

Regarding the classification of drones, Gupta et al. argued that there is no uniform classification due to the diversity of drone capabilities, size, and operational characteristics [16]. That means that we can have a categorical list of drones by the types of drones seen so far. Table 2 lists the categories and their associated parameters. These include the maximum total take-off weight (UAV with payload), regular operating altitude, mission radius, endurance, general use, and purpose of use.

Table 2. The classification of drones by drone type.

Classification	Weight	Normal Operating Altitude	Radius of Mission	Endurance	Normal Employment	Typical Uses
Mirco	<2 KG	Up to 200 ft	5 KM	Few hours	Tactical platoon (single operator)	R, I, S
Mini	2~20 KG	Up to 3000 ft	25 KM	Up to 2 days	Tactical subunit (manual launch)	S, DG
Small	20~150 KG	Up to 5000 ft	50 KM	Up to 2 days	Tactical unit (employs launch system)	S, DG
Tactical	150~600 KG	Up to 10,000 ft	200 KM	Up to 2 days	Tactical formation	S, DG
MALE	>600 KG	Up to 45,000 ft	Unlimited	Days/weeks	Operational/Theatre	S, CT
HALE	>600 KG	Up to 65,000 ft	Unlimited	Days/weeks	Strategy/National	S, DG, SR
Strike/Combat	>600 KG	Up to 65,000 ft	Unlimited	Days/weeks	Strategy/National	S, DG, SR

Table note for legends: R: reconnaissance, I: inspection, S: surveillance, DG: data gathering, CT: cargo transportation, SR: signal relay.

Grimaccia et al. proposed an effective method to classify drones according to their functionalities [21]. However, the U.S. Department of Defense provided other classifications, while NASA provided another "classification matrix" [15], as shown in Tables 3 and 4,

respectively. In Table 3, these classifications are based on weight, altitude, mission radius, and duration [13,22].

Table 3. U.S. DoD's classification for drones.

Weight (kg)	Normal Operating Altitude (ft.)	Mission Radius (km)	Endurance (hrs)	Representative UAV
<2	<400	5	<1	Black Widow, Raven
2~25	<3000	25	2–8	Aerosonde, Scan Eagle, Puma
25~150	<5000	50	4–12	Manta B
150~600	<10,000	200–500	8–14	SIERRA, Viking 400, Tiger Shark
>600	<18,000	1000	>20	Ikhana (Predator B)
>600	>18,000	5000	>24	Global Hawk

Table 4. NASA's drone classification matrix.

Category	I	II	III
Weight	<=55 lb (25 KG)	55–330 lb (25–150 KG)	>330 lb (150 KG)
Airspeed (kt)	<=70	<=200	>200
Type	Model or sUAS	sUAS	UAS

In Table 4, drones are classified by weight, airspeed, and type. However, it can be seen that, although there are different terms, weight can be used as the only common classification criterion, as other characteristics of drones are usually weight-related. Additionally, some studies [9,16,18] provided another means of drone classification, which is descriptive, telling the "feature descriptions" rather than the numerical parameters above. Table 5 shows the categorization of drones with this method.

2.2. Review for the Consideration Factors

In the last subsection, the history and classifications of drones, as well as the civilian uses of drones, were reviewed in general. In this subsection, a deepened review for the design and selection factors for civilian-drone applications is provided, because subsequent studies (i.e., the confirmation of the set of factors, the solidified basis of the AHP hierarchy that is established, and the final results obtained using the AHP) may heavily rely upon a set of factors that is grounded. Additionally, after the review of works, we found that the surveyed literature involves several categories, e.g., cost, performance and applications, operation, and maintenance, and we present the review to the relevant works by reference to these categories in order. In fact, as will be shown later, these four factor categories form exactly the four constructs to establish the AHP hierarchy.

2.2.1. Cost

Cost is always a concern for designing and applying any equipment and facilities. This also holds for drones. Many studies have explored related costs of drones. Aragão et al. [23] proposed a UAV selection model, and initial investment and maintenance cost are two main factors in their proposed selection model. In an exploration of life cycle costing (LCC), Kianian et al. [24] argued that the LCC should contain the acquisition costs, operation costs, maintenance costs, and disposal costs. In the study related to a stochastic facility location model for drones, Kim et al. [25] argued that, besides the purchase cost, it is critical whether the operation cost and maintenance cost are reasonable or not when considering the costs of a drone. They also mentioned that the total relevant costs of a

drone include the costs of opening drone facilities and the operation and maintenance of drones and drone facilities. Discussing the sustainability of small UAV, Figliozzi [26] highlighted some important trends, such as UAV tare, payloads, battery energy, purchase costs, and energy consumption per unit of time flown. He also argued that the cost of operating a drone should include UAV operation staff costs, maintenance costs, ground costs, energy costs, purchase costs, battery costs, software costs, and communications costs. In the study recommending the use of UAV platforms in precision agriculture in Brazil, Jorge et al. [27] mentioned that reduced operating costs is one of the consideration factors when purchasing a UAV. In another study about UAV's technology-supporting maintenance operations, Miari [28] emphasized the importance of UAV operation and maintenance costs in UAV usage. As for a drone's purchase cost and operation cost, Yu et al. [29] mentioned that these are very economical, with 1/5 of the purchase cost and 1/10 of the operation cost of unmanned helicopters.

Table 5. The categorization of drones with the "feature description" method.

Category	Feature Description
NAV (Nano Air Vehicles)	NAV are recommended for radar obfuscation or ultra-short-range monitoring if the camera, propulsion, and control subsystem can be small enough.
MAV (Micro UAV)	MAV were originally defined as a drone with a wingspan of no more than 150 mm. MAV are mainly used for operations in urban environments, especially when flying slowly in buildings, preferably stopping to sit on walls or columns. Micro-aircraft usually need to be launched manually because they are very susceptible to atmospheric turbulence, so the payload of a fixed-wing aircraft is very low. Such problems may exist in all types of MAV.
MUAV (Mini UAV)	Most of them refer to UAV that are less than a certain mass. They may be less than 20 kg, but they are not as small as micro-UAV. They can be launched manually and fly about 30 km at most. They are used by mobile battle groups and also for various civilian purposes.
Close-Range UAV	Usually, mobile forces use these drones to perform relatively simple military operations and a variety of civilian purposes. They typically execute a range of approximately 100 km and perform tasks such as reconnaissance, targeting, surveillance, airport security, ship-to-shore surveillance, power line inspection, crop spraying, and traffic monitoring.
TUAV (Medium-range/Tactical UAV)	Its operation range is from 100 to 300 km; compared to HALE and MALE, these drones are smaller and have a simpler control; they could be operated primarily by the Army and Navy.
MALE UAV (Medium-altitude long-endurance UAVs)	Its flight altitude is between 5000 and 15,000 m and its endurance time is 24 h. It functions like a HALE system, but it usually runs in a shorter range that still exceeds 500 km. It needs to operate at a fixed base.
HALE UAV (High-altitude long-endurance UAV)	Its flight altitude is more than 15,000 m; its endurance time is over 24 h. It can perform extremely long-range reconnaissance and surveillance. It is a trend for HALEs to arm them with weapons. Usually, the Air Force operates them at fixed bases.

Moreover, the study related to maintenance cost estimation of Royal Canadian Navy ships described that operating costs included three major categories: the cost of personnel operation, the cost of operation consumables, and the costs of all activities that support the system's operation. In addition, the study also had a description of maintenance costs. It was stated that maintenance costs covered all planned and unplanned activities to keep or return the system to a given state or provide the additional operational capability. These maintenance activities include detection; inspection; troubleshooting; prevention; testing and calibration; overhaul; and replacement of parts, components, or assemblies performed by the crew, by specialist repair personnel, by a depot or agency, and by the industry [30]. Based on the airlines' perspective, Dožić et al. [31] chose evaluation criteria to solve the aircraft type(s) selection problem. The chosen criteria include aircraft seat capacity, reflecting the measure of matching demand and capacity; aircraft price describing needed investment; total baggage related to the earning possibility from cargo transport; maximal take-off weight (MTOW), which is the main unit for calculation of airport and

navigation fees; payment conditions describing payment advantages offered by different manufacturers or leasing companies; and total cost per available seat miles (CASM), indicating the operational costs and aircraft performances. Gomes et al. [32] proposed a novel approach to imprecise assessment and decision environments (NAIADE) method. This proposed method is based on three criteria, financial, logistics, and quality, to select an aircraft for regional chartering. In a study about cost–benefit assessment and implications for service pricing of electric taxies, Wang et al. [33] argued that the total life-cycle cost model for cost–benefit assessment should consider purchase cost, usage cost, and other operation costs. Additionally, Yeh and Chang [34] claimed that purchase cost and operating cost are the two criteria that can be used to evaluate an aircraft's fuzzy rating performance.

In a study related to LCC, Woodward [35] mentioned that purchase costs are just one of the initial capital costs, and they should include land, buildings, fees, furniture, and equipment. It means that purchase costs should contain the costs of the purchase of equipment and facilities related to the equipment. Operation cost is usually to ascertain the costs of providing or operating a service. This method of costing is applied by those undertakings that provide services rather than the production of goods [36]. The role of operational cost is also evident in expected-value-approach (EVA) studies, while determining the best purchase portfolio, e.g., in the photovoltaic manufacturing industry [37]. Relatedly, in Bressani-Ribeiro et al. [38], it was shown that low operational cost is one of the primary reasons for users to adopt new technology. In their study, Nachimuthu et al. [39] mentioned that total maintenance costs should include maintenance personnel costs, maintenance ship costs, dedicated repair ship costs, spare parts costs, and production losses due to downtime.

Thus, it can be asserted that *purchase cost*, *operation cost*, and *maintenance cost* are the primary consideration factors for a civilian drone design and selection from the discussions above. For drones, the purchase costs would include flight vehicles, manipulation devices, and devices required to perform related applications. The operation costs would contain fuel/electricity, mission-related consumables, and the use of landing sites, and the maintenance would consist of flight vehicle and primary equipment maintenance and component replacement. In conclusion, this completes the review of the factors that should be included in the "cost" category.

2.2.2. Performance and Applications

A civilian drone's performance and applications are perhaps the most complicated category. Although a construct can be established to recapitulate all relevant factors, a thorough study should be exerted to clearly specify the initial set of factors that are to be included under the construct and sent for experts' approval during the Delphi process.

Performance and applications are usually the primary consideration factors when users try to adapt to any new equipment. For drone usage, many studies also discussed drones' performance and applications. In discussing drone performance, Hwang et al. [40] concluded that the key performance of a drone should include speed, altitude, range, payload, and specific operational activity. In the study about selection of UAV for precision agriculture, Petkovics et al. [41] argued that flight duration time, flight speed, on-board computer, sensors, payload, coverage area, and operational time are the UAV selection consideration factors for precise agricultural usage. In the study about imagery collection to aid Aedes aegypti (mosquito) breeding site identification, Aragão et al. [23] proposed a UAV selection model. The proposed model adopted weight, dimension, technique, performance, speed, and investment as the main criteria. There are 12 performance-related sub-criteria, such as maximum take-off weight, maximum payload weight, wingspan, take-off, landing, maximum range, maximum mapped area, wind resistance, maximum altitude, cruise speed, stall speed, and maximum level speed. For last-mile delivery drone selection, Nur et al. [42] proposed an evaluation model. There are 19 sub-criteria related to the "performance" main criterion in the proposed model: drone's overall size, weight, drone type, fuel type, internal computing components, location and proximity accuracy, communication and data quality,

traceability, reliability, required delivery distance, maximum flight time, charge and fuel usage rate, maximum load, maximum carry dimensions, maximum reachable altitude, drone speed, adaptability to a dynamic assignment, package handling flexibility, and delivery flexibility.

For the selection of the most proper UAV for transportation in emergency operations, Ulukavak and Miman [43] used eight factors to obtain an evaluation process: payload, UAV weight, maximum altitude, maximum ground speed, approximate flight time, remote controller range, landing field, and ease of use. For visual inspection, monitoring, and analysis of infrastructure using UAV, Duque et al. [44] also select drones that can meet their requirements based on eight evaluation factors, which are flying time, an additional camera on top of a drone, camera resolution with low illumination, video resolution, payload capacity, drone lights, remote control range, and price. For inspecting bridges with a drone, Duque et al. selected a drone with various consideration specifications. These specifications include user-controls and interface, maneuverability, software capability, adaptability, size, and payload [45]. Hoyas Ester [46] selected a drone for his study with another eight selection criteria: price, body size, drone weight, flight time, radio frequency (RF) range, lens field of view (FOV), and lens aperture.

Cesnik et al. [47] mentioned that payload mass, flight speed, fuel mass, time, flight altitude, and landing and flying distance are the important indicators to evaluate the vehicle flight performance of a drone. Chen et al. [48] argued that designers of a drone must consider the high mobility and flight time while minding the limited battery life; the flight duration time of a drone is a key performance indicator. In the study related to drone flight capabilities, Ajanic et al. [49] discussed the importance of manipulative ability for a drone. Therefore, in drone selection, the manipulative ability of a drone is a critical evaluation factor. Yang et al. [50] mentioned the operation range of a drone, the control distance of a drone's controller, the transmission bandwidth for a drone, and the signal interference of a drone are a drone's critical performance issues. Shakeri et al. compared the advantages and disadvantages of multi-UAV and single-UAV systems with several features: targeted area coverage, cost, task time, radar cross-section, power, network topology, application, and security [51].

In discussing disaster management with UAV, Erdelj et al. [52] also argued that airborne operation duration of a drone is an important consideration factor in disaster process operation. In fact, the application of UAV now plays a critical role in not only disaster management but also law enforcement and first responders, and these can be mapped to "Fire Service and Forestry" and "Police Authorities" in Table 1. Whilst the essence of these applications is quickness (i.e., for launching actions just in time for law enforcement (police), effective interventions made by the first responders (e.g., police officers, firefighters, and disaster managers), etc.), the design of drones may also address such a noteworthy feature (i.e., "quick reconnaissance"). For this specific domain, we cite Laszlo et al.'s work in 2018 [53] and the work of Restas in 2015 [54], which have shown the importance of this feature in the aforementioned application domains.

Aljehani and Inoue [55] discussed the coverage problem of a UAV and mentioned that the communication system's performance in a UAV is important for a UAV's flight control and operation. In the study related to design and trajectory control of universal drone system, Yıldırım et al. [56] argued that controllers and sensors of a drone are the components that directly affect the vehicle's flight performance, while other components directly affect the payload of a drone. Besides these basic components, other devices on a drone may be added to perform some specific requirements. Additionally, Amiri [57] argued that the manipulation's agility and stability for the required maneuvers are the key performance indicator for a drone. Pai et al. [58] mentioned that the drone operator should be familiar with the operation interface of a drone, as it involves the manipulative ability of a drone. Therefore, the operation interface of a drone might affect its manipulative ability. Liu et al. [59] also discussed the manipulative ability of robots. Manipulative ability refers to the manipulative ability of robots to perform certain tasks. In terms of maneuverability,

different types of rescue robots have different performances. Robots must be controllable and easy to control. The global manipulative ability embodies survivability, mobility, sensors, communication, and the human–machine interface.

Gomes et al. [32] used 12 sub-criteria to evaluate the selection of an aircraft. The performance-related sub-criteria include range, flexibility, cruising speed, landing and take-off distance, comfort, and avionics. Bruno et al. [60] proposed an aircraft evaluation model based on the airlines' requirements. Their proposed evaluation model contains four main criteria and eight sub-criteria. The one main criterion, technical performance, and two sub-criteria, cruise speed and autonomy, are related to a performance consideration for an aircraft evaluation. Yeh and Chang [34] used three main criteria and 11 sub-criteria to evaluate each aircraft's fuzzy rating performance. One of the three main criteria, technological advances, and two of the 11 sub-criteria, aircraft reliability and maximum range, are related to an aircraft's performance. See et al. [61] used speed, range, and the number of passengers as criteria to select the best aircraft among a set of alternatives with a multi-attribute methodology.

In the study about the classifications, applications, and design challenges of drones, Hassanalian and Abdelkefi [62] mentioned that drones' applications would cover a wide range of civilian and military fields. This is important. Drones can perform outdoor and indoor missions in very challenging environments. Drones can be equipped with a variety of sensors and monitors for intelligence, surveillance, and reconnaissance missions. Drone applications can be categorized into different channels. They can be based on mission type (military and civilian), flight area type (outdoor and indoor), and environmental type (underwater, water, ground, and air and space). Types of drone applications are shown in Figure 2. Depending on the type of drone, there are more than 200 drone applications in the future, including search and rescue missions, environmental protection, mailing and delivery, shooting and reconnaissance, performance, bird repellent, cleaning, agricultural spraying, missions at sea or on other planets, and other miscellaneous applications.

In discussing disaster management with UAV, Erdelj et al. [52] mentioned the applications of UAV, and they divided these applications into six categories: monitoring, forecasting, and early warnings; disaster information fusion and sharing; situational awareness, logistics, and evacuation support; support for a standalone communication system; support for search and rescue (SAR) missions; and damage assessment. Figure 3 shows a classification of drones' applications [62].
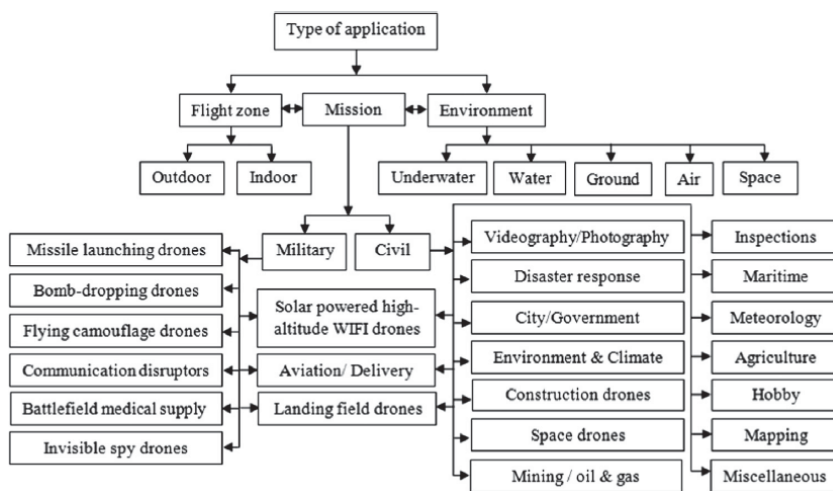
Figure 3. A classification of drones' applications.

In particular, Hassanalian et al. [62] mentioned that different types of drones use different types of power sources, such as fuel, battery, solar cells, and laser power beaming technology. They discussed the advantages and disadvantages of these power sources. Nur et al. [42] also mentioned that the types of power sources provided by UAV include batteries, solar energy, hydraulic fuel cells, internal combustion engines, and tethered and laser transmitters. In the invention related to the field of radiation detection and the "CdZnTe" aerial inspection system, Zhang et al. [63] emphasized the importance of a long operation duration. Pickett [64] also emphasized the importance of extended operation duration for applications of a drone in the patent about unmanned aerial vehicle boosters. Moreover, in rescue applications with an energy-constrained UAV, Liang et al. [65] argued that the longest operation duration of a UAV is a constraint factor in rescue applications. Erdelj et al. [52] also argued that airborne operation duration of a drone is an important consideration factor in disaster process operation in discussing disaster management with UAVs.

From the above long survey so far, we can find several critical factors that are significant to a drone's performance and applications. These critical factors include *vehicle flight performance*, *manipulative ability*, *flight power*, *main application*, and *operation duration*.

2.2.3. Operation(s)

Operation is another important category of concern when users use drones. Many studies discussed issues of drones' operation, and several patents are also related to this category.

There are several patents related to drone operation convenience. Zhang et al. [66] emphasized that operation convenience and operation security are critical for a drone; they had a rotary-wing invention to improve the operation convenience and the operational safety of the rotary-wing drones to a large extent. Ng [67] invented a mobile vehicle charging system that can improve the operation convenience of drones. Tang et al. [68] invented a remote controller of a UAV with a handle structure. This remote controller can simplify the control interface of a UAV to enhance the operation convenience of a UAV. From the above inventions related to UAVs, we can find that drone operational convenience is significant for users. Drone manufacturers can use those new inventions of UAV to improve the operation convenience of drones. Additionally, Zhou et al. [69] argued that the size of the landing site would affect the convenience of drone operations.

Xiao et al. [70] mentioned that UAV offer advantages, such as flexibility, ease of operation, convenience, safety, reliability, and low costs. Thus, ease of operation and safety are two of the reasons why users want to use UAV. In an exploration of the features of consumer UAV, Mao et al. [71] used the DJI UAV products to illustrate the characteristics of consumer UAV availability that include convenience, easy operation, safety, intelligence, and entertainment. That means safety is a critical consideration factor for a consumer UAV. In the study related to the risk, vulnerability, and safety improvement of the industrial UAV transportation system, Johnsen and Evjemo [72] explored the safety of UAS (unmanned aviation systems) based on drones and other UAVs. Safety is related to accidental harm, and security is related to intentional harm. They mentioned that drones have often been used in tasks that are dangerous, dirty, or dull. Thus, safety and security have often been the principal drivers when using UAS. Therefore, we must ensure high reliability, safety, and security when we use UAS in critical operations such as the transport of medical supplies. In the study related to operator engagement during UAV operation, Roy et al. [73] argued that bio-cybernetic systems could adapt the UAV operator's mental status to optimize UAV performance and increase UAV operation safety. Therefore, how to improve the safety of UAV operation is a critical issue. Jorge et al. [27] also mentioned that ease of operation and safety are two of the consideration factors in purchasing a UAV. Moreover, they also explored the advantages and disadvantages of UAV with type, applications, and operations.

In the book about UAV design, Gundlach [74] described the supportability of unmanned aircraft. He argued that the supportability covers activities required to sustain operations. That includes support equipment, spares management, and other items. Both the customer and the contractor can perform support activities. Hwang et al. [40] also argued that supportability is a key performance indicator of a drone. In the study related to UAV design, Sadraey [75] listed the design-related requirements as follows: performance, stability, handling qualities, operational requirements, low weight, affordability, reliability, maintainability, producibility, evaluability, usability, safety (airworthiness for aircraft and operator), supportability and serviceability, sustainability, disposability, marketability, environmental requirements, detectability (i.e., stealth), standards requirements, and legal requirements. In the design consideration of a precision aerial delivery system, Hall [76] argued that the design team should consider the operational supportability of a precision aerial delivery system.

Since drone applications kept growing for both civilian and military purposes, Candeloro et al. [77] also mentioned that this situation exacerbated the noise pollution problem caused by drones. In the study about a drone's noise scattering, Jiang et al. [78] described that both commercial and civil domains had many applications that caused growing environmental concerns on the noise emission. Thus, drone noise received much attention in recent years. In the study about an exploratory investigation of combustion and NVH emissions signature of a drone jet engine, Soloiu et al. [79] mentioned that the largest pollution source of greenhouse gas (GHG) emissions comes from aerospace transportation. The pollution caused by drones' fuel exhaust is also getting worse. Gaynutdinov and Chermoshentsev [80] mentioned that the avionics of UAV uses analog, digital, and RF devices to manipulate a UAV simultaneously over a wide frequency range (up to several gigahertz) of voltages and currents that lead to expansion of the paths' electromagnetic interactions. That obviously leads to deterioration in the electromagnetic environment. Petrov et al. [81] mentioned that mass electrification of UAV creates massive mobile sources of electromagnetic interference. This is worse in dense urban environments in particular.

From the abovementioned literature, we can find many factors that are related to drone operations. However, through this comprehensive literature survey, we can further locate several key consideration factors, such as *convenience*, *safety and security*, *supportability*, and *environmental impact*, for drone operations.

2.2.4. Maintenance

Users should consider the maintenance issue when they adopt new equipment or new facilities. Design factors under this category should also be critical for drones, so the literature is also abundant with articles about relevant issues.

In discussing the U.S. Army's light tactical vehicle solution, Metzler argued that the design of the U.S. Army's light tactical vehicle should keep maintenance requirements low and keep maintenance costs low as well. A possible design solution is to adopt commercial off-the-shelf parts found in civilian vehicles [82]. In a study related to the neural network control system of the UAV altitude dynamic, Muliadi et al. mentioned the reasons why a UAV becomes a popular type. The easiness of maintenance is one of the reasons [83]. Edgell et al. [84] argued that the development of modular aircraft results from highly reliable and easy-to-maintain systems. That will minimize logistical requirements and simplify maintenance requirements. They also mentioned that locally manufactured parts allow the maintenance process to reduce their dependence on the parts supply and described the importance of the acquisition processes for critical components.

In the study about trickling filters following anaerobic sewage treatment, Bressani-Ribeiro et al. [38] argued that maintenance simplicity is the key consideration factor for new technology adoption. In the study about the role of nanoparticles upon the productivity of solar desalination systems, Rashidi et al. [85] mentioned the advantages of solar distillation systems, including low costs of construction, repair, and maintenance, simplicity, portability, and use of solar energy resources. In the study related to a time

service improvement scheme for a nuclear power plant, Zhai and Bai [86] proposed the improvement scheme of time service system to solve the problems of redundant backup, system networking, convenient maintenance, and power supply optimization. Therefore, maintenance convenience is a critical issue for the operations of a system. In the study about point cloud processing system development, based on the proposed, Dingning and Qiong [87] improved system security and maintenance convenience of the point cloud processing system. This study showed the significance of maintenance convenience for an information system. In the patent about container-type data centers, Zhao et al. [88] also emphasized the importance of maintenance convenience for a mini data center in their patent application.

Moreover, in a study to compare life-cycle costing and performance parts costing, Adebimpe et al. [89] mentioned that maintenance cost involves the usage of consumables and spare parts. In another patent about a spare parts and consumables management system, Dellar et al. [90] used the wafer manufacture as an example to illustrate the importance of spare parts and consumables. They mentioned that a lack of required spare parts or consumables at critical points could mean damage to expensive wafers in the process and other wafers in pipelines waiting to process with closed machines. Additionally, the time it takes for a machine to drop reduces the wafer output, which can be very expensive. They also emphasized that it is critical to ensure that needed spare parts are available when designing a system. In an illustration of the life cycle of durable manufactured products, Oliva and Kallenberg [91] also mentioned that the acquisition assurance of spare parts and consumables is a critical issue for users.

The above literature study has described many consideration factors systematically related to maintenance for drones. Further, in the review process, a set of common critical factors has been identified in the literature, including *maintenance simplicity*, *maintenance convenience*, and *acquisition of parts and operation consumables*. These should be the critical factors placed under the drone maintenance construct.

2.2.5. Short Summary

In this subsection, a suitable set of criteria (design factors) for the application and selection of civilian drones is filtered and obtained on a solid basis. The constructs, each of which cover a separate subset of these criteria, are also identified. Therefore, the hierarchical tree structure for AHP investigation (i.e., AHP hierarchy) is justified and developed concretely in Section 3, so all of the subsequent works can begin based on (i.e., the Delphi process to confirm the included criteria and the tree's form) the main process of AHP to collect the opinions using the expert questionnaire designed to calculate the weights for the factors and prioritize them. The THM-integrated analysis is for the preferential orders toward the criteria and constructs in each opinion group, and the implicative discussions identify the emphases for law-making advice. In other words, the thoroughness of the reviewed literature that has been studied underlies all later results' credibility; even the comprehension of the process is, perhaps, sufficient to form a review study.

2.3. Methods: Delphi and AHP

After the previous use of THM in this field (see Section 1), this subsection gives a review at a higher level of Delphi and AHP, as they are the other two main methodological elements.

2.3.1. Delphi Method

Delphi is a survey method of research that aims to structure group opinions and discussions. The RAND Corporation developed the Delphi method. The purpose is to discuss and enable judgments on a specific topic, and then some synchronized decisions related to the specific topic can be made to represent a given group's opinions and views. The Delphi method can break the limitations when traditional methods were used to obtain

a specific group's opinion or judgments for policy making [92]. Woudenberg [93] evaluated the characteristics of Delphi, which are listed as follows:

1. Anonymity: Participants, almost all being experts, are interviewed by mail or a computer network.
2. Iteration: There are rounds for a Delphi process. The first round is inventory (probing). The number of rounds can be determined in advance or "on the fly" according to the stability of individual judgments.
3. Feedback: The results of the first (inventory) round are usually sent back to all participants. In the second round, the Delphi asks participants to make arguments about their deviational estimations for the criteria set fixed in the first round. It will feedback these arguments and the statistical results to all participants before any third and subsequent rounds begin.

Delphi is also helpful when using other methods would be not adequate or inappropriate. The following application contexts wherein it is particularly useful are summarized [94]:

1. The problem is not suitable for precise analytical techniques but can benefit from collective subjective judgments.
2. Individuals who contribute to the review of broad or complex issues do not have a sufficient history of communication and may have different backgrounds in experience and expertise.
3. In face-to-face communication, people need to communicate effectively.
4. Time and cost make frequent group meetings not feasible.
5. The supplementary group communication can improve a face-to-face meeting's efficiency.
6. Disagreements between individuals are serious or politically unpleasant, so the communication process must be reviewed and anonymity ensured.
7. Dominance due to quantity or personality power must be avoided.

Turoff and Linstone [95] have also summarized several application areas of Delphi, which are as follows:

1. To collect current and historical data, although the data cannot be accurately known.
2. To evaluate possible budget allocations.
3. To explore urban and regional planning options.
4. To build an educational model.
5. To describe the pros and cons associated with potential policy options.
6. To distinguish and clarify real and perceived human motivations.
7. To explore priorities of personal values, social goals, etc.

In this study, Delphi is used to confirm the criteria set, the proposed constructs, and the tree form of the AHP hierarchy, for the following studies and results to be made and justified on a solid basis (see Section 3.1).

2.3.2. Analytic Hierarchy Process (AHP)

AHP is a theoretical and methodological framework of humans' mental measurements by using a "pairwise comparison" repeatedly. It depends on the judgment of experts to get the priority and measure the relative values of intangible things, e.g., assets, alternatives, criteria, etc. Comparisons are carried out with an absolute "judgment scale" that represents the extent to which one element dominates another with respect to a given concept or content [96].

Specifically, if the things being compared are criteria in the MADM context, those relative values would mean the relative importance among the criteria (or alternatives). The vector-based form consisting of these values is called a "criteria weight vector," or CWV, which can be used to prioritize the criteria (or alternatives) (i.e., to order them or rank them) [7,97].

For AHP, the judgments may be inconsistent. How to measure the inconsistency is another focus of AHP. Saaty breaks down the decision-making process into several steps,

including a step called "CR-validation" to verify whether one's pairwise judgments made individually for each pair of things, when put together, are consistent or not [98].

Zhuang et al. [12] proposed another "two-phases" separation for the entire MADM process using AHP, namely, a first phase of "CWV-determination" and a second of "alternative ranking". As the research question of this study only concerned the first phase, we also refer to [12] for a summary of the formulas for the calculation process of CWV-determination. The other summary for these calculations is also seen in another mathematical expression form [8]. We also refer to [6] for a demonstration of CR-validation using a numerical example. The mathematical details of these are omitted here for space reasons, but similar full applications of AHP for the CWV-determination purpose (with CR-validation) have been illustrated in [8] and [9] to study the design factors for fighters and MALE UAS.

3. Processes and Results

3.1. Confirming the Factors with Delphi Method

According to Section 2.3.1, in the first round of Delphi in our study, three "almost experts" who are not familiar with each other were intentionally chosen to meet the selection standard of the method, and these participants gave their qualitative estimates. Their communication used e-mails. This confirmed that the 15 factors that were distilled from the literature review work in Section 2.2 in the original factor set—purchase cost, operation cost, maintenance cost, vehicle flight performance, manipulative ability, flight power, primary application, operation duration, operation convenience, operation safety and security, operation supportability, and operation environmental impact—are all effective, and there was no comment given to augment this factor set by adding any other factor. In addition, none of them opposed the four constructs (categories) that were established by the authors after the literature study and agreed with how each individual factor (criterion) could be placed (mounted) under its upper-level construct. This means that the hierarchical structure of the tree has been confirmed at this stage, and the "decision hierarchy" can therefore be ascertained in Figure 4 for AHP.
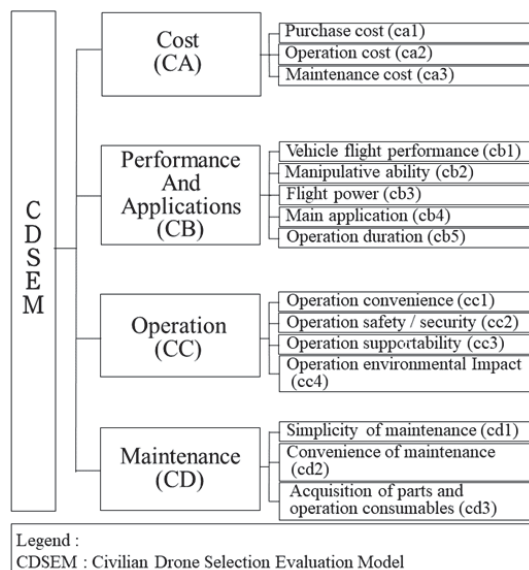
Figure 4. The decision hierarchy for civilian design/selection.

However, as in the first round the operational definitions for each factor were sent along with the data for polling, and they were slightly modified by the participants after returning, we present the modified version in Table 6.

Table 6. Operational definitions of the factors for civilian drone design/selection.

Criterion	Operational Definition
Purchase cost	The cost of purchase of drone flight vehicles, manipulation devices, and devices required to perform related applications.
Operation cost	The costs of using drones to perform related missions, such as the cost of flying power such as fuel and electricity, the cost of mission-related consumables, and the costs that may be involved in the use of landing sites.
Maintenance cost	The cost of maintenance and replacement of components for the flight vehicle and primary equipment that ensure the proper operation of a drone.
Vehicle flight performance	The critical flight performance considerations of a drone include flight speed, range, endurance, flight altitude, payload, and take-off and landing way.
Manipulative ability	The important considerations of a drone manipulation performance include operation range and distance, manipulation agility and stability, operation interface, and anti-interference of wireless control signal.
Flight power	The types of drone flight power include fuel, electricity, hybrid fuel and electricity, solar energy, and other possible power; different power systems have a relative impact on the flight performance of a drone.
Main application	The main applications of drones include logistics and transportation, agricultural plant protection, surveillance and security, geographic mapping, and aerial photography and performance.
Operation duration	The duration of time to perform the main application, such as spraying, monitoring, shooting, etc.
Operation convenience	The convenience of drone operation is restricted by the flight vehicle take-off and landing field and the open condition of the operating airspace also affects the convenience of drone operation.
Operation safety and security	Drone operations should consider the safety and security of flight and personnel.
Operation supportability	Related support required for drone operations, such as flight logistics support, hardware and software support for related equipment required to perform tasks, etc.
Operation environmental impact	The possible impact of drone operation on the surrounding environment, such as noise, pollution from fuel exhaust, electromagnetic wave emission, etc.
Maintenance simplicity	The maintenance simplicity of drone flight vehicles and related equipment means that maintenance personnel can easily repair drone flight vehicles and related equipment through modular components.
Maintenance convenience	The maintenance convenience of drone flight vehicles and related equipment means that the suppliers of drone flight vehicles and related equipment provide relevant maintenance and maintenance support in close and convenient.
Acquisition of parts and operation consumables	Drone flight vehicle and related equipment components and related consumables needed for operation are not in short supply.

Then, the second round of Delphi fed back the whole group's results on the previous round to all participants for subsequent evaluation. These included the hierarchical structure of the tree weaving the constructs and the criteria (i.e., the decision hierarchy) as shown in Figure 4 and the set of factors (although no change was made) and the revised operational definitions for the factors in Table 6. Finally, all participants returned with no other comments, and this confirmed that all the delivered data (i.e., the set of factors, the constructs, the decision hierarchy that reveals their relationships, and the operational definitions) are effective. Therefore, fortunately, the Delphi process does not involve a third round.

3.2. Prioritizing the Factors with AHP Method

Based on the confirmed decision hierarchy, as shown in Figure 4, a set of expert questionnaires using the pairwise-comparison scales of 9:1, 7:1, 5:1, 3:1, 1:1, 1:3, 1:5, 1:7, and 1:9 is designed for investigating the individual opinions of the experts (or decision-makers (DMs5)).

According to the THM, we would like to understand the opinions of the domain experts in the industry, academia, and research institutes. For this sake, the entire sample is designed to have 27 experts, and it is intentionally partitioned into three groups, with each group containing 9 experts. The researchers visited these 27 experts and performed investigations in terms of AHP using the designed questionnaire set, during the period from 3 January to 28 February 2021.

Eventually, for each expert interviewee (respondent), we successfully received five pairwise comparison matrices of the five AHP expert questionnaires that are consistent in the results. Note that among the five matrices, one of them connotes the results of pairwise comparison of the constructs (i.e., with respect to CDSEM, or the civilian drone selection evaluation model as shown in Figure 4), and for the remaining four, each connotes the results of a pairwise comparison of the individual factors with respect to some construct.

Table 7 gives the statistics for the backgrounds of the 27 interviewed experts overall, as the "respondent profiles" are also polled along with the AHP-style survey using an initial but anonymous block of questions. As can be observed, 24 of these experts are male and three are female; 13 have a Ph.D. and 14 have a master's degree. In terms of age, they are all 31–65 without exception. Finally, five of them have experienced the service for <10 years, 12 have experienced 10–20 years, while 10 of them have worked for over 21 years. The A, I, and R partitions of the sample of the experts are also clear in this table.

Table 7. Background statistics of the interviewed experts.

	Type	#DMs	Percentage
Gender	Male	24	88.89%
	Female	3	11.11%
Degree	Master's	14	51.85%
	Ph.D.	13	48.15%
Group of Expert	I: Industry	9	33.33%
	A: Academy	9	33.33%
	R: R&D Institute	9	33.33%
Age	31–40	7	25.93%
	41–50	11	40.74%
	51–65	9	33.33%
Years in Service	1–10	5	18.52%
	11–20	12	44.44%
	>21	10	37.04%

Surprisingly from these sample stratifications, no respondent in this survey possesses only a bachelor's degree (or under), even for the respondents in group I (industry). After a post-survey consultation, the fact is interesting. For group I, we interviewed respondents from a maker that is partially government-funded, because it is not only the largest aeronautic manufacturer in the studied country (as mentioned in Section 1) but also where people who have the decisive/influencing power for drones' law-making may come from. As such, the respondents whom we interviewed are all (very) high-level staff, but in such institutions, only people who possess a master's or Ph.D. degree can be promoted to these higher positions.

As usual, the investigation process required one to three rounds of interviews for all pairwise comparison matrices filled in by an expert to pass the CR-validation process, with a CR (consistent ratio) threshold set at 0.1 (see Section 2.3.2). Additionally, we also found that most DMs could pass the CR-validation easily with one round of interviews when they were requested to answer the questionnaires containing three items to be compared pair-wisely (i.e., for the three factors under construct CA and for another three under construct CD). Otherwise, many of them passed the CR-validation with two to three rounds of interviews, especially when they were asked to compare the five factors under CB pair-wisely.

After the consistencies in the results were all guaranteed, calculations to obtain the CWVs based on the data in the five pairwise comparison matrices were performed for each expert using the Expert-Choice software (and it was also installed on a laptop as a mobile office during the investigation to record the experts' answers in real time).

By reference to THM, we further combined the CWVs with respect to the same thing (i.e., CDSEM or one of the four constructs) for all experts in each expert group to obtain an "aggregated CWV." For more details, please see Appendix A. This aggregated CWV connotes a "group opinion" with respect to "that thing". As the different groups (i.e., A, I, and R) give various "group opinions" for "the same thing", the variety and heterogeneity can be observed, analyzed, and compared. The following sub-subsections present these results in a visualized manner.

3.2.1. Academia (A) Group's Opinions

The weights of the four main constructs are shown and ranked in Figure 5 based on the group opinion according to the "aggregated CWV" over the individual CWVs of the nine experts in the "A" group, with respect to CDSEM.

Figure 5. Academia group's opinion for the constructs.

Reviewing Figure 5, we can find the significance rankings of those four constructs: CB: Performance and Application ≻ CC: Operation ≻ CD: Maintenance ≻ CA: Cost. The sum of the relative weights of the two decision constructs, CB and CC, exceeds 70%; especially, the performance and application construct received nearly half of the relative weight, which is 0.463.

Figure 6 shows the 15 consideration factors' "absolute weights" when the aggregated CWV (for a subset of factors) with respect to each construct is multiplied with the associated element in the aggregated CWV with respect to CDSEM (i.e., a number in Figure 5, in its original non-ranked order), while the priority over these 15 factors is also visualized.

Combined instance -- Synthesis with respect to: a civilian drone selection assessment model

Overall Inconsistency = .00

Manipulative ability	.165
Vehicle flight performance	.142
Operation safety/security	.086
Operation duration	.076
Main application	.070
Flight power	.061
Acquisition of parts and operation consumables	.061
Maintenance simplicity	.059
Operation convenience	.049
Maintenance costs	.043
Operation supportability	.043
Operation cost	.042
Operation environmental impact	.035
Purchase cost	.034
Maintenance convenience	.033

Figure 6. Academia (A) group's opinion for the absolute weights of all factors.

Examining Figure 6, we find that only the top five factors are "more important" and the 10 decision criteria remaining are less important, according to the academia (A) group's overall opinion. The manipulative ability (cb2) and vehicle flight performance (cb1), both under construct CB, are the two most important factors. both absolute weights are over 0.1, and the sum of the two weights exceeds 30%. Relatively, operation convenience (cc1) is deemed the least important factor among the 15 by the experts in the A group; its absolute weight is less than 0.0335. Note that we have used ">0.7" as the rule to justify whether a factor is "more important" by seeing whether the absolute weight of the factor surpasses the threshold of 0.7 or not.

3.2.2. Industry (I) Group's Opinions

The weights of the four main constructs are shown and ranked in Figure 7 based on the group opinion according to the "aggregated CWV" over the individual CWVs of the nine experts in the "I" group, with respect to CDSEM.

Priorities with respect to:
a civilian drone selection assessment model

Combined

Performance and application	.288
Cost	.287
Maintenance	.245
Operation	.180

Inconsistency = 0.0052
with 0 missing judgments.

Figure 7. Industry group's opinion for the constructs.

Reviewing Figure 7, we can find the significance ranking of those four constructs: CB: Performance and Application ≻ CA: Cost ≻ CD: Maintenance ≻ CC: Operation. Among them, the industry (I) group thinks that CB and CA are the two most significant constructs for designing and selecting civilian drones. Their relative weights, 0.288 and 0.287, are almost even. The operation construct (CC) is the least significant one, because its relative weight is only 0.180. However, CB and CA are just a bit more important than CD, and the weight of CC is just 0.07 away from a quarter (0.25).

Figure 8 shows the 15 consideration factors' absolute weights, while the priority over these 15 factors is also visualized. The process to obtain this figure is analogous to what has been described in Section 3.2.1, but the studied sample group has been changed from A (academia) to I (industry).
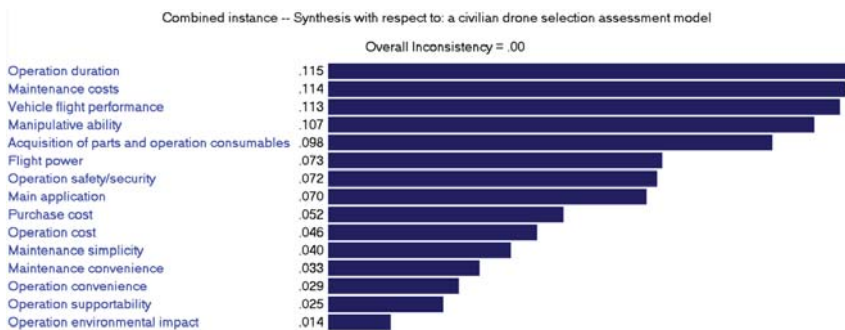
Figure 8. Industry (I) group's opinion for the absolute weights of all factors.

Examining Figure 8, we can see that eight of the 15 factors are "more important" and the other seven factors are "less important", according to the industry (I) group's overall opinion, while the same threshold (0.7) is used to justify such a classification. Among the eight "more important" factors, we found that there are also five factors whose weights may dominate the other three to a certain extent, and their order is: cb5: Operation duration ≻ ca3: Maintenance cost ≻ cb1: Vehicle flight performance ≻ cb2: Manipulative ability ≻ cd3: Acquisition of parts and operation consumables. These five factors, in sum, may occupy 55% of the total importance. Relatively, among the seven less important factors, operation environmental impact (cc4) is the least important decision criterion. This factor receives a weight of only 0.014, which is obviously lower than the other six less important ones. This means that experts in the industry (from the I group) think the possible environmental impacts caused by operating the civilian-use drones are of little significance.

3.2.3. Research Institute (R) Group's Opinions

Finally, this study explores the four main constructs' weights as shown and ranked in Figure 9 based on the group opinion according to the "aggregated CWV" over the individual CWVs of the nine experts in the research institute (R) group, with respect to CDSEM.
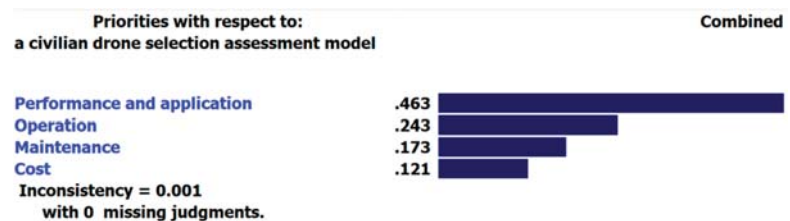

Figure 9. Research institute (R) group's opinion for the constructs.

Reviewing Figure 9, we can find that the significance rankings of those four constructs are CB: Performance and application ≻ CD: Maintenance ≻ CA: Cost ≻ CC: Operation. Among them, the research institute (R) group thinks that CB is the most significant factorial construct for designing and selecting civilian drones. Its relative weight, 0.315, may dominate the other three constructs, the importance of which is almost 1/3. In contrast, the cost construct (CA) and the operation construct (CC) are the less significant ones (see their weights, 0.221 and 0.211, in the figure). However, both of the weights are not far away from a quarter (0.25).

Figure 10 gives the absolute weights of the 15 consideration factors, while the priority over these 15 factors is also visualized further. The process to obtain this figure is analogous

to what has been described in Section 3.2.1, too, but the studied sample group has been changed from A (academia) to R (research institute).

Combined instance -- Synthesis with respect to: a civilian drone selection assessment model

Overall Inconsistency = .01

Main application	.123
Vehicle flight performance	.111
Acquisition of parts and operation consumables	.099
Maintenance costs	.086
Operation safety/security	.082
Manipulative ability	.080
Operation duration	.078
Flight power	.059
Maintenance simplicity	.058
Operation cost	.053
Operation supportability	.045
Purchase cost	.039
Maintenance convenience	.036
Operation convenience	.030
Operation environmental impact	.021

Figure 10. Research institute (R) group's opinion for the absolute weights of all factors.

Given the results in Figure 10, seven of the 15 factors' absolute weights have surpassed the used threshold, 0.7, so they can be classified as the "more important" factors. Besides these, the other eight factors should be less important for the design and selection of civilian drones. Further looking into these two groups, we find that the only three factors that have received a >0.10 or ~0.10 weight value, i.e., main application (cb4), vehicle flight performance (cb1) of civilian drones, and acquisition of parts and operation consumables (cd3), are the most important, as regarded by the experts who came from the R&D institutions. These factors should contribute a lot to CB and CD, as CB and CD have been shown to be the two more important constructs in Figure 9.

Relatively, the only two factors that received a weight value less than or equal to 0.03, i.e., operation convenience (cc1) and operation environmental impact (cc4), are deemed the two least important factors in minds of those experts who came from the research institute (R) group. The fact that the two least important factors are under the operation construct (CC) is reflective of the fact that CC is the least important construct in Figure 9.

3.3. A Short Summary

In this section, the process we have performed to conduct the analysis is demonstrated, and the results are shown and justified based on the empirical survey data, for retrieving a set knowledge about the design and selection factors of civilian drones, i.e., it is a mind-mining process for the experts' key opinions that will be reflected in law-making. This process involves the use of multiple theories and methods, including THM, Delphi, and AHP.

In Section 3.1, the Delphi method is used to confirm that the established set of influencing factors is effective after the thorough literature study, that the operational definitions made for these factors are correct, that the postulated set of constructs used to cover these factors is reasonable, and that the defined tree structure (i.e., the AHP hierarchy) is plausible, with the help from the selected "almost expert" participants.

In Section 3.2, the AHP survey is designed in such a way that it is linked with the THM, i.e., three groups of experts, A, I, and R, are intentionally organized and interviewed to understand the "group opinions," rather than the individual opinions. These "group opinions" are aggregated based on each individual expert's CWVs related to the civilian drone selection and design constructs and the selection and design criteria under each construct.

However, after the studies in Section 3.2, we may eventually see that there are heterogeneities and homogeneities in the opinions of the three groups as stratified by using the THM; the similarities and differences when these groups' opinions are compared subject to "the same thing" may require further exploration. This is the purpose of the next section.

4. Discussion and Implications

The priority and relative weights for the four constructs and for the 15 criteria were explored group by group in the previous section by aggregating the individual opinions (CWVs) in each group. Given the information, questions were raised as to the homogeneities and heterogeneities that exist across the different expert groups (i.e., A for academia, I for industry, and R for research institutes).

The first insight gained is that regardless of the subject group, the experts have a consensus that "CB: Performance and application" is the most significant construct to be considered while designing and selecting civilian drones. Such an outcome is persuasive, because no exception is found according to the group opinions.

Following the first insight, the *second insight* is that *there are varieties when the groups of experts are addressing the importance of another three constructs* while it is to design a civilian drone; these constructs are CA: Cost, CC: Operation, and CD: Maintenance. Among these, group A feels that operation is more important than cost and maintenance. Meanwhile, group I feels that cost is more important than maintenance and operation. However, group R feels that maintenance is more important than cost and operation. The differences in "which construct is more significant than the other two" *in the three expert groups' mind* tells a truth that for these constructs (CA, CC, and CD), *the group opinions are quite diversified* (except for the commonly agreed critical importance for CB).

Following from the former two insights, the *third insight* relates to a claim that *no construct is meaningless*. The I group's opinion for the constructs (with respect to CDSEM) (Figure 7) shows that the importance of the least important construct, operation, is 18.0%. The A group's opinion for the constructs (Figure 5) shows that the importance of the least important construct, cost, is 12.1% (still >10%), let alone for the operation construct that is regarded as the least important by the R group (whose relative importance is 21.1%; see Figure 9). These may imply that *the set of constructs proposed by this study is effective*, since each construct, either being critical or not, possesses a weight to a certain extent.

Before going on to discuss other insights about the consideration factors in more detail (in addition to those about the constructs), in Table 8, let us summarize the final ordinal ranks over all criteria (row-wise) as assessed by the three expert groups (column-wise), in terms of "rank order vector" (or ROV; see [7,12,99]) and analyze the ranking differences (or differences in rank alternative).

Table 8. Rankings for individual criteria and the ranking differences among the expert groups.

Construct	Criterion	Industry	Academia	Research	SRD *	ARD *
Cost	Purchase cost	9	14	12	10	10
	Operation cost	10	12	10	4	
	Maintenance cost	2	10	4	16	
Performance and application	Vehicle flight performance	3	2	2	2	8.4
	Manipulative ability	4	1	6	10	
	Flight power	6	6	8	4	
	Main application	8	5	1	14	
	Operation duration	1	4	7	12	
Operation	Operation convenience	13	9	14	10	7.5
	Operation safety and security	7	3	5	8	
	Operation supportability	14	10	11	8	
	Operation environmental impact	15	13	15	4	
Maintenance	Maintenance simplicity	11	8	9	6	6
	Maintenance convenience	12	15	13	6	
	Acquisition of parts and operation consumables	5	6	3	6	

* Table legend: SRD: sum of ranking difference, ARD: average ranking difference.

Scrutiny into this table finds the *fourth insight* that several factors (decision criteria) receive similar overall rankings from the three expert groups. Because the SRD (sum of ranking difference) aggregates the "difference in rank between each pair of groups" for some specific criteria, and there are always three pairs of groups in each case, SRD/3 can be used to measure the average diversity of the group opinions when the focus is a factor. If we set up a threshold "SRD/3 ≦ 2", which means that the three expert groups give similar rankings to the same factor (in that for this vector, the average diversities of the group opinions are quite converged), to filter the penultimate SRD column in Table 8, there are seven factors are under this threshold. Therefore, we can gain the knowledge that regardless of the expert group, experts in these three groups have reached *a consensus to a certain extent on the priorities of "operation cost" (ca2), "vehicle flight performance" (cb1), "flight power" (cb3), "operation environmental impact" (cc4), "maintenance simplicity" (cd1), "maintenance convenience" (cd2), and "acquisition of parts and operation consumables" (cd3)*. Note that here the "priority" of any factor, while being represented using a rank order number as shown in the middle three columns in Table 8, does not necessarily mean its importance in terms of absolute weight.

The *fifth insight*. As can be seen in the above list of seven factors, one is under CA and one is under CC, two are under CB, but three are under CD (and all criteria under construct D, CD, are listed). This tells a truth that under every construct, there is at least one factor that has received (very) similar rankings from the three groups of experts, and the real count varies construct by construct. Moreover, *compared to the factors under CA and CB regarding which the expert groups sometimes give very diversified opinions but sometimes do not* (see the gap in SRD, 12, for the factors under CA and the same gap size, 12, for the factors under CB), *their opinions* (among the groups) *are relatively stable* (with smaller variance; the gap in SRD is six) *for all factors under CC, and no variance is observed for the SRD values assessed for all factors under CD* (with the smallest possible variance, 0).

The *sixth insight*. The last column in Table 8, *"ARD" (average ranking difference), provides another measure*. Theoretically speaking, the ARD measures the degree to which the opinions for the factors included by a construct are diversified on average, i.e., 10, 8.4, 7.5, and 6.0 for construct CA (cost), CB (performance and application), CC (operation), and CD (maintenance), respectively. It is, in fact, a measure other than the "gap" between the highest and lowest of the SRD values used in the previous point to connote the variance (degree) in those SRD values for each construct. However, despite this, it is surprising that *the order of the constructs, while justified using the ARD measure, roughly concurs with the order while justified using the "gap" measure to see the variances in SRD under the constructs*. In other words, *these outcomes may cross-validate with each other, for how the group opinions of experts are diversified under each construct within which the individual factors are included*.

Then, following the fourth insight, the *seventh insight* relates to *the set of the remaining eight factors, which have more opinion differences among the three groups of experts* in terms of SRD. These include: "purchase cost" (ca1), "maintenance cost" (ca3), "manipulative ability" (cb2), "main application" (cb4), "operation duration" (cb5), "operation convenience" (cc1), "operation safety and security" (cc2), and "operation supportability" (cc3). Additionally, according to their SRD values (i.e., the degree to which their opinions diversify across the groups for each factor), these eight factors are sorted in descending order as: *ca3* (SRD = 16) > *cb4* (14) > *cb5* (12) > (*ca1, cb2, cc1*) (10) > (*cc2, cc3*) (8). Both the set of these factors and the order of them are worthwhile knowledge for the design and selection of civilian drones. These are also important for the different groups of experts to make the advice for law-making, because integrating their diversified opinions for these factors while defining the legislations is usually a tough task, but the results of this study may offer some supplemental information about the opinion gaps before they sit down together with real lawmakers.

The *eighth insight* pertains to *"what factors are the most critical ones to be watched for?"* Either the field of big data analytics or MADM usually gives more emphasis to the items (i.e., criteria or alternatives, and the factors as in the case here) that are extraordinary (i.e.,

the data points, the opinions from DMs, and the opinions for the factors here). For example, an MADM model may assign a heavier weight to a DM whose opinion is away from the average by using the opinion weight vector (OWV) concept [8]. For this sake, based on the information of the "diversified order" of those factors obtained in the previous point, we also find that the three groups of experts have the largest opinion differences for the maintenance cost (ca3), main application (cb4), and operation duration (cb5) factors for designing and selecting civilian drones. Following from the former insight, this implies that they (i.e., the three groups) may reach little consensus while the relevant drafts pertaining to these three factors are discussed among them for regulating the civilian use of drones (after they sit down together), if no extra (or at least sufficient) effort is made to coordinate their preferences and intentions toward civilian drones' design and selection and law-making.

5. Conclusions and Future Recommendations

This study, at the outset, aims to understand the expert opinions during a consultation process before law-making. These opinions will shape the related laws made and enacted to regulate the relevant matters of civilian drones (i.e., to control the design, manufacturing, and uses of civilian drones in Taiwan). As the consultation process involves polling the opinions from three expert groups, academy (A), industry (I), and research institutes (R), the main research question is thus about understanding their opinions and noting the similarities and differences in their group opinions. However, how can the relevant set of knowledge be explored thoroughly and "neatly"?

In this study, first, the literature was studied comprehensively to have a set of influencing factors for designing and selecting the civilian drones. Eventually, a set of 15 consideration factors was established, with four possible constructs covering these factors being summarized, i.e., CA: cost, CB: performance and application, CC: operation, and CD: maintenance. Therefore, a hierarchical tree weaving the 14 factors under the four constructs was postulated, and this formed the initial "AHP hierarchy" that awaited further confirmation. This rigorous process is critical, because drone technologies have been combined with the non-aeronautic emerging technologies for various application purposes nowadays, e.g., 5G [100], data integration techniques [101], the machine learning models [102], optimization routing algorithms [103], and the humanoid robots [104]. Thus, a multiplex of these advanced capabilities (and technologies) into existing areas of UAV [105] may become the interferences to exploit the key influencing factors.

In the next, the established initial AHP hierarchy was sent to several "almost experts" for evaluation using the Delphi process for two rounds. At last, the AHP hierarchy is confirmed to be effective, with minor corrections made for the operational definitions. Following this, the questionnaires were designed in AHP style, and using these, experts in the three groups were interviewed. Stratifying the respondent sample into three groups intentionally followed the proposed "modified THM" model, in which the "triple player parties" were altered from I, G, and A to A, I, and R. See former sections for the reasoning process.

The entire survey process spanned over two months in early 2021. It required one to three rounds of interviews for the expert opinions to pass the CR-validation check (of AHP). Eventually, the pairwise matrices collected from all of the 27 experts were used to calculate the CWVs (i.e., opinions in each expert's mind) for the constructs (with respect to the total goal) and for the criteria (factors) (with respect to some construct). Based on these individual CWVs, the "group opinions" are aggregated in terms of "group CWVs" for the relative importance (of the four constructs, and of the different factors under each construct).

For all the three groups, their group CWVs justified for the four constructs were dissected and analyzed. Furthermore, within each group, its group CWVs were "synthesized" to obtain the "absolute weights" for the 15 factors overall, and these weights were also ranked in each group. These overall ranks of the factors became another target to be compared across the THM groups. Through a process to understand the former results, several practical implications for drone design/selection and for the advice made by the

different expert groups for law-making were therefore drawn. As a short summary, the insights gained are summarized as follows:

1. Regardless of the subject group, the experts have a consensus that construct CB, performance and application, is the most significant construct to be considered without exception.

2. For the importance of the three remaining constructs, the opinions are quite diversified, because, except for CB, each group feels a different construct (either CA, or CC, or CD) to be more important than another two.

3. No construct proposed by this study is meaningless, since even the construct with the lowest importance among the three groups has a weight of 12.1% (i.e., CA by party A).

4. The three groups have reached a consensus on the overall rank (i.e., connoting the priority for its importance level) of many factors to a certain extent, among all of the 15 factors considered, which are ca2: operation cost, cb1: vehicle flight performance, cb3: flight power, cc4: operation environmental impact, cd1: maintenance simplicity, cd2: maintenance convenience, and cd3: acquisition of parts and operation consumables.

5. Compared to the situation in which the expert groups sometimes rank the factors under CA and CB very diversely but sometimes do not, their opinions are relatively stable for all factors under CC, and no variance in rank is observed for all factors under CD using the SRD measure.

6. Using ARD as the measure, CA (cost) is shown to have a larger average ranking difference (over all factors) than CB (performance and application), CC (operation), and CD (maintenance); such an order concurs with the order that is justified using the previous variance measure (in terms of the farthest distance in SRD between any two factors under the constructs). In other words, these outcomes may cross-validate with each other.

7. There is another set of eight factors that received more opinion differences from the three groups of experts. According to the SRD values of these factors (i.e., the degree to which the opinions of the groups are diversified), these factors can be sorted in descending order as: ca3 (16) > cb4 (14) > cb5 (12) > (ca1, cb2, cc1) (10) > (cc2, cc3) (8). Both the set of factors and the order of them are worthwhile knowledge to close the opinion gaps before the experts sit down together.

8. By reference to the theory in the field of big data or MADM, we put an emphasis on the opinions of the factors that are extraordinary. Therefore, the last insight is that the three groups of experts have the largest opinion differences on factors ca3: maintenance cost, cb4: main application, and cb5: operation duration. This implies that they may reach little consensus while the relevant drafts to regulate the civilian use of drones are discussed after they sit down together if no extra coordination about their preferences and intentions toward the factors is made.

As can be seen in the list of valuable insights gained, all this is critical for the different groups of experts to give their advice for law-making because investigating and integrating their opinions, either diversified or not, for these factors is usually a difficult task while defining the legislations. Moreover, the results may provide the knowledge to facilitate the communication processes and close the opinion gaps before the experts sit down together or even before a final draft is formally delivered for law-making. As from the perspective of operational research (OR) some law-relevant issues have just been addressed [106], these insights also encompass the general aim of this research line.

The THM has been popular for years, but studies based on it explored many other issues, such as innovation (or national innovation system), governmental aspects (e.g., smart city), the industrial revolution and cooperation, local economic or regional development, and knowledge production, transfer, and economy matters. Most of the studies were based on the academia (university)–industry–government interactions (i.e., A–I–G) to explore the concerned topics where appropriate. Analogously, this study proposed a "modified THM" to explore the factors for civilian drone design/selection in terms of

academia–industry–research (i.e., A–I–R) and identify the relationships between the group opinions (attitudes) toward those constructs and factors, so as to understand the required knowledge for law-making. In previous THM studies, e.g., in the field of smart city, only the sphere of drone applications has been touched. In this sense, this study not only fills the gap by using the modified THM to offer another set of in-depth knowledge about the design/selection of civilian drones with a systematic study flow, but also is helpful for lawmakers to develop regulations on drones during the formation process of law-making.

The future research directions may involve:

1. More deepened analysis about the group opinions, or even the individual opinions, based on the (human) data set as collected by this study; for this sake, the advanced visualization techniques [8,9] are perhaps helpful.
2. As the focus of this study is on the importance of the constructs and the factors (either relative or absolute), this study uses AHP for CR-validation and CWV-determination; the last phase of AHP or other MADM methodologies can be applied to the real selection problem of drones [6,9,97]. As current data profiles of different brands of drones can be aggregated as a "decision matrix" (which means a set of computer data), together with the human data polled in this study, integrating the heterogeneous data sets, solving the selection problem, and performing the decision analysis based thereon should be an interesting DDDM study [12].
3. Some techniques in the (big) data analytics field can be applied to test whether each pair of the group opinions of experts is "really dissimilar" or not, and recently this concept has become popular. For this, we refer to the non-parametric tests used by the "similarity confirmation method" [12,99]. Besides this, using other non-parametric-based measures and comparing the results should also be interesting.

Appendix A

This study also explores all twenty-seven DMs' decision opinions. Figure A1 shows the four decision constructs' relative weights for the civilian drone selection evaluation model. Looking at Figure 5, we can find that the significance ranking of those four decision constructs is "performance and application", "maintenance", "cost", and "operation." Except that the relative weight value of the most significant decision construct, "performance and application" is 0.363, there exists a big relative weight gap with the other three decision constructs. The other three decision constructs' relative weight values are relatively close; their relative weight values are all around 0.210.
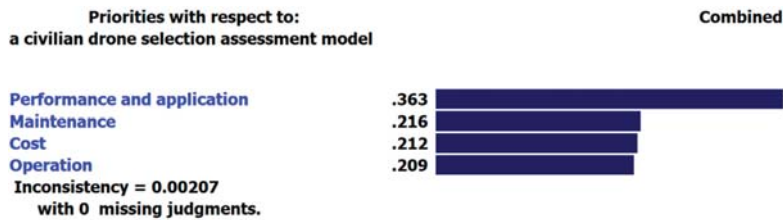
Figure A1. The four decision construct aggregated relative weights in the all group.

This study uses the mean value of all decision criteria's absolute weights as an evaluation criterion. A decision criterion will belong to a more significant group when its absolute weight is more than the mean value of all decision criteria's absolute weights; otherwise, the decision criterion will belong to a less significant group. Figure A2 shows that all the fifteen decision criteria absolute weights are under the total designed goal. Examining Figure A2, we can find that eight decision criteria belong to the more significant group; seven decision criteria belong to the less significant group. In the more significant group, the "vehicle flight performance" and "manipulative ability" are the two most significant decision criteria, and all those decision criteria's absolute weights exceed 0.1 (1.5 times the mean value); the absolute weight sum of those two decision criteria is over 25%. Relatively, in the less significant group, the "operation convenience", "operation supportability", and "operation environmental impact" are the three least significant decision criteria; their absolute weights are less than 0.0335 (half the mean value).
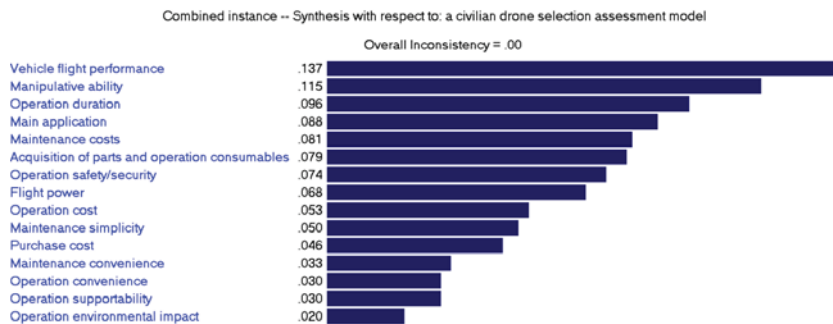
Figure A2. The fifteen decision criteria aggregated absolute weights in the all group.

References

1. Sorgedrager, N. Using Consumer Drones in Surveying Deltas and Coastal Systems. Master's Thesis, Water Science and Management, Universiteit Utrecht, Utrecht, The Netherlands, 2019.
2. Drone Industry Insights. The Drone Market Report 2020–2025. Available online: https://droneii.com/product/drone-market-report-2020-2025 (accessed on 8 February 2021).
3. Sah, B.; Gupta, R.; Bani-Hani, D. Analysis of barriers to implement drone logistics. *Int. J. Logist. Res. Appl.* **2020**. [CrossRef]
4. Simões, P.C.; Moreira, A.C.; Mendes Dias, C. Portugal's Changing Defense Industry: Is the Triple Helix Model of Knowledge Society Replacing State Leadership Model? *J. Open Innov. Technol. Mark. Complex.* **2020**, *6*, 183. [CrossRef]
5. Jia, L.; Alizadeh, R.; Hao, J.; Wang, G.; Allen, J.K.; Mistree, F. A rule-based method for automated surrogate model selection. *Adv. Eng. Inform.* **2020**, *45*, 101123. [CrossRef]
6. Zhuang, Z.-Y.; Chiang, I.-J.; Su, C.-R.; Chen, C.-Y. Modelling the decision of paper shredder selection using analytic hierarchy process and graph theory and matrix approach. *Adv. Mech. Eng.* **2017**, *9*, 1–11. [CrossRef]
7. Zhuang, Z.-Y.; Lin, C.-C.; Chen, C.-Y.; Su, C.-R. Rank-based comparative research flow benchmarking the effectiveness of AHP–GTMA on aiding decisions of shredder selection by reference to AHP–TOPSIS. *Appl. Sci.* **2018**, *8*, 1974. [CrossRef]
8. Chi, L.-P.; Fu, C.-H.; Chyng, J.-P.; Zhuang, Z.-Y.; Huang, J.-H. A post-training study on the budgeting criteria set and priority for MALE UAS design. *Sustainability* **2019**, *11*, 1798. [CrossRef]

9. Chi, L.-P.; Zhuang, Z.-Y.; Fu, C.-H.; Huang, J.-H. A knowledge discovery education framework targeting the effective budget use and opinion explorations in designing specific high cost product. *Sustainability* **2018**, *10*, 2742. [CrossRef]
10. Ulloa, C.; Nuñez, J.M.; Lin, C.; Rey, G. AHP-based design method of a lightweight, portable and flexible air-based PV-T module for UAV shelter hangars. *Renew. Energy* **2018**, *123*, 767–780. [CrossRef]
11. Song, C.; Zang, Y.; Zhou, Z.; Luo, X.; Zhao, L.; Ming, R.; Zi, L.; Zang, Y. Test and comprehensive evaluation for the performance of UAV-based fertilizer spreaders. *IEEE Access* **2020**, *8*, 202153–202163. [CrossRef]
12. Zhuang, Z.-Y.; Su, C.-R.; Chang, S.-C. The effectiveness of IF-MADM (intuitionistic-fuzzy multi-attribute decision-making) for group decisions: Methods and an empirical assessment for the selection of a senior centre. *Technol. Econ. Dev. Econ.* **2019**, *25*, 322–364. [CrossRef]
13. Gertler, J.U.S. *Unmanned Aerial Systems*; Congressional Research Service: Washington, DC, USA, 2012.
14. Ravich, T.M. The integration of unmanned aerial vehicles into the National Airspace. *NDL Rev.* **2009**, *85*, 597–622.
15. Fladeland, M.; Schoenung, S.; Lord, M. UAS platforms. In Proceedings of the NCAR/EOL Workshop–Unmanned Aircraft Systems for Atmospheric Research, Boulder, CO, USA, 21–24 February 2017; pp. 21–24.
16. Gupta, S.G.; Ghonge, M.M.; Jawandhiya, P.M. Review of unmanned aircraft system (UAS). *Int. J. Adv. Res. Comput. Eng. Technol.* **2013**, *2*, 1646–1658. [CrossRef]
17. Murphy, J.R.; Williams-Hayes, P.S.; Kim, S.K.; Bridges, W.; Marston, M. Flight test overview for UAS integration in the NAS project. In Proceedings of the AIAA Atmospheric Flight Mechanics Conference, San Diego, CA, USA, 4–8 January 2016; p. 1756.
18. Austin, R. *Unmanned Aircraft Systems: UAVS Design, Development and Deployment*; John Wiley & Sons: Hoboken, NJ, USA, 2011; Volume 54.
19. Grand View Research. Commercial Drone Market Size & Trends Report, 2019–2025. Available online: https://www.grandviewresearch.com/industry-analysis/global-commercial-drones-market (accessed on 6 February 2021).
20. Fuhrmann, M.; Horowitz, M.C. Droning on: Explaining the proliferation of unmanned aerial vehicles. *Int. Organ.* **2017**, *71*, 397–418. [CrossRef]
21. Grimaccia, F.; Aghaei, M.; Mussetta, M.; Leva, S.; Quater, P.B. Planning for PV plant performance monitoring by means of unmanned aerial systems (UAS). *Int. J. Energy Environ. Eng.* **2015**, *6*, 47–54. [CrossRef]
22. Davis, L.E.; McNerney, M.J.; Chow, J.; Hamilton, T.; Harting, S.; Byman, D. *Armed and Dangerous? UAVs and US Security*; RAND Corp.: Santa Monica, CA, US, 2014.
23. Aragão, F.V.; Zola, F.C.; Marinho, L.H.N.; de Genaro Chiroli, D.M.; Junior, A.B.; Colmenero, J.C. Choice of unmanned aerial vehicles for identification of mosquito breeding sites. *Geospat. Health* **2020**, *15*, 92–100. [CrossRef]
24. Kianian, B.; Kurdve, M.; Andersson, C. Comparing life cycle costing and performance part costing in assessing acquisition and operational cost of new manufacturing technologies. *Procedia CIRP* **2019**, *80*, 428–433. [CrossRef]
25. Kim, D.; Lee, K.; Moon, I. Stochastic facility location model for drones considering uncertain flight distance. *Ann. Oper. Res.* **2019**, *283*, 1283–1302. [CrossRef]
26. Figliozzi, M.A. *Modeling the Sustainability of Small Unmanned Aerial Vehicles Technologies: Final Report*; Portland State University: Portland, OR, USA, 2018.
27. Jorge, L.A.; Brandão, Z.N.; Inamasu, R.Y. Insights and recommendations of use of UAV platforms in precision agriculture in Brazil. In Proceedings of the Remote Sensing for Agriculture, Ecosystems, and Hydrology XVI (Proc. of SPIE Vol. 9239), Amsterdam, The Netherlands, 12 November 2014. Paper ID: 923911. [CrossRef]
28. Miari, B. A Qualitative Risk Assessment Applied Using SORA: UAV Technology Supporting Maintenance Operations on Rødsand II Offshore Wind Farm. Master Thesis, Risk and Safety Management, Aalborg University, Copenhagen, Denmark, 2018.
29. Yu, S.H.; Kim, Y.K.; Jun, H.J.; Choi, I.S.; Woo, J.K.; Kim, Y.H.; Lee, J. Evaluation of Spray Characteristics of Pesticide Injection System in Agricultural Drones. *J. Biosyst. Eng.* **2020**, 1–9. [CrossRef]
30. Bouayed, Z.; Penney, C.E.; Sokri, A.; Yazbek, T. *Estimating Maintenance Costs for Royal Canadian Navy Ships: A Parametric Cost Model*; Defence Research and Development Canada: North York, ON, Canada, 2017.
31. Dožić, S.; Kalić, M. An AHP approach to aircraft selection process. *Transp. Res. Procedia* **2014**, *3*, 165–174. [CrossRef]
32. Gomes, L.F.A.M.; de Mattos Fernandes, J.E.; de Mello, J.C.C.S. A fuzzy stochastic approach to the multi-criteria selection of an aircraft for regional chartering. *J. Adv. Transp.* **2014**, *48*, 223–237. [CrossRef]
33. Wang, N.; Liu, Y.; Fu, G.; Li, Y. Cost–benefit assessment and implications for service pricing of electric taxies in China. *Energy Sustain. Dev.* **2015**, *27*, 137–146. [CrossRef]
34. Yeh, C.H.; Chang, Y.H. Modeling subjective evaluation for fuzzy group multi-criteria decision making. *Eur. J. Oper. Res.* **2009**, *194*, 464–473. [CrossRef]
35. Woodward, D.G. Life cycle costing—Theory, information acquisition and application. *Int. J. Proj. Manag.* **1997**, *15*, 335–344. [CrossRef]
36. iEduNote. Operating Costing: Definition, Classification of Operating Cost. Available online: https://www.iedunote.com/operating-costing (accessed on 18 February 2021).
37. Chang, C.-T.; Chou, Y.-Y.; Zhuang, Z.-Y. A practical expected-value-approach model to assess the relevant procurement costs. *J. Oper. Res. Soc.* **2015**, *66*, 539–553. [CrossRef]
38. Bressani-Ribeiro, T.; Almeida, P.G.S.; Volcke, E.I.P.; Chernicharo, C.A.L. Trickling filters following anaerobic sewage treatment: State of the art and perspectives. *Environ. Sci. Water Res. Technol.* **2018**, *4*, 1721–1738. [CrossRef]

39. Nachimuthu, S.; Zuo, M.J.; Ding, Y. A decision-making model for corrective maintenance of offshore wind turbines considering uncertainties. *Energies* **2019**, *12*, 1408. [CrossRef]

40. Hwang, H.; Prasad, C.R.; Serino, R.M. Lean-Sensing: Intelligent, Low-Cost, Remote Detection by Integrating Currently Available Components for Distant Early Warning. *Hdiac J.* **2015**, *2*, 15–20.

41. Petkovics, I.; Simon, J.; Petkovics, Á.; Čović, Z. Selection of unmanned aerial vehicle for precision agriculture with multi-criteria decision-making algorithm. In Proceedings of the 2017 IEEE 15th International Symposium on Intelligent Systems and Informatics (SISY), Subotica, Serbia, 14–16 September 2017; pp. 151–156.

42. Nur, F.; Alrahahleh, A.; Burch, R.; Babski-Reeves, K.; Marufuzzaman, M. Last mile delivery drone selection and evaluation using the interval-valued inferential fuzzy TOPSIS. *J. Comput. Des. Eng.* **2020**, *7*, 397–411.

43. Ulukavak, M.; Miman, M. Selection of The Most Proper Unmanned Aerial Vehicle for Transportation in Emergency Operations by Using Analytic Hierarchy Process. *Int. J. Environ. Geoinform.* **2019**, *8*, 78–91. [CrossRef]

44. Duque, L.; Seo, J.; Wacker, J. Synthesis of unmanned aerial vehicle applications for infrastructures. *J. Perform. Constr. Facil.* **2018**, *32*, 04018046. [CrossRef]

45. Duque, L.; Seo, J.; Wacker, J. Timber bridge inspection using UAV. In Proceedings of the Structures Congress 2018: Bridges, Transportation Structures, and Nonbuilding Structures (ASCE), Reston, VA, USA, 19–21 April 2018; pp. 186–196.

46. Hoyas Ester, I. STAMP project. Master Thesis, Universitat Politècnica de Catalunya, Barcelona, Catalunya, Spain, 2018.

47. Cesnik, C.E.; Palacios, R.; Reichenbach, E.Y. Reexamined structural design procedures for very flexible aircraft. *J. Aircr.* **2014**, *51*, 1580–1591. [CrossRef]

48. Chen, Y.; Zhang, H.; Xu, M. The coverage problem in UAV network: A survey. In Proceedings of the IEEE Fifth International Conference on Computing, Communications and Networking Technologies (ICCCNT), Hefei, China, 11–13 July 2014; pp. 1–5.

49. Ajanic, E.; Feroskhan, M.; Mintchev, S.; Noca, F.; Floreano, D. Bioinspired wing a and tail morphing extends drone flight capabilities. *Sci. Robot.* **2020**, *5*, eabc2897. [CrossRef]

50. Yang, G.; Lin, X.; Li, Y.; Cui, H.; Xu, M.; Wu, D.; Redhwan, S.B. A telecom perspective on the internet of drones: From LTE-advanced to 5G. *arXiv* **2018**, arXiv:1803.11048.

51. Shakeri, R.; Al-Garadi, M.A.; Badawy, A.; Mohamed, A.; Khattab, T.; Al-Ali, A.K.; Guizani, M. Design challenges of multi-UAV systems in cyber-physical applications: A comprehensive survey and future directions. *IEEE Commun. Surv. Tutor.* **2019**, *21*, 3340–3385. [CrossRef]

52. Erdelj, M.; Natalizio, E.; Chowdhury, K.R.; Akyildiz, I.F. Help from the sky: Leveraging UAVs for disaster management. *IEEE Pervasive Comput.* **2017**, *16*, 24–32. [CrossRef]

53. Laszlo, B.; Agoston, R.; Xu, Q. Conceptual approach of measuring the professional and economic effectiveness of drone applications supporting forest fire management. *Procedia Eng.* **2018**, *211*, 8–17. [CrossRef]

54. Restas, A. Drone applications for supporting disaster management. *World J. Eng. Technol.* **2015**, *3*, 316–321. [CrossRef]

55. Aljehani, M.; Inoue, M. Performance evaluation of multi-UAV system in post-disaster application: Validated by HITL simulator. *IEEE Access* **2019**, *7*, 64386–64400. [CrossRef]

56. Yıldırım, Ş.; Çabuk, N.; Bakırcıoğlu, V. Design and trajectory control of universal drone system. *Measurement* **2019**, *147*, 106834. [CrossRef]

57. Amiri, N. *Control of an Unconventional VTOL UAV for Complex Maneuvers*; Graduate Studies, University of Calgary's; University of Calgary: Calgary, Italy, 2013.

58. Pai, N.S.; Zhou, Y.H.; Chen, P.Y.; Chen, W.L.; Chen, S.A. Realization of Person Tracking and Gesture Recognition with a Quadrotor System. *Sens. Mater.* **2019**, *31*, 2245–2262. [CrossRef]

59. Liu, J.; Wang, Y.; Li, B.; Ma, S. Current research, key performances and future development of search and rescue robots. *Front. Mech. Eng. China* **2007**, *2*, 404–416. [CrossRef]

60. Bruno, G.; Esposito, E.; Genovese, A. A model for aircraft evaluation to support strategic decisions. *Expert Syst. Appl.* **2015**, *42*, 5580–5590. [CrossRef]

61. See, T.K.; Gurnani, A.; Lewis, K. Multi-attribute decision making using hypothetical equivalents and inequivalents. *J. Mech. Des.* **2004**, *126*, 950–958. [CrossRef]

62. Hassanalian, M.; Abdelkefi, A. Classifications, applications, and design challenges of drones: A review. *Prog. Aerosp. Sci.* **2017**, *91*, 99–131. [CrossRef]

63. Zhang, L.; Wang, W.; Yingshuai, D.U.; Wu, Z.; Zhang, W.; Xuming, M.A.; Li, J. Aerial Cdznte Inspection System And Inspection Method. U.S. Patent Application No. 15/740,813, 4 October 2018.

64. Pickett, S. Unmanned Aerial Vehicle Boosters. U.S. Patent Application No. 16/108,495, 26 November 2019.

65. Liang, Y.; Xu, W.; Liang, W.; Peng, J.; Jia, X.; Zhou, Y.; Duan, L. Nonredundant information collection in rescue applications via an energy-constrained UAV. *IEEE Internet Things J.* **2018**, *6*, 2945–2958. [CrossRef]

66. Zhang, T.; Wang, M.; Wang, Z.; Zhang, X.; Zhang, G.; Gong, S.; Zhang, Y.; Wang, J.; Liu, L. Fully Protected Drone. U.S. Patent Application No. 15/117,829, 22 December 2016.

67. Ng, M. Mobile Vehicle Charging System. U.S. Patent No. 10,207,591, 22 October 2019.

68. Tang, Y.; Zhao, T.; Deng, L. Remote Controller and Handle Structure Thereof, and Method for Controlling a UAV. U.S. Patent No. 10,675,551, 9 June 2020.

69. Zhou, M.; Zhou, Z.; Liu, L.; Huang, J.; Lyu, Z. Review of vertical take-off and landing fixed-wing UAV and its application prospect in precision agriculture. *Int. J. Precis. Agric. Aviat.* **2020**, *3*, 8–17.
70. Xiao, X.; Guo, B.; Li, D.; Li, L.; Yang, N.; Liu, J.; Peng, Z. Multi-view stereo matching based on self-adaptive patch and image grouping for multiple unmanned aerial vehicle imagery. *Remote Sens.* **2016**, *8*, 89. [CrossRef]
71. Mao, X.; Li, Y.; Cheng, J.; Zhang, Y. International Investment Strategies of Chinese High-Tech Company—In the Example of DJI'Four Flyings Strategy. In Proceedings of the 4th International Symposium on Business Corporation and Development in South-East and South Asia under B&R Initiative (ISBCD 2019), Kunming, China, 24 November 2019; pp. 193–198.
72. Johnsen, S.O.; Evjemo, T.E. State of the art of unmanned aircraft transport systems in industry related to risks, vulnerabilities and improvement of safety. In Proceedings of the 29th European Safety and Reliability Conference (ESREL), Hannover, Germany, 22–26 September 2019.
73. Roy, R.N.; Bovo, A.; Gateau, T.; Dehais, F.; Chanel, C.P.C. Operator engagement during prolonged simulated uav operation. *Ifac-Pap. Line* **2016**, *49*, 171–176. [CrossRef]
74. Gundlach, J. Designing unmanned aircraft systems: A comprehensive approach. In Proceedings of the American Institute of Aeronautics and Astronautics (AIAA), Manassas, VI, USA, 9–12 January 2012.
75. Sadraey, M.H. Unmanned Aerial Vehicles Design Education; Techniques and Challenges. In Proceedings of the ASEE's Virtual Conference, Virtual, 22–26 June 2020. Paper ID: 28664. [CrossRef]
76. Hall, A.B. *Conceptual and Preliminary Design of a Low-Cost Precision Aerial Delivery System*; Naval Postgraduate School: Monterey, CA, USA, 2016.
77. Candeloro, P.; Pagliaroli, T.; Ragni, D.; Di Francesco, S. Small-scale rotor aeroacoustics for drone propulsion: A review of noise sources and control strategies. *Preprints* **2019**. [CrossRef]
78. Jiang, H.; Zhou, T.; Fattah, R.J.; Zhang, X.; Huang, X. Multi-rotor noise scattering by a drone fuselage. In Proceedings of the 25th AIAA/CEAS Aeroacoustics Conference, Delft, The Netherlands, 20–23 May 2019; p. 2586.
79. Soloiu, V.; Phillips, C.J.; Carapia, C.; Knowles, A.; Grall, D.; Smith, R. Exploratory Investigation of Combustion and NVH Signature of a Drone Jet Engine Fueled with IPK. In Proceedings of the AIAA SciTech 2021 Forum, Virtual, 19–21 January 2021; p. 1347.
80. Gaynutdinov, R.R.; Chermoshentsev, S.F. Emission of electromagnetic disturbances from coupling paths of avionics unmanned aerial vehicles. In Proceedings of the IEEE 2017 International Siberian Conference on Control and Communications (SIBCON), Astana, Kazakhstan, 29–30 June 2017; pp. 1–5.
81. Petrov, G.; Stancheva, A. Problems related to EMC caused by low-altitude flying drones in urban environment. *Electrotech. Electron. (E+E)* **2020**, *55*, 1–7.
82. Metzler, C.D.F. Logistics in the Contact Layer. *Marine Corps Gazette*, 20 May; 18–24.
83. Muliadi, J.; Kusumoputro, B. Neural network control system of UAV altitude dynamics and its comparison with the PID control system. *J. Adv. Transp.* **2018**, 3823201. [CrossRef]
84. Edgell, J.; Spangler, S.K.; Dragoo, G.F.; Jackson, L.W. *Logistics in 2025: Consider It Done!* Department of Defence: Washington, DC, USA, 1996.
85. Rashidi, S.; Karimi, N.; Mahian, O.; Esfahani, J.A. A concise review on the role of nanoparticles upon the productivity of solar desalination systems. *J. Therm. Anal. Calorim.* **2019**, *135*, 1145–1159. [CrossRef]
86. Zhai, S.; Bai, B. A Time Service Improvement Scheme for Clock System of Nuclear Power Plant. *Int. J. Comput. Electr. Eng.* **2014**, *6*, 501. [CrossRef]
87. Dingning, L.; Qiong, D. Point Cloud Processing System Development Based on PCL and Qt. *Int. J. Eng. Manag.* **2019**, *3*, 33. [CrossRef]
88. Zhao, J.; Zhuang, Z.; Hu, H.; Hao, M.; Peng, Y.; Zhang, W.; Xu, S. Container-Type Data Center. U.S. Patent Application No. 12/963,129, 25 May 2010.
89. Adebimpe, O.A.; Oladokun, V.; Charles-Owaba, O.E. Preventive maintenance interval prediction: A spare parts inventory cost and lost earning based model. *Eng. Technol. Appl. Sci. Res.* **2015**, *5*, 811–817. [CrossRef]
90. Dellar, C.; Morris, T.; Hendrikse, N.; Wainscott, K. Spare Parts and Consumables Management System. U.S. Patent Application No. 09/956,586, 20 March 2003.
91. Oliva, R.; Kallenberg, R. Managing the transition from products to services. *Int. J. Serv. Ind. Manag.* **2003**, *14*, 160–172. [CrossRef]
92. Goodman, C.M. The Delphi technique: A critique. *J. Adv. Nurs.* **1987**, *12*, 729–734. [CrossRef]
93. Woudenberg, F. An evaluation of Delphi. *Technol. Forecast. Soc. Change* **1991**, *40*, 131–150. [CrossRef]
94. Linstone, H.A.; Turoff, M. *The Delphi Method*; Addison-Wesley Publishing: Boston, MA, USA, 1975.
95. Turoff, M.; Linstone, H.A. *The Delphi Method: Techniques and Applications*; Advanced Book Program; Addison-Wesley Publishing: Boston, MA, USA, 2002.
96. Saaty, T.L. A scaling method for priorities in hierarchical structures. *J. Math. Psychol.* **1977**, *15*, 234–281. [CrossRef]
97. Zhuang, Z.-Y.; Yang, L.-W.; Lee, M.-H.; Wang, C.-Y. 'MEAN+ R': Implementing a web-based, multi-participant decision support system using the prevalent MEAN architecture with R based on a revised intuitionistic-fuzzy multiple attribute decision-making model. *Microsyst. Technol.* **2018**, *24*, 4291–4309. [CrossRef]
98. Saaty, T.L. Decision Making with the Analytic Hierarchy Process. *Int. J. Serv. Sci.* **2008**, *1*, 83–98. [CrossRef]

99. Zhuang, Z.-Y.; Chang, S.-C. Another empirical application of the Similarity Confirmation Method in evaluating the MADM methods for a type-selection decision case before bulk purchase. In Proceedings of the 11th Annual International Conference on Industrial Engineering and Operations Management (IOEM 2021), Singapore, 7–11 March 2021; ISBN 978-1-7923-6124-1.

100. Ferro, E.; Gennaro, C.; Nordio, A.; Paonessa, F.; Vairo, C.; Virone, G.; Bragagnini, A. 5G-Enabled Security Scenarios for Unmanned Aircraft: Experimentation in Urban Environment. *Drones* **2020**, *4*, 22. [CrossRef]

101. Rodríguez-Puerta, F.; Ponce, R.A.; Pérez-Rodríguez, F.; Águeda, B.; Martín-García, S.; Martínez-Rodrigo, R.; Lizarralde, I. Comparison of Machine Learning Algorithms for Wildland-Urban Interface Fuel-break Planning Integrating ALS and UAV-borne LiDAR Data and Multispectral Images. *Drones* **2020**, *4*, 21. [CrossRef]

102. Gorkin, R.; Adams, K.; Berryman, M.J.; Aubin, S.; Li, W.; Davis, A.R.; Barthelemy, J. Sharkeye: Real-time autonomous personal shark alerting via aerial surveillance. *Drones* **2020**, *4*, 18. [CrossRef]

103. Srivastava, K.; Pandey, P.C.; Sharma, J.K. An Approach for Route Optimization in Applications of Precision Agriculture Using UAVs. *Drones* **2020**, *4*, 58. [CrossRef]

104. Chatziparaschis, D.; Lagoudakis, M.G.; Partsinevelos, P. Aerial and Ground Robot Collaboration for Autonomous Mapping in Search and Rescue Missions. *Drones* **2020**, *4*, 79. [CrossRef]

105. Sigala, A.; Langhals, B. Applications of Unmanned Aerial Systems (UAS): A Delphi Study Projecting Future UAS Missions and Relevant Challenges. *Drones* **2020**, *4*, 8. [CrossRef]

106. Zhuang, Z.Y.; Vincent, F.Y. Analyzing the effects of the new labor law on outpatient nurse scheduling with law-fitting modeling and case study. *Expert Syst. Appl.* **2021**, *180*, 115103. [CrossRef]

Drone Control in AR: An Intuitive System for Single-Handed Gesture Control, Drone Tracking, and Contextualized Camera Feed Visualization in Augmented Reality

Konstantinos Konstantoudakis *,†, **Kyriaki Christaki** *,†, **Dimitrios Tsiakmakis, Dimitrios Sainidis, Georgios Albanis, Anastasios Dimou** * **and Petros Daras**

Visual Computing Lab (VCL), Centre for Research and Technology-Hellas (CERTH), Information Technologies Institute (ITI), 57001 Thessaloniki, Greece; tsiakmakis@iti.gr (D.T.); dsainidis@iti.gr (D.S.); galbanis@iti.gr (G.A.); daras@iti.gr (P.D.)

* Correspondence: k.konstantoudakis@iti.gr (K.K.); kchristaki@iti.gr (K.C.); dimou@iti.gr (A.D.)

† These authors contributed equally to this work.

Abstract: Traditional drone handheld remote controllers, although well-established and widely used, are not a particularly intuitive control method. At the same time, drone pilots normally watch the drone video feed on a smartphone or another small screen attached to the remote. This forces them to constantly shift their visual focus from the drone to the screen and vice-versa. This can be an eye-and-mind-tiring and stressful experience, as the eyes constantly change focus and the mind struggles to merge two different points of view. This paper presents a solution based on Microsoft's HoloLens 2 headset that leverages augmented reality and gesture recognition to make drone piloting easier, more comfortable, and more intuitive. It describes a system for single-handed gesture control that can achieve all maneuvers possible with a traditional remote, including complex motions; a method for tracking a real drone in AR to improve flying beyond line of sight or at distances where the physical drone is hard to see; and the option to display the drone's live video feed in AR, either in first-person-view mode or in context with the environment.

Keywords: drones; augmented reality; AR; gesture recognition

1. Introduction

Over the past decade commercial drones, and quadcopters in particular, have become increasingly popular and affordable. In addition to their use in professional or casual photography, they have grown into a transformative force in diverse sectors, including inspection [1,2], mapping [3,4], exploration [5], human–machine interaction [6], search-and-rescue missions [7,8], and more. More recently, their combination with virtual and augmented reality (VR and AR, respectively) has yielded new experiences such as first-person-view (FPV) fights (www.dji.com/gr/dji-fpv, accessed on 20 December 2021), AR training (vrscout.com/news/dronoss-training-drone-pilots-with-ar/, accessed on 20 December 2021), and mixed reality games (www.dji.com/newsroom/news/edgybees-launches-the-first-augmented-reality-game-for-dji-drone-users, accessed on 20 December 2021).

Learning to pilot a quadcopter effectively can be a challenging task: Conventional remote controllers are largely unintuitive, as they use two joysticks to control flight, with one corresponding to horizontal motions (pitch and roll) and the other to vertical (throttle) and rotational (yaw) motions. Additional wheels and buttons control the drone's camera. While basic motions in relaxed circumstances are achievable with short training sessions, complex motions can be more difficult. Moreover, in challenging or stressful circumstances (e.g., in disaster response or under tight time constraints), the lack of intuitive controls add additional cognitive load on the pilot, affecting his/her safety and efficiency. In addition,

the remote controller in itself, requiring the continuous use of both hands, can be restrictive. Although alternative remote controllers, such as the DJI motion controller, provide a less cumbersome solution, they cannot support the full range of motions executable by a traditional remote.

Another challenge stems from the difference in position and orientation between the drone and its pilot, which can make it difficult to match the drone's camera feed with the pilot's surroundings. In particular, especially when the drone is at some distance or out of direct line of sight, it can be challenging both to judge its position and orientation and have a direct understanding of where its camera is pointing at. Moreover, as the video feed is normally displayed on a screen attached to the remote, it requires users to constantly change their focus from the drone (in the air) to the screen (usually held at chest level, hence towards the ground), glancing from one to the other. This can be both tiring (mentally as well as visually) and adds to the cognitive load, as the user alternates between two different points of view. Although VR FPV mode eliminates the change of perspective, it leaves users unaware of their own surroundings, which can be prohibitive in many cases.

In this paper, we propose an AR solution that leverages gesture recognition, computer vision AI, and motion tracking techniques to provide a natural user interface for intuitive drone control and contextualized information visualization. Based on the Microsoft HoloLens 2 headset (https://www.microsoft.com/en-us/hololens/hardware, accessed on 20 December 2021), the presented system allows users to pilot a drone using single-hand gestures, improves tracking the position of the drone in an AR environment, and provides video feed visualization in either the contextualized or FPV modes. It allows for a comfortable flight, as both hands are free and can be used for other tasks when not directing the drone. AR tracking improves drone visibility in longer distances or in low light conditions. The visualization of the drone's video feed in the AR display means that users can view both the video and their surroundings without glancing towards different directions. In conjunction with tracking, a contextualized video view projects the video in the approximate location and/or direction of its contents, considering the drone's location and orientation, resulting in a mixed reality view combining the virtual video feed with the real world. The main contributions of this work are as follows:

- Gesture control for drones, supporting all drone and camera motions, including complex motions;
- Drone tracking in AR, based on cumulative Inertial Measurement Unit (IMU) readings and an initial relative pose calibration, while exploring visual-based drift correction;
- Visualization of the drone's camera feed in AR in context with the real world, considering the relative pose between drone and user, with the additional option to explore and integrate depth estimation for more accurate placement.
- A unified solution encompassing all of the above, consisting of a HoloLens 2 user interface app, an Android UAV interface app, and a Kafka message broker.

The rest of the paper is organized as follows: Section 2 discusses earlier work related to the presented solution, in particular regarding drone gesture control, drone tracking, and the visualization of information in AR; Section 3 presents the system's architecture, including hardware, software, communication, and data flow; Section 4 describes the primary technical tasks that were needed to realize the solution; Section 5 discusses the testing of the system, including subjective and objective measurements and feedback; and finally, Section 6 summarizes this work and outlines possible future developments.

2. Related Work

2.1. Gesture Control

With the ever growing accessibility of drones and the range of their potential applications, the users acting as pilots are no longer limited to highly-trained professionals. This, in turn, leads to a shift in the design of human–drone interfaces as there is a need for simplified control methods [9] that provide an easy way to control a drone without the need of extensive training. There are now several approaches that go beyond the standard

remote controller with joysticks and allow the user to use inherent expression and communication means such as gesture, touch, and speech. These methods are also known as Natural User Interfaces (NUI) and have the advantage, in some application domains, to feel intuitive and require less training time and cognitive effort. Suárez Fernández et al. [10] implemented and tested a gesture drone control interface utilizing a LeapMotion sensor (https://www.ultraleap.com/product/leap-motion-controller/, accessed on 20 December 2021). At the early stages of our work, we applied a similar approach using LeapMotion, but later, we abandoned this plan for more efficient AR interfaces. Herrmann and Schmidt [11] designed and evaluated an NUI for drone piloting based on gestures and speech in AR. Their study results indicate that the use of the designed NUI is not more effective and efficient than the use of a conventional remote controller. However, the selected gesture "alphabet" may have played a crucial role on the study results. For example, their input alphabet included combinations of head and hand movement in order to perform certain navigation tasks, something that many users of the study found confusing. In our approach, although head gestures do exist, they are not combined with hand gestures, and they are only used to perform auxiliary tasks in certain navigation modes. In their survey about human–drone interactions, Tezza and Andujar [9] classify gesture interaction as an intuitive and easy to learn control interface but with the disadvantages of high latency and low precision. However, we argue that the current technologies for gesture recognition are able to overcome the aforementioned disadvantages.

2.2. Tracking

Positional or motion tracking is the ability of a device to estimate its position in relation to the environment around it or the world coordinate system. As described by Kleinschmidt et al. [12], there are two fundamental solutions for positional tracking, marker- and non-marker-based methods. Marker-based methods require the use of standard tags such as ARTags and QR codes for the coupling between an agent's camera and the tracked element. In our application both approaches are available since each one has certain pros and cons: Our current non-marker-based approach does not require the use of tags, however, it requires a two-step calibration process. Marker-based approaches are used in time-critical tasks or in hostile environments where there is no sufficient time for calibration, however, they can only be performed with drones that are already equipped with the compatible tags. Regardless of the approach used, the tracking process is prone to the accumulation of errors and latency, and is in general computationally intensive. Several methods attempt to overcome these challenges. Islam et al. [13] introduced an indoor tracking system with a rotary-laser base station and photo-diode sensors on tracking objects. The base station scans the space and detects the UAV sufficiently. The error is almost negligible as the estimation in 5 m is only 13 cm. Arreola et al. [14] proposed a position estimation method using a low-cost GPS and optical flows provided by UAV's camera. This approach is available only outdoors since the system uses GPS measurements. In a hybrid case, Tsai and Zhuang [15] adapted optical flow and ultrasonic sensors on the drone and achieved better results than GPS positioning. A similar approach was implemented for real-time pose estimation by Hong et al. [16], combining the Cubature Kalman Filter on IMU readings with an optical-flow-based correction to minimize positioning error.

2.3. Computer Vision for AR

For successful AR use and application, a detailed understanding of the scene is required, a challenging task that includes multiple sensor fusion, object tracking and real, and virtual world registration [17]. Computer Vision approaches have been used in AR applications for object detection and tracking [18,19], object pose estimation [20], localization [21], and even gaze-based UAV navigation [22]. In our application, we utilize computer vision techniques for visual pose drone detection [23].

2.4. Situation Awareness and Virtual Information Visualization in AR

Situation awareness (SA) is related to the perception and comprehension of a dynamic environment. Increased SA is related to improved performance and efficiency in the completion of complex tasks and operations. According to Endsley's definition [24], SA comprises three main phases: perception of the relevant elements, their relation to the operation goals, and projection of the operation environment future states. In the context of disaster response and law enforcement operations, drones can provide a means to expand SA by providing video and images from advantageous vantage points [25,26]. Leveraging AR visualization and tools can have positive effects in SA as task-relevant information and feedback can be displayed on the same screen and in the context of real-world elements. The user can easily correlate the augmented information elements with the real world, avoiding additional cognitive load. Earlier work [27,28] has leveraged AR for vehicle operators in maritime applications. In the AR environment, information from maps, radars, and other instruments were fused with the real world view. Their results indicate improved SA of the operators. Lukosch et al. [29] used AR to support information exchange for operational units in the security domain. Their results showed improved SA for personnel that were not present in the scene.

2.5. Visualization in Context

Apart from visualizing virtual information with the aim of improved perception and SA, another key element in our application area is live video in contextualized mixed reality. Cameras are nowadays ubiquitous and used for a wide space of applications, quite often deploying multiple cameras at once. Having multiple views from an observed area, while useful, can also be straining for the observer who, in order to understand the situation, needs to mentally reconstruct the observed area and understand the spatial relations between the different views. In order to reduce this mental workload, new design approaches should be identified. Brejcha et al. [30] introduced a pipeline for aligning photographs in a reconstructed 3D terrain based on location and rotation metadata included in the photographs. The produced result offers improved spatial orientation and scene understanding and overall an enhanced first-person experience for the viewers. Wang et al. [31], suggested and tested different visualization techniques for embedding videos in a 3D spatial environment. One of their preferred approaches is the Billboard video view. In this approach, the video is projected in a rectangle that orients itself in order to face the user. A modified Billboard approach is utilized in our AR application.

3. Architecture

3.1. Overview

As stated in Section 1, the main focus of this work is to provide drone pilots with intuitive gesture control, drone tracking in AR, and a video feed displayed in context with the real environment. This section presents the system architecture developed (depicted in Figure 1) to support these functionalities.

The two end-points of the system are the pilot and the drone. The pilot interacts with the system via an autonomous mixed reality headset that provides hand-tracking capabilities along with visualization in AR. A HoloLens application was developed to support gesture acquisition, give feedback to the pilot, display the received video feed and the drone's tracked position in AR, and handle connectivity and common settings. The drone connects with the system via a direct wireless link with its remote controller, which is connected to a smartphone running a custom Android app to support the needed functionalities. These include transmitting telemetry data from the drone to the AR device and control commands from the AR device to the drone. The communication between the AR device and the drone is routed through a message broker, while the video data are streamed via a direct socket connection between the smartphone and the AR device.

Figure 1. System architecture and data flow between components.

There are three primary data flows pertinent to the desired functionalities:

- Hand gestures are captured, interpreted, translated to drone commands, and forwarded to the drone.
- Telemetry data are used to estimate the drone's current position, which is then sent to the AR device.
- Live video is captured by the drone's camera, transmitted to the remote controller, and then streamed to the AR device directly.

The remainder of this section further describes the individual system components and their functionalities, while the next section (Section 4) provides technical details regarding the main components of the solution.

3.2. Hardware

The main hardware devices used in the proposed solution are the drone, and the AR device used as a user-interface, both of which are briefly described below. Additional hardware, such as the smartphone connected to the drone's remote and the computer server hosting the message broker, are generic and need no further elaboration.

Developing and testing the architecture was performed using DJI's Mavic 2 Enterprise Dual and Mavic Mini drones. The DJI Mobile SDK platform offers high-level control of the aircraft and the camera–gimbal system, low latency video feed retrieval from the camera, and state information about the aircraft and the controller through various sensors, all of which are essential for development. For outdoor testing, we primarily used the larger Mavic 2 Enterprise Dual drone with its onboard obstacle avoidance system, which was important for safety reasons when implementing gesture control. For indoor testing, the smaller and lighter Mavic Mini was used.

Microsoft's HoloLens 2 was used as an augmented reality platform. HoloLens is a head-mounted system that can display virtual objects in the real world, with the use of two see-through holographic displays. It has a plethora of onboard sensors to understand its surrounding environment (spatial mapping) including four RGB cameras, which combined with a Time-of-Flight Depth sensor, are used to track the user's hands. In addition, two infrared cameras are tracking the user's eyes, optimizing object rendering, and a microphone array can be used to issue voice commands. We capture hand tracking data through the HoloLens interface and translate them into UAV commands to control the drone and the camera. We also use the head tracking information the HoloLens provides to rotate the drone in accordance to head movement. HoloLens was selected because it provides three features necessary for the presented application: AR visualization, hand tracking, and autonomous operation (i.e., not tethered to a computer).

3.3. Communication

Information exchange between the different modules of the presented architecture is achieved via the Kafka (https://kafka.apache.org/, accessed on 20 December 2021) message broker. We use Confluent's implementation (https://www.confluent.io/, accessed on 20 December 2021), which includes a built-in REST proxy and a corresponding API, which are necessary since there are no Kafka clients compatible with UWP (Universal Windows Platform) and the HoloLens. The broker's contents are organized into topics, and each topic corresponds to different functionality of the system (e.g., control commands, positioning info, etc.). The messages abide by the JSON protocol, which is natively supported by Kafka, and their structure is strictly defined. This not only ensures compatibility between modules but also provides significant modularity since new message types can be added, removed, or modified in future versions since they comply with the same JSON structure. Finally, our modules use HTTP operations (POST, GET) to produce and consume the stated messages.

3.4. Augmented Reality Application

The augmented reality app was developed for HoloLens using Unity3D (https://unity.com/, accessed on 20 December 2021) and the Mixed Reality Toolkit (https://github.com/microsoft/MixedRealityToolkit-Unity, accessed on 20 December 2021). The main functional modules of the application are as follows:

- **Drone control commands**: This module is responsible for capturing the gesture/voice interactions of the user, translating them to specific control commands (i.e., pitch, roll, yaw, and throttle values), and sending them to the the Android app via the Kafka broker.
- **Drone tracking**: The drone tracking module is responsible for monitoring the spatial relation between the real world elements (the drone and the app user) and its virtual representatives. Drone tracking is the backbone for many feedback cues (visual, textual, contextualized videos) that provide the user with enhanced spatial perception. Tracking is possible following an initial calibration process and an IMU-based approach.
- **Video feedback**: The live video feed from the drone's camera is projected on a canvas inside the augmented environment. The user can simultaneously be aware of his/her surroundings in the real environment while also viewing the drone's video feed in his/her field of view (FoV). With minimal head movement and loss of focus, the user can perceive the surrounding environment from two different viewpoints. This video projection is modifiable and can either be placed in the center of the user's FoV as shown in Figure 2 (FPV mode) or on a smaller panel projected from the drone's virtual counterpart (Figure 3). The center placement is useful in tasks where higher detail of the drone's camera feed is required. This contextualized video feed mode is called "egocentric" view with the drone at the center and allows for easier perception of what the drone "sees" during the flight and of the spatial correspondence between the drone's and the user's point of view. In contrast, the FPV mode is useful in tasks where higher detail of the drone's camera feed is required. In addition, when using a drone equipped with an infrared camera, the user can choose between three different modalities, visible (RGB), infrared (IR), or fused (MSX).
- AR feedback and visualization: GUI elements and various visualization features were added in the AR application to provide feedback and various controls. Emphasis was given to creating an easy-to-use application and increasing the SA of the user. In more detail:
    - Visualization of the virtual hand joints overlaying on top of the user hands, making it possible for the user to directly check if his/her hands are correctly perceived by HoloLens (Figure 4).
    - Drone visualization based on the drone tracking module. A virtual drone is overlaid on top of the real drone so that the user is aware of the drone's relative

position even if it is not in a direct line of sight (e.g., behind a wall or building) or too far to be easily visible with a naked eye.

– An extensive virtual menu that includes all high level commands and toggles for enabling the application features is present in the lower part of the application view. The menu can be be hidden in order to not obstruct the user's field of view.

– A navigation feedback panel is placed at the top part of the application's window. In the feedback panel, the current perceived navigation commands are listed alongside with other drone- and user-related information such as the drones's flying altitude and horizontal distance from the user, the drone heading, and the user heading.
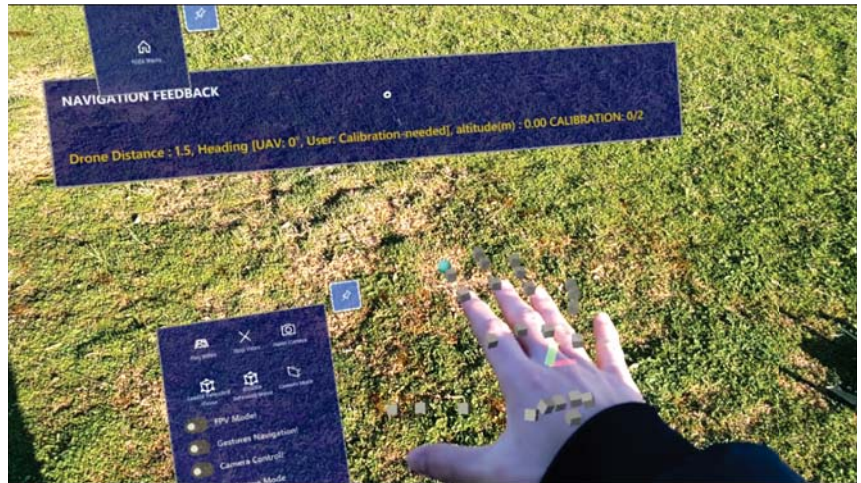

Figure 2. First Person View (FPV) into the Augmented Reality environment. Real and virtual drones are shown in the lower right corner.

Figure 3. The AR Egocentric View mode. The AR user can be shown in collinearity between the user and the drone's camera in the right corner.

Figure 4. Hand-tracking as visualized in our AR application. Cubes represent hand joints. (The displacement of joints is due to the location of camera capturing the screenshots; the user of the app can see the virtual joints on top of his/her actual joints.

3.5. UAV Interface Application

An application was developed to act as a communication bridge between the DJI drone and the rest of the system architecture. We chose the Android platform since it was the most mature and versatile Mobile SDK platform DJI had to offer at the time of development. The app is installed on an Android smartphone connected to the remote controller via a USB cable. The drone connects to the remote controller via DJI's proprietary communication protocol, OcuSync, while the smartphone connects to the rest of the system by WiFi or a commercial mobile network. The app's primary responsibilities are:

1. Receiving control commands from Kafka and forwarding them to the drone;
2. Collecting the drone's IMU readings, aggregating them to estimate its position, and posting this to Kafka at regular intervals;
3. Sending the drone's live video feed directly to the HoloLens via network sockets.

The application, depicted in Figure 5, displays practical information (e.g., battery status of the aircraft and of the remote controller), along with a live view of the drone's camera feed. Buttons are also present to perform various actions. The "Configurator" button exposes the user to a settings page shown on the left pane of Figure 5, where several parameters can be configured, including connection settings, the sensitivity of the drone to gesture commands, and infrared visualization options.
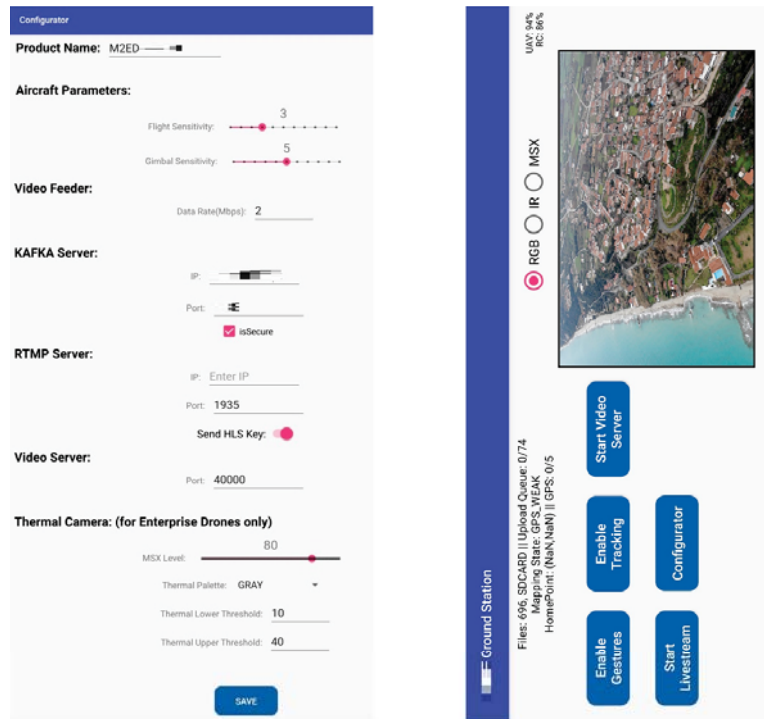
Figure 5. The Android UAV interface app. Left: the app's configurator page, with setting regarding connectivity, gesture command sensitivity, and infrared view display. Right (rotated): the app's main view, showing a live view of the drone's camera feed.

4. Methodology

The realization of the presented solution can be broken down into five tasks, each regarding a different aspect of the gesture control or the AR visualization pipeline:

- **Gesture definition**, in which an appropriate set of hand gestures was selected to control the drones, meeting requirements relating both to usability and control. This was the focus of earlier work ([32]), refined and updated for the current work;
- **Gesture acquisition**, in which users' hand gestures must be captured, interpreted, translated to flight or camera control commands, and forwarded to the drone via the UAV interface Android app;
- **Drone position tracking in AR**, in which the drone's motions must be tracked in reference to the virtual world, based on aggregated IMU reading and optionally improved by visual cues;
- **Calibration**, in which the virtual environment must be aligned with the real world, in terms of both translation and rotation, so that virtual objects can be displayed in the context of the environment. Calibration is necessary both for tracking and displaying the drone in AR and displaying a contextualized video feed, which depends on tracking;
- **Video transmission and visualization**, in which the drone's video feed must be transmitted to the HoloLens and displayed in AR in (near) real time, via the UAV interface Android app.

The rest of this section describes in detail each of these five tasks, presenting the methodologies followed, noting weaknesses, and outlining possible future improvements.

4.1. Gesture Definition

4.1.1. Requirements and Considerations

In order to develop a viable alternative drone control system, it should allow users to perform the same motions as a regular handheld remote: pitch, roll, yaw, throttle, and their combinations, as well as camera motions. Similarly, it should allow users to define the sensitivity of each command, and by extension, the amplitude of the corresponding motion.

Designing Natural User Interfaces (NUI), such as gestures, some additional requirements must be taken into account to achieve intuitive interaction. Peshkova et al. [33] explained that the gestures should be related to each other while following a single metaphor. In the same study, the use of multi-modal interaction, such as a combination of gesture and speech commands, is encouraged in order to increase naturalness. Hermann et al. [11] additional requirements were highlighted including avoidance of non-ergonomic positions (as described in [34]) and the presence of some form of feedback. In an AR environment, several forms of feedback can be integrated in the real-world view of the user as overlaid virtual objects.

Hence, UAV gesture control has three primary aims:

1. To provide an easy-to-learn and intuitive interface;
2. To be physically comfortable and ergonomic;
3. To allow the full extent of drone motions, including combination motions and variable velocities.

4.1.2. Gesture Vocabulary

In a previous user study and survey [32], we tested two sets of gesture vocabularies, a finger-based and a palm-based vocabulary in a simulated drone navigation environment. Users were required to navigate a virtual drone in an outdoor and an indoor environment. In the finger-based mode, each gesture is defined by which fingers are extended, and the velocity value is defined by the pointing direction of a selected extended finger. In the palm-based mode, the operator uses the positioning and orientation of his/her open palm (all finders extended) to control the drone. The subjective study results showed a clear user preference for the palm-based control, which was described as more comfortable and easier to learn and use. The objective metrics showed faster task completion using the palm-based controls, however, finger-based control offered more precise navigation. The overall objective score showed that the palm-based control has a slightly better performance.

The study results are aligned with findings in [33] that intuitive NUIs should be based on a common metaphor. In this case, the metaphor chosen is that the drone corresponds to the user's hand, and hence mimics and follows all its movements. Therefore, raising the hand up higher will correspond to an ascend (increase throttle) command; a tilt of the hand will correspond to the drone assuming a similar angle (pitch and/or roll); a horizontal rotation will correspond to yaw; and so on. This metaphor, validated by the user study, addresses the first aim of gesture control.

The second aim of gesture control is to avoid non-ergonomic, physically stressing hand gestures. It may be noted that even easy-to-perform gestures can be tiring when performed repeatedly or may oblige users to hold their hand/arm steady in the same height for a long time. In order to avoid the latter, we applied a relative gesture vocabulary based on a varying reference position. One key gesture is used as a reset and calibration command. When the user performs this key hand gesture, the current hand pose is set as the neutral (resting) position, and all following gestures are interpreted relative to this. This allows users to chose the resting position that is most comfortable to them and even define new resting positions in preparation for certain maneuvers.

Hence, a user wishing to command the drone to ascend may define a low resting position, allowing her to move her hand higher with no discomfort. Later, in preparation for a descent, a higher resting position may be chosen so that the user can lower her hand easily. The reset and calibration command is tied to the user opening the palm and extending the fingers. Hence, after a brake and stop command (closed fist), a new resting

position is always defined before the user issues a new command. While the hand is closed and no commands are issued, users can position their hand in preparation for the next gestures safely.

This palm-based gesture set was expanded in later work to include take-off and landing gestures [35]. Similar to a handheld remote, these gestures are mapped to hand positions assumed and held over a couple of seconds. To differentiate them from the other UAV control commands, take-off and landing use an upwards-facing palm. The full palm gesture vocabulary used for drone navigation is shown in Figure 6. Moreover, the user's other hand can be used to control the camera gimbal, where the same set of gestures are mapped to camera pitch and yaw.
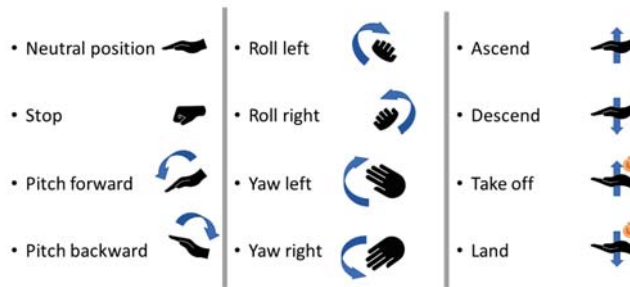

Figure 6. The palm gesture vocabulary used for drone navigation.

It can be noted that the selected gesture set can be used to perform any UAV motion achievable with the traditional handheld remote. Velocities of UAV commands are mapped directly to the angles or distances relative the resting position, allowing for a continuous control ranging from no motion at all to fast motion. Combination motions, such as pitching forward while yawing a little to the left and slowly descending are easily achievable. This can be further substantiated, as the human hand, like all real-world objects, has six degrees of freedom (translation and rotation along three axes), while a quadcopter's control has four (pitch, roll, yaw, and throttle). This demonstrates that movements are independent of each other and can hence be freely combined. Naturally, the same holds for the camera-controlling hand. Therefore, the third aim of gesture control is addressed.

4.1.3. Drone Control Features

The drone control module was implemented following an agile development process; starting from a set of basic features, continuous testing and user feedback led to the refinement of the user requirements. Initially, the **hand gesture drone control** was implemented and three additional features, **hand gesture camera control**, **periscope** mode, and high-level **voice control** commands were added.

The primary task was to accurately navigate the drone using the selected palm gestures. It should also be noted that when no gesture is performed or when the user hand is not visible, no command is sent, and the drone stops. Inside the AR application, visual cues were displayed providing feedback to facilitate the navigation task. Drone navigation is performed using the user's right hand by default, however, this can be a parameter.

In the hand gesture camera control, the unassigned user hand, by default the left hand, is used for controlling the view direction of the drone's camera. This feature is controlling the camera gimbal, which is able to perform 2DoF movements: rotation up/down (pitch) and rotation right/left (yaw). The gesture vocabulary used for camera control is similar to the vocabulary for drone navigation, however, there are less defined gestures since the camera's possible movements are fewer; by tilting the open palm left or right, the camera

turns to the corresponding direction in the vertical axis while, by tilting the palm up or down, the camera rotates in the corresponding direction in the horizontal axis.

Periscope mode is an additional form of gesture control, which does not involve the use of hands but it is based on the user's head direction. When Periscope mode is enabled, the drone viewing direction follows the user's head direction in real time. For example, when the user rotates his head to look 90° east, the drone rotates to the exact same direction. Periscope is an auxiliary feature allowing for a quick and intuitive inspection of the surrounding environment that has collected very positive reviews from the end-users.

Finally, voice commands are used to perform high-level commands such as resetting the camera direction. Voice commands are completely optional, as all the commands can be alternatively performed by buttons and controls available in the virtual application menu, however, they offer a multi-modal tool of interaction and at the same time allow the user to use their hands for controlling the drone or perform an other task and at the same time dictate the desired command using speech.

4.2. Gesture Acquisition

4.2.1. Background

Our early research [32] into gesture acquisition for drone control considered two different hardware peripherals: the AvatarVR glove (https://avatarvr.es/, accessed on 20 December 2021), a wearable with embedded IMU and touch sensors, and the LeapMotion controller (https://developer.leapmotion.com/, accessed on 20 December 2021), an infrared LED and camera device. The former was found to falsely report finger curl when rotating the hand, which made it incompatible with the open hand metaphor described in the previous subsection; hence, it was discarded for the current application. The LeapMotion controller performed well in a lab setting but the lack of wireless portability (as it needs a USB connection) and its inability to track hands in an sunlit outdoor environment were important limiting factors. However, it served well for the initial development phase of the solution, as it includes a Unity API. Most of the gesture recognition and interpretation functions were based on the LeapMotion API and later adapted for the HoloLens.

Google's MediaPipe Hands [36] was also considered for purely RGB-camera-based gesture acquisition. This has proved robust in a wide range of lighting conditions, making it suitable both indoors and outdoors. However, as it is compatible with Unix and Android systems only, the integration of this modality into the HoloLens has not been realized. It has been used with a webcam for training on a computer simulator, and it could be considered for future developments on different AR devices or standalone gesture control applications not including AR visualization.

4.2.2. Gesture Acquisition and Interpretation in HoloLens 2

Gesture recognition for the palm-based control in HoloLens 2 utilized the MRTK Unity3D plugin and more specifically, the Hand-tracking API. The MRTK hand-tracking API did not provide (at least during the time of the development) high-level functions for recognizing extended fingers or an open/closed palm. The main values provided are handedness (left or right hand), joint transform (the position and orientation in the 3D space), and joint type (e.g., index tip, index distal, metacarpals, etc.). As a result, the development of palm navigation had to start by implementing a Gesture Recognizer component able to detect an open palm gesture in real-life conditions where fingers are quite often occluded or not completely straight, etc. The gesture recognizer component is based on the work provided by Rob Jellinghaus (https://github.com/RobJellinghaus/MRTK_HL2_HandPose/, accessed on 20 December 2021), but is heavily modified to adjust to our case needs. The code takes into account finger–eye alignment and co-linearity between finger pairs to cope with finger occlusions. It also uses ratios between different hand's parts instead of absolute measurements to be able to handle different hand sizes. Since in the palm-based control we are only interested in two classes of gestures, open/extended palm and closed palm,

the gesture detector does not have to be very precise in recognizing gesture details. For that reason, the gesture classification criteria are modified to match the needs of the application: The criterion for an open palm classification is the detection of an extended thumb and at least three extended fingers. This way, the recognizer is more sensible in recognizing an open palm gesture, which is the main state of interest.

When the Gesture Recognizer module detects an open palm, the hand joints' information (position and rotation) is processed by the Palm Navigation module that calculates the navigation commands (pitch, yaw, roll, throttle, and take off/landing) and their amplitude (or velocity values) based on the hand joints' current and past rotation angles. As mentioned in Section 4.1.2, in order to avoid physical stress, the reference null position can change every time the user performs the reset command (closed palm gesture). The next open palm position after the reset command corresponds to the reference position and the joint angles and position at that point are stored as the neutral (or zero) transforms for the future commands.

In particular, three components of the hand's position are relevant: the hand's Up normal vector, perpendicular to the palm; the hand's Forward normal vector, perpendicular to Up, and facing forward, along the direction of the middle finger; and the hand's vertical position. An overview of the vectors and their correspondence with the drone control values is shown in Figure 7. Interpretation is relative to the reference hand position. The current position's normals are translated to the y-axis and analyzed into components. Pitch is computed by the angle of the Forward vector to the xz-plane. Yaw is tied to the angle of the Forward vector's xz-component to the x-axis. Roll is computed by the angle of the Up vector's yz-component to the y-axis. Throttle is proportionate to the vertical (y-axis) distance between the current position and the reference. All commands allow for a "neutral zone", so that minor or involuntary motions are not translated to a drone command.
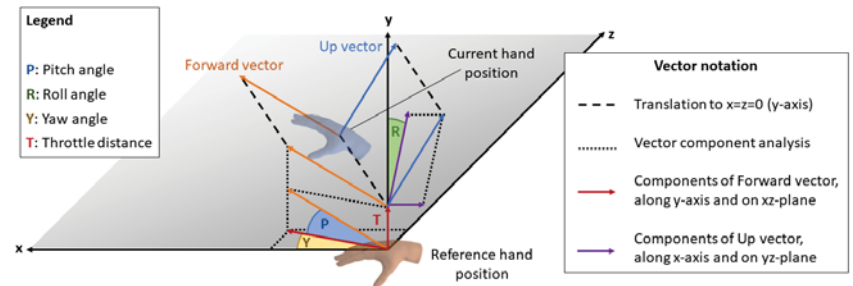
Figure 7. Palm vectors and angles used to interpret gesture commands. Interpretation is always relative to the reference position, whose normal vectors form the axes x, y, and z. The current position's normals are translated to the y-axis and analyzed into components. Pitch, roll, yaw, and throttle values are then computed according to the angles and distances between these component vectors and the reference axes.

4.3. Drone Position Tracking in AR

Drone tracking is used to monitor the physical location of the drone during a flight. In our case, this information is utilized in two different ways: to assist monitoring and piloting the drone when it is out of line of sight or too distant to distinguish it clearly using a virtual drone marker in the AR environment and to position the AR video canvas according to the drone's location and orientation and hence in context with the real environment.

Drones are commonly equipped with two positioning mechanisms: GPS and IMU. GPS is commonly used to provide an approximate location-based satellite communication. However, it presents two major drawbacks: It is only available outdoors, and its precision is limited, ranging from 2.5 m to 10 m or more [14]. This precision can be inadequate for flights that require precision. Hence, the presented system relies on IMU readings. The DJI SDK

offers no access to low-level IMU measurements; instead, it combines the readings from multiple sensors, including magnetometer, gyrospope, and accelerometer measurements to report the estimated velocity of the drone, at regular intervals. Velocity is reported in a North–East–Down (NED) coordinate system, with an origin point at the drone's starting location. The reported velocity measurements *V* are collected by the Android UAV interface app, multiplied by the interval time *T* to yield translations in distance, and summed to provide the estimate position of the drone *D* at time *t*, relative to its starting point:

$$D_t = \sum_{i=0}^{t} D_i = \sum_{i=0}^{t} V_i T_i \tag{1}$$

The above assumes that between reports, velocities remain constant, which is not the case when performing maneuvers. However, with a 100 ms reporting period, these errors are negligible. A more significant drawback to this procedure is the low precision — two decimal places—at which velocities are reported by the SDK. This makes for an average error of 0.005 m/s. Naturally, this becomes more significant at lower velocities, where it can account for up to 16% of the real velocity. Even without compensation, the position as derived by aggregated IMU readings is more accurate than GPS over short periods of time and short distances. With the error-correcting compensation described in Section 5, the accuracy improves significantly and is adequate for both locating and guiding the drone, perhaps excluding very precise maneuvering in tight spaces. For longer distances, GPS reading can be used correctively to ensure that the aggregated IMU drift is capped to the GPS precision.

The application posts the position related data presented in JSON format on the Kafka broker. The post frequency is four times per second in order to consume less network and computational process power. On the client side, the HoloLens application connects to the Kafka broker and consumes these messages on a specific topic. Based on the message information, it renders a virtual drone-like object into the augmented reality environment, overlaying the position of the real drone. In order to achieve this coupling, a prior calibration process is required to align the HoloLens's internal coordinate system with that of the drone.

4.4. Calibration of the AR Environment

Tracking a real object in augmented reality and visualizing it in context with the real environment requires a correspondence between two different coordinate systems: one based in the real world and one based in the virtual world, which will be superimposed on the real world to provide the AR graphics. As outlined in Section 4.3, the drone's position is continuously estimated based on aggregated IMU readings and its heading is supplied directly by its onboard compass. Hence, the calculated pose is expressed in relation to a system of coordinates with the drone's starting location as an origin point and its y-axis aligned with the north.

The HoloLens does not use its internal compass to orient its internal coordinate system, and the compass readings are not readily available to Unity apps. Therefore, the AR elements, including the virtual drone marker and the video panel, must be expressed in relation to the internal coordinate system, with an origin and y-axis direction equal to that at the user's location and heading, respectively, at the time of launching the application.

In order to link the two coordinate systems and place the virtual drone marker in the corresponding position of the physical drone and, by extension, for the video panel to be displayed correctly in context with the environment, a calibration procedure should be performed. The calibration process aims to calculate the relative translation and rotation between the two systems. Even though both real and virtual objects are mobile in 3D, with six DoF, the drone's altitude is tracked and reported independently via its altimeter. Hence, this can be viewed as a 2D problem of axis rotation and translation.

Keeping elementary linear algebra in mind [37], for two 2D coordinate systems with the same alignment (no rotation) and an offset of x'_0, y'_0, if x, y are the coordinates of a point in one system, then its coordinates in the rotated system will be:

$$\begin{bmatrix} x' \\ y' \end{bmatrix} = \begin{bmatrix} x \\ y \end{bmatrix} + \begin{bmatrix} x'_0 \\ y'_0 \end{bmatrix} \qquad (2)$$

Meanwhile, for two 2D coordinate systems with the same origin point (no translation) and a rotation of ϕ, if x, y are the coordinates of a point in one system, then its coordinates in the rotated system will be:

$$\begin{bmatrix} x' \\ y' \end{bmatrix} = \begin{bmatrix} cos(\phi) & sin(\phi) \\ -sin(\phi) & cos(\phi) \end{bmatrix} \begin{bmatrix} x \\ y \end{bmatrix} \qquad (3)$$

In the generic case of both translation and rotation, we have:

$$\begin{bmatrix} x' \\ y' \end{bmatrix} = \begin{bmatrix} cos(\phi) & sin(\phi) \\ -sin(\phi) & cos(\phi) \end{bmatrix} \begin{bmatrix} x \\ y \end{bmatrix} + \begin{bmatrix} x'_0 \\ y'_0 \end{bmatrix} \qquad (4)$$

Hence, using the real-world drone and its virtual marker in the AR coordinate system as the common point, we can link the two coordinate systems following a calibration procedure. The following text describes both the default, manual calibration method and two vision-based alternatives.

4.4.1. Manual Two-Step Calibration

The manual two-step calibration method relies on users performing the HoloLens's "air tap" gesture to mark the drone's location to the HoloLens app.

In the generic case, the HoloLens app will launch with the user some distance away from the drone and facing a random direction, forming an angle ϕ with the north. Figure 8 shows the two different coordinate systems and the devices' starting location with different colors. In order to translate coordinates from one system to the other, we need to calculate the coordinates of the origin of one with respect to the other (translation vector) and the angle ϕ, which can form the rotation matrix.

During the first step of calibration, the drone has not yet moved, and the user air-taps its present (starting) position, as shown in Figure 8 on the left. That position's HoloLens coordinates (x_0^H, y_0^H) are then captured and stored and form the translation vector.
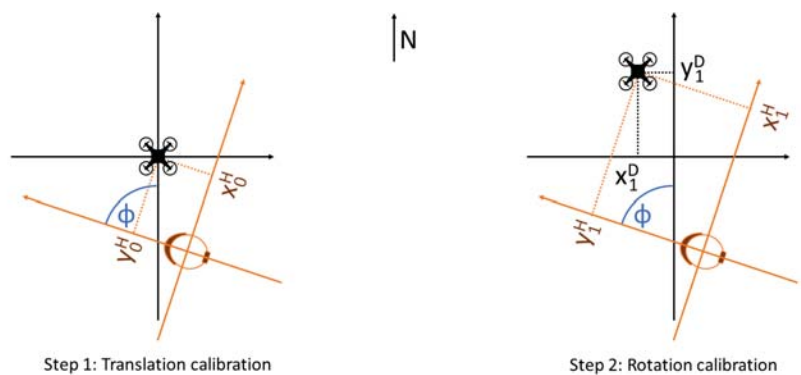
Figure 8. Axis translation and rotation via the two-step manual calibration process. Left: with the first tap on the drone, the translation offset is captured by the HoloLens. Right: after moving the drone a small distance, the second tap captures the drone's position in both coordinate systems (HoloLens and Drone), allowing the calculation of rotation angle ϕ.

To capture the rotation angle, the drone is moved from its starting position. The new position's HoloLens coordinates (x_1^D, y_1^D) are captured with a second air-tap. At the same time, the new position's Drone coordinates (x_1^H, y_1^H) are calculated based on the aggregated IMU readings. Figure 8, on the right, shows this second step. Hence, Equation (4) yields:

$$\begin{bmatrix} x_1^H \\ y_1^H \end{bmatrix} = \begin{bmatrix} cos(\phi) & sin(\phi) \\ -sin(\phi) & cos(\phi) \end{bmatrix} \begin{bmatrix} x_1^D \\ y_1^D \end{bmatrix} + \begin{bmatrix} x_0^H \\ y_0^H \end{bmatrix} \tag{5}$$

The only unknown being ϕ, the above can yield:

$$cos(\phi) = \frac{x_1^H - sin(\phi) y_1^D - x_0^H}{x_1^D}$$
$$sin(\phi) = \frac{x_1^H y_1^D - x_1^D y_1^H - x_0^H y_1^D + x_1^D y_0^H}{(x_1^D)^2 + (y_1^D)^2} \tag{6}$$

Therefore, Equation (6) can be used to obtain rotation angle ϕ, given any non-zero displacement (x_1^D, y_1^D). Knowing both translation and rotation, any future drone-system coordinates can be translated to HoloLens system coordinates to allow visualization in AR.

4.4.2. Visual Drone Pose Estimation

Instead of relying on user information (air-taps) a drone's relative pose (position and orientation) may be inferred from visual data, captured live from the HoloLens's onboard camera. To that end, we propose a method that exploits the latest advances in deep learning to automatically retrieve the 6DoF pose of a drone from a single image. An early version of this architecture, described in more detail in [23], uses a CNN encoder backbone followed by three fully connected layers that output two predictions, one for the translation components and one for the rotation. The translation prediction uses an L_2 loss, while the rotation prediction aims to minimize the angular difference L_R. The two loss functions are weighted by a balancing hyperparameter λ and combined to form the training loss function.

The newest update employs a state-of-the-art architecture, HRNet [38], as a landmark regression network to predict the eight landmark image positions. Then, we retrieve the pose using the predicted 2D–3D correspondences. However, this approach does not permit end-to-end training, as the pose retrieval step is not differentiable. Towards this end, we exploited the recently introduced BPnP algorithm [39], which has been proved to be effective for the pose estimation task [40].

For training our models and evaluating their performance, we have compiled and made publicly available the UAVA dataset (also in [23]), an extensive set of synthetic, photorealistic images of drones in indoor and outdoor environments, which provides ground truth annotations of 2D keypoints, pose, depth maps, normal maps, and more.

Accurate visual drone pose estimation can automate and simplify the calibration process, as both distance (step 1) and orientation (step 2) can be estimated by a single image, automatically, without user input. Visual recognition of the drone and its pose by HoloLens is robust at distances of a maximum of 5–10 m, depending on drone model and size. In addition, this method can be used to periodically correct the position computed by the aggregated IMU readings, offsetting IMU drift and any other errors. With the current version specifications of HoloLens, such an algorithm cannot run continuously in real time. However, even sparse inferences, performed every 5–15 s, can keep IMU drift at a minimum and improve tracking.

4.4.3. QR Code Reading

An alternative to the visual estimation of the drone's pose is to rely on QR codes pasted on the physical drones. The HoloLens provides a built-in capability to detect and read QR codes robustly. Hence, by pasting a QR code on top of the drone, the HoloLens can detect its starting position (analogous to step 1 in the manual calibration process) automatically, with no need of human intervention. While the air-tap determines a single point and hence

provides only position information, the QR code is an object, and its detection can provide both position and orientation. Hence, in conjunction with the heading provided by the drone's compass, both steps of the manual calibration process can be completed in a single QR code read.

Naturally, a QR code pasted on a drone's top is easily readable at short distances (perhaps a maximum of 2 m), i.e., while the drone is landed and the user stands close to it. Hence, while this method can provide fast and automated calibration, it cannot be used for correcting the drone's position during flight and offsetting IMU drift, as is the case with Section 4.4.2.

4.5. Video Transmission and Visualization

When implementing the live streaming feature of the drone's camera video feed to HoloLens 2, we had to consider specific requirements regarding latency and frame rate. In order for the video stream to be usable for piloting, it had to be low in latency and high in frame rate. Overall latency is the sum of two values: the latency from the drone to the remote controller, which depends on the drone manufacturer and the streaming protocols used, and the latency from the remote controller to the HoloLens, via the UAV interface app, which depends on the presented solution. In this case, DJI uses OcuSync for video transmission, which adds a nominal latency of 120 to 270 ms. The following text focuses on the latency between the remote controller and the HoloLens.

Ideally, the overall latency should be low enough to allow easy and safe control based solely on the video feed (e.g., in FPV mode) and frame rate should be high enough for the video to be viewable as a continuous stream. Therefore, we set targets for <350 ms overall latency (hence 120 ms for the Android-to-HoloLens latency) and >15 frames per second (FPS).

4.5.1. Video Streaming

Several methods and streaming protocols were considered for the transmission of live video to the HoloLens, including Real-Time Messaging Protocol (RTMP), Real-time streaming protocol (RTSP), sending frames as individual messages through Kafka, and direct connection via network sockets.

RTMP is a flash-based video streaming protocol routing the video stream through a server and supported natively by the DJI SDK. However, RTMP induces high latency, ranging from one to several seconds, depending on the the network conditions and server location and capabilities. This makes RTMP a good choice for non-reactive video watching (e.g., for a spectator) but unsuitable for remote control. RTSP and HLS (Http Live Streaming) exhibit similar behavior, and hence they were discarded for use in the presented solution.

Sending video frames through Kafka was implemented in an effort to simplify the architecture by routing all data through the same hub (Kafka). Two flavors were tested: sending encoded frames directly from the UAV interface app to the HoloLens and decoding the frames first on Android and then forwarding the decoded data to the HoloLens. Naturally, the first flavor minimizes bandwidth requirements, while the second minimizes the processing strain on the HoloLens. On a local (Wi-Fi) network, bandwidth is less of a concern, hence latency was reduced when streaming decoded frames. However, the frame rate has proved to be too low (at about 11 FPS) in both cases. This is attributed to the HoloLens using a REST API to connect to Kafka (as there are no clients available for UWP), which induces an overhead for each message request. Therefore, this approach was also discarded.

The solution finally selected made use of Network Sockets. This type of connection is Point-to-Point, meaning that once the connection is established, no additional overhead is required for the flow of data. With this implementation, in contrast to the two previous methods, there is no intermediate server between the drone and the HoloLens. The Android device running the UAV interface app acts as a server with the HoloLens being the client. To test this approach, we connected the drone and the HoloLens to alleviate network

bottlenecks. We measured the Android-to-HoloLens latency below 100 ms and the frame rate exactly 30 FPS, which is the native frame rate of the drone's camera. Since both requirements were met, this method is the most appropriate for piloting the drone through the live video feed from the camera.

4.5.2. Video Decoding

On the HoloLens side, the decoding process starts when the connection has been established. For the purposes of the decoding task, we have implemented a dedicated library using the FFmpeg tool, namely, Decoder, to handle video frames. The library has been implemented as a dynamic-link library for the Microsoft Windows operating system and built for UWP architecture compatible with HoloLens 2.

The Android app feeds the AR app with h.264 encoded frames. In the AR application decoding and visualization of the received video frames are handled in two background processing threads. The first thread runs the Decoder module while the second thread is responsible for the frame visualization. Decoding is performed in a 30Hz (native) rate while rendering in 15Hz for performance reasons and efficient management of computational resources. Rendered frames are displayed in a virtual projection panel. In contextualized video mode, this panel is placed in front of the drone, in the direction its camera is facing, while in FPV mode it is centered on the user's field of view.

During development, different methods of video streaming were implemented and tried (as shown in Figure 9). These included RTMP streaming (top left), sending video frames through Kafka (top right), and a direct connection using web sockets (bottom). The latter was finally selected, as it yields the lowest latency and requires no intermediaries.
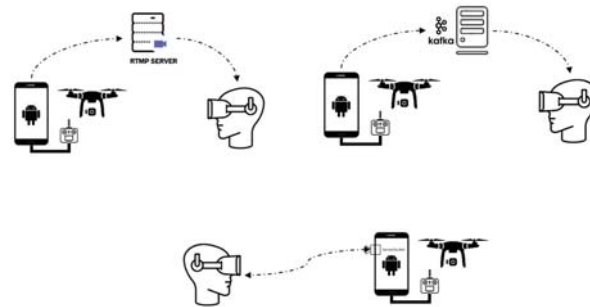

Figure 9. Diagrams of different streaming methods.

5. Testing and Evaluation

The presented solution was tested both subjectively and objectively. Subjective tests included a pre-development user study to define the gesture set used for drone control and a number of field trials where users had a chance to try the system in action. Objective measurements concerned the responsiveness time between gesture execution and drone reaction, IMU-based tracking error, and the latency in video transmission. Each of the above is presented in the following subsections.

5.1. Subjective User Evaluation

5.1.1. Gesture Usability

The gestures and underlying metaphor were selected in a pre-development user study, including a survey resulting from both subjective and objective measurements. Two gesture sets were considered: the palm-based gesture, where the drone mimics the orientation of the user's palm, and a finger-based gesture set with no common underlying metaphor, where three different commands (pitch, yaw, and throttle) were mapped to distinct gestures, differentiated by which fingers are extended. The study aimed to define a finger-based gesture set and then measure user preference and performance in the two gesture sets: the

mutually exclusive, rigidly defined finger-based gestures, and the freer and combinable palm-based gestures.

The study, conducted between December 2019 and February 2020, included two parts. The first part aimed to define the finger-based gesture set. Based on a questionnaire completed by 29 participants, we selected those finger-based gestures voted as both comfortable and intuitively appropriate and mapped them to the 3 drone control commands.

The second part employed a drone flight simulator developed in Unity and coupled with a gesture acquisition peripheral and gesture interpretation programming. It aimed at measuring the ease of learning, usability, and comfort of each control mode, as well as the performance in terms of mission completion time and collision avoidance. An outdoor and an indoor scene were prepared for testing. Participants, including 27 men and 12 women with varying degrees of familiarity with drone control, were asked to control a virtual drone in the simulator and pass through specific waypoints while avoiding collision with walls. Each participant tried both modes (palm- and finger-based) and both types of scenes (indoor and outdoor). Both objective and subjective results were obtained: the former by measuring the timings and collision from the simulator itself and the latter via a questionnaire.

An overview of the results can be seen in Figure 10. The results showed an overall preference for palm-based control. This included both faster timings and less collisions, and a subjective evaluation of it being easier to learn and more comfortable to use. In contrast, finger-based control was generally slower, but could be more precise, and hence useful in very tight environments (e.g., indoors). For more information and further results, the interested reader is referred to the full user study publication [32].
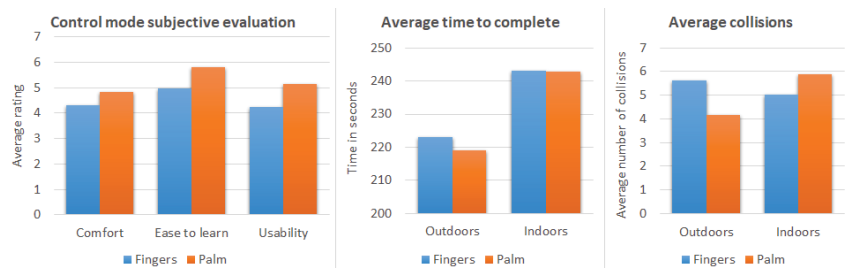
Figure 10. Overview of the gesture selection user study results.

5.1.2. Field Trials

Post-development, the complete system has been demonstrated to both drone pilots and non-expert users. While these evaluations are still ongoing, early results are being used to guide adjustments and improvements in the system. In these events, participants are first responders interested in using drones for search-and-rescue operations. Such mission are often stressful, highlighting the need for more comfortable and intuitive drone control and a video feed easily viewed and placed in context. Early demonstration and feedback sessions have been held in Japan (July 2021—9 participants), Greece (October 2021—6 participants), and France (November 2021—12 participants), with additional events planned for Italy, Finland, and Spain in the first half of 2022.

Initial feedback from these events indicate that gesture control with a real drone is easy to learn for inexpert users, comfortable, and allows full control, including any maneuver possible with a handheld remote. One setback noted concerned the use of the HoloLens in very bright sunlight or a hot day: Both of these conditions degraded the HoloLens's hand-tracking performance, and the heat caused it to shut down after a few minutes. This is expected, as the HoloLens employs passive cooling and is designed primarily for indoor use. However, under non-extreme heat and sunlight conditions, performance has been consistent and robust.

Two experienced drone pilots taking part in the demonstrations stated that they would feel comfortable using gesture control, provided conditions did not degrade the robustness of the HoloLens's hand tracking. The periscope mode, which keeps the drone motionless while tying its yaw to that of the HoloLens, has proven particularly popular and useful for scanning an area.

Regarding drone tracking in AR, feedback was mixed: The manual calibration process, in particular, often proves too difficult and complicated for users. This feedback has driven a turn towards implementing a easier, largely automated, vision-based calibration process, relying on AI visual pose estimation and/or QR codes, as described in Section 4.4. The new calibration process will be tested and evaluated in upcoming demonstration events.

Concerning visualization, users preferred the FPV mode rather than the contextualized view mode. This has been in part due to the difficult calibration process, which is a prerequisite for drone tracking and hence contextualized display. In addition, the size of the contextualized display was sometimes deemed too small. Based on this feedback, future versions will feature a larger canvas on which to display the video feed, as well as the option to scale this canvas using gestures on the camera-controlling hand.

5.2. Lab Testing and Objective Measurements

5.2.1. Drone Responsiveness

When testing alternative drone control methods, an important consideration is the response time of the drone. In the presented solution, this is the latency between the user performing a gesture and the drone responding to this command. In the presented architecture, commands are transmitted from the HoloLens to the UAV interface app via a Kafka broker on the Internet or a local network. The location of the broker, as well as network conditions, can impact drone response latency.

To measure this latency, a high-speed camera was used to capture both the user and the drone at 240 frames per second, also described in previous work [35]. Over a series of experiments, a counting of the number of elapsed frames between the user's gesture and the drone reaction yielded average latency timings. Different locations of the Kafka broker were considered and measured separately: the broker being on the same local network as the HoloLens and the UAV interface; the broker being in a different city in the same country; and the broker being in a different country. Figure 11 shows the minimum and the average timings measured in these experiments. With a camera frame rate of 240 frames per second, measurement error is less than 5 ms, which has has no significant impact on the conclusions of this experiment.

Since a DJI drone consumes commands from its remote controller every 40–200 ms, that degree of latency is unavoidable. In a local area network, the observed latency was minimal, at less than 200 ms, therefore, no worse than that of conventional, handheld remote controls. At more remote broker locales, response latency increases. However, even at around 300 ms, it is still within acceptable limits for drone piloting.
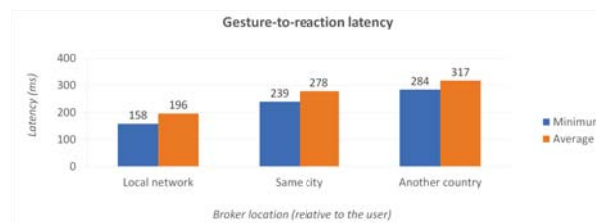
Figure 11. Drone response time measurements according to broker location.

5.2.2. Positioning Accuracy

The basic modality of drone tracking calculates the drone's position based on the IMU readings it reports. Even small error from individual reading aggregate over time resulting

in IMU drift. Hence, any error correction or compensation can improve the robustness of the system in a span of seconds or minutes.

To measure IMU positioning accuracy, an experiment was conducted where the drone would move forward close to ground level and the position as calculated from the IMU readings would be compared to the actual distance traveled, measured physically on the ground. The experiment was repeated for different values of pitch, corresponding to different velocities.

The results of these experiments are presented in Figure 12. The position estimated from the IMU is marked on the horizontal axis, while the ground truth is on the vertical. For reference, the yellow diagonal line marks the ideal of zero error, where IMU measurements equal the ground truth. It can be noted that the error is relatively small for higher pitch values and velocities, increasing when the drone moves slower. This is also evident by the angles of the different linear trendlines. For pitch = 0.3, the trendline is almost parallel to the zero-error line, while for lower pitches, the lines diverge. It may also be noted that IMU measurements steadily report a smaller than the actual distance. Using linear regression, the functions of each trendline can be calculated. In the following, GT is the ground truth, and IMU is the distance measured by the IMU readings aggregation:

$$GT = 1.31 * IMU + 0.20, \ for \ pitch = 0.05$$
$$GT = 1.17 * IMU + 0.27, \ for \ pitch = 0.1 \tag{7}$$
$$GT = 0.99 * IMU + 0.217, \ for \ pitch = 0.3$$

The observations of Figure 12 may be used to improve the IMU measurements by compensating for the error. As noted, this compensation must be inversely tied to the pitch value. Performing linear regression on the coefficients of Equation (7), we can approximate them as a function of the respective pitch value as $1 + (1/52.36 * pitch)$. As the $GT = IMU$ equation (with a coefficient of 1) is the ideal (i.e., no error), the $1/52.36 * pitch$ part expresses the error of the measurements.
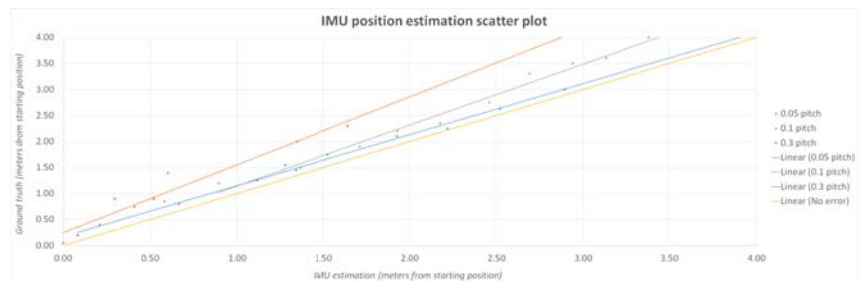
Figure 12. IMU measurements vs. ground truth for various pitch values, including linear trendlines and a no-error line for reference. Note how lower pitch values result in greater errors, and how the angle between the trendlines and the no-error line increases for slower speeds.

Hence, a simple, first-degree estimation of the error E per distance unit would be:

$$E = \frac{1}{52.36 * pitch} \tag{8}$$

Therefore, the compensated distance D_{comp} can be calculated from the measured distance D as:

$$D_{comp} = D * (1 + E) = D * (1 + \frac{1}{52.36 * pitch}) \tag{9}$$

Figure 13 shows the effect of error compensation on IMU measurements. The left graph shows the mean squared error (MSE) of measurements for different pitch values, without compensations (solid lines) and with (dashed lines). The right graph shows the

average MSE values for the different pitch values, again, with and without compensation. It can be seen that compensation has a huge impact, especially on lower pitches (slower drone speeds).

Compensation research is still ongoing. Future tests will include combination motions and different drone models, as well as higher-degree error modeling.
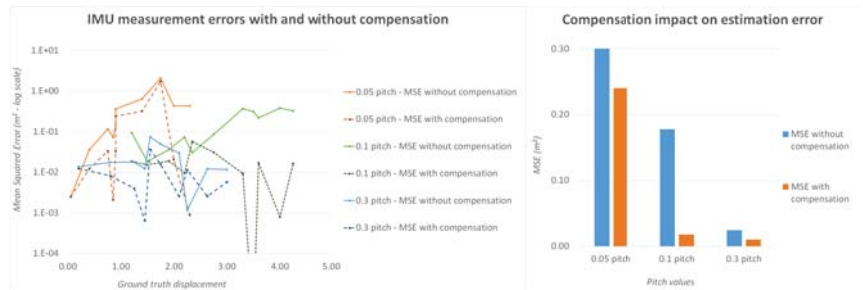
Figure 13. IMU measurement compensation. (**Left**): MSE of the error without compensation (solid lines) and with (dashed lines) for different pitch values. Note that the vertical axis is in logarithmic scale. (**Right**): Comparison of average MSE values with and without compensation, for different pitch values. Compensation has a drastic impact on slower speeds, where the error is greatest.

5.2.3. Video Transmission

A final measurement regarded the latency and frame rate of video transmission and display. End-to-end latency was measured, as above, with a high-frame-rate camera, which yielded an average measurement of 467 ms. While such latency is acceptable for inspection or searching, it is not ideal for piloting a drone in FPV, based on video feedback only. Video transmission latency can be considered in two steps: from the drone to the UAV interface app connected to the remote controller and from there to the HoloLens. The first part was measured at 386 ms, accounting for the larger part of the overall latency. However, this is significantly greater than the timings reported by DJI (170–240 ms) (https://www.dji.com/gr/mavic-mini/specs, accessed on 20 December 2021). Further investigation into this could result in decreased video latency. A full frame rate of 30 frames per second (native to the drone's camera) was achieved.

6. Conclusions and Future Steps

6.1. Conclusions

In this paper, we have presented a unified system for AR-integrated drone use, encompassing gesture control, tracking, and camera feed visualization in context with the user's environment. We have outlined the overall system architecture as well as individual components, described the mechanics of the vital tasks necessary for its function and conducted both objective and subjective evaluation experiments. Different aspects of the proposed solution were evaluated, with the results described in Section 5, including gesture selection and usability; drone responsiveness in terms of time lag; drone tracking accuracy and the efficacy of compensation; and video transmission quality.

Although the presented implementation focused on specific hardware (the HoloLens and DJI drones), the underlying logic and architecture are modular and not tied to the current hardware choices. As mentioned in the Section 4.2, the same gesture control methodology has been implemented and tested successfully with alternative hardware, including a regular webcam or smartphone camera. Hence, integration with different drone models or AR hardware is possible and mostly a matter of implementation.

The presented system has largely achieved its objectives, and future plans include both refinements and wider validation. In particular, gesture control has proved both intuitive and accurate, providing the same level of control as a traditional handheld remote.

However objective evaluation with real drones (i.e., not a simulator) has not yet been completed and is scheduled for the near future. This should be in comparison with the handheld remote controller, with pilots being asked to place the drone in a specified position. Measurements could include accuracy (distance from the specified position) and time (to achieve that position). In addition, more complex drone behaviors can be tied to either specific gestures or virtual buttons in future implementations; such behaviors can include flying in a circular or other pattern or returning to land either at the take-off location or near the user.

6.2. AR Tracking and Visualization Present and Future Vision

Work into the AR components—drone tracking, calibration, and visualization—of the presented solution is still ongoing. While the currently developed system is a working prototype, a number of possible future improvements have been outlined and planned for the medium term.

Figure 14 presents our vision for such future additions.
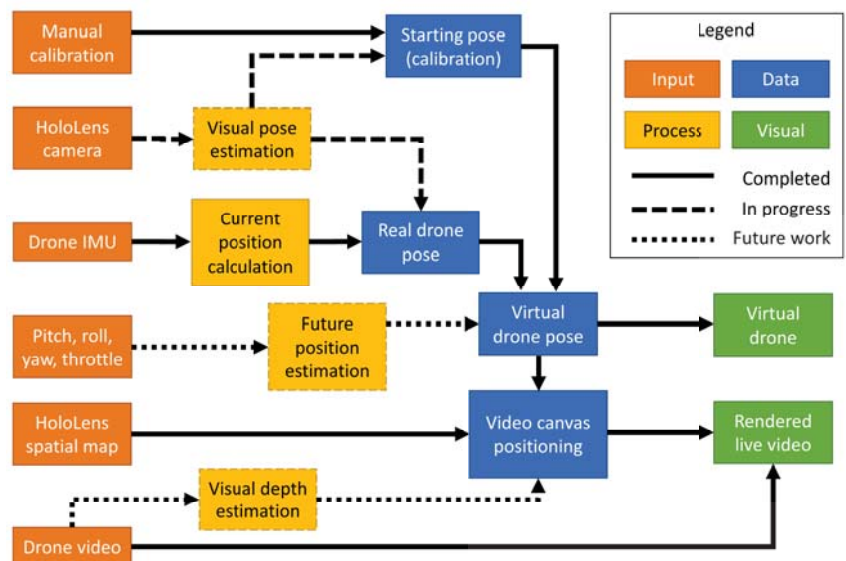
Figure 14. Present and future components of the AR part of the solution. Solid lines indicate completed modules, dashed lines work in progress, and dotted lines future plans.

Regarding calibration, the working prototype uses a manual, two-step calibration, which can prove both tiresome and challenging for inexpert users. Hence, work is already in progress to calibrate initial drone pose with a largely automated, visual method. Two options are currently considered, as outlined in the Section 4.4: a visual drone pose estimation AI and the reading of QR codes pasted on the drones. The former should also provide intermittent visual recognition of the drone during flight, correcting the IMU readings and eliminating any accumulated drift.

In addition, it can be noted that the position as tracked in AR will always lag some time behind that of the real drone, as IMU readings must be collected, read, and aggregated, a position estimated and forwarded to the HoloLens and there displayed. A future module could raw input from the flight control of the drone (pitch, roll, yaw, and throttle) and estimate a future position for the drone, offsetting the lag of data transmission and processing.

Finally, the AR video canvas is currently displayed a set distance in front of the virtual (tracked) drone. However, the actual distance between the drone and the objects in its field of view might range from a couple of meters to hundreds. A depth estimation algorithm could gauge this distance and position the video canvas appropriately, for a more realistic display in context with the environment.

References

1. Özaslan, T.; Loianno, G.; Keller, J.; Taylor, C.J.; Kumar, V.; Wozencraft, J.M.; Hood, T. Autonomous navigation and mapping for inspection of penstocks and tunnels with MAVs. *IEEE Robot. Autom. Lett.* **2017**, *2*, 1740–1747. [CrossRef]
2. Shihavuddin, A.; Chen, X.; Fedorov, V.; Nymark Christensen, A.; Andre Brogaard Riis, N.; Branner, K.; Bjorholm Dahl, A.; Reinhold Paulsen, R. Wind turbine surface damage detection by deep learning aided drone inspection analysis. *Energies* **2019**, *12*, 676. [CrossRef]
3. Wu, K.; Rodriguez, G.A.; Zajc, M.; Jacquemin, E.; Clément, M.; De Coster, A.; Lambot, S. A new drone-borne GPR for soil moisture mapping. *Remote Sens. Environ.* **2019**, *235*, 111456. [CrossRef]
4. Hill, A.C. Economical drone mapping for archaeology: Comparisons of efficiency and accuracy. *J. Archaeol. Sci. Rep.* **2019**, *24*, 80–91. [CrossRef]
5. Joyce, K.; Duce, S.; Leahy, S.; Leon, J.; Maier, S. Principles and practice of acquiring drone-based image data in marine environments. *Mar. Freshw. Res.* **2019**, *70*, 952–963. [CrossRef]
6. Karjalainen, K.D.; Romell, A.E.S.; Ratsamee, P.; Yantac, A.E.; Fjeld, M.; Obaid, M. Social drone companion for the home environment: A user-centric exploration. In Proceedings of the 5th International Conference on Human Agent Interaction, Bielefeld, Germany, 17–20 October 2017; pp. 89–96.
7. Mishra, B.; Garg, D.; Narang, P.; Mishra, V. Drone-surveillance for search and rescue in natural disaster. *Comput. Commun.* **2020**, *156*, 1–10. [CrossRef]
8. Burke, C.; McWhirter, P.R.; Veitch-Michaelis, J.; McAree, O.; Pointon, H.A.; Wich, S.; Longmore, S. Requirements and Limitations of Thermal Drones for Effective Search and Rescue in Marine and Coastal Areas. *Drones* **2019**, *3*, 78. [CrossRef]
9. Tezza, D.; Andujar, M. The State-of-the-Art of Human–Drone Interaction: A Survey. *IEEE Access* **2019**, *7*, 167438–167454. [CrossRef]
10. Suárez Fernández, R.A.; Sanchez-Lopez, J.L.; Sampedro, C.; Bavle, H.; Molina, M.; Campoy, P. Natural user interfaces for human-drone multi-modal interaction. In Proceedings of the 2016 International Conference on Unmanned Aircraft Systems (ICUAS), Arlington, VA, USA, 7–10 June 2016; pp. 1013–1022. [CrossRef]
11. Herrmann, R.; Schmidt, L. Design and Evaluation of a Natural User Interface for Piloting an Unmanned Aerial Vehicle: Can gestural, speech interaction and an augmented reality application replace the conventional remote control for an unmanned aerial vehicle? *i-com* **2018**, *17*, 15–24. [CrossRef]
12. Kleinschmidt, S.P.; Wieghardt, C.S.; Wagner, B. Tracking Solutions for Mobile Robots: Evaluating Positional Tracking using Dual-axis Rotating Laser Sweeps. In Proceedings of the ICINCO 2017, Madrid, Spain, 26–28 July 2017; pp. 155–164.
13. Islam, S.; Ionescu, B.; Gadea, C.; Ionescu, D. Indoor positional tracking using dual-axis rotating laser sweeps. In Proceedings of the 2016 IEEE International Instrumentation and Measurement Technology Conference Proceedings, Taipei, Taiwan, 23–26 May; IEEE: Piscataway, NJ, USA, 2016; pp. 1–6.

14. Arreola, L.; De Oca, A.M.; Flores, A.; Sanchez, J.; Flores, G. Improvement in the UAV position estimation with low-cost GPS, INS and vision-based system: Application to a quadrotor UAV. In Proceedings of the 2018 International Conference on Unmanned Aircraft Systems (ICUAS), Dallas, TX, USA, 12–15 June; IEEE: Piscataway, NJ, USA, 2018; pp. 1248–1254.
15. Tsai, S.E.; Zhuang, S.H. Optical flow sensor integrated navigation system for quadrotor in GPS-denied environment. In Proceedings of the 2016 International Conference on Robotics and Automation Engineering (ICRAE), Jeju, Korea, 27–29 August; IEEE: Piscataway, NJ, USA, 2016; pp. 87–91.
16. Hong, Y.; Lin, X.; Zhuang, Y.; Zhao, Y. Real-time pose estimation and motion control for a quadrotor uav. In Proceedings of the 11th World Congress on Intelligent Control and Automation, Shenyang, China, 29 June–4 July 2014; IEEE: Piscataway, NJ, USA, 2014; pp. 2370–2375.
17. Hoff, W.A.; Nguyen, K.; Lyon, T. Computer-vision-based registration techniques for augmented reality. In *Intelligent Robots and Computer Vision XV: Algorithms, Techniques, Active Vision, and Materials Handling*; International Society for Optics and Photonics: Bellingham, WA, USA, 1996; Volume 2904, pp. 538–548.
18. Deshmukh, S.S.; Joshi, C.M.; Patel, R.S.; Gurav, Y. 3D object tracking and manipulation in augmented reality. *Int. Res. J. Eng. Technol.* **2018**, *5*, 287–289.
19. Shreyas, E.; Sheth, M.H.; Mohana. 3D Object Detection and Tracking Methods using Deep Learning for Computer Vision Applications. In Proceedings of the 2021 International Conference on Recent Trends on Electronics, Information, Communication Technology (RTEICT), Bangalore, India, 27–28 August 2021; pp. 735–738. [CrossRef]
20. Rambach, J.; Deng, C.; Pagani, A.; Stricker, D. Learning 6DoF Object Poses from Synthetic Single Channel Images. In Proceedings of the 2018 IEEE International Symposium on Mixed and Augmented Reality Adjunct (ISMAR-Adjunct), Munich, Germany, 16–20 October 2018; pp. 164–169. [CrossRef]
21. Li, J.; Wang, C.; Kang, X.; Zhao, Q. Camera localization for augmented reality and indoor positioning: A vision-based 3D feature database approach. *Int. J. Digit. Earth* **2020**, *13*, 727–741. [CrossRef]
22. Yuan, L.; Reardon, C.; Warnell, G.; Loianno, G. Human Gaze-Driven Spatial Tasking of an Autonomous MAV. *IEEE Robot. Autom. Lett.* **2019**, *4*, 1343–1350. [CrossRef]
23. Albanis, G.; Zioulis, N.; Dimou, A.; Zarpalas, D.; Daras, P. Dronepose: Photorealistic uav-assistant dataset synthesis for 3D pose estimation via a smooth silhouette loss. In *European Conference on Computer Vision*; Springer: Cham, Switzerland, 2020; pp. 663–681.
24. Endsley, M.R. Toward a Theory of Situation Awareness in Dynamic Systems. *Hum. Factors* **1995**, *37*, 32–64. [CrossRef]
25. Silvagni, M.; Tonoli, A.; Zenerino, E.; Chiaberge, M. Multipurpose UAV for search and rescue operations in mountain avalanche events. *Geomat. Nat. Hazards Risk* **2017**, *8*, 18–33. [CrossRef]
26. Volckaert, B. Aiding First Incident Responders Using a Decision Support System Based on Live Drone Feeds. In Proceedings of the Knowledge and Systems Sciences: 19th International Symposium, KSS 2018, Tokyo, Japan, 25–27 November 2018; Springer: Berlin/Heidelberg, Germany, 2018; Volume 949, p. 87.
27. Hong, T.C.; Andrew, H.S.Y.; Kenny, C.W.L. Assessing the Situation Awareness of Operators Using Maritime Augmented Reality System (MARS). *Proc. Hum. Factors Ergon. Soc. Annu. Meet.* **2015**, *59*, 1722–1726. [CrossRef]
28. Rowen, A.; Grabowski, M.; Rancy, J.P. Through the Looking Glass(es): Impacts of Wearable Augmented Reality Displays on Operators in a Safety-Critical System. *IEEE Trans. Hum.-Mach. Syst.* **2019**, *49*, 652–660. [CrossRef]
29. Lukosch, S.; Lukosch, H.; Datcu, D.; Cidota, M. Providing information on the spot: Using augmented reality for situational awareness in the security domain. *Comput. Support. Coop. Work (CSCW)* **2015**, *24*, 613–664. [CrossRef]
30. Brejcha, J.; Lukáč, M.; Chen, Z.; DiVerdi, S.; Čadík, M. Immersive trip reports. In Proceedings of the 31st Annual ACM Symposium on User Interface Software and Technology, Berlin, Germany, 14–17 October 2018; pp. 389–401.
31. Wang, Y.; Krum, D.M.; Coelho, E.M.; Bowman, D.A. Contextualized Videos: Combining Videos with Environment Models to Support Situational Understanding. *IEEE Trans. Vis. Comput. Graph.* **2007**, *13*, 1568–1575. [CrossRef] [PubMed]
32. Konstantoudakis, K.; Albanis, G.; Christakis, E.; Zioulis, N.; Dimou, A.; Zarpalas, D.; Daras, P. Single-Handed Gesture UAV Control for First Responders—A Usability and Performance User Study. In Proceedings of the 17th International Conference on Information Systems for Crisis Response and Management (ISCRAM 2020), Blacksburg, VA, USA, 24–27 May 2020; Volume 17, pp. 937–951.
33. Peshkova, E.; Hitz, M.; Kaufmann, B. Natural Interaction Techniques for an Unmanned Aerial Vehicle System. *IEEE Pervasive Comput.* **2017**, *16*, 34–42. [CrossRef]
34. Nielsen, M.; Störring, M.; Moeslund, T.B.; Granum, E. A Procedure for Developing Intuitive and Ergonomic Gesture Interfaces for HCI. In *Gesture-Based Communication in Human-Computer Interaction*; Camurri, A., Volpe, G., Eds.; Springer: Berlin/Heidelberg, Germany, 2004; pp. 409–420.
35. Sainidis, D.; Tsiakmakis, D.; Konstantoudakis, K.; Albanis, G.; Dimou, A.; Daras, P. Single-handed gesture UAV control and video feed AR visualization for first responders. In Proceedings of the 18th International Conference on Information Systems for Crisis Response and Management (ISCRAM 2021), Blacksburg, VA, USA, 23–26 May 2021; Volume 18, pp. 835–848.
36. Zhang, F.; Bazarevsky, V.; Vakunov, A.; Tkachenka, A.; Sung, G.; Chang, C.L.; Grundmann, M. Mediapipe hands: On-device real-time hand tracking. *arXiv* **2020**, arXiv:2006.10214.
37. Anton, H.; Rorres, C. *Elementary Linear Algebra: Applications Version*; John Wiley & Sons: Hoboken, NJ, USA, 2013.

38. Sun, K.; Xiao, B.; Liu, D.; Wang, J. Deep high-resolution representation learning for human pose estimation. In Proceedings of the IEEE/CVF Conference on Computer Vision and Pattern Recognition, Long Beach, CA, USA, 15–20 June 2019; pp. 5693–5703.
39. Chen, B.; Parra, A.; Cao, J.; Li, N.; Chin, T.J. End-to-end learnable geometric vision by backpropagating PnP optimization. In Proceedings of the IEEE/CVF Conference on Computer Vision and Pattern Recognition, Seattle, WA, USA, 14–19 June 2020; pp. 8100–8109.
40. Albanis, G.N.; Zioulis, N.; Chatzitofis, A.; Dimou, A.; Zarpalas, D.; Daras, P. On End-to-End 6DOF Object Pose Estimation and Robustness to Object Scale. ML Reproducibility Challenge 2020. 2021. Available online: https://openreview.net/forum?id=PCpGvUrwfQB (accessed on 20 December 2021)

MDPI

Article

Demystifying the Differences between Structure-from-MotionSoftware Packages for Pre-Processing Drone Data

Taleatha Pell [1,*], Joan Y. Q. Li [2,*] and Karen E. Joyce [3]

[1] College of Science and Engineering, James Cook University Townsville, Bebegu Yumba Campus, 1 James Cook Drive, Douglas, QLD 4811, Australia
[2] GeoNadir, Trinity Beach, QLD 4879, Australia
[3] TropWATER/College of Science and Engineering, James Cook University Cairns, Nguma-bada Campus, 14-88 McGregor Road, Smithfield, QLD 4878, Australia; karen.joyce@jcu.edu.au
[*] Correspondence: taleatha.pell@my.jcu.edu.au (T.P.); joan@geonadir.com (J.Y.Q.L.)

Abstract: With the increased availability of low-cost, off-the-shelf drone platforms, drone data become easy to capture and are now a key component of environmental assessments and monitoring. Once the data are collected, there are many structure-from-motion (SfM) photogrammetry software options available to pre-process the data into digital elevation models (DEMs) and orthomosaics for further environmental analysis. However, not all software packages are created equal, nor are their outputs. Here, we evaluated the workflows and output products of four desktop SfM packages (AgiSoft Metashape, Correlator3D, Pix4Dmapper, WebODM), across five input datasets representing various ecosystems. We considered the processing times, output file characteristics, colour representation of orthomosaics, geographic shift, visual artefacts, and digital surface model (DSM) elevation values. No single software package was determined the "winner" across all metrics, but we hope our results help others demystify the differences between the options, allowing users to make an informed decision about which software and parameters to select for their specific application. Our comparisons highlight some of the challenges that may arise when comparing datasets that have been processed using different parameters and different software packages, thus demonstrating a need to provide metadata associated with processing workflows.

Keywords: unmanned aerial vehicle (UAV); digital elevation model (DEM); digital surface model (DSM); orthomosaic; photogrammetry; Earth observation; environmental monitoring

1. Introduction

Drone data use within environmental sciences has increased considerably over the past 20 y. This is due in part to the increased availability of drone platforms on the market, technological advances providing better sensors, a longer battery life, easier-to-use systems, and enhanced structure-from-motion (SfM) software that is able to process these datasets into orthomosaics and digital elevation models (DEMs) [1]. Further, in contrast to traditional aerial survey and satellite data capture, drones are able to survey at a fine resolution from a low altitude, be deployed on flexible time schedules, and fly below clouds for unobstructed data collection [2]. In some ways, a drone can capture data more akin to field surveys, though over larger and potentially inaccessible areas, thus effectively bridging the gap between satellite and on-ground data collection across terrestrial and marine environments [3].

Drone data have been captured to provide information across a range of environmental fields, predominantly to assess vegetation coverage, composition, and/or structure in the terrestrial environment (e.g., [4–8]). However, they have also been used to study a range of other environments, including mangroves [9–11], oyster reefs [12], coral reefs [13,14],

coastal dunes [15,16], and seagrass beds [17]. They have also been used to identify invasive plant species [18–20] and estimate animal populations [21–23]. Drones are also commonly used within agriculture (e.g., [24,25]), forestry [26], and urban settings (e.g., [27,28]).

Most of these environmental applications require the drone data to undergo some form of preprocessing before the data are suitable for mapping analyses. Typically, individual drone images will retain metadata not only of the time and date of capture, but also the x, y, z coordinate location of the drone (longitude, latitude, altitude), its orientation, and the angular rotations of the platform and camera. The combination of imagery and metadata is used by SfM photogrammetry software to commence the pre-processing workflow.

The two most commonly used outputs of an SfM workflow include a DEM and an orthomosaic. DEMs are spatial datasets that describe surface terrain features and are broken up into two categories: digital terrain models (DTMs) and digital surface models (DSMs) [29]. DTMs measure the elevation of the mapped surface, minus objects on the surface (e.g., trees, buildings), whereas DSMs measure the mapped elevation including surface objects. The derived DEM is then used in the process of building an orthomosaic.

Orthomosaics are created by stitching together a series of individual, overlapping orthorectified aerial images to produce a single continuous image/map [30]. This process corrects for distortions in the image, introduced by factors such as camera tilt, lens distortion, and environmental conditions [31]. The end product is a uniformly scaled, georeferenced image allowing for accurate estimation of the location, size, and shape of photographed objects.

The accessibility of drones and their derived data products allow scientists, land managers, and other users to collect and manage their own spatial datasets [1]. However, many end users remain unaware of the processes that take place within the workflow of a chosen software or the potential differences in the end product as a result of processing and software choices [32]. There are both proprietary and open-source software options available for conducting SfM photogrammetry. Provided one has sufficient skills in coding, open-source toolkits can be more flexible and allow customisation of many stages in the workflow. In contrast, proprietary software often provides a streamlined workflow to facilitate photogrammetric processing. However, these packages are often referred to as a "black box"-type solution because they offer little control or insight for users on the internal workings of the software, and in many cases, there is limited opportunity for customisation [33].

The uptake of SfM methods in research and monitoring requires some understanding of the data acquisition and image processing workflow to ensure research design repeatability and comparability [34]. Decisions in the image capturing process such as camera type, image resolution, level of image overlap, use of ground control points (GCPs), time of day, tides, and weather conditions can all affect the final orthomosaic and DEM [2]. Additionally, the different SfM software use different algorithms and processing options, which can also affect the final outputs [34]. The subtle difference in outputs between software types, combined with the limited photogrammetry background knowledge of many users of the software, means it is often difficult to reproduce or confidently compare results across photogrammetry studies.

While there have been some studies that have sought to compare the outputs provided by different photogrammetry software, they appear to have exclusively been conducted in the terrestrial environment, with a focus on forests [35,36], sandpits [37], agriculture [38,39], or urban environments [38]. Only Jiang et al. [38] investigated the output of different software across different types of datasets (urban and agricultural). There appear to be no assessments of the comparative accuracy or suitability of different photogrammetry software in processing unmanned aerial vehicle (UAV) data in marine or coastal environments that evaluate both orthomosaic and DSM outputs. This is particularly problematic since most terrestrial UAV mapping uses GCPs and real-time kinematic positioning (RTK) to enhance the accuracy of mapping outputs from photogrammetry software. Previous comparative studies that have assessed the performance of SfM software have focussed on

the accuracy of GCPs compared to ground truth GPS measurements under differing levels of GCPs [37]. However, in the marine environment, the placement of GCPs and the use of RTK is extremely difficult, requiring photogrammetry software to produce orthomosaics with limited or no GCPs and RTK.

Through this research, we aim to assist others in selecting an appropriate SfM software package for pre-processing drone data. In order to do this, we provide qualitative and quantitative assessments of four desktop-based SfM photogrammetry packages, assessing their output file dimensions and specifications, orthomosaics, and digital surface models using input aerial drone data across a variety of terrestrial and marine environments, both natural and built. Finally, we compare the outputs of the software packages and against satellite-derived data in the same locations. We hope that these comparisons highlight some of the challenges that may arise when comparing spatial datasets that have been processed using different parameters and different software packages, thus demonstrating the need to provide the metadata associated with a processing workflow.

2. Methods

There are a multitude of SfM photogrammetry software packages available designed to pre-process drone data and create DEMs and orthomosaics. Within this study, we focussed on a subset of these packages and selected four of those that are commonly cited and are available in the desktop processing environment, namely Pix4Dmapper [40], AgiSoft Metashape [41], Correlator3D [42], and WebODM [43].

2.1. Study Sites and Input Data

Using the online drone data platform GeoNadir [44], we downloaded datasets representing variable and commonly studied ecosystems (agriculture, marine, coastal, and urban) (Figure 1). All drone images were captured during mapping missions. As such, the images have a high degree of overlap and sidelap between adjacent photos, were captured using an RGB camera at nadir angle, and include a location at the time of capture in the image metadata. The dataset specifications are included in Table 1.

Table 1. Details of each drone image collection dataset.

	Common Features	No. of Images	Drone	Sensor	Array Size
A	Agricultural crops, road	282	DJI Phantom 3 Standard	1/2.3″ CMOS	4000 × 3000
B	Water, coral reef	340	DJI Phantom 4 Pro	1″ CMOS	5472 × 3648
C	Mangroves, tree, beach, water, road, residential buildings	189	DJI Phantom 4 Pro	1″ CMOS	4864 × 3648
D	Road, cars, residential buildings	587	Autel Robotics Evo II Pro	1″ CMOS	5472 × 3648
E	River, tree, forest	625	DJI Phantom 4 Pro	1″ CMOS	5472 × 3648

2.2. Software Packages

We selected three commercial and one open-source desktop SfM photogrammetry software packages to construct a DSM and orthomosaic for each sample area:

- AgiSoft Metashape 1.7.1 [41], formerly known as PhotoScan, is one of the most widely used commercial software packages and is frequently cited in academic literature. It supports a range of operating systems (OSs) including Linux, macOS, and Windows [45];
- SimActive Correlator 3D Version 9.0.2 (C3D) [42] processes drone data, as well as other aerial and satellite imagery. It is only supported on Windows OS [46];
- Pix4D Mapper (P4D) 4.2.26 [40] is available as a cloud-based solution, as well as supporting desktop OS (Windows, macOS) and mobile OSs (iOS and Android) [47];
- Web Open Drone Map Version 2.6.4 (WebODM) [43] is a commercial-grade open-source software for drone image processing. Based on the open-source command

line toolkit Open Drone Map [48], it can also be used across Linux, macOS, and Windows OS.
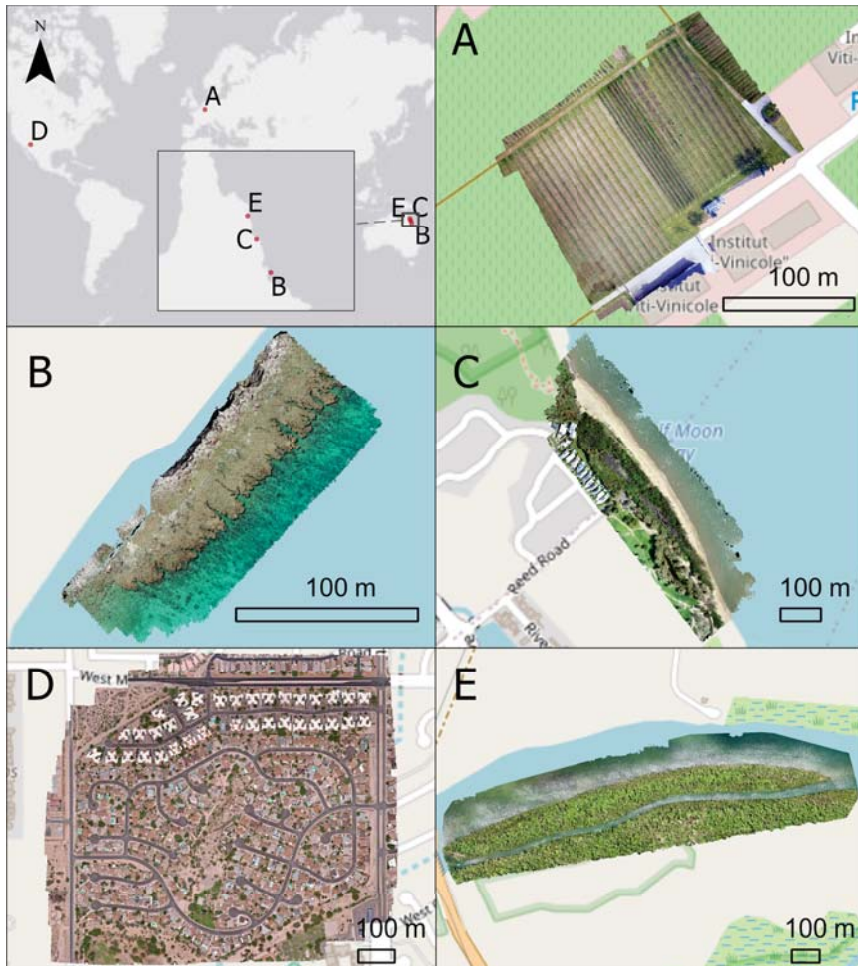
Figure 1. Study site locations and orthomosaic examples: (**A**) a vineyard (6°21′14.62042592″ E, 49°32′41.87405578″ N) located at Remich, Luxembourg [49]; (**B**) Fringing Reef on Yanooa (Pelorus) Island on the Great Barrier Reef (146°30′03.20650026″ E, 18°33′37.06807973″ S) located in Queensland, Australia [50]; (**C**) coastal suburban recreational beach (145°42′38.60723871″ E, 16°47′52.90367696″ S) in Trinity Park, Queensland, Australia [51]; (**D**) urban residential block (111°03′33.67593896″ W, 32°20′56.84116378″ N) located in Tucson, Arizona, USA [52]; and (**E**) Lung Island (145°13′49.31663938″ E, 15°31′16.66610816″ S) in Annan River (Yuku Baja-Muliku) National Park located in Cooktown, Queensland, Australia [53]. Service layer credits: HERE, Garmin, USGS, ESRI, ©OpenStreetMap (and) contributors, CC-BY-SA.

Each of the software packages have their own manufacturer-suggested workflows, in addition to a variety of parameters that can be manually altered depending on the user requirements. In this study, we opted to follow the suggested workflow of each package, based on the assumptions that many users are likely to opt for default settings at least initially and that the default settings have been selected by the manufacturer as producing

the most consistent and hopefully optimal outcomes. It was outside the scope of this study to evaluate each and every parameter within the software themselves, and we refer interested persons to the user manuals of each software for further details.

With minor variations in terminology between software packages, each follows a similar workflow including loading data, aligning photos, bundle adjustment, creating a dense point cloud and/or mesh, creating a DSM, and building an orthomosaic. We used the "True Ortho" Correlator3D wizard workflow; the "3D Maps—Standard" Pix4D workflow; and the default template for WebODM. As AgiSoftMS does not have a templated automated workflow, we selected the manufacturer-recommended components, namely align photos, optimise alignment, build dense cloud, build DEM, and build orthomosaic. We accepted the default recommended settings for each package.

While we recognise the benefit of including independent GCPs to improve the spatial registration of the output products, we did not have access to the required reference data for this study. Further, there are many circumstances where it may not be possible to obtain sufficient GCP data (e.g., in marine environments). This study therefore evaluated the software outputs in their absence, but remains relevant as a relative comparison of the "worst-case" spatial registration between each software package.

All processing was performed using a computer with Windows 10 Enterprise OS, an Intel(R) Core(TM) i7-7700 CPU @ 3.60 GHz, 32 GB of installed RAM, and an NVIDIA Quadro P1000 GPU with 4096 MB RAM. All spatial analyses to compare the output products were conducted in ArcGIS Pro [54], and quantitative analytics were completed using Python [55].

2.3. Comparing Output File Dimensions and Specifications

After processing all datasets using the manufacturer-recommended default parameters, we compared the output details for every software and dataset combination including output file size, projected coordinate system, geographic coordinate system, x and y resolution, absolute geographical coverage, and relative coverage. The areal coverage of each orthomosaic was obtained by extracting the polygon footprint of the projected DSM and orthomosaic boundary, excluding the "no data" values.

We selected the output from AgiSoft Metashape as the baseline product to which the other datasets were compared to obtain the relative areal coverage.

2.4. Comparing Orthomosaics

To compare the output orthomosaics, we assessed the following:

a   Colour correlation score: The luminance value of each pixel was extracted from each colour channel (red, green, and blue) from the original drone images, as well as the output orthomosaic. A density histogram was subsequently plotted to visualise the similarity between the unprocessed and the processed image of each colour band. A correlation score [56] was also calculated to quantify the resemblance of each histogram with each other using the equation below:

$$d(H_1, H_2) = \frac{\sum_l (H_1(I) - \bar{H}_1)(H_2(I) - \bar{H}_2)}{\sqrt{\sum_l (H_1(I) - \bar{H}_1)^2 \sum_i (H_2(I) - \bar{H}_2)^2}} \quad (1)$$

where H_1 and H_2 are the colour density histograms of any two out of five sources (original drone images and outputs from four software) being compared,

$$\bar{H}_k = \frac{1}{N} \sum_j H_k(J) \quad (2)$$

and N is the total number of histogram bins (256 for 8 bit true colour images). A correlation score close to one indicates high similarity between the colour density

of the input images and that of the orthomosaic, while a score approaching zero indicates low similarity;

b   Geographic shift: As no GCPs were available, traditional horizontal and vertical accuracy assessments (i.e., [37]) could not be conducted; instead, Dataset D had very clear and identifiable features within an urban environment, and we used it to calculate the geographic shift resulting after processing with the different software packages. We digitised the polygon boundaries of 20 identifiable features across each of the four orthomosaics, plus a reference satellite image available within the Esri ArcGIS Pro base maps [57]. We ensured that 50% of identifiable features were outlined in the centre region (within 150 m of the orthomosaic centre) and 50% around the edge (within 150 m of the orthomosaic edge). We then calculated the centroid coordinates of each polygon and the distance between feature locations in each software orthomosaic in relation to the same feature location within the satellite base map. Averages (±SE) of the distance from satellite features were calculated for each software at both the centre and edge of orthomosaics;

c   Visible artefacts: All orthomosaic outputs were visually scanned through to select obvious distortion and artefacts in the map, ensuring both the middle and edges of the datasets were evaluated.

2.5. Comparing Digital Surface Models

DSMs are often associated with various uncertainties and errors that could happen at either the data collection time or during the processing time [58]. In the absence of high-resolution LiDAR or field-verified elevation data, all DSM outputs were compared to each other and to the DSM derived from the Space Shuttle Radar Topography Mission (SRTM) DEM 1 Arc-Second Global data (approximately 30 m resolution) [59]. At each site, the four SfM-derived DSMs, in addition to the SRTM DSM, were paired up with each other (i.e., n = 10 combinations per site). Within each pair, both DSMs were resampled to the smaller pixel size of the pair and using the following statistical measures adapted from Szypuła [60]:

a   The mean bias error (MBE) measures the average magnitude of differences (i.e., errors) between any two DSM outputs. It also takes the error direction into consideration (Equation (3));

b   The mean absolute error (MAE) measures the average of the absolute differences between two DSM layers, where all individual differences have equal weight (Equation (4));

c   The root-mean-squared error (RMSE) is a quadratic scoring rule that also measures the average magnitude of the error and is the square root of the average of the squared differences between two observations (Equation (5)). Combining the MBE and MAE will demonstrate the magnitude and direction (i.e., higher or lower) of the difference between any two DSM datasets. Combining the MAE and RMSE, on the other hand, will provide the variance of the difference (i.e., all pixel have a relative uniform difference or not) between two DSMs.

$$MBE = \frac{\sum_{i=1}^{N}(a_i - b_i)}{N - 1} \qquad (3)$$

$$MAE = \frac{\sum_{i=1}^{N}|a_i - b_i|}{N - 1} \qquad (4)$$

$$RMSE = \sqrt{\frac{\sum_{i=1}^{N}(a_i - b_i)}{N - 1}} \qquad (5)$$

where a_i, b_i are the pixel values (i.e., elevation) at the same location of the paired up DSMs and N is the total number of overlapping pixels.

3. Results and Discussion

All software packages were able to successfully build a DSM and orthomosaic using the input datasets; however, we observed differences in the output file size, projected coordinate system, geographic coordinate system, x and y resolution, geographical coverage, relative coverage, and processing time between software packages.

Unsurprisingly, the total processing time was closely and linearly related to the number of images processed (Figure 2). In most cases, C3D was the fastest-performing software package, followed by AgiSoftMS. With the three smaller datasets, P4D was the slowest-performing software; however, with the two larger datasets, WebODM became the slowest. It is likely that the slow performance of WebODM for large datasets was due to it using the CPU for processing, while the other three packages are able to access the GPU for higher performance. Of particular note, P4D had a processing time of up to 348% more than that of C3D (Figure 3). The longer processing time for Pix4D is likely related to the additional processing steps requiring the software to generate a 3D mesh and also automatically exporting the DEM and orthomosaic. These features are not included in the recommended templates for the other packages, where 3D models are not required or where the export of files occurs after the processing stage. There was only one case where Correlator 3D was outperformed on speed (Dataset C—Trinity Park), where AgiSoftMS processed these data in 29 min compared to 34 min, or 85% of the time taken for C3D (Figure 3).
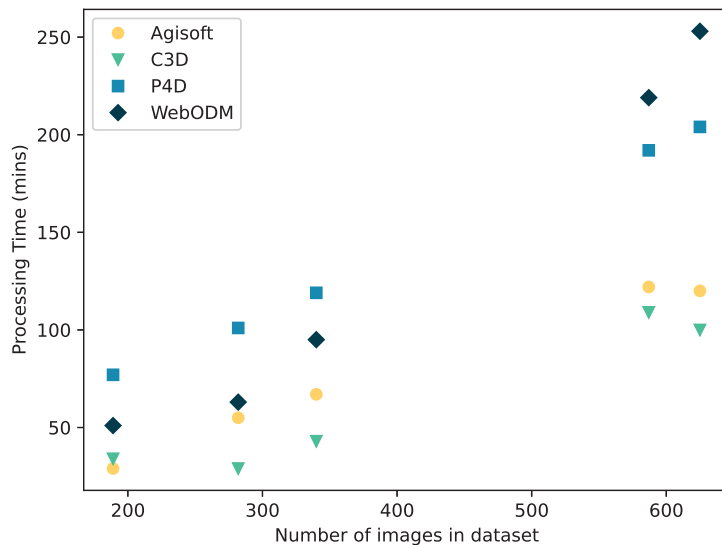
Figure 2. Comparison between the number of images to be processed and the time taken for each software package to complete the processing.

When time is money, the speed of processing is likely to influence software selection, particularly when multiple large datasets are captured. Yet, this cannot be considered in isolation, as the quality of the output is most likely the primary determinant of SfM software choice. We also note that it is possible to reduce the processing time of each of these packages by modifying the standard workflows (e.g., deselect the mesh option for P4D and WebODM), with the caveat that the modification may reduce the quality of the output products, so it should be evaluated accordingly.
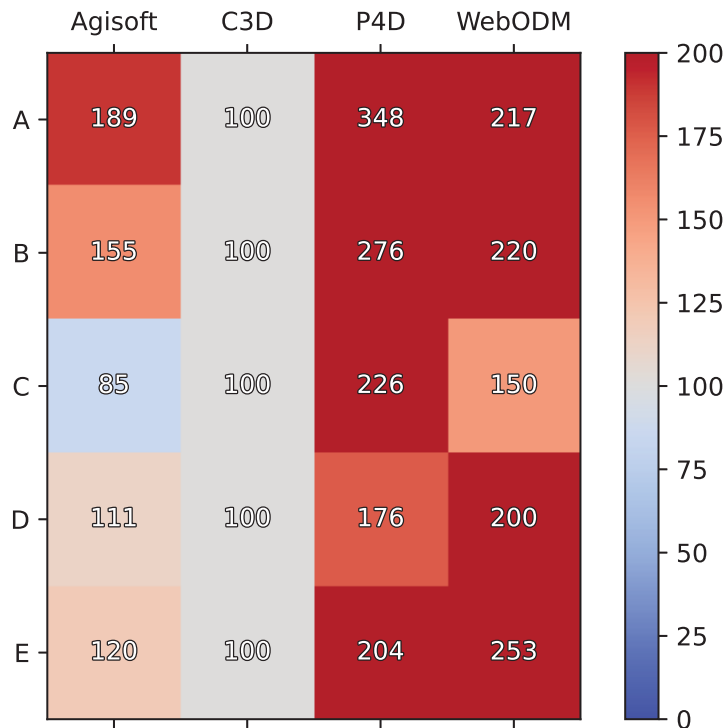
Figure 3. Comparison of the percentageof time taken for each software package to complete the processing, using Correlator 3D as the baseline. Blue shades depict a faster comparison time, while red shades indicate slower comparison times. The darker the tone, the greater the difference is.

3.1. Comparing Output File Dimensions and Specifications

The output orthomosaic and DSM file sizes varied considerably between the software packages (see the details in Tables A1 and A2). This is a result of a combination of the output image resolution and the area that was successfully processed. For example, the default WebODM processing resamples the output to a resolution of 5 × 5 cm per pixel. This lower resolution results in the lowest output file size among all software, which is useful for sharing data between collaborators or hosting on online servers. However, the loss of detail may prove problematic for some users. The other packages tend to generate the maximum resolution output by default, which is closer to the ground sample distance (GSD) of the original input drone images. As with all other parameters, the user can deviate from the default settings to stipulate the desired output resolution, and the software will resample the output accordingly. This might be important for maintaining consistency across multiple datasets, in particular for time series analysis, but resampling will inevitably alter the output image accuracy.

In combination with the output pixel size, the total areal coverage also impacts the file size. In Figure 4, we compare each of the software DSM and orthomosaic outputs to the areal coverage generated by AgiSoftMS and note the considerable differences. Pix4D in particular returns smaller areal coverages for both the DSM and orthomosaic in each of the datasets that contain water bodies (B, C, and E—Yanooa Reef, Trinity Park, and Lung Island). P4D and, to some extent, WebODM clearly have difficulty aligning and resolving water and submerged features—in particular where there is sunglint on the water's surface—and consequently crop these features from the final products (Figure 5).

WebODM failed to reconstruct the crop field on the right half of Dataset A, also resulting in a comparatively small areal coverage for those output products (Figure 6).
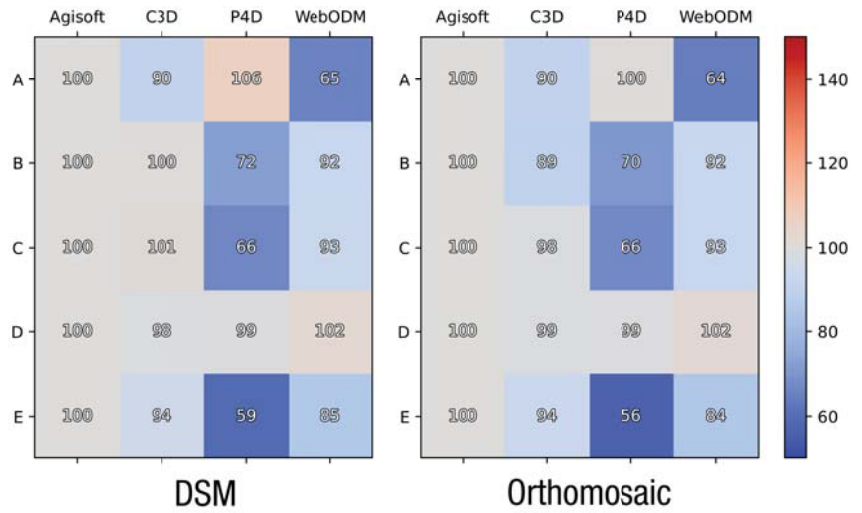
Figure 4. Relative coverage for the DSM (**left**) and orthomosaic (**right**) in all datasets where the cell colouring is blue, the output areal extent is smaller than the AgiSoft reference, while shades of red indicate an area larger in extent.

Figure 5. AgiSoft vs. P4D with Dataset B (**left**), Dataset C (**middle**), and Dataset E (**right**). The red shade and the inset at the bottom right corner are the coverage of the orthomosaic generated by P4D. The red cluster scattered in the shade is voids that have no value in the orthomosaic datasets. This is overlaid with the output from AgiSoft to show the difference of coverage.
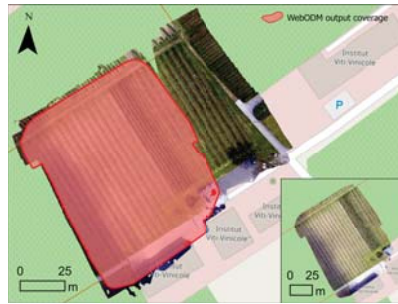
Figure 6. AgiSoft vs. WebODM with Dataset A. The red shade and the inset at the bottom right corner are the coverage of the orthomosaic generated by WebODM. The red cluster scattered in the bottom right edge of the shade is voids that have no value in the orthomosaic datasets. This is overlaid with the output from AgiSoft to show the difference of coverage.

3.2. Comparing Orthomosaics

In comparing the orthomosaics, we aimed to evaluate the similarity in colour between the input and output data; any geographic shift between the output products and reference satellite imagery; and the visual consistency between the output product and ground features.

3.2.1. Colour Density Correlation Score

During the process of building an orthomosaic, pixel values are averaged in areas of overlap, and as we already demonstrated with the coastal datasets, some pixels are excluded entirely. The colour density correlation score provides further evidence for the differences seen between the SfM packages and original drone images (Figures 7–9). In particular, the density histogram for the red channel for the P4D orthomosaics created from Dataset B (Figure 10A) are very different from the original images and other software outputs, which could be due to the cropped water feature pixels (Figure 5). The green and blue channels (Figure 10B,C) show closer alignment between all software packages with the exception of P4D, in particular in the middle range values for luminance (i.e., pixels that are neither very bright nor dark). This also results in decreased contrast across the orthomosaic scene. In cases where it is important to retain the input absolute pixel values (e.g., for quantitative mapping and assessments), it is worth further investigating the methods of feathering and averaging between images in overlapping areas to ensure the appropriate algorithms are used.
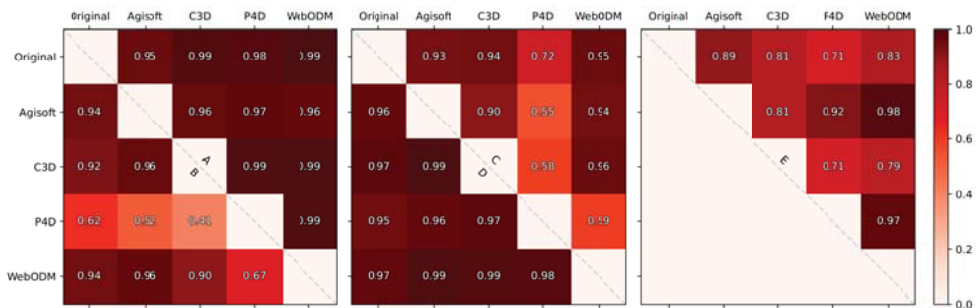
Figure 7. Correlation score of red pixel luminance values. The results from each dataset comprise half of the square presented, separated by the diagonal dashed line and labelled with the corresponding letter. Both columns and rows are labelled with orthomosaic sources, and "Original" refers to the original drone images. Darker shading denotes a higher correlation score, i.e., similar luminance value density.
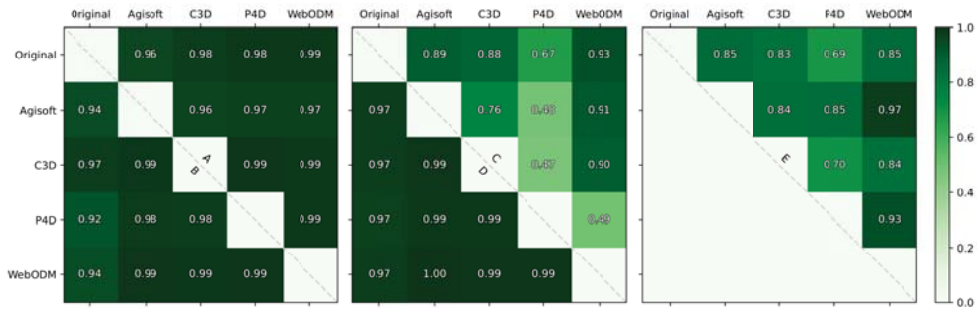
Figure 8. Correlation score of green pixel luminance values. The results from each dataset comprise half of the square presented, separated by the diagonal dashed line and labelled with the corresponding letter. Both columns and rows are labelled with orthomosaic sources, and "Original" refers to the original drone images. Darker shading denotes a higher correlation score, i.e., similar luminance value density.
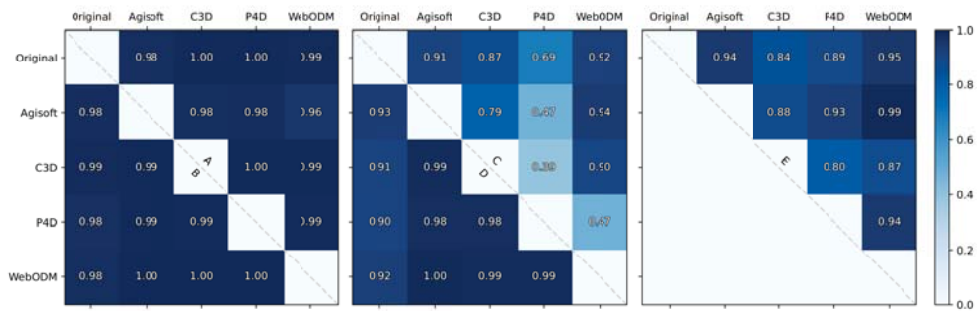
Figure 9. Correlation score of blue pixel luminance values. The results from each dataset comprise half of the square presented, separated by the diagonal dashed line and labelled with the corresponding letter. Both columns and rows are labelled with orthomosaic sources, and "Original" refers to the original drone images. Darker shading denotes a higher correlation score, i.e., similar luminance value density.
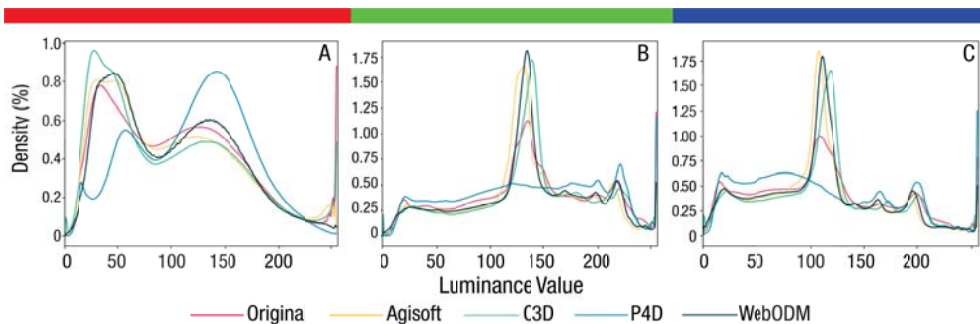
Figure 10. A subset of colour density histograms that show the most variance (i.e., lowest correlation score) between different software packages and original drone images. (**A**) Red channel colour density plot for Dataset B, where the lowest score (0.55) occurs between P4D and AgiSoft outputs. (**B**) Green channel colour density plot for Dataset C, where the lowest score (0.47) occurs between P4D and C3D outputs. (**C**) Blue channel colour density plot for Dataset C, where the lowest score (0.39) occurs between P4D and C3D outputs.

3.2.2. Geographic Shift

When compared to the satellite data available in Esri base maps within ArcGIS Pro [57], the drone data show between two and four metres of displacement (Figure 11), which is reasonable considering the positional accuracy of Global Navigation Satellite System (GNSS) units on drone platforms, in particular without additional ground control (Kalacska et al. 2020). The geographical shift is more prominent towards the edges of the orthomosaic than in the centre, due to the lower overlap of the input images in these areas. This reinforces the need to plan data capture missions that cover areas beyond the bounds of the central region of interest. In the centre of all software-generated orthomosaics, all features were within 2.50 m of the satellite features (WebODM: 1.86 ± 0.36 m, C3D: 2.06 ± 0.10 m, P4D: 2.44 ± 0.25 m, AgiSoftMS: 2.50 ± 0.26 m).
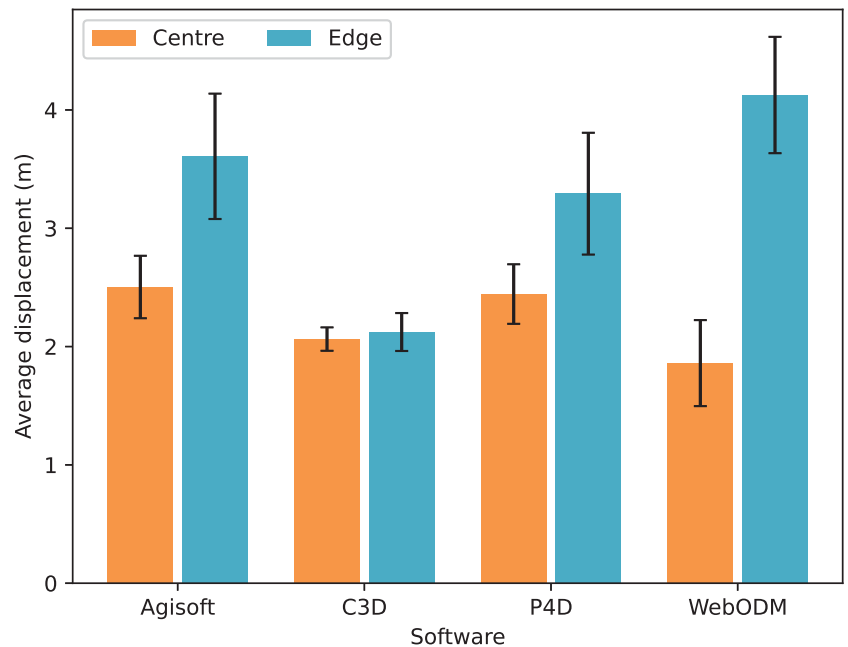
Figure 11. Average displacement (m) (±SE) of the centre and edge features on the AgiSoft Metashape, Correlator3D, Pix4DMapper, and WebODM Orthomosaics from satellite imagery [57]).

In contrast, at the orthomosaic edges, P4D, AgiSoftMS, and WebODM showed slightly larger displacement from the satellite features (Pix4DMapper: 3.29 ± 0.51 m, AgiSoftMS: 3.61 ± 0.53 m, WebODM: 4.13 ± 0.49 m). C3D, however, displayed similar displacement at the orthomosaic edges to the centre, (2.12 ± 0.16 m), making it the nearest to the satellite imagery at the orthomosaic edges. Interestingly, while WebODM appeared to be nearest to the satellite imagery in the centre of the orthomosaic, displacement at the edges was the furthest, at 2.2-times further from the satellite imagery than the centre features.

There are a range of factors in both the data collection and image processing phases that can influence geographic shift/geometrical accuracy. These include flight path, camera quality, calibration, georeferencing strategy (use of GCPs or reliance on the direct onboard georeferencing Global Navigation Satellite System (GNSS) with RTK), and the SfM algorithms [61]. While georeferencing strategies that have employed GCPs have been found to result in finer horizontal accuracy at the decimetre/centimetre scale [61–63], direct methods that rely on GNSS (i.e., non-RTK drones) alone have resulted in accuracies at the metre scale [31]. The metre scale of horizontal accuracy found in these previous studies that have

not employed GCPs or the GNSS with RTK appear to correspond to the results of this study where average displacement ranged from 1.86–2.50 m in the centre of the orthomosaics and 2.12–4.13 m at the orthomosaic edges. If users are seeking accuracy at much finer scales, the software choice is not likely to improve the outcome greatly, and they will need to consider the addition of GCPs or the use of a GNSS with RTK to achieve centimetre-scale accuracy [64,65]. The SfM algorithms employed by each software are another possible source of variation in the geographic shift observed. Although C3D appeared more consistent in the geographic shift across the orthomosaic, this is based on the assumption that the satellite imagery represents the true location of the features. A previous study comparing both horizontal and vertical accuracy across software platforms found AgiSoft PhotoScan to be more accurate than Pix4D web-based image processing and Bundler SfM algorithms [66], but did not evaluate C3D or WebODM. Additionally, a study that compared the accuracy of five different software packages that included AgiSoft and Pix4D in their assessment found little difference in accuracy; however, this was under differing levels of GCPs as opposed to what the software can produce without these inputs [37]. While these differences were attributed to differences in the algorithms in this case, it remains difficult to directly compare the cause due to the lack of detailed information released by proprietary software developers [34,66]. This however serves as a reminder to always retain copies of the original imagery so the data can be re-processed using the best available methods, as software packages and their algorithms will change and hopefully improve over time.

3.2.3. Visual Artefacts

The qualitative analysis of artefacts contained within orthomosaics found that all software contained more artefacts at the edges of the orthomosaic, compared to the centre. Centre artefacts were generally at a smaller scale and were only evident once viewed at increased zoom. Artefacts were also more evident in areas where DSM values in neighbouring pixels changed rapidly, such as at the edges of buildings or trees and forests (Figure 12). Artefacts presented in the form of missing data or gaps in information; "filled" data through smoothing, interpolation, extrapolation, or filtering; and cutlines at feature edges. Cutlines in the orthomosaic often produce visual artefacts at high zoom levels and will also present challenges for automated information extraction at later processing stages. Alternatively, the user can deviate from the standard workflow to create the orthomosaic using the derived DTM instead of the DSM, which tends to result in fewer visual artefacts, though can introduce a greater geographic shift of tall features in the imagery due to uncorrected radial displacement. The users must therefore determine for themselves the most suitable outcome for their specific application.

Each software's default appears to deal with missing data in different ways. C3D simply excludes pixels where it cannot reconstruct portions of the image, presenting them as "no data" fill in the orthomosaic (see Figure 12I). Pix4DMapper and AgiSoftMS have interpolation enabled in the default settings to fill the space based on surrounding values resulting in warped or shaded sections on an orthomosaic (see Figure 12G). However, interpolation will only fill when there are enough close points, and a lack of information from close points can result in areas that are filtered out of the final DSM and orthomosaic and present as holes (See Figure 12G,H). Close inspection of the DSM and the final orthomosaic is recommended to detect holes and warped areas, as these may not be detected until zooming in on smaller features in the orthomosaic.
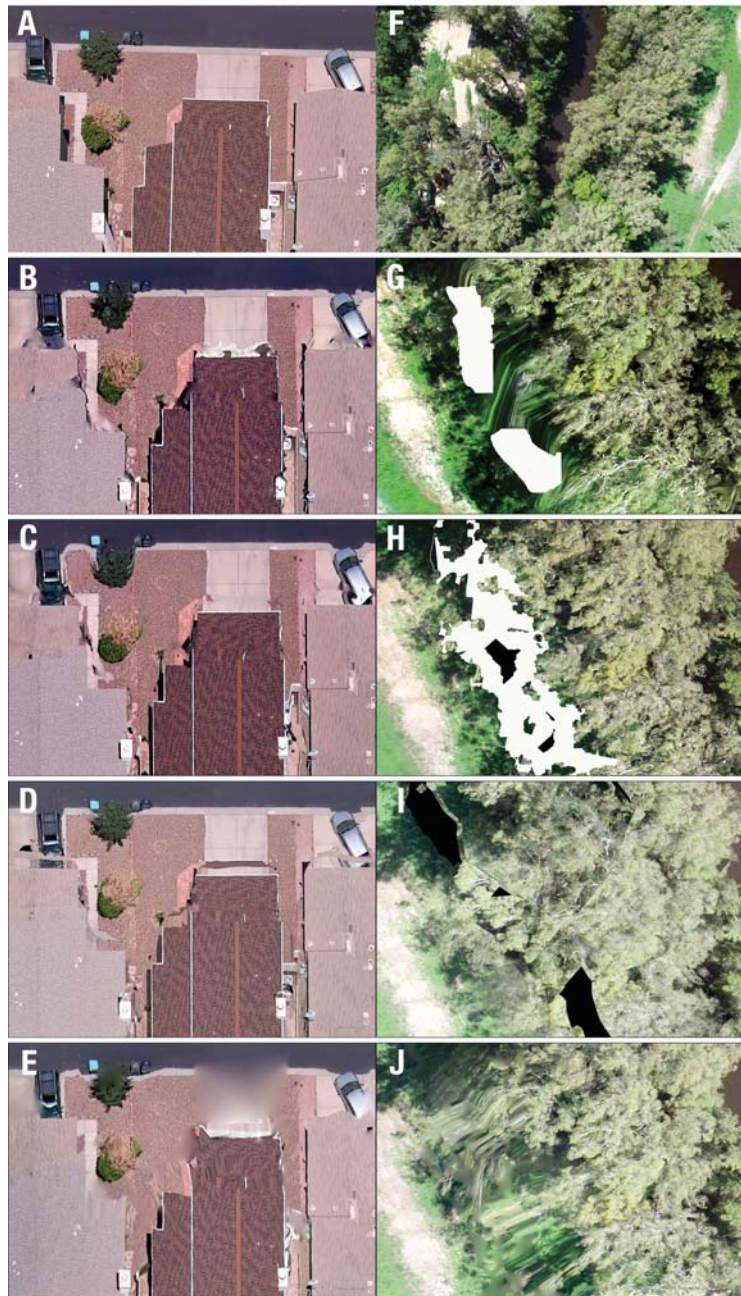
Figure 12. Examples of artefacts found in Dataset D (**A–E**) and Dataset C (**F–J**) orthomosaics generated from various image processing software where: (**A**) raw image, (**B**) AgiSoftMS, (**C**) Correlator3D, D: Pix4DMapper, and (**E**) WebODM for Dataset D; (**F**) raw image, (**G**) AgiSoftMS, (**H**) Correlator3D, (**I**) Pix4DMapper, and (**J**) WebODM for Dataset C.

3.2.4. Comparing Digital Surface Model

When using similarity metrics to evaluate the output DSMs, we found that there was very little overall difference between the software outputs except Dataset E, though all differed somewhat from the SRTM data. The MAE (Figure 13) and RMSE (Figure 14) had little difference in Datasets A, B, and D, between comparison pairs, which indicates that the difference between all the pixels was fairly even. A mixture of terrestrial and aquatic features yet led to a greater variance of the difference (the RMSE of Datasets C and E was higher than the MAE). The depth (or "negative elevation") of underwater features was inadequately represented across all models, though none of them boast a capability in this respect, and bathymetric LiDAR would certainly be a better option for deriving depth information [67].
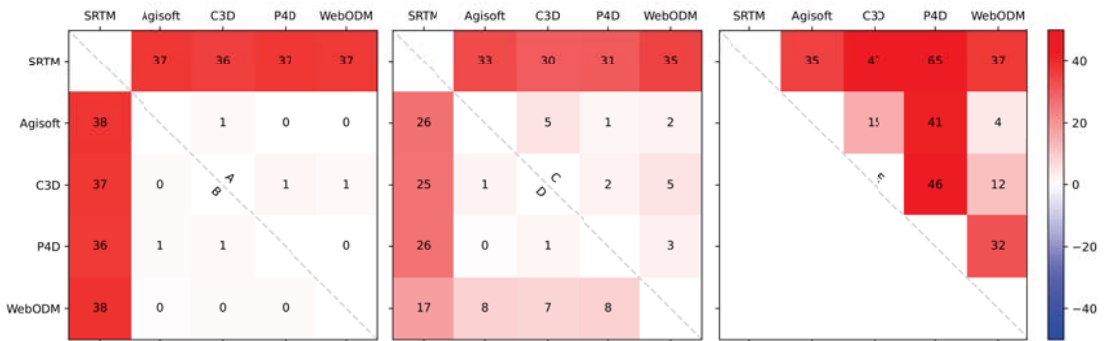
Figure 13. Mean absolute error (MAE) comparison between each DSM output. The results from each dataset comprise half of the square presented, separated by the diagonal dashed line and labelled with the corresponding letter. Both columns and rows are labelled with DSM sources (SRTM and drone derived). Darker shading denotes higher MAE values.
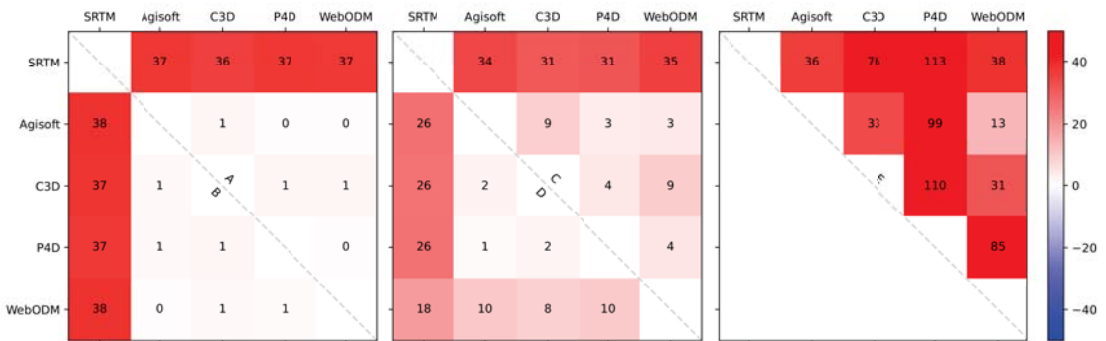
Figure 14. Root-mean-squared error (RMSE) comparison between each DSM output. The results from each dataset comprises half of the square presented, separated by the diagonal dashed line and labelled with the corresponding letter. Both columns and rows are labelled with DSM sources (SRTM and drone derived). Darker shading denotes higher RMSE values.

For the datasets dominated by terrestrial features, drone-derived elevation was overestimated, producing a positive MBE in Datasets A and D when compared to the SRTM data (Figure 15). Most of the differences between the drone-derived DSMs from AgiSoftMS, C3D, and P4D were minor (seen as light shading in Figure 15), indicating that the software algorithm is not the most important factor in obtaining an accurate elevation estimate.

However, WebODM displayed greater differences from the other drone-derived DSM values, in particular with Dataset D. WebODM was also more closely aligned to the SRTM data for Dataset D than the other software packages. As a previous review pointed out, the accuracies of UAV true colour image-derived DSM are comparable to those obtained by LiDAR [68]. Regardless of the usage of GCP or check points, the absolute difference between LiDAR and true colour image-derived DSM was less than 4 m [69,70]. The similarity between software outputs was as expected (Figures 13–15). On the other hand, the relatively large difference between SRTM data and the software outputs is worth noting since UAV imagery is considered as a new tool to fill in the gaps between satellite imagery and in-person field surveys. However, with such a small sample size, inconsistent findings between datasets, and no GCP information, these results are inconclusive. Given the significant difference in resolution between the SRTM and the true-colour-image-derived DSMs, this technique fits better for comparisons at the regional scale. Higher-resolution DSMs (e.g., derived from UAV-based LiDAR sensors or commercial-level satellites) would allow for more detailed comparison at the pixel level.
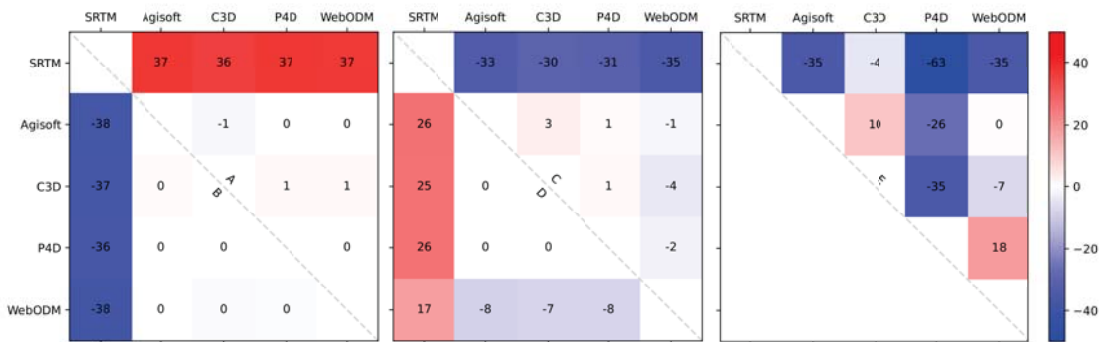
Figure 15. Mean bias error (MBE) comparison between each dataset. Each dataset takes up half of the quadrant, separated by the diagonal dash line and labelled with the corresponding letter. Both columns and rows are labelled with DSM sources (SRTM and drone derived). In each quadrant, for the top right half, $cellvalue = DSM_{row} - DSM_{column}$. For the bottom left half, $cellvalue = DSM_{column} - DSM_{row}$.

In most cases, if deriving absolute elevation is an important project consideration, using the standard processing workflows listed above will be insufficient. Similar to reducing geographic shift, large improvements in elevation accuracy are unlikely to be achieved through software or algorithm choice at this stage, based on the options available. Rather, previous research has indicated that the use of GCPs is highly important to calibrate DEMs [61], and additional direct georeferencing also improves the precision and accuracy [66]. There is growing potential for platforms with onboard RTK GNSS capability to also address this challenge [71]. Employing these technologies where available will undoubtedly increase the output product's accuracy, but will require an increase in the user's time and financial investment across both data capture and processing.

4. Conclusions

In this study, we tested the prescribed workflows and output products (DEMs and orthomosaics) of four different SfM photogrammetry packages using five drone image datasets. We observed considerable differences in processing times, with Correlator3D and AgiSoft outperforming Pix4Dmapper and WebODM, in particular with large datasets. It was also clear that Pix4Dmapper in particular struggled to reconstruct underwater features, while the other software packages provided suitable outputs in reef and coastal ecosystems. Each software package introduced visual artefacts in the output orthomosaic products,

in particular around the edges of buildings and tall vegetation, and we leave the opinion of the acceptable level of artefacts to the users and their particular application. Based on our qualitative and quantitative assessments of the output orthomosaics and DSMs, we caution users against comparing multitemporal drone datasets that have been processed using different software packages and algorithms. Using the same software will give users greater confidence that any detected change is in fact a change in an ecosystem and not due to the processing workflows. The information contained herein will allow users to make informed decisions about future software selections and the impact that their choices may have on the output product's accuracy.

Author Contributions: Conceptualisation, K.E.J., T.P., and J.Y.Q.L.; methodology, T.P. and J.Y.Q.L.; data collection: K.E.J.; formal analysis, T.P. and J.Y.Q.L.; original draft preparation: T.P., J.Y.Q.L., and K.E.J.; review and editing: T.P., J.Y.Q.L., and K.E.J. All authors have read and agreed to the published version of the manuscript.

Data Availability Statement: All data analysed in this study are available via https://www.geonadir.com: 1. https://data.geonadir.com/project-details/341 [49]; 2. https://data.geonadir.com/project-details/98 [50]; 3. https://data.geonadir.com/project-details/139 [51]; 4. https://data.geonadir.com/project-details/353 [52]; 5. https://data.geonadir.com/project-details/523 [53] (acessed on 13 December 2021).

Conflicts of Interest: The authors declare no conflict of interest.

Abbreviations

The following abbreviations are used in this manuscript:

AgiSoftMS	AgiSoft Metashape
C3D	Correlator3D
DEM	Digital elevation model
DSM	Digital surface model
DTM	Digital terrain model
ODM	OpenDroneMap
OS	Operating system
P4D	Pix4Dmapper
GCP	Ground control point
GNSS	Global Navigation Satellite System
GPS	Global Positioning System
GSD	Ground sampling distance
RTK	Real-time kinematic positioning
SfM	Structure-from-Motion
UAV	Unmanned aerial vehicle

Appendix A

Detailed output file dimensions and specifications.

Table A1. Output file specifications for the DSMs.

Features	Dataset	AgiSoft	C3D	P4D	WebODM
File size (MB)	A	63	134	482	3
	B	93	119	617	13
	C	106	145	410	84
	D	207	171	1590	242
	E	284.4	372.1	930	365.4
X resolution (cm)	A	3.7	4	0.76	5
	B	2.5	3.3	0.6	5
	C	8.6	10	2.1	5
	D	10.7	12.5	2.4	5
	E	10	12.5	2.55	5
Y resolution (cm)	A	3.7	4	0.76	5
	B	2.5	3.3	0.6	5
	C	8.2	10	2.1	5
	D	10.7	12.5	2.4	5
	E	10	12.5	2.55	5
Coverage (m^2)	A	13,541	12,286	14,437	8850
	B	12,507	12,591	9043	11,626
	C	149,168	151,489	99248	139,317
	D	537,804	531,526	534,683	55,1744
	E	544,650	517,100	322,233	465,383
Relative coverage (%)	A	100	91	107	65
	B	100	101	72	93
	C	100	102	67	93
	D	100	99	99	103
	E	100	95	59	85
Projected coordinate system	A			WGS 1984 UTM Zone 32N	
	B			WGS 1984 UTM Zone 55S	
	C	NA		WGS 1984 UTM Zone 55S	
	D			WGS 1984 UTM Zone 12N	
	E			WGS 1984 UTM Zone 55S	
Geographic coordinate system	A				
	B				
	C	WGS 1984			
	D				
	E				

Table A2. Output file specifications for the orthomosaics.

Features	Dataset	AgiSoft	C3D	P4D	WebODM
File size (MB)	A	1110	1520	617	12
	B	1510	2920	752	16
	C	1280	2810	620	150
	D	3270	3540	2160	565
	E	4290	6450	1310	674.2
X resolution (cm)	A	0.9	0.8	0.76	5
	B	0.6	0.6	0.6	5
	C	2.1	2	2	5
	D	2.7	0.25	2.4	5
	E	2.6	2.6	2.55	5
Y resolution (cm)	A	0.6	0.8	0.76	5
	B	0.6	0.6	0.6	5
	C	2.1	2	2	5
	D	2.3	2.5	2.4	5
	E	2.5	2.6	2.55	5
Coverage (m^2)	A	13,439	12,180	13,558	8640
	B	12,500	11,186	8833	11,584
	C	148,473	146,799	99,288	138,452
	D	536,672	532,164	532,849	549,017
	E	542,947	510,800	304,165	461,166
Relative coverage (%)	A	100	91	101	64
	B	100	89	71	93
	C	100	99	67	93
	D	100	99	99	102
	E	100	94	56	85
Projected coordinate system	A			WGS 1984 UTM Zone 32N	
	B			WGS 1984 UTM Zone 55S	
	C	NA		WGS 1984 UTM Zone 55S	
	D			WGS 1984 UTM Zone 12N	
	E			WGS 1984 UTM Zone 55S	
Geographic coordinate system	A				
	B				
	C	WGS 1984			
	D				
	E				

References

1. Anderson, K.; Westoby, M.J.; James, M.R. Low-Budget Topographic Surveying Comes of Age: Structure from Motion Photogrammetry in Geography and the Geosciences. *Prog. Phys. Geogr. Earth Environ.* **2019**, *43*, 163–173. [CrossRef]
2. Joyce, K.; Duce, S.; Leahy, S.; Leon, J.; Maier, S. Principles and Practice of Acquiring Drone-Based Image Data in Marine Environments. *Mar. Freshw. Res.* **2019**, *70*, 952–963. [CrossRef]
3. Anderson, K.; Gaston, K.J. Lightweight Unmanned Aerial Vehicles Will Revolutionize Spatial Ecology. *Front. Ecol. Environ.* **2013**, *11*, 138–146. [CrossRef]
4. Barnetson, J.; Phinn, S.; Scarth, P. Mapping Woody Vegetation Cover across Australia's Arid Rangelands: Utilising a Machine-Learning Classification and Low-Cost Remotely Piloted Aircraft System. *Int. J. Appl. Earth Obs. Geoinf.* **2019**, *83*, 101909. [CrossRef]
5. Almeida, A.; Gonçalves, F.; Silva, G.; Mendonça, A.; Gonzaga, M.; Silva, J.; Souza, R.; Leite, I.; Neves, K.; Boeno, M.; et al. Individual Tree Detection and Qualitative Inventory of a Eucalyptus Sp. Stand Using UAV Photogrammetry Data. *Remote Sens.* **2021**, *13*, 3655. [CrossRef]

6. Talucci, A.C.; Forbath, E.; Kropp, H.; Alexander, H.D.; DeMarco, J.; Paulson, A.K.; Zimov, N.S.; Zimov, S.; Loranty, M.M. Evaluating Post-Fire Vegetation Recovery in Cajander Larch Forests in Northeastern Siberia Using UAV Derived Vegetation Indices. *Remote Sens.* **2020**, *12*, 2970. [CrossRef]
7. Furukawa, F.; Laneng, L.A.; Ando, H.; Yoshimura, N.; Kaneko, M.; Morimoto, J. Comparison of RGB and Multispectral Unmanned Aerial Vehicle for Monitoring Vegetation Coverage Changes on a Landslide Area. *Drones* **2021**, *5*, 97. [CrossRef]
8. Lam, O.H.Y.; Dogotari, M.; Prüm, M.; Vithlani, H.N.; Roers, C.; Melville, B.; Zimmer, F.; Becker, R. An Open Source Workflow for Weed Mapping in Native Grassland Using Unmanned Aerial Vehicle: Using Rumex Obtusifolius as a Case Study. *Eur. J. Remote Sens.* **2021**, *54*, 71–88. [CrossRef]
9. Hsu, A.J.; Kumagai, J.; Favoretto, F.; Dorian, J.; Guerrero Martinez, B.; Aburto-Oropeza, O. Driven by Drones: Improving Mangrove Extent Maps Using High-Resolution Remote Sensing. *Remote Sens.* **2020**, *12*, 3986. [CrossRef]
10. Cohen, M.C.L.; de Souza, A.V.; Liu, K.b.; Rodrigues, E.; Yao, Q.; Ryu, J.; Dietz, M.; Pessenda, L.C.R.; Rossetti, D. Effects of the 2017–2018 Winter Freeze on the Northern Limit of the American Mangroves, Mississippi River Delta Plain. *Geomorphology* **2021**, *394*, 107968. [CrossRef]
11. Cohen, M.C.L.; de Souza, A.V.; Liu, K.B.; Rodrigues, E.; Yao, Q.; Pessenda, L.C.R.; Rossetti, D.; Ryu, J.; Dietz, M. Effects of Beach Nourishment Project on Coastal Geomorphology and Mangrove Dynamics in Southern Louisiana, USA. *Remote Sens.* **2021**, *13*, 2688. [CrossRef]
12. Windle, A.E.; Poulin, S.K.; Johnston, D.W.; Ridge, J.T. Rapid and Accurate Monitoring of Intertidal Oyster Reef Habitat Using Unoccupied Aircraft Systems and Structure from Motion. *Remote Sens.* **2019**, *11*, 2394. [CrossRef]
13. Fallati, L.; Saponari, L.; Savini, A.; Marchese, F.; Corselli, C.; Galli, P. Multi-Temporal UAV Data and Object-Based Image Analysis (OBIA) for Estimation of Substrate Changes in a Post-Bleaching Scenario on a Maldivian Reef. *Remote Sens.* **2020**, *12*, 2093. [CrossRef]
14. David, C.G.; Kohl, N.; Casella, E.; Rovere, A.; Ballesteros, P.; Schlurmann, T. Structure-from-Motion on Shallow Reefs and Beaches: Potential and Limitations of Consumer-Grade Drones to Reconstruct Topography and Bathymetry. *Coral Reefs* **2021**, *40*, 835–851. [CrossRef]
15. Laporte-Fauret, Q.; Marieu, V.; Castelle, B.; Michalet, R.; Bujan, S.; Rosebery, D. Low-Cost UAV for High-Resolution and Large-Scale Coastal Dune Change Monitoring Using Photogrammetry. *J. Mar. Sci. Eng.* **2019**, *7*, 63. [CrossRef]
16. Fabbri, S.; Grottoli, E.; Armaroli, C.; Ciavola, P. Using High-Spatial Resolution UAV-Derived Data to Evaluate Vegetation and Geomorphological Changes on a Dune Field Involved in a Restoration Endeavour. *Remote Sens.* **2021**, *13*, 1987. [CrossRef]
17. Rende, S.F.; Bosman, A.; Di Mento, R.; Bruno, F.; Lagudi, A.; Irving, A.D.; Dattola, L.; Giambattista, L.D.; Lanera, P.; Proietti, R.; et al. Ultra-High-Resolution Mapping of Posidonia Oceanica (L.) Delile Meadows through Acoustic, Optical Data and Object-based Image Classification. *J. Mar. Sci. Eng.* **2020**, *8*, 647. [CrossRef]
18. Benjamin, A.R.; Abd-Elrahman, A.; Gettys, L.A.; Hochmair, H.H.; Thayer, K. Monitoring the Efficacy of Crested Floatingheart (Nymphoides Cristata) Management with Object-Based Image Analysis of UAS Imagery. *Remote Sens.* **2021**, *13*, 830. [CrossRef]
19. Higgisson, W.; Cobb, A.; Tschierschke, A.; Dyer, F. Estimating the Cover of Phragmites Australis Using Unmanned Aerial Vehicles and Neural Networks in a Semi-Arid Wetland. *River Res. Appl.* **2021**, *37*, 1312–1322. [CrossRef]
20. Papp, L.; van Leeuwen, B.; Szilassi, P.; Tobak, Z.; Szatmári, J.; Árvai, M.; Mészáros, J.; Pásztor, L. Monitoring Invasive Plant Species Using Hyperspectral Remote Sensing Data. *Land* **2021**, *10*, 29. [CrossRef]
21. Drever, M.C.; Chabot, D.; O'Hara, P.D.; Thomas, J.D.; Breault, A.; Millikin, R.L. Evaluation of an Unmanned Rotorcraft to Monitor Wintering Waterbirds and Coastal Habitats in British Columbia, Canada. *J. Unmanned Veh. Syst. Virtual Issue* **2016**, *1*, 256–267. [CrossRef]
22. Oosthuizen, W.C.; Krüger, L.; Jouanneau, W.; Lowther, A.D. Unmanned Aerial Vehicle (UAV) Survey of the Antarctic Shag (Leucocarbo Bransfieldensis) Breeding Colony at Harmony Point, Nelson Island, South Shetland Islands. *Polar Biol.* **2020**, *43*, 187–191. [CrossRef]
23. Mustafa, O.; Braun, C.; Esefeld, J.; Knetsch, S.; Maercker, J.; Pfeifer, C.; Rümmler, M.C. Detecting Antarctic Seals and Flying Seabirds by UAV. *ISPRS Ann. Photogramm. Remote Sens. Spatial Inf. Sci.* **2019**, *IV-2/W5*, 141–148. [CrossRef]
24. Mhango, J.K.; Harris, E.W.; Green, R.; Monaghan, J.M. Mapping Potato Plant Density Variation Using Aerial Imagery and Deep Learning Techniques for Precision Agriculture. *Remote Sens.* **2021**, *13*, 2705. [CrossRef]
25. Tsouros, D.C.; Terzi, A.; Bibi, S.; Vakouftsi, F.; Pantzios, V. Towards a Fully Open-Source System for Monitoring of Crops with UAVs in Precision Agriculture. In Proceedings of the 24th Pan-Hellenic Conference on Informatics, Athens, Greece, 20–22 November 2020; Association for Computing Machinery: New York, NY, USA, 2020; pp. 322–326. [CrossRef]
26. Gallardo-Salazar, J.L.; Pompa-García, M. Detecting Individual Tree Attributes and Multispectral Indices Using Unmanned Aerial Vehicles: Applications in a Pine Clonal Orchard. *Remote Sens.* **2020**, *12*, 4144. [CrossRef]
27. Kucharczyk, M.; Hugenholtz, C.H. Pre-Disaster Mapping with Drones: An Urban Case Study in Victoria, British Columbia, Canada. *Nat. Hazards Earth Syst. Sci.* **2019**, *19*, 2039–2051. [CrossRef]
28. Jiménez-Jiménez, S.I.; Ojeda-Bustamante, W.; Ontiveros-Capurata, R.E.; Marcial-Pablo, M.d.J. Rapid Urban Flood Damage Assessment Using High Resolution Remote Sensing Data and an Object-Based Approach. *Geomat. Nat. Hazards Risk* **2020**, *11*, 906–927. [CrossRef]

29. Berra, E.F.; Peppa, M.V. Advances and Challenges of Uav Sfm Mvs Photogrammetry and Remote Sensing: Short Review. In *The International Archives of the Photogrammetry, Remote Sensing and Spatial Information Sciences*; Copernicus GmbH: Göttingen, Germany, 2020; Volume XLII-3-W12-2020, pp. 267–272. [CrossRef]

30. Xin, Y.; Li, J.; Cheng, Q. Automatic Generation of Remote Sensing Image Mosaics for Mapping Large Natural Hazards Areas. In *Geomatics Solutions for Disaster Management*; Li, J., Zlatanova, S., Fabbri, A.G., Eds.; Lecture Notes in Geoinformation and Cartography; Springer: Berlin/Heidelberg, Germany, 2007; pp. 61–73. [CrossRef]

31. Turner, D.; Lucieer, A.; Watson, C. An Automated Technique for Generating Georectified Mosaics from Ultra-High Resolution Unmanned Aerial Vehicle (UAV) Imagery, Based on Structure from Motion (SfM) Point Clouds. *Remote Sens.* **2012**, *4*, 1392–1410. [CrossRef]

32. James, M.; Robson, S.; d'Oleire-Oltmanns, S.; Niethammer, U. Optimising UAV Topographic Surveys Processed with Structure-from-Motion: Ground Control Quality, Quantity and Bundle Adjustment. *Geomorphology* **2017**, *280*, 51–66. [CrossRef]

33. Tmušić, G.; Manfreda, S.; Aasen, H.; James, M.R.; Gonçalves, G.; Ben-Dor, E.; Brook, A.; Polinova, M.; Arranz, J.J.; Mészáros, J.; et al. Current Practices in UAS-based Environmental Monitoring. *Remote Sens.* **2020**, *12*, 1001. [CrossRef]

34. Smith, M.; Carrivick, J.; Quincey, D. Structure from Motion Photogrammetry in Physical Geography. *Prog. Phys. Geogr. Earth Environ.* **2016**, *40*, 247–275. [CrossRef]

35. Brach, M.; Chan, J.C.W.; Szymanski, P. Accuracy Assessment of Different Photogrammetric Software for Processing Data from Low-Cost UAV Platforms in Forest Conditions. *iForest Biogeosci. For.* **2019**, *12*, 435. [CrossRef]

36. Gross, J.W.; Heumann, B.W. A Statistical Examination of Image Stitching Software Packages for Use with Unmanned Aerial Systems. *Photogramm. Eng. Remote Sens.* **2016**, *82*, 419–425. [CrossRef]

37. Casella, V.; Chiabrando, F.; Franzini, M.; Manzino, A.M. Accuracy Assessment of a UAV Block by Different Software Packages, Processing Schemes and Validation Strategies. *ISPRS Int. J. Geo-Inf.* **2020**, *9*, 164. [CrossRef]

38. Jiang, S.; Jiang, C.; Jiang, W. Efficient Structure from Motion for Large-Scale UAV Images: A Review and a Comparison of SfM Tools. *ISPRS J. Photogramm. Remote Sens.* **2020**, *167*, 230–251. [CrossRef]

39. Chen, P.F.; Xu, X.G. A Comparison of Photogrammetric Software Packages for Mosaicking Unmanned Aerial Vehicle (UAV) Images in Agricultural Application. *Acta Agron. Sin.* **2020**, *46*, 1112–1119. [CrossRef]

40. Pix4D. *Pix4Dmapper*; Pix4D: Denver, CO, USA, 2017. Available online: https://support.pix4d.com/hc/en-us/articles/202557839-Interface (accessed on 13 December 2021).

41. AgiSoft LLC. *AgiSoft Metashape*; AgiSoft LLC: St. Petersburg, Russia, 2021. Available online: http://agisoft.ca/ (accessed on 13 December 2021).

42. SimActive. *Correlator 3D*; SimActive: Montreal, QC, Canada, 2021. Available online: https://www.simactive.com/ (accessed on 13 December 2021).

43. OpenDroneMap. Web Open Drone Map (ODM). Available online: https://www.opendronemap.org/ (accessed on 13 December 2021).

44. Geonadir. Available online: https://data.geonadir.com/ (accessed on 13 December 2021).

45. AgiSoft LLC. *AgiSoft Metashape User Manual—Professional Edition*, Version 1.5; AgiSoft LLC: St. Petersburg, Russia, 2019.

46. SimActive. *Correlator3DTM User Manual*, Version 8.3.0; SimActive: Montréal, QC, Canada, 2019.

47. Pix4D. *Pix4Dmapper User Manual*, Version 4.1; Pix4D: Denver, CO, USA, 2017. Available online: https://support.pix4d.com/hc/en-us/articles/204272989-Offline-Getting-Started-and-Manual-pdf (accessed on 13 December 2021).

48. OpenDroneMap. *ODM-A Command Line Toolkit to Generate Maps, Point Clouds, 3D Models and DEMs from Drone, Balloon or Kite Images*; OpenDroneMap: Gurugram, India, 2020. Available online: https://opendronemap.org (accessed on 13 December 2021).

49. Bruscolini, M. Vineyard in Luxembourg. Available online: https://data.geonadir.com/project-details/341 (accessed on 13 December 2021).

50. Joyce, K.E.; Koci, J.; Duce, S. SE Pelorus March 2021 Part 1. Available online: https://data.geonadir.com/project-details/139 (accessed on 13 December 2021).

51. Joyce, K.E. Trinity Park January 2021. Available online: https://data.geonadir.com/project-details/98 (accessed on 13 December 2021).

52. Rogers, D. Tucson Arizona. Available online: https://data.geonadir.com/project-details/353 (accessed on 13 December 2021).

53. Hale, M. Lung Island Annan River Yuku Baja. Available online: https://data.geonadir.com/project-details/523 (accessed on 13 December 2021).

54. Esri Inc. *ArcGIS Pro*; Esri Inc.: Redlands, CA, USA, 2019.

55. Van Rossum, G.; Drake, F.L. *Python 3 Reference Manual*; CreateSpace: Scotts Valley, CA, USA, 2009.

56. Bradski, G. The OpenCV Library. *Dr. Dobb's J. Softw. Tools* **2000**, *25*, 120–123.

57. Esri. World Imagery—Overview. Available online: https://www.arcgis.com/home/item.html?id=10df2279f9684e4a9f6a7f08febac2a9 (accessed on 13 December 2021).

58. Wechsler, S.P. Uncertainties Associated with Digital Elevation Models for Hydrologic Applications: A Review. *Hydrol. Earth Syst. Sci. Discuss.* **2007**, *11*, 1481–1500. [CrossRef]

59. Observation, E.R.; Center, S.E. Shuttle Radar Topography Mission (SRTM) 1 Arc-Second Global. 2017. Available online: https://www.usgs.gov/centers/eros/science/usgs-eros-archive-digital-elevation-shuttle-radar-topography-mission-srtm-1?qt-science_center_objects=0#qt-science_center_objects (accessed on 13 December 2021).

60. Szypuła, B. Quality Assessment of DEM Derived from Topographic Maps for Geomorphometric Purposes. *Open Geosci.* **2019**, *11*, 843–865. [CrossRef]
61. Sanz-Ablanedo, E.; Chandler, J.H.; Rodríguez-Pérez, J.R.; Ordóñez, C. Accuracy of Unmanned Aerial Vehicle (UAV) and SfM Photogrammetry Survey as a Function of the Number and Location of Ground Control Points Used. *Remote Sens.* **2018**, *10*, 1606. [CrossRef]
62. Tonkin, T.N.; Midgley, N.G. Ground-Control Networks for Image Based Surface Reconstruction: An Investigation of Optimum Survey Designs Using UAV Derived Imagery and Structure-from-Motion Photogrammetry. *Remote Sens.* **2016**, *8*, 786. [CrossRef]
63. Agüera-Vega, F.; Carvajal-Ramírez, F.; Martínez-Carricondo, P. Accuracy of Digital Surface Models and Orthophotos Derived from Unmanned Aerial Vehicle Photogrammetry. *J. Surv. Eng.* **2017**, *143*, 04016025. [CrossRef]
64. Hutton, J.J.; Lipa, G.; Baustian, D.; Sulik, J.; Bruce, R.W. High Accuracy Direct Georeferencing of the Altum Multi-Spectral UAV Camera and Its Application to High Throughput Plant Phenotyping. In *The International Archives of the Photogrammetry, Remote Sensing and Spatial Information Sciences*; Copernicus GmbH: Göttingen, Germany, 2020; Volume XLIII-B1-2020, pp. 451–456. [CrossRef]
65. Hugenholtz, C.; Brown, O.; Walker, J.; Barchyn, T.; Nesbit, P.; Kucharczyk, M.; Myshak, S. Spatial Accuracy of UAV-Derived Orthoimagery and Topography: Comparing Photogrammetric Models Processed with Direct Geo-Referencing and Ground Control Points. *Geomatica* **2016**, *70*, 21–30. [CrossRef]
66. Turner, D.; Lucieer, A.; Wallace, L. Direct Georeferencing of Ultrahigh-Resolution UAV Imagery. *IEEE Trans. Geosci. Remote Sens.* **2014**, *52*, 2738–2745. [CrossRef]
67. Mandlburger, G.; Pfennigbauer, M.; Schwarz, R.; Flöry, S.; Nussbaumer, L. Concept and Performance Evaluation of a Novel UAV-Borne Topo-Bathymetric LiDAR Sensor. *Remote Sens.* **2020**, *12*, 986. [CrossRef]
68. Vélez-Nicolás, M.; García-López, S.; Barbero, L.; Ruiz-Ortiz, V.; Sánchez-Bellón, Á. Applications of Unmanned Aerial Systems (UASs) in Hydrology: A Review. *Remote Sens.* **2021**, *13*, 1359. [CrossRef]
69. Liao, J.; Zhou, J.; Yang, W. Comparing LiDAR and SfM Digital Surface Models for Three Land Cover Types. *Open Geosci.* **2021**, *13*, 497–504. [CrossRef]
70. Rogers, S.R.; Manning, I.; Livingstone, W. Comparing the Spatial Accuracy of Digital Surface Models from Four Unoccupied Aerial Systems: Photogrammetry Versus LiDAR. *Remote Sens.* **2020**, *12*, 2806. [CrossRef]
71. Ekaso, D.; Nex, F.; Kerle, N. Accuracy Assessment of Real-Time Kinematics (RTK) Measurements on Unmanned Aerial Vehicles (UAV) for Direct Geo-Referencing. *Geo-Spat. Inf. Sci.* **2020**, *23*, 165–181. [CrossRef]

Determining the Optimal Number of Ground Control Points for Varying Study Sites through Accuracy Evaluation of Unmanned Aerial System-Based 3D Point Clouds and Digital Surface Models

Jae Jin Yu, Dong Woo Kim, Eun Jung Lee and Seung Woo Son *

Korea Environment Institute, Bldg. B, 370 Sicheong-daero, Sejong 30147, Korea; jjyu@kei.re.kr (J.J.Y.); dwkim@kei.re.kr (D.W.K.); ejlee@kei.re.kr (E.J.L.)

* Correspondence: swson@kei.re.kr

Abstract: The rapid development of drone technologies, such as unmanned aerial systems (UASs) and unmanned aerial vehicles (UAVs), has led to the widespread application of three-dimensional (3D) point clouds and digital surface models (DSMs). Due to the number of UAS technology applications across many fields, studies on the verification of the accuracy of image processing results have increased. In previous studies, the optimal number of ground control points (GCPs) was determined for a specific area of a study site by increasing or decreasing the amount of GCPs. However, these studies were mainly conducted in a single study site, and the results were not compared with those from various study sites. In this study, to determine the optimal number of GCPs for modeling multiple areas, the accuracy of 3D point clouds and DSMs were analyzed in three study sites with different areas according to the number of GCPs. The results showed that the optimal number of GCPs was 12 for small and medium sites (7 and 39 ha) and 18 for the large sites (342 ha) based on the overall accuracy. If these results are used for UAV image processing in the future, accurate modeling will be possible with minimal effort in GCPs.

---

1. Introduction

Various studies have been conducted to investigate the utility of unmanned aerial systems (UASs) and unmanned aerial vehicles (UAVs) as the technologies have developed and popularized. These studies mainly acquire data through UAVs equipped with optical (RGB), multi-spectral, or infrared sensors [1–3], and produce 3D point clouds and digital surface models (DSMs) using image processing programs. Before the popularization of UAV technology, satellites, manned aircrafts, and professional surveillance cameras were the prominent methods of data acquisition for research [4,5].

The 3D point cloud is a set of data in which each point has a 3D coordinate value. The initial 3D point cloud was acquired through an expensive laser scanner [6,7]. However, recently, it could be constructed from images taken with a camera using the Structure from Motion-Multi View Stereo (SfM-MVS) algorithm [8–10]. DSM is a 2.5D raster format data generated with stereo images [5,11] and is also produced by interpolating point clouds built using the SfM-MVS algorithm [12,13]. Image processing results, such as 3D point clouds and DSMs built using UAV images, have been applied to various fields, such as geography, environment, administration, and industry [14–17].

Due to the increase in the number of studies that produce and utilize results of UAV image processing, studies that verify their accuracy are also increasing. Parameters that affect the accuracy of results are flight parameters [18–20], such as the front and side overlap and flight altitude, interior

orientation parameters of the camera [1,21–23], and exterior orientation parameters through ground control points (GCPs) [24,25]. The root-mean-square error (RMSE), which statistically represents the errors between the constructed results and the checkpoints (CPs), mainly evaluates the accuracy [25–28].

To verify the accuracy of image processing results, studies have been continuously conducted using flight parameters [18,29] or the interior orientation parameters and calibration of the camera as variables [1,22,30]. However, the most actively conducted studies on accuracy verification were focused on using the number of GCPs as the variable. Studies on 3D modeling using UAVs mainly used non-measurement cameras and low-cost UAVs [31–34], which requires an increasing number of GCPs [34]. Installing GCPs is labor-intensive and time-consuming work [35,36], and human access can be difficult depending on the terrain of the target site (e.g., steep mountain area and rock quarry) and the material of the ground surface (e.g., tidal flat and waste stock). In order to reduce the amount of time and labor required to install the GCPs, a real-time kinematic (RTK) and a post-processing kinematic (PPK) method have been recently introduced [25,27,37]. However, the RTK and PPK methods require expensive devices and need complex technologies that make them difficult to use. Therefore, many studies focus on the number of GCPs installed instead.

Previous studies have suggested the optimal number of GCP. Soo-Bong Lim [38] mentioned that 10–12 GCPs are appropriate per 100 ha. Yong-ho Yoo et al. [39] classified the number of GCPs into 0, 3, and 6. They reported that no significant difference exists in the deviation of the horizontal accuracy, depending on the number of GCPs. In contrast, the deviation of vertical accuracy decreased as the number of GCPs increased. Bu-yeol Yun et al. [40] reported that stable accuracy could be achieved when eight to nine GCPs are used to determine the precise position. Seung-woo Son [29] mentioned that two to three GCPs should be set per 1 ha to obtain a 3D model with high accuracy, although the number may differ depending on the flight altitude.

The accuracy was high when one GCP was used per 2 ha [41], and another study noted that one GCP is required per approximately 1.17 ha. This is because no change occurred when the number of GCP was 15 or higher for the study site (17.64 ha) [42]. A study on the appropriate amount of GCPs, in which more than 100 GCPs were installed in a study site of approximately 12 km^2 (1200 ha), reported that sufficiently high accuracy could be achieved when the number of GCPs was three or less per 100 photographs (a total of 2514 photographs) [43]. Patricio Martínez-Carricondo et al. [26] reported that GCPs must be placed at a density of 0.5–1 GCP $\times$ ha^{-1}.

These such studies indicate that 9–12 GCPs are generally required per 100 ha (1 km^2). As previous studies conducted research only in a single site to determine the optimal number of GCPs, the question is whether the results can be applied to study sites with various areas. In summary, when 9–12 GCPs were assumed to be optimal per 100 ha, examining whether the number of GCPs increases (or decreases) as the area increases (or decreases) is necessary. Additionally, the Public Surveying Regulation Using Unmanned Aerial Vehicle enacted recently in South Korea [44] specifies that nine or more GCPs are required per 1 km^2. However, it does not mention the number of GCPs changes according to the increase or decrease in the target site, and no criterion exists for areas less than 100 ha. 3D point clouds and DSMs were frequently constructed using UAVs in sites smaller than 100 ha [45–47] due to technical limitations, such as battery shortages [48–50], hence the need for research on GCP setting for various target sites.

In this study, the accuracy of 3D point clouds and DSMs were analyzed in three study sites with different areas according to the number of GCPs to determine the optimal number of GCPs, which is required when 3D modeling is performed for target sites with different areas using UAVs.

2. Materials and Methods

2.1. Study Sites

This study aimed to determine the optimal number of GCPs for each area by examining the accuracy of 3D point clouds and DSMs. Three differing sites were selected as study sites. The small

site (SS) was an aggregate yard located in Jiphyeon-ri, Sejong city, with 7 ha. The long-direction of the site was N-S with a length of approximately 0.34 km, whereas the short-direction was E-W with a distance of approximately 0.25 km. As SS was excessively small; one mission of a rotary-wing UAV could cover the entire area. The medium site (MS) was the Pado-ri coast located in Taean-gun, Chungcheongnam-do, with 39 ha. The long-direction of the site was N-S with a length of approximately 1.2 km, whereas the short-direction was E-W with a distance of approximately 0.3 km. The MS required four missions of a rotary-wing UAV. The large site (LS) was the Daedeok industrial complex in Daejeon metropolitan city, with an area of 342 ha. The long-direction of the site was NW-SE with a length of approximately 2.4 km, whereas the short-direction was NE-SW with a distance of approximately 1.7 km. As LS covers an extensive coverage even for a fixed-wing, which performs a longer flight time than the rotary-wing, three flight missions were performed using the fixed-wing UAV. The flight sites and their positions within the Korean peninsula are summarized in Figure 1.
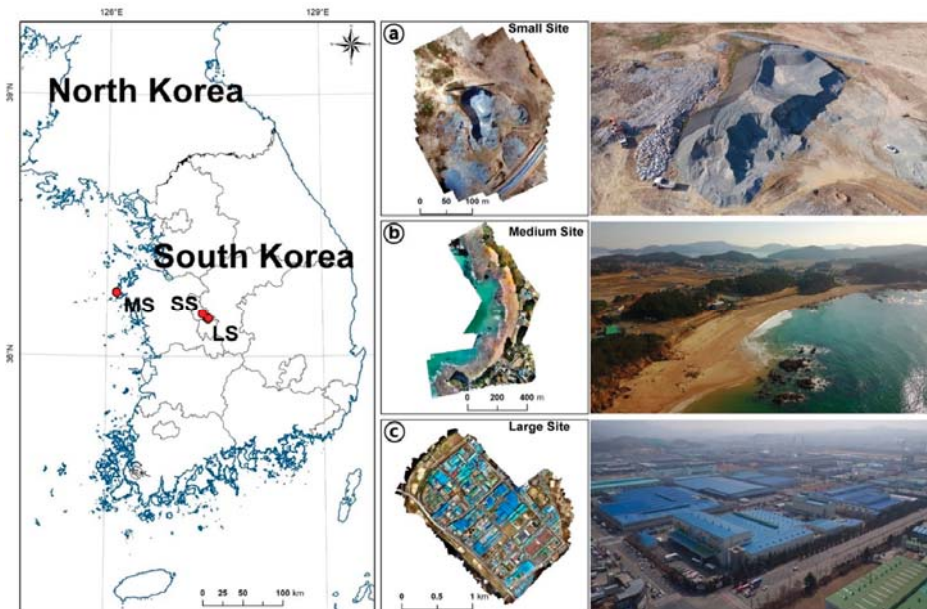
Figure 1. From left to right, a map of the Korean peninsula showing the locations of the three different study sites for (**a**) the small site, (**b**) medium site, and (**c**) large site, aerial orthomosaics of the three labeled study sites, next to images captured of the study sites from UAV.

In the SS, no vegetation growth was observed on the ground surface because aggregate was continuously carried in and out. The MS was composed of tidal flats, where flood and ebb tides were repeated, with artificial structures behind them; thus, no vegetation was in the tidal flats. The LS was also covered with buildings, pavements, and sidewalk blocks; therefore, there was no vegetation except street trees.

2.2. Data Collection and Photogrammetry Process

The target sites were classified as SS, MS, and LS; then, 3, 6, 9, 12, 15 (14 in the case of the SS, where the increase in the number of GCPs was halted owing to space restrictions), and 18 GCPs were placed in each target site to investigate the effects of the number of GCPs on the accuracy of 3D point clouds and DSMs for these sites. The 3D point clouds and DSMs were produced using each GCP as an

exterior orientation parameter in SfM-based image processing. The accuracy of the generated results was analyzed through CPs.

The research method can be divided into in situ operations, including UAV flights, image acquisition, and land survey; the photogrammetry process, where results are produced according to the number of GCPs; and accuracy analysis (Figure 2).
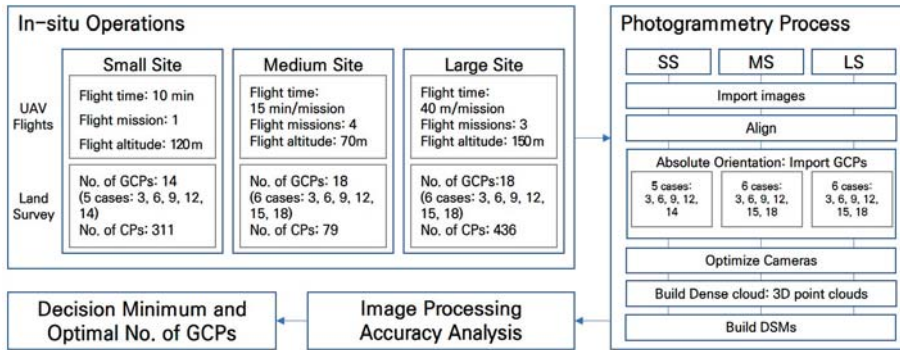
Figure 2. Flow of research, from in situ operations to the photogrammetry process, for each of the SS, MS, and LS.

2.2.1. In Situ Operations

The field survey was divided into UAV flight, image acquisition, and land survey using a global navigation satellite system (GNSS). A field survey for the SS was conducted on 10 October 2018. In the SS, the Inspire 1 Pro model was used, and images were captured using a Zenmuse X5 camera. As the area of the SS was small, imaging could be completed during a single flight.

A field survey for the MS was conducted on 2 December 2016. In the MS, the Phantom 3 Advanced model was used, and the camera mounted on the UAV (FC300S) was used. As the area of the MS exceeded the one-time flight coverage of the rotary-wing UAV, four missions were executed.

A field survey for the LS was conducted on 13 April 2017. In the LS, the QuestUAV DataHawk, a fixed-wing UAV, and ILCE-QX1 imaging camera were used. As the area of the LS exceeded the coverage of the fixed-wing UAV, which had a longer flight time than the rotary-wing UAV, three flight missions of the fixed-wing UAV were executed.

For land surveys, the Trimble R8s model was used for the SS and LS, and the Huace X90 model was used for the MS. This is summarized in Table 1.

Automatic path flight measurements for uniform image acquisition, SfM-based image processing, accuracy analysis, and mapping were processed using the same software for each site. Pix4d Capture was used for automatic path flight measurements. Agisoft Metashape (v. 1.5.3) was used for SfM-based image processing, CloudCompare (v. 2.10.2) for accuracy analysis, and ArcMap (v. 10.1) for mapping, as summarized in Table 2.

The coordinate system used for both flight and imaging was WGS 84 (EPSG: 4326), and the TM Korea 2000 or Central Belt 2010 (EPSG: 5186) coordinate system was used for GCP measurement. Although different coordinate systems for flight and measurement were used, absolute orientation was performed following the land survey performance during the image processing process.

Study Site	UAV	Camera	Land Survey
Small Site, SS: Jiphyeon-ri, Sejong city Area: 7 ha (0.07 km^2)	Aircraft: DJI Inspire 1 Pro Max speed: 18 m/s Weight: 3.4 kg Flight time: approximately 15 min	Camera: DJI X5(FC550) Image size: 4608 * 3456/px Max-Pixels: 16.0M Diagonal FOV: 72 degree Sensor Size: 17.3 × 13.0 mm	GNSS: Trimble R8s VRS H: 8 mm + 0.5 ppm RMS VRS V: 15 mm + 0.5 ppm RMS
Medium Site, MS: Pado-ri, Taean-gun Area: 39 ha (0.39 km^2)	Aircraft: DJI Inspire 1 Pro Max speed: 16 m/s Weight: 1.28 kg Flight time: approximately 23 min	Camera: DJI FC300S Image size: 4000 * 3000/px Max-Pixels: 12.76M Diagonal FOV: 94 degree Sensor Size: 6.16 × 4.62 mm	GNSS: Huace X90 VRS H: 5 mm + 1 ppm RMS VRS V: 10 mm + 2 ppm RMS
Large Site, LS: Daedeok industrial complex, Daejeon metropolitan city Area: 342 ha (3.42 km^2)	Aircraft: QuestUAV DataHawk (Fixed wing) Max speed: 25 m/s Weight: 2 kg Flight time: approximately 45 min	Camera: SONY ILCE-QX1 Image size: 5456 * 3632/px Max-Pixels: 20M Diagonal FOV: 73.7 degree Sensor Size: 23.2 × 15.4 mm	GNSS: Trimble R8s VRS H: 8 mm + 0.5 ppm RMS VRS V: 15 mm + 0.5 ppm RMS

Table 2. Software used in the research.

Automatic Mission Flight	3D Modeling Process	Accuracy Analysis and Mapping
Pix4d Capture	Agisoft Metashape (v.1.5.3)	CloudCompare (v.2.10.2) and ArcMap (v.10.1)

2.2.2. Construction of 3D Point Clouds and DSMs and Their Accuracy Evaluation

SfM is a technology for reconstructing the camera's position and direction from multi-shot two-dimensional (2D) images and restoring the subject and scene in 3D. This technology, based on computer vision, was developed in the 1990s and became widely used in the 2000s [31,51].

In this study, imaging (acquisition of 2D images) was performed in each study site using the UAVs. Based on this, 3D point clouds and DSMs were constructed as final results using Metashape, a software program based on the SfM algorithm. Metashape goes through the following: Camera calibration-align–absolute orientation–camera align optimization–3D point cloud generation–DSM generation (to produce the final results from 2D images).

This imaging process is a minimal procedure required to produce a 3D point cloud and DSM. As this study aims to identify the accuracy of 3D point clouds and DSMs according to the area of each study site and the number of GCPs, image processing was performed by applying multiple GCP sets for each study site.

The accuracy of the produced 3D point clouds and DSMs can be evaluated using various methods. In this study, the accuracy of *x*, *y*, *z*, *xy*, and *xyz* was evaluated for verification using the errors and *RMSE* between the constructed results and the measured CPs. The errors represent individual errors between the created point clouds and CPs. *RMSE* indicates the overall accuracy of the results by combining individual errors and is one of the generally used criteria for position accuracy [28,52].

The error between the 3D point cloud and the CP was calculated using the "Cloud/Cloud distance" tool in CloudCompare. Similarly, the error between the DSM and the CP was calculated using the "Extract Values to Point" tool in ArcMap. The mean distance and standard deviation were

calculated using the calculated error with the programs, and finally *RMSE x*, *y*, and *z* were produced (Equations (1)–(5)):

$$(RMSE)_x = \sqrt{\frac{\sum_{i=1}^{n} \Delta x_i^2}{n}}, \tag{1}$$

where Δx_i is the difference between the CP coordinates and coordinates determined from the 3D point cloud and DSM, and *n* is the number of points. The same equation applies to $RMSE_Y$ and $RMSE_Z$ mutatis mutandis:

$$(RMSE)_y = \sqrt{\frac{\sum_{i=1}^{n} \Delta y_i^2}{n}}, \tag{2}$$

$$(RMSE)_{xy} = \sqrt{(RMSE)_x^2 + (RMSE)_y^2}, \tag{3}$$

where $(RMSE)_x$ represents the *x*-direction error in the plane between the CPs and the produced 3D point cloud (Equation (1)) and $(RMSE)_y$ represents the *y*-direction error in the plane between the CPs and the generated 3D point cloud (Equation (2)). The individual *x*- and *y*-direction error is calculated as $(RMSE)_{xy}$, a radius error, which corresponds to the horizontal error of the 3D point cloud (Equation (3)):

$$(RMSE)_z = \sqrt{\frac{\sum_{i=1}^{n} \Delta z_i^2}{n}}, \tag{4}$$

$$(RMSE)_{xyz} = \sqrt{(RMSE)_x^2 + (RMSE)_y^2 + (RMSE)_z^2}. \tag{5}$$

Further, $(RMSE)_z$ represents the *z*-direction (vertical) error. For vertical accuracy testing, different methods are used in non-vegetated terrain (where errors typically follow a normal distribution suitable for RMSE statistical analyses) and vegetated terrain (where errors do not necessarily follow a normal distribution) [28]. In this study, $(RMSE)_z$ was applied for the evaluation of the vertical accuracy because all of the study sites were non-vegetated terrains (Equation (4)). $(RMSE)_{xyz}$ represents the error of the 3D point cloud in the overall direction (easting, northing, and elevation) (Equation (5)).

3. Results

3.1. In Situ Operation

In the SS, a total of 52 aerial images were acquired through a flight at an altitude of 120 m. The front and side overlap were 85% and 65%, respectively. In the MS, imaging was performed at an altitude of 70 m, and both the front and side overlap were 80%. As the site exceeded the flight radius of the rotary-wing UAV, four flights were performed, and a total of 1022 aerial images were acquired. In the LS, imaging was performed at an altitude of 150 m, and both the front and side overlap were 80%. As the site exceeded the flight radius of the fixed-wing UAV, three flights were performed, and 1163 aerial images obtained. The result of UAV and field survey is summarized in Table 3.

Table 3. Results of UAV flight and field survey.

Study Site	Flight Plan and Parameters		GNSS Survey
SS	Flight time: 10 m Flight mission: 1 Flight altitude: 120 m	Images: 52 Front overlap: 85% Side overlap: 65%	No. of GCPs: 14 (5 cases: 3, 6, 9, 12, 14) No. of CPs: 311
MS	Flight time: 15 m/mission Flight missions: 4 Flight altitude: 70 m	Images: 1022 Front overlap: 80% Side overlap: 80%	No. of GCPs: 18 (6 cases: 3, 6, 9, 12, 15, 18) No. of CPs: 79
LS	Flight time: 40 m/mission Flight missions: 3 Flight altitude: 150 m	Images: 1163 Front overlap: 80% Side overlap: 80%	No. of GCPs: 18 (6 cases: 3, 6, 9, 12, 15, 18) No. of CPs: 436

The arrangement adopted for the placement and the number of the GCPs is as follows: The number of GCPs was increased by a multiple of 3, starting with the minimum number of GCPs required to obtain an absolute orientation in Metashape. The GCPs were arranged to form a central polygon that covered the study area while keeping the gaps between the GCPs as uniform as possible.

Although the SS area was small, there was a difference in altitude between the aggregate stacked at the center of the site and the surroundings. Considering this, GCPs were evenly placed at the top of the aggregate and in the surrounding areas. A total of 14 GCPs were placed. Among them, 3, 6, 9, 12, and 14 GCPs were present in the absolute orientation process of image processing. The MS was long in the N-S direction due to the coastal area's nature, and GCPs were placed accordingly. A total of 18 GCPs were placed, and divided into six cases (3, 6, 9, 12, 15, and 18 GCPs). In the LS, there were 18 GCPs as in the MS.

At least 20 CPs are required to evaluate the accuracy of the produced image processing results [28]. Surveying CPs across the study area can ensure higher reliability. However, the limitations of time and labor restrict the number of CPs surveyed. Therefore, only the CPs that were around the main targets, such as aggregate mounds, sand beaches, and main streets in each study area, were measured. In the SS, 311 points were acquired in the upper and surrounding areas of the aggregate yard; the MS, 79 points were acquired by setting two survey lines across the sand beach; and in the LS, 436 points were acquired by planning one survey line in the long direction of the site and two lateral lines in the short direction, as shown in Figure 3.
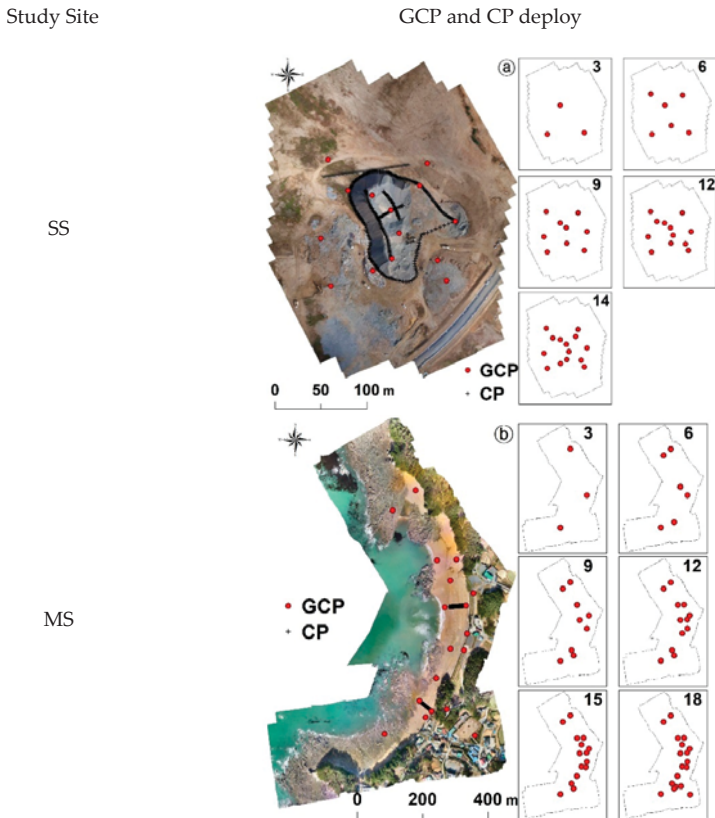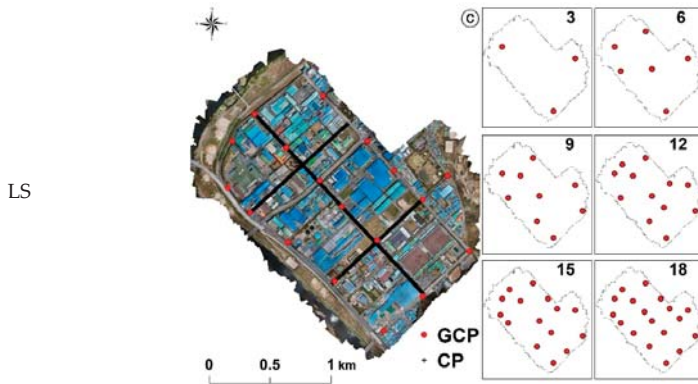

Figure 3. *Cont.*

Figure 3. Deployment of GCPs (red dots) and CPs (black crosses) for the (**a**) small site, (**b**) medium site), and (**c**) large site.

3.2. Photogrammetry Process

Constructing 3D Point Clouds and DSMs

The SS had five GCP sets generating five 3D point clouds and DSMs. For the MS and LS, they produced six 3D point clouds and DSMs because they had six GCP sets (Figure 4). There was a small difference in the number of points, point density, DSM, and orthomosaic of each 3D point cloud depending on the number of GCPs. Since the average number of points in a 3D point cloud is proportional to the area, a large difference in the average number of points is seen corresponding to the study area. Table 4 shows the average values of the produced results.

Table 4. Results of the field survey, summarizing the average number of points, density, and resolution of the 3–18 GCP results.

Study Site	Avg. Number of Points	Avg. Point Density (points/m^2)	Avg. Resolution of DSM (cm/px)	Avg. Resolution of Orthomosaic (cm/px)
SS	5,525,047	70.7	11.9	2.97
MS	53,859,773	86.4	10.8	2.69
LS	207,286,235	42.5	15.3	3.84

There were differences in the resolutions of DSM and orthomosaic because 3D point cloud processing was set to "Medium" in Metashape. "Medium" downscales the original scale at a ratio of 1:4. When a 3D point cloud and DSM are produced at the original scale in Metashape, the average resolution of the DSM (shown in Table 4) shows a 4-time increase, thereby increasing the value of the average resolution of DSM to become the same as the resolution of orthomosaic. The average point density and the average number of points also show an increase by 4 times. The image processing results were not produced on the original scale due to their capacity. The restriction on capacity is less for the SS and MS because the area is not large. In the case of the LS, however, the area is excessively large, and capacity can also become excessive if 3D point clouds and DSMs are produced in a 1:1 scale, making the post-processing of the results difficult.
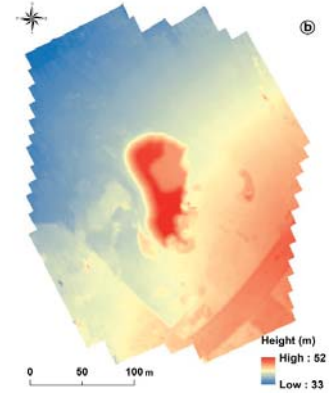
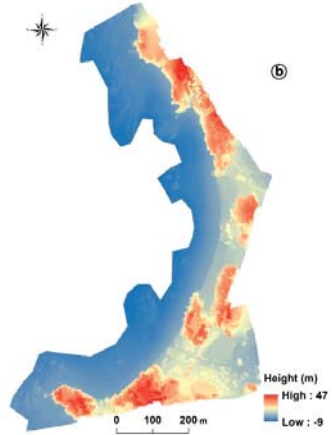| Study Site	3D point cloud	Digital surface model

SS

MS

LS
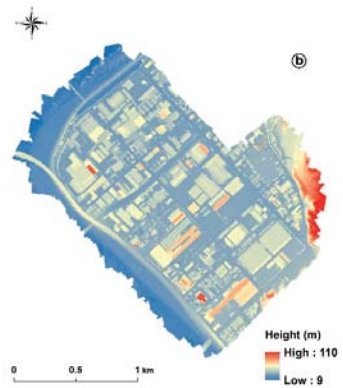
Figure 4. 3D point clouds (**a**) and DSMs (**b**) of the study sites.

3.3. Accuracy Analysis According to the Number of GCPs

3.3.1. Analysis of the Accuracy of 3D Point Clouds

The accuracy of 3D point clouds was evaluated using the horizontal (xy), vertical (z), and total (xyz) errors between the 3D point clouds and CPs. Figure 5 shows the average horizontal error between the 3D point cloud and CPs according to the number of GCPs. Figure 5a shows the average horizontal error distribution of the SS, and the error ranged from 0.046 to 0.050 m. Figure 5b shows the average horizontal error distribution of the MS. The average horizontal error was 0.103 m when the number of GCPs was three. This error ranged from 0.041 to 0.045 m when the number was six or larger. Figure 5c shows the average horizontal error distribution of the LS. The average horizontal error was 0.453 m when the number of GCPs was three, with a range of 0.061 to 0.063 m for other cases.
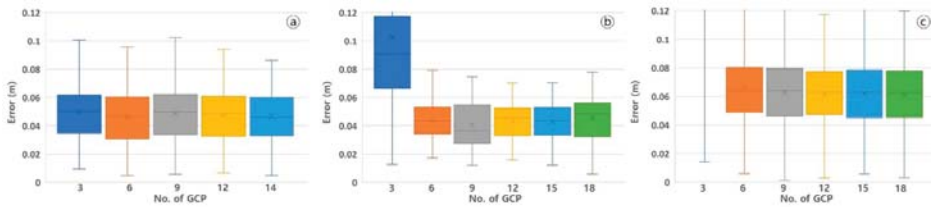
Figure 5. 3D point cloud horizontal error of the study areas: (**a**) SS, (**b**) MS, and (**c**) LS.

Figure 6 shows the average vertical errors between the 3D point clouds and CPs in each site and Figure 6a the vertical error distribution of the SS, and the error ranges from −0.004 to −0.063 m. Figure 6b shows the average vertical error distribution of the MS. The average vertical error was −0.916 m for three GCPs, ranging from −0.018 to −0.046 m. Figure 6c shows the average vertical error distribution of the LS. The average vertical error was 3.81 m for three GCPs, and it ranged from −0.004 to 0.114 m.
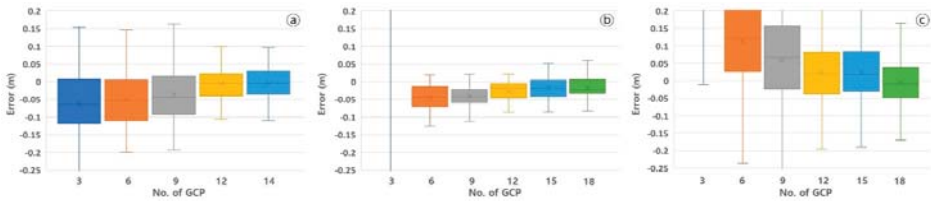
Figure 6. 3D point cloud vertical error of the study areas: (**a**) SS, (**b**) MS, and (**c**) LS.

Figure 7 shows the average total errors between the 3D point clouds and CPs in each site. Figure 7a shows the average total error distribution of the SS, and the error ranged from 0.063 to 0.111 m. The average total error of the MS was 0.972 m for three GCPs, as shown in Figure 7b, and it ranged from 0.055 to 0.07 m. Figure 7c shows the total error distribution of the LS. The average total error was 3.951 m for three GCPs, and it ranged from 0.088 to 0.174 m in other cases.
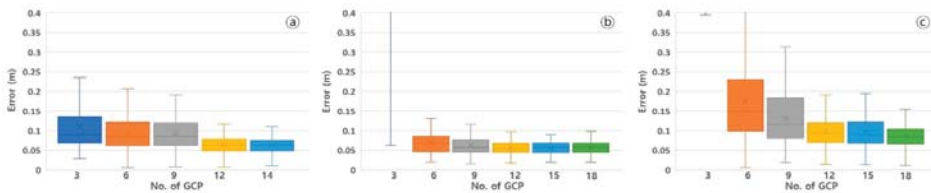
Figure 7. 3D point cloud total error of the study areas: (**a**) SS, (**b**) MS, and (**c**) LS.

The 3D point clouds produced for each GCP set were analyzed by using the average error range. In the case of the SS area, there was no significant difference observed in the average horizontal error corresponding to the increase or decrease in the GCP number. However, in the cases of the MS and LS areas, the average horizontal error showed a decrease when the number of GCPs was increased. Additionally, the average vertical error decreased significantly when six GCPs were used. The average total error showed a similar pattern to the average vertical error; however, when more than 12 GCPs were used, there was no significant decrease observed in the average total error.

3.3.2. Analysis of the Accuracy of DSMs

DSMs are produced by interpolating 3D point clouds. Their vertical errors were analyzed as the elevation of the surface is considered important. Figure 8 shows the average vertical errors between the DSMs, produced by varying the number of GCPs and CPs in each site.
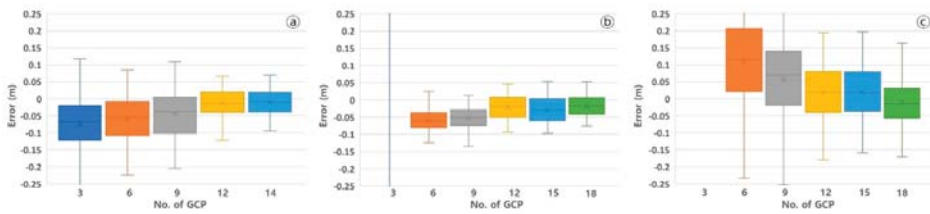
Figure 8. Vertical DSM accuracy of the study areas: (**a**) SS, (**b**) MS, and (**c**) LS.

Figure 8a shows the average vertical error distribution of the SS, which ranged from −0.011 to 0.074 m. Figure 8b shows the average vertical error distribution of the MS. The average error was −0.939 m for three GCPs, with a −0.019 to −0.061 m range in other cases. Figure 8c shows the average vertical error distribution of the LS. The average error was 3.986 m when three GCPs were used, and it ranged from −0.01 to 0.11 m in other cases. The vertical error observed in the DSMs was similar to the average vertical error observed in the 3D point clouds.

3.3.3. Comprehensive Comparison

The errors between the constructed results and CPs were analyzed in the above sections to verify the 3D point clouds and DSMs constructed for each site. RMSE by region and the number of GCPs were analyzed to evaluate the overall accuracy of the constructed results (Figure 9; Table 5).

Table 5. RMSEs of the 3D point clouds (in meters).

RMSE		Site	No. of GCPs						
			3	6	9	12	14	15	18
3D point cloud	Horizontal	SS	0.054	0.050	0.053	0.051	0.050	n/a	n/a
		MS	0.117	0.046	0.044	0.045	n/a	0.045	0.048
		LS	0.907	0.072	0.068	0.066	n/a	0.067	0.065
	Vertical	SS	0.114	0.092	0.087	0.045	0.044	n/a	n/a
		MS	1.148	0.058	0.051	0.038	n/a	0.036	0.036
		LS	4.101	0.188	0.131	0.082	n/a	0.082	0.067
	Total	SS	0.126	0.104	0.102	0.068	0.067	n/a	n/a
		MS	1.154	0.075	0.067	0.059	n/a	0.058	0.060
		LS	4.200	0.201	0.147	0.105	n/a	0.105	0.093
DSM	Vertical	SS	0.117	0.092	0.085	0.041	0.039	n/a	n/a
		MS	1.173	0.072	0.063	0.040	n/a	0.046	0.037
		LS	4.248	0.186	0.128	0.084	n/a	0.083	0.069
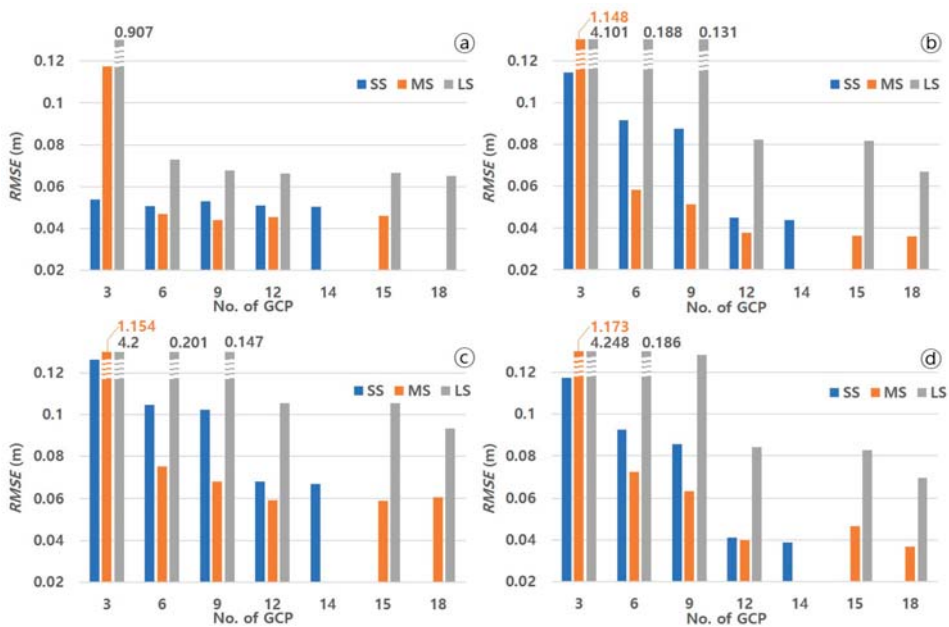
Figure 9. Comprehensive comparison of the RMSE results for the different study sites: (**a**) horizontal RMSEs of 3D point clouds, (**b**) vertical RMSEs of 3D point clouds, (**c**) total RMSEs of 3D point clouds, and (**d**) vertical RMSEs of DSMs.

The SS's horizontal RMSEs were 0.054 m (largest) for three GCPs and 0.050 m for 14 GCPs. The smallest RMSE of 0.050 m was observed when using 6 and 14 GCPs. The MS's horizontal RMSEs were 0.117 m (largest) for three GCPs and 0.048 m for 18 GCPs. The smallest RMSE of 0.044 m was observed when nine GCPs were used. The LS's horizontal RMSEs were 0.907 m (largest) for three GCPs and 0.065 m (smallest) for 18 GCPs.

The vertical RMSEs of the SS were 0.114 m (largest) for three GCPs and 0.044 m (smallest) for 14 GCPs. The vertical RMSEs of the MS were 1.148 m (largest) for three GCPs and 0.036 m for 18 GCPs. The smallest vertical RMSE of the MS was 0.036 m when 15 and 18 GCPs were used, and the vertical RMSEs of the LS were 4.101 m (largest) for three GCPs and 0.067 m for 18 GCPs. The smallest vertical RMSE was observed when the number of GCPs was largest.

The total RMSEs of the SS was 0.126 m (largest) for three GCPs and 0.067 m for 14 GCPs. The total RMSEs of the MS was 1.154 m (largest) for three GCPs and 0.060 m for 18 GCPs. The LS's total RMSEs were 4.200 m (largest) for three GCPs and 0.093 m for 18 GCPs.

The vertical RMSEs of DSMs for each site are as follows. Vertical RMSEs of the SS were 0.117 m (largest) for three GCPs and 0.039 m (smallest) for 14 GCPs. The MS had vertical RMSEs of 1.173 m (largest) for three GCPs and 0.037 m (smallest) for 18 GCPs. Finally, the LS's vertical RMSEs were 4.248 m (largest) for three GCPs and 0.069 m (smallest) for 18 GCPs, as in the previous case.

The RMSE analysis showed similarity to the error analysis. Excluding the case of the SS area, the RMSE showed a significant increase when 6 GCPs were used. The total RMSE seemed to be optimized when the 12 GCPs were used, although there were differences depending on the area of the study area.

4. Discussion

As mentioned in the introduction, the number of GCPs used in the study is important for performing absolute orientation in UAV surveys [24,53] because installing GCPs is not only labor

intensive but also time consuming [35,36]. In addition, a large number of GCPs may increase the time required to mark drone images during image processing. Therefore, determining the optimal number of GCPs to construct 3D point clouds and DSMs is significant as it enables time-efficient work without wasting labor.

To find the optimal number of GCPs according to each target sites area, the accuracy of the 3D point clouds and DSMs was calculated according to the number of GCPs. GCPs were evenly distributed in each target site so that the GCP network could form a central point polygon capable of covering the site [26,43,54].

Drone modeling has various end-users, and each end-user requires different types of accuracy (vertical, horizontal, or total accuracy) depending on their needs. Therefore, the horizontal, vertical, and total accuracy were calculated individually. Whether this accuracy met the horizontal/vertical accuracy criteria of the American Society for Photogrammetry and Remote Sensing (ASPRS) was assessed [25]. In the Accuracy Quality criteria of ASPRS, the ground sample distance (GSD) of the original image becomes the judgment criterion of accuracy for horizontal accuracy, but the vertical accuracy only distinguishes the absolute accuracy. However, all of the three study sites were non-vegetated terrains. Therefore, non-vegetated in the vertical accuracy class was considered for the judgment of the accuracy (Table 6).

Table 6. Horizontal accuracy quality examples for high-accuracy digital planimetric data and vertical accuracy quality examples for digital elevation data.

Horizontal Accuracy Class RMSEx, and RMSEy (cm)	RMSExy (cm)	Approximate GSD of Source Imagery (cm)	Vertical Accuracy Class (cm)	Absolute Accuracy: RMSEz Non-Vegetated (cm)
0.63	0.9	0.31–0.63	1 cm	1.0
1.25	1.8	0.63–1.25	2.5 cm	2.5
2.5	3.5	1.25–2.5	5 cm	5.0
5.0	7.1	2.5–5.0	10 cm	10.0
		…		

4.1. Horizontal Errors and RMSEs of 3D Point Clouds

In the SS, the average horizontal errors were 0.05 m for three GCPs and 0.047 m for 14 GCPs. The smallest average horizontal error was 0.046 m when using six GCPs. The standard deviation ranged from 0.019 to 0.020 m, indicating no significant difference between whether the number of GCPs was the largest and the smallest. RMSE also ranged from 0.050 to 0.054 m, corresponding to the range of less than 2 * GSD (5.94 cm) in all cases. In summary, using only three GCPs in the small area of the SS met the horizontal position accuracy criterion of ASPRS. Therefore, using only three GCPs is sufficient when only considering the horizontal accuracy.

The average horizontal error of the MS exceeded 0.1 m when the number of GCPs was three and became smaller when it was six. The error was the smallest (0.041 m) when the number of GCPs was nine. The standard deviation was 0.055 m for three GCPs and sharply decreased from six GCPs with a range of 0.014 to 0.016 m when the number of GCPs was between 6 and 18. RMSE was also inaccurate (approximately 5 * GSD) when three GCPs were used but exhibited an accuracy of less than 2 * GSD (5.38 cm) from six GCPs. As the horizontal accuracy criterion of ASPRS could be met when the number of GCPs was six or larger for the area of the MS, it is necessary to secure at least six GCPs when only the horizontal accuracy is considered.

The accuracy trend of the LS, according to the number of GCPs was very similar to that of the MS. When the number of GCPs was three, the average horizontal error was 0.453 m. However, the error sharply decreased and ranged from 0.061 to 0.067 m when the number of GCPs was between 6 and 18. The standard deviation also decreased from 0.78 m to 0.023–0.028 m when the number of GCPs increased from three. RMSE was also excessively large (close to 1 m) when the number of GCPs was three but decreased to less than 2 * GSD with six GCPs. This indicates that using at least six GCPs can

meet the horizontal accuracy criterion of ASPRS for sites whose area is similar to or larger than that of the MS.

4.2. Vertical Errors and RMSEs of 3D Point Clouds

In the SS, the average vertical error was the largest (−0.063 m) when the number of GCPs was three. As the number increased, the error slowly decreased and showed a tendency to converge to zero. The difference between the two cases was only 1 mm when using 12 and 14 GCPs. The standard deviation was also the largest for three GCPs. However, it slowly decreased and there was a small difference when 12 and 14 GCPs were used. RMSE also exceeded 0.1 m for three GCPs but was less than 0.1 m for six and nine GCPs. It was close to 0.04 m from 12 GCPs. These results indicate that at least six GCPs must be installed in small areas, such as SS, considering the vertical accuracy and that at least 12 GCPs must be used to achieve the 5 cm class of ASPRS.

The average vertical error of the MS was very inaccurate (approximately −0.9 m) with three GCPs. As the number increased from 6 to 12, the average vertical error tended to decrease, reaching −0.027 m when it was 12. The error was −0.018 m when 15 and 18 GCPs were used. The standard deviation amounted to 0.7 m when the number of GCPs was three. It was 0.036 m for six GCPs and approximately 0.03 m from nine GCPs. RMSE was 1.148 m for three GCPs and slightly exceeded 0.005 m for six and nine GCPs. It was close to 0.03 m from 12 GCPs. In summary, excellent accuracy could be secured for MS with six GCPs as in SS when considering the vertical position accuracy, the accuracy within 5 cm class was observed when 12 or more GCPs were used.

In the LS, the error was close to 3.8 m with three GCPs, and it exceeded 0.1 m even when the number increased to six. The error was 0.06 m for nine GCPs, and it recorded a stable error range only when the number of GCPs reached 12. The standard deviation also recorded a vast difference when the number of GCPs increased from three to nine but became less than 0.08 m when 12 GCPs were used. The RMSE of the LS became less than 0.1 m from 12 GCPs, unlike the SS and MS, which exhibited excellent accuracy from six GCPs, and the LS exhibiting the highest accuracy using 18 GCPs. In the LS with a large area, the accuracy showed a tendency to improve as the number of GCPs increased. Therefore, higher accuracy could have been achieved through the use of more GCPs. In many cases, however, UAV modeling is not performed in large areas, such as in LS [45].

4.3. Total Errors and RMSEs of 3D Point Clouds

While the horizontal and vertical errors represent xy- and z-direction errors, the total error determines the 3D error in the xyz direction. The mean total errors of the SS were approximately 1 m with three, six, and nine GCPs were used. They significantly decreased to 0.064 and 0.063 m when 12 and 14 GCPs were used. The standard deviation also exhibited the smallest difference when 12 or more GCPs were used. RMSE exceeded 0.1 m for three and six GCPs and presented the best results (0.068 and 0.067 m) when 12 and 14 GCPs were used. Therefore, for the area of the SS, 12 or more GCPs must be used to obtain high accuracy when considering the total accuracy.

In the case of the MS, the average error slightly changed by millimeters from 12 GCPs, which is also true of the standard deviation and RMSE. As RMSE converged to less than 0.06 m from 12 GCPs, it is necessary to install 12 or more GCPs to obtain high accuracy.

In the LS, the average error, standard deviation, and RMSE were significantly reduced when 12 or more GCPs were used as in MS. RMSE was approximately 0.08 m from 12 GCPs. However, the difference in the MS is that the error and standard deviation were somewhat reduced when 18 GCPs were used compared to 12 and 15 GCPs. Thus, 12 or more GCPs must be used to secure high accuracy in large areas, such as LS. If more than 18 GCPs are used, this may increase the accuracy slightly.

4.4. Vertical Errors and RMSEs of DSMs

As DSMs are produced by interpolating 3D point clouds, their accuracy is similar to that of 3D point clouds. In the SS, the average vertical error of DSM was the largest when the number of GCPs

was three. It decreased as the number of GCPs increased, and there was almost no difference when 12 and 14 GCPs were used. The standard deviation was also the smallest when using 12 and 14 GCPs similarly to 3D point clouds. Further, RMSE was approximately 0.04 m from 12 GCPs.

In both MS and LS, there was a small difference from the vertical errors of the corresponding 3D point clouds. In summary, in the case of DSM, at least 12 GCPs must be secured to ensure the accuracy of the result in a situation where vertical errors are considered.

4.5. Comprehensive Discussion

For each study site, the number of GCPs to be used to derive highly accurate horizontal, vertical, and total accuracy was different (Table 7). In this table, "minimum" represents the minimum number of GCPs to achieve the accuracy of approximately 0.1 m, which is "excellent" accuracy. Whereas, "optimal" is the number of GCPs required to meet the accuracy of ASPRS. The criteria for vertical and total errors are relative.

Table 7. Minimum and optimal number of GCPs for each area and accuracy (horizontal, vertical, and total).

	Horizontal		Vertical				Total	
	3D Point Cloud		3D Point Cloud		DSM		3D Point Cloud	
	Minimum	Optimal	Minimum	Optimal	Minimum	Optimal	Minimum	Optimal
SS (7 ha)	3	>3	6	>12	6	>12	6	>12
MS (39 ha)	6	>6	6	>12	6	>12	6	>12
LS (342 ha)	6	>6	12	>18	12	>18	12	>18

This study's results showed that using only three GCPs could result in the optimal accuracy when considering the horizontal accuracy in a small area. Regarding the vertical and total accuracy in typical drone survey areas, such as SS and MS, 6 GCPs are required for excellent accuracy and 12 GCPs for optimal accuracy. Therefore, installing more than 12 GCPs in an area of approximately 39 ha or less is inefficient.

In the LS, the optimal accuracy was observed from six GCPs when considering the horizontal accuracy. The vertical and total accuracy shown excellent results when at least 12 GCPs were used, and the optimal accuracy was observed using 18 GCPs. In previous studies, the accuracy improved as the number of GCPs increased for very large areas, but the accuracy improvement alongside the increase in the number of GCPs was unknown [19,24,26,43]. In this study, the degree of improvement was not evident, either.

Thus, in typical areas (such as SS and MS), using 12 GCPs will be able to produce highly accurate 3D point clouds and DSMs. In larger areas, the installation of more than 12 GCPs will be required depending on the needs. These results indicate that using too many GCPs may not be effective compared to the labor and cost [55,56], even if the area of the target site is diverse, unlike calculating the optimal number of GCPs per area in previous studies [26,29,41,43].

In order to find methods that can improve UAV modeling accuracy, research has been conducted on solutions, such as camera angle, altitude, overlap, interior orientation parameters of the camera, and calibration, rather than on exterior orientation parameters, such as GCPs. In addition, the need for GCP installation was significantly reduced through the RTK and PPK techniques [25,27,37]. Therefore, with the development of technology, the dependence on the number of GCPs is expected to decrease gradually. Nevertheless, discussion on the number of GCPs will continue, as the method of using GCPs is the most widely used UAV modeling method and the most accurate method.

There are extremely diverse target sites for UAV modeling, as almost all the surface of the earth can be targeted [57–61]. Thus, the elevation and roughness of the ground surface are different. In our study, the three study areas were similar because there was little or no vegetation. However, the main study areas showed variation as follows: (i) Aggregation and bare land (SS), (ii) sand and gravels of

beach (MS), and (iii) artificial/man-made areas (LS). In addition, the study on the number of GCPs mentioned in the introduction [38–43] also had a difference in elevation of less than 100 m in the study area except for the study of Enoc Sanz-Ablanedo et al. [43]. Generally, the distance between GCPs is referred to as the plane distance, but if the height difference in the study area is large, the height of the study area should be considered because the slant distance increases in proportion to the height difference. If the characteristics of the ground surface are considered in future studies, this may produce interesting results.

Herein, different UAVs and cameras were used for the three study sites. Various models and cameras were used as research materials because UAVs from hobby-type UAVs to industrial UAVs are routinely considered in UAV modeling. Therefore, it will be possible to apply the results of this study more universally. However, in future research, it will be essential to conduct research by reinforcing variable control and changing only the relative area for the same UAV, camera, and site.

Up to 18 GCPs were used for each site. LS exhibited the smallest RMSE with 18 GCPs. In future research, if the set interval for the number of GCPs is reduced to less than 3 and 18 GCPs or more are used, the results can be used to reinforce the results of this study.

5. Conclusions

In this study, the accuracy of 3D point clouds and DSMs were analyzed in three study sites with different areas according to the number of GCPs to propose the optimal number of GCPs for the 3D UAV modeling of various areas.

When the horizontal accuracy was considered, three or more GCPs had to be used in the SS, while six or more GCPs had to be used in the MS and LS. In terms of the vertical accuracy, using only 12 GCPs reached the optimal accuracy in SS and MS, and 18 GCPs in the LS. When considering the total accuracy that covers both the horizontal and vertical accuracy, using only 12 GCPs exhibited the optimal accuracy in SS and MS, and again 18 GCPs in the LS as with the vertical accuracy.

When 3D point clouds, DSMs, and orthomosaics are produced using UAVS, the installation of GCPs requires a lot of time and labor, both indoors and outdoors. Most of the previous studies discussed the number of GCPs in only one study area. On the other hand, our study selected various UAV modelling sites (encompassing natural environment, large industrial complexes, and environmental monitoring areas) based on different areas. We expect that if the results of this study are applied to actual UAV modeling, it may be possible to reduce the time and labor required for GCP installation.

References

1. Yu, J.J.; Son, S.W.; Park, H.S.; Jeon, H.J.; Yoon, J.H. Evaluation of DSM Accuracy Based on UAS with Respect to Camera Calibration Methods and Application of Interior Orientation Parameters. *Korean J. Remote Sens.* **2017**, *33*, 787–798.
2. Kim, D.; Yu, J.J.; Yoon, J.H.; Son, S.W. Analysis of urban surface temperature change during heat wave using UAV thermal infrared camera. *JAKG* **2019**, *8*, 47–60.
3. Burke, C.; Wich, S.; Kusin, K.; McAree, O.; Harrison, M.E.; Ripoll, B.; Ermiasi, Y.; Mulero-Pázmány, M.; Longmore, S. Thermal-Drones as a Safe and Reliable Method for Detecting Subterranean Peat Fires. *Drones* **2019**, *33*, 23. [CrossRef]
4. Baltsavias, E.P. Digital ortho-images—A powerful tool for the extraction of spatial-and geo-information. *ISPRS J. Photogramm. Remote Sens.* **1996**, *51*, 63–77. [CrossRef]
5. Zhang, L.; Gruen, A. Multi-image matching for DSM generation from IKONOS imagery. *ISPRS J. Photogramm Remote Sens.* **2006**, *60*, 195–211. [CrossRef]
6. Quinn, J.D.; Rosser, N.J.; Murphy, W.; Lawrence, J.A. Identifying the behavioural characteristics of clay cliffs using intensive monitoring and geotechnical numerical modelling. *Geomorphology* **2010**, *120*, 107–122. [CrossRef]
7. Kasperski, J.; Delacourt, C.; Allemand, P.; Potherat, P.; Jaud, M.; Varrel, E. Application of a terrestrial laser scanner (TLS) to the study of the Séchilienne Landslide (Isère, France). *Remote Sens.* **2010**, *2*, 2785–2802. [CrossRef]
8. Fleming, Z.; Pavlis, T. An orientation based correction method for SfM-MVS point clouds—Implications for field geology. *J. Struct. Geol.* **2018**, *113*, 76–89. [CrossRef]
9. Mali, V.K.; Kuiry, S.N. Assessing the accuracy of high-resolution topographic data generated using freely available packages based on SfM-MVS approach. *Meas. J. Int. Meas. Confed.* **2018**, *124*, 338–350. [CrossRef]
10. Meinen, B.U.; Robinson, D.T. Mapping erosion and deposition in an agricultural landscape: Optimization of UAV image acquisition schemes for SfM-MVS. *Remote Sens. Environ.* **2020**, *239*, 111666. [CrossRef]
11. Toutin, T. DSM generation and evaluation from QuickBird stereo imagery with 3D physical modelling. *Int. J. Remote Sens.* **2004**, *25*, 5181–5192. [CrossRef]
12. Ishiguro, S.; Yamano, H.; Oguma, H. Evaluation of DSMs generated from multi-temporal aerial photographs using emerging structure from motion–multi-view stereo technology. *Geomorphology* **2016**, *268*, 64–71. [CrossRef]
13. Dall'Asta, E.; Forlani, G.; Roncella, R.; Santise, M.; Diotri, F.; Cella, U.d. Unmanned aerial systems and DSM matching for rock glacier monitoring. *ISPRS J. Photogramm. Remote Sens.* **2017**, *127*, 102–114. [CrossRef]
14. Yu, J.J.; Kim, D.W.; Yoon, J.H.; Son, S.W. A Study on the Short-term Morphological Beach Changes of Pado-ri Using UAS-based DEM: Focusing on before and after Typhoon Soulik. *JAKG* **2018**, *7*, 303–317. [CrossRef]
15. Cardenal, J.; Fernández, T.; Pérez-García, J.L.; Gómez-López, J.M. Measurement of road surface deformation using images captured from UAVs. *Remote Sens.* **2019**, *11*, 1507. [CrossRef]
16. Drešček, U.; Kosmatin Fras, M.; Tekavec, J.; Lisec, A. Spatial ETL for 3D Building Modelling Based on Unmanned Aerial Vehicle Data in Semi-Urban Areas. *Remote Sens.* **2020**, *12*, 1972. [CrossRef]
17. Son, S.W.; Kim, D.W.; Sung, W.G.; Yu, J.J. Integrating UAV and TLS approaches for environmental management: A case study of a waste stockpile area. *Remote Sens.* **2020**, *12*, 1615. [CrossRef]
18. Udin, W.S.; Ahmad, A. Assessment of photogrammetric mapping accuracy based on variation flying altitude using unmanned aerial vehicle. *IOP Conf. Ser. Earth Environ. Sci.* **2014**, *18*, 12–27. [CrossRef]
19. Mesas-Carrascosa, F.J.; García, M.D.N.; de Larriva, J.E.M.; García-Ferrer, A. An analysis of the influence of flight parameters in the generation of unmanned aerial vehicle (UAV) orthomosaicks to survey archaeological areas. *Sensors* **2016**, *16*, 1838. [CrossRef]
20. Seifert, E.; Seifert, S.; Vogt, H.; Drew, D.; van Aardt, J.; Kunneke, A.; Seifert, T. Influence of drone altitude, image overlap, and optical sensor resolution on multi-view reconstruction of forest images. *Remote Sens.* **2019**, *11*, 1252. [CrossRef]
21. Shahbazi, M.; Sohn, G.; Theau, J.; Menard, P. Development and evaluation of a UAV-photo-grammetry system for precise 3D environmental modeling. *Sensors* **2015**, *15*, 27493–27524. [CrossRef] [PubMed]
22. Cucci, D.A.; Rehak, M.; Skaloud, J. Bundle adjustment with raw inertial observations in UAV applications. *J. Photogramm.* **2017**, *130*, 1–12. [CrossRef]

23. Lee, C.-N.; Oh, J.-H. A study on efficient self-calibration of a non-metric camera for closerange photogrammetry. *J. KSGPC* **2012**, *30*, 511–518.

24. James, M.R.; Robson, S.; d'Oleire-Oltmanns, S.; Niethammer, U. Optimising UAV topographic surveys processed with structure-from-motion: Ground control quality, quantity and bundle adjustment. *Geomorphology* **2017**, *280*, 51–66. [CrossRef]

25. Kalacska, M.; Lucanus, O.; Arroyo-Mora, J.P.; Laliberté, É.; Elmer, K.; Leblanc, G.; Groves, A. Accuracy of 3D landscape reconstruction without ground control points using different UAS platforms. *Drones* **2020**, *4*, 13. [CrossRef]

26. Martínez-Carricondo, P.; Agüera-Vega, F.; Carvajal-Ramírez, F.; Mesas-Carrascosa, F.J.; García-Ferrer, A.; Pérez-Porras, F.J. Assessment of UAV-photogrammetric mapping accuracy based on variation of ground control points. *Int. J. Appl. Earth Obs. Geoinf.* **2018**, *72*, 1–10. [CrossRef]

27. Taddia, Y.; Stecchi, F.; Pellegrinelli, A. Coastal mapping using DJI Phantom 4 RTK in post-processing kinematic mode. *Drones* **2020**, *4*, 9. [CrossRef]

28. American Society for Photogrammetry and Remote Sensing (ASPRS). *ASPRS Positional Accuracy Standards for Digital Geospatial Data (2014)*; ASPRS: Bethesda, MD, USA, 2015; pp. A1–A26.

29. Son, S.W.; Yoon, J.H.; Jeon, H.J.; Kim, D.W.; Yu, J.J. Optimal flight parameters for unmanned aerial vehicles collecting spatial information for estimating large-scale waste generation. *Int. J. Remote Sens.* **2019**, *40*, 8010–8030. [CrossRef]

30. Han, S.-H.; Park, J.-H.; Lee, W.-H. On-site vs. laboratory implementation of camera self-calibration for UAV photogrammetry. *J. KSGPC* **2016**, *34*, 349–356. [CrossRef]

31. Westoby, M.J.; Brasington, J.; Glasser, N.F.; Hambrey, M.J.; Reynolds, J.M. 'Structure-from-Motion' photogrammetry: A low-cost, effective tool for geoscience applications. *Geomorphology* **2012**, *179*, 300–314. [CrossRef]

32. Anderson, K.; Gaston, K.G. Lightweight unmanned aerial vehicles will revolutionize spatial ecology. *Front. Ecol. Environ.* **2013**, *11*, 138–146. [CrossRef]

33. Kršák, B.; Blišťan, P.; Pauliková, A.; Puškárová, P.; Kovanič, Ľ.; Palková, J.; Zelizňaková, V. Use of low-cost UAV photogrammetry to analyze the accuracy of a digital elevation model in a case study. *Measurement* **2016**, *91*, 276–287. [CrossRef]

34. Leica Geosystems. *Leica Photogrammetry Suite OrthoBASE & OrthoBASE Pro User's Guide, GIS & Mapping*; Leica Geosystems: Atlanta, Georgia, 2003.

35. Turner, I.L.; Harley, M.D.; Drummond, C.D. UAVs for coastal surveying. *Coast. Eng.* **2016**, *114*, 19–24. [CrossRef]

36. Forlani, G.; Dall'Asta, E.; Diotri, F.; di Cella, U.M.; Roncella, R.; Santise, M. Quality assessment of DSMs poroduced from UAV flights georeferenced with on-board RTK positioning. *Remote Sens.* **2018**, *10*, 311. [CrossRef]

37. Rabaha, M.; Basiouny, M.; Ghanem, E.; Elhadary, A. Using RTK and VRS in direct geo-referencing of the UAV imagery. *Nriag. J. Astron. Geophys.* **2018**, *7*, 220–226. [CrossRef]

38. Lim, S.B. Geospatial Information Data Generation Using Unmanned Aerial Photogrammetry and Accuracy Assessment. Ph.D. Thesis, Chungnam National University, DaeJeon, Korea, 2016.

39. Yoo, Y.H.; Choi, J.W.; Choi, S.K.; Jung, S.H. Quality evaluation of orthoimage and DSM based on fixed-wing UAV corresponding to overlap and GCPs. *J. Korean Soc. GIS* **2016**, *24*, 3–9.

40. Yun, B.Y.; Sung, S.M. Location accuracy of unmanned aerial photogrammetry results according to change of number of ground control points. *J. Korean Assoc. Geogr. Inf. Stud.* **2018**, *21*, 24–33.

41. Coveney, S.; Roberts, K. Lightweight UAV digital elevation models and orthoimagery for environmental applications: Data accuracy evaluation and potential for river flood risk modelling. *Int. J. Remote Sens.* **2017**, *38*, 3159–3180. [CrossRef]

42. Agüera-Vega, F.; Carvajal-Ramírez, F.; Martínez-Carricondo, P. Assessment of photogrammetric mapping accuracy based on variation ground control points number using unmanned aerial vehicle. *Measurement* **2017**, *98*, 221–227. [CrossRef]

43. Sanz-Ablanedo, E.; Chandler, J.H.; Rodríguez-Pérez, J.R.; Ordóñez, C. Accuracy of unmanned aerial vehicle (UAV) and SfM photogrammetry survey as a function of the number and location of ground control points used. *Remote Sens.* **2018**, *10*, 1606. [CrossRef]

44. National Geographic Information Institute (NGII). *Public Surveying Regulation Using Unmanned Aerial Vehicles*; NGII: Suwon, Korea, 2018.

45. Manfreda, S.; Dvorak, P.; Mullerova, J.; Herban, S.; Vuono, P.; Justel, J.J.A.; Perks, M. Assessing the accuracy of digital surface models derived from optical imagery acquired with unmanned aerial systems. *Drones* **2019**, *3*, 15. [CrossRef]

46. Gaey, C.; Bhardwaj, A. Applications of unmanned aerial vehicles in cryosphere: Latest advances and prospects. *Remote Sens.* **2020**, *12*, 948.

47. Rusnák, M.; Sládek, J.; Kidová, A.; Lehotský, M. Template for high-resolution river landscape mapping using UAV technology. *Measurement* **2018**, *115*, 139–151. [CrossRef]

48. Shima, T.; Rasmussen, S. *UAV Cooperative Decision and Control Challenges and Practical Approaches*, 1st ed.; SIAM: Philadelphia, PA, USA, 2008; pp. 15–35.

49. Avellar, G.S.C.; Pereira, G.A.S.; Pimenta, L.C.A.; Iscold, P. Multi-UAV routing for area coverage and remote sensing with minimum time. *Sensors* **2015**, *15*, 27783–27803. [CrossRef] [PubMed]

50. Zheng, X.; Wang, F.; Li, Z. A multi-UAV cooperative route planning methodology for 3D fine-resolution building model reconstruction. *ISPRS J. Photogramm. Remote Sens.* **2018**, *146*, 483–494. [CrossRef]

51. Snavely, N.; Seitz, S.M.; Szeliski, R. Modeling the world from Internet photo collections. *Int. J. Comput. Vis.* **2008**, *80*, 189–210. [CrossRef]

52. Julián, T.; Martin, M.; Šimon, S.; Františrek, C.; Daniel, T. Accuracy of photogrammetric UAV-based point clouds under conditions of partially-open forest canopy. *Forest* **2017**, *8*, 151.

53. Gindraux, S.; Boesch, R.; Farinotti, D. Accuracy assessment of digital surface models from unmanned aerial vehicles' imagery on glaciers. *Remote Sens.* **2017**, *9*, 186. [CrossRef]

54. Kim, Y.D.; Park, B.W.; Lee, H.S. Accuracy analysis according to GCP layout type and flying height in orthoimage generation using low-cost UAV. *J. Korean Soc. GIS* **2018**, *26*, 31–39.

55. Yang, H.; Li, H.; Gong, Z.; Dai, W.; Lu, S. Relations between the Number of GCPs and Accuracy of UAV Photogrammetry in the Foreshore of the Sandy Beach. *J. Coast. Res.* **2020**, *95*, 1372–1376. [CrossRef]

56. Zimmerman, T.; Jansen, K.; Miller, J. Analysis of UAS Flight Altitude and Ground Control Point Parameters on DEM Accuracy along a Complex, Developed Coastline. *Remote Sens.* **2020**, *12*, 2305. [CrossRef]

57. Yu, J.J.; Park, H.S.; Yang, Y.J.; Jang, D.H. Assessing the applicability of UAS for detecting geomorphological changes in coastal areas: A case study in the Baramarae Beach in Anmyeon-do. *J. Korean Geomorphol. Assoc.* **2016**, *23*, 113–126. [CrossRef]

58. Dąbskia, M.; Zmarz, A.; Pabjanek, P.; Korczak-Abshire, M.; Karsznia, I.; Chwedorzewska, K.J. UAV-based detection and spatial analyses of periglacial landforms on Demay Point (King George Island, South Shetland Islands, Antarctica). *Geomorphology* **2017**, *290*, 29–38.

59. De Beni, E.; Cantarero, M.; Messina, A. UAVs for volcano monitoring: A new approach applied on an active lava flow on Mt. Etna (Italy), during the 27 February–02 March 2017 eruption. *J. Volcanol. Geotherm. Res.* **2019**, *369*, 250–262. [CrossRef]

60. Nobajas, A.; Waller, R.I.; Robinson, Z.P.; Sangonzalo, R. Too much of a good thing? The role of detailed UAV imagery in characterizing large-scale badland drainage characteristics in South-Eastern Spain. *Int. J. Remote Sens.* **2017**, *38*, 2844–2860. [CrossRef]

61. Alexander, C.; Korstjens, A.H.; Hankinson, E.; Usher, G.; Harrison, N.; Nowak, M.G.; Abdullah, A.; Wich, S.A.; Hill, R.A. Locating emergent trees in a tropical rainforest using data from an Unmanned Aerial Vehicle UAV. *Int. J. Appl. Earth Obs.* **2018**, *72*, 86–90. [CrossRef]

Drone Magnetometry in Mining Research. An Application in the Study of Triassic Cu–Co–Ni Mineralizations in the Estancias Mountain Range, Almería (Spain)

Daniel Porras [1], Javier Carrasco [2], Pedro Carrasco [3], Santiago Alfageme [4], Diego Gonzalez-Aguilera [3,*] and Rafael Lopez Guijarro [5]

1 Geoland Services S.L., 28008 Madrid, Spain; dporras@geoland.es
2 Técnicas Geofísicas S.L., 05003 Avila, Spain; tgeofisicas@gmail.com
3 Departamento Ingeniería Cartográfica y del Terreno Geología, Escuela Politécnica Superior de Ávila, Universidad de Salamanca, Avd. Hornos Caleros 50, 05003 Avila, Spain; retep81@usal.es
4 Gesminle S.L., 24001 Leon, Spain; sca@gesminle.es
5 Exco Mining S.L., 28008 Madrid, Spain; rlopez@excomining.es
* Correspondence: daguilera@usal.es; Tel.: +34-920353500

Abstract: The use of drones in mining and geological exploration is under rapid development, especially in the field of magnetic field prospection. In part, this is related to the advantages presented for over ground surveys, allowing for high-density data acquisition with low loss of resolution, while being particularly useful in scenarios where vegetation, topography, and access are limiting factors. This work analyzes results of a drone magnetic survey acquired across the old mines of Don Jacobo, where Copper-Cobalt-Nickel stratabound mineralizations were exploited in the Estancias mountain range of the Betic Cordillera, Spain. The survey carried out used a vapor magnetometer installed on a Matrice 600 Pro Hexacopter. Twenty-four parallel survey lines were flown with a speed of 5 m/s, orthogonal to the regional strike of the geological structure, and mineralization with 50 m line separation and 20 m flight height over the ground was studied. The interpretation of the magnetic data allows us to reveal and model two high magnetic susceptibility bodies with residual magnetization, close to the old mines and surface mineral shows. These bodies could be related to potential unexploited mineralized areas whose formation may be related to a normal fault placed to the south of the survey area. Our geophysical survey provides essential data to improve the geological and mining potential of the area, allowing to design future research activities.

Keywords: aeromagnetics; drone survey; mineral exploration; geophysical prospecting

1. Introduction

The demand for raw materials is rapidly increasing, proving a fundamental pillar in modern development as well as the future prospects of European industries. The product of this is a rise in demand for new material extraction sites that are able to support this type of development. In the case of Europe, geological and mining research is currently hindered by the effectiveness and speed of traditional methodologies in this type of research. This has resulted in adaptations in the field of geophysics in response to increasingly stricter requirements.

In this context, the use of drones is under important development, incorporating more autonomous systems allowing for the integration of multiple sensors such as: RGB sensors, ultrasonic sensors, Infrared Sensors (IR), stereo camera, laser range finders (LRFs), Ultra-Wideband Radar (UWB), and hyperspectral sensors like hyperspectral cameras, which allows for its use in a variety of civilian and military applications [1,2] and missions including the magnetometer for geological and mining research [3–9]. Other authors have used drone magnetometry in the oil and gas industry to locate abandoned wells and other buried infrastructures such as pipelines over wide areas [10–12]. Traditionally, magnetic

surveys are performed on-site moving the sensor manually, thus capturing high resolution spatial data at the cost of low productivity. These approaches are additionally limited by access to the area of study. Other approaches consist in the installation of sensors on planes, increasing productivity by being able to study larger areas in smaller periods of time, at the cost of spatial resolution [13]. The use of drones is thus an alternative of interest presenting multiple operative advantages, such as flexibility, ease of use, and a lower logistic cost. Additionally, drones present high capacity for obtaining data over large areas in short periods of time, with less restrictions based on low accessibility, topographical, environmental, and vegetative conditions.

One of the most common techniques used in geological and mining research is magnetometry, employing the use of specially designed sensors that can be made airborne using drones [14–16]. This consists of a means of remotely carrying out geophysical surveys based on the measurement of terrestrial magnetic variations at regular intervals along a set of profiles. The majority of minerals present their own particular non-magnetic behavior. Nevertheless, another group of minerals exists, called ferromagnectic minerals, which include the cobalt ores frequently found in the Estancias mountain range of the Betic Cordillera, Spain, whose concentration in the Earth's crust generates detectable local variations in the magnetic field.

The present research project is focused on the analysis of the Don Jacobo mine, where copper and cobalt minerals were found in Triassic carbonates and have been extracted since the mid-19th century, up to the beginning of the 21st century [17]. These minerals include azurite, malachite, limonite, pyrite, galena, and erythrite. Mining works in the area were limited to small galleries that penetrated only few meters into the rock. There are no data from previous geophysical surveys or drilling activities.

This study thus has the primary objective of extracting information from this area in relation to the possible presence of mineral bodies located under areas of complex topographies where high slopes, scree debris, and vegetation make the application of ground geophysical techniques difficult. It is known that these topographic particularities make it difficult to study this area using other ground geophysical techniques such as, for example, electrical tomography, induced polarization, and ground magnetometry, which highlights the importance of research with drones in this application.

2. Geological Context and General Characteristics of the Locality

The region of interest is located in the Estancias mountain range, in the southeastern part of the Iberian peninsula, geologically positioned in the northern region of the Internal Betic Cordillera (Figure 1A), in materials of the The Alpujárride Complex, belonging to the Internal Zones of the Betic Cordillera. The diverse lithologies present can be organized into three large lithological units defining this complex. Stratigraphically, these three units correspond with, from bottom to top: Paleozoic shales, Triassic phyllite-quartzites, and Triassic carbonates (dolomitic-limestone). The first two units are additionally affected by Alpine metamorphism.

These units are presented with a general east-west orientation (N75-90E) (Figure 1B), conditioned by a strong deformation due to tectonic accidents [18,19]. These accidents have been interpreted mostly as fault propagation folds towards the south/south-east [20], thus conditioning the geological structures within this region (Figure 1B,C).

The area occupied by the Don Jacobo mine, and the general location of the target minerals, are dispersed in a topographically abrupt region, positioned on a 1000 m by 300 m (length × width) portion of the Triassic dolomitic-limestone unit. This unit is located above phyllites and is constricted towards the south by an interpreted as a possible normal tertiary fault, partially covered by plio-quaternary materials (Figure 1C).

From a metallogenetic perspective, the mineralizations are located within the Upper Triassic dolomites and limestones of the Alpujarride Complex, and are considered to be stratobound [18]. Rich Co-Cu mineralization can be found here alongside other minor elements

(Ni-Pb-Zn-Ag-Se-As-Hg) [21]. This is similar to the geological-lithological contexts of the Betic region, such as those found in Molvízar (Granada) and Huércal-Overa (Almería).
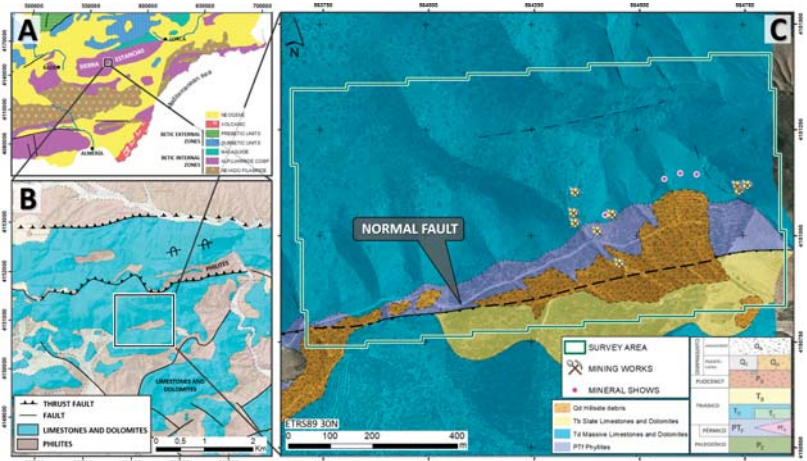
Figure 1. (**A**) Geological Context of the southeastern part of the Iberian Peninsula; (**B**) 1:50,000 Geological map (sheet 973—Chirivel and 995—Cantoria, Instituto Geológico y Minero de España, 1972 [18,19]), where the general east-west trend of the Alpujarride Complex can be observed; (**C**) 1:5000 cartographic revision of the Don Jacobo mine area, showing the main tectonic accident in the area (southern normal fault—black dashed line), survey area, and position of the Don Jacobo mines and outcropping mineral shows.

Genetically, these mineralizations have been attributed to a Mississippi Valley type, where metals are a product of the hydrothermal washing of marine series or from mafic intrusions, with carbonates acting as a reducing trap for the mineralization. The carbonated lithologies are constituted by large structures separated among themselves by phyllite lithologies, typically associated with important tectonic accidents. These accidents are then considered the potential channels for hydrothermal circulation [20].

The geochemical studies as well as nearby mineral indices documented from the initial exploitation of the Don Jacobo mine indicate the presence of Cu-Co-Ni primary mineralizations, with the presence of Pb-Zn (Ag), and with Cu and Co contents of >3% and 1%, respectively (Figure 2, [21]). No drilling data or geophysical surveys are available.
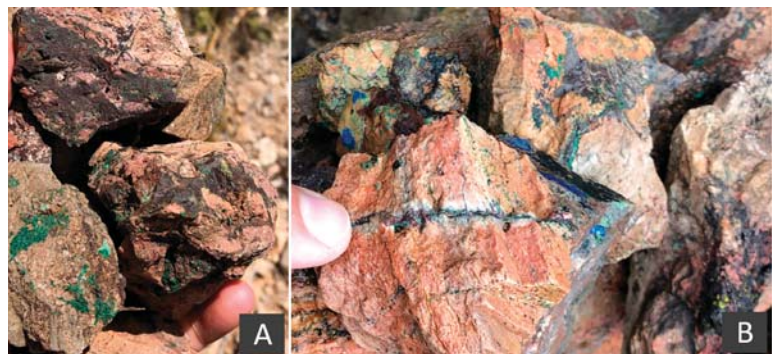
Figure 2. Mineralizations of the Don Jacobo mine; (**A**,**B**) Cu carbonates (green and blue colors) and veins of black Co oxides (black colors).

3. Materials and Methods

This research project consisted in the analysis of the mine's surroundings and out-cropping mineral shows. Additionally, this research has tried to analyze the carbonated outcrops that appear over the 80 ha area.

3.1. Site Conditions

Data collection was performed on 14 June 2020 in warm, sunny, uncloudy, and low wind speed (<16 m/s) day, and lasted a total of 4 h (from 10 am. to 2 pm.). The area under study is practically covered with matorral type shrub-land, and scattered with dense wooded areas (Corine Land Cover 2018 types 312 and 323—https://land.copernicus.eu/pan-european/corine-land-cover/clc2018—accessed on 1 November 2021). The area is accessible by only one track and is characterized by a low anthropogenic magnetic noise area and a severe topography, with an average slope of >26° (Figure 3). To minimize risks such as drone collision with topographic or vegetative elements (the tallest trees in the area reaching approximately 8 m Above Ground Level-AGL) and to ensure flight at a constant height above the ground, a digital elevation model (DEM) of the area was first generated. For this flight, the most important geometric criteria for photogrammetric applications were considered [22], allowing the generation of cartographic data of high quality and obtaining a Ground Sample Distance (GSD) of 4 cm/pixel. This DEM was calculated using a Dji Mavic 2 Pro drone with a 1" CMOS sensor, flying at 150 m AGL.
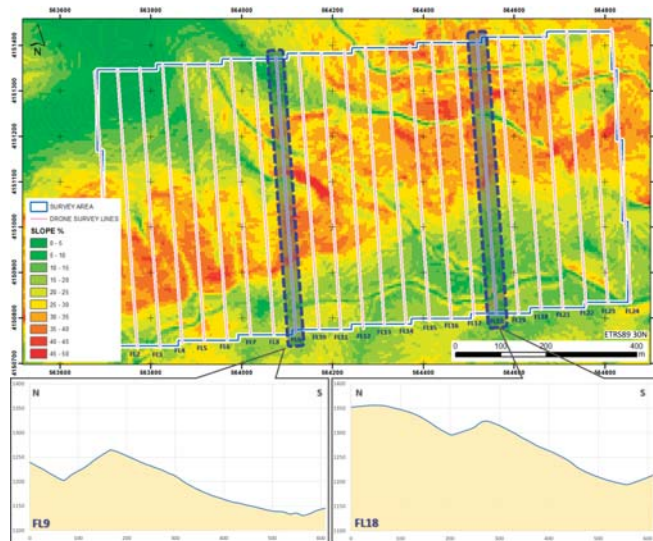
Figure 3. Slope map of the study area including drone flight lines (pink lines). The topographic profiles of flight lines 9 (FL9) and 18 (FL18) show the wild topographical characteristics of the area.

3.2. Platform and Flight Planning

The platform employed for the present study was the multi-rotor hexacopter Dji Matrice 600 Pro (Figure 5A), equipped with a A3Pro flight controller, and compatible with the UgCS mission planning tool software. This equipment has a total takeoff weight of 9.6 kg, and up to 6 kg payload, while being powered by 6 lithium polymer batteries (4500 mAh).

Flight software (UgCS) was used for the design and control of the survey. Twenty-four 650 m length parallel survey lines were flown trending N170E, orthogonal to the regional strike of the geological structure and mineralization (N75-90E), with a 50 m line separation in order to obtain a high spatial resolution that allows observing variations in the magnetic

field of target size. Due to the extension of the survey area, the total flight was divided into four flight blocks and two take-off and landing points taking into account the capacity of the batteries (Figure 4). The flight was programmed with a speed of 5 m/s and a sampling interval of 200 ms, obtaining measurements every meter along the registered profile. This selected configuration results in a total of 14,500 magnetic total field registration points. The altitude of the flight (20 m AGL) was selected to maximize the resolution of the sensor while guaranteeing safety against obstacles, integrating the DEM acquired previously. A 1 m tolerance level was also used for altitude adjustments.
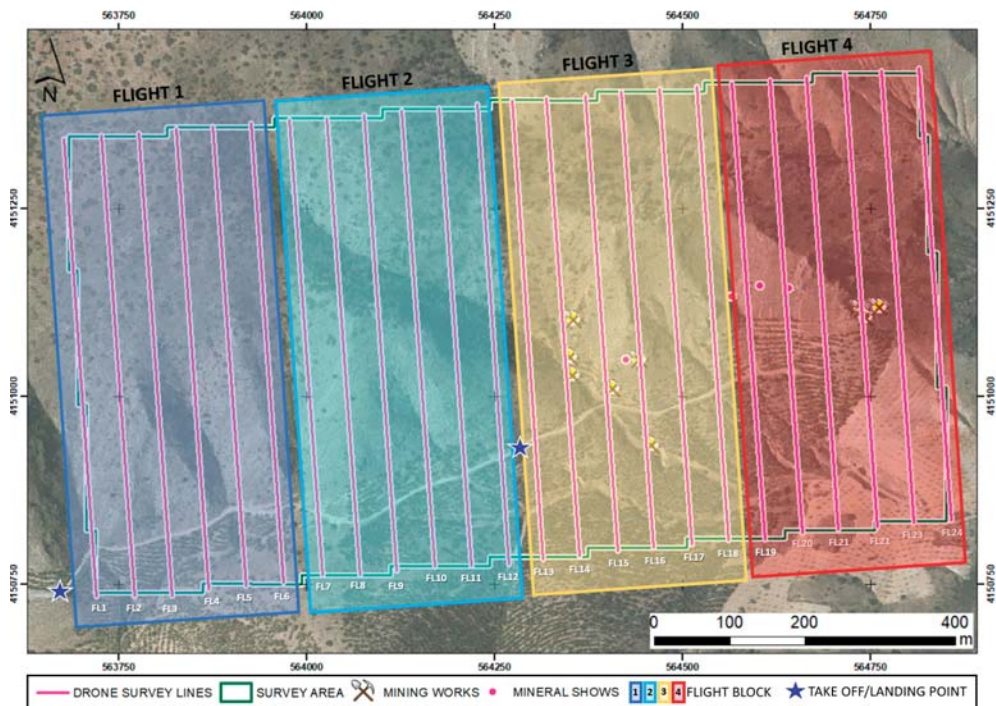
Figure 4. Survey design including flight lines (pink lines) and flying blocks division, including the take-off and landing points.

The effect produced by the distance between the sensor and the surface generates a low decrease of spatial resolution and intensity compared to ground surveys [16,23,24], compensated by a regular and higher density data acquisition.

3.3. Magnetometry

The drone was equipped with a GSMP-35U GEM-Systems potassium-vapor magnetometer, with a sensibility of 0.0002 nT/1 Hz. This system is additionally equipped with a simultaneous register of the magnetic field, as well as a real-time single-frequency (L1) GPS receiver with up to 0.7 m absolute accuracy in Satellite Based Augmentation System coverage areas.

This equipment consists of a sensor attached by cable to a controller, datalogger, 5 V battery power-source, and GPS, with a total weight of <2 kg. The datalogger and batteries were securely fixed and balanced in the payload container of the drone's undercarriage, while the GPS antenna was installed on the upper portion of the drone, so as to ensure a constant signal. Due to the magnetic interference that is generated by electromagnetic motors within the platform [5,24,25], the magnetic sensor was installed at a 3 m distance from the base of the drone, connected by cable, so as to counteract this electromagnetic

effect (Figure 5B). For this configuration, the magnetic field produced by the drone is attenuated and does not affect the measurements of the GSMP-35U magnetometer [20].
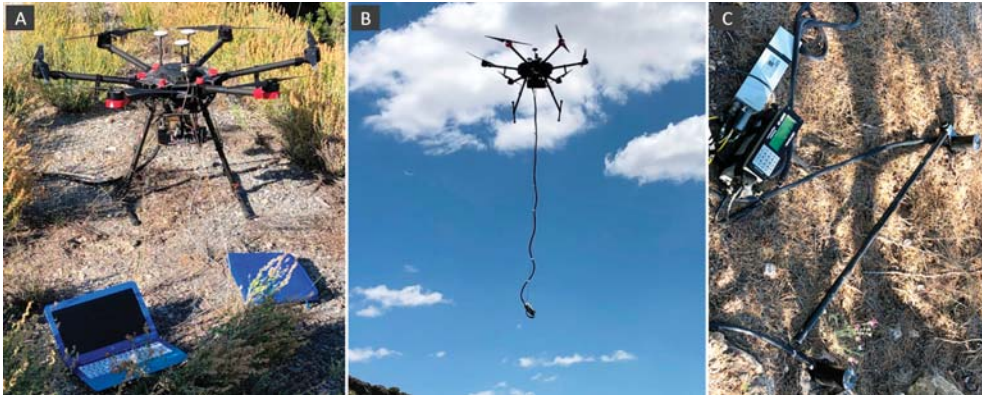
Figure 5. Registration system. (**A**) a Mavic Matrice 600 Pro Hexacopter drone; (**B**) static drone position with the magnetometer hanging below; (**C**) base magnetometer for diurnal corrections.

The magnetic sensor was deployed with no rotational restrictions about any of the axes. The survey was designed by adding an extra 25 m at each extremity of the flying lines at the 180° turn and reducing flight speed, preventing the pendulum motion of the sensor that creates yaw, pitch, and roll axis variations.

In parallel, a fixed magnetometer was installed in a nearby area away from sources of magnetic interference to calculate the diurnal effect correction caused by the temporal variation of the magnetic field throughout the day (Figure 5C). The magnetometer was set up with a 1 s time total field interval record, found to register a maximum of 11 nT throughout the data collection period.

3.4. Data Processing

Data were processed using the OASIS Montaj 9.8 software, using classic methods in the calculation of anomalies by applying a series of different filters so as to obtain anomaly residual maps. First, erroneous values due to drone position, take-off, landing, pitch, excess roll, and lag errors between the sensor and the drone are deleted. All points placed over the extended extremes of the survey lines and other outliners were discarded, applying a 1D median filter. Finally, diurnal variation of the Earth's magnetic field values caused by sun activity were used to correct the data obtained during the survey period [26].

Aeromagnetic data processing is based on a gridding computation routine that interpolates the observed aeromagnetic data from the survey data, placing these locations into a regular grid with the nodes displayed as a 2D total magnetic field contour map (RGB image). The minimum curvature gridding method was applied to the observed data [27], at $\frac{1}{4}$ of the flight line spacing (12.5 m) [28].

4. Results

4.1. Total Magnetic Field (TMF) and Reduction to Pole (TMFRP)

Data interpretation begins with the calculation of the Total Magnetic Field (TMF), from the filtered data (Figure 6A), and the Reduction to Pole (TMFRP). From this perspective, applying the data regarding magnetic inclination and declination of this area on the day of data collection, and in combination with the International Geomagnetic Reference Field (IGRF), a view of the central magnetic sources can be obtained directly for the bodies that generated them (Figure 6B).
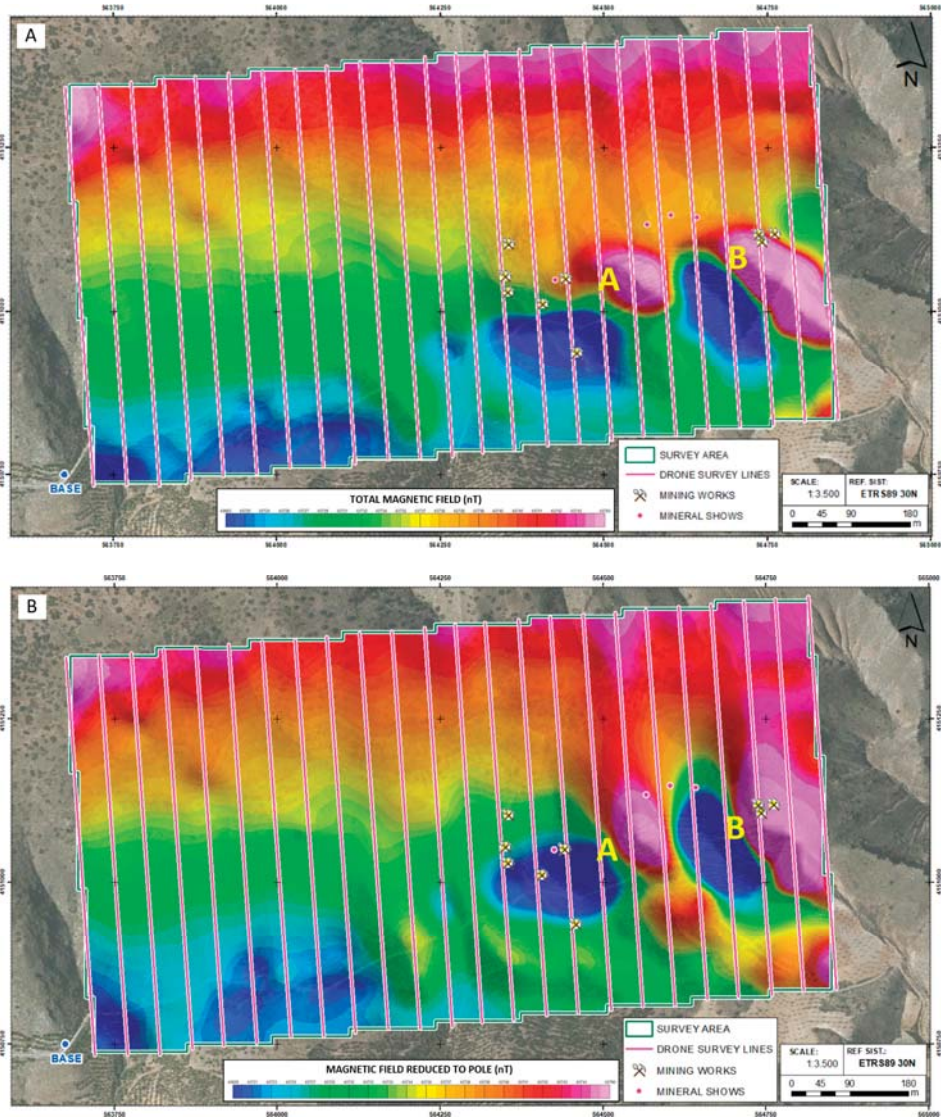
Figure 6. (**A**) Total Magnetic Field (TMF) and (**B**) Total Magnetic Field with Reduction to Pole (TMFRP). Dipoles A and B have been marked on each map, as well as the location of different mining activities and areas where the mineralization had been observed on the surface.

On both planes, the presence of two strong magnetic dipoles can be observed (A and B) towards the south-east quadrant of the region of interest. Both dipoles are located on carbonated materials and can be found in the immediate surroundings of the old mine as well as areas where the mineralization had originally been detected on surface.

TMFRP presents a slight variation in the position of the dipoles with reference to the TMF (Figure 6B), as well as an increase in its intensity, reaching a variation in the magnetic field of up to 88 nT (dipole A) and 165 nT (dipole B). The dipoles can be related to the

presence of ferromagnetic elements compatible with the paragenesis of the minerals from this locality.

It is important to point out that reduction to pole has not removed the dipolar character of the magnetic anomalies, which indicates a remaining magnetization of the materials found in this source. This is product of the natural axis of these dipoles, found approximately E-W and not N-S, as would be expected in the actual position of the magnetic field. Under this premise, the mineral bodies that generate these dipoles obtained the remaining magnetization at a moment in time when the magnetic field was different from present day.

4.2. Analytical Signal

The filtered Analytical Signal (AS) allows for the spatial identification of the two sources producing the observed dipoles. The calculation of AS is based on the execution of directional derivatives, where the obtained anomalies are organized in a bell-shape, and where the maxima are located directly on the edges of the anomalous bodies, with their amplitude being proportional to the depth of the location of the magnetic source [29].

The map displaying the computed analytical signal (Figure 7) presents a preferential lineation of anomalous areas with an approximate orientation of N80E, coinciding with the two maxima (A and B, Figure 7), and the general trend of the main geological contacts and structures, specially, with the normal fault defined through the geological cartography of the area (Figure 8).
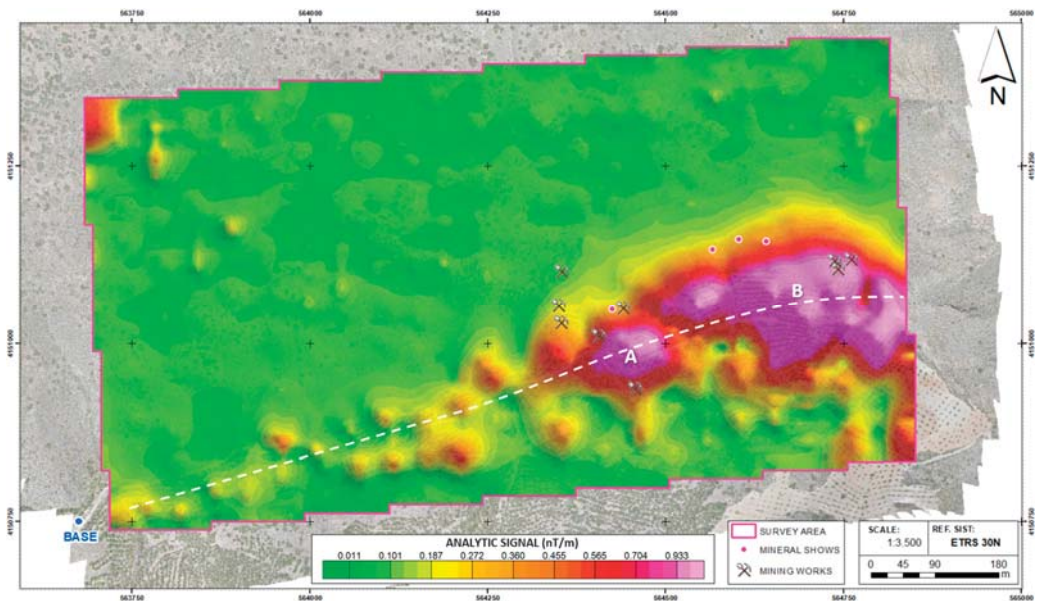
Figure 7. Analytical signal map over the aerial RGB image of the area of Don Jacobo with the position of the main mining works and outcropping mineral shows. Note the alignment of the analytical signal anomalies with approximate N80E orientation (white dashed line) and with the two AS maxima (A and B), as well as the position of the mining works and the outcropping mineral shows close to the main anomalies.

It is important to point out that all the mining works and outcropping mineral shows are located surrounding the northern part of the analytical signal anomalies, with all of them situated in the northern block of the normal fault.

4.3. D Inversion Model

The creation of a uniform grid with a high density of information obtained by drone allows to the creation of 3D models displaying magnetic susceptibility by applying the technique of Magnetic Vector Inversion (MVI) [30]. The model generated using the VOXI Earth Modeling software by OASIS Montaj is made up of a data mesh of $117 \times 69 \times 82$, generating a total of 661,986 cells of 10×10 m size. This model facilitated the spatial definition of the precise magnetic bodies of interest. These methods also allow for the characterization of these bodies, through computing magnetization vectors for each block that contain information about directionality as well as intensity.
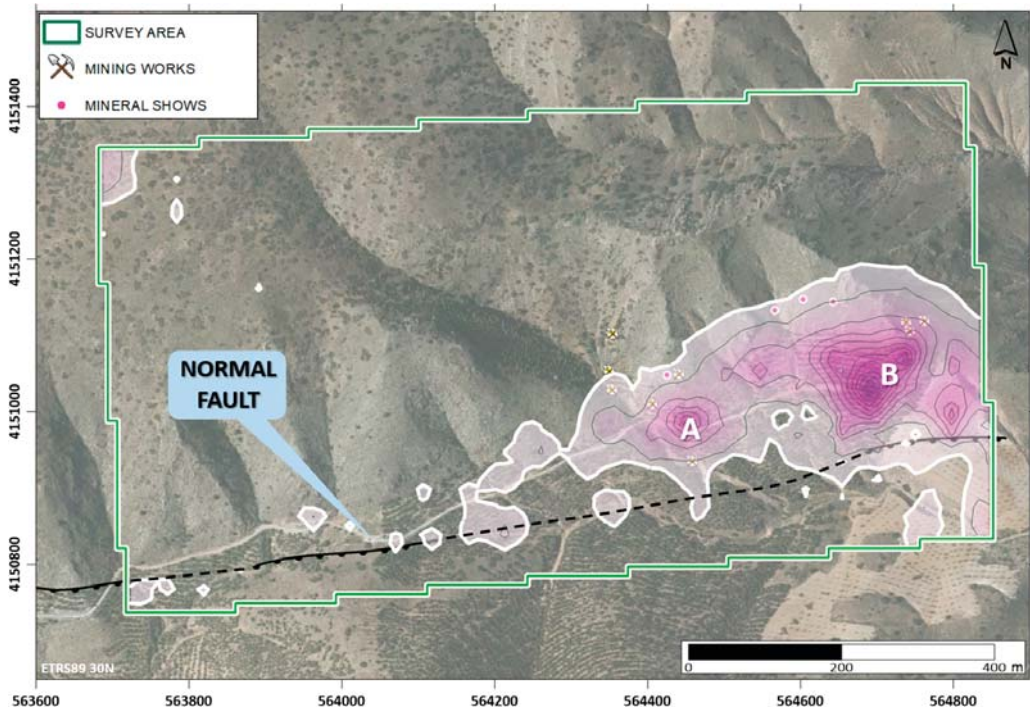
Figure 8. Analytical Signal anomalies over the aerial RGB image and normal fault trace from the 1:5000 geological cartography (Figure 1C) of the area of Don Jacobo. Note the alignment of analytical signal anomalies parallel to the normal fault placed at the south of the survey area.

The results from this modeling (Figure 9) reveals the presence of two bodies with high magnetic susceptibility (A and B), presenting susceptibility values over 12×10^{-4}, with peak values of 15×10^{-3}. Both bodies are modelled to prevent an oval morphology, with the maximal magnetization located at 45 m and 60 m in depth below surface (Figure 9A,B). This depth is an estimation and other methods such as drilling would be required to validate the proposed depth.

In the case of magnetization vectors, a preferential W-E orientation has been observed, different from the direction of the Earth's natural magnetic field. This model confirms the presence of a residual magnetization in the materials encountered here, coinciding with those observations obtained from TMFRP, and therefore, could be related to the presence of mineralized bodies.

Both bodies are located towards the south of the mining works and outcropping mineral shows and just at the north of the normal fault that crosses the southern border of the survey area (Figure 10), making it possible to interpret that the fault may have played

an important role in the formation of the mineralization, probably as a channel for the circulation of hydrothermal mineralizing fluids.
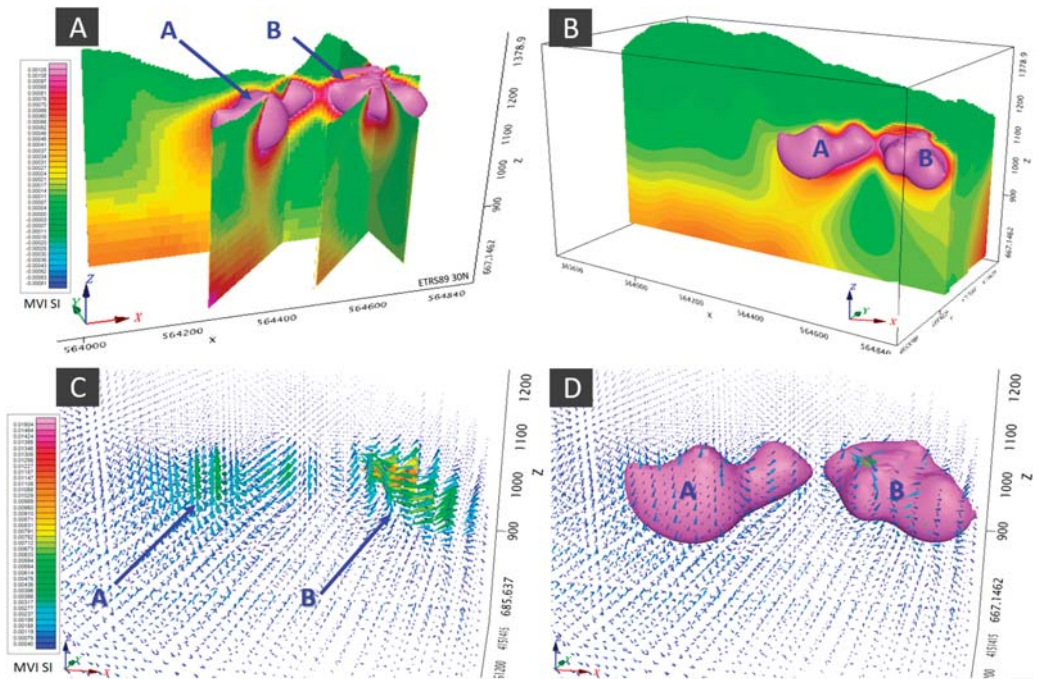
Figure 9. 3D model of the magnetic susceptibility in the area of Don Jacobo. (**A**,**B**) Different views and sections of the two magnetic bodies defined by the model. (**C**,**D**) Visualization of magnetization vectors obtained from each of the studies and their relationship with magnetic susceptibility.
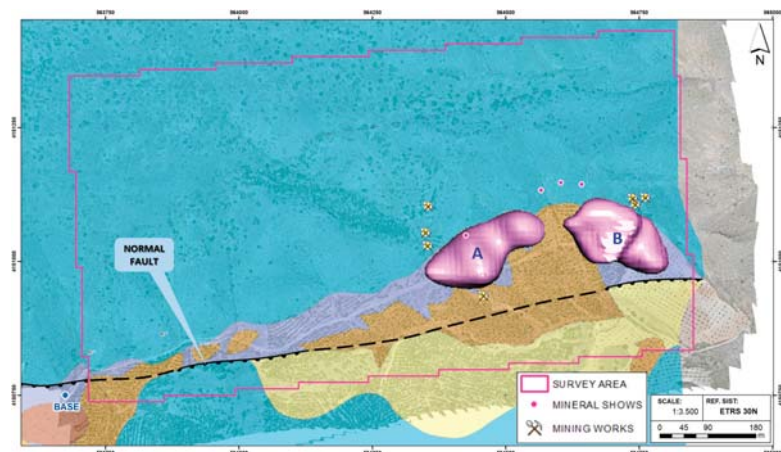
Figure 10. 3D model of the magnetic susceptibility of the Don Jacobo area, displaying the position of the two bodies of high magnetic susceptibility A and B (12×10^{-4} susceptibility threshold value); over the 1:5000 geological cartography and aerial RGB image of the area of Don Jacobo; normal fault placed at the south of the survey area and mining works and outcropping mineral shows.

5. Conclusions

We present results of the drone magnetometry survey for mineral exploration over the Don Jacobo mining area. We demonstrate the utility and advantages of using drone magnetometry in the study of mineral deposits, allowing for the acquisition of high-quality data in unfavorable conditions where traditional approaches are limited.

The present study was able to detect the presence of two magnetic dipoles with residuals magnetization in the nearby surroundings of old mining activities.

The use of 3D inversion was able to define the morphology and limits of the two potential mineral bodies, and further confirm their relation to the surrounding geological features, such as the normal fault to the south of the region of interest.

Our results strongly support that these dipoles are related to the potential presence of ferromagnetic mineral elements compatible with the Copper-Cobalt-Nickel paragenesis of the Don Jacobo area. The alignment of the analytical signal anomalies parallel and close to a normal fault indicate that this fault played an important role in the formation of the mineralization, probably as a channel for the circulation of hydrothermal mineralizing fluids.

We conclude that the drone magnetics survey method could be an important tool to study mineralized areas, such as the Don Jacobo mine, where precise modeling allows the precise definition of magnetic anomalies and the design and development of future investigation activities.

References

1. Giordan, D.; Adams, M.S.; Aicardi, I.; Alicandro, M.; Allasia, P.; Baldo, M.; De Berardinis, P.; Dominici, D.; Godone, D.; Hobbs, P.; et al. The use of unmanned aerial vehicles (UAVs) for engineering geology applications. *Bull. Eng. Geol. Environ.* **2020**, *79*, 3437–3481. [CrossRef]
2. Aleshin, I.M.; Ivanov, S.D.; Koryagin, V.N.; Matveev, M.A.; Morozov, Y.A.; Perederin, F.V.; Kholodkov, K.I. Review on the Use of Light Unmanned Aerial Vehicles in Geological and Geophysical Research. *Seism. Instrum.* **2020**, *56*, 509–515. [CrossRef]
3. Parvar, K.; Braun, A.; Layton-Matthews, D.; Burns, M. UAV magnetometry for chromite exploration in the Samail ophiolite sequence, Oman. *J. Unmanned Veh. Syst.* **2018**, *6*, 57–69. [CrossRef]
4. Shahmoradi, J.; Talebi, E.; Roghanchi, P.; Hassanalian, M. A comprehensive review of applications of drone technology in the mining industry. *Drones* **2020**, *4*, 34. [CrossRef]
5. Malehmir, A.; Dynesius, L.; Paulusson, K.; Paulusson, A.; Johansson, H.; Bastani, M.; Wedmark, P.; Marsden, P. The potential of rotary-wing UAV-based magnetic surveys for mineral exploration: A case study from central Sweden. *Lead. Edge* **2017**, *36*, 552–557. [CrossRef]
6. Park, S.; Choi, Y. Applications of unmanned aerial vehicles in mining from exploration to reclamation: A review. *Minerals* **2020**, *10*, 663. [CrossRef]
7. Kim, B.; Lee, S.; Park, G.; Cho, S.-J. Development of an unmanned airship for magnetic exploration. *Explor. Geophys.* **2020**, *52*, 1–6. [CrossRef]

8. Le Maire, P.; Bertrand, L.; Munschy, M.; Diraison, M.; Géraud, Y. Aerial magnetic mapping with an unmanned aerial vehicle and a fluxgate magnetometer: A new method for rapid mapping and upscaling from the field to regional scale. *Geophys. Prospect.* **2020**, *68*, 2307–2319. [CrossRef]
9. Schmidt, V.; Becken, M.; Schmalzl, J. A UAV-borne magnetic survey for archaeological prospection of a Celtic burial site. *First Break* **2020**, *38*, 61–66. [CrossRef]
10. Alex, N.; Timothy, S.d.S. A UAV-based magnetic survey method to detect and identify orphaned oil and gas wells. *Lead. Edge* **2019**, *38*, 447–452.
11. Hammack, R.W.; Veloski, G.A.; Lowe, R.; Zorn, A.; Wylie, L.; Schlagenhauf, M. *Using Drone-Mounted Geophysical Sensors to Map Legacy Oil and Gas Infrastructure*; National Energy Technology Laboratory (NETL): Pittsburgh, PA, USA; Medium: Morgantown, WV, USA, 2020.
12. De Smet, T.S.; Nikulin, A.; Romanzo, N.; Graber, N.; Dietrich, C.; Puliaiev, A. Successful application of drone-based aeromagnetic surveys to locate legacy oil and gas wells in Cattaraugus county, New York. *Appl. Geophys.* **2021**, *186*, 104250. [CrossRef]
13. Everett, M. *Near-Surface Applied Geophysics*; Cambridge University Press: Cambridge, UK, 2013.
14. Parvar, K. Development and Evaluation of Unmanned Aerial Vehicle (UAV) Magnetometry Systems. Master's Thesis, Department of Geological Sciences and Geological Engineering, Queen's University, Kingston, ON, Canada, 2016; pp. 1–141.
15. Parshin, A.; Morozov, V.; Blinov, A.; Kosterev, A.; Budyak, A. Low-altitude geophysical magnetic prospecting based on multirotor UAV as a promising replacement for traditional ground survey. *Geo-Spat. Inf. Sci.* **2018**, *21*, 1–8. [CrossRef]
16. Jackisch, R.; Madriz, Y.; Zimmermann, R.; Pirttijärvi, M.; Saartenoja, A.; Heincke, B.H.; Salmirinne, H.; Kujasalo, J.-P.; Andreani, L.; Gloaguen, R. Drone-borne hyperspectral and magnetic data integration: Otanmäki Fe-Ti-V deposit in Finland. *Remote Sens.* **2019**, *11*, 2084. [CrossRef]
17. Empresa Nacional Adaro de investigaciones Mineras (ADARO). *Programa de Investigación Sistemática de Recursos*; Zona Sureste, Sierra de Las Estancias; ADARO: Madrid, Spain, 1987.
18. IGME MAGNA; Instituto Geológico y Minero de España (IGME). *Hoja de Chirivel (973)*; Mapa Geológico de España (E. 1:50.000); Servicio de Publicaciones del Ministerio de Industria y Energía: Madrid, Spain, 1972; 46p.
19. IGME MAGNA; Instituto Geológico y Minero de España (IGME). *Hoja de Cantoria (995)*; Mapa Geológico de España (E. 1:50.000); Servicio de Publicaciones del Ministerio de Industria y Energía: Madrid, Spain, 1972; 51p.
20. EXCO MINING, SL. *Informe Geológico y Minero del Permiso de Investigación Burán*; Sierra de Oria, Informe Interno no Publicado; EXCO MINING SL: Madrid, Spain, 2019.
21. EXCO MINING, SL. *Análisis Geoquímico y Petrográfico de Muestras Superficiales Tomadas en el Permiso de Investigación Burán*; Informe Interno no Publicado; EXCO MINING SL: Madrid, Spain, 2020.
22. Hernandez-Lopez, D.; Felipe-Garcia, B.; Gonzalez-Aguilera, D.; Arias-Perez, B. An automatic approach to UAV flight planning and control for photogrammetric applications. *Photogramm. Eng. Remote Sens.* **2013**, *79*, 87–98. [CrossRef]
23. Cunningham, M.; Samson, C.; Wood, A.; Cook, I. Aeromagnetic Surveying with a Rotary-Wing Unmanned Aircraft System: A Case Study from a Zinc Deposit in Nash Creek, New Brunswick, Canada. *Pure Appl. Geophys.* **2018**, *175*, 3145–3158. [CrossRef]
24. Walter, C.A.; Braun, A.; Fotopoulos, G. Impact of three-dimensional attitude variations of an unmanned aerial vehicle magnetometry system on magnetic data quality. *Geophys. Prospect.* **2019**, *67*, 465–479. [CrossRef]
25. Jirigalatu, J.; Krishna, V.; Silva, E.; Døssing, A. Experiments on magnetic interference for a portable airbone magnetometry system using a hybrid unmanned aerial vehicle (UAV). *Geosci. Instrum. Methods Data Syst.* **2020**, *10*, 25–34. [CrossRef]
26. Telford, W.M.; Geldart, L.R.; Sheriff, R.E. *Applied Geophysics*, 2nd ed.; Cambridge University Press: Cambridge, UK, 1990; 770p.
27. Briggs, I.C. Machine contouring using minimum curvature. *Geophysics* **1974**, *39*, 39–48. [CrossRef]
28. Lee, M.; Morris, W. Quality assurance of aeromagnetic data using lineament analysis. *Explor. Geophys.* **2013**, *44*, 104. [CrossRef]
29. Nabighian, M.N.; Grauch, V.J.S.; Hansen, R.O.; LaFehr, T.R.; Li, Y.; Peirce, J.W.; Phillips, J.D.; Ruder, M.E. The historical development of the magnetic method in exploration. *Geophysics* **2005**, *70*, 33–61. [CrossRef]
30. MacLeod, I.N.; Ellis, R.G. Magnetic Vector Inversion, a Simple Approach to the Challenge of Varying Direction of Rock Magnetization. Australian Society of Exploration Geophysicists, Extended Abstracts. 2013, pp. 1–4, Melbourne. Available online: https://www.semanticscholar.org/paper/Magnetic-Vector-Inversion-%2C-a-simple-approach-to-of-Macleod-Ellis/9cd186fe7e6843baeb43c706d80fc64ffed3109a (accessed on 1 December 2021).

A Practical Validation of Uncooled Thermal Imagers for Small RPAS

George Leblanc [1,*], Margaret Kalacska [2], J. Pablo Arroyo-Mora [1], Oliver Lucanus [2] and Andrew Todd [3]

[1] Flight Research Laboratory, Aerospace, National Research Council Canada, 1200 Montreal Road, Ottawa, ON K1A 0R6, Canada; JuanPablo.Arroyo-Mora@nrc-cnrc.gc.ca

[2] Applied Remote Sensing Lab., McGill University, Montreal, QC H3A 0B9, Canada; Margaret.Kalacska@mcgill.ca (M.K.); Oliver.lucanus2@mcgill.ca (O.L.)

[3] Metrology, National Research Council Canada, 1200 Montreal Road, Ottawa, ON K1A 0R6, Canada; Andrew.Todd@nrc-cnrc.gc.ca

[*] Correspondence: George.Leblanc@nrc-cnrc.gc.ca

Abstract: Uncooled thermal imaging sensors in the LWIR (7.5 μm to 14 μm) have recently been developed for use with small RPAS. This study derives a new thermal imaging validation methodology via the use of a blackbody source (indoors) and real-world field conditions (outdoors). We have demonstrated this method with three popular LWIR cameras by DJI (Zenmuse XT-R, Zenmuse XT2 and, the M2EA) operated by three different popular DJI RPAS platforms (Matrice 600 Pro, M300 RTK and, the Mavic 2 Enterprise Advanced). Results from the blackbody work show that each camera has a highly linearized response ($R^2 > 0.99$) in the temperature range 5–40 °C as well as a small (<2 °C) temperature bias that is less than the stated accuracy of the cameras. Field validation was accomplished by imaging vegetation and concrete targets (outdoors and at night), that were instrumented with surface temperature sensors. Environmental parameters (air temperature, humidity, pressure and, wind and gusting) were measured for several hours prior to imaging data collection and found to either not be a factor, or were constant, during the ~30 min data collection period. In-field results from imagery at five heights between 10 m and 50 m show absolute temperature retrievals of the concrete and two vegetation sites were within the specifications of the cameras. The methodology has been developed with consideration of active RPAS operational requirements.

Keywords: drone; UAV; UAS; thermal imaging; blackbody; emissivity; thermography

1. Introduction

With the nearly ubiquitous use of small (under 25 kg) Remotely Piloted Aircraft Systems (RPAS), there are incredibly versatile, capable and, cost-effective systems being applied to a diverse span of applications [1–4] that can acquire very high quality (4K) optical video and other sensor data, with exceptional stability. Only a few years ago, this ability did not exist or belonged solidly in the realm of high-cost, much larger and lower performing systems. For optical cameras and RPAS, it is clear that very small systems (sensor, avionics, and airframe) are now very capable of producing high quality images and video; but what about the Thermal InfraRed (TIR) and, specifically, TIR Imaging (TIRI) within the Long Wave InfraRed (LWIR) from 7.5 μm to 14.0 μm?

Within less than half a decade, capable small RPAS TIRI systems have been employed in a wide variety of studies, such as forestry [5–7], wildlife surveys [8–11], natural hazards [12–14], urban environments [15–18], archeology [19–21], mining [22–24], building inspection [25–27], etc. These works, as well as many others, have aided the overall technology push toward the use of thermography with small RPAS. This, in turn, has driven the demand for the technology to deliver more robust, accurate, easier to use and, lower cost sensor systems.

The heart of the new breed of easily accessible TIRI cameras is an uncooled radiometrically calibrated microbolometer that is able to produce usable data [28–31]. Relatively recently, TIRI detectors required cryogenic environments (operating temperatures $< -150\,^{\circ}$C) in order to produce useful data—due to the inherent thermal noise sources associated with environmental and electronics temperatures [32]. However, present day uncooled TIRI detectors have devised clever ways around this thermal noise barrier, such that the performance of uncooled calibrated TIRI instruments are now sufficient to produce very useful data [28,29,33,34].

With the wide accessibility of low-cost, uncooled TIRI cameras and RPAS platforms, their coalescence was, as with optical systems, inevitable. However, unlike optical imagery, the proper collection and use of TIRI requires greater user knowledge about TIR, including the behavior of materials, sensors, and calibration [35]. One concern is that many users of TIRI are unaware that the calibration of the instrument is obtained in a highly idealized laboratory-based environment and also, that it may change over the course of transport and real-world conditions.

Within the following work, we present the development of, and present our approach to, collecting and validating TIRI from real-world field examples. This work relies on validation of indoor (non-laboratory) blackbody measurements, and in-field surface temperature measurements of common target materials. We evaluate three different uncooled manufacturer radiometrically calibrated TIRI cameras of various ages and abilities, on three different RPAS airframes taken under the same environmental conditions. From those data, we analyze and show the abilities of these systems to replicate surface temperature measurements of known sources, and provide examples of the applicability of the uncooled TIRI cameras for RPAS in real-world environments.

Finally, it is important to explicitly state that our objective was to do a validation that can be done by most RPAS operators of TIRI systems, either pre- and/or post- campaign, to ensure that their cameras are operating within the specifications of the calibration. We are not seeking to do a field-based calibration of the camerasince true calibrations are an entirely different process requiring a highly controlled environment for temperature, pressure, humidity, air movement, etc.

Previous Work

Principally, due to the "newness" of the small RPAS TIRI ability, there are relatively few studies in the literature [36–39] that endeavor to address the issue of TIRI sensor calibration or validation. In [36], an in-field (non-laboratory and exposed to the natural environment) blackbody was used as a thermal target within the imagery with the development of a vicarious calibration method. This work included the environmental influences (e.g., wind, humidity, etc.) as part of an overall correction factor, along with other sensor-specific influences on the data. In a different approach than [36], Ribeiro-Gomes, K. et.al. [37] used a blackbody source to characterize their TIRI system before flight and also use a variety of methods—including artificial neural networks—to perform a calibration of the instrument from the blackbody measurements. The results of the analysis of the calibration method, image filtering, and geocorrection improvements were applied to a field-level data collection campaign over a vineyard. This method resulted in an increased accuracy with the use of neural networks and a requirement to use more accurate spectroradiometers in follow-on work for the blackbody calibration process.

Work by [38] using TIRI on RPAS and piloted aircraft produced results from snow, water and forest canopy as validation targets. The conclusions of this work were that there is a significant component of instrument bias in the resulting TIRI data as well as difficult spectral mixing conditions at boundaries of the validation material. Still more recently [39], a calibration procedure applied to thermographic RPAS cameras for use in the field has developed new electrical hardware and methodology for RPAS TIRI calibration within a controlled laboratory environment that provided the necessary calibration function to go from digital numbers through to calibrated temperatures.

2. Materials and Methods

2.1. RPAS Airframes and Cameras

Da-Jiang Innovations, Shenzhen, China (most commonly referred to as DJI) is the largest and most popular civilian multirotor VTOL (Vertical Take-Off and Landing) RPAS manufacturer in the world. As of 2019, DJI systems comprised 76.8% of the market in the USA (based on FAA registrations) [40]. As such, we have chosen three DJI RPAS models with TIRI capabilities, they are: the Mavic 2 Enterprise Advanced (hereafter M2EA), the Matrice 600 Pro (hereafter M600P) and, the Matrice 300-RTK (hereafter M300) (Figure 1). Table 1 contains general physical [41–43] and costing information for each of the RPAS airframes.

The M2EA airframe is the only one of the three tested here that has the dual TIRI/visible camera and gimbal system form-integrated into its airframe. Therefore, unlike the M600P and the M300 airframes, the M2EA is not suitable for interchanging with other camera systems. Both the M2EA and M300 geotag the thermal images with RTK (Real Time Kinematics) corrected positional information, which allows for accurate (<3 cm horizontal) geopositioning [44]. However, because it does not use a local base station, in order for RTK to be enabled on the M2EA, an external cellular internet connection and incoming corrections are necessary. While the M600P uses the RTK module in differential mode for flight control, the geotags of the XT-R are based on the basic GNSS (Global Navigation Satellite System) position.

Figure 1. RPAS systems and cameras in this study. (**A**) The M600P (left), M2EA (center) and M300 (right). (**B**) the Zenmuse XT-R with gimbal, (**C**) the M2EA form-integrated thermal (upper) and visible (lower) cameras and, (**D**) the Zenmuse XT2 thermal (right) and visible (left) cameras. The cameras are shown in the same order from L-R as the airframes with which they are compatible.

Table 1. Physical and costing information on the 3 DJI airframes (unfolded, base-level batteries, no payload configuration for the M600P and M300) used in this work. The costing was accurate as of the date of the data collection (5 July 2021).

RPAS	Take-Off Weight (kg)	Max. Take-Off Weight (Kg)	Max. Flight Time (min.)	Dimensions L × W × H (mm)	~Cost (USD)	Year of Launch
M2EA	0.909 *	1.10	31	322 × 242 × 125	7200	2021
M600P **	9.5	21.0	38	1668 × 1518 × 727	9200	2016
M300	6.3	9.0	55	810 × 670 × 430	12,000	2020

* M2EA camera is form-integrated as part of the airframe. ** The M600P used here has the integrated D-RTK upgrade and Max. Take-off Weight updated from [41] by personal communication (K. Toderel, RMUS Canada).

Unlike the M2EA, the M600P and the M300 airframes are able to carry a wide range of payloads, including various TIRI systems and gimbals. This is due to their payload carrying capacity—up to 11.5 kg and 2.7 kg, for the M600P and M300, respectively. The M600P and the M300 airframes are also more robust than many similarly classed airframes in terms of general physical presence, flight endurance and having a wider operational envelope. The M300 has an Ingress Protection (IP) rating of IP45, meaning it is protected against solid objects that are >1.0 mm in diameter, and also from water coming from any direction.

As this study is focused on TIRI for RPAS, we have selected DJI's M2EA, the Zenmuse XT-R and the Zenmuse XT2 cameras for comparison. We distinguish the XT-R (radiometrically calibrated) version from the non-calibrated performance version not tested here. Standard specifications of each camera is shown in Table 2 [41,45,46]. The XT2 is the only camera tested that has an Ingress Protection (IP) rating (IP44), which indicates that it is protected from solid (i.e., dust) and water particles/drops larger than 1 mm. Considering that these cameras are some of the most popular models for RPAS TIRI, the outcome of this comparison is expected to bring some insight into the potential impacts that newer/older, smaller/larger and, expensive/cost-effective technology may have on the quality of data produced. For greatest accuracy of measurement, all three cameras are recommended for use by the manufacturer in applications where the emissivity (see Section 2.2.1) of the material under study exceeds 0.9. All three cameras have high and low gain modes; in this study, all data were acquired in high gain mode to increase sensitivity (at a loss of the overall usable scene temperature range).

Table 2. Standard information on each of the TIRI camera systems.

Camera	Weight (g)	Range (μm)	Resolution (pixels)	FOV (°)	Pixel Pitch (μm)	Visual Camera	~Cost (USD)	Year of Launch
M2EA	639	8–14	640 × 512	46.2	12	Y	Incl.	2021
XT-R	270	7.5–13.5	640 × 512	45° × 37°	17	N	12,000	2016
XT2	588	7.5–13.5	640 × 512	45° × 37°	17	Y	12,000	2018

Both the XT-R and XT2 used here were equipped with non-interchangeable 13 mm lenses. The M2EA's focal length is reported as ~9 mm. All three models have a frame rate of 30 Hz. The reported sensitivity (Noise Equivalent Differential Temperature (NEdT)) of the XT-R and XT2 is <50 mK @ f1.0 and <50 mK @f1.1 for the M2EA (personal communication from K. Toderel, RMUS Canada).

2.2. Blackbody Indoor Camera Validation

2.2.1. Thermal Radiation

In considering the thermal behavior of a material, it is very useful to invoke the construct of a "blackbody"—a theoretically perfect radiator that absorbs all incoming energy (no reflection) and, when in equilibrium, becomes a perfect emitter. Therefore, when in thermal equilibrium, a blackbody is both a perfect absorber and emitter of incident radiation. An important quality of the surface is that it is perfectly isotropic, emitting and absorbing incident radiation without directional bias.

To understand the blackbody energy relationships of interest to this study, we begin with Planck's blackbody radiation law (Equation (1)), which describes the intensity of the

electromagnetic radiation emitted by a blackbody at a given wavelength as a function of its temperature,

$$I_\lambda = \frac{2\pi hc^2}{\lambda^5 \left(e^{\left(\frac{hc}{\lambda kT}\right)} - 1 \right)} \tag{1}$$

where, I_λ is the spectral emissive intensity (W·m^{-2}·sr^{-1}·μm^{-1}) of the radiation emitted by the blackbody at a given wavelength, λ (in μm), T (in kelvin) is the absolute temperature, h is Planck's constant (6.626 × 10^{-34} J·s), c is the speed of light (2.9979 × 10^8 m·s^{-1}) and k is the Boltzmann constant (1.380649 × 10^{-23} J·K^{-1}).

In work with electromagnetic sensors and imaging systems, one of the main quantities of interests is the energy at which a system radiates. Therefore, with Equation (1) as a basis, the total emitted radiation (E) of a thermal system is well-known to be a function of the temperature associated with the body and is given as:

$$E = \sigma T^4 \tag{2}$$

where, σ is the Stefan–Boltzmann constant (5.670374 × 10^{-8} W·m^{-2}·K^{-4}) [47]. Equation (2) shows that there is a relatively simple relationship between the temperature of a body and the energy of that body and that it is proportional (by the Stefan–Boltzmann constant) to the 4th power of the temperature. The important behavior that Equation (2) is able to determine is that a change in temperature within a system (a body) produces a large change (relative to the magnitude of the temperature change) in energy output for the system.

While Equation (2) is certainly useful in many respects, for this work, we are primarily interested in a subset of wavelengths due to the fact that imagers have a finite sensitivity over specific wavelength ranges (7.5–14 μm in our case—from Table 2). Fortunately, there is a well-known derivation (Wien's law) of Equation (1) that determines the wavelength at which the maximum radiant energy (λ_{max}) is produced as a function of temperature, and is given below as:

$$\lambda_{max} = \frac{b}{T} \tag{3}$$

where, b, is Wien's constant (2.8978 × 10^{-3} m·K). We note that while Equation (3) determines the maximum, or peak, wavelength, it cannot be forgotten that there remains a continuum of wavelengths produced from a body, at temperature T above 0 K. This continuum is fully described by Equation (1) and is the blackbody curve for that temperature.

Although the construct of a perfectly emissive radiator (blackbody) is well-defined, real-world materials deviate from this perfect behavior by emitting less energy than that predicted by blackbody theory. This deviation is captured by the emissivity coefficient (ε) and is quantified as the ratio of the energy emitted from a material's surface (E_m) to that emitted by a blackbody (E_b):

$$\varepsilon = \frac{E_m}{E_b}. \tag{4}$$

Emissivity is a unit-less characteristic of real-world materials that is dependent on several factors including: wavelength, temperature, material composition and surface characteristics (including, roughness, angle and direction). It is the most important factor of a surface that affects the amount of energy radiating from it [48]. The closer the value of ε is to 1, the greater is that material's thermal behavior approximating that of a blackbody. Accordingly, objects with high ε absorb and radiate large amounts of energy, while those with low ε, such as most metals, absorb and radiate low amounts of energy but are highly reflective. Therefore, in order to retrieve accurate surface temperatures of real-world materials, it is fundamentally important to correct for the ε of the materials. In general, when collecting the raw TIRI data, the radiative temperature is often acquired and expressed as Brightness Temperature (BT). The BT represents the temperature that a blackbody would be at in order to generate the observed radiance at the given wavelength (as ε = 1 in this case). It is important to note that BT produces incorrect surface temperatures

for real materials; therefore, it is necessary to apply the correct emissivity value (from Equation (4)) in order to determine the true surface temperature of a material.

While emissivity is certainly important, there are also energy contributions from a number of other factors that need to be taken into account with typical RPAS TIRI estimations of surface temperature (Figure 2). As an example, sky/cloud contributions heavily depend on the condition (i.e., percent cloud cover and cloud type) with clear skies contributing the least. In contrast, thick cumulus clouds contribute considerably more energy to the measurement [49].
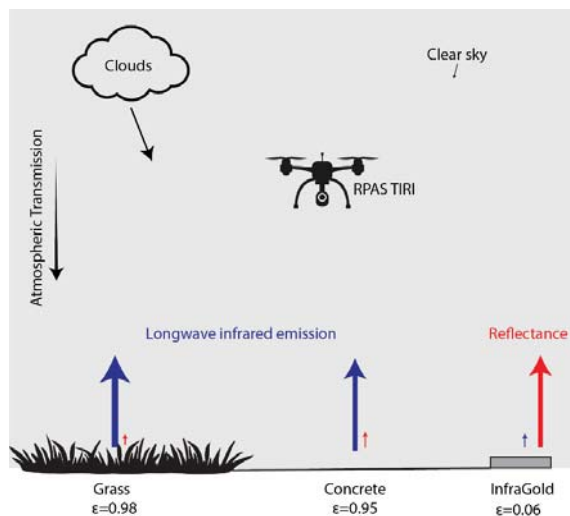
Figure 2. Illustration of the various sources of thermal infrared radiation to be considered with RPAS estimations of surface temperature in absence of nearby objects which would radiate energy into the scene. The arrows are representative of the relative contribution of each source. Three materials (grass, concrete, InfraGold) with a range of emissivity values considered in this study are shown. Atmospheric transmission decreases with increased distance between the TIRI sensor and the target. Atmospheric constituents such as water, smoke, dust, etc. all influence thermal transmission, with increasing significance at greater distances and/or as the concentration of the constituents increases.

2.2.2. Indoor Camera Validation—Blackbody Radiator

While it is often the case that small RPAS radiometric TIRI cameras come with a factory calibration certification, it is important (often necessary in practice) to validate if the calibration remains accurate at or near the time of the survey. The two primary reasons are that, (1) often there has been some physical jarring action during transport, which can potentially cause the unit to become uncalibrated and (2) all camera systems are not created equal, with quality greatly differing between them. The validation of TIRI systems involves the use of a stable calibrated blackbody source. In this study, we used the FLUKE 4180 Calibrator (Fluke Corporation, Everett, WA, USA) [50] as the target source for the validation. The FLUKE 4180 is a well-known portable blackbody operating within the $-15\,°C$ to $120\,°C$ temperature range with a large 15.24 cm diameter target radiator. Over the temperature range of this work, the calibration error was $0.4\,°C$ (obtained via the instrument's calibration certificate) at each temperature measured. The unit has a stability of $+/-0.05\,°C$ and $+/-0.10\,°C$ at $0\,°C$ and $120\,°C$, respectively. Over the central 12.7 cm diameter of the target, the radiator has a uniformity of $+/-0.1\,°C$ and $+/-0.20\,°C$ at $0\,°C$ and $120\,°C$, respectively. The unit has a nominal emissivity of 0.95 but is applicable over the range of emissivities (0.9 to 1.0) via thermometer emissivity compensation. As it was calibrated for $\varepsilon = 0.95$, all the imaging measurements for this work have used the 0.95 nominal emissivity value. As per

the instructions of the manufacturer, the unit requires 10 min of settling time after reaching the desired testing temperature to ensure the stability of the target radiator. Figure 3 shows the set-up of the indoor validation exercise.

Figure 3. Validation set-up that would be typical of a workspace pre/post RPAS operations. The tripod (**A**) that carries the environmental sensors for air temperature, RH, pressure and air movement, the FLUKE 4180 blackbody (**B**) and the M600P airframe with the XT-R camera (**C**).

The motivation of this validation process was to set the blackbody source at a distance away from the cameras that is greater than the minimal focal distance of the camera (for the XT-R and XT the minimum focus distance is 7.6 cm and ~3.2 cm for the M2EA [41,45,46]). Then set the temperature of the blackbody and let it settle to ensure uniformity. After settling, image the blackbody source with the central pixels of the camera and then go to the next temperature, let settle and image—repeat as per necessary for the temperature range expected by the phenomena under investigation. Then, to ensure the instrument and related software are properly accounting for distance, we doubled the distance and re-image at the same temperatures. In this process, we have used the central pixels as they are often (but not always) the ones of concern when we investigate any phenomena. This method, of course, is not entirely complete as the non-central pixels do not image the blackbody; however, we are proposing a realistic method to field-validate RPAS imagers. In order to fully validate the imager, each pixel of the imaging camera should image the central area of the blackbody target. Since we are interested in field-applicable methods, and our imager is 640 × 512 pixels, it is not at all practical (to the RPAS operations) to test more than the central pixels.

We set-up air temperature, pressure, humidity and air speed monitors within the indoor space using the HOBO™ (Honest Observer By Onset) smart sensor system (Onset Computer Corporation, Bourne, MA, USA). The HOBO system is a well-known and highly used suite of field-proofed environmental measurement instruments [51–54]. During the entire time of the exercise, there was no measurable flow of air, which was not unexpected as we performed this work indoors with no forced air circulation. However, it was necessary to ensure this wasthe case.

Each RPAS camera was positioned at 2 m distance to the blackbody and normal (90°) to the center of the face of the radiator target, so that any angular dependence of measurement was fundamentally restricted to being perpendicular to the measured surface. We then allowed the blackbody to come to the first temperature (5 °C) and once at that temperature, we let it stabilize for 10 min. With each camera in succession, the blackbody radiator target was imaged with the central portion of the camera's FOV. The blackbody temperature remained constant at the set point while the camera was moved to 4 m from the blackbody target and then each camera re-imaged the blackbody target again. The use

of two distances (2 m and 4 m) was an exercise to determine if there were considerable differences in measured temperature as a function of distance, even though each camera has a small focal length of 9 mm (M2EA) or 13 mm (XT-R and XT2). Once all cameras had imaged the blackbody target at both distances for each temperature, the temperature was increased to the next setting and the process was repeated. We selected eight temperature settings (5, 10, 15, 20, 25, 30, 35 and, 40 °C), over a range of 35 °C, that are uniformly spaced and would replicate the air and target temperatures expected in real-world environmental applications. As well, this process ensures the evaluation of the camera performance near to, and including, temperatures beyond those of interest to the application. In our case, the application temperatures of interest were from 15 °C to 25 °C.

The indoor blackbody validation data were acquired over a period of 2.5 h, after set-up, where the majority of that time was dedicated to allowing the blackbody target radiator to settle after reaching the testing temperature. Once the temperatures were recorded by the TIRI cameras, the images were processed in FLIR Thermal Studio (Teledyne FLIR, Wilsonville, OR, USA) in order to account for emissivity, distance to source, air temperature, humidity, and optics temperature. As the images from the M2EA cannot be directly read by FLIR Thermal Studio, they were first converted to a standard FLIR radiometric jpg with ThermoConverter (Aethea, London, UK).

2.3. Outdoor Field Trial
2.3.1. Study Site Set-up

The location of the field trial was at a private RPAS test site near Vaudreuil-Dorion, QC, Canada (45°26′23″ N, 74°13′05″ W). The extensively instrumented ground site is shown in Figure 4. The ground site set-up and the instrument distribution included: 2 differential RTK base stations supporting the M300 and M600P, HOBO environmental measurement station, vegetation validation targets, an InfraGold target panel and, concrete slab validation targets. The RTK base stations were used during the trial to replicate flight conditions appropriate to larger area TIRI acquisitions.

The HOBO environmental monitoring instrumentation (Figure 5) consisted of measuring the following (with model numbers): an anemometer (S-WSA-M003) for measuring wind speed, and wind gust, air temperature (T_{air}) and relative humidity (RH) ((A-THB-M002), solar shielding (RS3), air pressure (S-BPB-CM50), two in-canopy vegetation temperatures (S-TMB-M006), and two soil temperature probes (S-TMB-M002). The electronics and data collection units (H21-USB) were stored under the tripod. T_{air} and RH are integrated into one unit (S-THB-M002), and were placed under the solar shield (RS3) in order to obtain accurate T_{air} and RH measurements free from the effects of direct solar radiative heating [51].

While, T_{air} will have a large impact on surface temperature, wind speed has been shown to induce substantial localized cooling depending on its value over a sustained period of hours. Wind-induced surface cooling arises as a case of forced convective cooling and is proportional to the temperature differential between the air in motion and the surface [55]. Several studies using TIRI have shown and measured this effect on surfaces of buildings [56,57], and on the bare ground overtop of heating pipe systems [58]. In general, these studies show that with wind speeds below 2 m/s the effect is negligible, or at least at the limit of the resolution of the TIRI data. The work of [58] remains as one of the few examples of TIRI-derived temperature measurement as a function of increasing wind speed. In [58], TIRI taken overtop of buried heating pipes have shown that winds below ~2 m/s did affect the measurements but the value of this effect (~+/−0.2 °C) is less than the error in the TIRI data. In more recent work, [56] found that for many building surfaces, winds up to even 5 m/s did not significantly alter the values obtained via a TIRI survey. In an even more recent work, [57] generalized that wind pulsations (gusting) induced changes with TIRI data as being "not-critical" for speeds of up to 2 m/s. Sustained wind periods of several hours before data collection did have an impact on the surface temperature and should be avoided during those times. As a result of this known wind-induced cooling,

the majority of past studies identified that it is often necessary to install the environmental monitoring equipment (Figure 5), at least several hours before TIRI data collection.
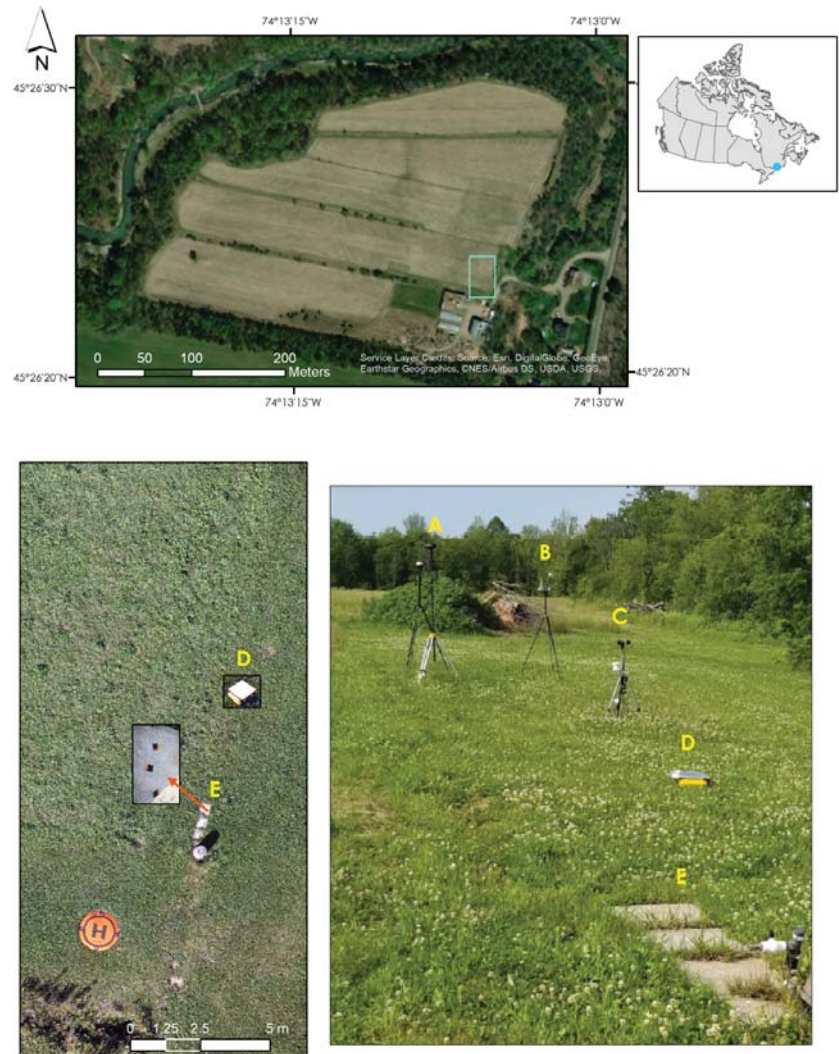
Figure 4. Field site near Vaudreuil-Dorion, QC (top panel) with the light blue/green box representing the area of the investigation and the instrumented ground site location. Ground site set-up (lower panels) including: differentialRTK base station for the M300 (**A**), and for the M600P (**B**), environmental monitoring station and vegetation validation site (**C**), the InfraGold dark sky diffuse reflectance panel (**D**) with foil protection covering that was removed before data collection, and the concrete slab target (**E**) with three thermal flux sensors (used for deriving temperature) indicated by the red arrow in the lower left panel. Photographs were taken during the day for clarity. The orange circular feature in the lower left panel (with an "H") shows the launch area for the RPAS vehicles.
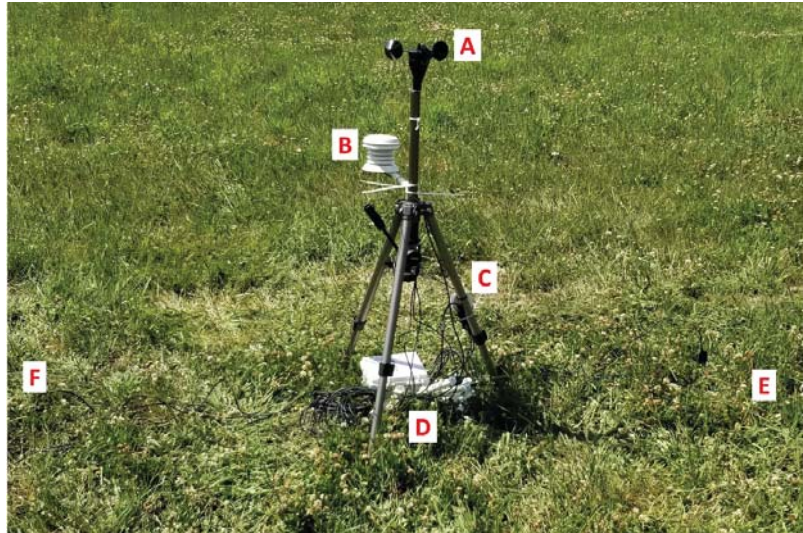
Figure 5. Environmental monitoring station and vegetation target from Figure 4. The photograph shows the emplacement of the anemometer (**A**) at 1.0 m height, the T_{air} and RH (one unit) under a solar radiative shield (**B**), air pressure (**C**) and, control electronics and data collection units (**D**). Also shown are the vegetation/soil target areas of T1/T2 (**E**) and T3/T4 (**F**) at 1.0 m distance from the center of the tripod location. Soil temperature probes (T2 and T4) were implanted at a depth of 5 cm directly below the in-canopy temperature sensors (T1 and T3).

Figure 6 shows the three targets of interest for this study, the InfraGold panel, the concrete slabs and, the in-canopy vegetation and soil targets. The diffuse InfraGold panel (25.5 cm × 25.5 cm), is being used only to determine if there is a significant contribution to the signal from the downwelling irradiance of the open sky [49]. Having an $\varepsilon = 0.06$ means that it is highly reflective and as it faces the sky, the conditions it presents to the imager is that of the sky with negligible contribution from its own emission (i.e., less than the detection limit of the TIRI camera) at most ambient air temperatures at which RPAS TIRI is carried out.

The patio stone concrete target, Figure 6B, were in place for several years prior to the experiment and, therefore, was in good contact with the underlying soil. The surfaces of the concrete slabs were weathered. Three FluxTeq^{TM} PHFS-01-e 1 × 1" standard heat flux sensors (Flux Teq, Balcksburg, VA, USA) were connected to a high resolution, 8 channel thermocouple data acquisition device (TC-DAQ) logging to a laptop. The PHFs-01e have a nominal sensitivity of 9.0 mV/(W/cm^2) and a specific thermal resistance of 0.9 K/(kW/m^2) [59]. The PHFs-01e heat flux sensors were adhered to the concrete using Arctic MX-4-4G thermal compound paste (carbon micro-particle based) (Arctic GmbH, Braunschweig, Germany). One of the three flux sensors did not properly adhere to the surface of the concrete, and thus those data were ignored in this study.
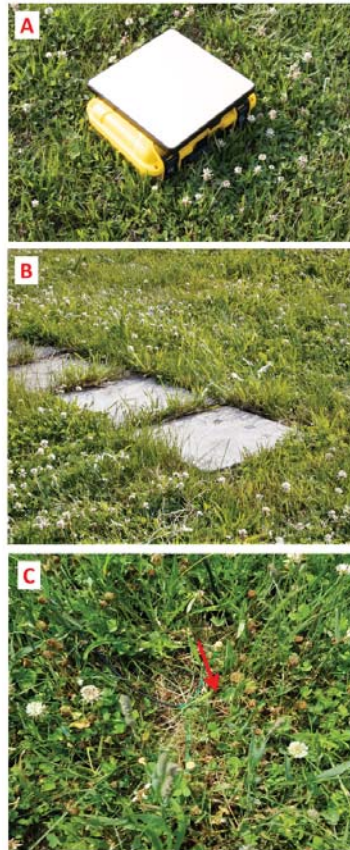
Figure 6. Target materials used for comparison. (**A**) InfraGold panel atop a plastic storage box, used as a platform to keep the surface debris free. (**B**) Concrete patio stones with three heat flux sensors (black squares on the concrete slab—as also indicated in Figure 4 label E) from which temperature was derived. The left-most sensor did not stay adhered to the surface and therefore, the data were not used. (**C**) In-canopy temperature sensor T1 (located with the red arrow) within the living and detritus vegetation canopy. The in-canopy temperature sensors (T1 and T3) were positioned at a height of approximately 2–3 cm above the soil.

The soil and in-canopy temperature sensors were configured to work in pairs where the soil temperature probes were placed directly below the in-canopy temperature probes at a depth of 5 cm from the surface. In our set-up, shown in Figure 5E and in detail in Figure 6C, the T1 and T2 sensor pair was located 1 m north of the middle of the anemometer tripod. The in-canopy sensor (T1), located by the red arrow in Figure 6C, was held in place by a nylon cord that was attached to wooden stakes driven into the ground approximately 5 cm on either side of the sensor. This was necessary as curious field animals have a tendency to remove these sensors when left in place overnight. The other pair of in-canopy and soil temperature sensors, respectively, T3 and T4, were installed in the same manner, 1 m south of the anemometer tripod (location F in Figure 5). The vegetation target area is composed of a heterogeneous mix of grasses, white clover, dandelion and detritus, as well as void space. The overall result is that the soil is fully overlaid by the living vegetation canopy and its detritus. At the time of the TIRI measurements, the height of vegetation

was ~10 cm. The soil and in-canopy sensors were installed and logged continuously for 12 days prior to the acquisition of the RPAS TIRI images.

2.3.2. RPAS TIRI Acquisition

The TIRI RPAS measurements were made after twilight (21:25 EST) on 5 July 2021 in order to ensure that solar irradiance would not influence the measurements. For a large amount of TIRI work, it is highly desirable to work after twilight in order to eliminate the potentially large non-linear differential solar contribution to the measured signal (Holtz 2000). For the TIRI acquisition starting at 10 m height above the study area, the first RPAS airframe hovered over the targets and acquired a thermal image—manually triggered by the operator. It then ascended to 20 m and repeated the acquisition. In this manner all three airframes completed the acquisition of the TIRI at heights of 10, 20, 30, 40 and, 50 m. The multi-altitude data set was acquired over a period of ~30 min. Even though each of the thermal cameras carry out flat field corrections (FCC) at power up and periodically during use, a supplemental FCC was triggered by the operator prior to the acquisition of each image. The FCC compensates for errors that occur during operation—such as those induced by temperature change at altitude. The images were processed in FLIR Thermal Studio to account for height (i.e., distance from target), atmospheric temperature, relative humidity and reflected temperature. The external optics temperature was set to *Tair* recorded at the time of acquisition. The images were processed with three different emissivity values, 1 for BT, 0.98 for grass and 0.95 for concrete. As with the blackbody radiator experiment, the M2EA images from this test were also first converted to a standard FLIR radiometric jpg with ThermoConverter.

In this work, we have used the value of $\varepsilon = 0.98$ for vegetation, which is based upon [60] (as cited in [61]) who have suggested this value for a general canopy emissivity. The value is further supported by [62] who have described grass emissivities for complete and partial canopy covers ranging from 0.956 to 0.986. More recently, [16] have used $\varepsilon = 0.979$ for grasses and $\varepsilon = 0.977$ for canopy cover, and [61] used $\varepsilon = 0.98$ as the vegetation canopy emissivity in non-arid environments. The emissivity value used for concrete (grey weathered, rough surface) was obtained from [63] where a large number of urban materials have undergone emissivity determination within the 8–14 μm range.

3. Results

3.1. Indoor Blackbody Validation

During the indoor trial, the environmental parameters were reported as: T_{air} average of 20.6 °C (ranged from 20.2 °C to 21.0 °C), RH average of 70.9% (ranged from 69% to 71.7%) and barometric pressure average of 1009.2 mbar (ranged from 1008.5 mbar to 1009.9 mbar). For the purposes of this work, we used the average T_{air}, pressure and RH for the calculation of the environmental temperature, in the vicinity of the blackbody, by each camera. The imagery obtained from each camera showed that the blackbody radiator target was well identified at each of the eight temperature settings. Examples of the imagery are shown in Figure 7 for the XT2 camera, at 2 m and 4 m distance, for 5 °C and 40 °C, respectively. The pixels in the central portion of the blackbody radiator (all within the 12.7 cm diameter of the central area of the radiator) were used in the subsequent analysis of the temperature measurements. The portion of the image outside of the area of the circular blackbody radiator exhibits less detail (lower contrast) as the material within the room was at or near the average indoor ambient temperature of 20.6 °C. A total of 830–950 pixels comprised the area extracted for analysis at 2 m and 220–230 pixels at the 4 m distance.
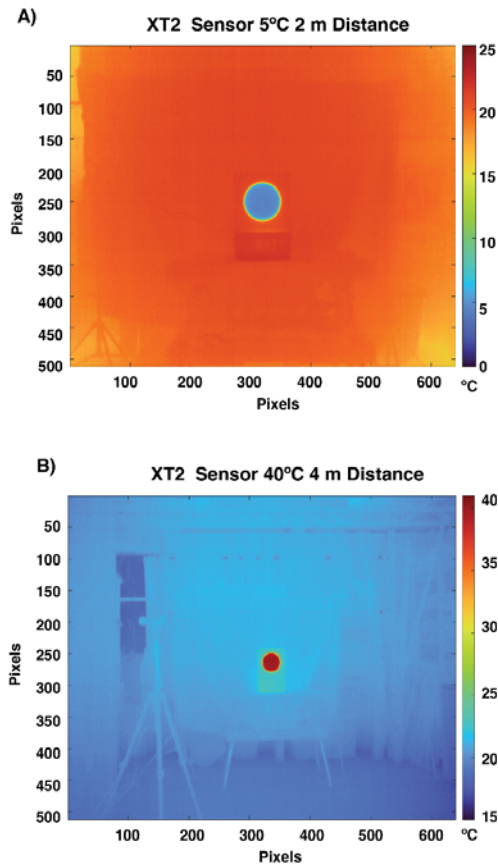
Figure 7. Example results at different distances and temperatures of imaging the variable temperature blackbody with the Zenmuse XT2. (**A**) 2 m distance and a blackbody temperature of 5 °C, and, (**B**) 4 m distance with 40 °C blackbody temperature. The lack of contrast in the objects outside of the circular blackbody radiator (in the center of the images) is due to the objects' temperatures being nearly at the ambient room temperature of 20.6 °C.

The measured results for each camera at all temperatures and distances, are shown in Figure 8 along with the best fit lines and uncertainties related to the measurements. The data used for Figure 8 is provided in Table A1 in Appendix A. The error bars shown for each plot arise from the range (minimum and maximum values of the central pixels) of the measurements themselves. Also presented in each plot is the corresponding 1:1 temperature line (black solid) that represents the theoretically perfect blackbody target temperature and the uncertainty (black dashed lines) corresponding to the +/−0.4 °C uncertainty value that was supplied by the calibration certificate. For each data set shown in Figure 8, statistical analytics describing the linearity of the response and the deviation from the blackbody source are shown in Table 3.
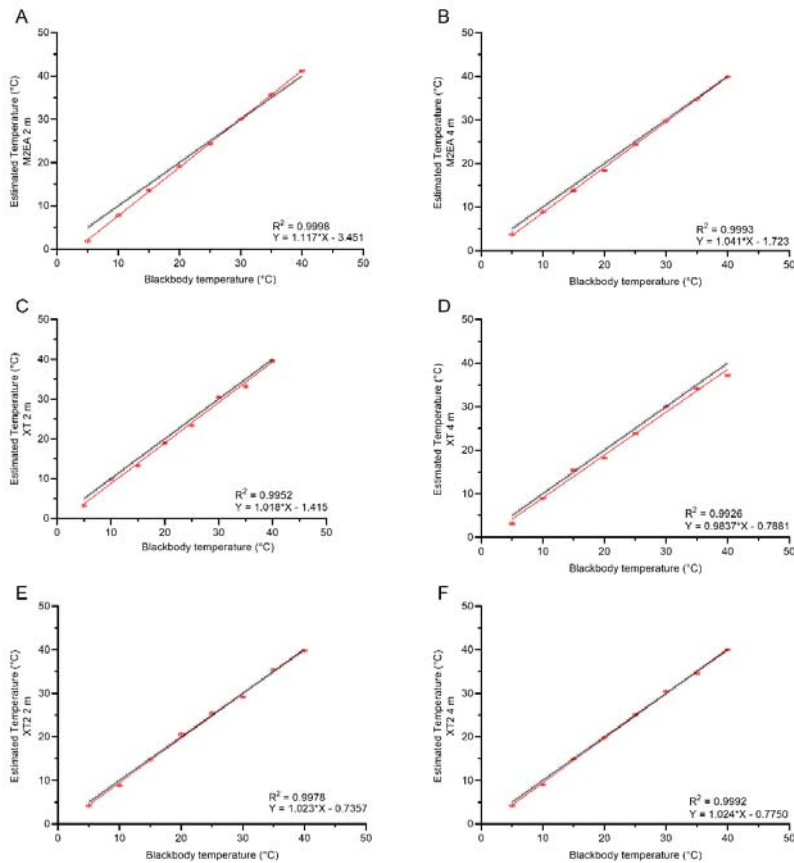
Figure 8. Results of the indoor validation with error bars derived from blackbody errors. (**A**) M2EA at 2 m, (**B**) M2EA at 4 m, (**C**) XT-R at 2 m, (**D**) XT-R at 4 m (**E**) XT2 at 2 m, (**F**) XT2 at 4 m. Red line is the best fit line between the TIRI calculated temperature and the blackbody set temperature. The red error bars illustrate the uncertainty of the FLUKE 4180 (x-axis) and the minimum and maximum calculated TIRI temperature (y-axis). The black line is the 1:1 blackbody temperature line with the dashed lines on either side illustrating the 0.4 °C FLUKE 4180 temperature uncertainty.

Table 3. Results from the indoor validation exercise for the M2EA, XT-R and XT2 cameras at 2 m and 4 m distance from the blackbody radiator over the 5 °C to 40 °C range. The coefficient of determination (R^2) is a measure of the variability explained by the linear regressions, the root mean square error (RMSE) is a measure of the difference between predicted and observed temperatures and the bias is a measure of the over or under prediction of temperature by the cameras. SD is the standard deviation of the temperature recorded by the cameras.

Camera	Dist. (m)	Best Fit Equation	R^2	RMSE (°C)	95% CI Slope	Bias (°C)	Mean Diff. (°C)	SD (°C)
M2EA	2	1.117X − 3.451	0.9998	0.18	1.104X − 1.131	−0.81	0.29	0.11
M2EA	4	1.041X − 1.723	0.9993	0.36	1.014X − 1.068	−0.80	0.18	0.13
XT-R	2	1.018X − 1.415	0.9952	0.94	0.947X − 1.089	−1.00	0.26	0.09
XT-R	4	0.984X − 0.788	0.9926	1.12	0.899X − 1.069	−1.15	0.29	0.08
XT2	2	1.023X − 0.736	0.9978	0.63	0.975X − 1.071	−0.21	0.13	0.09
XT2	4	1.024X − 0.775	0.9992	0.39	0.995X − 1.054	−0.23	0.08	0.10

Overall, Figure 8 shows that each camera is highly linear over the temperature testing range of 5 °C to 40 °C. The linear relationship for each camera shown in Figure 8 is reflected, numerically, in the results of Table 3 with each best fit line having an $R^2 > 0.99$ The 95% confidence intervals of the slope for the M2EA at both distances are the only ones that do not span 1.0 (i.e., slope of the 1:1 line) substantiating the larger underestimation of the blackbody temperatures of 5 °C and 10 °C see in Figure 8A,B. Over the temperature range investigated with the blackbody (35 °C), the M2EA had the greatest temperature difference (ΔT) (36.2 °C at 2 m and 39.3 °C at 4 m) from the ΔT of the blackbody (35 °C). In contrast, the XT2 had the least difference with a ΔT of 35.8 °C and 35.6 °C at 2 m and 4 m, respectively. The standard deviation for the measurements at each temperature was less than 0.15 °C for all cameras indicating a consistency in pixel values across the imaged surface of the blackbody (Table A1).

The analysis results for each camera at each distance are summarized in Table 3 and indicate that all cameras, in general, underestimated the blackbody temperatures. At the 2 m distance, the greatest deviations in the measured temperatures were found to be −3.1 °C and −2.2 °C for the M2EA at blackbody temperatures of 5 °C and 10 °C, respectively. At the 4m distance, the XT-R camera had the greatest deviations from the blackbody with −2.9 °C and −1.9 °C at 40 °C and 5 °C respectively (apparent in Figure 8 as well). The largest RMSE values at both distances are seen for the XT-R (0.94 °C and 1.12 °C). It also presents the greatest bias at both distances of −1.00 °C and −1.15 °C (Table 3, Figure 8). Consistently at both distances, the XT2 has the lowest bias (−0.21 °C and −0.23 °C). While its RMSE values were not as low as that of the M2EA (<0.4 °C), they were still less than 0.7 °C for both distances.

3.2. Outdoor Field Trial

Environmental Conditions

As previously noted, when considering doing TIRI work, the need to collect environmental data (T_{air}, wind and gust speed, RH, and air pressure) for several hours prior to taking thermal measurements is imperative. In our work, the results of these environmental measurements for the two hours prior to the end of the RPAS TIRI collection are shown in Figure 9 (along with the start time of the RPAS survey). On the day of the survey, twilight occurred at a time of 21:25 EST.

Figure 9A shows the temperature profiles of each sensor that measured the vegetation (T1 and T3), soil (T2 and T4) as well as that of T_{air}, for direct comparison. As a result, it is clear that variation in soil temperatures (1.0 °C) does not experience the larger fluctuations evident in the vegetation (3.3 °C) or T_{air} (2.1 °C). The soil profiles (T2 and T4) are also very similar in values, having a maximum difference of 0.07 °C (well within the +/−0.2 °C accuracy of the sensors); they also show a constant cooling slope over the first 90 min and again over the last half hour of the trial period (~2 h). The small change in cooling slope for the soil is likely due to the delayed effects of the increasing T_{air} and vegetation temperatures. A similar relationship to soil exists for the vegetation sensors (T3 and T4) where they mimic each other's profiles, however, there are differences that amount to ~0.7 °C (nearly 10 times that of the soil profiles) which is larger than the error of the sensors and is therefore, real but still quite small. T1 and T3 also mimics T_{air} (with some offset in time and a larger offset in temperature) but to a lesser degree. It is also evident that T_{air} has the most influence on the variability of T1 and T3; moreover, during the time of the RPAS survey (shown in Figure 9A), T_{air}, T1 and T3 experience ~0.5 °C of variability, which will be considered as remaining essentially constant for the duration of the survey.

(A)

(B)
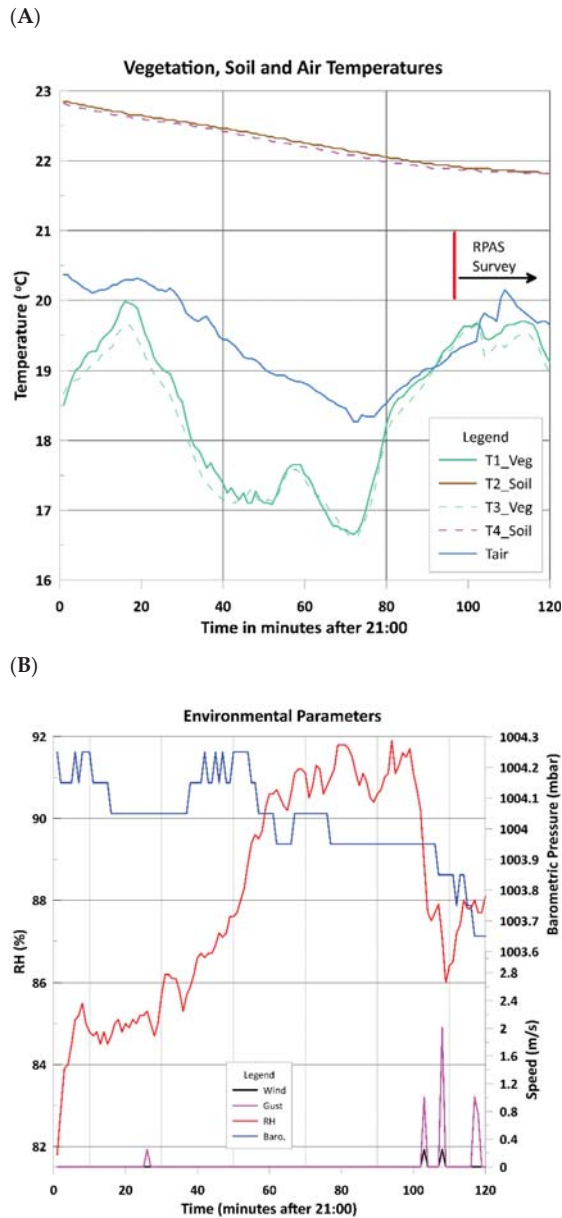
Figure 9. Two hours (of the 12 days of continuous logging) of environmental parameter data from 5 July—21:00 to 23:00. (**A**) Temperature data, (**B**) Environmental data, Wind, RH, Barometric pressure. RPAS data collection started at minute 94 and ceased after minute 116. The blocky nature of the barometric signal is a result of resolution effects near the threshold levels (0.1 mbar) of the instrument.

For the environmental factors in Figure 9B, the time during the RPAS TIRI data collection period shows small amounts of variability—with barometric pressure varying by 0.2 mbar and RH by 5.9%. Therefore, we are treating these parameters as being essentially constant for the purposes of calculating source temperatures from TIRI. In this study, the

wind and gust averages for the 2 h prior to the end of the trial were 0.01 m/s and 0.03 m/s, respectively—well below the 2.0 m/s value where they would start to influence the surface temperature measurements. Moreover, the maximum gust speed obtained was 2.0 m/s for a single point anomaly (at time point 108 in Figure 9B). Under these conditions, we can confidently say that the wind had no effect on the targets of interest.

While the environmental parameters in this study have been shown to be essentially constant or insignificant, it is important to measure the variables, in situ [14], as it could easily have been the case that the conditions exceeded the bounds of influence for TIRI temperature retrieval. Furthermore, the variables of humidity and T_{air}, along with an assumption of constant and near standard air pressure (1000 mbar), are required input values (or assumptions) for the radiometric correction software.

3.3. TIRI

3.3.1. Brightness Temperature

As previously discussed, BT is the collection of TIR measurements with $\varepsilon = 1$. It assumes all radiating surfaces in the scene are blackbodies. While BT is not an accurate measure of surface temperature for real materials, it is useful to compare these values across the scene and for quickly identifying changes in the thermal properties of the area under investigation. The relative differences within the imagery can provide a "quick view" of the potential areas of interest. As an example, Figure 10 shows the results of collecting 20 m and 50 m height TIRI with each camera in this study. It is clear from the 20 m data that all the features we are interested in, (i.e., InfraGold panel, vegetation and, the concrete patio stones), are all identifiable, while the larger area of the 50 m data also shows a curious high temperature linear feature (shown by the red arrow) cross-cutting the direction of the dirt road (brightest feature in the imagery from all three cameras). This feature was later investigated and found to be a buried drainage pipe under the roadway.

3.3.2. InfraGold Panel

To reiterate, the InfraGold panel ($\varepsilon = 0.06$) is used in this study as an indicating tool to determine if the thermal contribution from the sky is, or is not, significantly contributing to the TIRI data. Results from FLIR Thermal Studio of the InfraGold panel derived temperatures (at $\varepsilon = 0.06$) produced open sky average temperatures <-60.13 °C. This value derived for the panel constitutes the lowest temperatures that FLIR Thermal Studio could produce, however, the lowest limit for all three cameras in high gain mode is -25 °C. Therefore, we can only state that the reflected sky temperature from the panel is <-25 °C (as shown in Figure 11) indicating a negligible downwelling contribution. From Equations (1) and (3), the <-25 °C contribution provides a corresponding intensity of <3.85 W/m^2/sr/µm at a maximal peak wavelength at ~11.678 µm for the panel surface. Comparing this with an average temperature for the vegetation scene at 19.5 °C, which, through Equations (1) and (3), gives an energy of ~8.79 W/m^2/sr/µm at a peak wavelength of ~9.9 µm. In addition, because the 11.678 µm peak is near the edge of the sensors' measurable response, the effects from the downwelling irradiance are not appreciably impacting this work.

3.3.3. Concrete Patio Stone Target

Figure 12 provides an example of the results of imaging the concrete target with the XT-R camera at 20 m altitude with an emissivity of 0.95. Because of the 41 cm width of the concrete tiles, only the 10–30 m altitude images were included in the analysis. Considering the largest pixel pitch (i.e., 17 µm for the XT-R and XT2) and the 13mm lens, in order to retain the recommended minimum region of interest size of 10 pixels diameter [41,45,46], ensuring accurate temperature retrievals, the sensor/target separation can have a maximum value of 30 m. With fewer pixels, the spot size effect results in lower accuracy measurements due to contamination (spectral mixing) from neighboring materials.
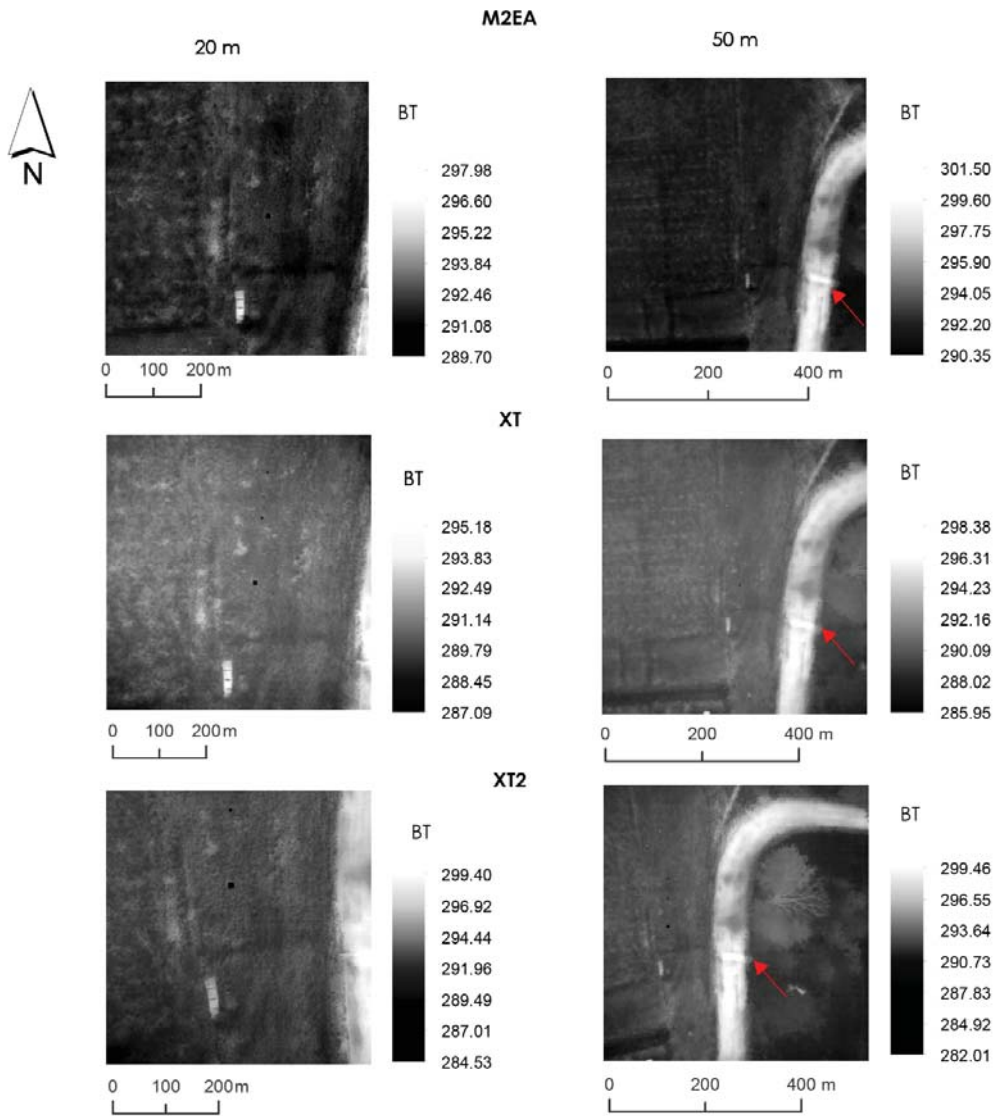
Figure 10. Brightness temperature (BT) in kelvin for all TIRI RPAS systems in this study at 20 m (left column of images) and 50 m (right column of images) with the M2EA (**top**), XT-R (**middle**) and XT2 (**lower**) cameras. The red arrow in the 50 m column indicates the location of a buried drainage pipe.
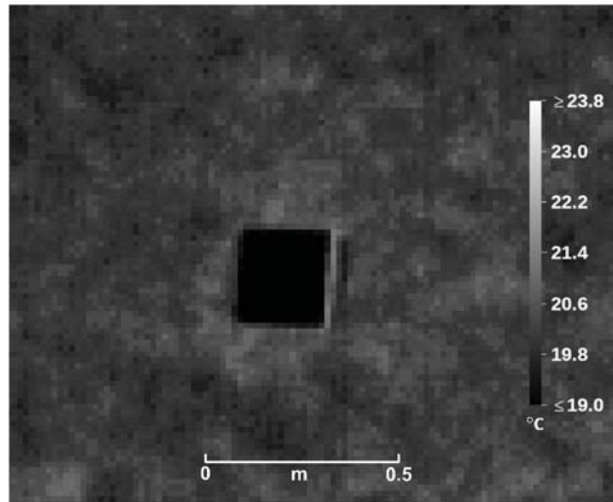
Figure 11. Thermal imaging results at 10 m AGL with the M2EA camera of the InfraGold panel (dark square in the center of the image). Evaluation of the panel area with $\varepsilon = 0.06$, produces a sky reflected temperature <-25 °C, below the lower limit of the camera in high gain mode.
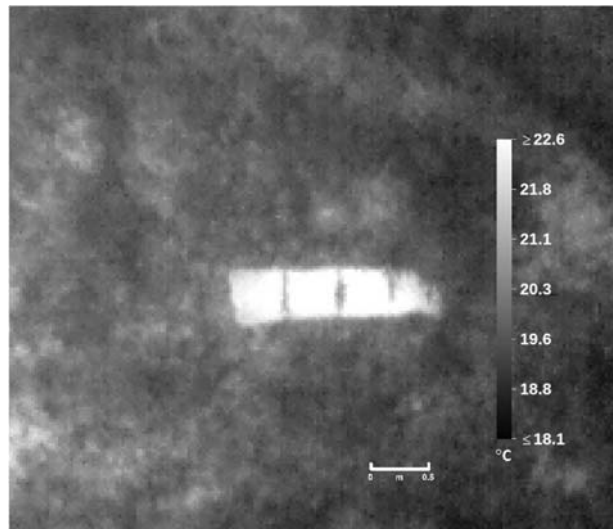
Figure 12. Subset of a TIRI from the XT-R camera over the concrete target from 20 m height. In this version of the image, only the concrete pixels provide valid temperature measurements due to the scene being processed with $\varepsilon = 0.95$.

The results of applying the emissivity corrections for concrete to the TIRI data from each camera are shown in Figure 13. The contact measurements from the PHFS-01-e sensors indicated a temperature of 23.8 °C during the data collection. At 20 m and 30 m, the M2EA reports the closest surface temperature to the PHFS-01-e (over estimation of 0.3–0.5 °C.) At the 10 m height, however, the M2EA overestimated the concrete temperature by 1.8 °C. At 20 m and 30 m both the XT-R and XT2 have a similarly large deviation from the in situ measurement, although in opposite directions (-1.1 °C, -1.2 °C for the XT-R

and 1.0 °C, 1.1 °C for the XT2). At 10 m height, the XT-R was the most similar to the in-situ temperature of concrete (−0.3 °C difference) in comparison to the M2EA and the XT2, which both overestimated the surface temperature by 1.8 °C. In context, however, while the deviations from the in situ measurements are greater than the bias reported with the blackbody experiment (Table 3), they are all relatively small (<2 °C).
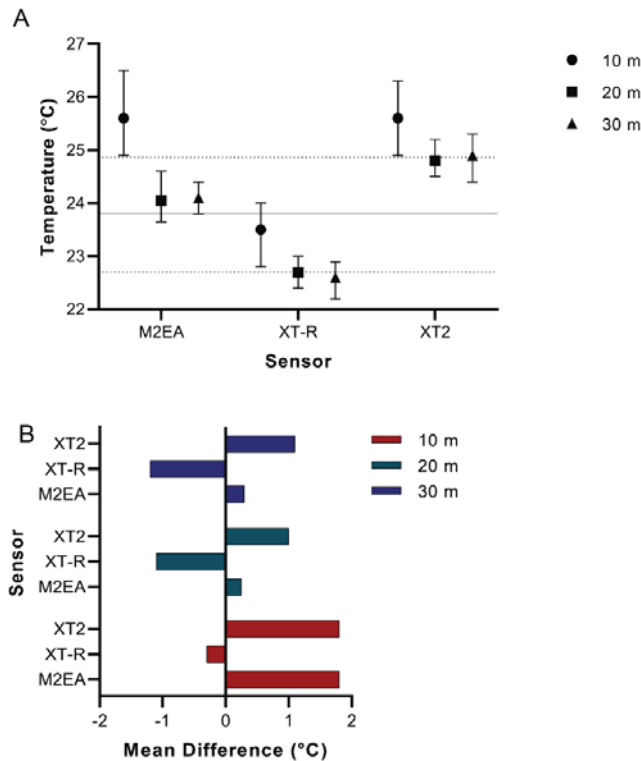
Figure 13. Results of comparing the TIRI data from each camera at 10–30 m height to the temperature determined by the PHFS-01-e heat sensors. (**A**) Mean with error bars representing the min and max of the temperature of the concrete tile from the TIRI. The solid line represents the temperature of the in-situ measurement of surface temperature from the PHFS-01-e heat sensors, the dotted lines represent the uncertainty of the PHFS-01-e in situ calculated temperature. (**B**) Mean difference between the TIRI estimated surface temperature and the PHFS-01-e heat sensors.

3.3.4. Grass and Soil

While vegetation targets are complex, due primarily to water content, air space and canopy distribution, they are, nevertheless, important to include as a great deal of outdoor work involves their measure [64,65]. Figure 14 shows an example of a TIRI image of the grass (ε = 0.98) from the XT2 camera at 40 m height. In the image are two black squares (10 cm × 10 cm) of aluminum tape that have been used as markers (due to their very low emissivity- providing high thermal contrast) to locate the areas of the in situ temperature sensors in the resulting TIRI. The markers were placed ~10 cm adjacent to the areas of the in-canopy temperature sensors, bookending the areas of investigation.
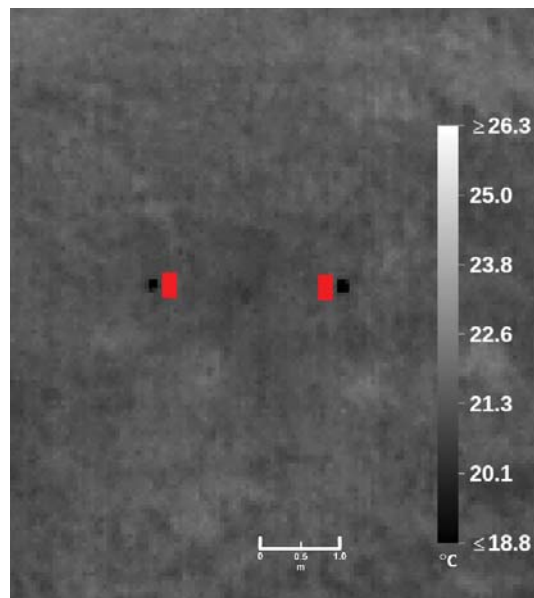
Figure 14. TIRI from the XT2 camera at 40 m height over the areas of vegetation identified by the red rectangles adjacent to the black squares. Validation sites for Vegetation 1 (left red rectangle) and Vegetation 2 (right red rectangle) correspond to locations E and F, respectively, in Figure 4. The black squares are metal 10 cm × 10 cm markers that have been used in all the TIRI to locate the areas of the in-situ temperature sensors, due to their high thermal contrast to the rest of the material in the image. The geometrical relationship of the location of the red validation sites, w.r.t. the true ground coordinates relies on the visual identification of the corners of the black markers in the image.

Results for vegetation was obtained by comparing the TIRI data from each camera at each height with that of the in situ ground measurements are shown in Figures 15 and 16. For the most part, the grass temperature estimate from the M2EA lies between the in situ temperatures obtained for grass canopy and soil for both T1/T2 (Figure 15) and T3/T4 locations (Figure 16). The actual location (on the temperatures axis) that the grass and the image measurements lies at is a function of air temperature, air space within the canopy and the coverage of the vegetation over the soil. As the soil sensor was emplaced 5 cm below the surface, and below the root mat, its value represents the true temperature of the upper surface of the soil. As seen in Figure 13, the TIRI temperature values from the M2EA camera, exhibit the greatest deviation from the in situ measurements. As with the concrete example in Figure 13, the source of this anomaly has yet to be determined. At both vegetation sites, across heights, the XT-R camera is most similar to the measurements of the in situ soil probes (0.3–0.8 °C difference). In contrast, the XT2 is most similar to the grass canopy in situ probes at both vegetation sites (0.7–1.3 °C difference) (Figures 15 and 16). As expected, for all three cameras, the greatest variability in the temperature of the grass pixels is seen at the 10 m height (smallest pixels). For the XT-R and XT2, the range of grass pixel values is lowest but similar across the 30–50 m heights. As seen with the concrete target (Figure 13), the deviation of the TIRI estimated temperatures is mostly greater than the bias determined from the blackbody experiment (Table 3); nevertheless, the differences seen for the grass canopies and soil are small for all sensors (<2.5 °C and <2.0 °C respectively).
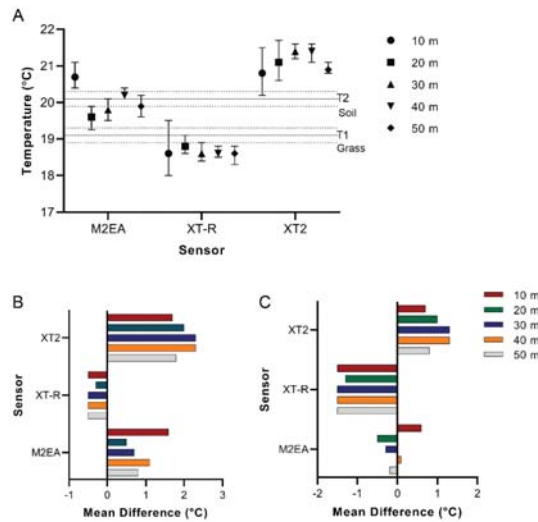
Figure 15. Comparison of TIRI from the three cameras with the grass region of interest surrounding temperature probes T1 (canopy) and T2 (soil) for Vegetation site 1. (**A**) Mean with error bars representing the minimum and maximum TIRI estimated temperature value. Solid lines indicate the temperature recorded in situ by the HOBO sensors. The dotted lines represent the uncertainty of the HOBO in situ temperature measurement (**B**) Mean difference between the soil in situ temperature measurement (T2) and the TIRI estimated temperature. (**C**) Mean difference between the grass canopy in situ temperature measurement (T1) and the TIRI estimated temperature.
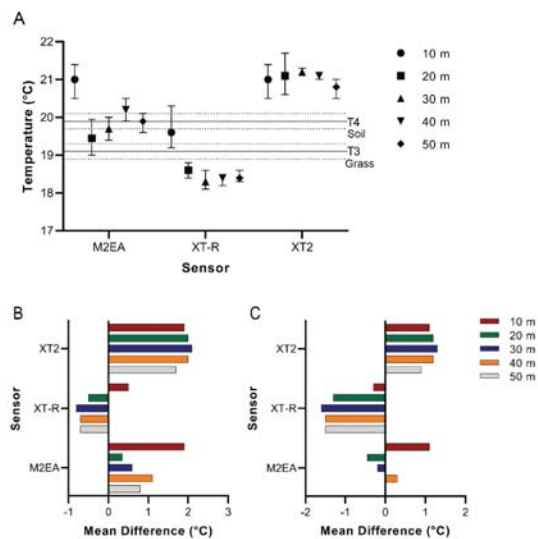
Figure 16. Comparison of TIRI from the three cameras with the grass region of interest surrounding temperature probes T3 (canopy) and T4 (soil) for Vegetation site 2. (**A**) Mean with error bars representing the minimum and maximum TIRI estimated temperature value. Solid lines indicate the temperature recorded in situ by the HOBO sensors. The dotted lines represent the uncertainty of the HOBO in situ temperature measurement. (**B**) Mean difference between the soil in situ temperature measurement (T4) and the TIRI estimated temperature. (**C**) Mean difference between the grass canopy in situ temperature measurement (T3) and the TIRI estimated temperature.

4. Discussion

The overall results obtained from the blackbody work, show that each camera has performed within the uncertainty envelopes of their calibration, and thus, are validated for use within the constraints of that calibration. Further, this work has shown that there is essentially, no appreciable difference in validation results or camera performance as a function of distance—under the constraints of 2 m and 4 m distances—which may be extended with caution to suggest that these same results hold when the distance is doubled if the source is relatively close to the camera. All three cameras showed high linearity in their response and low errors for all targets (blackbody, concrete, soil) with differences <2 °C between them (except for the blackbody measurements with the XT-R camera at 5 °C and 40 °C—which are outside of the environmental range of the field study).

It is evident from the results of the concrete targets and both vegetation sites, that temperatures retrieved with the XT-R camera are consistently lower than those of the other two cameras. While the temperature retrievals for the vegetation and soil plots show that the XT2 overestimates the grass temperature they also show that the M2EA falls between the values for the vegetation and the soil. However, all the systems generally performed within 2 °C (i.e., $\Delta T \leq 2$ °C) of the in situ measured temperatures of the targets.

In the context of how this work fits into that of previous studies, our methodology and results have taken several parameters into account that were either missing or were identified as topics of further work. For example, the process we showed herein is very different from [36], due primarily to our night time operations at the field site; further, we also consider environmental factors, such as air temperature and humidity. In [36], the in-field blackbody target was imaged; however, no accounting for environmental factors such as wind, humidity or air temperature was performed but rather considered as a portion of a common residual bias offset of 2.67 °C. Furthermore, the work was performed during the daytime (between 07:10 and 14:00) when solar heating effects have a significant non-linear impact [54,66,67] even over the timespan of an RPAS flight—typically under 30 min.

Comparing our current work to that in [37], shows the similarities in thought behind the use of the indoor blackbody to characterize the sensor before flight campaigns. While [37] provides a vicarious calibration, we have focused on validation for the reasons outlined previously in this work (calibration requires a highly controlled environment and exceedingly accurate radiometric instrumentation—as was the outcome concluded in [37]). Further, in [37], there was no mention of collecting or addressing environmental data nor the use of any in-field thermal calibration targets, although they did validate their neural network-based photogrammetry process which aided in improving the accuracy of their imaging. Also, as in [36], [37] collected their field-based TIRI during the daytime and therefore, previous statements for [36] on that practice also apply to the work of [37].

In the work by [38], a constant 0 °C value for the imaged surface of melting snow targets was used; however, it was identified that the vicarious calibration method employed, performed better without the natural target of the melting snow surface. The melting snow target temperature was found to be variable and correlated to underlying forest vegetation conditions. Moreover, retrieved TIRI data showed spatial pixel size temperature dependencies, angular dependencies as well as mixed pixel issues with more dense forest canopy. In our work, we have developed a method that is not being influenced by such sources.

The calibration work of [39] produced TIRI of an ice bath for evaluation. While [39] provides support for the idea of requiring accurate RPAS TIRI, it has not provided those results in a field environment under RPAS flight conditions—which is stated within [39] as a suggestion for further work. The work of this study has developed a field-level validation method (not the same as calibration) in order to determine if the calibration (be it manufacturer or based on [39], or similar methods) remains applicable near the time of the RPAS work.

In our study, all cameras have performed as per specifications, and therefore, it may be difficult to decide which of these cameras to use. As all three produce essentially identical ground pixel sizes (the M2EA produces slightly larger pixels, due to the slightly larger FOV, ~0–2 mm difference within an image square pixel of ~10 cm side length, and have nearly the same noise floors (<50 mK), the decision may be best decided by the non-thermal portions of the system. Both the M300 airframe and XT2 camera have ratings of IP45 and IP 44, respectively, and are thus, essentially waterproof—neither of the other two cameras, nor airframes, have an IP rating. The XT-R camera requires a stationary drone to take the images (otherwise the results have considerable blur), while the XT2 and M2EA can acquire with slow but continuous flight speeds. The M2EA is, by far, the easiest to transport, followed by the M300 and finally the M600P, which is difficult due to the 67 cm length of side and cube shaped case. While the M300 and M600P require a separate ground station with tripod to function in RTK mode, the M2EA is fully self-contained and only requires a Wi-Fi connection and incoming corrections for RTK mode. The inclusion of a 4K visible RGB camera coincident with the thermal cameras with the M2EA and XT2 is a large advantage in many applications during daytime hours. However, care must be taken with all three cameras not to burn the thermal sensor from incoming solar radiation. For applications that require stealth, such as wildlife studies [9,11], RPAS size and rotor noise (more significant with the M600P) is a primary concern. Further, payload and ancillary sensors (hyperspectral, LiDAR, etc) are often a complementary desire with TIRI, therefore RPAS payload capability will play a dominant part of the selection criteria. Finally, one other non-technical consideration that has a tremendous impact on operations is that the XT-R camera has an Export Control Classification Number (6A003.b.4.b., [46]) and is therefore, very difficult to travel across international borders.

While it is also important to note that the XT-R and XT2 are no longer manufactured, they, continue to be very much in use [9,11,13,17,18,21–24,26–28,68,69] and are sure to be primary instruments in new works to come. The M2EA is relatively new and highly capable, being able to compete (results-wise) with the XT2 system.

Finally, although this work has been applied to TIRI in the LWIR region, it has been derived in accordance with basic properties and principles of the TIR region of the electromagnetic spectrum. As a result, we suggest that it is also applicable to the Mid-Wave InfraRed (3–7.5 µm) region and, therefore, it can be used with all TIRI data from within the TIR.

5. Conclusions

In this work, we have developed a new TIRI validation methodology that has been applied to LWIR imagery (7.5 µm to 14 µm) taken of a blackbody source (indoors) and to real-world field conditions (outdoor) using instrumented concrete and vegetation sites as validation targets. We have tested our method on three popular LWIR TIRI cameras (the Zenmuse XT-R, Zenmuse XT2 and the M2EA) that are operated by three different popular DJI RPAS platforms—the Matrice 600 Pro, the M300 RTK and the Mavic 2 Enterprise Advanced. Results of the blackbody work over the temperatures expected in the field site show a highly linearized response for each sensor as well as a small temperature bias. All TIRI camera measurements were validated (by surface thermal sensors) to be within the stated tolerances of uncertainty for the cameras. Environmental parameters (air temperature, humidity, pressure and wind) were measured for several hours before TIRI data was collected. Wind cooling was not a factor up to 2 h prior to data collection. In-field TIRI results from 10 m to 50 m heights, images show absolute temperature retrievals of the target materials (concrete and two vegetation sites) that were within the specifications of the cameras. The methodology has been developed under the condition that it should be applicable to RPAS operators who need to verify their equipment either pre or post operations.

Appendix A

Table A1. Summary data from the blackbody measurements.

Camera	Distance (m)	Mean Blackbody Temp. (+/−0.4 °C)	Mean Measured Temp. (°C)	Stdev. (°C)
M2EA	2	5	1.87	0.13
M2EA	2	10	7.77	0.12
M2EA	2	15	13.57	0.11
M2EA	2	20	19.10	0.10
M2EA	2	25	24.37	0.11
M2EA	2	30	30.03	0.10
M2EA	2	35	35.63	0.11
M2EA	2	40	41.20	0.10
M2EA	4	5	3.70	0.16
M2EA	4	10	8.90	0.15
M2EA	4	15	13.77	0.10
M2EA	4	20	18.35	0.10
M2EA	4	25	24.40	0.11
M2EA	4	30	29.80	0.12
M2EA	4	35	34.77	0.13
M2EA	4	40	39.97	0.13
XT-R	2	5	3.23	0.11
XT-R	2	10	9.83	0.09
XT-R	2	15	13.27	0.09
XT-R	2	20	18.93	0.07
XT-R	2	25	23.33	0.08
XT-R	2	30	30.53	0.07
XT-R	2	35	33.20	0.09
XT-R	2	40	39.60	0.08
XT-R	4	5	3.13	0.10
XT-R	4	10	8.97	0.10
XT-R	4	15	15.43	0.07
XT-R	4	20	18.17	0.08
XT-R	4	25	23.80	0.06
XT-R	4	30	30.00	0.06
XT-R	4	35	34.13	0.07
XT-R	4	40	37.13	0.08
XT2	2	5	4.23	0.11
XT2	2	10	8.87	0.10
XT2	2	15	14.80	0.09

Table A1. *Cont.*

Camera	Distance (m)	Mean Blackbody Temp. (+/−0.4 °C)	Mean Measured Temp. (°C)	Stdev. (°C)
XT2	2	20	20.57	0.10
XT2	2	25	25.43	0.08
XT2	2	30	29.17	0.08
XT2	2	35	35.43	0.08
XT2	2	40	39.80	0.08
XT2	4	5	4.23	0.12
XT2	4	10	9.03	0.10
XT2	4	15	14.90	0.10
XT2	4	20	19.90	0.08
XT2	4	25	25.07	0.09
XT2	4	30	30.43	0.09
XT2	4	35	34.57	0.08
XT2	4	40	40.07	0.10

References

1. Stanković, M.; Mirza, M.M.; Karabiyik, U. UAV Forensics: DJI Mini 2 Case Study. *Drones* **2021**, *5*, 49. [CrossRef]
2. Burgués, J.; Marco, S. Environmental chemical sensing using small drones: A review. *Sci. Total Environ.* **2020**, *748*, 141172. [CrossRef]
3. Lakshman, S.A.; Ebenezer, D. Ebenezer, Integration of internet of things and drones and its future applications. *Mater. Today Proc.* **2021**, *47*, 944–949. [CrossRef]
4. Shahmoradi, J.; Talebi, E.; Roghanchi, P.; Hassanalian, M. A Comprehensive Review of Applications of Drone Technology in the Mining Industry. *Drones* **2020**, *4*, 34. [CrossRef]
5. Witczuk, J.; Pagacz, S.; Zmarz, A.; Cypel, M. Exploring the feasibility of unmanned aerial vehicles and thermal imaging for ungulate surveys in forests—Preliminary results. *Int. J. Remote Sens.* **2018**, *39*, 5504–5521. [CrossRef]
6. Ellsäßer, F.; Röll, A.; Ahongshangbam, J.; Waite, P.-A.; Schuldt, B.; Hölscher, D. Predicting Tree Sap Flux and Stomatal Conductance from Drone-Recorded Surface Temperatures in a Mixed Agroforestry System—A Machine Learning Approach. *Remote Sens.* **2020**, *12*, 4070. [CrossRef]
7. Alekseychik, P.; Katul, G.; Korpela, I.; Launiainen, S. Eddies in motion: Visualizing boundary-layer turbulence above an open boreal peatland using UAS thermal videos. *Atmos. Meas. Tech.* **2021**, *14*, 3501–3521. [CrossRef]
8. Hyun, C.-U.; Park, M.; Lee, W.Y. Remotely Piloted Aircraft System (RPAS)-Based Wildlife Detection: A Review and Case Studies in Maritime Antarctica. *Animals* **2020**, *10*, 2387. [CrossRef]
9. Ireland, A.W.; Palandro, D.A.; Garas, V.Y.; Woods, R.W.; Davi, R.A.; Butler, J.D.; Gibbens, D.M.; Gibbens, J.S., Jr. Testing unmanned aerial systems for monitoring wildlife at night. *Wildl. Soc. Bull.* **2019**, *43*, 182–190. [CrossRef]
10. Beaver, J.T.; Baldwin, R.W.; Messinger, M.; Newbolt, C.H.; Ditchkoff, S.S.; Silman, M.R. Evaluating the Use of Drones Equipped with Thermal Sensors as an Effective Method for Estimating Wildlife. *Wildl. Soc. Bull.* **2020**, *44*, 434–443. [CrossRef]
11. Scholten, C.N.; Kamphuis, A.J.; Vredevoogd, K.J.; Lee-Strydhorst, K.G.; Atma, J.L.; Shea, C.B.; Lamberg, O.N.; Proppe, D.S. Real-time thermal imagery from an unmanned aerial vehicle can locate ground nests of a grassland songbird at rates similar to traditional methods. *Biol. Conserv.* **2019**, *233*, 241–246. [CrossRef]
12. Melis, M.T.; Da Pelo, S.; Erbì, I.; Loche, M.; Deiana, G.; Demurtas, V.; Meloni, M.A.; Dessì, F.; Funedda, A.; Scaioni, M.; et al. Thermal Remote Sensing from UAVs: A Review on Methods in Coastal Cliffs Prone to Landslides. *Remote Sens.* **2020**, *12*, 1971. [CrossRef]
13. Zhang, R.; Li, H.; Duan, K.; You, S.; Liu, K.; Wang, F.; Hu, Y. Automatic Detection of Earthquake-Damaged Buildings by Integrating UAV Oblique Photography and Infrared Thermal Imaging. *Remote Sens.* **2020**, *12*, 2621. [CrossRef]
14. Marotta, E.; Peluso, R.; Avino, R.; Belviso, P.; Caliro, S.; Carandente, A.; Chiodini, G.; Macedonio, G.; Avvisati, G.; Marfè, B. Thermal Energy Release Measurement with Thermal Camera: The Case of La Solfatara Volcano (Italy). *Remote Sens.* **2019**, *11*, 167. [CrossRef]
15. Gaitani, N.; Burud, I.; Thiis, T.; Santamouris, M. High-resolution spectral mapping of urban thermal properties with Unmanned Aerial Vehicles. *Build. Environ.* **2017**, *121*, 215–224. [CrossRef]
16. Naughton, J.; McDonald, W. Evaluating the Variability of Urban Land Surface Temperatures Using Drone Observations. *Remote Sens.* **2019**, *11*, 1722. [CrossRef]
17. Bayomi, N.; Nagpal, S.; Rakha, T.; Fernandez, J.E. Building envelope modeling calibration using aerial thermography. *Energy Build.* **2021**, *233*, 110648. [CrossRef]
18. Park, S.-I.; Ryu, T.-H.; Choi, I.-C.; Um, J.-S. Evaluating the Operational Potential of LRV Signatures Derived from UAV Imagery in Performance Evaluation of Cool Roofs. *Energies* **2019**, *12*, 2787. [CrossRef]

19. Hill, A.C.; Laugier, E.J.; Casana, J. Archaeological Remote Sensing Using Multi-Temporal, Drone-Acquired Thermal and Near Infrared (NIR) Imagery: A Case Study at the Enfield Shaker Village, New Hampshire. *Remote Sens.* **2020**, *12*, 690. [CrossRef]
20. DiNapoli, R.J.; Lipo, C.P.; de Smet, T.S.; Hunt, T.L. Thermal Imaging Shows Submarine Groundwater Discharge Plumes Associated with Ancient Settlements on Rapa Nui (Easter Island, Chile). *Remote Sens.* **2021**, *13*, 2531. [CrossRef]
21. Adamopoulos, E.; Rinaudo, F. UAS-Based Archaeological Remote Sensing: Review, Meta-Analysis and State-of-the-Art. *Drones* **2020**, *4*, 46. [CrossRef]
22. Turner, R.M.; MacLaughlin, M.M.; Iverson, S.R. Identifying and mapping potentially adverse discontinuitie in underground excavations using thermal and multispectral UAV imagery. *Eng. Geol.* **2020**, *266*, 105470. [CrossRef]
23. He, X.; Yang, X.; Luo, Z.; Guan, T. Application of unmanned aerial vehicle (UAV) thermal infrared remote sensing to identify coal fires in the Huojitu coal mine in Shenmu city, China. *Sci. Rep.* **2020**, *10*, 13895. [CrossRef] [PubMed]
24. Zhao, Y.; Sun, B.; Liu, S.; Zhang, C.; He, X.; Xu, D.; Tang, W. Identification of mining induced ground fissures using UAV and infrared thermal imager: Temperature variation and fissure evolution. *ISPRS J. Photogramm. Remote Sens.* **2021**, *180*, 45–64. [CrossRef]
25. Zheng, H.; Zhong, X.; Yan, J.; Zhao, L.; Wang, X. A Thermal Performance Detection Method for Building Envelope Based on 3D Model Generated by UAV Thermal Imagery. *Energies* **2020**, *13*, 6677. [CrossRef]
26. Rakha, T.; Gorodetsky, A. Review of Unmanned Aerial System (UAS) applications in the built environment: Towards automated building inspection procedures using drones. *Autom. Constr.* **2018**, *93*, 252–264. [CrossRef]
27. Leggiero, M.; Andrew, B.; Elliott, R.; Indergaard, J.; Sharma, J.B.; Vogel, T. Radiative heat loss estimation of building envelopes based on 3D thermographic models utilizing small unmanned aerial systems (sUAS). *Energy Build.* **2021**, *244*, 110957. [CrossRef]
28. Deane, S.; Avdelidis, N.P.; Ibarra-Castanedo, C.; Zhang, H.; Nezhad, H.Y.; Williamson, A.A.; Mackley, T.; Maldague, X.; Tsourdos, A.; Nooralishahi, P. Comparison of Cooled and Uncooled IR Sensors by Means of Signal-to-Noise Ratio for NDT Diagnostics of Aerospace Grade Composites. *Sensors* **2020**, *20*, 3381. [CrossRef]
29. Crastes, A., Sr.; Ruiter, M.; Gierkink, S., Sr.; Brunelle, J., Sr. Recent uncooled IR development based on state of the art digital ROIC. Infrared Sensors, Devices, and Applications XI. *Int. Soc. Opt. Photonics* **2021**, *8*, 118310H. [CrossRef]
30. Tankut, F.; Cologlu, M.H.; Askar, H.; Ozturk, H.; Dumanli, H.K.; Oruc, F.; Tilkioglu, B.; Ugur, B.; Akar, O.S.; Tepegoz, M.; et al. An 80 × 80 microbolometer type thermal imaging sensor using the LWIR-band CMOS infrared (CIR) technology. Infrared Technology and Applications XLIII. *Int. Soc. Opt. Photonics* **2017**, *10177*, 101771X. [CrossRef]
31. Laurent, L.; Yon, J.-J.; Moulet, J.-S.; Roukes, M.; Duraffourg, L. 12-μm-Pitch Electromechanical Resonator for Thermal Sensing. *Phys. Rev. Appl.* **2018**, *9*, 024016. [CrossRef]
32. Kennedy, H.V. Modeling noise in thermal imaging systems. Infrared Imaging Systems: Design, Analysis, Modeling, and Testing IV. *Int. Soc. Opt. Photonics* **1993**, *1969*, 66–77. [CrossRef]
33. Sharma, P.; Dell, J.; Parish, G.; Keating, A. Engineering 1/f noise in porous silicon thin films for thermal sensing applications. *Microporous Mesoporous Mater.* **2021**, *324*, 111302. [CrossRef]
34. Yu, L.; Guo, Y.; Zhu, H.; Luo, M.; Han, P.; Ji, X. Low-Cost Microbolometer Type Infrared Detectors. *Micromachines* **2020**, *11*, 800. [CrossRef]
35. Holst, G.C. *Common Sense Approach to Thermal Imaging*; SPIE Optical Engineering Press: Washington, DC, USA, 2000.
36. Torres-Rua, A. Vicarious calibration of suas microbolometer temperature imagery for estimation of radiometric land surface temperature. *Sensors* **2017**, *17*, 1499. [CrossRef] [PubMed]
37. Ribeiro-Gomes, K.; Hernández-López, D.; Ortega, J.F.; Ballesteros, R.; Poblete, T.; Moreno, M.A. Uncooled Thermal Camera Calibration and Optimization of the Photogrammetry Process for UAV Applications in Agriculture. *Sensors* **2017**, *17*, 2173. [CrossRef]
38. Pestana, S.; Chickadel, C.C.; Harpold, A.; Kostadinov, T.S.; Pai, H.; Tyler, S.; Webster, C.; Lundquist, J.D. Bias correction of airborne thermal infrared observations over forests using melting snow. *Water Resour. Res.* **2019**, *55*, 11331–11343. [CrossRef]
39. Aragon, B.; Johansen, K.; Parkes, S.; Malbeteau, Y.; Al-Mashharawi, S.; Al-Amoudi, T.; Andrade, C.F.; Turner, D.; Lucieer, A.; McCabe, M.F. A Calibration Procedure for Field and UAV-Based Uncooled Thermal Infrared Instruments. *Sensors* **2020**, *20*, 3316. [CrossRef] [PubMed]
40. Drone Industry Insights. *Top 10 Drone Manufacturers' Market Shares in the US*; Drone Industry Insights UG: Hamburg, Germany, 2019.
41. DJI Science and Technology Co., Ltd. Mavic 2 Enterprise Advanced User Manual v 1.0. 03, Shenzhen, China. 2021. Available online: https://dl.djicdn.com/downloads/Mavic_2_Enterprise_Advanced/20210331/Mavic_2_Enterprise_Advanced_User_Manual_EN.pdf (accessed on 13 October 2021).
42. DJI Science and Technology Co., Ltd. Matrice 600 Pro User Manual V1.0. Shenzhen, China. 2018. Available online: https://dl.djicdn.com/downloads/m600%20pro/1208EN/Matrice_600_Pro_User_Manual_v1.0_EN_1208.pdf (accessed on 13 October 2021).
43. DJI Science and Technology Co., Ltd. Matrice 300 RTK User Manual V1.8. Shenzhen, China. 2021. Available online: https://dl.djicdn.com/downloads/matrice-300/20210419UM/M300_RTK_User_Manual_EN_v1.8_20210419.pdf (accessed on 13 October 2021).
44. Kalacska, M.; Lucanus, O.; Arroyo-Mora, J.P.; Laliberté, É.; Elmer, K.; Leblanc, G.; Groves, A. Accuracy of 3D Landscape Reconstruction without Ground Control Points Using Different UAS Platforms. *Drones* **2020**, *4*, 13. [CrossRef]

45. DJI Science and Technology Co., Ltd. Zenmuse XT2 Thermal by FLIR User Manual v1.0, 04, Shenzhen, China. 2018. Available online: https://dl.djicdn.com/downloads/Zenmuse%20XT%202/Zenmuse_XT_2_User_Manual_v1.0_en_.pdf (accessed on 13 October 2021).
46. DJI Science and Technology Co., Ltd. Zenmuse XT Powered by FLIR User Manual v1.2, 05, Shenzhen, China. 2016. Available online: https://dl.djicdn.com/downloads/zenmuse_xt/en/Zenmuse_XT_User_Manual_V1.2_en_0708.pdf (accessed on 13 October 2021).
47. Tiesinga, E.; Mohr, P.J.; Newell, D.B.; Taylor, B.N. CODATA recommended values of the fundamental physical constants: 2018. *Rev. Mod. Phys.* **2021**, *93*, 025010. [CrossRef]
48. Minkina, W.; Dudzik, S. *Infrared Thermography: Erros and Uncertainties*; John Wiley & Sons: Hoboken, NJ, USA, 2009.
49. Garcia-Santos, V.; Valor, E.; Caselles, V.; Mira, M.; Galve, J.M.; Coll, C. Evaluation of Different Methods to Retrieve the Hemispherical Downwelling Irradiance in the Thermal Infrared Region for Field Measurements. *IEEE Trans. Geosci. Rem. Sens.* **2013**, *51*, 4. [CrossRef]
50. Fluke Corporation. Fluke Calibration 4180, 4181 Precision Infrared Calibrator. Operators Manual. November 2020. Available online: https://us.flukecal.com/products/process-calibration-tools/temperature-calibrators/infrared-calibrators/4180-4181-precision-?quicktabs_product_details=4 (accessed on 13 October 2021).
51. da Cunha, A.R. Evaluation of measurement errors of temperature and relative humidity from HOBO data logger under different conditions of exposure to solar radiation. *Environ. Monit. Assess.* **2015**, *187*, 236. [CrossRef]
52. Abdullahi, M.G.; Husini, E.M.; Ibrahim, A.O.; Collins, K.; Arabi, O.F.; Bashir, F.M. Architectural Experimental Field Measurement Process and Procedure using Case Study. *Solid State Technol.* **2021**, *64*, 2.
53. Shawesh, R.; Mohamed, M. Post-occupancy evaluation of outdoor thermal comfort in hot arid zone. *Int. J. Low Carb. Technol.* **2020**, *16*, 1. [CrossRef]
54. Lozano-Parra, J.; Pulido, M.; Lozano-Fondón, C.; Schnabel, S. How do Soil Moisture and Vegetation Covers Influence Soil Temperature in Drylands of Mediterranean Regions? *Water* **2018**, *10*, 1747. [CrossRef]
55. Cengal, Y.A. *Heat Transfer: A Practical Approach*, 2nd ed.; McGraw–Hill: New York, NY, USA, 2002.
56. Balaras, C.A.; Argiriou, A.A. Infrared thermography for building diagnostics. *Energy Build.* **2002**, *34*, 2. [CrossRef]
57. Lehmann, B.; Wakili, K.G.; Frank, T.; Collado, B.V.; Tanner, C. Effects of individual climatic parameters on the infrared thermography of buildings. *Appl. Energy* **2013**, *110*, 29–43. [CrossRef]
58. Jonsson, B.; Zinko, H. *Quantitative Heat Loss Analysis of Heat- and Coolant Distribution Pipes by Means of Thermography*; NOVEM: Vorbach, Germany, 1993; ISBN 90-72130-95-2.
59. FluxTeq LLC. PHFS-01e Heat Flux Sensor Datasheet. Available online: https://d7c61e62-ec2b-486f-b3c3-d005ddd2f7d8.filesusr.com/ugd/b0a63e_e2f8d1846d244ead8946fe3d870ce7e2.pdf (accessed on 13 October 2021).
60. Davies, J.A.; Idso, S.B. *Estimating the Surface Radiation Balance and Its Components. Modification of the Aerial Environment of Plants. ASAE Monograph*; American Society of Agricultural: St. Joseph, MI, USA, 1979; pp. 183–210.
61. Tu, L.; Qin, Z.; Yang, L.; Wang, F.; Geng, J.; Zhao, S. Identifying the Lambertian Property of Ground Surfaces in the Thermal Infrared Region via Field Experiments. *Remote Sens.* **2017**, *9*, 481. [CrossRef]
62. Humes, K.S.; Kustas, W.P.; Moran, M.S.; Nichols, W.D.; Weltz, M.A. Variability of emissivity and surface temperature over a sparsely vegetated surface. *Water Resour. Res.* **1994**, *30*, 1299–1310. [CrossRef]
63. Kotthaus, S.; Smith, T.E.L.; Wooster, M.J.; Grimmond, C.S.B. Derivation of an urban materials spectral library through emittance and reflectance spectroscopy. *ISPRS J. Photogramm. Remote Sens.* **2014**, *94*, 194–212. [CrossRef]
64. Sagan, V.; Maimaitijiang, M.; Sidike, P.; Eblimit, K.; Peterson, K.T.; Hartling, S.; Esposito, F.; Khanal, K.; Newcomb, M.; Pauli, D.; et al. UAV-Based High Resolution Thermal Imaging for Vegetation Monitoring, and Plant Phenotyping Using ICI 8640 P, FLIR Vue Pro R 640, and thermoMap Cameras. *Remote Sens.* **2019**, *11*, 330. [CrossRef]
65. Hackl, H.; Baresel, J.P.; Mistele, B.; Hu, Y.; Schmidhalter, U. A Comparison of Plant Temperatures as Measured by Thermal Imaging and Infrared Thermometry. *J. Agron. Crop Sci.* **2012**, *198*, 415–429. [CrossRef]
66. Brevik, E.C.; Fenton, T.E.; Horton, R. Effect of Daily Soil Temperature Fluctuations on Soil Electrical Conductivity as Measured with the Geonics® EM-38. *Precis. Agric.* **2004**, *5*, 145–152. [CrossRef]
67. Singh, R.K.; Sharma, R.V. Numerical analysis for ground temperature variation. *Geotherm. Energy* **2017**, *5*, 22. [CrossRef]
68. Patrucco, G.; Cortese, G.; Tonolo, F.G.; Spanò, A. Thermal and optical data fusion supporting built heritage analyses. *Int. Arch. Photogramm. Remote Sens. Spat. Inf. Sci.* **2020**, *43*, 619–626. [CrossRef]
69. Kuczyńska, A.; Jarnuszewski, G.; Nowakowska, M.; Wexler, S.K.; Wiśniowski, Z.; Burczyk, P.; Durkowski, T.; Woźnicka, M. Identifying causes of poor water quality in a Polish agricultural catchment for designing effective and targeted mitigation measures. *Sci. Total Environ.* **2021**, *765*, 144125. [CrossRef]

![drones logo]

Advanced Leak Detection and Quantification of Methane Emissions Using sUAS

Derek Hollenbeck, Demitrius Zulevic and Yangquan Chen *

Mechatronics Embedded Systems and Automation (MESA) Lab, Department of Mechanical Engineering, University of California at Merced, Merced, CA 95343, USA; dhollenbeck@ucmerced.edu (D.H.); dzulevic@ucmerced.edu (D.Z.)
* Correspondence: ychen53@ucmerced.edu

Abstract: Detecting and quantifying methane emissions is gaining an increasingly vital role in mitigating emissions for the oil and gas industry through early detection and repair and will aide our understanding of how emissions in natural ecosystems are playing a role in the global carbon cycle and its impact on the climate. Traditional methods of measuring and quantifying emissions utilize chamber methods, bagging individual equipment, or require the release of a tracer gas. Advanced leak detection techniques have been developed over the past few years, utilizing technologies, such as optical gas imaging, mobile surveyors equipped with sensitive cavity ring down spectroscopy (CRDS), and manned aircraft and satellite approaches. More recently, sUAS-based approaches have been developed to provide, in some ways, cheaper alternatives that also offer sensing advantages to traditional methods, including not being constrained to roadways and being able to access class G airspace (0–400 ft) where manned aviation cannot travel. This work looks at reviewing methods of quantifying methane emissions that can be, or are, carried out using small unmanned aircraft systems (sUAS) as well as traditional methods to provide a clear comparison for future practitioners. This includes the current limitations, capabilities, assumptions, and survey details. The suggested technique for LDAQ depends on the desired accuracy and is a function of the survey time and survey distance. Based on the complexity and precision, the most promising sUAS methods are the near-field Gaussian plume inversion (NGI) and the vertical flux plane (VFP), which have comparable accuracy to those found in conventional state-of-the-art methods.

Keywords: advanced leak detection; advanced leak quantification; remote sensing; source estimation; environmental monitoring; landfill; natural gas

1. Introduction

Why is methane so important? Methane is a greenhouse gas (GHG) that has a global warming potential 86 times that of carbon dioxide in a 20 year time window and is even larger for smaller time-scales. The mitigation of methane and reducing methane emissions can help reduce global warming in the near term. The first step is improving the way we measure emissions in practice, both in accuracy and in frequency. The overall measurement of methane emissions in oil and gas for example, (top-down vs bottom-up) has been shown to have discrepancies and is often underestimated [1,2].

For example, 190 oil and gas production sites were explored in [3,4], and the measurements indicated that well completion emissions were lower than previously estimated. The data also showed how emissions from pneumatic controllers and equipment leaks were higher than the Environmental Protection Agency (EPA) national emission projections. In a report titled, "Lessons from a decade of emissions gap assessments" [5], the authors argued about where we need to be and where we think we are, including the Paris climate agreement and what steps to take in order to keep global warming below 2 °C. One way to combat this is by detecting super emitters through tiered remote sensing strategies, which is outlined in [6].

This approach aims to focus on the detecting and repairing the largest emitters first, which can contribute a significant portion of the overall emissions of oil and gas systems. Furthermore, pressure to reduce contributions of climate change from customers and investors has been seen, insisting on reducing carbon footprints, including from landfills with much needed debate on inventory methods, direct emission measurements, and accountability [7]. The importance of mitigating methane emissions on a wide array of mitigation strategies is needed to stay on track with the Paris agreement [8].

Who is currently looking at methane? From an anthropogenic point of view (e.g., oil and gas), companies, such as Picarro (Santa Clara, CA, USA), Aerodyne Research (Billerica, MA, USA), Bridger Photonics (Bozeman, MT, USA), SeekOps (Austin, TX, USA), Heath Consultants (Houston, TX, USA), Flir (Global), Scientific Aviation (Boulder, CO, USA), Avitas (Houston, TX, USA), Ventus Geospatial (Houston, TX, USA), Aerometrix (Canada), and many more have provided methane detection and quantification solutions in a variety of technologies.

For example, A quantum cascade laser spectrometer is deployed on a small unmanned aircraft system (sUAS) for measuring facility-scale emissions using a mass balance approach with kriging [9]. For biogenic sources in ecosystems, there has been work looking at permafrost bogs [10,11], lakes [12], small ponds, wetlands [13], and vernal pools [14–17] to name a few. Seasonal dynamics of methane emissions from permafrost landscapes are explored in [18], specifically a lagoon pingo, and emissions estimated using a Thin Boundary Layer approach.

Porewater samples were analyzed using a Quantum Cascade Laser Spectrometer and combined with high resolution images from sUAS as an input into a neural network for creating a prediction map to upscale methane flux [19]. The spatial distribution of methane in the Artic permafrost bluffs was explored in [20] with a backscatter tunable diode laser absorption spectrometer (bs-TDLAS), namely the Pergam Laser Methane mini.

Flux estimates can be made, typically, using methods based on static measurements, on foot, by vehicle, manned aircraft, and by satellite. Static measurements consist of: (1) Eddy Covariance (EC) towers: A footprint modeling technique that looks at the turbulent exchange with the environment and utilizes meteorological conditions with precision concentration measurements to estimate the flux, (2) Chambers (autochambers): An enclosed chamber is placed over a target piece of land and is sampled with a syringe occasionally (to be analyzed at a later time, typically with gas chromatography) or dynamically sampled within a closed loop (such as GASMET's Fourier Transform Infrared (FTIR) analyzer [21]).

Measurements made on foot consist of handheld sensors that are used with survey equipment and the surface. Surface emission monitoring (SEM) is typically a routine operation for landfills, done quarterly, to maintain compliance with local regulations to account for emissions lost from gas control systems. SEM is a point-based scanning technique that can take on the order of a week or so to complete. The concentrations are measured with devices, such as the flame ionization detector (FID) (regulated by EPA's guidance and Method 21), and are integrated along sub divided grids looking for elevated methane levels (greater than 500 ppmv) [22].

Landfill emissions are generally calculated using inventory-type estimates. Measurements by vehicle consist of methods, such as the Tracer Correlation Method (TCM) and the environmental protection agency (EPA)'s other test method 33A (OTM33A) [23]. In [24], they explored vehicle-based advanced leak detection (ALD) with a cavity ring-down spectrometer (CRDS) from Picarro and determined that five to eight drives will capture a majority of leaks (>90%) as well as indicate detection limitations (such as wind and soil conditions and variations in methane enhancements making quantifying emissions difficult).

In [25], a vehicle mounted CRDS (Picarro G2301 and G4302) used empirical formulation to turn elevated concentration levels (or leak indications), C, to emission rates , Q (based on the work of [26], $\ln C = -0.988 + 0.817 \ln Q$) and used Gaussian plume model to quantify emissions from site-level emissions in Utrecht and Hamburg, Germany. In work by [27],

6650 sites were evaluated using inventory and inverse point source Gaussian measurements, and they found that the methane inventory was underestimated by a factor of 1.5.

A series of campaigns were carried out utilizing TCM and downwind mobile measurements to explore the accuracy of different TCM approaches as well as compare CRDS with FTIR instrumentation in multiple source separation [28]. Measurements from manned aircraft have been done using FID, mounted on both fixed wing (Piper (Vero Beach, FL, USA) Seneca or Piper Navajo twin engine) and helicopter (Bell (Fort Worth, TX, USA) 206 Long Ranger) to detect liquid hydrocarbons from pipelines [29]. In [30,31], they utilize the next generation Airborne Visible/Infrared Imaging Spectrometer (AVIRIS-NG) to retrieve methane, carbon dioxide, and water vapor.

In [32], AVIRIS-NG was used to generate the VIsta-CA geospatial dataset to provide a comparison to the attribution of sources with Calfornia Air Resources Board (CARB) Pollution Mapping Tool (CARB PMT) and the U.S. Environmental Protection Agency (EPA) Facility Level Information on Greenhouse gases Tool (EPA FLIGHT). In [33], they investigate the uncertainty for estimating urban fluxes by an aircraft-based mass balance approach. They assess the sensitivity of the estimated city-wide CO_2 and CH_4 fluxes for several flight experiments, including the regional background concentration, depth of the convective boundary layer, magnitude of the wind speed, and type of interpolation technique.

In [34], they utilized a Sky Arrow Environmental Research Aircraft to measure emissions from multiple landfills and combined steady state Gaussian models to distinguish the emission coefficients for each individual site. A Bridger Photonics Gas Mapping LiDAR (GML) system was deployed on a Cessna 172 and blindly evaluated where the detection limits were as low as 1 kg/h depending on the wind conditions [35].

This method was also introduced to the Fugitive Emissions Abatement Simulation Toolkit (FEAST) [36] and shown to be comparable to OGI-based methods at equivalent survey frequencies for the detection and repair of emissions. Optical Gas Imaging (OGI) was explored in [37,38] and the effectiveness was evaluated in [38]. NASA's Alpha Jet Atmospheric eXperiment (AJAX) and the AutoMObile greenhouse Gas (AMOG) surveyor were used to fuse airborne and ground-based data together (as part of the GOSAT-COMEX Experiment) using an anomaly approach instead of the typical mass balance approach [39]. Measurements by satellite have been explored in [40], where a ResNet-50 was trained from ESA's Sentinel-2 data and labeled with a U-Net to detect smoke plumes.

Other works in the literature where emissions are detected, quantified, mapped, or localized include: A mid-wave infrared (MWIR) camera was used to compare eight supervised multivariate methods for detecting oil spills along the coastline in [41]. Using an array of stationary laser fetches, a controlled release emission is estimated using a Bayesian Markov chain Monte Carlo (MCMC) approach in [42]. There have been several works devoted to gas distribution mapping (GDM) using the Kernel DM/V methodology [43], including simultaneous localization and mapping (SLAM) [44].

GDM and gas source localization (GSL) with micro-drones have been explored in [45]. GDM has also been used in olfactory simulations in [46]. In [47], different GSL strategies (spiral, surge-cast, spiral-surge, and particle filter) were evaluated using the GADEN gas dispersion simulator. A mobile ground robot system named ARMEx was used to perform gas distribution mapping with a Heath Consultants remote methane leak detector (RMLD) [48].

In recent years, sUAS-based sensing approaches have become increasingly popular amongst practitioners for a variety of reasons, such as the ability to not be restricted to roadways or land locked areas, the ability to operate within the class G airspace at altitudes that traditional manned aircraft cannot operate at (improving resolution), the low cost, and the ability for high frequency deployment for capturing temporal changes.

Here, we provide an overview of some of the recent literature works utilizing sUAS, such as: a fixed-wing SIERRA sUAS with off axis integrated cavity output spectrometer (OA-ICOS) instrument was deployed in Svalbard, Norway prior to the NASA Characterization of Arctic Sea Ice Experiment (CASIE) [49]; single and multi-sUAS systems for source seeking based on the Luenberger observer were explored in [50]; an open path

GHG analyzer based on vertical cavity surface emitting laser (VCSEL) was developed and tested in [51] with an aim to provide improved measurements compared to satellites; and volcanic emissions were captured using thermal cameras [52].

In [53], detection and spatial temporal analysis of a thermokarst lake was done with RGB images taken from a plane and sUAS. They looked at the bubble characteristics of the images to determine methane ebulliton. The use of long wave infrared (LWIR), short wave infrared (SWIR), hyperspectral, and visible cameras were used to detect liquid hydrocarbons with machine learning in [54]. Detection of methane gas from a custom open path absorption spectroscopy , mounted on fixed-wing sUAS, was explored in [55]. Emission factors from a combustion source using the EPA-based sensor, Kalibri, were calculated using a sUAS in [56]. Profiling GHG using sUAS-based AirCore system was analyzed with CRDS in [57].

Terra Sana Consultants developed a sUAS system with a path-integrated laser absorption (10 Hz at 30 m with 1 ppm-m) used in the detection of landfill gas. In a field trial, they compared the sUAS results to ground-based walk-over survey, reporting good correlation between the two [58]. A bs-TDLAS equipped drone with laser rangefinder was used to reconstruct 2D plumes under realistic conditions [59]. SEM, drone emission monitoring (DEM), and downwind plume emission monitoring (DWPEM) with CRDS are used with a genetic algorithm (GA) to estimate methane emissions from a landfill [60].

The AlphaSense electro-chemical sensor suite was used on a DJI 100 series sUAS that conducted ziz-zag and spiral localization flights of a stationary source [61]. In [62], red green blue (RGB), near infrared (NIR), and thermal infrared (TIR) cameras were used to map the topography and create digital elevation maps for identifying problematic areas where localized CH4 emissions were present using a static prototype semiconductor sensor. In [63], a sUAS equipped with a Pergam (Renton, WA, USA) backscatter-based tunable diode laser absorption spectrometer (bs-TDLAS) and OGI camera were used to detect and quantify pipeline leaks. The sUAS traveled 4 m from the pipeline during the surveys and had a minimum detection limit of 0.06 g/s.

In [64], atmospheric particulate matter and carbon dioxide were measured using sUAS sampling and a bag collection system. The bags were collected and analyzed in a lab. characterizing termite mounds using ground and sUAS-based laser scanning [65]. In a recent paper, ref. [66] utilized a NDIR instrument to measure CO_2 flux (characterized, corrected, and validated in laboratory experiment at the Integrated Carbon Observation Station (ICOS) in Steinkimmen, Germany) at an ExxonMobil (Irving, TX, USA) natural gas processing facility in Germany. They used an on-board anemometer (FT-205) that was gain and bias corrected prior to the field experiments, where flux measurements were calculated using the mass balance approach.

General questions one can ask are, "What technologies and methods fall under advanced leak detection and quantification (LDAQ)?" Does this include mobile and sUAS-based approaches? These questions, in practice, are unfortunately up to the owners and operators of natural gas facilities, as they have the choice regarding what becomes adopted. However, the potential impact that LDAQ can have on improving methane mitigation is yet to be seen. Is leak grading quantification? What is accurate enough? What size leaks should we (or can we) care about? In the literature, it is often observed that leak quantification estimates and variability are reported in the place of accuracy and uncertainty. How can we determine the necessary and sufficient conditions for application of these methodologies? To the best of our knowledge, these questions remain unsolved in practice.

In the literature, there have been several reviews conducted on topics that deal with emissions, including remote sensing, source term estimation, and fugitive gas emissions. A remote sensing review paper in [67] describes many applications and topics within remote sensing, including the environmental sensing of volcanic eruptions, soil erosion, and geological related areas. A thorough review paper on source term estimation techniques is presented in [68]. In [69], a review was conducted on chemical sensing drones, which includes the sUAS platforms, sensors, and a brief overview of methodologies.

In [70], a review was conducted measuring fugitive gas emissions from landfills using various methodologies, including surface chambers (closed and open), EC towers, stationary mass balance, aerial mass balance, vertical radial plume mapping (VRPM), differential absorption LiDAR (DiAL), tracer gas dispersion (stationary and dynamic), and inverse modeling approaches (stationary, dynamic, and aerial [71]). In [72], several biogas plants in the UK were evaluated using the point source Gaussian plume model.

In this manuscript, we provide a review on the literature regarding the source rate estimation of continuous emission sources, focused around UAV-based methodology. We provide an overview of theoretical methodology as well as establish a quantitative comparison (for papers that have shown validated accuracy) between existing/current approaches and with UAV-based approaches in an attempt to shed light on the current accuracy of these methods. In Section 2, we discuss the problem overview. In Section 3, we overview some common sensors (chemical and wind). In Section 4, we overview the LDAQ methodology. In Section 5, we analyze the reported accuracy. Section 6 summarizes the methodologies, Section 7 discusses possible future directions, and in Section 8, we conclude the paper.

2. Problem Overview

The general problem in this work looks at methane emissions released into the air in gaseous form. The release mechanism or interface can vary depending on the application or system. For instance, in the oil and gas industry, leaks generally appear from tanks, valves, or hatches in the form of a point source, typically an above ground leak. Underground leaks also occur in practice, and the resulting emissions can manifest on the surface in many ways.

This may also be the case for landfills, where many small sources can be present across a very large area. If the distribution of sources is spatially uniform, we refer to this as an area source. The distribution of emissions may also vary, as in the case of natural ecosystems where the amount of methane may be produced at different rates depending on key factors of natural methane and carbon dioxide production (e.g., temperature, soil properties, water properties, etc.). Examples of different types of leaks are shown in Figure 1.
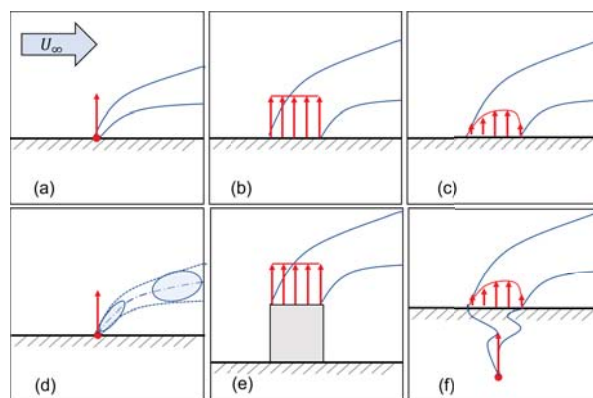
Figure 1. Example illustration for source types: (**a**) continuous point source, (**b**) uniform area source, (**c**) distributed area source, (**d**) intermittent point source, (**e**) elevated area source, and (**f**) underground point source.

Landfills, which typically have area sources, are required to do quarterly walkover surveys, based on landfill regulations [73], using SEM on gas collection facilities. Landfills also have to consider the production and control of hydrogen sulfide gas, which is reviewed in [74]. Assuming some level of uniformity, chamber measurements have been taken and

compared against atmospheric tracer methods (or TCM) [75]. The mass flux for chamber measurements can be calculated as

$$E = \frac{V}{A} p \left(\frac{\Delta C}{\Delta t} \right),$$ (1)

where V is the volume of the chamber, A is the area covered, p is the gas density given the headspace temperature, and $(\Delta C / \Delta t)$ is the change in mixing ratio, which is derived from linear regression of the temporal observations (four to five headspace measurements to achieve an acceptable correlation coefficient). However, due to the large size of these sites they are difficult to accurately measure. For example, four methods (aircraft mass balance, tracer correlation (TCM), vertical radial plume mapping (VRPM), and static chambers) and the California Landfill Methane Inventory Model (CALMIN) were compared in a landfill study in Indiana [76].

A field study comparison of different landfill methods for assessment of fugitive gas emissions was explored in [77]. This included VRPM, TDM, DiAL, MicroMeteoroligcal (Eddie Covariance method), and Flux chamber, and VRPM (close to the source, ≈10 m) and TDM (≈400 m) performed quite well against DiAL. In a paper from the UK, a review quantification of biogas plants was undertaken with inverse dispersion modeling (e.g., bLS), a tracer dispersion model, and OGI for different feedstock cases [72]. Mass balance approaches have also been applied using UAVs developed in [78].

In [79], chamber measurements were used to compare TIR images to quantify emissions in two landfills. The overall site emissions were verified using TCM (which tends to be the gold standard). The methane flux from different types of surface emissions were explored using chamber and FID measurements in [80]. A point-based scanning method, utilizing a portable gas detector (bs-TDLAS based), was correlated in lab testing using chamber methods and deployed on a landfill experimentally. This study showed a positive correlation between ambient methane concentrations and flux as well as directly proportional to flow rates [81]. Then, using this relation, a spatial map of the emissions was derived.

In a landfill study, the TCM was quantified for a 6 day campaign during different wind conditions and found that the methane emitted accounted for 31% of the generated methane [82]. Based on these findings, it is clear that fast and effective methods for estimating emissions from landfills are needed.

In natural ecosystems, which typically manifest as distributed sources (sometimes point sources distributed across a landscape) are generally much lower emissions than anthropogenic sources. It has been thought that these emissions are small; however, recent research has suggested that they are still not well understood. For example, digital elevation maps with SWIR imagery have been used to detect temporal trends in ombrotrophic peatland [83].

A Patagonia peat bog was examined with a UAV with high resolution color infrared (CIR). The images were classified using chamber measurements and different microforms in an attempt to upscale the plot-scale fluxes [84]. Thawing permafrost, peatland bogs, etc. have been typically measured using chambers [85], autochambers, and Eddy covariance (EC) towers. Commercialized chambers include those from LICOR, Picarro, and GASMET [21].

Aside from types of sources, wind is a direct input into the flux calculation and it can introduce a lot of uncertainty into the emission estimation. There are many important weather related measurements that can provide metrics for quantification methods, such as atmospheric stability. These stability classification schemes can depend on mechanical turbulence (roughness length and friction velocity), convective turbulence (mixing depth, Monin–Obukhov length, and heat flux), wind speed, and wind direction fluctuations [86,87]. These meteorological measures are summarized here: the Monin–Obukhov length is given as

$$L = -\frac{u_*^3 \overline{T}}{\kappa g \overline{w'T'}},$$ (2)

where κ is the von Karman constant, g is the acceleration of gravity, $\overline{T}$ is the average temperature, $\overline{w'T'}$ is the mean covariance between the vertical wind speed and sonic temperature [88]; and the friction velocity is given as

$$u_* = \sqrt{-\overline{u'w'}},\tag{3}$$

where $\overline{u'w'}$ is the mean covariance between the horizontal and vertical wind speed components. The effective plume height, $\overline{z}$, can be determined using the following two equations,

$$L_{x,eff} + x_0 =$$
$$\begin{cases} (\overline{z}/\kappa^2)[\ln(c\overline{z}/z_0) - \Psi(c\overline{z}/L)][1 - pa_1\overline{z}/(4L)]^{-1/2}, & L < 0, \\ (\overline{z}/\kappa^2)[(\ln(c\overline{z}/z_0) + 2b_2p\overline{z}/(3L))(1 + b_1p\overline{z}/(2L)) + \\ (b_1/4 - b_2/6)]p\overline{z}/L, & L > 0. \end{cases}\tag{4}$$

This equation is first initialized by setting the effective distance $L_{x,eff} = 0$, the effective plume height to the source height $\overline{z} = z_s$, and solving for the integration constant x_0. $L_{x,eff}$ is calculated from the longitudinal distance to the source using the angle to the center of the plume θ_p by, $L_{x,eff} = L_x \cos(\theta - \theta_p)$, where L_x is the longitudinal distance from the source. The stability parameter, Ψ, which is dependent on the effective plume height $\overline{z}$ and Monin–Obukhov length L [89], can be calculated (for a given height) as,

$$\Psi(z/L) = \begin{cases} (1 - a_2 z/L)^{1/4} - 1, & L < 0, \\ -b_2 z/L, & L > 0. \end{cases}\tag{5}$$

The coefficient c is dependent on the shape function parameter, s, described in [89] and given as

$$s = \begin{cases} \frac{1 - a_1 c\overline{z}/(2L)}{1 - a_1 c\overline{z}/L} + \frac{(1 - a_2 c\overline{z}/L)^{-1/4}}{\ln(c\overline{z}/z_0) - \Psi(c\overline{z}/L)}, & L < 0, \\ \frac{1 + b_1 c\overline{z}/L}{1 + b_1 c\overline{z}/L} + \frac{1 + b_2 c\overline{z}/L}{\ln(c\overline{z}/z_0) + \Psi(c\overline{z}/L)}, & L > 0. \end{cases}\tag{6}$$

The remaining coefficients (also from [89]) p, a_1, b_1, and b_2 can be set to 1.55, 16, 5, and 5, respectively (as used in [88]). The speed of the plume is given as

$$U(z) = \frac{u_*}{\kappa}[\ln(z/z_0) - \Psi(z/L)].\tag{7}$$

For the interested reader, the Monin–Obukhov similarity theory overview is given in [90].

3. Sensors and Equipment

There are many types of sensors that can be used on-board sUAS, granted they are light enough for a given platform's payload capacity. In this section, we overview a few key sensors used and refer interested readers to a thorough review paper for more on chemical sensing drones [69]. Sensors used in many of the works reviewed here are briefly overviewed.

There are generally two types of sensing modalities, passive and active. Passive sensing encompasses any sensor that receives information from the environment. A common example of this includes optical cameras, such as visual spectrum cameras (e.g., RGB), thermal cameras (e.g., thermal infrared (TIR) [79,91], near infrared (NIR), short-wave infrared (SWIR), mid-wave infrared (MWIR), and long-wave infrared (LWIR)).

TIR cameras tend to span a larger bandwidth of wavelengths, whereas hyperspectral cameras can control which wavelengths to focus on. For example, in [92], Telops (Quebec, Canada) used a standoff tripod mounted hyperspectral camera to estimate the flow rate by integrating the mass per unit area and multiplying by the mean velocity of the gas. They utilized a two layer model to calculate the background radiance,

$$L_{tot} = [L_{bkg}\tau_{plume} + L_{plume}(1 - \tau_{plume})]\tau_{atm} + L_{atm}(1 - \tau_{atm}). \tag{8}$$

When the hyperspectral camera was optimized for methane detection (as in [93], 7.7 μm band), two controlled release tests showed flow rates calculated (measured) were found to be 25.3 ± 2.8 g/h (23 ± 2.3 g/h) and 102.9 ± 5.8 g/h (100 ± 10 g/h). The authors claimed that the approach is 40 to 100 times more sensitive and can potentially be mounted to an aerial platform, remotely sensing from several hundred meters, deeming it suitable for both natural and anthropogenic sources. Active sensing encompasses any sensor that actively transmits information into the environment, probing a response.

An example of active sensing includes tunable diode laser absorption spectroscopy (TDLAS), which can come in several forms. The working principle relies on the gas species entering the sensor region or laser path, such that some of the power is absorbed by the gas, and a power drop is detected. One form of TDLAS is the closed path TDLAS (e.g., sensing region enclosed in controlled environment), where the emitter and detector are apart of the same device at a fixed distance apart, optimized for a desired detection species.

Other variations of the TDLAS include: the open path TDLAS (e.g., sensing region is open to the environment (see the open path laser spectrometer (OPLS) [94])), the backscatter TDLAS (bs-TDLAS) where the laser is reflected off the natural environment before being received at the detector, and long path TDLAS (e.g., used with retro-reflectors not connected to the physical instrument). Several examples of bs-TDLAS include: LiDAR based (Continuous wave laser absorption LiDAR, Pulsed Differential Absorption LiDAR (DIAL)), Pergam Laser Methane Mini [95], RMLD, Gasfinder2 [96], and Gasfinder3 [97]) [98].

Other more sensitive laser based instruments are also used in practice, such as cavity ring-down spectroscopy (CRDS) and off-axis integrated cavity output spectroscopy (ICOS). An example of these types of instruments can be seen from the Los Gatos Research Inc. (LGR) micro greenhouse gas analyzer (MGGA) (also referred to in the literature as the ultra-portable greenhouse gas analyzer (UGGA)) or the Picarro G2301 and G4302. These instruments are typically the gold standard for sensing gas, albeit they are also typically the most heavy as well. Other sensors used consist of non-dispersive infrared (NDIR), ceramic metal oxide sensors (CMOS) [99–102], photo-ionization detectors (PID, such as the Honeywell MiniRAE® 3000) and electro-chemical sensors (review of applications [103].

A recent survey paper in [104] outlined new electronic nose technologies and applications. As the need for low cost sensing solutions increases and becomes commercially available, we are faced with evaluating the accuracy and characteristics of these sensors for practical use, such as in the work by [105] where low cost commercially available sensors were evaluated for precision and accuracy in a gas mixing chamber, providing promise for applications in continuous monitoring applications. Once these sensors can be evaluated and integrated on a platform with suitable sensor characteristics, they can be applied in practice.

For example, in [102], they demonstrated a proof of concept using a chemical multi-sensor payload for gas monitoring based on the DJI S900 platform. Or in [106], a semiconductor type sensor (Testo Gas Detector, Testo SE & Co. KGaA, Titisee-Neustadt, Germany) was used on a DJI M600 to analyze the spatial distribution of methane at a landfill, as well as compared different spatial interpolation techniques. This required calibration and consideration of the vehicle's critical velocity.

For sUAS, lightweight and accurate wind sensors are needed to provide in situ measurements that can be used in the quantification methodology. Some examples of lightweight sensors can range from five hole probes (or multi-hole probes) to ultrasonic anemometers that utilize time of flight (e.g., Anemoment (Longmont, CO, USA) Trisonica used in [107] or the Gill (Lymington, Hampshire, UK) WindMaster used on the OP-TOKopter [108]) and resonance based (FT Technologies FT742 and FT205 used in [109]) to more custom micro electrical mechanical systems (MEMS)-based solutions (such as in [110]). These wind sensors can also be applied to general wind profiling and mapping applications. For example, in [111], they used in situ wind measurements on sUAS for understanding the atmospheric boundary layer by developing wind profiling measurements using wind-induced perturbations. Mapping wind distributions over complex terrain

was explored in [112], where they utilized a Gill WindMaster 3D ultrasonic anemometer mounted on a octocopter (called the WindLocater).

Wind and temperature profiling from fires were explored in [113] based on wind measurements using the Trisonica. Vertical velocity measurements of aerosol cloud interactions were compared with ground-based radar in [114]. If payload limitations prevent integration of an on-board wind sensor, wind estimation techniques can also be explored, such as in [115,116]. For a more thorough understanding of different sensors and estimation techniques, we refer the reader to [117].

The choice of a platform and ancillary equipment depends directly on the choice payload system (e.g., the collection of on-board sensors) that needs to be integrated onto the sUAS. For LDAQ, this typically includes lightweight methane and wind sensors. Due to sUAS payload capacity limitations, this often leads to integration problems as the weight of methane sensors can vary greatly depending on the desired sensitivity and response time (e.g., from a couple hundred grams to a couple kilograms). Lightweight and low cost methane sensors (such as CMOS) are slower in response and are less sensitive. For high accuracy and fast response sensors, which typically weigh more, this ultimately affects the selection process of sUAS, requiring bigger and more costly platforms to maintain safe stability and control.

For this reason, ground-based wind sensors are often used (placed adjacent to operating area) with smaller sUAS platforms gathering the in situ methane measurements. The data from these two systems are collected by a local data acquisition system for live observation and post-processing. This kind of configuration, implicitly assumes that the average wind, or mean wind field, represents the overall sensing region quite well. This is usually only the case in rural areas, where there are little to no obstructions (i.e., trees, hills, buildings, infrastructure, etc.). Most of the scenarios faced in practice, however, deal with obstructions and require on-board, or in situ, wind measurements.

This decision requires platform specific knowledge (e.g., hardware setup, autopilot, co-pilot software, etc.) as well as desired payload knowledge, which will vary depending on the desired application, sensitivity, measurement mode, and so on. For these reasons, and since this manuscript's focus is on detection and quantification methodologies, we omit these details in this manuscript, and suggest that the interested reader see [118] for a guide on sUAS platform selection.

Payload integration strategies for methane sensors include several configurations, such as the boom-mounted, bottom-mounted, or top-mounted (see Figure 2). Boom-mounted approaches typically consist of TDLAS based sensors, which are subject to disturbances in the measurement from downwash of the propellers. This is avoided by placing the sensor out front of the aircraft along a boom and sampling when the effective wind speed over the sensor is greater than 2 m/s [119].

(a) (b) (c)
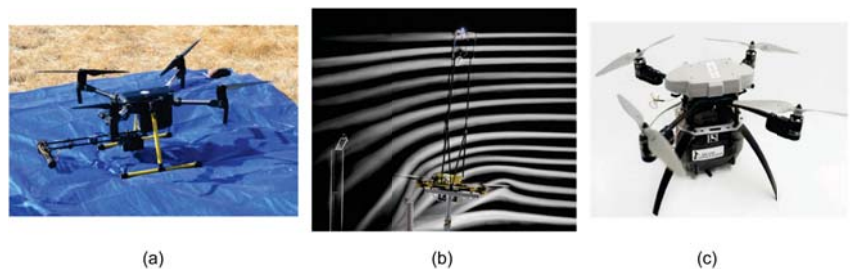
Figure 2. Payload configuration examples of (**a**) boom-mounted TDLAS on a DJI M210 used in [120], © 2020 IEEE, used with permission, (**b**) top-mounted anemometer in a wind tunnel showcasing the effect of propellers on the streamlines used in [108], and (**c**) bottom-mounted RMLD used in [121].

Bottom-mounted approaches are typically used with bs-TDLAS or OGI. The sensor is mounted on a gimbal system or sometimes hard mounted to the aircraft frame. Top-

mounted approaches on typically only suitable for bs-TDLAS or OGI based methods. Point source measurements with TDLAS will, on average, underestimate the concentration (see [69] for more details). On the contrary, top-mounted wind sensors can provide high accuracy if translational and induced wind velocities can be removed [108].

4. Advanced Leak Detection and Quantification Methods

In this section, we overview the conventional and sUAS-based advanced leak detection and quantification (LDAQ) methodology. The LDAQ methods utilize several concepts and approaches within numerics, control, and optimization as well as approaches based on different available sensing modalities (see Figure 3 for effective length-scales). In this manuscript, we divided these approaches into five general categories, namely: Simulation-based (Section 4.1), Optimization-based (Section 4.2), Mass-Balance-based (Section 4.3), Imaging-based (Section 4.4), and Correlation-based (Section 4.5).

In the Simulation-based approaches, the methods depend heavily on simulation and computational tools for solving dynamic partial differential equations, which are used to determine the source rate estimation. Sometimes other source parameters are also estimated in the process and this is typically referred to as source term estimation (STE) or the source determination problem (SDP). Two methods that show up in the literature are backwards Lagrangian stochastic (bLS) and mesoscale recursive Bayesian least squares inverse (RB-LSI).

The optimization-based methods showcased in this manuscript depend on some form of a parameterized system model, which undergoes a model fitting or recursive optimization (statistical or information based). Many of these methods include several variations of the point source Gaussian (PSG) solution of the classical Gaussian plume model. This is seen in the PSG approach based on the EPA's other test method (OTM) 33A, where the data is gathered from a single sensor downwind and undergoes model fit of the peak concentration measured.

Next is the conditionally sampled PSG (PSG-CS) approach that utilizes meteorological data in the model fitting process using conditionally sampled concentration data based on the incremental changes in wind direction. Another variation to this is the recursive Bayesian PSG (PSG-RB) that utilizes a moving sensor and meteorological data to condition the models likelihood function and prior for updating the posterior distribution that is used to quantify the source estimate. This approach also considers past knowledge about equipment characteristics if this is known.

A different approach to the Bayesian way of thinking is to solve for the parameters of the model conditioned on the observations. This approach also utilizes a particle filter and Markov Chain Monte Carlo (MCMC) to update the posterior and is referred to as the PSG sequential Bayesian MCMC (PSG-SBM). The last optimization approach mentioned in this manuscript is the Near-Field Gaussian Plume Inversion (NGI) approach.

The NGI utilizes fitting the Gaussian plume model based on sampling of a perpendicular plane downwind of the source. The vertical and horizontal dispersion relations are used to find the center of the plume within the perpendicular plane and minimize, by least square fit, the difference between the modeled concentration and the observed concentration (integrated over the lateral dispersion direction).

The next category is the Mass-Balance-based approaches, which includes methods that utilize equations based on mass conservation and continuity. The simplest approach is the vertical flux plane (VFP), which takes a control volume approach to estimating the emission rate by measuring the flux entering and leaving the control volume. Traditionally, the plume is sampled using a raster scanning approach in a perpendicular plane upwind and downwind of the source. The sparse set of observations within the plane undergo a spatial interpolation process and are combined with the wind to estimate the source rate.

A direct variation to this approach is the cylindrical flux plane (CFP), which the sensing system measures concentrations on successive loops around the source at different altitudes. The flux going into and out of this cylindrical plane is used to estimate the

flux. Using different sensing modalities (such as imaging or backscatter-based sensors), a path integrated vertical flux plane (PI-VFP) method can be formulated. Both aircraft and sUAS-based approaches to PI-VFP have been implemented, which rely on horizontal scanning of the area of interest.

For sUAS-based PI-VFP, concentric circles are flown to confirm that sources are contained inside the path before estimating the source rate. A flux plane approach has also been explored using a series of TDLAS-based laser fetches at different altitudes and utilizes the time-average of the line-integral of the instantaneous product of the wind speed and concentration. This is advantageous to other VFP approaches as it provides very good performance and does not take time to scan the plane. However, it is in ways impractical as it requires setup of the laser fetches and knowledge of the source geometry.

The next method is the Gauss divergence theorem (GDT) approach. It utilizes the CFP approach with mass flux continuity as well as the expected time rate of change of the mass within the control volume to estimate the source rate. Another VFP approach was included in this review that uses Gaussian plume model optimization with a general linear model (GLM) to help determine the contributions of multiple sources. This approach is referred to as the VFP-GLM.

The last Mass-Balance-based approach is vertical radial plume mapping (VRPM). The VRPM approach uses a ground based laser with retro-reflectors at different altitudes downwind of the source. The path integrated concentrations are measured at different radial angles and used to estimate the flux.

The next category is the Imaging-based approaches that utilize MWIR, hyperspectral cameras, and absorption spectroscopy (such as iterative maximum a posteriori differential optical absorption spectroscopy (IMAP-DOAS)).

The last category covered in this manuscript is the correlation-based approaches, which includes the traditional Eddy covariance (EC) method (in brief) and the tracer correlation method (TCM). The TCM has also been referred to in the literature as the tracer dispersion method (TDM) and atmospheric tracer method (ATM).
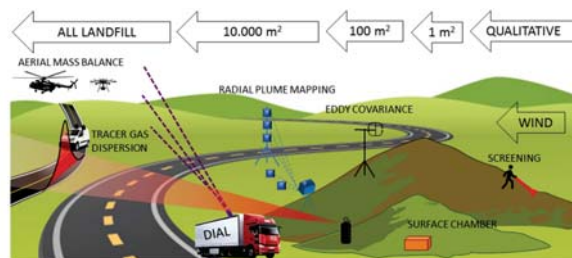
Figure 3. Conventional methods and their effective emission quantification length-scales [70], © 2019 Elsevier, used with permission.

4.1. Simulation-Based

4.1.1. Forward Modeling

Forward modeling is typically used for projecting or forecasting dispersion. Forward modeling is not directly used in emission quantification by itself, but rather paired with feedback in the optimization sense. This can include numerically solving a governing set of equations, such as the advection diffusion equation (ADE) or applying a parameterized general model (such as the Gaussian plume). It is also common in practice to utilize existing numerical models, such as the WindTrax 2.0, WRF model, FLEXible PARTicle-Weather Research and Forecasting (FLEXPART-WRF), SCIPUFF, QUIC, and others that can be Lagrangian-base, include turbulence e.g., Large eddie simulation (LES), and Reynolds averaged Navier Stokes (RANS). Interested readers can check the review paper from [122] on dispersion models.

4.1.2. Backward Lagrangian Stochastic (bLS)

The accepted backward modeling approach used in the draft OTM- 33A document [23] and in several applications (e.g., Dairy Farm [123], etc.) is the backwards Lagrangian stochastic (bLS) approach by [124]. The bLS approach aims to answer the general questions: What is the proper form of the LS trajectory model? As well as, how can source estimates be extracted from the particle's backward LS trajectory? The forward model, formulated as a generalized Langevin equation, is evolved jointly as a Markov process,

$$du_i = a_i(\mathbf{x}, \mathbf{u}, t)dt + b_{i,j}(\mathbf{x}, \mathbf{u}, t)d\xi_j, \quad dx_i = u_i dt, \tag{9}$$

where the particle position is given by $\mathbf{x} = (x_1, x_2, x_3) = (x, y, z)$, and $d\xi_j$ is a random increment governed by Gaussian process. The functions a_i and $b_{i,j}$ have to be specified such that the velocity probability density function, $g_a(\mathbf{x}, \mathbf{u}, t)$, satisfies the Fokker–Planck equation (FPE) [124],

$$\frac{\partial g_a}{\partial t} = \frac{\partial}{\partial x_i}(u_i, g_a) - \frac{\partial}{\partial u_i}[a_i(\mathbf{x}, \mathbf{u}, t)g_a] + \frac{\partial}{\partial x_i}[B_{i,j}(\mathbf{x}, \mathbf{u}, t)g_a]. \tag{10}$$

This method provides a source estimation for an area source given the source location (with unknown source rate) and assuming horizontally uniform surface source atmosphere in horizontal equilibrium (see Figure 4). To make an emission estimate using bLS, the method utilizes the dispersion model relation,
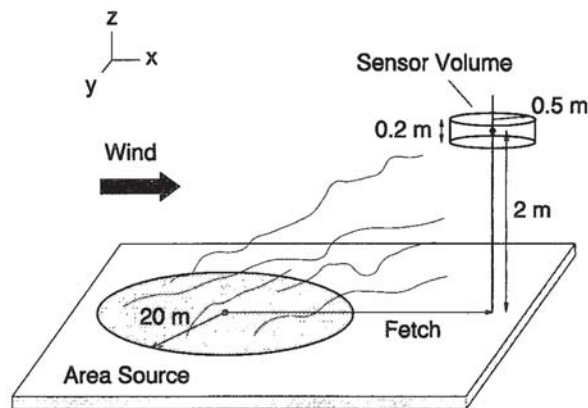
Figure 4. A diagram depicting the bLS approach [124], © American Meteorological Society, used with permission.

$$\frac{UC}{Q} = n = f(z_m, z_0, L, h, G), \tag{11}$$

where L is the Monin–Obukhov length, h is the depth of the mixing layer, G describes the set of parameters characterizing the plume, and z_m represents the measurement height. As the particles from the back trajectories touchdown in the source area, the vertical velocities, w_0 are logged and used to estimate n,

$$n(z_m) = \frac{C(z_m)U(z_m)}{Q} = \frac{1}{N}\sum \left| \frac{2}{w_0/U(z_m)} \right|. \tag{12}$$

Once n is known, an estimate of the source rate can be determined using the measured concentration and wind speed, $Q = n/(CU)$. In this approach, due to the time-averaged

ensemble, the accuracy improves over time (nominal averaging period of 15 min [124]). An alternate expression for the emission estimate is given as

$$Q_{bLS} = \frac{C - C_b}{(C/Q)_{sim}},$$ (13)

where C_b is the background concentration and $(C/Q)_{sim}$ is calculated using

$$(C/Q)_{sim} = \frac{1}{N} \sum |\frac{2}{w_0}|.$$ (14)

This Monin–Obukhov similarity theory (MOST)-based bLS emission estimation methodology was validated against the mass balance approach (given the along-wind distance of the source D),

$$Q_m = \frac{1}{D} \int_0^\infty C(z)U(z)dz,$$ (15)

and field tested in [96,125,126]. A lagoon environmental leak was simulated and explored with the bLS approach by constructing a large 45 m by 45 m emission source on a pond. The accuracy was shown to be lower during the summer period due to more frequent unstable atmospheric conditions [127].

4.1.3. Mesoscale Recursive Bayesian Least Squares Inverse (RB-LSI)

Utilizing the NOAA P-3 aircraft and a wavelength-scanned CRDS, ref. [71] used a mesoscale bayesian least squares approach to solve the inverse problem of estimating emissions. They use the FLEXPART-WRF to model the forward problem, which was compared to physical observations and minimized on an iterative cost function that assumes lognormal distributions,

$$J = \frac{1}{2}(\ln(y_0) - \ln(Hx))^T (\ln(y_0) - \ln(Hx))$$
$$+ \frac{1}{2}\alpha(\ln(x) - \ln(x_b))^T (\ln(x) - \ln(x_b)),$$ (16)

where the observed concentration enhancements are given as y_0, posterior solutions are x, FLEXPART-WRF outputs are H, prior fluxes are x_b, error covariance matrix from observations are R, and error covariance matrix from prior fluxes are B in the lognormal space.

4.2. Optimization-Based

In this section, we discuss the emission quantification techniques that utilize some form of optimization in the methodology that fits a model.

4.2.1. Point Source Gaussian (PSG)—OTM33A

In [88], the point source Gaussian (PSG) is discussed. The measurement involves a vehicle with a concentration measurement instrument (CMI) to park downwind of the known source with the vehicle off. The CMI (such as Picarro or LGR UGGA) collects data at roughly 2.5 m above ground at a known distance from the source. The variations in the wind direction are measured using a sonic anemometer (e.g., R.M. Young). The PSG calculations are based off of enhanced emission levels and can be calculated as the fifth percentile of the concentration time series signal [88]. The PSG estimate then becomes a simple 2-D Gaussian integration with no reflection term,

$$S_E = 2\pi \sigma_y \sigma_z U_m C_p,$$ (17)

where C_p is the peak concentration from the Gaussian fit, U_m is the mean wind speed, σ_z and σ_y are the vertical and lateral plume dispersion that can be determined from the meteorological conditions, such as the Pasquill–Gifford stability classification curves [128] (see Figure 5). The accuracy of the OTM33A method is explored in [129,130].
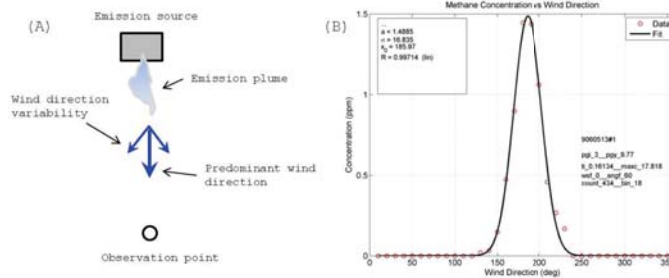
Figure 5. (**A**) Depiction of Gaussian plume dispersion with an observer making a stationary measurement downwind. (**B**) Resulting time-integrated data with a Gaussian fit applied [23].

4.2.2. Conditionally Sampled PSG (PSG-CS)

To capture the ensemble mean of the downwind plume behavior, a dispersion model is used in [88]. The model is a function of downwind distance and dispersion factors $D_y(x,y)$ and $D_z(x,z)$, given as

$$C_m(x,y,z) = \frac{S}{\overline{U}} D_y(x,y) D_z(x,z). \tag{18}$$

This method essentially aims to determine the source rate, S, using the conditional mean concentration data, C_m, of the downwind plume. The lateral dispersion downwind of a continuous point source can be shown to have a Gaussian distribution such that it can be represented as

$$D_y(x,y) = \frac{1}{\sqrt{2\pi}\sigma_y} [-\frac{1}{2}(\frac{y}{\sigma_y})^2)]. \tag{19}$$

However, the vertical dispersion (assuming vertical eddy diffusivity and wind speed that scales vertically to a power law) can be formulated as a parameterized stretched exponential (originally expressed in [131]),

$$D_z = D_z(x,z) = \frac{A}{\overline{z}} \exp[-(\frac{Bz}{\overline{z}})^s]. \tag{20}$$

The parameters $\overline{z}$, s, A, and B are functions of the atmospheric stability and downwind distance, x. A and B can be described using the usual Gamma function, $\Gamma(\cdot)$ as

$$A = s\Gamma(2/s)[\Gamma(1/s)]^2, \tag{21}$$

$$B = s\Gamma(2/s)\Gamma(1/s). \tag{22}$$

The conditional averaged concentration can be calculated using

$$\langle C|\theta \rangle = \frac{1}{n} \sum_{\theta_i \in \Theta}^{n} C(\theta_i), \tag{23}$$

where the set $\Theta(\theta) = \{\theta_i : |\theta - \theta_i| < \Delta\theta/2, \forall i = 1,2,...,n\}$ and $\Delta\theta = 2°$. The basic idea is to capture the plume geometry in the crosswind direction, which is further used to derive the least squares source estimate,

$$S = \Big[\sum_{i=1}^{N} \frac{D_y D_z}{\overline{U}} \langle C|\hat{Y}_i \rangle \Big] / \Big[\sum_{i=1}^{N} (\frac{D_y D_z}{\overline{U}})^2 \Big]. \tag{24}$$

As shown in [88], the lateral dispersion can be determined in two ways: classically, using atmospheric stability (for constants a_y and p_y) [132],

$$\sigma_y = a_y z_0 1.9 (L_x/z_0)^{p_y};$$

(25)

and by reconstructing the lateral dispersion,

$$\sigma_y = \sqrt{\frac{1}{N} \sum_{i=1}^{N} \hat{Y}_i},$$

(26)

where the N is the number of values in $\langle C|\underline{\hat{Y}}\rangle$, and $\underline{\hat{Y}}$ are $\hat{Y}$ values that are greater than the minimum concentration (i.e., background) and $\pm 40°$ off the plume center θ_p. The distance $\hat{Y}$ is calculated as

$$\hat{Y}(\theta) = L_x \sin(\theta - \theta_p),$$

(27)

with $\theta_p = \arg\max_\theta \langle C|\theta\rangle$ (see Figure 6).
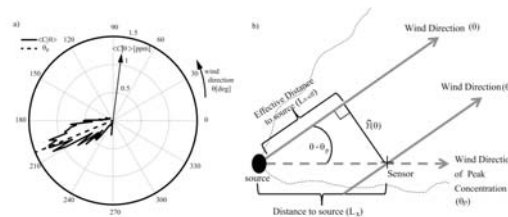
Figure 6. (**a**) Polar plot with the wind direction, θ as the radial axis, and the conditionally averaged concentration, $\langle C|\theta\rangle$ as the distance from the center. θ_p is the peak wind direction located at the maximum conditionally averaged concentration. (**b**) Illustration of the wind direction geometry for conversion of θ to crosswind position $\hat{Y}$ with the source plume represented by the dashed lines [88], © 2015 Atmospheric Environment, used with permission.

4.2.3. Recursive Bayesian Point Source Gaussian Method (PSG-RB)

In work from [133,134], a moving sensor measured a point source concentration that can be formulated as

$$C(x, y, z) = \frac{S}{\overline{U}} D_y(x, y) D_z(x, z).$$

(28)

The source rate is given as S, the effective wind speed is $\overline{U}$, and the lateral and vertical dispersion is characterized by $D_y(x, y)$ and $D_z(x, z)$, respectfully. The equation is formulated such that the downwind distance, x, is aligned with the predominant wind direction. Since the measurement is taken at closer distances to the source, the lateral dispersion is taken as a random function such that

$$\int_{-\infty}^{\infty} D_y(x, y) dy = 1.$$

(29)

This can be advantageous for instantaneous plumes. The integrated lateral concentration can be written as

$$C^y(x, z) = \frac{S}{\overline{U}} D_z(x, z).$$

(30)

The choice of the vertical dispersion D_z (originally expressed in [131]) is that of a parameterized stretched exponential function,

$$D_z = D_z(x, z) = \frac{A}{\bar{z}} \exp\left[-\left(\frac{Bz}{\bar{z}}\right)^s\right],$$

(31)

where $\bar{z}$, s, A, and B are functions of atmospheric stability and downwind distance, x. The lateral dispersion is given as

$$D_y = \frac{1}{\sqrt{2\pi}\sigma_y} \exp\left[-\frac{1}{2}\left(\frac{y_i}{\sigma_y}\right)^2\right]. \tag{32}$$

Then, by numerically integrating (28) and incorporating the vehicle movement V,

$$C^y = \sum_{i=0}^{\infty} C(x_i, y_i, z_i)\Delta t V = S \sum_{i=0}^{\infty} \frac{\Delta t V}{\overline{U_i}} D_z(x_i, z_i) D_y(x_i, y_i). \tag{33}$$

The recursive Bayesian approach described here is based on well pads and oil and gas production, which are used to help inform the path planning of the mobile sensor. For brevity, we will only cover the formulation of the quantification only. Starting with the definition of the posterior distribution,

$$p(S|M, W, \Lambda) = \frac{p(S|W)p(M|S, \Lambda)}{p(M|\Lambda)}, \tag{34}$$

where M is the concentration data, W is the ancillary information (e.g., well pad characteristics), Λ is the meteorological conditions, $p(S|W)$ is the prior, $p(M|S, \Lambda)$ is the likelihood, and $p(M|\Lambda)$ is the evidence (which can be thought of as a normalization constant for the likelihood [135]). The prior is given as

$$p(S|W) = \frac{1}{\beta} \exp\left[-\left(1 + \gamma\frac{S-\mu}{\beta}\right)^{-\frac{1}{\gamma}}\right]\left(1 + \gamma\frac{S-\mu}{\beta}\right)^{-1-1/\gamma}, \tag{35}$$

where the hyperparameters need to be fit to the application (for well-pad source, $\gamma = 1$, $\mu = 0.19$, $\beta = 0.23$ based on [136]). The likelihood function is chosen to be a Gaussian,

$$p(M|S, \Lambda) = \frac{1}{\sqrt{2\pi}\sigma_e} \exp\left[-\frac{1}{2}\left(\frac{C^y - C^{y,M}}{\sigma_e}\right)^2\right], \tag{36}$$

where $C^{y,M}$ is the modeled concentration for a given source rate, and σ_e is the combined model and measurement error (outlined in [137]). The recursive approach involves replacing the prior with the previous posterior distribution found using the likelihood function,

$$p(S|W)_i = \begin{cases} p(S|W), & i = 1, \\ p(S|M, W, \Lambda)_{i-1}, & i > 1. \end{cases} \tag{37}$$

As the number of passes increases, the posterior distribution improves and can be used to estimate the source rate,

$$S = \int_{S_{min}}^{S_{max}} Sp(S|M, W, \Lambda)dS. \tag{38}$$

Variations of this method were seen in [134], where the measurement noise was assumed to be Gaussian and also included a UAV with sensor noise and utilized the flux plane mass balance method to estimate the source rate, which was used in the calculation of the posterior distribution. Further field tests of this method were carried out in [138].

4.2.4. Point Source Gaussian Sequential Bayesian Markov Chain Monte Carlo (PSG-SBM)

Utilizing the Gaussian plume model for the likelihood of a sequential Bayesian Markov Chain Monte Carlo (MCMC) method, a UAV scans horizontally to update the estimated posterior distribution in [139]. The parameters are given as $\Theta_k = [\mathbf{p}_s^T, q_s, u_s, \phi_s, \zeta_s]^T$, were the position is $\mathbf{p}_s$, source rate q_s, wind speed and direction u_s and ϕ_s, and the model diffusion coefficients $\zeta_s = [\zeta_{s1}, \zeta_{s2}]^T$. The point source observations, $\mathbf{z}_{1:k} = \{z_1, z_2, ..., z_k\}$ are used within Bayes rule to update the posterior,

$$p(\Theta_{k+1}|\mathbf{z}_{1:k+1}) = \frac{p(\mathbf{z}_{k+1}|\Theta_{k+1})p(\Theta_{k+1}|\mathbf{z}_{1:k})}{p(z_{k+1}|\mathbf{z}_{1:k+1}}. \tag{39}$$

The likelihood model, $\mathcal{M}(\mathbf{p}_k, \zeta_k)$, in [139], based on observational data, $\bar{z}_k = \mathcal{M}(\mathbf{p}_k, \zeta_k)$ + $\bar{v}_k$, was taken to be detection event, $p(\bar{z}_k|\Theta_k)$, if $z_k > z_{thr}$,

$$p(\bar{z}_k|\Theta_k) = \frac{1}{\sigma_k\sqrt{2\pi}}\exp[-\frac{(\bar{z}_k - \mathcal{M}(\mathbf{p}_k, \zeta_k))^2}{2\sigma_k^2}], \tag{40}$$

and a non-detection event otherwise,

$$p(z_k|\Theta_k) = (\frac{p_b}{2}[1 + \text{erf}(\frac{z_{thr} - \mu_b}{\sigma_b\sqrt{2}})]) + p_m + (\frac{p_s}{2}[1 + \text{erf}(\frac{z_{thr} - (\mu_b + \mathcal{M}(\mathbf{p}_k, \zeta_k))}{\sigma_b\sqrt{2}})]). \tag{41}$$

The three terms in the non-detection event account for instrument noise, turbulence, and observing concentrations above the threshold, where $p_b + p_m + p_s = 1$, and μ_b and σ_b are mean background noise and standard deviation, respectively. Using a particle filter, the posterior can be approximated by a set of n weighted random samples $\{\Theta_k^{(i)}, w_k^{(i)}\}_{i=1}^n$,

$$p(\Theta_k|\bar{z}_{1:K}) \approx \sum_{i=1}^n w_k^{(i)}\delta(\Theta_k - \Theta_k^{(i)}), \tag{42}$$

where δ is the Dirac delta function. The un-normalized weights are then updated using

$$\overline{w}_{k+1}^{(i)} = w_k^{(i)} \cdot p(z_{k+1}|\Theta_{k+1}^{(i)}). \tag{43}$$

Once the weights are determined they can be normalized by dividing by the summation of all the weights. Additionally, an effective sample size must be considered to avoid the degeneracy problem. The new samples undergo a MCMC step that is accepted with the likelihood probability distribution described earlier (see Figure 7).
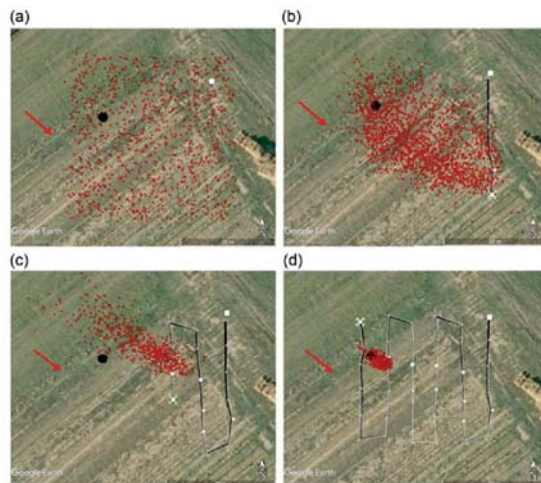
Figure 7. Example run of the PSG-SBM method at time steps: (**a**) k = 0, (**b**) k = 6, (**c**) k = 16, and (**d**) k = 36. The white lines indicate the path of the UAV starting at from the beginning at the white rectangle to the UAV's current positions—the white quadrotor symbol. The black circle is the source location, and the red arrow is the wind direction. The red dots are the random sample approximation of the source parameter estimates at that respective time step [139], © 2019 Field Robotics, used with permission.

4.2.5. Near-Field Gaussian Plume Inversion (NGI)

The near-field Gaussian plume inversion (NGI) method [140,141] is a mass continuity model in principle, where the upwind and downwind concentration measurements, combined with wind measurements, of an emission source are differenced to quantify emission flux. The NGI method is typically sampled around 100 m from the source. The sampling aims to capture the time-invariant behavior of the plume, which, under turbulent conditions, may not map out the characteristic Gaussian plume shape.

This is because it is assumed that spatial variability in the time-averaged plume is Gaussian. This method was initially carried out with a DJI S900 equipped with a ultra portable greenhouse gas analyzer (UGGA) by Los Gatos Research Inc. (LGR). The flux estimate is derived by fitting the experimentally measured flux values, q_{me}, to the modeled flux values, q_{m0} given as,

$$q_{me} = (C - C_b)U(z)\rho, \tag{44}$$

where the modeled flux is given by the Gaussian model,

$$q_{m0} = \frac{F_e}{2\pi\sigma_y(x)\sigma_z(x)} \exp\left(\frac{-(y - y_c)^2}{2\sigma_y(x)^2}\right)\left(\exp\left(\frac{-(z - h)^2}{2\sigma_z(x)^2}\right) + \exp\left(\frac{-(z + h)^2}{2\sigma_z(x)^2}\right)\right). \tag{45}$$

The lateral and vertical dispersion relations are typically looked up in the PGT stability tables, however, in this method, they are assumed to be linearly proportional to downwind distance,

$$\tau_y = \sigma_y(x)/x, \quad \tau_z = \sigma_z(x)/x. \tag{46}$$

Trying to solve (45) is not always well constrained, and thus the method proposes to separate (45) and fit the model along the z-direction,

$$q_{me,y} = q_{me} \frac{\tau_z x \sqrt{2\pi}}{\left(\exp\left(\frac{-(z-h)^2}{2(\tau_z x)^2}\right) + \exp\left(\frac{-(z+h)^2}{2(\tau_z x)^2}\right)\right)}. \tag{47}$$

The spatial variability in the z-direction has to be sampled to determine τ_z. The lateral spatial variability τ_y and plume center y_c are determined simultaneously,

$$y_c = \frac{\sum_j (q_{me,y} y_j)}{\sum_j (q_{me,y})}, \tag{48}$$

$$\tau_y = \sqrt{\frac{\sum_j (q_{me,y_j} (\frac{y_j - y_c}{x_j})^2)}{\sum_j (q_{me,y_j})}}. \tag{49}$$

Once the unknowns, τ_z, τ_y, and y_c are determined, the source emission rate, F, can be estimated by minimizing the least square fit between q_{me} and q_{mo}, given F_e and τ_z. The uncertainty in F and the impact of limiting τ_z are given in [140].

4.3. Mass Balance Based

The mass balance approach aims to estimate an emission source by balancing the mass flux leaving or entering a control volume. Generally, there are two path planning approaches to the mass balance method: (1) rectangular vertical flux plane (or curtain) downwind of the source and (2) a cylindrical flux plane enclosing the source. For a well behaved plume under stable atmospheric conditions, the downwind plume contains all the flux. The sampling distance from the source may vary based on each submethod. The measured flux plane data can be sparse and is typically subject to spatial interpolation.

4.3.1. Vertical Flux Plane (VFP)

The flux plane method generally involves sampling within a plane, vertically or horizontally, upwind and downwind, of an emission source. It has been applied in several works [9,33,37,66,76,78,120,142–149]. The plane is typically sampled using a raster-

scanning approach, capturing the plume within the width and height of the plane. The emission rate (in moles s^{-1}) can be estimated as,

$$Q_c = \int_0^z \int_A^B n_{ij}(C - C_b)\mathbf{u} \cdot \mathbf{n}_f dx dz, \tag{50}$$

where n_{ij} is the mole density of air (given standard temperature and pressure), $(C - C_b)$ is the enhanced mole fraction (referenced to air), C_b is the background mole fraction, $\mathbf{u}$ is the wind speed vector, and $\mathbf{n}_f$ is the flux plane normal vector (see Figure 8). Since the measurements are sparse, the integral irregularly spaced. To combat this, the sparsely sampled points are spatially interpolated using techniques, such as inverse distance weighting (IDW) [150] or kriging [151]. This is a common problem in geostatistics to interpret unknown data, $z(s_0)$, from desired spatial locations s_0 in domain $\Omega \in \mathbb{R}^2$, only using N sparse sampling points, $z(s_i)$, based on some optimal weights, λ_i,

$$\hat{z}(s_0) = \sum_{i=1}^N \lambda_i z(s_i). \tag{51}$$

For example, in ordinary kriging [151], a semivariogram is used to model the spatial variability and, given a spatial distance, h, is defined as,

$$\hat{\gamma}(h) = \frac{1}{2N(h)} \sum_{i=1}^{N(h)} (z(s_i) - z(s_i + h))^2. \tag{52}$$

This experimental semivariogram can be fitted to the model semivariogram with one of several common functions: circular, spherical, exponential, Gaussian, or linear. The weights are determined by solving

$$\sum_{j=1}^N \lambda_j C(\mathbf{s}_i - \mathbf{s}_j) + \mu(\mathbf{s}_0) = C(\mathbf{s}_i - \mathbf{s}_0), \text{ for } i = 1, 2, ..N, \tag{53}$$

where $C(\cdot)$, in this context, represents the point support covariance matrix. This matrix is related to the semivariogram, $\gamma(h) = C(0) - C(h)$ [151], and the mean square prediction error is $\sigma_e^2 = Var(z(s_0) - \hat{z}(s_0))$, which, for ordinary kriging, is minimized to make the estimated values $\hat{z}(s_0)$ optimal. Furthermore, the estimator should be unbiased (e.g., $E[\hat{z}(s_0)] = E[z(s_0)]$), which requires $\sum \lambda_i = 1$ and the spatial mean to be stationary $E[z(s)] = \mu$, $\forall s \in \Omega$.

If the kriging process is not stationary, it is considered, at best, an approximate solution to the spatial interpolation problem and incorrect at worst. A better approach could be to apply a spectral method that takes into consideration non-stationarity and higher frequencies, namely, the high frequency kriging method [152]. Consideration of temporal observations could be included as well, see quantile kriging in [153].

An enhanced version of the IDW was proposed in [154] to include an adaptive distance-decay parameter based on the density characteristics of the sampled points. Available tools, such as Kriging Assistant (KA) [155], Golden Software Surfer, or ESRI Geostatistical Analyst for ArcMap have been used in the literature before. For irregular geographical units with different sizes and shapes, the interested reader should consult [156].

A variation of the VFP technique is illustrated in [157], where a path-averaged long open path duel-comb spectroscopy is operated from a ground vehicle to a sUAS with a retro-reflector. A vertical profile is flown downwind of the source to conduct the VFP. This technique is also vary similar to VRPM.
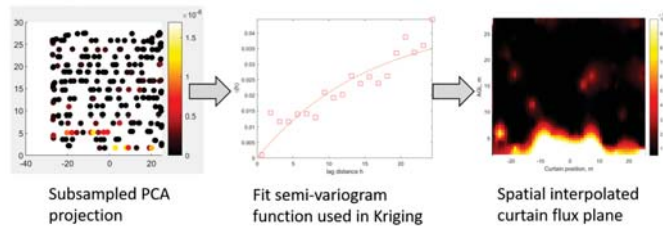
Figure 8. Demonstration of using sampled flux plane data and applying kriging to it for spatial interpolation [11].

4.3.2. Cylindrical Flux Plane (CFP)

A variation to the VFP is the Cylindrical Flux Plane (CFP). This method has been used with manned aircraft as it is not as easy to raster-scan a rectangular flux plane. The methodology is essentially vary similar to the VFP and can be found in the work by [158], omitted here for brevity.

4.3.3. Path Integrated Vertical Flux Plane (PI-VFP)

A variation of the VFP is the path integrated vertical flux plane (PI-VFP). This method utilizes a bs-TDLAS approach in that the instrument points straight down and scans or circles the emission source (see Figure 9). In [159], the AVIRIS-NG manned aircraft used IMAP-DOAS technique to retrieve methane concentrations and estimated fluxes using a PI-VFP type calculation. This approach was compared with the GDT and Gaussian inverse approaches during a joint-flight campaign.
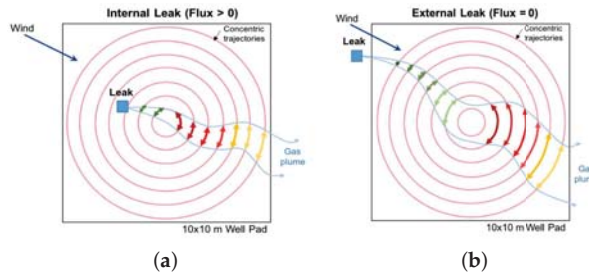
Figure 9. Example of the VFP-PI strategy via a UAV sensing in circular trajectories with (**a**) being an internal leak producing a net positive flux and (**b**) being an external leak producing a net zero flux. The color of the arcs are indicative of methane flux strength with green being more negative and red being more positive [121].

The emission rates were estimated by, $Q \approx \mathbf{u} \cdot \mathbf{n} \sum_i V_i \Delta s_i$, were V_i represents the vertically integrated concentration, and Δs_i is a path segment along the boundary. The individual measurements are integrated together (referred to as integrated methane enhancement (IME)) such that $IME = k \sum XCH_4(i) \cdot S(i)$. The value XCH_4 is the methane plumes that exceed the minimum threshold of 200 ppm/m and k is a conversion factor.

Using an RMLD sensor fitted to a small quadrotor UAV, a circular scanning approach can be applied to sample horizontally a site of interest. The sensor uses a bsTDLAS to measure integrated methane emissions from a known height. The resulting measurements are then combined with wind measurements to estimate the flux [121,160],

$$q = \int_0^H \int_{-W/2}^{W/2} \mathbf{u} \times (X - X_b) dx dz, \tag{54}$$

where H and W are the vertical and lateral dimensions, and X_b is the background concentration. This calculation encompasses a single circular loop and if the source is encapsulated, multiple passes can be used to estimate the source,

$$Q = \frac{1}{n} \sum q_i. \tag{55}$$

In practice, the circular flight path is actually made up of line segments that are box-like. The source location was also identified by course raster scanning over the area of interest followed by a more fine flight pattern free approach combined with triangular natural neighbor interpolation. The maximum observed concentration was used for the source location.

4.3.4. Micrometeorological Mass Difference (MMD)

Utilizing the technique from [161], sampling the plume far enough downwind of the source, the averaged MMD can be calculated as

$$Q = \overline{\iint U_{(y,z)} (\rho_{(y,z)} - \rho_b) dy dz} = \int \chi(z) dz. \tag{56}$$

The work in [162] utilized the time-average of the line-integral of the instantaneous product of U and ρ in the y-direction. Alternatively, while using a laser fetch, an instantaneous product of a single wind measurement U and line-averaged laser concentration was used,

$$\chi \approx \Delta y \overline{U_{(z)}} (\rho_{L(z)} - \rho_b). \tag{57}$$

This method can also be used to calculate the turbulent fluxes,

$$\frac{Q_{tur}}{Q} = \frac{(Q_{\overline{U}\overline{\rho}} - Q_{\overline{U\rho}})}{Q_{\overline{U\rho}}}, \tag{58}$$

where $Q_{\overline{U\rho}}$ is calculated from the flux term in (57) and $Q_{\overline{U}\overline{\rho}}$ in (59),

$$\chi \approx \Delta y \overline{U_{(z)}} \overline{(\rho_{L(z)} - \rho_b)}. \tag{59}$$

This prescription of the flux does not capture the turbulent component of the horizontal flux (albeit wrong), is often necessary due to the short time-scale behavior of the wind (e.g., limitations in wind measurement devices).

4.3.5. Gauss Divergence Theorem (GDT)

In the paper by [163], Conley et al. they focused on the continuity equation,

$$Q_c = \left\langle \frac{\partial m}{\partial t} \right\rangle + \iiint \nabla \cdot c\mathbf{u} \, dV, \tag{60}$$

where m is the mass of the aerosol, $\langle \cdot \rangle$ is the expectation or average, $c = C + c'$ is the concentration (comprised of an average term and a deviation term), $\mathbf{u}$ is the wind speed, and V is the volume of the area of interest. The flux divergence can be expanded as,

$$\nabla \cdot c\mathbf{u} = \mathbf{u} \cdot \nabla c + c\nabla \cdot \mathbf{u}. \tag{61}$$

The surface integral is taken to be a cylinder, which can be broken into several parts: the floor, the walls of the cylinder, and the top. The height of the cylinder is taken such that the emission is encapsulated with the minimum and maximum height. The resulting emission rate can be calculated as

$$Q_c = \left\langle \frac{\partial m}{\partial t} \right\rangle + \int_0^{z_{max}} \oint c' \mathbf{u}_h \cdot \hat{\mathbf{n}} \, dl \, dz, \tag{62}$$

where z represents the altitude, and l the flight path. The temporal trend of the total mass ($\frac{\partial m}{\partial t}$) within the volume can be estimated from the measurements. The cylinder passes can be vertically binned and discretely summed up,

$$Q_c = \frac{\Delta m}{\Delta t} + \sum_{z=0}^{z=Z_t} \left(\sum_{0}^{L} \rho \cdot u_n \right) \cdot \Delta z. \tag{63}$$

4.3.6. Vertical Flux Planes with GLM (GLM-VFP)

In [34], a 3D grid of airborne measurements are collected across multiple landfill sites. The resulting downwind observational points are then spatially interpolated with IDW and used to calculate the total mass flux. The multiple steady state Gaussian dispersion models,

$$C(x, y, z) = \frac{Q}{2\pi \sigma_y \sigma_z U} \exp\left(\frac{-y^2}{2\sigma_y^2}\right) \left(\frac{1}{\sqrt{2\pi}\sigma_z}\right) \exp\left[\frac{-(z-L)^2}{2\sigma_z^2}\right], \tag{64}$$

are applied to a fixed grid (50 by 50 m), where the mixing ratios found over each individual landfill was used to calculate a model mass flux (for each site, integrated along the x, y, and z directions). The experimental measurements are then used with simulation measurements and a general linear model,

$$\min_{\alpha} \left| MF - \sum_{i=1}^{max} (MMF_i \cdot \alpha_i) \right|, \tag{65}$$

to approximate the emission coefficient, α_i, from multiple landfill sources. The emission findings are further corroborated with a local Eddie covariance tower measurement.

4.3.7. Vertical Radial Plume Mapping (VRPM)

The vertical radial plume mapping approach (compared with other methods in [77]), utilizes a long path TDLAS instrument from the ground. The laser is aimed at retro-reflectors, situated perpendicular and downwind of the source. The height of the retro-reflector constitutes the different radial angles where the path-integrated concentrations are combined with the normal wind component to estimate the flux (similar to VFP or MMD). An illustration of this is seen in Figure 10.
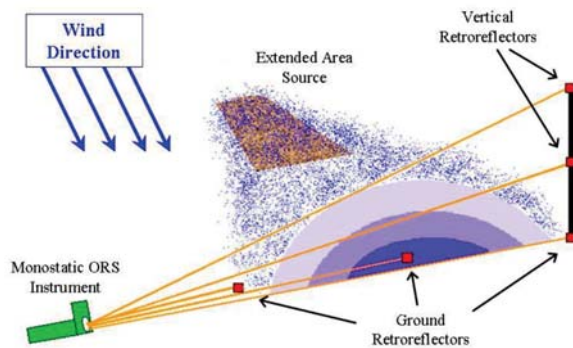
Figure 10. A diagram of the VRPM method [77].

4.4. Imaging-Based

In this section, we overview the imaging-based methodology for quantifying methane emissions. This typically includes techniques that sample images passively, such as TIR, MWIR, or other OGI-based instrumentation. The methods mentioned here that can quantify methane emissions are considered as quantitative optical gas imaging (QOGI).

4.4.1. Mid-Wave Infrared (MWIR) and Hyperspectral

In the work by [164], the detection limits of MWIR band of a hyperspectral data was explored using the Spatially-Enhanced Broadband Array Spectrograph System (SEBASS) airborne instrument. They also provided a comparison between LWIR and MWIR (see Figure 11) using the radiative transfer model,

$$R_s = (R_T^\uparrow + R_S^\uparrow) + t\{\epsilon_s B(T_s) + (1 - \epsilon_s)[\frac{R_T^\downarrow + R_S^\downarrow}{1 - S(1 - \epsilon_s)}]\}, \tag{66}$$

where R_s is th etotal radiance at the sensor, $R_T^\uparrow$ is the upwelling emitted atmospheric path radiance, $R_T^\downarrow$ is the downwelling emitted atmospheric path radiance, $R_S^\uparrow$ is the scatter path radiance at the sensor, $R_S^\downarrow$ total solar radiance that reaches the surface, t is the atmospheric transmittance, ϵ_s is the surface emissivity, and $B(T_s)$ is the blackbody radiation at the surface temperature.
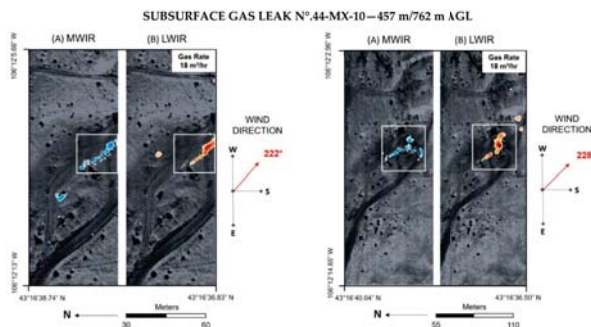
Figure 11. Methane plume detections in the (**A**) MWIR and (**B**) LWIR ranges [164].

Other works, such as [98], have used MWIR cameras combined with two Pergam Methane Mini G lasers in pipeline leak detection. In [165], a FLIR GF320 and a RMLD were used together to make volumetric flow rate calculations in the laboratory using a data fusion approach. In [166], they utilized a thermal camera and steady state energy balance approach to estimate methane emissions from thermal anomalies in urban landfills.

4.4.2. Iterative Maximum a Posteriori Differential Optical Absorption Spectroscopy (IMAP-DOAS)

The IMAP-DOAS method was applied to the AVIRIS-NG [30,31] aircraft and measures reflected solar radiation between 0.35 μm and 2.5 μm with 5 nm spectral resolution and sampling. Using a nonlinear iterative minimization of the differences between modeled and measured radiance. The measured concentrations can be applied to the PI-VFP method to calculate fluxes [159]. Variations in this approach for retrieving methane concentrations has been seen in [167] for albedo correction and [39] anomaly-based mass balance.

4.5. Correlation-Based

4.5.1. Tracer Correlation (TCM)

The tracer correlation method, or isolated source tracer ratio method, initially proposed and implemented in works by Lamb et al. [168] and Czepiel et al. [75], aims to quantify the emission rate of an unknown gas species by releasing a tracer gas at a known flow rate while measuring both the tracer and the unknown signals collocated downwind. This method assumes that the location of the source is known and, at the measurement location, the plume is well mixed. The elevated signal downwind also needs to typically be greater than 50 ppb. The authors report uncertainty estimates of ±15%. The general equation is given as

$$Q_m = Q_t \frac{C_m}{C_t}, \tag{67}$$

where Q_t is the tracer release rate, and C_m and C_t are the elevated mixing ratios of the unknown source gas and tracer gas, respectively. A comparison study between TCM and other fugitive emission quantification methods are studied in [77]. The effect of wind on accuracy of the TCM was explored for landfills using WRF model [169]. An in situ method was used to evaluate the collection efficiency of gas extraction wells based on tracer gas [170].

Variations of the quantification of TCM were explored in [28], which quantified emission rates based on the plume integration of a transect, peak height of the transect using a scatter plot to calculate the ratio (best fit line), and comparison with fitted Gaussian plume model. A landfill field comparison of methane emission models were compared to measured emissions using TCM [171]. The TCM method was also applied to quantifying emissions from dairy farms in [123].

A dual tracer method was explored in [172]. The second tracer provides for closer downwind measurements that can be refined by assessment of plume position as well as in the far-field measurements the second tracer becomes an internal standard to the measurement. A mobile version of the TCM approach was proposed in [173].

4.5.2. Eddy Covariance (EC)

The Eddy covariance method aims to estimate the emission flux from a footprint area given the boundary layer meteorology. Historical developments and current implementations of this method are summarized in [174]. This method generally assumes stationarity of the measured data and fully developed turbulent conditions [175]. One way it can be expressed is,

$$Q = \frac{1}{t_f - t_i} \int_{t_i}^{t_f} (C(t) - \overline{C})(w(t) - \overline{w}) dt, \tag{68}$$

where the time-averaged concentration and vertical wind speed is $\overline{C}$ and $\overline{w}$, respectively. There are several assumptions required to make this flux calculation.

5. Analysis of Methods and Assessment

In an attempt to analyze the methods covered in this paper, we decided to use the following metrics: required assumptions, sample distance, survey time, complexity, average precision, average accuracy, and average cost. The required assumptions are meant to inform the practitioner so that the best method can be applied to a given problem. For example, if the source location is unknown, the PSG method may not be directly applicable unless a source location estimate is supplied. The sample distance is defined as the distance from the source at which the required method needs measurements taken from.

The survey time consists of the time required to make a single flux estimate. Understandably, some methods may require multiple flux estimates in order to approximate the emission source to within an acceptable error. Complexity is the measure of how difficult it is to implement any given method. In order to determine a value for complexity, a scheme was developed using figures of merit (FOM) that assigns factors and weights to the metrics (detailed in Table 1). Determining the values for these factors were based on loose estimates, inferred from papers found in the literature.

Ranges were assigned to the metrics to capture variations in the factors due to either the operators or the equipment being used, and are given in Table 2. For example, some setups may use more expensive equipment or more people for the same method and, as a result, are reflected in the complexity metric.

Table 1. Figures of merit for defining complexity of an estimation method.

FOM	(%)	Low (2.5)	Medium (5)	Med-High (7.5)	High (10)
Operator skill	30	Little	Moderate	Professional	Expert
Number of operators	25	1	2	3	3+
Equipment cost	15	<$10,000	<$50,000	<$100,000	>$100,000
Setup Time	20	<1 h	<4 h	<8 h	8+ h
Survey Time	10	<0.5 h	<1 h	<2 h	2+ h

Evaluating methane quantification techniques is important, and much work has already gone into this topic through controlled release experiments and evaluation frameworks. Examples from controlled release facilities (CRF) consist of but are not limited to the following:

In the Joint Urban 2003 study [176,177], static sensors were distributed in an urban setting to measure the dispersion of tracer particulates. In [178], area-averaged velocity and turbulent kinetic energy profiles were derived from data collected at the Mock Urban Setting Test (MUST). Mock Urban Setting test (MUST) was also evaluated with photo-ionization detectors (PID) [179,180]. MUST was further simulated using MISKAM 6 [181]. In [182], the WRF model was used to model wind and turbulence inside the Quick Urban and Industrial Complex (QUIC) model for comparing simulated and observed plume transport. A test plan for Jack Rabbit II was developed in [183], which aimed to improve chemical hazard modeling, produce better planning for release incidents, improve emergency response, and improve mitigation measures.

More recently, single-blind tests at the Methane Emission Technology Evaluation Center (METEC) in Fort Collins, Colorado evaluated several types of LDAQ sensing modalities as apart of the Standford/EDF Mobile Monitoring Challenge (MMC) and the Advanced Research Projects Agency-Energy (ARPA-E) MONITOR program (such as by vehicle, plane, and drone—shown in Figures 12 and 13). In the Standford EDF MMC it was observed that the drone based technologies performed quite well (e.g., SeekOps) with an $R^2 = 0.42$ [144].

While the results shown in Figure 12 seem quite promising, there is still exists some improvements in precision that can be made. In the ARPA-E MONITOR program, 6 of the 11 participants tested their technologies at the METEC facility in [184] against six other industry-based participants. Due to confidentiality agreements at the time of testing, the data gathered from the 12 participants were aggregated to compare the methodologies based on measurement type (handheld, mobile and continuous monitoring). However, to the best of authors knowledge, only four of the MONITOR program participants have published data regarding the METEC tests (shown in Figure 13).

In a white paper by Bridger Photonics, a sUAS-based approach using LiDAR-based sensor, also demonstrated promising results even though the uncertainty is not given. In [121], a RMLD was used on a sUAS with the PI-VFP method. In contrast, ref. [185] utilized a portable TDLAS-based instrument and the PSG method to quantify emissions. Lastly, ref. [186] used a dual frequency comb spectrometer (from over one kilometer away) with the non-zero minimum bootstrap method (see [187]) and the Gaussian plume model to estimate the source rate.

Examples from active operations with comparison to conventional OGI-based methods are conducted in the Alberta Methane Field Challenge (AMFC) [147,188,189], which aimed to answer the questions: Are Leak detection and repair (LDAR) programs effective at reducing methane emissions? As well as, Can new technologies provide more cost-effective leak detection compared to existing approaches?
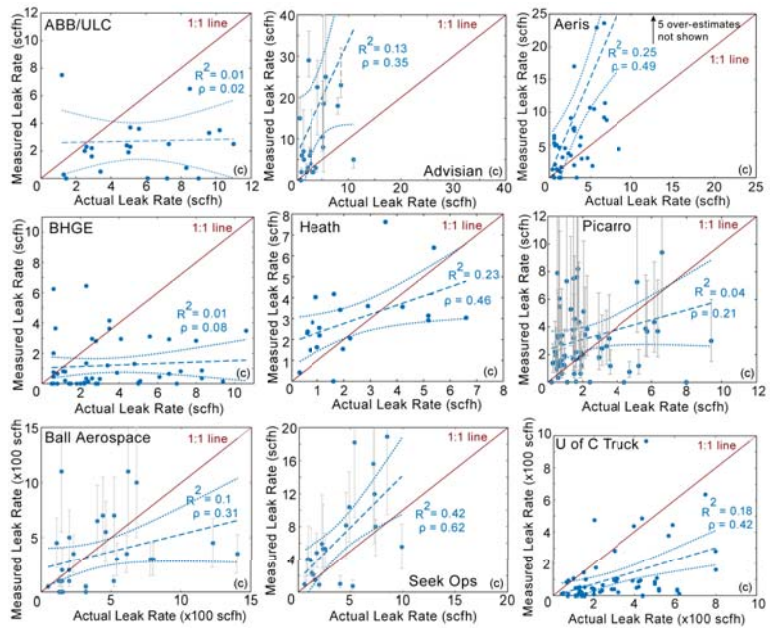
Figure 12. METEC results from the Standford EDF Mobile Monitoring Challenge [144].
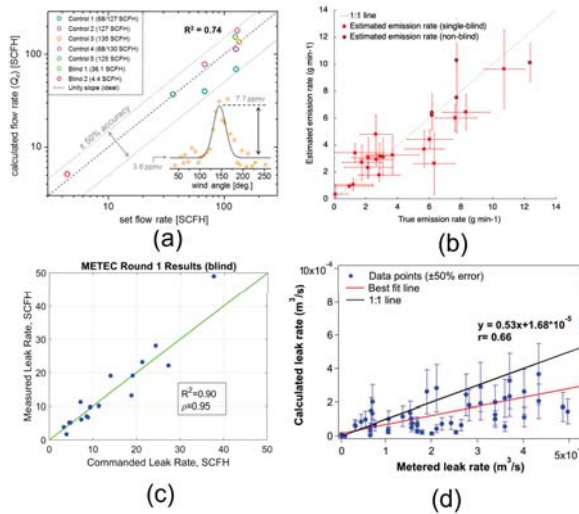
Figure 13. Published METEC results of ARPA-E MONITOR program participants from: (**a**) [185] using a static on-site portable TDLAS and PSG method, (**b**) [186] using the dual frequency comb spectrometer and non-zero minimum bootstrap (NZMB) method [187] with Gaussian plume model, reprinted (adapted) with permission from [186], © 2019 American Chemical Society (**c**) Bridger Photonics' group white paper using Gas Mapping LiDAR [190], used with permission, © 2019 Bridger Photonics, Inc., and (**d**) [121] using the bs-TDLAS and PI-VFP methods.

Table 2. Summary of methods and their assumptions, operational details, complexity, cost, average precision, and average accuracy are generalized over implementations found in the literature. The average precision and accuracy are given as unitless values, normalized by the true source rate (estimated source rate). (measured using [1] fixed, [2] foot, [3] vehicle, [4] manned aircraft, or [5] UAV; cost with $ ≤ $10,000, $$ ≤ $50,000, $$$ ≤ $100,000, $$$$ ≥ $100,000; (·) represents precision normalized on estimated source rate.).

Method	Assumptions	Sample Distance	Survey Time	Complexity (1–10)	Avg Precision	Avg Accuracy	Avg Cost
bLS	x_s, horizontally uniform surface source atmosphere in horizontal equilibrium	20–441 m [1]	15 min–4 days [1]	3.8–8.5 [1]	±0.16–0.36 [1] (±0.07–0.85) [1]	±0.02–0.30 [1]	$–$$$ [1]
PSG	x_s, steady state source rate, point source, plume evolution via ground-level Gaussian dispersion with no obstructions	441 m [1] 18–500 m [3] 50 m [5]	4 days [1] 37–58 min [3] 7.22–20 min [5]	4.5–8 [1] 3.6–6.1 [3] 3.3–5.5 [5]	(±0.30) [1], ±0.20–0.67 [3] (±0.19–0.47) [3] ±0.31 [5]	±0.0022–0.43 [3] ±0.50 [5]	$$–$$$ [3]
PSG-RB	*PSG assumptions*, vertical eddy diffusivity and wind speed approximated by power law scheme	20–200 m [3]	6 min [3]	3.6–6.4 [3]	—	±0 [3]	$$–$$$
PSG-CS	*PSG assumptions*, continuous source emission, constant wind speed, vertical eddy diffusivity and wind speed approximated by power law	18–106 m [3]	20 min [3]	3.6–5.9 [3]	±0.20–0.67 [3] (±0.19–0.47) [3]	±0.02–0.26 [3]	$$–$$$ [3]
NGI	constant source rate, σ_x and σ_y linear functions of distance to source, plume not capped by atmospheric temp. inversion in z-direction	50–82.25 m [5]	7.35–29.62 min [5]	3.3–5.5 [5]	±0.21–0.58 [5] (±0.06–0.53) [5]	±0.11–0.13 [5]	$–$$ [5]
MMD	x_s	12–27 m [1]	15 min [1]	4.5–8.1 [1]	±0.06 [1]	±0.10 [1]	$$$–$$$$ [1]
GDT	near to no meandering, steady state source rate	3–8 km [4]	1 hr [4]	5.5–7.8 [4]	±0.07 [4] (±0.08) [4]	±0.13 [4]	$$$–$$$$ [4]

Table 2. *Cont.*

Method	Assumptions	Sample Distance	Survey Time	Complexity (1–10)	Avg Precision	Avg Accuracy	Avg Cost
VFP	*GDT assumptions*	4.875–10 km [4] 19.08–510 m [5]	1.5–4.5 h [4] 20–30 min [5]	5.8–8.3 [4] 3.3–5.5 [5]	(±0.30–0.53) [4] ±0.17–0.37 [5] (±0.013–0.62) [5]	±0.10–0.50 [4] ±0.03–0.50 [5]	$$$–$$$$ [4] $–$$ [5]
PI-VFP	*GDT assumptions*	3 km [4] 0–6.77 m [5]	20–30 min [4] 15–20 min [5]	5.3–7.5 [4] 3.3–5.5 [5]	(±0.34–0.58) [4] ±0.82 [5]	±0.27–52 [5]	$$$–$$$$ [4] $–$$ [5]
CFP	*GDT assumptions*	3–17.84 km [4]	1 h [4]	5.5–7.8 [4]	—	—	$$$–$$$$ [4]
GLM-VFP	*GDT assumptions*	0.4–2.2 km [4]	2.5 h [4]	6–8.3 [4]	(±0.21) [4]	—	$$$–$$$ [4]
VRPM	*GDT assumptions*	10–100 m [1]	1 h [1]	7.1–8.6 [1]	±0.18–0.21 [1] (±0.21–0.33) [1]	±0.05–0.43 [1]	$–$$$ [1]
QOGI	temperature and pressure of gas at leak location are the same, gas plume length in direction of optical path is small	30 m [1]	1 min [1]	3–6.3 [1]	±0.01–0.02 [1] (±0.02–0.03) [1]	±0.20–0.24 [1]	$–$$$ [1]
TCM	leak plume and tracer plume are well mixed	100–3546 m [3]	0.5–2 h [3]	4.6–7.6 [3]	±0.06–0.24 [3] (±0.06–0.74) [3]	±0.0056–0.17 [3]	$$–$$$ [3]
EC	stationarity, fully developed turbulent conditions	25–228 m [1]	—	4.5–7.8 [1]	(±0.08) [1]	—	$–$$$ [1]

In order to compare the performances of the each of the methods to one another, their performance metrics were garnered from different studies where the method was utilized in either a field study or a controlled release scenarios and recorded in Table 2. Performance values were gathered from the standard deviations of consecutive flux estimates of a singular source leak scenario. Accuracy pertains to error of the flux estimate to the known source rate.

This information was limited primarily to controlled release scenarios. For each method, performances and details were separated into the broad types of sampling strategies: fixed/ static, on foot, mounted on a vehicle, mounted on an aircraft, and mounted on a sUAS. This prevents convolution of performance values between, for example, long aircraft sampling flights at far distances and short sampling flights near the source via sUAS.

6. Summary of Methods

After analyzing the quantification methods, we can separate the methods based on whether they have used sUAS or not. In this manuscript, we observed that the sUAS-based methods consist of near-field Gaussian plume inverse (NGI), vertical flux plane (VFP), and the path-integrated vertical flux plane (PI-VFP). The non-sUAS-based methods consist of backwards Lagragian Stochastic (bLS), point source Gaussian (PSG), recursive Bayesian point source Gaussian (PSG-RB), conditionally sampled point source Gaussian (PSG-CS), micrometeorological mass difference (MMD), Gauss divergence theorem (GDT), VFP, PI-VFP, cylindrical flux plane (CFP), general linear model verticl flux plane (GLM-VFP), vertical radial plume mapping (VRPM), quantitative optical gas imaging (QOGI), tracer correlation method (TCM), and Eddy covariance (EC).

When comparing their performances in Table 2, it can be seen that, when categorizing by means of mobility (i.e., fixed, on-foot, etc.), methods using static sensors show a trend of having higher complexity values while UAV-based methods display generally lower complexity values. For a subset of the methods, the survey times, sample distances, and average accuracies can be seen in Figure 14. This subset was specifically displayed for these methods had both upper and lower bounds for survey times and sample distances along with accuracy data, which allowed for the plotting of these quantities for each method in the form of ellipses on a log–log plot.

When analyzing this plot, it can be seen that the sUAS-based methods are generally lower in sample distances and survey times as opposed to the aircraft-based method being the one of the highest in both. The bLS and TCM methods are shown to have the best average accuracy with several sUAS and mobile methods close in accuracy. The long sample times of bLS method are due to the values reported in [191], and it is possible that these values don't reflect typical bLS sample times. The advantages and disadvantages of each of the methods can be seen in Table 3 along with what typical application fields that they were applied in.

The final ranking of the methods depends heavily on the desired application, which also depends on factors, such as sample distance, sample time, and desired accuracy. For that reason, it is difficult to rank the methods in general. Thus, we provide a ranking of the methods in terms of complexity (outlined in Table 1) with highlights from the precision and cost in Figure 15. The results indicate that the simplest methods, in terms of complexity, are the sUAS-based NGI[5] and VFP[5] as well as fixed QOGI[1].

The most complex methods include bLS[1] and manned aircraft-based approaches. In terms of precision, bLS[1], NGI[5], GDT[4], VFP[5], QOGI[1], TCM[3], and EC[1] tend to be the best. Thus, for sUAS-based methods, NGI[5] and VFP[5], are the most promising approaches. Additionally, the GDT[4], TCM[3], and EC[1] approaches can be treated as candidate methods for future implementation using sUAS.
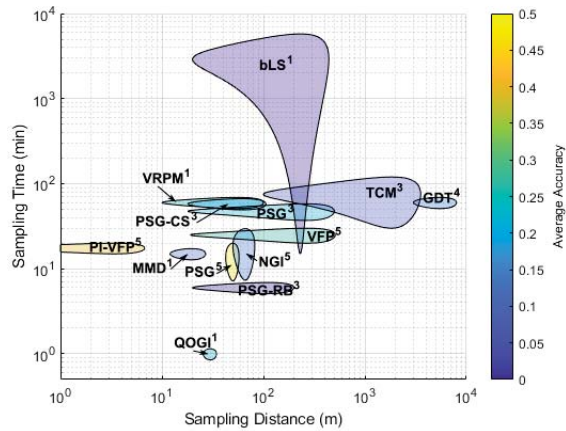
Figure 14. Diagram of summary of methods (based on Table 2) showing the relationship between typical survey time versus sample distance and there associated normalized accuracy, where lower values represent more accurate measurements. (measured using [1]fixed, [2]foot, [3]vehicle, [4]manned aircraft, or [5]UAV).
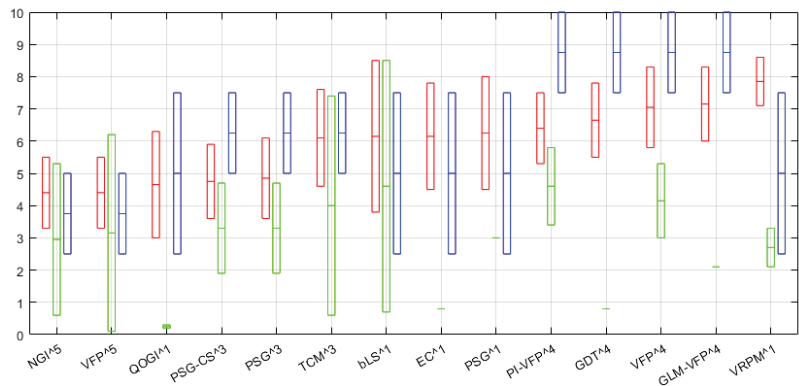
Figure 15. Diagram of the complexity ranking of the methods (based on Table 1), showing the relationship between the method complexity (red), precision (green), and cost (blue). The precision is normalized on the source estimate multiplied by 10 and the cost is ranked from 0 to 10. (measured using [1]fixed, [2]foot, [3]vehicle, [4]manned aircraft, or [5]UAV).

Table 3. Summary of the method advantages and disadvantages along with fields of application.

Method	Application	Advantages	Disadvantages
bLS	General, Oil and Gas, Agriculture	Able to quantify area source and point source emissions	Sensor is fixed, multiple measurements, negatively impacted by obstacles
PSG	Biogas, Oil and Gas	No tracer required	Negatively impacted by obstacles and low wind speeds due to plume advection, mobile sensors limited to roads
PSG-RB	Oil and Gas	No tracer required, accurate source quantification in open environments	*PSG limitations*
PSG-CS	Oil and Gas	No tracer required	*PSG limitations*
NGI	General, Oil and Gas	Assumes near-field plume turbulence and wind meandering, No assumption of atmospheric stability class	Near-field (100 m), prop-wash interference if unaccounted for
MMD	Agriculture	Able to give instantaneous flux estimates	Fixed sensors
GDT	Regional	Capable of giving emission quantifications of large areas	Sample around closed volume typically large areas, unable to capture instantaneous methane flux
VFP	General, Oil and Gas, Landfill	Does not require exact source location, ease of mobility	Stable atmospheric conditions, unable to capture instantaneous methane flux
PI-VFP	General, Oil and Gas	*VFP advantages*	*VFP limitations*
CFP	General, Urban	Capable of giving emission quantifications of large areas	*GDT limitations*
GLM-VFP	Landfill	*VFP advantages*	*VFP limitations*
VRPM	Landfill	Able to give instantaneous flux estimates	Fixed sensors
QOGI	Biogas	Able to give instantaneous flux estimates	Gas velocity determined via gas camera–velocity component parallel to image plane, can be difficult to process images
TCM	General, Oil and Gas, Landfill, Urban	Does not rely on meteorological measurements	Mobile sensors limited to roads, application difficulty due to outside methane source interference
EC	General, Oil and Gas	Can capture emission variations due to long time series	Fixed sensor(s), stable atmospheric conditions, sensitive to time of day, typically requires long sampling times

7. Future Directions

What areas should we begin to focus and invest in, and where is the field going? One approach is by looking more into smart sensing using sensor arrays and machine learning [192]. Leveraging gas dispersion modeling in path planning with source estimation approaches. A recent paper in [193] showed a joint estimation method (wind and gas) that performed fairly well compared to existing methods at reconstructing plumes within enclosed structures.

Can these approaches be used with sUAS for smarter path planning to improve LDAQ methodology? As these methods develop for outdoor gas dispersion modeling,

sUAS could potentially use these concepts for improved sensor placement, which can yield improved quantification results. For techniques, such as SEM of landfills as well as any 2D plume reconstruction problems, the sUAS-based complex tomography techniques outlined in [59] could be applied. Additionally, the combination of gas tomography with mass balance approaches or model-based optimizations could yield improved emissions estimates as well.

As survey areas become larger and harder to capture with single sUAS systems, the use of swarms can also be leveraged to improve VFP mass balance based approaches, such as in [194], or can be applied to the Bayesian inference framework, which aims to maximize the mutual information, such as in [195] to estimate source parameters. Currently regulatory hurdles and cost may prevent these systems from being applied in practice today. Given that low cost methane sensors are being actively researched, it is possible that swarms of sUAS may be used in the near future.

Considering that some non-sUAS methods (overviewed in this manuscript) may be adopted by sUAS that require longer sampling times (such as PSG and TCM), the use of power-over-tether may become desirable for increasing the survey time of sUAS. This is demonstrated for meteorological applications in [196] and has nearly indefinite flight times. There has also been advances in the digital transformation of technological applications and control, where concepts, such as Digital twins are being applied to perform smart control engineering or industrial artificial intelligence (IAI).

These techniques utilize modeling, machine learning, edge computing, and or internet of things (IOT) approaches to create digital representations of physical assets that evolve system parameters over time. They can be used to understand remaining useful life (RUL) of equipment and perhaps be coupled with LDAQ to understand when to survey equipment that is projected to fail in the near-term. This can allow the limited resources of companies and practitioners to focus on problematic areas in an attempt to detect and mitigate super emitters.

In a previous work, [120], plume modeling was applied to not only improve on methodology but also aide in smarter path planning (as mentioned above). As low cost methane sensors become more sensitive, they can be integrated into existing infrastructures to give system status updates that can be fed back into modeling approaches, such as with PSG-RB method's a priori well information [133] and PSG-SBM [139]. Furthermore, having access to a priori information and digital twins of the plume (e.g., a model of the system), can allow for improved autonomy of the sUAS. Ultimately, by applying sUAS in this context, early detection, and repair of methane leaks can be better approached.

8. Conclusions

Overall, this manuscript serves to capture the majority of sUAS-related emission quantification strategies as well as provide some accuracy comparisons to more conventional and non-sUAS quantification strategies. LDAQ methods based on sUAS can provide accuracy close to the state-of-the-art conventional methods, while improving the sampling distances and sampling times (see Figure 14). The advantage to using sUAS in some cases allows for better localization of emission sources and provides more flexibility in deployment.

Taking into consideration the operator skill, number of operators, equipment cost, setup time, and survey times, the complexity of the methods were derived. The complexity ranking of the methods indicated that NGI[5], VFP (sUAS-based), and QOGI[1] have the simplest complexity, while bLS[1] and the manned aircraft-based approaches have the highest. Comparing the precision of each method indicated that bLS[1], NGI[5], GDT[4], VFP[5], QOGI[1], TCM[3], and EC[1] have the most precise estimations, while VFP[4] and PI-VFP[4] are the least precise. To conclude, for sUAS-based methods, NGI[5] and VFP[5] are the most promising approaches.

Additionally, the GDT[4], TCM[3], and EC[1] approaches can be treated as candidate methods for future implementation using sUAS. Lastly, sUAS-based quantification approaches,

outlined in this manuscript, can be combined with new modeling and control approaches and a priori information (e.g., digital twins, machine learning, or the joint estimation method) to improve autonomy and estimation. For interested readers, the papers and bib file can be made available upon request.

Author Contributions: Conceptualization, D.H. and Y.C.; writing—original draft preparation, D.H. and D.Z.; and writing—review and editing, D.H., D.Z., and Y.C. All authors have read and agreed to the published version of the manuscript.

Conflicts of Interest: The authors declare no conflict of interest.

Abbreviations

The following abbreviations are used in this manuscript:

ADE	Advection diffusion equation
AJAX	Alpha Jet Atmospheric eXperiment
ALD	Advance Leak Detection
AMFC	Alberta Methane Field Challenge
AMOG	AutoMObile greenhouse Gas
ARPA-E	Advanced Research Projects Agency-Energy
AVIRIS-NG	Next generation Airborne visible/infrared imaging spectrometer
bLS	Backward Lagrangian Stochastic dispersion technique
bs-TDLAS	Back scatter tunable diode laser absorption spectrometer
CALMIM	California Landfill Methane Inventory Model
CARB	California Air Resources Board
CASIE	Characterization of Arctic Sea Ice Experiment
CFP	Cylindrical Flux Plane
CRDS	Cavity ring-down spectrometer
DiAL	Differential Absorption LiDAR Method
DT	Digital Twin
EC	Eddy Covariance
EDF	Environmental Defense Fund
EPA	Environmental Protection agency
EPA FLIGHT	EPA Facility Level Informationon Greenhouse gases Tool
FEAST	Fugitive Emissions Abatement Simulation Toolkit
FID	Flame Ionization Detector
FLEXPART-WRF	FLEXible PARTicle-Weather Research and Forecasting
FPE	Fokker–Planck equation
FTIR	Fourier Transform Infrared
GADEN	A 3D Gas Dispersion Simulator for Mobile Robot Olfaction in Realistic Environments
GDT	Gauss Divergence Theorem
GDM	Gas distribution mapping
GHG	Greenhouse gas
GLM	General linear model
GLM-VFP	General linear model vertical flux plane
GML	Gas Mapping LiDAR™ technology
GSL	Gas source localization
QOGI	Quantitative optical gas imaging
ICOS	Integrated cavity output spectroscopy
IDW	Inverse distance weighted
IMAP-DOAS	Iterative maximum a posteriori differential optical absorption spectroscopy
LDAQ	Leak detection and quantification

LDAR	Leak detection and repair
LES	Large eddie simulation
LiDAR	Light detection and ranging
LGR	Los Gatos Research
MCMC	Markov Chain Monte Carlo
MEMS	Micro electrical mechanical systems
METEC	Methane Emission Testing and Evaluation Center
MGGA	Micro greenhouse gas analyzer
MOX, CMOS, MOS	Ceramic Metal oxide sensor
MMC	Standford EDF Mobile Monitoring Challenge
MMD	Micrometeorological mass difference method
MONITOR	Methane Observation Networks with Innovative Technology to Obtain Reductions
MUST	Mock Urban Test Setting
MWIR	Mid-wave infrared
NDIR	Non-dispersive Infrared
NZMB	Non-zero minimum bootstrap
NGI	Near-field Gaussian plume inversion
OA-ICOS	Off axis integrated cavity output spectrometer
OGI	Optical gas imaging
OPLS	Open path laser spectrometer
OTM	Other test method
PID	Photo-ionization detector
PI-VFP	Path Integrated Vertical Flux Plane
PMT	Pollution mapping tool
PSG	Point source Gaussian
PSG-CS	Conditionally sampled point source Gaussian
PSG-RB	Recursive Bayesian point source Gaussian
PSG-SBM	PSG sequential Bayesian MCMC
QOGI	Quantitative Optical gas imaging
RANS	Reynolds averaged Navier Stokes
RB-LSI	Recursive Bayesian least squares inverse
RMLD	Remote methane leak detector
SDP	Source determination problem
SEBASS	Spatially-Enhanced Broadband Array Spectrograph System
SEM	Surface emission monitoring
SLAM	Simultaneous localization and mapping
STE	Source term estimation
sUAS	Unmanned aircraft system
SWIR	Short-wave infrared
TDLAS	Tunable diode laser absorption spectroscopy
TDM	Tracer dispersion method
TCM	Tracer correlation (or dilution) method
ATM	Atmospheric tracer method
TSEB	Two source energy balance
UA	Ultrasonic Anemometer
UGGA	LGR Ultraportable GHG analyzer
VCSEL	Vertical cavity surface emitting laser
VFP	Vertical Flux Plane
VRPM	Vertical Radial Plume Mapping Method
WRF	Weather Research and Forecasting Model

References

1. Alvarez, R.A.; Zavala-Araiza, D.; Lyon, D.R.; Allen, D.T.; Barkley, Z.R.; Brandt, A.R.; Davis, K.J.; Herndon, S.C.; Jacob, D.J.; Karion, A.; et al. Assessment of methane emissions from the US oil and gas supply chain. *Science* **2018**, *361*, 186–188.
2. Allen, D.T. Methane emissions from natural gas production and use: Reconciling bottom-up and top-down measurements. *Curr. Opin. Chem. Eng.* **2014**, *5*, 78–83. [CrossRef]

3. Allen, D.T.; Torres, V.M.; Thomas, J.; Sullivan, D.W.; Harrison, M.; Hendler, A.; Herndon, S.C.; Kolb, C.E.; Fraser, M.P.; Hill, A.D.; et al. Measurements of methane emissions at natural gas production sites in the United States. *Proc. Natl. Acad. Sci. USA* **2013**, *110*, 17768–17773. [CrossRef]

4. Allen, D. Measurements of methane emissions at natural gas production sites in the United States (Supplementary). *GPA Annu. Conv. Proc.* **2013**, *2013*, 36–50.

5. Christensen, J.; Olhoff, A. *Lessons from a Decade of Emissions Gap Assessments*; United Nations Environment Programme: Nairobi, Kenya, 2019; pp. 1–14.

6. Jones, K.L.; Tratt, D.M. Mapping methane super-emitters in oil and gas fields: A tiered remote sensing strategy. *arXiv* **2020**, arXiv:1011.1669v3.

7. Nemo, B.L. Renewed Focus on Landfill Calculations as Waste Industry Faces Pressure to Reduce Emissions. Available online: https://www.wastedive.com/news/landfill-emissions-greenhouse-gas-climate-change-esg/596313/ (accessed on 29 September 2021).

8. Nisbet, E.; Fisher, R.; Lowry, D.; France, J.; Allen, G.; Bakkaloglu, S.; Broderick, T.; Cain, M.; Coleman, M.; Fernandez, J.; et al. Methane mitigation: Methods to reduce emissions, on the path to the Paris Agreement. *Rev. Geophys.* **2020**, *58*, e2019RG000675. [CrossRef]

9. Morales, R.P.; Ravelid, J.; Brennan, K.P.; Tuzson, B.; Emmenegger, L.; Brunner, D. Estimating Local Methane Sources from Drone-Based Laser Spectrometer Measurements by Mass-Balance Method. In Proceedings of the EGU General Assembly Conference Abstracts, Online, 4–8 May 2020; p. 14778.

10. Manies, K.; Yates, E.; Christensen, L.; Fladeland, M.; Kolyer, R.; Euskirchen, E.; Waldrop, M. Can a drone equipped with a miniature methane sensor determine methane fluxes from an Alaskan wetland? *Earth Space Sci. Open Arch.* **2018**, doi:10.1002/essoar.10500765.1. [CrossRef]

11. Hollenbeck, D.; Manies, K.; Chen, Y.; Baldocchi, D.; Euskirchen, E.; Christensen, L. Evaluating a UAV-based mobile sensing system designed to quantify ecosystem-based methane. *Earth Space Sci. Open Arch.* **2021**, 15. [CrossRef]

12. Bastviken, D.; Cole, J.; Pace, M.; Tranvik, L. Methane emissions from lakes: Dependence of lake characteristics, two regional assessments, and a global estimate. *Glob. Biogeochem. Cycles* **2004**, *18*, 1–12. [CrossRef]

13. Kyzivat, E.D.; Smith, L.C.; Gleason, C.J.; Pavelsky, T.; Langhorst, T.; Fayne, J.V.; Kuhn, C.; Harlan, M.; Ishitsuka, Y.; Feng, D.; et al. Boreal Wetland Mapping by UAV to Upscale Greenhouse Gas Emissions. *AGU Fall Meet. Abstr.* **2019**, *2019*, B24F-01.

14. Kuhn, M. Methane Dynamics in Vernal Pools. Ph.D. Thesis, Wheaton College, Norton, MA, USA, 2015.

15. Holgerson, M.A.; Zappa, C.J.; Raymond, P.A. Substantial overnight reaeration by convective cooling discovered in pond ecosystems. *Geophys. Res. Lett.* **2016**, *43*, 8044–8051. [CrossRef]

16. Holgerson, M.A.; Farr, E.R.; Raymond, P.A. Gas transfer velocities in small forested ponds. *J. Geophys. Res. Biogeosci.* **2017**, *122*, 1011–1021. [CrossRef]

17. Kifner, L.H.; Calhoun, A.J.; Norton, S.A.; Hoffmann, K.E.; Amirbahman, A. Methane and carbon dioxide dynamics within four vernal pools in Maine, USA. *Biogeochemistry* **2018**, *139*, 275–291. [CrossRef]

18. Hodson, A.J.; Nowak, A.; Redeker, K.R.; Holmlund, E.S.; Christiansen, H.H.; Turchyn, A.V. Seasonal dynamics of Methane and Carbon Dioxide evasion from an open system pingo: Lagoon Pingo, Svalbard. *Front. Earth Sci.* **2019**, *7*, 30. [CrossRef]

19. McArthur, K.J. Using vegetation cover type to predict and scale peatland methane dynamics. *AGU Fall Abstr.* **2015**, *2015*, B41C-0454.

20. Oberle, F.K.; Gibbs, A.E.; Richmond, B.M.; Erikson, L.H.; Waldrop, M.P.; Swarzenski, P.W. Towards determining spatial methane distribution on Arctic permafrost bluffs with an unmanned aerial system. *SN Appl. Sci.* **2019**, *1*, 1–9. [CrossRef]

21. GASMET. *How to Measure Greenhouse Gas Soil Fluxes*; Gasmet Technologies Oy: Vantaa, Finland, 2020.

22. Pickering, D. *New Solutions for Landfill Surface Emissions Monitoring*; Waste Today; Valley View, OH, USA, 2021.

23. U.S. EPA. Draft Other Test Method 33A: Geospatial Measurement of Air Pollution, Remote Emissions Quantification—Direct Assessment (GMAP-REQ-DA). 2014. Available online: https://www3.epa.gov/ttnemc01/prelim/otm33a.pdf (accessed on 29 September 2021).

24. Luetschwager, E.; von Fischer, J.C.; Weller, Z.D. Characterizing detection probabilities of advanced mobile leak surveys: Implications for sampling effort and leak size estimation in natural gas distribution systems. *Elem. Sci. Anth.* **2021**, *9*, 00143. [CrossRef]

25. Maazallahi, H.; Fernandez, J.M.; Menoud, M.; Zavala-Araiza, D.; Weller, Z.D.; Schwietzke, S.; von Fischer, J.C.; Denier van der Gon, H.; Röckmann, T. Methane mapping, emission quantification, and attribution in two European cities: Utrecht (NL) and Hamburg (DE). *Atmos. Chem. Phys.* **2020**, *20*, 14717–14740. [CrossRef]

26. Weller, Z.D.; Yang, D.K.; von Fischer, J.C. An open source algorithm to detect natural gas leaks from mobile methane survey data. *PLoS ONE* **2019**, *14*, e0212287. [CrossRef]

27. MacKay, K.; Lavoie, M.; Bourlon, E.; Atherton, E.; O'Connell, E.; Baillie, J.; Fougère, C.; Risk, D. Methane emissions from upstream oil and gas production in Canada are underestimated. *Sci. Rep.* **2021**, *11*, 8041. [CrossRef]

28. Mønster, J.G.; Samuelsson, J.; Kjeldsen, P.; Rella, C.W.; Scheutz, C. Quantifying methane emission from fugitive sources by combining tracer release and downwind measurements—A sensitivity analysis based on multiple field surveys. *Waste Manag.* **2014**, *34*, 1416–1428. [CrossRef] [PubMed]

29. Riquetti, P.V.; Fletcher, J.I.; Minty, C.D. Aerial Surveillance for Gas and Liquid Hydrocarbon Pipelines Using a Flame Ionization Detector (FID). In Proceedings of the 1996 1st International Pipeline Conference, Calgary, AB, Canada, 9–13 June 1996; American Society of Mechanical Engineers: New York, NY, USA, 1996; Volume 2, pp. 681–687.

30. Thorpe, A.K.; Frankenberg, C.; Thompson, D.R.; Duren, R.M.; Aubrey, A.D.; Bue, B.D.; Green, R.O.; Gerilowski, K.; Krings, T.; Borchardt, J.; et al. Airborne DOAS retrievals of methane, carbon dioxide, and water vapor concentrations at high spatial resolution: Application to AVIRIS-NG. *Atmos. Meas. Tech.* **2017**, *10*, 3833–3850. [CrossRef]

31. Thorpe, A.; Frankenberg, C.; Roberts, D. Retrieval techniques for airborne imaging of methane concentrations using high spatial and moderate spectral resolution: Application to AVIRIS. *Atmos. Meas. Tech.* **2014**, *7*, 491–506. [CrossRef]

32. Rafiq, T.; Duren, R.M.; Thorpe, A.K.; Foster, K.; Patarsuk, R.; Miller, C.E.; Hopkins, F.M. Attribution of methane point source emissions using airborne imaging spectroscopy and the Vista-California methane infrastructure dataset. *Environ. Res. Lett.* **2020**, *15*, 124001. [CrossRef]

33. Cambaliza, M.; Shepson, P.; Caulton, D.; Stirm, B.; Samarov, D.; Gurney, K.; Turnbull, J.; Davis, K.; Possolo, A.; Karion, A.; et al. Assessment of uncertainties of an aircraft-based mass balance approach for quantifying urban greenhouse gas emissions. *Atmos. Chem. Phys.* **2014**, *14*, 9029–9050. [CrossRef]

34. Gasbarra, D.; Toscano, P.; Famulari, D.; Finardi, S.; Di Tommasi, P.; Zaldei, A.; Carlucci, P.; Magliulo, E.; Gioli, B. Locating and quantifying multiple landfills methane emissions using aircraft data. *Environ. Pollut.* **2019**, *254*, 112987. [CrossRef]

35. Johnson, M.R.; Tyner, D.R.; Szekeres, A.J. Blinded evaluation of airborne methane source detection using Bridger Photonics LiDAR. *Remote Sens. Environ.* **2021**, *259*, 112418. [CrossRef]

36. Kemp, C.E.; Ravikumar, A.P.; Brandt, A.R. Comparing natural gas leakage detection technologies using an open-source "virtual gas field" simulator. *Environ. Sci. Technol.* **2016**, *50*, 4546–4553. [CrossRef]

37. Allen, D.; Stokes, S.; Tullos, E.; Smith, B.; Herndon, S.; Flowers, B. Field Trial of Methane Emission Quantification Technologies. In Proceedings of the SPE Annual Technical Conference and Exhibition, Virtual, 26–29 October 2020; Society of Petroleum Engineers: Houston, TX, USA, 2020.

38. Ravikumar, A.P.; Wang, J.; Brandt, A.R. Are optical gas imaging technologies effective for methane leak detection? *Environ. Sci. Technol.* **2017**, *51*, 718–724. [CrossRef]

39. Leifer, I.; Melton, C.; Fischer, M.L.; Fladeland, M.; Frash, J.; Gore, W.; Iraci, L.T.; Marrero, J.E.; Ryoo, J.M.; Tanaka, T.; et al. Atmospheric characterization through fused mobile airborne and surface in situ surveys: Methane emissions quantification from a producing oil field. *Atmos. Meas. Tech.* **2018**, *11*, 1689–1705. [CrossRef]

40. Mommert, M.; Sigel, M.; Neuhausler, M.; Scheibenreif, L.; Borth, D. Characterization of Industrial Smoke Plumes from Remote Sensing Data. *arXiv* **2020**, arXiv:2011.11344.

41. Gómez-Carracedo, M.; Fernández-Varela, R.; Ballabio, D.; Andrade, J. Screening oil spills by mid-IR spectroscopy and supervised pattern recognition techniques. *Chemom. Intell. Lab. Syst.* **2012**, *114*, 132–142. [CrossRef]

42. Hirst, B.; Randell, D.; Jones, M.; Chu, J.; Kannath, A.; Macleod, N.; Dean, M.; Weidmann, D. Methane emissions: Remote mapping and source quantification using an open-path laser dispersion spectrometer. *Geophys. Res. Lett.* **2020**, *47*, e2019GL086725. [CrossRef]

43. Lilienthal, A.J.; Reggente, M.; Trincavelli, M.; Blanco, J.L.; Gonzalez, J. A statistical approach to gas distribution modeling with mobile robots-the kernel dm+ v algorithm. In Proceedings of the 2009 IEEE/RSJ International Conference on Intelligent Robots and Systems, St. Louis, MO, USA, 10–15 October 2009; pp. 570–576.

44. Lilienthal, A.J.; Loutfi, A.; Blanco, J.L.; Galindo, C.; Gonzalez, J. A rao-blackwellisation approach to GDM-SLAM: Integrating SLAM and gas distribution mapping (GDM). In Proceedings of the 3rd European Conference on Mobile Robots, ECMR'07, Freiburg, Germany, 19–21 September 2017; pp. 126–131.

45. Neumann, P.P. Gas Source Localization and Gas Distribution Mapping with a Micro-Drone. Ph.D. Thesis, Bundesanstalt für Materialforschung und-prüfung (BAM), Berlin, Germany, 2013.

46. Luo, B.; Meng, Q.H.; Wang, J.Y.; Ma, S.G. Simulate the aerodynamic olfactory effects of gas-sensitive UAVs: A numerical model and its parallel implementation. *Adv. Eng. Softw.* **2016**, *102*, 123–133. [CrossRef]

47. Ojeda, P.; Monroy, J.; Gonzalez-Jimenez, J. An evaluation of gas source localization algorithms for mobile robots. In Proceedings of the 3rd International Conference on Applications of Intelligent Systems, Las Palmas de Gran Canaria, Spain, 7–9 January 2020; pp. 1–6.

48. Arain, M.A.; Hernandez Bennetts, V.; Schaffernicht, E.; Lilienthal, A.J. Sniffing out fugitive methane emissions: Autonomous remote gas inspection with a mobile robot. *Int. J. Robot. Res.* **2021**, *40*, 782–814. [CrossRef]

49. Berman, E.S.; Fladeland, M.; Liem, J.; Kolyer, R.; Gupta, M. Greenhouse gas analyzer for measurements of carbon dioxide, methane, and water vapor aboard an unmanned aerial vehicle. *Sens.... Actuators B Chem.* **2012**, *169*, 128–135. [CrossRef]

50. Court, J. Estimation of the Concentration from a Moving Gaseous Source in the Atmosphere Using a Guided Sensing Aerial Vehicle. Ph.D. Thesis, Worcester Polytechnic Institute, Worcester, MA, USA, 2012.

51. Khan, A.; Schaefer, D.; Roscoe, B.; Sun, K.; Tao, L.; Miller, D.; Lary, D.J.; Zondlo, M.A. Open-path greenhouse gas sensor for UAV applications. In *CLEO: Applications and Technology*; Optical Society of America: Washington, DC, USA, 2012; p. JTh1L–6.

52. Amici, S.; Turci, M.; Giammanco, S.; Spampinato, L.; Giulietti, F. UAV thermal infrared remote sensing of an Italian mud volcano. *Adv. Remote Sens.* **2013**, *2*, 358–364. [CrossRef]

53. Lindgren, P.; Grosse, G.; Walter Anthony, K.; Meyer, F. Detection and spatiotemporal analysis of methane ebullition on thermokarst lake ice using high-resolution optical aerial imagery. *Biogeosciences* **2016**, *13*, 27–44. [CrossRef]
54. Araujo, M.; Siebenaler, S.; Baldor, S.; Dupont, E.; Davila, D.; Blaisdell, S. Automated Small Leak Detection from Hazardous Liquid Pipelines Using Multi-Platform Remote Sensing. In Proceedings of the 11th Pipeline Technology Conference, Estrel, Berlin, Germany, 23–25 May 2016; Volume 2016.
55. Barchyn, T.E.; Hugenholtz, C.H.; Myshak, S.; Bauer, J. A UAV-based system for detecting natural gas leaks. *J. Unmanned Veh. Syst.* **2017**, *6*, 18–30. [CrossRef]
56. Aurell, J.; Mitchell, W.; Chirayath, V.; Jonsson, J.; Tabor, D.; Gullett, B. Field determination of multipollutant, open area combustion source emission factors with a hexacopter unmanned aerial vehicle. *Atmos. Environ.* **2017**, *166*, 433–440. [CrossRef]
57. Andersen, T.; Scheeren, B.; Peters, W.; Chen, H. A UAV-based active AirCore system for measurements of greenhouse gases. *Atmos. Meas. Tech.* **2018**, *11*, 2683–2699. [CrossRef]
58. Gargiulo, G.; Martin, A. Detection of landfill gas emissions using drones. *Air Qual. Clim. Chang.* **2019**, *53*, 16.
59. Neumann, P.P.; Kohlhoff, H.; Hüllmann, D.; Krentel, D.; Kluge, M.; Dzierliński, M.; Lilienthal, A.J.; Bartholmai, M. Aerial-based gas tomography–from single beams to complex gas distributions. *Eur. J. Remote Sens.* **2019**, *52*, 2–16. [CrossRef]
60. Bel Hadj Ali, N.; Abichou, T.; Green, R. Comparing estimates of fugitive landfill methane emissions using inverse plume modeling obtained with Surface Emission Monitoring (SEM), Drone Emission Monitoring (DEM), and Downwind Plume Emission Monitoring (DWPEM). *J. Air Waste Manag. Assoc.* **2020**, *70*, 410–424. [CrossRef]
61. Araujo, J.O.; Valente, J.; Kooistra, L.; Munniks, S.; Peters, R.J. Experimental flight patterns evaluation for a UAV-based air pollutant sensor. *Micromachines* **2020**, *11*, 768. [CrossRef]
62. Daugėla, I.; Visockienė, J.S.; Kumpienė, J. Detection and analysis of methane emissions from a landfill using unmanned aerial drone systems and semiconductor sensors. *Detritus-Multidiscip. J. Waste Resour. Residues* **2020**, *10*, 127–138.
63. Li, H.Z.; Mundia-Howe, M.; Reeder, M.D.; Pekney, N.J. Gathering pipeline methane emissions in utica shale using an unmanned aerial vehicle and ground-based mobile sampling. *Atmosphere* **2020**, *11*, 716. [CrossRef]
64. Li, C.; Han, W.; Peng, M.; Zhang, M.; Yao, X.; Liu, W.; Wang, T. An Unmanned Aerial Vehicle-Based Gas Sampling System for Analyzing CO2 and Atmospheric Particulate Matter in Laboratory. *Sensors* **2020**, *20*, 1051. [CrossRef] [PubMed]
65. D'hont, B.; Calders, K.; Bartholomeus, H.; Whiteside, T.; Bartolo, R.; Levick, S.; Krishna Moorthy, S.M.; Terryn, L.; Verbeeck, H. Characterising Termite Mounds in a Tropical Savanna with UAV Laser Scanning. *Remote Sens.* **2021**, *13*, 476. [CrossRef]
66. Reuter, M.; Bovensmann, H.; Buchwitz, M.; Borchardt, J.; Krautwurst, S.; Gerilowski, K.; Lindauer, M.; Kubistin, D.; Burrows, J.P. Development of a small unmanned aircraft system to derive CO2 emissions of anthropogenic point sources. *Atmos. Meas. Tech.* **2021**, *14*, 153–172. [CrossRef]
67. Pajares, G. Overview and current status of remote sensing applications based on unmanned aerial vehicles (UAVs). *Photogramm. Eng. Remote Sens.* **2015**, *81*, 281–330. [CrossRef]
68. Hutchinson, M.; Oh, H.; Chen, W.H. A review of source term estimation methods for atmospheric dispersion events using static or mobile sensors. *Inf. Fusion* **2017**, *36*, 130–148. [CrossRef]
69. Burgués, J.; Marco, S. Environmental chemical sensing using small drones: A review. *Sci. Total Environ.* **2020**, *748*, 141172. [CrossRef] [PubMed]
70. Mønster, J.; Kjeldsen, P.; Scheutz, C. Methodologies for measuring fugitive methane emissions from landfills—A review. *Waste Manag.* **2019**, *87*, 835–859. [CrossRef] [PubMed]
71. Cui, Y.Y.; Brioude, J.; McKeen, S.A.; Angevine, W.M.; Kim, S.W.; Frost, G.J.; Ahmadov, R.; Peischl, J.; Bousserez, N.; Liu, Z.; et al. Top-down estimate of methane emissions in California using a mesoscale inverse modeling technique: The South Coast Air Basin. *J. Geophys. Res. Atmos.* **2015**, *120*, 6698–6711. [CrossRef]
72. Bakkaloglu, S.; Lowry, D.; Fisher, R.E.; France, J.L.; Brunner, D.; Chen, H.; Nisbet, E.G. Quantification of methane emissions from UK biogas plants. *Waste Manag.* **2021**, *124*, 82–93. [CrossRef]
73. Drotman, C. Updates to GHG Regulations and Impacts to the Waste Industry. 2021. Available online: https://wasteadvantagemag.com/updates-to-ghg-regulations-and-impacts-to-the-waste-industry/ (accessed on 29 September 2021).
74. Ko, J.H.; Xu, Q.; Jang, Y.C. Emissions and control of hydrogen sulfide at landfills: A review. *Crit. Rev. Environ. Sci. Technol.* **2015**, *45*, 2043–2083. [CrossRef]
75. Czepiel, P.; Mosher, B.; Harriss, R.; Shorter, J.; McManus, J.; Kolb, C.; Allwine, E.; Lamb, B. Landfill methane emissions measured by enclosure and atmospheric tracer methods. *J. Geophys. Res. Atmos.* **1996**, *101*, 16711–16719. [CrossRef]
76. Cambaliza, M.O.L.; Bogner, J.E.; Green, R.B.; Shepson, P.B.; Harvey, T.A.; Spokas, K.A.; Stirm, B.H.; Corcoran, M.; Helmig, D.; Wisthaler, A. Field measurements and modeling to resolve m2 to km2 CH4 emissions for a complex urban source: An Indiana landfill study. *Elem. Sci. Anthr.* **2017**, *5*, 36. [CrossRef]
77. Babilotte, A. *Field Comparison of Methods for Assessment of Methane Fugitive Emissions from Landfills*; Environmental Research and Education Foundation (EREF): Raleigh, NC, USA, 2011.
78. Bourn, M.; Allen, G.; Hollingsworth, P.; Kababbe, K.; Williams, P.I.; Ricketts, H.; Pitt, J.R.; Shah, A. The development of an unmanned aerial system for the measurement of methane emissions from landfill. In Proceedings of the Sixteenth International Waste Management and Landfill Symposium, S. Margherita di Pula, Cagliari, Italy, 2–6 October 2018.
79. Fjelsted, L.; Christensen, A.; Larsen, J.; Kjeldsen, P.; Scheutz, C. Assessment of a landfill methane emission screening method using an unmanned aerial vehicle mounted thermal infrared camera—A field study. *Waste Manag.* **2019**, *87*, 893–904. [CrossRef]

80. Irandoost, E. An Investigation on Methane Flux in Landfills and Correlation with Surface Methane Concentration. Master's Thesis, Schulich School of Engineering, Calgary, AB, Canada 2020.
81. Lando, A.T.; Nakayama, H.; Shimaoka, T. Application of portable gas detector in point and scanning method to estimate spatial distribution of methane emission in landfill. *Waste Manag.* **2017**, *59*, 255–266. [CrossRef]
82. Rees-White, T.; Mønster, J.; Beaven, R.; Scheutz, C. Measuring methane emissions from a UK landfill using the tracer dispersion method and the influence of operational and environmental factors. *Waste Manag.* **2019**, *87*, 870–882. [CrossRef]
83. Arroyo-Mora, J.P.; Kalacska, M.; Lucanus, O.; Soffer, R.; Leblanc, G. Spectro-spatial relationship between UAV derived high resolution DEM and SWIR hyperspectral data: Application to an ombrotrophic peatland. In Proceedings of the Remote Sensing for Agriculture, Ecosystems, and Hydrology XIX, Warsaw, Poland, 11–14 September 2017; International Society for Optics and Photonics: Bellingham, WA, USA, 2017; Volume 10421, p. 104210.
84. Lehmann, J.R.; Münchberger, W.; Knoth, C.; Blodau, C.; Nieberding, F.; Prinz, T.; Pancotto, V.A.; Kleinebecker, T. High-resolution classification of south patagonian peat bog microforms reveals potential gaps in up-scaled CH4 fluxes by use of Unmanned Aerial System (UAS) and CIR imagery. *Remote Sens.* **2016**, *8*, 173. [CrossRef]
85. Fall, T.; Heiden, K.; Smyth, A.R.; Brym, Z.; Adamczyk, B. Greenhouse Gas Emissions from Subtropical Agriculture Fields Decrease Over Time. *Exp. Results* **2021**, *2*, 1–8. [CrossRef]
86. Daniels, F. Meeting Review: AMS Workshop on Stability Classification Schemes and Sigma Curves—Summary of Recommendations. *Am. Meteorol. Soc.* **1977**, *58*, 1305–1309.
87. Pasquill, F; Smith F.B. *Atmospheric Diffusion*; Ellis Hardwood Ltd.: Liverpool, UK, 1983.
88. Foster-Wittig, T.A.; Thoma, E.D.; Albertson, J.D. Estimation of point source fugitive emission rates from a single sensor time series: A conditionally-sampled Gaussian plume reconstruction. *Atmos. Environ.* **2015**, *115*, 101–109. [CrossRef]
89. Gryning, S.E.; Holtslag, A.; Irwin, J.S.; Sivertsen, B. Applied dispersion modeling based on meteorological scaling parameters. *Atmos. Environ. (1967)* **1987**, *21*, 79–89. [CrossRef]
90. Foken, T. 50 years of the Monin–Obukhov similarity theory. *Bound.-Layer Meteorol.* **2006**, *119*, 431–447. [CrossRef]
91. Fjelsted, L.; Thomasen, T.; Valbjørn, I.; Scheutz, C.; Christensen, A.; Kjeldsen, P. Development of an innovative UAV-mounted screening tool for landfill gas emissions. In Proceedings of the Sardinia 2015-15th International Waste Management and Landfill Symposium, S. Margherita di Pula, Cagliari, Italy, 5–9 October 2015; CISA Publisher: Padua, Italy, 2015.
92. Gagnon, J.P. *Quantification of VOC Emissions Using Remote Thermal Infrared Hyperspectral Imaging*; Telops, Jean Baptiste: Québec, QC, Canada, 2020.
93. Gålfalk, M.; Olofsson, G.; Crill, P.; Bastviken, D. Making methane visible. *Nat. Clim. Chang.* **2016**, *6*, 426–430. [CrossRef]
94. Christensen, L.E. Miniature Tunable Laser Spectrometer for Detection of a Trace Gas. U.S. Patent 9,671,332, 6 June 2017.
95. Emran, B.J.; Tannant, D.D.; Najjaran, H. Low-altitude aerial methane concentration mapping. *Remote Sens.* **2017**, *9*, 823. [CrossRef]
96. Flesch, T.K.; McGinn, S.M.; Chen, D.; Wilson, J.D.; Desjardins, R.L. Data filtering for inverse dispersion emission calculations. *Agric. For. Meteorol.* **2014**, *198*, 1–6. [CrossRef]
97. DeBruyn, Z.J.; Wagner-Riddle, C.; VanderZaag, A. Assessment of open-path spectrometer accuracy at low path-integrated methane concentrations. *Atmosphere* **2020**, *11*, 184. [CrossRef]
98. Bretschneider, T.R.; Shetti, K. UAV-based gas pipeline leak detection. In Proceedings of the 35th Asian Conference on Remote Sensing 2014, ACRS 2014: Sensing for Reintegration of Societies, Nyaung Lay Pin, Myanmar, 27–31 October 2014.
99. Bastviken, D. Supplement of Technical Note: Cost-efficient approaches to measure carbon dioxide (CO_2) fluxes and concentrations in terrestrial and aquatic environments using mini loggers. *Suppl. Biogeosci.* **2015**, *12*, 3849–3859. [CrossRef]
100. Bastviken, D.; Sundgren, I.; Natchimuthu, S.; Reyier, H.; Gålfalk, M. Cost-efficient approaches to measure carbon dioxide (CO2) fluxes and concentrations in terrestrial and aquatic environments using mini loggers. *Biogeosciences* **2015**, *12*, 3849–3859. [CrossRef]
101. Bastviken, D.; Nygren, J.; Schenk, J.; Parellada Massana, R.; Thanh Duc, N. Technical note: Facilitating the use of low-cost methane (ch4) sensors in flux chambers-calibration, data processing, and an open-source make-it-yourself logger. *Biogeosciences* **2020**, *17*, 3659–3667. [CrossRef]
102. Carrozzo, M.; De Vito, S.; Esposito, E.; Salvato, M.; Formisano, F.; Massera, E.; Di Francia, G.; Veneri, P.D.; Iadaresta, M.; Mennella, A. UAV intelligent chemical multisensor payload for networked and impromptu gas monitoring tasks. In Proceedings of the 5th IEEE International Workshop on Metrology for AeroSpace, MetroAeroSpace, Rome, Italy, 20–22 June 2018; pp. 112–116. [CrossRef]
103. Arduini, F.; Cinti, S.; Scognamiglio, V.; Moscone, D.; Palleschi, G. How cutting-edge technologies impact the design of electrochemical (bio) sensors for environmental analysis. A review. *Anal. Chim. Acta* **2017**, *959*, 15–42. [CrossRef] [PubMed]
104. Karakaya, D.; Ulucan, O.; Turkan, M. Electronic nose and its applications: A survey. *Int. J. Autom. Comput.* **2020**, *17*, 179–209. [CrossRef]
105. Honeycutt, W.T.; Ley, M.T.; Materer, N.F. Precision and limits of detection for selected commercially available, low-cost carbon dioxide and methane gas sensors. *Sensors* **2019**, *19*, 3157. [CrossRef]
106. Kim, Y.M.; Park, M.H.; Jeong, S.; Lee, K.H.; Kim, J.Y. Evaluation of error inducing factors in unmanned aerial vehicle mounted detector to measure fugitive methane from solid waste landfill. *Waste Manag.* **2021**, *124*, 368–376. [CrossRef]

107. Hollenbeck, D.; Nunez, G.; Christensen, L.E.; Chen, Y. Wind measurement and estimation with small unmanned aerial systems (suas) using on-board mini ultrasonic anemometers. In Proceedings of the 2018 International Conference on Unmanned Aircraft Systems (ICUAS), Dallas, TX, USA, 12–15 June 2018; pp. 285–292.

108. Thielicke, W.; Hübert, W.; Müller, U.; Eggert, M.; Wilhelm, P. Towards accurate and practical drone-based wind measurements with an ultrasonic anemometer. *Atmos. Meas. Tech.* **2021**, *14*, 1303–1318. [CrossRef]

109. Hollenbeck, D.; Oyama, M.; Garcia, A.; Chen, Y. Pitch and roll effects of on-board wind measurements using sUAS. In Proceedings of the 2019 International Conference on Unmanned Aircraft Systems (ICUAS), Atlanta, GA, USA, 12–14 June 2019; pp. 1249–1254.

110. Bruschi, P.; Piotto, M.; Dell'Agnello, F.; Ware, J.; Roy, N. Wind speed and direction detection by means of solid-state anemometers embedded on small quadcopters. *Procedia Eng.* **2016**, *168*, 802–805. [CrossRef]

111. González-Rocha, J.; De Wekker, S.F.; Ross, S.D.; Woolsey, C.A. Wind profiling in the lower atmosphere from wind-induced perturbations to multirotor UAS. *arXiv* **2020**, arXiv:2001.02740.

112. Ingenhorst, C.; Jacobs, G.; Stößel, L.; Schelenz, R.; Juretzki, B. Method for airborne measurement of the spatial wind speed distribution above complex terrain. *Wind Energy Sci.* **2021**, *6*, 427–440. [CrossRef]

113. Brewer, M.J.; Clements, C.B. Meteorological profiling in the fire environment using UAS. *Fire* **2020**, *3*, 36. [CrossRef]

114. Calmer, R.; Roberts, G.C.; Preissler, J.; Sanchez, K.J.; Derrien, S.; O'Dowd, C. Vertical wind velocity measurements using a five-hole probe with remotely piloted aircraft to study aerosol–cloud interactions. *Atmos. Meas. Tech.* **2018**, *11*, 2583–2599. [CrossRef]

115. Brosy, C.; Krampf, K.; Zeeman, M.; Wolf, B.; Junkermann, W.; Schäfer, K.; Emeis, S.; Kunstmann, H. Simultaneous multicopter-based air sampling and sensing of meteorological variables. *Atmos. Meas. Tech.* **2017**, *10*, 2773–2784. [CrossRef]

116. Brosy, C. Hexacopter-Based Three-Dimensional Measurements of Hydrometeorological Variables and Methane. Ph.D. Thesis, Universität Augsburg, Augsburg, Germany, 2019.

117. Tian, P.; Chao, H.; Rhudy, M.; Gross, J.; Wu, H. Wind Sensing and Estimation Using Small Fixed-Wing Unmanned Aerial Vehicles: A Survey. *J. Aerosp. Inf. Syst.* **2021**, *18*, 132–143.

118. Stark, B.; Smith, B.; Chen, Y. A guide for selecting small unmanned aerial systems for research-centric applications. *IFAC Proc. Vol.* **2013**, *46*, 38–45. [CrossRef]

119. Smith, B.; John, G.; Stark, B.; Christensen, L.E.; Chen, Y. Applicability of unmanned aerial systems for leak detection. In Proceedings of the 2016 International Conference on Unmanned Aircraft Systems (ICUAS), Arlington, VA, USA, 7–10 June 2016; pp. 1220–1227.

120. Hollenbeck, D.; Chen, Y. Characterization of ground-to-air emissions with sUAS using a digital twin framework. In Proceedings of the 2020 International Conference on Unmanned Aircraft Systems (ICUAS), Athens, Greece, 1–4 September 2020; pp. 1162–1166. [CrossRef]

121. Yang, S.; Talbot, R.W.; Frish, M.B.; Golston, L.M.; Aubut, N.F.; Zondlo, M.A.; Gretencord, C.; McSpiritt, J. Natural gas fugitive leak detection using an unmanned aerial vehicle: Measurement system description and mass balance approach. *Atmosphere* **2018**, *9*, 383. [CrossRef]

122. Holmes, N.S.; Morawska, L. A review of dispersion modeling and its application to the dispersion of particles: An overview of different dispersion models available. *Atmos. Environ.* **2006**, *40*, 5902–5928. [CrossRef]

123. Arndt, C.; Leytem, A.; Hristov, A.; Zavala-Araiza, D.; Cativiela, J.; Conley, S.; Daube, C.; Faloona, I.; Herndon, S. Short-term methane emissions from 2 dairy farms in California estimated by different measurement techniques and US Environmental Protection Agency inventory methodology: A case study. *J. Dairy Sci.* **2018**, *101*, 11461–11479. [CrossRef] [PubMed]

124. Flesch, T.K.; Wilson, J.D.; Yee, E. Backward-time Lagrangian stochastic dispersion models and their application to estimate gaseous emissions. *J. Appl. Meteorol. Climatol.* **1995**, *34*, 1320–1332. [CrossRef]

125. Flesch, T.; Wilson, J.; Harper, L. Deducing ground-to-air emissions from observed trace gas concentrations: A field trial with wind disturbance. *J. Appl. Meteorol.* **2005**, *44*, 475–484. [CrossRef]

126. Flesch, T.K; Wilson, J.D; Harper, L.A; Crenna, B.P; Sharpe, R.R. Deducing ground-to-air emissions from observed trace gas concentrations: A field trial. *J. Appl. Meteorol.* **2004**, *43*, 487–502. [CrossRef]

127. Ro, K.S.; Johnson, M.H.; Stone, K.C.; Hunt, P.G.; Flesch, T.; Todd, R.W. Measuring gas emissions from animal waste lagoons with an inverse-dispersion technique. *Atmos. Environ.* **2013**, *66*, 101–106. [CrossRef]

128. Hunter, C. *A Recommended Pasquill-Gifford Stability Classification Method for Safety Basis Atmospheric Dispersion Modeling at SRS*; Technical Report; Savannah River Site (SRS): Aiken, SC, USA, 2012.

129. Edie, R.; Robertson, A.M.; Field, R.A.; Soltis, J.; Snare, D.A.; Zimmerle, D.; Bell, C.S.; Vaughn, T.L.; Murphy, S.M. Constraining the accuracy of flux estimates using OTM 33A. *Atmos. Meas. Tech.* **2020**, *13*, 341–353. [CrossRef]

130. Edie, R.; Robertson, A.M.; Soltis, J.; Field, R.A.; Snare, D.; Burkhart, M.D.; Murphy, S.M. Off-site flux estimates of volatile organic compounds from oil and gas production facilities using fast-response instrumentation. *Environ. Sci. Technol.* **2019**, *54*, 1385–1394. [CrossRef]

131. Van Ulden, A. Simple estimates for vertical diffusion from sources near the ground. *Atmos. Environ. (1967)* **1978**, *12*, 2125–2129. [CrossRef]

132. Eckman, R.M. Re-examination of empirically derived formulas for horizontal diffusion from surface sources. *Atmos. Environ.* **1994**, *28*, 265–272. [CrossRef]

133. Albertson, J.D.; Harvey, T.; Foderaro, G.; Zhu, P.; Zhou, X.; Ferrari, S.; Amin, M.S.; Modrak, M.; Brantley, H.; Thoma, E.D. A mobile sensing approach for regional surveillance of fugitive methane emissions in oil and gas production. *Environ. Sci. Technol.* **2016**, *50*, 2487–2497. [CrossRef]

134. Gemerek, J.R.; Ferrari, S.; Albertson, J.D. Fugitive gas emission rate estimation using multiple heterogeneous mobile sensors. In Proceedings of the 2017 ISOCS/IEEE International Symposium on Olfaction and Electronic Nose (ISOEN), Montreal, QC, Canada, 28–31 May 2017; pp. 1–3.

135. Yee, E.; Flesch, T.K. Inference of emission rates from multiple sources using Bayesian probability theory. *J. Environ. Monit.* **2010**, *12*, 622–634. [CrossRef] [PubMed]

136. Brantley, H.L.; Thoma, E.D.; Squier, W.C.; Guven, B.B.; Lyon, D. Assessment of methane emissions from oil and gas production pads using mobile measurements. *Environ. Sci. Technol.* **2014**, *48*, 14508–14515. [CrossRef] [PubMed]

137. Yee, E. Probability theory as logic: Data assimilation for multiple source reconstruction. *Pure Appl. Geophys.* **2012**, *169*, 499–517. [CrossRef]

138. Zhou, X.; Yoon, S.; Mara, S.; Falk, M.; Kuwayama, T.; Tran, T.; Cheadle, L.; Nyarady, J.; Croes, B.; Scheehle, E.; et al. Mobile sampling of methane emissions from natural gas well pads in California. *Atmos. Environ.* **2021**, *244*, 117930. [CrossRef]

139. Hutchinson, M.; Liu, C.; Chen, W.H. Source term estimation of a hazardous airborne release using an unmanned aerial vehicle. *J. Field Robot.* **2019**, *36*, 797–817. [CrossRef]

140. Shah, A.; Allen, G.; Pitt, J.R.; Ricketts, H.; Williams, P.I.; Helmore, J.; Finlayson, A.; Robinson, R.; Kabbabe, K.; Hollingsworth, P.; et al. A near-field Gaussian plume inversion flux quantification method, applied to unmanned aerial vehicle sampling. *Atmosphere* **2019**, *10*, 396. [CrossRef]

141. Shah, A. Supplement to A Near-Field Gaussian Plume Inversion Flux Quantification Method, Suitable For Unmanned Aerial Vehicle Sampling. *arXiv* **2020**, arXiv:1011.1669v3.

142. Allen, G.; Hollingsworth, P.; Kabbabe, K.; Pitt, J.R.; Mead, M.I.; Illingworth, S.; Roberts, G.; Bourn, M.; Shallcross, D.E.; Percival, C.J. The development and trial of an unmanned aerial system for the measurement of methane flux from landfill and greenhouse gas emission hotspots. *Waste Manag.* **2019**, *87*, 883–892. [CrossRef]

143. France, J.L.; Bateson, P.; Dominutti, P.; Allen, G.; Andrews, S.; Bauguitte, S.; Coleman, M.; Lachlan-Cope, T.; Fisher, R.E.; Huang, L.; et al. Facility level measurement of offshore oil and gas installations from a medium-sized airborne platform: Method development for quantification and source identification of methane emissions. *Atmos. Meas. Tech.* **2021**, *14*, 71–88. [CrossRef]

144. Ravikumar, A.P.; Sreedhara, S.; Wang, J.; Englander, J.; Roda-Stuart, D.; Bell, C.; Zimmerle, D.; Lyon, D.; Mogstad, I.; Ratner, B.; et al. Single-blind inter-comparison of methane detection technologies–results from the Stanford/EDF Mobile Monitoring Challenge. *Elem. Sci. Anthr.* **2019**, *7*, 37. [CrossRef]

145. Shah, A.; Allen, G.; Ricketts, H.; Pitt, J.; Williams, P. Methane flux quantification from lactating cattle using unmanned aerial vehicles. *Eur. Geophys. Union* **2018**, *20*, 7655.

146. Shah, A.A. Methane Flux Quantification Using Unmanned Aerial Vehicles. Ph.D. Thesis, University of Manchester, Manchester, UK, 2020.

147. Whiticar, M.; Hollenbeck, D.; Billwiller, B.; Salas, C.; Christensen, L. Application of the BC GHGMapper™ platform for the Alberta Methane Field Challenge (AMFC). In *Geoscience BC Summary of Activities 2019: Energy and Water, Geoscience BC, Report 2020-02*; EERI: Vancouver, BC, Canada, 2020; pp. 87–102.

148. Whiticar, M.; Christensen, L.; Salas, C.; Reece, P. Ghgmap: Detection of fugitive methane leaks from natural gas pipelines British Columbia and Alberta. In *Geoscience BC Summary of Activities 2018: Energy and Water, Geoscience BC, Report 2019-2*; EERI: Vancouver, BC, Canada, 2019; pp. 67–76.

149. Whiticar, M.; Christensen, L.; Salas, C.; Reece, P. GHGMap: Novel approach for aerial measurements of greenhouse gas emissions British Columbia. In *Geoscience BC Summary of Activities 2017: Energy, Geoscience BC, Report 2018-4*; EERI: Vancouver, BC Canada, 2018; pp. 1–10.

150. Cressie, N. Kriging nonstationary data. *J. Am. Stat. Assoc.* **1986**, *81*, 625–634. [CrossRef]

151. Wackernagel, H. Ordinary Kriging. In *Multivariate Geostatistics*; Springer: Berlin/Heidelberg, Germany, 2003; pp. 79–88.

152. Fuentes, M. A high frequency kriging approach for non-stationary environmental processes. *Environm. Off. J. Int. Environm. Soc.* **2001**, *12*, 469–483. [CrossRef]

153. Lebrenz, H.; Bárdossy, A. Geostatistical interpolation by quantile kriging. *Hydrol. Earth Syst. Sci.* **2019**, *23*, 1633–1648. [CrossRef]

154. Lu, G.Y.; Wong, D.W. An adaptive inverse-distance weighting spatial interpolation technique. *Comput. Geosci.* **2008**, *34*, 1044–1055. [CrossRef]

155. Mazzella, A.; Mazzella, A. The importance of the model choice for experimental semivariogram modeling and its consequence in evaluation process. *J. Eng.* **2013**, *2013*, 960105. [CrossRef]

156. Goovaerts, P. Kriging and semivariogram deconvolution in the presence of irregular geographical units. *Math. Geosci.* **2008**, *40*, 101–128. [CrossRef]

157. Cossel, K.C.; Waxman, E.M.; Hoenig, E.; Cermak, M.; Choate, C.; Hesselius, D.; Coddington, I.; Newbury, N.R. Micrometeorological flux measurements using spatially- scanned open-path dual-comb spectroscopy.Optical Sensors and Sensing Congress, Virtual, 22–26 June 2020; Volume 2020, p. EM3C.2. [CrossRef]

158. Ryoo, J.M.; Iraci, L.T.; Tanaka, T.; Marrero, J.E.; Yates, E.L.; Fung, I.; Michalak, A.M.; Tadić, J.; Gore, W.; Bui, T.P.; et al. Quantification of CO2 and CH4 emissions over Sacramento, California, based on divergence theorem using aircraft measurements. *Atmos. Meas. Tech.* **2019**, *12*, 2949–2966. [CrossRef]

159. Frankenberg, C.; Thorpe, A.K.; Thompson, D.R.; Hulley, G.; Kort, E.A.; Vance, N.; Borchardt, J.; Krings, T.; Gerilowski, K.; Sweeney, C.; et al. Airborne methane remote measurements reveal heavy-tail flux distribution in Four Corners region. *Proc. Natl. Acad. Sci. USA* **2016**, *113*, 9734–9739. [CrossRef]

160. Frish, M.B. *Monitoring Fugitive Methane Emissions Utilizing Advanced Small Unmanned Aerial Sensor Technology*; Physical Sciences Inc.: Andover, MA, USA, 2016.

161. Denmead, O.; Harper, L.; Freney, J.; Griffith, D.; Leuning, R.; Sharpe, R. A mass balance method for non-intrusive measurements of surface-air trace gas exchange. *Atmos. Environ.* **1998**, *32*, 3679–3688. [CrossRef]

162. Gao, Z.; Desjardins, R.L.; Flesch, T.K. Comparison of a simplified micrometeorological mass difference technique and an inverse dispersion technique for estimating methane emissions from small area sources. *Agric. For. Meteorol.* **2009**, *149*, 891–898. [CrossRef]

163. Conley, S.; Faloona, I.; Mehrotra, S.; Suard, M.; Lenschow, D.H.; Sweeney, C.; Herndon, S.; Schwietzke, S.; Pétron, G.; Pifer, J.; et al. Application of Gauss's theorem to quantify localized surface emissions from airborne measurements of wind and trace gases. *Atmos. Meas. Tech.* **2017**, *10*, 3345–3358. [CrossRef]

164. Scafutto, R.D.P.M.; Filho, C.R.d.S. Detection of methane plumes using airborne midwave infrared (3–5 μm) hyperspectral data. *Remote Sens.* **2018**, *10*, 1237. [CrossRef]

165. Dierks, S.; Kroll, A. Quantification of methane gas leakages using remote sensing and sensor data fusion. In Proceedings of the 2017 IEEE Sensors Applications Symposium (SAS), Glassboro, NJ, USA, 13–15 March 2017; pp. 1–6.

166. Tanda, G.; Balsi, M.; Fallavollita, P.; Chiarabini, V. A uav-based thermal-imaging approach for the monitoring of urban landfills. *Inventions* **2020**, *5*, 55. [CrossRef]

167. Foote, M.D.; Dennison, P.E.; Thorpe, A.K.; Thompson, D.R.; Jongaramrungruang, S.; Frankenberg, C.; Joshi, S.C. Fast and accurate retrieval of methane concentration from imaging spectrometer data using sparsity prior. *IEEE Trans. Geosci. Remote Sens.* **2020**, *58*, 6480–6492. [CrossRef]

168. Lamb, B.K.; McManus, J.B.; Shorter, J.H.; Kolb, C.E.; Mosher, B.; Harriss, R.C.; Allwine, E.; Blaha, D.; Howard, T.; Guenther, A.; et al. Development of atmospheric tracer methods to measure methane emissions from natural gas facilities and urban areas. *Environ. Sci. Technol.* **1995**, *29*, 1468–1479. [CrossRef] [PubMed]

169. Imhoff, P.T.; Chow, F.K. *Assessing Accuracy of Tracer Dilution Measurements of Methane Emissions from Landfills with Wind Modeling*; Environmental Research and Education Foundation, Raleigh, NC, USA, 2014.

170. Imhoff, P.; Yazdani, R.; Han, B.; Mei, C.; Augenstein, D. Quantifying capture efficiency of gas collection wells with gas tracers. *Waste Manag.* **2015**, *43*, 319–327. [CrossRef]

171. De la Cruz, F.B.; Green, R.B.; Hater, G.R.; Chanton, J.P.; Thoma, E.D.; Harvey, T.A.; Barlaz, M.A. Comparison of field measurements to methane emissions models at a new landfill. *Environ. Sci. Technol.* **2016**, *50*, 9432–9441. [CrossRef] [PubMed]

172. Roscioli, J.; Yacovitch, T.; Floerchinger, C.; Mitchell, A.; Tkacik, D.; Subramanian, R.; Martinez, D.; Vaughn, T.; Williams, L.; Zimmerle, D.; et al. Measurements of methane emissions from natural gas gathering facilities and processing plants: Measurement methods. *Atmos. Meas. Tech.* **2015**, *8*, 2017–2035. [CrossRef]

173. Foster-Wittig, T.A.; Thoma, E.D.; Green, R.B.; Hater, G.R.; Swan, N.D.; Chanton, J.P. Development of a mobile tracer correlation method for assessment of air emissions from landfills and other area sources. *Atmos. Environ.* **2015**, *102*, 323–330. [CrossRef]

174. Hicks, B.B.; Baldocchi, D.D. Measurement of Fluxes Over Land: Capabilities, Origins, and Remaining Challenges. *Bound.-Layer Meteorol.* **2020**, *177*, 365–394. [CrossRef]

175. Göckede, M.; Rebmann, C.; Foken, T. A combination of quality assessment tools for eddy covariance measurements with footprint modeling for the characterisation of complex sites. *Agric. For. Meteorol.* **2004**, *127*, 175–188. [CrossRef]

176. Allwine, K.J.; Flaherty, J.E. *Joint Urban 2003: Study Overview and Instrument Locations*; Technical Report; Pacific Northwest National Lab. (PNNL): Richland, WA, USA, 2006.

177. Leach, M. *Final Report for the Joint Urban 2003 Atmospheric Dispersion Study in Oklahoma City: Lawrence Livermore National Laboratory Participation*; Technical Report; Lawrence Livermore National Lab.(LLNL): Livermore, CA, USA, 2005.

178. Nelson, M.A.; Brown, M.; Pardyjak, E.; Klewicki, J. *Area-Averaged Profiles Over the Mock Urban Setting Test Array*; Technical Report; Los Alamos National Laboratory: Santa Fe, NW, USA, 2004.

179. Biltoft, C.A. *Customer Report for Mock Urban Setting Test*; DTC Project No. 8-CO-160-000-052; DPG Document No. WDTC-FR-01-121; Defense Threat Reduction Agency: Alexandria, VA, USA, 2001.

180. Biltoft, C.A.; Yee, E. Overview of the Mock Urban Setting Test (MUST). In Proceedings of the AMS Fourth Symposium on the Urban Environment, Norfolk, VA, USA, 20–24 May 2002.

181. Eichhorn, J.; Balczó, M. Flow and dispersal simulations of the Mock Urban Setting Test. *Hrvat. Meteorološki časopis* **2008**, *43*, 67–72.

182. Nelson, M.A.; Brown, M.J.; Halverson, S.A.; Bieringer, P.E.; Annunzio, A.; Bieberbach, G.; Meech, S. A case study of the Weather Research and Forecasting Model applied to the Joint Urban 2003 tracer field experiment. Part 2: Gas tracer dispersion. *Bound.-Layer Meteorol.* **2016**, *161*, 461–490. [CrossRef]

183. Nicholson, D.K.; Hedrick, A.; Serguievski, P.; Martinez, A.A. *Detailed Test Plan for Jack Rabbit (JR) II*; Technical Report; West Desert Test Center Dugway Proving Ground: Dugway, UT, USA, 2015.

184. Bell, C.S.; Vaughn, T.; Zimmerle, D.; Helmig, D.; Lamb, B. Evaluation of next generation emission measurement technologies under repeatable test protocols. *Elem. Sci. Anthr.* **2020**, *8*, 32. [CrossRef]
185. Zhang, E.J.; Teng, C.C.; van Kessel, T.G.; Klein, L.; Muralidhar, R.; Wysocki, G.; Green, W.M. Field deployment of a portable optical spectrometer for methane fugitive emissions monitoring on oil and gas well pads. *Sensors* **2019**, *19*, 2707. [CrossRef] [PubMed]
186. Alden, C.B.; Coburn, S.C.; Wright, R.J.; Baumann, E.; Cossel, K.; Perez, E.; Hoenig, E.; Prasad, K.; Coddington, I.; Rieker, G.B. Single-blind quantification of natural gas leaks from 1 km distance using frequency combs. *Environ. Sci. Technol.* **2019**, *53*, 2908–2917. [CrossRef] [PubMed]
187. Alden, C.B.; Ghosh, S.; Coburn, S.; Sweeney, C.; Karion, A.; Wright, R.; Coddington, I.; Rieker, G.B.; Prasad, K. Bootstrap inversion technique for atmospheric trace gas source detection and quantification using long open-path laser measurements. *Atmos. Meas. Tech.* **2018**, *11*, 1565–1582. [CrossRef]
188. Ravikumar, A.P.; Barlow, B.; Wang, J.; Singh, D. Results from the Alberta Methane Measurement Campaigns: New Insights into Oil and Gas Methane Mitigation Policy. *AGU Fall Meet. Abstr.* **2019**, *2019*, A41D-08.
189. Singh, D.; Barlow, B.; Hugenholtz, C.; Funk, W.; Robinson, C.; Ravikumar, A.P. Field Performance of New Methane Detection Technologies: Results from the Alberta Methane Field Challenge. *EarthArXiv* **2021**.. [CrossRef]
190. Bridger Photonics. *Gas Mapping LiDAR™ METEC Round 1 Results*; Bridger Photonics Inc.: Bozeman, MT, USA, 2019.
191. Shaw, J.T.; Allen, G.; Pitt, J.; Shah, A.; Wilde, S.; Stamford, L.; Fan, Z.; Ricketts, H.; Williams, P.I.; Bateson, P.; et al. Methane flux from flowback operations at a shale gas site. *J. Air Waste Manag. Assoc.* **2020**, *70*, 1324–1339. [CrossRef] [PubMed]
192. Feng, S.; Farha, F.; Li, Q.; Wan, Y.; Xu, Y.; Zhang, T.; Ning, H. Review on smart gas sensing technology. *Sensors* **2019**, *19*, 3760. [CrossRef] [PubMed]
193. Gongora, A.; Monroy, J.; Gonzalez-Jimenez, J. Joint estimation of gas and wind maps for fast-response applications. *Appl. Math. Model.* **2020**, *87*, 655–674. [CrossRef]
194. Hollenbeck, D.; Chen, Y. Multi-UAV Method For Continuous Source Rate Estimation of Fugitive Gas Emissions From a Point Source. In Proceedings of the 2021 International Conference on Unmanned Aircraft Systems (ICUAS), Athens, Greece, 15–18 June 2021.
195. Madankan, R.; Singla, P.; Singh, T. Optimal information collection for source parameter estimation of atmospheric release phenomenon. In Proceedings of the 2014 American Control Conference, Portland, OR, USA, 4–6 June 2014; pp. 604–609.
196. Rico, D.A.; Detweiler, C.; Muñoz-Arriola, F. Power-over-Tether UAS Leveraged for Nearly-Indefinite Meteorological Data Acquisition. In Proceedings of the 2020 ASABE Annual International Virtual Meeting. American Society of Agricultural and Biological Engineers, Omaha, NE, USA, 12–15 July 2020; pp. 1–12.

MDPI

Article

Numerical Fluid Dynamics Simulation for Drones' Chemical Detection

Fabio Marturano [1], Luca Martellucci [1,*], Andrea Chierici [1], Andrea Malizia [2], Daniele Di Giovanni [1,3], Francesco d'Errico [4], Pasquale Gaudio [1] and Jean-François Ciparisse [1]

[1] Department of Industrial Engineering, University of Rome Tor Vergata, 00133 Rome, Italy; fabio.marturano@am.difesa.it (F.M.); a.chierici@studenti.unipi.it (A.C.); daniele.di.giovanni@uniroma2.it (D.D.G.); gaudio@ing.uniroma2.it (P.G.); ciparisse@uniroma2.it (J.-F.C.)

[2] Department of Biomedicine and Prevention, University of Rome Tor Vergata, 00133 Rome, Italy; malizia@ing.uniroma2.it

[3] School of Medicine and Surgery, Unicamillus-Saint Camillus International University of Health Sciences, 00131 Rome, Italy

[4] Department of Civil and Industrial Engineering, University of Pisa, 56122 Pisa, Italy; francesco.derrico@unipi.it

* Correspondence: luca.martellucci@uniroma2.it

Abstract: The risk associated with chemical, biological, radiological, nuclear, and explosive (CBRNe) threats in the last two decades has grown as a result of easier access to hazardous materials and agents, potentially increasing the chance for dangerous events. Consequently, early detection of a threat following a CBRNe event is a mandatory requirement for the safety and security of human operators involved in the management of the emergency. Drones are nowadays one of the most advanced and versatile tools available, and they have proven to be successfully used in many different application fields. The use of drones equipped with inexpensive and selective detectors could be both a solution to improve the early detection of threats and, at the same time, a solution for human operators to prevent dangerous situations. To maximize the drone's capability of detecting dangerous volatile substances, fluid dynamics numerical simulations may be used to understand the optimal configuration of the detectors positioned on the drone. This study serves as a first step to investigate how the fluid dynamics of the drone propeller flow and the different sensors position on-board could affect the conditioning and acquisition of data. The first consequence of this approach may lead to optimizing the position of the detectors on the drone based not only on the specific technology of the sensor, but also on the type of chemical agent dispersed in the environment, eventually allowing to define a technological solution to enhance the detection process and ensure the safety and security of first responders.

Keywords: detection; CBRNe; drone; MOX; chemical sensor; simulation; fluid dynamics simulations

1. Introduction

The rise of new technologies, such as drones, and the improvement of their capabilities, nowadays allows to potentially design and develop useful detection and sampling systems that may be aimed at limiting the exposure to hazardous agents of the workforce and of the population following a chemical, biological, radiological, nuclear, and explosive (CBRNe) event. Factors such as early detection and alarms are primary requirements to consider when designing and deploying new technologies in the field of CBRNe events' management [1–4].

CBRNe events may belong to either the hostile or accidental dimensions. Intervention by responder teams is quite complex and needs to be structured in many phases. When approaching a dangerous scenario, the first and most critical phase is usually considered "situational awareness"; indeed, the right perception of the potential hazards is the basis for the future decision-making process. Being able to characterize a CBRNe event in terms

of time, space, required actions, and operations is a fundamental step to successfully protect the public, the workforce, and the environment. Such an approach is commonly the best suited to ensure a fast and effective operative response when facing a wide range of dangerous situations. A good situational awareness could mean the difference between life and death of both rescuers and responders; in order to protect themselves and others against a CBRNe event, responders must assess as soon as possible the nature and proportion of the threat/hazard for subsequent life-saving and decontamination operations. In order to possess the right situational awareness, first responders not only need to be very well prepared, but they shall use whatever tool or technology available to them to enhance their response capabilities [5].

Mobile robot olfaction (MRO), the field of robotics where intelligent mobile platforms are equipped with a mixture of chemical sensors, has made tremendous progress in the last few years. Monitoring of environmental gases for risk assessment both indoors and outdoors usually requires a complex sensor system and a long operational time. A typical application field is gas pipelines' monitoring, where MRO equipped drones are used to monitor and localize a dangerous dispersion along the pipeline. The idea of installing a portable gas detector in a mobile robotic platform was first described in [6] for the localization of gas dispersion in nuclear power plants with the aim to minimize workforce exposure to dangerous environments. From the advancement of autonomous robots, different application results from the integration of specific sensor, to different kinds of mobile platforms [7], such as for firefighting, demining, environmental monitoring, and search and rescue [8–11]. Mobile robots are effective tools for replacing the workforce in repetitive tasks, such as continuous monitoring; they can work in a hostile environment (e.g., chemical and radioactive dispersion, oxygen-deficient, or hostile environment) and explore impervious areas that cannot be easily reached by human operators. Moreover, the use of this kind of system is twofold: support and monitoring application of the chemical dispersion, whereas it could be used even for direct response to the event [12]. Such aspects make drones a suitable platform in the context of CBRNe events' management [13–16].

MRO systems need on one hand to satisfy the requirements of early disaster response, where a high degree of mobility, fast operation, and highly efficient collaboration with human operators and decision makers are crucial; on the other end, MRO systems also need to satisfy the needs of long-term monitoring when less critical events affecting permanent infrastructures may exist.

Recent advances in mobile robot platforms, specifically in drones' technology, together with the improvements in the performance of chemical detectors, nowadays present a great prospect to deploy an integrated platform in a wide range of applications. Furthermore, recent advances in the miniaturization of chemical instrumentation as well as data processing algorithms and methodologies allow to better understand the nature and the origin of the chemical dispersion event [17–19]. For example, micro aerial vehicles (MAVs) equipped with gas detection systems and/or sampling devices have already been used in the field of environmental monitoring [11–27], volcanic gas sampling [28–32], localization of gas dispersion [33,34], early fire detection [35,36], precision agriculture [37–39] landfill monitoring [40–42], disaster response [43,44], demining [45], and others [46–48].

The use of inexpensive, low complexity sensors mounted on small commercial drones for the detection of specific substances could respond to the requisites of rapid response to a threat and allow to satisfy the safety requirements for the operators involved in a chemical release event. However, a potential problem in the accuracy of the acquired data arises when low-cost chemical sensors are used on board a drone because of the vortexes generated by the propellers mainly during the approaching phase, thus preventing the sensor from correctly detecting the presence of hazard substances or misreading the real concentration of the substance. Several works indicate that the problem of the turbulence generated by drone propellers may strongly affect the chemical sensor signals. In the work of Rossi et al. [26] and Burgues [22], the applicability of nano-drones for gas sensing tasks is explored: preliminary indoor experiments using nano-drones equipped with metal-oxide

semiconductor (MOX) gas sensors showed that the air drawn around the airframe strongly affects the sensor response, basically resulting in useless signals.

To reduce the interferences of the drone propellers on the behavior of the chemical sensors, this work is aimed at optimizing the position of the detectors on the drone platform in order to maximize the effectiveness of sensor detection. A series of fluid dynamic simulations have been performed, aimed at improving the capability and the proficiency of such mobile systems to correctly collect data during the drone approaching phase by optimizing the position of the sensors on the drone body.

2. Materials and Methods

In this section, the authors describe the methodology to evaluate and improve the performances of metal oxide chemical sensors when used on board a drone, taking into account the fluid-dynamics interaction through the software COMSOL Multiphysics® (COMSOL Inc., Stockholm, Sweden [49]). The authors provide an explanation of the advantages of using numerical simulation versus experiments followed by the case study analyzed in this work. The last two parts of these sections are devoted to explaining the models and the designed geometry, respectively.

The design of a mobile system, such as a drone platform for the detection, identification, and monitoring of a chemical substance release, requires a deep analysis of the interference that the propulsion of the drone itself produces owing to the volatile nature of the chemical substances that the system needs to analyze. In order to understand if a specific design of a drone equipped with chemical sensors will be able to correctly detect the target substance/particles during different phases of flying, such as approaching and hovering, studies on the fluid-dynamics of the vortexes generated by the propellers need to be performed.

Drones come in different shapes, sizes, and configurations. Among the most used configurations are the quadcopter and hexa-copter. While the first is more commercially and widely available for hobbyist, the hexa-copter configurations are usually aimed at professional and specialized applications. To carry out a simulation of a realistic drone platform, a 3D drone was modelled based on an existing prototype. A specific commercial drone that has already been the object of trials in the CBRNe domain is the SR-SF6 (Figure 1). It is a hexa-drone created by Skyrobotics, which has shown good performance when applied in a wide range of applications. For example, it has been modified to host a bio-chemical aerosol detector and sampler system with the goal of being used as a tool in the management of CBRNe scenarios. In this work, the hexa-drone was chosen as the reference drone to be modelled in the simulation thanks to its relatively simple structure and good performance balance in terms of speed, stability, and aerodynamic control compared with commercially available quad-copters and octa-copters.

Figure 1. SR-SF6 by Skyrobotics.

Because of the volatile nature of the substances, experimental tests could lead to unpredictable results and require a strong effort to define an experimental set. Moreover, the repeatability of the experimental set between different cycle makes it hard to achieve particularly in the particle dispersion flow. Fluid-dynamic simulations, mainly carried out to optimize the positioning of the chemical sensors on a drone platform to minimize the fluid dynamics interference of the propeller, could lead to an optimal system able to correctly acquire the data from the chemical sensors used. In computational fluid dynamics (CFD), finite volume algorithms subdivide the fluid domain into several little volumes in which, once the boundary conditions are imposed, the Navier–Stokes equations solve the problem using an iterative method [50]. Each fluid is then characterized by its macroscopic properties such as density, viscosity, pressure, and so on. The CFD equations can predict with a reasonable degree of approximation the behavior of fluid flow with a mathematical model and numerical methods. A set of pre- and post-processing algorithms are usually applied to visually correct the error in the resolution of the system and to help perform the virtual simulations. To correctly set up the variables in the CFD simulation, attention should be paid to the following properties:

- Aerodynamics of the model;
- Weather conditions;
- Particle characteristics and type of dynamics.

At the end, the CFD simulation provides a solution for complex flow problems that may be expensive and not reliable in real experimentation.

2.1. Aim of the Investigation

The present study addresses the problem of the optimization of the chemical sensor location on the drone to avoid the interference on the sensors owing to the propulsion used in the drones. Specifically, the flow from the propellers could cause the loss or corruption of the data collected from the sensors owing to the turbulence area and the dispersion of the concentration around the propeller.

2.2. Fluid Dynamics Models

In this work, the dispersion of ammonia due to an accidental release is being simulated, and the sensitivity of sensors placed in different areas of the drone is analysed. As ammonia is a common by-product of several chemical industrial processes, and as it is an irritant, toxic, and uncoloured gas, it was chosen as the representative chemical substance of choice in this study. Because of its molecular characteristics, ammonia is more dangerous compared with more volatile substances, and its stagnation could create a dangerous area. Moreover, the use of ammonia in low concentrations does not represent a large threat to human life; therefore, it represents a good candidate to perform an experimental campaign aimed at characterizing the detecting capabilities of different kinds of chemical sensors, such as MOXs. It has to be highlighted that such an approach should be avoided for concentrations larger than the lower explosion limit (LEL).

The numerical model is a multiphase mixture model, where two phases are considered: air and ammonia. The first equation used to simulate the event is the continuity equation, which describes the conservation of the mass:

$$\frac{\partial \rho}{\partial t} + \nabla(\rho \boldsymbol{u}) = 0 \tag{1}$$

where $\boldsymbol{u}$ is the velocity vector and ρ is the density of the mixture. The momentum conservation is taken into account by a set of three equations:

$$\rho \frac{\partial \boldsymbol{u}}{\partial t} + \rho \boldsymbol{u} \nabla(\boldsymbol{u}) = -\nabla p + \rho \boldsymbol{g} + \nabla \mathbf{K} \tag{2}$$

where p is the pressure and

$$K = (\mu + \mu_t)\left(\nabla u + (\nabla u)^T\right) - \frac{3}{2}(\mu + \mu_t)(\nabla \cdot u)I - \frac{2}{3}\rho k I \tag{3}$$

where μ is the dynamic viscosity, μ_t is the turbulent viscosity, I is the identity matrix, and k is the turbulent energy. The turbulent variables are calculated by the k-ε turbulent model, which describes, using a two equations approach, the turbulent kinetic energy (k) and the turbulent dissipation ratio (ε):

$$\rho\frac{\partial k}{\partial t} + \rho u \nabla k = \nabla\left(\left(\mu + \frac{\mu_t}{\sigma_k}\right)\nabla k\right) + P_k - \rho\varepsilon \tag{4}$$

$$\rho\frac{\partial \varepsilon}{\partial t} + \rho u \nabla \varepsilon = \nabla\left(\left(\mu + \frac{\mu_t}{\sigma_\varepsilon}\right)\nabla \varepsilon\right) + C_{\varepsilon 1}\frac{\varepsilon}{k}P_k - C_{\varepsilon 2}\rho\frac{\varepsilon^2}{k} \tag{5}$$

where

$$P_k = \mu_t\left(\nabla u : \left(\nabla u + (\nabla u)^T\right) - \frac{2}{3}(\nabla \cdot u)^2\right) - \frac{2}{3}\rho k \nabla \cdot u \tag{6}$$

$$\mu_t = \frac{\rho C_\mu k^2}{\varepsilon} \tag{7}$$

The turbulent model constants are $C_\mu = 0.09$, $C_{\varepsilon 1} = 1.44$, $C_{\varepsilon 2} = 1.92$, $\sigma_k = 1$, and $\sigma_\varepsilon = 1.3$. The mixture properties are calculated by the mixture flux equation:

$$\rho\frac{\partial \alpha_i}{\partial t} + \alpha_i \rho \nabla(u) + \nabla j_i = 0 \tag{8}$$

where α_i is the mass fraction of the i-th phase and j_i is the mass flux vector, calculated taking into account both diffusion and convection.

2.3. Settings of COMSOL Multiphysics Parameters

To run a CFD simulation, the software needs to process the data modelling the drone and the volume where the simulation is going to be carried out with well-defined boundaries. For this simulation, it was decided to consider a cube of air with a linear length of 50 m (**L**) (Figure 2), assuming the drone position is at the centre of the volume.

Figure 2. Schematics of the numerical simulation geometry.

Transforming partial differential equations (PDEs) into algebraical equations while working on the entire model might introduce significant errors into the results. To avoid

this problem, the surface is divided into a number of sub-elements of geometrical simple shapes (tetrahedrons) to be studied one by one in order to increase the goodness of the approximation and remove the final errors. The mesh settings determine the resolution of the finite element mesh used to discretize the model. The mesh used in a fluid flow simulation depends on the fluid flow model and on the accuracy required in the simulation. Generally, a fluid flow model requires a fine resolution to converge. The finer the resolution (number of sub cells), the better the goodness of the approximation and the lower the error of the final result.

Two different meshes are used for the simulation: a first one for the reference volume, characterized by larger sub-elements; and a second one for the drone, whose dimensions require the sub-elements to be much smaller. Once an assessment about the virtual environment is completed, with the fundamental boundary conditions, the geometry of the drone can be created by choosing a simplified geometric shape and by providing the spatial information to the system. The geometry of the drone was created starting from a three-element shaped body using an ellipsoid for the central body, while cylindrical shapes were used to model the rotor and the ducted propeller. The cylindrical shape is an approximation of the propeller area for simulating the inlet and outlet surface in the simulation of the flow, whereas the ducting effects are not taken into account. These components are joined by the arm connecting the rotor shape with the central body, respectively. The union of these three separate parts was then used to define the final ensemble shape into a single body. Finally, the drone was completed, with the exception of the sensors, by maintaining the center of the ellipsoid as a fulcrum and applying a rotation on the XY plane by an alpha angle equal to 60 degrees five times and gluing all the parts together (Figure 3).
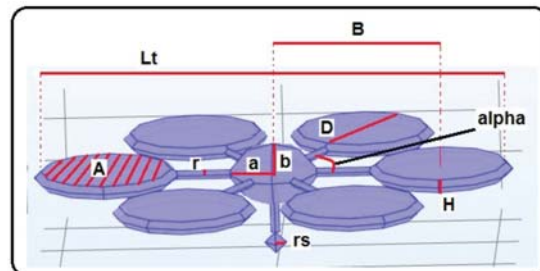

Figure 3. Schematics of the drone geometric components.

In order to validate the CFD simulation results by comparing them with experimental data, a fundamental step involves the choice of the model of the chemical sensors, which needs to take into account both the availability of the sensor in the market and the volatile substance to analyze. The aim of the simulations is the analysis of a specific area contaminated with ammonia, thus an MQ137 chemical sensor was selected as the detector to be modeled in the simulation thanks to its low cost, commercial availability, and ease of use in a real environment. Moreover, MOX technology is today one of the most used in the context of MRO thanks to the relative rapid prototyping requirements. MOX sensors in the simulation are modelled as a sphere with radius of 5 cm to better approximate the shape and simplify the fluid dynamics computation. To simulate a release of ammonia in the environment for the bi-component simulation, a solid sphere releasing the particles in all directions at a speed of 0.5 m/s was configured. In the first set of simulations, aimed at evaluating the propeller interference, the releasing source was located at 5 meters on the X-axis, at 15 meters form the ZX plane along the Y-axis, and at 25 meters from the ZY plane along the X-axis. Wind was introduced as a parameter, blowing along the Y-axis direction at a speed of 3 m/s.

The simulation will run with configurations having two different locations of the sensors positioned on the drone. The first configuration considered is the nadir position

(underneath the central body ellipsoid) of the drone hosting a single sensor, whereas the radial configuration of the sensors hosted six sensors radially displaced around the outer edge of each propeller (Figure 4).
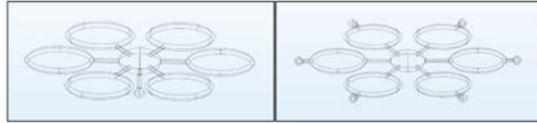
Figure 4. Nadir (**left**) and radial (**right**) sensors' displacement.

The study of the flow and the interference of the propeller were carried out for two different virtual environment settings: the first setting considers only the presence of the air as a unique fluid flow, namely mono-component CFD simulation, whereas the other setting takes into account the presence of the dispersion source (inlet) of ammonia that spreads the volatile substance into the air at a specific height, namely bi-component CFD (owing to the mixing of ammonia with the surrounding air). Regarding the latter configuration, the simulation of fluid flow is more complex compared with the single fluid because the different properties of the molecules give rise to different behaviors when mixed together.

The last groups of settings required to define the simulation, taking into account the prototype of the drone with the sensors and the releasing point (modelled as a sphere) had to be positioned inside the reference volume.

3. Results and Discussion

To test the optimal positioning of the detectors, two simulations were carried out, each characterized by different displacement of chemical sensors on the drone body. A first check of the goodness of the simulations could be performed during the run of the simulation itself. The convergence of the velocity, pressure, volume fraction of the dispersion, and turbulence variables can always be observed on the run. Therefore, it was observed that the errors of the solutions just stabilized to a constant value as the number of iterations was increasing. The difference of a 10^{-3} factor between the error values was assumed to be dictated by the numerical model used and the computational algorithms.

By examining the flow lines in the simulation, the air flow follows the expected path; that is, it exits from the reference volume into the upper side of the ducted propeller and re-enters the reference volume from the lower side (Figure 5a). It is important to note that the flow re-entering into the volume is accelerated and concentrated in a coherent downwash until the ground interference dissipates it radially (Figure 5b). Moreover, it is important to consider that the air flow that enters into the propeller duct not only is directly influenced by the propeller action on the vertical space, but also derives from the outer boundaries of the ducts; in fact, the fluid starts its acceleration downward, and the mass flow claimed from the propeller increases with the propeller velocity.

By analyzing the air speed and fluid flow, we can instead observe that the air is being accelerated on top of the ducted propeller with a speed close to 8–9 m/s, and the same value is maintained for almost 2 meters downward, where it starts to slow down at 5–6 m/s (Figure 6). The speed of air is still effective as the air flow hits the ground at 25 m with a speed of 1–3 m/s. Furthermore, the air flow assumes a larger radial angle as it leaves the drone such that the flow cross section at ground level is almost double with respect to the cross section below the drone.
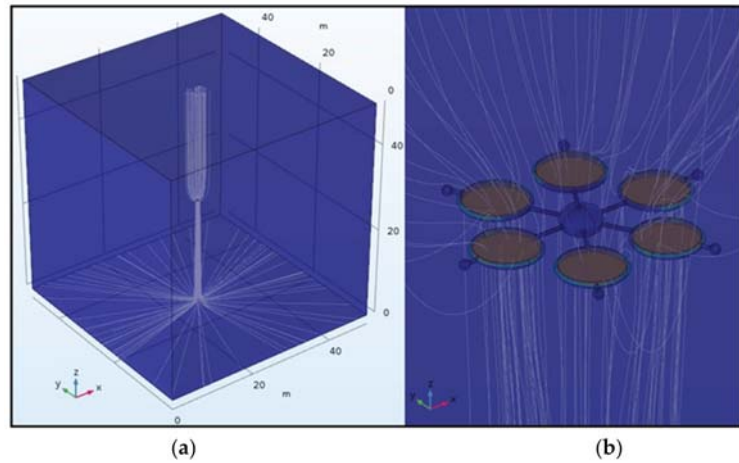
Figure 5. (**a**). Flow ground radial dissipation (**b**). Fluid Flow simulation lines.
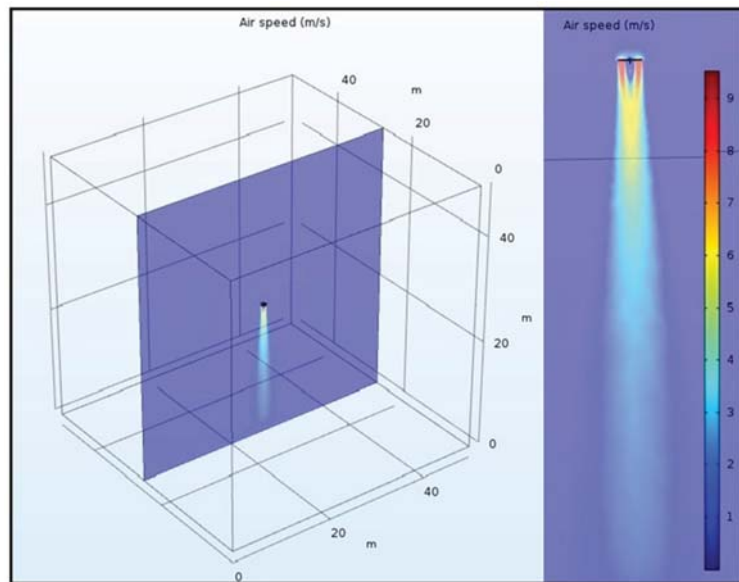

Figure 6. Air speed behaviour.

The air flow section underneath the central ellipsoid shows an interesting feature: the air flow has an acceleration between 2 and 4 m/s. As the air flow downstream expands below the propeller, it merges down at 2 meters with another air flow. This phenomenon creates a vortex (a local vorticity generated by the drone propeller) that redirects upward the flow under the nadir area and finally forces it to re-join the mainstream downward from the propeller (Figure 7). The toroidal recirculation under the nadir made by the six propellers creates the increment in speed toward the sensor located under the centre of the drone. This implies that, in order to detect chemical substances under the drone, the aerosol/particles first need to be attracted by the propeller, then pushed downward, and finally reach the sensor after being recirculated upward in the toroidal pattern.
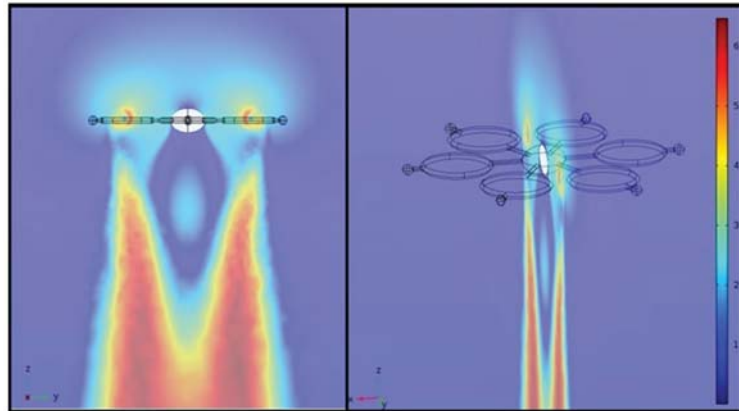
Figure 7. Downstream of the hexacopter.

Given the strength of the downstream, which creates a virtual wall around the sensor, it may be difficult for the drone to detect anything when flying at medium to high altitudes unless the plume is higher than the propellers. Flying at low altitudes will instead facilitate the detection as the downstream of the air flow will increase the terrain turbulence by impacting with the ground at a high speed. Furthermore, once the chemical substance is accelerated through the ducted propeller and reaches the sensor, its concentration could change enough to be detectable during a measurement.

In the other setting, namely the radial configuration, the sensors are displaced in the outer ring of the propeller; here, the presence of several other surfaces gives rise to a fluctuating error affecting the convergence of the variables considered in the simulation.

Most of the considerations and analysis for the nadir configuration are applicable for the radial configuration as well, where the sensors are placed in the outer ring of the propellers. The pressure velocity values as well as the turbulent variables need to converge to a constant value as the number of iterations increases. Given the presence of several other aerodynamic surfaces, in this configuration, the pressure and velocity values will converge too, but they will maintain a fluctuating error range with an average value of 10^{-9}. Despite this fluctuation error in the convergence of the values of the variables, the radial setting seems to offer an interesting solution for enhancing the detection compared with the nadir sensor location. Whereas the nadir sensor is limited to sampling the particles that arise from the below vortex that redirect the flow upward, sensors in the radial configuration appear not to be influenced by the acceleration of the air flow (Figure 8). As the drone hovers on a stationary plane and is reached by a chemical plume, none of its rotors downstream flows should affect it before it detects the chemical presence from a lower altitude. Moreover, if the chemical plume flows at the same altitude of the drone, then the upper rotor air-need would accelerate the air radially from outside, forcing the mixture to impact the sensors before it is sucked into the ducted propeller rotors.

Bi-Component Simulation

In the bi-component (ammonia and air) simulation, where the ammonia source is introduced into the environment, the influence of the wind direction and intensity (3 m/s) results in a turbulence both in proximity to the drone air flow and in proximity to the release point (Figure 9). As the wind velocity is higher than the normal air flow in the reference volume above the drone, the flow lines coming from the propeller described by the simulation are dominated by the wind direction and intensity. After entering the rotors, they are twisted and accelerated downwards, but are still affected by the external wind direction.
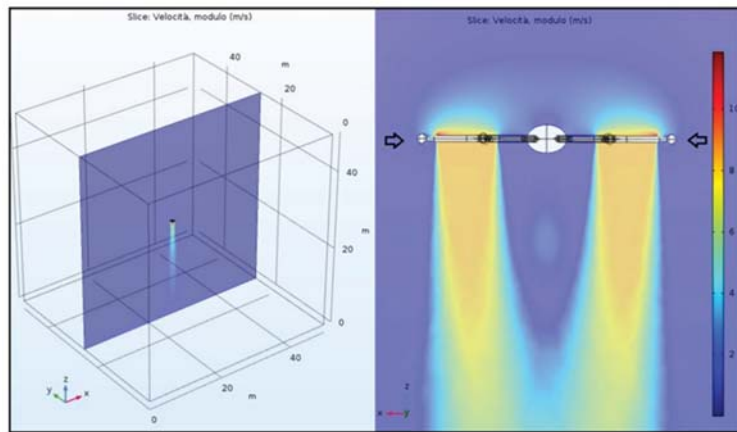
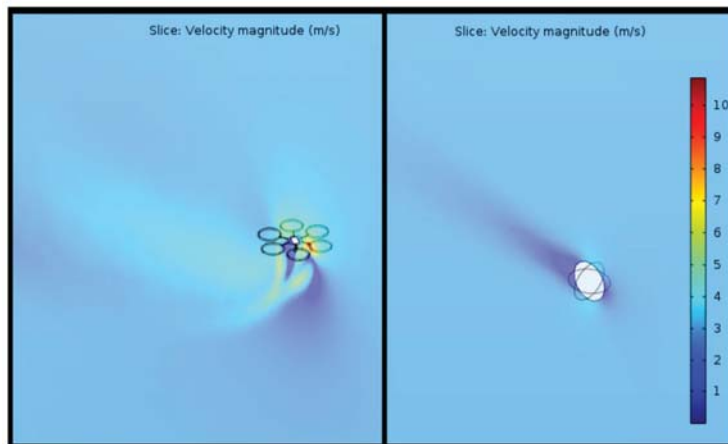**Figure 8.** Air flow behavior for the radial configuration.

Figure 9. Turbulence around the drone (**left**) and around the emission sphere (**right**) owing to the introduction of the wind vector.

In the final simulation, the reference volume was resized to become a parallelepiped (50 m × 50 m × 300 m) with the drone positioned at 225 meters from the ammonia source and lowered to be 5 meters higher than the source. The nadir drone bi-component simulation in the new reference volume shows the same results for both velocity magnitude and flow lines behavior graphs as for the previous reference volume (cube). It should be noted that the different speed in the volume around the drone is not related to the reference plane (ZX) including two ducted propeller rotors (as for the first mono component simulation), but it is related to the reference plane (ZY) passing for the ammonia sphere and crossing the drone between its rotors. The nadir drone bi-component simulation in the new reference volume shows the same results for both the velocity magnitude and flow lines behavior graphs found for the previous reference volume (cube). It should be noted that the different speed areas around the drone in the section view are not related to the reference plane (ZX) including two ducted propeller rotors (as for the first mono component simulation), but they are necessarily connected to the reference plane (ZY) passing for the ammonia sphere and crossing the drone between its rotors.

The nadir drone simulation provides interesting results when analyzing the mass fraction and, more specifically, to understand if the sensor detects a certain concentration of ammonia particles. Mass fraction is defined as the mass of one chemical species in a set volume divided by the total mass of species in the same volume. It is normally calculated in parts per million (ppm). With COMSOL software, it is possible to calculate the concentration of ammonia at any specific point, thus it is possible to assess if any sensor in a specific location on the drone will be able to detect the presence of the contaminant. By focusing on the mass fraction of the contaminants around the drone, different concentration may result owing to propeller flow. In front of the drone, such as the radial position, the mass fraction appears uninterrupted, whereas under the drone, it decreases. By comparing the mass fraction in front of the forward rotor ducts (where the sensors are located on the radial position) and below the nadir of the central body of the drone, the difference in the concentration sampling of the two configurations is evident (Figure 10). Ranging from a minimum of 122.60 ppm to a maximum of 169.17 ppm with an average value of 151.8 ppm, the radial design shows a detection capability 5.8 times higher than the nadir configuration, where the average sensor value is 26.089 ppm.
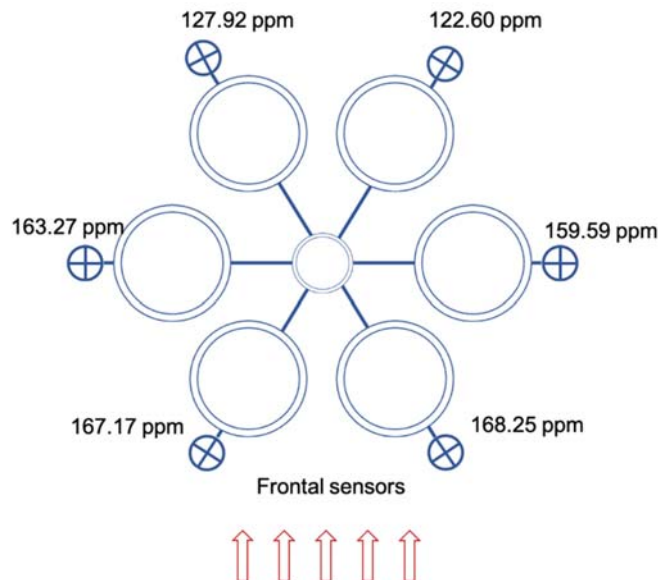
Figure 10. As the gas dispersion reaches the sensor in the radial configuration, frontal sensors detect the highest values in ppm, followed by the lateral sensors and thus back sensors, where a lower concentration level is detected.

When considering an inexpensive commercial portable detector for industrial and domestic uses and sensitivity to ammonia such as the MQ137, and by comparing its mass fraction detecting threshold against the values for both the nadir sensor and the radial ones, the advantage of the radial configuration is evident. When a dispersed concentration changes (for example, by changing the relative distance to the emission source), and considering a reduction of 1/10 of the concertation, the limit of detection (LoD) of a real sensors could make the sensor unable to detect the dispersion itself. In the case of MQ137, with an LoD of 5 ppm, a relative detection of 1/10 of the mass fraction implies that, in the nadir position, the possible detected concentration drops to 2.6 ppm, thus under the LoD of the sensor, whereas for the radial configuration, it drops to a 12.26 ppm. This implies

that the nadir detection is under the threshold, whereas the radial sensor is still able to detect a useful level of concentration.

4. Conclusions and Prospects

Both CBRNe threats and hazards have evolved significantly over the last decades. Know-how and dangerous elements have become more accessible; consequently, the probability of a chemical or biological attack or casualty has grown significantly all over the world. It is obvious that every country in the world should be prepared to respond to a CBRNe event. Such a response is provided by the intervention of first responder teams, whose main task is focused on acquiring the correct situational awareness in order to save lives, rescue people, and decontaminate the hazardous area. A good situational awareness could mean the difference between life and death of both rescues and responders. In order to possess the right situational awareness, first responders not only need to be very well prepared, but they need to use whatever tool or technology available to enhance their capabilities. By providing all first responder teams with commercial drones equipped with inexpensive, low complexity sensors, capable of detecting a wide range of substances, the risk assessment process could be improved, ensuring the safety and security of the operators through a fast and effective response to the threat.

The main problem to be solved when sensors for chemical and biological detection are used on board of a drone is related to the vortexes generated by the drone propellers. Two different sets of computational fluid-dynamics simulations, using COMSOL software and starting from a drone specific design, were carried out to demonstrate the effectiveness and advantage of correct positioning of the sensors.

In this work, the simulation of the fluid-dynamics variables in proximity to the drone and the sensors on two different configurations helped to identify the optimal positioning of the detectors in the case of a chemical release/dispersion scenario. The distribution of the concentrations of the particles around the drone with and without the wind interference allowed to identify a radial configuration as an optimal solution for the detection of the chemical particles' release. The results of the simulation emphasized how radial positioned sensors would be less affected by the rotors downstream of the drone compared with the one placed on the central belly. Moreover, as the virtual drone is a hexa-copter able to carry up to six radial sensors, a similar model could be considered a recommendation for further simulations and experimentations; for example, it may be equipped with six different low-cost and selective sensors among those to detect nerve agents, blister agents, chocking agents, blood agents, and riot control agents. If such a low-cost device will prove effective, it could determine an improvement in the detection of hazardous agents following a CBRNe event. By providing first responder teams of any organization in the world with such a kind of platform, a fast and full situational awareness and risk assessment could be easily achieved in order to face any challenge in different hostile environments.

References

1. Singh, V.K.; Garcia, M.; Wise, S.Y.; Seed, T.M. Medical countermeasures for unwanted CBRN exposures: Part I chemical and biological threats with review of recent countermeasure patents. *Expert Opin. Ther. Patents* **2016**, *26*, 1431–1447. [CrossRef]
2. Bruno, F.; Carestia, M.; Civica, M.; Gaudio, P.; Malizia, A.; Troiani, F.; Sciacqua, R.; Spezia, U. CBRN Risk Scenarios. In *Nanomaterials for Security*; Springer: Dordrecht, The Netherlands, 2018; pp. 309–317. [CrossRef]
3. Fumian, F.; Di Giovanni, D.; Martellucci, L.; Rossi, R.; Gaudio, P. Application of Miniaturized Sensors to Unmanned Aerial Systems, A New Pathway for the Survey of Polluted Areas: Preliminary Results. *Atmosphere* **2020**, *11*, 471. [CrossRef]
4. Rossi, R.; Gelfusa, M.; Malizia, A.; Gaudio, P. Adaptive Quasi-Unsupervised Detection of Smoke Plume by LiDAR. *Sensors* **2020**, *20*, 6602. [CrossRef]
5. Carestia, M.; Troiani, F.; Caldari, R.; Civica, M.; Bruno, F.; Vicini, C.; Di Giovanni, D.; Iannotti, A.; Russo, C.; Thornton, M.; et al. CBRNe as Conceptual Frame of an All Hazards Approach of Safety and Security: The Creation of Organic Networks of Military, Civil, Academic/Research and Private Entities at National and International Level to Generate Solutions for Risk Reduction—A European and Italian Perspective. In *Nanomaterials for Security*; Springer: Dordrecht, The Netherlands, 2020; pp. 307–315. [CrossRef]
6. Larcombe, M.H.E. *Robotics in Nuclear Engineering: Computer Assisted Teleoperation in Hazardous Environments with Particular Reference to Radiation Fields*; Graham and Trotman, Inc.: Gaithersburg, MD, USA, 1984.
7. Peng, C.-C.; Hsu, C.-Y.; Chao-Chung, P. Integration of an unmanned vehicle and its application to real-time gas detection and monitoring. In Proceedings of the 2015 IEEE International Conference on Consumer Electronics-Taiwan, Taipei, Taiwan, 6–8 June 2015; pp. 320–321. [CrossRef]
8. Siegel, M.W. Olfaction Metal Oxide Semiconductor Gas Sensors and Neural Networks. In *Traditional and Non-Traditional Robotic Sensors*; Springer: Berlin/Heidelberg, Germany, 1990; pp. 143–157. [CrossRef]
9. Genovese, V.; Dario, P.; Magni, R.; Odetti, L. Self-organizing behaviour and swarm intelligence in a pack of mobile miniature robots in search of pollutants. In Proceedings of the IEEE/RSJ International Conference on Intelligent Robots and Systems, Raleigh, NC, USA, 7–10 July 1992; Volume 3, pp. 1575–1582. [CrossRef]
10. Mächler, P. Detection technologies for anti-personnel mines. In Proceedings of the Autonomous Vehicles in Mine Countermeasures Symposium, Monterey, CA, USA, 4–6 April 1995; pp. 6–150.
11. Trevelyan, J.P.; Kang, S.-C.; Hamel, W.R. Robotics in Hazardous Applications. In *Springer Handbook of Robotics*; Springer: Berlin/Heidelberg, Germany, 2008; pp. 1101–1126. [CrossRef]
12. Restas, A. Drone applications for preventing and responding HAZMAT disaster. *World J. Eng. Technol.* **2016**, *4*, 76–84. [CrossRef]
13. Gardner, C.W.; Wentworth, R.; Treado, P.J.; Batavia, P.; Gilbert, G. Remote chemical biological and explosive agent detection using a robot-based Raman detector. In *Unmanned Systems Technology X*; International Society for Optics and Photonics: Orlando, FL, USA, 2008; Volume 6962, p. 69620T. [CrossRef]
14. Humphrey, C.M.; Adams, J.A. Robotic tasks for cbrne incident response. *Adv. Robot.* **2009**, *23*, 1217–1232. [CrossRef]
15. Chierici, A.; Malizia, A.; di Giovanni, D.; Fumian, F.; Martellucci, L.; Gaudio, P.; D'Errico, F. A low-cost radiation detection system to monitor radioactive environments by unmanned vehicles. *Eur. Phys. J. Plus* **2021**, *136*, 1–18. [CrossRef]
16. Marturano, F.; Ciparisse, J.F.; Chierici, A.; d'Errico, F.; Di Giovanni, D.; Fumian, F.; Malizia, A. Enhancing Radiation Detection by Drones through Numerical Fluid Dynamics Simulations. *Sensors* **2020**, *20*, 1770. [CrossRef]
17. Asad, M.; Al Aidaros, O.; Beg, R.; Al Dhahri, M.; Al Neyadi, S.; Hussein, M. Development of autonomous drone for gas sensing application. In Proceedings of the 2017 International Conference on Electrical and Computing Technologies and Applications, Ras Al Khaimah, United Arab Emirates, 21–23 November 2017; pp. 1–6. [CrossRef]
18. Rossi, M.; Brunelli, D.; Adami, A.; Lorenzelli, L.; Menna, F.; Remondino, F. Gas-Drone: Portable gas sensing system on UAVs for gas leakage localization. In Proceedings of the IEEE SENSORS 2014, Valencia, Spain, 2–5 November 2014; pp. 1431–1434. [CrossRef]
19. Tosato, P.; Facinelli, D.; Prada, M.; Gemma, L.; Rossi, M.; Brunelli, D. An Autonomous Swarm of Drones for Industrial Gas Sensing Applications. In Proceedings of the 2019 IEEE 20th International Symposium on "A World of Wireless, Mobile and Multimedia Networks" (WoWMoM), Washington, DC, USA, 10–12 June 2019; pp. 1–6. [CrossRef]
20. Khan, A.; Schaefer, D.; Tao, L.; Miller, D.J.; Sun, K.; Zondlo, M.A.; Harrison, W.A.; Roscoe, B.; Lary, D.J. Low Power Greenhouse Gas Sensors for Unmanned Aerial Vehicles. *Remote Sens.* **2012**, *4*, 1355–1368. [CrossRef]
21. Berman, E.S.; Fladeland, M.; Liem, J.; Kolyer, R.; Gupta, M. Greenhouse gas analyzer for measurements of carbon dioxide, methane, and water vapor aboard an unmanned aerial vehicle. *Sensors Actuators B Chem.* **2012**, *169*, 128–135. [CrossRef]
22. Burgués, J.; Hernández, V.; Lilienthal, A.J.; Marco, S. Smelling Nano Aerial Vehicle for Gas Source Localization and Mapping. *Sensors* **2019**, *19*, 478. [CrossRef]
23. Carrozzo, M.; De Vito, S.; Esposito, E.; Salvato, M.; Formisano, F.; Massera, E.; Mennella, A. UAV intelligent chemical multisensor payload for networked and impromptu gas monitoring tasks. In Proceedings of the 2018 5th IEEE International Workshop on Metrology for AeroSpace (MetroAeroSpace), Rome, Italy, 20–22 June 2018; pp. 112–116. [CrossRef]
24. Chang, C.-C.; Wang, J.-L.; Liang, M.-C.; Lin, M.-R. Development of a multicopter-carried whole air sampling apparatus and its applications in environmental studies. *Chemosphere* **2016**, *144*, 484–492. [CrossRef]
25. Xie, T.; Liu, R.; Hai, R.; Hu, Q.; Lu, Q. UAV Platform Based Atmospheric Environmental Emergency Monitoring System Design. *J. Appl. Sci.* **2013**, *13*, 1289–1296. [CrossRef]

26. Rossi, M.; Brunelli, D. Autonomous Gas Detection and Mapping with Unmanned Aerial Vehicles. *IEEE Trans. Instrum. Meas.* **2015**, *65*, 765–775. [CrossRef]

27. Rossi, M.; Brunelli, D. Gas Sensing on Unmanned Vehicles: Challenges and Opportunities. In Proceedings of the 2017 New Generation of CAS (NGCAS), Genova, Italy, 6–9 September 2017; pp. 117–120. [CrossRef]

28. Mcgonigle, A.J.S.; Aiuppa, A.; Giudice, G.; Tamburello, G.; Hodson, A.; Gurrieri, S. Unmanned aerial vehicle measurements of volcanic carbon dioxide fluxes. *Geophys. Res. Lett.* **2008**, *35*. [CrossRef]

29. Shinohara, H. Composition of volcanic gases emitted during repeating Vulcanian eruption stage of Shinmoedake, Kirishima volcano, Japan. *Earth Planets Space* **2013**, *65*, 667–675. [CrossRef]

30. Rudiger, J.; Tirpitz, J.L.; Moor, J.; Bobrowski, N.; Gutmann, A.; Liuzzo, M.; Hoffmann, T. Implementation of electrochemical, optical and denuder-based sensors and sampling techniques on UAV for volcanic gas measurements: Examples from Masaya, Turrialba and Stromboli volcanoes. *Atmos. Meas. Tech.* **2018**, *11*, 2441–2457. [CrossRef]

31. Mori, T.; Hashimoto, T.; Terada, A.; Yoshimoto, M.; Kazahaya, R.; Shinohara, H.; Tanaka, R. Volcanic plume measurements using a UAV for the 2014 Mt. Ontake eruption. *Earth Planets Space* **2016**, *68*, 1. [CrossRef]

32. Astuti, G.; Giudice, G.; Longo, D.; Melita, C.D.; Muscato, G.; Orlando, A. An Overview of the "Volcan Project": An UAS for Exploration of Volcanic Environments. *J. Intell. Robot. Syst.* **2008**, *54*, 471–494. [CrossRef]

33. Neumann, P.P.; Kohlhoff, H.; Hüllmann, D.; Lilienthal, A.J.; Kluge, M. Bringing Mobile Robot Olfaction to the next dimension —UAV-based remote sensing of gas clouds and source localization. In Proceedings of the 2017 IEEE International Conference on Robotics and Automation (ICRA), Singapore, 29 May–3 June 2017; pp. 3910–3916. [CrossRef]

34. Golston, L.M.; Aubut, N.F.; Frish, M.B.; Yang, S.; Talbot, R.W.; Gretencord, C.; Zondlo, M.A. Natural gas fugitive leak detection using an unmanned aerial vehicle: Localization and quantification of emission rate. *Atmosphere* **2018**, *9*, 333. [CrossRef]

35. Krüll, W.; Tobera, R.; Willms, I.; Essen, H.; von Wahl, N. Early Forest Fire Detection and Verification using Optical Smoke, Gas and Microwave Sensors. *Procedia Eng.* **2012**, *45*, 584–594. [CrossRef]

36. Merino, L.; Caballero, F.; de Dios, J.R.M.; Ferruz, J.; Ollero, A. A cooperative perception system for multiple UAVs: Application to automatic detection of forest fires. *J. Field Robot.* **2006**, *23*, 165–184. [CrossRef]

37. Pfeifer, J.; Khanna, R.; Constantin, D.; Popovic, M.; Galceran, E.; Walter, A.; Siegwart, R.; Liebisch, F. Towards automatic UAV data interpretation. In Proceedings of the International Conference of Agricultural Engineering 2016, Aahus, Denmark, 26–29 June 2016.

38. Roldán, J.J.; Joossen, G.; Sanz, D.; Del Cerro, J.; Barrientos, A. Mini-UAV Based Sensory System for Measuring Environmental Variables in Greenhouses. *Sensors* **2015**, *15*, 3334–3350. [CrossRef]

39. Pobkrut, T.; Eamsa-Ard, T.; Kerdcharoen, T. Sensor drone for aerial odor mapping for agriculture and security services. In Proceedings of the 2016 13th International Conference on Electrical Engineering/Electronics, Computer, Telecommunications and Information Technology (ECTI-CON), Chiang Mai, Thailand, 28 June–1 July 2016; pp. 1–5. [CrossRef]

40. Lega, M.; Napoli, R.M.A. A new approach to solid waste landfills aerial monitoring. *Waste Manag. Environ. IV* **2008**, *109*, 193–199. [CrossRef]

41. Allen, G.; Hollingsworth, P.; Kabbabe, K.; Pitt, J.; Mead, M.; Illingworth, S.; Roberts, G.; Bourn, M.; Shallcross, D.E.; Percival, C.J. The development and trial of an unmanned aerial system for the measurement of methane flux from landfill and greenhouse gas emission hotspots. *Waste Manag.* **2019**, *87*, 883–892. [CrossRef]

42. Emran, B.J.; Tannant, D.D.; Najjaran, H. Low-Altitude Aerial Methane Concentration Mapping. *Remote Sens.* **2017**, *9*, 823. [CrossRef]

43. Daniel, K.; Dusza, B.; Lewandowski, A.; Wietfeld, C. AirShield: A system-of-systems MUAV remote sensing architecture for disaster response. In Proceedings of the 2009 3rd Annual IEEE Systems Conference, Vancouver, BC, Canada, 23–26 March 2009; pp. 196–200. [CrossRef]

44. Murphy, R.R.; Tadokoro, S.; Kleiner, A. Disaster Robotics. In *Springer Handbook of Robotics*; Springer: Cham, Switzerland, 2016; pp. 1577–1604.

45. Alvarado, M.; Gonzalez, F.; Fletcher, A.; Doshi, A. Towards the development of a low-cost airborne sensing system to mon-itor dust particles after blasting at open-pit mine sites. *Sensors* **2015**, *15*, 19667–19687. [CrossRef]

46. Villa, T.F.; Gonzalez, F.; Miljievic, B.; Ristovski, Z.D.; Morawska, L. An Overview of Small Unmanned Aerial Vehicles for Air Quality Measurements: Present Applications and Future Prospectives. *Sensors* **2016**, *16*, 1072. [CrossRef] [PubMed]

47. Pajares, G. Overview and Current Status of Remote Sensing Applications Based on Unmanned Aerial Vehicles (UAVs). *Photogramm. Eng. Remote Sens.* **2015**, *81*, 281–330. [CrossRef]

48. Siciliano, B.; Khatib, O. *Handbook of Robotics*; Springer: Cham, Switzerland, 2016.

49. COMSOL. Available online: https://www.comsol.com/ (accessed on 22 July 2021).

50. Wendt, J.; Bourzutschky, M.; Mallinckrodt, A.J.; McKay, S. Computational Fluid Dynamics: An Introduction. *Comput. Phys.* **1993**, *7*, 542. [CrossRef]

Convolutional Neural Networks for Classification of Drones Using Radars

Divy Raval [1,2], Emily Hunter [1,3], Sinclair Hudson [4], Anthony Damini [1] and Bhashyam Balaji [1,*]

[1] Defence Research and Development Canada, 3701 Carling Avenue, Ottawa, ON K2K 2Y7, Canada; divy.raval@ecn.forces.gc.ca (D.R.); emily.hunter@ecn.forces.gc.ca (E.H.); Anthony.Damini@ecn.forces.gc.ca (A.D.)

[2] Institute of Biomedical Engineering, University of Toronto, 27 King's College Cir, Toronto, ON M5S 1A1, Canada

[3] School of Computing, Queen's University, 99 University Ave, Kingston, ON K7L 3N6, Canada

[4] Cheriton School of Computer Science, University of Waterloo, 200 University Ave W, Waterloo, ON N2L 3G1, Canada; sshudson@uwaterloo.ca

[*] Correspondence: Bhashyam.Balaji@ecn.forces.gc.ca

Abstract: The ability to classify drones using radar signals is a problem of great interest. In this paper, we apply convolutional neural networks (CNNs) to the Short-Time Fourier Transform (STFT) spectrograms of the simulated radar signals reflected from the drones. The drones vary in many ways that impact the STFT spectrograms, including blade length and blade rotation rates. Some of these physical parameters are captured in the Martin and Mulgrew model which was used to produce the datasets. We examine the data under X-band and W-band radar simulation scenarios and show that a CNN approach leads to an F_1 score of 0.816 ± 0.011 when trained on data with a signal-to-noise ratio (SNR) of 10 dB. The neural network which was trained on data from an X-band radar with 2 kHz pulse repetition frequency was shown to perform better than the CNN trained on the aforementioned W-band radar. It remained robust to the drone blade pitch and its performance varied directly in a linear fashion with the SNR.

Keywords: drone classification; CNN; machine learning; HERM lines; micro-Doppler; radars

1. Introduction

Modern drones are more affordable than ever, and their uses extend into many industries such as emergency response, disease control, weather forecasting, and journalism [1]. Their increased military use and the possible weaponization of drones have caused drone detection and identification to be an important matter of public safety.

There are several types of technology which can facilitate drone detection and classification. Some sensors employ sound-based or acoustic technology to classify drones. Drones give off a unique acoustic signature ranging from 400 Hz to 8 kHz, and microphones can capture this information. Unfortunately, this technology can only be used at a maximum range of 10 meters, and the microphones are sensitive to environmental noise [2]. When tracking drones through the air, this method becomes impractical.

Optical sensors use one or more cameras to create a video showing the target drone. The classification problem then becomes the identification of specific patterns in the shapes and colours of the drones. This approach is a popular technique because it is intuitive and enables the use of image processing and computer vision libraries [3] as well as neural networks [4]. However, optical sensors have a limited range and require favourable weather conditions. For these reasons, they are not reliable enough to use for drone classification, especially at longer ranges.

Drones and other unmanned aerial vehicles (UAVs) rely on (typically hand-held) controllers, which send radio frequency signals to the drone. These signals have a unique

radio frequency fingerprint that depends on the circuitry of the controller, drone, and the chosen modulation techniques. Radio frequency fingerprint analysis has been studied as a method to detect and classify drones [5].

Finally, radar sensors for drone tracking and classification have been extensively studied [6–9]. Radars are capable of detecting targets at longer ranges than other sensors and perform reliably in all weather conditions at any time of day [10].

The classification technique investigated in this paper is based on the target drone's micro-Doppler signature. A micro-Doppler signature is created when specific components of an object move separately from the rest. The rotation of propeller blades on a drone is sufficient to generate these signatures. The use of radars for studying micro-Doppler signatures has been shown effective [11] and has been used in conjunction with machine learning for many UAV classification problems [12–19]. As such, radars are the chosen technology for this paper.

Previous work has shown that an analysis of the radar return, including the micro-Doppler signature, can reliably distinguish drones from birds [7,8,20]. We now turn to the problem of distinguishing different types of drones. Standard analyses of the radar return include using the short-window and long-window Short Time Fourier Transform (STFT). The short- and long- window labels refer to the rotation period of the drone, or the time it takes for the drone's blades to make a complete 360-degree rotation. A short-window STFT is when the window length is less than a rotation period, while a long-window STFT is when the window length exceeds the rotation period. The long-window STFT generates a unique signature of the drones in the form of Helicopter Rotation Modulation (HERM) lines. The number of HERM lines and their frequency separation can be used to distinguish between the different drones.

For situations where the pulse repetition frequency (PRF) of the radar is not high enough to extract the full micro-Doppler signature, Huang et al. proposed a log harmonic summation algorithm to use on the HERM lines [21]. This algorithm estimates the micro-Doppler periodicity and performs better than the previously used cepstrum method [8] in the presence of noise. Huang also showed using collected radar data that the Minimum Description Length Parametric Spectral Estimation Technique reliably estimates the number of HERM lines. This information can be used to determine whether the target is a rotary drone with spinning propellers [22].

When the full micro-Doppler signature is available (using a high PRF radar), the short-window STFT can be utilized for analysis. Klaer et al. used HERM lines to estimate the number of propeller blades in these situations [23]. They also proposed a new multi-frequency analysis of the HERM lines, which enables the approximation of the propeller rates [23]. In this paper, we leverage the work of Hudson et al., who demonstrated the potential of passing STFT spectrograms into a Convolutional Neural Network (CNN) to classify drones [13].

Recently, Passafiume et al. presented a novel micro-Doppler vibrational spectral model for flying UAVs using radars. This model incorporates the number of vibrational motors in the drone and the propeller rotation rates. They showed that this model is able to reliably simulate the micro-Doppler signature of drones. Furthermore, they proposed that the model could be further studied for use in unsupervised machine learning [24].

In another study, Lehmann and Dall trained a Support Vector Machine (SVM) on simulated data. They simulated their data by considering the drone as a set of point scatterers and superimposing the radar return of each point [25]. However, their work modelled the data as free from thermal noise. Using the Martin and Mulgrew model instead, we can simulate varying signal-to-noise ratio (SNR) conditions in this paper. Doing so provides a more realistic situation in which to apply machine learning. Additionally, our use of CNN provides better classification accuracy than their SVM.

In our investigation, we use the updated versions of the Martin and Mulgrew model [26] to simulate drone signals and perform additional augmentation to improve the data's realism. We used the model to produce datasets distinguished by the SNR and PRFs of the

contained samples. A CNN was trained for each of these datasets, and their performances were analyzed with the F_1 metric. Our findings suggest that it is possible to train a robust five-drone classifier (plus an additional noise class) using just one thousand data samples, each 0.3 s in duration. Furthermore, we show it is possible to train CNN classifiers robust to SNR-levels not included in training while maintaining performance that is invariant to the blade pitch of the drones.

The work presented in this paper contributes to the field of drone classification in several ways. Many studies explore the use of neural networks for a specific SNR. Here, we provide an analysis for a wide range of SNR values, thus making our results more generalizable to different situations. We also show that the selected model is robust against varying pitches of the propeller blades, maintaining its performance when tested on drones whose blade pitch is outside of the training range. Additionally, we find that X-band radars provide better data than W-band radars for this application within the studied SNR range. This last result is likely due to the configuration of our neural network and may not be true in general cases. Finally, we leverage the Martin and Mulgrew model for data simulation, a model that is not commonly used for drone classification.

This paper is organized as follows. Section 2 introduces the reader to the concepts used in our work. We review some of the important radar parameters in Section 2.1, paying close attention to their use in our context. The Martin and Mulgrew model is used to simulate returns from different types of radars and is summarized in Section 2.2. Drone parameters and data generation are discussed in Section 2.3, and an overview of the machine learning pipeline is presented in Section 2.4. The results of the machine learning model are shown and discussed in Sections 3 and 4, respectively. Finally, we present our conclusions and future steps in Section 5.

2. Materials and Methods

2.1. Radar Preliminaries

As discussed previously, radar (RAdio Detection And Ranging) systems are advantageous over other surveillance systems for several reasons. This subsection will define the radar parameters and discuss the signal-to-noise ratio and the radar cross-section, two significant quantities for drone classification.

2.1.1. Radar Parameters

There are two main classes of radars: active and passive. Active radars emit electromagnetic waves at the radio frequency and detect the pulse's reflection off of objects. Passive radars detect reflections of electromagnetic waves that originated from other sources or other transmitters of opportunity. In this paper, we will be focusing our attention on active radars. Such radars may be either pulsed or frequency modulated continuous wave (FMCW) radars. Pulse radars transmit pulses at regular intervals, with nominal pulse duration (or pulse width) of the order of a micro-second and pulse repetition interval of the order of a millisecond. Many variables related to the radar and target dictate a radar's performance. These variables are presented in Table 1.

Table 1. The radar parameters and pre-determined quantities which describe the radar-drone interaction.

Symbol	Parameter Name and Interpretation
PRF	Pulse repetition frequency—The number of pulses emitted by the transmitting antenna every second in pulsed radars
SRF	Sweep repetition frequency—The number of sweeps emitted by the transmitting antenna every second in FMCW radars
P_t	Transmitter power—The power of the transmitted signal in Watts

Table 1. *Cont.*

Symbol	Parameter Name and Interpretation
G_t	Transmitting antenna gain—The gain of the transmitting antenna compared to an isotropic antenna [27]
G_r	Receiving antenna gain—The gain of the receiving antenna compared to an isotropic antenna. The radars simulated in this paper are monostatic radars, meaning that there is just one antenna for transmitting and receiving. Hence, $G_t = G_r$
λ	Wavelength—The wavelength of the light in the emitted pulse
σ	Radar cross-section (RCS)—The surface area of the target that is "visible" to the radar. More technically, it is defined as the surface area of a metal sphere which reflects the same amount of power as the object does [10]
τ	Pulse width—The width or duration of the pulses in pulsed radar or sweep duration in FMCW radar
R	Range—the distance from the radar to the target
T_n	Noise temperature—The combined temperature of external radiating sources, thermal energy lost in the receiving/transmitting lines, and any internal receiver noise [27]
k_b	Boltzmann's constant—The product $T_n \times k_b$ yields the power density in Watts per hertz of bandwidth that is lost due to temperature noise [27]
L	Loss—The loss incurred by transmission lines, an imperfect antenna, and the propagation medium (the air) [27]

For more information about radar types and their operations, we direct interested readers to the text by Dr. Skolnik [28]. We will now turn our attention to some of the specific measurements that help describe how radars can detect and classify drones.

2.1.2. Radar Cross-Section

The radar cross-section (RCS) is critical when working with drones. As explained in Table 1, the RCS of a target is the surface area that is visible to the radar. The RCS varies with the target's size, shape, surface material, and pitch. Typical drones have an RCS value from −15 dBsm to −20 dBsm for X-band frequencies and smaller than −20 dBsm for frequencies between 30–37 GHz [29]. The RCS of drones varies significantly with the drone model and position in the air. A comprehensive study of drone RCS was performed by Shröder et al. They reported that the material is a significant factor in the blade RCS as metal blades have a much higher RCS than plastic ones [30].

The strength of the returned radar signal varies directly with the RCS, making it a critical factor in drone classification using radars. This paper will utilize the micro-Doppler effects from drone propeller blades. Thus, the RCS of the drones' blades is much more important for this investigation than that of the body.

2.1.3. Signal-to-Noise Ratio

Another important quantity for radar studies is the signal-to-noise ratio (SNR). The SNR measures the ratio of received power from the target(s) and the received power from noise. The expression for the SNR depends on the radar parameters previously introduced, including the RCS, and is provided by the radar range equation [31]:

$$\text{SNR} = \frac{P_t G_t G_r \lambda^2 \sigma \tau}{(4\pi)^3 R^4 T_n k_b L} \tag{1}$$

One would expect that classification performance decreases with the SNR because the target becomes less clear. Dale et al. showed this to be true when distinguishing drones from birds [32]. As seen in Equation (1), the SNR is directly related to the RCS and so consequently tends to be small for drones. It is, therefore, crucial to understand and appreciate the signal SNR because it will significantly impact the quality of the trained model. If the training data has an SNR that is too high, the model will not generalize well to realistic scenarios with a lower SNR. The work later in this paper analyzes model performance as a function of the SNR of the signals in the training data.

It is often more convenient to express Equation (1) in decibels (dB), which is a logarithmic scale. The log-scale simplifies the calculation of the SNR quantity by adding the decibel equivalents of the numerator terms and subtracting those in the denominator. A Blake Chart clarifies this process. Table 2 shows an example of such a calculation where the radar operates in the X-band (10 GHz frequency) and the object is 1 km away.

Table 2. Example usage of a Blake Chart for calculating the SNR of a particular drone using a given radar.

Parameter	Unit Value	+ (dB)	− (dB)
Peak Power (W)	1 W	0	0
Gain (dB)	25 dB	50	0
Wavelength (m)	0.03 m	−30.464	0
Cross Section (m^2)	0.01 m^2	−20	0
Range (m)	1000 m	0	120.0
$1/k_b$ (m^{-2} · kg^{-1} · s^2 · K)	1.380649e−23	228.599	0
System Temperature (K)	290 K	0	24.624
Pulse Width (s)	0.001 s	−30	0
$(4\pi)^3$	1984.402	0	32.976
Losses (dB)	7 dB	0	7
Totals		198.135	−184.6
SNR Per Pulse		13.535 dB	

Blake Charts make it easy to see how slightly adjusting one parameter can impact the SNR per pulse. It is important to note that for a particular radar and object at a specified range, the only parameters that can be adjusted are the P_t, λ, and τ. Each of these parameters comes with an associated cost due to limited power supply or the specifications of the radar, and so it is not always possible to achieve a desirable SNR. Due to this, classification models need to perform well in low-SNR conditions.

2.2. Modelling Radar Returns from Drones

The Martin and Mulgrew equation models the complex radar return signal of aerial vehicles with rotating propellers [26]. The model assumes that the aerial vehicle (or drone in our context) has one rotor. The formulation of the model is presented in Equation (2) and was used to simulate radar return signals of five different drones under two different radar settings. French [33] provides a derivation and detailed insights on the model.

$$\psi(t) = A_r e^{j\left(2\pi f_c t - \frac{4\pi}{\lambda}(R + v_{\mathrm{rad}}t)\right)} \sum_{n=0}^{N-1} (\alpha + \beta \cos \Omega_n) e^{-j\frac{L_1+L_2}{2}\gamma_n} \mathrm{sinc}\left(\frac{L_2 - L_1}{2}\gamma_n\right) \quad (2)$$

where

$$\alpha = \sin\big(|\theta| + \phi_p\big) + \sin\big(|\theta| - \phi_p\big) \tag{3}$$

$$\beta = \text{sign}(\theta)\big(\sin\big(|\theta| + \phi_p\big) - \sin\big(|\theta| - \phi_p\big)\big) \tag{4}$$

$$\Omega_n = 2\pi\Big(f_r t + \frac{n}{N}\Big) \tag{5}$$

$$\gamma_n = \frac{4\pi}{\lambda}\cos\theta\sin\Omega_n \tag{6}$$

Table 3 provides a complete description of each of the parameters within the model. Excluding time, t, the model has eleven parameters approximately categorized as radar and drone parameters. Radar parameters include the carrier frequency, f_c, and the transmitted wavelength, λ. The latter set of parameters depends on the position of the drone relative to the radar and the characteristics of the drone's propeller. In particular, the strength of the presented model over the initial version of the Martin and Mulgrew equation is its ability to account for variation in blade pitch of the drones, ϕ_p [26,34].

Table 3. Interpretation of all the parameters in the Martin and Mulgrew model. f_c and λ depend on the specific radar. θ, R, and v_{rad} depend on the position of the drone, while f_r, N, L_1, and L_2 are characteristic of the drone's blades.

Parameter	Interpretation
A_r	Real valued scalar, the scale factor
t	Time
f_c	Frequency of the transmitted signal
λ	Wavelength of the transmitted signal
θ	Angle between the target's plane of rotation and the line of sight from the radar to the target's center of rotation
R	Range of the target
v_{rad}	Radial velocity of the target with respect to the radar
N	Number of propeller blades on target
f_r	Frequency of rotor rotation
L_1	Distance of the blade roots from the target's centre of rotation
L_2	Distance of the blade tips from the target's centre of rotation
ϕ_p	Pitch of the blades relative to horizontal

For several reasons, the Martin and Mulgrew model was the chosen data simulation model. It is a model based on electromagnetic theory and Maxwell's equations. Despite this, it is computationally efficient compared to more sophisticated models. Additionally, the drone parameters used were previously compiled and demonstrated by Hudson et al. [13]. The following section of this paper will strengthen confidence in the model by comparing it to an actual drone signal. It is found that the Martin and Mulgrew model produces distinct HERM line signatures (dependant on the parameters), as seen in the collected data—a fact that is crucial for this investigation. Although the number of rotors on the drone is not the focus of this paper, it is helpful to note that the model assumes that there is a single rotor. A proposed extension to the model sums the signal over the different rotors [35], but it has not been extensively studied.

2.3. Data Generation and Augmentation

This section describes the different sampling and augmentation considerations taken to simulate a Martin and Mulgrew signal. As will be elaborated in Section 2.4, many simulated signals were put together to produce datasets for machine learning.

The data simulation step involved two sets of radar parameters, representing an X-band and W-band radar, respectively. Furthermore, five sets of drone parameters corresponding to different commercial drones were used. Tables 4 and 5 have the parameters for the radars and drones' blades. Note that along with the five drones (classes), a sixth Gaussian-noise class was produced to investigate the possibility of false alarms during classification and their impact.

Table 4. Transmission wavelength and frequency values for a W-band and X-band radar.

Radar	λ (cm)	f_c (GHz)
W-band	0.32	94.00
X-band	3.00	10.00

Table 5. Approximate drone-blade parameters of five drones.

Drone	N	L_1 (cm)	L_2 (cm)	f_r (Hz)
DJI Mavic Air 2	2	0.50	7.00	91.66
DJI Mavic Mini	2	0.50	3.50	160.00
DJI Matrice 300 RTK	2	5.00	26.65	70.00
DJI Phantom 4	2	0.60	5.00	116.00
Parrot Disco	2	1.00	10.40	40.00

Although the selected drones have fixed blade pitches, the parameter was assumed to be variable for modelling purposes since some drones can have adjustable blade pitches. This assumption can improve the generalizability of the analysis. Moreover, θ and R were similarly considered as variable parameters while v_{rad} and A_r were set to be constant (zero and four, respectively) for simplicity. As seen in Table 6, these variable parameters were uniformly sampled to produce meaningful variations between each simulated drone signal.

Table 6. Sampling distributions for some variable parameters.

Variable Parameter	Distribution
ϕ_p (rad)	$\sim \mathcal{U}(0, \pi/4)$
θ (rad)	$\sim \mathcal{U}(\pi/16, \pi/2)$
R (m)	$\sim \mathcal{U}(500, 2000)$
v_{rad} (rad/s)	Asserted to be 0
A_r	Asserted to be 4

Besides varying the above parameters, additional methods were used to produce differences between the simulated signals. We applied shifts in the time domain, adjusted the signal to reflect the probability of detection, and added noise to augment each sample. The time shift was introduced by randomly selecting a t_s such that the resulting signal would be $\psi(t + t_s)$. Next, a probability of detection (p_d) of 0.8 was asserted by removing some data from the signal, simulating the amount of information typically present in real scenarios. Finally, Gaussian-normal noise was introduced to produce a signal of the desired SNR. The added noise, **n**, was sampled from $\mathcal{N}(0, \sigma_0)$ where the standard deviation was

given by the rearranged form of Equation (7). Equation (8) presents the final augmented signal produced using the Martin and Mulgrew equations. Each simulated sample used for machine learning was 0.3 s in length.

$$\text{SNR} = 10\log_{10}\left(\frac{A_r^2}{\sigma_0^2}\right) \quad \xleftrightarrow{\text{rearranged}} \quad \sigma_0 = \sqrt{10^{-\text{SNR}/10}A_r^2} \tag{7}$$

$$\psi_{\text{final}}(t) = \text{detection}(\psi(t+t_s), p_d = 0.8) + \mathbf{n} \tag{8}$$

The use of a convolutional network requires data with spatially relevant information. The long-window STFT was applied to produce a spectrogram representation of the simulated signals [36]. The STFT is one of many methods used to produce spectrograms for convolutional learning [18]. Recall that a short-window STFT has a window size smaller than the rotation period of the drone. However, according to the Nyquist Sampling Theorem, using a short window requires that the radar PRF is at least four times the maximum Doppler shift of the propeller blades to detect micro-Doppler blade flashes unambiguously. In contrast, a long-window STFT cannot detect blade flashes because the window size is larger than the rotational period of the propellers. The long-window method only requires that the PRF is at least twice the propeller rotation rate, making this method more versatile for different radars. Previous work suggests that the long-window STFT can reveal HERM micro-Doppler signatures of drones even under low PRF conditions [21,23].

We used two configurations of the long-window STFTs. The first has a window size of 512 for the X-band radar with a PRF of 2 kHz, while the second is a window size of 2048 for the W-band radar with a PRF of 20 kHz. Due to its higher PRF value, the latter requires a larger window size.

Figure 1 shows a long-window STFT spectrogram for each of the five drones outlined in Table 5. The signals were produced using radar parameters with the X-band (left column) and W-band (right column). For demonstration purposes, these signals have no augmentation. Notice the unique HERM line signature, or bands, within each spectrogram. These signatures are not an exact representation of the drones, but the important fact is that they are distinct from one another—just as we would expect in practice. Furthermore, these spectrograms would be easily identifiable by a convolutional network. We will investigate whether this remains true for signals that have undergone the previously discussed augmentation.
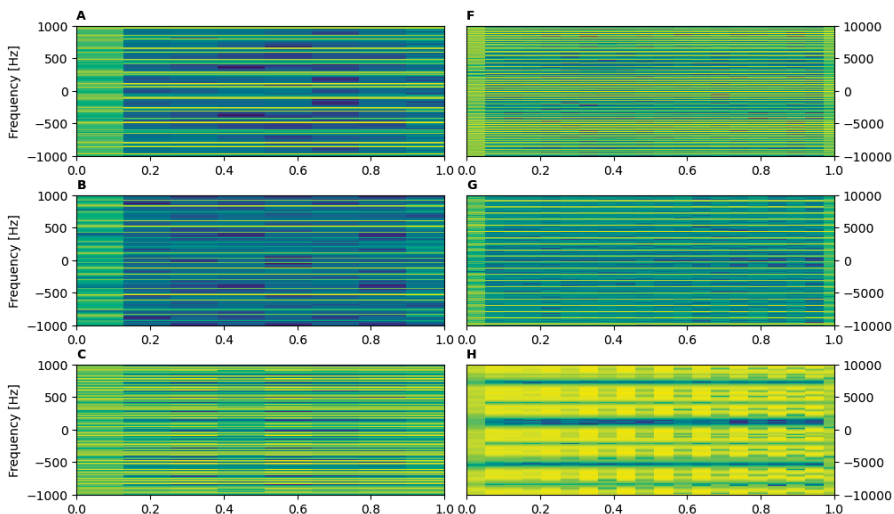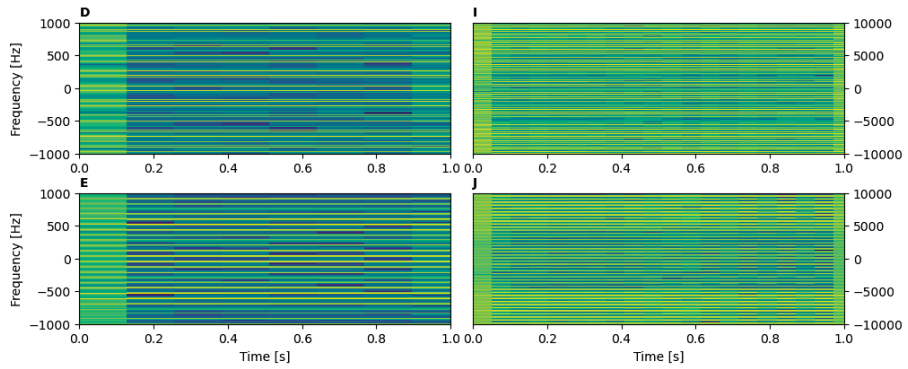

Figure 1. *Cont.*

Figure 1. Long-window STFTs displaying the HERM line signatures of five different drones under (**A–E**) X-band and (**F–J**) W-band simulation conditions. (**A,F**) Mavic Air 2, (**B,G**) Mavic Mini, (**C,H**) Matrice 300 RTK, (**D,I**) Phantom 4, (**E,J**) Parrot Disco. For demonstration, $v_{rad} = 0$, $\theta = \pi/4$, $R = 1000$, $\phi_p = \pi/8$, and $A_r = 4$ were enforced. Signals were produced using no augmentation, and a p_d of 1.

Before continuing with the creation of our neural network, it is prudent to examine whether the radar simulation is suitable for our purposes. To validate the Martin and Mulgrew model, we used the results of a laboratory experiment involving a commercial Typhoon H hexacopter drone. An X-band radar measured the drone, which was fixed in place and operating at a constant blade rotation frequency. Figure 2 shows the reflected radar signal and its corresponding long-window STFT spectrogram. This measured time-series is periodic, just like the simulated signals produced using Equation (2). Additionally, there appear to be HERM line signatures in the STFT, verifying the reasonability of the artificial data spectrograms shown previously. The spectrogram is not as clean as those seen in Figure 1 owing to background noise in the collected signal. This fact is addressed by our augmentation methods which make the simulated signals more realistic. Further validation would have been performed; however, the authors were limited by data access. From this point on, the Martin and Mulgrew model was pursued because it can capture many of the physical drone-blade parameters that contribute to the micro-Doppler signature.
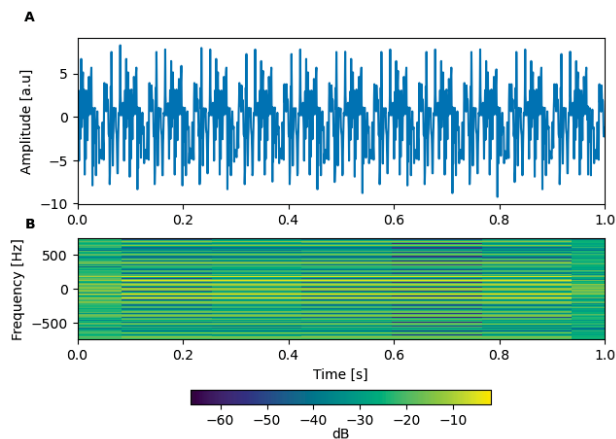

Figure 2. (**A**) Radar return signal and (**B**) its corresponding long-window STFT. Captured using a TyphoonH hexacopter and an X-band radar with $f_c = 9.8$ GHz and 1.5 kHz PRF.

2.4. Machine Learning Pipeline

Datasets were produced using the described data generation and augmentation methodology. A new dataset was created for each combination of radar specification and SNR, where the SNR ranged between 0 dB and 20 dB, in increments of 5 dB. The range for the SNR was motivated by the expected SNR of actual signals collected by our available radars. It is not easy to collect large real-drone datasets of high fidelity in practice. Thus, each dataset contained only 1000 spectrogram-training samples, equally-weighted among the six classes (five drones and noise). A smaller validation set of 350 samples was created to follow an approximate 60-20-20 percentage split. However, having the ability to produce the artificial data with relative ease, three test datasets—each with 350 samples— were uniquely generated. Therefore, when models were evaluated, the results contained standard deviation measures.

The architecture of the neural network has a convolutional and a linear portion. Given an input batch of spectrograms, they undergo three layers of convolution, SoftPlus activation, instance normalization, dropout, and periodic max pooling. The batch then undergoes linearization and passes through three hidden layers with ReLU activation. Finally, the loss is computed using the logits and cross-entropy. Figure 3 demonstrates this pipeline, with the dashed outline representing the model itself.
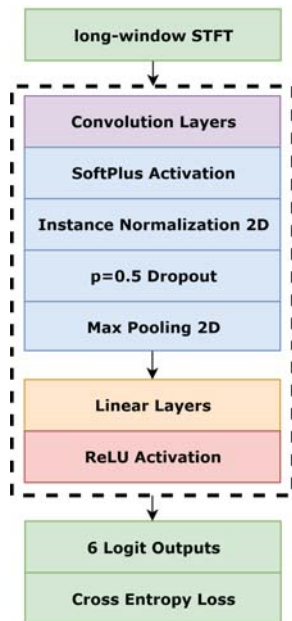
Figure 3. Machine learning pipeline where the data input is a batch of spectrograms. The dashed portion is the neural network.

Recall that the two simulated radars used different PRF values, resulting in the size of the input spectrograms being different. A PRF of 20 kHz produces more data points per 0.3 s in the signal, resulting in a larger spectrogram than a PRF of 2 kHz. The spectrogram sizes are 512×4 and 2048×7 for the 2 kHz PRF and 20 kHz PRF, respectively. This required the creation of two (similar) networks, one for each radar. The general architecture still holds because both networks differ only in kernel sizes and the number of hidden units in the linear layers.

A CNN model was trained for each training dataset (each dataset represents a unique radar and SNR combination). The training was conducted for 300 epochs, and the most

generalizable models were selected through consideration of the training and validation loss and accuracy. All training occurred using PyTorch, a Python machine learning library, on an RTX 2060S GPU.

From the work of El Kafrawy et al. [37], the macro-F_1 score, referred to as the F_1 score, was used to evaluate the performance of the trained models against the three test datasets. In many cases, the F_1 score can be similar to pure accuracy. However, it benefits from considering false positives and false negatives through precision and recall, respectively, making it a preferred metric to accuracy. The formulation is provided in Equation (9), where C represents the number of classes (six), P_c is the precision and R_c is the recall, both of class $c \in \{1, 2, \ldots, C\}$ [37]. In their definitions, TP_c, FP_c, and FN_c are the number of true positives, false positives, and false negatives for class c, respectively.

$$F_1 = \frac{2}{C} \sum_{c=1}^{C} \frac{P_c R_c}{P_c + R_c} \tag{9}$$

where

$$P_c = \frac{TP_c}{TP_c + FP_c} \tag{10}$$

$$R_c = \frac{TP_c}{TP_c + FN_c} \tag{11}$$

3. Results

Presented in Figure 4 are the F_1 score results of the trained models. The model for the X-band 2 kHz PRF radar achieved an F_1 score of 0.816 ± 0.011 at an SNR of 10 dB. The W-band 20 kHz PRF radar performed much worse, only reaching comparable results at 20 dB SNR. A W-band radar with a 2 kHz PRF was trained as a control model, which demonstrated weaker performance against the X-band radar at the same PRF. The X-band 2 kHz PRF radar, trained on 10 dB SNR, was used for further investigation moving forward due to its ability to perform relatively well under high noise conditions.
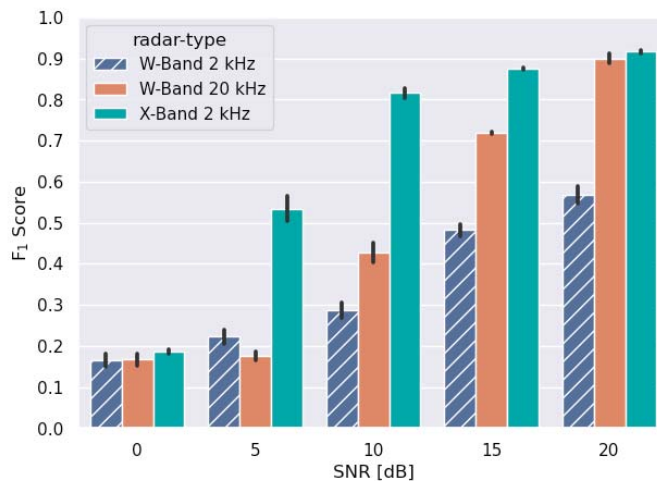
Figure 4. F_1 score of various models versus the SNR of the training data. The vertical black line at the top of each bar shows the standard deviation of that model. The standard deviations were created using three test datasets.

A multi-class confusion matrix and Receiver Operating Characteristic (ROC) curve were used to gain insight into the performance of the selected X-band model for each class.

The selected model performs well at classifying drone classes. However, the classifier demonstrates a high false-negative rate when a false alarm sample (noise) is presented. As seen in Figure 5, noise is most often confused with the Matrice 300 RTK. Similarly, within Figure 6, noise has the lowest area under the ROC curve. Nevertheless, the model maintains a high average ROC area of 0.9767, suggesting a minimal compromise between true positives and false negatives.
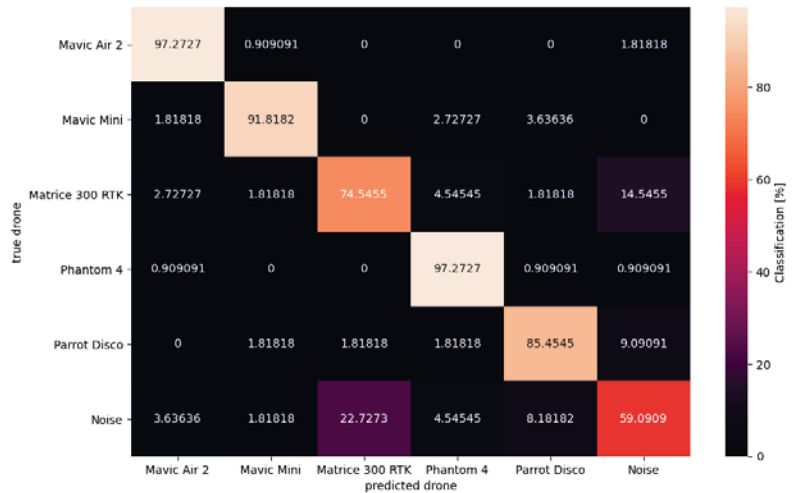
Figure 5. Row-normalized confusion matrix results of the X-band 2 kHz PRF model trained on 10 dB training data. Order of the classes as follows: Mavic Air 2, Mavic Mini, Matrice 300 RTK, Phantom 4, Parrot Disco, and Noise (false alarm).
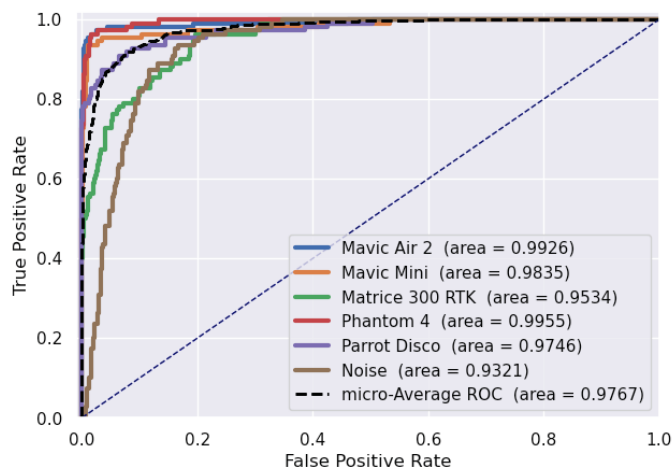
Figure 6. Multi-class ROC curves of the X-band 2 kHz PRF model trained on 10 dB training data. The micro-Average ROC, an aggregate representation, is shown as the black dotted-line.

Next, the robustness of the model against blade pitch and varying SNR values was investigated. The inclusion of blade pitch was a driving factor in using the more complex version of the Martin and Mulgrew equations to produce the artificial dataset. The results of the trained X-band 2 kHz PRF model against the blade pitch, ϕ_p, are in Figure 7. The

model's F_1 score for the bins between 0 and $\pi/4$ remains close to the mean of 0.816 as expected. More importantly, the model remained robust, maintaining comparable performance when tested with ϕ_p values outside those used in training.
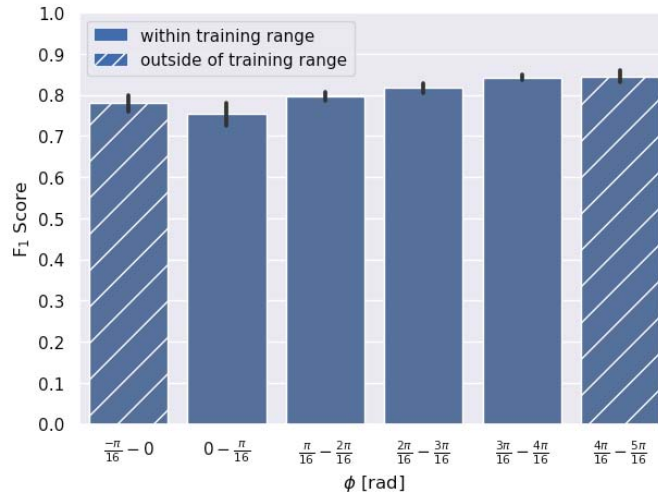
Figure 7. F_1 score versus different blade pitch, ϕ_p, bins for the X-band 2 kHz PRF model trained on the data within the ϕ_p range shown by the solid bins. The striped bins show the performance when tested on data with ϕ_p values not used in training. The standard deviations were created using three test datasets.

In Figure 8, a similar analysis was conducted to determine the model's robustness to varying SNR values. The model performs worse when tested on data with an SNR lower than 10 dB. In contrast, the same model can classify much more effectively as the SNR of the provided test data increases.
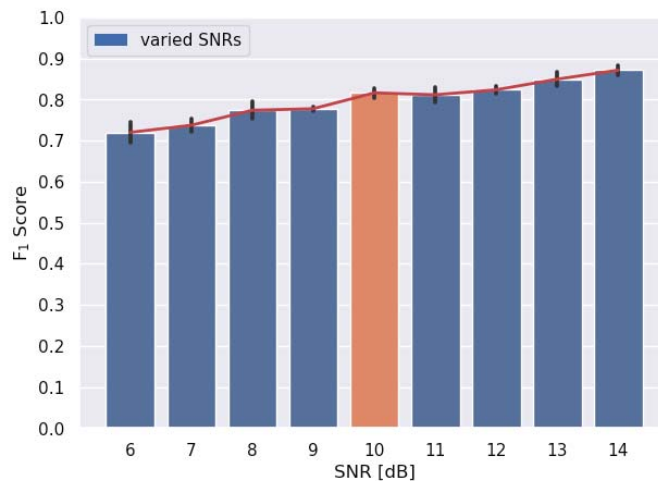
Figure 8. F_1 score versus varying SNR values for the X-band 2 kHz PRF model trained on 10 dB SNR data, where the blue bars strictly represent test data with SNR values not used in training. The standard deviations were created using three test datasets.

4. Discussion

Following the processes outlined in Section 2.3, artificial datasets were generated using the Martin and Mulgrew model, and CNN classifiers were trained for each dataset. Training each of these models enables us to quickly identify the required SNR of the data for drone classification and compare the performance of different radars for this application. Of particular importance, only 1000 spectrograms were present in each training set. This small size reflects the case where real drone data is minimal in applications. Obtained from the work of El Kafrawy et al., and presented in Equation (9), the multi-class F_1 score metric was used to measure the performance of each trained model [37].

As found in Figure 4, the performance in the X-band is superior to that of the W-band for the chosen CNN. This is somewhat surprising as the W-band corresponds to a shorter wavelength and would intuitively result in better classification performance. There could be several reasons for this. Firstly, the 20 kHz PRF spectrogram is quite dense and holds a lot more information than a 2 kHz PRF STFT in the X-band. The additional complexity and detail may not be as robust against noise. By simulating a W-band radar at the same PRF as the X-band, we identify the reason for the discrepancy in performance lies in the transmitted wavelength parameter in the simulation. Note that we do not claim the X-band frequency is the best, but rather that it is better than W-band radars for typical parameters. Furthermore, X-band radars offer superior all-weather capabilities over other frequency bands. The W- and X- band radars were chosen for this paper because they are lighter and more portable than other band radars; however, it is possible that lower frequency bands (e.g., S-band and L-band) may provide superior performance over the X-band. This is undoubtedly a topic of exploration in future work. Additionally, our conclusion is limited to the choice of the model. A deeper CNN might yield a different conclusion, and it is something we plan to explore in future work.

In any case, the result is interesting and valuable. It suggests that an X-band radar with a PRF on the order of a few kHz can be highly effective in classifying drones under our simulation model. The lower PRF requirement in the X-band is also welcome as this leads to a longer unambiguous range. The 2 kHz PRF X-band classifier, trained on 10 dB SNR data, was selected for further investigation.

A multi-class confusion matrix and ROC curve were produced in Figures 5 and 6, respectively, which revealed shortcomings in the selected model. The noise class exhibits the weakest performance in both, and the confusion matrix reveals that noise is most often misclassified as a DJI Matrice 300 RTK drone. The reasoning for this misclassification is not immediately apparent. However, a qualitative consideration of Figure 1 suggests that spectrograms with a dense micro-Doppler signature (HERM lines) might be more easily confused with noise. The Matrice 300 RTK, in particular, has a very dense signature. On the other hand, an STFT of Gaussian noise contains no distinct signature or obvious spatial information. Under the low, 10 dB SNR conditions, the Matrice 300 RTK spectrogram likely becomes augmented to the point where it begins to resemble the random-looking noise STFTs. This result emphasizes the need for reliable drone detection models and algorithms, as false alarms can easily be confused with some drone types during the classification process.

Consideration of Figure 7 shows that model performance is invariant to different values of ϕ, even for values not included in the training dataset. This result is important because it suggests that classification performance is mostly unaffected by the pitch of the drone blades. In a similar analysis against varying SNR, the trained model demonstrated a linear trend in performance. The model performed worse when evaluated using data with an SNR lower than the 10 dB used for training while showing superior performance on less noisy, higher dB data samples. This result is shown in Figure 8. Both of these results inform that when training drone classifiers, the blade pitch of the samples is not critical. Additionally, models should maintain linear performance near the SNR of the training samples.

In Figures 4, 7 and 8 we observe the standard deviation of the test results shown by vertical lines. These were produced by evaluating the model's performance on three different test sets. The small size of the standard deviations strengthens our results' confidence and, therefore, the efficacy of our CNN classifier.

5. Conclusions

This paper investigated the feasibility of classifying drones using radar signals and machine learning. The utilized datasets were generated using the Martin and Mulgrew model with realistic drone parameters. Five distinct drones were classified, and a sixth noise (false alarm) class was also considered during our analysis. We show that it is possible to train a CNN model to classify drones in low SNR scenarios, using a signal of just 0.3 s in duration. We find that practically realizable radars (e.g., X-band with 2 kHz PRF) can lead to a F_1 performance of 0.816 ± 0.011 using training data of 10 dB SNR. Further analysis of the trained model shows that it remains robust to varying drone blade pitch and linearly decreases and increases in performance with the SNR of the signal. However, the model becomes less viable when false alarms are presented, as they can be confused with some drone classes. We wish to stress that the presented analysis is based on a simple model and should be corroborated with higher-fidelity models.

Our goals are to continue exploring the Martin and Mulgrew model for the purpose of constructing drone classifiers. Specifically, we wish to investigate the effect of transmitted wavelengths on model performance. An in-depth comparison of the classification results using a more comprehensive range of radars is a good topic for future work. Further exploration should uncover why the W-band radar signals provided worse data than the X-band for use in our CNN. As stated previously, the Martin and Mulgrew model assumes that the modelled drone has a single rotor; however, many real drones have up to eight rotors. Future work could investigate an adapted Martin and Mulgrew model proposed in [35] which considers multiple rotors. Moreover, it would be interesting to compare the performance of models trained using samples of shorter duration but with higher PRF against training samples of longer duration with lower PRF values. Consideration of different machine learning approaches and more complex CNN architectures will also be of interest. In parallel, recognizing that simulations produce results under controlled and ideal conditions, we wish to elucidate the applicability of the trained CNN models on real drone data. This can be investigated via a direct application of the model on real data or through a transfer learning process where the trained models are used as a starting point for further training.

Abbreviations

The following abbreviations are used in this manuscript:

CNN	Convolutional Neural Network
HERM	Helicopter Rotor Modulation
PRF	Pulse Repetition Frequency
RCS	Radar Cross-Section
ROC	Receiver Operating Characteristic
SNR	Signal-to-Noise Ratio
STFT	Short-Time Fourier Transform
UAV	Unmanned Aerial Vehicle

References

1. 38 Ways Drones Will Impact Society: From Fighting War to Forecasting Weather, UAVs Change Everything. Available online: https://www.cbinsights.com/research/drone-impact-society-uav/ (accessed on 5 August 2021).
2. Nijim, M.; Mantrawadi, N. Drone classification and identification system by phenome analysis using data mining techniques. In Proceedings of the 2016 IEEE Symposium on Technologies for Homeland Security (HST), Waltham, MA, USA, 10–11 May 2016; pp. 1–5. [CrossRef]
3. Gökçe, F.; Üçoluk, G.; Şahin, E.; Kalkan, S. Vision-Based Detection and Distance Estimation of Micro Unmanned Aerial Vehicles. *Sensors* **2015**, *15*, 23805–23846. [CrossRef] [PubMed]
4. Aker, C.; Kalkan, S. Using deep networks for drone detection. In Proceedings of the 2017 14th IEEE International Conference on Advanced Video and Signal Based Surveillance (AVSS), Lecce, Italy, 29 August–1 September 2017; pp. 1–6. [CrossRef]
5. Ezuma, M.; Erden, F.; Anjinappa, C.K.; Ozdemir, O.; Guvenc, I. Micro-UAV Detection and Classification from RF Fingerprints Using Machine Learning Techniques. In Proceedings of the 2019 IEEE Aerospace Conference, Big Sky, MT, USA, 2–9 March 2019; pp. 1–13. [CrossRef]
6. Fioranelli, F.; Ritchie, M.; Griffiths, H.; Borrion, H. Classification of loaded/unloaded micro-drones using multistatic radar. *Electron. Lett.* **2015**, *51*, 1813–1815. [CrossRef]
7. Fuhrmann, L.; Biallawons, O.; Klare, J.; Panhuber, R.; Klenke, R.; Ender, J. Micro-Doppler analysis and classification of UAVs at Ka band. In Proceedings of the 2017 18th International Radar Symposium (IRS), Prague, Czech Republic, 28–30 June 2017; pp. 1–9. [CrossRef]
8. Harmanny, R.I.A.; de Wit, J.J.M.; Cabic, G.P. Radar micro-Doppler feature extraction using the spectrogram and the cepstrogram. In Proceedings of the 2014 11th European Radar Conference, Rome, Italy, 8–10 October 2014; pp. 165–168. [CrossRef]
9. Molchanov, P.; Harmanny, R.I.; de Wit, J.J.; Egiazarian, K.; Astola, J. Classification of small UAVs and birds by micro-Doppler signatures. *Int. J. Microw. Wirel. Technol.* **2014**, *6*, 435–444. [CrossRef]
10. Fell, B. Basic Radar Concepts: An Introduction To Radar For Optical Engineers. In *Effective Utilization of Optics in Radar Systems*; International Society for Optics and Photonics: Huntsville, AL, USA, 1977; Volume 128. [CrossRef]
11. Chen, V.C. Analysis of radar micro-Doppler with time-frequency transform. In Proceedings of the Tenth IEEE Workshop on Statistical Signal and Array Processing (Cat. No.00TH8496), Pocono Manor, PA, USA, 16–16 August 2000; pp. 463–466. [CrossRef]
12. Rahman, S.; Robertson, D.A. Multiple drone classification using millimeter-wave CW radar micro-Doppler data. In *Radar Sensor Technology XXIV*; Ranney, K.I., Raynal, A.M., Eds.; International Society for Optics and Photonics, SPIE: Bellingham, WA, USA, 2020; Volume 11408, pp. 50–57. [CrossRef]
13. Hudson, S.; Balaji, B. Application of machine learning for drone classification using radars. In *Signal Processing, Sensor/Information Fusion, and Target Recognition XXX*; Kadar, I., Blasch, E.P., Grewe, L.L., Eds.; International Society for Optics and Photonics, SPIE: Bellingham, WA, USA, 2021; Volume 11756, pp. 72–84.
14. Kim, B.K.; Kang, H.S.; Lee, S.; Park, S.O. Improved Drone Classification Using Polarimetric Merged-Doppler Images. *IEEE Geosci. Remote. Sens. Lett.* **2020**, 1–5. [CrossRef]
15. Brooks, D.; Schwander, O.; Barbaresco, F.; Schneider, J.Y.; Cord, M. Deep learning and information geometry for drone micro-Doppler radar classification. In Proceedings of the 2020 IEEE Radar Conference (RadarConf20), Florence, Italy, 21–25 September 2020; pp. 1–6. [CrossRef]
16. Brooks, D.; Schwander, O.; Barbaresco, F.; Schneider, J.Y.; Cord, M. Complex-valued neural networks for fully-temporal micro-Doppler classification. In Proceedings of the 2019 20th International Radar Symposium (IRS), Ulm, Germany, 26–28 June 2019; pp. 1–10. [CrossRef]
17. Brooks, D.A.; Schwander, O.; Barbaresco, F.; Schneider, J.; Cord, M. Temporal Deep Learning for Drone Micro-Doppler Classification. In Proceedings of the 2018 19th International Radar Symposium (IRS), Bonn, Germany, 20–22 June 2018; pp. 1–10. [CrossRef]
18. Gérard, J.; Tomasik, J.; Morisseau, C.; Rimmel, A.; Vieillard, G. Micro-Doppler Signal Representation for Drone Classification by Deep Learning. In Proceedings of the 2020 28th European Signal Processing Conference (EUSIPCO), Amsterdam, The Netherlands, 18–21 January 2021; pp. 1561–1565. [CrossRef]

19. Kim, B.K.; Kang, H.; Park, S. Drone Classification Using Convolutional Neural Networks With Merged Doppler Images. *IEEE Geosci. Remote. Sens. Lett.* **2017**, *14*, 38–42. [CrossRef]
20. Rahman, S.; Robertson, D.A. Radar micro-Doppler signatures of drones and birds at K-band and W-band. *Sci. Rep.* **2018**, *8*, 17396. [CrossRef] [PubMed]
21. Huang, A.; Sévigny, P.; Balaji, B.; Rajan, S. Fundamental Frequency Estimation of HERM Lines of Drones. In Proceedings of the 2020 IEEE International Radar Conference (RADAR), Washington, DC, USA, 28–30 April 2020; pp. 1013–1018. [CrossRef]
22. Huang, A.; Sévigny, P.; Balaji, B.; Rajan, S. Radar Micro-Doppler-based Rotary Drone Detection using Parametric Spectral Estimation Methods. In Proceedings of the 2020 IEEE SENSORS, Rotterdam, The Netherlands, 25–28 October 2020; pp. 1–4. [CrossRef]
23. Klaer, P.; Huang, A.; Sévigny, P.; Rajan, S.; Pant, S.; Patnaik, P.; Balaji, B. An Investigation of Rotary Drone HERM Line Spectrum under Manoeuvering Conditions. *Sensors* **2020**, *20*, 5940. [CrossRef] [PubMed]
24. Passafiume, M.; Rojhani, N.; Collodi, G.; Cidronali, A. Modeling Small UAV Micro-Doppler Signature Using Millimeter-Wave FMCW Radar. *Electronics* **2021**, *10*, 747. [CrossRef]
25. Lehmann, L.; Dall, J. Simulation-based Approach to Classification of Airborne Drones. In Proceedings of the 2020 IEEE Radar Conference (RadarConf20), Florence, Italy, 21–25 September 2020; pp. 1–6. [CrossRef]
26. Martin, J.; Mulgrew, B. Analysis of the effects of blade pitch on the radar return signal from rotating aircraft blades. In Proceedings of the 92 International Conference on Radar, Brighton, UK, 12–13 October 1992; pp. 446–449.
27. Blake, L.V. Recent Advancements in Basic Radar Range Calculation Technique. *IRE Trans. Mil. Electron.* **1961**, *MIL-5*, 154–164. [CrossRef]
28. Skolnik, M. *Radar Handbook*, 3rd ed.; Electronics Electrical Engineering, McGraw-Hill Education: New York, NY, USA, 2008.
29. Semkin, V.; Haarla, J.; Pairon, T.; Slezak, C.; Rangan, S.; Viikari, V.; Oestges, C. Analyzing Radar Cross Section Signatures of Diverse Drone Models at mmWave Frequencies. *IEEE Access* **2020**, *8*, 48958–48969. [CrossRef]
30. Schröder, A.; Aulenbacher, U.; Renker, M.; Böniger, U.; Oechslin, R.; Murk, A.; Wellig, P. Numerical RCS and micro-Doppler investigations of a consumer UAV. In *Target and Background Signatures II*; International Society for Optics and Photonics Security + Defence: Edinburgh, UK, 2016. [CrossRef]
31. Budge, M.C. Radar Range Equation. University Lecture. 2011. Available online: http://www.ece.uah.edu/courses/material/ EE619-2011/RadarRangeEquation(2)2011.pdf (accessed on 14 July 2021).
32. Dale, H.; Baker, C.; Antoniou, M.; Jahangir, M.; Atkinson, G.; Harman, S. SNR-dependent drone classification using convolutional neural networks. *IET Radar Sonar Navig.* **2021**. Available online: https://ietresearch.onlinelibrary.wiley.com/doi/pdf/10.1049/ rsn2.12161 (accessed on 13 December 2021). [CrossRef]
33. French, A. Target Recognition Techniques for Multifunction Phased Array Radar. Ph.D. Thesis, University College London, London, UK, 2010.
34. Martin, J.; Mulgrew, B. Analysis of the theoretical radar return signal form aircraft propeller blades. In Proceedings of the IEEE International Conference on Radar, Arlington, VA, USA, 7–10 May 1990; pp. 569–572. [CrossRef]
35. Regev, N.; Yoffe, I.; Wulich, D. Classification of single and multi propelled miniature drones using multilayer perceptron artificial neural network. In Proceedings of the International Conference on Radar Systems (Radar 2017), Belfast, UK, 23–26 October 2017; pp. 1–5. [CrossRef]
36. Markow, J.; Balleri, A. Examination of Drone Micro-Doppler and JEM/HERM Signatures. In Proceedings of the 2020 IEEE Radar Conference (RadarConf20), Florence, Italy, 21–25 September 2020; pp. 1–6. [CrossRef]
37. ElKafrawy, P.; Mausad, A.; Esmail, H. Experimental Comparison of Methods for Multi-label Classification in different Application Domains. *Int. J. Comput. Appl.* **2015**, *114*, 1–9. [CrossRef]

Article

Ice Detection on Aircraft Surface Using Machine Learning Approaches Based on Hyperspectral and Multispectral Images

Maria Angela Musci [1,2]**, Luigi Mazzara** [1,2,*] **and Andrea Maria Lingua** [1,2]

[1] DIATI, Department of Environment, Land and Infrastructure Engineering, Politecnico di Torino, Corso Duca degli Abruzzi 24, 10129 Torino, Italy; mariaangela.musci@polito.it (M.A.M.); andrea.lingua@polito.it (A.M.L.)

[2] PIC4SeR, Politecnico Interdepartmental Centre for Service Robotics, 10129 Torino, Italy

[*] Correspondence: luigi.mazzara@polito.it; Tel.: +39-3453183320

Abstract: Aircraft ground de-icing operations play a critical role in flight safety. However, to handle the aircraft de-icing, a considerable quantity of de-icing fluids is commonly employed. Moreover, some pre-flight inspections are carried out with engines running; thus, a large amount of fuel is wasted, and CO_2 is emitted. This implies substantial economic and environmental impacts. In this context, the European project (reference call: MANUNET III 2018, project code: MNET18/ICT-3438) called SEI (Spectral Evidence of Ice) aims to provide innovative tools to identify the ice on aircraft and improve the efficiency of the de-icing process. The project includes the design of a low-cost UAV (uncrewed aerial vehicle) platform and the development of a quasi-real-time ice detection methodology to ensure a faster and semi-automatic activity with a reduction of applied operating time and de-icing fluids. The purpose of this work, developed within the activities of the project, is defining and testing the most suitable sensor using a radiometric approach and machine learning algorithms. The adopted methodology consists of classifying ice through spectral imagery collected by two different sensors: multispectral and hyperspectral camera. Since the UAV prototype is under construction, the experimental analysis was performed with a simulation dataset acquired on the ground. The comparison among the two approaches, and their related algorithms (random forest and support vector machine) for image processing, was presented: practical results show that it is possible to identify the ice in both cases. Nonetheless, the hyperspectral camera guarantees a more reliable solution reaching a higher level of accuracy of classified iced surfaces.

Keywords: hyperspectral images; multispectral data; machine learning; ice detection

1. Introduction

Human safety is one of the main concerns at airports and aircraft icing represents a significant hazard in aviation [1]. The ice formation leads the aircraft's balance in a loss of control, and de-icing and anti-icing are necessary treatments for flight safety during the winter [2,3]. However, de-icing operations require the employment of chemicals such as ethylene glycol- (EG-) or propylene glycol- (PG-) that can cause damage to the environment, in particular for the nearby surface and groundwater [3].

Ice accumulation can occur due to the supercooled droplets colliding with a hard surface forming an ice film [4] with an air temperature between 0 and −20 °C [5]. As reported by the FAA (Federal Aviation Administration), structural or in-flight ice and ground ice can be identified [6,7]. The former occurs when the aircraft is flying through visible water such as rain or cloud droplets. The latter, instead, may accumulate on parked aircraft due to precipitation and atmospheric conditions.

According to the temperature, liquid water content, speed of the formation process, aircraft surface temperature and shape, particle concentration and size, it is possible to distinguish three different types of structural ice [8] (Figure 1):

- Rime ice that is a milky-white deposit of the ice, and it is the result of rapidly freezing of small droplets at low temperature after impacting with the aircraft surfaces. It grows at low temperature (<15 °C) with low water liquid content. The rime density is lower than 0.2–0.3 g cm^{-3}, and it is composed mainly of discrete ice granules [9].
- Clear or glaze ice, glassy transparent ice, caused by large droplets that run back on the aircraft surface with slow freezing, has a density higher than 0.8 or 0.9 g cm^{-3} [10].
- Mixed-ice that has mixed features of the previous ones, because it forms when both rime and clear ice accumulate on the aircraft.

Figure 1. Ice types: rime ice, clear ice, and mixed-ice. (Photo credit: NASA, adapted from [8]).

Frost, snow (or slush), fog, drizzle, rain (and their freezing states), and ice pellets can be considered the foremost examples of ground icing.

The sublimation of deposited water vapor on the aircraft can form frost when the temperature is at or below freezing. A fog formed of supercooled water droplets which freeze upon the impact with the aircraft surface, also known as freezing fog, produces a coating of rime/clear ice.

Rain and drizzle, uniform precipitations of liquid water particles, can be distinguished by drop diameters and proximity. The rain is characterized by drops with a diameter more than 0.5 mm very separated, instead of drizzle, that has close drops with diameters less than 0.5 mm. These two kinds of precipitations, in the freezing state, can create ice deposits with a transparent appearance. Snow or slush are precipitations of ice crystals. The slush is formed by water-saturated snow.

As gathered from the Manual of Aircraft Ground De-icing/Anti-icing Operations [2], the difference between in flight and on ground icing is not referred mainly on the characteristics of the ice but the impacts on the flight and the de-icing procedures. As it is possible to notice from the definitions of freezing fog or frost and freezing rain, clear and rime ice can also occur on the ground.

Due to the physical characteristics of these types of ice, their identification is currently based on visual (e.g., for rime ice, snow) and tactile (e.g., for clear ice, frost) inspections carried out by trained and qualified ground crew or flight crew [11].

The cleaning process moreover involves the use of a considerable amount of aircraft de-icing fluids (ADFs), because targeted operations are not achievable. The contamination check shall cover all surfaces that have aerodynamic-, control-, sensing-, movement- or measuring-function such as wings, tail surfaces, engine, fuselage, antennas, and sensors. This investigation requires enough visibility of these parts. A verification of cleaned surfaces shall always be made after the de-icing/anti-icing, and this inspection can be either visual or tactile. The whole procedure is time-consuming and demanding, especially since it is crucial to maintain the flight's schedule. A time-effective strategy for ice detection is required to limit ADFs use and improve the management of the crew's operations.

In this context, UAV (uncrewed aerial vehicle) [12] imagery combined with machine learning algorithms has shown excellent potential for rapid, remote, cost-effective detection tasks. This approach allows ice identification from multiple views with an automatic check-up operation.

The SEI (Spectral Evidence of Ice) project [13,14] proposes to provide an integrated solution that can handle the automatic pre-deicing inspection, ice detection, and cleaning verification procedure. The expert crew manages the request of de-icing and sends the UAV to the parking area (or hangar) of a specific aircraft that needs the procedure. The UAV can autonomously recognize the location of the aircraft and starts the inspection. Indeed, the multi-sensor UAV platform, equipped with a hyperspectral or multispectral camera, has been designed to monitor and inspect aircraft in the specific de-icing area of the airport. The main task of the drone is the identification of the location and the extension of the ice-contaminated area. For this purpose, an automatic methodology for geometric and radiometric detection of the ice has been determined. The development of computer-oriented methods for ice detection is still challenging due to the physical characteristics of the ice, variable atmospheric condition, and lack of autonomous technology in this application field.

Several devices have been developed for ice characterization for on-ground and in-flight inspection [15,16]. Some examples are based on ultrasonic, magnetostrictive, and electromagnetic sensors [17,18]. Some researchers such as Gong et al. [19] have discussed the use of the mid-infrared sensor for ice detection. In this field, the spectral imagery, not only in the mir-infrared but also in all electromagnetic range, is an emerging technology because of its high spectral and spatial resolution [20]. Our study would fulfil the gap and present the potential of hyperspectral or multispectral imaging technique in the ice detection on aircraft.

Regardless of devices for data acquisition, machine learning approaches, such as random forest (RF) [14] and support vector machine (SVM) [15], have been utilized for material detection and their characterization [21]. These algorithms perform well in reducing the complexity of the classification task associated with spectral data because they can handle the high dimensionality input space and noisy dataset [22,23].

This work, within the activities of the SEI project, tests the feasibility to use spectral sensors, such as hyperspectral and multispectral cameras, and random forest and support vector machine, as machine learning algorithms.

Firstly, the purpose is the selection of the most suitable sensor to mount on a UAV prototype that has to respond to cost requirements. For this reason, a multispectral camera, as a low-cost sensor, was examined to reduce the system production cost. At the same time, the paper addresses the definition of the time-effective automatic methodology for ice detection using the machine learning approach. As known, the hyperspectral camera has a spectral resolution of more than 100 bands instead of the multispectral camera that has a few bands (most of the cases from three to 15). A dimensionality reduction process has been applied to accurately compare the performance of the two algorithms on images with sharply different spectral resolution.

Since the UAV prototype is under construction, the experimental analysis was performed with a simulation dataset acquired on the ground. However, the methodology can be easily transferred to a UAV application.

2. Materials and Methods

This section describes the two sensors (Section 2.1), the methodology (Section 2.2), and the algorithms and accuracy assessment (Sections 2.3–2.5).

2.1. Sensor Description

The data acquisition was performed by a hyperspectral camera (Senop Rikola) and a multispectral camera (MAPIR Survey 3N). Senop Rikola hyperspectral camera is a snapshot camera based on a Fabry–Perot Interferometer [24,25]. It includes two not aligned sensors: one sensor acquires near-infrared bands (659.2–802.6 nm) and the second captures visible bands (from 502.8 to 635.1 nm). The MAPIR survey 3N is a multispectral camera, and it records RGN (red, green, and near-infrared bands) images as red (660 nm), green (550 nm), and near-infrared (850 nm) bands [26]. An RGB camera with specifications comparable with the MAPIR (same spatial resolution, optics, and pixel size) was

used to include the blue band (475 nm). The reason for the introduction of an additional band is explained in the Methodology (Section 2.2).

The Senop and the MAPIR are lightweight UAV sensors, and they were selected because they have a similar spectral range from 500 to 950 nm. Table 1 summarizes the specifications of the two sensors.

Table 1. Sensor specifications: the Senop Rikola hyperspectral camera and the MAPIR Survey3N multispectral camera.

| Camera	Senop Rikola	MAPIR Survey3N
Lens optics	H 36.5°, V 36.5°	H 41° HFOV (47 mm)
Spectral range	500–900 nm	550–850 nm
Spectral channels	380	3
Spectral resolution	1 nm	-
Shutter type	Global	Rolling
Focal length	9 mm	8.25 mm
Image resolution	1010 × 1010 pixels	4000 × 3000 pixels
Pixel size	5.5 μm	1.55 μm
Weight	720 g	75.4 g
Dimensions	172.7 × 89 × 77 mm	59 × 41.5 × 36 mm
Cost	≈60,000€	≈700€

2.2. Methodology

The overall methodology is shown in the schema below (Figure 2).

For data collection, ice samples were generated in the laboratory using molds and a real section of the aircraft wing. Since the idea was to have ice samples similar to rime (white ice) and clear ice (transparent ice), two types of ice were created. Snow or other varieties of ice cited above are not considered in this analysis because its production in our laboratory was not possible. The details of sample production and data acquisition will be explained in Section 3.

The hyperspectral and multispectral images were radiometrically corrected using the empirical line method (ELM) and the reference panel.

After that, the dimensionality reduction with principal component analysis (PCA) was executed on the hyperspectral data. This step allows defining two new datasets, the one composed by principal component hypercubes and the ones with a reduced number of bands. The original hyperspectral dataset and both the new ones also with multispectral images were classified to evaluate the performance of the detection and the computational time. Moreover, for the multispectral case, further analysis was made using the RGBN (red, green, blue, near-infrared) images, to understand the improvement of the additional band on the classification.
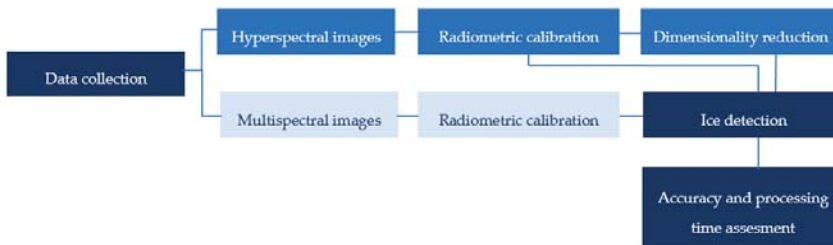
Figure 2. Methodology workflow.

2.3. Dimensionality Reduction of Hyperspectral Images: Feature Extraction and Feature Selection

The high dimensionality of hyperspectral images is a crucial problem in real-time application because it takes time both in the acquisition and in ice detection steps. Moreover, it can produce the so-called Hughes phenomenon [27]. For addressing this issue, the most popular methods for

dimensionality reduction are feature extraction and feature selection. Feature extraction refers to a linear or nonlinear transformation procedure that reduces the data redundancy in the spatial and spectral domain. Feature selection refers to a process to define a subset of the original features without a transformation [28–30]. PCA is widely used as a feature extraction method, but it can also be used for feature selection.

The PCA dimensionality reduction is based on the estimation of the eigenvalues of the covariance matrix [31–33]. For each pair of bands, the covariance is calculated as (1):

$$\sigma_{i,j} = \frac{1}{N-1} \sum_{p=1}^{N} (DN_{p,i} - \mu_i)(DN_{p,j} - \mu_j) \tag{1}$$

where $DN_{p,j}$ and $DN_{p,j}$ are digital numbers of a pixel p in the bands i and j, respectively, and the μ_i and μ_j are the averages of the DN for bands i and j. Then the covariance matrix is defined as (2):

$$C_{b,b} = \begin{pmatrix} \sigma_{1,1} & \dots & \sigma_{1,j} \\ \dots & \dots & \dots \\ \sigma_{i,1} & \dots & \sigma_{i,j} \end{pmatrix} \tag{2}$$

The roots of the characteristic equation provide the eigenvalues λ (3):

$$\det(C - \lambda I) = 0 \tag{3}$$

where C refers to the covariance matrix (2), and I is the diagonal identity matrix.

The eigenvalues indicate the quantity of original information that they compress. The variance percentage for each principal component is calculated as the ratio of each eigenvalue and the sum of all of them. Those components which contain minimum variance and, thus, the minimum number of information can be discarded. The matrix form of the principal components can be expressed as (4):

$$Y_i = \begin{pmatrix} w_{1,1} & \dots & w_{1,j} \\ \dots & \dots & \dots \\ w_{i,1} & \dots & w_{i,j} \end{pmatrix} X_j \tag{4}$$

where Y is the vector of the principal components (PC), W the transformation matrix, and X the vector of the original data, the coefficients $w_{i,j}$ are the eigenvectors, and they link the PC with the real variable providing information on their relationship. The eigenvectors can be calculated for each λ_k as (5):

$$(C - \lambda_k I)w_k = 0 \tag{5}$$

where C and I can be defined as the (3), while λ_k is the k eigenvalues and w_k is the k eigenvectors.

There are three practical criteria to select the most representative PCs [34]:

- Cumulative percentage of total variation: the representative PCs must contribute to the cumulative percentage of total variation to achieve 80% or 90%.
- Kaiser's criterion: the selected PCs must have a variance that exceeds 1, which means that if all the variables are independent, the PCs have variance equal to 1 in the correlation matrix.
- Screen graph: it is the plot of eigenvalues λ_k related to the order number of that eigenvalue k. The PC number can be selected looking at the 'elbow' in the graph, that indicates the components to retain. The number of PCs to use will be given by the smallest k characterized by the trend of λ_k. The trend of the function must be sharply decreasing on the left of 'elbow' point, while on the right, it has to be constant or weakly decreasing [35].

Once the PCs have been chosen, the interpretation of them is based on eigenvectors, derived from the (5). The meaning of PCs can be determined looking at the coefficient ($w_{i,j}$) of variables X_j. The greater $w_{i,j}$ is, the higher the correlation, and X_j is the most important for the PC [36].

2.4. Machine Learning: Random Forests and Support Vector Machine

Random forest (RF) algorithm builds multi-decision trees (forest) that operate as an ensemble trained with a bagging mechanism [37,38]. The bagging mechanism samples N random bootstraps of the training set with replacement. The number of trees characterized the forest, and the higher the number of trees, the more accurate the classification [39]. Moreover, the following parameters can affect the performance of the RF classifier: the tree depth, that is the number of splits for each tree, the split criteria, that handle the split at each node (such as GINI index), and the minimum split [40,41].

Support vector machine (SVM) is a binary algorithm and constructs an optimal hyperplane or a set of hyperplanes, that can be employed for the classification task [42]. The best hyperplane can separate data points of different classes, and it is usually the plane that has the most significant margin between the two classes [40]. SVM can be extended to the multiclass problem through two different approaches: the one-against-all or the one-against-one. In the one-against-all approach, a set of N binary classifiers is applied to the N-class problem. The second approach, one-against-one, carries out a series of binary classifiers to each pair of classes. The training sample size has a high impact on the performance of the SVM, as defined in Myburgh G. et al. [43].

2.5. Evaluation Metrics

Either for the random forest and the support vector machine, the accuracy assessment for the performance evaluation can be achieved with different parameters based on the error matrix. According to the literature, the selected parameters are the following [44,45]:

- Overall accuracy (OA) that is the ratio of the total number of correctly classified pixels with respect to the total number of reference pixels;
- User's accuracy (UA) that is the ratio of pixels correctly classified in given class with respect to all pixels classified in the specific category.

Moreover, in this specific real-time application, the computational time for the classification part was assessed. The processing time of the training procedure was not taken into account because the final goal was to use transfer learning.

3. Ice Detection: An Experimental Analysis

For the experimental analysis, it was not possible to collect the real types of ice; thus, different kinds of ice were generated in the laboratory as much as similar to the case study. Two types of ice were produced: the first one similar to the rime ice with milky-white color and the second one to the glassy clear ice.

The former was created using the water vapor condensed into the freezer at a temperature of −15 °C and its thickness reaches values between 2 and 6 cm. The latter was generated by freezing tap water within plastic molds at a temperature of −15 °C. Different plastic molds were used for producing different blocks of ice that contained from 5 to 20 mL of water with a thickness of approximately around 3 cm. The ice blocks were located on a section of an aircraft wing to simulate the typical conditions in which the ice is present.

The aluminum panel used in the tests was a section of a Socata MS.894 Rally Minerva with a dimension of $400 \times 400 \times 2$ mm. Before icing, the panel was stored in a freezer so the icing would start with low surface temperature. Figure 3 shows the configuration of the samples.

Figure 3. Example of annotated image with reference data. Training set sample (**a**) and validation set sample (**b**).

3.1. From Data Collection to Sample Annotation

The dataset was built by collecting a ground measurement. The acquisitions were performed at Photogrammetry, Geomatics and GIS Laboratory of DIATI (Department of Environment, Land and Infrastructure Engineering) at Politecnico di Torino (Italy) [46]. During this campaign, 10 images for the hyperspectral and eight for the multispectral sensor with different illumination conditions were collected (18 images in overall). The various illumination conditions were generated using a different number of lamps and a combination of lamps and natural light to simulate the real scenario in which the drones will be used in the parking area or the hangar. The term "Test" refers to each image with different environmental conditions in this paper. All data were recorded, maintaining stable positions and varying rotations of the camera slightly.

The hyperspectral camera was used in manual mode connected to the computer through a USB cable. The selected image resolution was 1010×1010 pixels. The images were composed by 100 bands covering the spectral range from 502 to 906 nm, with a wavelength step of 4 nm and a Full with Half Maximum resolution (FWHM, where Wide means low gap index). The integration time was set at 450 ms based on the environmental illumination condition. The sequence of the bands was automatically generated using the Rikola Hyperspectral Imager software v2.0. These parameters were chosen to cover the whole spectral range. The whole electromagnetic spectrum was also covered to identify the most characteristic bands and features of studied materials. For the MAPIR instead, the camera's sensitivity was set to ISO- 800, and the exposure time was fixed to 1/15 s.

The two datasets of images were radiometrically calibrated using the Empirical Line Calibration tool of ENVI 4.7 [47]. Then, the images of each sensor were manually annotated. In both cases, the same 10 classes were considered: rime ice, clear ice, white aluminum, aluminum, floor tile, wood and reference panel (white, black, grey 21%, and grey 27%). The representative classes were only the rime ice, the clear ice, and the white aluminum (Figure 3). These classes were chosen according to the materials that it was possible to distinguish in the real case at aircraft scale. The selected materials were related to the object (in our case, the aircraft) and the ice. Other materials were included in the background in different classes to improve the performance of the classification. The option of a single class for background materials would alter the accuracy of outcomes. The number of samples per class for each dataset are reported in Table 2.

Table 2. Hyperspectral and multispectral reference samples per class.

| Class	Hyperspectral Samples (Pixels)	Multispectral Samples (Pixels)
Rime ice	10,156	101,797
Clear ice	10,457	104,819
White aluminum	11,632	116,588
Aluminum	3580	35,912
Wood	10,896	93,624
Floor tile	19,812	198,572
White reference panel	9545	95,672
Black reference panel	16,024	160,617
21% grey reference panel	12,980	130,089
27% grey reference panel	10,670	106,949
Average pixels per class	10,523	104,058

The training and test samples were collected based on visual interpretation. ArcGIS Pro 2.5.0 toolbox was used to create polygons as reference data for each class.

3.2. Dimensionality Reduction of Hyperspectral Data: Results

To reduce the hyperspectral data dimensionality, PCA was carried out using the "Principal components tools" of ArcGIS Pro 2.5.0 [48]. As described in Section 2.3, it was possible to adopt the PCA as feature extraction and band selection method.

As the first step, the feature extraction was performed to define the principal components. In the second step, the selected PCs were used for significative band selection. Both feature extraction and band selection methods were applied for understanding the best solution for ice detection.

Therefore, for the feature extraction, the eigenvalue and cumulative variance were obtained to identify the number of principal components (PCs), which means the new dimensionality. The outcomes of the first image only were reported as an example because the selection process and conclusions were the same for the other pictures. Table 3 shows the percentages of the primary five components of the sample image. As can be seen from Table 3, three PCs reach 90.31% of the total variance in original data for the first criterion and pass the 1% for Kaiser's rule (Section 2.3). As a consequence, the dimensionality of the new representation is three, and the rest of the component can be discarded. Moreover, also the screen plot in Figure 4 illustrates that it is possible to identify three as the number of PCs (third rule described in Section 2.3).
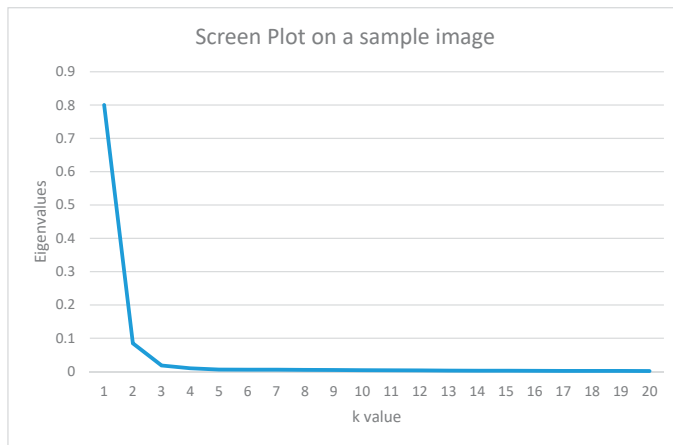

Figure 4. Screen graph on a sample image. Zoom of the 'elbow'.

Table 3. Principal component analysis (PCA): example of eigenvalue and cumulative variance in percentage on a single sample image.

Component	Percent %	Cumulative%
1	80.0010	80.0010
2	8.4818	88.4828
3	1.8341	90.3169
4	0.9935	91.3104
5	0.5888	91.8992

After the identification of the PC number, the first three principal components were used to select a reduced number of original bands for the classification task. The band selection process was carried out using the eigenvectors for each PC. The higher the absolute value of the band eigenvector, the higher the importance of that band for the specific principal component. According to this criterium, considering that the number of significative bands is strictly related to the application, a threshold of eigenvector values, defined for each component, allows to identify the significative bands. The plot of eigenvector values reports the correlation between spikes of the function and the representative bands. Figures 5–7 represent the eigenvector values with respect to the band number for the three selected principal components in four representative images (Test1, Test2, Test6, Test10) among 10 hyperspectral images. Different illuminations and the change of the state of ice characterize these four tests, and this comparison was made to check the recurrence of the most significant bands, that can be selected. The presence of spikes in the eigenvectors function allows to recognize the bands, for all the images for the three selected PCs (Table 4):
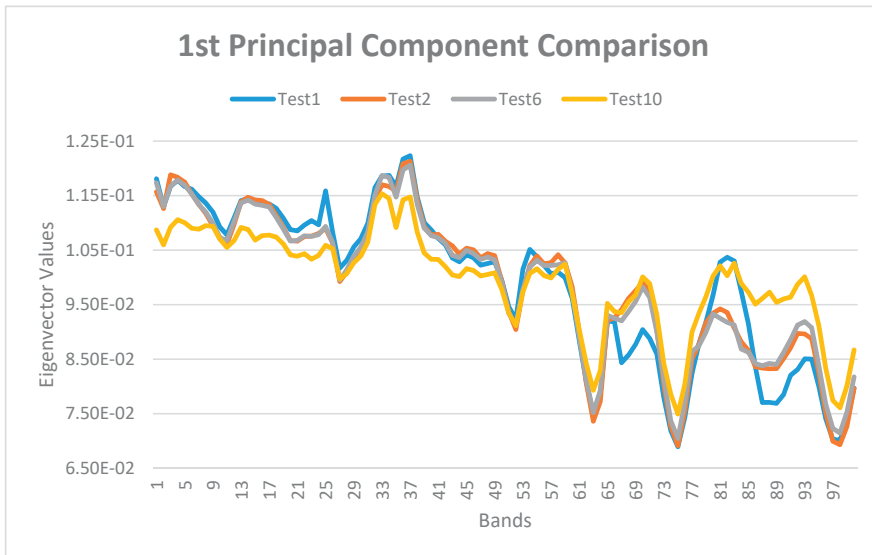
Figure 5. First principal component eigenvalues plot.
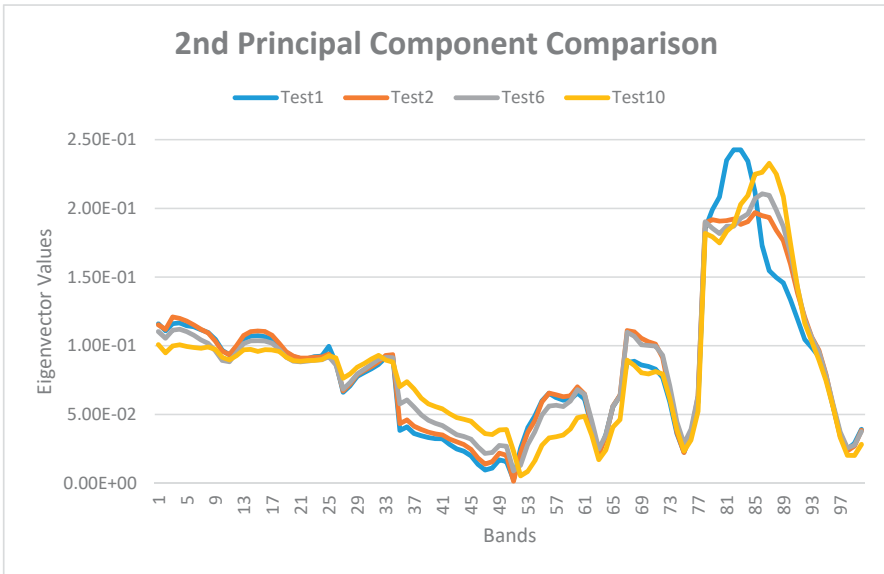
Figure 6. Second principal component eigenvalues plot.
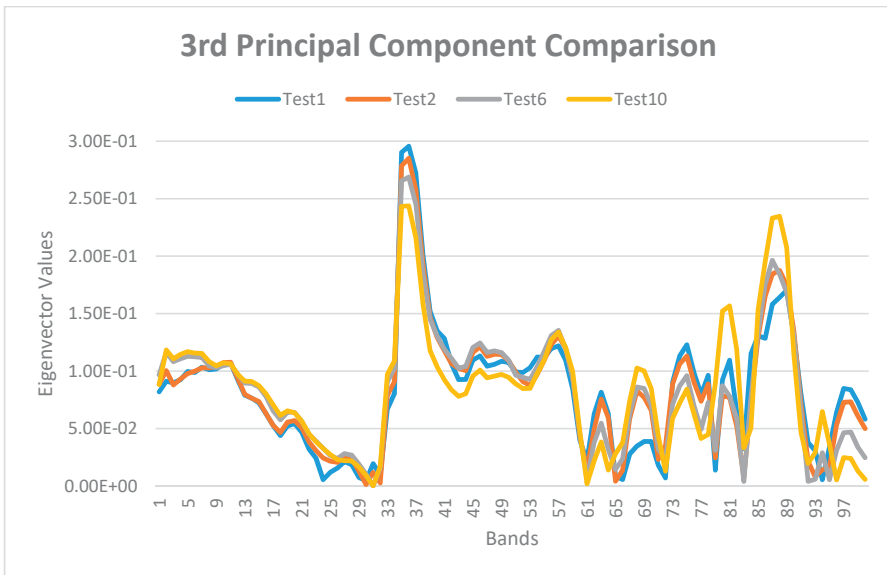
Figure 7. Third principal component eigenvalues plot.

As it is possible to notice in Table 4, there are recurring bands in each test. Taking into account all the identified bands, a new hypercube with 27 bands, that are 1 (506.31 nm), 3–7 (from 514.48 to 530.11 nm), 14 (558.28 nm), 25 (602.47), 32–38 (from 630.2 to 654.19 nm), 78–89 (from 817.58 to 861.65 nm) can be generated. However, considering only the popular bands in each principal component of all images, the number of significative bands can be further reduced to 10. The significative bands, in this latter case, are 4–5 (from 518.12 to 522.48 nm), 33–37 (from 634.36 to 650.38 nm), 83–85 (from 837.98 to 846.21 nm).

Table 4. Band selection for the three principal components (PC) in the representative tests (Test1, Test2, Test6, Test10).

Principal Component	Test1	Test2	Test6	Test10
1	1, 3–7, 25, 32–38	1, 3–6, 14, 33–37	1, 3–6, 32–37	4, 5, 32–34, 36, 37
2	80–85	80–85	78–89	83–89
3	35–37	35–37	35–37	35–37, 86–89

Three new datasets came from the dimensionality reduction process: 10 new images composed by the three PCs, 10 new hypercubes with 10 bands and 10 hypercubes with 27 bands. The first set of modified hypercubes was created through the toolbox "Principal Component Analysis" of ArcGIS Pro 2.5.0 selecting three as a maximum number of principal components. The two remaining datasets with reduced hypercubes were generated using a customized routine of Matlab for hyperspectral data decomposition and the "Composite Bands" tool of ArGIS Pro 2.5.0 [49] for the selected band composition.

3.3. Hyperparameter Tuning for Random Forest and Support Vector Machine

The hyperparameter tuning process plays a crucial role in improving the accuracy of RF and SVM algorithms.

Before starting with the hyperparameters adjustment, data were split in 80% for training and 20% for testing. The tuning of hyperparameters was made on the training set for defining a model. Accuracy assessment was carried out for either the training and testing set to verify the performances of the model in the classification task. The validation curve allows to visualize the values of the model hyperparameters, and it shows different values of the single hyperparameter related to the accuracy trend.

The optimized hyperparameters were chosen according to two criteria. The first one is the minimum difference between the overall accuracy of training and validation models, and the second one is the best user's accuracy only for the validation. It is necessary to notice that for the evaluation of the accuracy the random choice of the samples has to be taken into account; thus, tolerance has to be considered. Accuracy analysis of training and validation are presented for both the algorithms.

Moreover, the accuracy assessment of the rime ice, clear ice, and white aluminum is under the attention among the other classes. These three classes are distinctive in the real de-icing application. The clear ice, as explained in the Introduction (Section 1), is critical to identify by visual inspection. Thus, it has a relevant weight in this analysis.

The tuning was implemented either for RF or SVM on a single image (Test_1) of both datasets (hyperspectral and multispectral images) and the "Segmentation and Classification tools" of ArcGIS Pro 2.5.0 [50]. The tests were made on a window workstation (Windows 10) with an Intel® Core™ I7-6500U CPU at 2.50 Ghz, GPU AMD Radeon™ R7 M360 (Iceland) (six compute units at 980 MHz, 2048 MB) and 16 GB of RAM.

Since SEI project application requires a near real-time approach (Section 1), in this section, the computational time was evaluated because one of the aims of the optimization is the definition of the trade-off between accuracy and processing time.

As described in Section 2.4, the hyperparameters for each classifier have to be tuned. They are the same either for hyperspectral and multispectral. The optimization was executed in manual mode. For the RF algorithm, the maximum number of samples for each class was fixed; we tuned two hyperparameters: the tree depth and the number of trees. For what concerns the SVM instead, only the maximum number of samples per class was tuned.

3.3.1. Hyperparameters Tuning for the Hyperspectral Dataset

Starting for the RF, the sample size was set to 2000 for each class for tuning the tree depth and the number of the trees. The tree depth optimization was done varying its value from 5 to 30. Instead,

the number of trees was fixed to 50. As reported in Table 5, the difference between the overall accuracy (OA) is comparable in all training and validation configuration. The case with a depth equal to 5 was kept out because it was not reasonable with a low number of trees. Therefore, looking just to the validation results, the tree depth equal to 30 produces the best value of OA and clear ice accuracy. For these reasons, the selected tree depth was equal to 30.

Table 5. Training accuracy (on the left) and validation accuracy (on the right) for random forest (RF) tree depth optimization. R_i stands for rime ice, C_i for clear ice, and W_a for white aluminum. In yellow, the selected optimized hyperparameter.

D_Trees	Training Accuracy (%)				Validation Accuracy (%)			
	R_i	C_i	W_a	Overall	R_i	C_i	W_a	Overall
5	73.6842	91.0615	74.7475	92.5425	42.4802	92.9577	64.8855	85.5371
10	80.1887	98.8636	92.9412	97.0971	44.4992	94.9346	69.5067	87.7175
15	78.8018	98.8506	93.4524	96.8969	43.128	95.0083	68.9602	87.0574
20	84.6535	93.956	93.8547	97.2472	41.2747	94.108	68.7908	86.6773
25	79.3427	97.1429	93.4911	96.8468	42.2256	92.5159	68.932	86.5173
30	81.6038	99.422	95.3757	97.2472	43.6863	95.7816	70.8692	87.83

Instead, for the number of tree selection, the tree depth value was fixed to 30, according to Table 5. The number of trees was varied from 5 to 50 (Table 6). Following the same reasoning defined for the selection of tree depth, the cases with a lower number of trees were excluded. Indeed, the differences among the OA is comparable in the other configurations. Concerning Table 6, the cases 15, 30, and 50 were characterized by a similar OA value that is also the highest one (87.9% on average). However, the accuracy of the C_i class leads with a gap in the case 50. As a consequence, the number of trees equal to 50 was the optimized value.

Table 6. Training accuracy (on the left) and validation accuracy (on the right) optimization of RF number of trees. R_i stands for rime ice, C_i for clear ice, and W_a for white aluminum. In yellow the selected optimized hyperparameter is shown.

N_Trees	Training Accuracy (%)				Validation Accuracy (%)			
	R_i	C_i	W_a	Overall	R_i	C_i	W_a	Overall
5	85,3403	96.5909	91.0053	97.1471	39.0855	93.9542	66.8908	86.0172
10	83.3333	99.422	95.4802	97.5475	41.1854	93.9344	67.7368	86.6573
15	**82.381**	**99.422**	**94.2529**	**97.3974**	**45.4699**	**95.1604**	**71.3681**	**87.9587**
20	80.7512	98.3051	95.2663	97.2472	43.2602	94.2122	71.205	87.2575
25	85.8586	97.2067	95.0549	97.6977	42.8571	93.4959	72.0339	87.3253
30	**82.6923**	**97.7011**	**93.2203**	**97.1972**	**44.0476**	**94.3548**	**71.1538**	**87.8743**
35	86.8687	99.4253	95.6522	97.998	44.081	93.75	70.892	87.3375
40	83.0846	96.4912	90.3226	96.9469	42.1217	94.2997	68.7988	86.5973
45	81.6425	98.8506	92.1348	97.0971	42.6404	95.098	69.9681	87.4375
50	**81.6038**	**99.422**	**95.3757**	**97.2472**	**43.6863**	**95.7816**	**70.8692**	**87.83**

In Figure 8, the comparison between training and validation overall trends among all the considered depths and numbers of trees can be appreciated. The validation curves confirm the previous observations and the criteria used for the optimized hyperparameters selection.

Table 7 presents the RF processing time for the training in the analyzed configurations considering the tuning of both the hyperparameters. In the case of D_Trees, the processing times are not excessively influenced by the increase of the depth number. While in the case of N_trees, the higher the number of trees, the higher the computational time. However, the computational time is stable after 15 N_tree because the selected sample size does not affect the number of trees. It is possible, thus, to choose 50 as N_trees value.

Figure 8. RF validation curve for maximum depth (on the **left**) and maximum number of trees (on the **right**).

Table 7. Processing time for the training in RF using different values of tree depth (on the left) and the number of trees (on the right). In yellow the time for training the model with the selected optimized hyperparameter is shown.

D_Trees	Processing Time	N_Trees	Processing Time
5	34″	5	14″
10	31″	10	26″
15	26″	15	32″
20	26″	20	31″
25	27″	25	32″
30	33″	30	29″
-	-	35	33″
-	-	40	30″
-	-	45	33″
-	-	50	33″

For what concerns the SVM instead, the maximum number of samples per class ranged between 100 and 5000 samples. The differences between OA training and validation remains 8% on average in all configurations (Table 8). The highest value of the OA (validation) occurs in the case of 5000 samples, but this configuration was excluded because the related computational time is too long (3h4′25″) (Table 9). Thus, the cases of 100, 750, and 1000 were taken into account. The configuration 100 was discarded because the sample size was small, and the random choice of the sample hugely affects the overall accuracy in the images.

Table 8. Training accuracy (on the left) and validation accuracy (on the right) optimization of support vector machine (SVM) number of the sample. R_i stands for rime ice, C_i for clear ice, and W_a for white aluminum. In yellow the selected optimized hyperparameter is shown.

N_Samples	Training Accuracy (%)				Validation Accuracy (%)			
	R_i	C_i	W_a	Overall	R_i	C_i	W_a	Overall
100	77.6744	97.7401	92.1687	96.3964	56.6879	99.1667	72.4719	91.4671
250	86.8687	97.7401	96.7568	97.9980	46.8354	96.4567	74.5247	89.7206
500	86.6667	1.0000	94.6237	97.9479	44.7059	95.2756	73.1707	88.6228
750	93.5135	99.4382	98.4615	99.0490	51.8644	**93.9623**	90.9091	90.9182
1000	91.8919	98.895	97.3822	98.7487	52.8571	**92.6740**	89.0000	91.0679
2000	91.5344	1.0000	97.8836	98.9990	49.6815	93.8697	89.4444	89.8204
5000	97.1910	1.0000	98.4925	99.5996	52.9825	92.8058	91.1917	91.3673

Table 9. Processing time for the training in SVM using different values of sample size. In yellow the time for training the model with the selected optimized hyperparameter is shown.

N_Samples	Processing Time
100	2′8″
250	12′26″
500	24′51″
750	47′21″
1000	1h18′2″
2000	1h33′36″
5000	3h4′25″

For the remaining cases, since OA is comparable, thus the hyperparameter selection was based on the accuracy of the clear ice. In the validation, the C_i accuracy is 94.0% in the 750 sample case, instead of 92.7% in the 1000 sample case. According to this consideration, the selected number of samples was 750. The validation curves confirm that this parameter is the best fit (Figure 9).
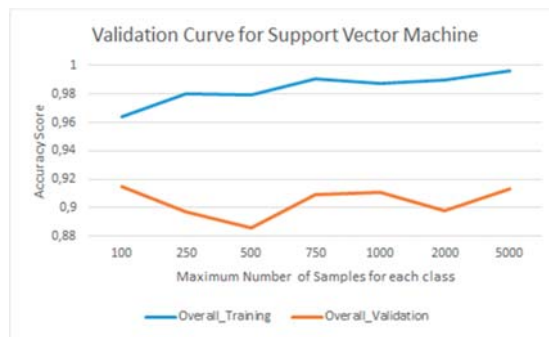
Figure 9. SVM validation curve for the maximum number of samples.

Table 9 reports the processing time for each configuration. It is possible to notice that, as expected, the computational time increases according to the increase of the sample size.

3.3.2. Hyperparameter Tuning for the Multispectral Dataset

With the RF, the samples size was set to 10,000 for each class. Tree depth and the number of trees ranges were chosen according to the number of samples and the image resolution. For multispectral images, the training sample size is five times greater than the hyperspectral, and the resolution is 4000×3000 pixels instead of 1010×1010 pixels. The case 50_30 was chosen as starting point according to the previous tuning on hyperspectral data (Section 3.3.1). The tree depth optimization was done, varying its value from 30 to 60. The number of trees ranged from 50 to 125.

Table 10 presents the training and validation accuracies considering all the combinations of the number of trees (xx in the test code) and the depth tree (yy in the test code).

The OA in training and validation is constant in all configurations, 81% and 77%, respectively. As a consequence, the best configuration can be defined, looking only to the validation accuracy. The OA accuracy is not strongly affected by the different hyperparameters. However, the test 100_30 presents the highest value of OA (77,8%). Looking at the clear ice UA, the best case should be 125_40 with a value of 69.8% instead of 69.7% in the case 100_30. From these observations, it is not possible to recognize this case as the best fit without the computational time analysis because the UA for C_i is quite similar (Table 11).

Table 10. Training accuracy (on the left) and validation accuracy (on the right) RF tree depth and the number of trees optimization. R_i stands for rime ice, C_i for clear ice, and W_a for white aluminum. The test name is defined as xx_yy, where xx is the number of trees, yy is the depth. In yellow the selected optimized hyperparameter is shown.

Test (xx_yy)	Training Accuracy (%)				Validation Accuracy (%)			
	R_i	C_i	W_a	Overall	R_i	C_i	W_a	Overall
50_30	70.5078	66.9162	56.3398	81.6832	55.3701	68.7615	60.2531	77.1311
50_40	69.8004	67.3592	56.2977	816582	54.1104	67.8014	60.6952	77.0461
50_50	69.5568	67.5865	55.8317	81.5282	53.0954	68.4173	60.8929	77.2861
50_60	70.0849	67.6036	54.2184	81.4681	53.5284	68.5125	60.6882	77.6211
75_30	68.8278	67.2374	55.5764	81.4281	53.9481	67.9496	60.4317	77.1311
75_40	69.9799	67.5952	56.2234	81.7932	53.4521	68.7778	59.3454	76.9912
75_50	69.5681	66.3261	55.0188	81.5732	53.0235	67.9594	59.4336	77.0561
75_60	68.8259	66.6204	53.4672	81.2381	54.9031	68.4853	61.2722	77.3711
100_30	67.2472	67.9566	54.3531	81.4881	56.2536	**69.6554**	61.6554	77.8161
100_40	71.1968	67.5524	56.8807	81.8782	54.2343	69.0955	60.4542	77.6161
100_50	70.6303	67.463	57.5832	81.3081	54.5098	68.7132	61.0991	77.3811
100_60	69.8595	67.5313	55.8442	81.3281	54.0376	69.2891	60.8715	77.5611
125_30	68.8588	66.3749	54.7497	81.2081	53.224	69.2393	59.2529	77.4511
125_40	69.0385	67.5875	55.7325	81.7182	52.5876	**69.8535**	60.451	77.6211
125_50	69.5795	67.8422	56.7398	81.7282	53.6558	69.1431	59.2657	77.3261
125_60	691205	66.6516	55.627	81.4181	53.7237	69.7354	60.792	77.7861

Table 11. Processing time for the training in RF using different values of tree depth and the number of trees. In yellow the time for training the model with the selected optimized hyperparameter is shown.

Test	Processing Time
50_30	2'59"
50_40	2'54"
50_50	2'57"
50_60	3'4"
75_30	4'50"
75_40	5'8"
75_50	5'4"
75_60	5'13"
100_30	6'55"
100_40	7'23"
100_50	7'25"
100_60	7'24"
125_30	9'23"
125_40	8'58"
125_50	9'1"
125_60	9'25"

For what concerns the processing time, in all configurations, the trend increases according to the number of trees increasing. The case 100_30 was selected because it has a good trade-off between processing time (6'55" instead of 8'58" for the case 125_40), overall and glassy ice accuracy.

For the SVM classifier, only the sample size per class ranged between 500 and 2000 samples. In Table 12, it can be noticed that cases with 1500 and 2000 samples have the best OA and the latter also has the highest value for the C_i accuracy (68.6%). Nonetheless, taking into account the computational time (Table 13), the test with 2000 samples lasts around 20 min more than the test with 1500 samples (1h5'43"). The best fit can be considered the configuration with 1500 samples.

Table 12. Training accuracy (on the left) and validation accuracy (on the right) optimization of SVM number of the sample. R_i stands for rime ice, C_i for clear ice, and W_a for white aluminum. In yellow the selected optimized hyperparameter is shown.

N_Samples	Training Accuracy (%)				Validation Accuracy (%)			
	R_i	C_i	W_a	Overall	R_i	C_i	W_a	Overall
500	67.8201	62.1644	54.3074	80.9231	51.924	64.772	60.339	75.9512
1000	67.1179	64.2766	57.4959	80.463	51.8227	66.7797	62.0635	76.6062
1500	66.7683	64.8352	54.526	80.213	52.5362	67.6934	61.0333	77.0711
2000	68.616	66.6042	54.0258	80.283	53.9737	68.603	61.3453	77.0461

Table 13. Processing time for the training in SVM using different values of the number of samples. In yellow the time for training the model with the selected optimized hyperparameter is shown.

N_Samples	Processing Time
500	24′47″
1000	50′47″
1500	1h5′43″
2000	1h23′20″

Table 13 provides the computational time in all configurations and displays that the increase of sample size defines the increasing of the processing time trend in a proportional way.

3.4. Ice Detection using Hyperspectral Data: Results

The ice detection was performed on three types of hypercubes:

1. the original hypercubes collected with the Senop Rikola (Section 3.1);
2. the reduced hypercubes composed by the selected bands (27 bands and 10 bands) (Section 3.2);
3. the images formed by the three principal components (PC images) (Section 3.2).

For the classification, the "Classify Raster" tool of ArcGIS Pro 2.5.0 [51] and the Test_1 was employed for the training. The analysis, in this section, is focused on two main parameters: the accuracy and the computational time for the classification only.

In general, as explained in Section 2.5 both overall accuracy and user's accuracy were used for assessing the classification. As mentioned in Section 3.1, some materials are included in the background, but at the same time annotated as different classes to check the performance on different materials. Since these classes were not included in the real scenario, because in that case, the background will be different (e.g., asphalt instead of floor tile), the overall accuracy was included just to show the general performance of the algorithms. However, the primary parameter is the user's accuracy, because the object of this study is the detection of the ice and in detail the clear ice due to its transparent property.

For each dataset (original hypercubes, reduced hypercubes, and PC images), random forest and SVM with the optimized hyperparameters derived from Section 3.3.1 were used. For the RF, the hyperparameters selected for the classification are the number of trees equal to 50, tree depth equal to 30 and 2000 samples. For the SVM, the classification with 750 samples was performed.

As in the case of PCA (Section 3.2), the classification evaluation is shown only in four representative images (Test_1, Test_2, Test_6, and Test_10). Test_1, Test_2 and Test_6 present varied environmental conditions and Test 10 was included to display the behavior of the model in the presence of ice phase transition.

For what concerns the original dataset classified with the RF, the overall accuracy reaches a maximum value of 88%, and the computational time is 14 min on average (Table 14). The classification performs better on the clear ice than the other classes, reaching a maximum value of ca. 96%. Regarding the rime ice, its accuracy is on average under 50% since the radiometric response is similar to that related to the white aluminum (67% on average).

Table 14. Accuracy and processing time on the original dataset with random forest. R_i stands for rime ice, C_i for clear ice, and W_a for white aluminum.

Test	Accuracy (%)				Processing Time
	R_i	C_i	W_a	Overall	
Test_1	41.7311	96.3272	69.0852	87.3775	13′22″
Test_2	46.3158	96.3636	70.9497	88.8378	14′38″
Test_6	53.2446	81.6364	69.1238	86.9974	12′37″
Test_10	43.3428	52.7938	59.5405	81.5763	16′9″

With SVM classifier (Table 15), the overall accuracy reaches a maximum value of 92%, and the computational time is 17 min on average. Additionally, in this case, C_i user's accuracy is higher than the other significant classes, reaching a maximum value of ca. 97%. Rime ice accuracy is on average under 60% since the radiometric response is similar to that related to the white aluminum (78% on average).

Table 15. Accuracy and processing time on the original dataset with SVM. R_i stands for rime ice, C_i for clear ice, and W_a for white aluminum.

Test	Accuracy (%)				Processing Time
	R_i	C_i	W_a	Overall	
Test_1	50.4886	95.1975	88.0297	90.39	15′2″
Test_2	56.6781	97.0843	82.5337	91.91	16′48″
Test_6	56.5801	80.2994	72.5888	88.39	15′4″
Test_10	63.1236	55.4054	64.4209	84.54	21′29″

As presented in Tables 14 and 15, the SVM reaches better accuracy on average than the RF. Indeed, the overall accuracy is 86.2% for the RF and 88.8% for SVM. The drawback of the SVM is the processing time. The average computational time is 14′22″ for the RF and the 17′5″ for the SVM. Therefore, the RF is faster than the SVM in the classification process.

For both algorithms, Test_10 reports low user's accuracy values compared with the other tests, because in this case, ice was starting to melt. This evidence also recurs in the reduced hypercube datasets and the PCA dataset. There is only one test in which the ice is starting to melt. Thus, it is predictable that the algorithm, in this case, works worst and the detection of the ice in other physical states was out of this preliminary study. It is well known that the ice changes its features according to its state. Thus, for the real case application, further acquisitions will be made for training the algorithm and improving the detection of the ice while changing its state to the liquid one.

The same analysis was carried out for the reduced hypercube datasets (27 bands and 10 bands) (Table 16). The reached OA with RF classifier has a maximum value of 83.8% for the hypercubes with 27 bands and 80.6% for the hypercubes with 10 bands. The computational time varies from 28.5″ for the 27 bands to 26.5″ for the 10 bands. These observations demonstrate that the two cases are comparable, and the dataset with 10 bands can be considered reliable. Moreover, the C_i user's accuracy stands that the model has in any way a good performance. As a consequence, it verifies that the set of bands selected using the PCA is adequate for the classification task.

Table 16. Accuracy and processing time on the reduced hypercube (27 and 10 bands) with RF. R_i stands for rime ice, C_i for clear ice, and W_a for white aluminum.

Bands N°	Test	Accuracy (%)				Processing Time
		R_i	C_i	W_a	Overall	
27	Test_1	41.7047	92.7769	69.1438	82.5365	25″
	Test_2	52.2158	93.28	74.6367	**86.0572**	28″
	Test_6	40.4255	70.997	67.0165	80.3561	31″
	Test_10	34.1797	54.2955	56.0549	76.3753	30″
10	Test_1	43.5185	95.4392	69.9213	80.8962	24″
	Test_2	50.1825	94.8074	74.7238	**83.2366**	27″
	Test_6	38.9886	80.3754	59.7285	77.0154	26″
	Test_10	30.7018	57.7818	56.6897	73.0546	29″

Table 17 presents the outcomes of the SVM. The overall accuracy reaches a maximum value of 87.3% for the 27 bands-hypercubes and 80.8% for the 10 bands-hypercubes. The processing time varies from 1′50″ to 1′40″, respectively, for the 27 bands and the 10 bands. Regarding the clear ice, the dimensionality reduction does not affect accuracy. Even if the SVM accuracy has the same trend of RF for the two datasets, there are still slight differences (Tables 16 and 17). Referring to the average OA for the 27 bands, the SVM performs better than the RF, while for the 10 bands is the opposite. For both reduced datasets, the SVM has a higher user's accuracy of C_i class, and it is slower compared with the RF.

Table 17. Accuracy and processing time on the reduced hypercube (27 and 10 bands) with SVM. R_i stands for rime ice, C_i for clear ice, and W_a for white aluminum.

Bands N°	Test	Accuracy (%)				Processing Time
		R_i	C_i	W_a	Overall	
27	Test_1	45.2203	94.4217	70.1794	82.84	1′33″
	Test_2	62.4833	96.7882	72.6236	**87.32**	1′52″
	Test_6	53.3607	84.0215	68.2892	82.18	1′58″
	Test_10	45.7447	61.0082	59.3465	78.02	1′57″
10	Test_1	44.1153	94.9749	70.038	79.37	1′35″
	Test_2	48.8522	96.144	72.9124	**80.84**	1′43″
	Test_6	49.3736	84.3806	67.8459	78.89	1′42″
	Test_10	33.6364	61.4594	55.3836	72.78	1′40″

Turning now to the analysis on the PC dataset, for the RF algorithm, Table 18 indicates that there is a perceivable reduction of the accuracy rate concerning original and reduced hypercubes. The average OA does not overcome the value of 72%. Regarding the computational time, it is around 38″ on average.

Table 18. Accuracy and processing time on the PC images with RF. R_i stands for rime ice, C_i for clear ice, and W_a for white aluminum.

Test	Accuracy (%)				Processing Time
	R_i	C_i	W_a	Overall	
Test_1	37.8215	94.8214	65.92	75.8552	34″
Test_2	41.1435	75.6241	78.6325	73.5947	39″
Test_6	33.5897	68.3121	57.9747	69.4139	39″
Test_10	46.1314	54.9505	72.1607	70.9542	41″

For the SVM algorithm, Table 19 presents findings comparable to the RF one. The average OA does not overcome the value of 76%. Moreover, the computational time is around 1′17″ on average.

Table 19. Accuracy and processing time on the PC images with SVM. R_i stands for rime ice, C_i for clear ice, and W_a for white aluminum.

Test	Accuracy (%)				Processing Time
	R_i	C_i	W_a	Overall	
Test_1	42.4956	95.3888	68.2451	78.16	59″
Test_2	42.7742	81.6558	80.7923	78.24	1′5″
Test_6	45.1613	77.8899	64.8072	76.05	1′16″
Test_10	45.9184	56.5625	71.4886	72.29	1′48″

These observations demonstrate that either SVM and RF produce ambiguous and inaccurate outcomes in some cases and the resulting average accuracy for clear ice (77.8% for SVM and 73.4% for RF) could be not acceptable for our applications. Finally, the comparison between the two algorithms proves that SVM behaves better than RF. Overall and user's accuracy for all classes always have a higher value in SVM, but its computational time is twice as much as RF's one. Hence the classification with the SVM is still slower than the RF's.

According to the above analysis, for the ice detection in all datasets (original, reduced 27 bands, reduced 10 bands and PC), it is possible to make some general considerations. SVM and RF accuracy are comparable in all cases. Indeed, the difference between the accuracies is from 0.1% to 2%. Despite these minimal differences, the SVM presents the higher values of the user's and overall accuracy on average than the RF classifier. The reduction of dimensionality affects the overall accuracy slightly. Considering the difference between the original hypercube and the PC hypercube, the OA decreasing on average is 12% for the SVM classifier, instead of 14% for the RF one.

For the user's accuracy of the C_i, a descending trend based on the dimensionality of the feature space cannot be defined. However, the differences of clear ice accuracy between the best case (10 bands hypercube) and the worst case (PC images) is 7% for the SVM and 9% for the RF.

The processing time is strictly related to the size of the feature space. The dimensionality reduction helps to contract the processing time. In general, the analysis on the computational time shows that the RF is faster than the SVM, both in training and classification parts.

Figure 10 illustrates the results of the classification for each dataset. It can be appreciated graphically the discrepancy related to the reduction of the number of bands. Specifically, Figure 10 refers to the Test_1 hypercube classified with SVM. The RF graphical results are not included because it is impossible to detect the visual differences compared with the SVM accuracy. As can be seen, the clear ice is well detected in all the cases; while the rime ice identification gets worse according to the reduction of the bands.
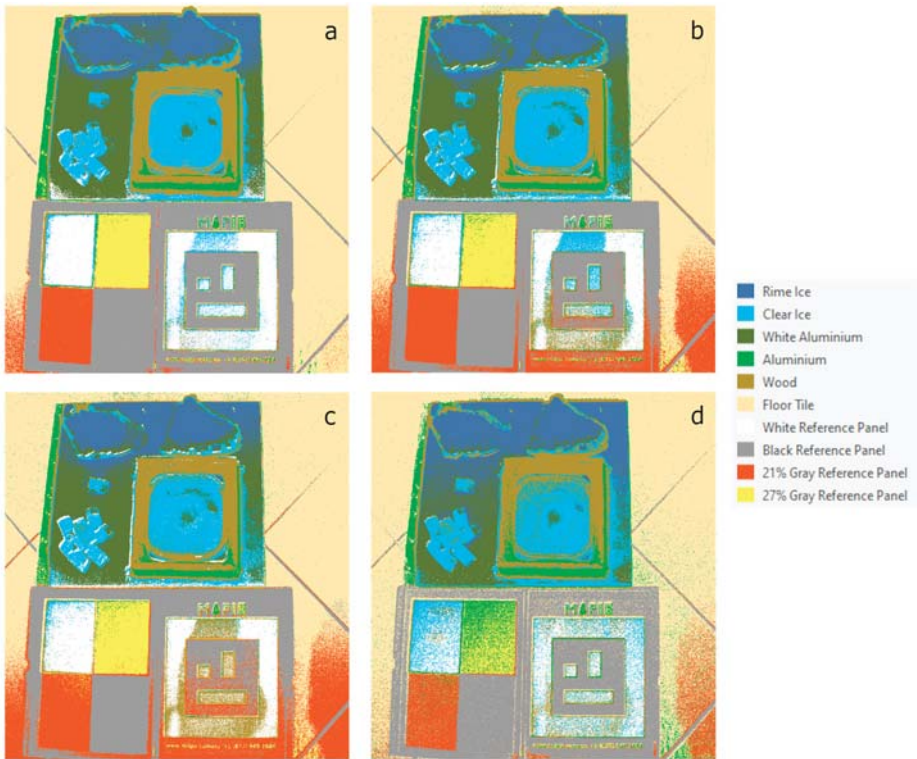
Figure 10. The classification results on Test_1 with SVM. (**a**) Original classified hypercube, (**b**) reduced classified hypercube-27 bands, (**c**) reduced classified hypercube-10 bands, and (**d**) PC classified hypercube.

3.5. Ice Detection Using Multispectral Data: Results

The ice detection was performed in the case of multispectral images on two datasets:

1. the original data acquired with the MAPIR (RGN images);
2. the multispectral data composed with the blue band of the RGB (RGBN images).

The optimized hyperparameters identified after the tuning (Section 3.3.2) were used. For the RF, the hyperparameters selected for the classification are the number of trees equal to 100, tree depth equal to 30 and 10,000 samples. For the SVM, the number of samples is 1500.

Considering the RGN dataset, the classification assessment is described in four representative images (Test_1, Test_2, Test_6, and Test_10) that have the same characteristics of the hypercubes described in Section 3.4. For the RGBN dataset, only the Test_1 integrated with the blue band is cited to demonstrate the improvement related to the blue presence in terms of accuracy.

With the RF, the evaluation of the outcomes on RGN images shows that OA is on average 49.5%. Instead, the computational time on average is 6′43″ (Table 20). As expected, the lack of blue band alters deeply also values of UA compared with hyperspectral hypercubes. For example, the maximum value for the glassy ice accuracy is lower than the 80%. Thus, it is not sufficient to be considered correct and accurate.

Table 20. Accuracy and processing time on the RGN (red, green, and near infrared) images with RF. R_i stands for rime ice, C_i for clear ice, and W_a for white aluminum.

Test	Accuracy (%)				Processing Time
	R_i	C_i	W_a	Overall	
Test_1	54.9565	69.7936	60.7158	77.6311	6'40"
Test_2	36.1789	42.5788	35.2851	47.9226	6'36"
Test_6	25.2031	33.7942	8.2353	30.9185	6'30"
Test_10	34.7062	33.3841	44.8087	41.34	7'5"

With the SVM, the accuracy assessment of the RGN dataset shows that OA is on average 49.2%. Instead, the computational time on average is 23'40" (Table 21). The missing blue band problem is still visible. Indeed, the clear ice accuracy does not surpass the value of 67% in the best configuration.

Table 21. Accuracy and processing time on the RGN images with SVM. R_i stands for rime ice, C_i for clear ice, and W_a for white aluminum.

Test	Accuracy (%)				Processing Time
	R_i	C_i	W_a	Overall	
Test_1	52.2795	67.3587	63.1305	76.9362	22'13"
Test_2	34.8404	41.2713	32.8609	46.8527	23'9"
Test_6	25.8493	35.6347	10.6874	30.6135	23'55"
Test_10	40.3123	37.1409	42.4566	42.375	25'21"

Nonetheless, the comparison among the two algorithms shows that RF performs better classification on average and its computational time is lower than SVM's one.

Considering that the accuracy assessment for the RGN dataset is not comparable with the ones obtained using the hypercube with similar feature space size (e.g., PC images), the blue band was added to create RGBN images. Indeed, looking to the results of the band selection (Section 3.2) it is possible to notice that the blue band has essential weight.

Table 22 illustrates an overview of the accuracy and the processing time in the RGBN case. As can be seen, the OA reported a significant increase compared with the RGN images. Indeed, it overcomes the value of 80% for both the algorithms. The UA values are higher than the average of the respective values in the RGN case. At the same time, the computational time decreases for the RGBN images.

Table 22. Accuracy and processing time on the RGBN(red, green, blue, near-infrared) image with RF and SVM. R_i stands for rime ice, C_i for clear ice, and W_a for white aluminum.

Classifier	Accuracy (%)				Processing Time
	R_i	C_i	W_a	Overall	
RF	57.9867	54.2284	83.7163	84.495	4'49"
SVM	62.3726	57.3843	88.1515	86.695	8'18"

Regarding the comparison between the two algorithms in the RGBN case, the SVM produces a better classification, but its computational time is longer than the RF's one.

Figure 11 highlights the results of the classification in the two datasets using the SVM. The improvement related to the introduction of the additional band is evident. The blue band allows to reduce the classification noise and at the same time a better identification of all materials. Moreover, the enhancement of the distinction between rime ice or clear ice and white aluminum is clear.
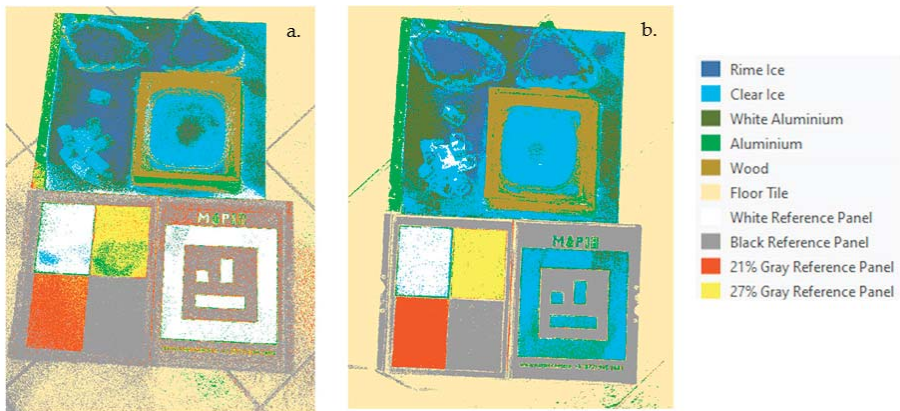
Figure 11. The classification results on Test_1 with SVM. (**a**) RGN classified images and (**b**) RGBN classified images.

4. Discussion

Since the previous section describes already the outcomes related to the dimensionality reduction of hyperspectral data and the classification with the two algorithms on the different datasets, the discussion focuses on:

- the consideration related to the use of hyperspectral or multispectral images for the ice detection task;
- the comparison between the two classifiers in terms of computation time and accuracy;
- the comparison among the detection of the different material.

For what concern the first point, this study confirms that for the ice detection task, the use of hyperspectral images is more reliable. However, on the other hand, highlights that the advantage of operating with multispectral data (with the same spatial resolution of the hyperspectral images) is related to the computational time. The latter, indeed, is one of the crucial problems in real-time application.

The outcomes demonstrate that the hyperspectral data are suitable for real-time applications after a priori analysis. A dimensionality reduction process can easily compress the size of hyperspectral data preparing the data for the classification task. This step leads to breaking down the limits related to the computational time of the original hypercubes. The experimental analysis shows that the processing time can be improved, downscaling the spectral resolution. The case of reduced hypercube with 10 bands can be considered a trade-off between accuracy and computational time, regardless of the employed algorithm.

Moreover, starting with the analysis of significative bands, a multispectral sensor can be defined for facilitating the acquisition and classification operations. It is crucial to take into account, in the case of multispectral images, that the spatial resolution is four times greater than the hyperspectral. The results obtained with the introduction of a significative band (in this case, the blue band) shows the effectiveness of predefined-band knowledge in the classification.

Regarding the classifiers, it is possible to state that the SVM performs better in terms of accuracy; on the opposite, the RF classifier is faster than the SVM. This observation is valid for both datasets: the multispectral and the hyperspectral dataset. However, the accuracy reached with the multispectral data is not comparable with ones of the hyperspectral camera regardless of the selected algorithm.

Finally, turning now to material detection, this study focuses the attention on the classification of clear ice. As explained in the Introduction (Section 1), the clear ice is not visible with the naked eye and requires tactile inspection. The ice, in the real case, could have different features (e.g., density, shape) than the ice samples that were generated in this study. At this stage of our work, other types of ice

were examined to understand if the classification was able to distinguish, as two classes, the different condition of the same material, such as transparent ice and rime ice. Due to its characteristics, the rime ice is more visible; thus, the detection is more straightforward. Concerning the ice detection reliability, it is possible to underline that both algorithms conservatively recognize both forms of ice. For instance, if an area is contaminated by ice, conservative way means that it is much more unlikely that the algorithms recognize that area as aluminum or as other material instead of ice (this is the case of a false negative). This example implies that even if the algorithms recognize an area of aluminum as ice, it is very improbable that the contrary occurs. It is possible to notice in Figures 10 and 11 that the main false negative can be associated with the white aluminum, that is identified as ice.

In the real case, not to apply de-icing fluids to some areas with ice is more dangerous than applying the de-icing procedure on some other areas that do not need it. Therefore, it could be possible that some de-icing fluids will be wasted for areas in which actually ice is not present; however, the safety, that is a primary goal, is not compromised.

Moreover, although the radiometric classification is noisy for the rime ice, the results can be improved with the use of geometric features. The previous activities of the SEI project [14] demonstrated that the rime ice is accurately identifiable in this application, using the RGB sensor and a photogrammetric approach.

5. Conclusions

In this paper, the feasibility to use spectral images for ice detection was studied, testing different sensors with different spectral resolutions such as the Senop Rikola and the MAPIR. To address this purpose, two different types of ice samples were created to understand if it was possible to distinguish clear ice (transparent ice) from rime ice (white ice). Then, images were collected in different illumination conditions, because there is no open-source and ready to use dataset to face this specific task. Moreover, semantic segmentation algorithms (such as RF and SVM) were defined, also evaluating the accuracy and the processing time.

The main challenges of this work were the definition of the efficient use of hyperspectral data in the near real-time application and the research of spectral resolution and algorithms capable of providing higher accuracy and limited computational time.

This experimental analysis demonstrates the possibility to use the reduced hypercubes and both the RF and SVM as a classifier with an OA higher than 80% on average.

As feature work, we plan to transfer the knowledge and the promising outcomes acquired through this simulation in a drone application. Moreover, the drone's application can help to consider also other kinds of ice that are not possible to reproduce in the laboratory, such as snow and freezing rain.

References

1. European Organisation for the Safety of Air Navigation. The Flight Safety Foundation Aircraft Ground De/Anti-Icing. Available online: https://www.skybrary.aero/index.php/Aircraft_Ground_De/Anti-Icing (accessed on 28 June 2020).

2. International Civil Aviation Organization (ICAO) Aircraft Ground De-Icing/Anti-Icing Operations. Available online: https://www.icao.int/safety/airnavigation/OPS/Pages/Aircraft-Ground-De-IcingAnti-Icing-Operations.aspx (accessed on 25 June 2020).
3. Castro, S.; Davis, L.C.; Erickson, L.E. Plant-Enhanced Remediation of Glycol-Based Aircraft Deicing Fluids. *Pract. Period. Hazard. Toxic Radioact. Waste Manag.* **2001**, *5*, 141–152. [CrossRef]
4. Hoover, G.A. *Aircraft Ice Detectors and Related Technologies for Onground and Inflight Applications*; U.S. Department of Transportation, Fedaral Aviation Administration Technical Center, Atlantic City International Airport: Atlantic County, NJ, USA, 1993; p. 54.
5. Mingione, G.; Barocco, M.; Denti, E.; Bindi, F.G. *Flight in Icing Conditions*; Direction Générale de l'Aviation civile (DGAC): Paris, France, 1997; p. 188.
6. Federal Aviation Administration, United States Department of Transportation. *AC 00-6A—Aviation Weather for Pilots and Flight Operations Personnel*; Fedaral Aviation Administration: Washington, DC, USA, 1975.
7. Federal Aviation Administration, United States Department of Transportation. *AC 00-6B—Aviation Weather 2016*; Fedaral Aviation Administration: Washington, DC, USA, 2016.
8. Icing Hazards. Available online: https://www.weather.gov/source/zhu/ZHU_Training_Page/icing_stuff/icing/icing.htm (accessed on 28 June 2020).
9. American Meteorological Society Rime. Available online: http://glossary.ametsoc.org/wiki/Rime (accessed on 29 July 2020).
10. American Meteorological Society Glaze. Available online: http://glossary.ametsoc.org/wiki/Glaze (accessed on 29 July 2020).
11. Federal Aviation Administration, United States Department of Transportation Standardized International Aircraft Ground Deice Program (SIAGDP). Available online: https://www.faa.gov/other_visit/aviation_industry/airline_operators/airline_safety/deicing/media/standardized_international_ground_deice_program.pdf (accessed on 25 June 2020).
12. Garr-Schultz, A.; Gardner, W. Strategic Self-Presentation of Women in STEM. *Soc. Sci.* **2018**, *7*, 20. [CrossRef]
13. Falcone, A.; Miccone, D.; Eytan, A.; Theoharatos, C.; Stavropoulos, P.; Aicardi, I.; Musci, M.A.; Maria, A. Spectral Evidence of Ice on Aircrafts—The SEI Project. *Inf. Intell. Syst. Appl.* **2020**, *1*, 69–73.
14. SEI Project Consortium SEI Project. Available online: https://www.sei-project.eu/ (accessed on 7 July 2020).
15. Rizk, P.; Al Saleh, N.; Younes, R.; Ilinca, A.; Khoder, J. Hyperspectral imaging applied for the detection of wind turbine blade damage and icing. *Remote Sens. Appl. Soc. Environ.* **2020**, *18*, 100291. [CrossRef]
16. Bassey, C.E.; Simpson, G.R. Aircraft Ice Detection using Time Domain Reflectometry with Coplanar Sensors. In Proceedings of the 2007 IEEE Aerospace Conference, Big Sky, MT, USA, 3–10 March 2007; pp. 1–6.
17. Roy, C. Remote Sensing in Precision Agriculture: An Educational Primer. Master's Thesis, Iowa State University, Ames, IA, USA, July 1999.
18. Breda, J.-M.; Choisnet, J.; Naim, M. Optical Device for the Detection of Icing Conditions on Aircraft 2000. U.S. Patent US6091335A, 18 July 2000.
19. Gong, X.; Bansmer, S. 3-D ice shape measurements using mid-infrared laser scanning. *Opt. Express* **2015**, *23*, 4908. [CrossRef] [PubMed]
20. Nakauchi, S.; Nishino, K.; Yamashita, T. Selection of optimal combinations of band-pass filters for ice detection by hyperspectral imaging. *Opt. Express* **2012**, *20*, 986. [CrossRef] [PubMed]
21. Huber, N.; Kalidindi, S.R.; Klusemann, B.; Cyron, C.J. *Machine Learning and Data Mining in Materials Science*; Frontiers Media SA: Lausanne, Switzerland, 2020; ISBN 978-2-88963-651-8.
22. Camps-Valls, G.; Bruzzone, L. Kernel-based methods for hyperspectral image classification. *IEEE Trans. Geosci. Remote Sens.* **2005**, *43*, 1351–1362. [CrossRef]
23. Adam, E.M.; Mutanga, O.; Rugege, D.; Ismail, R. Discriminating the papyrus vegetation (Cyperus papyrus L.) and its co-existent species using random forest and hyperspectral data resampled to HYMAP. *Int. J. Remote Sens.* **2012**, *33*, 552–569. [CrossRef]
24. Tommaselli, A.M.G.; Santos, L.D.; de Oliveira, R.A.; Honkavaara, E. Refining the Geometric Calibration of a Hiperspectral Frame Camera with Preliminary Bands Coregistration. In Proceedings of the IGARSS 2018 IEEE International Geoscience and Remote Sensing Symposium, Valencia, Spain, 22–27 July 2018; pp. 6468–6471.

25. Saari, H.; Aallos, V.-V.; Holmlund, C.; Mäkynen, J.; Delauré, B.; Nackaerts, K.; Michiels, B. Novel hyperspectral imager for lightweight UAVs. In *Airborne Intelligence, Surveillance, Reconnaissance (ISR) Systems and Applications VII*; Henry, D.J., Ed.; International Society for Optics and Photonics: Bellingham, WA, USA, 2010; p. 766805.

26. MAPIR Survey3 Cameras. Available online: https://www.mapir.camera/collections/survey3 (accessed on 28 June 2020).

27. Landgrebe, D.A. *Signal. Theory Methods in Multispectral Remote Sensing*; John Wiley & Sons: Hoboken, NJ, USA, 2005; ISBN 978-0-471-72125-3.

28. Preet, P.; Batra, S.S. Jayadeva Feature Selection for classification of hyperspectral data by minimizing a tight bound on the VC dimension. *arXiv* **2015**, arXiv:1509.08112.

29. Chang, C.I.; Du, Q.; Sun, T.L.; Althouse, M.L. A joint band prioritization and band-decorrelation approach to band selection for hyperspectral image classification. *IEEE Trans. Geosci. Remote Sens.* **1999**, *37*, 2631–2641. [CrossRef]

30. Li, F.; Lu, H. Hyperspectral images band selection using multi-dictionary based sparse representation. In Proceedings of the 2016 IEEE International Geoscience and Remote Sensing Symposium (IGARSS), Beijing, China, 10–15 July 2016; pp. 2769–2772.

31. Estornell, J.; Martı-Gavila, J.M.; Sebastia, M.T.; Mengual, J. Principal component analysis applied to remote sensing. *Model. Sci. Educ. Learn.* **2013**, *6*, 83–89. [CrossRef]

32. Fauvel, M.; Chanussot, J.; Benediktsson, J.A. Kernel Principal Component Analysis for the Classification of Hyperspectral Remote Sensing Data over Urban Areas. *EURASIP J. Adv. Signal. Process.* **2009**, *2009*, 783194. [CrossRef]

33. Torbick, N.; Becker, B. Evaluating Principal Components Analysis for Identifying Optimal Bands Using Wetland Hyperspectral Measurements from the Great Lakes, USA. *Remote Sens.* **2009**, *1*, 408–417. [CrossRef]

34. Jolliffe, I.T. *Principal Component Analysis*, 2nd ed.; Spinger Sieries in Statistics; Springer: New York, NY, USA, 2002; ISBN 978-0-387-22440-4.

35. Cattell, R.B. The Scree Test for the Number of Factors. *Multivar. Behav. Res.* **1966**, *1*, 245–276. [CrossRef] [PubMed]

36. Csillag, F.; Pásztor, L.; Biehl, L.L. Spectral band selection for the characterization of salinity status of soils. *Remote Sens. Environ.* **1993**, *43*, 231–242. [CrossRef]

37. Breiman, L. Random Forests. *Mach. Learn.* **2001**, *45*, 5–32. [CrossRef]

38. Richards, J.A.; Jia, X. *Remote Sensing Digital Image Analysis: An Introduction*, 4th ed.; Springer: Berlin, Germany, 2006; ISBN 978-3-540-25128-6.

39. Zhang, C.; Kovacs, J.M. The application of small unmanned aerial systems for precision agriculture: A review. *Precis. Agric.* **2012**, *13*, 693–712. [CrossRef]

40. Khan, M.N.; Ahmed, M.M. Snow Detection using In-Vehicle Video Camera with Texture-Based Image Features Utilizing K-Nearest Neighbor, Support Vector Machine, and Random Forest. *Transp. Res. Rec.* **2019**, *2673*, 221–232. [CrossRef]

41. Hanselmann, M.; Köthe, U.; Kirchner, M.; Renard, B.Y.; Amstalden, E.R.; Glunde, K.; Heeren, R.M.A.; Hamprecht, F.A. Toward Digital Staining using Imaging Mass Spectrometry and Random Forests. *J. Proteome Res.* **2009**, *8*, 3558–3567. [CrossRef]

42. Bruzzone, L.; Persello, C. Approaches Based on Support Vector Machine to Classification of Remote Sensing Data. In *Handbook of Pattern Recognition and Computer Vision*; World Scientific: Singapore, 2009; pp. 329–352. ISBN 978-981-4273-38-1.

43. Myburgh, G.; van Niekerk, A. Impact of Training Set Size on Object-Based Land Cover Classification: A Comparison of Three Classifiers. *Int. J. Appl. Geosp. Res.* **2014**, *5*, 49–67. [CrossRef]

44. Lillesand, T.M.; Kiefer, R.W.; Chipman, J. *Remote Sensing and Image Interpretation*, 7th ed.; Wiley: Hoboken, NJ, USA, 2015; ISBN 1-118-34328-X.

45. Thanh Noi, P.; Kappas, M. Comparison of Random Forest, k-Nearest Neighbor, and Support Vector Machine Classifiers for Land Cover Classification Using Sentinel-2 Imagery. *Sensors* **2017**, *18*, 18. [CrossRef] [PubMed]

46. Geomatics Group of Politecnico di Torino Our Labs- Geomatics Labs. Available online: https://areeweb. polito.it/geomatics_lab/en/geomatic-lab/ (accessed on 4 July 2020).

47. L3 Harris Geospatial Docs Center—Using ENVI- Atmospheric Correction. Available online: https://www. harrisgeospatial.com/docs/AtmosphericCorrection.html#empirical_line_calibration (accessed on 4 July 2020).

48. ESRI. Principal Components. Available online: https://pro.arcgis.com/en/pro-app/tool-reference/spatial-analyst/principal-components.htm (accessed on 3 July 2020).
49. ESRI. Composite Bands—Data Management Toolbox. Available online: https://pro.arcgis.com/en/pro-app/tool-reference/data-management/composite-bands.htm (accessed on 5 July 2020).
50. ESRI. An Overview of the Segmentation and Classification Toolset. Available online: https://pro.arcgis.com/en/pro-app/tool-reference/spatial-analyst/an-overview-of-the-segmentation-and-classification-tools.htm (accessed on 30 June 2020).
51. ESRI. Classify Raster. Available online: https://pro.arcgis.com/en/pro-app/tool-reference/spatial-analyst/classify-raster.htm (accessed on 5 July 2020).

Deep Learning Classification of 2D Orthomosaic Images and 3D Point Clouds for Post-Event Structural Damage Assessment

Yijun Liao, Mohammad Ebrahim Mohammadi and Richard L. Wood *

Department of Civil and Environmental Engineering, University of Nebraska-Lincoln,
Lincoln, NE 68588-531, USA; yijun.liao419@huskers.unl.edu (Y.L.); me.m@huskers.unl.edu (M.E.M.)
* Correspondence: rwood@unl.edu

Abstract: Efficient and rapid data collection techniques are necessary to obtain transitory information in the aftermath of natural hazards, which is not only useful for post-event management and planning, but also for post-event structural damage assessment. Aerial imaging from unpiloted (gender-neutral, but also known as unmanned) aerial systems (UASs) or drones permits highly detailed site characterization, in particular in the aftermath of extreme events with minimal ground support, to document current conditions of the region of interest. However, aerial imaging results in a massive amount of data in the form of two-dimensional (2D) orthomosaic images and three-dimensional (3D) point clouds. Both types of datasets require effective and efficient data processing workflows to identify various damage states of structures. This manuscript aims to introduce two deep learning models based on both 2D and 3D convolutional neural networks to process the orthomosaic images and point clouds, for post windstorm classification. In detail, 2D convolutional neural networks (2D CNN) are developed based on transfer learning from two well-known networks AlexNet and VGGNet. In contrast, a 3D fully convolutional network (3DFCN) with skip connections was developed and trained based on the available point cloud data. Within this study, the datasets were created based on data from the aftermath of Hurricanes Harvey (Texas) and Maria (Puerto Rico). The developed 2DCNN and 3DFCN models were compared quantitatively based on the performance measures, and it was observed that the 3DFCN was more robust in detecting the various classes. This demonstrates the value and importance of 3D datasets, particularly the depth information, to distinguish between instances that represent different damage states in structures.

Keywords: convolutional neural network; deep learning; transfer learning; point clouds; structural damage assessment

1. Introduction

One of the emerging approaches for aerial image collection is to utilize the unpiloted (or unmanned) aerial system (UAS), commonly known as a drone [1–3]. Following natural hazard events, the data collection is often limited by time and site accessibility imposed by precarious structures, debris, road closures, curfews, and other restrictions. However, UAS imagery enables first responders and emergency managers to perform effective logistical planning, loss estimates, and infrastructure assessment for insurance adjusters, engineers, and researchers [4]. UAS with an onboard camera enables assessors to collect numerous images from large areas efficiently as well as to reconstruct the three-dimensional (3D) scene via three steps, including Scale Invariant Feature Transform (SIFT), Structure-from-Motion (SfM), and Multi-View Stereo (MVS). Here, SfM is generated using two-dimensional (2D) aerial images [5]. The SfM derived point cloud has relative accuracy at the centimeter level [1]. The creation of a 3D SfM point cloud is a time-consuming process; however,

it enables a reconstruction of the depth information in the scene, which may improve various analyses. Recently, deep learning techniques have become a more common approach to develop various computer vision workflows. These techniques have been utilized to create workflows to investigate damage in the aftermath of extreme events from aerial images, in particular for large areas and at the community scale.

The main objective of this manuscript is to study and compare three deep learning models based on 2D aerial images and 3D SfM derived point clouds to detect damaged structures following two hurricanes. In addition, the study investigates the application of transfer learning for the 2D convolutional neural network (CNN) as a rapid post-event strategy to develop a model for damage assessment of built-up areas with minimal to no prior data. The model created for damage assessment using 2D images is developed based on transfer learning from two well-known image classification networks, namely AlexNet and VGGNet [6]. During the training process, the pre-trained weights of these models were further modified to match the user-defined classes. Moreover, a 3D fully convolutional network (3D FCN) with skip connections is developed based on expanding the 3D FCN model proposed by Mohammadi et al. [7]. While the goal of 2DCNN is to classify the aerial images based on the most prominent object observed in the images, the 3D FCN with skip connections semantically classifies the SfM derived point cloud. Both 2D and 3D models were trained on similar datasets with identical numbers of classes and were compared based on precision, recall, and overall accuracy. The comparison between 2D and 3D models is to demonstrate the entropy and value associated with the depth-information that is present in the 3D datasets.

2. Literature Review

2.1. Studies Used 2D Images for Detection and Classification

The task of object detection or classification of a set of images has been investigated by various studies using CNNs with different architectures. Among all proposed methods, transfer learning has become one of the most popular techniques. Transfer learning corresponds to the process of fine-tuning the upper layers of a pre-trained model based on a new dataset for a newly proposed task(s) [8]. Models developed based on a transfer learning strategy demonstrated not only improved performance in comparison to other models but also that such models could be developed more efficiently. In an early study within the area of deep learning, Bengio discussed transfer learning algorithms and their effectiveness in classifying new instances based on pre-trained models and demonstrating the process through numerous examples of transfer learning [8]. One of the most referenced studies was performed by Krizhevsky et al. [9]. The authors within this study developed a CNN model through transfer learning from the subset of the ImageNet network [10]. Krizhevsky et al. modified the fully connected layers to accommodate classifying the new labels [9]. The modified network architecture contained eight layers to maximize the correct label under prediction distribution. The authors reported that the validation of the results showed test error rates of 17% to 37.5% for the used datasets. Another application of transfer learning was studied by Oquab et al. [11]. The authors developed various CNN models for the task of visual recognition based on transfer learning from the pertained ImagetNet model [10]. Within this study, the training images are mainly comprised of centered objects with a clear background in the image, and authors reported that the model was able to classify images with a high level of accuracy after an extended training process. Different CNN performs distinctively as the network architecture varies. As a result, Shin et al. listed a few popular image-based classification transfer learning networks, such as CifarNet, AlexNet, and GoogleNet [6]. These network performances were compared based on a set of medical images via transfer learning. It was concluded that transfer learning has been consistently beneficial for classification experiments.

Various studies have investigated the application of CNN models for post-event assessments using aerial images. For example, Hoskere et al. proposed post-earthquake inspections based on UAS imagery and CNN models [12]. Within this study, the authors developed a fully convolutional network to semantically segment images into three classes of pixels. The developed model was

able to segment the images with an average accuracy of 91.1%. More recently, Xu et al. studied the post-earthquake scene classification task using three deep learning methods. These methods included a Single Shot MultiBox Detector (SSD), post-earthquake multiple scene recognition (PEMSR) based on transfer learning from SSD, and Histogram of Oriented Gradient along with Support Vector Machine (HOG+SVM) [13]. Within the proposed method, the aerial images were initially classified into six classes, including landslide, houses, ruins, trees, clogged, and ponding. The dataset was created via web-searched images of the 2014 M_W 6.5 Ludian earthquake (China), which were later preprocessed and degraded into 300×300 pixels and manually classified into the six classes aforementioned. The authors reported that the PEMSR model demonstrated a higher efficiency of 0.4565 s comparing to HOG+SVM of 8.3472 s as well as higher accuracy. In their work, the transfer learning strategy also improved the overall accuracy and performance, although the average processing time was slightly higher than the SSD method. Moreover, in addition to the effect of transfer learning in the increasing accuracy and performance of 2D CNN models, Simonyan and Zisserman pointed out the CNN performance improvement can be achieved by increasing the network depth [14]. As a result, Gao and Masalam developed a deep 2D CNN based on transfer learning from the VGGNet model for Structural Health Monitoring (SHM) and rapid post-event damage detection [15]. The 2D image-based SHM used red, green, blue (RGB) information based unsupervised training algorithms and was able to obtain 90% accuracy for binary classification.

2.2. Studies Used 3D Point Clouds for Detection and Classification

With the rapid development of technologies to collect remotely sensed 3D point clouds and the growing application of these data in various fields of civil engineering, many researchers have proposed various methods to analyze 3D point clouds, in particular for routine inspections or post-event data collection and analyses [16,17]. The datasets here are considered to be non-temporal, which is a single post-event only dataset that does not utilize change detection from a baseline (or pre-event) dataset. For example, Axia et al. proposed a workflow to classify an aerial 3D point cloud into damaged and undamaged classes [18]. Within the proposed workflow, Axia et al. estimated a normal vector for each point within the point cloud data as the key damage sensitive feature and identified the variation of these normal vectors with respect to a global reference vector. Lastly, the study used a region growing approach based on the variation of normal vectors to classify the point cloud. Axia et al. reported that while the proposed method can classify the collapsed structures, the developed method may misclassify the partially damaged structures.

In general, one of the main steps in point cloud analysis workflows is to classify the points into a set of predefined classes. As a result, multiple workflows have been introduced to classify point clouds through machine learning and more recently deep learning techniques. Hackel et al. introduced one of the most successful workflows to classify dense point clouds of urban areas into multiple classes [19]. These classes include building façades, ground, cars, motorcycles, traffic signals, and pedestrians. Within this study, authors extract a series of features for each point based on various neighboring sizes using eigendecomposition, the height of points, and first and second statistical moments and used random forest learning algorithm to classify each point. The proposed method results in the main overall accuracy of 95%. More recently, Xing et al. used the Hackel et al. workflow as a basis and developed a more robust workflow by adding a series of features computed based on the difference of normal vectors for better identification [19,20]. Their study demonstrated a 2% improvement on average.

Recently deep learning method applications become more widespread to analyze 3D datasets in science and engineering fields. Various deep learning-based workflows have been developed to classify the 3D point cloud datasets. The main advantage of deep learning-based learning algorithms over the more traditional learning algorithms (e.g., artificial neural networks) is the capability of the algorithms to learn the feature extractors from the input data directly. Therefore, deep learning algorithms, in particular CNN architectures, eliminate the need for engineering feature extractors based on the

geometry of the objects within the dataset and background. One of the early studies to investigate the application of deep learning for 3D point cloud classification was performed by Prokhorov [21]. Prokhorov proposed a 3D network architecture similar to CNN to classify point cloud of various objects by converting the point cloud data into 3D grid representations. The developed 3D CNN network had one convolutional layer, one pooling layer, and two fully connected layers, which was followed by a 2-class output layer. The weights or parameters within the convolutional layers were pre-trained using lobe component analysis and were updated using the stochastic meta-descent method [22]. Following this study, Maturana and Scherer proposed a 3D CNN for object recognition similar to that of Prokhorov [22,23]. The proposed 3D network had two tandem convolutional layers, one max-pooling layer, and one fully connected layer, which was followed by the output layer. In contrast to the study conducted by Prokhorov [22], Maturana and Scherer did not pre-train the developed network while the network resulted in a performance on par or better than the network proposed by Prokhorov. This highlights that the developed 3D CNN network was able to extract features during the training process effectively.

Recently, Hackel et al. introduced a point cloud classification network based on 3D CNN architecture. The proposed network accepts five occupancy grid models with different resolutions for each instant as input and has five convolutional layers in parallel with an organization similar to VGGNet, which followed by a series of fully connected and one output layers [14,24]. The authors have reported a maximum overall accuracy of 88% and an intersection over the union value of 62% for datasets collected from urban environments. This work classifies the scene into classes of natural terrain, high vegetation, low vegetation, buildings, hardscape, vehicles, and human-made terrains. More recently, Zhang et al. proposed a network to semantically segment point clouds based on a model that consists of three distinct networks [25]. The first network encodes the point cloud into 2D instances. The second network consists of a series of fully connected and max-pooling layers, which are followed by convolutional layers. Finally, the third and last network goal converts the 2D encoded data into 3D grid models, which semantically classify the voxels in the grid and creates a bounding box for each detection object. The authors reported that the experimental results demonstrate an overall improvement in accuracy of 10% in comparison to the network developed by Maturana and Scherer [25].

2.3. Knowledge Gap

Previous studies have explored the application of CNNs in post-natural hazard event assessment using aerial images. Both deep learning-based methods and unsupervised learning were implemented for 2D and 3D datasets, while the difference between 2D and 3D datasets in deep learning has yet to be fully understood by quantitative comparisons. As reviewed, the majority of studies developed to analyze the 3D point clouds for post-event applications were created based on traditional methods. In contrast, the applications of deep learning models developed based on transfer learning for 2D aerial images was investigated in various studies. However, due to the lack of depth information, limitations of the damage and structural component recognition still exist. As a result, this study investigates the application of deep learning-based models using 2D images and 3D SfM derived point clouds corresponding to the same post-event scenes.

3. Datasets

3.1. Introduction to Hurricane Harvey and Maria

Within this study, three othomosiac image and point cloud datasets were collected in the aftermath of Hurricanes Harvey and Maria. Hurricane Harvey made landfall on 25 August 2017 on the coastline of Texas. Hurricane Harvey was a Category 4 hurricane and produced wind gusts over 215 km/h, and storm surges as high as 3.6 m. This incident resulted in the destruction of more than 15,000 partial damage, 25,000 residential and industrial structures, as well as other critical infrastructure in coastal

communities, including the towns of Rockport and Port Aransas [26]. Hurricane Maria made landfall on 19 September of 2017 in Puerto Rico. Hurricane Maria was classified as Category 5 hurricane and produced wind guests over 280 km/h, and storm surges as high as 2.3 m, which makes it the most severe natural hazard event recorded in history to affect Puerto Rico and other Islands in the region [27]. As a result of this extreme event, the power grid of Puerto Rico was significantly damaged, a major dam for the Guajataca reservoir sustained critical structural damage, and more than 60,000 buildings were damaged [28].

3.2. Data Collection Method

To carry out the data collection task of the selected areas, a medium-size drone with an onboard camera was deployed. A DJI Phantom 4 UAS collected high-resolution aerial images with an onboard camera. The selected flight paths were fully controlled autonomously with the Pix4dcapture application on a handheld tablet. The data collection in Puerto Rico produced 4077 images in 7 flights, which covered approximately 1.75 km^2 area with a 53.5 m elevation change. The Texas Salt Lake dataset contained 1379 images in 2 flights with 0.75 km^2 area coverage with an elevation range of 9.3 m. The Texas Port Aransas site had 1424 images collected from four flights, with a 0.88 km^2 area coverage with an elevation range of 1.9 m. The collected images were further processed using SfM workflow, which used a series of two-dimensional images with sufficient overlap to generate 3D point cloud and further processed orthomosaic datasets of the surveyed area [1]. The SfM derived point clouds for the two sites are shown in Figures 1–3. Other key characteristics of these datasets are presented in Table 1.

(a)

(b)
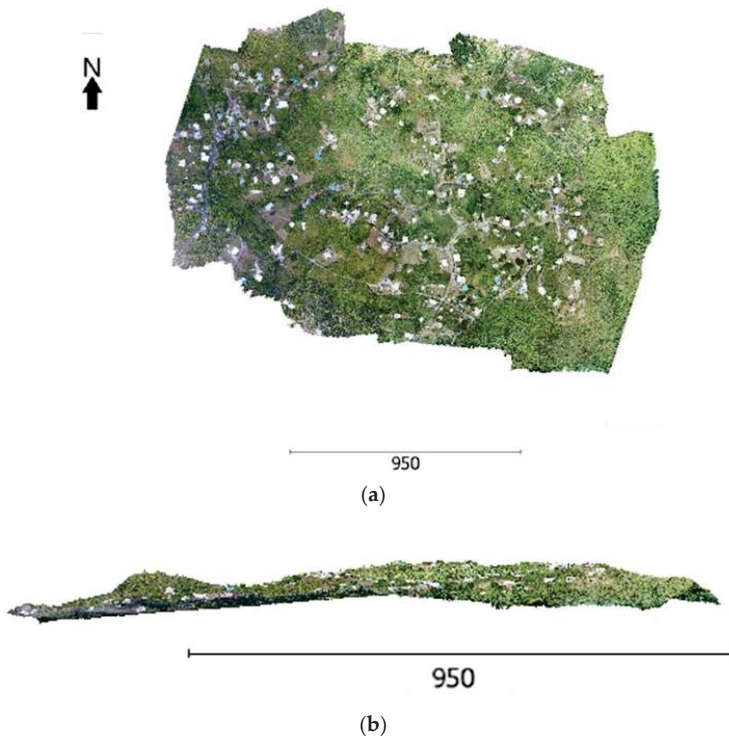
Figure 1. Puerto Rico point cloud (scale in meters): (**a**) top view and (**b**) side view.

(**a**)

(**b**)
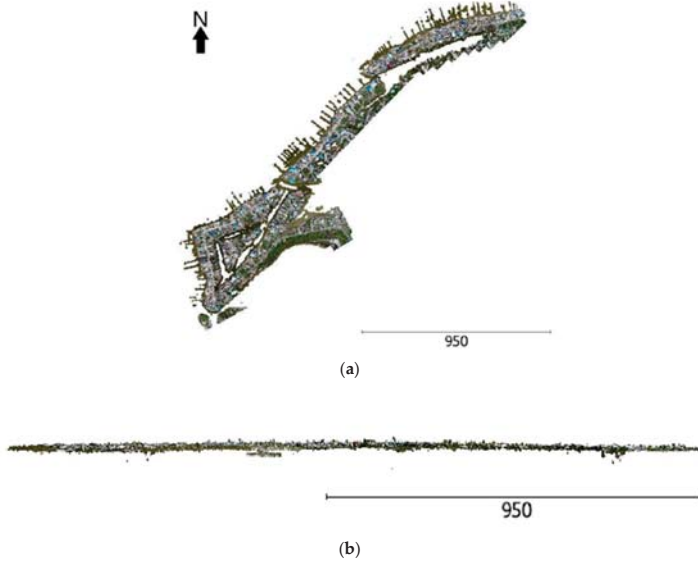
Figure 2. Texas Salt Lake point cloud (scale in meters): (**a**) top view and (**b**) side view.


(**a**)

(**b**)
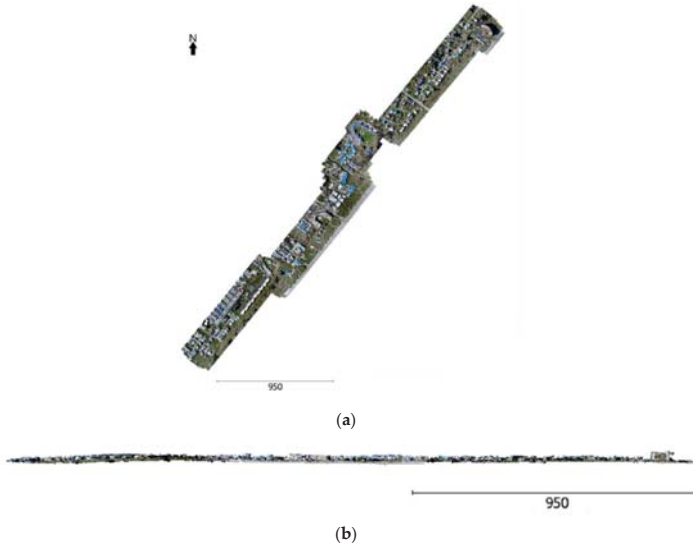
Figure 3. Texas Port Aransas point cloud (scale in meters): (**a**) top view and (**b**) side view.

Table 1. Summary characteristics of the datasets.

Dataset	Characteristics		
	GSD (cm)	Orthomosaic Dimensions (pixels)	Point Cloud Number of Vertices (count)
Puerto Rico	1.09	29,332 × 39,482	393,764,295
Texas—Salt Lake	2.73	61,395 × 61,937	78,830,950
Texas—Port Aransas	2.69	96,216 × 84,611	131,902,480

3.3. Dataset Classes

Within this study, each dataset was segmented manually into one of the following seven classes: Undamaged structures, partially damaged structures, completely damaged structures, debris, roadways, terrain, and vehicles. An earlier study by Mohammadi et al. informs the classification used here [7]. However, the scope of damaged structures is expanded where the instances are modified into two damaged structure classes based on the level of damage sustained during the event, which relates to the degree of damage sustained. A structure that sustained partial damage includes any building that does not represent any physical changes while the roof of the structure is covered by tarps, which are typically blue or red. Completely damaged structures are buildings that underwent physical changes due to the event, such as roof damage without tarp coverings with visible structural components such as beams, columns, or walls. If a structure is collapsed such that no structural component can be identified, the structure is classified as debris. The class of debris consists of everything that is not in its native state. Debris, in general, is comprised of rooftop shingles, fallen trees, downed utility or light poles, and other wind-blown objects. Terrain incorporates any region that is comprised of grass, low-height vegetation, water, sand, trees, exposed soil, fences, or utility poles. Note that any nonbuilding structural objects that are represented by a cylindrical shape (e.g., utility and light poles) are considered as terrain [29]. Lastly, the vehicle class corresponds to objects used for the transportation of people or goods. This includes cars, SUVs, trucks, carts, recreational vehicles, trailers, construction vehicles (e.g., excavators), or any water-borne vessels that can be propelled on water by oar, sail, or engine. Figures 4 and 5 demonstrate the example of each class point cloud and its corresponding images. Lastly, Tables 2 and 3 illustrate the number of point cloud and image instances that were manually identified from the datasets, respectively.

(a)

(b)

(c)

(d)

(e)

(f)
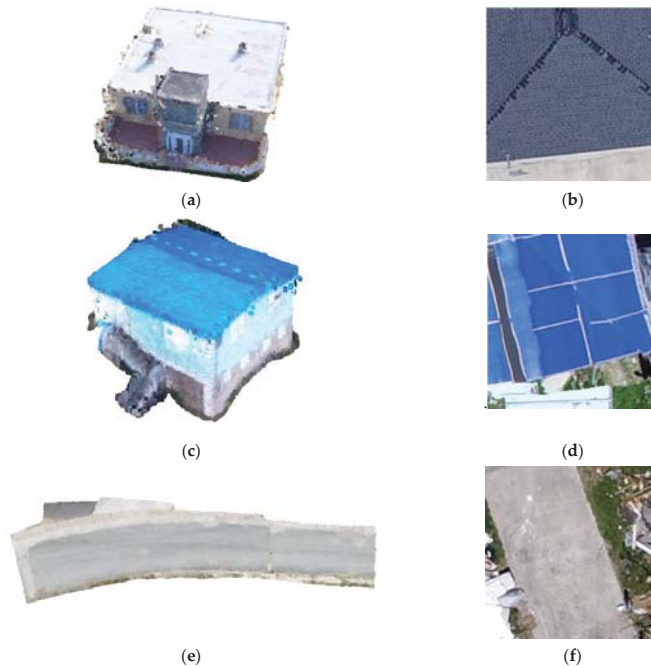
Figure 4. Examples of instances from all datasets: (**a**,**b**) Undamaged structure, (**c**,**d**) partially damaged structure, and (**e**,**f**) roadways.

(**a**)

(**b**)

(**c**)

(**d**)

(**e**)

(**f**)

(**g**)

(**h**)
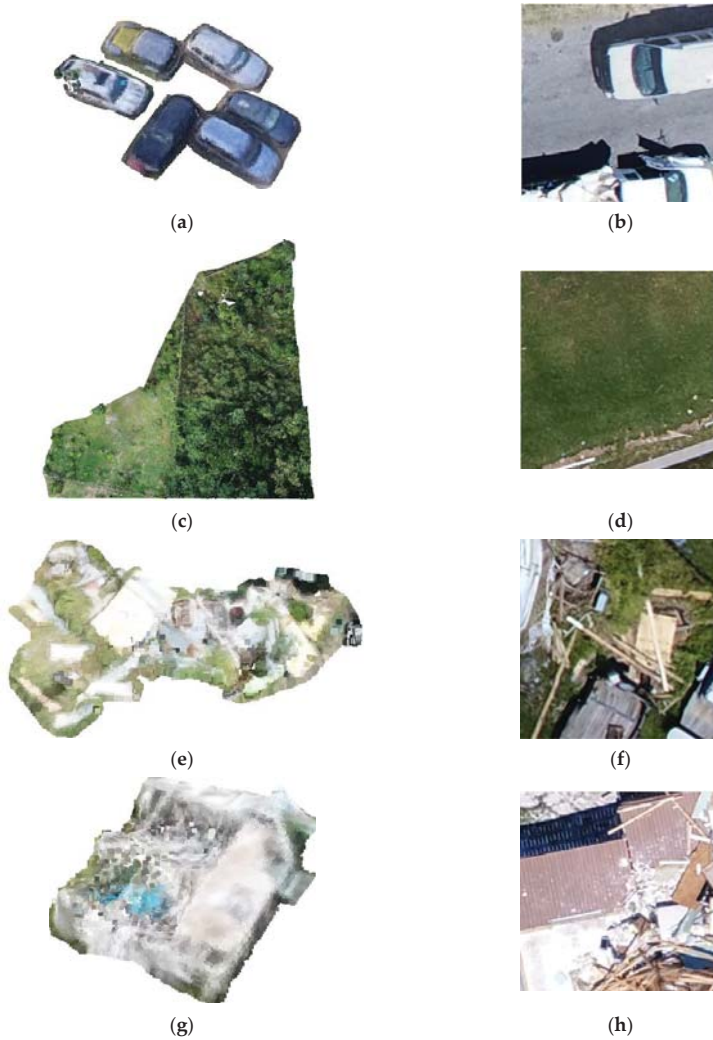
Figure 5. Examples of instances existed from all datasets: (**a**,**b**) vehicles, (**c**,**d**) terrain, (**e**,**f**) debris field, and (**g**,**h**) completely damaged structure.

Table 2. Summary of point cloud instances for Salt Lake, Puerto Rico, and Port Aransas.

Instance	Number of Instances		
	Texas-Salt Lake	Puerto Rico	Texas-Port Aransas
Terrain	719	224	665
Undamaged Structure	307	97	355
Debris	404	764	257
Partially Damaged Structure	99	76	115
Completely Damaged Structure	146	364	76
Vehicle	256	198	224
Roadway	57	166	87

Table 3. Summary of image instances for Salt Lake, Puerto Rico, and Port Aransas.

Instance	Number of Instances		
	Texas-Salt Lake	**Puerto Rico**	**Texas-Port Aransas**
Terrain	1972	5238	3288
Undamaged Structure	138	610	688
Debris	296	247	71
Partially Damaged Structure	236	223	485
Completely Damaged Structure	152	74	33
Vehicle	67	160	53
Roadway	246	864	904

4. Methodology

4.1. Dataset Preparation for 2D Images

The process of creating image instances was started by creating an orthomosaic image of the entire scene. This was done using Pix4Dmapper. Afterward, the orthomosaic image was segmented into a series of to 256×256 images. As a result, approximately a total of 18,000 images were created from the Puerto Rico dataset, the Salt Lake dataset resulted in a total of 60,000 images, and Port Aransas dataset was divided into 120,000 segmented images. The next step within the preparation image instances was to assign a label to each 256×256 image based on the seven classes mentioned in Section 3. Within this study, the image classes are determined by the most prominent object that is visible in the image. Moreover, the Salt Lake and Puerto Rico datasets were used for model development, and the Port Aransas dataset was used to test and validate the developed models.

4.2. 2D Convolutional Neural Network Architecture

Pre-trained CNNs have advantages due to their relative stability during the training process, efficiency, and higher performance over various diverse tasks. Among the various networks available to select for transfer learning, AlexNet and VGGNet were selected as a basis to develop the 2D CNN models in MATLAB 2020a. These two networks were pre-trained by millions of images for more than 1000 classes. These selected networks for transfer learning, on the other hand, represented different architectures. AlexNet model was developed in 2012 and was the first CNN model to perform well on the ImageNet database, and it still performed consistently well on diverse datasets [9,30]. This network contained five layers, including convolutional and max-pooling layers, and two fully connected layers, as illustrated in Figure 6. The developed model based on AlexNet had identical architecture to the AlexNet network; however, within the fully-connected layers, the dropout regularization method was applied to combat the overfitting while training [31]. The input images were also augmented through rotation and reflection processes to reduce the generalization error of the models. The second CNN model was developed based on transfer learning from VGGNet from 2014. The VGGNet model had 16 convolutional and max-pooling layers, which was followed by the fully connected layers, as shown in Figure 7. These small filter sizes (i.e., 3×3 kernels) in VGGNet captured and learned the small details of input instances while larger filter sizes of the network (i.e., 5×5) permitted the network to extract features that corresponded to larger regions. Development of the networks based on transfer learning permitted to modify the previously learned feature extractors of these networks according to a new task using a smaller number of training images and epochs [30].
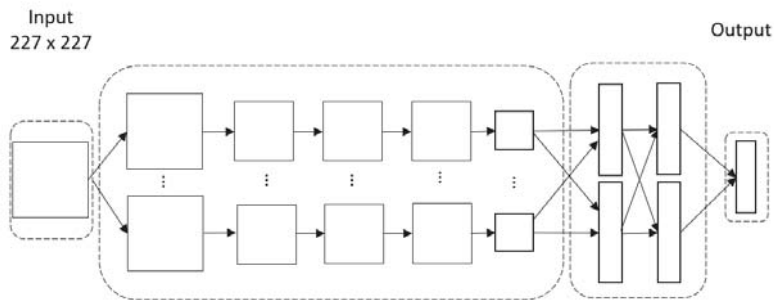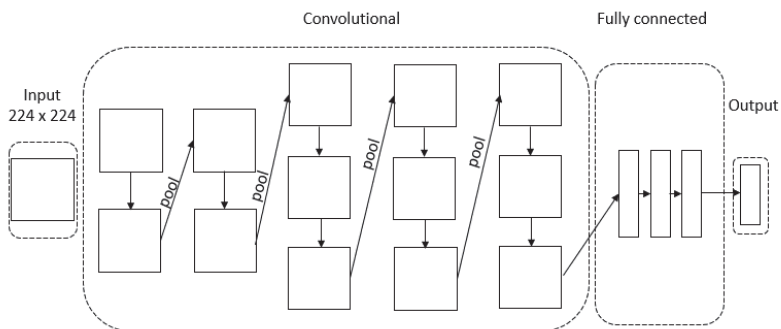
Figure 6. AlexNet network architecture.

Figure 7. VGGNet network architecture.

During the training process of models developed based on the transfer learning strategy, the 256 × 256 image instances were rescaled to 227 × 227 and 224 × 224 for AlexNet and VGGNet, respectively. In addition, the batch size, which represents the number of images input into the network at once, was set to 64 [15]. While the number of epochs was originally set as high as 2000, the training was terminated when the computed losses reached a plateau to combat the overfitting. The learning rate was set as 0.01 for both networks. Besides these parameters, the remaining hyperparameters were kept identical to the original networks [32]. Note that the training images for both AlexNet and VGGNet are identical in order to compare the results, and because of the augmentation process, approximately over 10,000 images within seven classes are used within the network training. The training performance was evaluated by computing the losses and validation accuracy. Generally, the training of AlexNet contained approximately 300 iterations, while VGGNet has a higher number of approximately 500 iterations. Both developed networks resulted in optimized accuracy for seven classes, which is 88.7% of AlexNet and 91.0% of VGGNet. Figure 8 shows the confusion matrices for the developed networks, which demonstrates that both networks were able to detect the majority of class terrain with high-level accuracy.

The evaluation of the results indicated that the model struggled to learn differences in some of the original classes, particularly as related to structural damage assessment. Consequently, a selected number of classes were merged to reduce the total number of classes from the original seven to specific five and four classes. This was done to demonstrate if the model was able to distinguish between a structural class in general, and an improvement was noted. However, none of the networks were able to learn the other classes, including the partially damaged structure, completely damaged structure, and debris, due to significant similarities between partially damaged and completely damaged structures within the segmented orthoimages.
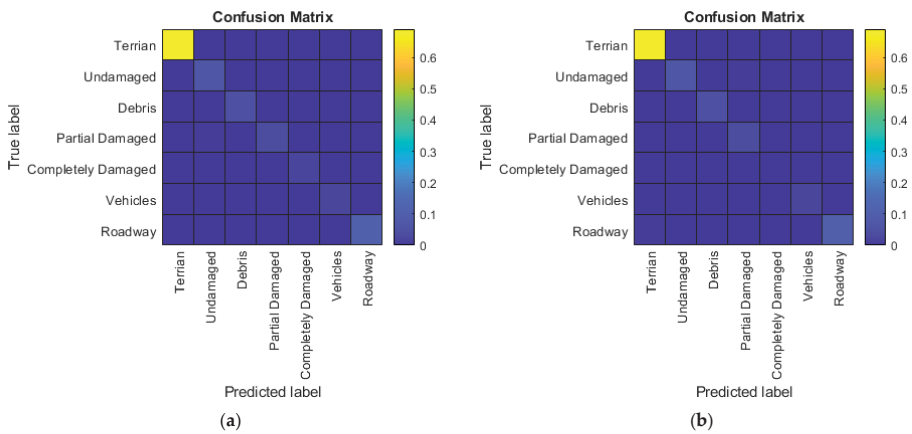
Figure 8. 2D convolutional neural network (CNN) confusion matrices during the training process: (**a**) AlexNet and (**b**) VGGNet models.

4.3. Dataset Preparation for 3D Point Clouds

Raw and unstructured point clouds were typically incompatible with CNN architectures. This was due to the issue that point clouds generally lack a grid structure, unlike images. Consequently, the raw point cloud instances were converted into volumetric or occupancy gird models, which were 3D arrays. Occupancy grid models provided a suitable data structure for point clouds that can be used within robust CNN learning models. To convert the point clouds instances to occupancy grid models, a method as proposed by Mohammadi et al. was used [7]. Within this study, initially, the point cloud instances were created by slicing the labeled point cloud dataset into roughly 10 m × 10 m segments. Then, the coordinates within each segment, which consisted of objects with various labels, were processed to have only positive values and normalized [7]. Afterward, each segment was downsampled based on the selected occupancy grid dimensions. Within this study, the occupancy grid model of 64^3 was used as it results in a sampling of 10 to 16 cm for 10 m × 10 m segments, which was a sufficient resolution to perform per building damage assessment in the aftermath of wind storm events [17]. Lastly, an extra-label corresponding to the empty cells within the 3D arrays was assigned to each instance and denoted as neutral. This allowed the network not only to learn the label instances but also to learn the geometry of the output based on the input instances as well since occlusion or gaps in point clouds are common.

4.4. 3D Fully Convolutional Network Architecture with Skip Connections

The model developed to learn 3D point cloud instances was guided by the previous work of Long et al. and, as discussed in Mohammadi et al. [7,33]. However, the authors reported that developed 3D FCN required a large number of training iterations to achieve an acceptable level of accuracy. As a result, the 3D FCN architecture was modified within this study with skip connections, such that the network can recover the most useful features during the training process at a faster rate [25,34]. The 3D FCN was implemented in TensorFlow v1.15 within this study, and the developed 3D FCN model had an overall general architecture similar to that presented in Mohammadi et al. [7]. In summary, the network was comprised of an input layer that accepted three 3D arrays corresponding to red, green, and blue channels. In addition, the network consisted of an encoding part and decoding parts. The encoder was comprised of 6 3D convolutional layers. The decoding segment of the network consisted of a total of 6 3D transpose convolutional layers. Note that the network did not use any max-pooling layers. Lastly, the output layer was a single-occupancy grid model, each of which cells represented the label of the input point cloud instance (Figure 9). Skip connections added the output

of the convolutional layers within the encoder to the corresponding input of transpose convolutional layers in the decoder. The skip connections conceptually helped the network to recover the fine details in the prediction and reduce any gradient vanishing issues. Figure 9 illustrates the skip connections by arrows.
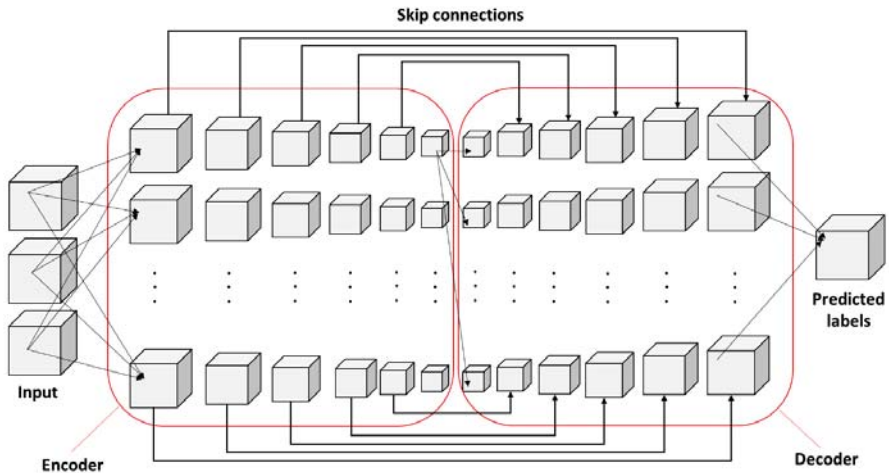

Figure 9. The developed 3D fully convolutional network with skip connections pipeline.

The developed 3D FCN with skip connections was optimized based on stochastic gradient descent, and the cells that contained labels except neutral classes were waited by a factor of 2.0 while updating the learnable parameters to increase boost training and reduce the convergence time. The model was trained on instances from the Salt Lake and Puerto Rico datasets. To further improve the network for generalization, the training instances were augmented by randomly rotating each instance two times. This resulted in a total of 10,958 training instances. In addition, it was observed that network convergence improved as the number of mini-batches increased from 64 to 256. Therefore, the model was trained based on the minibatch size of 256. To evaluate the training process, three performance measures were also calculated, including precision, recall, and cell accuracy in addition to loss, as shown in equations below:

$$Recall = \frac{C_{ii}}{C_{ii} + \sum_{j \neq i} C_{ij}} \tag{1}$$

$$Presicion = \frac{C_{ii}}{C_{ii} + \sum_{j=i} C_{ji}} \tag{2}$$

$$Cell\ accuracy = \frac{\sum C_{ii}}{\sum_i \sum_j C_{ji}} \tag{3}$$

where C_{ii} represents the diagonal of the confusion matrix, which also corresponds to true predictions, $\sum_{j \neq i} C_{ij}$ denotes to the false negatives, $\sum_{j \neq i} C_{ji}$ denotes the false positive predictions, $\sum C_{ii}$ represents the total count of true predictions, and $\sum_i \sum_j C_{ji}$ represents the total count of all predictions. Table 4 demonstrates the result of these performance measures for the developed model during training for a total of 2500 epochs, and Figure 10 shows the training losses, which was measured based on mean squared error (MSE). Lastly, Figure 11 demonstrates the confusion matrix for the trained model. The training results demonstrated that while the model had learned the geometry of the input instances with a high level of accuracy, cell accuracy of 98.1%, it cannot distinguish the discrepancy between partially damaged structures, completely damaged structures, debris, and vehicles. Lastly,

the developed network with skip connections demonstrated massive improvement in comparison to the 3D FCN model introduced by Mohammadi et al. as the network was able to achieve a similar level of accuracy with almost 25% training iterations [7].

Table 4. Quantified performance measures for the training dataset.

Classes	3D FCN	
	Precision	Recall
Neutral	100	100
Terrain	85	70
Undamaged Structure	15	37
Debris	31	33
Partially Damaged Structure	8	26
Completely Damaged Structure	14	8
Vehicle	4	4
Roadway	94	94
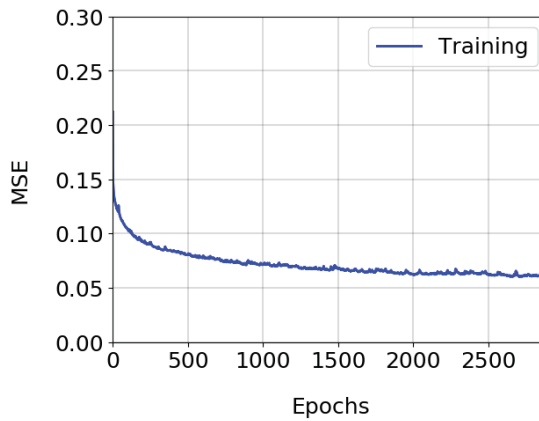
Figure 10. Loss progress (MSE) during model training.
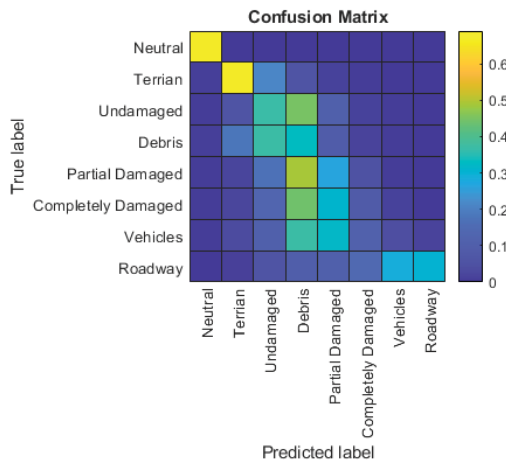
Figure 11. 3D fully convolutional network (FCN) confusion matrix for the training dataset.

5. Discussion

5.1. 2D CNN Experiment

The developed 2D CNN networks have demonstrated a significant difference between training and testing performance measures. The network accuracy during training reached 88.7% and 91.0% for AlexNet and VGGNet, respectively, while lower accuracy was demonstrated in testing. This could be caused by the limitation of the 2D CNN classification based only on RGB information with the lack of depth information. Moreover, this demonstrates that the network was not able to learn useful features to distinguish between different classes. To further investigate this thought, the model developed based on transfer learning form VGGNet was trained using five and four classes, where the classes related to the structures were grouped together. As VGGNet demonstrates a better performance, this model was selected as the network for a more detailed performance investigation. The combined classes represent more general object classes than the original seven class instances. To reduce the classes to five, the classes comprising of completely damaged and partially damaged were merged to create the class named damaged. Similarly, to reduce the total number of classes to a total of four classes, the classes completely damaged structures, partially damaged, and undamaged structures were combined to create a general class of structures. Identical parameters and architecture were used to train the new networks based on the reduced number of classes. It was observed that the training has improved in terms of accuracy, which turned out to be 92.0% and 94.6% for the five and four classes, respectively. Original confusion matrix of seven classes is shown in Figure 12. As for testing results, confusion matrices of merged five and four classes are shown in Figures 13 and 14, respectively. In the end, the VGGNet transfer learning using four classes has a significant improvement in both training accuracy and testing performance as expected. However, this model is not ideal for the targeted structural damage classification following natural hazards events. This is because the structural classes were combined, and the VGGNet training (in all models) cannot reliably distinguish between undamaged, partially damaged, and completely damaged structures. Instead, the general object classification of structure, roadway, terrain, and vehicles was proved to perform well. The improved performance when the classes combined demonstrate that depth information within 3D point clouds is critical to classify damaged structures from undamaged structures automatically.
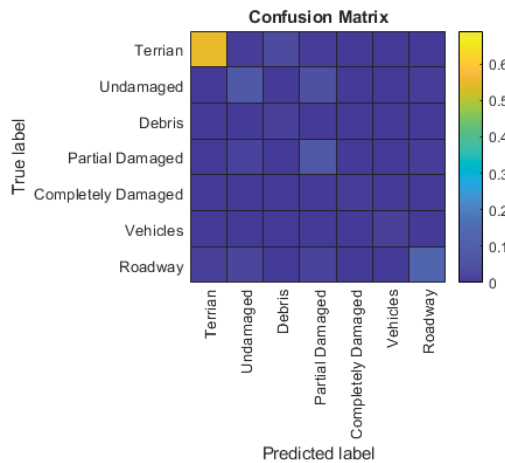

Figure 12. VGGNet transfer learning confusion matrix of testing results on the Port Aransas dataset in seven classes.
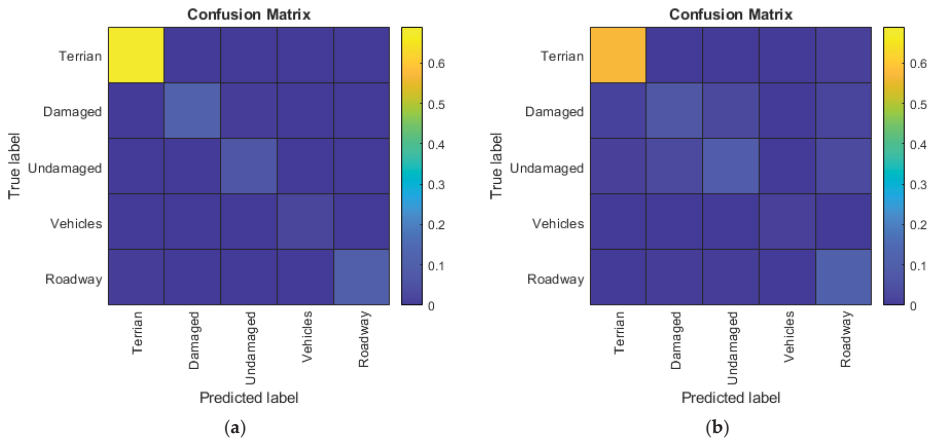
Figure 13. VGGNet transfer learning confusion matrix results for five classes: (**a**) training and (**b**) testing.
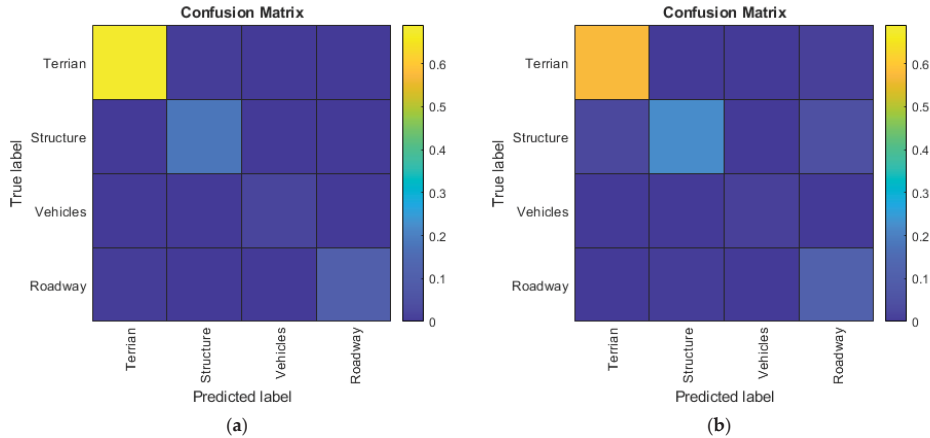

Figure 14. VGGNet transfer learning confusion matrix results for four classes: (**a**) training and (**b**) testing.

5.2. 3D FCN Experiment

Similar to the 2D CNN network, the 3D FCN model was developed and trained based on Salt Lake and Puerto Rico instances and was tested on the Port Aransas instances. To create the testing dataset, a procedure similar to that of creating the training dataset was followed; however, the testing instances were not augmented. Figure 15 shows the confusion matrix for testing on the Port Aransas dataset, and Table 5 provides the performance measures for each class.

The 3D FCN network prediction results on the test dataset demonstrated an overall similar performance measure in comparison to resulted performance measures observed during the training process. The overall cell accuracy of the network was 97.8%. The network was able to predict the class of terrain instances with a high level of accuracy while this was unexpected as the general terrain within the testing dataset in terms of texture and geometry differs in comparison to the training dataset. This suggests that the model was able to learn features that can generalize well between datasets with moderate to low similarities. A similar pattern in detecting the classes of partially damaged structures, completely damaged structures, debris, and vehicles to that of training was observed. Authors expect

that by performing extended training and using more learnable parameters, the network will learn features to distinguish between these classes with a higher level of accuracy.
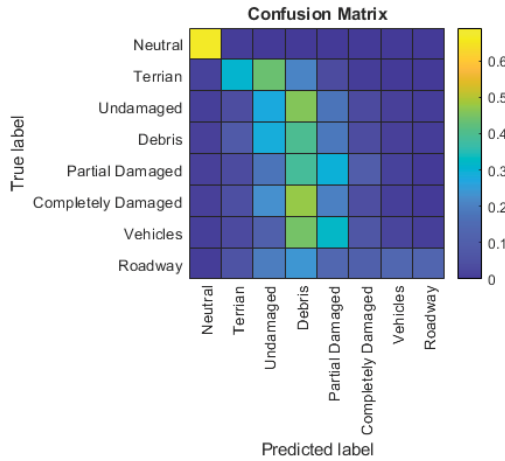

Figure 15. 3D FCN confusion matrix for the Port Aransas dataset (in 7 classes).

Table 5. Quantified performance measures on the Port Aransas dataset.

Classes	3D FCN	
	Precision	Recall
Neutral	100	100
Terrain	61	31
Undamaged Structure	12	28
Debris	3	40
Partially Damaged Structure	10	29
Completely Damaged Structure	1	4
Vehicle	1	2
Roadway	95	13

5.3. Comparison of 2D CNN and 3D FCN

The detection accuracies of the 2D CNN models were consistently lower than the performance obtained based on the 3D FCN network, which is 91.0% for the 2D model and 97.8% for the 3D model. Comparing the structural damage detection performance, 3D FCN demonstrated a superior advantage over 2D models developed based on various class numbers. Keen advantages of 2D CNN and images relate to the smaller number of learnable parameters and reduced data sizes in comparison to the 3D FCN model. While 2D CNN performance improved from 92.0% to 94.6% in general object classification such as structures, terrain, roadway, or vehicles. This basic detection was not adequate for damage detection between structural classes like completely damaged, partially damaged, debris, and other classes. These results demonstrate a significant classification limitation when it is solely based on RGB information (which corresponds to 2D images) in comparison to RGB with depth information (which corresponds to 3D point clouds). Consequently, 3D FCN performs with a marked improvement in structural damage detection when comparing to 2D CNN.

6. Conclusions

Aerial image data collection provides an efficient technique to collect perishable data following a natural hazard event. Both 2D orthomosaic images and the 3D point clouds can be obtained and

processed for analyses and automated classification. This study compared post-event site damage classification using 2D and 3D datasets following two separate hurricanes from 2017 using 2D CNN and 3D FCN. The 2D CNN was conducted via transfer learning of two pre-trained networks: AlexNet and VGGNet. The inputs to the 2D CNN networks are 2D segmented images for unsupervised training and outputs the label for each image segment. The 3D FCN was conducted using aerial image-derived point clouds. Within the FCN method, point clouds are semantically classified into various classes. To keep the parameters consistent, both 2D CNN and 3D FCN have identical classes initially. To further demonstrate the 2D CNN classification performance, a reduction and combination of the classes were used for performance evaluation. The combination was aimed to eliminate the narrative of the classes of damage detection, which combines the structural damage and undamaged classes together.

Within the reduced numbers of classes for 2D CNN training, the accuracy improved at the cost of reducing and eliminating the classes corresponding to structural damage. The accuracy improvement demonstrates the 2D deep learning classifications are ideal for general object detection such as terrain, structures, vehicles, roadway, etc. However, they have a demonstrated limited learning capability to predict distinct structural characteristics from undamaged, partially damaged, and completely damaged as well as debris. However, this limitation was overcome when using a 3D point cloud dataset in deep learning, which contains both RGB and depth information. The model developed based on 2D data was only able to learn the dominant class (i.e., terrain) effectively. This results in lower precision and accuracy for other classes for both training and testing phases. On the contrary, the model developed based on 3D point clouds was able to learn other classes in addition to the dominant class. Classification within damage detection is known to be a class imbalance scenario, where the instances that represent damaged or debris are often the minority class that follows a random and unique geometric and color patterns.

Comparing the training durations, 2D CNN requires a significantly shorter time from a few hours to a day, while 3D FCN requires numerous days. The 2D CNN training accuracy achieved 88.7% and 91.0% for seven classes, and the highest accuracy was achieved by VGGNet training using four classes of 94.6%, while 3D FCN training accuracy was as high as 97.8%. However, when it comes to testing accuracy, the 2D CNN has significantly lower accuracy compared to 3D FCN. The accuracy decrease in the 2D dataset is expected due to the lack of depth information. Classification on 2D images is RGB based only, which can be influenced by the object surface reflection, sunlight, existence of shadows, etc. Moreover, despite 3D dataset preparation and network development is more time consuming, higher accuracy and reliability can be guaranteed. This is especially true when classifying the location and severity of damage following natural hazard events.

References

1. Liao, Y.; Wood, R.L.; Mohammadi, M.E.; Hughes, P.J.; Womble, J.A. *Investigation of Rapid Remote Sensing Techniques for Forensic Wind Analyses*, 5th, ed.; American Association for Wind Engineering Workshop: Miami, FL, USA, 2018.

2. Adams, S.M.; Levitan, M.L.; Friedland, C.J. High resolution imagery collection utilizing unmanned aerial vehicles (UAVs) for post-disaster studies. In *Advances in Hurricane Engineering: Learning from Our Past*; American Society of Civil Engineers: Reston, VA, USA, 2013; pp. 777–793.

3. Chiu, W.K.; Ong, W.H.; Kuen, T.; Courtney, F. Large structures monitoring using unmanned aerial vehicles. *Procedia Eng.* **2017**, *188*, 415–423. [CrossRef]

4. Zhou, Z.; Gong, J.; Guo, M. Image-based 3D reconstruction for posthurricane residential building damage assessment. *J. Comput. Civil Eng.* **2016**, *30*, 04015015. [CrossRef]

5. Fernandez Galarreta, J.; Kerle, N.; Gerke, M. UAV-based urban structural damage assessment using object-based image analysis and semantic reasoning. *Nat. Hazards Earth Syst. Sci. Discuss.* **2014**, *2*, 5603–5645. [CrossRef]

6. Shin, H.-C.; Roth, H.R.; Gao, M.; Lu, L.; Xu, Z.; Nogues, I.; Yao, J.; Mollura, D.; Summers, R.M. Deep convolutional neural networks for computer-aided detection: CNN architectures, dataset characteristics and transfer learning. *IEEE Trans. Med. Imaging* **2016**, *35*, 1285–1298. [CrossRef] [PubMed]

7. Mohammadi, M.E.; Watson, D.P.; Wood, R.L. Deep Learning-Based Damage Detection from Aerial SfM Point Clouds. *Drones* **2019**, *3*, 68. [CrossRef]

8. Bengio, Y. Deep learning of representations for unsupervised and transfer learning. In *Proceedings of ICML Workshop on Unsupervised and Transfer Learning*; Workshop and Conference Proceedings: Pittsburgh, PA, USA, 2012; pp. 17–36.

9. Krizhevsky, A.; Sutskever, I.; Hinton, G.E. Imagenet classification with deep convolutional neural networks. In *Proceedings of Advances in Neural Information Processing Systems*; Communication of the ACM: Silicon Valley, CA, USA, 2017; pp. 1097–1105.

10. Berg, A.; Deng, J.; Fei-Fei, L. Large Scale Visual Recognition Challenge. 2010. Available online: http://www.image-net.org/challenges/LSVRC/2010/ (accessed on 1 May 2010).

11. Oquab, M.; Bottou, L.; Laptev, I.; Sivic, J. Learning and transferring mid-level image representations using convolutional neural networks. In Proceedings of the IEEE Conference on Computer Vision and Pattern Recognition, Columbus, OH, USA, 23–28 June 2014; pp. 1717–1724.

12. Hoskere, V.; Narazaki, Y.; Hoang, T.A.; Spencer, B.F., Jr. Towards automated post-earthquake inspections with deep learning-based condition-aware models. *arXiv* **2018**, arXiv:1809.09195.

13. Xu, Z.; Chen, Y.; Yang, F.; Chu, T.; Zhou, H. A Post-earthquake Multiple Scene Recognition Model Based on Classical SSD Method and Transfer Learning. *ISPRS Int. J. Geo-Inf.* **2020**, *9*, 238. [CrossRef]

14. Simonyan, K.; Zisserman, A. Very deep convolutional networks for large-scale image recognition. *arXiv* **2014**, arXiv:1409.1556.

15. Gao, Y.; Mosalam, K.M. Deep transfer learning for image-based structural damage recognition. *Comput. Aided Civil Infrastruct. Eng.* **2018**, *33*, 748–768. [CrossRef]

16. Olsen, M.J.; Kayen, R. Post-earthquake and tsunami 3D laser scanning forensic investigations. In *Forensic Engineering 2012: Gateway to a Safer Tomorrow*; Sixth Congress on Forensic Engineering: San Francisco, CA, USA, 2013; pp. 477–486.

17. Womble, J.A.; Wood, R.L.; Mohammadi, M.E. Multi-scale remote sensing of tornado effects. *Front. Built Environ.* **2018**, *4*, 66. [CrossRef]

18. Aixia, D.; Zongjin, M.; Shusong, H.; Xiaoqing, W. Building damage extraction from post-earthquake airborne LiDAR data. *Acta Geol. Sin. Engl. Ed.* **2016**, *90*, 1481–1489. [CrossRef]

19. Hackel, T.; Wegner, J.D.; Schindler, K. Fast Semantic Segmentation of 3d Point Clouds with Strongly Varying Density. *Int. Arch. Photogramm* **2016**, *3*, 177–184. [CrossRef]

20. Xing, X.-F.; Mostafavi, M.A.; Edwards, G.; Sabo, N. An improved automatic pointwise semantic segmentation of a 3D urban scene from mobile terrrstrial and airborne lidar point clouds: a mechine learning approach. *ISPRS Ann. Photogramm. Remote Sens. Spat. Inf. Sci.* **2019**, *4*.

21. Prokhorov, D. A convolutional learning system for object classification in 3-D lidar data. *IEEE Trans. Neural Netw.* **2010**, *21*, 858–863. [CrossRef]

22. Weng, J.; Luciw, M. Dually optimal neuronal layers: Lobe component analysis. *IEEE Trans. Auton. Ment. Dev.* **2009**, *1*, 68–85. [CrossRef]

23. Maturana, D.; Scherer, S. Voxnet: A 3d convolutional neural network for real-time object recognition. In Proceedings of the 2015 IEEE/RSJ International Conference on Intelligent Robots and Systems (IROS), Hamburg, Germany, 28 September–2 October 2015; pp. 922–928.

24. Hackel, T.; Savinov, N.; Ladicky, L.; Wegner, J.D.; Schindler, K.; Pollefeys, M. Semantic3d. net: A new large-scale point cloud classification benchmark. *arXiv* **2017**, arXiv:1704.03847.

25. Zhang, F.; Guan, C.; Fang, J.; Bai, S.; Yang, R.; Torr, P.; Prisacariu, V. Instance segmentation of lidar point clouds. *ICRA Cited* **2020**, *4*.

26. Blake, E.S.; Zelinsky, D.A. *National Hurricane Center Tropical Cyclone Report: Hurricane Harvey*; National Hurricane Center, National Oceanographic and Atmospheric Association: Washington, DC, USA, 2018.

27. Smith, A.; Lott, N.; Houston, T.; Shein, K.; Crouch, J.; Enloe, J. *US Billion-Dollar Weather and Climate Disasters 1980–2018*; National Oceanic and Atmospheric Administration: Washington, DC, USA, 2018.

28. Pasch, R.J.; Penny, A.B.; Berg, R. *National Hurricane Center Tropical Cyclone Report: Hurricane Maria*; Tropical Cyclone Report Al152017; National Oceanic And Atmospheric Administration and the National Weather Service: Washington, DC, USA, 2018; pp. 1–48.

29. ASCE (American Society of Civil Engineers). Minimum design loads and associated criteria for buildings and other structures. ASCE standard ASCE/SEI 7–16. Available online: https://ascelibrary.org/doi/book/10.1061/9780784414248 (accessed on 1 May 2019).

30. Beale, M.H.; Hagan, M.T.; Demuth, H.B. *Neural Network Toolbox™ User's Guide*; The MathWorks: Natick, MA, USA, 2010.

31. Srivastava, N.; Hinton, G.; Krizhevsky, A.; Sutskever, I.; Salakhutdinov, R. Dropout: a simple way to prevent neural networks from overfitting. *J. Mach. Learn. Res.* **2014**, *15*, 1929–1958.

32. Ghazi, M.M.; Yanikoglu, B.; Aptoula, E. Plant identification using deep neural networks via optimization of transfer learning parameters. *Neurocomputing* **2017**, *235*, 228–235. [CrossRef]

33. Long, J.; Shelhamer, E.; Darrell, T. Fully convolutional networks for semantic segmentation. In Proceedings of the IEEE Conference on Computer Vision and Pattern Recognition, Boston, MA, USA, 7–12 June 2015; pp. 3431–3440.

34. Ronneberger, O.; Fischer, P.; Brox, T. U-net: Convolutional networks for biomedical image segmentation. In Proceedings of the International Conference on Medical Image Computing and Computer-Assisted Intervention, Munich, Germany, 5–9 October 2015; pp. 234–241.

MDPI